NASA SP-365

Part I

NATIONAL GEODETIC SATELLITE PROGRAM

A REPORT COMPILED AND EDITED FOR NASA BY THE AMERICAN GEOPHYSICAL UNION

PARTICIPATING ORGANIZATIONS

Applied Physics Laboratory/The Johns Hopkins University
Department of Commerce/National Ocean Survey
Department of Defense
Air Force Cambridge Research Laboratories
Engineer Topographic Laboratories
Defense Mapping Agency/Aerospace Center
Defense Mapping Agency/Topographic Command
Naval Surface Weapons Center/Dahlgren Laboratory
National Aeronautics and Space Administration
Goddard Space Flight Center
Jet Propulsion Laboratory/California Institute of Technology
Wallops Flight Center
Ohio State University
Smithsonian Astrophysical Observatory
University of California, Los Angeles

Scientific and Technical Information Office 1977
NATIONAL AERONAUTICS AND SPACE ADMINISTRATION
Washington, D.C.

Foreword

The National Aeronautics and Space Administration was created in 1958 and had as one of its principal objectives to extend man's domain farther into and beyond the Earth's atmosphere. However, it quickly became apparent that an Earth-based applied science, geodesy, would be among the first to benefit from its activities, and soon a new discipline, satellite geodesy, was born. A major series of early results associated with an unexpected value for the polar flattening, asymmetries in the zonal gravity field (the "pear-shape" component), and, in the nonzonal, the ellipticity of the equator, were developed in gravimetric geodesy. Also in geometric geodesy, the first interconnection of major geodetic datums in a center-of-mass system was achieved. Thus one small step in satellite geodesy had been taken; the giant leap came in 1964. After prior recommendations to proceed had come from the National Academy of Sciences and the Congress, and after agreement had been reached on the division of responsibility with other agencies having geodetic activities and requirements, the NASA National Geodetic Satellite Program (NGSP) was launched.

Now, a decade later, this volume is dedicated to recording the major results obtained as a consequence of this program. Although no attempt has been made to report on all the research that has taken place directly in support of or as a result of the impetus of the NGSP, this work does record that the objectives of the program have been met. The gravity field has been determined to 5 parts in 10^8 for a field of degree and order 15, and numerous geodetic datums have been connected in a common center-of-mass world datum in such a way that the control stations have relative accuracies of ± 10 meters. The data from several electronic and optical geodetic satellite instrument systems have been compared and correlated so that errors in each system could be reduced and the geodetic parameters improved by combined analyses.

The activities of the NGSP have benefited other NASA programs. All programs that require precise trajectory calculations—Apollo, OGO, and ERTS, for example—have drawn on NGSP advances. In addition, an Earth and Ocean Dynamics Applications Program (EODAP) has emerged from the NGSP in which many of the same techniques and approaches are used to measure not the static but the dynamic characteristics of the Earth that affect man's daily life in so many ways.

—FRANCIS L. WILLIAMS

Preface

In assembling this final report on the National Geodetic Satellite Program (NGSP), the editor was guided by the recommendations of a committee that met in 1971 to help the National Aeronautics and Space Administration (NASA) plan the structure of the final report. The committee was made up both of participants in the program and representative future users of the program's results. The committee's recommendations reflected the desire of its members to see the results not only fairly presented but also widely used. The essence of the recommendations was that the complete results should be given together with as much other material as necessary to support them, and that all the material should be presented in a form useful to the largest number of scientists, engineers, and educators. Because the committee realized that the results reported by the participants were not going to be in agreement and because it realized that there were more advantages than disadvantages in this diversity, it recommended that the results not be combined and homogenized before publication but be presented separately.

The editor agreed completely with these recommendations. Since the results were to be kept separate, each of the major original participating organizations—Department of Defense (DOD), NASA/Goddard Space Flight Center (GSFC), National Geodetic Survey, Ohio State University (OSU), and Smithsonian Astrophysical Observatory (SAO)—wrote its own chapter as a complete entity. To make the presentations coherent, each chapter was organized in the same way. An introductory section described the organization's purpose in participating in the program and presented a brief history of the participation. A section then described the instruments used in getting the data, another section described the data itself, another gave the theory used in processing the data, and a final section gave and evaluated the results. Additional chapters were needed to complete the programs and history or to provide additional support to the results. These chapters, by the Applied Physics Laboratory (APL), Jet Propulsion Laboratory (JPL), NASA/Wallops Flight Center (WFC), and University of California, Los Angeles (UCLA), were organized in the same way as the other chapters, insofar as possible.

This scheme could not be adhered to in all cases; the chapters by JPL and UCLA are organized to best present their special topics. On the other hand, the result of applying the scheme to chapters 3 and 5, which actually describe several individual projects, has been to break the continuity of these subprojects. The editor decided that maintaining the continuity of each subproject, from instrumentation to results, was less important than keeping the results together for ease of reference. Accordingly, the reader of chapters 3 and 5 who is more interested in the development of a particular subproject than in the total picture will have to skip over intervening material.

NATIONAL GEODETIC SATELLITE PROGRAM

To assemble in 18 months a final report on the results of a program that extended over the entire globe for a period of 10 years was of course far more than a one-man effort, particularly since results were still being revised well into the final stage of assembly. Before beginning the task, the editor therefore asked the NGSP's participating organizations for advice and assistance. The response of these organizations was immediate and whole-hearted. With the help of these organizations, two boards were formed. One, the Editorial Board, was responsible for passing on the general format and content of the report to ensure that these had the approval of the participating organizations. The members of this board were Dr. R. Kershner of APL; Mr. O. W. Williams of DOD (Dr. A. Mancini, alternate); Dr. D. W. Trask of JPL; Dr. F. Vonbun of NASA/GSFC; Mr. J. McGoogan of NASA/WFC; Dr. H. Schmid of the National Geodetic Survey (NGS); Dr. I. I. Mueller of OSU; Dr. E. M. Gaposchkin (Dr. G. C. Weiffenbach, alternate) of SAO; Dr. A. F. Spilhaus, Jr., of the American Geophysical Union (AGU); and Mr. J. Milwitzky (Mr. J. Murphy, alternate) of NASA Headquarters. A Technical Advisory Board was formed to pass on specific format and content and to advise on technical problems. In keeping with the highly technical nature of this board's work, its members represented disciplines or projects rather than organizations. Its members were Dr. R. Kershner (Mr. H. Black and Dr. S. M. Yionoulis, alternates) of APL; Dr. A. Mancini, Dr. R. Anderle, and Mr. G. Hadgigeorge of DOD; Dr. D. W. Trask of JPL; Dr. D. Smith and Mr. J. H. Berbert of NASA/GSFC; Mr. H. R. Stanley of NASA/WFC; Dr. H. Schmid of NGS; Dr. I. I. Mueller of OSU; and Dr. E. M. Gaposchkin of SAO. Without the help given freely by the two boards, the report would not have been possible, and the editor gives sincere acknowledgment of help of the boards and particularly of the individual members.

Although the work of copy editors is usually accepted by contributors without acknowledgment (but frequently with resentment), Mrs. Holoviak of the AGU staff has contributed to the volume beyond what duty called for, and the editor feels deeply indebted to her.

—S. W. HENRIKSEN

Contents

CHAPTER		PAGE
	FOREWORD	iii
	PREFACE	v
1	Introduction S. W. HENRIKSEN	1
2	Applied Physics Laboratory C. A. DUNNELL, P. FERRITER, G. GEBEL, H. S. HOPFIELD, M. M. SCHAEFER, S. M. YIONOULIS	87
3	Department of Defense R. ANDERLE, D. C. BROWN, E. CYRAN, D. H. ECKHARDT, G. DUDLEY, W. D. GOOGE, G. HADGIGEORGE, D. HUBER, R. L. ILIFF, N. MASON, R. H. NICHOLS, R. H. RAPP, F. W. ROHDE, C. R. SCHWARTZ, R. W. SMITH, J. TROTTER, M. A. WARDEN, H. L. WHITE, O. W. WILLIAMS	139
4	Jet Propulsion Laboratory P. B. ESPOSITO, N. A. MOTTINGER, T. D. MOYER, D. W. TRASK	247
5	National Aeronautics and Space Administration/Goddard Space Flight Center J. H. BERBERT, J. BROWND, T. FELSENTREGER, D. HARRIS, T. S. JOHNSON, M. A. KHAN, F. LERCH, J. MARSH, J. MURPHY, B. PUTNEY, J. REECE, J. RICHARDSON, M. SANDSON, P. SCHMIDT, D. SMITH, S. VINCENT, C. WAGNER	293
6	National Aeronautics and Space Administration/Wallops Flight Center J. BELGIN, A. BORREGO, R. L. BROOKS, D. J. DEMPSEY, N. M. FUBARA, K. GUARD, M. HILLHOUSE, C. D. LEITAO, C. F. MARTIN, G. MOURAD, N. A. ROY, H. R. STANLEY	485
7	National Geodetic Survey H. SCHMID	525
8	Ohio State University I. I. MUELLER	645

CHAPTER		PAGE
9	Smithsonian Astrophysical Observatory D. A. ARNOLD, E. M. GAPOSCHKIN, Y. KOZAI, J. LATIMER, C. G. LEHR, C. A. LUNDQUIST, G. MENDES, M. R. PEARLMAN, J. M. THORP, C. R. H. TSIANG, G. VEIS, F. L. WHIPPLE, M. R. WILLIAMSON, J. WOHN	793
10	University of California, Los Angeles W. M. KAULA	941
11	Evaluation S. W. HENRIKSEN	949
	NOTATION	985
	REFERENCES	989
	INDEX	1019

1

INTRODUCTION

S. W. Henriksen

1.1 INTRODUCTION

Every major science or discipline has its development marked by epochs during which the creation of new ideas and the influx of new data increase beyond the ability of the science to absorb them. The science loses for a time its sense of direction and purpose, and results, while spectacular, are often inconsistent and appear unrelated to each other and to the science as a whole. In 1964, geodesy found that it had entered such an epoch several years earlier and began to worry about the consequences. It had achieved its breakthrough seven years earlier by launching an artificial satellite for use as a geodetic tool and had been "going ahead in all directions" ever since. The period between 1957 and 1965 saw the growth of geodetic satellite networks, the start of work on geodetic satellites, and a vast increase in the amount of satellite-tracking data that could be used for determining the shape and figure of the Earth. Although the growth of this body of knowledge was exciting, there was little evidence of its having direction.

While each scientist reveled in the abundance of data and rejoiced in his ability to mold them into new results, the ultimate users of geodetic information had no reliable means of choosing among the results or judging their suitability for any one application. And of course there was absolutely no way of estimating the value of the results as a function of the cost of the satellites, because there was no comprehensive geodetic satellite program whose results could be evaluated in terms of cost. Since the National Aeronautics and Space Administration (NASA) was in one way or another carrying by far the greatest part of the costs of satellite geodesy and was also a major user of the results, it was natural that the push toward a coordinated and comprehensive national program in satellite geodesy should come from NASA.

The National Geodetic Satellite Program (NGSP) was started in 1965 by NASA primarily in response to pressures from within NASA for improvements in the geodetic and geophysical constants used by NASA in its computation of orbits. There were also pressures from outside NASA for a program that would correlate the diverse efforts of several groups engaged in satellite geodesy: Ohio State University, Smithsonian Astrophysical Observatory, European Satellite Triangulation Network, and others. Furthermore, when the program was started, there was very little systematic work being done on calibration and intercomparison of the different kinds of satellite-tracking systems. The need for reliable information on the calibration constants of the tracking systems and on how the systems compared in accuracy and precision with each other was considered great enough to warrant a special place in the proposed program.

NASA's own requirements were many (ch. 5 and ch. 6). *First,* it needed more accurate geodetic coordinates for its PRIME MINITRACK and radar tracking systems, and these coordinates had to be in a reference system common to all the systems. Figure 1.1 shows the distribution of NASA's tracking stations in 1964, as well as the locations of other tracking stations whose data were used by NASA. The locations of these stations with respect to one another were known partly by connections through classical triangulation networks and partly by connections through the orbits of artificial satellites as computed from the tracking data of these stations. The errors in these locations were greater than could be allowed in future NASA programs. They would have to be reduced. The NGSP was therefore planned to provide more accurate coordinates for tracking systems. In figure 1.2 the 86 stations (not all of which existed in 1965) that were to be located are shown as dots on a background indicating the networks (and their datums) in which they lay.

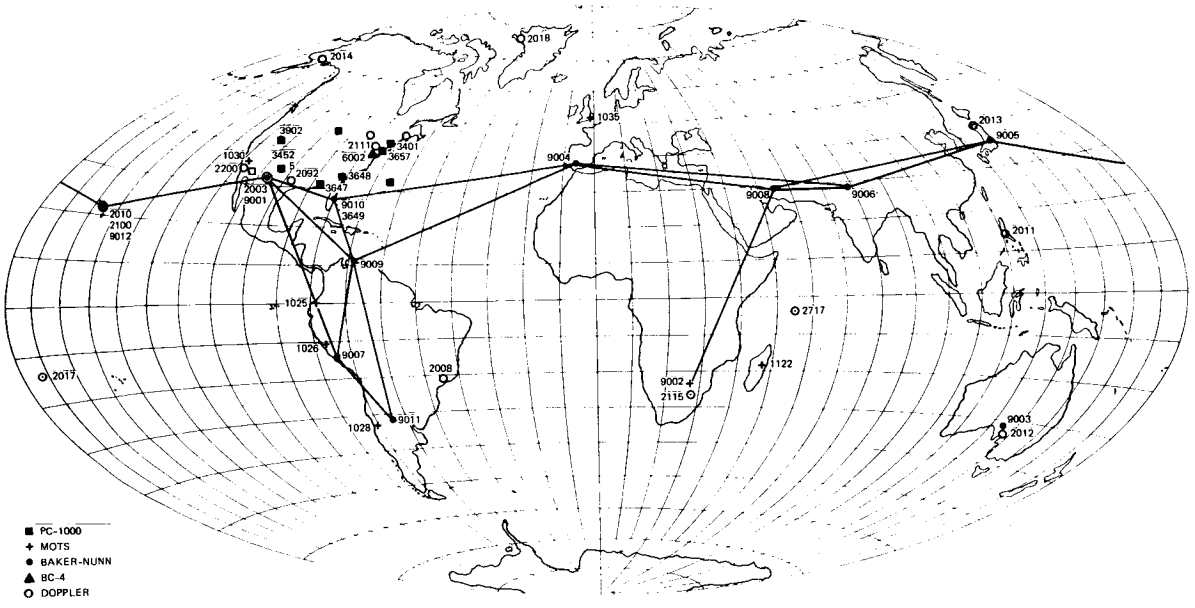

FIGURE 1.1.—Locations of tracking stations at start of NGSP. Solid lines show correction already made between SAO's Baker-Nunn stations.

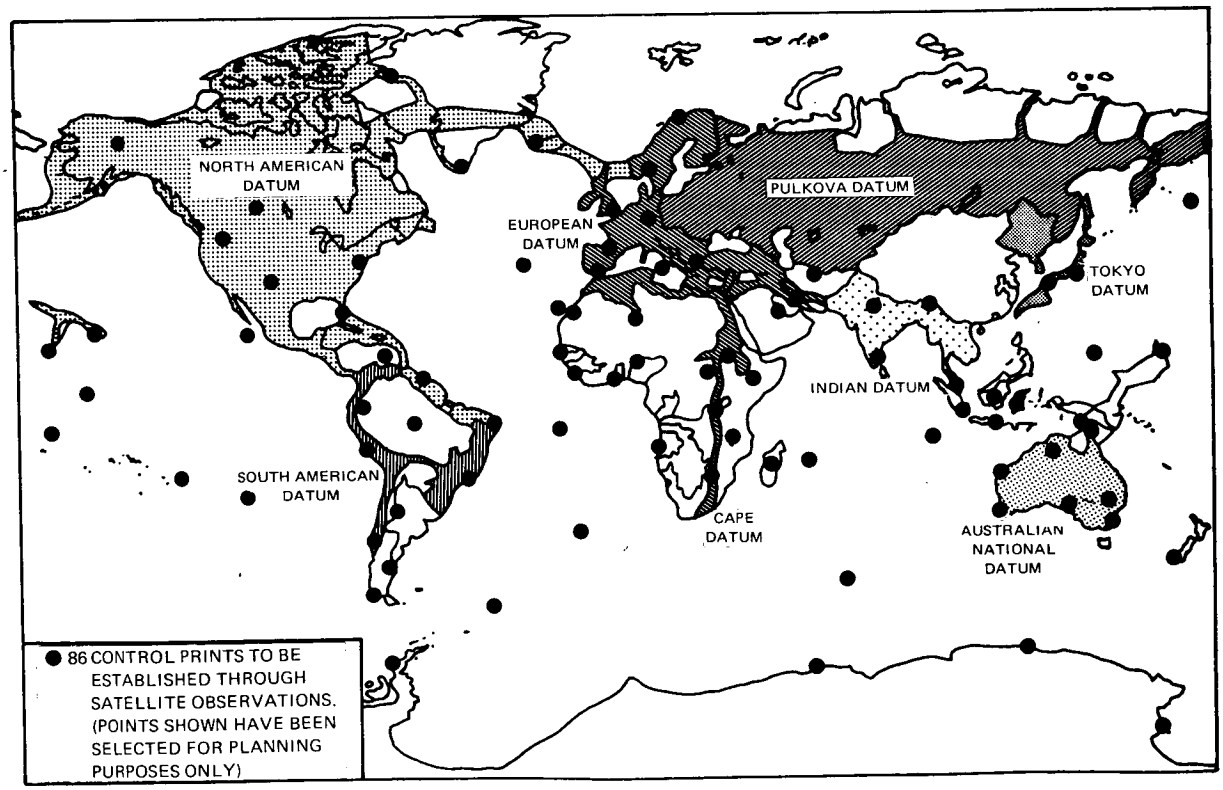

FIGURE 1.2.—National Geodetic Satellite Program objective 1: unified world reference system.

Second, some of these programs required prediction of accurate orbits. This meant not only more accurate locations for the tracking stations but also more accurate descriptions of the Earth's gravity field (fig. 1.3).

These requirements of NASA paralleled requirements of other groups both in the United States and abroad. The U.S. Coast and Geodetic Survey was starting its World Geometric Net (ch. 7, fig. 7.4) but needed help in carrying out its field operations and data reduction. The Smithsonian Astrophysical Observatory had the same requirements for its observing network of cameras that NASA had. The U.S. Navy wanted to improve the navigational accuracies of its navigation satellite system (NNSS), and the Army Map Service (AMS) wanted satellites suitable for use in constructing its geometric equatorial network (ch. 3).

Besides the purely geodetic and geophysical requirements, there was also a strong requirement for evaluating the performance of various satellite-tracking instruments then in use and for calibrating these instruments. Although there were eight major kinds of tracking equipment in use or under development (short-focal-length photogrammetric cameras, long-focal-length reconnaissance cameras, Schmidt-type cameras, 5-cm radar, 10-cm radar, laser distance-measuring equipment (DME), CW radar, and frequency-measuring equipment), the accuracies of these instruments, and sometimes even their precision, were not known, or at least not well enough known to permit useful comparison of the performance of one instrument with respect to that of another.

Therefore, in 1965 NASA started the NGSP by setting up an extensive program of observation and data reduction (e.g., Bowker, 1967). The major participants in this program were NASA's Goddard Space Flight Center (NASA/GSFC), the Smithsonian Astrophysical Observatory (SAO), Ohio State University (OSU), the Department of Defense (DOD), and the National Geodetic Survey (NGS), a part of the former U.S. Coast and Geodetic Survey. The many activities involved were centralized by designating certain persons in the participating organizations as principal investigators.

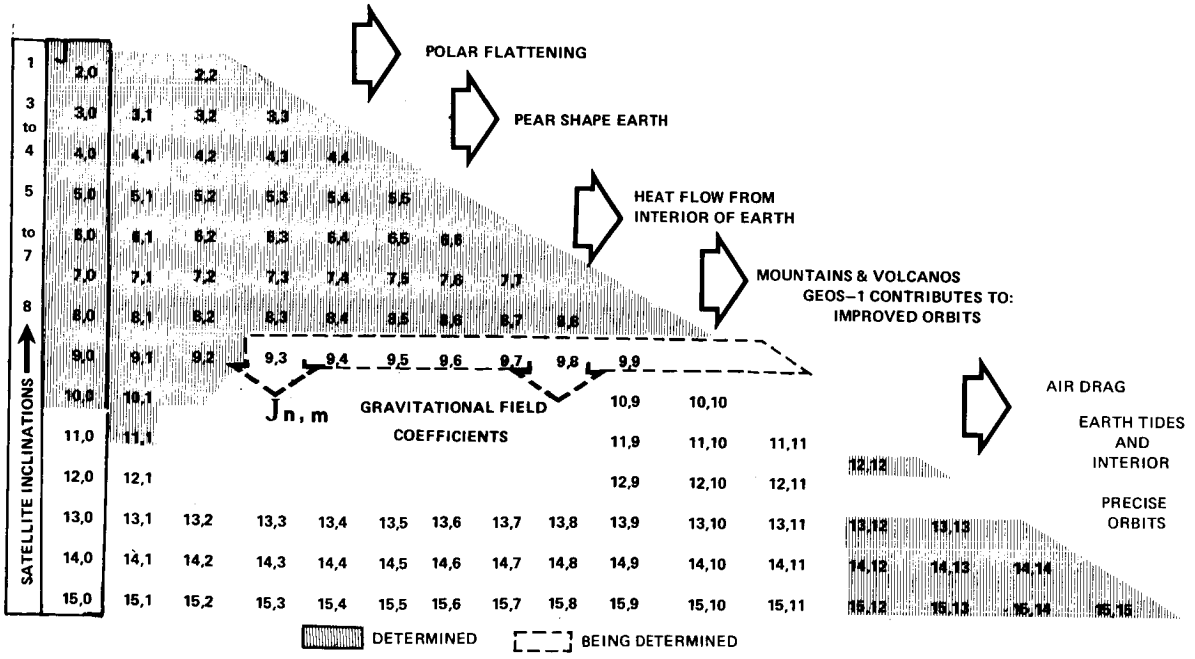

FIGURE 1.3.—National Geodetic Satellite Program objective 2: determination of gravitational field.

These investigators would monitor the contributions of their organizations and would be responsible for processing and distributing these contributions. Overall direction lay with J. Rosenberg of NASA Headquarters, and the principal investigators were J. Berbert and W. Kaula of NASA/GSFC, C. Lundquist of SAO, I. Mueller of OSU, J. McCall, M. Rosenbaum, and R. Anderle of DOD, and L. W. Swanson of NGS. During the lifetime of the NGSP some of these investigators left the program and were replaced by others. Other organizations such as Applied Physics Laboratory (APL), Jet Propulsion Laboratory (JPL), and Wallops Flight Center of NASA (NASA/WFC), while not directly incorporated into the NGSP, made contributions that had important effects on the results of the program. Because the NGSP had strong and capable administrative control throughout its history and because the organizations involved in the program cooperated so well, changes in principal investigators and overall direction did not affect the progress of the program, and the contributions of organizations outside the program considerably furthered it.

The following pages of this chapter provide a historical background for the NGSP and a historical summary of the program itself and then the technical structure. Without this historical overview the results of the program could not be seen in their proper places in the geodetic picture as a whole. The technical structure of the program—its instrumentation, data, and theory—is described in enough detail that the reader can relate the work of the individual contributors (given in chs. 2 through 10) to each other and to the NGSP. The results of the program are summarized and evaluated in the final chapter (ch. 11).

1.1.1 Historical Survey of Geodesy

To understand the NGSP, we must first have at least a feeling for the long development that went into bringing geodesy and geophysics to the state in which it was at the start of the NGSP (1964). The development took place (from our point of view) in two stages—the presatellite stage, from prehistory up to 1957, when Sputnik–1 was launched, and the post-Sputnik stage from 1958, when a value of the flattening of the earth (1/298.3) was first derived from artificial satellite data alone, to 1964, when work began on setting up the NGSP.

1.1.1.1 Era Preceding Artificial Satellites

Before the advent of artificial satellites, geodesy was essentially four different disciplines which only rarely (as in the hands of the 19th century geodesist, Helmert) were coordinated and synthesized. The work in horizontal control, vertical control, astrogeodesy, and physical geodesy usually went on independently, and the development of geodesy reflected this separation.

For a closer look at the geodetic background we select a particular epoch at which to summarize the state of the sciences. The obvious epoch in this case is the beginning of 1957, just before the launching of Sputnik–1.

Datums.—A datum is a set of numbers defining a coordinate system. Until the early part of the 20th century, each country, from choice or necessity, used its own coordinate system. As a consequence, whenever such problems as the calculation of the points in two countries or the determination of the location of a point in one country with respect to the reference system of another country were undertaken, difficulties arose because there was no accurately known relationship between the datums used by the countries involved. This situation troubled the engineers occasionally and the scientists frequently, but only when it had political or economic effects was there any strong agitation to do something about it. Until artificial satellites became a possibility in the early 1950's, datums were related to one another by the following methods.

(1) When only political barriers were to be overcome, connection of coordinate systems to each other was accomplished by conventional triangulation and, sometimes, by

leveling. The principal examples of this approach were the completion of the arc of the 30th meridian, connecting European to Cape datums, and completion of the triangulation between European and Indian datums (Adams, 1960).

(2) When short stretches of water intervened, the datums were connected by flare triangulation, as in the connection of Danish and Norwegian datums across the Kattegat (Simonsen, 1949).

(3) Longer distances over water were bridged by use of HIRAN, as in the connection of the Hawaiian Islands to each other (Thomas, 1962), the connection of Crete to North Africa (Owen, 1960), and the connection of North American Datum 1927 to European Datum 1950 via Greenland and Iceland (Hopke, 1959; Owen, 1960).

(4) Very long distances over water could not be bridged with high accuracy. Methods used for the purpose all (except for the gravimetric method, of course) depended on using the moon as an intermediary (Lambert, 1969). The costs of getting up expeditions for surveying in this way were very high, and because of persistently bad weather the chances of a successful survey were low. Lunar surveying expeditions were therefore infrequent. Various organizations used solar eclipses or occulations by the moon to get data that would permit connecting North American Datum 1927 to European Datum 1950 and to Tokyo Datum. Few results were published until long after the observations had been made, partly because there were military restrictions and partly because of the difficulty of measurement and the length of time needed for precise reduction. (See Kukkamaki, 1954; Schauer, 1952.)

As was mentioned before, the long-distance connections were highly inaccurate. Also, like the HIRAN-based connections, their values were never published in the open literature. For all practical purposes the situation in 1957 was therefore still one in which datums were continental in scope. Table 1.1 in the appendix lists those datums that provide the framework for points in regions covering more than 200,000 km^2.

Besides these "major" datums, there were a very large number (well over 100) of minor or provisional datums, each dominating a very small isolated region, such as an oceanic island. Furthermore, there were (and still are) many datums that in theory had been superseded by newer datums but that were the only referents for existing geodetic markers. (See, for example, Mueller, 1966, and ch. 8, table 8.4 for an extensive list of datums.)

Closely connected with the datums (and the reason for their existence) are the sets of geodetic control points that form the geometric framework of countries. These sets are called geodetic networks. Figure 1.4 shows the extent of the networks associated with the datums of table 1.1.

Station Coordinates.—Although 1957 was the year that the first artificial satellite was launched, the setting up of permanent stations for satellite tracking had been started several years earlier. The United States' Vanguard satellites were to be launched in 1958, and the U.S. government had provided funds for two independent networks of satellite-tracking stations. (See Greene and Lomask, 1970.) These stations were the SAO optical (camera) tracking stations—not in operation until mid-1958—and the electronic tracking stations (PRIME MINITRACK) of the Naval Research Laboratories (NRL)—seven such stations were in operation at the end of 1957. The stations, except in a few cases, were connected to the geodetic control of the country in which they were located.

The tracking stations planned for 1958 are listed in table 1.2 of the appendix (Wilson, 1959; Hyneck, 1959). The only ones of these functioning at the beginning of 1958 are the six marked by asterisks.

Note that neither NRL (Project Vanguard) nor SAO located its tracking stations with geodetic research in mind. Both were first concerned with ensuring that satellites launched under the Vanguard project would be detected and tracked at least once every revolution. PRIME MINITRACK could track at any time of the day or night and in

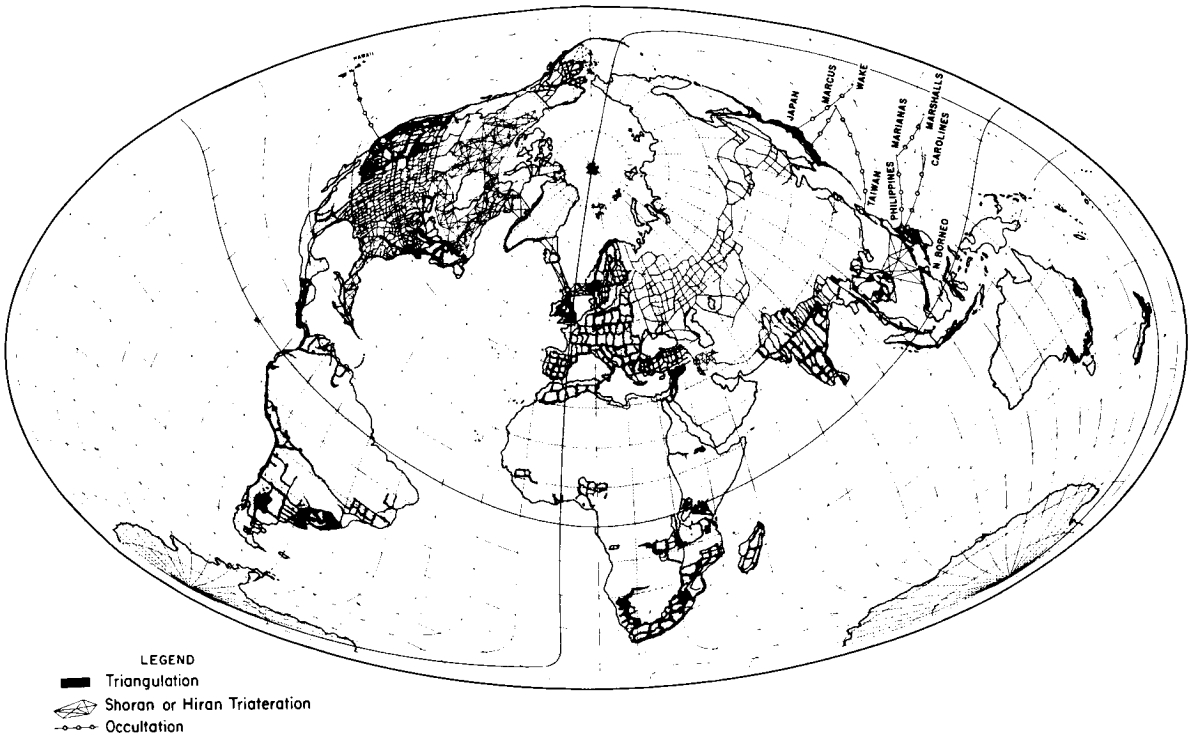

FIGURE 1.4.—Horizontal geodetic networks controlled by major datums (1957).

most kinds of weather. NRL was therefore able to set up its tracking stations so close together along the 75th meridian that it created an electronic fence which any satellite would have to cross every revolution (Mengel, 1956). SAO, on the other hand, had two important limitations on where it could place its stations. First, the stations had to be located in regions with a large percentage of clear weather. (Many stations were therefore located near astronomical observatories.) Second, since SAO had to plan on photographing satellites by sunlight reflected from the satellites, the satellites would be detectable only during twilight hours at any particular station. SAO stations therefore had to be spaced longitudinally about the globe in order to ensure that a reasonable number of observations could be obtained from the network (Hynek, 1959).

A large number of radar stations were in operation in 1957. These, for the most part, were operated by the U.S. Air Force and were used for tracking missiles launched from bases in Florida and California. Only a very few had the ability to track at ranges over a few hundred kilometers (it was the FPS–16 radar at Cape Canaveral that tracked the Vanguard–1 and Explorer–1).

The Geoid.—In 1957 there was no such thing as *the* geoid, even in theory. There were a *number* of geoids devised in different parts of the world by different methods and according to different definitions. The two principal types of geoids were the astrogeodetic geoid (derived by comparing astronomic place coordinates with geodetic ones) and the gravimetric geoid (derived by means of Stokes' formula—or some modification of it—with gravity measurements). There were also mixtures of the two types of geoids. The principal gravimetric geoid of global extent was the Columbus geoid of 1957 (Heiskanen, 1957), derived by the Mapping and Charting Research Laboratory of Ohio State University (fig. 1.5). (Gravity values were scarce in the southern hemi-

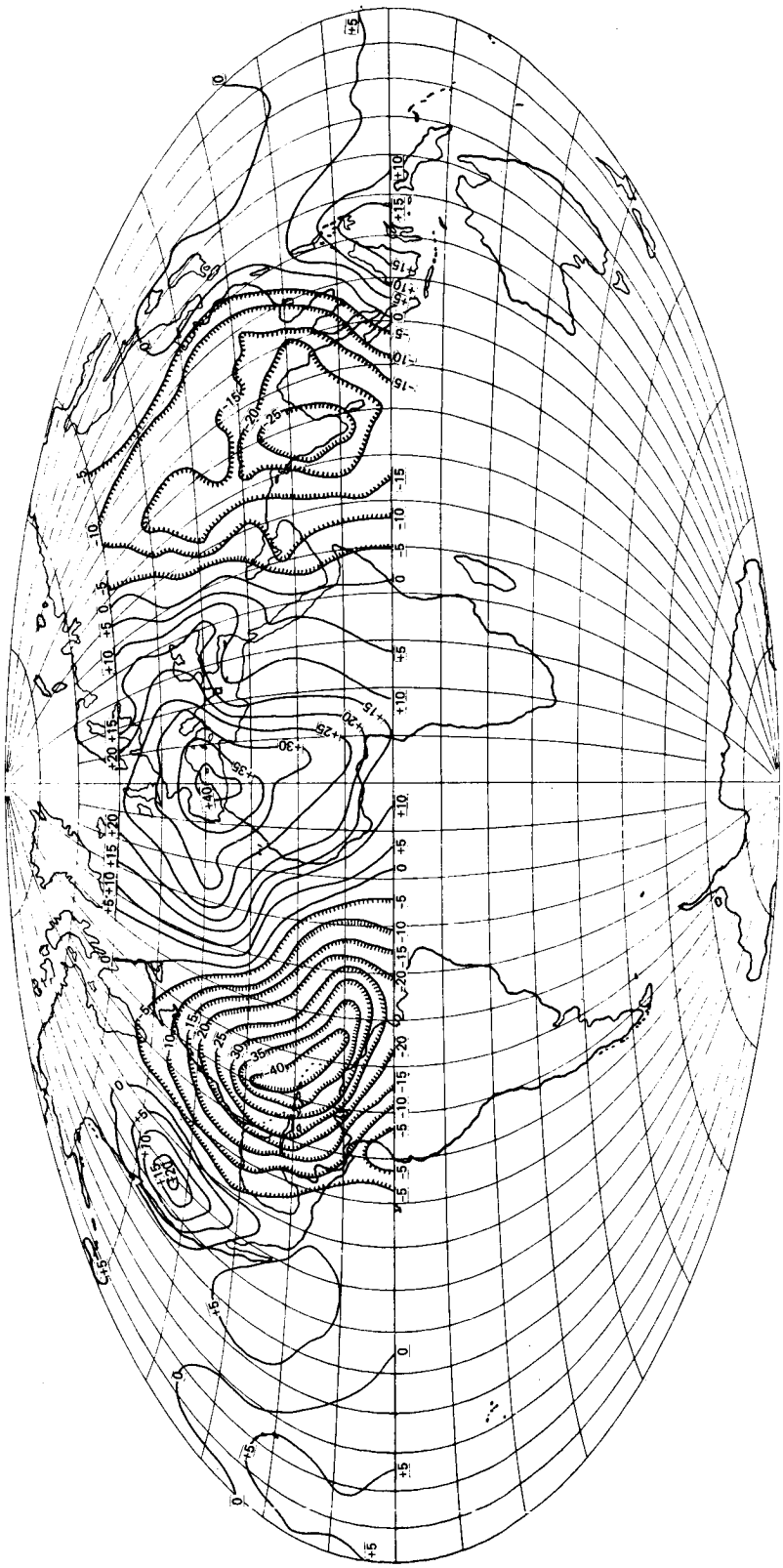

FIGURE 1.5.—The Columbus geoid (Heiskanen, 1957) based on spheroid $a=6378388$, $f=1/297.0$.

sphere; therefore the geoid was not computed for that region.) There were no corresponding astrogeodetic geoids, of course. However, bits and pieces of astrogeodetic geoids, such as the one for Europe (Lieberman, 1955; Bomford, 1956), the one for India (Survey of India, 1957), and the one for Eurasia and northern Africa (Tanni, 1948) did exist. Fischer (1959) assembled a number of these geoids, using the Columbus geoid to connect the regional geoids. The result is shown in figure 1.6. (Original values were with respect to the Hough ellipsoid, $a=6{,}378{,}224$ and $1/f=297$.)

Gravity and Gravitation.—Although a knowledge of gravity is important to most science and engineering disciplines, it is extremely important in three applications: geophysical exploration, prediction of trajectories and orbits, and calculation of the geoid. The prospector needs to know the value of gravity accurately over small regions but at points close together; the trajectory specialist needs to know them over large areas but can make do with approximate, representative values. The geodesist, for calculating the geoid, needs average values of gravity over small (1′ x 1′) or large (10° x 10°) regions, depending on the resolution wanted. Because the surface gravity values were far from being uniformly distributed over the globe and were at all levels of error, from less than 1 $\mu m/s^2$ to more than 100 $\mu m/s^2$, there was little point in using the values themselves. Instead, average values over 5° x 5° quadrangles were quite good enough, considering immediate purpose and material available. Table 1.3 in the appendix shows the values of the coefficients C^m_n, S^m_n of the gravitational potential as it was known in 1957. (Note that in 1957 the existence of nonzero values for odd values of n and of nonzero values of m was considered impossible. A body in hydrostatic equilibrium, such as the Earth was thought to be, must be symmetric about the axis of rotation and with respect to a plane perpendicular to that axis. Nonzero values for the coefficients with $n=2k+1$ or $m=0$, k being an integer, imply lack of symmetry.)

1.1.1.2 The Era of Artificial Satellites (1958 to 1964)

The groundwork for the era of satellite geodesy was laid well before 1957 in the work of V. Väisälä, W. De Sitter, D. Brouwer, W. Lambert, J. O'Keefe, and other geodesists. Results of geodetic importance did not start to come in until after the launching of Sputnik–1. The first definite new result was the derivation of the value 1/298.3 for the Earth's flattening by O'Keefe *et al.* (1958), Buchar (1958), and King-Hele and Merson (1958), using observations of Explorer–1 and Sputnik–2. From that time on, derivation of further constants defining the earth's gravity field and of geometric data on the Earth's shape followed swiftly. Some of the major events are listed in table 1.4 of the appendix.

Not all important events of this era were connected with satellites, however. The classical methods were still superior to satellite methods when they could be applied properly, and important geodetic measurements were made by classical methods in Africa, Australia, and the United States.

By 1964 many of the problems that had been bothering geodesists in 1957, and to whose solution they had been devoting years of study, had been solved with an accuracy unhoped for in earlier years. A practically definitive value had been obtained for the Earth's flattening, the major datums (North American 1927, European 1950, Tokyo, South African, and others) had been connected with an error of less than ± 50 meters (compared to ± 100 to 200 meters of earlier years), the geoid was now known, at least in its larger aspects, over the oceans and in unexplored or unknown continental interiors, and the gross features (low-frequency components) of the gravitational potential were known.

Datums.—By 1964 there were only two methods being used for connecting widely separated datums: that using HIRAN (radar) systems and that using satellites. Flare triangulations, so successfully used in Scandinavia (Simonsen, 1949) and by the

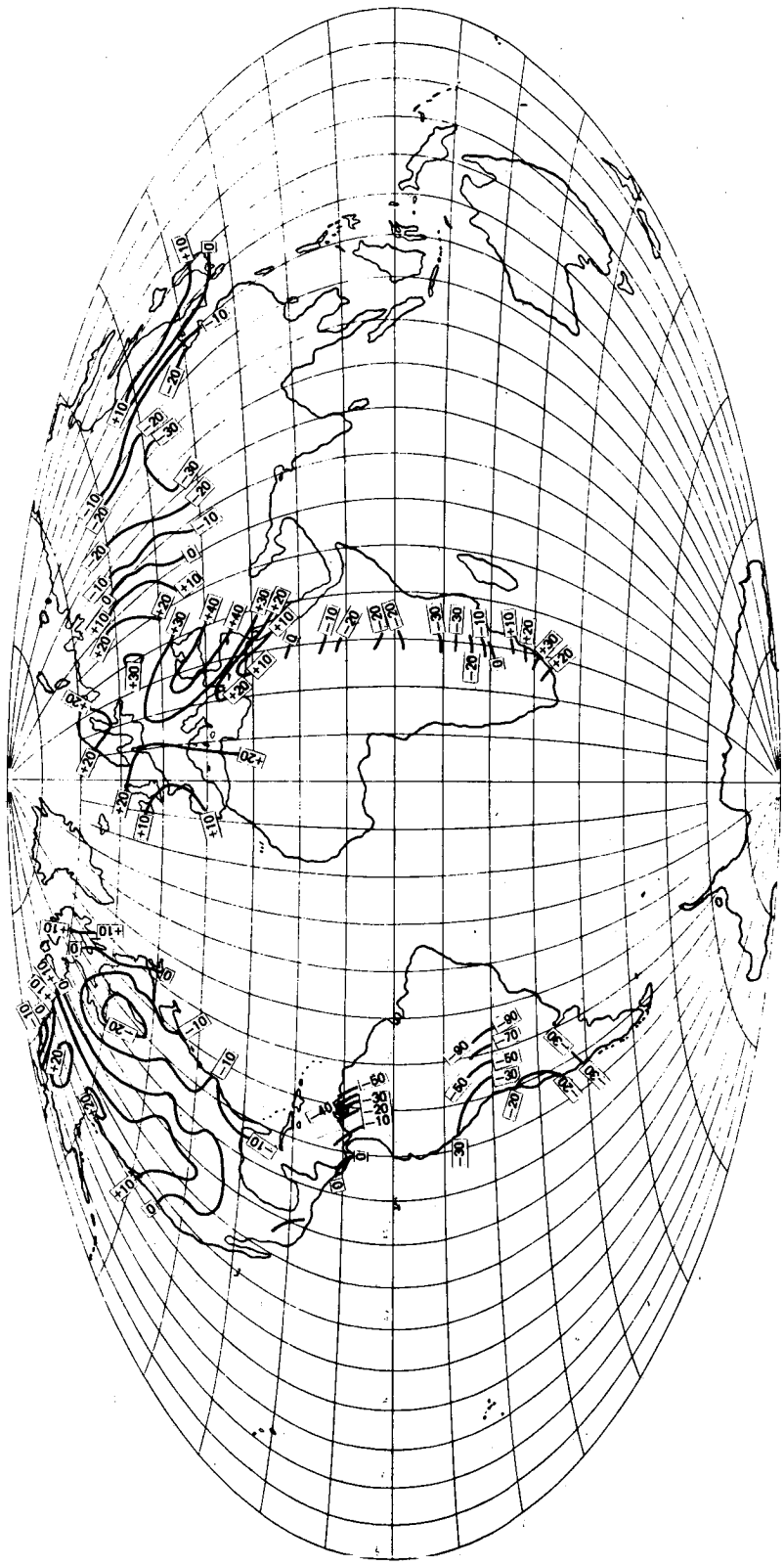

FIGURE 1.6.—Global astrogeodetic geoid (Fischer, 1959; contours in meters) based on spheroid with $a=6378199$, $f=1/298.3$.

United States, were being used for primary triangulation in Finland, but not elsewhere. (See Ewing *et al.*, 1959, for a novel method of trilateration over great distances, which used oceanic layers of low sonic attenuation, the SOFAR channel, as a medium.) Ties between datums using HIRAN were still being made, but published results were scarce.

Fortunately, satellite geodesy was beginning to provide ties almost as accurate as those provided by using HIRAN. The points shown in figure 1.7 represent locations that had been determined to within ±50 meters. (Within a few years this value would shrink to +10 to +15 meters.) Table 1.5 in the appendix (Kaula, 1963b) gives the "shifts" Kaula found in six datums. These shifts are approximately the coordinates of the spherical center of each datum in an earth-center-of-mass system with axes parallel to the Earth's axis of rotation and the Greenwich meridian.

Locations of Stations.—In 1957 only three organizations, Smithsonian Astrophysical Observatory (SAO), Naval Research Laboratory (NRL), and Army Map Service (AMS), were engaged in large programs involving satellite geodesy. The SAO was using Baker-Nunn cameras, NRL was using PRIME MINITRACK, and AMS was using MINITRACK–MII. By 1964 the number of organizations involved had grown, as had the number of tracking stations and the variety of instruments. The NRL Vanguard project had been absorbed in NASA, and PRIME MINITRACK was supplemented by 40-in. (100 cm) cameras (ch. 5). The Coast and Geodetic Survey was getting its geometric world network underway, using Wild BC–4 cameras (ch. 7), and the TRANSIT project (ch. 2) of the Applied Physics Laboratory (APL) was using 11 or more receiving stations. Figure 1.8 shows the most important (with respect to volume of output data) tracking stations existing in 1964, at the start of the NGSP.

By 1964 global geoids based on surface gravity data or astrogeodetic data alone were almost entirely replaced by geoids based on satellite-tracking data. The role of the satellite in this situation is that of a free-fall type of gravimeter that is being transported around the Earth 12 to 16 times daily. Be-

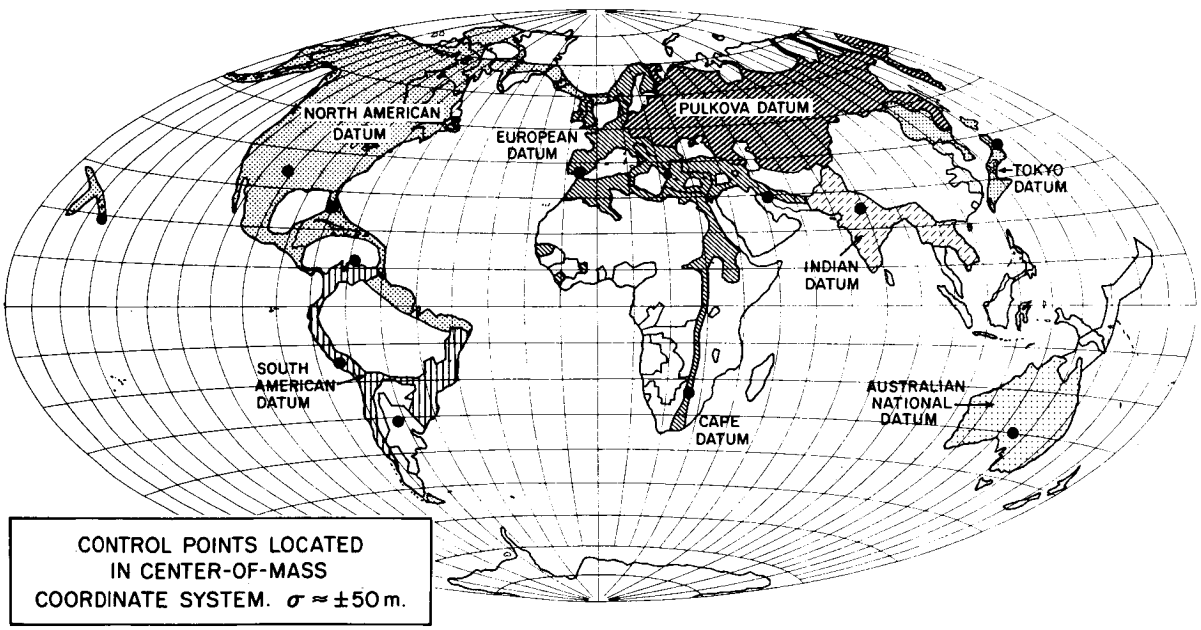

FIGURE 1.7.—Locations determined to ±50 m.

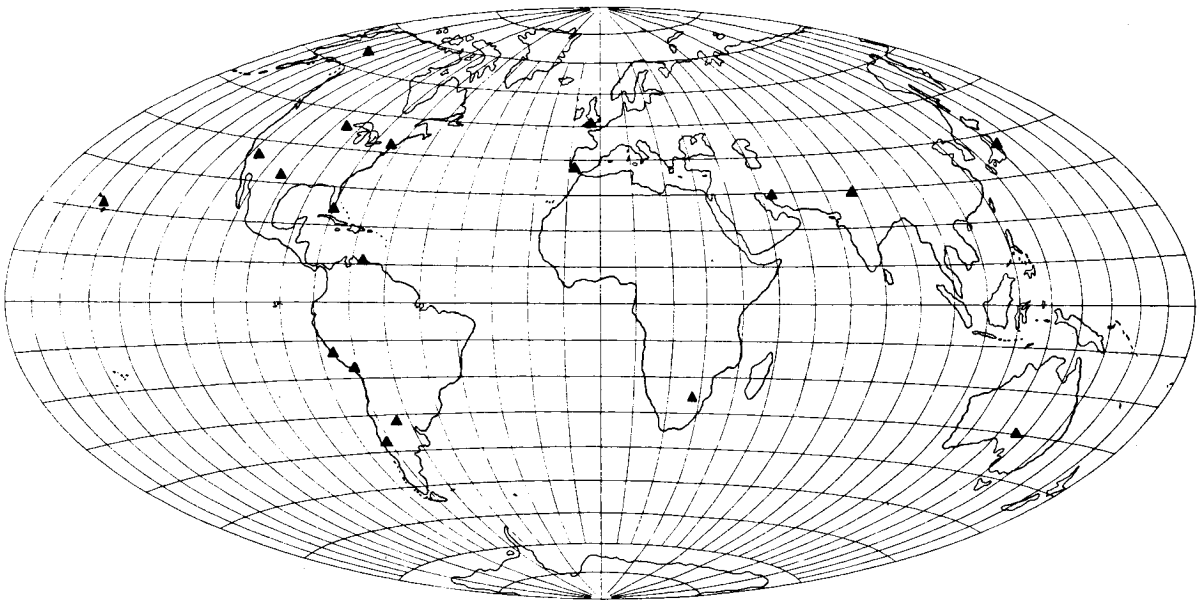

FIGURE 1.8.—Most important tracking stations (with respect to volume of output data), 1964.

cause of its distance from the surface, such a gravimeter is not sensitive to small variations of gravity (say, 10–30 $\mu m/s^2$) nor is it able to distinguish between large variations close together. Furthermore, unless the satellite is in an orbit of very high inclination, it is not able to measure gravity from pole to pole but only over a restricted zone. Within these limitations, however, the satellite, used as gravimeter, did provide many data leading to geoids somewhat distorted through poor distribution of data. Figure 1.9 shows a geoid determined by Uotila (1962) from an analysis of gravity in Legendre harmonics. Figure 1.10 shows a geoid (Izsak, 1964) based on data obtained by photographic observation of satellites. A comparison of these figures with figures 1.5 and 1.6 shows the difference between the situation in 1964 and that in 1957.

Gravity and Gravitation.—By 1964 a large amount of data on surface gravity had been added to what was available in 1957. But the increase was not large in proportion to the total volume of gravity data or in proportion to the amount still to be gotten. Large areas of the world (particularly in oceanic or inaccessible land regions) had no measurements at all within them or had a measurement density of only one value per 500 km^2. This situation was particularly true of the southern hemisphere.

The situation was far different for average values of gravitation as derived from satellite observations. In 1964 there were values of the coefficients C^m_n, S^m_n for all n,m through $n=7$, $m=6$, for values of $n=9$ through 13 with $m=0$, and for various special higher values of n,m such as (13,13), (15,13), (15,14), etc. Table 1.6 in the appendix shows the status as of 1964.

The quantity GM, the gravitational attraction of the earth, appears in the formula for the gravitational potential V as

$$V=\frac{GM}{a_e}L(\lambda,\psi,r)$$

where L is a function (usually a finite Legendre series) in λ, ψ, and r. The best value for GM was obtained by the Jet Propulsion Laboratory from data on the tracking of lunar "probes" and was $[3.986\ 00(9\pm6)]\times 10^{14}$ m^3/sec^2 (Sjogren *et al.*, 1964).

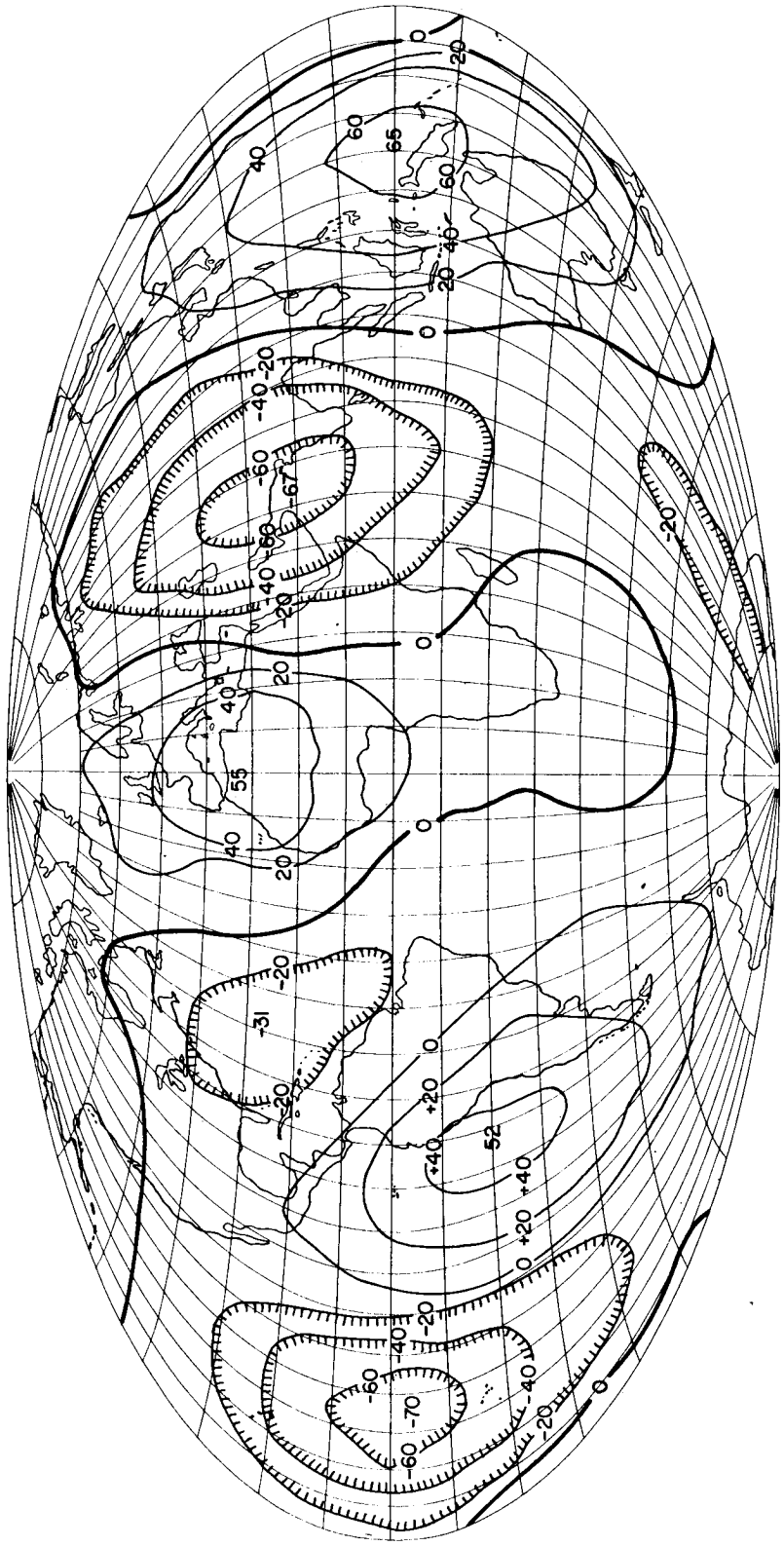

FIGURE 1.9.—Geoid based on surface gravity data (Uotila, 1962).

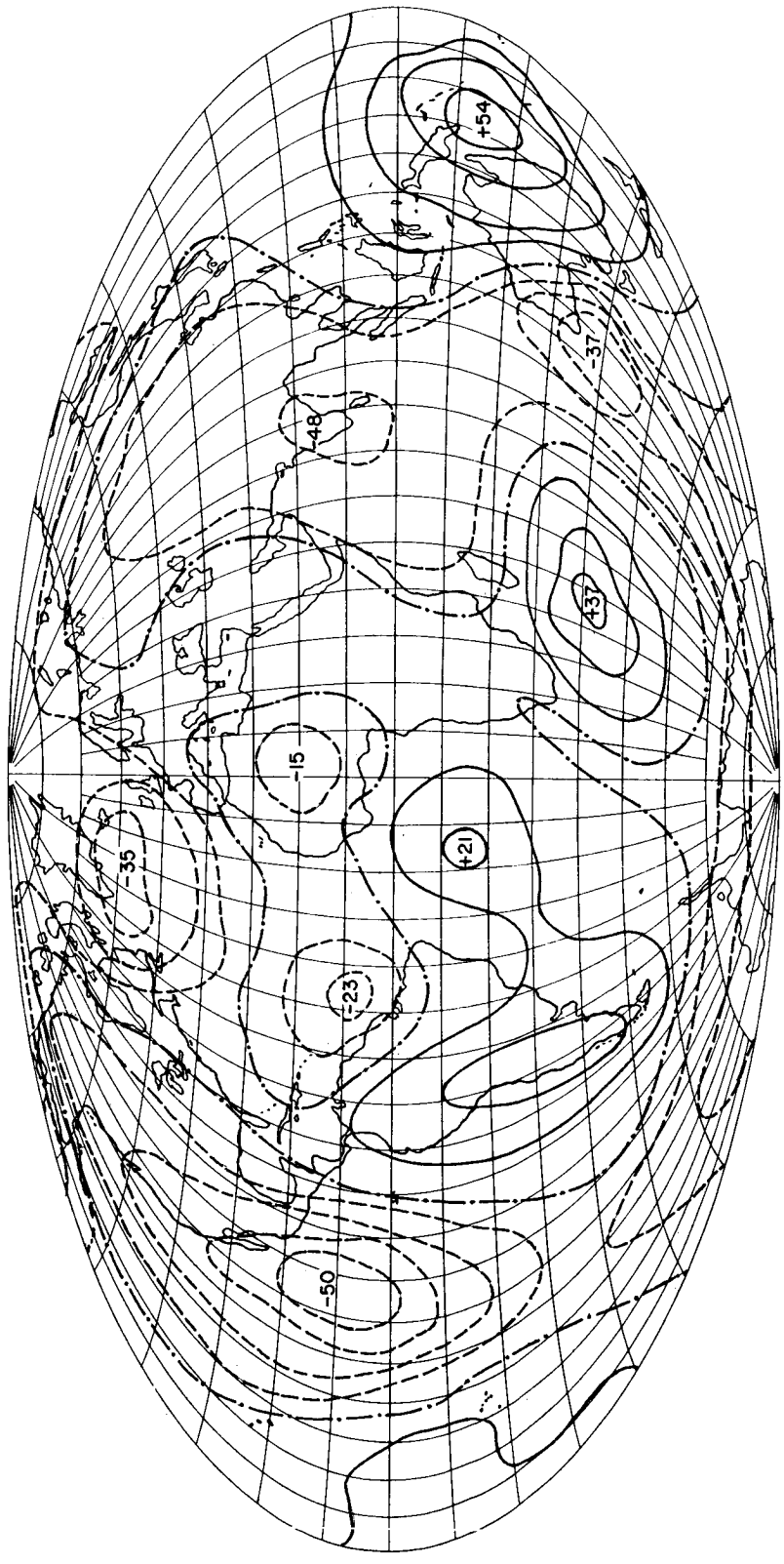

FIGURE 1.10.—Geoid based on data from cameras (Izak, 1964).

1.1.2 Organization of the NGSP

As was mentioned earlier, the overall responsibility for the program lay with J. Rosenberg of NASA Headquarters. There were eight individual but coordinated projects under Rosenberg's guidance. Those concerned with geodetic problems were carried out by the Army Topographic Command (ATC, formerly AMS) using SECOR (ch. 3), the Aeronautical Chart and Information Service (ACIC) using PC–1000 cameras (ch. 3), the Naval Weapons Laboratories (NWL) using TRANET (ch. 2 and ch. 3), NASA/GSFC and UCLA using a variety of data from MOTS cameras and from other participants (chs. 5 and 10), the U.S. Coast and Geodetic Survey and the U.S. Army Topographic Command using observations with BC–4 cameras of PAGEOS (ch. 7), Ohio State University (OSU) using those data from the other participants that could be fitted into a geometric theory (ch. 8), and Smithsonian Astrophysical Observatory (SAO) using data from Baker-Nunn cameras as well as data from other participants.

In addition, there was a separate effort by NASA/GSFC to evaluate the various tracking systems used by the participants in order to find a valid way of assessing the data and better ways of processing the data (ch. 5).

The data resulting from each participant's activities were to be sent, in a form specified for each kind of instrument, to a central collecting, storing, and distributing center. This center was the Geodetic Satellite Data Service (GSDS). (See sec. 1.3.4.1.) (Not all data collected during the NGSP reached the GSDS for several reasons, such as that data were gathered as part of special projects or were not in standard format.) Among the organizations whose data were used in the NGSP were NASA/WFC, which participated with its radar network in many evaluations, and the Jet Propulsion Laboratory, whose computations of GM and of its station coordinates were used by many of the NGSP participants.

Finally, to provide a suitable and uniformly available set of satellites for the NGSP, the program was planned to concentrate efforts on three satellites designed especially for geodetic application: GEOS–1, GEOS–2, and PAGEOS. The first two of these were constructed by the Applied Physics Laboratory (ch. 2) and the last by NASA/Langley (ch. 5).

The work of the major participants and of the assisting organizations is discussed in detail in the following chapters. Each chapter is organized approximately under the headings: introduction, instrumentation, theory, and results. A final chapter analyzes the results of chapters 2 through 10 and evaluates the results on the basis of their applications.

1.1.3 European Satellite Triangulation Programs

In 1965 a commission was organized in Europe to take advantage of the geodetic satellite that NASA had announced would be launched. NASA actively supported the commission's activities by providing predictions and other help. This commission, organized under the auspices of the International Association of Geodesy (IAG) and known as the International Commission for Artificial Satellites, was divided into two subcommittees: the Western European Satellite Triangulation (WEST) subcommittee and the Eastern European Satellite Triangulation (EEST) subcommittee. Very few data or results have been published by EEST, but the WEST group was quite active until 1972, when observations ceased and full attention was concentrated on data reduction (Various, 1972). Although neither WEST nor EEST networks have ever taken formal part in the NGSP, data from many of the cameras have been used by NASA/GSFC (ch. 5), by OSU, and by SAO (ch. 9). Dobaczewska (1972) and Massevitch (1965) have reported on EEST work, and there have been other reports submitted at the General Assemblies of the IAG. WEST's work is effectively summarized by Lefebvre (1969) and in the proceedings of a symposium at Graz (Various, 1972).

1.2 INSTRUMENTATION (TRACKING SYSTEMS)

It has frequently been pointed out that great advances in science generally follow great advances in instrumentation rather than the other way around. This is a humbling thought for the theoretician, but it is well illustrated by the development of geodesy over the period following the launching of Sputnik–1. Until 1958 the results of geodesy were essentially those obtainable with classical instrumentation and methods. With the introduction of the artificial satellite as a geodetic tool, not only did new results appear but new theories had to be provided to explain these results.

Consequently, it is not only desirable but essential that a description of the instrumentation (including satellites) developed for and during the NGSP be a major element in this report. However, we will confine our attention to the instruments directly involved in measuring the distance, direction, or velocity of a satellite. They will be called, in this book, "tracking systems" or "satellite-tracking systems" to adhere to common usage, although the term is also applied to non-tracking systems. Where the distinction is important, it will be explicitly noted.

A typical tracking system consists of four to six distinct subsystems, as shown in figure 1.11. There is also interest at present in tracking systems involving two satellites simultaneously, one of which is continuously measuring its distance from or velocity with respect to the other. See, for example, Schwartz (1972) for a discussion of one such kind of system and Martin *et al.* (1972) for discussion of another. Table 1.7 in the appendix lists the types of satellite-tracking systems used for the NGSP and gives those characteristics with geodetic significance.

1.2.1 Satellites

Although the fact is often overlooked, a satellite is an indispensable part of any tracking system. Not only is the system in-

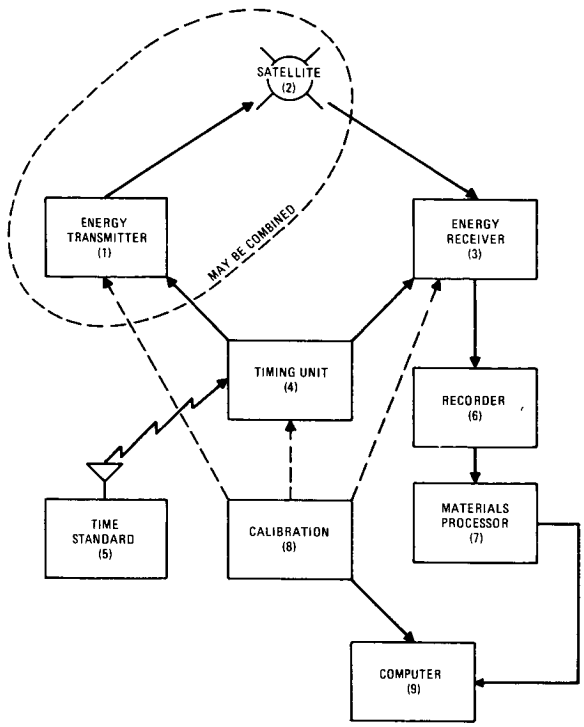

FIGURE 1.11.—Subsystem of a general tracking system.

operative without the satellite, but the measurements made by the system depend in type and value and in precision and accuracy on the satellite. This influence of satellites on geodetic data is analyzed in table 1.8 of the appendix, and the satellites that have formed part of tracking systems are listed and their main characteristics given in table 1.9 of the appendix. Those satellites of major importance to the NGSP are described in more detail by the organizations responsible for designing and/or building them. Satellites TRANSIT–1B, ANNA–1B, GEOS–1, GEOS–2, BE–B, and BE–C are described in chapter 2. Satellites ECHO-1, ECHO–2, and PAGEOS are described in chapter 5, and the SECOR series of satellites is described in chapter 3. Specific instrumentation in or on the satellite is also covered. The SECOR transponder is described in chapter 3; the 5–cm radar transponder is described in chapter 6. The ANNA and GEOS satellites carried flashing lamps, which are described in chapter 3 and are pictured in chapter 2. Cor-

ner-cube reflectors, used with laser DME, are described in this section and in chapter 9.

1.2.2 Tracking Equipment on the Ground

Most present-day tracking equipment (including MINITRACK, the 5–cm radars, SECOR, GRARR, and the BC–4 cameras) can trace its descent from equipment developed for tracking ballistic missiles. Of course, many kinds of equipment originally developed for use on ballistic missiles saw little or no further development for use on satellites (e.g., Marquis, 1960; Mertens and Tabeling, 1965). Almost all other tracking equipment—the Baker-Nunn, PC–1000, and MOTS cameras—is descended from astronomical prototypes. Only one instrument, the laser DME, is entirely of the space age.

Table 1.10 in the appendix shows the most important characteristics of the satellite-tracking instruments used in the NGSP. The precision shown is of course approximate and is not clearly distinguishable from accuracy. In spite of the considerable and important work done by Berbert and others on calibration and comparison of instruments (see sec. 1.3.4 and chs. 5 and 6), one still has a hard time finding a reliable way of evaluating either the precision or the accuracy of an instrument and of separating the one from the other. Note that the measurements are shown as having been made either *along* the line from observer to satellite or *transversely* thereto. Measurements made in one mode are therefore not directly comparable to those made in another. See chapters 5 and 11 on evaluation of tracking systems for further discussion of this point. Note also that FME equipment does not even measure distances but measures one component of the velocity (or a quantity that can be converted into one component of velocity); thus comparisons are even more difficult to make.

1.2.2.1 Camera-Type Tracking Systems

The development of camera-type tracking systems can be traced back to two special types of cameras developed in the 19th century. (See fig. 1.12.) One is the camera invented by B. Schmidt (1932). His intention was to get a wide-angle, large-aperture camera that could be constructed easily. The wide angle and large aperture were obtained by using a short-focal-length reflector as the principal element (Bowen, 1960). This camera, the "super-Schmidt" (Whipple, 1949) then became the starting point for design of cameras for satellite photography. Other cameras have followed the same line of development. The best known is perhaps the f/1 camera of Hewitt (1960), which was developed in Britain. The Soviet VAU (Massevich and Lozinsky, 1970) is a spectacular variation from the main line. Because of the influence of Maksutov, inventor of the Maksutov camera (a Schmidt camera derivative), many Soviet satellite-tracking cameras follow his design. The AFU–75 is the Russian camera from which most data have been obtained and used.

The second line of development was through the aerial camera. Here again the line split. One group selected aerial mapping cameras because the resulting photographs had very little distortion and because they had been used on missile testing ranges. The

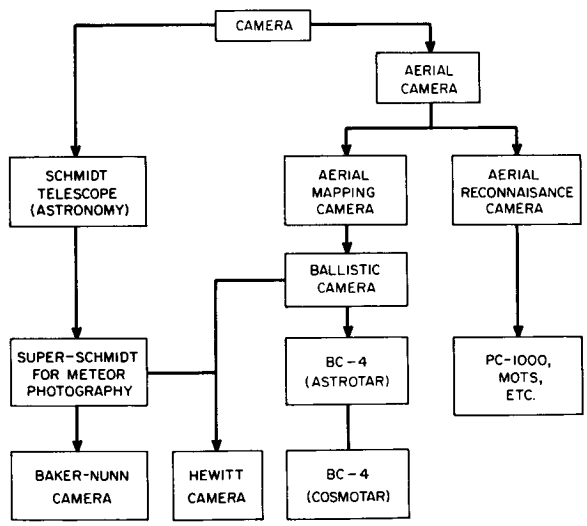

FIGURE 1.12.—Family tree of satellite-tracking cameras.

result was the BC–4 series of cameras used by NGS (ch. 7). Other groups selected aerial reconnaissance cameras because of their availability and low cost, and the results were the DMA/AC PC–1000 cameras (ch. 3) and the NASA/GSFC MOTS cameras (ch. 5).

Table 1.11 of the appendix lists the most important characteristics of the cameras used during the NGSP. Note that no values are given for the accuracies obtainable with these cameras. Although one can find in the literature values given for precision and accuracy of various camera systems, such values must be considered qualitative in nature. (The values given in table 1.7 and in chapter 11, for instance, are indicative rather than definitive.) The accuracy of a camera type of tracking system depends not only on the design of the camera, but also on the method used for measuring the photographs and reducing the data. Not only are differences in methods of reduction great but the effects of these differences on the overall accuracy are difficult to estimate. For example, one would perhaps expect that the accuracy of a camera would be related to its focal length—the greater the focal length, the larger the scale (microns per second of arc) of the photograph, and the less important the measuring errors. But with increased focal length usually comes decreased field of view, and thus fewer stars with accurate coordinates are available against which to compare the locations of a satellite. If the aperture is increased in order to increase the field of view, errors become larger in the outer parts of the field. The NGS has done a particularly thorough job of analyzing the factors affecting camera accuracy, and a reading of chapter 7 and the references cited therein is well worthwhile. See also the NASA/GSFC evaluation of camera performance (ch. 5). Note that SAO uses two different values for the σ of the same laser DME system in order to absorb into one number the errors in the gravitational potential used with its data (ch. 9). Information on Russian cameras can be found in Massevich *et al.* (1969), Massevich and Lozinsky (1970), Lozinsky and Leikin (1969), and Lapushka (1972).

Calibration of Camera Systems.—One of the most interesting aspects of the camera type of tracking system is that it can be calibrated by using only its own observational material. This apparent "bootstrapping" paradox is a consequence of the fact that the stars themselves, whose images appear on the photographs, constitute a set of points with accurately known coordinates. The procedures used for calibrating the camera portion of the system are discussed by DMA/AC (ch. 3), NASA/GSFC (ch. 5), NGS (ch. 8), and SAO (ch. 9). The differences in approach are not as great as the discussions might indicate. All organizations use forms that can be reduced to:

$$\epsilon_i = \sum_{j,k,l} a_{ijkl} x^j y^k r^l \quad j,k,l = 0 \text{ to } J,K,L, \text{ respectively}$$

where ϵ_i, (ϵ_r) is the error in coordinate $x(y)$, the a_{ijkl} are constants, and

$$r^2 \equiv x^2 + y^2$$

The difference between the photogrammetric (projective) method used by DMA/AC (ch. 3) and NGS (ch. 7), and, on observations of GEOS–1 and –2, by NASA/GSFC (ch. 5), and the astrometric (Turner's) method used by SAO (ch. 9) and on some occasions by NASA/GSFC (ch. 5) lies simply in the fact that in the photogrammetric method there are, between the constants $\{a_{ijkl}\}$, relations derived from optical considerations, whereas in the astrometric method no such relations are specified. Which method is preferable will depend on the system being calibrated. A system with a wide field of view (BC–4, MOTS, PC–1000) will either require more terms in the above equation to account for distortion and aberration than will a system with a narrow field of view, or for the same number of terms will require assumptions of relations between coefficients.

Hornbarger (1968) studied this question with some thoroughness. Whether his conclusion (the photogrammetric equations are preferable for use with wide-angle cameras) is in general correct is still not known. One

indication of our uncertainty of what the photogrammetric version of the calibration equations should look like can be gotten by comparing the equations used by the various authors in this work (chs. 3, 7, and 9). Berbert and others (unpublished reports) have compared results of using particular equations.

Because of the peculiar nature of the camera data, there is little difference between the calibration process and the ordinary process of photographic data reduction. The descriptions given in the sections on preprocessing of data therefore apply almost unchanged to the calibration process. The most significant difference is that calibration may, as in the case of the PC–1000 cameras (ch. 3), occur long after the photographs of a satellite have been taken. If the experiences of users of other cameras is applicable to PC–1000 camera systems, then such long times between calibration degrade the data on satellite tracking.

Measuring Engine.—The camera type of tracking system is unusual in that the measuring part, the comparator, is usually hundreds or thousands of kilometers away from the rest of the system. But the comparator, unless care is taken, can contribute from 10 to 50 percent of the total error to the data, and it is therefore as important as any other portion of the system. Almost all of the measurements used for the NGSP were made on the D. Mann Company's comparators, and that company's literature can be consulted for information on specific instruments. Most of the measurements have been with instruments in which the point of measurement was selected by a human operator (NGS, SAO, NASA/GSFC), but some were made with an instrument that itself selected the precise point of measurement (DMA/AC). The distinction is important because the latter type is capable of attaining greater precision than the former.

The least reading—that is, the shortest distance shown directly on the machine—is, for most of the measuring engines used by NGSP participants, 1μ along each axis. Shorter distances can be estimated by interpolating visually between graduations if the measuring engine is appropriately equipped. If the machine indicates its readings digitally, as is most often the case, no interpolation is possible. The least reading is then often taken to be the resolution of the machine, and the precision and accuracy are assumed to be limited by the least reading. This assumption is not correct, however. The precision and accuracy attainable depend on many more factors than just the least reading, and some of these are much more important. Table 1.12 in the appendix lists the most important factors. Note that the accuracy of the instrument does not depend on the accuracy of the screws or scales. This apparent paradox is readily explainable. The explanation lies in the method used for calibration.

For a discussion of standard methods of calibration, see Hotter (1967), Rosenfield (1963), and Hallert (1963). For a discussion of optimal methods of calibration, see Marckwardt (1971), Bennett (1961), and Henriksen (1965). The entire system can be calibrated without separate calibration of the camera portion and the comparator portion. (See Hotter, 1967, and ch. 7.)

1.2.2.2 PRIME MINITRACK

The original frequency allocated to MINITRACK was 108 MHz. This region of the spectrum was, however, part of the general band intended for use by commercial television. When pressure for reallocation of the 108-MHz frequency band to commercial use became heavy, MINITRACK was modified to work at around 136 MHz and remained there. Data used in NGSP were taken by the 136-MHz version.

The basic PRIME MINITRACK system (Watkins, 1969; Wilson, 1959; Mengel, 1956) consists of (1) pairs of linear antenna arrays arranged on base lines perpendicular to each other (fig. 5.7, ch. 5), (2) a set of radio receivers and phase comparators, and

(3) a radio beacon emitting a signal at a fixed frequency around 136 MHz. The arrays are connected in pairs by coaxial cables to the receivers. The phase of a signal arriving at one array of a pair is compared with the phase of the signal arriving at the other array, and these phases are converted to direction cosines.

Because of the long wavelength (2.2 m) compared with the distance between the arrays (125 m), the standard deviations of the directions measured by PRIME MINITRACK are about $\pm 20''$ at best. This value is considerably worse when the sun is very active. The characteristics of PRIME MINITRACK are summarized in table 1.13 of the appendix.

1.2.2.3 Distance-Measuring Equipment

From the geodetic point of view, a basic difference between distance-measuring equipment (DME) and angle-measuring equipment (AME) is that the latter can, in principle at least, provide the data in a celestial (stellar) reference system, whereas the former provides its data in the system of the local datum. Furthermore, there is a difference between types of DME that divides such equipment into two groups. Instruments in one group measure the time it takes a pulse to travel from the transmitter on the ground up to the satellite and then back to the receiver. Instruments in the second group measure difference in phase between a continuous wave traveling from the transmitter up to the satellite and back to the receiver. Although this distinction is justified by the very different construction of equipment in the two groups, it is just as important from the geodetic point of view because of the effect it has on the way the data from each group are treated.

A pulse travels at the velocity v_g of the group of waves composing it, and the measured distance is equal to

$$s = \oint v_g \, dt$$

whereas the distances obtained by phase measurement depend on the phase velocity v of the single frequency involved

$$s = \lambda = \oint \lambda v_\phi \, dt$$

In the ionosphere, v_g and v_ϕ behave quite differently and this difference must be taken into account in the reductions. Table 1.14 in the appendix summarizes the principal characteristics of DME as used with satellites.

Pulse-Type DME—Laser DME.—A laser DME system consists of the following essential components: (1) a generator and transmitter of light pulses, (2) a reflector of the pulses, (3) a detector of the light pulses, and (4) a timing device for measuring the time interval between emission of the pulse and detection of its return.

In addition, since measuring satellite distances simultaneously from several stations is very difficult, each station also has a clock for giving the time of pulse emission. The time and distance (calculated from the time interval) are then used to compute the satellite orbit. Table 1.15 of the appendix compares the major characteristics of systems giving data used in the NGSP. Table 1.16 of the appendix lists the satellites that, because they carry corner-cube reflectors (sec. 1.2.4), have been much tracked by laser systems.

5-cm Radar.—The 5-cm (C-band)[1] radar systems discussed in chapter 6 consist basically of (1) a transmitter, composed of a pulse generator and amplifier, (2) a paraboloidal antenna, (3) a receiver, and (4) time-interval-measuring devices. It may include a transponder carried on the satellite, and the distance at which a satellite can be tracked is then greater because the signal-to-noise ratio at the receiver of the tracking station

[1] What is here termed 5-cm radar is also called C-band radar. The designation by letter is an inheritance from World War II days, when the Allies assigned letters in random fashion to various parts of the radio spectrum. The radar systems operating in these frequency ranges were then designated by the same letters.

is improved. (See table 1.17 in the appendix.) If the transponder is not present, the pulses of the radar system are simply reflected from the surface of the satellite. When the pulses are reflected in this manner, the radar is sometimes said to be "skin tracking." When a transponder is used, the pulse from the tracking station is picked up by the satellite antennas, amplified, and reemitted. Since the 5–cm radars were originally designed and are still mostly used for tracking rocket-propelled missiles, they also measure azimuth (A_z) and elevation (E_l) components of the direction to the satellite. The errors in these quantities are of the same size as those in directions measured by PRIME MINITRACK (1.2.2.2) but are 10 to 20 times larger than those measured by camera systems (1.2.2.1). The angular measurements are therefore not of great importance for geodetic purposes. Table 6.2 (ch. 6) lists the radar systems used on geodetic or calibration projects during the NGSP. Although some nine different models of radar are listed, the differences are often only as simple as, for example, whether vacuum tubes or transistors are used in the circuitry or whether the system is mobile or fixed. There are more significant differences within different systems of the same model; for example, FPS–16's may have different radio-power outputs. The characteristics of the two major varieties of 5-cm radar, the AN/FPS–16 and the AN/FPQ–6, are given in table 1.17 in the appendix. A block diagram of the AN/FPS–16 is shown in fig. 1.13.

It should be noted that large radar systems, such as those used in the NGSP, are invariably subject to engineering mutation. This means that each radar system is structurally unique and that no two radars have the same geodetically significant measuring characteristics. It also means that no one system can be depended on to retain its characteristics unchanged over a long period. Even the strictest supervision has never been able to prevent the personnel operating a radar system from "improving" (the engineering term is "tweaking") the equipment. As a result, published values for the characteristics of one radar cannot be used for another system even of the same model. Furthermore, calibration constants determined for one epoch cannot be relied upon at a later epoch. For these reasons the calibration projects carried out under the NGSP are of great importance.

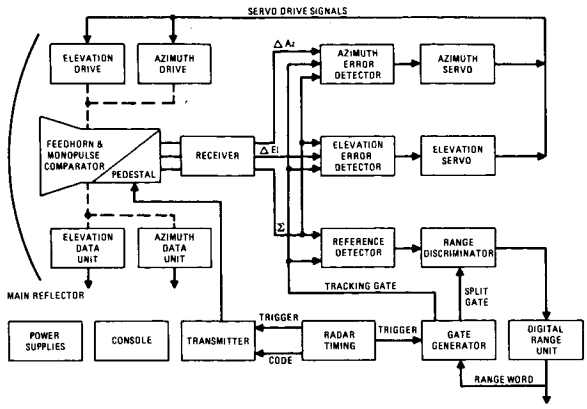

FIGURE 1.13.—Basic AN/FPS–16 (simplified block diagram).

Phase-Type DME.—There is a close relationship between the principle on which phase-type AME like PRIME MINITRACK works and that on which phase-type DME like SECOR and GRARR works (and on which, for that matter, the Michelson interferometer works). This relationship is indicated by the sketch in figure 1.14. The figure shows, first, a MINITRACK system with two antennas, 1 and 2, separated by a distance d. The beacon in the satellite emits CW radiation and the phase of the wavefront at an-

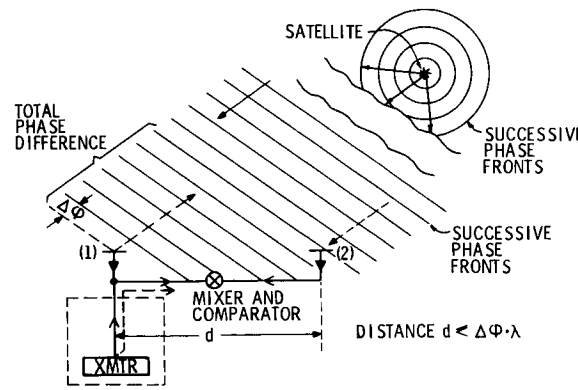

FIGURE 1.14.—Principle of phase-type DME.

tenna 2 is compared to that at antenna 1. There is an ambiguity of an integral number of wavelengths in the total phase.

If we add to antenna 1 a transmitter (shown enclosed by dashed lines) and decrease the distance d to a quantity smaller than the expected resolution of the system (say, 10 cm) and if we replace the beacon by a receiver/transmitter unit (transponder), we have essentially a phase-measuring system whose observations can be translated directly into distance (with, of course, the usual ambiguity). If the phase difference is $\Delta\phi$, then the distance r to the transponder is

$$r=\frac{\Delta\phi}{2}\lambda+n\lambda$$

where λ is the wavelength and n is an unknown integer.

Ambiguity can be resolved by either of two methods.

If r is known to within $\pm\lambda/2$, the correct distance is

$$r=\left[\frac{r_0}{\lambda}\right]+\frac{\Delta\phi\cdot\lambda}{2}$$

where r_0 is the approximately known distance.

The distance can be measured at wavelengths $\lambda_1,\lambda_2, \ldots, \lambda_N$, where

$$\lambda_i=k_i(\lambda_{i-1})$$

and k_i is an integer such that λ_i/k_i is greater than the smallest resolution interval on λ_{i-1}. This method is used on data from SECOR and GRARR.

1.2.2.4 Frequency-Measuring Equipment

Two "range rate," or frequency-shift-measuring, instruments have been used in the NGSP to an extent great enough to warrant detailed description. One, TRANSIT (or AN/ASN–8) developed by the Applied Physics Laboratory (APL), is described in detail in chapter 2. The other, developed by MOTOROLA, ADCOM, and others for NASA/Goddard Space Flight Center and referred to as GRARR (or STADAN RR, GRR), is described in detail in chapter 5. A third system, DSS, developed by Jet Propulsion Laboratory for tracking spacecraft at very great distances, has been of less importance for geodesy. Data from it have been used, however, to derive values for *GM* and for the coordinates of the stations themselves. The system is discussed briefly in chapter 4.

All the systems compare the frequency of radio waves received at a station with the frequency emitted from some source of known frequency. The TRANSIT system places the emitter in the satellite; the GRARR and DSS systems place the emitter at the same point as the receiver and place a relay (transponder; receiver/transmitter) in the satellite. The TRANSIT system has the advantage of simplicity but depends for its accuracy on the stability of the source. The GRARR and DSS systems are much more complex than the TRANSIT but give the operator exact knowledge of the emitted frequencies. The observation equations for the three systems are of course similar. They differ mainly because a transponder cannot simultaneously receive and transmit signals of the same frequencies unless the antennas are designed to ensure that the transponder does not receive its own emitted signals. A transponder could be designed to alternately receive and transmit. But designers of GRARR and DSS systems (and of SECOR) preferred to have the transponder receive signals at one frequency and transmit at another. The observation equations are therefore written to take this fact into account.

In the TRANSIT systems (fig. 2.7, ch. 2) the incoming waves are separated by two (or more) tuning sections into component signals of frequencies f_1, f_2, and so on. (TRANSIT uses two frequencies, but four frequencies have been used in earlier work.) Each separated frequency is heterodyned down to the frequency:

$$\Delta f_i\equiv f_{ri}-\bar{f}_{oi}$$

where the frequency $\bar{f}_{oi}$, obtained from a frequency standard at the station, is a close approximation to the frequency f_{oi} used in the satellite. This frequency is then "tracked" —that is, a reasonably stable, local oscillator is locked in phase to the frequency Δf, and the output of the local oscillator is then measured and recorded. The phase-locking circuit provides a filtering action, since it responds slowly to sudden changes. The output of the local oscillator (also denoted as Δf for convenience) is sent to a counter which measures the period of Δf_1. The result, times of starting the count, and the number of cycles counted are recorded.

For the design of GRARR system, see chapter 5; for the design of DSS systems, see chapter 4.

Table 1.18 in the appendix lists the satellites which have carried beacons for use with FME.

The velocity $\mathbf{v}_s$ of a source and the volocity $\mathbf{v}_r$ of a receiver are related to the frequencies f_o and f_r, emitted and received, respectively, by the Doppler equation:

$$f_r = f_o\left[1 - \frac{(\mathbf{v}_s - \mathbf{v}_r)\cdot\mathbf{r}}{c}\right]$$

where $\mathbf{r}$ is the vector from source to receiver. See section 1.4 and chapter 2.

Besides the work of APL on the theory of FME, there should be mentioned the analyses of Lorens (1959) and Mendoca and Garrioff (1962).

1.2.3 Timing Subsystems

In theory, two different kinds of time-measuring systems should be used for satellite geodesy. One kind, of only fair accuracy (say, 1 part in 10^8), would be adequate for static satellite geodesy, since this kind of geodesy uses observations taken nearly simultaneously. The timing subsystem at a tracking station would then need to be just good enough to allow adjustment of all observations to a single, common time and to allow accurate compensation for the rotation of the Earth. Of this type are timing subsystems used in camera-type tracking stations where the light flashes from GEOS are photographed simultaneously at other tracking stations (such as DOD's and WEST's tracking stations) or where they are photographed by reflected light in near simultaneity with other cameras (such as the NGS network). SECOR, an electronic DME which measures phase simultaneously with similar DME, is also of this type. On the other hand, cameras and electronic instruments making their observations independently of all other systems would require highly accurate clocks (errors of 1 part in 10^{11} in rate or better) to give the times used in the equations of dynamic satellite geodesy. APL's (ch. 2) system is certainly of this type, as are the instruments in the JPL network (ch. 4) and those in NASA's PRIME MINITRACK network (ch. 5).

It turns out that most tracking systems have the same general kind of timing subsystem. The timing subsystem is composed of two different kinds of components. One kind is concerned with putting out extremely accurate or precise time intervals. It furnishes the time scale for the station (Essen, 1962). Its most important unit is the frequency standard (Essen, 1962; Behler, 1967). This unit provides time intervals with a precision of 1 part in 10^{10} to 10^{12} (table 1.19 of the appendix) depending on whether the oscillator in it is a quartz crystal, cesium beam, or hydrogen gas (Mainberger, 1958; Throne, 1968). The frequency of this oscillator is monitored by means of VLF broadcasts from one of a number of stations (table 1.20 of the appendix). The frequency standard sends the time intervals to a clock. The epoch of the clock is set according to pulses received from one of a number of VHF time-broadcasting stations (table 1.20 of the appendix). Time established in this way is accurate to from about 0.2 msec to perhaps 1 msec, depending on the state of the atmosphere, distance of the broadcasting station from the receiver, and so on.

Since this accuracy is not good enough for many applications, a portable cesium or

rubidium clock is carried from a primary time station, such as the U. S. Naval Observatory (cesium only), to the field stations and then back to the primary time station. This procedure, begun by Rader and others in 1960 (Rader *et al.*, 1961) is now used by almost all organizations that run tracking systems. Clocks can be synchronized to better than 10 μsec as a routine matter, and to 1 μsec with care.

The second kind of component of a timing system is of course that directly concerned with timing or controlling the scheme of measurements at the station. At stations with camera-type tracking systems, the clock is used to time, and sometimes to control, the opening and closing of the camera shutters. At stations with laser DME, the clock, acting as frequency divider, provides accurate time intervals, which are sent to the counting or timing instrument. This measures the time elapsed between pulse emission and pulse return. It also provides the time of pulse emission and/or pulse return. At stations using phase measurement for finding distance (such as SECOR and GRARR), the frequency standard ensures that the modulating frequencies are of correct wavelength.

It is worthwhile mentioning here some relatively new timing subsystems. One of these, the subsystem that controls synchronism in television receivers and transmitters, is unlikely to be of great importance to satellite geodesy of the future. It can provide a frequency referent with a precision of 1 part in 10^{11} and is immediately available to anyone with a television receiver (Davis *et al.*, 1970; Davis, 1971). Another subsystem is that contained in the Navy Navigation Satellite System (NNSS) satellites. This subsystem provides time (not frequency) to ± 0.2 msec. A third is the timing subsystem in TIMATION satellites. Experiments were made by S. C. Laios at GSFC in 1969 using GEOS–2 as a carrier of time from the Rosman, North Carolina, tracking station to other tracking stations. Time derived in this way agreed to within 25 μsec with time given by cesium clocks whose time was carried from Rosman. (See also Mueller, 1969.)

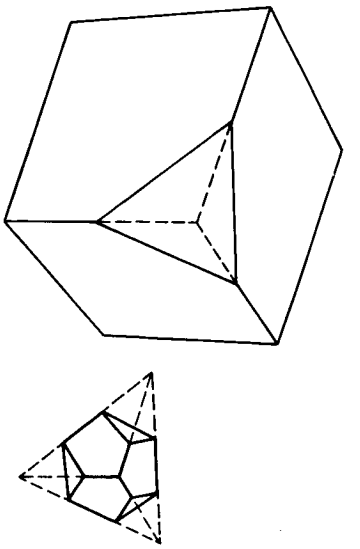

FIGURE 1.15.—Corner-cube reflector.

1.2.4 Corner-Cube Reflector

Although they are not usually thought of as instruments, corner-cube reflectors (CCR)[2] are an important part of many satellites and of many distance-measuring systems. They have the property of reflecting incident energy back in the direction from which it came. The CCR gets its name from the fact that it can be (and sometimes is) made by removing a corner from a cube (fig. 1.15). The theory of the corner-cube reflector at optical wavelengths is covered in detail by Yoder (1958), Chandler (1960), Karube (1967), and Chang *et al.* (1971), and at radio wavelengths by Spencer (1944), and Blank and Sacks (1965). The earliest attempt at using CCR's in satellite geodesy was not done with lasers but with 60-inch searchlight beams. The initial experiments carried out by J. A. O'Keefe in 1957, using corner-cube reflectors on the earth's surface, were unsuccessful because of the large amount of

[2] These are also referred to as cube-corner reflectors, corner reflectors, and retroreflectors. The first of these terms would be best, but it is not as common as "corner-cube reflectors." Retroreflector is definitely inappropriate as a synonym for the CCR, since other prisms than the CCR are retroreflectors.

backscattered light involved. Not until the narrow laser beam was available did the CCR idea become practicable at optical wavelengths for satellite geodesy.

Note that the CCR for radio waves is much larger than that for light. This size makes it impracticable to form large arrays. Other forms such as the Laneburg lens and the Helisphere (Schrank and Grove, 1968) are also used. NASA/WFC uses the Van Atta array (see ch. 6).

1.2.5 Evaluation of Performance of Tracking Systems

A tracking system can be considered as being made up of two parts, the physical and the mathematical. The physical part is the obvious part; the mathematical part, which is just as important and consists of the calibration constants and error estimates, is often overlooked. NASA in setting up the NGSP realized the importance not only of the physical machinery for observing the satellites but also of the calibration constants and the error estimates. It ensured that these mathematical components of the systems would be adequately dealt with by making them the particular responsibility of a group within NASA. This group, headed by J. Berbert of GSFC, undertook its task by making an extensive and exhaustive series of comparisons of the performance of the tracking systems participating in the NGSP. Most of the work done by the group is presented in a long series of internal reports of GSFC, but a considerable portion has not yet been put together. Other personnel at GSFC and Wallops Flight Center also compared systems of the NGSP. A report (X–514–67–315 GSFC) of J. Berbert's represents the status as of July 1967.

But as Socrates put it, "Comparisons are slippery," and very great care is needed in interpreting the results of such an evaluation. The subject is examined critically in chapters 5 and 11.

1.3 DATA

The preceding sections on the origin and development of the NGSP, on its place in the geodetic scheme, and on the instrumentation used to acquire data [3] are important if one wishes to understand the theory and results presented in this book. The data themselves, however, are the basic life-stuff from which the results are built up, and these are always the first interest of the geodesist and of other users. The scientist takes the data, molds them into the skeleton provided by theory, and produces a new creation that can be utilized to produce newer versions, in steadily progressing cycles of improvement.

So with this section we enter on a discussion of purely geodetic aspects of the NGSP. It is of course impossible to give here, or even in the individual chapters, the totality of data that the NGSP produced. There were, for instance, over 200 000 observations made by Baker-Nunn cameras alone, and the total number of observations made during the NGSP and available from the Goddard Science Data Center (sec. 1.3.4.1) is probably over 2 000 000.

The data used for the NGSP fall into four categories—(1) constants, (2) locations of and geometric relations between observers, (3) models of the geopotential and/or gravitational potential, and (4) measurements giving the satellite's distance or direction with respect to the observer, or the difference in frequency between signals from the satellite and signals from a standard. An additional category, auxiliary data, contains all those data such as temperature, pressure, calibration constants, etc., which are used to correct the measurements for their departure from their "ideal" values. Such data are of ephemeral value and are not listed in this volume.

1.3.1 Constants

Although the participants in the NGSP had common geodetic objectives, they took

[3] By data is meant, of course, the set of all numbers inserted into the theory (sec. 1.4) and from which values of the unknown are then derived.

completely independent paths toward them. As a consequence, the results from each participant are derived not only from different observational material and from different theories but also from different values for the fundamental constants or even from different fundamental standards.

For the benefit of those who will be working with data or results from the NGSP, a summary is given of the sources of standards and reference values that should be used.

1.3.1.1 International Standards

The units adopted by the General Conference on Weights and Measures are as follows:

Meter	(length)	m
Kilogram	(mass)	kg
Second	(time)	s
Ampere	(electric current)	A
Degree kelvin	(temperature)	K
Mole	(amount of matter)	mol
Candela	(luminous intensity)	cd

These units have the status of international standards and form the basis for the set of units known as the "Systeme International" (SI). Besides these fundamental units, there are a number of supplementary and derived units. The derived units are defined in terms of the fundamental units. Their definitions and symbols are given in table 1.21 of the appendix; for full discussion see, for example, Page *et al.* (1966), Page and Vigoreaux (1970), and Markowitz (1973).

1.3.1.2 Defined Physical Constants

Table 1.22 of the appendix lists those quantities which are of particular interest to geodesists and for which values have been recommended for common use. Two sets of quantities are listed. Set I (table 1.22a) consists of physical quantities. Its values were recommended by the NAS/NRC Committee on Fundamental Constants in 1963 (Jet Propulsion Laboratory, 1964). The U.S. National Bureau of Standards has published a revised list (Abramowitz and Stegun, 1971). The revised list is based on the 1969 adjustment by Taylor *et al.* (1969a,b). However, the International Council of Scientific Unions has not yet (1973) finished an official readjustment, so adherence to the older values is advisable.

Set II (table 1.22b) consists of astronomical quantities for which conventional values have been adopted. These conventional or defined values are, unlike the older set that they replace, self-consistent (Kulikov, 1964). Since they have the sanction of the International Astronomical Union (Wilkins, 1964, 1965), they are being used in the computation of the national ephemerides and in other computations. The geodesist should therefore use these values in all cases where data from national ephemerides are used. JPL's and SAO's results (ch. 4) should of course be evaluated with their use in mind.

1.3.1.3 Time

Time as a fourth coordinate in geodesy and in satellite geodesy in particular is important for at least three reasons. First, positions on the earth's surface are not fixed but vary slowly with time. For every set of coordinates of a point in 3-space, the time at which these coordinates were determined should also be given. See, e.g., the discussions of polar motion in chapters 3 and 5 and of continental drift in chapter 3. Motions of this kind are slow and do not require measurement of time to better than an hour at the least. Second, the theory of motion of a satellite was used either entirely or in part by eight of the investigators (chs. 2, 3, 4, 5, 6, and 9) in the NGSP for finding positions and the gravitational field. Time is the only independent variable in these theories, and the times of measurement should be known to better than ± 0.1 msec in order that final errors be acceptably small. Third, even in the cases where the theory did not involve satellite motion and was nominally geometric (chs. 5, 7, 8, and 9) because observations were made simultaneously, time was involved

through the rotation of the earth. The observations were only simultaneous in small subsets of the total set of observations, and the times between subsets (or equivalently, times of subsets) had to be determined accurately (but not as accurately as in the second case, because the angular velocities were less). Unfortunately, time is measured in a number of different systems and the relations among them are not in every case carefully stated.

Table 1.23 of the appendix lists the epochs of major importance in the NGSP; Table 1.24 of the appendix lists the time scales of major importance. The most valuable source of information on epochs of astronomical importance is the *Explanatory Supplement to the Astronomical Ephemeris and the American Ephemeris and Nautical Almanac* (1961). Because time scales have been changed repeatedly since 1961, each change marking a discontinuity in the corresponding time and epoch, the *Explanatory Supplement* is not satisfactory for information on time scales. For this, Hudson (1967), Preuss (1966), Mueller (1969), Guinot and Feisel (1969), Smith (1972), Henderson (1972), and Chi and Fosque (1973) should be consulted.

All investigators used either universal time coordinated (UTC) or atomic time (AT) during the NGSP (see table 1.24). Those observers having atomic clocks generally used portable clocks to relate the time from the atomic clock to time of the U.S. Naval Observatory and used portable frequency standards or VLF broadcasts to maintain the AT scale.

1.3.2 Coordinate Systems

Satellite geodesy is carried out in two different kinds of coordinate systems: the system defined by reference to fixed points on the earth and the system defined by fixed points (stars) in the heavens. The theory of transformations between these systems is discussed in succeeding chapters (e.g., chs. 5, 7, and 8). Their definitions, however, occur in the NGSP as data and therefore are given here. The first kind of system is defined by datums (1.3.2.1), the second kind by, in a practical sense, star catalogs (1.3.2.2). Because the coordinates of satellite-tracking stations bear in many cases the same relation to datums that stars do to astronomic reference systems, these coordinates are given here rather than being discussed in the section on unknowns in section 1.4.1.

1.3.2.1 Datums

The set of constants that defines the relationship between a coordinate system (which is a mathematical abstraction) and the real earth is called a datum. The number of constants in this set depends on the kind of coordinate system chosen. From elementary mechanics it is known that the motion of a rigid body (such as a coordinate system) is completely specified by six quantities: three linear quantities that give the translation of a point in the body and three angular quantities that give the rotation of the body about the point. (Time is not relevant here.) Therefore, a datum for a Cartesian orthogonal coordinate system contains six constants (some of which, of course, can be made equal to zero by suitable definition). If a geodetic coordinate system is to be used, the datum must also specify the size and shape of the ellipsoid. This means three additional constants if the ellipsoid is triaxial, two if the ellipsoid is a spheroid, and one if the ellipsoid is a sphere. Since all geodetic reference systems in use at present specify an oblate spheroid as the reference surface, all the corresponding datums should contain eight constants. If, as is usually the case, the axes of the spheroid are defined to be parallel to the earth's axes of rotation and to the meridian of Greenwich (or some other standard meridian), then only five constants need be given explicitly.

It has been customary to specify different datums for horizontal and vertical coordinates, and usually to specify them in such a way that there is no defined relationship between the two. The consequent errors induced in each coordinate begin to appear

as the accuracy of three-dimensional geodesy increases, and care must therefore be used when dealing with datums or interpreting the meaning of coordinates in them.

Every satellite-tracking instrument used to gather the data for the NGSP is located in some reference system for which a datum exists, but they are far from all being in the same reference system or datum. Table 1.1 in the appendix lists those datums which control regions of more than 200 000 km. The majority of the satellite-tracking instruments are on one or more of these datums. Datums of smaller extent are described in chapters 3 and 8 and in *NASA Directory of Observation Station Locations* (1973). Although the above definition of a datum is theoretically correct, the geodesist applying it to the "datums" now existing will find that very few of these meet all the conditions necessary to make them well-defined. This means, of course, that calculations made with such existing ill-defined datums are erroneous. Fortunately, the errors are, as was mentioned earlier, insignificant by present-day standards. Excellent references on the pitfalls of datum definition are Yeremeyev and Yurkina (1969), Isotov (1968), and Hristow (1968).

Besides the absolute or geometric datums, there are a large number of datums established for use in orbit computation. These "dynamic" datums are all defined to have their origins at the earth's center of mass; their axes are oriented relative to various arbitrary choices. The most common orientation used because of the characteristics of the tracking systems involved is to have one axis in BIH's (Bureau International de l'Heure) meridian of zero longitude (Guinot and Feisel, 1969) and the other parallel to the 1903 mean axis of rotation of the earth. However, in execution these intended systems are not necessarily adhered to. (See chs. 3 and 7.)

Locations of Stations.—Locations (coordinates) of satellite-tracking stations are properly classified as unknowns (see ch. 4). However, the importance of the surveyed coordinates in fixing the local datums makes it desirable to use them as data also. For this reason, the coordinates on local datums are discussed here.

Until such a time as one datum is adopted by all countries, points on the Earth's surface will occur in sets, each set belonging to a different datum. This diversity of datums was first caused by the political nature of survey activities, but it also has good technical justification. One reason is that at present all so-called "World Geodetic Systems" are defined in such a way as to give large (5 m to 50 m) values for the rms error of all points on the earth's surface. A suitably chosen absolute reference system, on the other hand, can give from 0 to 4 m rms error for most of the points within the region governed by the datum. Another reason is that a datum designed particularly for a specific region can usually provide a better local fit of spheroid to the geoid than does a datum specifying a single spheroid for the world (for examples, the Great Lakes Datum, Australian Geodetic Datum, and Old Hawaiian Datum). Furthermore, it should be noted that while the coordinates of points in World Geodetic Systems (WGS) must change every time a change is made in the theory connecting the WGS's origin to surface points, no change due to theory is introduced into coordinates on local datums. Such coordinates are absolute and are not relative to a particular theory.

For these and other reasons, coordinates on the local datums are very important. It is therefore these coordinates that are given for the observing stations. Coordinates in relative coordinate systems as derived through the theory of satellite motion are given among the results in the various chapters following. Table 1.25 of the appendix lists the stations in order of increasing longitude. (In order to keep European stations close together in the table, the list begins at longitude –30°.) The last column tells what sets of results used these stations in their derivation.

Locations of radar stations other than NASA's that participated in the NGSP are given in the *NASA Directory* (Anonymous, 1973). Locations of TRANET stations whose positions were determined by NWL are given in chapter 3 and are the coordinates of the phase centers of the antenna arrays (ch. 2). They differ from the coordinates given in the *NASA Directory* for the same stations by the difference between phase center and geometric center.

1.3.2.2 Stellar Positions

All data from camera-type tracking systems in the NGSP were reduced by using stellar positions taken from one of two star catalogs, the *Fourth Fundamental Catalog* (FK4) (Fricke and Kopff, 1963) or the *SAO Star Catalog* (Staff of Smithsonian Astrophysical Observatory, 1966). The former has been used by European tracking stations, the latter by DOD, NASA, NGS, OSU, and, of course, SAO. The SAO catalog, described by K. Haramundanis (1967) and H. Eichhorn (Mueller, 1969), is made up of positions taken from nine different sources. The coordinate system is that of the FK4 (whose positions are included); the Boss catalog (Boss, 1936), AGK2 catalog (Schorn and Kohlschutter, 1951–1953), Yale Zone catalogs, and Cape Zone catalogs contributed most of the positions. Figure 1.16 (Hadaramundas, 1967) shows the distribution of stars according to magnitude and spectral

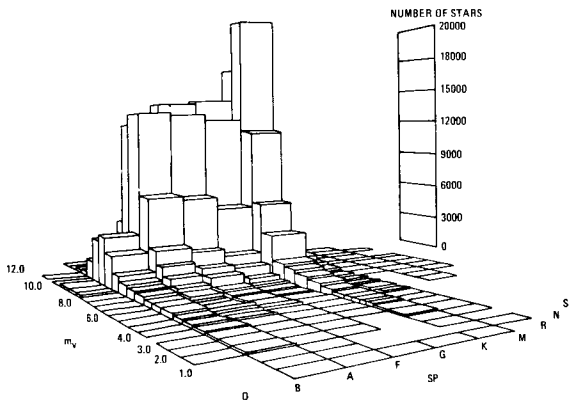

FIGURE 1.16.—Distribution of stars, SAO catalog.

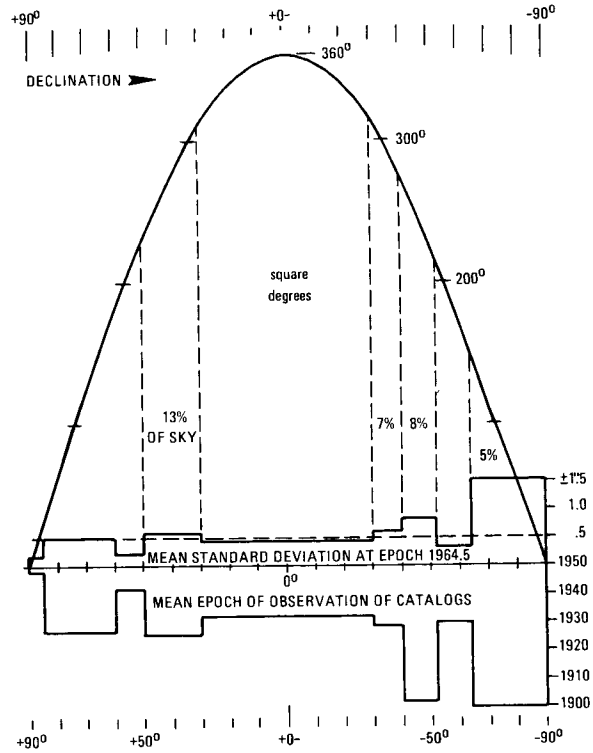

FIGURE 1.17.—Distribution of standard deviations, SAO catalog.

type; figure 1.17 (Hadaramundas, 1967) shows the distribution of the standard deviations of the positions according to declination.

Besides being needed for reduction of data from camera-type tracking stations, stellar positions are needed for the determination of time and polar motion. Whenever an observatory changes the characteristics of the set of stars it uses for time determination, it changes the epoch as well as the accuracy of its determinations. The geodesist need not concern himself with the mechanics of this process, but should keep track of the ensuing changes in time. See section 1.3.2.2 for a discussion of the effects of star position on time determination. See also Mueller (1969) and Melchior *et al.* (1972).

1.3.3 Gravity and Gravitation

Most of the results given in this report were derived from observations on the satel-

lites alone. This is, of course, obvious for the results of static satellite geodesy, and many of the results on the gravitational field of the earth were also derived as part of a general solution based on observations alone. A few results were, however, based in part on either computed values for the gravitational potential or average gravity anomalies.

APL's results (ch. 2) were derived with the use of values for coefficients of the zonal harmonics provided by Anderle and Smith of Naval Weapons Laboratory. These values are listed in chapter 2.

Both SAO and NASA/GSFC used average gravity anomalies as additional input for their solutions. GSFC's GEM–6 used Rapp's averages over 555×555 km^2 areas (ch. 5). The gravimetric geoid was based on average gravity anomalies obtained from DMA/AC, University of Hawaii, and other sources, as well as on measurements. SAO's data on gravity were obtained from DMA/AC (ch. 9).

1.3.4 Observational Data

The volume of data accumulated by observations on satellites exceeds that of all other categories of data by several orders of magnitude. Almost every satellite launched by the United States has had its distances, direction, and/or velocity measured, and for the NGSP some data on satellites not launched by the United States and on planetary probes also have been used. These data are contained in the archives of the organizations that collected for the NGSP and are stored in NASA's Space Science Data Center.

1.3.4.1 Storage and Retrieval of Data

Anticipating that during the NGSP a large volume of data would have to be transferred among the five or more major participants, the organizers of the program asked the NASA Space Science Data Center (NSSDC) to act as data storage, retrieval, and distribution center for NGSP data. Since NSSDC considered the NGSP data to be of a considerably different kind from the data NSSDC had been organized to handle, it set up within itself a separate group, the Geodetic Satellite Data Service (GSDS) to handle data accumulated during the NGSP.

To ensure that data passing through GSDS were handled efficiently within GSDS and were intelligible to and usable by those receiving the data, GSDS established a set of rules that controlled the quality of data accepted by the service and required that the data submitted to it be in a standard format acceptable to all NGSP participants. The quality control rules require data submitted to be grouped in distinct sets, each set consisting of all those data gathered during *one* passage of a satellite through the observation region of a single station. Data other than photographic were to be on ½-inch tapes usable on IBM computers and in BCD (even parity) form.

Data submitted to GSDS for storage must be in the prescribed format, and data received from GSDS also will be in that format. The format varies with the type of data. Formats, specified by reference to the columns of a standard 82-column computer card, can be found in Hotter (1967) for camera data and in Gross (1968) for range and Doppler data.

The data stored by GSDS are listed in catalogs published by the service, and directions for obtaining these data are also available from GSDS. The data are copied from GSDS files onto magnetic tape and sent out in this form. Punched cards are prepared only for small volumes of data. Requests should be sent to:

NASA Space Science Data Center
Geodetic Satellite Data Service
Goddard Space Flight Center
Greenbelt, MD 20771

Table 1.26 of the appendix summarizes most of the data available in the GSDS. These data are the results of observations on GEOS–1, GEOS–2, ECHO–1, ECHO–2, PAGEOS, BE–B, BE–C, D1–C, and D1–D. Not all available data are stored in the GSDS, nor are all data stored in GSDS sum-

marized in the table. To find out exactly what data are available, letters to the GSDS and to each of the participating agencies are required.

A comprehensive summary (to 1970) of data accumulated during the NGSP is given in a report by Clavelaux and Strange (1973, unpublished). Most of these data are available from GSDS; some are available from the investigators at GSFC, Wallops Flight Center, and SAO.

1.3.4.2 Preprocessing of Observational Data

Observations produce observational material. This material may be in the form of photographs, graphs, magnetic tape, printed paper, and so on. The data, which are numbers, may be already on the material (magnetic tape, punched paper tape, filled-out forms, printed sheets, etc.) or may be created by making measurements on the materials (e.g., putting photographs or oscillographic recordings on a measuring engine). The data, which in this first form are called raw data, are transformed by certain procedures into other numbers called processed data. The processed data are the numbers stuck into the observation equations (sec. 1.4.2) and "reduced." The process of turning raw data into processed data is "preprocessing."

The exact structure of a particular preprocessing scheme depends of course on what kind of data are involved. The general structure, however, is the same for all kinds of observational data used in satellite geodesy (fig. 1.18). The differences induced in preprocessing by the nature of the measurements are displayed in table 1.27 of the appendix. Note that six different kinds of data are involved. Only five are considered in the following sections, since the (A_z, E_l) variety are of minor importance for geodesy. (See, however, ch. 6.) We will consider the various kinds in this order: cameras, MINITRACK, DME, and FME. For details, see Hotter (1967) and Gross (1968).

Preprocessing of Data From Cameras.—Three separate preprocessing procedures are applied to data from cameras. One is applied

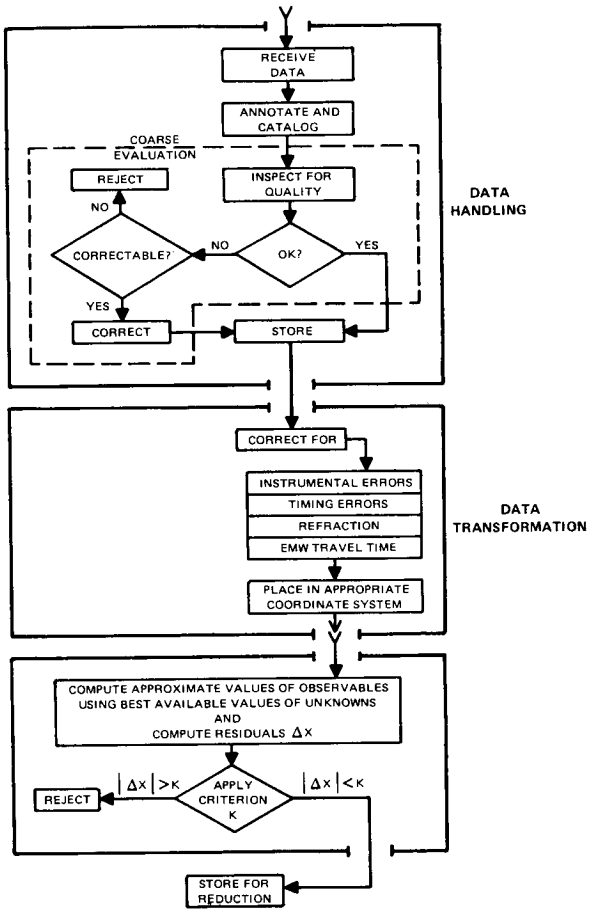

FIGURE 1.18.—General scheme for preprocessing of data.

to the measured x,y coordinates of images to correct for errors introduced by the measuring engine, camera, and atmosphere. Another is applied to the astronomic coordinates of the stars which are photographed to bring them from their cataloged values to their values at the time of the photograph. The third is applied to the time and may be simply a correction for the clock errors, or it may be more complicated and may take into account the travel time of the light, etc. Table 1.28 of the appendix lists the most important corrections applied during preprocessing. Detailed discussions are given in chapters 3, 5, 7, and 9. The chart in chapter 8 refers to preprocessing applied to data from GSDS (sec. 1.3.4.1) and not to preprocessing by the organizations themselves.

It should be noted that a very important consideration in the usefulness of the preprocessing is the timeliness of the calibration constants used. Some organizations, like NASA/GSFC, NGS, and SAO, calibrate the camera either very close to the time of photography or solve for the calibration constants as a part of the reduction procedure. DMA/AC, on the other hand, let a long time elapse between calibration and photography, consequently with greater danger of using obsolete values in the preprocessing.

Preprocessing of MINITRACK Data.—For various reasons, most of them connected with the MINITRACK use of 2.2–m radiation and the large area covered by the antenna, PRIME MINITRACK data require treatment considerably different from that given other kinds of data. Only the fact that users of PRIME MINITRACK are satisfied with 20″ to 40″ standard deviation keeps preprocessing from being almost impossible. A discussion is given in Gross (1968) and Watkins (1969), and a summary is given in chapter 5.

Preprocessing of Data From DME.—The four kinds of DME considered are (1) laser DME, which measures the travel time of short pulses of 6943–A light, (2) 5–cm radar of the FPS–16 type, which measures the travel time of short pulses of 5–cm radio waves, and (3) the GRARR, and (4) SECOR DME, which measures phase differences in radio waves—GRARR at wavelengths of 600 m to 18 740 000 m being present as modulation on a number of VHF or UHF carrier waves, the latter at wavelengths of 512 m to 1 048 576 m present as modulation on carrier waves of 224.5–, 420.9–, and 449–MHz frequency. In spite of the substantial differences in wavelength and measuring techniques, the preprocessing procedures are in general much alike. Table 1.29 of the appendix shows the steps taken in preprocessing the data from each type of instrument. There are, besides the differences (for each type) arising from inclusion or omission of various steps, also differences in the equations used. The greatest difference is found in computing the correction for refraction (table 1.30 of the appendix). See chapters 3, 5, 6, 7, and 9 for details.

Preprocessing of Data From FME.—As would be expected, data from FME get a considerably different treatment during preprocessing than do data from AME or DME. A typical procedure is shown in figure 1.19 (based on APL's procedures as given by Guier, 1966a). It is obvious that a great deal of attention is paid to smoothing the data by comparing them with values computed from the equations of motion of the satellite.

1.4 THEORY

Among those engaged in deriving geodetic quantities from observations on artificial satellites, it is common to think that there are two kinds of theory involved: (1) geometric or static and (2) dynamic. The former is based almost entirely on analytic geometry, does not contain time as an essential variable, and uses an absolute (i.e., Euclidean and fundamental) system of coordinates. The latter is based almost entirely on the theory of motion of a particle in a noncentral force field, contains time as an essential independent variable, and uses a coordinate system defined in terms of the motion of the particle. Which kind of theory is adopted and which variations are introduced depends essentially on (1) what kind of instrument was used for the observations

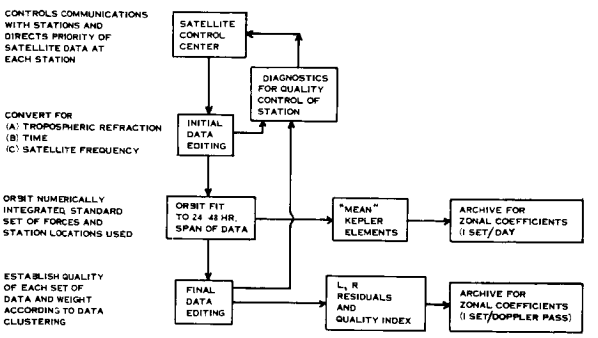

FIGURE 1.19.—General scheme for preprocessing data from FME (Guier, 1966a).

and (2) how the observers were placed with respect to each other, i.e., whether they could observe simultaneously or not. NGS (ch. 7), DMA/AC (ch. 3), and OSU (ch. 8) adopted geometric theory; SAO (ch. 9) used geometric theory with some success but relied principally on dynamic theory, as did DMA/AC (ch. 3). APL (ch. 2), DOD/NWL (ch. 3), JPL (ch. 4), and NASA (chs. 5 and 6) relied almost entirely on the dynamic theory.

But the dichotomy between static and dynamic satellite geodesy is based on differences which, though practically important, are less significant from a mathematical point of view than the very great basic similarity underlying all the methods (fig. 1.20). The following section therefore concentrates on the common part of the mathematics used. The differences in methods are found almost entirely in the way the observations are expressed as a function of the unknowns, and these will be discussed only enough to bring the reader up to where the specialized treatments in the following chapters start off. The fundamental and most valuable reference for geodesy is Helmert's two-volume work (1880–1884). Notable later works are those of Molodensky *et al.* (1960), giving the views of the Russian school; Hotine (1969), giving the theory in tensorial notations; and Levallois and Kovalevsky (1971), giving a clear exposition of three-dimensional (including satellite) geodesy. Heiskanen and Moritz (1967) is a good exposition of physical geodesy, as are the various editions of H. Jeffreys' "The Earth" (e.g., 1970). See also Bomford (1971) and Mueller (1969).

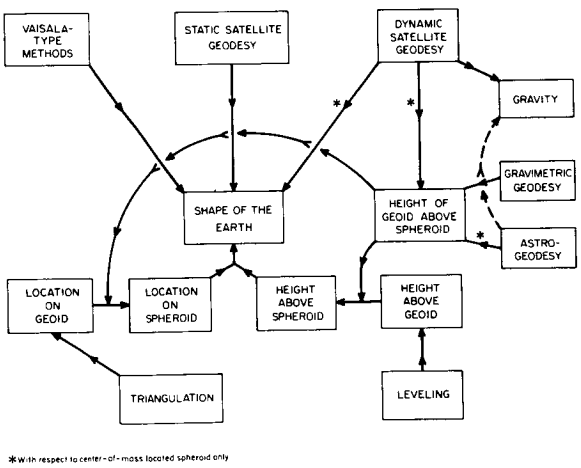

FIGURE 1.20.—Relations between geodetic methods and concepts.

For satellite geodesy alone, the works of Levallois and Kovalevsky (1971), Mueller (1964), and Kaula (1966b) are detailed; Bursa's (1970) paper is an excellent summary of the status in 1970.

1.4.1 General

All investigators, regardless of the particular methods they used in getting the results put down in the following chapters, followed the same general theoretical procedures in obtaining the results.

(1) To start with, each investigator selected or was assigned a set of quantities as unknowns, quantities whose values were to be determined. The set differed from investigator to investigator and depended on the interests or responsibilities of the organization involved. Table 1.31 of the appendix lists the unknowns (called "solve-for's" by JPL) of concern to the NGSP.

(2) Measurements were made of certain properties of the satellite or of the observer's environment that could be related, mathematically, to the investigator's unknowns. These properties, called basic observables, are listed in table 1.32 of the appendix. The basic observables were themselves affected by other properties of the environment of the observer, the satellite, or both. Data on these other properties, called auxiliary observables, also had to be collected. Table 1.33 of the appendix lists the most important of the auxiliary observables. Note that time may be either a basic observable or an auxiliary observable.

(3) Each investigator derived, from geometric considerations, from the equations of motion of a satellite or from other considerations, equations relating the K observables $\{y_k\}$ to the M unknowns $\{x_m\}$. A typical equation would be

$$f_{1n}(y_1, y_2, \ldots y_K) = f_{2n}(x_1, x_2, \ldots x_M) \quad (1.1)$$

This is an observation equation. In all cases considered in this book, f_{1n} and f_{2n} were nonlinear. The investigators therefore linearized the equations by expanding f_{1n} and f_{2n} into Taylor series and dropping terms of order higher than the first (the Einstein summation convention is used).

$$\frac{\partial f_{1n}}{\partial y_k} dy_k = \frac{\partial f_{2n}}{\partial x_m} dx_m \quad (1.2)$$

(4) Using approximate values $\{x_m^o\}$ (called by various investigators assumed values or a priori values) assumed to be close to the true values of the unknown quantities, the investigators computed from the n equations of the form of (1.1) approximate values $\{y_{kn}^o\}$. Subtracting the y_{kn}^o from the observed values y_{kn} gave residuals Δy_{kn} related to the unknowns Δx_m $(\equiv x_m - x_m^o)$ by the approximation

$$[\Delta y_{kn}] = \left[\frac{\partial f_1}{\partial y_k}\right]_n^{-1} \left[\frac{\partial f_2}{\partial x_m}\right]_n [\Delta x_m] \equiv [F]^{-1} [A] [\Delta x_m] \quad (1.3)$$

where the matrices of coefficients are evaluated with values a_{knm} of the variables. The matrix F in all work done in the NGSP has been made an identity matrix by suitable derivation of (1.1) above, so the equation (1.3), called also a (matrix) observation equation, is

$$[\Delta y_{kn}] = [A] [\Delta x_m] \quad (1.4)$$

(5) All of the investigation procedures used in the work reported on here ensured the existence of relations between the $\{x_m\}$ which did not depend on the observables. These relations, L in number,

$$0 = g_2(x_1, x_2, \ldots x_m) \quad (1.5)$$

were treated like equation (1.1) to give

$$[\Delta g_2] = [B] [\Delta x_m] \quad (1.6)$$

Equations (1.5) and (1.6) are to be solved simultaneously. Several methods have been used by the investigators.

(5.1) Equation (1.6) may be solved for those $\{\Delta x_m\}$ which are not of interest, such as coordinates of satellites, etc., and the resulting expressions substituted into (1.4). This procedure was used by many of the investigators such as OSU, NASA/GSFC and NASA/WFC.

(5.2) Equation (1.6) may be treated as an observation equation with large weights associated,

$$[W_l]^{1/2} [\Delta g_l] = [W_l]^{1/2} [\Delta x_m] \quad (1.7)$$

so that when combined with the weighted, true observation equation (1.4)

$$[W_n]^{1/2} [\Delta y_n] = [W_n]^{1/2} [A] [\Delta x_m]$$

the result is

$$[A^T B^T] [W] \begin{bmatrix} \Delta y_n \\ \Delta g_l \end{bmatrix} = [A^T B^T] [W] \begin{bmatrix} A \\ B \end{bmatrix} [\Delta x_m]$$

This procedure has been used by, among others, DOD/AFCRL, NGS, and OSU. See, for example, chapter 2 (D. Eckhardt).

(5.3) An additional set of L unknowns $\{\kappa_l\}$ can be introduced (these are called Lagrangian multipliers or correlates), so that the total number of equations can be set equal to the number $(M+L)$ of unknowns:

$$\begin{bmatrix} AW^T \\ I \end{bmatrix} \begin{bmatrix} \Delta y_n \\ \Delta g_l \end{bmatrix} = \begin{bmatrix} A^T W_n A & B^T \\ B & O \end{bmatrix} \begin{bmatrix} \Delta x_m \\ \kappa_l \end{bmatrix} \quad (1.8)$$

This method has been used by, among others, DMA/AC, NASA/GSFC, OSU, and SAO in developing their theory. However, because the multipliers $\{\kappa_l\}$ are not of geodetic interest, it would be a waste of effort to actually compute them. Equation (1.8) is therefore solved for the $\{\kappa_l\}$ and the result used to eliminate them from (1.8). See, for instance, chapters 5, 8, and 9.

(6) Once the observation equations and condition equations have been set up, application of the theory of least squares leads to

a "best" set of values for the unknowns—best in the sense that the set found has the highest probability (or at least, minimum variance) of yielding the values found by measurement. (See Bjerhammer, 1951, 1973; Anderson, 1958, Cramer, 1946; Carlton, 1962; and Baarda, 1960, for detailed analysis.) Weights are assigned to the observations—either by a study of the dispersion of the observation or from prior knowledge, or whatever—and the equations solved for the unknowns $[\Delta x_m]$ as, for example,

$$\begin{bmatrix} \Delta x_m \\ \kappa_l \end{bmatrix} = \begin{bmatrix} A^T W A & B^T \\ B & O \end{bmatrix}^{-1} \begin{bmatrix} A^T W \Delta y_n \\ \Delta g_l \end{bmatrix} \quad (1.9)$$

This equation will have a different appearance if the method of using condition equations as observations has been employed (5.2 above) or if the Lagrangian multipliers $\{\kappa_l\}$ have been eliminated (5.1 above), or if any one of a number of other minor modifications has been made. It can be shown, however, that all these modifications are merely variants of equation (1.9). That is, they can be transformed into (1.9) by matrix manipulation and will give approximately the same values for $[\Delta x_m]$ (approximately, because round-off errors in computation increase differently according to the method).

Among the modifications that will be found in following chapters, some are worth special mention here.

(6.1) The mathematics given above assumes that the equations are divided into "observation equations" and "condition equations" as indicated. But the problem can be restated in such a way that the relations expressed as observation equations

$$[\Delta y_n] = [A]\,[\Delta x_m]$$

are instead expressed as condition equations

$$[\Delta h_j] = [A]\,[\Delta x_m]$$

where the values Δh_j are of the same kind as Δg_c. There are J conditions of this type. This different viewpoint does not mean that there are no observation equations but that the observation equations are now the simple set

$$[\Delta y_n] = [D]\,[\Delta x_m]$$

where the rows of D are unit vectors. The resulting normal equation is then

$$\begin{bmatrix} AWA^T & A \\ A^T & O \end{bmatrix} \begin{bmatrix} K \\ \Delta x \end{bmatrix} = \begin{bmatrix} \Delta y \\ O \end{bmatrix}$$

This equation can be derived by the usual methods used in deriving (1.9). This method of working entirely with observables is preferable to (1.9) if the number of observations is only a little greater than the number of unknowns. For this reason, it was used by DMA/AC (ch. 3) and NASA/GSFC (ch. 5). (The method has certain dangerous aspects which must be well understood before it is used.)

(6.2) It is frequently possible to get, from previous solutions by oneself or others, values for and standard deviations of the unknowns being sought in the current computation. This information can be used to improve the current solution by applying directly to laws of propagation of errors (see, e.g., Anderson, 1958). However, a more interesting derivation, because it appeals to Bayes' theorem, is that of C. Goade in chapter 6. One must, of course, always be careful in using Bayes' theorem not to push the assumptions too far. One of these assumptions, seldom correct, is that the earlier information is from the same population as the later. Another, even less frequently satisfied, is that either the original information results from a sufficient sample of the population or the original plus later information will be sufficient samples. See the IEEE *Transactions on Reliability* (1972) for a thorough discussion of Bayes' theorem, its applicability, and its limitations.

(7) Finally, the validity of the results, the solutions for the unknowns, $[\Delta x]$, is tested by computing the covariance matrix $\sum^2_{\Delta x}$ of these quantities, using the well-known theorem that if

$$\underline{X}=\underline{\underline{D}}\,\underline{Y}$$

then

$$\sum_{\underline{X}}^{2}=\underline{\underline{D}}\sum_{\underline{Y}}^{2}\underline{\underline{D}}^{T}$$

The eigenvalues of $\sum_{\underline{X}}^{2}$ give the dimensions of the m-dimensional error ellipsoid. Usually, these are computed only for $m=2$ or $m=3$. (See chs. 9, 3, and 8.) The validity of the $\sum_{\underline{X}}^{2}$ matrix itself is, of course, another matter, and for $m>3$ this testing, which involves the Wishart distribution, is seldom done. Fortunately, most problems in satellite geodesy can be broken down into subproblems in which only 3×3 matrices are involved at any one step, and for these Fischer's t test or the X^2 test may be applied. See Anderson (1958), Cramer (1946), and Carlton (1962) for general discussion, and Baarda (1960) and Baarda and Alberda (1962) for geodetic applications.

1.4.1.1 Coordinate Systems

Geodesy per se is interested only in absolute or Euclidean systems of coordinates, that is, systems definable in terms of (accessible) points, distances, and directions, systems in which coordinates are defined in terms of distance and direction and can be measured in terms of the same fundamental units. The data and results of NGS (ch. 7) and OSU (ch. 8) have relevance primarily to such systems. Some of the data and results of SAO (ch. 9) also are in an absolute system, but because the geometric arrangement of the observing stations (ch. 9) is unfavorable to determination of corresponding coordinates, the system ultimately selected is a barycentric one (see below). Until the completion of NGS's and OSU's World Geometric Networks, a major disadvantage of absolute systems was that each geographically or politically isolated government set up its own system, and it was often impossible to find, accurately, the transformations between systems. As is known from elementary mathematics or physics, one Euclidean system is completely defined with respect to another if six quantities are given: three defining the location of the origin of the one system and three defining its orientation. These six quantities, plus two defining the size and shape of the spheroid to be used, are necessary and sufficient. A penetrating discussion of the geodetic significance of these quantities is given by Isotov (1968) and by Yeremeyev and Yurkina (1969).

1.4.1.2 Transformations

In satellite geodesy there is need for the following transformations:

Transformation of Coordinates
- (1) Geodetic coordinates ↔ Cartesian coordinates

Transformation between Systems
- (2) Geodetic (datum) ↔ Geodetic (datum)
- (3) Geodetic ↔ Astronomic
- (4) Geodetic (datum) ↔ Dynamic (datum)

(1) Transformation 1 is

$$\begin{bmatrix} X_1 \\ X_2 \\ X_3 \end{bmatrix}=\begin{bmatrix} (N+h)\cos\lambda\cos\phi \\ (N+h)\sin\lambda\cos\phi \\ [N(1-e^2)+h]\sin\phi \end{bmatrix}$$

and its inverse. Levallois (Levallois and Kovalevsky, 1971) describes an iterative method and a one-step approximate method of getting $\{\lambda, \phi, h\}$ from $[X]$; H. Schmidt (ch. 7) describes a one-step exact method.

(2) Conversion from a geodetic system (datum) to an astronomic system is a transformation between mutually rotating systems. The usual procedure is to convert from geodetic to Cartesian coordinates, rotate to bring the Z axis parallel to the instantaneous axis of rotation and the X axis parallel to the instantaneous meridian of Greenwich, then rotate about the Z axis, using the rate of rotation of the Earth; see, e.g., Mueller (1969) or Veis (1960).

(3) No exact transformation from a geodetic datum to a center of mass system is pos-

sible. However, an approximate transformation is possible when coordinates of at least three points are known in both systems. See chapters 5 and 8.

(4) A geodetic datum involves, in general, eight quantities. To effect a transformation from one datum to another, there must be known (measured) relations between the origin and orientation constants of one datum and those of the other. In general, these relations do not exist. When they are known, however, the transformation is usually accomplished by conversion of geodetic to Cartesian coordinates, rotation to an astrogeodetic system, translation to a new origin, rotation into the new datum, and conversion to geodetic coordinates with the new a and f. See, for example, Veis (1960).

1.4.2 Observation Equations

For convenience, the observation equations used in this volume are considered as belonging to static (geometric) satellite geodesy or to dynamic satellite geodesy. Since all observation equations are put in linear form before being used for computation, the division is not sharp. That is, the equations of dynamic satellite geodesy can be considered as an augmentation of those of static geodesy. The unknowns $\{\Delta X_s, \Delta Y_s, \Delta Z_s\}$, corrections to the satellite coordinates, are replaced by the unknown $\{\Delta a, \Delta e, \Delta i, \Delta\Omega, \Delta\omega, \Delta\sigma\}$, corrections to the orbital elements, and, in some cases, also by $\{\Delta C^m_n, \Delta S^m_n\}$, corrections to the coefficients $\{C^m_n, S^m_n\}$ in the expansions in Legendre series of the gravitational potential.

1.4.2.1 Static (Geometric) Satellite Geodesy

Only three kinds of geometry have arisen in the NGSP: (1) only directions to the satellite are measured; (2) only distances are measured, and (3) both distance and direction are measured. As far as the observation equations are concerned, only two kinds need be considered. One relates the measurements (x,y) of the image of a satellite to the coordinates X_o, Y_o, Z_o of the projection center of the camera and to the coordinates X_s, Y_s, Z_s of the satellite. Letting

$$R^2 \equiv (X_s - X_o)^2 + (Y_s - Y_o)^2 + (Z_s - Z_o)$$

and

$$r^2 \equiv x^2 + y^2 + f^2$$

where f is the distance of the projection center from the principal point, we have, first,

$$\begin{aligned} \xi &= \sum_{i,j} a_{ij} x^i y^j \\ \eta &= \sum_{i,j} b_{ij} x^i y^j \end{aligned} \tag{1.10}$$

where the a_{ij}, b_{ij} are constants (see chs. 1 and 5). Then

$$\begin{aligned} \xi/r &= (X_s - X_o)/R \\ \eta/r &= (Y_s - Y_o)/R \\ f/r &= (Z_s - Z_o)/R \end{aligned} \tag{1.11}$$

Linearized, these equations become

$$\begin{bmatrix} \Delta x \\ \Delta y \end{bmatrix} = [A] \begin{bmatrix} X_s \\ Y_s \\ Z_s \\ X_o \\ Y_o \\ Z_o \end{bmatrix} \tag{1.12}$$

The observation equation for observation of distance is

$$r^2 = (X_s - X_o)^2 - (Y_s - Y_o)^2 + (Z_s - Z_o)^2$$

and this, on linearization, also turns into an equation like (1.12).

Equations (1.11) appear in many forms—as projection equations (ch. 8) or as vector equations for the volume of a parallelopiped (chs. 3 and 5).

1.4.2.2 Dynamic Satellite Geodesy

Dynamic satellite geodesy (DSG) can be defined as that branch of satellite geodesy in

which the observation equations contain, as unknowns, orbital elements (or corrections thereto) of a satellite. It has been used principally where the arrangement of instruments used for observing does not allow simultaneous observations with strong geometry, for example, APL (ch. 2), NWL (ch. 3), JPL (ch. 4), NASA/GSFC (ch. 5), NASA/WFC (ch. 6), and SAO (ch. 9). However, it was used when the gravitational potential also had to be determined, as was necessary for NASA/GSFC and SAO. The constants determining this potential are easily added to the list of unknowns involved. (See, for example, Mueller, 1964; Kaula, 1966a; Arnold, 1968; Chapront-Touze, 1972.) A third reason for sometimes using DSG is that the precision of the resulting coordinates is higher than that obtained with static satellite geodesy. This can be seen, for example, by comparing the results of DOD/NWL (ch. 3) with those of NGS (ch. 7). One must be careful not to regard this higher precision as being, at present, a very important consideration. There are several reasons why the differences in precision are not indicative of better (i.e., more accurate) results, and these are discussed further in chapter 11.

1.4.2.2.1 THE BASIC EQUATIONS

Dynamic satellite geodesy starts with Newton's equation for the motion of a small body.

$$\begin{aligned} m\frac{d^2\mathbf{X}}{dt^2} &= m\nabla V+\mathbf{F}_{\text{atmosphere}}+\mathbf{F}_{\text{radiation}}+\mathbf{F}_{\text{luni-solar}} \\ &\quad +\mathbf{F}_{\text{electromagnetic}} \qquad (1.13) \\ &= m\nabla V+\mathbf{F} \end{aligned}$$

where $\mathbf{F}$ is the resultant of the individual forces $\mathbf{F}_{\text{atmospheric}}, \mathbf{F}_{\text{radiation}}, \mathbf{F}_{\text{luni-solar}}, \mathbf{F}_{\text{electromagnetic}}$, other than $m\nabla V$. The potential V is different from that of a spherical homogeneous solid but close enough to it that an expansion of V in a series of associated Legendre polynomials is practical:

$$V=\frac{k^2M}{a_o}\sum_{n=0}^{N}\sum_{m=0}^{n}\left(\frac{a_o}{r}\right)^{n+1}P_n^m(\sin\psi) \qquad (1.14)$$
$$[C_n^m\cos m\lambda+S_n^m\sin m\lambda]$$

The usual first step in solving (1.13) is to set

$$\mathbf{F}=0$$
$$\{C_n^m, S_n^m\}=0,\ n>0$$

The result is the "basic" equation of orbit theory and of dynamic satellite geodesy:

$$\frac{d^2\mathbf{X}}{dt^2}=\frac{GM\mathbf{X}}{r^3} \qquad (1.15)$$

where

$$r^2\equiv\mathbf{X}\cdot\mathbf{X}$$

This is the equation of motion of a particle in the field of a Newtonian (inverse-square) central force. The equation has an exact solution, which is simplest in a coordinate system defined as follows with respect to a rectangular coordinate system.

(1) Define the orientation of a certain set of axes by three Eulerian angles Ω, i, and ω. If the coordinates implicit in (1.15) are rotated through these angles, the new Z (X_3) coordinate disappears. Furthermore, the relationship between the new X_1 and X_2 coordinates can be shown to be

$$\frac{(\bar{X}_1-\bar{X}_1^o)^2}{a^2}+\frac{\bar{X}_3}{a^2(1-e^2)}=1 \qquad (1.16)$$

which is the equation of an ellipse with its major diameter (length $2a$) along the new X_1 axis, a minor diameter of $a(1-e^2)^{1/2}$, and its center at

$$\bar{X}_1^o=-\dot{a}e$$

(2) A final transformation is therefore made to a system specified by the constants a, e, and ν_o (the angle between the $\bar{X}_1$ axis and a radius vector to the particle at time T_o). In this system, only the time T is an independent variable. The angle ν, the true anomaly, is a complicated function of T, which is usually broken up into a sequence of three functions:

$$M\equiv\bar{n}(T-T_o) \qquad (1.17)$$

where $\bar{n}$, the mean motion, is a constant,

$$M = E - \sin E, \tag{1.18}$$

and

$$\cos \nu = \frac{\cos E - e}{1 - e \cos E} \tag{1.19}$$

The radius vector r is

$$r = \frac{a(1-e^2)}{1 + e \cos \nu} \tag{1.20}$$

This basic orbit is extensively used as a first approximation to the true orbit. It is also much used, as by DOD/AFCRL (ch. 3) and NASA/GSFC (ch. 5) as a curve for fitting to a short series of observations by one observer. Used in this way, the method is referred to as the "short-arc" method (see next section). Finally, the basic orbit was used by SAO for its "differential orbit improvement" (DOI) method (Veis and Moore, 1960; Izsak, 1961c; Gaposchkin, 1964). This method expresses the orbit as an empirical formula composed of two parts: a basic portion which is an analytic solution of (1.15) (or, in later developments, of the more general equations), and a series portion composed of power series and trigonometric series. The orbital elements a, e, i, Ω, ω, ν_o and the coefficients of the various terms in the series are determined from the data.

It should be noted that the expression of V as a series of associated Legendre polynomials (see Macmillan, 1930; Helmert, 1880-1884) is not the only form nor even the best. Lamé functions (Morse and Feshbach, 1953; Hobson, 1931) are theoretically more suitable for the gravitational potential near the surface of the earth, while expression as the result of surface layers (Orlin, 1959) is frequently used (Koch and Morrison, 1970; Morrison, 1972). Weightman (1967) proposed using point masses, and this procedure also has been used successfully.

1.4.2.2.2 SHORT-ARC METHODS

The short-arc method is a generalization, using dynamic geodesy, of the method used in static geodesy for getting rid of the time variable. In the static case, polynomials of low degree in the time t are fitted to the measurements $x(t)$ and $y(t)$

$$x(t) = \sum_1^n a_n t^n$$
$$y(t) = \sum_1^n b_n t^n \tag{1.21}$$

or to the satellite, coordinates $\alpha(t)$ and $\delta(t)$

$$\alpha(t) = \Sigma a_n t^n$$
$$\delta(t) = \Sigma b_n t^n \tag{1.22}$$

and so on. (See ch. 8 and Bialas, 1967.) In the dynamic case, the functions used are the equations of motion of the satellite

$$X = X(a, e, i, \Omega, \omega, \nu_o; t)$$
$$Y = Y(a, e, i, \Omega, \omega, \nu_o; t) \tag{1.23}$$
$$Z = Z(a, e, i, \Omega, \omega, \nu_o; t)$$

Because the time t covers an interval of only a few periods (and usually an interval considerably shorter than a full period), those perturbing forces which produce appreciable effects only after many revolutions can be neglected. So atmospheric drag, solar radiation pressure, and luni-solar gravitation do not enter into the equations. Nor need the high-degree terms in the Legendre series for terrestrial gravitation be included.

Equations (1.23) contain, besides the orbital elements, the constants that characterize the gravitational field. Under certain conditions, these also can be treated as unknowns.

1.4.2.2.3 PERTURBATIONS OF THE BASIC ORBIT

Methods and Terrestrial Gravitational Perturbations.—The basic orbit described above is inadequate for describing the motion of a satellite if an arc longer than about one-

eighth of a revolution is to be accurately computed. Methods which require use of orbits more complicated than the basic orbit are called "long-arc" methods. There are numerous variants, but three major varieties have been used by the investigators in the NGSP.

(1) The quasi-empirical method of SAO, the DOI method, was described previously in scetion 1.4.2.2.1.

(2) Equation (1.21) with appropriate expressions for the $\{\mathbf{F}_i\}$, can be left as is and integrated numerically. If the $\{\mathbf{F}_i\}$ involves only second-order or zero-order derivatives, Cowell's method (e.g., Brouwer and Clemence, 1961), which takes advantage of the fact that first-order derivatives are missing, can be used. Otherwise, more general methods of numerical integration must be used. Because the formulas involved are simple, are easily programed, and provide an accuracy dependent only on the size of the computing machinery available, this method was the choice of most investigators (chs. 2, 3, 4, 5, and 6).

Most investigators started with equation (1.21). A few, however, started with equation (1.23) and integrated the perturbations on this orbit.

(3) Equation (1.21) can be solved analytically, although not in closed form except for special cases. The usual procedure is to start with the basic orbit (sec. 1.4.2.2.1). If we denote the potential $(GM/a_o)(a_o/r)$ leading to the basic orbit by V_s and the perturbing potential by V_p, so that $V \equiv V_s + V_p$, and if we regard the orbital elements $(a, e, i, \Omega, \omega, M_o)$ as functions of time,

$$\{P_i\} = \left\{P_{i_o} + \frac{dP_i}{dt}\Delta t\right\} \qquad (1.24)$$

where P_i is one of the orbital elements and t is the time, then the coefficients dP_i/dt can be found from Lagrange's equations

$$\begin{Bmatrix} \frac{\partial}{\partial a} \\ \frac{\partial}{\partial e} \\ \frac{\partial}{\partial i} \\ \frac{\partial}{\partial \Omega} \\ \frac{\partial}{\partial \omega} \\ \frac{\partial}{\partial M_o} \end{Bmatrix} V_p =$$

$$\begin{Bmatrix} 0 & 0 & 0 & [a,\Omega] & [a,\delta] & [a,M_o] \\ 0 & 0 & 0 & [e,\Omega] & [e,\omega] & 0 \\ 0 & 0 & 0 & [i,\Omega] & 0 & 0 \\ [\Omega,a] & [\Omega,e] & [\Omega,i] & 0 & 0 & 0 \\ [\omega,a] & [\omega,e] & 0 & 0 & 0 & 0 \\ [M_o,a] & 0 & 0 & 0 & 0 & 0 \end{Bmatrix} \begin{Bmatrix} \frac{da}{dt} \\ \frac{de}{dt} \\ \frac{di}{dt} \\ \frac{d\Omega}{dt} \\ \frac{d\omega}{dt} \\ \frac{dM_o}{dt} \end{Bmatrix}$$

Here [ ] denotes Lagrangian brackets,

$$[\rho_i, \rho_k] \equiv \sum_j \left(\frac{\partial q_j}{\partial \rho_i}\frac{\partial q_j}{\partial \rho_k} - \frac{\partial q_j}{\partial \rho_i}\frac{\partial q_j}{\partial \rho_k}\right) \qquad (1.26)$$

This equation (1.26) was used extensively by Murphy and Felsentreger (ch. 5) for their analysis of perturbations caused by lunar and solar gravitation and by solar radiation pressure and by SAO (ch. 9) for development of their equations. (See also Gaposchkin, 1966c.)

Unlike the theory involving solution by numerical integration, that involving analytic solutions is extremely complicated even for motion of a single particle in a given force field. General treatises like those of Wintner (1941), Siegel (1956), Tisserand (1960), Brouwer and Clemence (1961), Stumpf (1959, 1965), and Hagihara (1972) are valuable for the fundamentals but are primarily concerned with motion of a particle in the Newtonian gravitational fields of other particles. Dynamic satellite geodesy is pri-

marily interested in motion of a particle in a non-Newtonian field, and for this theory the works of Mueller (1964), Kaula (1966b), A. H. Cook (1967), and Levallois and Kovalevsky (1971) are more useful.

The basis of dynamic satellite geodesy was laid by D. Brouwer in his papers of 1946, 1958, and 1959, in which he proceeded from Delauney's form of the Hamiltonian equations using a method of successive approximation called von Zeipel's method. (See Hutcheson, 1964; see also Lyddane and Cohen, 1962, for comparison with numerical integrations.) This same method was used later by Kozai (1962b), and Kozai's equations were adopted by SAO for the zonal harmonics (Gaposchkin, 1966c). For orbits involving tesseral harmonics, one generally proceeds from Lagrange's equations, as did Kaula (1961a), whose method was also adopted by SAO.

Besides these methods, which are the most important ones for the NGSP, a number of other methods have been used for DSG. The most important of these is that of King-Hele (1964; A. H. Cook, 1967), which has been used in England very successfully for both close and distant satellites. Hansen's theory as applied to Earth's satellites by Musen (1954, 1961) and Bailie and Bryant (1960) has not yet been much used. Nor have most of the theories designed to deal with particular kinds of orbits, such as those with small e or i (Kozai, 1961b; Izsak, 1961a; Lyddane and Cohen, 1962), large i (Cunningham, 1957), or i near the vertical inclination (Hori, 1960; Hagihara, 1961a; Lubowe, 1969), been extensively used. Most of the problems involving singularity in coordinates can be eliminated, in analytic solutions, by choice of a nonsingular set. (See, e.g., Eckert and Brouwer, 1937; Newton, 1961; Cohen and Hubbard, 1962; Lyddane, 1963; Musen, 1963b.)

The basic orbit (sec. 1.4.2.2.1) is not the only closed solution to equation (1.13). If spheroidal coordinates are used, a solution in closed form for more general U involving the C_4^0 coefficient can be found. This was first suggested by Sterne (1958), investigated by Garfinkel (1958, 1959), and put into elegant and final form by Vinti (1959, 1961).

Other Perturbations.—Besides the gravitational attraction of the Earth as a rigid body, there are a number of other forces acting on the satellite. One of these is a fictitious force originating in the deformation of the earth by the attraction of the sun and moon. The deformed Earth exerts a different force than a rigid Earth does, and the amount of deformation is a function of Love's number, k_2, which is a measurement of the rigidity of the solid Earth; k_2 can be taken as one of the unknowns to be solved for. The first values, based on tracking data, were found by Kozai (1965, 1968a) and Newton (1960). More recent work by Anderle (DOD) is reported in chapter 3 and by D. Smith (NASA/GSFC) in chapter 5. See also Musen and Estes (1972) for another viewpoint. Other forces of appreciable size which are usually taken into account are summarized in table 1.34 of the appendix.

In regard to solar radiation pressure, note that the equation accounts only for radiation direct from the sun. Radiation reflected by or otherwise coming from the Earth is not included. Studies of the effect of this secondary radiation, especially in the ECHO and PAGEOS satellites, have been made by, among others, Wyatt (1963), D. Smith (1969), and Prior (1970).

Other sources of perturbation are relativity (McVittie, 1963; Gilvarry, 1959; Krause, 1964; Jenkins, 1969 and 1971; Moyer, 1971) and, since a satellite is an extended body, the gravitational gradient (Chin, 1962; Fleig, 1970).

Polar motion is not a perturbating force, but is in the nature of a variation in the coordinate system used. It can be measured if the observing systems are sufficiently precise. The theory is given by, among others, Munk and MacDonald (1960), Fedorov (1963), and Woolard (1953); a survey is given by Gaposchkin (1966). Rikhlova (1969) gives a summary of polar motion for 119 years. Determination from tracking data is discussed here by D. Smith (ch. 5) and

R. Anderle (ch. 3) while still further information is available in Lambeck (1971a), Beuglass and Anderle (1972), Kane (1972), D. Smith *et al.* (1972a), and Melchoir *et al.* (1972).

Resonance.—One important exception to the statement above that theories concerned with special kinds of orbits have been little used in the NGSP is the theory dealing with orbits whose periods have some simple ratio to the length of a day. For such orbits, the satellite finds itself at equal intervals of time above the same part of the gravitational field, and resonance is thereby induced in the satellite motion. Even very small gravitational forces can then build up into respectable perturbations on the orbit. This effect was first pointed out by A. Cook (1960, 1961); its presence in orbits of 24-hour period was analyzed by Blitzer *et al.* (1962) and Morando (1963). It was used for finding various tesseral harmonic coefficients by Yionoulis (1965, 1966a) and Anderle (1965a) and has been extensively used since then by many other researchers. (See, for example, Wagner and Douglas (1970), Cazenave *et al.* (1972b), Gedeon *et al.* (1967), and Allan (1964, 1965, 1967); see also chapter 2.)

Comprehensive studies of perturbation of orbits of Earth satellites were made by Porter (1958) and Challe and Laclaverie (1969).

Numerical Integration.—Of the various contributors to the NGSP, only SAO places its entire dependence on literal functions as solutions to the differential equations of motion (Lundquist and Veis, 1966). NASA/GSFC uses literal functions only for projects of special purpose. The other contributors all depend on numerical integration to solve the differential equations. The theory of numerical integration is simple in concept. It is in essence the fitting of a polynomial to a small set of consecutive points and the extrapolation of the polynomial to give one further point. The process is then repeated as often as desired. The coefficients of the extrapolation polynomial are determined by (1) the set of points already given and (2) the derivatives of these points as given by the equations of motion. Theories differ according to the number of data points required, the distances which a point is extrapolated, the fitting process used, and so on. These theories are treated at great length in many texts. Among the best of these is that of Henrici (1962), which goes into great detail about the errors caused by integration. Other excellent sources are Scarborough (1966), Collatz (1966), Milne (1949), and Buckingham (1966). The methods used in this volume are listed in table 1.35 of the appendix. A useful analysis of the stability of the major procedures is given by Lomax (1967). The Runge-Kutta method (Runge, 1895; Kutta, 1899) becomes too complicated for easy programming if the order is higher than 4. Rosen (1965) and Fehlberg (1966a, b, 1969) have done much to generalize the method and work out the specific equations for higher order.

1.4.3 Condition Equations

The use of condition equations is for the most part straightforward and was treated in an earlier section. A more detailed exposition of the various kinds is given by J. Reece in chapter 5. One kind which deserves special comment, however, is that of "inner constraint" used by OSU (Blaha, 1971; ch. 8). The condition imposed is that the trace of the normal equation be a minimum. This is equivalent to selecting an origin and orientation of the coordinate system which depend on the assemblage of points. It results in smaller σ's for the unknowns. The method is perfectly valid but its usefulness may be limited. (See, for example, ch. 11.)

1.4.4 The Geoid

At present, geoidal heights, N, are not among the unknowns present in the observation equations of either static or dynamic satellite geodesy. However, they do appear in OSU's work in the condition equations used for determining the size and flattening of the best fitting ellipsoid (ch. 8) and are

used for the same purpose but in a different way by NASA/GSFC (ch. 5). In this work, N has been determined either by solving equation 1.24 for r, after adding on the centrifugal force and deciding on a value $W_o \equiv V_o$ + centrifugal force and then subtracting the length of the radius vector to the spheroid (see, for example, ch. 5) or by using Stokes' formula or some modification thereof. A slightly different procedure is that by which Rapp (ch. 3) derived his geoids. A geoid based on isostatic anomalies is given by Kahn in chapter 5.

The theory of the geoid since Bruns (1878) and Sludskii (1888) and of geops (equipotential surfaces in general) even yet is not completely rigorous. Excellent treatments are those of Hirvonen (1962), Bjerhammar (1962), Hunter (1960), Egyed (1964), and Zhongolovich (1956, 1962).

Note that part of the reason for disagreement on geoidal heights lies in the fact that there is still no universal agreement on what a geoid is (as was obvious from proceedings of a 1973 GEOP conference). The original definition as "that equipotential surface which best fits mean sea level on the oceans" became inadequate when geoidal heights could be determined so precisely that a significant difference could be found between mean sea level and the defined geoid. Another part lies in the method of determining the geoid, i.e., from tracking data, gravimetric data, or astrogeodetic data. Only the first two of these methods have been used in the NGSP; astrogeodetic geoids have been used as checks on the others. (See, for example, ch. 5.)

APPENDIX

TABLE 1.1.—*Datums Controlling More Than 200 000 Square Km*

Datum	Area controlled (millions of sq km)	Regions involved	Origin (horizontal control)	Connections to other datums
NAD 1927	24.4	Canada, U.S.A., Mexico, Central America	Meades Ranch, Kansas	SAD, European 1950
Pulkova 42	17.1	USSR	Pulkova Observatory	European 1950
European 1950	10.7	Europe, Near East	Helmert Tower Potsdam, Germany	NAD 1927, Indian Cape, Pulkova
Peiping 1954	9.60	China	Peiping	Tokyo Datum
SAD	9.13	All South America Except Argentina	La Canoa, Venezuela	NAD 1927
Australian	7.80	Australia, New Guinea	Johnston Geodetic Station	SW and Central Pacific Islands, Papua
Cape	5.02	South Africa	Boffelsfontein	European 50
Indian	4.38	India, Thailand, Burma	Kalianpur	European 50
Blue Nile	3.74	Ethiopia, Sudan	Station 15, Adindan baseline	European 50
Argentinean	2.70	Argentina	S.E. end of Castelli Base	SAD 1969
Angola	1.25	Angola	Camp de Avinco	
Manchurian Principal	1.10	Manchuria	Shinkyo	Tokyo Datum
Nigerian	0.928	Nigeria	Menna	----------
----------	0.590	Malagasy	----------	----------
Tokyo	0.369	Japan	Tokyo Observatory	Manchurian, Peiping
Malayan Revised	0.333	Malaysia	Kertau	Luzon
Luzon	0.302	Philippines	Arbitrary	Malaysian
Guinean	0.260	Guinea	Conakary	----------
Papataki	0.258	New Zealand	Papataki	----------

TABLE 1.2.—*Tracking Stations Planned for 1958*

PRIME MINITRACK	Baker-Nunn Cameras
1001 Blossom Point, Maryland[a]	9001 Las Cruces, New Mexico
Fort Stewart, Georgia[a]	9012 Maui, Hawaii
1005 Quito, Ecuador[a]	9007 Arequipa, Peru
1006 Lima, Peru[a]	9011 Villa Dolores, Argentina
1007 Antofagasta, Chile[a]	9002 Olifantsfontein, South Africa
1008 Santiago, Chile[a]	9004 San Fernando, Spain
	9006 Naini Tal, India
	9008 Shiraz, Iran
	9003 Woomera, Australia
	9005 Tokyo, Japan
	9010 Jupiter, Florida
	9009 Curacao, Neth. Antilles

[a] Stations functioning at the beginning of 1958.

TABLE 1.3.—*Coefficients of Gravitational Potential Terms* ($\times 10^6$)

C_n^m/S_n^m

n,m	1927 (De Sitter)	1941 (Jeffreys)	1948 (Jeffreys)	1957 (Zhongolovich)
2, 0	1092.5 ± 0.7	1091.8 ± 4.2	1089.7 ± 2.1	-----
2, 2	----------	----------	+4.1 ± 1.4	+4.74
				−1.58
3, 0	----------	----------	----------	-----
3, 1	----------	----------	+3.1 ± 1.2	+1.99
				−0.96
3, 2	----------	----------	+0.66 ± 0.35	+0.36
				−0.50
3, 3	----------	----------	2.0 ± 1.1	+0.42
			0.13 ± 0.08	−0.34
4, 0	----------	----------	----------	-----
4, 1	----------	----------	----------	−0.67
				−0.40
4, 2	----------	----------	----------	0
				+0.08
4, 3	----------	----------	----------	+0.05
				−0.01
4, 4	----------	----------	----------	+0.01
				+0.02

TABLE 1.4.—*Significant Geodetic Events Between 1957 and 1965*

Date	Event	Name	Scale
1957	Launching of Sputnik–1	----------	Global
1958	Flattening from satellite data (1/298.3)	O'Keefe, Marchant, and Herz; Buchar, King-Hele	Global
1958	Launching of Explorer–1	----------	Global
1959	Third Zonal Harmonics	O'Keefe, Eckels, and Squires	Global
1959	Theory of motion of artificial satellite	Brouwer	None (math.)
1960	Launching of TRANSIT–1B	----------	Global
1960	Launching of ECHO–1	----------	Global
1960	Theory for satellite orbits	Kaula	None (math.)
1962	Launching of ANNA–1B	----------	Global
1962	Connection of France-Algeria	IGN	Continental
1965	APL geodetic constants 4.5	APL	Global
1965	Connection of Europe-Azores	IGN	Continental

TABLE 1.5.—*Shifts in Datum Points (Kaula, 1963b)*[a]

Datum	Shift in coordinate (meters)					
	Δx		Δy		Δz	
NAD 1927	−24	±6	−32	±5	−3	±1
European 1950	+37	±4	−56	±3	+13	±1
Australian	−111	±10	+33	±12	+67	±3
Tokyo	−57	±3	+60	±4	+10	±5
Argentine	+245	±10	−15	±4	+37	±23
Hawaiian	−26	±10	+59	±17	−291	±24

[a] These values are shifts from a system with center at center of mass of the Earth, x, y, z axes directed toward 0°, 0°, and 90° N, respectively (Kaula, 1963a).

TABLE 1.6.—*Status of Gravitational Potential in 1964*

Date	Determined by	Zonals	Principal Tesserals	Other
From tracking data				
1964	Kozai	C_2^0 to C_{14}^0	----------	----------
1968	Anderle	C_2^0 to C_7^0	C_2^1, S_2^1 to C_7^6, S_7^6	$C_{13}^{13}, C_{15}^{13}, C_{15}^{14}$ $S_{13}^{13}, S_{15}^{13}, S_{15}^{14}$
From gravimetry				
1962	Uotila	----------	C_2^2, S_2^2 to C_4^4, S_4^4	---------- ----------
1964	Uotila	C_{36}^0	C_2^1, S_2^1 to C_{36}^{36}, S_{36}^{36}	---------- ----------

TABLE 1.7.—*Satellite-Tracking Systems Used in NGSP*

Type	Satellites	Measured	Used by
Camera, PC–1000	Bright reflectors or beacons	Angles	DOD
Camera, MOTS	Bright reflectors or beacons	Angles	GSFC
Camera, BC–4	Bright reflectors or beacons	Angles	NGS,DOD
Baker-Nunn	All	Angles	SAO, DOD
Radar, 5-cm	GEOS	Distance	WFC, DOD
MINITRACK	All with MINITRACK beacon	Angles	GSFC
SECOR	SECOR and GEOS	Distance	DOD
GRARR	GEOS	Distance and Doppler-shift	GSFC
Laser DME	Reflecting	Distance	DOD,GSFC,SAO
TRANET FME	GEOS, Navigation	Doppler-shift	DOD

TABLE 1.8.—*Geodetically Important Characteristics of a Satellite*

Characteristic	Effect
Structural	
Reflectivity	Affects signal-to-noise ratio at a receiver
Mass/area ratio	Affects size of atmospheric-drag and solar-radiation-pressure perturbations
Shape	Affects atmospheric-drag perturbations and radiation pressure perturbations
Instrumental	
Active or passive	Has big effect on instrumentation design, on distance at which satellite can be detected, etc.
Type of stabilization	Affects visibility and may affect frequencies in signal
Frequency and type of signals	Determines what kind of tracking-station is needed
Orbital	
Apogee/perigee	Affects signal-to-noise ratio, how many stations can observe simultaneously, and length of time satellite is visible; also satellite sensitivity to gravitation
Inclination	Determines, along with apogee/perigee heights, those zones of earth from which satellite is visible; also affects satellite sensitivity to certain zonal harmonics
Period	Helps determine frequency of observation, extent of resonance between satellite period and earth's rotation

TABLE 1.9.—*Characteristics of Satellites*

Satellite	Date of launch	Elements of initial orbit			Period (minutes)	Height (km) at perigee	Mass (kg) / Area (m^2) [a]	Geodetic Instruments[b]	Stabilization[c]
		a (km)	e	i (degrees)					
SAS-1 (1970-107A)	12 Dec 1970	6922.505	0.002	3.0	95.6	530	79.5 / 0.4	MR	MAG
DIAL (1970-17A)	10 Mar 1970	7344	0.09	5.4	104.4	310	61.7 / ---	CC	ROT
PEOLE (1970-109A)	12 Dec 1970	7006.155	0.02	15.0	97.3	530	55 / ---	CC	GG
Courier-1B (1960 ν1)	4 Oct 1960	7474.289	0.017	28.3	107	965	227 / ---	MR	----
TRANSIT-3B (1961 η)	22 Feb 1961	6876	0.04	28.4	94.5	187	110 / 2.8	DR	MAG
Explorer-2 (1961 ν)	27 Apr 1961	7509	0.086	28.8	108	490	43 / 0.3	MR	NS
Pegasus-3 (1965-60A)	30 Jul 1965	6906	0.002	28.9	95.2	483	10 430 / ---	MR	NS
LCS-1 (1965-34C)	6 May 1965	9162	0.00	32.1	145.6	2788	34 / ---	NI	NS
TRANSIT-4B (1961 $\alpha\eta$1)	5 Nov 1961	7415	0.013	32.4	105.6	970	90 / 0.4	DR	MAG
OSO-3 (1967-20A)	8 May 1957	6916	0.002	32.9	45.4	910	281 / ---	MR	MAG ROT JET
Vanguard-2 (1959 α1)	17 Feb 1959	8306.760	0.165	32.9	126	557	9.3 / 0.2	MR	NS
Explorer-1 (1958 α)	1 Feb 1958	8157	0.18	33	114.8	358	8.3 / 0.15	MR	NS
Vanguard-3 (1959 η)	18 Sep 1959	8433	0.190	33.4	130	510	23 / 0.2	MR	NS
Vanguard-1 (1958 β2)	17 Mar 1958	8680	0.19	34.1	133.8	691	1.5 / 0.2	MR	NS
Explorer-9 (1961 δ1)	16 Feb 1961	7960	0.121	38.9	118	636	6.8 / 1.6	MR	NS
DIADEME-2 DI-D (1967-14-01)	15 Feb 1967	7337	0.052	39.5	109.2	591	22.7 / 0.3	DR CC MR	MAG ROT

TABLE 1.9.—*(Cont'd)*

Satellite	Date of launch	Elements of initial orbit			Period (minutes)	Height (km) at perigee	Mass (kg) / Area (m^2) [a]	Geodetic Instruments[b]	Stabilization[c]
		a (km)	e	i (degrees)					
DIADEME-1 DI-C (1967-11-01)	8 Feb 1967	7336	0.053	39.9	104.3	557	22.7 / 0.13	CC MR	MAG ROT
BE-C (Explorer-27) (1965-32A)	29 Apr 1965	7311	0.026	41.1	108	927	54 / ---	DR CC	MAG
TELSTAR-1 (1962 $\alpha\epsilon$)	10 Jul 1962	9669.530	0.242	44.8	158	950	77 / 0.6	MR	ROT
ECHO-1 Rocket (1960 $\iota 2$)	12 Aug 1960	7568.579	0.011	47.2	118	1501	---	NI	NS
ECHO-1 (1960 $\iota 1$)	12 Aug 1960	8966	0.01	47.2	118.3	1524	76 / 700	MR RF	NS
RELAY-1 (1962 β)	13 Dec 1962	10 736	0.284	47.5	184.9	1317	78.2 / ---	N/A	ROT
GRS (1963-26A)	28 Jun 1963	7228.289	0.060	49.7	102.1	421	100 / ---	SR	ROT
ANNA-1B (1962 $\beta\mu 1$)	31 Oct 1962	7504.951	0.008	50.1	107.8	1080	250 / 1.5	FL DR MR SR	MAG
TRANSIT-1B (1960 $\gamma 2$)	13 Apr 1960	6936	0.03	51.28	95.8	379	125 / 0.5	DR	MAG
TIROS-6 (1962 $\alpha\psi 1$)	18 Sep 1962	8020.761	0.026	58.1	120	590	128 / 0.5	MR	ROT
TIROS-7 (1963-24A)	19 Jun 1963	7003	0.003	58.2	97.4	615	130 / ---	MR	ROT MAG
GEOS-1 (Explorer-29) (1965-89A)	6 Nov 1965	8067.354	0.080	59.4	120.3	1115	175 / 1.23	DR GR SR CC FL	GG
Elektron-3 (1964-38A)	11 Jul 1964	10 080	0.34	61	168	408	------	N/A	----
DOD (1963-55A)	21 Dec 1963	6607	0.001	64.9	89.3	173	------	N/A	----

TABLE 1.9.—*(Cont'd)*

Satellite	Date of launch	Elements of initial orbit			Period (minutes)	Height (km) at perigee	Mass (kg) / Area (m^2) (^{a})	Geodetic Instruments^b	Stabilization^c
		a (km)	e	i (degrees)					
Sputnik–1 (1957 α)	4 Oct 1957	6959	0.052	65	96.1	227	83.6 / 1	N/A	NS
INJUN–1 (1961 $o2$)	29 Jun 1961	7313.542	0.008	66.8	103.8	895	93 / ---	MR	MAG
TRANSIT–4A (1961 $o1$)	29 Jun 1961	7321.522	0.008	66.8	103.8	880	79 / 0.4	DR	MAG
TRANSIT–2A (1960 $\eta 1$)	22 Jun 1960	7221	0.03	67	102	630	101 / 0.5	DR	MAG
EGRS–5 (1965–63A)	10 Aug 1965	8194.970	0.080	69.2	122.2	1140	20 / 0.02	DR SR	MAG
Agena Rocket (1969–1A)	11 Jan 1964	7297.252	0.001	69.9	103.5	920	-------	NI	NS
DOD Vehicle (1964–1A)	11 Jan 1964	7301	0.002	69.9	103.5	921	-------	-----	----
TIMATION–2 (1969–082B)	30 Sep 1969	7289	0.002	70	103.5	905	-------	DR	----
EGRS–3 (1965–16E) (SECOR–3)	9 Mar 1965	7289.5	0.003	70.1	103.5	900	18 / 0.02	SR	MAG
FR–1 (1965–101A)	6 Dec 1965	7126	0.001	75.9	99.9	740	60 / ---	MR	ROT
Explorer–19 (1963–53A)	19 Dec 1963	7857	0.11	78.6	115.9	589	8 / 10.5	MR	NS
BE–B (Explorer–22) (1964–64A)	10 Oct 1964	7354.785	0.014	79.7	105	874	53 / ---	DR CC	MAG
ALOUETTE–2 (1965–98A)	28 Nov 1965	8097.474	0.151	79.8	125	502	145 / 0.7	MR	ROT
ECHO–2 (1964–4A)	25 Jan 1964	8267	0.03	81.5	108.8	1029	256 / 1260	MR RF	NS
PAGEOS (1966–56A)	24 Jun 1966	10 614.790	0.0025	87.1	181.4	4207	54 / 700	RF	NS
OGO–2 (1965–81A)	14 Oct 1965	7345.634	0.074	87.4	104.4	424.8	450 / --	MR	GG JET

TABLE 1.9.—*(Cont'd)*

Satellite	Date of launch	Elements of initial orbit			Period (minutes)	Height (km) at perigee	Mass (kg) / Area (m^2) ([a])	Geodetic Instruments[b]	Stabilization[c]
		a (km)	e	i (degrees)					
DASH-2 (1963-30-D)	19 Jul 1963	9342	0.074	88.4	168	2280	-------	-----	----
ISIS-1 (1969-9A)	30 Jan 1969	8240	0.175	88.4	128.2	586	241 / 0.5	MR	ROT
MIDAS-7 (1963-30A)	19 Jul 1963	9337	0.074	88.4	167.9	2277	1032 / 3.5	N/A	ROT
OSCAR-7 (1966-$o\zeta$A)	28 Jan 1966	7404.041	0.024	89.7	105.6	868	60 / 0.98	DR	GG
5 BN-2 (1963-48C)	6 Dec 1963	7463.227	0.0058	89.95	106.9	1062.5	75 / 0.5	DR	GG MAG
DOD Vehicle (1963-49B)	5 Dec 1963	7477	0.004	90.0	107.2	1108	-------	DR	----
EGRS-7 (1966-77B)	19 Aug 1966	10 057	0.001	90.11	167.6	3679	20.4 / 0.02	SR	MAG
MIDAS-4 (1961 $\alpha\delta$1)	21 Oct 1961	10 005	0.012	96	166	3496	1576 / 7	N/A	ROT
TIROS-9 (1965-4A)	22 Jan 1965	8020.761	0.117	96.4	119.2	690	139 / 0.6	MR	ROT
ESSA-1 (1966-8A)	3 Feb 1966	7141	0.010	97.9	100.1	710	135 / 0.6	MR	ROT

TABLE 1.9.—*(Cont'd)*

Satellite	Date of launch	Elements of initial orbit			Period (minutes)	Height (km) at perigee	Mass (kg) / Area (m^2) ([a])	Geodetic Instruments[b]	Stabilization[c]
		a (km)	e	i (degrees)					
GEOS-2 (Explorer-36) (1968-2A)	11 Jan 1968	7710.807	0.031	106	111.6	1084	213 / 1.3	MR,GR, RR, SR, RFR, DR, FL	GG
OVI-2 (1965-78-01)	15 Oct 1965	8314.7	0.164	144.3	126	418	170 / ---	N/A	ROT
EGRS-9 (1967-65A)	29 Jun 1967	10 237	0.007	172.1	172.1	3794	20.4 / 0.02	SR	MAG

[a] Cross-sectional area in direction of motion. Many of the satellites have complex surfaces and change orientation with respect to direction of motion. Areas are not usually given for such satellites or, if given, are estimated maxima.

[b] CC Corner-cube reflector
DR Doppler beacon
FL Flashing light
GR Grarr transponder
MR MINITRACK radio (sometimes used primarily for telemetry)
NI Not instrumented
RF Reflecting surface
RFR Radar reflector
RR Radar transponder
SR Secor transponder
N/A Instrumentation not used geodetically or unknown

[c] GG Gravity-gradient stabilized
MAG Magnetically stabilized
ROT Stabilized by rotation
NS Not stabilized
JET Orientation partly or entirely controlled by jet engines

TABLE 1.10.—*Characteristics of Satellite-Tracking Equipment*

Type	Precision/Accuracy/Direction	Meteorological Requirements	Portable/ Fixed	Users[a]
1000–mm camera	± 10 m/transverse	Darkness; clear weather	Portable	DMA/AC (3.2.1) NASA/GSFC (5.2.1)
450–mm camera	± 5 m/transverse	Darkness; clear weather	Portable	NGS (7.2)
300–mm camera	± 5 m/transverse	Darkness; clear weather	Portable	NGS (7.2)
Baker-Nunn	± 10 m/transverse	Darkness; clear weather	Fixed	SAO (9.2.1)
Radar FPS–16	± 1 m / ± 2–5 m /radial	Any conditions except thunderstorm	Fixed	NASA/WFC (6.2) USAF (6.2)
Radar FPR–6	± 1 m / ± 2–5 m /radial	Any conditions except thunderstorm	Fixed	NASA/WFC (6.2) USAF (6.2)
MINITRACK	± 100 m / ± 300 m /transverse	Not effective in rain or thunderstorm, nor in times of very active sun	Fixed	NASA/GSFC (5.2.2)
SECOR	± 5–10 m/radial	Not effective in thunderstorm	Portable	DMA/TC (3.2.3)
FME (TRANSIT)	± 2 cm/sec (radial)	Not effective in thunderstorm	Portable	APL (2.2) NWL
GRARR	± 5 m/radial	Not effective in thunderstorm	Fixed	NASA/GSFC (5.2.3)
Laser DME	0.2 m / 1.0–2.0 m /radial	Clear weather	Portable	SAO (9.2.2) AFCRL (3.2.2) NASA/GSFC (3.2.2)

[a] Numbers in parentheses refer to sections in subsequent chapters.

TABLE 1.11.—*Camera Characteristics*

Focal length (cm)	Field of view (deg)	Aperture (cm)	Type	Mounting	Shutter	Designation	Originator	Stations at which used	References	Additional comments
103.13	5° × 5°	34.0	Schmidt-Vaissala	----------	---------	Schmidt-Vaissala	Finnish Geodetic Institute	Finnish Geodetic Stations, Upsala (8000)	Jaernefelt (1961)	Used for Vaissala-type triangulation
101.6	11° × 14°	20.3	Aerial reconnaissance	Equatorial	Inter-lens	MOTS 40	NASA/GSFC	See chapter 5	Berbert *et al.* (1963); Harris *et al.* (1963); see chapter 5	27μ
101.6	10°	20.3	Aerial reconnaissance	Fixed	Inter-lens	PTH–100	----------	See chapter 3	Williams (1963)	27μ
100.0	15°	25.0	Aerial reconnaissance	Fixed and tracking	Rotating	K–50 (modified) (geodetic 36)	SAO J. G. Baker and Perkin-Elmer)	Atlas, Greece	----------	Temporary use only
100.0	10° × 10°	20.0	Aerial reconnaissance	Fixed	Rotating	PC–100	USAF	See chapter 3	Williams (1963); see chapter 3	27μ

TABLE 1.11.—*(Con'd)*

Focal length (em)	Field of view (deg)	Aperture (cm)	Type	Mounting	Shutter	Designation	Originator	Stations at which used	References	Additional comments
76.0	11.3°	42.5	Schmidt	Tracking 4-axis	Capping only special device for trial interpretation	SBG 420/500 760	Carl-Zeiss Jena	----------	Steinbach 1967	---------
73.6	10° × 14°	21.0	URAN-16	Equatorial 4-axis	---------	AFU-75	Riga U.	EEST network (9431, 9432, 9434)	Massevich and Lozinsky (1970)	---------
70.0	35.0°	50.0	Astrotar lens and mirror	3-axis paralactic	Rotating	VAU	Moscow	----------	Massevich and Lozinsky (1970)	Mirror 107-cm diameter
61.0	18 × 23	10.2	Aerial reconnaissance lens assembly	Equatorial	Inter-lens	MOTS 24	NASA/ GSFC	No longer used	----------	----------
60.0	10°	63.0	Schmidt (modified)	Altazimuth	Rotating	Grubb-Parsons Hewitt f/1	RAF	Malvern, England	Hewitt (1960, 1965)	30μ circle of least confusion

TABLE 1.11.—*(Cont'd)*

Focal length (em)	Field of view (deg)	Aperture (cm)	Type	Mounting	Shutter	Designation	Originator	Stations at which used	References	Additional comments
60.0	20°	17.0	Aerial reconnaissance camera	Fixed	Inter-lens	K–17 (modified)	----------	WEST stations	----------	----------
50.0	5° × 30°	50.0	Schmidt (modified)	Equatorial altazimuth	Focal surface	Baker-Nunn	SAO	See sec. 1.2 and chapter 9	Henize (1957), Brandenberger (1962)	20μ circle of least confusion, 50% transmission
46.3	31°	23.0	–10 ASTRO-TOPAR	Equatorial	Rotating	BMK 46/18/1:2	Zeiss-Jena; Tech. U. Berlin	Tech. U. Berlin	Schwebel (1970), Hirsch (1970), Seeber and Campbell (1972)	4–mm maximum distortion
45.0	22° × 22°	11.5	Aerial mapping lens assembly	Fixed	Rotating	BC–4 COSMOTAR	Wild/ Heerbrug USC and GS	See chapter 7	See chapter 7	20μ longer focal length version of BC–4
30.3	33° × 33°	11.5	Aerial mapping lens assembly	Fixed	Rotating	BC–4 ASTROTAR	Wild/ Heerbrug USC and GS	USC and GS program stations; see sec. 1.2 and chapter 7	Taylor (1963); see chapter 7	20μ

TABLE 1.12.—*Factors Affecting Precision and Accuracy of Measuring Engine*

1. Method of calibration
2. Stability of instrument as function of
   a. Time
   b. Temperature
   c. Position of carriage
3. Method for identifying points
   a. Human observer
   b. Impersonal observer
4. Treatment of data
5. Resolution

TABLE 1.13.—*Characteristics of PRIME MINITRACK*

Baseline length	125.5 m	Polar fine	
	101.4 m	Equatorial fine	
Resolution	0.1 milliradian		
Calibration	Against beacon carried in airplane located by camera		
Beamwidth	10° E–W, 100° N–S	or	100° N–S, 10° E–W
Phase equation	$\delta\theta = [\lambda/(2\pi\rho \cos \theta)]\, d\phi$		
Perturbations			
Ionosphere	Large		
Troposphere	Small		
Array alignment	Calibrated		
Cable lengths	Calibrated		
Phase-measurement error	Calibrated		

TABLE 1.14.—*Characteristics of DME*

	Type			
	5-cm Radar	Laser DME	SECOR	GRARR
Carrier frequency (MHz)	5400–5900	4.32×10^5	449 224.5	1500
Pulse or CW	Pulse	Pulse	CW	CW
Power output (kW)	250, 100[1], 2500[2]	1000–500 000	2	10
Maximum range (m)	[a]2 000 000[1] [a]60 000 000[2]	----------	5000 But depends on transponder	400 000 km
Precision (m)	±1 m	±0.2–±1	---------	----------
Accuracy (m)	±2–5	±0.5–2	[b]3–10 m	----------
Resolution	0.5 m	0.1 m	0.25 m	15 m
Used by	NASA, DOD	NASA, DOD, SAO	DOD	NASA

[a] Barton (1964)
[b] Prescott (1965) unpublished

TABLE 1.15.—*Characteristics of Typical Laser DME* (6943 Å)

	NASA/GFSC (Chapter 5)	CNES	SAO (Chapter 9)	AFCRL[a] (Chapter 3)
Transmitter pulse				
Energy	1 J	1 J	7 J	0.5 J
Length	30 ns	30 ns	13–18 ns	30 ns
Repetition rate	60 ppm	15 ppm	4 ppm	----------
Beamwidth	60″ (variable)	30″	200″	290″
Receiver				
Aperture	40 cm	30 cm	49 cm	−22 cm
Resolution	1 ns	10 ns	1 ns	1 ns
Timer				
Type	Quartz clock	Quartz clock	Quartz clock	Cesium clock
Control	VLF	VLF	VLF	UNS Obs and portable clocks
Precision (estimated)	0.5 m	[b]1.5 m	[c]0.01 m	<0.5 m

[a] Ranging system.
[b] Bracket and Brossier (1972, unpublished).
[c] Lehr *et al.* (1971, unpublished).

TABLE 1.16.—*Satellites With Corner-Cube Reflectors*

Satellite	Apogee (Mm)	Perigee (Mm)	Inclination (deg)	Period (min)	Number of cube corners	Effective area (cm^2)	Divergence	Stabilization
BE–B (1964–64A)	1.09	0.89	80	105	360	80	12″	Magnetic
BE–C (1965–32A)	1.32	0.94	41	108	360	80	12″	Magnetic
GEOS–1 (1965–89A)	2.27	1.12	59	120	334	940	20″	Gravitational
D1–C (1967–11A)	1.35	0.53	40	104	144	[a]20–100	[a]16″	Magnetic
D1–D (1967–14A)	1.85	0.58	39	110	144	[a]20–100	[a]16″	Magnetic
GEOS–2 (1968–2A)	1.61	1.08	74	112	400	1100	20″	Gravitational
PEOLE (1970–109A)	0.73	0.53	15	97	-----	-----	-----	----------

[a] The retroreflectors on D1–C or D1–D shape the returning beam so as to compensate most effectively for velocity aberration. Consequently, a characterization of its properties in terms of effective area and divergence is an approximation. Lehr *et al.* (1970, unpublished).

TABLE 1.17.—*Major Characteristics of 5-cm Radars Used in NGSP*

Characteristics	Values (Nominal)	
	FPS-16 (modified) (CAPRI, HAIR, MPS-25)	FPQ-16 (TPQ-18)
Frequency	5400–5900 MHz	
Transmitter		
Power, peak	1–3 MW	
Pulse width	0.25, 0.5, 1 μsec	
Repetition	285 to 1707 pps	2.5 to 640 pps
Antenna		
Type	Paraboloidal	
Diameter	4 m	4 m (9 m)
Beamwidth	1.1°	0.4°
Gain	44 db	51
Scan	Monopulse	
Receiver		
Bandwidth	1.6 MHz	0.5 MHz
	8.0 MHz	----------
Noise figure	4–12 db	8 db
Range		
General (1 m^2)	560 km (275 km)	1 400 km
[a]Reflector (1 m^2)	3 000 km	7 500 km
[b]Transponder (100 w)	32 000 km	100 000 km (60 000)
Accuracy	± 5–10 m	± 3 m
Precision	± 1–2 m	± 1 m
Resolution	0.5 m	2 m
Angle		
Resolution	0.1 mil	0.1 mil

[a] For reflector characteristics, see chapter 6.
[b] For transponder characteristics, see chapter 6.

TABLE 1.18.—*Satellites Carrying Highly Stable CW Beacons*[a]

Name	Designation	Transmitted frequencies	Launch date	Transmitting (T) or not transmitting (NT) (or ceased transmitting)
TRANSIT-1B	1960 $\gamma 2$	B,C	13 Apr 60	11 Jul 60
TRANSIT-2A	1960 $\eta 1$	B,C	22 Jun 60	26 Oct 62
TRANSIT-3B	1961 $\eta 1$	B,C	22 Feb 61	1 Apr 61
TRANSIT-4A	1961 $o1$	C,Z	29 Jun 61	
TRANSIT-4B	1961 $\alpha\eta 1$	C,Z	15 Nov 61	2 Aug 62
TRAAC	1961 $\alpha\eta 2$	C	15 Nov 61	12 Aug 62
ANNA-1B	1962 $\beta\mu 1$	B,C	31 Oct 62	
5A1	1962 $\beta\psi 1$	Z	19 Dec 62	19 Dec 63
5A3	1963-22A	Z	16 Jun 63	
5BN-1	1963-38B	Z	28 Sep 63	22 Dec 63
5E-1	1963-38C	Y	28 Sep 63	
5BN-2	1963-49B	Z	5 Dec 63	
5E-3	1963-49C	C,Y,X	5 Dec 63	9 Mar 64
5C-1	1964-26A	Z	3 Jun 64	23 Aug 65
Oscar-01	1964-63A	Z	6 Oct 64	8 Oct 64
BE-B	1964-64A	Y	9 Oct 64	
Oscar-02	1964-83D	Z	12 Dec 64	31 Dec 64
5E-5	1964-83C	Y	12 Dec 64	
Oscar-03	1965-17A	Z	11 Mar 65	6 Apr 65
BE-C	1965-32A	Y	29 Apr 65	
Oscar-04	1965-48C	Z	24 Jun 65	
Oscar-05	1965-65F	Z	13 Aug 65	
GEOS-A	1965-89A	Y	6 Nov 65	
Oscar-06	1965-109A	Z	22 Dec 65	
Oscar-07	1966-05A	Z	28 Jan 66	
D1-A	1966-13A	Z	17 Feb 66	
Oscar-08	1966-024A	Z	25 Mar 66	
Oscar-09	1966-41A	Z	19 May 66	
Oscar-10	1966-76A	Z	18 Aug 66	T
D1-C	1967-11D	Z	8 Feb 67	
D1-D	1967-14A	Z	15 Feb 67	
Oscar-12	1967-34A	Z	14 Apr 67	T
Oscar-13	1967-48A	Z	18 May 67	T
Timation-1	1967-53F	400 Hz	31 May 67	
Oscar-14	1967-92A	Z	25 Sep 67	T
GEOS-B	1968-02A	T	11 Jan 68	NT
Oscar-18	1968-12A	Z	1 Mar 68	T
Timation-2	1969-82B	Z	30 Sep 69	
Oscar-19	1970-67A	Z	27 Aug 70	T
Doppler Beacon-1	1970-16A	Y	4 Mar 70	NT
Doppler Beacon-2	1970-40A	Y	20 May 70	NT
Doppler Beacon-3	1970-98A	Y	18 Nov 70	NT
Doppler Beacon-5	1971-22A	Y	24 Mar 71	NT
Doppler Beacon-6	1971-76A	Y	10 Sep 71	NT
Doppler Beacon-7	1973-19A	Y	9 Mar 73	NT

[a] B = 162/216 MHz; C = 54/324 MHz; Z = 150/400 MHz; T = 162/324/972 MHz; Y = 162/324 MHz; X = 648 MHz. From Gross (1968) and other sources.

T-lines — 1 hr. 5 minutes
input — 1 hr. 30 minutes

TABLE 1.19.—*Quantitative Characteristics of Frequency Standards*

	Quartz crystal oscillator	Rubidium-gas-cell-controlled oscillator	Cesium-beam-tube-controlled oscillator		Hydrogen maser
Resonator frequency	5 MHz	6834.682 608 MHz	9192.631 770 MHz		[a]1420.405 751 786 4 MHz
Systematic drift	$<5 \times 10^{-10}$ per 24 hrs	$<2 \times 10^{-11}$ per month	None detected within resolution of current measurements; estimated at $<3 \times 10^{-12}$ for life		None detected within resolution of current measurements; estimated at $<1 \times 10^{-12}$ for life
Short-term stability (rms fractional frequency fluctuations for typical units in constant environments)[b]			Loop time constant τ_0 = 1 *s*	60 *s*	
Averaging time:					
1 msec	5×10^{-10}	5×10^{-10}	5×10^{-10}	5×10^{-10}	------
10 msec	1×10^{-10}	1×10^{-10}	1×10^{-10}	1×10^{-10}	------
100 msec	1×10^{-11}	1.5×10^{-11}	4×10^{-11}	1×10^{-11}	5×10^{-12} extrapolated
1 sec	5×10^{-12}	5×10^{-12}	4×10^{-11}	5×10^{-12}	5×10^{-13} measured
1 min	5×10^{-12}	6×10^{-13}	7×10^{-12}	5×10^{-12}	7×10^{-15} measured
1 hr	5×10^{-12}	5×10^{-13}	1×10^{-12}	1×10^{-12}	7×10^{-15} estimated
1 day	------	5×10^{-13}	2×10^{-13}	2×10^{-13}	7×10^{-15} estimated

[a] Manufacturer's values.
[b] Systematic drift removed from for quartz and rubidium-controlled clocks.

TABLE 1.20.—*Time Signals*

Stationary frequencies (VHF)			Stable frequencies (VLF)		
Call	City	MHz	Call	City	kHz
FFH	Paris	2.5			
HBN	Neuchabel	5	GBR	Rugby	16
IAM	Rome	5	MSF	Rugby	60
JJY	Tokyo	2.5,5,10,1	NBA	Balboa	24
MSF	Rugby	5.10	NSS	Annapolis	21.4
RWV	Moscow	5,10,15	RWM	Moscow	100
WWV	Fort Collins	5 to 25	WWVB	Fort Collins	60
WWV-U	Hawaii	5 to 25			

TABLE 1.21.—*Defined Quantities*

Meter (1960, 11th General Conference on Weights and Measures)

The length equal to 1 650 763.73 wavelengths in vacuum of the radiation corresponding to the undisturbed transition between the levels $2p_{10}$ and $5d_5$ of the atom of krypton—86.

Kilogram (1901, 3rd General Conference on Weights and Measures)

The unit of mass represented by the mass of the International Prototype Kilogram at Sevres, France.

Second (1964, 12th CGPM and ICWM)

The standard to be used is the transition between the hyperfine levels $F = 4, M = 0$ and $F = 3, M = 0$ of the fundamental state $^2S_{1/2}$ of the cesium-133 atom unperturbed by external fields. The value 9 192 631 770 hertz is assigned to the frequency of this transition.[a]

Degree Kelvin (1954, 10th CGPM)

Define the thermodynamic scale of temperature by means of the triple-point of water as a fixed point, attributing to it the temperature 273.16 degrees kelvin, exactly.

[a] Second (11th General Conference on Weights and Measures): $(31\ 556\ 925.9747)^{-1}$ of the tropical year 1900 January 0 at 12 hours of ephemeris time.

TABLE 1.22a.—*The NAS-NRC System of Physical Constants (Adjusted Values of Constants)*

Constant	Symbol	Value	Est. error limit[a]	Unit (MKSA)
Speed of light in vacuum	(c)	$2.997\,925 \times 10^{8}$	3	$m\ s^{-1}$
Elementary charge	(e)	$1.602\,10 \times 10^{-19}$	7	C
Avogadro constant	(N_A)	$6.022\,52 \times 10^{23}$	28	mol^{-1}
Planck's constant	(h)	$6.625\,6 \times 10^{-34}$	5	J s
Charge to mass ratio for electron	(e/m_e)	$1.758\,796 \times 10^{11}$	19	$C\ kg^{-1}$
Gas constant	(R)	$8.314\,3 \times 10^{0}$	12	$J\ K^{-1}\ mol^{-1}$
Normal volume perfect gas	(V_n)	$2.241\,36 \times 10^{-2}$	30	$m^3\ mol^{-1}$
Boltzmann constant	(k)	$1.380\,54 \times 10^{-23}$	18	$J\ K^{-1}$
Stefan-Boltzmann constant	(σ)	$5.669\,7 \times 10^{-8}$	29	$W\ m^{-2}\ K^{-4}$
Gravitational constant	(G)	6.670×10^{-11}	15	$N\ m^2\ kg^{-2}$

[a] Based on three standard deviations, applied to last digits in "value" column. Electromagnetic system: C—coulomb J—joule Hz—hertz W—watt N—newton t—tesla G—gauss.

TABLE 1.22b.—*Set II—The IAU System of Astronomical Constants*

Defining constants		
Number of ephemeris seconds in 1 tropical year (1900)	s	= 31 556 925.974 7
Gaussian gravitational constant, defining the a.u.	k	= 0.017 202 098 95
Primary constants		
Measure of 1 a.u. in meters	A	$= 149\,600 \times 10^{6}$
Velocity of light in meters per second	c	$= 299\,792.5 \times 10^{3}$
Equatorial radius for Earth in meters	a_e	= 6 378 160
Dynamical form factor for earth	J_2	= 0.001 082 7
Geocentric gravitational constant (units: $m^3\ s^{-2}$)	GE	$= 398\,603 \times 10^{9}$
Ratio of the masses of Moon and Earth	μ	= 1/81.30
Sidereal mean motion of Moon in radians per second (1900)	$n_{\leftmoon}^{*}$	$= 2.661\,669\,489 \times 10^{-6}$
General precession in longitude per tropical century (1900)	p	= 5 025".64
Obliquity of the ecliptic (1900)	ϵ	= 23°27′ 08".26
Constant of nutation (1900)	N	= 9".210
Derived constants		
Solar parallax	$\pi\odot$	= 8".794
Light-time for unit distance	τA	= 499s.012
Constant of aberration	κ	= 20".496
Flattening factor for Earth	f	= 1/298.25
Heliocentric gravitational constant (units: $m^3\ s^{-2}$)	GS	$= 132\,718 \times 10^{15}$
Ratio of masses of Sun and Earth		332 958
Ratio of masses of Sun and Earth + Moon		328 912
Perturbed mean distance of Moon in meters	$a_{\leftmoon}$	$= 38\,440 \times 10^{3}$
Constant of sine parallax for Moon	$\sin \pi_{\leftmoon}$	= 3 422".451
Constant of lunar inequality	$L_{\leftmoon}$	= 6".440
Constant of parallactic inequality	$P_{\leftmoon}$	= 124".986

System of planetary masses (ratio of masses of Sun and planet)

Mercury	6 000 000	Mars	3 093 500	Uranus	22 869
Venus	408 000	Jupiter	1 047.355	Neptune	19 314
Earth + Moon	329 390	Saturn	3 501.6	Pluto	360 000

TABLE 1.23.—*Major Epochs Used in Satellite Geodesy (NGSP)*

Epoch	For	Distance (in J.D.) From	
		1900 Jan 0^d12^h	Julian day number 0.0
1900 Jan 0^d12^h	Definition of Ephemeris Time, Universal Time Ephemeris Second, Calculation of Fundamental Ephemerides (Anonymous, 1961, p. 69; Trans. IAU 10:172, 1960)	0	2 415 020.0
1950.0	General (Boss) Catalog, Zodiacal Catalog, FK3, FK4, Yale (Zone) Catalogs, Smithsonian Star Catalog (See catalogs mentioned; also Anonymous, 1961)	0^d313	2 433 282.423
Julian day number 0	Chronological reckoning by days elapsed; calculation of sidereal time, etc. (Anonymous, 1961, p. 21)	2 415 020.0	0
Julian day modified number 0	Same as Julian day number (ch. 9)	15 019.5	2 400 000.5
1967 Jan 1	CIO Adopted (BIH Report, 1965; Trans. IAU, 1967)	24 471.5	2 439 491.5
1972 Jan 1	Discontinuity in UTC (BIH Circular D.59; Chi and Fosque, 1973)	26 293.5	2 441 317.5
1964 Apr 1	Discontinuities in UTC on 1964/5/1, 1964/9/1, 1965/1/1, 1965/3/1, 1965/7/1, 1965/9/1, 1966/1/1, 1968/2/1	Various	Various

TABLE 1.24.—*Time Scales of Major Importance in NGSP*

Name	Symbol	Basis and reference	Test object
Unit: second of atomic time			
Atomic time A.1	A.1	Initially, a set of eight cesium-beam frequency standards at USNO, NRL, NBS, Cruft Lab., NPL, Neuchatel, Bayneux Epoch of $0^h0^m0^s$ 1 Jan 1958 (UT2). Various standards since. (Audoin, 1973; USNO Time Bulletins)	Cesium-beam clocks; hydrogen maser
Atomic time TA.1	TA.1	Time Standard of Laboratory Suisse Recherche Horologenes (Neuchatel) (Audoin, 1973)	Cesium-beam clock; ammonia maser
Atomic time A3	A3	Cesium-beam clocks at NBS, NPL, LSRH (Neuchatel) and averaged by BIH (Guinot and Feisel, 1969; Guinot, 1972)	Cesium-beam clocks; radio broadcasts
Atomic time NBS	NBS–A	Times of two cesium-beam clocks. Epoch of A.1 ± 0.001 *S* (Behler, 1967)	Cesium-beam clocks
Ephemeris time	ET	Motion of Earth about the Sun and Newcomb's Tables of the Sun. In practice, motion of the Moon and the ephemeris of the Moon (Anonymous, 1961)	Moon and Brown's equations for motion of the Moon
Unit: second of mean solar time			
Universal time TO	UTO	Rotation of Earth. Time between successive passages of point with right ascension $\alpha = 18^h38^m45^s.836 + 86'40\ 184.542\ T + 0.0929\ T^2$ Measured by successive passages of ϒ, which are then converted to UTO. (Trans. IAU 7, 1950)	ϒ, *o* stars
Universal time T1	UT1	UT0 corrected for motion of pole. (Melchior *et al.*, 1972; Dejaffe, 1972; Trans. IAU 7:75, 1950; Rice, 1959; Anonymous, 1961)	UT0 and stars
Universal time T2	UT2	UT1 corrected for seasonal variations (Anonymous, 1961; Guinot and Feisel, 1969)	UT1 and stars
Unit: second of mean sidereal time			
Sidereal time, apparent	STA	Time between two successive passages of true equinox of date = $24^h = 86.400^s$	Stars
Sidereal time, mean	STM	Greenwich Hour Angle of Mean Equinox of Date (Anonymous, 1961)	Stars
Unit: second of solar time			
Solar time, apparent	---	Time between two successive passages of true Sun through lower meridian = $24^h = 86\ 400^s$	Sun

TABLE 1.25.—*Stations in Order of Increasing Longitude*

Number[a]	Name[b]	Coordinates[c] λ	φ	H_{msl}(m)	Datum[d]	Instrument[e]	Model[f]
5715	Dakar	342° 30′ 59″.794	14° 44′ 36″.678	27.3	Adindan	SECOR	5, 10
2813	Dakar	53″.268	-----	---	YOF Astro 67	Doppler	2*
6063	Dakar	31′ 02″.452	39″.899	26.3	Adindan	BC–4	1, 6, 9, 10
8820	Dakar	342° 35′ 29″.321	46′ 00″.548	28.5	Adindan	Laser (CNES)	8, 9
9020	Dakar	29″.795	01″.645	24.6	Adindan	B–N	9
5736	Ascension	345° 35′ 32″.385	−7° 58′ 15″.200	74.0	Ascensión 1958	SECOR	5, 10
6055	Ascension	32″.764	16″.634	70.9	Ascensión 1958	BC–4	1, 6, 9, 10
2722	Ascension	38″.840	-----	---	Ascensión 1958	Doppler	1, 2*
4080	Ascension	345° 35′ 53″.898	−07° 58′ 22″.779	125.4	Ascensión 1958	TPQ–18	4
6069	Tristan da Cunha	347° 40′ 53″.555	−37° 03′ 26″.257	24.8	Local	BC–4	1, 6, 9, 10
5740	Rota	Insufficient data				SECOR	5, 10
5741	Roberts Field	Insufficient data				SECOR	5, 10
8804	San Fernando	353° 47′ 41″.286	36° 27′ 50″.119	---	EU–50	Laser (CNES)	8, 9
9004	San Fernando	42″.09	51″.37	---	EU–50	B–N	1, 8, 9, 10
DSS 62	Madrid	355° 38′ 00″.572	40° 27′15″.273	783.3	EU–50	DSS	9, J
DSS 61	Madrid	45′ 08″.278	25′ 47″.717	788.4	EU–50	DSS	9, J
8818	Colomb-Bechar	357° 34′ 54″.06	31° 43′ 19″.25	855.7	EU–50	Laser (CNES)	9*
8011	Malvern	358° 01′ 59″.47	52° 08′ 39″.13	113.2	EU–50	Camera	8, 9, 10
2106	Lasham	358° 58′ 30″.21	51° 11′ 12″.32	190.3	EU–50	Doppler	1
1035	Winkfield	359° 18′ 14″.10	51° 26′ 49″.11	67.37	EU–50	MOTS	1, 8
8030	Meudon	2° 13′ 51″.339	42° 48′ 25″.354	165.5	EU–50	Camera	8, 10
8009	Delft	4° 22′ 21″.23	52° 00′ 09″.24	24.7	EU–50	Camera	8, 10
8815	St. Michel de Provence	5° 42′ 48″.382	43° 55′ 59″.183	657.83	EU–50	Laser (CNES)	8, 9*

TABLE 1.25.—*(Cont'd)*

Number[a]	Name[b]	Coordinates[c] λ	φ	H_{msl}(m)	Datum[d]	Instrument[e]	Model[f]
8015	Haute Provence	49″.277	56′ 01″.14	658.8	EU-50	Camera	8, 9, 10
8809	Haute Provence	48″.788	00″.190	657.8	EU-50	Laser (CNES)	8, 9*
8019	Nice	7° 18′ 03″.309	43′ 36″.496	377.4	EU-50	Camera (Antares)	8, 9, 10
8010	Zimmerwald	27′ 58″.239	46° 52′ 40″.318	903.4	EU-50	Camera	8, 9, 10
9426	Oslo	10° 45′ 08″.74	60° 12′ 40″.38	575.9	EU-50	B-N	1, 8, 9, 10
6065	Hohenpeissen-berg	11° 01′ 28″.574	47° 48′ 07″.009	943.2	EU-50	BC-4	1, 6, 9, 10
2830	Hohenpeissen-berg	30″.259	-----	---	EU-50	Doppler	2*
2812	Catania	14° 55′ 05″.883	-----	---	EU-50	Doppler	2*
2822	Ft. Lamy (Chad)	15° 02′ 05″.680	12° 07′ 50″.895	298.4	Adindan	Doppler	1, 2
5717	Ft. Lamy (Chad)	06″.232	49″.291	298.5	Adindan	SECOR	5, 10
6064	Ft. Lamy (Chad)	06″.234	51″.741	295.4	Adindan	BC-4	1, 6, 9, 10
5744	Catania	15° 02′ 44″.955	37° 26′ 40″.831	11.8	EU-50	SECOR	5, 10
6016	Catania	47″.696	42″.345	9.2	EU-50	BC-4	1, 6, 9, 10
2818	Tromsø	18° 56′ 30″.700	-----	---	EU-50	Doppler	2*
9432	Uzhgorod	22° 17′ 57″.88	48° 38′ 04″.56	189	EU-50	AFU-75	8, 9,* 10
8816	Stephanion	23° 49′ 43″.313	37° 45′ 17″.043	803.1	EU-50	Laser (CNES)	1, 9*
9051	Stephanion	46′ 42″.89	37° 58′ 40″.31	---	EU-50	36″ Camera	9, 10
9930	Dionysos	23° 55′ 59″.99	38° 04′ 46″.157	472.4	EU-50	Laser (SAO)	8, 9
9030	Dionysos	56′ 00″.13	46″.56	472.64	EU-50	B-N	9*
9091	Dionysos	01″.587	48.215	466.3	EU-50	B-N	1, 8, 9, 10
9431	Riga	24° 03′ 37″.81	56° 56′ 54″.98	8	EU-50	AFU-75	8, 9, 10
8435	Helsinki	24° 57′ 11″.07	60° 09′ 44″.06	40	EU-50	B-N	8
DSS 51	Johannesburg	27° 41′ 08″.53	−25° 53′ 21″.150	1391.0	Cape	DSS	9, 10, J

TABLE 1.25.—*(Cont'd)*

Number[a]	Name[b]	Coordinates[c] λ	φ	H_{msl}(m)	Datum[d]	Instrument[e]	Model[f]
6068	Johannesburg	42′ 25″.17	52′ 56″.98	1523.8	Cape	BC-4	1, 6, 9, 10
1031	Johannesburg	42′ 27″.931	−25° 52′ 58″.862	1522.3	Cape	MOTS-40	1, 8
9002	Olifantsfontein	28° 14′ 53″.91	57′ 33″.85	1544.1	Cape	B-N	1, 8, 9, 10
9902	Olifantsfontein	53″.909	33″.851	1543.88	Cape	Laser (SAO)	8, 9*
9022	Olifantsfontein	54″.351	33″.82	1543.3	Cape	B-N	1, 9*
2115	Pretoria	28° 20′ 53″.205	-----	---	Cape	Doppler	1, 2*
4050	Pretoria	21′ 29″.948	−25° 56′ 35″.336	1584	Cape	MPS-25	1, 4, 10
5719	Cyprus	Insufficient data				SECOR	5, 10
9028	Addis Ababa	38° 57′ 30″.48	6° 44′ 47″.23	1925.2	Adindan	B-N	1, 8, 9, 10
6042	Addis Ababa	59′ 49″.164	08″.501	1886.5	Adindan	BC-4	1, 6, 9, 10
5720	Addis Ababa	59′ 49″.196	09″.479	1889.4	Adindan	SECOR	5, 10
1043	Tananarive	47° 18′ 00″.461	−19° 00′ 27″.097	1377.9	Tananarive	MOTS-40	1, 8
1122	Tananarive	09″.45	01′ 13″.32	1403	Tananarive	GRARR	1
1123	Tananarive	12″.56	09″.33	1399	Tananarive	GRARR	1
4741	Tananarive	54″.191	00′ 00″.991	1338.3	Tananarive	FPS-16	4
9008	Shiraz	52° 31′ 11″.445	29° 38′ 18″.112	1597.4	EU-50	B-N	1, 8, 9, 10
2020	Mahe	55° 28′ 48″.63	-----	---	Local	Doppler	2*
2717	Mahe	48″.738	-----	---	Local	Doppler	2*
6075	Mahe	55° 28′ 50″.38	−4° 40′ 07″.23	588.98	Local	BC-4	1, 6, 9, 10
2838	Mauritius	57° 25′ 07″.503	-----	---	Local	Doppler	2*
6045	Mauritius	07″.661	−20° 13′ 41″.942	---	Local	BC-4	1, 6, 9, 10
5721	Mashad	59° 37′ 40″.105	36° 14′ 30″.404	994.4	EU-50	SECOR	5, 10
6015	Mashad	42″.729	29″.527	991.0	EU-50	BC-4	1, 6, 9, 10
2817	Mashad	42″.916	-----	---	EU-50	Doppler	1, 2*
6051	Mawson Station	62° 52′ 24″.41	−67° 36′ 03″.28	11.3	Local	BC-4	1, 6, 9, 10

TABLE 1.25.—*(Cont'd)*

Number[a]	Name[b]	Coordinates[c] λ	φ	H_{msl}(m)	Datum[d]	Instrument[e]	Model[f]
5722	Diego Garcia	72° 28′ 31″.570	−7° 20′ 57″.440	6.7	Local	SECOR	5, 10
6073	Diego Garcia	32″.156	58″.527	3.9	Local	BC-4	1, 6, 9, 10
6044	Heard I.	73° 23′ 27″.42	−53° 01′ 12″.03	3.8	Local	BC-4	1, 6, 9, 10
9006	Naini Tal	79° 27′ 25″.51	29° 21′ 38″.97	1927	EU-50	B-N	1, 8, 9, 10
6040	Cocos	96° 49′ 47″.08	−12° 11′ 57″.91	4.4	Local	BC-4	1, 6, 9, 10
2723	Cocos	47″.730	-----	---	Local	Doppler	1, 2*
5723	Chiang Mai	Insufficient data				SECOR	5, 10
2765	Chiang Mai	98° 58′ 14″.812	-----	---	Indian	Doppler	2*
6072	Chiang Mai	98° 58′ 15″.123	18° 46′ 06″.149	308.4	1968 Astro	BC-4	1, 6,* 9, 10
5724	Singapore	Insufficient data				SECOR	5, 10
6052	Wilkes Station	110° 32′ 04″.61	−66° 16′ 45″.12	18	Local	BC-4	1, 6, 9, 10
7054	Carnarvon	113° 42′ 53″.892	−24° 54′ 19″.908	31.4	AGD	Laser (NASA)	1, 8
1152	Carnarvon	54″.938	14″.964	37.9	AGD	GRARR	1
4761	Carnarvon	57″.765	−24° 53′ 50″.755	49.0	AGD	FPQ-6	4
7079	Carnarvon	43′ 11″.592	−24° 54′ 26″.914	23.6	AGD	PTH-100	1, 8
5725	Hong Kong	Insufficient data				SECOR	5, 10
2709	Caversham	115° 55′ 47″.572	----- ---		AGD	Doppler	2*
6032	Caversham	115° 58′ 26″.618	−31° 50′ 28″.992	26.3	AGD	BC-4	1, 6, 9, 10
5726	Zamboanga	122° 04′ 03″.558	6° 55′ 26″.213	---	Luzon 1911	SECOR	5, 10
2821	Zamboanga	03″.700	-----	---	Luzon 1911	Doppler	2*
6047	Zamboanga	04″.838	6° 55′ 26″.132	---	Luzon 1911	BC-4	1, 6, 9, 10
2832	Japan	129° 42′ 43″.640	-----	---	Tokyo	Doppler	2*
5727	Darwin	Insufficient data				SECOR	5, 10
6013	Kanoya	130° 52′ 24″.860	31° 23′ 30″.140	65.9	---	BC-4	1, 6, 9, 10
5742	Palau	Insufficient data				SECOR	5, 10
9003	Woomera	136° 46′ 58″.70	−31° 06′ 07″.261	159.2	---	B-N	1, 9

TABLE 1.25.—*(Cont'd)*

Number[a]	Name[b]	Coordinates[c] λ	φ	H_{msl}(m)	Datum[d]	Instrument[e]	Model[f]
4946	Woomera	50′ 13″.120	−30° 49′ 11″.003	124.7	AGD	FPS–16	1, 4
1024	Woomera	52′ 11″.022	−31° 23′ 30″.07	129.5	AGD	MOTS–40	1, 8
9023	Woomera	52′ 39″.016	30″.816	137.9	AGD	B–N	1, 8, 9
DSS 41	Woomera	53′ 10″.124	−31° 22′ 59″.431	140.3	AGD	DSS	J
9025	Dodaira	139° 11′ 43″.159	36° 00′ 08″.606	855.89	Tokyo	B–N	1, 8, 9
9005	Tokyo	32′ 28″.222	35° 40′ 11″.078	59.8	Tokyo	B–N	1, 8, 9, 10
6023	Thursday Island	142° 12′ 35″.496	−10° 35′ 08″.037	60.5	AGD	BC–4	1, 6, 9, 10
2744	Thursday Island	36″.990	-----	---	AGD	Doppler	2*
5728	Guam		Insufficient data			SECOR	5, 10
7060	Guam	144° 44′ 05″.374	13° 18′ 28″.614	85.9	Local	Laser (NASA)	8, 9
5729	Manus		Insufficient data			SECOR	5, 10
1038	Orroral	148° 57′ 10″.705	−35° 37′ 37″.501	931.3	AGD	MOTS–40	1, 8
DSS 42	Tidbinbilla	58′ 48″.206	24′ 08″.038	655.8	AGD	DSS	9, 10, J
2805	Culgoora	149° 33′ 36″.622	-----	---	AGD	Doppler	2*
6060	Culgoora	36″.892	−30° 18′ 39″.418	211.1	AGD	BC–4	1, 6, 9, 10
5731	Guadalcanal		Insufficient data			SECOR	5, 10
2708	Wake Island	166° 36′ 39″.128	-----	---	Local	Doppler	2*
6012	Wake Island	39″.780	19° 17′ 23″.227	3.5	Local	BC–4	1, 6, 9, 10
6066	Wake Island	41″.206	24″.100	5.3	Local	BC–4	10
5730	Wake Island	41″.206	24″.100	8.1	Local	SECOR	5, 10
2019	McMurdo Station	166° 40′ 03″.444	-----	---	Local	Doppler	1, 2*
6053	McMurdo Station	38′ 07″.585	−77° 50′ 46″.249	19.0	Local	BC–4	1, 6, 9, 10
6078	Port Vila	168° 17′ 57″.921	−17° 41′ 46″.966	15.2	Local	BC–4	1, 9, 10
6031	Invercargill	168° 19′ 31″.155	−46° 25′ 03″.491	0.9	New Zealand	BC–4	1, 6, 9, 10

TABLE 1.25.—*(Cont'd)*

Number[a]	Name[b]	Coordinates[c] λ	φ	H_{msl}(m)	Datum[d]	Instrument[e]	Model[f]
2809	Invercargill	18′ 13″.206	-----	---	New Zealand	Doppler	2*
2739	Shemya	174° 06′ 51″.482	-----	---	NAD 1927	Doppler	2*
6004	Shemya	07′ 37″.87	52° 42′ 54″.89	36.8	NAD 1927	BC-4	1, 6, 9, 10
5734	Shemya	37″.870	54″.894	39.3	NAD 1927	SECOR	5, 10
5410	Midway	182° 37′ 49″.531	28° 12′ 32″.061	6.1	Local	SECOR	5, 10
2117	Tafuna	189° 17′ 07″.643	-----	---	Am. Samoa 62	Doppler	1, 2*
2017	Tafuna	07″.87	−14° 20′ 07″.99	6.7	Am. Samoa 62	Doppler	1*
6022	Tafuna	13″.242	12″.216	5.3	Am. Samoa 62	BC-4	1, 6, 9, 10
5732	Pago Pago	Insufficient data				SECOR	5, 10
9427	Johnston Island	190° 29′ 05″.59	16° 44′ 45″.39	5	Local	B-N	1, 8, 9, 10
4742	Kauai	200° 19′ 53″.962	22° 07′ 35″.828	1155	Old Hwn.	FPS-16	4, 10
2100	Wahiawe	202° 00′ 00″.63	21° 31′ 26″.86	395	Old Hwn.	Doppler	1
5733	Christmas Island	202° 35′ 21″.962	2° 00′ 35″.622	3.5	Local	SECOR	5, 10
6059	Christmas Island	21″.962	35″.622	2.8	Local	BC-4	1, 6, 9, 10
2849	Christmas Island	21″.036	-----	---	Local	Doppler	2*
6123	Pt. Barrow	203° 21′ 20″.720	71° 18′ 49″.882	8.3	NAD 1927	BC-4	1, 9, 10*
2811	Maui	203° 31′ 52″.080	-----	---	Old Hwn.	Doppler	2*
5411	Maui	52″.77	20° 49′ 37″.00	32.3	Old Hwn.	SECOR	5
9012	Maui	44′ 24″.08	42′ 37″.50	3034.1	Old Hwn.	B-N	1, 8, 9, 10
6011	Maui	44′ 28″.529	20° 42′ 38″.561	3049.3	Old Hwn.	BC-4	1, 6, 9, 10
2014	Anchorage	210° 10′ 37″.46	61° 17′ 01″.98	68	NAD 1927	Doppler	1
1033	Fairbanks	212° 09′ 47″.168	64° 52′ 19″.721	162.7	NAD 1927	MOTS-40	1, 8, 10
1036	Fairbanks	28′ 40″.898	64° 58′ 38″.600	289.6	NAD 1927	MOTS-40	1, 8

TABLE 1.25.—*(Cont'd)*

Number[a]	Name[b]	Coordinates[c] λ	φ	H_{msl}(m)	Datum[d]	Instrument[e]	Model[f]
1128	Fairbanks	29′ 22″.415	20″.886	346.6	NAD 1927	GRARR	1
6039	Pitcairn	229° 53′ 11″.882	−25° 04′ 07″.146	339.4	Local	BC–4	1, 6, 9, 10
4280	Vandenberg AFB	239° 25′ 10″.428	34° 39′ 57″.140	123.0	NAD 1927	TPQ–18	4, 10
2738	Moses Lake	240° 39′ 47″.400	-----	---	NAD 1927	Doppler	1, 2*
6003	Moses Lake	48″.118	47° 11′ 07″.132	368.7	NAD 1927	BC–4	1, 6, 9, 10
5201	Moses Lake	50″.463	05″.916	368.9	NAD 1927	SECOR	5, 10
9425	Edwards AFB	242° 05′ 11″.584	34° 57′ 50″.742	784.23	NAD 1927	B–N	1, 8, 9, 10
6134	Wrightwood	242° 19′ 09″.259	34° 22′ 44″.444	2198.4	NAD 1927	BC–4	1, 9, 10*
6111	Wrightwood	09″.484	34° 22′ 54″.54?	2284.3	NAD 1927	BC–4	1, 6, 9, 10*
1030	Mojave	243° 06′ 02″.73	35° 19′ 48″.088	929.1	NAD 1927	MOTS–40	1, 8, 10
DSS 14	Goldstone	243° 06′ 40″.850	35° 25′ 33″.340	1031.8	NAD 1927	DSS	9, 10, J
DSS 11	Goldstone	09′ 05″.262	23′ 22″.346	1036.3	NAD 1927	DSS	9, 10, J
DSS 12	Goldstone	11′ 43″.414	17′ 59″.854	988.9	NAD 1927	DSS	9, 10, J
DSS 13	Goldstone	12′ 21″.573	35° 14′ 51″.788	1093.5	NAD 1927	DSS	J
6038	Socorro Island	249° 02′ 39″.28	18° 43′ 44″.93	23.2	Local	BC–4	1, 6, 9, 10
2831	Socorro Island	40″.587	-----	---	Local	Doppler	2*
9021	Mt. Hopkins	249° 07′ 21″.35	31° 41′ 02″.67	2383.1	NAD 1927	B–N	1, 8, 9, 10
9921	Mt. Hopkins	21″.35	31° 41′ 02″.87	2383.1	NAD 1927	Laser (SAO)	8, 9
9424	Cold Lake	249° 57′ 26″.389	54° 44′ 33″.858	704.6	NAD 1927	B–N	1, 8, 9, 10
6020	Easter Island	250° 34′ 17″.495	−27° 10′ 39″.213	230.8	Local	BC–4	1, 6, 9, 10
2846	Easter Island	18″.384	-----	---	Local	Doppler	2*
2103	Las Cruces	253° 14′ 48″.25	32° 16′ 43″.75	1203	NAD 1927	Doppler	1
9001	Organ Pass	253° 26′ 51″.17	32° 25′ 24″.56	1651.33	NAD 1927	B–N	1, 8, 9, 10
9901	Organ Pass	51″.17	32° 25′ 24″.56	1651	NAD 1927	Laser (SAO)	9

TABLE 1.25.—*(Cont'd)*

Number[a]	Name[b]	Coordinates[c] λ	φ	H_{msl}(m)	Datum[d]	Instrument[e]	Model[f]
3400	Colorado Springs	255° 07′ 01″.01	39° 00′ 22″.44	2184.1	NAD 1927	PC–1000	10
3902	Cheyenne	255° 08′ 02″.65	41° 07′ 59″.200	1882.2	NAD 1927	PC–1000	10
7045	Denver	255° 23′ 41″.19	39° 38′ 48″.026	1789.6	NAD 1927	MOTS–40	1, 7, 8, 10
7036	Edinburg (Tex.)	261° 40′ 09″.03	26° 22′ 45″.443	59.59	NAD 1927	MOTS–40	1, 7, 8, 10
5709	Austin		Insufficient data			SECOR	5, 10
7034 (1034)	E. Grand Forks	262° 59′ 21″.56	48° 01′ 21″.40	253	NAD 1927	MOTS–40	1, 7, 8, 10
5706	Worthington		Insufficient data			SECOR	5, 10
7037	Columbia (Mo.)	267° 47′ 42″.12	38° 53′ 36″.068	272.7	NAD 1927	MOTS–40	1, 7, 8, 10
2745	Stoneville	269° 05′ 10″.70	33° 25′ 31″.57	44	NAD 1927	Doppler	1
5333	Stoneville	10″.78	32″.342	38.7	NAD 1927	SECOR	7
3334	Stoneville	11″.35	31″.95	39.0	NAD 1927	PC–1000	10
3402	Semmes Island	271° 44′ 52″.37	30° 46′ 49″.35	73	NAD 1927	PC–1000	3, 7, 10
3647	Dauphin	271° 55′ 17″.598	30° 14′ 48″.229	1.2	NAD 1927	PC–1000	7
3404	Swan Island	276° 03′ 29″.87	17° 24′ 16″.57	40.4	Local	PC–1000	3, 7, 10
1126	Rosman	277° 07′ 26″.230	35° 11′ 45″.051	873.9	NAD 1927	GRARR	1
7051	Rosman	26″.23	46″.60	879	NAD 1927	Laser (NASA)	7
1042	Rosman	41″.008	12′ 06″.926	909.4	NAD 1927	MOTS–40	1, 7, 8, 10
1037	Rosman	41″.308	35° 12′ 06″.911	909.27	NAD 1927	MOTS–40	1, 8
1022	Ft. Meyers	278° 08′ 03″.926	26° 32′ 51″.891	4.8	NAD 1927	MOTS–40	1, 7, 8, 10
5648	Ft. Stewart	278° 26′ 00″.260	31° 55′ 18″.405	27.8	NAD 1927	SECOR	5, 10
3648	Hunter AFB	278° 50′ 46″.359	32° 00′ 05″.868	12	NAD 1927	PC–1000	3, 7, 10
7075	Sudbury (Ont.)	279° 03′ 10″.354	46° 27′ 20″.988	281.9	NAD 1927	MOTS–40	1, 7, 8, 10
4082	Merritt Island	279° 20′ 07″.376	28° 25′ 27″.928	11.3	NAD 1927	TPQ–18	1, 4, 10
3861	Homestead	279° 36′ 42″.69	25° 30′ 24″.686	2.4	NAD 1927	PC–1000	3, 7, 10

TABLE 1.25.—*(Cont'd)*

Number[a]	Name[b]	Coordinates[c] λ	ϕ	H_{msl}(m)	Datum[d]	Instrument[e]	Model[f]
5861	Homestead	279° 37′ 39″.35	25° 29′ 21″.18	6.4	NAD 1927	SECOR	5
7071	Jupiter	279° 53′ 12″.312	27° 01′ 12″.769	14.0	NAD 1927	MOTS-24	1, 8
7072	Jupiter	12″.485	13″.168	14.2	NAD 1927	MOTS-40	1, 7, 8, 10
9049	Jupiter	12″.636	12″.726	12.9	NAD 1927	Geodetic-36	1
7073	Jupiter	12″.722	13″.107	13.56	NAD 1927	PTH-100	1
7074	Jupiter	12″.761	13″.333	14.2	NAD 1927	BC-4	1
9010	Jupiter	13″.008	12″.882	15.1	NAD 1927	B-N	1, 9, 10
3649	Jupiter	13″.72	14″.80	15	NAD 1927	PC-1000	7
5711	Panama	Insufficient data				SECOR	5, 10
1025	Quito	281° 25′ 17″.939	−00° 37′ 20″.621	3568.6	SAD 1969	MOTS-40	1
6009	Quito	34′ 49″.212	− .5′ 50″.468	2682.1	SAD 1969	BC-4	1, 3, 6, 9, 10
2844	Quito	50″.213	-----	---	SAD 1969	Doppler	2*
5001	Herndon	282° 40′ 16″.705	38° 59′ 37″.697	127.8	NAD 1927	SECOR	5, 7, 10
1021	Blossom Pt.	282° 54′ 48″.225	38° 25′ 49″.628	5.8	NAD 1927	MOTS-40	1, 7, 8, 9, 10
2111	Howard County APL	283° 06′ 11″.07	39° 09′ 47″.83	145	NAD 1927	Doppler	1
7077	Greenbelt	283° 09′ 37″.31	38° 59′ 56″.73	50.9	NAD 1927	MOTS-40	1
7050	Greenbelt	10′ 18″.04	39° 01′ 13″.676	54.8	NAD 1927	Laser (NASA)	1, 8, 9
7043	Greenbelt	19″.93	15″.004	53.5	NAD 1927	PTH-100	1, 7, 10
6002	Beltsville	26″.942	39″.003	44.3	NAD 1927	BC-4	1, 3, 6, 9, 10
2742	Beltsville	27″.170	-----	---	NAD 1927	Doppler	2*
7076	Kingston	283° 11′ 26″.528	18° 04′ 31″.980	445.9	NAD 1927	MOTS-40	1, 7, 8, 10
3657	Aberdeen	283° 55′ 44″.780	39° 28′ 18″.971	5.5	NAD 1927	PC-1000	3, 7, 10
7052	Wallops Flight Center	284° 29′ 23″.333	37° 51′ 33″.432	8.6	NAD 1927	Laser (NASA)	1, 8

TABLE 1.25.—*(Cont'd)*

Number[a]	Name[b]	Coordinates[c] λ	φ	H_{msl}(m)	Datum[d]	Instrument[e]	Model[f]
4860	Wallops Flight Center	25″.236	36″.509	14.9	NAD 1927	FPQ-6	1, 4
2203	Wallops Flight Center	31″.414	51″.314	13.6	NAD 1927	Doppler	1
4840	Wallops Flight Center	30′ 52″.378	50′ 28″.393	12.4	NAD 1927	FPS-16	1, 4
3477	Bogotá	285° 55′ 35″.482	4° 49′ 2″.379	255.8	SAD 1969	PC-1000	3
9027	Arequipa	288° 30′ 26″.578	−16° 27′ 54″.365	2450.2	SAD 1969	B-N	9
9007	Arequipa	26″.814	55″.085	2451.9	SAD 1969	B-N	1, 8, 9, 10
9907	Arequipa	26″.81	−16° 27′ 55″.08	2452.3	SAD 1969	Laser (SAO)	8, 9
9050	Cambridge	288° 26′ 28″.71	42° 30′ 20″.97	187.2	NAD 1927	Geodetic-36	1, 8
3401	Bedford (Mass.)	288° 43′ 35″.03	27′ 17″.530	83.0	NAD 1927	PC-1000	7, 10
3405	Grand Turk	288° 51′ 13″.796	21° 25′ 46″.796	2.2	NAD 1927	PC-1000	3, 7, 10
4081	Grand Turk	52′ 03″.051	21° 27′ 43″.487	36.00	NAD 1927	TPQ-18	10
1028	Santiago	289° 19′ 56″.40	−33° 08′ 57″.24	693.4	SAD 1969	MOTS-40	1, 8
2847	Cerro Sombrero	290° 46′ 29″.005	-----	---	Prov. S. Chile	Doppler	2*
6043	Cerro Sombrero	29″.573	−52° 46′ 52″.468	80.7	Prov. S. Chile	BC-4	1, 6, 9, 10
9009	Curaçao	291° 09′ 46″.078	12° 05′ 25″.912	8.7	SAD 1969	B-N	1, 8, 9, 10
3406	Curaçao	45″.80	12° 05′ 26″.843	6.8	SAD 1969	PC-1000	3, 7, 10
2018	Thule	291° 13′ 21″.472	-----	---	Quornoq	Doppler	1, 2*
6001	Thule	27′ 51″.887	76° 30′ 03″.411	206.0	NAD 1927	BC-4	6, 9, 10
9031	Comodora Rivadavia	292° 23′ 12″.215	−45° 53′ 11″.028	186.5	SAD 1969	B-N	1, 8, 9, 10
5738	Puerto Rico	Insufficient data				SECOR	5, 10
7040	San Juan	294° 00′ 22″.174	18° 15′ 26″.216	49.7	NAD 1927	MOTS-40	1, 7, 8, 10
2820	Villa Dolores	294° 53′ 39″.460	-----	---	SAD 1969	Doppler	2*

TABLE 1.25.—*(Cont'd)*

Number[a]	Name[b]	Coordinates[c] λ	φ	H_{msl}(m)	Datum[d]	Instrument[e]	Model[f]
9011	Villa Dolores	38″.95	−31° 56′ 33″.228	608	SAD 1969	B–N	1, 8, 9, 10
6019	Villa Dolores	41″.342	33″.954	608.2	SAD 1969	BC–4	1, 3, 6, 9, 10
3471	Bermuda	295° 18′ 59″.824	32° 22′ 54″.204	51.9	Bermuda 1957	PC–1000	3
5710	Bermuda	Insufficient data				SECOR	5, 10
7039	Bermuda	295° 20′ 34″.49	32° 21′ 44″.529	53.1	Bermuda 1957	MOTS–40	1, 7, 8, 10
4740	Bermuda	46″.321	32° 20′ 48″.033	19.9	Bermuda 1957	FPS-10	1, 4, 10
4760	Bermuda	46″.532	47″.530	21.1	Bermuda 1957	FPQ–6	1, 4
2825	Palmer Station	295° 56′ 29″.748	-----	---	Local	Doppler	2*
6050	Palmer Station	37″.040	−64° 46′ 37″.04	16.4	Local	BC–4	1, 6, 9, 10
4061	Antigua	298° 12′ 24″.472	17° 08′ 34″.777	42.3	NAD 1927	FPQ–6	4, 10
3106	Antigua	37″.552	52″.685	1.9	NAD 1927	PC–1000	3, 7, 10
3407	Trinidad	298° 23′ 25″.652	10° 44′ 35″.844	254.8	SAD 1969	PC–1000	3, 7, 10
3478	Manaus	300° 00′ 59″.620	−3° 08′ 44″.820	84	SAD 1969	PC–1000	3*
3451	Asunción	302° 25′ 15″.376	−25° 18′ 56″.192	150	SAD 1969	PC–1000	3*
6008	Paramaribo	304° 47′ 42″.35	05° 26′ 54″.97	18.38	SAD 1969	BC–4	1, 3, 6, 9, 10
3476	Paramaribo	43″.744	54″.292	18.3	SAD 1969	PC–1000	3, 10
5712	Paramaribo	44″.52	05° 26′ 59″.46	21.5	SAD 1969	SECOR	5, 10
2815	Paramaribo	46″.590	-----	---	SAD 1969	Doppler	2*
1032	St. Johns	307° 16′ 43″.369	47° 44′ 29″.739	69	NAD 1927	MOTS–40	1, 8, 10
3414	Brasilia	312° 06′ 02″.679	−15° 51′ 35″.540	10.58	SAD 1969	PC–1000	3
6061	S. Georgia	323° 30′ 42″.531	−54° 16′ 39″.515	4.2	Local	BC–4	1, 6, 9, 10
3413	Natal	324° 49′ 57″.605	−5° 54′ 56″.253	36.9	SAD 1969	PC–1000	3, 10
5735	Natal	57″.605	56″.253	39.5	SAD 1969	SECOR	5, 10

TABLE 1.25.—*(Cont'd)*

Number[a]	Name[b]	Coordinates[c] λ	φ	H_{msl}(m)	Datum[d]	Instrument[e]	Model[f]
2837	Natal	57".617	-----	---	SAD 1969	Doppler	1, 2
6067	Natal	50' 06".200	37".414	40.63	SAD 1969	BC-4	1, 3, 6, 9, 10
9029	Natal	08".660	38".62	45.3	SAD 1969	B-N	8, 9, 10
9039	Natal	09".401	38".62	41.6	SAD 1969	B-N	9*
9929	Natal	08".68	38".62	45.6	SAD 1969	Laser (SAO)	8, 9
2727	Terceira	332° 54' 18".919	-----	---	Local	Doppler	2*
5739	Terceira	19".686	38° 45' 36".311	56.1	Local	SECOR	5, 10
5713	Terceira	21".064	36".725	56.0	Local	SECOR	5, 10
6007	Terceira	21".064	36".725	53.3	Local	BC-4	1, 6, 9, 10

[a] These are the numbers assigned to stations for the NGSP and are the ones given preference in the *NASA Directory of Observation Station Locations* (Anon., 1971). Other numbers have been assigned by some participants to some stations. (TRANET numbers + 2000 = NGSP numbers; NGS numbers + 6000 = NGSP numbers; SAO has erratic numbering differences.)

[b] These names are in general those given in the NASA directory (1971) or by the organization occupying the station. The same location may have several names. Since the names have no official status, the differences are unimportant.

[c] Coordinates given for stations in the 2000 series (NWL) and the 8000 and 9000 series (SAO and associated groups) must be used with caution. Coordinates given in the *NASA Directory* (Anonymous, 1971) for Doppler-tracking stations refer to the geometric center of the antennas. This center differs from the phase center of the antennas given in section 2.3. The coordinates (Z-coordinates) of the phase center are given by R. Anderle in chapter 3. Corrections should be made, when necessary, for differences between geometric center and phase center and, if this is indicated, between phase centers of 162/324-Mc/s pair and 150/400-Mc/s pair.

Some of SAO's Baker-Nunn cameras were moved to another site by a laser-type DME. In a few cases, the DME was given the same coordinates as the camera had had. It is unlikely that the true coordinates could be exactly the same, since the structures are quite different. When accuracy is essential, special investigation should be made.

λ and φ are geodetic coordinates; H_{msl} is height above mean sea level.

[d] Most of the minor datums have no official designation, and slight variations will be found. See section 8.3 for an extensive list.

[e] B-N designates a Baker-Nunn camera (section 9.2). For a list of characteristics of most of the cameras involved, see section 1.2.

1 - Chapter 5, GEM
2 - Chapter 3, NWL-9D
3 - Chapter 3, DMA/AC
4 - Chapter 6, WFC
5 - Chapter 3, SEN
6 - Chapter 7, WGN
7 - Chapter 3, AFCRL
8 - Chapter 5, GSFC '73
9 - Chapter 10, SE-III
10 - Chapter 8, WN14
J - Chapter 4, JPL

[f] The references are to chapters and models where original and/or new coordinates may be found. The coordinates given are, where possible, these in the NASA directory (1971). Only longitude is given unless there is some special reason for also giving latitude and height above mean sea level. Where the directory did not describe a particular station or where a contributor's coordinates were considered considerably more reliable, the contributor's coordinates are given.

An asterisk (*) indicates source (see list in (e) above) of coordinates cited in this table. If not specifically indicated by asterisk, source is Anon., 1971.

TABLE 1.26.—*Geodetic Satellite Data Service Reduced Data Received and Processed as of 24 September 1973*

Network	Observations	Passes	Period Covered		
		GEOS-1			
Camera network					
SAO	11 371	1 701	8 Nov	1965—29 Nov	1966
NASA MOTS	22 618	2 219	18 Nov	1965—24 Nov	1966
USAF	1 101	164	20 Dec	1965—20 Nov	1966
USAF (revised)	4 642	550	25 Nov	1965—30 Nov	1966
USAF (special preprocessing)	1 328	213	25 Nov	1965—30 Nov	1966
U.S. Coast and Geodetic Survey	130	19	28 Nov	1965—27 Jul	1966
International[a]	1 803	201	8 Dec	1965—21 Nov	1966
Electronic network					
AMS SECOR[a]	78 357	756	25 Mar	1966— 8 Feb	1967
USN doppler[a]	683 478	19 088	14 Nov	1965—17 Dec	1967
NASA range and range rate	42 417	1 308	17 Nov	1965—28 Nov	1966
NASA MOTS	14 291	9 525	6 Nov	1965—14 Jan	1967
USA SECOR[a] (reduced by GIMRADA)	43 241	90	11 Jan	1966—25 Apr	1966
Laser network					
SAO laser[a]	796	140	27 Jan	1966—24 Jun	1967
NASA laser	4 849	19	11 Apr	1966—21 Nov	1966
	5 602	8	23 Apr	1969—30 May	1969
		GEOS-2			
Camera network					
SAO	10 806	1 736	20 Feb	1968—31 Jan	1970
NASA MOTS	20 033	2 488	20 Feb	1968—12 Dec	1969
USAF	21	3	7 Oct	1968— 7 Dec	1968
USAF (special preprocessing)	54	8	28 Mar	1968— 8 Jan	1969
International	7 938	948	20 Feb	1968—27 Mar	1973
Electronic network					
AMS SECOR	11 359	88	1 Apr	1968—29 Jun	1968
USN doppler	86 097	3 110	11 Jan	1968—30 Dec	1968
Laser network					
SAO laser	385	97	2 Sep	1969—31 Jan	1970
NASA laser	166 014	368	7 Feb	1968—13 May	1970
		BE-B			
Electronic network					
USN doppler	26 957	1 635	11 Nov	1964—30 Mar	1965
Laser network					
SAO laser	98	31	10 Mar	1966—26 Jun	1967
NASA laser	5 481	13	12 May	1967—17 Apr	1971

TABLE 1.26.—*(Cont'd)*

Network	Observations	Passes	Period Covered		
		BE-C			
Electronic network					
USN doppler[a]	73 108	4 102	2 May	1965—24 Feb	1966
Laser network					
SAO laser	661	161	25 Jan	1966—24 Jun	1967
NASA laser	11 081	41	3 Apr	1967— 2 May	1970
		D1-C			
Laser network					
SAO laser	207	44	17 Feb	1967—29 Jun	1967
NASA laser	47 868	(*b*)	23 Apr	1967— 9 Sep	1971
		D1-D			
Laser network					
SAO laser	238	38	9 Mar	1967— 2 Jun	1967
NASA laser	24 433	61	10 May	1967—23 Jun	1971
		ECHO-1			
Camera network					
U.S. Coast and Geodetic Survey	865	2	1 Feb	1967— 1 Feb	1967
		ECHO-2			
Camera network					
U.S. Coast and Geodetic Survey	824	4	15 Dec	1966—17 Jan	1967
		PAGEOS			
Camera network					
U.S. Coast and Geodetic Survey	70 743	244	20 Jul	1966—31 Mar	1967
USAF (special preprocessing)	212	30	20 Sep	1967—10 Jan	1969
Number of tapes					
U.S. Coast and Geodetic Survey	49[c]	(*b*)	20 Jul	1966—12 Jun	1970

[a] Catalog prepared.
[b] Unknown.
[c] Tapes are not in NGSP format.

TABLE 1.27.—*Differences in Preprocessing Procedures as Functions of Kind of Raw Data*

Raw data	Corrections	Transformations	Processed data	From instrument type
x,y	Camera errors Measuring engine errors Refraction Aberration of EMW Target phase Timing errors Star catalog errors	From x,y to α,δ at catalog epoch From α,δ at catalog epoch to α,δ at appropriate epoch	α,δ	Camera
Δt	Instrument errors Pulse threshold Refraction Aberration of EMW Target phase Timing errors	From Δt to distance s	s	Laser DME Radar DME
A_z,E_l	Instrument errors Beam pattern Refraction Aberration of EMW Timing errors	From A_z,E_l in local system to A_z,E_l in appropriate system	A_z,E_l	Radar
ϕ_m	Instrument errors Calibration errors Refraction Aberration Timing errors Wavelength errors	From phase difference to direction cosines l,m,n	l,m,n	MINITRACK
ϕ_s	Instrument errors Phase center Refraction Timing errors Wavelength errors	From phase difference to distance s	s	SECOR
Δf	Instrument errors Beacon frequency errors Refraction	No change	Δf	
n	Aberration Timing errors	From number of cycles to change in radial distance	Δr	FME

TABLE 1.28.—*Corrections Introduced During Preprocessing*

	NGS	SAO	DMA/AC	NASA[a]
Proper motion	[b]√		√	√
Precession	√	√	√	√
Nutation	√		√	√
Precession + nutation	--			
Parallax, annual	√		--	--
Aberration, annual	√	√	√	√
Aberration, diurnal	√	--	--	√
Refraction, astronomic	√	--	√	√
Refraction, parallactic	√	√	√	√
Polar motion	√	√	--	
Calibration, comparator	√	√	√	√
Calibration, camera				
separate	√	--	√	√
combined	√	√	--	--
Time				
Shutter	√	√	--	--
Instrumental delay	√	--	√	--
Propagation	--	√	√	√
Light	√	√	--	√
UTI-AT	√	√	√	--

[a] Erratic; various procedures applied at various times.
[b] Including radial proper motion.

TABLE 1.29.—*Preprocessing of Data From DME*

Item	Laser DME	5-cm Radar	GRARR	SECOR
Receive material	√	√	√	√
Inspect	√	√	√	√
Catalog and annotate	√	√	√	√
Combine wavelengths	--	--	√	√
Resolve ambiguities	--	--	√	√
Calculate distance	√	√	√	√
Quality control	√	√	√	√
Correction of errors	√	√	√	√
Correct ranges				
Calibration constants	√	√	√	√
Refraction				
Troposphere	√	√	√	√
Ionosphere				
Multi-Hz	--	--	√	√
Mono-Hz	√	√	√	--
Time Correction				
Calibration constants	√	√	√	√
Travel time	√	√	√	√
Compute ranges from orbit	√	√	√	√
Compute residuals	√	√	√	√
Quality control	√	√	√	√

TABLE 1.30.—*Formulae for Correction of Range*

The correction ΔR to the measured distance is computed as a function of the distance R, and of time *derivatives* of distance, time t, and elevation angle ϕ. The general formula is

$$\Delta R = a_1 + a_2 R + a_3 \dot{R} + A_4 \ddot{R} + a_5 R^{(3)} + a_6 t + a_7 t^2 + a_8 R t + a_9 \dot{R}/R + a_{10} \csc \phi$$

	Instrument Type			
Constant	Laser DME	5-cm Radar	GRARR	SECOR
a_1	✓	✓	✓	✓
a_2	✓	--	✓	✓
a_3	✓	--	✓	✓
a_4	--	--	✓	--
a_5	--	--	--	--
a_6	✓	--	✓	✓
a_7	--	--	--	--
a_8	--	--	--	✓
a_9	--	--	✓	--
a_{10}	✓	--	✓	✓

TABLE 1.31.—*Unknowns of Concern to the NGSP*

Unknown	Symbol	Organization
Station location Coordinates in barycentric system	x, y, z	APL[a], DOD/NWL, JPL[b], NASA/GSFC, NASA/WFC, SAO
Coordinates in absolute system	λ, ϕ, h x, y, z	DOD/DMA/TC, NGS, OSU, SAO, DOD/AFCRL, DOD/DMA/AC
Relative coordinates	$\Delta\lambda, \Delta\phi, \Delta h$	JPL, DOD/AC, DOD/TC
Gravitational potential	C_n^m, S_n^m	APL, DOD/NWO[a], DOD/DMA/AC[a], NASA/GSFC, SAO
Polar motion	x, y	APL[a], DOD/NWL, NASA/GSFC, SAO
Earth tides	k	APL[a], NASA/GSFC, SAO
Geocentric gravitational constant	GM	JPL *et al.*

[a] Results not given in this book.
[b] Distance from axis of rotation and distance above equatorial plane.

TABLE 1.32.—*Observables Used in NGSP*

Observable	Symbol	Used by
Distance to satellite	d, r, s	DOD/DMA/TC, DOD/AFCRL, NASA, OSU, SAO
Direction to satellite		
Right ascension, Declination	α, δ	DOD/AFCRL, DOD/DMA/AC, NASA/GSFC, NGS, USO, SAO
Direction cosines	$l, m, n, \mu_1, \mu_2, \mu_3$	NASA/GSFC
Altitude, azimuth	A_z, E_l	JPL, NASA/WFC
Frequency	f	APL, DOD/NWL, JPL, NASA/GSFC
Gravity	g	NASA/GSFC, SAO
Distance between surface points (SP's)	d, s	NASA/GSFC, OSU, SAO
Direction between SP's	A_z	NASA/GSFC, OSU, SAO
Elevation of SP	H	NASA/GSFC, OSU, SAO
Time	t	All investigators

TABLE 1.33.—*Auxiliary Observables Used in NGSP*

Observable	Symbol	Used to Compute
Temperature	T	Tropospheric refraction
Pressure	P	Tropospheric refraction
Humidity	e	Tropospheric refraction
Electron content	N_e	Ionospheric refraction
Density of atmosphere	ρ	Drag
Solar radiation constant	S	Solar radiation pressure
Time	t	Time of observation; position from equations of motion

TABLE 1.34.—*Formulae for Forces of Appreciable Size (Other Than Terrestrial Gravitation)*

Force	Formula
Lunar[a]	$\frac{GM_{\leftmoon}}{r_{\leftmoon}}\left[\frac{r_{\leftmoon}}{r_{s_{\leftmoon}}}-\frac{r\cos\theta_{\leftmoon}}{r_{\leftmoon}}\right]$
Solar[a]	$\frac{GM_{\odot}}{r_{\odot}}\left[\frac{r_{\odot}}{r_{s_{\odot}}}-\frac{r\cos\theta_{\odot}}{r_{\odot}}\right]$
Atmospheric drag[b]	$\rho C_D \frac{A_a}{M_s}\frac{V\,\mathbf{V}}{2}$
Pressure of solar radiation[c]	$\pi\frac{R_s^2}{M_s}k\frac{S}{C}$ or $\frac{A_s}{M_s}k\frac{S}{C}$

$M_{\leftmoon}, M_{\odot}, M_s$ masses of the Moon, Sun, and satellite, respectively.
$r_{\leftmoon}, r_{\odot}$ geocentric distances of the Moon and Sun, respectively.
$r_{s_{\leftmoon}}, r_{s_{\odot}}$ distances of the satellite from the Moon and the Sun, respectively.
$\theta_{\leftmoon}, \theta_{\odot}$ angles between the radius to the disturbing body (Moon and Sun, respectively) and the radius to the satellite.
ρ atmospheric density at the height of the satellite.
C_D drag coefficient.
$\mathbf{V}$ velocity vector of the satellite relative to the atmosphere.
A_a, A_s cross-sectional areas of the satellite in a plane perpendicular, respectively, to the direction of motion and to the direction of the Sun.
S solar radiation constant; 1.94 cal/cm² min or 1.5×10^{-6} newton/m².
k reflection factor.

[a] Kozai (1959a, 1966b), Blitzer (1959), Kaula (1962a), G. Cook (1962), Newton (1965), Murphy and Felsentreger (1966), Berger and Boudon (1972), Challe and Laclaverie (1969).
[b] Parkyn (1960), Izsak (1960b), Brouwer and Hori (1961), G. Cook (1963a), Ewart (1962), King-Hele (1964).
[c] Geyling (1960), Musen (1960), Bryant (1961), Brouwer (1963), Lala (1971).

TABLE 1.35.—*Methods of Numerical Integration Used in NGSP*

Name	Used by	Type	General Form[a]
Runge-Kutta	APL	One-step	$Y_{n+1} = Y_n + h\Phi_{(X_n, Y_n, h)}$
Cowell[b]	NASA	Multi-step	$Y_{n+1} = 2Y_n - Y_{n-1} + h^2\sum_m \gamma_m \nabla^m f_{n+1}$
Störmer[b]	NASA	Multi-step	$Y_{n+1} = 2Y_n - Y_{n-1} + h^2\sum_m \gamma_m \nabla^m f_n$
Adams-Bashford[b]	NASA	Multi-step	$Y_{n+1} + Y_n + h\sum_m \gamma_m \nabla^m f_n$
Adams-Moulton[b]	NASA	Multi-step	$Y_{n+1} + Y_n + h\sum_m \gamma_m \nabla^m f_{n+1}$
Second-sum	JPL	Multi-step $\left\{\begin{matrix}2\text{ sum}\\10\text{ diff}\end{matrix}\right\}$	Moyer (1971)
Second-difference	DOD/NWL	Multi-step	Herrick (1971)

[a] h = step size
γ_m = constant
f_m = given function
Φ = adjustment function
[b] Note that Cowell's and Störmer's methods apply to function f without first derivative, whereas the Adams-type equations apply to first-order equations.

2

APPLIED PHYSICS LABORATORY

C. A. Dunnell

P. Ferriter

G. Gebel

H. S. Hopfield

M. M. Schaefer

S. M. Yionoulis

2.1 INTRODUCTION

The satellite-geodesy research program at the Johns Hopkins University Applied Physics Laboratory (APL) was initiated as part of a major effort to develop a Doppler navigation satellite system for the U.S. Navy. The concept of this system was proposed by F. T. McClure, head of the laboratory's research center, after reviewing the results of an experiment performed by W. H. Guier and G. C. Weiffenbach.

When the Russians orbited the first Sputnik satellite on 4 October 1957, Guier and Weiffenbach (1958) demonstrated that the satellite orbit could be determined from an analysis of the Doppler shift on transmissions of the satellite. Later, using more sensitive tracking equipment designed by H. B. Riblet and J. W. Hamblen, they were able to repeat these experiments with the Sputnik 2 signal (40 MHz) and also with the 108-MHz signals from the Explorer and Vanguard satellites.

McClure, noting the accuracy with which the orbits were being predicted from the Doppler-shift measurements, realized that if the satellite position could be determined by measuring the Doppler shift at a station of known position, it would also be possible to determine the position of a station if the position of the satellite was known. He also recognized that this ability could provide the Navy with a precise all-weather navigation system (McClure, 1965).

By 1959 the first experimental satellite, TRANSIT 1A, had been designed and constructed, the computer tracking programs had been prepared, and five tracking stations had been constructed by APL. Although this satellite failed to achieve orbit, sufficient data were obtained to demonstrate the feasibility of the Doppler navigation satellite system as proposed to the Navy.

To establish this system for the Navy, it was necessary for APL to design and fabricate satellites (and satellite-tracking equipment) and begin geodetic studies. A development program was officially begun in 1959.

It was recognized from the beginning that the success of this system would depend mainly on the ability to provide an accurate satellite ephemeris to the users. It was also recognized that the largest force affecting the motion of a near-Earth satellite was the Earth's gravitational field. Therefore the main emphasis of the developmental program was directed toward obtaining an accurate model of this field.

Inasmuch as the Doppler shift in the frequency of the radio signal transmitted by the satellite is a strong function of the motion of the satellite relative to the observer, Doppler shifts are an excellent source of data for determining a model of the Earth's gravitational field. Therefore a worldwide network of tracking stations was established (Newton and Kershner, 1962) and a constellation (set) of geodetic satellites proposed to obtain the necessary Doppler data.

It would be impossible, in the space allocated, adequately to describe and present the analyses used and results obtained in all the geodetic studies performed at APL. The major effort of the laboratory's space research program has been directed toward modeling the Earth's gravitational field from an analysis of the Doppler shifts on the transmitted frequencies of the satellites as obtained by the tracking stations. Therefore the emphasis in this chapter is on the satellites involved and the methods used in accomplishing this goal.

Section 2.2 describes some of the satellites built by APL that contributed significantly to the geodetic programs of many of the organizations associated with the NGSP. Section 2.3 presents a discussion of the Doppler tracking station network (TRANET) and describes the operation of the network and

the instrumentation needed by each tracking station. Additional information on TRANET can be found in chapter 3. Section 2.4 summarizes the data and the preprocessing applied to them. The methods of analyzing the data that culminate in an improved model of the Earth's gravitational field are presented in section 2.5, and the results of the last determination of this model are given in section 2.6.

2.2 SATELLITES

Figure 2.1 gives the overall status of APL satellites covering the period from 1959 through early 1969. Six of these satellites, which made a significant contribution to the development of the navigational system and to geodetic research programs, are described in the following pages: TRANSIT 1B, ANNA 1B, Beacon Explorer–B, Beacon Explorer–C, GEOS–A, and GEOS–B. Doppler data from observations on the last four of these are stored in the Geodetic Satellite Data Center. (See chapter 1.) Data from satellites that carried TRANSIT beacons were used by APL and the Naval Weapons Laboratory (NWL) in the results given in this chapter and in chapter 3. Section 2.2.3 describes the TRANSIT beacon.

2.2.1 TRANSIT 1A

TRANSIT 1A was the "granddaddy" of all TRANSIT-type navigation satellites, and its design was adhered to for a long time. Unfortunately it failed to acquire orbital velocity after launch on 17 September 1959. The next satellite, TRANSIT 1B, which was almost identical to TRANSIT 1A in design, was successfully launched 13 April 1960, with an electronic system almost identical to that of TRANSIT 1A. Other satellites similar in design to TRANSIT 1A and successfully put into orbit were TRANSIT 2A, 3B, 4A, 4B, and 5A. Model 3B was launched together with satellite LOFTI, which failed to separate. TRANSIT 4B was launched together with satellite TRAAC. The shape was changed from spherical to octagonal.

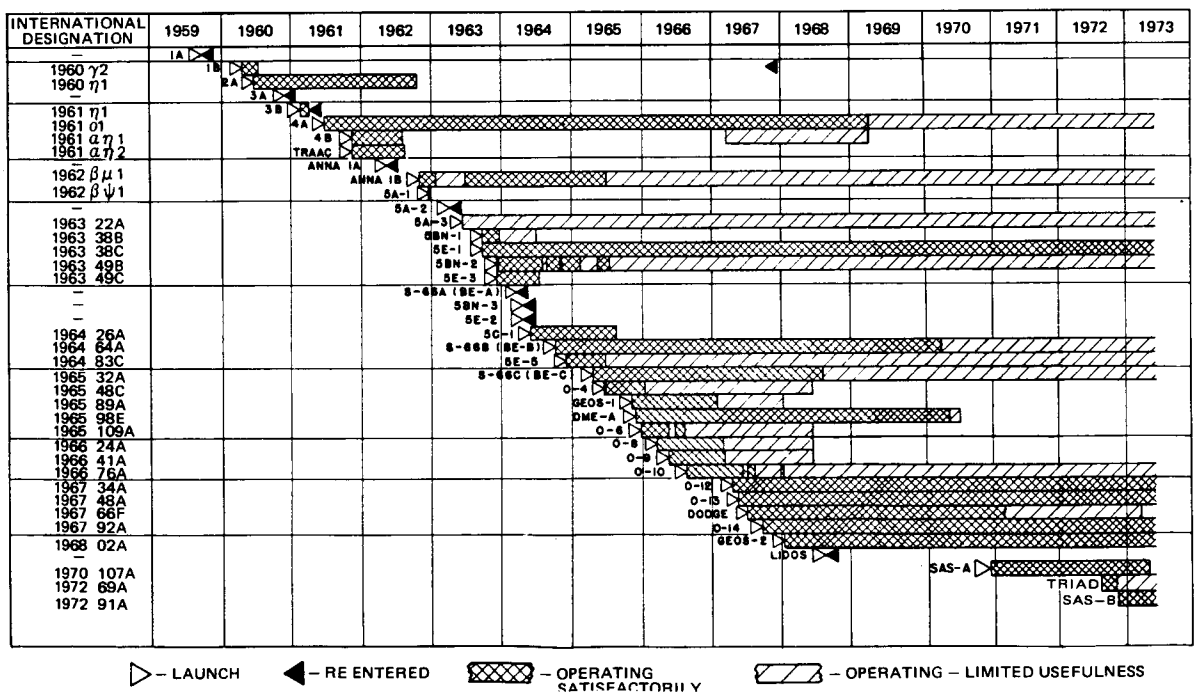

FIGURE 2.1.—Overall status of APL satellites for period 1959–1969.

2.2.2 TRANSIT 1B (1960–γ2)

TRANSIT 1B lasted 89 days after launch. Replacing TRANSIT 1A, it had the same objectives, i.e., to demonstrate the feasibility of the Doppler navigation concept and to test various items of equipment involved in the Doppler navigation system. It also carried instruments for measuring the Earth's albedo in the infrared. Table 2.1 gives the characteristics of the satellite. Figure 2.2 shows the satellite construction.

TRANSIT 1B was similar in mechanical and electrical structure to TRANSIT 1A except that the modulated 108–MHz carrier of TRANSIT 1A was replaced by an unmodulated 324–MHz signal in TRANSIT 1B. General descriptions of the satellite and project TRANSIT can be found in articles by Kershner (1960) and Nicolaides (1961). The circuitry of TRANSIT 1A and 1B is described by Hamblen and Oakes (1961) and Schreiber and Wyatt (1960). The antenna, of a broadband spiral type used in many succeeding satellites, is described by Riblet (1960).

2.2.3 ANNA 1B (1962–βμ1)

Satellite ANNA 1B was launched 31 October 1962 as part of a joint Army, Navy, NASA, and Air Force project to improve geodetic control and to compare the performance of the various tracking instruments of the services. The satellite therefore contained a transponder as part of the Army's SECOR tracking system; flashing lights for photography by the PC–1000 cameras of the Air Force, the MOTS cameras of NASA, and the BC–4 cameras of the U.S. Coast and Geodetic Survey (CGS); and a TRANSIT beacon for use in the APL and NWL tracking systems.

The characteristics of ANNA 1B are given in table 2.2. Figure 2.3 is a schematic of the satellite. Details on the flashing light subsystem and on the SECOR transponder are given in chapter 3.

Except for the painted pattern on the outside of the satellite, ANNA 1B was identical to ANNA 1A, which was to have been launched on 10 May 1962 but did not go into orbit because the second-stage rocket engine failed.

ANNA 1B was important for several reasons: it was the first satellite launched specifically for geodesy; it provided data over a long period of time to many groups; and finally, it was the prototype of the GEOS series of satellites (see secs. 2.2.6 and 2.2.7).

2.2.4 Beacon Explorer–B (1964–64A)

The satellite Beacon Explorer–B (also called BE–B, S–66, and Explorer 22) was launched 9 October 1964 by a Scout rocket, Beacon Explorer–A having failed to go into orbit. It carried a TRANSIT-type beacon, an array of corner-cube reflectors to allow tests of the newly developed laser-type distance-measuring equipment (DME), and a photo-

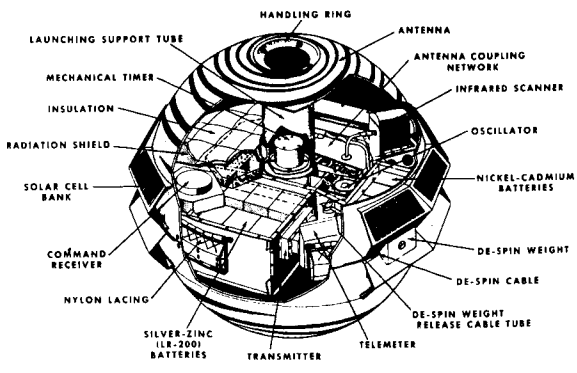

FIGURE 2.2.—TRANSIT 1B.

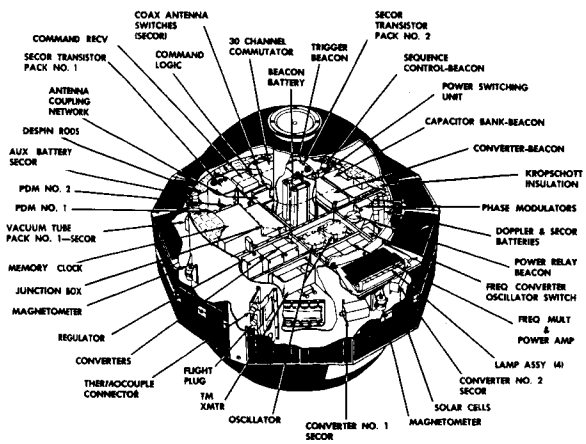

FIGURE 2.3.—Schematic diagram of ANNA 1B.

detector for measuring the intensity of incident light from the laser. It also carried a three-axis, flux-gate magnetometer and two probes for investigating electron density in the neighborhood of the satellite. Table 2.3 gives the satellite's characteristics; figure 2.4, an exploded view of the satellite, shows the instrumentation.

2.2.5 Beacon Explorer–C (1965–32A)

This satellite (also called BE–C and Explorer 27) was launched on 29 April 1965 by a four-stage Scout rocket. Its purpose and instrumentation were identical to those of Beacon Explorer–B and therefore need not be discussed. Table 2.4 lists those characteristics that differed from the characteristics of Beacon Explorer–B.

2.2.6 GEOS–A (1965–89A)

Satellite GEOS–A (also called GEOS–1 or Explorer 29) was launched 6 November 1965. (See fig. 2.5.) It was intended that the satellite orbit reach apogee at 1480 km, but because the fuel of the second stage of the rocket burned to completion, the apogee was 2294 km instead.

In structure, function, and purpose, GEOS–A (see table 2.5) was a direct descendant of ANNA 1B, described previously. Two ANNA satellites were built. The first, ANNA 1A, never achieved orbit. The second,

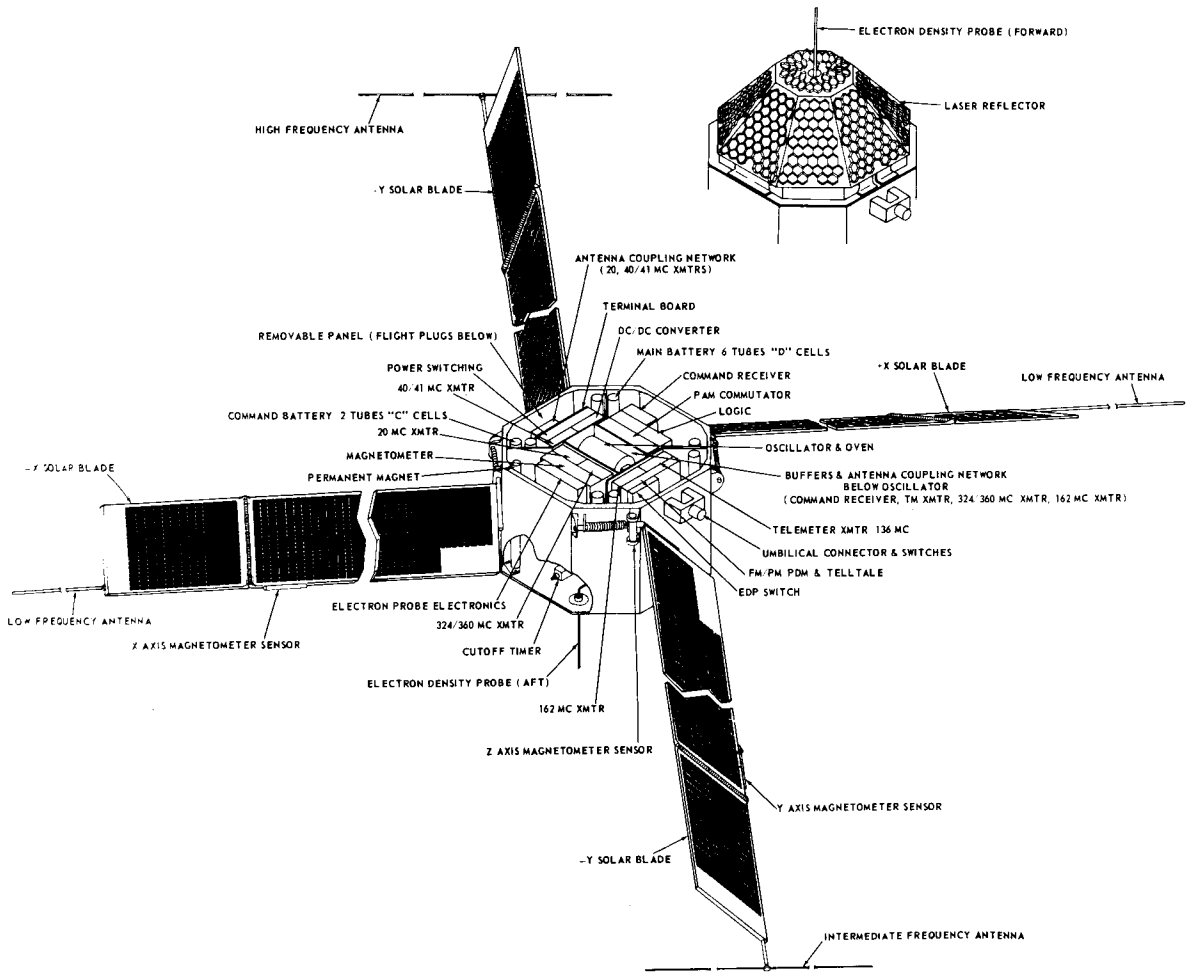

FIGURE 2.4.—Instrumentation of Beacon Explorer.

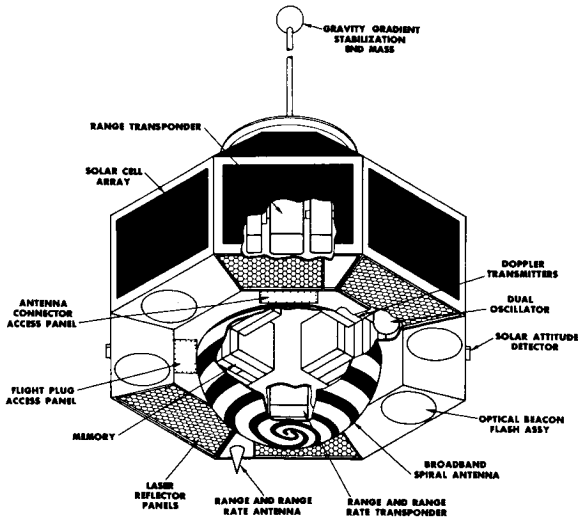

FIGURE 2.5.—GEOS–A.

ANNA 1B, did get satisfactorily into orbit and continued functioning even after GEOS–A was launched. As a consequence of the success of ANNA 1B, more satellites patterned after ANNA were planned. R. B. Kershner, writing in 1964 just before GEOS–A was launched (Kershner, 1965), gave an excellent description not only of the situation at that time, but also of GEOS–A itself. The following paragraphs are from his paper.

> "Although the ANNA satellite is the only one launched to date which was intended to provide broad geodetic usefulness, it was by no means the only satellite which contributed to the current advanced state of geodetic knowledge. The photographic approach has also been used during dawn and dusk periods for satellites which are illuminated by the sun against a dark background. The Navy's Doppler system has been used with a large number of satellites containing stable transmitters which have been launched in connection with the development of their satellite navigation system. Finally, the Army has launched several small satellites containing SECOR transponders which have been successful.
>
> "By all odds the greatest amount of data of geodetic quality has resulted from the use of the Applied Physics Laboratory/Navy Doppler system. This results from a combination of the rather large number of satellites with appropriate stable transmissions launched in connection with the development of a satellite navigation system together with an extensive global network of Doppler receiving stations.
>
> "Although progress to date [1965] has been quite rapid using, largely, satellites of opportunity with only one general and a few special satellites primarily intended for geodetic purposes, it is quite clear that, in the future, things will be more difficult. The honeymoon is over. Just because the progress to date has been so impressive further progress will require considerably more effort, with satellites very specifically designed for geodetic purposes.
>
> "By now two new elements have altered the situation. First, it has been determined that further progress in geodesy has no real military significance and, accordingly, the responsibility for geodesy has been transferred to the National Aeronautics and Space Administration (NASA). Secondly, two new measurement techniques have been developed which have precision of geodetic quality; namely, a range and range rate system developed by the Goddard Space Flight Center of NASA and a laser corner reflector system developed for NASA by General Electric. [See ch. 5.]
>
> "The laser system has already been tested. The concept is very simple—a laser (coherent light) pulse is sent to an orbiting satellite which contains a corner reflector capable of returning the incident energy back to the source point. The total time of travel is measured and a very accurate range measurement results. This system has been tested with the S–66 satellite, launched on October 10, 1964, which was primarily intended for ionospheric research, but which also carried an appropriate corner reflector. The range/range rate system was incorporated in the SYNCOM satellite and has already been useful in confirming the values for the

zonal harmonics obtained from other sources.

"In view of the situation outlined above, the NASA has asked the Applied Physics Laboratory of the Johns Hopkins University to develop a series of satellites to advance the state of knowledge of geodesy. . . .

"The first satellite under the NASA sponsorship intended from the beginning for geodetic research has been named GEOS and is under construction at the Applied Physics Laboratory intended for launching in the fall [1965]. It contains provisions for the use of all five of the systems currently considered to have sufficient accuracy to contribute to geodetic research; namely, flashing light, Doppler, SECOR, range/range rate, and laser reflector. A block diagram of GEOS–1 is shown in Figure 1. [See fig. 2.6.]

"The configuration of the GEOS satellite differs quite markedly from that of ANNA. The major differences in external configuration are a result of the decision to use gravity gradient stabilization for GEOS. This means that one face of the satellite can be assumed always to face the earth. This allows the solar cells to be concentrated on those faces of the satellite that do not face the earth while the antennae, the flashing lights and the laser reflectors can be mounted on the earth-facing side of the satellite.

"The flashing light system of GEOS is greatly improved over that incorporated in ANNA. A total of four independent flashing light systems are incorporated. This provides a considerable increase in reliability through redundancy and also great flexibility in use. By flashing all four lights simultaneously a very bright intensity is available. Alternatively somewhat weaker flashes extending over a longer period can be obtained by commanding separate flashing of individual light systems. [See ch. 3.]

"The Doppler transmitters in GEOS differ in two ways from those used in ANNA. First the basic oscillator stability is slightly better than that of the ANNA

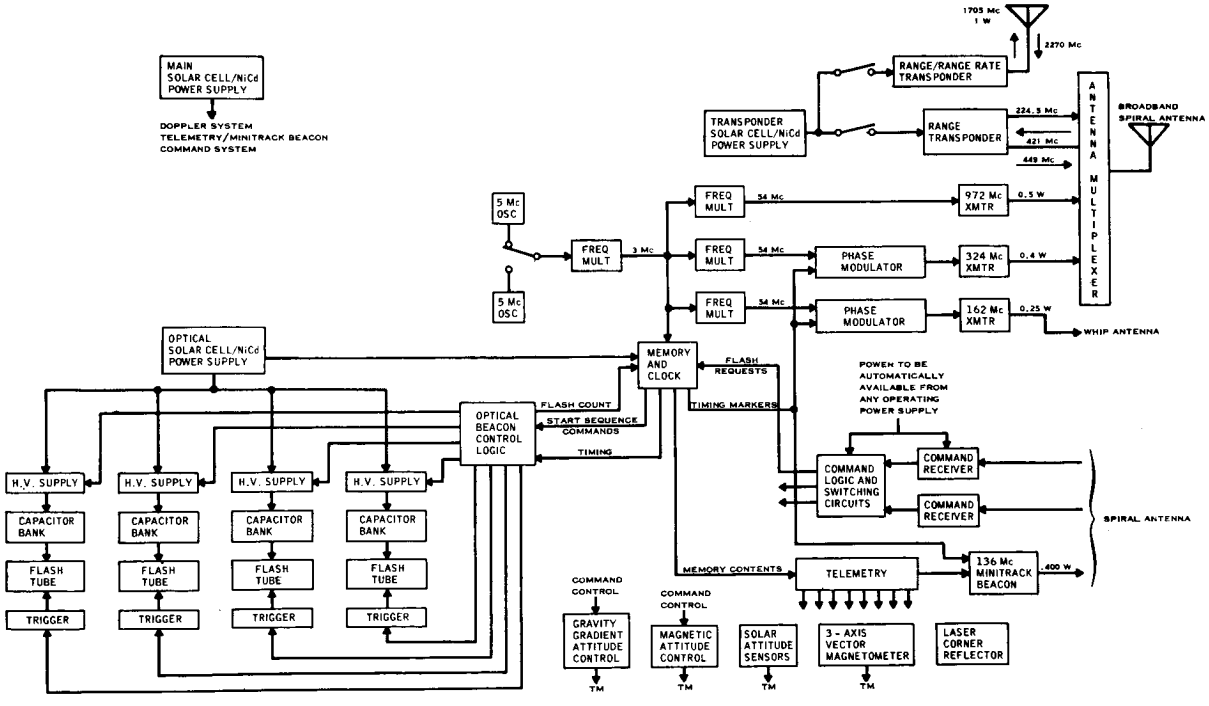

FIGURE 2.6.—Block diagram of GEOS A.

oscillator, being about 3×10^{-11} as compared to 5×10^{-11} for ANNA. In addition, transmitters are provided not only at 162 and 324 Mc [MHz] as in ANNA, but also at 972 Mc. This made it possible to make a more sophisticated correction for ionospheric refraction using all three frequencies rather than the first-order two-frequency correction used with the ANNA transmissions. Even with the same two-frequency correction technique the results are greatly improved by the use of the 972-Mc transmission as one of the two frequencies.

"The remaining systems, i.e., the SECOR, range/range rate, and laser reflector, are described elsewhere and their implementation in GEOS contains no special features except for the obvious advantage of gravity gradient stabilization in making possible convenient orientation of antennae and the laser corner reflector.

"In order to make a maximum contribution to geodesy, it is necessary to consider carefully not only the satellite design but also the orbit into which it is launched. The primary consideration is the following: There is a limit to the number of gravitation field force terms that can be determined from any particular satellite orbit. Since the satellite is responsive to a specific summation of all the force terms it is always possible, for any particular orbital inclination, to change the value of some force term coefficients by making compensatory changes in other coefficients, without appreciably altering the effect on that particular satellite. However, the effect of the altered gravitational field model would be appreciably different for satellites at another inclination. The more different inclinations there are for which precision tracking data are available, the more force terms can be computed. Data of geodetic quality were already available at inclinations of 32°, 50°, 67°, 80°, 90°. The BE–C (back-up) ionospheric research satellite is planned for a 41° orbit. GEOS A is planned for 59°."

2.2.7 GEOS–B (1968–002–A)

Satellite GEOS–B (also called GEOS 2, S–11, and Explorer 36) was launched 11 January 1968. It was placed in a retrograde orbit of 105°.977 or −75° as compared to the 59° orbit of GEOS–A. Also it was placed in an approximately circular orbit ($e=0.0308$). Except for this difference in orbits and the addition of a transponder (5 cm, C–band) and reflector to work with the 5-cm (C–band) radars, the two satellites were much alike. The main power source, the flashing light system, and the satellite clock began to develop problems soon after the satellite was in orbit. Table 2.6 lists the principal characteristics of GEOS–B.

2.3 INSTRUMENTATION EXCLUSIVE OF SATELLITES

2.3.1 TRANET Network

The Doppler tracking station network TRANET was established in the early 1960's under U.S. Navy sponsorship. It was a necessary part of the Navy Navigation Satellite System (NNSS) development effort. Once the NNSS requirements had been satisfied, TRANET observations of the Doppler shift were applied to other problems: determination of geocentric coordinates of earth-fixed points, establishment of ties between the several world datums, determination of tides in the crust (Newton, 1968), and further refinements to the model of the gravitational field.

Thirteen of the stations constitute a basic network that has remained essentially intact over the past decade. The basic network is augmented for special missions or short-term requirements by van-mounted or otherwise transportable equipment. Operation of the stations is a responsibility of the Doppler Satellite Office at the Pacific Missile Range and is carried out by contract with the Physical Science Laboratory of the New Mexico State University and through operating agreements with other agencies, including

the governments of foreign countries. Several cooperating stations sponsored by the National Science Foundation are operated in the Antarctic in support of U.S. Geological Survey projects by contract with the Applied Research Laboratories of the University of Texas at Austin.

TRANET stations automatically acquire signals and produce data from satellites transmitting on the frequency pairs 150/400 and 162/324 MHz. With suitable modifications, other frequencies can be and have been received. Stations operate largely unattended, accumulating Doppler shift data on punched paper tape. The data are transmitted via the Autodin network of the Department of Defense (DOD) to the Satellite Control and Communication Center (SCC) at APL.

Communication by high-speed teletypewriters ensures early receipt and processing of the data and more rapid return of station diagnostic results to the stations than would be possible if the data were mailed. It also simplifies the assembling and processing of data in the SCC by reducing the time required to assemble each day's data and the amount of data accumulating in the SCC at any given time.

2.3.2 Satellite Control Center

Data are received more or less continuously in the SCC on punched paper tape. The data may be in one of four formats: TRANET CCID, TRANET Sampled, GEOCEIVER, or ITT 5500. The data are logged and transferred to magnetic tape for further processing by computer.

Soon after 0500 UT each day, the magnetic tape containing the data from the previous 24-hour period is taken to a computer for processing. The processing includes, among other things, checking for format errors, correcting data identification errors, creating data files from which the corrected data can be retrieved by giving satellite, day, and station, and generating seven-track magnetic tape for subsequent transmission.

2.3.3 Tracking Station Instrumentation

Measurement of the Doppler shift in signals received from satellites requires the measurement of frequency and time. (In a strict sense, all frequency measurements are made by measuring time interval; however, it is convenient to speak of frequency measurement without this qualification.) It requires that the frequencies radiated by the satellite be derived from a "highly stable" frequency source and that the receiving station have "stable" frequency and time references. In practice, the satellite signals are radiated in pairs of phase-coherent frequencies, i.e., frequencies derived from a common crystal. Use of two frequencies enables a correction to be made for the frequency-dependent refractive effects of the ionosphere.[1]

TRANET stations are designed to receive signals on certain specified frequency pairs, nominally 150/400 and 162/324 MHz, to correct for ionospheric refraction effects, to measure the Doppler shift on the refraction-corrected signal, to receive timing signals from NNSS satellites, and to record both the Doppler shift and the timing data on punched paper tape.

For convenience in specifying the performance required of a TRANET station, specific frequencies in the satellite signal have been used to define modes of operation. Each mode defines a set of station-operating conditions that must be satisfied to produce data from the specified frequencies. Table 2.7 gives the currently defined modes for automatic and manual operation of TRANET stations. When operated manually, the stations are capable of receiving signals on frequency offsets other than those listed, the limiting condition being the frequency range of the voltage-controlled oscillator (VCO) of the receiver. This range is approximately 0.2 to

[1] This is, of course, not the only approach. If the frequency is high enough, ionospheric refraction effects are negligible. Experience indicates that 2.5 GHz is high enough that correlated ionospheric errors are rarely seen in the data.

80 kHz below the nominal frequencies listed in table 2.7.

A complete tracking station (fig. 2.7) consists of the following components: (1) antennas and preamplifiers, (2) dual-channel, phase-lock tracking receivers, or separate fixed-frequency receivers and phase-lock tracking filters, (3) a refraction-correction analog system, (4) a digital processor, comprising a Doppler shift-and-timing data digitizer and station clock, and a header programmer, (5) a frequency standard, typically a crystal oscillator and VLF receiver for frequency determination, (6) a device for recognizing 2-min time marks from NNSS satellites, (7) a WWV receiver and time comparator, (8) a paper-tape punch and analog-signal recorders, and (9) power supplies, standby batteries, test equipment, displays, and station-control devices for automatic operation.

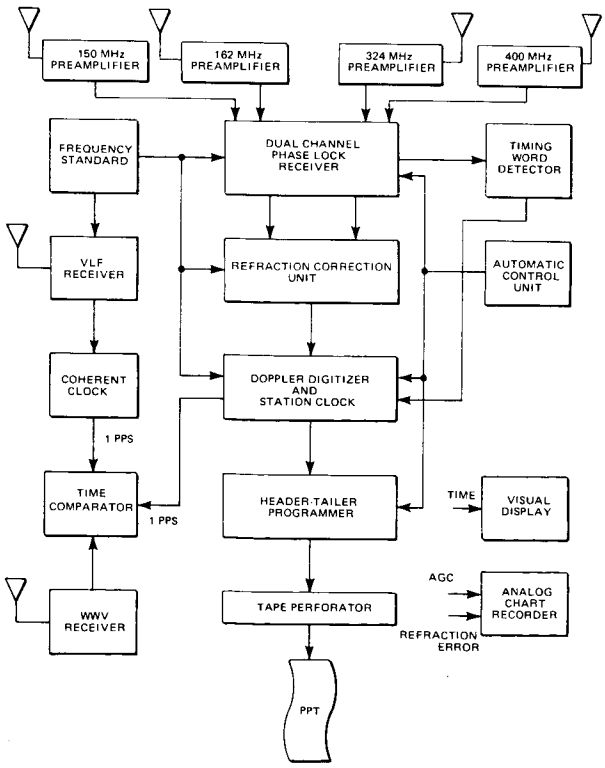

FIGURE 2.7.—Simplified block diagram of typical tracking station instrumentation using phase-lock receiver.

2.3.3.1 Antennas and Preamplifiers

Ideally, ground station (tracking station) antennas should be chosen to match the signal polarization and the gain pattern of the satellite antenna. Geodetic and navigational satellites flown in the past decade have radiated signals with linear, left-circular, and right-circular polarization. The TRANET ground-station system began with quarter-wave vertical antennas and has continued to use them successfully to receive signals from numerous satellites of opportunity—the French-built D1A, D1C, D1D and the U.S.-built nongeodetic satellites—as well as those intended specifically for geodetic purposes. Circularly polarized receiving antennas have been used on occasion for test purposes, with fair success.

Before 1969, station antennas were generally arranged in a square array, with the two antennas of each pair on diagonally opposite corners. In 1969, analysis and experiment determined the effective measurement center of a pair of vertical antennas (see 2.3.3.3). Since 1969 all new antenna installations have been linear arrays of whip antennas having a common measurement center for both frequency pairs.

Low-noise preamplifiers, mounted near the individual antennas, establish a system noise figure at 5 dB or better on all frequencies.

2.3.3.2 Receivers

The phase-lock receivers used by most stations may be one of two models: the Space General Model 104751 or the ITT Model 1004AB. Although they differ in detail, both are dual-channel receivers incorporating a second-order, phase-lock demodulator. Some stations of the TRANET use instead separate fixed-frequency receivers and phase-lock demodulators.

In any case, the inputs to the receivers are the satellite signals and a local reference signal derived from the station's frequency standard. The receiver amplifies and translates the noisy, Doppler-shifted signal, as

received, to a new frequency, which serves as the input to the receiver or tracking filter phase-lock demodulator. The outputs of the phase-lock demodulator consist of the filtered Doppler-shifted signal offset by a certain fixed frequency and the demodulated phase signals, which contain the satellite time word.

In the phase-lock receivers the Doppler-shifted signal is offset in frequency by 26 MHz. In the tracking filter the corresponding offset is 250 kHz. In either case the offset is removed by the operation of the refraction corrector.

The phase-lock demodulator acts as a variable-frequency band-pass filter. For such filters, output rms phase-noise is related to the input signal-to-noise ratio and the tracking bandwidth by (Interstate Electronics Corporation, 1960)

$$\text{output rms phase-noise} = \frac{N}{a}\frac{B_t}{B_i}$$

where

N rms noise voltage at the input
a rms signal voltage (sinusoidal) at the input
B_t tracking loop bandwidth, typically 10 Hz
B_i bandwidth of input, established by the receiver, typically 50 kHz or less

Output rms phase-jitter for either type of receiver is typically less than 0.01 Hz.

2.3.3.3 Refraction Corrector

The effect of ionospheric refraction on the Doppler shift of a satellite signal is a function of the signal frequency. It can therefore be eliminated, to first order, by transmitting two phase-coherent signals of different frequencies and combining the data as follows:

The total Doppler shift Δf in the frequency f of either transmitted signal as measured at the tracking station can be written, correct to $0(1/f^3)$, as (Guier, 1961)

$$\Delta f = -\frac{f}{c}\dot{\rho} + \frac{a_1}{f} + \frac{a_2}{f^2} + \frac{a_3}{f^3} + \ldots \qquad (2.1)$$

where

$\dot{\rho} \equiv d\rho/dt$ the geometric range rate (uncorrected for tropospheric effects)
c the velocity of light
a_1/f the first-order ionospheric refraction contribution; a_1 is proportional to the time derivative of the total electron content along the geometric slant-range vector from station to satellite.
a_2/f^2 the second-order ionospheric refraction contribution; a_2 depends on signal polarization (choice of sign depends on direction of circular polarization) and on the magnetic field component in the direction of travel of the signal; a_2 is related to Faraday rotation; the a_2 term is typically 1 percent of the a_1 term
a_3/f^3 the third-order inospheric refraction contributions; a_3 has several components and involves, among other things, the difference between the signal path and the slant range vector.

The validity of this expansion depends explicitly on the fact that the frequency of the transmitted signal is large in comparison with the (so-called) electron plasma resonance frequency of the ionosphere. This latter quantity depends on the local electronic density and therefore varies from point to point in the ionosphere. The plasma resonance frequency is typically a few megahertz and rarely exceeds 10 MHz. To ensure that the expansion is valid, the transmission frequency for Doppler satellites should exceed 100 MHz.

If higher order terms are neglected, equation (2.1) yields for the two frequencies

$$\begin{aligned} \Delta f_1 &= -\frac{f_1}{c}\dot{\rho} + \frac{a_1}{f_1} \\ \Delta f_2 &= -\frac{f_2}{c}\dot{\rho} + \frac{a_1}{f_2} \end{aligned} \qquad (2.2)$$

We can eliminate the a_1 term and obtain

$$\Delta f_1 - \lambda \Delta f_2 = -\frac{f_1(1-\lambda^2)}{c}\dot{\rho} \qquad (2.3)$$

where

$$\lambda \equiv f_2/f_1 < 1 \qquad (2.4)$$

When equations (2.3) and (2.1) are compared, $f_1(1-\lambda^2)$ can be interpreted as an effective frequency of a transmitter in the absence of the ionosphere. Since, however, we can multiply equation (2.3) by any constant, we can make the effective frequency any convenient value.

In practice, the refraction corrector operates on the above principle: combining signals from the two voltage-controlled oscillators of the receiver (or tracking filter) to produce a single refraction-corrected Doppler signal. The frequency to which this resulting signal is scaled depends not only on the input frequency ratio, as shown above, but also on the choice of multiplying factors, i.e., on the instrumentation. (The system contains frequency synthesizers to provide the required frequencies.)

Table 2.8 gives the effective signal frequency corresponding to the refraction-corrected, Doppler-shifted frequencies for each of the standard frequency pairs. The effective frequencies listed in the last column of the table are derived from the third column, but a further correction for the satellite frequency offsets listed in table 2.7 has been made.[2]

To complete the explanation of correction for ionospheric refraction, we recognize that the two antennas associated with the frequency pair are not precisely at the same point. If we repeat the above analysis and insert this detail, the result is unchanged, providing we take for the station position

$$\bar{r}_e = \bar{r}_1 - \frac{\lambda^2}{1-\lambda^2}(\bar{r}_2 - \bar{r}_1) \qquad (2.5)$$

where $\bar{r}_1$ is the position of the antenna associated with the higher frequency, f, of the two and $\bar{r}_2$ is the position of the other (lower frequency) antenna.

It is a beguiling fact (eq. (2.5)) that the station position lies outside the line connecting the two antennas and close to the higher-frequency element of the pair.

The paired antennas for both the 162/324– and 150/400–MHz channels are located so that, consistent with equation (2.5), a common set of station coordinates can be used for both frequency pairs. (R. Anderle of the Naval Weapons Laboratory suggested this refinement.)

In summary, the refraction-corrected Doppler signal is derived as follows. Doppler-shifted, refraction-corrupted satellite signals appearing at the antennas are amplified and mixed with local reference signals to produce beat notes, each containing the Doppler signal, a frequency bias, modulation if present, ionospheric refraction errors, and noise. The phase-lock demodulators reduce noise on the Doppler signals and remove any modulation. The signals from phase-locked loops in the demodulator are combined in correct proportions to produce a single refraction-corrected signal containing the Doppler shift plus a frequency bias, scaled to a new frequency.

2.3.3.4 Doppler Digitizer and Station Clock

The Doppler digitizer and station clock is a self-contained unit incorporating a time-of-day clock and all counters and registers required to count accurately cycles of the Doppler-shifted signal, to perform time and time-interval measurements, and to furnish signals in the proper format to operate a paper-tape punch. It is used to provide accurate period measurements on the Doppler-shifted signal from the refraction corrector.

Until 1971 a 4-sec interval between samples and approximately 1-sec counting periods were used. Every 4 sec, the digitizer counted a preset number of cycles of Doppler shift frequency and recorded the time required for such a count. The count began at the first positive-going zero crossover of the Doppler signal, 100 μsec after an integral second. It ended at the positive-going zero crossover of the N_c^{th} cycle, where N_c is the preset number of counted cycles. The resolution of the time measurement was either 10^{-6} or 0.2×10^{-6} sec,

[2] Satellites rarely transmit frequencies having integer values. The difference, the actual transmitter frequency less the nearest integral megahertz value, is defined as the offset.

depending on the equipment; the preset count was almost continuously variable between 1 and 99 999. The preset count was chosen to make the counting interval just under 1 sec at the beginning of a pass, when the difference between the station frequency and the Doppler-shifted carrier is least.

When the TRANET stations were converted from manual to semiautomatic operation in 1971, the data format was modified to provide counts over contiguous time intervals spanning 10 to 30 sec. The beginning and end time of each interval is now recorded to 10^{-6}-sec resolution and the counts are continuous. This procedure has permitted a reduction in the amount of data transmitted (over ground lines) by a factor of four or five and yet resulted in a higher theoretical accuracy and total information content.

2.3.3.5 Frequency and Time Standards

As the measured physical quantities are frequency and time, the station must have accurate time and precise frequency standards.

Oscillator stability required for specified accuracy of position determination involves two main considerations: (1) If the frequency drift is continuous and monotonic, an error in the Doppler-frequency measurement can result from neglecting oscillator drift parameters. A neglected drift rate of a few parts in 10^{11} per day corresponds to a position error of about 2 cm. (2) Although short-term stability is a commonly used measure of oscillator quality, short-term variations in frequency do not have an important influence on system accuracy unless the variations have a period comparable to 10^3 sec, the duration of a satellite pass. Oscillator variations of a few parts in 10^{12} over the period of a pass correspond to a position error of one meter in the worst case. The stability characteristic of crystal frequency standards of the type used in TRANET stations typically exhibits short-term rms variations of about one part in 10^{11}.

TRANET station clocks are maintained at the UTC rate by monitoring one of the coordinated VLF stations (ch. 1). Typically, a separate clock slaved to the received VLF frequency produces a once-per-second reference pulse. A phase shifter allows the reference pulse to be set to an external standard (NNSS, WWV, portable clock); after the reference pulse has been set to this external standard, it follows the phase of the received VLF signal.

The NNSS satellites provide both UTC for clock control and data from which the station clock error can be determined. In tracking NNSS satellites, the station clock times are recorded at the satellite. These times are later processed to remove propagation and equipment delays, to recalibrate the satellite clocks against a station clock selected as standard, and to compute a station clock error for each satellite pass. These station clock errors can be used to correct the times, but not all users of Doppler data have followed this practice. The computed station clock errors are also fed back to the stations and used to maintain the UTC epoch (ch. 1).

The largest error in using satellite time is thought to be caused by the variability in equipment delay times. These variations currently limit the accuracy attained in station timekeeping to about 0.1 msec at most TRANET stations.

A measure of the attainable accuracy in using NNSS satellites as source of UTC is afforded by comparing the independent measurements of satellite clock error made (1) by the U.S. Navy Astronautics Group, using data from the Navy's four tracking stations in setting the satellite clocks, and (2) in the programs that compute satellite and station clock errors for the TRANET stations. The agreement between these two measurements is usually good to a few tens of microseconds. Both Navy Astronautics Group time standards and the TRANET time standard at APL are related to the U.S. Naval Observatory time by periodic portable clock visits, LORAN C monitoring, or similar means.

2.3.3.6 Satellite Time-Mark Detector

Several devices have been used in the TRANET to recognize the occurrence of the

2-min mark that is broadcast by NNSS satellites. Most stations are equipped with a device that produces a fiducial pulse at the 2-min mark. Another device used at several stations produced a pulse at a bit transition that occurs in the satellite time encoder 775 434 μsec after the 2-min mark. In either case, the fiducial pulse triggers a readout of the tracking station clock with a resolution of 1 μsec. These time readouts are interspersed with Doppler data points.

Accuracy of the first device is limited by the variability of delays through the equipment and decoder to about 100 μsec. Accuracy of the other is about 10 μsec.

2.3.3.7 Automatic Control Unit

Acquisition of satellite signals and the production of data on punched paper tape can be under the manual control of an operator, but normally are controlled by the station automatic control unit (ACU). Functions performed by the ACU include control of the receiver or tracking-filter signal search operation, automatic acquisition of signals, validation of satellite signals, and operation of the digitizer and paper-tape punch to produce data and headers.

2.3.4 The Doppler Beacon

Instrumentation required in a satellite for Doppler tracking includes a highly stable oscillator, a frequency synthesizer, and power amplifiers and antennas for the signals to be radiated. These components make up a Doppler beacon, a system that has been used with minor variations from the earliest TRANSIT satellites to the most recent satellites carrying Doppler beacons. In some applications the RF carriers may be phase-modulated to provide telemetry and timing signals. NNSS satellites also broadcast the ephemeris of the satellite and time marks in UTC each even minute. The time marks are of particular interest to the TRANET system, since they provide time reference for the system.

The typical Doppler beacon consists basically of a low-frequency oscillator of high stability, a frequency synthesizer, and power amplifiers and antennas for 162– and 324–MHz signals. The signal source is an ultrastable crystal oscillator using redundant, fifth-overtone, 5–MHz crystals. Temperature control is provided by redundant, proportional control heaters. Either oscillator or heater is selectable by command: The 5–MHz signal is used to synthesize a 54–MHz signal. Two buffered 54–MHz signals from the synthesizer drive the two power amplifiers, which multiply the 54–MHz signal by the appropriate factor and amplify the signal to a level suitable for radiation. Typical output levels are 0.25 watt at 162 MHz and 0.4 watt at 324 MHz. Antennas are selected to provide left-hand circular polarization with hemispheric coverage.

Short-term variations of the Doppler beacon frequency are typically a few parts in 10^{11}, measured on the ground. Oscillator drift rates when the satellite is in orbit average two parts in 10^{11} per day for the more recent satellites.

2.4 DATA

This section summarizes the data used by APL in producing the model of the gravitational field given in section 2.6.1. It also describes the procedures used in preparing the observational data (Doppler shifts and corresponding times) for use in observation equations.

2.4.1 Summary of Data

The data used in producing the results given in section 2.5 are summarized in tables 2.9 through 2.12. Table 2.9 gives the approximate values of the elements of the orbits of the satellites involved. Table 2.10 summarizes for each satellite the amount of data acquired from that satellite. Table 2.11 gives the values of the zonal harmonic coefficients used (these were provided by Anderle and Smith of the Naval Weapons Laboratory,

Dahlgren, Virginia, in a private communication). Table 2.12 gives values of miscellaneous quantities used in the computations.

2.4.2 Doppler Data Preprocessing

2.4.2.1 Introduction

The observations of the tracking station must be processed before they can be used for orbit determination. This processing consists of two steps. The first, usually performed at the station, consists of correction for first-order ionospheric refraction. The second, performed at the computing center, consists of converting the observation (as corrected for refraction) from a Doppler cycle count over a stated time interval into a Doppler frequency at a stated epoch. A fixed number of cycles of the Doppler shift to be counted is selected so that the count for each observation will require less than 1 sec. The counts are started every 4 sec. This sampling frequency, used in the National Geodetic Satellite Program, differs from other later sampling frequencies (in Continuous Count, SRN–9, and GEOCEIVER equipment) in which counting periods are longer and contiguous and in which the count is equated to a range difference rather than a frequency. As will be seen, the later sampling frequencies have certain practical advantages.

2.4.2.2 Refraction Correction (Ionosphere)

The satellite transmits signals at two frequencies, obtained from the same oscillator so that the transmissions are coherent. A typical pair of frequencies would be 162 and 324 MHz. These frequencies are offset (reduced) by a small amount, typically 80 parts per million. The reference frequencies of the tracking station are not offset, so that the resulting Doppler shift frequencies never go through zero. The station thus observes two Doppler signals simultaneously. It is the combination of these two signals that results in the elimination of the first-order ionospheric refraction contribution.

The phase of the q^{th} Doppler signal is

$$\varphi_q = 2\pi \int_0^t dt \left[F_{Tq} - (F_{Sq} + \Delta f_q + \sum_k \Delta f_q^{(k)} + R_{Tq}) + N_q \right]$$

This is an all-inclusive expression, which we now simplify. The summation over k, representing the ionospheric contribution, is replaced by the first term $\Delta f_q^{(1)}$. The remaining terms have been ignored at this time as having negligible effect. The noise term N_q represents the contribution of many noise sources. No attempt has been made to include their effect analytically. Experience indicates that the contributions may be ignored.

Since both the Doppler shift and the tropospheric refraction correction (see sec. 2.5) are proportional to transmitted frequency, their sum can be rewritten in terms of values scaled to the standard frequency:

$$\Delta f = \Delta f_q \cdot \frac{f_R \times 10^6}{F_{Sq}}$$

$$R_T = R_{Tq} \cdot \frac{f_R \times 10^6}{F_{Sq}}$$

so that

$$\Delta f_q + R_{Tq} = m_q (\Delta f + R_T)$$

The first-order, ionospheric refraction correction is inversely proportional to the frequency of the transmitted signal. We rewrite it scaled to the standard frequency:

$$\Delta f^{(1)} = \frac{f_R \times 10^6}{F_{Sq}} \cdot \Delta f_q^{(1)} = \Delta f_q^{(1)} / m_q$$

Assembling the above, we have finally

$$\varphi_q = 2\pi \int_0^t dt \left[\frac{n_q}{f_R} \Delta F - m_q (\Delta f + R_T) - \frac{\Delta f^{(1)}}{m_q} \right]$$

in which the q dependence has been confined to the coefficients n_q and m_q. It is now seen that if the two φ_q are multiplied by the proper

constants and subtracted, the refraction term $\Delta f^{(1)}$ will vanish. We choose as constants i_q and $i_{q'}$ such that

$$i_q/n_q = i_{q'}/n_{q'}$$

Multiplying by i_q and $i_{q'}$ and subtracting yields

$$i_q\varphi_q - i_{q'}\varphi_{q'} = \varphi_{q''} = 2\pi \int_0^t dt \left[\frac{n_{q''}}{f_R}\Delta F - m_{q''}(\Delta f + R_T)\right] \quad (2.6)$$

where

$$n_{q''} = i_q n_q - i_{q'} n_{q'}$$

$$m_{q''} = \frac{n_{q''}}{f_R} \cdot F_S$$

$$F_S = \frac{F_{Sq}}{n_q \times 10^6}$$

for either $q=1$ or $q=2$. A typical value of "equivalent" frequency $(n_{q''}/f_R)$ is 687.5 MHz, based on values of 600 and 225 for i_q and $i_{q'}$, respectively. It is now apparent that the equation for $\varphi_{q''}$ is the same form as that for φ_q except that the ionospheric refraction contribution has been removed and equivalent frequencies have replaced the actual frequencies. The computations outlined above are accomplished by a device that produces the corrected signal continuously.

2.4.2.3 Digitization Process

In this process the signal corrected for ionospheric refraction, $\varphi_{q''}$, is observed for a specified number of cycles and the count time T is recorded. The time of count initiation t_b and the count time T constitute the observations for one point. These data are converted into a Doppler frequency and an epoch by the method described subsequently.

The details of the counting process are shown diagrammatically in figure 2.8. The count initiation signal activates a gate that passes the next positive zero-crossing of the Doppler signal to a circuit, which in turn activates a gate and starts the clock at the next zero crossing of the counting signal. At the end of count, a gate passes a signal that turns off the clock, leaving a fraction of the counting signal uncounted. The three short time intervals, ϵ_0, ϵ_1, and ϵ_2, incident to the start and stop of the counting process represent such fractions of a single cycle of counting frequency. They are assumed to have uniform distributions, so that their first and second moments are

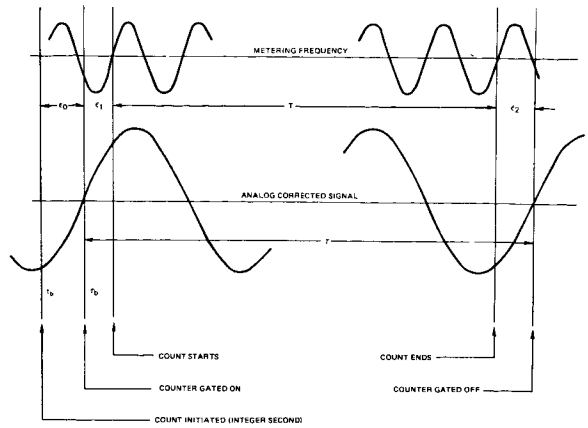

FIGURE 2.8.—Timing and signals involved in digitization.

$$\langle \epsilon_0 \rangle = \frac{T}{2n_c}$$

$$\langle \epsilon_0^2 \rangle = \frac{1}{3}\left(\frac{T}{n_c}\right)^2$$

$$\langle \epsilon_1 \rangle = \langle \epsilon_1 \rangle = \frac{1}{2f_M}$$

$$\langle \epsilon_1^2 \rangle = \langle \epsilon_2^2 \rangle = \frac{1}{3(f_M)^2}$$

Thus

$$\langle \tau \rangle = T + \langle \epsilon_1 + \epsilon_2 \rangle = T + (1/f_M)$$

Equation (2.6) is now solved for the desired quantity Δf and the epoch at which it occurs. The equation is rewritten to substitute q for q'' throughout to simplify notation.

$$\varphi_q = 2\pi \int_0^t dt \left[\frac{n_q}{f_R}\Delta F - m_q(\Delta f + R_T)\right]$$

The integration limits from the figure are τ_b and $(\tau_b+\tau)$, and the total phase change is $2\pi n_c$. Hence

$$2\pi n_c = 2\pi \int_{\tau_b}^{\tau_b+\tau} dt \left[\frac{n_q}{f_R} \Delta F - m_q (\Delta f + R_T) \right]$$

Although both ΔF and ΔR_T have some time dependence, we assume that they are constant during a pass, so that

$$n_c = \frac{n_q}{f_R} \Delta F \tau - m_q R_T \tau - \int_{\tau_b}^{\tau_b+\tau} dt\,(m_q \cdot \Delta f)$$

and the problem resolves into evaluating this integral. We evaluate ΔF and R_T at some arbitrary epoch during the count interval. In order to evaluate the integral, Δf is expanded in a Taylor series to the quadratic term about some arbitrary epoch during the counting interval. It is this epoch that will be the desired epoch t_D corresponding to the desired Doppler frequency $\Delta f\ (t_D)$:

$$\Delta f(t) = \Delta f(t_D) + \Delta \dot{f}(t_D)\,(t-t_D) + \frac{\Delta \ddot{f}}{2}(t_D)\,(t-t_D)^2$$

Inserting this expansion, we find

$$\int_{\tau_b}^{\tau_b+\tau} dt\,(m_q \cdot \Delta f) = m_q \tau \left\{ \Delta f(t_D) + \frac{\Delta \dot{f}(t_D)}{2} [\tau + 2(t_b - t_D)] + \frac{\Delta \ddot{f}(t_D)}{6} [\tau^2 + 3\tau(\tau_b - t_D) + 3(\tau_b - t_D)^2] \right\}$$

Note that t_D is an arbitrary epoch in the τ interval. We now select t_D to make the expected value of the coefficient of $\Delta \dot{f}$ vanish.

$$\langle \tau + 2(\tau_b - t_D) \rangle = 0$$

This choice is made to avoid dealing with $\Delta \dot{f}$. The rate of change of Doppler shift is not known and is not readily available. It is a larger rate than $\Delta \ddot{f}$, which should be quite small in the 1-sec interval during which the Doppler shift is counted. Noting that

$$\langle \tau \rangle = \langle T + \epsilon_1 + \epsilon_2 \rangle = T + \frac{1}{f_M}$$

$$\langle \tau_b \rangle = \langle t_b + \epsilon_0 \rangle = t_b + \frac{T}{2n_c}$$

we find that

$$t_D = t_b + \frac{T}{2}\left(1 + \frac{1}{T f_M} + \frac{1}{n_c} \right)$$

This is just what might be expected. If $\Delta \ddot{f}$ were zero and $\Delta \dot{f}$ constant, then the Doppler frequency at the midpoint of the observation period would be the average frequency over the time span, and the total count could be computed without knowing $\Delta \dot{f}$. The small time corrections represent the effects of starting and stopping the count. Finally, the station clock correction is added.

$$t_T = t_D + \Delta t$$

If the derived value of t_D is now substituted in the integral and solved for the corresponding Doppler frequency, we obtain

$$\Delta f(t_D) = \frac{n_q}{m_q f_R} \Delta F - \frac{m_c}{m_q T}\left(1 - \frac{1}{T f_M} \right) - R_T - \frac{T^2}{24} \Delta \ddot{f}(t_D)$$

This Doppler frequency together with the corresponding time t_T noted above constitute the output of the preprocessing stages for each point. The two inputs t_b and T are used directly in computing t_D. In the computation of Δf, two corrections are required from another source. One is R_T, the correction to Doppler frequency due to tropospheric refraction. This is in part a function of satellite elevation (hence of the orbit) and of the weather. The other is the contribution of $\Delta \ddot{f}$, which is also a function of the orbit. Both corrections can be added later in the computation as they become known during the

iterations that eventually produce the orbital parameters.

2.4.2.4 Problems

The tracking system is sensitive to noise and disturbances of different kinds. Phase jitter and phase modulation arising out of amplitude modulations induced by propagation effects, satellite motion, and receiver noise are among the sources of distortion. Timing errors are serious because the satellite travels at the rate of about 7 m/msec. The volume of data may be a problem. At a sampling rate of one measurement every 4 sec, a 15-min pass produces 225 measurements. It is customary to reduce the computational load by processing only a fraction of the data. Another approach is to condense several observations. This can be done by fitting a curve to 10 observations (say) and interpolating for the Doppler frequency and epoch at the midpoint of the arc. It is estimated that the perturbations that may be considered irreducible at the current state-of-the-art contribute an error of about 5 m to satellite position. The conversion procedure described herein has been used successfully for counting intervals of 10 sec. Historically, the conversion of cycles of Doppler counts to Doppler frequency was the approach in determining the orbit. It was later realized that the count over a given time interval was equivalent to the difference of slant ranges over that interval. This "integrated Doppler" approach dispensed with the need for determining a Doppler frequency, minimized some of the phase distortion and noise effects, and reduced the number of observations without discarding data. It has thus become the currently prefered method of orbit determination. The two-frequency method of removing first-order ionospheric refraction effects continues to be used.

2.4.2.5 Other Preprocessing Material

The process of eliminating blunders and errors from the data is included by many people as part of preprocessing and is in fact so treated in most of this report. APL developed its data reduction procedures specifically as part of the development of NNSS and in addition used an approach peculiar to APL. As a consequence, the APL theory for data reduction cannot easily be separated into the customary categories. The theory given in section 2.5.3, together with the material in this section, covers what could be closest to what is covered under "Preprocessing" in other chapters of this report.

2.5 THEORY

2.5.1 Introduction

The main emphasis of the APL geodetic program was the determination of the coefficients associated with the tesseral harmonics in the gravitational potential and the determination of the position of tracking stations. However, some early studies on the effects of the zonal harmonics were also made. Different analytical techniques were used in the two studies on gravitation, and both are presented here.

Raw data are submitted by the TRANET stations as sets of ordered pairs consisting of reception time and a quantity referred to as "period count." The period count is simply the ratio of the number of cycles of the Doppler signal to the counting frequency. These ordered pairs are generated every 4 sec during the passage of the satellite over a given station, augmented with an identifying heading called an identification header, and submitted to the computing facility on five-level, punched paper tape. The sampling interval lasts approximately 0.5 sec. (The TRANET stations were modified in 1971 to count continuously.) The computing facility accumulates these paper tapes from all the tracking stations, batches them according to some appropriate time span (one or two days), and puts each Doppler pass (see following) on magnetic tape in the order of time of observation.

A typical Doppler pass contains between 200 and 400 individual data points. (By Dop-

pler pass we mean the Doppler shift data measured by a tracking station during a single transit of a satellite.) Obviously, for geodetic purposes, where several hundred Doppler passes are needed, the problem of coping with this much data would prove to be quite formidable. Thus it was decided to process the data in two stages.

The objective of the first stage of processing is to condense the information contained in the Doppler data into a small set of parameters. These parameters consist of a set of mean Keplerian elements for each orbital arc used and a set of "aggregation" parameters associated with each Doppler pass. The Keplerian elements constitute the data base from which the zonal harmonic effects are computed. A set of aggregation parameters consists of three quantities S, $\mathcal{L}$, and Δf. These parameters are determined via a least-squares fit of the Doppler shift residuals generated from the observations at a particular station during a particular pass (sec. 2.5.3.3). S and $\mathcal{L}$ are modeled as corrections to the station coordinates used in generating the residuals; Δf is modeled as a correction to the estimated current satellite frequency offset (sec. 2.3). The theory leading from the raw data to the aggregation parameters and other quantities is given in section 2.5.3. (This section constitutes approximately what is called "theory of preprocessing" in other chapters.)

The Doppler residuals analyzed in this first stage reflect not only station coordinate errors but also satellite ephemeris errors resulting from the theoretical model used in generating the ephemeris. Data measurement errors are also reflected in these residuals but are assumed to be negligible in comparison to the other error sources. By minimizing these residuals with respect to S, $\mathcal{L}$, and Δf we were able to demonstrate that the final or adjusted residuals were reduced to the estimated noise level in the data measurements themselves (i.e., that all significant errors in the Doppler residuals for a given pass were removed by an adjustment of these three parameters). These parameters are saved and archived into special data sets, one for each collection of Doppler passes discussed earlier. These data together with additional parameters associated with each pass (which allow us to reconstruct the satellite-station geometry during the time of the pass) serve as the experimental data to be processed in the second stage of analysis.

The objective of the second stage is to derive results of geodetic significance (station locations and values of the gravitational potential) from the results of the first stage (mean Keplerian elements, a set of aggregation parameters, and associated pass geometry). Sections 2.5.4 through 2.5.7 deal with this stage. Section 2.5.4 presents a theoretical analysis of the residuals of the Doppler data (referred to hereafter as Doppler residuals), which defines the parameters as a function of station position errors and orbital errors. The theory relating orbital errors to errors in the gravitational potential coefficients is given in section 2.5.5. Sections 2.5.6 and 2.5.7 describe the algorithms used in processing the aggregation parameters to obtain better models of the earth's gravitational field.

2.5.2 Notations and Definitions Peculiar to This Chapter

(1) Coordinate systems

$\hat{H}$, $\hat{L}$, $\hat{Z}$ coordinate system = right-handed coordinate system with axes defined as:

- $\hat{H}$: direction of radius vector from Earth's center of gravity to satellite at a given epoch
- $\hat{L}$: direction of that component of the satellite velocity vector, at the same epoch, perpendicular to its radius vector and lying in the osculating plane of the computed orbit
- $\hat{Z}$: direction of angular momentum vector of the theoretical orbit at the same epoch.

$\hat{S}$, $\hat{\mathcal{L}}$, $\hat{C}$ (minimum slant range) coordinate system = right-handed coordinate system with axes in the three directions:

$\hat{S}$: direction of radius vector from station to satellite at time of closest approach of satellite to station

$\hat{\mathcal{L}}$: direction of satellite velocity vector at time of closest approach of satellite to station

$\hat{C}$: $\hat{S} \times \hat{\mathcal{L}}$ direction.

(2) Potential

N_{nm} = normalization used for spherical harmonics

$$= \left[\frac{(n-m)\,!\,(2n+1)\,(2-\delta_{om})}{(n+m)\,!}\right]^{\frac{1}{2}}$$

$$\delta_{om} = \begin{cases} 0 \text{ for } m \neq 0 \\ 1 \text{ for } m = 0 \end{cases}$$

$$\bar{C}_n^m = \frac{1}{N_{nm}} C_n^m$$

$$\bar{S}_n^m = \frac{1}{N_{nm}} S_n^m$$

α_G = right ascension of Greenwich

(3) Data

t_b = station clock time at start of count (generally an integral second) (sec)

τ_b = station clock time when counter is turned "on" (sec)

τ = actual time required to count n_c cycles (sec)

Δt = correction to station clock relative to WWV time (sec)

t_D = station clock time (computed) corresponding to computed Doppler frequency (sec)

$t_T = t_D + \Delta t$ (corrected t_D) (sec)

T = approximate time required to count n_c cycles (sec)

q = index of satellite signal (q = 1, 2)

F_{Tq} = station reference frequency (as estimated at station) corresponding to q^{th} signal (Hz)

$n_q = F_{Tq} \times 10^{-6}$ (MHz)

f_R = standard reference frequency (MHz) (=300 MHz)

f_M = counting frequency (=5 MHz)

N_q = noise term for q^{th} signal (Hz)

F_{Sq} = frequency of q^{th} transmitter in satellite (Hz)

$\Delta F_q = F_{Tq} - F_{Sq}$ (satellite transmitter frequency bias) (Hz)

$m_q = (F_{Sq}/f_R) \times 10^6 = F_{Sq}$ scaled to f_R

$\Delta F = \Delta F_q \cdot f_R / n_q$

= fractional ΔF_q scaled to f_R

Δf_q = Doppler shift of q^{th} satellite signal in vacuum (Hz)

$\Delta f_q^{(k)}$ = k^{th}-order refraction contribution to q^{th} satellite signal (Hz)

R_{Tq} = tropospheric refraction contribution to q^{th} transmitted signal (Hz)

n_c = preset number of complete cycles counted of the analog Doppler signal

f_T = effective transmitted frequency (Hz)

(4) Satellite position and motion

f = true anomaly

$\beta = f + \omega$

$\bar{n} = \dot{\beta}$

$\mathbf{r}_s(t)$ = satellite position in true equatorial system of date

$\delta\mathbf{r}_s(t)$ = error in satellite position

r_s, ϕ_s, α_s = radial distance, latitude, and longitude of the satellite

δr_s, δl_s, δZ_s = components of satellite position errors in the $\hat{H}$, $\hat{L}$, $\hat{Z}$ coordinate system

(5) Tracking station position

$\mathbf{r}_T$ = station position vector in true equatorial system of date

$\mathbf{r}_c$ = station position vector in Earth-fixed system

δr_c, $\delta\phi_c$, $\delta\lambda_c$ = errors in station radial distance, latitude, and longitude

S, $\mathcal{L}$ = corrections to station slant range and along-track components which minimize the sum of the

squares of the Doppler residuals at a station for a given Doppler pass.

(6) Geometry of satellite and station

t_c = time of closest approach of satellite to station

$\varrho(t) = \mathbf{r}_s(t) - \mathbf{r}_T(t)$

= slant range vector from station to satellite

$\rho(t) = |\varrho(t)|$

$\hat{\rho}(t) = \frac{\varrho(t)}{\rho(t)}$

$\delta\varrho(t)$ = error in slant range vector

$\varrho_c = \varrho(t_c)$

$\rho_s = \frac{|\varrho_c|}{|\mathbf{r}_s(t_c)|}$

E_l, A_z = elevation and azimuth at station of ϱ_c

a_z, e_l = pseudo azimuth and pseudo elevation of ϱ_c

θ = angle between $\mathbf{r}_s(t_c)$ and ϱ_c at position of satellite

$\alpha_p = 1 - \rho_s \cos\theta$

t_R = time at which satellite rises above minimum elevation for acceptable tracking data from stations

t_S = time at which satellite sets below minimum elevation for acceptable tracking data from station

$\Delta M = \bar{n}(t - t_c)$

$\Delta M_o = \frac{\bar{n}}{2}(t_R + t_S - 2t_c)$

2.5.3 Determination of Aggregation Parameters and Mean Orbital Elements

As stated in the introduction, the objective of the first stage of analysis is to condense the pertinent information content contained in the raw Doppler-shift measurements into a smaller and more easily analyzed set of parameters. Also accomplished at this stage is an editing of the Doppler data, the objective being to delete from further consideration those individual Doppler measurements (or even an entire Doppler pass) if preestablished criteria are not satisfied. To achieve these objectives, it is also necessary to determine an improved satellite orbit for each group of Doppler passes to be processed. (By satellite orbit, in this context, we mean a set of six orbital elements at a specified epoch which can be used in generating a satellite ephemeris, via a numerical integration scheme, for the time span covered by the Doppler data.)

The Doppler shift measurements from each satellite are processed in groups, each consisting of from 24 to 48 hours of data. If the primary objective is to obtain aggregation parameters for each pass, then Doppler passes covering a 48-hour time span are used. For defining mean orbital elements, 24-hour data spans are used.

Processing of the Doppler data is done in six steps. The first of these merely formats (rearranges) the data and need not be described.

In the second step, period counts (sec. 2.4.2) are converted into frequencies (sec. 2.4.2.3). First-order ionospheric refraction effects are computed and removed from the frequencies if this was not done by the refraction corrector unit (sec. 2.3.3.3) at the tracking station. When a weather report is submitted with the data, effective "wet" and "dry" refractive indices are computed, to be used later to calculate the tropospheric refraction correction (sec. 2.5.3.2) to the Doppler shift. Gaps in the measurements within each Doppler pass are identified, and a record is kept of the number of gaps and length of the maximum gap.

To continue the analysis from this point, it is necessary to generate the satellite ephemeris for the time span covered by the Doppler data. This is accomplished via a numerical integration procedure (sec. 2.5.3.1) using an initial estimate of the satellite orbit. The main objective of step 3 is to identify and delete poor-quality data. Each Doppler pass is first analyzed separately. After the satellite ephemeris has been combined with the station coordinates, a theoretical Doppler shift is computed, which is then differenced with the experimental measurements (now with tropospheric (sec. 2.5.3.2) and first-order ionospheric (sec. 2.3.3.3) refraction

effects removed) to produce the Doppler shift residuals for the pass being processed. [In this chapter, residuals are defined to be the theoretical value minus the experimental value. This is the negative of the convention used in the rest of the book.] These Doppler residuals for each pass are then minimized with respect to S, $\mathcal{L}$, and Δf (sec. 2.5.3.3) by means of a least-squares iterative procedure. After each iteration a 3σ "stripping" is performed on the adjusted residuals. This processing continues until a stable solution is found or until a maximum number of iterations has been performed.

This method of editing the Doppler shift measurements is useful in detecting noisy data. However, this approach cannot detect (for example) station timing or frequency bias errors. Therefore an additional method of editing the data is used. In section 2.5.4 a theoretical analysis of the Doppler shift residuals is presented. This analysis shows that the pass-determined parameters S and $\mathcal{L}$ as computed (by means of the theory given in sec. 2.5.3.3) are a function not only of station position errors but also of satellite ephemeris errors. Utilizing these results, we now assume that the pass-determined parameters S and $\mathcal{L}$ are functions only of satellite ephemeris errors via equations (2.58) and (2.59) in section 2.5.4, and that these in turn are caused by the propagation effects of the errors in the satellite initial orbit given by equation (2.91) in section 2.5.5. Under these assumptions we perform a least-squares fit to these pass-determined parameters with respect to the six orbit error parameters of equation (2.91). Doppler pass deletion is then performed on the basis of the statistics of the adjusted S and $\mathcal{L}$ values.

The six orbit parameters obtained in the above minimization could also be used to correct the initial orbit needed for the numerical integration scheme (sec. 2.5.3.1); however, this approach was not used in the programs being described here.

In step 4 the results of the previous step are used to compute pass weights. The frequency offset parameters, Δf, are used to compute a correction for the drift in the satellite oscillator. (Any frequency change in time as measured by these pass parameters is attributed to the satellite oscillator.) Finally, a representative subset of the surviving Doppler shift measurements from all the passes in the data span is selected for use in step 5.

The objective of step 5 is to determine an improved orbit. This is accomplished by performing a least-squares fit to the subset of Doppler shift measurements selected in step 4 with respect to the six Keplerian elements. The partial derivatives of the satellite motion with respect to these parameters are obtained by means of an analytic theory that includes only the central body and C_2^0 effects of the potential. However, for each iteration the satellite ephemeris, including all modeled forces acting on the satellite, is recomputed numerically (sec. 2.5.3.1) to accurately reflect the effects of the adjusted orbit parameters.

This final ephemeris (derived from the "best" determined orbit) is used in the final step to repeat the computations performed in step 3.

Information determined from this final analysis of the Doppler shift measurements is then saved for further analysis by the geodetic research programs. This information consists of the pass-determined parameters S, $\mathcal{L}$, and Δf, as well as computed parameters that enable us to reconstruct the satellite-station geometry during the time of each pass (sec. 2.5.4). In addition, pass weights are also saved.

A set of eight mean orbital parameters describing a constantly precessing ellipse are determined from a least-squares fit to the satellite ephemeris given for a 24-hour time span. This ephemeris is generated from the final "best" orbit by numerical integration (sec. 2.5.3.1).

2.5.3.1 Determination of Orbit

Two factors control the accuracy of numerical integration. The first is the choice of orbit parameters (elements). The parameters should be chosen so that there is a mini-

mum variation of the parameters with time. The second is the choice of the algorithm that approximates differential equations by difference equations. Table 2.13 indicates the basic orbital parameters that have been chosen (Newton, 1961). The second part of table 2.13 indicates the definition of these parameters in terms of the usual Keplerian elements and consequently defines the scaling (units) of the parameters. With the semimajor axis, a, scaled by the mean radius of the earth, the magnitude of the **P** vector is about unity. The magnitude of the **e** vector is the eccentricity of the osculating arbit. The independent variable has been chosen to be the argument of the latitude β rather than time t because the largest forces acting on the satellite are functions of its position, with only a weak, explicit dependence upon time. Consequently, a variable is numerically integrated along with the three components of the **P** and **e** vectors. However, there are only six independent parameters, since by definition the **P** and **e** vectors are orthogonal.

For an unperturbed orbit, the parameters in table 2.13 are constant. Consequently, the fixed word-length of a computer can be better utilized by using, instead of the parameters themselves, the changes in these parameters due to perturbing forces on the satellite.

The difference parameters and variables are shown in table 2.14. After integration the actual orbital parameters and time are computed as also shown in table 2.14. The most sensitive parameters affecting the accuracy of the satellite's computed position are the magnitude of **P** and the time. These are computed separately from the components of the two vectors. Consequently, six parameters and two variables (one a function of the parameters) are numerically integrated (the two variables are carried in double precision in the computer). Since the nodal (draconic) period of the unperturbed satellite is constant, the times in an unperturbed orbit can be computed as indicated in the last equation in table 2.14.

The method used for integrating the differential equations of motion for the $\Delta\mathbf{P}(\beta)$ and $\Delta\mathbf{e}(\beta)$ vectors and the time $\Delta t(\beta)$ is that of Runge-Kutta, using fourth-order integration (ch. 1). Considering the rapid variation of the forces with β, 64 steps of the independent variable β are taken per revolution.

The differential operations of motion and the forces involved are given in chapter 1. In addition to the Earth's gravitational forces, the gravitational effects of the Sun and Moon are computed. Also included are the contributions of solar radiation pressure and atmospheric drag. The drag force is based on a model of atmospheric density developed by Jacchia (1965).

2.5.3.2 Refraction Correction (Troposphere)

The lower, un-ionized part of the atmosphere and the higher, ionized part have different effects on the velocity of an electromagnetic signal. This section deals with the un-ionized part, which thus includes both the troposphere and stratosphere; some 80 percent of the combined effect of the troposphere and stratosphere is, however, produced by the troposphere proper, below the tropopause. The index of refraction of un-ionized air is independent of frequency in the radio region, at least up to a frequency of 15 GHz. The two-frequency method that corrects radio Doppler data for ionospheric errors (ch. 3) therefore does not remove tropospheric effects. A correction based on an atmospheric model has been developed for this purpose.

Passage of a satellite radio or optical signal through un-ionized air delays the arrival of the signal. The resulting error in the measured range (or range rate) is a function of atmospheric conditions along with the signal path and of the satellite elevation angle. The effect in the zenith direction is the height integral

$$\Delta h_{tro} = \int (n-1)\, dh \qquad (2.7)$$

through the un-ionized atmosphere, where n is the index of refraction. If horizontal gradients in the atmosphere are negligible, the range effect at an elevation angle E_l is a function of the effect at the zenith.

It is convenient to define the refractivity N as

$$N \equiv 10^6 (n-1) \tag{2.8}$$

and also to separate N into its so-called dry and wet components (Smith and Weintraub, 1953):

$$\left.\begin{aligned} N &= N_d + N_w \\ N_d &= 77.6\frac{P}{T} \\ N_w &= 3.73\times 10^5 \frac{e}{T^2} \end{aligned}\right\} \tag{2.9}$$

where T is the Kelvin temperature, P is the total pressure in millibars, and e is the partial pressure of water vapor, also in millibars. Both N_d and N_w normally decrease with height above the earth, but at different rates.

Equations (2.9) pertain to radio frequencies. In the optical region, n is a function of wavelength but is little affected by water vapor. The results given below for the radio dry component are applicable also to optical studies (e.g., laser ranging) if a wavelength correction of a few percent is made.

For a dry atmosphere, it can be shown theoretically (Hopfield, 1971; Haurwitz, 1941) that

$$\int N_d \, dh = k P_s \tag{2.10}$$

where P_s is the surface pressure and k is a constant at a given location. Equation (2.10) is also valid for the dry component of real atmospheres. This has been verified by a study of meteorological balloon data from several thousand balloon ascents in one-year sets (two balloons per day) at several widely separated locations (Hopfield, 1971). The observed values of the parameter k show a small latitudinal variation (Hopfield, 1972). The value of k is approximately 2.28 mm of zenith range effect per millibar of surface pressure.

Equation (2.10), though useful, is not sufficient. A model of both the N_d and the N_w profiles is needed for correcting radio data.

In a dry, isothermal atmosphere the refractivity would decrease exponentially with height (Bean and Dutton, 1959); but if there is a constant lapse rate α of temperature ($\alpha \equiv -dT/dh$), theoretically the refractivity varies with height according to the equation (Hopfield, 1969; Haurwitz, 1941)

$$N = N_o \left[\frac{T_o/\alpha - h}{T_o/\alpha}\right]^{\mu} \tag{2.11}$$

where

$$\mu = \frac{g}{R\alpha} - 1 \tag{2.12}$$

In equation (2.11) the subscript O refers to the surface, assumed at sea level; in equation (2.12), g is the acceleration of gravity, assumed constant through the lower atmosphere, and R is the gas constant for a unit mass of air.

It has been found empirically from meteorological balloon data that an expression of the form of equation (2.11), with $\mu = 4$ (corresponding to $\alpha = 6.8°\text{C/km}$), can be satisfactorily used to represent the dry-component profile N_d in the real atmosphere. The expression is rewritten below for this purpose, for a station at the surface but not at sea level, where the subscript s refers to the surface. The quantity T_o/α of equation (2.11), which is a height, is replaced here by the height parameter h_d (later called h_1). Theoretically, h_d depends on T_o; i.e., it has a temperature coefficient, here called a_d.

The wet-component profile is written in a similar form for convenience, although doing so does not have the same theoretical justification. The complete expression becomes

$$\left.\begin{aligned} N &= \sum_{i=1,2} N_i \\ N_i &= \frac{N_{s_i}}{(h_i - h_s)^4}(h_i - h)^4 \qquad h \le h_i \\ N_i &= O \qquad\qquad\qquad\qquad h > h_i \end{aligned}\right\} \tag{2.13}$$

where $i = 1,2$ refers to the dry and wet components, respectively. All heights are meas-

ured above the geoid. The values of h_i must at present be specified differently:

$$\left.\begin{aligned} h_1 &= h_{d_0} + a_d T_{sc} \\ h_2 &= \text{const (for a given location and data sample)} \end{aligned}\right\} \quad (2.14)$$

where h_{d_0} is the value of h_1 at 0°C and T_{sc} is the Celsius temperature at the surface.

The theoretical radio range effect of the troposphere at the zenith is the height integral of this composite N profile:

$$\Delta h_{tro} = 10^{-6} \times \frac{1}{5} \sum_{i=1,2} N_{s_i}(h_i - h_s) \quad (2.15)$$

With suitable height parameters, the dry part of the theoretical Δh_{tro} matches observed data within 2 mm rms. Deviations in matching the wet part of the observed integrals are an order of magnitude larger, i.e., a few centimeters.

The values of the height parameters are tabulated for several geographic locations, in Hopfield (1972). The following are nominal values:

$$\begin{aligned} h_{d_0} - h_s &= 40.1 \text{ km} \\ a_d &= 0.149 \text{ km/°C} \\ h_w &\cong 10 \text{ km} \end{aligned}$$

The empirical values obtained for $(h_{d_0} - h_s)$ and a_d are nearly the same for all the locations studied, and are in good agreement with theory for a dry atmosphere. The values obtained for h_w at different locations are far more variable and not now theoretically predictable. Fortunately, the wet component of Δh_{tro} seldom contributes more than 10 percent of the total effect and often much less (Hopfield, 1971).

The N profile of equations (2.13) leads to the following expression for the range effect $\Delta\rho_{tro}$ at any elevation angle E_l (Hopfield, 1969). Path curvature of the signal is neglected here; however, this is very small except at low elevation angles, where satellite data are seldom used. The total range effect is the sum of the dry and wet contributions $\Delta\rho_i$.

$$\Delta\rho_{tro} = \sum_{i=1,2} \Delta\rho_i$$

$$\begin{aligned} \Delta\rho_i = 10^{-6} N_{s_i} \Bigg\{ & -l_1 + \frac{4}{h_{tro_i}^4} \Bigg[\frac{1}{3} r_s^2 l_1^3 \\ & - \frac{2}{15} l_1^5 - \frac{3}{4} r_s r_{tro_i} l_1 \left(l_1^2 + \frac{1}{2} l_2^2 \right) \\ & + r_{tro_i}^2 l_1^3 - \frac{1}{2} r_{tro_i}^3 r_s l_1 \\ & - \frac{1}{3} r_{tro_i}^2 l_{3i}^3 + \frac{2}{15} l_{3i}^5 \\ & + \frac{3}{4} r_{tro_i}^2 \left(l_{3i}^3 + \frac{1}{2} l_{3i} l_2^2 \right) \\ & - r_{tro_i}^2 l_{3i} \left(l_{3i}^2 - \frac{1}{2} r_{tro_i}^2 \right) \\ & + \frac{1}{2} r_{tro_i} l_2^2 \left(\frac{3}{4} l_2^2 + r_{tro_i}^2 \right) ln \frac{r_s + l_1}{r_{tro_i} + l_{3i}} \Bigg] \Bigg\} \end{aligned} \quad (2.16)$$

In this expression, r_s and r_{tro_i} are distances from the center of the earth to the tracking station and to the top of the troposphere (dry or wet component), respectively. Also, where $h_1 = h_d$ and $h_2 = h_w$,

$$\begin{aligned} h_{tro_i} &= h_i - h_s \qquad & r_{tro_i} &= r_s + h_{tro_i} \\ l_1 &= r_s \sin E_l \qquad & l_2 &= r_s \cos E_l \\ & & l_{3i} &= (r_{tro_i}^2 - l_2^2)^{1/2} \end{aligned}$$

The tropospheric contribution to the Doppler shift of the satellite signal of frequency f is, again, the sum of the dry and wet contributions; c is the velocity of light:

$$\Delta f_{tro} = 10^{-6} \frac{f}{c} r_s \dot{E}_l \sum_{i=1,2} [N_{s_i} F_{4i}(E_l)] \quad (2.17)$$

The function $F_{4i}(E_l)$ for either component (subscript 4 to refer to the quartic N profile) is

$$\begin{aligned} F_{4i}(E) = \cos E \Bigg\{ & 1 + \frac{4 l_1}{h_{tro_i}^4} \Bigg[\frac{l_{3i}^3 - l_1^3}{3} + l_{3i} \left(l_2^2 + \frac{3 r_{tro_i}^2}{2} \right) \\ & - l_1 \left(l_2^2 - \frac{3 r_s r_{tro_i}}{2} + 3 r_{tro_i}^2 \right) \\ & + \left(\frac{3 r_{tro_i} l_2^2}{2} + r_{tro_i}^3 \right) ln \frac{r_s + l_1}{r_{tro_i} + l_{3i}} \Bigg] \Bigg\} \end{aligned} \quad (2.18)$$

In practice, the computation of $\Delta\rho_i$ or $F_{4i}(E_l)$ is done in double precision to avoid excessive rounding errors. $\Delta\rho_i$ is particularly hard to compute with enough precision, and two algorithms for this purpose, based on series expansions, have been developed by Yionoulis (1970). These may be used to replace equation (2.16). One is intended for high, the other for low, values of E_l.

The observed range at any point is too great, because of tropospheric delay, and the amount of the error is greater near the horizon than at the point of closest approach. The observed range rate or Doppler shift therefore appears too large in magnitude and changes too rapidly; i.e., the slope of the observed Doppler curve is too steep. Geometrically (and somewhat paradoxically), this makes the satellite pass appear closer to the station that it really is.

Figure 2.9 shows the Doppler residuals for a satellite pass without and with tropospheric correction. The upper graph shows the residuals without correction; they show a large systematic increase in magnitude toward the ends of the pass. The computed but unused correction is shown also as a solid line. The lower graph shows the residuals for the same pass, recomputed after the use of the tropospheric correction. Nontropospheric errors were small in this pass, and the residuals now show little systematic variation. A small overcorrection may, however, be noted at the end of the pass. This is the effect of neglecting signal path curvature in the model and is noticeable here only below 2-deg elevation.

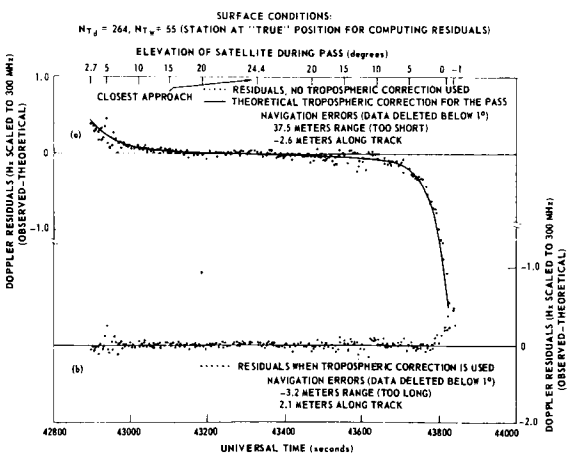

FIGURE 2.9.—Tropospheric effect on Doppler data during pass of satellite 1967 34A, Lasham, England, 2 September 1967.

2.5.3.3 Procedure for Determining S, $\mathcal{L}$, and Δf

The aggregation parameters S, $\mathcal{L}$, and Δf associated with each Doppler pass being processed are determined by minimizing the function F:

$$F=\frac{1}{N}\sum_{\mu=1}^{N}\{\Delta f_D^{(T)}(\rho_e, l_e, \Delta f; t_\mu)-\Delta f_D^{(E)}(t_\mu)\}^2 \tag{2.19}$$

In equation (2.19), N is the number of data points in the Doppler pass, ρ_e and l_e are parameters associated with the position of the station (fig. (2.10)), and Δf is a correction for the difference between the frequencies generated by the satellite oscillator and the station oscillator. A formula for the experimental Doppler shift $\Delta f_D{}^{(E)}$ is given in section 2.4.2.2. A tropospheric refraction correction is applied to this function (sec. 2.5.3.2), so that the theoretical representation $\Delta f_D{}^{(T)}$ of the Doppler shift in vacuo is given by

$$\Delta f_d^{(T)}=-f_T\left[\rho\cdot\frac{\dot{\boldsymbol{\varrho}}}{c}\left(1-\frac{\dot{\mathbf{r}}_s}{c}\cdot\hat{\rho}\right)\right]$$

In this equation the slant-range vector is defined as

$$\boldsymbol{\varrho}=\mathbf{r}_s(t_\mu{}^*)-\mathbf{r}_T(t_\mu)$$

The instants t_μ^*, t_μ are related by the equation

$$t_\mu^*=t_\mu-\frac{|\boldsymbol{\varrho}|}{c}$$

which must be solved by iteration. The instant t_μ^* represents time of emission of the signal received by the station at t_μ.

The coordinate system used in the analysis is based on the theoretical Doppler shift. At the time t_c of closest approach of the satellite to the station, the range rate $\dot{\varrho}$, and consequently the theoretical Doppler shift, is zero. Therefore at this instant the range ϱ and range rate $\dot{\varrho}$ are orthogonal, and their unit vectors, as computed at the time of closest approach, become the basis of an orthogonal coordinate system. The third component of this system is obtained from the cross product of these two vectors.

It is now necessary to show how these vectors define the Earth-fixed coordinate system in which the station position is "navigated." Components defined in this Earth-fixed system are referred to as the minimum-slant-range (MSR) coordinates. The three different coordinate systems used are shown in figure 2.10. The subscript T denotes inertial system components, and the subscript e denotes the Earth-fixed system components. It should be noted that the x–y plane of the Earth-fixed coordinate system coincides with that of the inertial system.

The desired relationship between the station-inertial system components as a function of time and the Earth-fixed MSR system components is given by

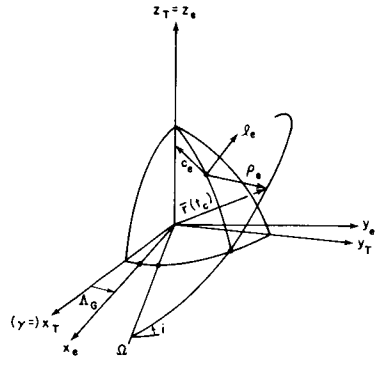

x_T, y_T, z_T denote components in inertial coordinate system.

x_e, y_e, z_e denote components in earth fixed coordinate system.

ρ_e, ℓ_e, c_e denote components in MSR coordinate system.

Λ_G = right ascension of Greenwich relative to Aries.

FIGURE 2.10.—Coordinate systems.

$$\begin{pmatrix} x_T \\ y_T \\ z_T \end{pmatrix}_t = R(t)\,R^{-1}(t_c)\,M(t_c)\begin{pmatrix} \rho_e \\ l_e \\ c_e \end{pmatrix} \qquad (2.20)$$

where

$$R(t) = \begin{pmatrix} \cos\alpha_G(t) & -\sin\alpha_G(t) & 0 \\ \sin\alpha_G(t) & \cos\alpha_G(t) & 0 \\ 0 & 0 & 1 \end{pmatrix} \qquad (2.21)$$

(In the period 1963–1966, when these equations were being used for geodetic research, the effects of polar motion were not included. However, $R(t)$ is easily modified to include this effect, and the procedure otherwise remains the same.) The functional form of the matrix $M(t_c)$ is given by eq. (2.22) in inset, where the elements are functions of the components of the MSR system unit vectors in the inertial coordinate system defined at the time of closest approach of the satellite to the station. It can be shown that $M(t_c)$ is an orthogonal matrix, if it is noted that the dot product of ϱ and $\dot{\varrho}$ is zero at t_c. In the actual adjustment the station is "navigated" in only two (S and $\mathcal{L}$) of the three coordinates. This is in the plane defined by the slant-range and velocity vectors at t_c.

After a minimum has been found, the final adjusted station position is compared with the original position. The differences are then expressed in the MSR system coordinates and are referred to as the station along-track, $\mathcal{L}$, and slant range, S, differences.

These aggregation parameters, as computed in the final step in the processing of the Doppler shift residuals (sec. 2.5.3), constitute the data base from which the determination of improved tesseral harmonic coefficients and station coordinates are made.

2.5.4 Theoretical Analysis of Doppler Shift Residuals

In section 2.5.3.3 the theory used in obtaining the aggregation parameters was described. In order to use these quantities for determining improved station coordinates and values of the gravitational potential,

$$M(t_c)=\begin{pmatrix} \frac{x-x_T}{|\varrho|} & \frac{\dot{x}-\dot{x}_T}{|\dot{\varrho}|} & \frac{(y-y_T)(\dot{z}-\dot{z}_T)-(z-z_T)(\dot{y}-\dot{y}_T)}{|\varrho|\ |\dot{\varrho}|} \\ \frac{y-y_T}{|\varrho|} & \frac{\dot{y}-\dot{y}_T}{|\dot{\varrho}|} & \frac{(z-z_T)(\dot{x}-\dot{x}_T)-(x-x_T)(\dot{z}-\dot{z}_T)}{|\varrho|\ |\dot{\varrho}|} \\ \frac{z-z_T}{|\varrho|} & \frac{\dot{z}-\dot{z}_T}{|\dot{\varrho}|} & \frac{(x-x_T)(\dot{y}-\dot{y}_T)-(y-y_T)(\dot{x}-\dot{x}_T)}{|\varrho|\ |\dot{\varrho}|} \end{pmatrix} \tag{2.22}$$

Guier (1966a) derived the functional dependence of these quantities on station position and orbital errors. This derivation and the resulting formulas are presented in this section. In section 2.5.5 the functional dependence of errors in the coefficients C_n^m and S_n^m on errors in the satellite motion are given.

The following simplifying assumptions are made in obtaining the results of this section:

(1) The orbit is assumed to be nearly circular and near the Earth. This assumption allows for the expansion of complex expressions in powers of quantities approximately proportional to the ratio of the satellite altitude to the radius of the orbit and allows the neglect of terms proportional to the eccentricity of the orbit times the first-order effects of the errors.

(2) Errors in station position and satellite orbit are small enough that the second-order effects of the errors are negligible.

(3) The receiving station is rigidly connected to the Earth's surface. This assumption justifies the neglect of velocity errors in the station trajectory in inertial space.

(4) Ionospheric and tropospheric refraction contributions as well as errors in the measurements of the Doppler shift residuals are negligible.

The first step in the analysis is to formulate a mathematical model that can be used to describe the time dependence of the Doppler residuals for a given pass. The Doppler residuals including a frequency correction parameter can be written as

$$\delta f_D(t)=-\frac{f_T}{c}\frac{d}{dt}[\delta\rho(t)]+\delta f \tag{2.23}$$

where $\delta\rho$ is the error in the slant range and δf represents the error in the estimate of the satellite frequency offset. The slant range error can be reexpressed as

$$\delta\rho(t)=\frac{\varrho(t)}{|\bar{\rho}(t)|}\cdot\delta\varrho(t)=\hat{\rho}(t)\cdot\delta\varrho(t) \tag{2.24}$$

where

$$\delta\varrho(t)=\delta\mathbf{r}_s(t)-\delta\mathbf{r}_T(t) \tag{2.25}$$

In section 2.5.3 the Doppler shift residuals are minimized under the assumption that the errors are a function only of two components of the station position (S and $\mathcal{L}$) and a frequency offset parameter (Δf). Therefore this theoretical model can be parameterized as

$$\Delta f_D(t)=\frac{f_T}{c}\frac{d}{dt}[\hat{\rho}(t)\cdot\Delta\mathbf{r}_T(t)]+\Delta f \tag{2.26}$$

and the function that is minimized can be approximated by (differencing eqs. (2.23) and (2.26))

$$\delta^2 f_D(t)=\frac{f_T}{c}\frac{d}{dt}\{\hat{\rho}(t)\cdot\delta^2\varrho(t)\}+\delta^2 f \tag{2.27}$$

where

$$\left.\begin{aligned} \delta^2\varrho(t)&=\delta^2\mathbf{r}_T(t)+\delta\mathbf{r}_s(t) \\ \delta^2\mathbf{r}_T(t)&=\Delta\mathbf{r}_T-\delta\mathbf{r}_T \\ \delta^2 f&=\Delta f-\delta f \end{aligned}\right\} \tag{2.28}$$

Two different coordinate systems are predominantly utilized in the analysis. They are defined through the geometry of the satellite relative to the station at the time of closest approach, $t=t_c$. The station errors are resolved into the MSR system coordinates defined in section 2.5.3, the unit vectors being given by $\hat{S}$, $\hat{\mathcal{L}}$, and $\hat{C}$. They are then transformed into the $\hat{H}_c$, $\hat{L}_c$, $\hat{Z}_c$ system defined in section 2.5.5. The c subscript is used to

denote the directions as defined at $t=t_c$. These coordinate systems are fixed in the true equatorial system of date and are shown in figures 2.11 through 2.13. Figure 2.11 illustrates the motion of the satellite and the station in an inertial system during the time that the satellite is above the horizon of the station. The X–Y plane of the coordinate system of figure 2.11 is the osculating orbital plane of the orbit at t_c, where the Z axis is in the direction of the satellite angular momentum vector and is the $\hat{Z}_c$ coordinate axis of the $\hat{H}_c$, $\hat{L}_c$, $\hat{Z}_c$ system. We define

$$\beta(t)-\beta(t_c)=\Delta M=\bar{n}\ (t-t_c) \tag{2.29}$$

and the maximum value attained by ΔM during a satellite pass by ΔM_0. Also, to simplify the analysis, we assume the pass to be symmetric with respect to the in-plane angular distance traveled by the satellite before and after $t=t_c$.

In the analysis, two quantities related to the elevation E_l and azimuth A_z (of the satellite) are used. These quantities, the "pseudo-elevation," e_l, and "pseudo-azimuth," a_z, are shown in figure 2.12, and their relation to E_l and A_z is summarized in table 2.15. The use of e_l and a_z allows the form of the transformation equations to remain invariant for all quadrants of the azimuth and for all inclinations of the orbital plane.

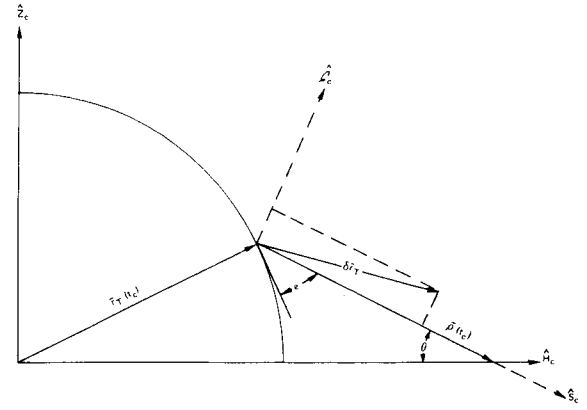

FIGURE 2.12.—Geometry at time of minimum slant range (H_c—Z_c plane, satellite motion into page).

To facilitate the analysis, the time derivative of the slant-range error is written as

$$\frac{d}{dt}[\hat{\rho}(t)\cdot\delta^2\varrho(t)]=\frac{1}{\rho^3(t)}\{\rho^2(t)\frac{d}{dt}[\varrho(t)\cdot\delta^2\varrho(t)]-\frac{1}{2}\varrho(t)\cdot\delta^2\rho(t)\frac{d}{dt}\rho^2(t)\} \tag{2.30}$$

In order to evaluate this derivative, we first obtain expressions for $\rho^2(t)$ and $\varrho(t)\cdot\delta^2\varrho(t)$ expanded in terms of the functions $\sin\Delta M$ and $C(\Delta M)$, where

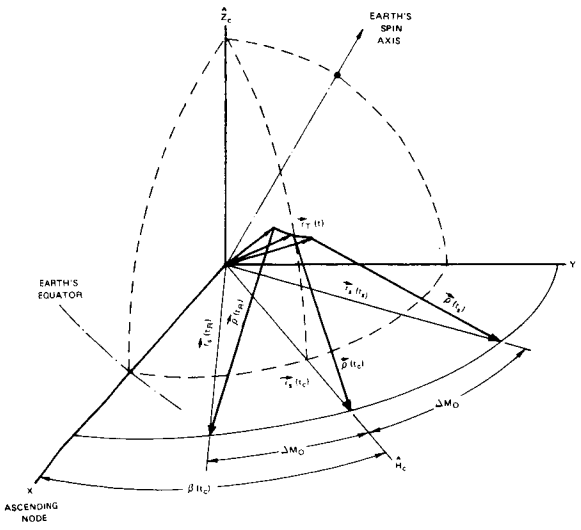

FIGURE 2.11.—Geometry during satellite pass (X—Y plane=orbital plane).

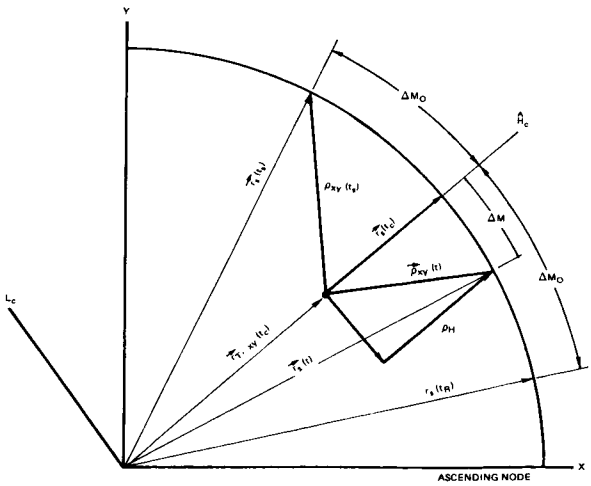

FIGURE 2.13.—Geometry of pass (orbital plane).

$$C(\Delta M) = 1 - \cos(\Delta M) \qquad (2.31)$$

A justification for using these as expansion functions is given by Guier (1966a) and will not be presented here.

We begin by writing the slant-range vector as

$$\begin{aligned}\varrho(t) &= \mathbf{r}_s(t) - \mathbf{r}_T(t) \\ &= \mathbf{r}_s(t) - \mathbf{r}_s(t_c) + [\mathbf{r}_s(t_c) - \mathbf{r}_T(t_c)] \\ &\quad - [\mathbf{r}_T(t) - \mathbf{r}_T(t_c)]\end{aligned} \qquad (2.32)$$

Regrouping, we get

$$\begin{aligned}\rho(t)\left\{\hat{\rho}(t) + \frac{\mathbf{r}_T(t) - \mathbf{r}_T(t_c)}{\rho(t)}\right\} \\ = \mathbf{r}_s(t) - \mathbf{r}_s(t_c) + \varrho(t_c)\end{aligned} \qquad (2.33)$$

Since for near-Earth satellites

$$\left|\frac{\mathbf{r}_T(t) - \mathbf{r}_T(t_c)}{\rho(t)}\right| \leq \frac{|\mathbf{r}_T|\,\omega_e(t - t_c)}{\rho(t)} \ll 1$$

this term can be neglected.

If all vectors are defined in the $\hat{H}_c$, $\hat{L}_c$, $\hat{Z}_c$ coordinate system, using figures 2.11–2.13, we can then write equation (2.33) as

$$\begin{aligned}\varrho(t) = r_s\{[\rho_s \cos\theta - C(\Delta M)]\,\hat{H}_c + \sin\Delta M\,\hat{L}_c \\ - \rho_s \sin\theta\,\hat{Z}_c\}\end{aligned} \qquad (2.34)$$

where terms that depend on the eccentricity of the orbit have been neglected. For convenience we have defined

$$\begin{aligned} r_s &= |\mathbf{r}_s(t_c)| \\ \rho_s &= \frac{|\varrho(t_c)|}{r_s}\end{aligned}$$

From equation (2.34) we can now obtain

$$\rho^2(t) = r_s^2[\rho_s^2 + 2\alpha_p C(\Delta M)] \qquad (2.35)$$

where

$$\alpha_p = 1 - \rho_s \cos\theta \qquad (2.36)$$

In equation (2.28) we defined

$$\delta^2\varrho(t) = \delta^2\mathbf{r}_T(t) + \delta\mathbf{r}_s(t)$$

in which

$$\delta^2\mathbf{r}_T(t) = \Delta\mathbf{r}_T - \delta\mathbf{r}_T$$

We defined $\Delta\mathbf{r}_T$ to be the parameterized station correction in the MSR coordinate system determined from the least-squares fit to the Doppler residuals. This is represented as

$$\Delta\mathbf{r}_T = \mathcal{L}\,\hat{\mathcal{L}} + S\,\hat{S} \qquad (2.37)$$

Since the Doppler shift is relatively insensitive to out-of-plane motion of the satellite with respect to the tracking station, the inclusion of a $\hat{C}$-component correction in the determination results in ill-conditioned equations. Therefore the correction to the station coordinates is confined to the plane defined by the unit vectors $\hat{\mathcal{L}}$ and $\hat{S}$. The estimated errors in the station coordinates are given by

$$\delta r_T = E_S\,\hat{S} + E_{\mathcal{L}}\hat{\mathcal{L}} + E_C\hat{C} \qquad (2.38)$$

and therefore

$$\delta^2\mathbf{r}_T = (S - E_S)\,\hat{S} + (\mathcal{L} - E_{\mathcal{L}})\,\hat{\mathcal{L}} - E_C\hat{C} \qquad (2.39)$$

Transforming to the $\hat{H}_c$, $\hat{L}_c$, $\hat{Z}_c$ system, we get

$$\begin{aligned}\delta^2\mathbf{r}_T = [(S - E_S)\cos\theta - E_C\sin\theta]\,\hat{H}_c \\ + (\mathcal{L} - E_{\mathcal{L}})\,\hat{L}_c + [(S - E_S)\sin\theta \\ + E_C\cos\theta]\,\hat{Z}_c\end{aligned} \qquad (2.40)$$

where we have assumed that $\hat{\mathcal{L}} = \hat{L}_c$. The results given in equation (2.40) are easily verified by figure 2.12.

In 2.5.5 we defined the satellite position error by

$$\delta\mathbf{r}_s(t) = \delta r_s(t)\,\hat{H} + \delta l_s(t)\,\hat{L} + \delta Z_s(t)\,\hat{Z} \qquad (2.41)$$

where the unit vector directions are also time dependent. Transforming to the Earth-fixed coordinate system, we get

$$\left.\begin{aligned}\delta\mathbf{r}_s(t)\cdot\hat{H}_c &= \delta r_s(t) - \delta l_s(t)\sin\Delta M - \delta r_s(t)\,C(\Delta M) \\ \delta\mathbf{r}_s(t)\cdot\hat{L}_c &= \delta l_s(t) + \delta r_s(t)\sin\Delta M - \delta l_s(t)\,C(\Delta M) \\ \delta\mathbf{r}_s(t)\cdot\hat{Z}_c &= \delta z_s(t)\end{aligned}\right\} \qquad (2.42)$$

Finally, in equation (2.42) we expand the time dependent components of the errors in the satellite position in terms of their values at $t=t_c$. It is desirable that this expansion represent accurately the position error at the time of closest approach of the satellite to a given station and a first-order estimate of the time dependence of the position error (relative to its value at closest approach) during the time that the satellite is above the horizon of the station for that pass. One alternative would be to use the complete solution to the differential equations given in section 2.5.5 (including the force contributions), at epoch t_c. However, this introduces complexities that are not warranted in this analysis. The best compromise is to use a Taylor series expansion in time about t_c and transform the time differentials to functions of sin ΔM and $C(\Delta M)$. This gives

$$\left.\begin{aligned}
\delta r_s(t) &= \delta r_c + \frac{\delta \dot r_c}{\overline{n}}\sin\Delta M + \frac{\delta \ddot r_c}{\overline{n}^2}C(\Delta M)\\
\delta l_s(t) &= \delta l_c + \frac{\delta \dot l_c}{\overline{n}}\sin\Delta M + \frac{\delta \ddot l_c}{\overline{n}^2}C(\Delta M)\\
\delta Z_s(t) &= \delta Z_c + \frac{\delta \dot Z_c}{\overline{n}}\sin\Delta M + \frac{\delta \ddot Z_c}{\overline{n}^2}C(\Delta M)
\end{aligned}\right\} \quad (2.43)$$

We again use a subscript c to denote that the functions are evaluated at $t=t_c$. Substitution of these results into eq. (2.42) then gives the desired form of the satellite position errors.

where

$$\left.\begin{aligned}
U_f(t) &= 1\\
U_0(t) &= -\alpha_p\,\rho_s\,\overline{n}\frac{f_T}{c}\left(\frac{r_s}{\rho(t)}\right)^3\sin\Delta M\\
U_1(t) &= \overline{n}\frac{f_T}{c}\left(\frac{r_s}{\rho(t)}\right)^3\\
&\quad [\rho_s^2-\rho_s^2 C(\Delta M)-C^2(\Delta M)]\\
U_2(t) &= \overline{n}\frac{f_T}{c}\left(\frac{r_s}{\rho(t)}\right)^3\\
&\quad [\rho_s^2+\alpha_p\,C(\Delta M)]\sin\Delta M\\
U_3(t) &= \overline{n}\frac{f_T}{c}\left(\frac{r_s}{\rho(t)}\right)^3\\
&\quad [3\rho_s^2+4\,C(\Delta M)]\,C(\Delta M)
\end{aligned}\right\} \quad (2.47)$$

Now let the mean square value of the Doppler residuals be given by

$$F=\frac{1}{2\Delta M_0}\int_{-\Delta M_0}^{\Delta M_0}[\delta^2 f_D(t)]^2\,d(\Delta M) \quad (2.48)$$

where we seek to minimize F with respect to Δf, $\mathcal{L}$, and S. We define the partials of F as

$$\begin{aligned}
B_f &= \frac{\partial F}{\partial \Delta f}\\
B_K &= \frac{\partial F}{\partial R_K} \qquad K=0,1,2,3
\end{aligned} \quad (2.49)$$

so that

$$\frac{\partial F}{\partial \mathcal{L}}=\sum_{K=0}^{3}B_K\frac{\partial R_K}{\partial \mathcal{L}} \qquad \frac{\partial F}{\partial S}=\sum_{K=0}^{3}B_K\frac{\partial R_K}{\partial S} \quad (2.50)$$

Using this together with the results given by equations (2.34) and (2.40), we obtain

$$\varrho(t)\cdot\delta^2\varrho(t)=r_s\{\rho_s R_0+R_1\sin\Delta M+R_2\,C(\Delta M)+R_3\sin\Delta M\,C(\Delta M)+R_4\,C^2(\Delta M)\} \quad (2.44)$$

where

$$\left.\begin{aligned}
R_0 &= S\text{-}E_S+[\delta r_c\cos\theta-\delta Z_c\sin\theta]\\
R_1 &= \mathcal{L}\text{-}E_{\mathcal{L}}+\alpha_p\,\delta l_c+\rho_s\cos\theta\frac{\delta\dot r_c}{\overline{n}}-\rho_s\sin\theta\frac{\delta\dot Z_c}{\overline{n}}\\
R_2 &= -[(S\text{-}E_S)\cos\theta-E_C\sin\theta]+\alpha_p\left[\delta r_c+2\frac{\delta\dot l_c}{\overline{n}}\right]+\rho_s\cos\theta\frac{\delta\ddot r_c}{\overline{n}^2}-\rho_s\sin\theta\frac{\delta\ddot Z_c}{\overline{n}^2}\\
R_3 &= \alpha_p\left[\frac{\delta\dot r_c}{\overline{n}}+\frac{\delta\dot l_c}{\overline{n}^2}\right] \qquad R_4=\alpha_p\left[\frac{\delta\ddot r_c}{\overline{n}^2}-\frac{\delta\dot l_c}{\overline{n}}\right]
\end{aligned}\right\} \quad (2.45)$$

Equations (2.30), (2.35), and (2.44) are now used to obtain the desired form of the function to be minimized in a least-squares sense:

$$\delta^2 f_D(t)=\delta^2 f\,U_f(t)+R_0\,U_0(t)+R_1\,U_1(t)+R_2\,U_2(t)+R_3\,U_3(t) \quad (2.46)$$

Consider first B_f. Using equation (2.27) to define $\delta^2 r_D(t)$, we get

$$B_f = 0 = \frac{1}{\Delta M_0}\int_{-\Delta M_0}^{\Delta M_0} \frac{d}{dt}\left(\hat{\rho}(t)\cdot\delta^2\varrho(t)\right) + \delta^2 f\, d(\Delta M)$$

$$\delta^2 f = -\frac{f_T}{c}\mathbf{n}\frac{\hat{\rho}(\Delta M_0)\cdot\delta^2\varrho(\Delta M_0) - \hat{\rho}(-\Delta M_0)\cdot\delta^2\varrho(-\Delta M_0)}{2\Delta M_0}$$

Using equation (2.53), we then obtain

$$\delta^2 f = -\frac{f_T}{c}\bar{n}\left(\frac{r_s}{\rho(\Delta M_0)}\right)\left[R_1\frac{\sin\Delta M_0}{\Delta M_0} + R_3\frac{\sin\Delta M_0}{\Delta M_0}C(\Delta M_0)\right] \tag{2.51}$$

which, if the values of R_1 and R_3 are known, yields the value for $\delta^2 f$. We now use equation (2.51) to eliminate the frequency parameters in $\delta^2 f_D(t)$, thus getting

$$\delta^2 f_D(t) = R_0\, U_0(t) + R_1\, U_{1,f}(t) + R_2\, U_2(t) + R_3\, U_{3,f}(t) \tag{2.52}$$

where

$$U_{1,f}(t) = U_1(t) - \bar{n}\frac{f_T}{c}\left(\frac{r_s}{\rho(\Delta M_0)}\right)\frac{\sin\Delta M_0}{\Delta M_0} \tag{2.53}$$

$$U_{3,f}(t) = U_3(t) - \bar{n}\frac{f_T}{c}\left(\frac{r_s}{\rho(\Delta M_0)}\right)\frac{\sin\Delta M_0}{\Delta M_0}C(\Delta M_0) \tag{2.54}$$

From equations (2.47) and (2.53) we see that $U_0(t)$ and $U_2(t)$ are antisymmetric functions and that $U_{1,f}(t)$ and $U_{3,f}(t)$ are symmetric functions of ΔM. Noting this and substituting equation (2.52) into equation (2.49), we get

$$\left.\begin{aligned}
\frac{B_0}{2} &= R_0\, I_{00} + R_2\, I_{02}\\
\frac{B_1}{2} &= R_1\, I_{11} + R_3\, I_{13}\\
\frac{B_2}{2} &= R_0\, I_{02} + R_2\, I_{22}\\
\frac{B_3}{2} &= R_1\, I_{13} + R_3\, I_{33}
\end{aligned}\right\} \tag{2.55}$$

where

$$\left.\begin{aligned}
I_{00} &= \frac{1}{\Delta M_0}\int_0^{\Delta M_0}[U_0(t)]^2\, d(\Delta M)\\
I_{02} &= \frac{1}{\Delta M_0}\int_0^{\Delta M_0}U_0(t)\, U_2(t)\, d(\Delta M)\\
I_{22} &= \frac{1}{\Delta M_0}\int_0^{\Delta M_0}[U_2(t)]^2\, d(\Delta M)\\
I_{11} &= \frac{1}{\Delta M_0}\int_0^{\Delta M_0}[U_{1,f}(t)]^2\, d(\Delta M)\\
I_{13} &= \frac{1}{\Delta M_0}\int_0^{\Delta M_0}U_{1,f}(t)\, U_{3,f}(t)\, d(\Delta M)\\
I_{33} &= \frac{1}{\Delta M_0}\int_0^{\Delta M_0}[U_{3,f}(t)]^2\, d(\Delta M)
\end{aligned}\right\} \tag{2.56}$$

Using these results in equation (2.50), we have

$$\frac{\partial F}{\partial \mathcal{L}} = 0 = B_1 = 2\,[R_1\, I_{11} + R_3\, I_{13}]$$

$$\frac{\partial F}{\partial S} = 0 = B_0 - B_2\cos\theta = 2R_0\,[I_{00} - \cos\theta\, I_{02}] + 2R_2\,[I_{02} - \cos I_{22}] \tag{2.57}$$

Solving these equations for S and $\mathcal{L}$, we have

$$S = E_S - \frac{1}{(1-\alpha_1\cos\theta)}\left[E\sin\theta\alpha_I + \cos\theta\delta r_c - \sin\theta\,\delta Z_c\right] - \frac{\alpha_I}{(1-\alpha_I\cos\theta)}\left[\alpha_p\left(\delta r_c + 2\frac{\delta\dot{l}_c}{\bar{n}}\right) + \rho_s\left(\cos\theta\frac{\delta\ddot{r}_c}{\bar{n}^2} - \sin\theta\frac{\delta\ddot{Z}_c}{\bar{n}^2}\right)\right] \tag{2.58}$$

$$\mathcal{L} = E_L - \alpha_p\,\delta l_c - \left[\rho_s\cos\theta + \frac{I_{13}}{I_{11}}\alpha_p\right]\frac{\delta\dot{r}_c}{\bar{n}} + \rho_s\sin\theta\frac{\delta\dot{Z}_c}{\bar{n}} - \frac{I_{13}}{I_{11}}\alpha_p\frac{\delta\dot{l}_c}{\bar{n}^2} \tag{2.59}$$

where

$$\alpha_l = \frac{I_{02} - \cos\theta\, I_{22}}{I_{00} - \cos\theta\, I_{02}} \tag{2.60}$$

Equations (2.58) and (2.59) define the aggregation parameters obtained from the least-squares fit to the Doppler residuals in terms of the station position and satellite orbit errors that are contained in the data.

The station MSR-system positional errors can be expressed as functions of errors in their spherical coordinates by using the pseudo-elevation and pseudo-azimuth angles defined earlier.

$$\begin{aligned} E_S &= \sin e_l \delta r_c - [\cos a_z (r_c\, \delta\varphi_c) \\ &\quad - \sin a_z\, (r_c \cos\varphi_c\, \delta\lambda_c)] \cos e_l \\ E_L &= \sin a_z\, (r_c\, \delta\varphi_c) + \cos a_z\, (r_c \cos\varphi_c\, \delta\lambda_c) \\ E_C &= \cos e_l \delta r_c + [\cos a_z (r_c\, \delta\varphi_c) \\ &\quad - \sin a_z\, (r_c \cos\varphi_c\, \delta\lambda_c)] \sin e_l \end{aligned} \tag{2.61}$$

These can be verified from figure 2.12.

As an aid in determining the relative importance of terms appearing in the derived equations the following results are presented without further discussion:

$$C(\Delta M_0) \approx \frac{\rho(t_c) \sin e_l}{r_T + \rho(t_c) \sin e_l}$$

$$I_{22} = 0\ (\sqrt{C(\Delta M_0)}\ I_{02}) = 0\ (C(\Delta M_0)\ I_{00})$$

$$I_{33} = 0\ (\sqrt{C(\Delta M_0)}\ I_{13}) = 0\ (C(\Delta M_0)\ I_{11})$$

2.5.5 Special Procedure for Near-Earth Satellites

The equations of motion of a satellite in an inertial coordinate system under the influence of the Earth's gravity field can be written as

$$\ddot{\mathbf{r}}_s + \frac{GM_e}{r_s^3}\mathbf{r}_s = \mathbf{F} \tag{2.62}$$

Applying a first-order perturbation, we obtain

$$\delta\ddot{\mathbf{r}}_s + \frac{GM_e}{r_s^3}\delta\mathbf{r}_s - 3\frac{GM_e}{r_s^4}\delta r_s\, \mathbf{r}_s = \delta\mathbf{F} \tag{2.63}$$

Equation (2.62) represents the perturbed equations of motion which result from incorrect coefficients in the series expansion of the gravitational potential.

Guier (1966a) showed that if the error vector was transformed into a certain coordinate system, the resulting equations were more amenable to an analytic solution. He chose an orthogonal coordinate system that moved in an inertial coordinate system and that had its origin located at the satellite position as defined by a reference orbit. The unit vectors which specify the coordinate systems directions are defined by (see sec. 2.5.2) $\hat{H}$, $\hat{L}$, and $\hat{Z}$.

If we now define δr_s, δl_s, and δZ_s to be the components of the difference vector in this new coordinate system, then

$$\delta\mathbf{r}_s = \delta r_s\, \hat{H} + \delta l_s\, \hat{L} + \delta Z_s\, \hat{Z} \tag{2.64}$$

In the inertial coordinate system we have

$$\delta\mathbf{F} = \frac{\partial(\delta V)}{\partial x_s}\hat{\imath} + \frac{\partial(\delta V)}{\partial y_s}\hat{\jmath} + \frac{\partial(\delta V)}{\partial v_s}\hat{k} \tag{2.65}$$

where δV represents the error in the potential resulting from errors $\delta\bar{C}^m_n$, $\delta\bar{S}^m_n$ in the harmonic coefficients. On transforming to the new system we get

$$\begin{aligned} \delta\mathbf{F} = &\frac{\partial(\delta V)}{\partial r_s}\hat{H} + \frac{1}{r_s}\frac{\partial(\delta V)}{\partial\beta}\hat{L} \\ &+ \frac{1}{r_s \sin\beta}\frac{\partial(\delta V)}{\partial i}\hat{Z} \end{aligned} \tag{2.66}$$

The unit vectors in this system are time dependent. However, we can easily obtain

$$\left.\begin{aligned} \frac{d\hat{H}}{dt} &= \dot{\beta}\,\hat{L} + \text{terms of order } O\ (C^m_n, S^m_n) \\ \frac{d\hat{L}}{dt} &= -\dot{\beta}\,\hat{H} + \text{terms of order } O\,(C^m_n, S^m_n) \\ \frac{d\hat{Z}}{dt} &= 0 + \text{terms of order } O\ (C^m_n, S^m_n) \end{aligned}\right\} \tag{2.67}$$

Substituting equation (2.64) into equation (2.63) and neglecting terms of the order $C^m_n\, \delta S^m_n$, $\bar{S}^m_n\, \delta\bar{C}^m_n$, etc., we get

$$\delta\ddot{r}_s-\left(\dot{\beta}^2+\frac{2GM_c}{r_s^3}\right)\delta r_s-2\dot{\beta}\,\delta\dot{l}_s-\ddot{\beta}\,\delta l_s=\frac{\partial(\delta V)}{\partial r_s} \tag{2.68}$$

$$\delta\ddot{l}_s+2\dot{\beta}\,\delta\dot{r}_s+\ddot{\beta}\,\delta r_s+\left(\frac{GM_c}{r_s^3}-\dot{\beta}^2\right)\delta l_s=\frac{1}{r_s}\,\frac{\partial(\delta V)}{\partial\beta} \tag{2.69}$$

$$\delta\ddot{Z}_s+\frac{GM_c}{r_s^3}\delta Z_s=\frac{1}{r_s\sin\beta}\,\frac{\partial(\delta V)}{\partial i} \tag{2.70}$$

Note that in these equations the effects of errors in the $\hat{Z}$ component of the difference vector are uncoupled from the remaining two.

In nonzonal harmonic analysis the eccentricity of the orbit is neglected in solving the above equations. After this simplification is made, equations (2.68)–(2.70) reduce to

$$\delta\ddot{r}_s-3\bar{n}^2\delta r_s-2\bar{n}\delta\dot{l}_s=\frac{\partial(\delta V)}{\partial r_s} \tag{2.68'}$$

$$\delta\dot{l}_s+2\bar{n}\delta\dot{r}_s=\frac{1}{r_s}\,\frac{\partial(\delta V)}{\partial\beta} \tag{2.69'}$$

$$\delta\ddot{Z}_s+\bar{n}^2\delta Z_s=\frac{1}{r_s\sin\beta}\,\frac{\partial(\delta V)}{\partial i} \tag{2.70'}$$

The forces on the right-hand side of these equations are derived from a model of the Earth's perturbing potential expressed in terms of a series expansion in spherical harmonics.

$$V=\frac{GM_c}{a_c}\sum_{n=2}^{\infty}\sum_{m=0}^{l}N_{nm}\left(\frac{a_c}{r_s}\right)^{n+1}P_n^m(\sin\varphi_s')\left[\bar{C}_n^m\cos m(\alpha_s-\alpha_G)+\bar{S}_n^m\sin m(\alpha_s-\alpha_G)\right] \tag{2.71}$$

where the notation used is given in section 2.5.2. We assume that all errors in the expansion are a result of using incorrect coefficients for the spherical harmonics. Thus a mathematical description of δV is obtained from equation (2.71) by replacing $\bar{C}_n^m$ and $\bar{S}_n^m$ by $\delta\bar{C}_n^m$ and $\bar{S}_n^m$, respectively.

To derive a more useful expansion, we define the complex function

$$\psi_n^m=N_{nm}\left(\frac{a_c}{r_s}\right)^{n+1}[u_n^m+jv_n^m] \tag{2.72}$$

where

$$\left.\begin{aligned}u_n^m&=P_n^m(\sin\varphi_s)\cos m(\alpha_s-\alpha_G)\\ v_n^m&=P_n^m(\sin\varphi_s)\sin m(\alpha_s-\alpha_G)\end{aligned}\right\} \tag{2.73}$$

We then have that

$$\delta V=\sum_{n=2}^{\infty}\sum_{m=0}^{n}\delta V_n^m \tag{2.74}$$

where

$$\delta V_n^m=\frac{GM_c}{a_c}\{\delta\bar{C}_n^m Re[\psi_n^m]+\delta\bar{S}_n^m\,\mathrm{Im}[\psi_n^m]\} \tag{2.75}$$

From spherical geometry we note the following identities:

$$\left.\begin{aligned}\sin\varphi_s'&=\sin i\sin\beta\\ \cos\varphi_s'\cos(\alpha_s-\Omega)&=\cos\beta\\ \cos\varphi_s'\sin(\alpha_s-\Omega)&=\cos i\sin\beta\end{aligned}\right\} \tag{2.76}$$

Also, the Legendre polynomials are rewritten as

$$P_n^m(\sin\varphi_s')=\cos^m\varphi_s' T_n^m(\sin\varphi_s') \tag{2.77}$$

where

$$T_n^m(\sin\varphi_s')=\frac{1}{2^n}\sum_{t=0}^{\left[\frac{n-m}{2}\right]}(-1)^t\frac{(2n-2t)!\,(\sin i\sin\beta)^{n-m-2t}}{t!\,(n-t)!\,(n-m-2t)!}$$

$$\left[\frac{n-m}{2}\right]=\begin{cases}\dfrac{n-m}{2} & \text{for } n-m \text{ even}\\ \dfrac{n-m-1}{2} & \text{for } n-m \text{ odd}\end{cases} \tag{2.78}$$

When equations (2.76)–(2.78) are used, the complex function ψ_n^m takes the form

$$\psi_n^m=N_{nm}\left(\frac{a_c}{r_s}\right)^{n+1}T_n^m(\sin\varphi_s')[\cos\beta+j\cos i\sin\beta]^m e^{jm(\Omega-\alpha_G)} \tag{2.79}$$

The trigonometric functions of argument β in this equation are redefined in exponential form and then expanded to obtain

$$\psi_n^m = \frac{N_{nm}}{2^n}\left(\frac{a_e}{r_s}\right)^{n+1} \sum_{t=0}^{\left[\frac{n-m}{2}\right]} (-1)^t \frac{(2n-2t)!}{t!\,(n-t)!\,(n-2t)!}\left(\frac{-j}{2}\right)^{n-m-2t} \sum_{s=0}^{m}\sum_{c=0}^{n-m-2t} (-1)^c \cos^{2(m-s)}\frac{i}{2}\sin^{2s}\frac{i}{2}\binom{m}{s}\binom{n-m-2t}{c} \exp j\{[n-2(t+c+s)]\beta + m(\Omega-\alpha_G)\} \quad (2.80)$$

The above equation can be rewritten, collecting the coefficients of each argument of the function exp $j\{[n-2(t+c+s)]\beta+m(\Omega-\alpha_G)\}$. Let

$$p = t+c+s \quad (2.81)$$

where $0 \le p \le n$. In adding the summation on p we can eliminate one of the other summations. In this case we set $s=p-t-c$ and eliminate the summation on s. Finally,

$$\psi_n^m = (-j)^{n-m}\left(\frac{a_e}{r_s}\right)^{n+1} \sum_{p=0}^{n} I_{nmp}^{(0,0)} \exp j\{(n-2p)\beta + m(\Omega-\alpha_G)\} \quad (2.82)$$

where

$$I_{nmp}^{(g,h)} = \frac{N_n^m}{2^n}\sum_t \frac{(2n-2t)!\left[\sin\frac{i}{2}\cos\frac{i}{2}\right]^{n-m-2t-g}}{t!\,(n-t)!\,(n-m-2t-g)!} \sum_c (-1)^c \binom{n-m-2t-g}{c}\binom{m-h}{s}\cos^{2(m-h-s)}\frac{i}{2}\sin^{2s}\frac{i}{2} \quad (2.83)$$

and the limits on t and c are given by

$$0 \le t \le \begin{cases} p & ; p \le \left[\frac{n-m-g}{2}\right] \\ \left[\frac{n-m-g}{2}\right] & ; \left[\frac{n-m-g}{2}\right] \le p \le \left[\frac{n+m-g}{2}\right]-h \\ n-p-g-h & ; p \ge \left[\frac{n+m-g}{2}\right]-h \end{cases} \quad (2.84)$$

$$\begin{cases} 0 & ; p-t \le m-h \\ p-t-m+h & ; p-t \ge m-h \end{cases} \le c \le \begin{cases} n-m-2t-g & ; p-t \ge n-m-2t-g \\ p-t & ; p-t \le n-m-2t-g \end{cases}$$

The additional parameters g and h are introduced into the definition of the inclination function to facilitate the computation of the forces derived from the potential, specifically, that component of the force which is in the $\hat{Z}$ direction. For this computation we first take the derivative of equation (2.79) with respect to the satellite inclination i. This yields a sin β factor which cancels with the one appearing in the denominator.

Since we neglect eccentricity effects in modeling the contribution of potential errors in the satellite motion, no further expansion of equation (2.82) is needed. Using this form in equation (2.75), we can then express the error in the potential resulting from a harmonic of degree and order (n, m) as

$$\delta V_n^m = \frac{GM_e}{a_e}\left(\frac{a_e}{r_s}\right)^{n+1} \sum_{p=0}^{n} I_{nmp}^{(g,h)(0,0)} S_{nmp} \quad (2.85)$$

where

$$S_{nmp}=S(\Phi_{nmp})$$
$$=(-1)^{\left[\frac{n-m}{2}\right]}\left\{\begin{bmatrix}\delta\bar{C}^{\,m}_{n}\\ -\delta\bar{S}^{\,m}_{n}\end{bmatrix}_{(n-m)\text{ odd}}^{(n-m)\text{ even}}\cos\Phi_{nmp}+\begin{bmatrix}\delta\bar{S}^{\,m}_{n}\\ \delta\bar{C}^{\,m}_{n}\end{bmatrix}_{(n-m)\text{ odd}}^{(n-m)\text{ even}}\sin\Phi_{nmp}\right\} \quad (2.86)$$
$$\Phi_{nmp}=(n-2p)\beta+m(\Omega-\alpha_G)$$

Utilizing the above results, we can now write the desired form of the forces to be used in solving equations (2.68′) and (2.70′) :

$$\frac{\partial(\delta V^m_n)}{\partial r_s}=-(n+1)\frac{GM_e}{a_e^{\,2}}\left(\frac{a_e}{a}\right)^{n+2}\sum_{p=0}^{n}I^{(0,0)}_{nmp}S_{nmp} \quad (2.87)$$

$$\frac{1}{r_s}\frac{\partial(\delta V^m_n)}{\partial\beta}=\frac{GM_e}{a_e^{\,2}}\left(\frac{a_e}{a}\right)^{n+2}\sum_{p=0}^{n}(n-2p)\,I^{(0,0)}_{nmp}S'_{nmp} \quad (2.88)$$

$$\frac{1}{r_s\sin\beta}\frac{\partial(\delta V^m_n)}{\partial i}=\frac{GM_e}{a_e}\left(\frac{a_e}{a}\right)^{n+2}\sum_{p=0}^{n-1}[\cos i\,I^{(1,0)}_{nmp}-m\sin j\,I^{(0,1)}_{nmp}]D_{nmp} \quad (2.89)$$

where r_s is replaced by a, the orbit semi-major axis. The frequency dependence of the $\hat{Z}$ component of the force vector for a given harmonic is slightly different from the other two. For emphasis, a different symbol is used, which we define as

$$D_{nmp}=D(\Phi_{n-1,\,mp})=-S'_{nmp}(\Phi_{n-1,\,mp})$$
$$=(-1)^{\left[\frac{n-m}{2}\right]}\left\{\begin{bmatrix}\delta\bar{C}^{\,m}_{n}\\ -\delta\bar{S}^{\,m}_{n}\end{bmatrix}_{(n-m)\text{ odd}}^{(n-m)\text{ even}}\sin\Phi_{n-1,\,mp}-\begin{bmatrix}\delta\bar{S}^{\,m}_{n}\\ \delta\bar{C}^{\,m}_{n}\end{bmatrix}_{(n-m)\text{ odd}}^{(n-m)\text{ even}}\cos\Phi_{n\,1,\,mp}\right\} \quad (2.90)$$

The prime used with S_{nmp} denotes the derivative with respect to its argument Φ_{nmp}.

The general solution to the differential equations given in equations (2.68′)–(2.70′) consists of two parts, a complementary and a particular solution. The complementary solution reflects how orbital errors at a given epoch will propagate as a function of time. In a least-squares determination of a satellite orbit, orbital errors are introduced as a result of both measurement noise and deficiencies in modeling the data. Thus, if adjustments are made to the data, the orbit parameters must also be modified to reflect these changes. In an analysis of residuals, this modification can be accomplished, with sufficient accuracy, by a least-squares fit of the adjusted data to the six orbital parameters specified by the complementary solution given below.

$$\delta r_s^{(0)}=-\frac{2}{3}A_1-\frac{A_3}{2}\cos\bar{n}(t-t_0)+\frac{A_2}{2}\sin\bar{n}(t-t_0)$$
$$\delta l_s^{(0)}=A_0+A_1\bar{n}(t-t_0)+A_2\cos\bar{n}(t-t_0)+A_3\sin\bar{n}(t-t_0)$$
$$\delta Z_s^{(0)}=A_4\cos\bar{n}(t-t_0)+A_5\sin\bar{n}(t-t_0) \quad (2.91)$$

The A_i's are referred to as the orbit parameters and the superscript zero is used to denote their contribution to the total solution. (Since the principal frequency contributions of zonal harmonics to the motion of a satellite are similar to those in equation (2.91), it is clear that short arcs of satellite data are not very useful in estimating zonal values.)

The particular solution to the differential equations reflects the contribution of the forces acting on the system. This contribution for a given (n,m,p) combination is given in equation (2.92) on page 124. Since the differential equations solved are linear, the complete solution consists of the sum of all the individual contributions.

2.5.6 Determination of Station Positions and Tesseral Harmonics

As was stated earlier, the main emphasis of the geodetic research program at APL was directed towards obtaining improved coefficients of the tesseral harmonics in the series expansion of the gravitational potential. Improved coordinates for the TRANET stations were also found in this analysis.

$$\left.\begin{aligned}
\delta r_s^{(p)} &= -\frac{GM_e}{a_e^2}\left(\frac{a_e}{a}\right)^{n+2}\left[n+1-\frac{2\bar{n}(n-2p)}{\dot{\Phi}_{nmp}}\right]\frac{I_{nmp}^{(0,0)}}{\bar{n}^2-\dot{\Phi}_{nmp}^2}S_{nmp}\\
\delta l_s^{(p)} &= -\frac{GM_e}{a_e^2}\left(\frac{a_e}{a}\right)^{n+2}\left[2\bar{n}(n+1)-\frac{(n-2p)(3\bar{n}^2+\dot{\Phi}_{nmp}^2)}{\dot{\Phi}_{nmp}}\right]\frac{I_{nmp}^{(0,0)}S'_{nmp}}{\dot{\Phi}_{nmp}(\bar{n}^2-\dot{\Phi}_{nmp}^2)}\\
\delta Z_s^{(p)} &= \frac{GM_e}{a_e^2}\left(\frac{a_e}{a}\right)^{n+2}\frac{1}{\bar{n}^2-\dot{\Phi}_{n-1,\,mp}^2}[\cos i\, I_{nmp}^{(1,0)}-m\sin i\, I_{nmp}^{(0,1)}]D_{mnp}
\end{aligned}\right\} \qquad (2.92)$$

This section describes the algorithms used in processing the pass-determined parameters to achieve this goal. It is also pertinent, at this point, to discuss some of the criteria established for selecting and processing the raw Doppler data (Guier, 1963a).

A uniform distribution of tracking stations over the Earth's surface is desirable to avoid overweighting of data from a given region. As far as possible, uniform coverage of the satellite orbit by the data is obtained. Data are considered only from those periods for which the satellite oscillator is sufficiently stable. Selection is also made on the basis that the data are the best available with respect to noise level, absence of second-order refraction effects, and timing errors. To further minimize refraction errors, only those passes with maximum elevations of less than 80 deg and greater than 20 deg are used. Individual data points within a pass corresponding to instantaneous elevations less than 13 deg are also eliminated.

The selected Doppler passes from a given satellite are grouped into 48-hour time spans and processed by the method discussed in section 2.5.3. For studying the effects of resonance harmonics the data are grouped into spans comparable to 1½ times the resonance period. These resonance coefficients are obtained in a separate analysis of the data and will be discussed later.

The aggregation parameters obtained from each 48-hour group of data are stored on tapes. These tapes are then processed by a special program designed by W. H. Guier and called GEOFIT. This program seeks a minimum to the following function:

$$F=\frac{1}{N}\sum_{\gamma=1}^{N}W_\gamma\{\delta S_\gamma^2+\delta\mathcal{L}_\gamma^2\} \qquad (2.93)$$

where the weights W_γ are based on information obtained from the analysis presented in section 2.5.3. The functions δS_γ and $\delta\mathcal{L}_\gamma$ represent the theoretical minus experimental station coordinates determined from one Doppler pass. The experimental values are those produced in section 2.5.3 and their theoretical representation defined by equations (2.58) and (2.59) of section 2.5.4.

The minimization parameters consist of the following: (1) six orbit-parameters for each 48-hour span of data used, as defined by equation (2.91); (2) a predetermined set of tesseral-harmonic coefficient corrections as defined by equation (2.92); and (3) three position-coordinate parameters associated with each tracking station from which Doppler data were received. These minimization parameters are determined by an iterative procedure. To avoid the problem of inverting large matrices, the parameters associated with the tesseral harmonics are partitioned into subgroups according to the order of the harmonics (i.e., all coefficients associated with the harmonics of order m_i constitute the minimization parameters in the i^{th} subgroup).

The orbit parameters are adjusted to the data before and after each adjustment for station parameters and for each determined subgroup of harmonic coefficient corrections. This iterative procedure is followed until a stable solution is found for all the desired minimization parameters.

By this method of analysis of Doppler data, the approximations in the theory preclude obtaining more than a three-to-five factor improvement in the rms of the residuals. To seek improvements beyond this point, the entire procedure of processing the

Doppler data should be repeated with the improved parameters available at this stage of the analysis.

Resonance harmonic coefficients have been determined exclusively from an analysis of the station along-track movements, $\mathcal{L}$, given in section 2.5.3 (Yionoulis, 1965). Equation (2.58) of section 2.5.4 shows that the major orbital error absorbed by this parameter is the along-track component δl_s. From equation (2.92) we have that the contribution from the tesseral harmonics to the satellite along-track errors for a given (n,m,p) combination is

$$\delta l_s = -\frac{GM_e}{a_e^2}\left(\frac{a_e}{a}\right)^{n+2}\left[2\bar{n}(n+1) - \frac{(n-2p)(3\bar{n}^2+\dot{\Phi}_{nmp}^2)}{\dot{\Phi}_{nmp}}\right]\frac{I_{nmp}^{(0,0)}S'_{nmp}}{\dot{\Phi}_{nmp}[\bar{n}^2-\dot{\Phi}_{nmp}^2]}$$

where the frequency associated with the given term is

$$\dot{\Phi}_{nmp} = (n-2p)\,\dot{\beta} + m(\dot{\Omega}-\dot{\alpha}_G)$$

This form of the solution clearly illustrates the two types of resonance effects that are possible. From the frequency contribution to the amplitude we see that $\dot{\Phi}_{nmp} \approx \pm\bar{n}$ and $\dot{\Phi}_{nmp} \ll 1$ results in an amplification of the effect associated with the corresponding harmonic. The first type produces a nearly orbital frequency oscillation with a long-period envelope. The second type produces a long-period oscillation in the satellite motion. If a very strong resonance exists with a given orbit, it may be necessary to include the effects of eccentricity in the solution. Since the near-resonance phenomenon occurs for all near-Earth satellites, it admits the estimation of harmonic coefficients whose effects might otherwise be negligible.

2.6 RESULTS

The Applied Physics Laboratory's program to develop a Doppler satellite navigational system for the U.S. Navy began in 1959. Since the success of this system depended heavily on our ability to provide an accurate satellite ephemeris to the navigator, a major effort was directed toward improving this capacity. It was soon recognized that an elaborate model of the Earth's potential would be needed in order to satisfy the accuracy requirements established for this system. This was initially set at 0.1 nmi (0.18 km) for fixed-site navigation. To achieve this goal, a worldwide network of tracking stations (Newton and Kershner, 1962) was established and a constellation of geodetic satellites was proposed to provide the data needed for this analysis. A system of programs was designed by W. H. Guier for the IBM 7094 computer to be used for the geodetic determinations.

The first major results from this program were obtained in 1963 from an analysis of Doppler data from satellites in three distinct orbits (Guier, 1963a). Estimates for the harmonic coefficients through degree and order (4,4) were determined, and this model provided a satellite tracking capability of about 200 meters, rms error.

In 1964 the potential coefficients through degree and order (8,8) were determined from an analysis of Doppler data from five different satellites. This model, when it was used to process the satellite data, revealed the large contributions made by high-order resonant harmonic terms (Yionoulis, 1965, 1966a) to the satellite motion. This effect was first noticed in the processed Doppler data from satellite 1963–49B. Figures 2.14a and 2.14b are plots of station along-track errors as a function of time covering a 6-day period.[3] In figure 2.14a the effects of a 60-hour resonant period with the 13th-order harmonics in the potential expansion is clearly discernible. The amplitude of the oscillation is 130 meters. This effect was removed from the residuals (fig. 2.14b) on including appropriate values for coefficients of the 13th degree and order in

[3] The TRAFAC stations consist of four Doppler tracking stations, located in the United States which constitute the satellite tracking network for the Navy Navigation Satellite System (NNSS).

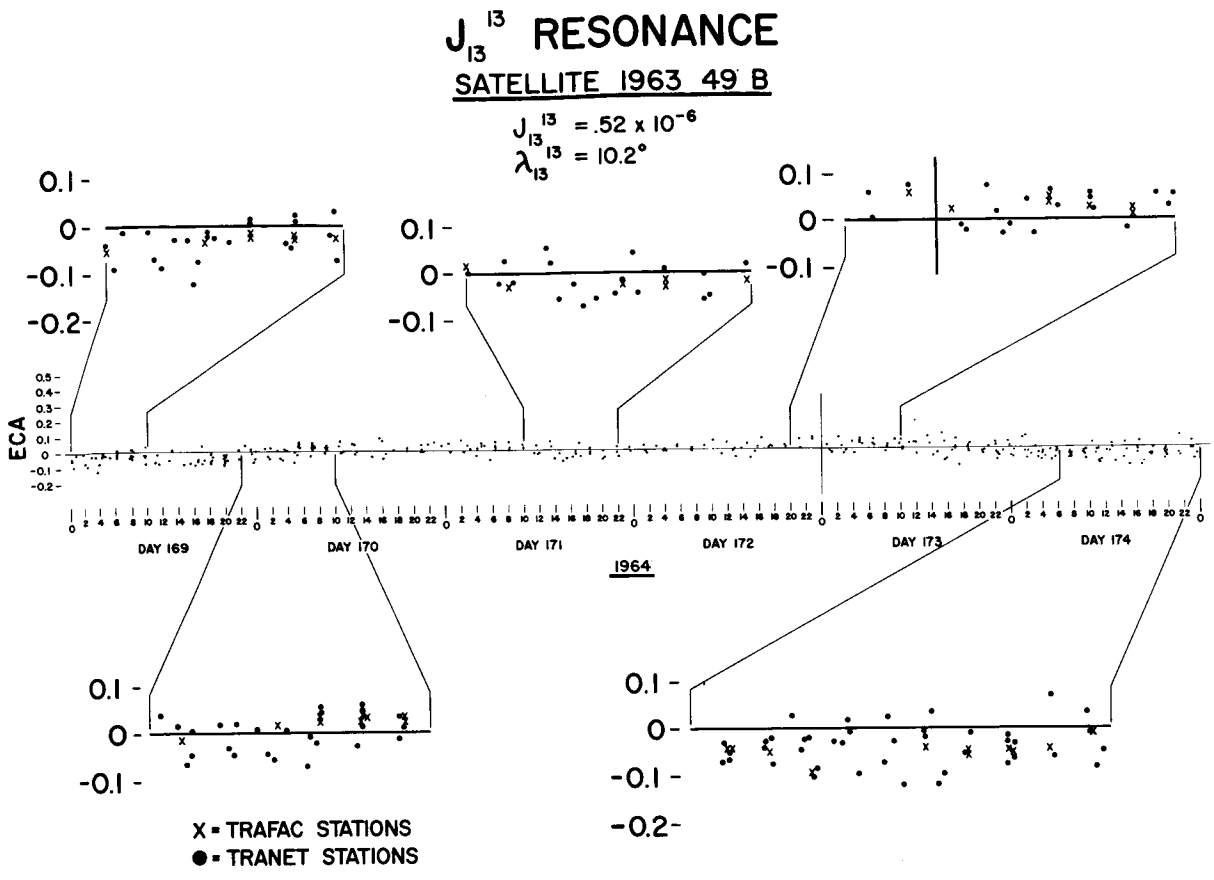

FIGURE 2.14a.—Plot of station along-track residuals (ECA) versus time showing the effect of resonance with the 13th-order harmonics.

computing the gravitational forces acting on the satellite.

After the resonance effect had been removed from the data, the coefficients were readjusted (Guier and Newton, 1965), and the resulting model became the first to satisfy the accuracy requirements established for the Navy Navigation Satellite System (NNSS).

Gravitational Potential Model APL 5.0–1967.—The last major redetermination of the potential coefficients was made in 1966. This model was deduced from the Doppler tracking of satellites in seven different orbital inclinations and is currently (1974) being used by the operational NNSS.

An extensive refinement of this model (Yionoulis *et al.*, 1972) was made in 1967. (The zonal harmonic coefficients are a set determined by the Naval Weapons Laboratory (table 2.11) (Anderle and Smith, private communication).) The characteristics of the satellites and the data used are presented in tables 2.9 and 2.10. Since the residuals associated with each pass have the dimensions of length, the rms of these residuals for all passes associated with a given satellite serves as a measure of the errors still remaining in the data. These final rms values, after fitting to new station coordinates and potential coefficents, are listed for each satellite in table 2.16. At the time that these computations were made, the effects of polar motion had not been incorporated. Neglecting this effect can contaminate the station coordinates and rms of the residuals by as much as 10m or more. Because computer runs are costly the residuals

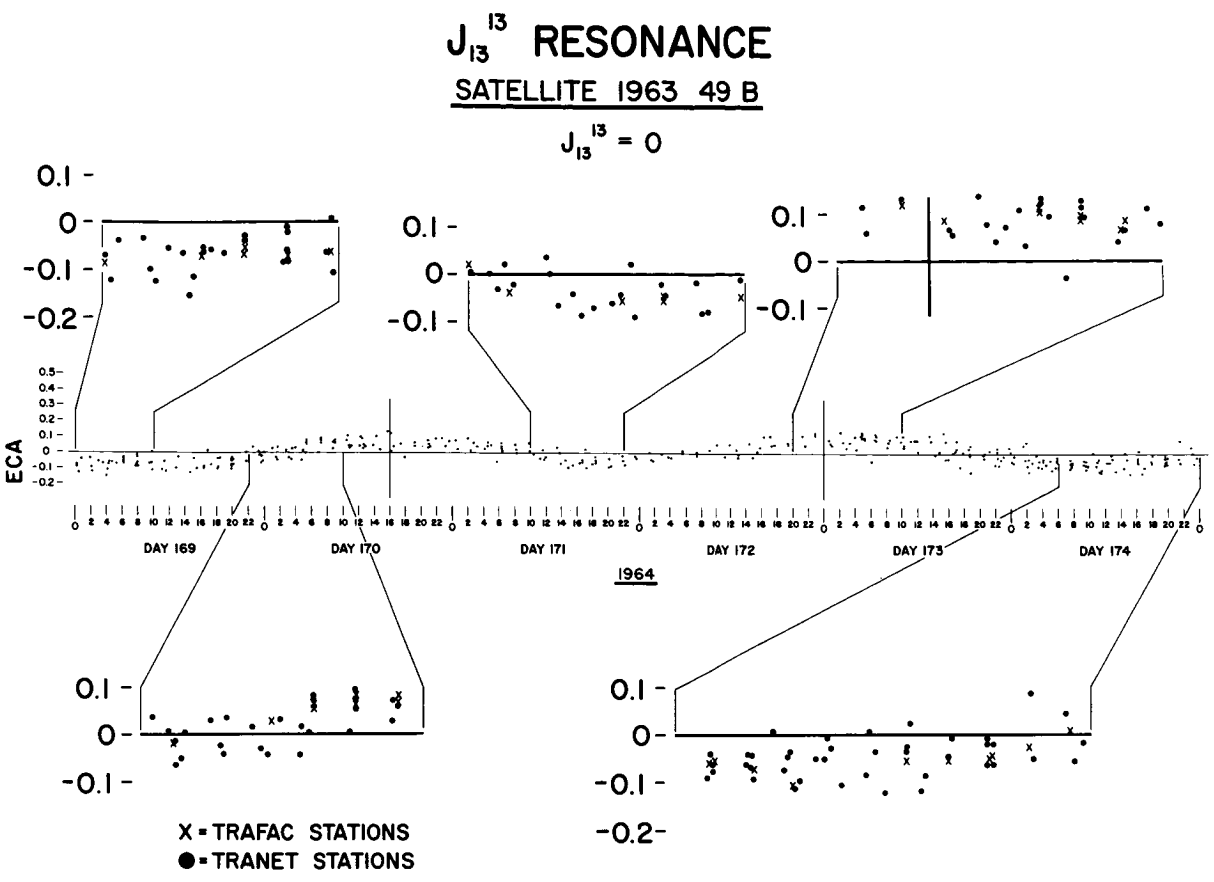

FIGURE 2.14b.—Plot of station along-track residuals (ECA) versus time with resonance effects removed by using values shown.

shown in table 2.16 were not recomputed to reflect this effect. It should also be noted that the rms of the residuals for 1961 $o1$ and 1961 $\delta\eta 1$ are significantly poorer than those for the other satellites, mainly because the tracking stations during these early years had poorer-quality instrumentation and lesser ability to maintain accurate time. For this reason fewer passes from these satellites were used in the determination.

The final values of the coefficients are listed in table 2.17. The geoidal heights based on this model are given in figure 2.15. The reference surface is defined by the central term and by the C_2^0 and C_4^0 values. This surface is very closely approximated by an ellipsoid with a semimajor axis of 6378.140 km and flattening 1/298.26.

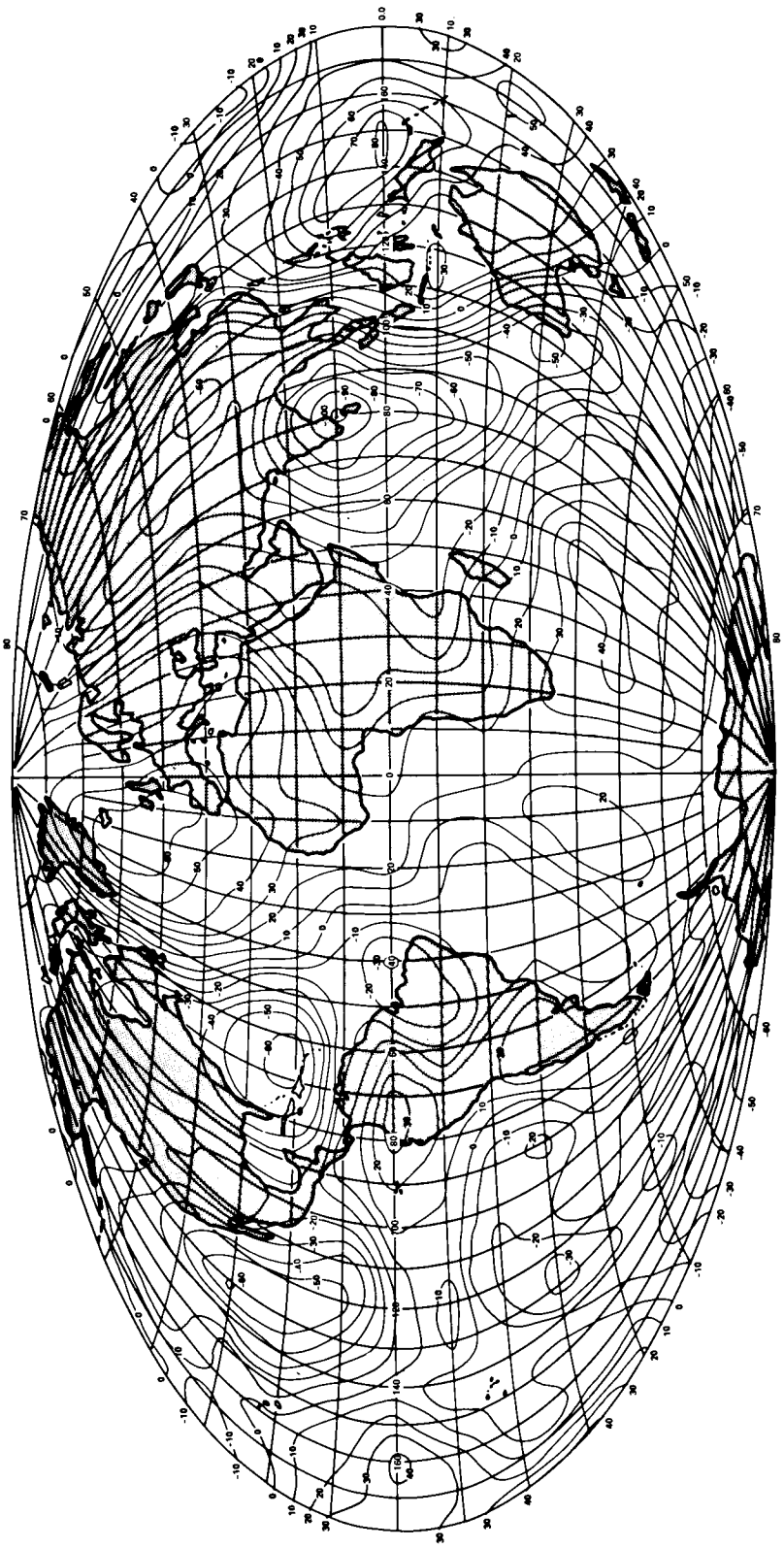

FIGURE 2.15.—Geoidal height contours (meters). Gravity model 5.0–1967.

APPENDIX

TABLE 2.1.—*Characteristics of TRANSIT 1B (1960 γ2)*

Launch

Date: 13 April 1960
From: Cape Kennedy, Florida
Rocket: Thor-Able-Star (two stages)

Orbital elements

Date	a	e	i	Period	Height at perigee	Height at apogee
13 April 1960	6 944 160	0.027	51°3	95.78 min	378 km	754 km

Lifetime

89 days

Physical characteristics

Shape: Spherical; 91.44-cm diameter (36 inches)
Weight: 120.5 kg

Equipment

Transmitters:	TRANSIT beacon (Hamblen and Oakes, 1961) B-system: 162-MHz and 216-MHz frequencies ±5 parts in 10^9 rms variations C-system: 54-MHz and 324-MHz frequencies ±5 parts in 10^{10} rms variations
Antenna:	Logarithmic spiral antenna painted on each hemisphere (Riblet, 1960) with silver paint
Power supply:	B-system: solar cells/nickel-cadmium batteries C-system: silver-zinc batteries (operated for 67 days)
Clock:	Mechanical
Orientation control:	Magnetic (Hamblen and Oakes, 1961) Yo-yo despinning (Hamblen and Oakes, 1961) Magnetic hysteresis despinning (Hamblen and Oakes, 1961)
Remarks:	An unmodulated 324-MHz carrier replaced the modulated 108-MHz carrier in TRANSIT 1A.

TABLE 2.2.—*Characteristics of ANNA 1B (1962 βμ)*

Launch

Date: 31 October 1962
From: Atlantic Missile Range, Florida
Rocket: Thor-Able-Star (two stages)

Orbital elements

Date	a	e	i	Period	Height at perigee	Height at apogee
31 October 1962	7 504 951	0.0070	50°.1	107.92 min	1077 km	1184 km

Lifetime

In orbit (1973)

Physical characteristics

Shape: Prolate spheroid 107.7-cm diameter, 36-cm wide, 119-cm diameter, 12-sided polygonal band of solar cells about the equator
Material: Aluminum and fiberglass
Weight: 159 kg

Equipment

Transmitters:	TRANSIT beacon		
	Frequency	Power	Stability
	54 MHz	450 mW	7×10^{-11} day^{-1}
	216 MHz	225 mW	6×10^{-11} day^{-1}
	MINITRACK		
	136 MHz	400 mW	----------
Transponders:	SECOR		
	224.5 MHz	100 mW	----------
	449.0 MHz	1 W	----------
Flashing lights:	See ch. 3 (Tomlinson, 1962)		
Antennas:	Logarithmic spiral painted on each hemisphere in silver		
Power supply:	Solar cells and rechargeable nickel/cadmium batteries 22 watts continuously		
Clock:	Electronic counter with 352-bit magnetic arc shift register		
Orientation control:	Magnetic despin by magnetic hystersis		

TABLE 2.3.—*Characteristics of Beacon Explorer B (1964–64A)*

Launch

Date: 9 October 1964
From: Point Arguello, California
Rocket: Scout (four stages)

Orbital elements

Date	a	e	i	Period	Height at perigee	Height at apogee
9 October 1964	7 362 000	0.012	79°.7	104.7 min	874 km	1077 km

Lifetime

Still in orbit (1974)

Physical characteristics

Shape: Octagonal prism with truncated octagonal pyramids at ends
Four panels, 46 cm in diameter and 25 cm high, carrying solar cells extended radially from prism 122 cm × 25 cm, each with 46 cm × 25 cm appendage
Weight: 32 kg

Equipment

Transmitters:
TRANSIT beacon

Frequency	Stability
162 MHz	3-MHz oscillator: 1×10^{-10} day^{-1}
324 MHz	5-MHz oscillator: 2×10^{-10} day^{-1}

Ionospheric experiment 4
20, 40, 41, 360 MHz
MINITRACK
136 MHz
Corner-cube reflectors: 160
Antennas: Whip antenna and dipole antenna
Power supply: Solar cells
Orientation control: Initially spin-stabilized; yo-yo despinning mechanism used after panels were extended; magnetic stabilization.

TABLE 2.4.—*Characteristics of Beacon Explorer–C*
(See table 2.3 for characteristics not listed)

Launch

Date: 20 April 1965
From: Wallops Island, Virginia
Rocket: Scout (four stages)

Orbital elements

Date	a	e	i	Period	Height at perigee	Height at apogee
20 April 1965	7 504 564	0.0252	41°.168	107.8 min	927 km	1310 km

Physical characteristics

Weight: 54.5 kg

Equipment

Transmitters:	Stability
System 1	2×10^{-11} day^{-1}
System 2	5×10^{-11} day^{-1}
5–MHz oscillator	6.3×10^{-10} day^{-1}

TABLE 2.5.—*Characteristics of GEOS-A (1965 89A)*

Launch

Date: 6 November 1965
From: Cape Kennedy, Florida
Rockets: Thor-Delta-X258 (three stages, improved Delta)

Orbital elements

Date	a	e	i	Period	Height at perigee	Height at apogee
6 November 1965	8 067 354	0.0725	59°.38	120.2 min	1115 km	2277 km

Lifetime

Still in orbit (1974)

Physical characteristics

Shape: Truncated octagon with octagonal prism (1.32 m outside diameter, 0.5 m high with 0.6-m-diameter hemisphere at one end (down) and truncated octagonal pyramid on other (fig. 2.5))
Weight: 175 kg

Equipment

Transmitters:	TRANSIT beacon:	162, 324, 972 MHz (operation ended 15 January 1966)
	Oscillator stability:	No. 1: $4–6 \times 10^{-12}$ (½-hour average) No. 2: $1–3 \times 10^{-11}$ (¼-hour average)
	SECOR transponder:	421 MHz (receive); 224.5 and 449 MHz (transmit) failed 8 February 1967
	GRR:	2.270 GHz (receive); 1.705 GHz (transmit)
	MINITRACK:	136 MHz, turned off 14 January 1967
Flashing lights:	4 xenon 670-watt flash tubes (see Table 2.6)	
Corner-cube reflectors:	322 reflectors mounted on bottom rim; 0.18 m^2 of surface; 50 percent within 20°	
Other:	Vector magnetometer; solar aspect detector	
Clock and storage unit:	Microelectronic circuitry	
Antenna:	Equiangular spiral slot antenna on each hemisphere; cone antenna (GRRR): 150° beam width	
Power supply:	Solar cells	
Stabilization:	Gravity-gradient-stabilized; magnetially anchored, eddy current damper; eddy-current-rod despinning system.	

TABLE 2.6.—*Characteristics of GEOS-B (1968 02-A)*

Launch

Date: 11 January 1968
From: Vandenberg Air Force Base, California
Rockets: Thor-Delta (Augmented)—FW-4 (three stages)

Orbital elements

Date	a	e	i	Period	Height at perigee	Height at apogee
11 January 1968	7 710 807	0.0308	105°.977	111.3 min	1084.0 km	1577.0 km

Lifetime

Still in orbit

Physical characteristics

Shape: Octagonal prism with hemispherical cap (1.32 m in outside diameter, 0.5 m height) (0.3 m in radius) on down end and octagonal prism on top
Weight: 213 kg

Equipment

Transmitters:	TRANSIT beacons:	162, 324, 972 MHz; timing markers on 162- and 324-MHz frequencies
	SECOR transponder:	421 MHz (receive); 224.5 MHz and 449 MHz (transit)
	GRR transponder:	2270 GHz (receive); 1.705 MHz (transmit)
	MINITRACK:	136.83 MHz
	5-cm (C-band) transponder:	5.690 MHz (receive); 5.765 MHz (transmit)
	Flashing lights:	Four 670-watt (1580 candle sec per flash) xenon flash tubes; Beacon 4 failed soon after launch; other beacons used until 31 January 1970
Corner-cube reflectors:	Optical 332 (0.18-m^{-2} reflecting surface) radar	
Other:	Vector magnetometer; solar aspect detector; Precipitating electron detector; laser light detector	
Clock and memory:	Same as for GEOS-A	
Antennas:	(1) Equiangular spiral slot antennas on each of two hemispheres (2) Conical antenna for GRRR (3) Two button-type, circularly polarized antennas for 5-cm (C-band) radar	
Power supply:	Solar cells (N-on-P) covering more than 50 percent of exposed area on prism; three independent power supplies (10, 10, and 20 watts)	
Stabilization:	Same as that for GEOS-A (See Whisnant *et al.*, 1969.)	

TABLE 2.7.—*TRANET Station Operating Modes*

Type of satellite	Mode designation	Frequencies (MHz)	Frequency, offset (ppm)	Station capabilities
GEOS, Doppler Beacon (DB)	Y_0	162/324	−50	Manual or automatic
NNSS	Z_0	150/400	−80	Manual or automatic
TRIAD	Z_1	150/400	−140	Manual or automatic
TIMATION	Z_2	149.5/399.4	None	Manual only, by equipped stations
As above	Z_0/Z_1	As above	As above	Automatic; station searches alternatively for Z_0 and Z_1 signals

TABLE 2.8.—*Scaling of the Frequencies by the Station Refraction-Corrector*

Satellite mode	Station Q number[a]	Formula	Effective frequency (MHz)
Y_0	351	$3/2\frac{\dot{\rho}(t)}{c}(162)$	242.98785
Z_0	261	$55/72\frac{\dot{\rho}(t)}{c}(150)$	114.5742
Z_0	266	$55/24\frac{\dot{\rho}(t)}{c}(150)$	343.7225
Z_1	261	$55/72\frac{\dot{\rho}(t)}{c}(150)$	114.5673
Z_1	266	$55/24\frac{\dot{\rho}(t)}{c}(150)$	343.7019
Z_2	261	$55/72\frac{\dot{\rho}(t)}{c}(150)$	114.4458
Z_2	266	$55/24\frac{\dot{\rho}(t)}{c}(150)$	343.3296

[a] The station Q number identifies the manner in which the refraction correction was performed and hence the effective frequencies to which the Doppler solution is scaled and corrected for frequency offset (Table 2.7).

TABLE 2.9.—*Satellites Used*

Satellite	Orbital elements[a]			
	Semimajor axis, a, km	Eccentricity, e	Inclination, i, deg	Nodal (draconic) period, p, min
1961 $\alpha\eta 1$	7414.482	0.010	32.4	104.9
1965 32A	7503.564	0.026	41.2	108.0
1962 $\beta\mu 1$	7504.951	0.006	50.1	108.0
1965 89A	8067.354	0.072	59.4	120.4
1961 $o1$	7321.522	0.008	66.8	103.9
1964 64A	7354.781	0.012	79.7	104.9
1965 48C	7460.782	0.009	90.0	107.0
1963 49B	7470.846	0.004	90.0	107.3

[a] Approximate values given.

TABLE 2.10.—*Observational Data Used*

Satellite	Number of 2-day arcs	Total number of passes[a]
1961 $\alpha\eta 1$	4	78
1965 32A	4	106
1962 $\beta\mu 1$	3	116
1965 89A	3	174
1961 $o1$	3	96
1964 64A	3	115
1965 48C	2	106
1963 49B	2	96

[c] A typical satellite pass above a station's horizon contains 200–400 data points. A data point consists of a pair of numbers specifying frequency and time.

TABLE 2.11.—*Coefficients of Zonal Harmonics*[a]

n	m	$\bar{C}_n^0 \times 10^6$
2	0	−484.257
3	0	0.953
4	0	0.718
5	0	0.074
6	0	−0.411
7	0	0.096
8	0	0.298
9	0	0.018
10	0	−0.191
11	0	−0.006
12	0	0.140

[a] Anderle and Smith, private communication.

TABLE 2.12.—*Miscellaneous Quantities*

Quantity	Value
GM_e	3.986015×10^{14} m^3/sec^2
a_e	6 378 166 m (used for length scaling only)

TABLE 2.13.—*Numerical Integration—Orbital Parameters*

I. Parameters
- β = argument of latitude (independent variable)
- $t(\beta)$ = time corresponding to β
- $\mathbf{P}(\beta)$ = angular momentum vector (normal to plane of osculating instantaneous orbit)
- $\mathbf{e}(\beta)$ = "eccentricity" vector (in direction of perigee)

II. Definition in terms of Keplerian elements
- $\mathbf{P} \cdot \mathbf{e} = 0$
- $|\mathbf{P}|^2 = a\,(1 - e^2)$
- $P_1 = |\mathbf{P}| \sin i \sin \Omega$; $P_2 = -|\mathbf{P}| \sin i \cos \Omega$;
- $P_3 = |\mathbf{P}| \cos i$
- $e_1 = e\,(\cos \omega \cos \Omega - \sin \omega \sin \Omega \sin i)$
- $e_2 = e\,(\cos \omega \sin \Omega + \sin \omega \cos \Omega \cos i)$
- $e_3 = e \sin \omega \sin i$

TABLE 2.14.—*Numerical Integration—Change in Orbital Parameters*

$t_0(\beta)$	= time corresponding to β in unperturbed orbit
$\mathbf{P}_0$	= $\mathbf{P}(\beta = 0)$ = angular-momentum vector of unperturbed orbit
$\mathbf{e}_0$	= $\mathbf{e}(\beta = 0)$ = eccentricity vector of unperturbed orbit
$\Delta t(\beta)$	= $t(\beta) - t_0(\beta)$
$\Delta\mathbf{P}(\beta)$	= $\mathbf{P}(\beta) - \mathbf{P}_0$
$\Delta\mathbf{e}(\beta)$	= $\mathbf{e}(\beta) - \mathbf{e}_0$
$\lvert\mathbf{P}(\beta)\rvert^2$	= $\lvert\mathbf{P}_0\rvert^2 + 2\,\mathbf{P}_0\cdot\Delta\mathbf{P}(\beta) + \Delta\mathbf{P}(\beta)^2$ (double precision)
$t(\beta)$	= $t_0(\beta) + \Delta t(\beta)$ for n^{th} revolution after epoch
$t_0(\beta)$	= $n\,[t_0(2\pi) - t_0(0)] + [t_0(\beta - 2\pi n) - t_0(2\pi n)] + t_0(0)$ (double precision)

TABLE 2.15.—*Relationship Between Pseudo Angles and Angles as a Function of Pass Direction*

Azimuth	Pass Direction	
	North	South
$0 < A_z < \pi$	$a_z = \pi - A_z$ $e_l = E_l$	$a_z = -A_z$ $e_l = \pi - E_l$
$\pi < A_z < 2\pi$	$a_z = -A_z$ $e_l = \pi - E_l$	$a_z = \pi - A_z$ $e_l = E_l$

E_l = elevation
A_z = azimuth
e_l = pseudo elevation
a_z = pseudo azimuth

TABLE 2.16.—*Data Residuals*

Satellite	RMS value of residuals[a] (meters)
1961 $\alpha\eta 1$	46.9
1965 32A	26.2
1962 $\beta\mu 1$	27.0
1965 89A	23.9
1961 $o1$	40.2
1964 64A	29.8
1965 48C	17.0
1963 49B	18.7

[a] Computed with program that did not include effects of polar motion.

TABLE 2.17.—*Fully Normalized Coefficients of the Spherical Harmonic Expansion of the Gravitational Potential*

n	m	$\bar{C}_{nm} \times 10^6$	$\bar{S}_{nm} \times 10^6$
2	1	0.0	0.0
2	2	2.443	−1.341
3	1	2.030	0.293
3	2	0.911	−0.602
3	3	0.643	1.396
4	1	−0.492	−0.446
4	2	0.370	0.536
4	3	0.964	−0.165
4	4	−0.135	0.292
5	1	−0.109	−0.270
5	2	0.502	−0.231
5	3	−0.321	−0.140
5	4	−0.196	−0.134
5	5	0.135	−0.745
6	1	−0.191	0.040
6	2	−0.130	−0.206
6	3	0.264	−0.035
6	4	−0.094	−0.564
6	5	−0.032	−0.489
6	6	0.046	−0.156
7	1	0.293	0.261
7	2	0.407	−0.132
7	3	0.172	−0.190
7	4	−0.179	−0.164
7	5	−0.062	0.033
7	6	−0.383	0.279
7	7	0.173	0.015
8	1	0.106	−0.040
8	2	0.144	−0.091
8	3	−0.192	−0.047
8	4	−0.054	0.019
8	5	−0.141	0.090
8	6	−0.749	0.379
8	7	0.126	0.107
8	8	−0.146	0.088
9	1	0.076	−0.131
9	2	−0.042	0.208
9	3	0.117	−0.227
9	4	−0.213	−0.064
9	5	−0.020	−0.018
9	6	0.065	0.166
9	7	−0.089	0.007
9	8	0.077	−0.094
9	9	−0.086	0.035
10	1	0.007	−0.017
10	2	−0.008	0.104
10	3	0.195	−0.205
10	4	−0.246	0.037
10	5	0.043	−0.063
10	6	−0.115	−0.123
10	7	0.067	0.094
10	8	0.039	−0.232
10	9	0.040	−0.014
10	10	0.060	0.008

TABLE 2.17.—*(Cont'd)*

n	m	$\bar{C}_{nm} \times 10^6$	$\bar{S}_{nm} \times 10^6$
11	1	0.073	0.121
11	2	0.163	−0.263
11	3	−0.176	−0.011
11	4	0.145	−0.119
11	5	−0.171	0.003
11	6	0.121	0.004
11	7	−0.092	−0.267
11	8	−0.026	0.128
11	9	−0.033	0.176
11	10	−0.126	−0.037
11	11	0.052	0.009
12	3	−0.120	0.039
12	4	0.019	−0.000
12	5	−0.104	−0.036
12	6	0.100	−0.144
12	7	−0.058	−0.110
12	8	−0.000	0.117
12	9	0.097	−0.023
12	10	0.051	−0.013
12	11	−0.061	−0.068
12	12	0.010	−0.003
13	4	−0.133	0.138
13	5	0.170	0.139
13	6	−0.097	0.021
13	7	−0.088	0.144
13	8	0.217	−0.254
13	9	−0.147	0.034
13	10	0.045	0.054
13	11	−0.036	−0.164
13	12	−0.048	0.034
13	13	−0.069	0.055
14	5	−0.012	−0.048
14	6	−0.177	0.067
14	7	0.189	−0.106
14	8	0.122	0.164
14	9	−0.000	0.006
14	10	0.037	−0.054
14	11	−0.019	−0.012
14	12	−0.013	−0.028
14	13	0.010	0.005
14	14	−0.039	−0.016
15	6	−0.116	−0.074
15	7	−0.046	−0.086
15	8	−0.082	0.176
15	9	0.125	−0.113
15	10	0.098	0.004
15	11	−0.086	−0.068
15	12	−0.038	−0.073
15	13	−0.041	−0.020
15	14	−0.003	−0.011
15	15	−0.009	−0.009
16	13	0.040	0.011
16	14	−0.043	−0.031
17	13	0.006	0.010

3

DEPARTMENT OF DEFENSE

R. Anderle
D. C. Brown
E. Cyran
D. H. Eckhardt
G. Dudley
W. D. Googe
G. Hadgigeorge
D. Huber
R. L. Iliff
N. Mason
R. H. Nichols
R. H. Rapp
F. W. Rohde
C. R. Schwartz
R. W. Smith
J. Trotter
M. A. Warden
H. L. White
O. W. Williams

3.1 INTRODUCTION

(Owen W. Williams, DMA)

The global responsibilities of the Department of Defense (DOD) encouraged an early interest in satellite geodesy. This interest considerably predated the formal National Geodetic Satellite Program (NGSP) and led to the use of satellites of opportunity for both positional and gravimetric investigations. The unique problems of the overwater missile test ranges and the requirements associated with development of worldwide navigation systems provided much of the early impetus to intercontinental geodetic programs. Uniquely, these activities also developed the skills and equipment that provided an initial base for subsequent developments in satellite geodesy by both the military and the civil communities. Early efforts included camera and electronic measuring techniques based on ranging, phase comparison, and Doppler. They culminated in Project ANNA, a truly cooperative effort involving the three military services, NASA, and other civil agencies. The basic concept of ANNA fostered by DOD in 1958 resulted in the first real geodetic satellite and the precursor of the NGSP.

Project ANNA was a test bed for satellite geodetic methods. The three military services concentrated their efforts in research and development in distinctly different techniques that were incorporated into the ANNA satellite (ch. 2 and ch. 3). This same division continued through the early portion of the NGSP.

The U.S. Army developed the sequential collation of range (SECOR) system at the Geodesy, Intelligence, Mapping Research and Development Agency (now the U.S. Army Engineer Topographic Laboratories (USAETL)). The system was subsequently exploited by the Army Map Service (currently known as the Defense Mapping Agency Topographic Center (DMATC)). The first SECOR transponder was orbited on ANNA 1B in 1962. SECOR systems continued in use through 1970.

Navy developments in satellite geodesy have used the Doppler technique and have grown out of the TRANSIT navigation satellite system developed by the Johns Hopkins Applied Physics Laboratory. The Naval Weapons Laboratory (NWL) has been the primary proponent of this system for geodetic applications. This system, its beacon having been first flown in 1960 as a navigation satellite and later included on the ANNA and GEOS (ch. 2) satellites, continues in use today as both a navigation and a geodetic system. Continued system development has resulted in the GEOCEIVER survey system. The Doppler system has proven more accurate, versatile, and efficient than other systems in early use within DOD and has been adopted by the Defense Mapping Agency as the primary DOD geodetic satellite system.

The U.S. Air Force, primarily as a result of encouraging experiences in conducting large-scale rocket-flare triangulations on the Eastern Test Range, pursued optical methods for satellite geodesy. The Air Force Cambridge Research Laboratories (AFCRL) developed xenon strobe lights for satellite applications. They also developed the PC–1000 camera which, together with the Wild BC–4 (ch. 7), was used for photographic satellite observations. In addition, AFCRL pioneered and has continued the development of laser illuminating and ranging equipment within the DOD.

Field observations using camera equipment were conducted by the 1381st Geodetic Survey Squadron (GSS). Data reduction was done by AFCRL and by the Aeronautical Chart and Information Center (ACIC) of the Air Force. (Both ACIC and the 1381st GSS have been incorporated into the Defense

Mapping Agency Aerospace Center (DMAAC) and continue to be active in satellite geodesy using the GEOCEIVER system.)

Significant contributions to satellite geodesy theory and to the practical methodology of data reduction involving active, passive, and cooperative satellites have been made by NWL, DMATC, DMAAC, AFCRL, and USAETL.

The early diversity of equipment and techniques within DOD has been reduced as a result of operational evaluations carried out during the NGSP. The following sections describe the theory, instrumentation, and data reduction methods used and some results obtained during the NGSP period.

3.2 INSTRUMENTATION

Data used in deriving the results given in this chapter were obtained primarily by means of three tracking systems: the PC–1000 camera system (sec. 3.2.1), SECOR, a distance-measuring system (sec. 3.3.2), and the TRANET Doppler-frequency measuring system (ch. 2). In addition, some data have been obtained by using laser DME (sec. 3.2.3), BC–4 cameras (ch. 7), and GEOCEIVER. The GEOCEIVER is basically a miniaturized version of the TRANET Doppler frequency measuring equipment, and the principles of its operation can be inferred from the description of TRANET in chapter 2.

3.2.1 PC–1000 Geodetic Camera System

(Maj. Norman Mason, DMA/AC/GSS)

Development of the PC–1000 camera system began at The Air Force Cambridge Research Center in the year 1959. Initial development of these cameras was undertaken for the purpose of testing the concept of long-range space triangulation using missile-borne flares. As the geodetic programs evolved from using missiles to using satellites, in the early 1960's, these cameras were modified so that they could observe flashing-light satellites as well as sun-illuminated satellites.

(1) Camera: Figure 3.1 shows a model of the PC–1000, which was used in several large-scale satellite triangulation missions. This camera consists of an eight-element lens with a focal length of about 1 meter and a relative aperture of f/5.0. The camera uses a photographic plate 190 mm × 215 mm × 6 mm, with a field of view 10° square (table 3.1).

(2) Other components: The other components of the PC–1000 camera system consist of the chopping shutter, camera controller, timing equipment, a digital recorder and data storage, and the power source.

(3) Shutter: The chopping shutter (Rapidyne) allows exposure times from 1 msec to infinity, but with a maximum of three exposures per second. It is electrically operated and driven by signals from the solid-state controller. Signals triggered by shutter cause the recording of time by the high-speed digital printer.

(4) Controller: The controller was developed to open and close automatically both internal and external shutters at precise predetermined times. The fully automatic mode can be overriden to permit manual operation.

(5) Timing equipment: The timing equipment consists of a timing generator (digital clock), a precise frequency standard, and three types of radio receivers. The method used to establish and maintain accurate time can produce UTC over long periods to within ±10 μsec (internal precision).

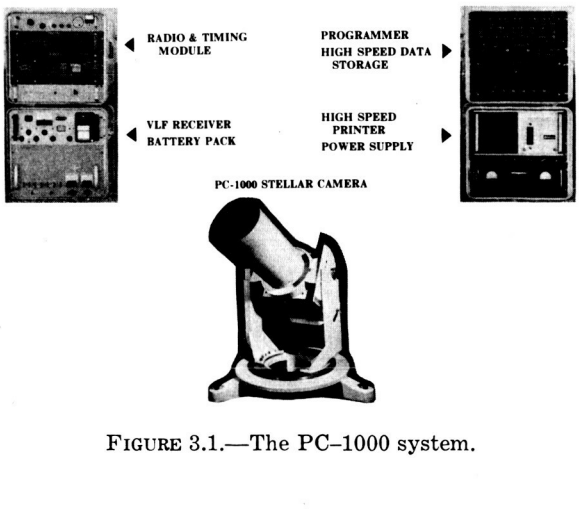

FIGURE 3.1.—The PC–1000 system.

(6) Recording equipment: Time data in binary coded decimal (BCD) format from the timing generator are printed on paper tape and are also stored in the 84-bit data storage system when the shutter is activated. This yields a record of the actual time of operation of the shutter that is not affected by the speed of the printer, and allows actual time differences to ± 10 μsec to be printed every 50 msec.

(7) Operation and calibration: Figure 3.2 shows a star trace (not to scale) and a satellite trace as recorded on a photograph. The first operation (precalibration) begins with the chopping shutter open and the camera's internal shutter operating. Openings and closings of a shutter produce five images on the plate of each star in the field of view. The time for each exposure varies from 1 to 0.1 sec. The intervals between exposures are equal (usually 10 sec). Varying the exposure times makes it possible to select the star images, for each calibration sequence, whose densities appear to equal the densities of the satellite images. This sequence of five exposures is then repeated to end the precalibration operation.

If the satellite contains flashing lights (such as ANNA 1B or GEOS A), the internal shutter is left open during the predicted time of the burst of flashes. The chopping shutter is not used for active satellite observation. If a passive satellite (such as ECHO or PAGEOS) is being observed, the internal shutter is left open and the chopping shutter is operated. Exposures are 0.02 in duration and approximately 0.5 sec apart. Two or three times during the overall exposure period a special exposure, called the signature, is made. Exposure time for the signature varies from 2 to 4 sec, and its purpose is to provide easy identification of time and image.

Postcalibration is a repetition of the precalibration operation. It is done to allow selection of images before and after the main event in order to detect any movement of the camera during the exposure sequence.

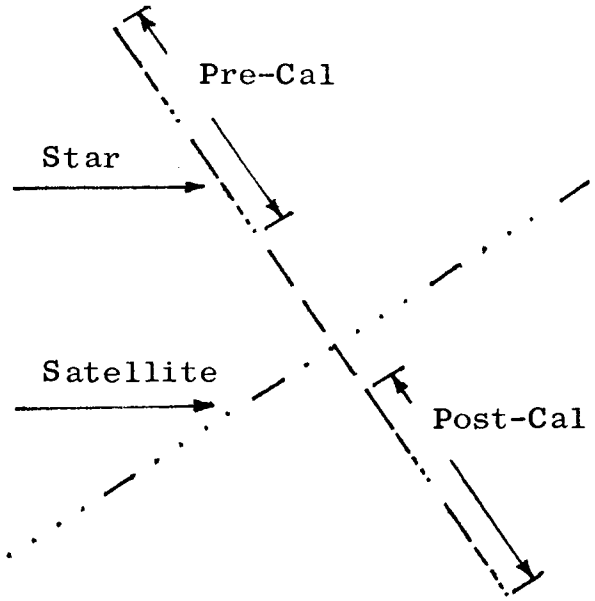

FIGURE 3.2.—Star and satellite trace.

3.2.2 Geodetic SECOR System

(F. W. Rohde)

3.2.2.1 Principles of the Geodetic SECOR System

SECOR consists of four ground stations and an Earth-orbiting satellite. Each ground station contains a transmitter, a dual-frequency receiver, data-processing equipment, and data display and recording equipment. The most important part of the satellite is a transponder, which receives the signals from the ground stations and returns them on two carriers back to the ground stations. Each of the ground stations is electronically identical and is capable of two modes of operation; namely, as master station and as slave station. The master station is in control of the operation and provides, in addition to the ranging signals, commands to the satellite and certain timing signals to the slave stations. The slave stations transmit only ranging signals.

SECOR operates on the principle that an electromagnetic wave propagated through space undergoes a phase shift proportional to the distance traveled. A ground station transmits a phase-modulated signal which is

received by the satelliteborne transponder and returned to the ground. The phase shift experienced by the signal during the round trip from ground to satellite and back to ground is measured by an electronic servo at the ground station, which provides as its output a digitized representation of range.

The modulation of the signal is determined by the requirements for accuracy and unambiguity. For accuracy, since phase is compared, the shortest possible wavelength should be used. For unambiguity the longest wavelength compatible with the required range should be used. Unambiguous and accurate measurements are achieved by modulating with more than one frequency. Four modulation frequencies are included in the signals to provide adequate data on range.

SECOR can be operated in three different modes. If the satellite is visible from all four stations, the stations can interrogate (the process of obtaining distance to the satellite, including also the activation of the transmitter portion of the satellite and the providing of timing signals to the slave stations) the satellite nearly simultaneously. Three ground stations are therefore placed in known locations, and the fourth station is put in an unknown location. Figure 3.3 shows the simultaneous mode of operation. Range measurements from the three known ground stations to the satellite determine the position of the satellite with respect to the known stations. Range measurements from the unknown station to at least three properly spaced positions of the satellite determine the location of the unknown station relative to the known stations. If the unknown station is too far from the known station, observation of the satellite simultaneously by all four ground stations is impossible, and another mode of operation may be used. This mode of operation is called the "orbital mode" and is shown in figure 3.4. Again, three stations placed on known locations simultaneously measure ranges to the satellite. These ranges are used to determine short arcs of the satellite orbits in the region above the three ground stations. The short arcs can be extrapolated into the region above the unknown station. Interrogation of the satellite by this station provides the data for positioning the unknown station with respect to the known stations. If the clocks of the stations can be synchronized, each station can observe independently of the other, which is the third mode of operation.

Signal Structure.—To meet the requirements of both accuracy and range, SECOR incorporates a multiple-frequency ranging technique. The range to the satellite is measured in terms of the wavelengths and fractions thereof of four ranging frequencies, which are listed in table 3.2. The range resolution is the smallest fraction of a ranging frequency that can be measured by

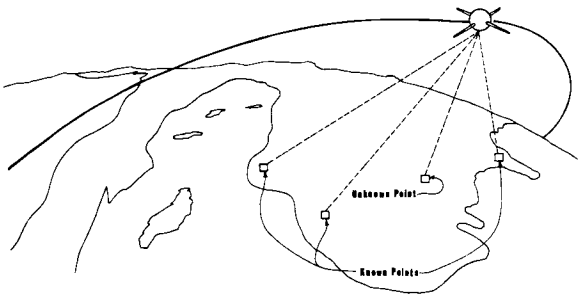

FIGURE 3.3.—Simultaneous mode of operation.

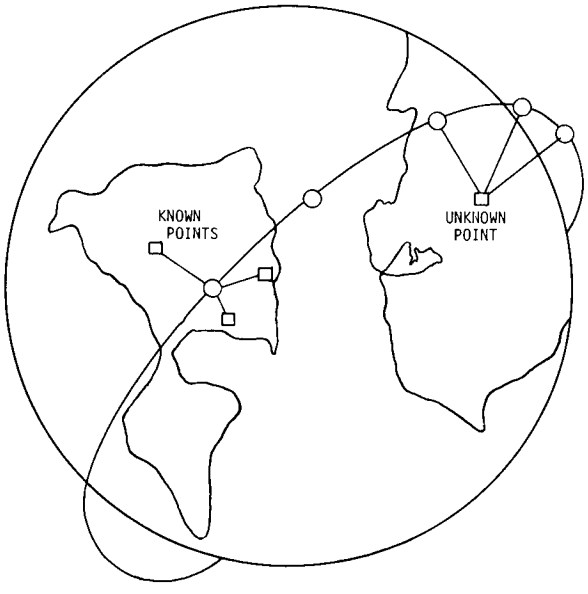

FIGURE 3.4.—Orbital mode of operation.

SECOR. Since the unambiguous range of a ranging wavelength is large in comparison to the resolution of the next larger ranging wavelength, ranges up to 524 288 meters can be measured unambiguously to an accuracy of 0.25 meter. A further extension of range is made possible by measuring the time for a pulse to travel to the satellite and back.

For reason of optimum modulation the ranging frequencies, except for the highest, appear in the signal as difference frequencies of a frequency group between 548 and 585 kHz. The signal of the master station is modulated by more frequencies in addition to the ranging frequencies. One frequency is received only by the satellite and is used to turn the transmitter part of the transponder on and off. The other frequency is transmitted through the satellite to the slave stations and provides timing signals to the slave stations. The ranging frequencies exist as beat frequencies in the modulation of the carrier. Because of the narrow bandwidth, the selection of the carrier frequencies, and the small modulation index, the dispersive distortion of the SECOR signal along its propagation path is smaller than 1 part in 10^6, and the group velocity is practically constant within the bandwidth. Because of the altitude of the satellites used, the signals travel through the ionosphere and experience a delay that must be considered in the calculation of distance. By using two frequencies a correction for the ionospheric error in range is provided. In order to avoid overlapping of arriving signals at the satellites, the ground stations transmit the signals in sequentially arranged pulses.

Interrogation Cycle.—The interrogation cycle is one complete sequence of interrogations of a satellite from four stations. The signal from each station must arrive at the satellite at different times. An overlap, at the satellite, of interrogations from two or more ground stations results in a degradation of range data. The degradation is proportional to the degree of overlap. The interrogation cycle is 50 msec long and divided into four intervals. Each interval consists of a 10-msec signal pulse and a 2.5-msec isolation band. A delay is provided at each station to adjust to time of transmission as required.

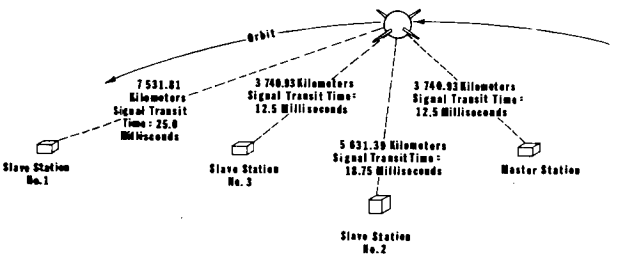

	Interrogation Sequence	Time Of Transmission	Time Of Signal's Arrival At Satellite
Master Station	1	0.0 MS	+12.5 MS
Slave Station 1	2	0.0 MS	+25.0 MS
Slave Station 2	3	+18.75 MS	+37.5 MS
Slave Station 3	4	+37.5 MS	+50.0 MS

FIGURE 3.5.—Example for interrogation cycle.

Figure 3.5 shows an example of interrogation cycle timing. The master station establishes the 0.0 time reference. It is evident from this example that any combination of station transmission times could occur during a pass of the satellite over the SECOR. The operator at a slave station monitors the signals returning from the satellite and adjusts this transmission to remain in the allotted time slot.

3.2.2.2 Ground Station Equipment

Figure 3.6 is a block diagram of a ground station. A SECOR ground station includes

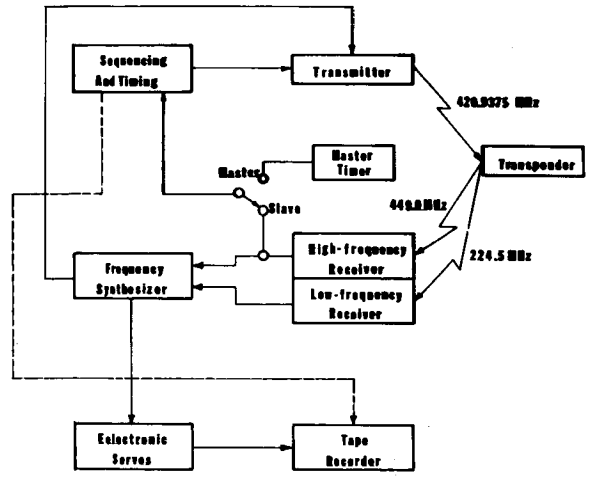

FIGURE 3.6.—Block diagram of ground station.

two major equipments: radio frequency (RF) equipment and data-handling (DH) equipment. These major equipments are housed in two separate shelters, the RF shelter and the DH shelter.

3.2.2.2.1 DESCRIPTION OF THE RF EQUIPMENT

The RF equipment comprises (1) the antennas, (2) a transmitter, (3) a high-frequency receiver, and (4) a low-frequency receiver.

Antennas.—Two 10-foot (3-meter) parabolic antennas serve as the ground terminal of the radio link between the satellite and the ground station. The high-frequency antenna is used for transmitting signals on the 420.9-MHz carrier to the satellite and receiving signals on the 449-MHz carrier from the satellite. The low-frequency antenna receives signals on the 224.5-MHz carrier from the satellite. Both antennas can radiate in two polarizations that are perpendicular to each other. The change from one polarization to the other is achieved by polarization switches. The gain of the high-frequency antenna is about 18 dB and the gain of the low-frequency antenna about 12 dB. The high-frequency antenna is connected to the transmitter and the high-frequency receiver through a diplexer. The diplexer allows simultaneous reception and transmission of two closely spaced frequencies. It prevents transmitted power from entering the receiver and prevents the leakage of received signals into the transmitter circuit. The diplexer is essentially a pair of band-pass filters. In order to track the satellite, the antenna must be pointed in the direction of the satellite. This positioning is accomplished by the antenna servo system, which moves the antennas about the azimuth and elevation axes. The movement of the antennas is manually controlled and visually displayed on a panel.

Transmitter.—The transmitter (fig. 3.7) provides a fixed-frequency, crystal-controlled, phase-modulated source of RF power. The

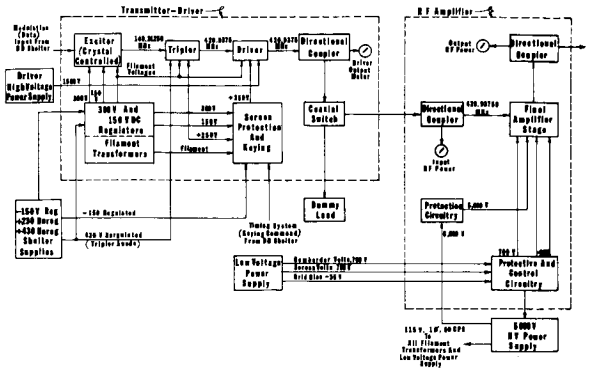

FIGURE 3.7.—Block diagram of transmitter.

basic function of the transmitter is to interrogate the transponder. The transmitter operates in three modes: (1) CW (continuous wave), (2) keyed standby, and (3) keyed transmit.

In the CW and keyed transmit mode the transmitter output is fed through a coaxial switch and diplexer directly to the antenna. In the keyed standby mode the output is switched into a dummy load. In both keyed modes the transmitter output is an RF pulse whose width is determined by the input key pulse. Keying and modulation signals are furnished by the frequency synthesizer in the DH shelter.

The basic RF signal is generated by a 35.07812-MHz, crystal-controlled oscillator in the exciter. This signal is first phase modulated by data input from the DH shelter and then doubled twice in amplifier stages to provide a 140.31250-MHz signal to the tripler. The tripler subsequently supplies 420.9375 MHz (the final output frequency) to the driver, which increases the signal to 100 watts. The directional coupler provides a means of monitoring the driver output power. A coaxial switch routes the output of the driver to the RF amplifier or to a dummy load when the final amplifier is switched off.

The 100 watts of the 420.9375-MHz signal from the driver is fed to the final amplifier, where the power is increased to 2 kW. The output of the final amplifier is passed through a low-pass filter to a coaxial switch. The output is switched to a dummy load when operating in the keyed standby mode or to

the diplexer when operating in CW or keyed transmit mode.

Receivers.—A ground station uses two receivers: a high-frequency (449 MHz) and a low-frequency (224.4 MHz) receiver. The basic function of each receiver is to amplify and demodulate signals from the transponder. Both receivers use carrier phase lock, correlation detection, and modulation feedback techniques. The high-frequency receiver provides ranging data to the data-handling equipment; the low-frequency receiver provides ionospheric correction data. These signals are shifted in phase by an amount proportional to the distance traveled during the round trip between the ground station and the transponder. The high-frequency receiver also detects the timing signal transmitted by the master station and directs this timing signal to the sequencing and timing circuits in the DH shelter.

The high-frequency receiver (fig. 3.8) accepts a phase-modulated 449-MHz carrier from the antenna and demodulates this signal to recover the individual frequencies. The data frequencies are individually filtered and then delivered to the DH shelter.

The incoming 449-MHz signal received by the antenna is amplified by the RF preamplifiers and applied to the first mixer. The amplified 449-MHz signal is heterodyned with a 403-MHz signal from the high-frequency local oscillator, and the 46-MHz difference frequency is selected and amplified by the first IF amplifier. The amplified 46–MHz signal is heterodyned in a second mixer with a 35.5–MHz signal from the second local oscillator. The 10.7–MHz difference frequency is selected and amplified by the second IF amplifier. A portion of the amplified 10.7–MHz signal is fed to the correlation detector, narrow-band IF amplifier, which generates frequency correction and automatic gain control (AGC) voltages. The amplified 10.7–MHz signal is also fed to the correlation detector, wide-band IF amplifier, which amplifies the total modulation content of the received signal.

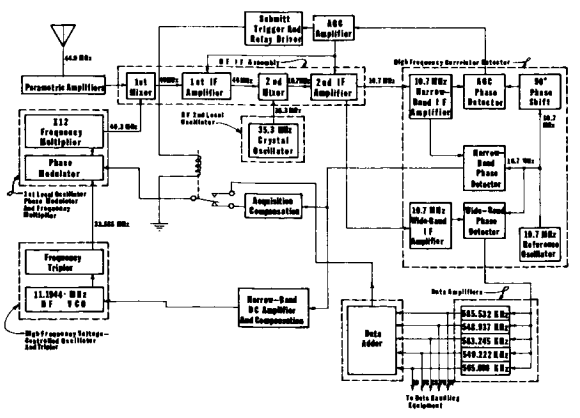

FIGURE 3.8.—Block diagram of high-frequency receiver.

The output of the narrow-band IF amplifier is applied to the narrow-band phase detector along with a 10.7–MHz signal from the reference oscillator. The detector provides an output that is proportional to the phase shift between the two 10.7–MHz signals. This output is used for acquisition compensation and for frequency control of the voltage-controlled oscillator (VCO) to obtain and maintain phase lock to the carrier. The narrow-band IF amplifier also drives an AGC phase detector, which supplies AGC voltage to the IF amplifier. In the AGC phase detector the 10.7–MHz IF signal is phase-compared to the 10.7–MHz reference signal, which is shifted 90° in phase. The resulting output of the detector is a function of RF input level when the carrier is phase-locked.

The output of the wide-band IF amplifier is applied to the correlation detector. This circuit demodulates the 10.7–MHz output of the wide-band amplifier and provides a composite signal consisting of four ranging modulation frequencies and a timing signal. This composite signal is fed to five data amplifiers, where it is separated into four individual data signals and a timing signal. These signals are sent to the DH shelter for processing. They are also fed into a data adder and recombined into a composite signal. This composite signal is used as a negative-feedback signal to phase-modulate the local oscillator carrier. This technique provides excellent phase stability for tracking the received signal.

During a no-signal condition the output of the IF amplifier and the following phase detectors is a noise voltage centered around zero. Since this output controls the VCO frequency, a small but insignificant variation of the VCO frequency around the center frequency will occur.

When a signal is received, the second IF output is a sinusoidal signal, which is phase-compared to the narrow-band reference signal in the narrow-band phase detector. This results in a "beat-note" output: its amplitude is proportional to the RF signal level, and its frequency is equal to the difference between second IF and narrow-band reference frequency. A difference in frequency can be considered as a continuously varying phase difference. The beat-note signal is fed back through a low-pass filter and the acquisition DC amplifier to the phase modulator in the local oscillator. This results in a phase difference and consequently a frequency deviation of the local oscillator signal, which in turn causes the beat-note frequency to vary. At the same time the beat-note is fed back through a narrow-band compensation network and DC amplifier to the VCO but, because of the roll-off characteristics and the narrow bandwidth of this feedback path, no substantial action is obtained in this loop when the beat-note frequency is high. However, the resulting action of the acquisition loop varies this frequency, and when it comes within the capture range of the narrow-band loop, the loop acquires the data RF input because of its higher loop gain characteristics. The beat-note from the narrow-band DC amplifier also causes a deviation of the VCO output frequency around its center frequency. When this deviation matches the deviation of the RF signal, the beat-note frequency becomes zero, and the output of the narrow-band detector is a DC voltage proportional to the phase difference between the second IF signal and the narrow-band reference signal. The receiver is now phase-locked, and any change in the received RF frequency results in a proportional change of the DC control voltage and thus an equal change in the output frequency of the local oscillator.

In summary, during acquisition the output of the narrow-band phase detector is a beat-note because the phase difference between the second IF signal and narrow-band reference signal varies continuously. This output is used for feedback in the acquisition and narrow-band loop to obtain phase lock of the carrier. After the phase lock is obtained, the output of the narrow-band phase detector is a DC voltage that is proportional to the constant phase difference between the second IF signal and the narrow-band reference signal.

Prior to obtaining a phase lock to a received RF signal, the output of the AGC detector is a beat-note. This varying voltage is filtered out by a low-pass filter and does not affect the AGC line. After phase lock is achieved, the output of the AGC detector is a negative DC voltage. The output is proportional not only to the RF level, but also to the phase difference between the second IF signal and the AGC reference signal.

This negative output is amplified and applied as AGC voltage to the IF amplifier. A decrease in its level will result in an increase of IF amplifier gain, which in turn results in an increased negative output. Therefore, change in AGC detector output due to phase variation is counteracted almost completely, and the effective AGC is mainly determined by the RF input level. Owing to the AGC loop action, the second IF output level and thus the narrow-band and wide-band detector output levels are held relatively constant.

A second output of the AGC amplifier is applied to a Schmit trigger and relay driver circuit. When phase lock occurs, the high AGC level triggers the Schmit trigger, and the relay driver actuates a relay. The relay contacts transfer the phase modulator input from the acquisition network to the output of the data adder. Thus the acquisition loop is opened, and the data feedback loop is closed.

During acquisition, the wide-band detector output consists of a wide noise spectrum in addition to the beat-note and the composite

data. Until the second IF carrier is phase-locked to the reference signal by the narrow-band loop, the data are useless for phase comparison in the phase meter. After phase lock is obtained, the output of the wide-band detector consists of noise, a DC voltage, and the composite data signal.

The DC voltage is present because of a small phase difference between the second IF carrier and the wide-band reference signal; it is not used for any control purposes. The composite data signal is the recovered modulation. It comprises five data signals: four ranging modulation frequencies and a timing signal. Each of the five signals is separately selected and amplified in a narrow-band amplifier and then routed to the DH shelter for processing.

The five data signals are also recombined into a composite signal in the data adder. The composite signal is used to phase-modulate the local oscillator after acquisition is accomplished. This feedback effectively flattens out the phase and amplitude responses of the filter and practically eliminates phase shift and amplitude variation due to frequency shift (Doppler) of the data signals. Although a relatively small modulation index (0.7) is used for each modulation frequency in the transmitter output, the fact that five modulation signals are used adds up to a relatively large instantaneous modulation index. Therefore, a larger bandwidth is needed to accommodate the second-order side bands that are significant. The modulation feedback results in a large reduction of the side bands; therefore, the wide-band IF channel has to accommodate only the first-order side bands.

The low-frequency receiver accepts a 224.5–MHz phase-modulated carrier from the antenna and demodulates this signal to recover the data. The demodulated information is sent to the DH equipment as ionospheric correction data for the very fine wavelength.

In the low-frequency receiver, only three data signals are used to phase-modulate the first local oscillator signal, and one data signal is fed to the data-handling equipment. In the high-frequency receiver, all five data signals are used to phase-modulate the first local oscillator signal and are also sent to the data-handling equipment. Except for the aforementioned difference, the acquisitions, narrow-band, and AGC data feedback loops in the low-frequency receiver operate the same as those in the high-frequency receiver.

3.2.2.2.2 DATA-HANDLING EQUIPMENT

(F. W. Rohde, USAETL; E. Cyran, DMA/TC)

The DH equipment provides all ranging and timing signals necessary for the operation of SECOR. Figure 3.9 is a block diagram of the DH equipment. Input and output of the DH equipment are the ranging and timing signals coming from and going to the RF shelter. The DH equipment converts the signals received in analog form to digital form and extracts the range information. The digitized ranges, including ionospheric corrections, time, quality, and identification data, are arranged in a suitable format and recorded on magnetic tape.

Frequency Synthesizer.—The frequency synthesizer generates the following signals.

(1) Basic ranging: These are the frequencies that provide for adequate range resolution and unambiguity. They are called

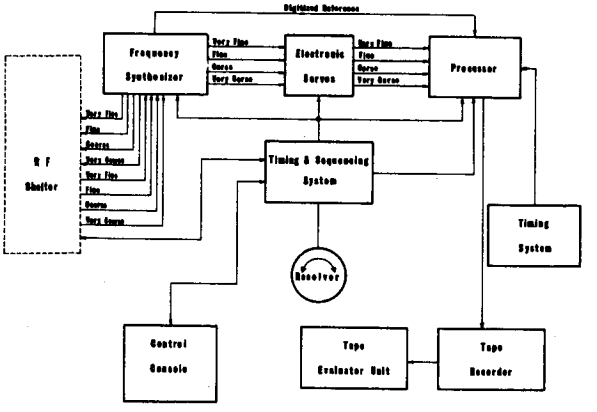

FIGURE 3.9.—Block diagram of DH equipment.

the very fine tone (585 533 kHz), the fine tone (36 596 kHz), the coarse tone (2287 Hz), and the very coarse tone (286 Hz).

(2) Ranging modulation: These are the frequencies that are synthesized from the basic ranging signals. They are the very fine modulation (585.533 kHz), the fine modulation (548.937 kHz), the coarse modulation (583.245 kHz), and the very coarse modulation (549.223 kHz). The ranging modulation signals are used to modulate the carriers of the radio links between ground station and satellite. The basic ranging signals are translated into the ranging modulation signals in order to make the bandwidth of the radio links sufficiently small.

(3) Servo data: Each of the received and demodulated ranging modulations is translated down to 1144 Hz. The four resulting signals of 1144 Hz contain the phase information that is proportional to the range to the satellite. These signals are called the servo data signals.

(4) Servo reference: This frequency (1144 Hz) is used in the translation process for the servo data signals and for the range measurement process.

A stable oscillator operating at 1 171 065.625 Hz drives a binary frequency divider. The output of the frequency divider is the four basic ranging signals and the servo reference signal. In order to maintain high signal-to-noise ratio, the translation processes are achieved by phase-lock techniques. Since all signals generated by the frequency synthesizer are derived from the same source, the signals are coherent.

The stable oscillator also drives the reference slave counter. This counter provides the processor with a digital signal corresponding to the count contained in the frequency divider. The count in the frequency divider is representative of the phase of the range modulation at the time of transmission. Control gates permit the reference slave counter to be used as binary counter or as shift register.

Electronic Servos.—The electronic servos convert the servo data signals into a digital representation of each cycle. The phase of the signal is therefore available as a binary word which is further processed by the processor. Each electronic servo comprises a phase-locked mixer loop and a slave counter. The servo data signal is applied to a phase detector. The 1144–Hz reference signal to the phase detector is derived from a VCO by means of a frequency divider, which functions also as a loop counter. The VCO drives a slave counter in parallel with the loop counter. If the input signals to the phase detector have the same phase, the output of the phase detector is zero. As the phase of the servo data signal changes with respect to the reference signal, the phase detector develops a DC voltage output which is proportional to the phase difference. This voltage is amplified and applied to the VCO. The oscillator adjusts its phase in such a manner as to reduce the phase detector to a minimum. Loop counters and slave counters continuously indicate the phases of the servo data signals and by them the range to the satellite. A simultaneous stopping of all counters (very fine, fine, coarse, very coarse, very fine ionospheric correction, and reference slave) then indicates the range at that particular instant of time. This indication is a set of binary numbers representing the count contained by the counter when they were stopped. The true range is computed from this set of binary numbers.

Timing and Sequencing System.—Sequential interrogation of the satellite requires that transmission from each ground station be received by the satellite at a known and separate portion of the interrogation cycle. The allocation of portions of the interrogation cycle to the various ground stations is based on a calculated optimum sequence dictated by the orbit of the satellite. Each interrogation cycle is started by a timing or synchronization signal provided by the ground station designated the master station. The slave stations use this signal as a time reference to control their transmission.

The timing and sequencing system performs the following functions: (1) initiation

of master timing signal during master station operation, (2) synchronization of the station to the master timing signal, (3) control of transmissions, (4) control of the processor, and (5) oscillographic presentation of the interrogation cycle.

The extended range portion of this system is used to resolve any ambiguities that might occur in the measurement of range by the very coarse channel.

The master identification burst is detected by the amplitude modulation detector. The resulting envelope has a repetition rate of 20 times per second. The phase of this pulsed signal is compared with the phase of the divided-down signal from the voltage-controlled oscillator in the phase detector. If there is a phase difference, the voltage-controlled oscillator will adjust to minimize this difference. Range is measured by starting the counter with the transmitter key pulse and stopping it with the received data burst. This range count is then sent to the processor.

Timing System.—Each DH originally had a digital clock that provided time information for each record of range and station-constant data. The information included hours, minutes, seconds, and milliseconds. Initially, stable crystal oscillators were used along with WWV radio receivers to synchronize the clock. Later, rubidium oscillators replaced the crystal oscillators in each station.

3.2.2.3 Satellites

(Robert H. Nichols, USAETL)

3.2.2.3.1 DESIGN

The first SECOR satellite (fig. 3.10) was a reflecting ball 51 cm in diameter. Its surface was made of polished aluminum with a thin layer of silicon monoxide; this composition helped to regulate internal temperatures. The satellite contained six circular solar-cell panels, 20 cm in diameter, and nine spring-loaded dipole antennas: four antennas for 449–MHz signals, four antennas for 224.5–MHz signals, and a single antenna attached

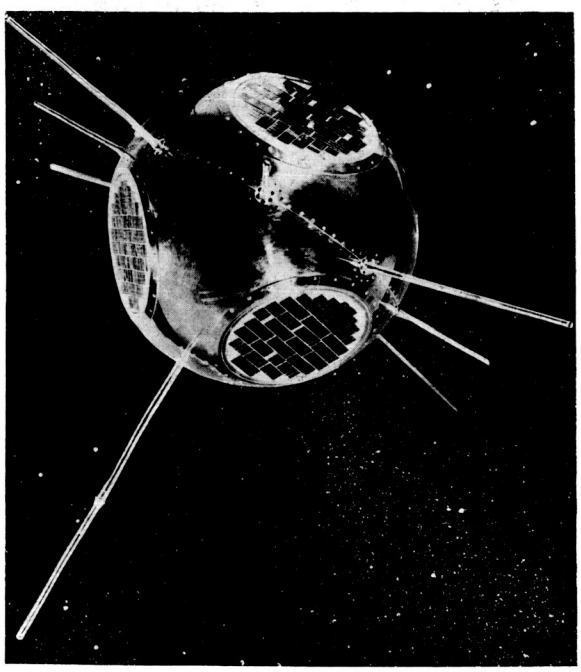

FIGURE 3.10.—First SECOR satellite.

at the apex of the satellite for telemetry at 136 MHz. The satellites averaged 17 kg in weight. Most of this weight was in a power system built to receive continuously and to transmit for at least 45 to 60 min per day.

The second SECOR satellite (fig. 3.11) was built in the shape of a cube, measuring $23 \times 28 \times 33$ cm and weighing nearly 18 kg. The size and shape of this satellite made it easily adaptable to be a secondary payload on many rockets. The cubical satellite carried the same transponder as the spherical satellite. The history of SECOR satellites is summarized in table 3.3.

3.2.2.3.2 OPERATION

The transponder on the satellite was normally in a standby condition (minimum circuitry energized in the receiver) to conserve power. Upon reception of a command tone, "select call," the transponder became fully activated, and electronic switching circuits applied power to all remaining electronics in the satellite.

The transponder received and demodulated the signals of the ground station and retrans-

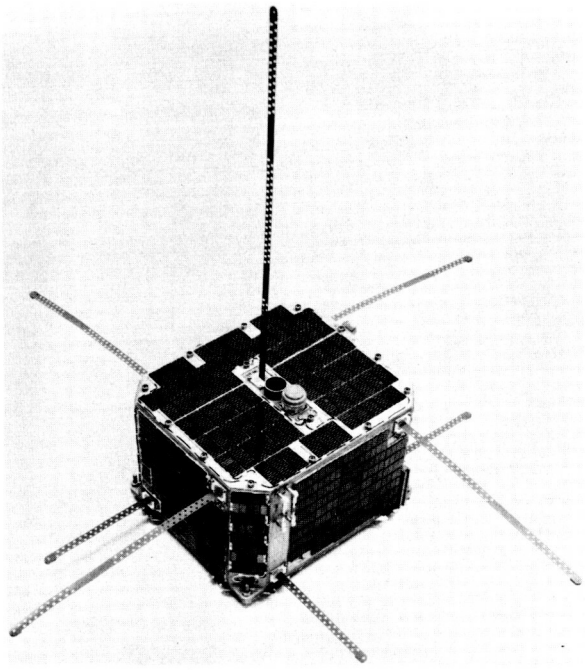

FIGURE 3.11.—Second SECOR satellite.

mitted the ranging and timing subcarriers on two coherently related frequencies, 449 and 224.5 MHz. The lower frequency was used for correcting for ionospheric refraction. Four multiple-frequency ranging tones of overlapping wavelength values were used for increased accuracy (table 3.1).

The satellite remained active throughout each pass (12 to 15 min) until the strength of the "select call" faded. Eight seconds thereafter the satellite returned to its standby mode of operation.

3.2.2.3.3 EQUIPMENT IN THE SATELLITE

Transponder.—The transponder consisted primarily of a receiver and a transmitter. Normally in a standby condition, the dual-conversion receiver accepted a 420.9375–MHz carrier modulated with a "select call" tone from the ground station. The signal passed through an antenna and a diplexer to an RF amplifier. From there it was fed into a mixer, which was also being fed by a signal from a standby local oscillator. These two signals were mixed, and the resultant passed directly into an AGC-controlled IF amplifier. The detected signal went to a data amplifier, where it was routed through a "select call" circuit to a switch that turned on the power to the remainder of the transponder circuitry. Two command signals were routed to the telemetry portion of the circuitry. Other modulation signals from the ground station (four subcarrier frequencies for range measuring and a timing signal) followed the same path, but the data amplifier routed them to the transmitter section of the transponder. They were fed into the phase modulator and multiplier circuit and from there to an exciter. The exciter doubled the frequency, yielding 224.5 MHz. This signal was routed to an antenna and used at the ground station as an offset frequency for ionospheric refraction correction.

The 224.5–MHz signal was also doubled to 449 MHz and routed into diplexer network associated with an antenna. A small portion of the transmitted output was tapped off and used as local oscillator voltage for the transponder receiver. Thus the transponder was caused to operate as a negative feedback amplifier for the modulation signals. The feedback effect stabilized the phase relationship between the received and retransmitted modulation signals.

A phase-lock loop was used to provide correlation detection, allowing automatic acquisition and phase tracking at signal levels of -120 dBm or lower, depending on the modulation index used. Also, the phase-lock feature allowed easy adaptation of the transponder to coherent-carrier systems.

The earliest transponder had a power output of 1 watt. Later, transistorized versions were capable of putting out 4 watts with modulation indices of 0.7 to 2.4. All parameters were thoroughly tested before launch.

There were several variations in physical appearance of the different transponders. Early vacuum-tube models were packaged in three individual units: transmitter, receiver, and power converter. Later models were condensed into one unit. All transponders weighed approximately the same: 3 to 5 kg.

Antennas.—The spherical SECOR satellites used aluminum rods approximately 1.27 cm in diameter and cut to match frequencies of 224, 449, and 136 MHz. The nine antennas (four at 224 MHz, four at 449 MHz, and the single telemetry antenna for 136 MHz) were simple dipoles having no gain and producing regularly shaped "donut" patterns. They were spring-loaded and collapsed about the satellite, erecting automatically upon separation of the spacecraft from the rocket.

The antennas on the cubical SECOR satellite were identical in electrical characteristics to those on the spherical satellites but radically different in physical construction. Elements of the antennas were fabricated of hardened, tempered steel strips 1.27 cm wide by 0.025 cm thick and formed to a 1.9–cm radius. Each antenna was plated with silver and then coated with Teflon. Numerous perforations were made throughout the antenna length to minimize the effect of shadows cast on the solar cell panels.

Orientation Device.—The device used in the spherical satellite for stabilization consisted of a bar magnet, 7.6 cm long and 1.27 cm in diameter, and two damping rods, 0.1651 cm in diameter. Each magnet had a magnetic moment of greater than 6000 unit-pole/cm. A slightly larger magnet was provided for the cubical satellite.

3.2.3 AFCRL Geodetic Laser System

(Robert L. Iliff, AFCRL)

3.2.3.1 Introduction

This system, designed and developed for measuring distances and direction to a satellite, is based on the use of two ruby lasers and a camera. It obtains ranges from station to satellite with a Q-switched laser and determines directions to the satellite by photographing the satellite against a stellar background with a PC–1000 camera using pulses from a high-energy, normal-mode laser for illumination. The two lasers and the ranging receiver are shown in figure 3.12, and the PC–1000 camera is shown in figure 3.1.

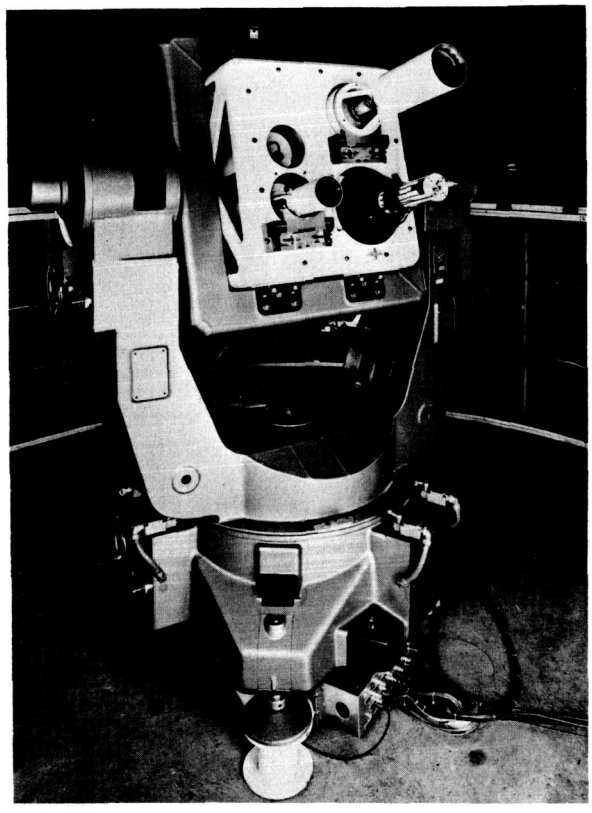

FIGURE 3.12.—AFCRL geodetic laser: Range laser at lower left, Pockels-cell high-voltage supply above it, receiver at lower right, and photographic laser at upper right.

3.2.3.2 Description of System

The characteristics of the two lasers are summarized in table 3.4.

(1) Photographic laser: The "photographic" ruby-laser is capable of about 500 J output but is generally operated at about 250 J to give longer life to the components. The normal-mode pulse of 2–msec duration is collimated to a width at half-power of 2 mrad. The two flash lamps are water-cooled and the 300-mm-long by 19-mm-diameter ruby is cooled with liquid nitrogen to an operating temperature of about 150 K (λ= 6936Å) to avoid excessive atmospheric absorption. The cavity is evacuated to 1 mm Hg or less to limit convection losses to the metal housing and to prevent freezing of the water. The maximum firing rate is once

every 3 sec because of the time needed to recharge the capacitors. The banks of capacitors are capable of storing 60 000 J total, 30 000 J for each lamp.

(2) Ranging laser: Ranges are determined by using pulses from a Q-switched laser capable of emitting bursts of 10 pulses per pumping period.

(3) Receiver (telescope): The pulses reflected from the satellite are collected by a 22-cm aperture, f/2 telescope, focused through a field stop at the prime focus; the beam is collimated, passed through a temperature-controlled, 5-Å interference filter, and then converted to electrical pulses by an RCA 4459 photomultiplier. The field of view is 1.7 mrad for operation at night and 1.1 mrad for operation in daytime.

(4) Timing subsystem: Time is kept by a cesium-controlled clock whose output is compared continuously with LORAN-C signals. The combination of delay time in propagation and electronics is determined by comparison with U.S. Naval Observatory and traveling atomic clocks. The precision of the calibration is about 1 μsec, and the accuracy (as compared to LORAN-C) is of the same order. The travel time counter uses a separate crystal oscillator, which is calibrated against the cesium clock. The drift is kept below 1 part in 10^9, which corresponds to an error of less than 3 mm for a 3-mm range.

(5) Retroreflectors: The targets of interest with a laser system are those satellites equipped with retroreflectors. There are six satellites that can be observed from the AFCRL station at 42° latitude. These are BE-B, BE-C, GEOS-1, GEOS-2, D1-C, and D1-D. The orbital characteristics of these satellites are given in chapter 2; the characteristics of the retroreflectors are given in chapter 1 and in chapter 2.

3.2.3.3 Operation

The PC-1000 camera with its 10° field of view is used to photograph reflections from the satellite. Four or five images from the satellites are obtained with the camera oriented in one direction; the camera is swung to another position and another set of images recorded on the same pass. Ranges, of course, are measured during the entire pass.

3.2.3.4 Precision

The change in distance to the satellite during the 400- to 500-μsec time for observation of the 10-pulse burst was observed. The standard deviation of the average range was found to be 45 cm.

No degradation in the range rms error was observed during daylight operations. For use of this system in daylight, the receiver field of view must be reduced to limit background noise, and the atmosphere must be more haze-free than it would be for nighttime operation. This requirement is made necessary by the scattering of sunlight into the receiver.

The multipulse approach to ranging reduces noise in the system by approximately $1/\sqrt{n}$ as compared to a system operating with single pulses. The accuracy of the present system is estimated to be about 1 meter.

3.2.4 DOD (Navy) Doppler

The Doppler system developed by DOD for the Navy TRANSIT program is described in chapter 2.

3.2.5 Flashing Beacons

(Theodore E. Wirtanen, AFCRL)

3.2.5.1 Beacon on ANNA 1B (1962 $\beta\mu$)

The flashing beacon designed for the ANNA 1B satellite (ch. 2) was the first beacon designed and flown specifically for geodetic operations. Several prototypes were developed to study light intensity and light distribution patterns, but the configuration eventually adapted to ANNA consisted of four linear flashtubes (EG&G, Inc., Type XEX-40). These four tubes were mounted in pairs on each side of the equatorial band of solar cells on the satellite (fig. 2.2, ch. 2). Each flashtube was mounted over a flat re-

flector that was canted outward at an angle of 5° with the equatorial plane of the satellite in order to eliminate obstruction of the emitted light by the polar areas of the spacecraft.

Lamps on each side of the band of solar cells were necessary because ANNA was magnetically stabilized; hence one pole faced the earth when in the northern hemisphere and the other pole faced the earth when in the southern hemisphere.

The flashing beacons were designed to give their greatest amount of light energy at approximately 50°–60° off the mechanical axis of the satellite (fig. 3.13). This arrangement provided higher intensity for the more distant observers. Light from the flashtube had a uniform distribution of energy at wavelengths from 4000 out to 8500 Å; 40 percent of the total output energy was at wavelengths longer than 8500 Å and 20 percent of the energy was at wavelengths shorter than 4000 Å. This made the light somewhat comparable to sunlight, with a substantial amount in the blue to make it suitable for photography against a stellar background.

The entire beacon assembly on ANNA 1B consisted of flashtube-reflector assemblies, a trigger circuit, a capacitor bank, a converter circuit, a sequence controller, a power relay, and a battery (ch. 2). Each flashtube-reflector assembly consisted of an XFX–40 linear tube and flat reflector. The flashtubes were 15.24 cm long. The flat reflectors consisted of rectangular, quartz, second-surface mirrors. A summary of the flashing beacon characteristics is given in table 3.5.

3.2.5.2 Triggering

The trigger circuit started the ionization of the xenon within the flashtubes causing the main electrical discharge to occur and a flash of light to be given off. It consisted of solid-state switch, an energy-storing coupling capacitor, a pulse transformer, and associated components. It was activated by a signal from a sequence controller and coupled the energy stored in the capacitor to the pulse

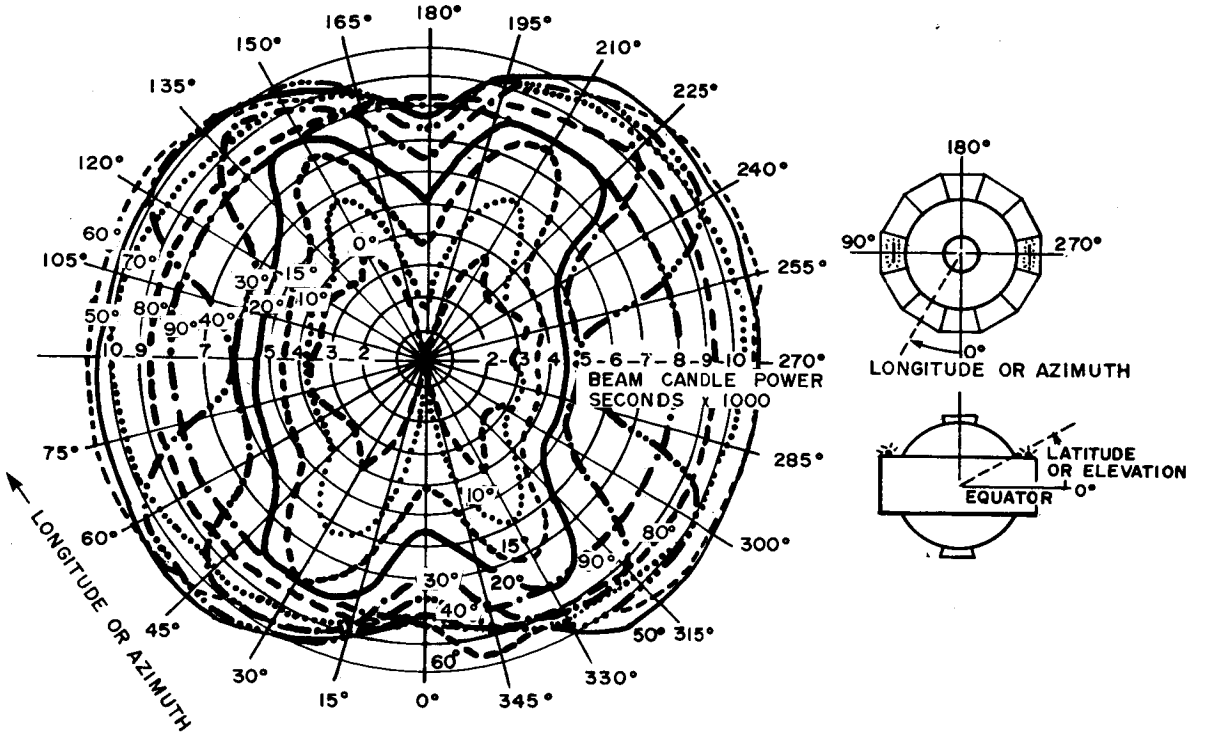

FIGURE 3.13.—Optical beam pattern of ANNA 1B.

transformer primary. The pulse transformer applied a high-voltage pulse to the flashtube to cause ionization of the gas inside the tube. Silicon-controlled rectifiers were used as the switching devices for the trigger circuit.

3.2.5.3 Beacons on GEOS–A and GEOS–B

The beacon on GEOS was made up of four helical xenon flashtubes. The lamps operated from a common battery, but were otherwise independent, with separate banks of capacitors. The reflectors were spun aluminum with foam backing. Because GEOS–A was gravity-gradient-stabilized, the four lamps were all mounted on that surface of the satellite facing the earth.

The pattern of the beam from each lamp was symmetric about an axis parallel to the vertical axis of the spacecraft. Figure 3.14 shows a pattern from measurements on the lamp-reflector combination; the luminous intensity produced at the camera is shown in figure 3.15.

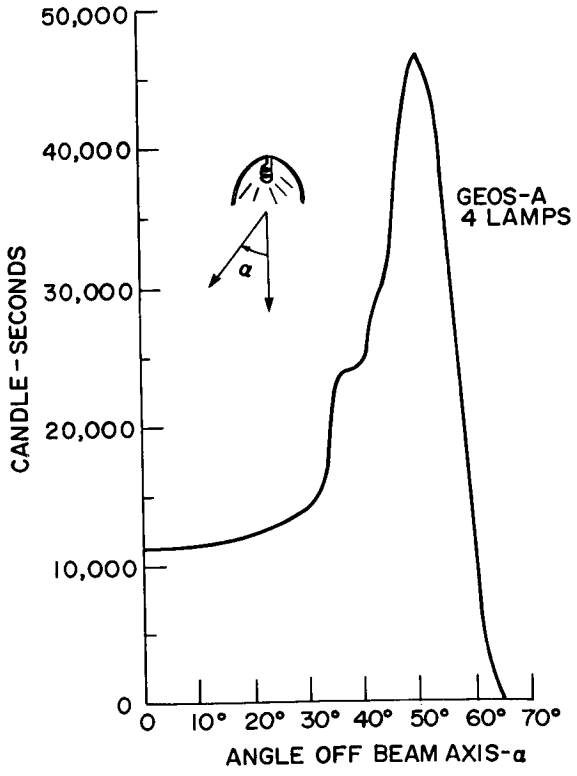

FIGURE 3.14.—Output of four lamps flashed simultaneously (based on measurements of prototype lamp reflector).

The xenon flashtubes were made to flash at a specified time with very high precision. The lamps operated in sequences of five or seven flashes, any specified combination of one to four lamps being flashed simultaneously in each sequence. The first flash of each sequence was started at an integral minute (UT ±0.4 msec relative to WWV), and the interval between successive flashes in each sequence was 4 sec ±0.4 msec. The satellite memory was used to store those times at which the flashing sequences were to occur.

3.3 DATA

The results of DOD's geodetic activities in the NGSP were obtained by several different organizations. The data used in getting these results are summarized in this section and are connected to the results (sec. 3.5) as follows.

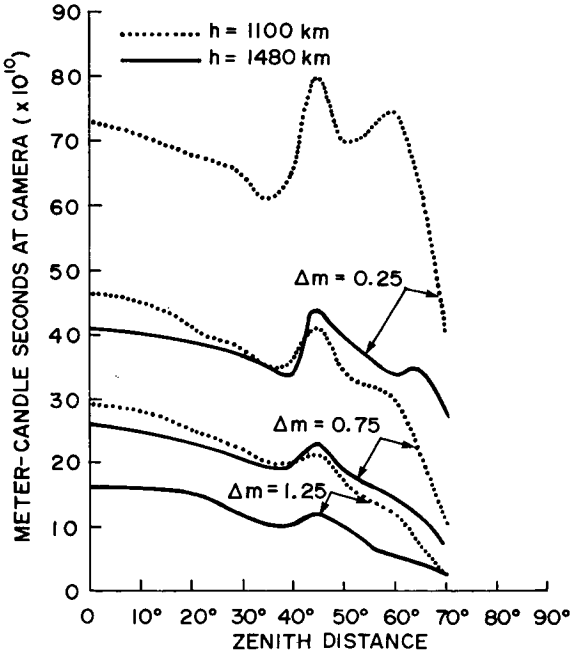

FIGURE 3.15.—Illumination at camera versus zenith distance using four lamps at those levels of atmospheric extinction and altitudes of 1100 (dotted curve) and 1480 (solid curve) kilometers.

The results given in section 3.5.1.1 (coordinates of stations in the western hemisphere; DMAAC) were derived by means of the observational data summarized in section 3.3.1. Results given in section 3.5.1.2 (coordinates of stations in North America, the West Indies, and Bermuda; AFCRL) used observational data summarized in section 3.3.2. Results given (sec. 3.5.1.3) for the SECOR Equatorial Belt Project (DMATC) depend on observational data summarized in section 3.3.3. Results given (sec. 3.5.1.4) for the TRANET Global Network used the data summarized in section 3.3.4. The fundamental or accepted coordinates of these points in their appropriate datums are given in chapter 1. The preprocessing techniques used on these data are described in section 3.3.5.

Satellites are described in chapter 2 and chapter 5. Their approximate orbital elements are given in chapter 1, table 1.10.

3.3.1 Data Used in Solution for Coordinates in Western Hemisphere

Table 3.6 lists the PC–1000 and BC–4 camera stations that contributed data to the four projects whose results are given in section 3.5.1.1. The number of simultaneous events used from each of the satellites and the period of observation are tabulated in columns 5 and 6.

A typical photograph is shown in figure 3.16. This is a photograph of the flashing lights of the ANNA 1B. The images are at the centers of the heavy cricles.

3.3.2 Data Used in the Solution for Coordinates in North America, the West Indies, and Bermuda

The observational data used in getting the results shown in section 3.5.1.2 are summarized in table 3.7. The satellites used and their approximate orbital characteristics are described in chapter 1, chapter 2, chapter 3, and chapter 5. Section 3.3.5.3 describes the preprocessing applied to the data from laser DME, section 3.3.5.1 that applied to data from the PC–1000, and section 3.3.5.2 that applied to data from SECOR. The stations involved are shown in figure 3.17. Their coordinates are given in section 3.1.3.1, table 3.3. The constraints applied between stations are given in figure 3.18.

3.3.3 Data for SECOR Equatorial Network

The SECOR data and the global stations making up the SECOR Equatorial Network are summarized in table 3.8; the distribution of stations is shown in figure 3.19. The constraints imposed on the station positions are given in tables 3.20a and 3.20b of section 3.5.1.3.

3.3.4 Doppler Data

3.3.4.1 Satellites

The first geodetic results based on Doppler satellite observations were obtained by using data from the TRANSIT 1B (1960 $\alpha 2$) and TRANSIT 2A (1960 $\eta 1$) satellites. Analysis of these data yielded determinations of the third zonal coefficient (Cohen and Anderle, 1960) and the second and fourth zonal coefficients. However, the perigee heights of these satellites were too low for the observations to be of use in current geodetic analyses. Current analyses of Doppler data are based on observations of the TRANSIT 4A and 4B satellites (1961 $o1$ and 1961 $\alpha\eta 1$), the ANNA 1B geodetic satellite (1962 $\beta\mu 1$), the Beacon Explorer satellites B and C (1964–64A and 1965–32A), GEOS A and B satellites (1965–89A and 1968–002A), the DIADEME 1 and DIADEME 2 satellites (1967–11D and 1967–14A), the TIMATION II satellite (1969–082B), and a number of Navy navigation satellites, such as 1967–92A. Each of these satellites radiated at a pair of frequencies synthesized from one stable oscillator to permit correction for first-order ionospheric effects on the Doppler signal. The navigation satellites radiated at approximately 150 and 400 MHz, while the other satellites

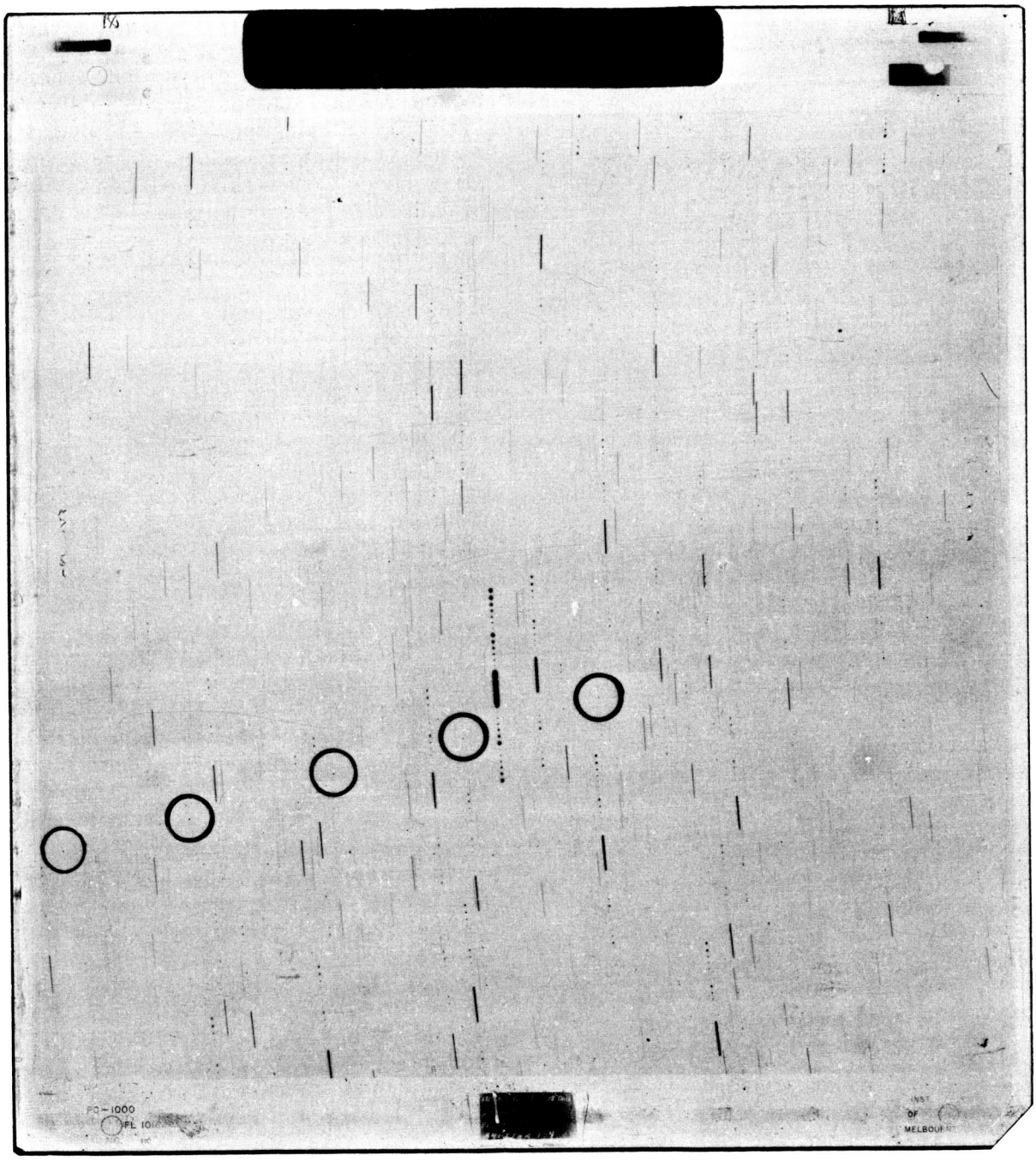

FIGURE 3.16.—Photograph of the ANNA 1B flashing light taken by PC–1000 camera.

radiated either at similar frequencies or at 162 and 324 MHz. The lifetime of the electronics system in the satellites varied from a few weeks to over 5 years. Oribtal data for the satellites are given in table 3.9.

3.3.4.2 Ground Stations

Only six stations were operating in 1960, when the first geodetic results were obtained by analysis of Doppler observations of arti-

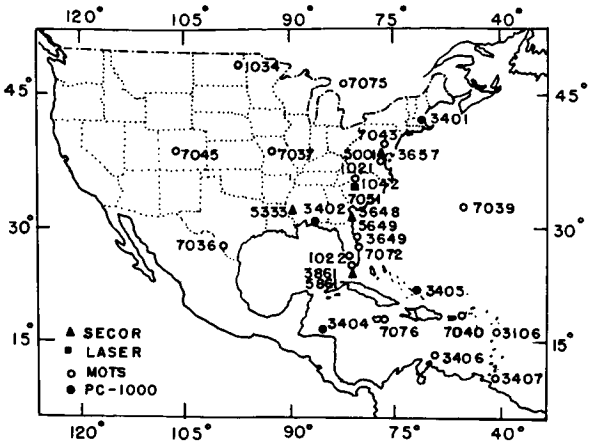

FIGURE 3.17.—Tracking network.

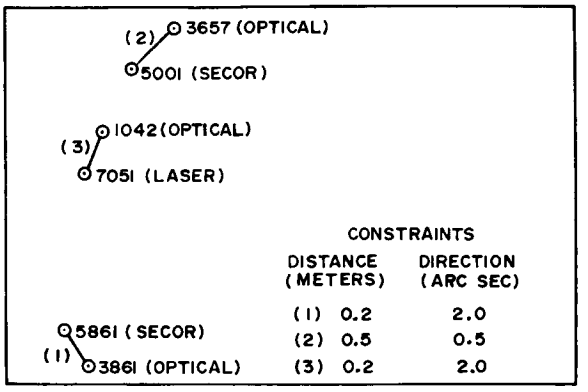

FIGURE 3.18.—Constraints between stations.

ficial Earth-satellites. By 1972, 19 Doppler stations were contributing data used in geodetic analyses including 11 stations operated by the Defense Mapping Agency, 4 stations in the Navy Navigation Satellite System, and 4 other cooperating stations. Stations operating during various time periods are shown in figure 3.20. Station antennas were moved at the times shown by the arrows on the figure. The changes in position were generally less than a few meters except that the movement from station 106 to 16 was 20 km and the change from station 10 to 100 was 200 km. The stations shown in figure 3.20 are termed "permanent" stations; mobile equipment has been placed at over 200 stations for short periods of time. Coordinates of stations involved in the solution given in section 3.5.1.4 are given in table 3.10. The distribution of these 39 stations is shown in figure 3.21.

The stations originally recorded observations at two coherent frequencies which were combined in a large-scale digital computer to obtain a correction for first-order ionospheric refraction effects. The stations were soon modified so that they produced data that had been corrected for first-order ionospheric

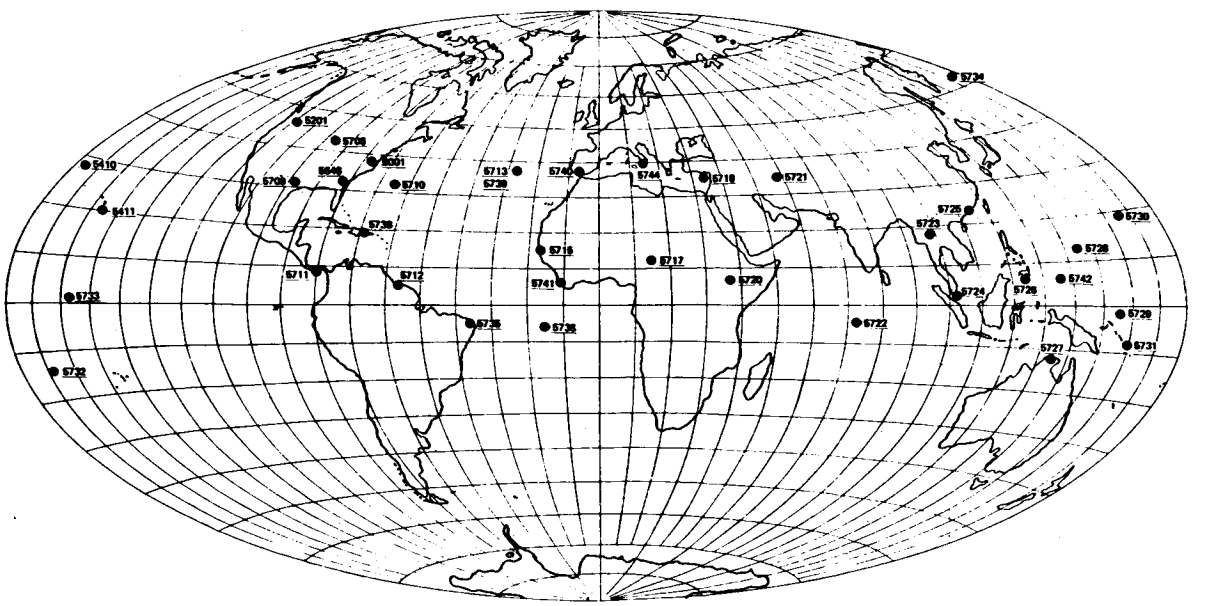

FIGURE 3.19.—SECOR equatorial networks (SEN).

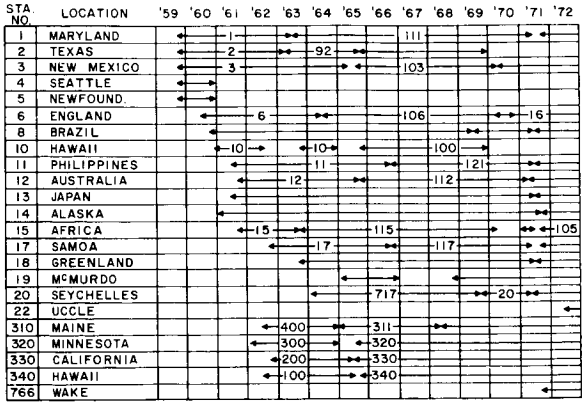

FIGURE 3.20.—Periods of operation of Doppler stations.

refraction by analog combination of the two frequencies at the station site.

Most geodetic results of current interest derived from Doppler observations were based on observations made with equipment which produces data in one of three forms.

(1) Sampled Doppler data: Most of the NGSP results were based on measurements of time required to count a present number of beat cycles between an analog combination of received frequencies and a frequency generated by a ground oscillator. The measurements were typically made every 4 sec, and the number of cycles to be counted was set so that the count would be completed in just under 1 sec.

(2) Continuous-count integrated Doppler (CCID) data: In 1971 the Doppler stations, except those in the Navy Navigation Satellite System, were modified so that they would operate more automatically. As part of the modification, the counting device was modified so that the time for the completion of one count is now identical to the time for the start of the next count. For the modified equipment the number of cycles to be counted is usually set so that the count lasts 10 to 20 sec.

(3) GEOCEIVER data: Production of GEOCEIVER equipment commenced in 1971. This equipment produces a beat-cycle count at fixed time intervals. For Navy navigation satellites, the time intervals are approximately 30 sec long as defined by time ticks generated by the satellite. For other satellites the GEOCEIVER clock terminates the count at 30-sec intervals. The GEOCEIVER equipment records the refraction correction and the count at the high frequency so that the ionospheric refraction correction is made digitally.

Preprocessing techniques are described in section 3.3.5.4.

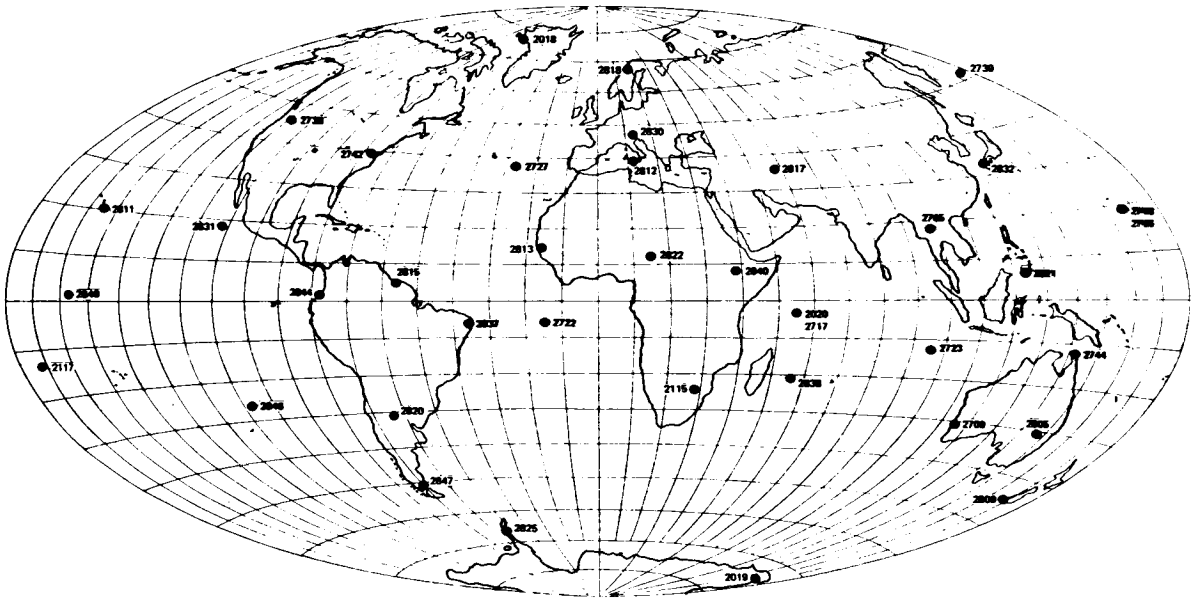

FIGURE 3.21.—Doppler station locations.

3.3.5 Preprocessing of Data

3.3.5.1 PC–1000 Camera

(Donovan N. Huber, DMA/AC)

3.3.5.1.1 PLATE PREPARATION AND MEASUREMENTS

The plate reduction process begins with the selection of four of the 25 to 30 reference stars measured and used in the final adjustment. These four stars (employed for automatic star-identification purposes) as well as the remaining reference stars are selected so that they form an even distribution around the satellite images and are selected also for sharpness of image, size, and clarity of image. All images of reference stars are marked and numbered for the plate mensuration phase. A generalized flow diagram of the plate reduction procedure as employed by DMAAC is contained in figure 3.22 at the end of this section.

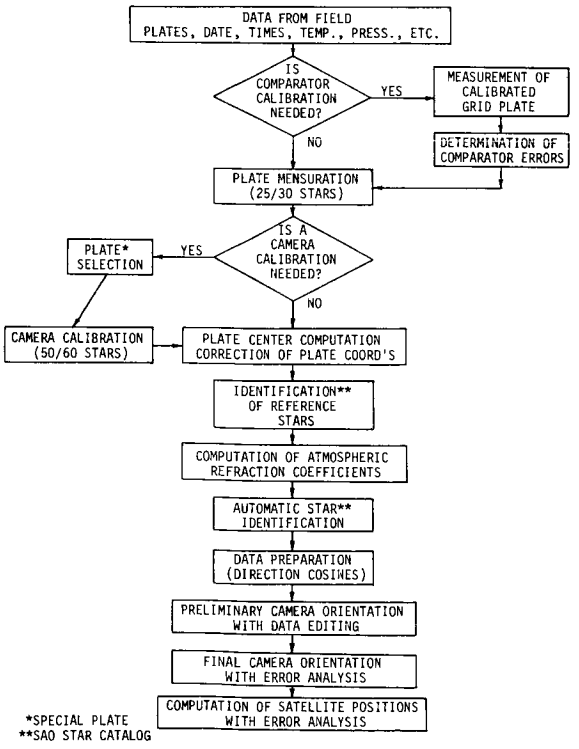

FIGURE 3.22.—Generalized flow diagram of DMA photographic plate reduction.

Plate measurement involves the precise determination of distances of the centers of density of satellites and stellar images from an arbitrary origin. The measurements on the PC–1000 plates are made with a semiautomatic comparator. Since the center of density of each image is determined electronically by the comparator, the error arising from manual setting is avoided, and the need for repeated settings is eliminated. The ability of the comparator to repeat readings was tested and the precision found to be 1 μm.

3.3.5.1.2 CALIBRATION OF COMPARATOR

The stellar comparator is calibrated periodically to ensure continued integrity of measured plate coordinates. A least-squares adjustment is made between coordinates of 49 points (X_c, Y_c) of a calibrated grid and the actual measurements (X_m, Y_m) of the same points. The result of this adjustment produces the amount of rotation (Φ) and translation (X_p, Y_p), a scale factor (K_x, K_y) for each coordinate axis, the orthogonal deviation (ϵ) of the comparator axes, and the standard deviation in the plate measurements. The equations used that relate these quantities are

$$X_c = X_p + K_x X_m \cos \Phi + K_y Y_m \cos (\epsilon + \Phi)$$

$$Y_c = Y_p + K_x X_m \sin \Phi + K_y Y_m \sin (\epsilon + \Phi)$$

where X_c, Y_c, X_m, Y_m are known quantities and X_p, Y_p, Φ, ϵ, K_x, K_y are the unknowns sought and used subsequently to correct the measured plate coordinates.

3.3.5.1.3 CORRECTION FOR ATMOSPHERIC REFRACTION

From observed barometric pressure and temperature at the camera site and an abbreviated version of Garfinkel's (1967) atmospheric table, an approximation to the atmospheric refraction is computed. This approximation is used to determine the correction δ_ξ (to be applied to the star images

for computing the initial camera orientation) and is obtained from

$$\delta_\zeta = \eta_1 \tan\theta + \eta_2 \tan^3\theta + \eta_3 \tan^5\theta + \eta_4 \tan^7\theta$$

where

$$\tan\theta = (1+\gamma_0^2 \cot^2\zeta)^{1/2} - \gamma_0 \cot\zeta$$

γ_0 is computed from the temperature at the camera site; η_1, η_2, η_3, η_4 are the refraction coefficients interpolated from Garfinkel's table; and ζ is the observed zenith distance.

3.3.5.1.4 CORRECTED PLATE COORDINATES

The plate coordinates resulting from section 3.3.5.1.2 are next referred to the plate center. Coordinates for the plate center (x^0, y^0) are computed by determining the point of intersection of the two lines connecting the diagonally opposite fiducial marks (x_i, y_i) $i=$ 1, 2, 3, 4. The quantities x^0, y^0 are obtained from

$$x^0 = (P_1R_2 - R_1P_2)/(P_2Q_1 - P_1Q_2)$$
$$y^0 = (x^0\, Q_1/P_1) + (R_1/P_1)$$

where

$$P_1 = x_3 - x_1 \qquad P_2 = x_4 - x_2$$
$$Q_1 = y_3 - y_1 \qquad Q_2 = y_4 - y_2$$
$$R_1 = y_1 P_1 - x_1 Q_1 \qquad R_2 = y_2 P_2 - x_2 Q_2$$

The plate coordinates are now adjusted for radial and decentering distortion of the camera lens. These corrections are determined according to adjustments (sec. 3.3.5.1.10) which are performed at least every 30 days or when the camera system is moved from one site to another. The corrected plate coordinates (x, y) now become

$$x = \overline{x} + \delta x + \Delta x$$
$$y = \overline{y} + \delta y + \Delta y$$

where $\overline{x}$, $\overline{y}$ are coordinates corrected for comparator errors and referred to plate center, δx, δy are corrections for radial distortion in x and y, and Δx, Δy are corrections for decentering distortion in x and y. The apparent local sidereal time (ALST) for each exposure is also computed at this time for use in subsequent computations.

3.3.5.1.5 AUTOMATIC IDENTIFICATION OF STARS

The corrected plate coordinates for the four manually identified stars, along with their apparent positions, are used to determine an approximate exterior camera orientation ν', ω', κ'. The corrected plate coordinates for all other selected star images are then converted to their corresponding right ascension (α) and declination (δ) on the basis of this preliminary orientation. The α and δ computed for each image are then compared with the stellar positions for that general area of the sky, and the actual stars corresponding to the selected stellar images are identified. The fiducial marks in each corner of the plate are used to define the limits in right ascension and declination for searching by the computer.

From the 1950.0 mean place (α^0, δ^0) and values for annual (a_v, a_v') and secular (s_v, s_v') variation and the integral number of years (t) from 1950 (catalog epoch) to the beginning of the year nearest the date of observation, the mean place (α_0, δ_0) for the beginning of the appropriate Besselian year is computed by

$$\alpha_0 = \alpha^0 + t\ (a_v + s_v\, t/200)$$
$$\delta_0 = \delta^0 + t\ (a_v' + s_v'\, t/200)$$

The α_0, δ_0 are then updated to the apparent place (α, δ) for the time of observation by the equations

$$\alpha = \alpha_0 + \tau\mu + Aa + Bb + Cc + Dd + E + J\tan^2\delta_0$$
$$\delta = \delta_0 + \tau\mu' + Aa' + Bb' + Cc' + Dd' + E + J'\tan\delta_0$$

where τ is the fraction of the tropical year elapsed since the beginning of the year nearest the date of observations, μ, μ' indicate the proper motion of the star in right ascension and declination, respectively, and A,B,C,D,E

are Besselian day numbers linearly interpolated to the time of observation, J, J' are second-order day numbers interpolated to time of observation, and a, b, c, d, a', b', c', and d', are Besselian star constants.

Standard deviations in right ascension and declination for α and δ are determined for each star from the values for probable error given in the star catalog. The standard deviations σ_α, σ_δ are obtained from

$$\sigma_\alpha = f\{PE_\alpha^2 + (PE_{c_\alpha})^2 (t/100)^2\}^{1/2} / .6745$$

$$\sigma_\delta = f\{PE_\delta^2 + (PE_{c_\alpha})^2 (t/100)^2\}^{1/2} / .6745$$

where f is the scale factor for star catalog errors, PE_α, PE_δ are the probable errors in star position at epoch 1950.0, and PE_{c_α}, PE_{c_δ} are the centennial probable errors in proper motion.

3.3.5.1.6 THE COMPUTATION OF DIRECTION COSINES

Two sets of direction cosines for the reference stars are computed next: the first set (χ, μ, γ) without the refraction correction and the second set (χ_R, μ_R, γ_R) with the refraction correction included. The corresponding χ_R, μ_R, γ_R directions are used in a preliminary camera orientation in which the refraction coefficients η_1, η_2, η_3, and η_4 are carried as known quantities and χ, μ, γ directions are used for the final camera orientation adjustment. Using the apparent star positions α, δ for all reference stars and the ALST, the values of χ, μ, γ are obtained from

$$\chi = \sin A_z \cos E_l$$

$$\mu = \cos A_z \cos E_l$$

$$\gamma = \sin E_l$$

where

$$\sin E_l = \sin \phi \sin \delta + \cos \phi \cos \delta \cos h$$

$$\cos E_l = (1 - \sin^2 E_l)^{1/2}$$

$$\sin A_z = -\cos \delta \sin h / \cos E_l$$

$$\cos A_z = -(\sin \phi \cos \delta \cos h + \cos \phi \sin \delta) / \cos E_l$$

E_l = elevation angle
A_z = azimuth angle
h = local hour angle = ALST $-\alpha$
α = right ascension of the star (apparent)
ϕ = geodetic latitude of the camera.

The second set of direction cosines is obtained in a similar fashion using elevation angles compensated for refraction δ_ζ,

$$\chi_R = \sin A_z \cos E_{l_R}$$

$$\mu_R = \cos A_z \cos E_{l_R}$$

$$\gamma_R = \sin E_{l_R}$$

where $E_{l_R} = E_l + \delta_\zeta$ and other symbols denote the same quantities as above.

3.3.5.1.7 PRELIMINARY COMPUTATION OF THE CAMERA ORIENTATION

Input data for this step of the plate reduction include corrected plate measurements x, y and direction cosines χ_R, μ_R, γ_R for all star images and an approximation of the elements of exterior orientation ν', ω', κ' and the three interior elements (x_p, y_p, k). A weighted least-squares adjustment is performed through repeated differential correction. The primary benefit from this adjustment is the editing of plate measurements where those with large errors are rejected, leaving a set of screened measurements for the final steps of the reduction. The results also provide a good approximation of orientation x_p, y_p, k, ν, ω, κ parameters usable for starting the final calibration without using excessive computer time. The orientation of camera in space is defined by matrix A

$$A = \begin{bmatrix} A^\circ & B^\circ & C^\circ \\ A'^\circ & B'^\circ & C'^\circ \\ D^\circ & E^\circ & F^\circ \end{bmatrix}$$

The elements of A are the direction cosines relating the coordinate system of object space (X, Y, Z) to that of image space (x, y, z). For example, A°, B°, and C° are the di-

rection cosines of the x axis relative to axes X, Y, and Z, respectively. Similar definitions apply to the elements of the second and third rows of the A matrix with respect to the x and y axes.

3.3.5.1.8 FINAL DETERMINATION OF ORIENTATION

The final camera orientation is now computed using the screened plate measurements, the direction cosines (χ, μ, γ), and the six preliminary orientation values resulting from the last step. Two of Garfinkel's refraction coefficients (η_1 and η_2) are used as partially constrained parameters which are allowed to adjust in the final orientation solution. The apparent coordinates of the stars, which were assumed known in previous computations, are also allowed to adjust. The lens distortion parameters are taken from a separate adjustment (sec. 3.3.5.1.10) and are not allowed to adjust. The linearized projective equations for the i^{th} image of the j^{th} star are described in matrix form as

$$V_{ij}+\dot{B}_{ij}\,\delta_j+\ddot{B}_{ij}\,\ddot{\delta}_{ij}=\epsilon_{ij}$$

where

$$V_{ij}=\begin{bmatrix} V_{1_{ij}} \\ V_{2_{ij}} \end{bmatrix}$$

$=$the residuals of the corresponding measured plate coordinates (x, y) for the i^{th} image of the j^{th} star

$\dot{B}_{ij}=$matrix of partial derivatives with respect to the orientation parameters, $(\psi, \omega, \kappa, x_p, y_p, k)$ and the refraction coefficients (η_1, η_2)

$\delta_j=$vector of corrections to preceding parameters

$\ddot{B}_{ij}=$matrix of partial derivatives with respect to α and δ computed from data taken from a star catalog and current ephemeris

$\ddot{\delta}_{ij}=$corrections to computed α and δ

$\epsilon_{ij}=$residuals being minimized in the adjustment

At the end of each adjustment computation, an error analysis is made and several tests are performed to determine the need for more iterations. The items in the error analysis and testing include residual errors in the plate measurements (V_x, V_y); unweighted mean measuring error (V_{xy}); unweighted mean error in star coordinates $(V_{\alpha\delta})$; composite weighted mean error (V_t) (reflects errors in measurements, positions from star catalogs and the adjusted orientation and refraction parameters); unweighted mean error from the preliminary camera orientation adjustment; and the principal point coordinates from the preliminary adjustment along with those for the current and immediately preceding iterations of this final adjustment. Iterations are continued until the criteria set for these tests are satisfied. The various errors are computed from

$$V_{xy}^2=\sum_{i=1}^{n_x}V_{x_i}^2+\sum_{i=1}^{n_y}V_{y_i}^2/(n_x+n_y)$$

where n_x and n_y are the number of x and y measurements used.

$$V_{\alpha\delta}^2=\sum_{i=1}^{n_s}\frac{(\Delta\alpha_i)^2+(\Delta\delta_i)^2}{2n_s}$$

where n_s equals the number of stars used. $\Delta\alpha$ and $\Delta\delta$ are corrections to the computed α and δ of the stars.

$$V_i^2=\frac{\sum_{i=1}^{n_x}(V_xW_x)_i^2+\sum_{i=1}^{n_y}(V_yW_y)_i^2+\sum_{i=1}^{n_s}[(\Delta\alpha W_\alpha)_i^2+(\Delta\delta W_\delta)_i^2]+\sum_{i=1}^{P}(\delta\dot{W})_i^2}{n_x+n_y-2n_s-P}$$

where

$W_x, W_y=$ weights in measured x, y $\quad W=$ weights for parameters

$W_\alpha, W_\delta=$ weights of star coordinates α, δ

$P=$ number of parameters in final solution

$\delta=$ parameter corrections from final solution

3.3.5.1.9 COMPUTATION OF SATELLITE POSITIONS

Finally, the plate measurements and the apparent local sidereal times of the satellite observations are used with the final adjusted parameters from the general analytical plate reduction (sec. 3.5.1.8) to obtain the azimuth, elevation, apparent right ascension, and apparent declination for each image of the satellite. Standard errors in each coordinate are also computed for evaluating the reliability of the computed positions. The azimuth and elevation of the satellite are computed first, where refraction (adjusted for parallax) is removed from the elevation. Then, the azimuth (A_z) and elevation (E_l) are used to compute the final topocentric right ascension (α) and declination (δ) using:

$$\sin \delta = \sin E_l \sin \phi + \cos A_z \cos E_l \cos \phi$$
$$\alpha = \mathrm{ALST} - h$$
$$\sin h = -\sin A_z \cos E_l / \cos \delta$$

3.3.5.1.10 CALIBRATION OF CAMERA

The plate reduction procedure discussed in the preceding sections employs certain constants (κ_0', κ_1', κ_2', J_1, J_2, $\phi°$, k) for each PC–1000 camera system which are derived from special exposures specifically designed to calibrate each camera system. Unlike some other camera reduction procedures, the PC–1000 plate adjustment does not involve a simultaneous calibration and orientation reduction for each individual plate. Calibration of the PC–1000's, as performed within elements of DMA, was done only intermittently to check the calibration values or done after the camera systems had been dismantled and reassembled, or shipped to other locations. In the latter case, a recalibration was performed before any satellite observations were started.

The camera calibration procedure is much like the plate reduction procedure just described, but there are some differences which warrant discussion. Instead of 25 to 30 stars distributed evenly around the satellite images, 50 to 60 stars were selected covering the entire exposed area of the plate. Plate coordinates were corrected for comparator errors and referred to the plate center. Stars were automatically identified, direction cosines computed, and a preliminary camera orientation computed just as was done in plate reduction except that the solution included approximate values for the distortion parameters.

Adjustments for errors in the cataloged coordinates were added when determining the final orientation and distortion parameters. The first part of this adjustment, along with curve balancing (see below), produced the coefficients of radial distortion (κ_0, κ_1, κ_2, κ_3) and their standard deviations. The displacement, d, of a point due to radial distortion, at distance r from the plate center, is expressed by the radial distortion function:

$$d = \kappa_0 r + \kappa_1 r^3 + \kappa_2 r^5 + \kappa_3 r^7$$

in which κ_0 (by definition) is equal to zero. The relationship between the principal distance (k), radial distance, and displacement due to radial distortion is expressed by

$$\frac{r+d'}{r+d} = \frac{k+\Delta k}{k}$$

When the radial distance is held constant and the principal distance is changed by Δk, the d is the distortion with principal distance k, and d' is the distortion with principal distance $k+\Delta k$. This relationship is expressed by

$$\Delta k = \frac{kd' - kd}{r+d}$$

A balanced curve is obtained by forcing the distortion d' to become zero at distance r. The change in principal distance becomes

$$\Delta k = kd/(r+d)$$

The balanced curve is

$$d' = \kappa_0' r + \kappa_1' r^3 + \kappa_2' r^5 + \kappa_3' r^7$$

and the new radial distortion coefficients are computed by

$$k_1' = k + \Delta k$$

$$\kappa_0' = \kappa_0 + (1+\kappa_0)\ \Delta k/k$$

$$\kappa_1' = (1+\Delta k/k)\ \kappa_1$$

$$\kappa_2' = (1+\Delta k/k)\ \kappa_2$$

$$\kappa_3' = (1+\Delta k/k)\ \kappa_3$$

The second part of the final adjustment produces auxiliary decentering parameters (P_1, P_2, P_3) which are then used to compute the coefficients of decentering distortion (J_1 and J_2) and phase angle ($\phi°$).

$$J_1 = [P_1^2 + P_2^2]^{1/2}$$

$$J_2 = P_3[P_1^2 + P_2^2]^{1/2}$$

$$\phi° = \tan^{-1}[-P_1/P_2]^{1/2}$$

3.3.5.2 AFCRL Geodetic Laser System

(Robert L. Iliff, AFCRL)

The operations performed on the data adjust the recorded values according to the amplitudes of the individual returning pulses and correct for bias. The corrected travel times of pulses within each burst (of up to 10 pulses) are then averaged, resulting in a single time per burst. The correct time for this resultant range must then be calculated. Time of observation is carried to the nearest microsecond. Corrections for refractive index are made in the final reduction by using atmospheric conditions as measured at the site. The process used to obtain the corrected range is shown below.

The travel time is obtained from

$$\tau_c = \frac{\Sigma\, \tau_m}{n} - C_f$$

where τ_c is the corrected travel time, τ_m is the measured travel time, n is the number of measured travel times in the burst, and C_f is a calibration factor obtained by ranging to a known fixed target.

The range is calculated by

$$R = \frac{\tau_c}{2}(299\,792\,462) - \frac{2.238 + 0.414\,PT^{-1} - 0.238H}{\sin E_l + (10^{-3}\cot E_l)}$$

where E_l is the elevation angle of the satellites, P is the atmospheric pressure in millibars, T is the temperature in degrees Kelvin, H is the height of the laser above mean sea level in kilometers, and R is the corrected range in meters.

The time of observation corresponding to R is obtained by a weighted average of time delays by

$$T_m = t_p + t_d + \frac{t_1 + t_2 + \ldots t_{10}}{n} \pm t_c + \frac{\tau_c}{2}$$

where T_m is the corrected observation time, t_p is the recorded time (coincident with flashlamp firing), t_d is the delay from flashlamp trigger pulse to the first laser pulse (this time is controlled by the operator), t_1, t_2 . . . t_{10} is the time of delays from the first programmed pulse to subsequent pulses (each referred to first pulse), and t_c is the time difference between station clock and Loran C and can be positive or negative.

3.3.5.3 SECOR

(Marvel A. Warden and George Dudley, DMA/TC)

3.3.5.3.1 PREPARATION OF DATA

Data received from a field station were analyzed to evaluate their quality. This preliminary evaluation served to detect gross errors which had escaped detection at the tracking station. Since shipment of the tapes from remote sites was often slow, an undetected abnormality could have resulted in costly and time-consuming re-observation.

The tape was next translated by means of a Honeywell H–200 computer and a printout made. Figure 3.23 illustrates how the five channels overlap to make up the full range word. The raw data on tape from a single station include quality codes, run number,

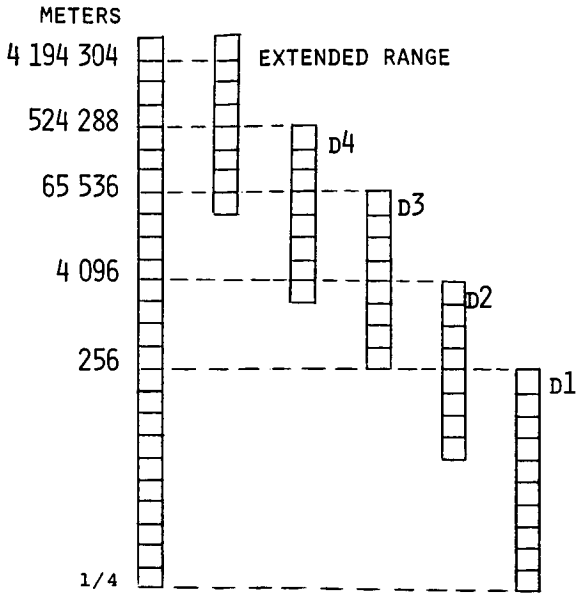

FIGURE 3.23.—Channel overlap.

day and month of track, and five individual channels of binary range data, the raw ionospheric correction, and the time of each observation in hours, minutes, seconds, and milliseconds. These data were screened for quality and grouped with data from other tapes carrying data for the same pass.

The combined data were then arranged in order of time, edited (by examining first differences), and packed onto a single tape. No data smoothing was done at this time. Where an ambiguity was detected, the range was corrected and the correction noted. Incorrect ranges were flagged and data were prepared for preprocessing.

A flow diagram of the SECOR data processing procedure is shown in figure 3.24.

3.3.5.3.2 CORRECTIONS TO THE RANGE

Calibration Correction.—The system circuitry, both on the ground and in the satellite, introduces a phase shift and consequent bias in the measured ranges; hence, a calibration must be performed to determine its magnitude. Insofar as the transponder was concerned, careful measurements of its contributions to the phase shifts of the signal

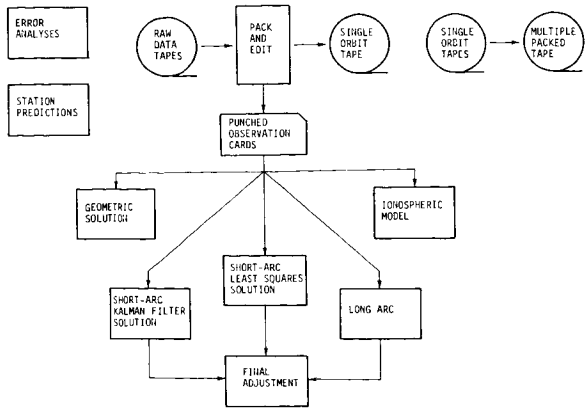

FIGURE 3.24.—SECOR data processing.

were made before it was launched and it was presumed that this value (SAT DELAY) remained the same when the transponder was in orbit. In any case, as long as the phase delay in the transponder did not change, any bias from this source was the same at all stations.

At the original SECOR ground station, calibration was performed by introducing, at a point just before the antenna, a known signal similar to that received from the satellite. The antenna was therefore outside the calibration loop. After removal of the phase delay within the loop it was still necessary to range to a transponder placed at a known distance from the station in order to determine the phase delay in the antenna. Because of multipath reflection and radio interference this method proved very unreliable. As a consequence, undetermined bias, probably varying from station to station, was a source of error in early SECOR measurements in the Pacific area. By the time the SECOR Equatorial Network (SEN) was begun, modifications to the equipment had been made to bring the antenna within the calibration loop by placing a small dipole within the near field of the antenna and it was possible to remove all of the phase delay due to the equipment itself. This was done before each period of observation and was checked immediately afterwards. In both pre-track calibration (PRE CAL) and post-track calibration (POST CAL) a known range was

also measured to verify the validity of the calibration and to measure any drift in phase during the track. Data from each step of the calibration process were recorded on data tapes in the same manner as observational data.

A calibration constant, or zero-set bias, is added to take care of the phase delay in the satellite's transponder, and any drift in the zero setting noted between the pre- and post-calibration. This correction is computed for both the VF and VFIC channels. The total correction for the VF channel is

$$\mathrm{CAL_{vf}}=\frac{\mathrm{PRE\ CAL_{vf}}+\mathrm{POST\ CAL_{vf}}}{2}-\mathrm{SAT\ DELAY_{vfic}}$$

and for the VFIC channel it is

$$\mathrm{CAL_{vfic}}=\frac{\mathrm{PRE\ CAL_{vfic}}+\mathrm{POST\ CAL_{vfic}}}{2}-\mathrm{SAT\ DELAY_{vfic}}$$

Elimination of Ambiguities.—Ranges were next corrected for any obvious ambiguities (multiples of 256 meters). This correction was not made easily in the early SECOR operations but, as a result of improvements in engineering and observation procedures, ambiguities presented only minor problems during the observational phase of the SECOR Equatorial Network project. Only on rare occasions was there any question as to the amount of ambiguity, but even then this question was easily resolved once a preliminary solution had been obtained and the unknown station positioned approximately.

Tropospheric Refraction.—Refraction causes both a bending and a phase shift of the electromagnetic wave. Empirical formulas were used to correct both elevation angles and ranges for the effect of tropospheric refraction. These formulas require only a minimum of meteorological data and are accurate to about 10 percent of the correction or within 1 meter for the case of a range measured at a 15° elevation angle. The empirical correction was obtained from

$$\Delta R_i=\frac{K_1[1-e^{(R_i/7000)}]}{\sin E_0+0.0236\cos E_0}$$

where K_1 is the refraction value at zenith in meters, E_0 is the elevation angle, and R_i is the range observation.

Ionospheric Correction.—By far the greatest correction to range measurements is that due to ionospheric refraction. In some cases the magnitude of this correction becomes as large as 500 meters.

The phase delays in the SECOR modulations induced by traversing the ionized regions of the Earth's atmosphere are dependent upon the frequency of the carrier wave. Therefore by transmitting the modulations on two different carrier frequencies, two different ranges will be observed for a particular satellite position. Knowing the differential effects enables a correction to be made to either range to remove the ionospheric delay.

The total phase-shift of a carrier wave of frequency f in propagating a distance R_s is determined by integrating the phase index of refraction of the medium along the propagation path (ds) so that

$$\Phi=k=\int_0^{R_s} n_p(f)\,ds \qquad (3.1)$$

where

ϕ = phase
k = wave number of beat frequency
$n_p(f)$ = phase index of refraction

The phase shift measured in units of distance (electrical path length) is then

$$R=\frac{\phi}{k}\int_0^{R_s} n_p(f)\,ds \qquad (3.2)$$

The total phase shift of the beat frequency modulation is measured as the carrier wave is modulated. The group index of refraction must replace the phase index in equation (3.1). The two ranges measured by SECOR

(½ round trip distance) can then be expressed as

$$R_1 = \tfrac{1}{2}\int_0^{R_s} n_g(f_1)\,ds + \tfrac{1}{2}\int_0^{R_s} n_g(f_2)\,ds$$
$$R_2 = \tfrac{1}{2}\int_0^{R_s} n_g(f_1)\,ds + \tfrac{1}{2}\int_0^{R_s} n_g(f_3)\,ds \qquad (3.3)$$

where

$f_1 = 420.9$ MHz
$f_2 = 449.0$ MHz
$f_3 = 224.5$ MHz

and the range difference ΔR becomes

$$\Delta R = R_2 - R_1 = \tfrac{1}{2}\int_0^{R_s} n_g(f_3)\,ds - \tfrac{1}{2}\int_0^{R_s} n_g(f_2)\,ds \qquad (3.4)$$

The phase index of refraction describing the propagation of electromagnetic waves in an ionized medium can be derived by considering the waves' interaction with the individual ions of the medium. Such an analysis leads to the Appleton-Hartree dispersion equation for the phase index of refraction in the ionosphere:

$$n_p^2(f) = 1 - \frac{X}{1 - jZ - \dfrac{Y_t^2}{2(1-X-jZ)} \pm \sqrt{\dfrac{Y_t^2}{4(1-X-jZ)^2} + Y_L^2}} \qquad (3.5)$$

where

$$X = \frac{Ne^2}{mE_0\omega^2}$$
$$Y_t = -\frac{H_e\, e\, \mu_0}{m\omega}\sin\theta_p$$
$$Y_L = -\frac{H_e\, e\, \mu_0}{m\omega}\cos\theta_p$$
$$Z = \frac{\nu}{\omega}$$

where

θ_p = angle between the ray path and the magnetic field
ν = electron collision frequency
N = electron density
H_e = magnetic field strength
m = electron mass
e = electron charge
$\omega = 2\pi\nu$

Analysis of the contribution of each term to $n_p(f)$ and ultimately to ΔR for the frequencies used in SECOR leads to the conclusion that the effects of collisions and of the magnetic field are negligible (less than 4 meters in ΔR under the most extreme conditions). It is therefore adequate to approximate $n_p(f)$ by

$$n_p(f) = 1 - \frac{X}{2}$$

since $X \ll 1$.

The group index of refraction is defined as

$$n_g(f) = n_p(f) + f\frac{\partial}{\partial f} n_p(f) \qquad (3.6)$$

hence

$$n_g(f) = 1 + \frac{X}{2}$$

If we let $\alpha = 1.0666$, $\beta = 0.5333$, the range difference becomes

$$\Delta R = \tfrac{1}{2}\int_0^{R_s}\left[1 + \tfrac{1}{2}\frac{\eta N(s)}{\beta^2 f_1^2}\right]ds - \tfrac{1}{2}\int_0^{R_s}\left[1 + \tfrac{1}{2}\frac{\eta N(s)}{\alpha^2 f_1^2}\right]ds = \tfrac{1}{4}\frac{\eta}{f^2}\left[\frac{1}{\beta^2} - \frac{1}{\alpha^2}\right]\int_0^{R_s} N(s)\,ds \qquad (3.7)$$

If the integral is defined as the total electron content along the path of propagation N_T, ΔR becomes

$$\Delta R = \tfrac{1}{4}\frac{\eta}{f_1^2}\left[\frac{1}{\beta^2}-\frac{1}{\alpha^2}\right]N_T \qquad (3.8)$$

This relationship establishes the proportionality of N_T to the measured range difference (ΔR). When this expression is substituted into equation (3.3) for the high-frequency range, the following correction term is obtained:

$$\begin{aligned} R_1 &= R_s + \tfrac{1}{4}\frac{1}{f_1^2}\left[1+\frac{1}{\alpha^2}\right]N_T \\ &= R_s + \Delta R\frac{1+\frac{1}{\alpha^2}}{\frac{1}{\beta^2}-\frac{1}{\alpha^2}} \\ &= R_s + 0.7125\,\Delta R \end{aligned} \qquad (3.9)$$

The true range is then expressed as the measured range minus a correction term dependent on the measured range difference. The error introduced into R_s by the assumptions made in the derivation of the two frequency corrections can be determined by numerically integrating equation (3.1) through a model ionosphere. The assumption of a linear propagation path produces the largest error at lower elevation angles, and consequently residual error in corrected range due to ionospheric delays increases as the elevation angle decreases.

For the region of SECOR operation (elevation angles $> 15°$) the residual ionospheric error in extreme cases was less than 4 meters and under normal conditions was less than 1 meter.

In the dual-frequency technique the correction for ionospheric refraction was therefore computed by

$$\Delta R_i = K\,[D1-IC)_i - \mathrm{CAL_{vf}} + \mathrm{CAL_{vfic}}]$$

where

$K = -0.7125$ as defined above

$$D1-IC = \frac{R_{\mathrm{vfic}}-R_{\mathrm{vf}}}{2}$$

$\mathrm{CAL_{vf}}$ and $\mathrm{CAL_{vfic}}$ are as previously defined.

Travel Time.—At some instant of time, t_0, a pulse transmitted by the master station leaves the satellite and travels to each station in the quadrilateral, where it causes a range and a time to be recorded. The recorded range will be that to the satellite position at the time t_0, but the time recorded will be $t_0+\Delta t$, where Δt is the time of propagation of the signal from the satellite to the station. In order to bring range and time into correspondence, all ranges are adjusted to their proper value for the time recorded at the master station. The correction added to the observed range at any station, i, is

$$\Delta R_i = \frac{R_m}{c}\dot{R}_i + \frac{\ddot{R}_i R_m^2}{2c^2} + \cdots$$

where

R_m = range to master station
c = speed of light
$\dot{R}_i$ = rate of change of range to i^{th} station

Scale Factor.—Each station has a reference frequency oscillator, which is set to a certain value. This setting can be related to the value of the assumed velocity of light. It was determined that this assumed value differed from the internationally accepted value of 299 792 500 m/sec by $.98\times10^{-6}$ and thus a correction is made to each measured range.

$$\Delta R_i = -.98\times10^{-6}\,R_i$$

where R_i = measured range with ambiguity applied, if an ambiguity existed in the initial measured range.

3.3.5.4 Doppler Shift

(R. J. Anderle, NWL)

The principal objectives of the data-processing programs are to change the data format, to calibrate the station clock, to detect and eliminate erroneous data points or passes, and to determine weights for the observations. No corrections are made for higher order ionospheric-refraction correc-

tion; corrections for tropospheric refraction and aberration are made only as an aid in the filtering and must still be applied to the filtered observations for any subsequent calculations. Most of the data placed in the National Geodetic Data Service Center were preprocessed without the aberration correction; thus there resulted a bias in the base frequencies reported with the data. The bias is of no consequence when the frequency is a parameter of the solution.

Doppler data received on punched paper tapes from teletype machines are first transferred to magnetic tapes for use in orbital computations. Data recorded automatically are compared with times of predicted passes in order that the satellite may be identified and a header message inserted in front of each pass containing the satellite number, station number, and calibration constants; the inserted data are copied from a header which had been placed manually by the station operator before an earlier pass. Generally, the foregoing work is performed at the Applied Physics Laboratory of Johns Hopkins University (ch. 2), and the results are transmitted to the Naval Weapons Laboratory (NWL) by telephone data line. At NWL, data are rejected if illegal characters or formats occur as a result of transmission errors, or if unusual time gaps or reversals in the time order occur in the series of observations within any individual satellite pass. Sampled Doppler data are converted to frequency as follows:

$$f_0 = f_r - \frac{N_c}{T}$$

$$t_0 = t_1 + \frac{T}{2}$$

where f_r is the effective ground frequency against which the combined frequencies are beat, N_c is the number of beat-cycles counted, T is the time to count N_c beats, and t_1 is the time of the start of the count. If the data are from the CCID or GEOCEIVER, the range-difference $\Delta\rho$ is

$$\Delta\rho = -c\,(N_c - \Delta f \Delta t)\,/\,(f_r - \Delta f)$$

where c is the velocity of light and Δf is the offset between the satellite frequency and the ground station frequency. Station clock and frequency calibration constants provided in the header message by the station operator are applied in the course of these conversions.

The times of observation are then adjusted by means of the recorded times of receipt of timing signals from the satellite. Four to eight timing points are recorded for each pass of the satellite over each station. The time of receipt of the signal is corrected for the travel time from the satellite to the station by using predicted positions for the satellite. The relative error between the satellite and station clock is the difference between this corrected time and the nearest even minute. First the satellite clock epoch and rate are calibrated for the day by use of the timing data from a group of stations equipped with the most accurately calibrated clocks. The clock epoch and rate are found by a least-squares solution, minimizing the satellite clock errors. An iteration of the least-squares solution is performed after the clock errors exceeding 2.5 times the standard deviations of all clock errors are rejected. The corrected satellite-clock signals are then used to obtain a mean time correction for each pass of the satellite over the remaining stations. The mean corrections are applied to the time of observations of sampled Doppler, GEOCEIVER, or CCID data for the corresponding passes. If inconsistent time corrections are obtained for the individual time signals within a given pass, the mean correction for the day is applied to observations for that satellite pass.

The sampled Doppler, GEOCEIVER, and CCID data are then filtered to detect erroneous data. The observations are compared with computed data corresponding to the predicted satellite positions from the previous orbit computation. Residuals exceeding a coarse tolerance are rejected, and a least-squares solution is made for a modified station position for each satellite pass. This station navigation, which is performed to linearize residuals for filtering purposes, is constrained to lie in the plane containing the

slant range vector to the satellite and the satellite velocity vector at the time of closest approach of the satellite to the station. The navigation errors are called the along-track error and the range error. Residuals for the modified station position are then rejected if they are larger than 2.5 (2.0 for CCID or GEOCEIVER data) times the standard deviation of all the residuals in the pass. The least-squares solution and navigation are iterated for CCID or GEOCEIVER data until no further data points are rejected.

Each filtered CCID or GEOCEIVER data point in a pass is assigned a weight equal to the inverse square of the standard deviation of the residuals for use in subsequent calculations. In the case of the more numerous sampled Doppler data points, eight raw data points are condensed to one data point. The condensation is accomplished by making a fit to the filtered residuals in a time span corresponding to eight data points, after which the fitted residual at the mid data point is added to the computed Doppler value for that point. The resulting condensed observation is assigned a weight equal to the inverse square of the standard error of the linear fit.

After all passes have been filtered in the two-day span used for orbit computations, the navigation errors are filtered. Passes giving slant-range navigation errors larger than 2.5 times the standard deviation of the errors or passes giving along-track navigation errors that depart from a linear fit through the errors by more than 2.5 times the standard deviation of the differences from the linear fit are rejected. This filtering is relaxed to the extent that errors less than 10 meters are automatically accepted and all passes from new site locations are accepted.

3.4 THEORY

This section gives the equations and describes the procedures used to determine station coordinates by simultaneous observations by PC–1000 cameras (secs. 3.4.1 and 3.4.2.1), nearly simultaneous observation by cameras and DME (sec. 3.4.2.2), nearly simultaneous observation by SECOR (sec. 3.4.3), and observations by frequency-measuring equipment (sec. 3.4.4).

The theory involved in determining the potential by combining gravimetric data with the gravitational potential determined by satellite geodesy is described in section 3.4.5.

Also given in section 3.4.4 is the theory by which the potential, polar motion, Love's number, and so on may be derived from using data collected by the frequency-measuring equipment.

3.4.1 Satellite Triangulation

(Donovan N. Huber, DMA/AC)

The theory on which satellite triangulation is based is the same as the theory used by Väisälä (1947) in solving the flare triangulation problem (see also ch. 7). When the satellite is at position j_1 (fig. 3.25), the cameras at stations i and k are operated and the satellite is photographed against a stellar background. At some later time, when the satellite is at position j_2 (not necessarily on the same pass as j_1), another photograph of the satellite is taken. It is the geometric relationship between the satellite and the ground station positions that allows the determination of interstation directions and hence a solution.

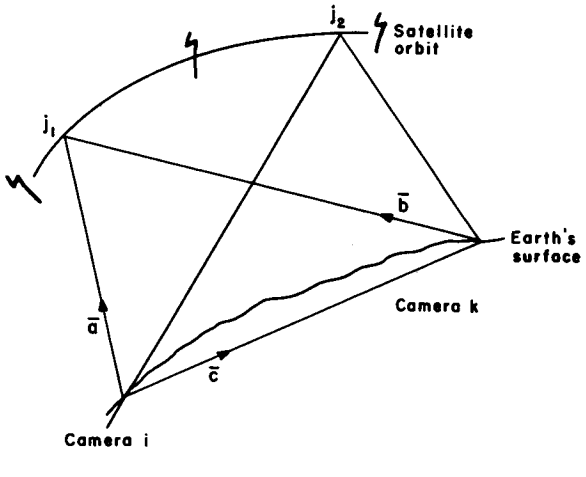

FIGURE 3.25.—Satellite triangulation.

3.4.1.1 Basic Conditions

The vectors **a**, **b**, and **c** are all unit vectors associated with the recording of event 1 (the appearance of the satellite at point j_1). Vectors **a** and **b** represent the directions from stations i and k, and vector **c** represents the direction of the chord between stations i and k. The three vectors must all be coplanar; hence

$$\mathbf{a}\times\mathbf{b}\cdot\mathbf{c}=0 \qquad (3.10)$$

A similar condition holds for the second recorded event, which defines a second triangle. It is obvious from this that the chord between the two camera stations is the line formed by the intersection of the two planes.

3.4.1.2 Coordinate and Time Systems

The reduction employs two coordinate systems, the Cartesian rectangular system (X, Y, Z) with its origin at the center of the ellipsoid and a topocentric, true right ascension and declination system (α, δ). There are also two time systems used in the computations, the sidereal and universal systems. The universal time (UTI) of an observation is converted to sidereal time and added to the apparent Greenwich sidereal time (AGST) for O^h to obtain the exact angle between the mean astronomic meridian at Greenwich and the meridian of the true vernal equinox for the time of the observation.

3.4.1.3 Observation Equations

Let

α,δ = topocentric, true right ascension and declination
x_p,y_p = polar motion (in radians)
$G=\alpha-\delta$
$T=-x_p\cos\delta\cos G+y_p\cos\delta\sin G$
$S=-y_p\sin\delta$
$R=x_p\sin\delta$
$u=\sin\delta_k+T_k$
$t=\cos\delta_k\sin G_k+S_k$
$s=\cos\delta_k\cos G_k+R_k$
$r=\sin\delta_i+T_i$
$n=\cos\delta_i\sin G_i+S_i$
$m=\cos\delta_i\cos G_i+R_i$
$C=sn-tm$
$B=um-sr$
$A=tr-un$

where the subscripts i and k denote the respective ground stations.

Using the simultaneous observations of the satellite at j from the unknown stations i and k, we obtain from equation (3.10) the equation (case 1)

$$A\Delta X_{ij}+B\Delta Y_{ij}+C\Delta Z_{ij}-A\Delta X_{kj}-B\Delta Y_{kj}-C\Delta Z_{kj}+L_{ikj}=0$$

where

$$L_{ijk}=A(X_{ij}-X_{kj})+B(Y_{ij}-Y_{kj})+C(Z_{ij}-Z_{kj}) \qquad (3.11)$$

If the assumption is made that station k is the known station and station i is the unknown, the equation above reduces to (case 2)

$$A\Delta X_{ij}+B\Delta Y_{ij}+C\Delta Z_{ij}+L_{ijk}=0 \qquad (3.12)$$

3.4.1.4 Adjustment Procedures

A least-squares procedure (see ch. 1) is used to determine values for X_{ij}, Y_{ij}, and Z_{ij}. The station coordinates in the reduction can be weighted, and other constraints, such as the known chord length between two camera stations, can also be introduced. The results achieved from this procedure with PC–1000 camera data are given in section 3.5.1.

3.4.2 Short-Arc Method

(George Hadgigeorge, AFCRL; Duane C. Brown and Jerry Trotter, DBA)

3.4.2.1 Observational Equations for Camera Data

The equations for the plate coordinates x, y are of the form

$$\left.\begin{aligned} x &= f_1\,(X^c, Y^c, Z^c, X_{00}, Y_{00}, Z_{00}, \\ &\qquad x_0, y_0, z_0, \dot{x}_0, \dot{y}_0, \dot{z}_0; t) \\ y &= f_2\,(X^c, Y^c, Z^c, X_{00}, Y_{00}, Z_{00}, \\ &\qquad x_0, y_0, z_0, \dot{x}_0, \dot{y}_0, \dot{z}_0; t) \end{aligned}\right\} \tag{3.13}$$

in which X^c, Y^c, Z^c are station coordinates, X_{00}, Y_{00}, Z_{00} are center of mass coordinates, and x_0, y_0, z_0, $\dot{x}_0$, $\dot{y}_0$, $\dot{z}_0$ are orbital elements at $t=0$.

If x^0, y^0 denote the observed values of x, y, the adjusted values corrected for systematic error can be expressed as

$$\left.\begin{aligned} x &= x^0 + v_x + \dot{x}v_t + \dot{x}\,\delta t + \delta x \\ y &= y^0 + v_y + \dot{y}v_t + \dot{y}\,\delta t + \delta y \end{aligned}\right\} \tag{3.14}$$

where δx, δy are given by equation (3.15). In equation (3.14), v_x, v_y denote residuals in x and y, and v_t denotes the residual in timing. The terms in δt account for the bias in timing. The ν, ω, and κ are the inner orientation angles defined in chapter 7 (α is used there for ν); k is the focal length.

$$\begin{bmatrix} \delta x \\ \\ \delta y \end{bmatrix} = \begin{bmatrix} -k\left(1+\dfrac{x^2}{k^2}\right) & \dfrac{xy}{k} & y\,\dfrac{x}{k} \\ \\ \dfrac{xy}{k} & k\left(1+\dfrac{y^2}{k^2}\right) & -x\,\dfrac{y}{k} \end{bmatrix} \begin{bmatrix} \delta\nu \\ \delta\omega \\ \delta\kappa \\ \delta k \end{bmatrix} \equiv \underset{=}{B}^{(4)} \cdot \underset{-}{\delta}^{(4)} \tag{3.15}$$

We now set up the relations

$$\left.\begin{aligned} X^c &= (X^c)^{00} + \delta X^c \\ X_{00} &= X_{00}^{00} + \delta X_{00} \\ x_0 &= x_0^{00} + \delta x_0 \\ \dot{x}_0 &= \dot{x}_{00}^{0} + \delta \dot{x}_0 \end{aligned}\right\} \tag{3.16}$$

in which the superscripts $(^{00})$ denote approximations and the δ are the corresponding corrections. Substituting these into the right-hand side of equation (3.13) and linearizing the resulting expressions by Taylor's series, we obtain equations (3.17) and (3.18). To arrive at explicit expressions for the elements of the linearized observational equations, we let X^{00}, Y^{00}, Z^{00}, $\dot{X}^{00}$, $\dot{Y}^{00}$, $\dot{Z}^{00}$ denote the components of position and velocity for the time τ of the observation. Then we define the auxiliary vector

$$\begin{bmatrix} m^{00} \\ n^{00} \\ q^{00} \end{bmatrix} = \begin{bmatrix} A & B & C \\ A' & B' & C' \\ D & E & F \end{bmatrix} \begin{bmatrix} X^{00} - (X^c)^{00} \\ Y^{00} - (Y^c)^{00} \\ Z^{00} - (Z^c)^{00} \end{bmatrix} \tag{3.19}$$

where the orientation matrix has been computed from the data. The values of the plate coordinates thus computed then become

$$\begin{bmatrix} x^{00} \\ \\ y^{00} \end{bmatrix} = \frac{k}{q^{00}} \begin{bmatrix} m^{00} \\ \\ n^{00} \end{bmatrix} \tag{3.20}$$

The partial derivatives of the plate coordinates with respect to the station coordinates are given by

$$\underset{(2,3)}{\underset{=}{B}}{}^{(1)} = \frac{\partial(x,y)}{\partial(X^c,Y^c,Z^c)} = \frac{-k}{q^{00}} \begin{bmatrix} 1 & 0 & -x^{00}/k \\ 0 & 1 & -y^{00}/k \end{bmatrix} \begin{bmatrix} A & B & C \\ A' & B' & C' \\ D & E & F \end{bmatrix} \tag{3.21}$$

In terms of this the partial derivatives of the plate coordinates with respect to center of mass and in terms of orbital elements are given by

$$\underset{(2,9)}{\underset{=}{B}}{}^{(2)} = \frac{\partial(x,y)}{\partial(X_{00},Y_{00},\ldots,\dot{Z}_0)} = -\underset{(2,3)}{\underset{=}{B}}{}^{(1)}\ \underset{(3,9)}{\underset{=}{\Phi}} \tag{3.22}$$

$$x = x^{00} + \frac{\partial x}{\partial(X^c,Y^c,Z^c,X_{00},Y_{00},Z_{00},x_0,y_0,z_0,\dot{x}_0,\dot{y}_0,\dot{z}_0)} (\delta X^c, \ldots, \delta\dot{z}_0)^T \tag{3.17}$$

$$y = y^{00} + \frac{\partial y}{\partial(X^c,Y^c,Z^c,X_{00},Y_{00},Z_{00},x_0,y_0,z_0,\dot{x}_0,\dot{y}_0,\dot{z}_0)} (\delta X^c, \ldots, \delta\dot{z}_0)^T \tag{3.18}$$

The time derivatives of the plate coordinates required in equation (3.14) can be computed from

$$\begin{bmatrix} \dot{x} \\ \dot{y} \end{bmatrix} = \underset{(2,3)}{\underline{\underline{B}}^{(1)}} \begin{bmatrix} \dot{X}^{00} \\ \dot{Y}^{00} \\ \dot{Z}^{00} \end{bmatrix} \tag{3.23}$$

If we partition $\underset{(2,9)}{\underline{\underline{B}}^{(2)}}$ as

$$\underset{(2,9)}{\underline{\underline{B}}^{(2)}} = \left[\frac{\partial(x,y)}{\partial(X_{00},Y_{00},Z_{00})} \;\middle|\; \frac{\partial(x,y)}{\partial(x_0,y_0,z_0,\dot{x}_0,\dot{y}_0,\dot{z}_0)} \right] = \left[\underset{(2,3)}{\underline{\underline{B}}^{(2a)}} \;\middle|\; \underset{(2,6)}{\underline{\underline{B}}^{(2b)}} \right] \tag{3.24}$$

the linearized observation equations can be put into the form

$$\underset{(2,3)}{\underline{\underline{A}}} \underset{(3,1)}{\underline{v}} - \underset{(2,3)}{\underline{\underline{B}}^{(1)}} \underset{(3,1)}{\underline{\delta}^{(1)}} - \underset{(2,3)}{\underline{\underline{B}}^{(2a)}} \underset{(3,1)}{\underline{\delta}^{(2a)}} - \underset{(2,6)}{\underline{\underline{B}}^{(2b)}} \underset{(6,1)}{\underline{\delta}^{(2b)}} - \underset{(2,1)}{\underline{\underline{B}}^{(3)}} \underset{(1,1)}{\underline{\delta}^{(3)}} - \underset{(2,4)}{\underline{\underline{B}}^{(4)}} \underset{(4,1)}{\underline{\delta}^{(4)}} = \underset{(2,1)}{\underline{\epsilon}} \tag{3.25}$$

in which

$$\left.\begin{aligned} \underset{(2,3)}{\underline{\underline{A}}} &= \begin{bmatrix} 1 & 0 & \dot{x} \\ 0 & 1 & \dot{y} \end{bmatrix} & \underset{(6,1)}{\underline{\delta}^{(2b)}} &= \begin{bmatrix} \delta x_0 \\ \delta y_0 \\ \cdot \\ \cdot \\ \cdot \\ \delta \dot{z}_0 \end{bmatrix} \\ \underset{(3,1)}{\underline{v}} &= \begin{bmatrix} v_x \\ v_y \\ v_t \end{bmatrix} & \underset{(2,1)}{\underline{\underline{B}}^{(3)}} &= \begin{bmatrix} \dot{x} \\ \dot{y} \end{bmatrix} \\ \underset{(3,1)}{\underline{\delta}^{(1)}} &= \begin{bmatrix} \delta X^c \\ \delta Y^c \\ \delta Z^c \end{bmatrix} & \delta^{(3)} &= (\delta t) \\ \underset{(3,1)}{\underline{\delta}^{(2a)}} &= \begin{bmatrix} \delta X_{00} \\ \delta Y_{00} \\ \delta Z_{00} \end{bmatrix} \end{aligned}\right\} \tag{3.26}$$

At this point we shall recognize that as many as four plates may be acquired at a given station for a given pass. Accordingly, there may be as many as four sets of error coefficients. Letting p denote the p^{th} plate (max $p=4$) taken and introducing the subscript j to denote the j^{th} point observed by the station, we may express the pair of linearized observational equations generated by point j on plate p as in equations (3.27)-(3.29). The dimension l denotes the total number of error coefficients needed for the given pass at the station. The quantity ξ_{ip} is defined as

$$\left.\begin{aligned} \underline{\xi}_{ip} &= 1 \qquad \text{if } i=p \\ \underline{\xi}_{ip} &= 0 \qquad \text{if } i \neq p \end{aligned}\right\} \tag{3.30}$$

It is understood that the number of parameters generated by a given station for a given pass increases by 4 with each plate successfully recorded. Thus $\underset{(2,l)}{\underline{\underline{B}}_j}$ may range from a (2, 17) matrix for a single plate to a (2, 29) matrix for a set of four plates.

3.4.2.2 Normal Equations (Optical and Electronic)

We are now in a position to consider the formation of the normal equations for optical and electronic observations. We first form the normal equations for a given station and pass, ignoring the existence of other stations and other passes. If the covariance matrix of the random errors in plate coordinates and timing for the j^{th} point from the given station is denoted by

$$\underset{(3,3)}{\Lambda_j} = \begin{bmatrix} \sigma_{x_j}^2 & 0 & 0 \\ 0 & \sigma_{y_j}^2 & 0 \\ 0 & 0 & \sigma_{t_j}^2 \end{bmatrix}$$

$$\underline{\underline{A}}_j \underline{v}_j + \underline{\underline{B}}_j \underline{\delta} = \underline{\epsilon}_j \tag{3.27}$$

in which

$$\underset{(2,\,12+l)}{\underline{\underline{B}}_j} = -\left[\underset{(2,3)}{\underline{\underline{B}}_{pj}^{(1)}} \; \underset{(2,3)}{\underline{\underline{B}}_{pj}^{(2a)}} \; \underset{(2,6)}{\underline{\underline{B}}_{pj}^{(2b)}} \; \underset{(2,1)}{\underline{\underline{B}}_{pj}^{(3)}} \; \underset{(2,4)}{\underline{\xi}_{1p}\underline{\underline{B}}_{pj}^{(4)}} \; \underset{(2,4)}{\underline{\xi}_{2p}\underline{\underline{B}}_{pj}^{(4)}} \; \underset{(2,4)}{\underline{\xi}_{3p}\underline{\underline{B}}_{pj}^{(4)}} \; \underset{(2,4)}{\underline{\xi}_{4p}\underline{\underline{B}}_{pj}^{(4)}} \right] \tag{3.28}$$

$$\underset{(12+l,\,1)}{\underline{\delta}} = \left[\underset{(1,3)}{\underline{\delta}^{(1)T}} \; \underset{(1,3)}{\underline{\delta}^{(2a)T}} \; \underset{(1,6)}{\underline{\delta}^{(2b)T}} \; \underset{(1,2)}{\underline{\delta}^{(3)T}} \; \underset{(1,4)}{\underline{\delta}^{(4)T}} \; \underset{(1,4)}{\underline{\delta}^{(4)T}} \; \underset{(1,4)}{\underline{\delta}^{(4)T}} \; \underset{(1,4)}{\underline{\delta}^{(4)T}} \right]^T \tag{3.29}$$

the system of normal equations generated by the point can be expressed as

$$N_j\delta = c_j$$

in which

$$\left.\begin{aligned} &N_j = B_j^T (A_j \Lambda_j A_j^T)^{-1} B_j, \\ &\text{and, for optical observations,} \\ &N_j = \frac{1}{\sigma_{r_t}^2} B_j^T B_j \\ &c_j = B_j^T (A_j \Lambda_j A_j^T)^{-1} B_j \\ &\text{and, for electronic observations,} \\ &c_j = \frac{1}{\sigma_{r_t}^2} B_j^T B_j \end{aligned}\right\} \quad (3.31)$$

in which $\sigma_{r_t}^2$ denotes the expression $(\sigma_\tau^2 + r^2\sigma_\tau^2)^{1/2}$. It is to be noted that since

$$A_i \Lambda_j A_j^T = \begin{bmatrix} \sigma_{x_j}^2 + \dot{x}_j^2\sigma_{\tau_j}^2 & 0 \\ 0 & \sigma_{y_j}^2 + \dot{y}_j^2\sigma_{\tau_j}^2 \end{bmatrix}$$

the results of the multiplication by $(A_j \Lambda_j A_j)^{-1}$ can also be effected by treating this matrix as a unit matrix in equation (3.31) after modifying B_j and ϵ_j by dividing their first and second rows, respectively, by $(\sigma_{x_j}^2 + \dot{x}_j^2\sigma_{\tau_j}^2)^{1/2}$ and $(\sigma_{y_j}^2 + \dot{y}_j^2\sigma_{\tau_j}^2)^{1/2}$.

The system normal equation generated by all points from the given station pass is simply

$$N\delta = c$$

where

$N = \Sigma N_j$
$c = \Sigma c_j$

3.4.3 Reduction of Data From SECOR

(M. A. Warden, W. D. Googe, and R. W. Smith, DMA/TC)

3.4.3.1 Trilateration

The geometric solution is based on the assumption that coordinates of three stations in a four-station quadrilateral are known. Satellite coordinates are determined uniquely from the coordinates of three known stations and from three simultaneous ranges. Coordinates of the fourth (unknown) station are then developed from the assemblage of ranges of this station from the satellite. The solution takes the well-known form of

$$\Delta R_4 = \left[\sum_{i=1}^{n} (B_\theta^T B_\theta)_i\right]^{-1} \sum_{i=1}^{n} (B_\theta^T Y_\theta)_i$$

where

$$\Delta R_4 = \begin{bmatrix} \Delta X \\ \Delta Y \\ \Delta Z \end{bmatrix}_4$$

= corrections to the assumed coordinates of the unknown site

$$B_{\theta_i} = \left[\frac{\partial R_i}{\partial X_4} \frac{\partial R_i}{\partial Y_4} \frac{\partial R_i}{\partial Z_4}\right]$$

= partial derivatives of observables with respect to the unknown site coordinates

$Y_{\theta_i} = R_{m_i} - |\underline{R}_i - \underline{R}_4|$
= discrepancy
$\underline{R}_i$ = satellite coordinates
R_{m_i} = measured distance to the unknown site from the i^{th} position of the satellite
n = the number of satellite positions available for the adjustment
$\underline{R}_4$ = estimated coordinates of the unknown station

The summation includes all observations to the unknown station. After each summation, the correction is applied by

$$\underline{R}_4 = \underline{R}_4 + \Delta\underline{R}_4$$

3.4.3.2 Short-Arc Theory

A short-arc, batch, least-squares procedure was used for final adjustment of all data observed as part of the SECOR Equatorial Network. The basic range equation is

$$r_{t_j} = (\underline{R}_t\ (\underline{R}_0, \underline{V}_0) - \underline{P}_j)^2$$

where r_{t_j} is the range at time t measured from station j, $\underline{p}_j$ is the position vector of sta-

tion j and $\underline{R}_t = \underline{R}_t(\underline{R}_0, \underline{V}_0)$ is the position vector of the satellite at time t and as such is a function of the position $\underline{R}_0$ and velocity $\underline{V}_0$ of the satellite at initial epoch for the short arc in question. The short-arc, batch, least-squares procedure is developed as

$$\Delta\underline{X} = \left[\sum_{i=1}^{n} \underline{\underline{Q}}_i^T \underline{\underline{W}}_i \underline{\underline{Q}}_i\right]^{-1} \sum_{i=1}^{n} \underline{\underline{Q}}_i^T \underline{\underline{W}}_i Y_i \quad (3.32)$$

where

$$\underline{X} = \begin{bmatrix} \underline{R}_{0_1} \\ \underline{V}_{0_1} \\ \underline{R}_{0_2} \\ \cdot \\ \\ \\ \underline{R}_{0_n} \\ \underline{V}_{0_n} \\ \underline{P}_1 \\ \underline{P}_2 \\ \\ \\ \\ \underline{P}_m \end{bmatrix}$$

$\begin{bmatrix} \underline{R}_{0_j} \\ \underline{V}_{0_j} \end{bmatrix}$ = nominal orbital vectors for the j^{th} epoch where $j = 1,n$

$\begin{bmatrix} \underline{P}_j \end{bmatrix}$ = site coordinates where $j = 1,m$

$\underline{X}$ = estimated state vector

$\Delta\underline{X}$ = correction to state vector

$\underline{\underline{W}}_i$ = weight matrix of the i^{th} observation $= 1/\sigma_{\theta_i}^2$ where σ_{θ_i} is the estimated standard deviation

$\underline{\underline{Q}}_i$ = matrix of partial derivatives of the observables with respect to the elements of the state vector

$Y_i = \theta_{m_i} - \theta_{i_i}$ = discrepancy between measured and computed observations

θ_i = observation at the time t

$i = 1,n$ observations in the adjustment

In the short-arc, batch, least-squares procedure, orbit-to-orbit correlation is neglected; however, the cumulative site-to-orbit correlation is maintained. Also the short-arc, batch, least-squares procedure allows an adjustment of more than four ground stations. The procedure is begun by setting

$$\Delta X = \left[\sum_{i=1}^{n} \underline{\underline{Q}}_i^T \underline{\underline{W}}_i \underline{\underline{Q}}_i + \underline{\underline{W}}_0^{-1}\right]^{-1} \sum_{i=1}^{n} \underline{\underline{Q}}_i^T \underline{\underline{W}}_i Y_i$$

where

$$\underline{\underline{W}}_0 = \begin{bmatrix} \sigma^2_{\underline{R}_0 V_{01}} & 0 & 0 & 0 & \cdots & 0 \\ 0 & \sigma^2_{\underline{R}_0 V_{02}} & 0 & 0 & & 0 \\ \cdot & \cdot & \cdot & \cdot & & \cdot \\ \cdot & \cdot & \cdot & \cdot & & \cdot \\ \cdot & & \cdot & \cdot & & \\ 0 & 0 \cdots & \sigma^2_{\underline{R}_0 V_{0n}} & 0 & \cdots & 0 \\ 0 & 0 \cdots & 0 & \sigma^2_{\underline{P}_1} & 0 \cdots & 0 \\ \cdot & & & & & \\ \cdot & & & & & \\ \cdot & & & & & \\ 0 & 0 \cdots & 0 & 0 & \sigma^2_{\underline{P}_2} \cdots & 0 \\ \cdot & \cdot & \cdot & \cdot & \cdot & \cdot \\ \cdot & \cdot & \cdot & \cdot & \cdot & \cdot \\ \cdot & \cdot & \cdot & \cdot & \cdot & \cdot \\ 0 & 0 \cdots & 0 & 0 & 0 \cdots & \sigma^2_{\underline{P}_m} \end{bmatrix}$$

The coefficients of the normal equations are

$$\underline{\underline{N}}(t_i) = \sum_{i=1}^{n} \underline{\underline{Q}}_i^T \underline{\underline{W}}_i \underline{\underline{Q}}_i + \underline{\underline{W}}_0^{-1}$$

and the covariance matrix is

$$\underline{\underline{C}}(t_i) = \underline{\underline{N}}(t_i)^{-1}$$

The structure of $\underline{\underline{N}}$ determines the correlation carried in the adjustment. $\underline{\underline{N}}$ has the form

$$\underline{\underline{N}} = \begin{bmatrix} I & 0 \cdots & 0 & \underline{\underline{B}}_{11} & \underline{\underline{B}}_{12} & \cdots & \underline{\underline{B}}_{1m} \\ 0 & I_2 \cdots & 0 & \underline{\underline{B}}_{21} & \underline{\underline{B}}_{22} & \cdots & \underline{\underline{B}}_{2m} \\ \cdot & \cdot \ \cdot & \cdot & \cdot & \cdot & & \\ \cdot & \cdot \quad \cdot & \cdot & \cdot & \cdot & & \\ \cdot & \cdot \quad \cdot & \cdot & \cdot & \cdot & & \\ 0 & 0 & I_n & \underline{\underline{B}}_{n1} & \underline{\underline{B}}_{n2} & \cdots & \underline{\underline{B}}_{nm} \\ \underline{\underline{B}}^T_{11} & \underline{\underline{B}}^T_{21} \cdots & \underline{\underline{B}}^T_{n1} & \underline{\underline{S}}_1 & 0 & \cdots & 0 \\ \underline{\underline{B}}^T_{12} & \underline{\underline{B}}^T_{22} \cdots & \underline{\underline{B}}^T_{n2} & 0 & \underline{\underline{S}}_2 & & 0 \\ \cdot & & & \cdot & & \cdot & \cdot \\ \cdot & & & \cdot & & \cdot & \cdot \\ \cdot & & & \cdot & & \cdot & \cdot \\ \underline{\underline{B}}^T_{1m} & \underline{\underline{B}}^T_{2m} & \underline{\underline{B}}^T_{nm} & 0 & 0 & & \underline{\underline{S}}_m \end{bmatrix}$$

The correlation terms $\underline{\underline{B}}_{ij}$ will be nonzero when the particular station tracks the corresponding orbit. Off-diagonal terms in the $\underline{\underline{I}}$ matrix portions are zero because each orbit is assumed to be independent. Off-diagonal terms in the $\underline{\underline{S}}$ matrices are zero because the observations are made via the satellite rather than from site to site, as would be the case with land surveys.

The short-arc, batch, least-squares procedure used here is iterative. After each iteration the increment $\Delta\underline{X}$ is applied to the state vector $\underline{X}$ and the procedure is repeated; hence

$$\underline{X}_L = \underline{X}_{L-1} + \Delta\underline{X}_L$$

where L is the number of the iteration.

Once a correction adjustment $\Delta\underline{X}$ is applied to $\underline{X}_{L-1}$, the new state vectors $\underline{X}_L$ are used in the next set of computations.

3.4.3.2.1 INTEGRATION OF EQUATIONS OF MOTION

The total acceleration of a satellite can be represented as

$$\frac{d^2\underline{R}}{dt^2} = \nabla U + \underline{A}_G + \cdots \qquad (3.33)$$

where ∇U is the two-body attraction and $\underline{A}_G$ are the higher order terms in the accelerations caused by the earth's gravitational field. Other forces (e.g., drag, radiation pressure) are not considered for the short-arc orbit integration procedure, since the effects of these are primarily of long period.

The general solution of equation (3.33) cannot be obtained in closed form. However, the equation may be partitioned as follows

$$\left.\begin{aligned} \frac{d^2\underline{R}_T}{dt^2} &= \nabla U \\ \frac{d^2\Delta\underline{R}}{dt^2} &= \underline{A}_P \\ \underline{A}_P &= \underline{A}_G \end{aligned}\right\} \qquad (3.34)$$

Now, equation (3.34) is the two-body equation whose solution may be expressed as

$$\underline{R}_T(t_2) = f_1(t_1, t_2)\,\underline{R}_T(t_1) + g_1(t_1, t_2)\,\underline{v}_T(t_1) \qquad (3.35)$$

$$v_T(t_2) = f_2(t_1, t_2)\,\underline{R}_T(t_1) + g_2(t_1, t_2)\,\underline{v}_T(t_1) \qquad (3.36)$$

where $\underline{R}_T$ is the location vector and $\underline{v}_T$ is the velocity vector. The solution for $\Delta\underline{R}$ is found numerically as follows:

(1) $\underline{R}_T(t_0+\Delta t)$, $\underline{v}_T(t_0+\Delta t)$ are calculated by means of equations (3.35) and (3.36).

(2) The perturbationary acceleration, $\underline{A}_p$, is calculated at t_0 by using $\underline{R}_T(t)$, $\underline{v}_0(t)$ and at $t+\Delta t$ by using $\underline{R}_T(t+\Delta t)$, $\underline{v}_T(t+\Delta t)$.

(3) $\Delta\underline{R}\ (t_0+\Delta t)$, $\underline{v}(t_0+\Delta t)$ are calculated from

$$\Delta\underline{R}\ (t_0+\Delta t) = \frac{\Delta t^2}{6}\left[2\,\underline{A}_p(t_0) + \underline{A}_p(t_0+\Delta t)\right]$$

$$\Delta\underline{v}\,(t_0+\Delta t) = \frac{\Delta t}{2}\left[A_p(t_0) + A_p(t_0+\Delta t)\right]$$

The position at $t_0+\Delta t$ is then

$$\underline{R} = \underline{R}_T + \Delta\underline{R}$$

$$\underline{v} = \underline{v}_T + \Delta\underline{v}$$

Implicit in the calculations of step (3) is the assumption that the perturbating accelerations may be approximated by a linear function over the rectification interval, Δt.

In fact, the rectification interval must be chosen to make this assumption valid if no significant error buildup is to occur. For purposes of predicting the positions of a satellite in a near circular orbit, the rectification interval is held constant (normally 5 sec).

3.4.3.2.2 PARTIAL DERIVATIVES OF THE OBSERVABLES

The procedure used here requires the evaluation of the partial derivatives of the observables with respect to the position and velocity components of a satellite. For con-

venience, the partial differentiation operators are defined as

$$\nabla_{OBS}=\begin{bmatrix}\frac{\partial_{OBS}}{\partial X}\\ \frac{\partial_{OBS}}{\partial Y}\\ \frac{\partial_{OBS}}{\partial Z}\end{bmatrix}=\frac{\partial\theta}{\partial\underline{R}}$$

$$\dot{\nabla}_{OBS}=\begin{bmatrix}\frac{\partial_{OBS}}{\partial \dot{X}}\\ \frac{\partial_{OBS}}{\partial \dot{Y}}\\ \frac{\partial_{OBS}}{\partial \dot{Y}}\end{bmatrix}=\frac{\partial\theta}{\partial\underline{V}}$$

where X, Y, Z, $\dot{X}$, $\dot{Y}$, $\dot{Z}$ are the components of the satellite position and velocity described in a topocentric coordinate system.

The partial derivatives of the range r_{t_j} with respect to X, Y, Z, $\dot{X}$, $\dot{Y}$, $\dot{Z}$ at the time of the observation are

$$\nabla r=\frac{1}{r}(R_T-P_j)=\hat{R}$$

$$\dot{\nabla} r=0$$

The partial derivatives of the range r_{t_j} with respect to the station position P_j are

$$\frac{\partial\theta}{\partial P_j}=\frac{\partial r_{t_j}}{\partial P_j}=-\nabla R=-\hat{\underline{R}}$$

3.4.4 Doppler

(R. J. Anderle, NWL)

3.4.4.1 Organization of Computations

The principal parameters of recent general geodetic solutions include 450 gravitational coefficients and 150 components of positions of observing stations. Incidental parameters include thousands of orbital constants, pole positions, and instrument bias parameters. In order to reduce the problem to manageable size without loss of accuracy, the normal equations are considered to have parameters of two types: geodetic parameters $\mathbf{P}_G$ and bias parameters $\mathbf{P}_B$. The normal equations are then partitioned as follows:

$$\begin{bmatrix}[B_G] & [A]\\ [A^*] & [B_B]\end{bmatrix}\begin{bmatrix}\mathbf{P}_G\\ \mathbf{P}_B\end{bmatrix}=\begin{bmatrix}\mathbf{E}_G\\ \mathbf{E}_B\end{bmatrix} \quad (3.37)$$

Operation on these equations yields

$$[B_G]\mathbf{P}_G=\mathbf{E}_G-[A]\mathbf{P}_B \quad (3.38a)$$

$$\mathbf{P}_B=[B_B^{-1}](\mathbf{E}_B-[A^*]\mathbf{P}_G) \quad (3.38b)$$

so that

$$[B'_G]\mathbf{P}_G=\mathbf{E}'_G \quad (3.39a)$$

where

$$[B'_G]=[B_G]-[A][B_B^{-1}][A^*] \quad (3.39b)$$

$$\mathbf{E}'_G=\mathbf{E}_G-[A][B_B^{-1}]\mathbf{E}_B \quad (3.39c)$$

The weighted residuals for the solution are

$$\mathbf{R}^{s*}[W]\mathbf{R}^s=\mathbf{R}^*[W]\mathbf{R}-\mathbf{P}_B^*\mathbf{E}_B-\mathbf{P}_G^*\mathbf{E}_G \quad (3.40a)$$

$$=\mathbf{R}^*[W]\mathbf{R}-\mathbf{E}_B^*[B_B^{-1}]\mathbf{E}_B-\mathbf{P}_G^*\mathbf{E}'_G \quad (3.40b)$$

When $\mathbf{P}_B$ are considered to be instrumental biases, then $[B_B]$ is block diagonal when partitioned according to the instrumental biases in each pass. Therefore, the normal equations can be formed and accumulated on a pass-by-pass basis for a given set of orbital constants, where the orbit constants are considered part of the $\mathbf{P}_G$ parameter set for the moment. The weighted residuals are adjusted by the second term of the last equation. A series of such matrices is generated for various spans of data and is stored in a library. Periodically, the stored matrices are combined. In order to permit processing of data for an unlimited number of time spans, the orbital constants are eliminated and the weighted residuals are again adjusted, where now the orbital constants are considered to be $\mathbf{P}_B$; that is, $[B_B]$ is block diagonal when partitioned according to the set of orbital constants (including the pole position) for a given span of data. Orbital constants are obtained by back substitution in the normal equations saved for each span of data. Instrumental biases can only be obtained by reintegration of the orbit using the improved

geodetic and orbital parameters, because the partitions of the matrix corresponding to instrument biases are not saved.

3.4.4.2 Reference Frames and Constants

The reference frame used in integrating the equations of motion for a given span of data is an inertial frame defined by mean equator and equinox at zero hours on the first day of data. The Earth's gravity field is rotated to this frame from a frame aligned with the instantaneous axis of the Earth's rotation. In the course of calculating residuals, the coordinates are rotated from the inertial frame to an Earth-fixed frame oriented with respect to the CIO pole. Transformation from the inertial to the Earth-fixed frame is performed by successive matrix multiplications

$$\mathbf{r}' = [A][B][C][D]\mathbf{r}$$

where $\mathbf{r}'$ are the Earth-fixed coordinates, $\mathbf{r}$ are the inertial coordinates, the $[D]$ matrix corrects for precession, the $[C]$ matrix introduces nutation, the $[B]$ matrix accounts for rotation about the spin axis, and $[A]$ corrects for the polar motion. The time argument for the integration is taken to be UT2 in the geodetic solution, although ephemeris time would have been a better choice. The appropriate value of (UT2–UT1) is used in computing station positions in inertial space; therefore the difference in the ET rate and UT2 rate is equivalent to a trivial error in GM, the balance of the difference being absorbed in the arbitrary orbit constants. The elements for the matrices $[B]$, $[C]$, and $[D]$ are obtained from the American Ephemeris and Nautical Almanac and its supplement. Initial values for the pole position are taken from Circulaire D of Bureau International de l'Heure (BIH). Corrections to the pole positions provided by the BIH are also parameters of the solution, but the BIH values are taken as a priori data and are assigned an accuracy of 1 meter. The corrections are considered constant for the length of the arc, which is at most 16 days.

3.4.4.3 Force and Perturbation Equations

3.4.4.3.1 GENERAL EQUATIONS OF MOTION AND PERTURBATION EQUATIONS

The equations of motion may be expressed as

$$\ddot{\mathbf{r}} = \mathbf{G}_E + \mathbf{D}_g + \mathbf{G}_m + \mathbf{G}_s + \mathbf{R}_p + \mathbf{T}_m + \mathbf{T}_s$$

Contributions to the force terms arise from

$\mathbf{G}_E$	gravitational field of the Earth
$\mathbf{G}_m$	gravitational field of the Moon
$\mathbf{G}_s$	gravitational field of the Sun
$\mathbf{D}_g$	atmospheric drag
$\mathbf{R}_p$	radiation pressure
$\mathbf{T}_m$	tidal distortion due to the Moon
$\mathbf{T}_s$	tidal distortion due to the Sun

The maximum numbers of force parameters are about 500 in $\mathbf{G}_E$, 10 in $\mathbf{D}_g$, three in $\mathbf{R}_p$, and one to correct Love's number, K_L. (In addition there are six parameters corresponding to the orbital elements, two parameters to correct the nominal pole position, and two arc parameters to account for the dominant effect of higher order resonance gravitational coefficients.)

The pertubational equations are given by

$$\ddot{\boldsymbol{\xi}}_k = \left[\frac{\partial \ddot{\mathbf{r}}}{\partial \mathbf{r}^*}\right]\boldsymbol{\xi}_k + \left[\frac{\partial \ddot{\mathbf{r}}}{\partial \dot{\mathbf{r}}^*}\right]\dot{\boldsymbol{\xi}}_k + \frac{\partial \ddot{\mathbf{r}}}{\partial p_k}$$

where

$$\boldsymbol{\xi} = \frac{\partial \mathbf{r}}{\partial p_k}, \quad \ddot{\boldsymbol{\xi}} = \frac{\partial^2 \boldsymbol{\xi}}{\partial t^2}, \quad \dot{\mathbf{r}} = \frac{\partial \mathbf{r}}{\partial t}, \quad \ddot{\mathbf{r}} = \frac{\partial^2 \mathbf{r}}{\partial t^2},$$

and p_k refers to the k^{th} parameter.

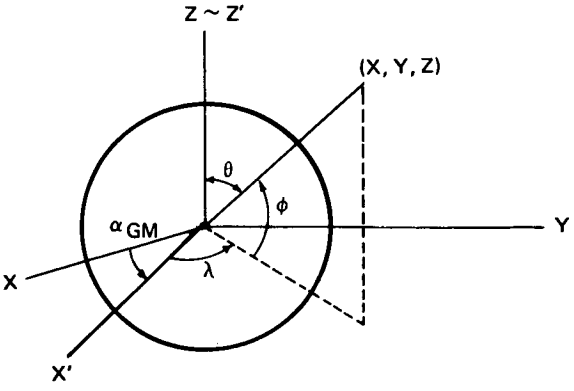

3.4.4.3.2 GRAVITATIONAL FIELD CONTRIBUTION FROM THE EARTH

We write the Earth's potential in an Earth-fixed coordinate frame (x', y', z') as

$$V=\frac{GM}{a_e}\sum_{n=0}^{N}(a_e/r)^{n+1}\sum_{m=0}^{n}P_n^m(\sin\psi)\ (C_n^m\cos m\lambda+S_n^m\sin m\lambda)$$

where a_e is the Earth's radius, $z'/r=\sin\psi$, where ψ is the geocentric latitude, λ is longitude with respect to Greenwich meridian, and

$$r=(x^2+y^2+z^2)^{1/2}=(x'^2+y'^2+z'^2)^{1/2}$$

The contributions to the force terms are obtained from

$$\mathbf{G}_E=\frac{\partial V}{\partial \mathbf{r}}$$

We write

$$V=\sum_{n=0}^{N}\sum_{m=0}^{n}[C_n^mU_n^m+S_n^mV_n^m]\qquad n\neq 1$$

where

$$U_n^m=\frac{GMa_e^n\,P_n^m\left(\frac{z'}{r}\right)\cos m\lambda}{r^{n+1}}$$

$$V_n^m=\frac{GMa_e^n\,P_n^m\left(\frac{z'}{r}\right)\sin m\lambda}{r^{n+1}}$$

α_{GM} is the rotation of the Greenwich meridian from the reference equinox used in forming $[B]$. We recall that the inertial coordinate system is based upon the mean pole and equinox for the starting time of the arc, t_0. We use

$$\alpha_{GM}=H_0+\dot{H}t_0+\bar{\omega}t$$

where H_0 is the hour angle of the vernal equinox at the start of the current year, $\dot{H}$ is the rate of change of hour angle, and $\bar{\omega}$ is the mean angular rotation velocity of the Earth.

3.4.4.3.3 EVALUATION OF U_n^m, V_n^m RECURRENCE RELATIONS

The recurrence relations obtained by R. N. DeWitt in 1962 are used to evaluate spherical harmonics. The procedure calls for repetitions of horizontal stepping followed by a diagonal step. (See fig. 3.26.)

Horizontal stepping:

$$U_{n+1}^m=\frac{\rho}{(n-m+1)}\rho[E_3]\mathbf{r}\,(2n+1)\,U_n^m-(n+m)\,\rho U_{n-1}^m$$

$$V_{n+1}^m=\frac{\rho}{(n-m+1)}\rho[E_3]\mathbf{r}\,(2n+1)\,V_n^m-(n+m)\,\rho V_{n-1}^m$$

where $[E_3]$ is the third row of $[E]$.

We note that $V_n^o=0$, $C_1^1=S_1^1\equiv 0$. The longitude is introduced through

$$C(\lambda)=\cos\psi\cos\lambda=\frac{a_e}{r}[E_1]\cdot\bar{r}'\qquad S(\lambda)=\cos\psi\sin\lambda=\frac{a_e}{r}[E_2]\cdot\bar{r}'$$

where $[E_1]$ and $[E_2]$ are the first two rows of

$$E=\frac{B}{a_e}CD\qquad C=\begin{bmatrix}1-\frac{\Delta\psi^2}{2} & -\Delta\psi\cos\epsilon & -\Delta\psi\sin\epsilon\\ \Delta\psi(\cos\epsilon-\Delta\epsilon\sin\epsilon) & 1-\frac{\Delta\epsilon^2}{2}-\frac{\Delta\psi^2}{2}\cos^2 & \epsilon-\Delta\epsilon-\frac{\Delta\psi^2}{2}\sin\epsilon\cos\epsilon\\ \Delta\psi(\sin\epsilon+\Delta\epsilon\cos\epsilon) & \Delta\epsilon-\frac{\Delta\psi^2}{2}\sin\epsilon\cos & \epsilon\,1-\frac{\Delta\epsilon^2}{2}-\frac{\Delta\psi^2}{2}\sin^2\epsilon\end{bmatrix}$$

and the $[B]$ and $[D]$ were defined earlier.

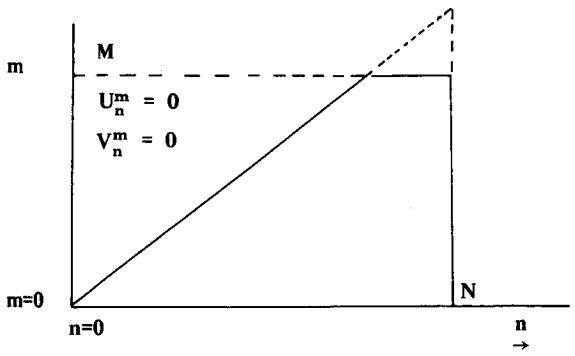

FIGURE 3.26.—Horizontal/diagonal stepping.

Diagonal stepping:

$$U_{n+1}^{n+1} = (2n+1)\rho[U_n^n C(\lambda) - V_n^n S(\lambda)]$$
$$V_{n+1}^{n+1} = (2n+1)\rho[V_n^n C(\lambda) - U_n^n S(\lambda)]$$

where

$$\rho = \frac{a_e}{r}$$

Using the values

$$U_0^0 = \frac{a_e}{r},\quad U_1^0 = \frac{GMa_e(a_e[E_3]\mathbf{r})}{r^3},\quad V_0^0 = 0,\quad V_1^0 = 0$$

we start at $n=1$, $m=0$ in the horizontal stepping equation and compute U_1^0, V_1^0 for $i=2, 3, \ldots, N$. We then utilize diagonal stepping, and calculate U_1^1, V_1^1. Returning to horizontal stepping enables calculation of U_1^i, V_1^i for $i=2, 3, \ldots, N$. This process is repeated until $m=M$, where $M \leq N$.

We note that

$$U_n^{-m} = \frac{(-1)^m (n-m)!}{(n+m)!} U_n^m$$

and

$$V_n^{-m} = \frac{(-1)^{m+1} (n-m)!}{(n+m)!} V_n^m$$

3.4.4.3.4 EVALUATION OF DERIVATIVES OF U_n^m, V_n^m

We use the notation

$$\mathbf{G}_E = \bar{\nabla}_R V$$

and define the rotation matrix

$$[R_\omega] = [E^*]$$

where the gradient operator $\bar{\nabla}_R$ is defined to take into account the rotation of the Earth. We use

$$\bar{\nabla}_R V = [R_\omega] \sum_{n=0}^{N} \sum_{m=0}^{n} (C_n^m a_e \bar{\nabla} U_n^m + S_n^m a_e \bar{\nabla} V_n^m)$$

($\bar{\nabla} U_n^m$ and $\bar{\nabla} V_n^m$ refer to Earth-fixed coordinates.)

The recurrence relations for $\partial U_n^m / \partial \mathbf{r}^*$ are obtained from

$$a_e \bar{\nabla} U_n^m = \begin{bmatrix} \frac{1}{2} A_n^m V_{n+1}^{m-1} - \frac{1}{2} U_{n+1}^{m+1} \\ -\frac{1}{2} A_n^m V_{n+1}^{m-1} - \frac{1}{2} V_{n+1}^{m+1} \\ -(n-m+1) U_{n+1}^m \end{bmatrix}$$

$$A_n^m = (n-m+1)(n-m+2)$$

and similarly

$$a_e \bar{\nabla} V_n^m = \begin{bmatrix} \frac{1}{2} A_m^n V_{n+1}^{m-1} - \frac{1}{2} V_{n+1}^{m+1} \\ \frac{1}{2} A_n^m U_{n+1}^{m-1} + \frac{1}{2} U_{n+1}^{m+1} \\ -(n-m+1) V_{n+1}^m \end{bmatrix}$$

$$\mathbf{G}_E = [R_\omega] \sum_{n=0}^{N} \sum_{m=0}^{n} C_n^m a_e \frac{\partial U_n^m}{\partial \mathbf{r}^*} + S_n^m a_e \frac{\partial V_n^m}{\partial \mathbf{r}^*}$$
$$= [R_\omega] \sum_{n=0}^{N} \sum_{m=0}^{N} C_n^m a_e \boldsymbol{\pi}_n^m + S_n^m a_e \boldsymbol{\Theta}_n^m$$

3.4.4.3.5 EVALUATION OF DERIVATIVES OF $\mathbf{G}_E$

The matrix of gradients is obtained from

$$\left[\frac{\partial \mathbf{G}_E}{\partial \mathbf{r}^*}\right] = [R_\omega]\left[\sum_{n=0}^{N} \sum_{m=0}^{N} \left(C_n^m a_e^2 \frac{\partial \boldsymbol{\pi}_n^m}{\partial \mathbf{r}^*} + S_n^m a_e^2 \frac{\partial \boldsymbol{\Theta}_n^m}{\partial \mathbf{r}^*}\right)\right][R_\omega^*]$$

where

$$a_e^2\left[\frac{\partial \boldsymbol{\pi}_n^m}{\partial \mathbf{r}^*}\right]=\begin{bmatrix} \tfrac{1}{2}A_n^m a_e\dfrac{\partial U_{n+1}^{m-1}}{\partial \mathbf{r}^*}-\tfrac{1}{2}a_e\dfrac{\partial U_{n+1}^{m+1}}{\partial \mathbf{r}^*} \\ -\tfrac{1}{2}A_n^m a_e\dfrac{\partial V_{n+1}^{m-1}}{\partial \mathbf{r}^*}-\tfrac{1}{2}a_e\dfrac{\partial V_{n+1}^{m+1}}{\partial \mathbf{r}^*} \\ -(n-m+1)\,a_e\dfrac{\partial U_{n+1}^{m}}{\partial \mathbf{r}^*} \end{bmatrix}$$

$$a_e^2\left[\frac{\partial \boldsymbol{\Theta}_n^m}{\partial \mathbf{r}^*}\right]=\begin{bmatrix} \tfrac{1}{2}A_n^m a_e\dfrac{\partial V_{n+1}^{m-1}}{\partial \mathbf{r}^*}-\tfrac{1}{2}a_e\dfrac{\partial V_{n+1}^{m+1}}{\partial \mathbf{r}^*} \\ \tfrac{1}{2}A_n^m a_e\dfrac{\partial U_{n+1}^{m-1}}{\partial \mathbf{r}^*}+\tfrac{1}{2}a_e\dfrac{\partial U_{n+1}^{m+1}}{\partial \mathbf{r}^*} \\ -(n-m+1)\,a_e\dfrac{\partial V_{n+1}^{m}}{\partial \mathbf{r}^*} \end{bmatrix}$$

The derivatives for U's and V's are obtained from the recurrence relations given earlier.

For $p_k=C_r^s$ or S_r^s

$$\frac{\partial \mathbf{G}_E}{\partial p_k}=[R_\omega]\,\boldsymbol{\pi}_r^s \text{ or } [R_\omega]\,\boldsymbol{\Theta}_r^s, \text{ respectively}$$

but

$$p_k\neq C_r^s \text{ or } S_r^s, \qquad \frac{\partial \mathbf{G}_E}{\partial p_k}=0$$

3.4.4.3.6 EVALUATION OF SOLAR AND LUNAR GRAVITATIONAL TERMS

The solar terms are as follows:

$$\mathbf{G}_s=-GM_s\left(\frac{\mathbf{r}-\mathbf{r}_s}{|\mathbf{r}-\mathbf{r}_s|^3}+\frac{\mathbf{r}_s}{|\mathbf{r}_s|^3}\right)$$

where

$$r_s^2=x_s^2+y_s^2+z_s^2$$

and GM_s is an input gravitational constant for the Sun.

The Sun's coordinates, x_s, y_s, z_s are supplied on tape at one-day intervals. A sixth-order Lagrangian interpolation is used to evaluate current coordinates. Exactly analogous procedures apply for the Moon. The Moon's coordinates are supplied on the coordinate tape at half-day intervals and a similar interpolation formula is applied.

3.4.4.3.7 EVALUATION OF DERIVATIVES OF $\mathbf{G}_s$ AND $\mathbf{G}_m$

Setting $P_s^2=(x-x_s)^2+(y-y_s)^2+(z-z_s)^2$, the derivatives are given by the following formulas:

$$\frac{\partial G_{sx}}{\partial \mathbf{r}}=-\frac{GM_s}{p_s^5}\begin{bmatrix} -3(x-x_s)^2+p_s^2 \\ -3(x-x_s)(y-y_s) \\ -3(x-x_s)(z-z_s) \end{bmatrix}$$

$$\frac{\partial G_{sy}}{\partial \mathbf{r}}=-\frac{GM_s}{p_s^5}\begin{bmatrix} -3(x-x_s)(y-y_s) \\ -3(y-y_s)^2+p_s^2 \\ -3(z-z_s)(y-y)_s \end{bmatrix}$$

$$\frac{\partial G_{sz}}{\partial \mathbf{r}}=-\frac{GM_s}{p_s^5}\begin{bmatrix} -3(x-x_s)(z-z_s) \\ -3(y-y_s)(z-z_s) \\ -3(z-z_s)^2+p_s^2 \end{bmatrix}$$

$$\frac{\partial \mathbf{G}_s}{\partial p_k}=0 \qquad \text{for all } p_k$$

Similar expressions apply for lunar terms.

3.4.4.3.8 EVALUATION OF DRAG CONTRIBUTION

The relative velocity of the satellite with respect to the atmosphere is

$$\mathbf{v}_r=\dot{\mathbf{r}}-\boldsymbol{\omega}\times\mathbf{r}\approx\begin{pmatrix}\dot{x}+\omega y\\ \dot{y}-\omega x\\ \dot{z}\end{pmatrix}$$

where ω is the average angular velocity of Earth's rotation with $\omega=|\boldsymbol{\omega}|$.

The acceleration of the satellite due to drag is the vector

$$\mathbf{D}=-\gamma\rho\frac{s}{2m}|\mathbf{v}_r|\mathbf{v}_r$$

in which s is the cross-section area and m the mass of the satellite, ρ is the upper atmosphere air density taken from

$$\rho=\exp\{Ah-B-\sqrt{Ch^2+Dh-E}\}$$

and the height of the satellite above Earth is

$$h=r\left\{1-\frac{a_e}{\sqrt{r^2+\dfrac{e^2}{1-e^2}z^2}}\right\}$$

where e and a_e are the eccentricity and semi-major axis of the reference ellipsoid.

The effective coefficient of drag is in step form, γ_i, $i=1, \ldots n \leq 10$, where the values are entries of a table separated by given times t_i of drag break.

3.4.4.3.9 EVALUATION OF DERIVATIVES OF THE DRAG ACCELERATION

Noting that drag acceleration is an explicit function of $\mathbf{v}_r$ and other positionally dependent quantities, we write

$$\frac{\partial \mathbf{D}}{\partial \mathbf{r}^*}=\left(\boldsymbol{\omega}\times\frac{\partial \mathbf{D}}{\partial \dot{\mathbf{r}}^*}\right)^*-|\mathbf{v}_r|\mathbf{v}_r\frac{\partial}{\partial \mathbf{r}^*}\left(\frac{|\mathbf{D}|}{|\mathbf{v}_r|^2}\right)$$

or using

$$\frac{1}{\rho}\frac{\partial \rho}{\partial h}=A+\frac{Ch+D/2}{\sqrt{Ch^2+Dh-E}}$$

and

$$\mathbf{w}=\frac{|\mathbf{D}|}{|\mathbf{v}_r|}\left\{\frac{1}{\rho}\frac{\partial \rho}{\partial h}\left[\left(1-\left(1-\frac{h}{r}\right)^3\frac{z^2}{a^2}\frac{e^2}{1-e^2}\right)\frac{\mathbf{r}}{|r|}+\left(1-\frac{h}{r}\right)^3\frac{rz}{a_e^2}\frac{e^2}{1-e^2}\begin{pmatrix}0\\0\\1\end{pmatrix}\right]\right\}$$

the positional gradient of the drag acceleration is then a matrix whose three rows are

$$\frac{\partial D_x}{\partial \mathbf{r}}=-\frac{|\mathbf{D}|\omega}{|\mathbf{v}_r|^3}\begin{pmatrix}-v_{rx}v_{ry}\\ [v_{rx}]^2+[\mathbf{v}_r]^2\\ 0\end{pmatrix}-v_{rx}\mathbf{w}$$

$$\frac{\partial D_y}{\partial \mathbf{r}}=-\frac{|D|\omega}{|v_r|^3}\begin{pmatrix}-[v_{ry}]^2-|v_r|^2\\ v_{rx}v_{ry}\\ 0\end{pmatrix}-v_{ry}\mathbf{w}$$

$$\frac{\partial D_z}{\partial \mathbf{r}}=-\frac{|D|\omega}{|\mathbf{v}_r|^3}\begin{pmatrix}-v_{ry}v_{rz}\\ v_{ry}v_{rx}\\ 0\end{pmatrix}-v_{rz}\mathbf{w}$$

The velocity gradient is more simply expressed as the symmetric matrix

$$\frac{\partial D}{\partial \dot{\mathbf{r}}^*}=-\frac{|\mathbf{D}|}{|\mathbf{v}_r|}\left(1+\frac{\mathbf{v}\mathbf{v}^*}{|\mathbf{v}|^2}\right)$$

$$=-\frac{|\mathbf{D}|}{|\mathbf{v}_r|^3}\begin{pmatrix}|v_r|^2+[v_{rx}]^2 & v_{rx}v_{ry} & v_{rx}v_{rz}\\ v_{rx}v_{ry} & |v_r|^2+[v_{ry}]^2 & v_{ry}v_{rz}\\ v_{rx}v_{rz} & v_{ry}v_{rz} & |v_r|^2+[v_{rz}]^2\end{pmatrix}$$

For the parameter derivatives we note that all vanish except those for the current drag constant. With subscript implied, these are

$$\frac{\partial D}{\partial \rho}=-\rho\frac{s}{2M}|v_r|\mathbf{v}_r$$

To allow for possible negative effective drag acceleration coefficient in these formulas use

$$|\mathbf{D}|=\gamma\rho\frac{s}{2m}|\mathbf{v}_r|^2$$

3.4.4.3.10 CALCULATION OF RADIATION PRESSURE TERM

Radiation pressure is calculated from the formula

$$\mathbf{R}_p=-\frac{K_R}{m}\frac{\mathbf{r}_s-\mathbf{r}}{|\mathbf{r}_s-\mathbf{r}|^3}\qquad\text{when sunlit}$$

$$\mathbf{R}_p=0\qquad\text{in Earth's shadow}$$

K_R is the radiation parameter.

3.4.4.3.11 EVALUATION OF DERIVATIVES OF RADIATION PRESSURE

The derivatives of $\mathbf{R}_p$ are almost identical with those of $\mathbf{G}_{(S)}$ with GM_s replaced by K_R. However, we also have the requirement

$$\frac{\partial \mathbf{R}_p}{\partial \mathbf{r}^*}=0 \text{ in the shadow}$$

Also, we have

$$\frac{\partial \mathbf{R}_p}{\partial p_k}=\frac{\mathbf{R}_p}{K_{R_m}}$$

if $p_k=K_{R_m}$ $m=1, 2, \ldots 6$

but

$$\frac{\partial \mathbf{R}_p}{\partial p_k}=0 \text{ in shadow}$$

3.4.4.3.12 TIDES AND TIDAL DERIVATIVES

The differential gravitational (tidal) attraction of the Sun or Moon causes the

Earth to become elongated on an axis pointing toward the disturbing body. This redistribution of mass results in a perturbation of the Earth's own gravitational field, which can be represented by potentials.

$$U_s = -k_L \frac{GM_s}{r_s^3}\frac{a_e^5}{r^3}P_2(\mathbf{r}^*\mathbf{r}_s)$$

$$U_m = -k_L \frac{GM_s}{r_m^3}\frac{a_e^5}{r^3}P_2(\mathbf{r}^*\mathbf{r}_m)$$

where k_L is Love's constant, presumed equal for both solar and lunar effects, and P_2 is the Legendre polynomial. The associated force, obtained by differentiation, is

$$\mathbf{T}_s = \frac{\partial \mathbf{T}_s}{\partial k_L}k_L$$

$$\frac{\partial \mathbf{T}_s}{\partial k_L} = \frac{GM_s}{r_s^3}\frac{a_e^5}{r^5}\left(\left(-\frac{15}{2}\left(\frac{\mathbf{r}^*\mathbf{r}_s}{rr_s}\right)^2+\frac{3}{2}\right)\mathbf{r}+3\left(\frac{\mathbf{r}^*\mathbf{r}_s}{rr_s}\right)\mathbf{r}_s\right)$$

The lunar term is identical with subscript m for s. The force gradient contribution is

$$\frac{\partial \mathbf{T}_s}{\partial \mathbf{r}^*} = -\frac{k_L}{2}\frac{GM_s}{r_s^3}\frac{a_e^5}{r^5}\left[\left(3-15\left(\frac{\mathbf{r}^*\mathbf{r}_s}{rr_s}\right)^2\right)I+6\frac{\mathbf{r}_s\mathbf{r}_s^*}{r_s^2}\right.$$
$$\left.+\left(105\left(\frac{r^*r_s}{rr_s}\right)-15\right)\frac{\mathbf{r}\mathbf{r}^*}{r^2}-30\frac{\mathbf{r}^*\mathbf{r}_s}{rr_s}\left(\frac{\mathbf{r}\mathbf{r}_s^*+\mathbf{r}_s\mathbf{r}^*}{rr_s}\right)\right]$$

with a similar term for the moon. The only nonvanishing parameter derivative of either tide is for Love's constant and

$$\frac{\partial \dot{\mathbf{r}}}{\partial k_L} = \frac{\partial \mathbf{T}_s}{\partial k_L}+\frac{\partial \mathbf{T}_m}{\partial k_L}$$

3.4.4.3.13 INTEGRATION METHOD

A "second difference" integration process is used (Herrick, 1971). A 12th order is normally used for the position integration, but recent geodetic solutions were based on sixth-order integration, because of computer storage limitation. Velocity integration performed for geodetic solutions is based on fourth-order integration, since less accuracy is required for the velocity used in the drag equations. When a low-order process is used for the velocity integration, an accurate velocity for use in Doppler calculations is obtained by differentiating position.

3.4.4.3.14 TRUNCATION ERRORS

Computations at the Naval Weapons Laboratory are performed on a computer with 14 or more significant decimal figures. Therefore round-off errors have not been found to be a significant source of error in geodetic computations. The principal source of numerical error occurs in the integration of the equations of motion and variational equations. In the general geodetic solutions, truncation errors in integrating the variational equations for gravity coefficients are the critical quantities.

For ephemeris computation, a 12th-order, 60-sec interval of integration can be used, yielding an ephemeris to 1-meter accuracy and perturbations for orbit constants to 1 part in 10^6. This accuracy is achieved over a span of several days for a variety of orbital conditions and a complex field. But accuracies in the perturbation in position due to potential coefficients must be better than 1 part in 10^6, because of the correlations among coefficients as well as correlation between coefficients and both orbit constants and station coordinates. Therefore in general geodetic solutions a sixth-order process and a 20-sec integration interval are used. Under these conditions, or with a 12th-order process and a 30-sec interval, the truncation errors for the 25th harmonic reach 1 part in 10^5.

The goal of 1 part in 10^6 is achieved for coefficients of 25th degree 15th order and coefficients of 20th degree and order.

The sixth-order process is used in place of the 12th-order process, despite the fact that a smaller integration interval is required at this order, because of computer storage limitations.

Interpolation Errors.—The program is designed so that the equations of motion and variational equations are integrated for the maximum length of time allowed, considering the disc storage space available for the results

of the integration. Interpolations are then made to obtain data at the times of observation, equations of condition are formed for data observed in the time segment, and increments are made to the normal equations. The integrations are then restarted at the end of the segment. Therefore, it is desirable to store data for the minimum number of integration steps required to yield accurate interpolated values at the time of observation. Eighth-order integration in data stored at 240-sec intervals is adequate for this purpose. Figure 3.27 shows that this choice results in errors in position of less than 1 meter for a variety of orbital conditions.

Figure 3.28 shows little gain by increasing the order of interpolation. Studies have shown that this interpolation process is also consistent with the accuracy with which the variation equations are integrated.

3.4.4.3.15 EXTRANEOUS RESONANCE PARAMETERS

In treating gravitational resonance effects we generally select for special treatment

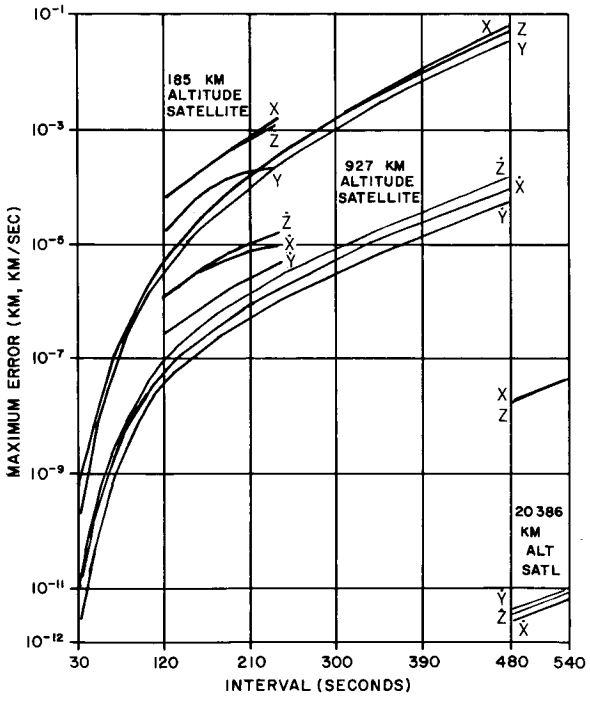

FIGURE 3.27.—Interpolation errors for Lagrangian eight-point interpolation.

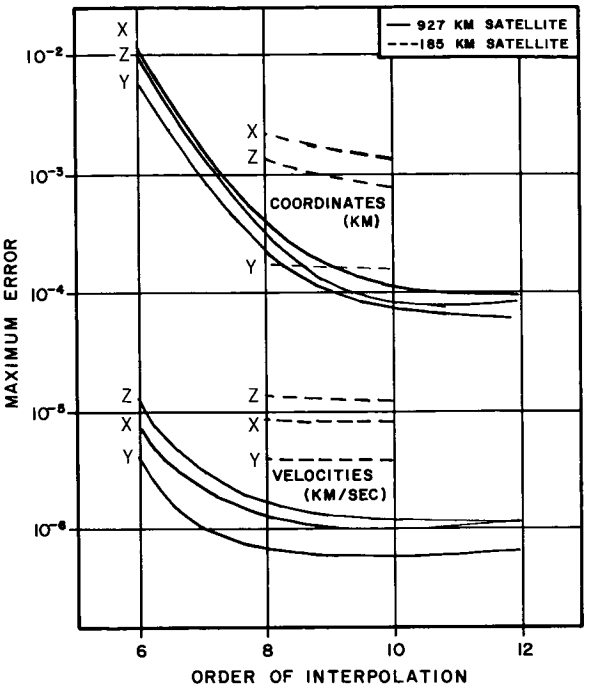

FIGURE 3.28.—Interpolation errors for 240-second interpolation interval.

three orders, m, of coefficients for which $m\omega \sim n_0$, where ω is the Earth's angular rate and n_0 is the mean motion of the satellite. One of the orders is the smallest m for which $m\omega > n_0$, and the other two orders are the two largest m for which $m\omega < n_0$. Gravitational coefficients of degree m through about $m+11$ are introduced as parameters of the solution for these orders. We are also concerned about resonance effects for coefficients of order m such that $m\omega \sim 2n_0$. Effects of these coefficients are generally about 20 meters for polar satellites in the along-track direction for the coefficient nearest resonance, and the effects are below 2 meters for other orders of coefficient or in other directions. Effects at lower orbital inclinations are smaller. Rather than integrate perturbation equations for these high orders of coefficients, we sometimes account for the dominant effects of these coefficients by introducing additional arbitrary parameters applicable to each time span of data. These parameters, which are termed "extraneous resonance parameters," are the coefficients

a and b of terms additive to the true anomaly of the satellite $a \cos \omega_{ep} t + b \sin \omega_{ep} t$ where ω_{ep} is the calculated beat frequency between m_ω and $2n_o$.

3.4.4.3.16 DIMENSIONAL (BLP) CHECK OF NORMAL EQUATIONS

C. J. Cohen discovered a nontrivial relation between system parameters and system observables that has been found useful in checking for formulation, coding, numerical, and computer operating errors. The relation is $BLP=0$, where B is the normal matrix augmented to include a scale parameter, L is the length dimension of each parameter, and P is the initial value of each parameter used in forming the normal matrix. Therefore this BLP scale parameter, σ, is introduced in the normal matrix as it is generated. (The check for $BLP=0$ is performed before the solution for the conventional parameters, and if it is found satisfactory, the row and column of the normal matrix corresponding to the scale parameters are then deleted.) The scale parameter adds no force on the satellite and makes no contribution for any derivative of force except its own perturbatonal force, which is a sum of contributions from the drag and the solar and lunar satellite perturbations

$$\ddot{\xi}_\sigma = \mathbf{G}_s + \mathbf{G}_m - 4\mathbf{T}_s - 4\mathbf{T}_m - \mathbf{D}\frac{1}{\rho}\frac{\partial s}{\partial n} - \left(\frac{\partial \mathbf{G}_s}{\partial \mathbf{r}^*} + \frac{\partial \mathbf{G}_m}{\partial \mathbf{r}^*} + \frac{\partial \mathbf{T}_s}{\partial \mathbf{r}^*} + \frac{\partial \mathbf{T}_m}{\partial \mathbf{r}^*}\right)\mathbf{r}$$

The starting conditions for $\dot{\xi}_\sigma$ and ξ_σ at arc epoch are zero as they are for most other parameters.

3.4.4.3.17 EQUATIONS OF CONDITION AND NORMAL EQUATIONS

The principal geodetic results are obtained by observations of frequency, range, range difference, right ascension, and declination. Therefore this section is limited to these data classes, although the computer programs described process additional types of data.

Processing of Doppler Frequency Observations.—Doppler frequency is that received deviation from the satellite oscillator frequency caused by relative motion of the satellite and the receiving station. In the simplest case this deviation is proportional to the time rate of change of the electromagnetic path length from the satellite to receiver.

The objective of this section is to give explicit formulas for the coefficient in the differential

$$df = \sum_k \frac{\partial f}{\partial p_k} dp_k$$

which are to be used in parameter improvement and to explain other details of Doppler pass processing. The parameters to be estimated fall into classes:

(1) Orbit: satellite initial conditions, coefficients of the gravity field, and constant of radiation pressure, drag, and tide.

(2) Station: the geocentric polar coordinates.

(3) Bias: frequency offset, drift rate, and clock error for the pass.

(4) BLP: velocity of light and scale parameter.

Weighted partial derivatives of frequency, with respect to these parameters, and the weighted discrepancy of observation are the coefficients in the observation equations to be generated.

The observable is the total received frequency approximated by

$$f = f_s\left(1 - \frac{1}{c\rho}\boldsymbol{\varrho}^* \dot{\boldsymbol{\varrho}}\right) + \delta f_r$$

where $f_s = f_b + f_b(t - t_b)$ gives the drifting reference frequency and δf_r the correction to frequency compensating for tropospheric refraction. The vector $\boldsymbol{\varrho}$ is related to the satellite position $\mathbf{r}$, the station position $\mathbf{r}_s$, and the time of observation t_r implicitly

$$\varrho = \mathbf{r}(t_a) - \mathbf{r}_s(t_r)$$

$$t_a = t_r - \frac{1}{c}\rho$$

Here t_a is the time at which the currently received signal presumably left the satellite. ρ and t_r are defined by iteration starting with $t_a = t$. The actual position of the satellite used is the sum of the trajectory position and the long-period perturbation.

$$\mathbf{r}(t_a) = \mathbf{r}_{\text{traj}}(t_a) + \frac{\dot{\mathbf{r}}_{\text{traj}}(t_a)}{\dot{r}_{\text{traj}}(t_a)} (a \cos \omega_{\text{ep}} t_a + b \sin \omega_{\text{ep}} t_a)$$

Therefore the derivatives of $\mathbf{r}$ are sums (evaluate at t_a)

$$\dot{\mathbf{r}} = \dot{\mathbf{r}} + \omega_{\text{ep}} \frac{\dot{\mathbf{r}}}{\dot{r}} (-a \sin \omega_{\text{ep}} t_a + b \cos \omega_{\text{ep}} t_a) + \frac{1}{|\dot{r}|}\left(\mathrm{I} - \frac{\ddot{\mathbf{r}}\dot{\mathbf{r}}^*}{\dot{r}^2}\right)\ddot{\mathbf{r}} (a \cos \omega_{\text{ep}} t_a + b \sin \omega_{\text{ep}} t_a)$$

$$\ddot{\mathbf{r}} = \ddot{\mathbf{r}} - \omega_{\text{ep}} \frac{\dot{\mathbf{r}}}{\dot{r}} (a \cos \omega_{\text{ep}} t_a + b \sin \omega_{\text{ep}} t_a) + 2\omega_{\text{ep}} \frac{1}{\dot{r}}\left(\mathrm{I} - \frac{\ddot{\mathbf{r}}\dot{\mathbf{r}}^*}{\dot{r}^2}\right)\ddot{r} (-a \sin \omega_{\text{ep}} t_a + b \cos \omega_{\text{ep}} t_a) + \left(\frac{1}{\dot{r}}\left(\mathrm{I} - \frac{\ddot{\mathbf{r}}\dot{\mathbf{r}}}{\dot{r}^2}\right)\ddot{\mathbf{r}} - \frac{2}{|\dot{r}|^3}(\dot{\mathbf{r}}^*\ddot{\mathbf{r}})\left(\mathrm{I} - \frac{\dot{\mathbf{r}}\dot{\mathbf{r}}^*}{\dot{r}^2}\right)\ddot{\mathbf{r}} - \frac{1}{\dot{r}^3}\dot{\mathbf{r}}\ddot{\mathbf{r}}^*\left(\mathrm{I} - \frac{\dot{\mathbf{r}}\dot{\mathbf{r}}^*}{\dot{r}^2}\right)\ddot{\mathbf{r}}\right)(a \cos \omega_{\text{ep}} t_a + b \cos \omega_{\text{ep}} t_a)$$

in which everything on the right is taken from the trajectory at t_a. Corresponding to the parameters, we approximate and ignore the long-period corrections

$$\frac{\partial \mathbf{r}}{\partial P_k} = \frac{\partial \mathbf{r}}{\partial P_k}\Big|_{\text{traj}} \quad \text{or} \quad \xi_p$$

$$\frac{\partial \dot{\mathbf{r}}}{\partial P_k} = \frac{\partial \dot{\mathbf{r}}}{\partial P_k}\Big|_{\text{traj}} \quad \text{or} \quad \dot{\xi}_p$$

in anticipation of $a = b = 0$ for the grand geodetic solution. The tables of $\mathbf{r}$, $\dot{\mathbf{r}}$ and ξ can be used to obtain $\mathbf{r}$, $\dot{\mathbf{r}}$, $\ddot{\mathbf{r}}$, ξ, and $\dot{\xi}$ by interpolation.

The station position and velocity at observation time are taken from the definitions given earlier. The station velocity is due almost entirely to the motion of Earth, not to the drift in station coordinates. Therefore

$$\mathbf{r}_0' = [ABCD]^* \mathbf{r}_0$$

$$\mathbf{r}_0' = \boldsymbol{\omega} \times \mathbf{r}_0$$

$$\boldsymbol{\omega}' = [CD]^* \begin{pmatrix} 0 \\ 0 \\ 1 \end{pmatrix} \omega$$

$$\omega = .729\,211\,585\,5 \times 10^{-4} \text{ rad/sec}$$

This approximation to ω is in error at about the eighth digit because of the precessional velocity of the Earth's axis. Finally, the slant range rate is

$$\dot{\varrho} = (\dot{\mathbf{r}} - \dot{\mathbf{r}}_0') - \frac{1}{c\lambda\rho}\varrho^* (\dot{\mathbf{r}} - \dot{\mathbf{r}}_0')\dot{\mathbf{r}}$$

with

$$\lambda = 1 + \frac{1}{c\rho}\varrho^* \dot{\mathbf{r}}$$

It should be noted that unless otherwise specified all station-related quantities are evaluated at t_r while all satellite-related quantities are evaluated at t_a.

In geodetic solutions conducted to date, the refraction correction is given by the expression

$$\delta f_r = -\frac{fs}{c}\frac{1}{\rho}\frac{\Delta N_x - \Delta N_s}{\cos \zeta}(\dot{\mathbf{r}} - \boldsymbol{\omega} \times \mathbf{r})^* \left(\frac{\varrho}{\rho} - \frac{1}{\cos \zeta}\frac{\mathbf{r}_0}{r_0}\right)$$

Here

$$\Delta N_s = C_0 (1 - e^{C_1 h_s}) + \frac{C_2}{\cos^2 \zeta}$$

$$\cos \zeta = \frac{\hat{\mathbf{o}}^* \mathbf{r}_s}{\rho r_s}$$

ΔN_x, C_0, C_1, C_2 are input constants and ω is as previously defined. The refraction correction is not differentiated to give corrections to the partials in the observation equation.

However, the model has been revised and computations are currently based on the following mathematics of first-order, closed

form, tropospheric refraction correction for Doppler range and range difference types of data. The model of the differential tropospheric refractivity is a polynominal in altitude closely resembling that of H. S. Hopfield (APL; see ch. 2) but modified by Mark Tanenbaum to allow somewhat more rapid machine calculations.

The theoretical forms of the basic first-order refraction corrections are

(range)

$$\Delta R = \int (n-1)\frac{r}{\sqrt{r^2-k^2}}dr$$

(range rate)

$$\Delta \dot{R} = k\dot{k}\int (n-1)\frac{r}{\sqrt{(r^2-k^2)^3}}dr$$

in which the geometric zenith angle ζ from the reference ellipsoid normal is defined by

$$\cos\zeta = \frac{u_0^* \varrho}{u_0 \rho} \qquad \text{with} \qquad u_0 \approx \begin{pmatrix} x_0' \\ y_0' \\ z_0'(1+e^2) \end{pmatrix}$$

and

$$k = r_0 \sin\zeta$$

$$k\dot{k} = \frac{r_0^2}{\rho}\cos\zeta\left[\left(I - \frac{\varrho\varrho^*}{\rho^2}\right)\dot{\varrho} - \omega\times\varrho\right]^* \frac{\mathbf{u}_0}{u_0}$$

Also r_0 is the magnitude of the station position vector, ρ is the slant range vector and r_{sat} is the magnitude of the satellite position vector. All integrals are assumed to be taken between the limits of r_0 and r_{sat}.

The differential refractivity is modeled

$$n-1 = N_{T1} + N_{T2}$$

$$N_{Ti} = \begin{cases} N_i\left(\dfrac{r^2-r_i^2}{r_0^2-r_i^2}\right)^4 & \text{if } r_0 \le r \le r_i \\ 0 & \text{otherwise} \end{cases}$$

given as a function of radius rather than height. The coefficients in this model are determined from thermodynamic variables: temperature, T, in degrees centigrade; pressure, P, in millibars; and relative humidity, H, in percent present, in that order as the first three time corrections on the pass header of the observation tape. With these we get

kelvin temperature $TK = T + 273$

water vapor pressure
$$E = H\exp\{-37.246\,5 + .213\,166\,TK - .000\,256\,908\,TK^2\}$$

refractivities
$$N_1 = (.776\times10^{-4})P/TK^2$$
$$N_2 = \begin{cases} (.373\times10^{-2})E/TK^2 \\ 0 \text{ for optical data} \end{cases}$$

radii
$$r_1 = r_0 + 40.1 + .149T$$
$$r_2 = r_0 + 12.0$$

Evaluation of the integrals given above proceeds as follows: In the case of electronic-type data, the differential refractivity is split into its two component parts and each is integrated separately. (In the case of optical data, only the part subscripted 1 is nonvanishing.) A look at the model reveals that the effective upper limit of integrals is r_i not r_{sat}. The separated integrands are exact derivatives and easily handled; in particular

$$I_i = \int (r^2-r_i^2)^n \frac{rdr}{(\sqrt{r_a-k^2})^m}$$
$$= \int \{(r^2-k^2)+(k^2-r_i^2)\}^n \frac{rdr}{(\sqrt{r^2-k^2})^m}$$
$$= \int \sum_{j=0}^{n}\binom{n}{j}(r^2-k^2)^{j-\frac{m}{2}}(k^2-r_0^2)^{n-j}\,rdr$$

Now interchange integration and summation and evaluate at the limits r_0 and r_i to get

$$I_i = \sum_{j=0}^{n}\binom{n}{j}\frac{1}{2j-m+2}(r^2-k^2)^{j\frac{m}{2}+1}(k^2-r_i^2)^{n-j}\Big]_{r=r_0}^{r=r_i}$$

Unfortunately, though these integrals may have terms near r^{2n-m+2}, their values are close to $r_0^{n-m+1}(r_i-r_0)^{n+1}$. Thus as many as

$$d_i \approx (n+1)\log\frac{r_0}{r_i-r_0} < \begin{cases} 10.9 \text{ for subscript 1} \\ 13.5 \text{ for subscript 2} \end{cases}$$

digits may be lost in the process of summation, possibly making the result too inaccurate. Double precision evaluation of I_i is therefore recommended. Finally, for the two integrals of interest we have

$$\int (n-1)\frac{rdr}{\sqrt{r^2-k^2}}=\sum_{i=1}^{2}\frac{Ni}{(r_0^2-r_1^2)^4}\sum_{j=0}^{4}\frac{1}{2j+1}\binom{4}{j}(r^2-k^2)^{j+1/2}\,(k^2-r_1^2)^{4-j}\Bigg]_{r_0}^{r_1}$$

$$\int (n-1)\frac{rdr}{(\sqrt{r^2-k^2})^3}=\sum_{i=1}^{2}\frac{Ni}{(r_0^2-r_1^2)^4}\sum_{j=0}^{4}\frac{1}{2j-1}\binom{4}{j}(r^2-k_i^2)^{j-1/2}\,(k^2-r_1^2)^{4-j}\Bigg]_{r_0}^{r_1}$$

Substitution of values computed from these formulas into the theoretical forms given earlier is straightforward.

The final forms of the tropospheric refraction corrections to be added to the computed values of the observable are, for Doppler,

$$\Delta f_{\text{ref}}=-\frac{fs}{c}\Delta\dot{R},$$

$$\Delta R_{\text{ref}}=\Delta R$$

as given earlier, and, for range difference,

$$\Delta(\Delta R)_{\text{ref}}=\Delta R(t_n)-\Delta R(t_{n-1}).$$

Note that although Doppler data are always electronic, range may be either electronic or optical. In order that this class obtain proper treatment it will be expected that humidity values of 0 are inserted by the laser range preprocessors.

Observation Equation.—The grand geodetic normal equations use the same type of information as the navigation equations. The quantities required for the observation equations are the weighted partial derivatives for all parameters and the weighted discrepancy

$$A_{ik}=\sqrt{w_i}\frac{\partial f_i}{\partial p_k}$$

$$\epsilon_i=\sqrt{w_i}\,(f_{obs}-f)_i$$

for each acceptable observation (indexed by i). The observed value and weight are taken from tape input. The computed value has already been given. The partial derivatives are computed as follows:

Bias:

$$\frac{\partial f}{\partial f_b}=1-\frac{1}{c\rho}\boldsymbol{\varrho}^*\dot{\boldsymbol{\varrho}}$$

$$\frac{\partial f}{\partial \dot{f}_b}=(t-t_b)\frac{\partial f}{\partial f_b}$$

$$\frac{\partial f}{\partial \tau}=-\frac{fs}{\lambda c}\left\{\frac{\boldsymbol{\varrho}^*}{\rho}\left[\left(1-\frac{1}{c\rho}\boldsymbol{\varrho}^*\dot{\boldsymbol{\varrho}}\right)^2\ddot{\mathbf{r}}-\ddot{\mathbf{r}}_0\right]+\frac{1}{\rho}\dot{\boldsymbol{\varrho}}^*\left(I-\frac{\boldsymbol{\varrho}\boldsymbol{\varrho}^*}{\rho^2}\right)\dot{\boldsymbol{\varrho}}\right\}$$

Orbit:

$$\frac{\partial f}{\partial p_k}=\left(\frac{\partial f}{\partial \mathbf{r}}\right)^*\frac{\partial \mathbf{r}}{\partial p_k}+\left(\frac{\partial f}{\partial \dot{\mathbf{r}}}\right)^*\frac{\partial \dot{\mathbf{r}}}{\partial p_k}$$

$$\frac{\partial f}{\partial \mathbf{r}}=-\frac{fs}{\lambda c}\left\{\frac{1}{|\boldsymbol{\varrho}|}\left(I-\frac{\boldsymbol{\varrho}\boldsymbol{\varrho}^*}{\rho^2}\right)\dot{\boldsymbol{\varrho}}-\frac{1}{c\lambda\rho}\left[\left(1-\frac{1}{c\rho}\boldsymbol{\varrho}^*\dot{\boldsymbol{\varrho}}\right)\boldsymbol{\varrho}^*\ddot{r}+\frac{\dot{\boldsymbol{\varrho}}^*}{\rho^2}\left(I-\frac{\boldsymbol{\varrho}\boldsymbol{\varrho}^*}{\rho^2}\right)\dot{\mathbf{r}}\right]\boldsymbol{\varrho}\right\}$$

$$\frac{\partial f}{\partial \dot{\mathbf{r}}}=-\frac{fs}{\lambda c\rho}\left(1-\frac{1}{c\rho}\boldsymbol{\varrho}^*\dot{\boldsymbol{\varrho}}\right)\boldsymbol{\varrho}$$

For the long-period parameters a and b, use

$$\frac{\partial \mathbf{r}}{\partial a}=\frac{\dot{\mathbf{r}}}{\dot{r}}\cos\omega_{ep}t_a$$

$$\frac{\partial \mathbf{r}}{\partial a}=-\omega_{ep}\frac{\partial \mathbf{r}}{\partial b}+\cos\omega_{ep}t_a\frac{1}{\dot{r}}\left(I-\frac{\dot{\mathbf{r}}\dot{\mathbf{r}}^*}{\dot{r}^2}\right)\ddot{\mathbf{r}}$$

$$\frac{\partial \mathbf{r}}{\partial b}=\frac{\dot{\mathbf{r}}}{\dot{r}}\sin\omega_{ep}t_a$$

$$\frac{\partial \dot{\mathbf{r}}}{\partial b}=\omega_{ep}\frac{\partial \mathbf{r}}{\partial a}+\sin\omega_{ep}t_a\frac{1}{\dot{r}}\left(I-\frac{\dot{\mathbf{r}}\dot{\mathbf{r}}^*}{\dot{r}^2}\right)\ddot{\mathbf{r}}$$

For corrections to the geocentric station position, $d\mathbf{s}^*=(dr_0 d\psi_0 d\lambda_0)$,

$$\frac{\partial f}{\partial \boldsymbol{\varrho}^*}=\left(\frac{\partial f}{\partial s}\right)^*\frac{\partial \mathbf{r}_0}{\partial s^*}+\left(\frac{\partial f}{\partial \mathbf{r}_0}\right)^*\frac{\partial \dot{\mathbf{r}}_0}{\partial \mathbf{s}^*}$$

$$\frac{\partial f}{\partial r_0}=-\frac{\partial f}{\partial \mathbf{r}}$$

$$\frac{\partial f}{\partial \dot{\mathbf{r}}_s}=\frac{fs}{\lambda c_\rho}\boldsymbol{\varrho}$$

$$\frac{\partial \dot{\mathbf{r}}_0}{\partial s^*}=\left[\frac{\mathbf{r}_0}{r_0},\frac{\mathbf{r}_0^*}{r_0}\times(\mathbf{P}\times\mathbf{r}_0),\mathbf{P}\times\mathbf{r}_0\right]\quad\text{by columns}$$

$$\frac{\partial \dot{\mathbf{r}}_0}{\partial s^*}=\boldsymbol{\omega}\times\frac{\partial \mathbf{r}_0}{\partial \mathbf{s}^*}$$

The vector

$$\mathbf{P}=[ABCD]^*\begin{pmatrix}0\\0\\1\end{pmatrix}$$

defines the instantaneous direction of the polar axis of the reference system in which λ and ψ are given for dimensional check, BLP,

$$-\frac{\partial f}{\partial \sigma}=-\frac{fs}{\lambda c}\left\{\frac{\boldsymbol{\varrho}^*\dot{\boldsymbol{\varrho}}}{\rho}-\frac{1}{c\lambda}\left(\boldsymbol{\varrho}^*\ddot{\mathbf{r}}+\dot{\boldsymbol{\varrho}}\left(I-\frac{\boldsymbol{\varrho}\boldsymbol{\varrho}^*}{\rho^2}\right)\dot{\mathbf{r}}\right)\right.$$
$$\left.-\left(\frac{\partial f}{\partial \mathbf{r}}\right)^*\xi_\sigma-\left(\frac{\partial f}{\partial \mathbf{r}}\right)^*\xi_\sigma\right.$$

in which σ is the scale parameter.

The required output is the matrix observation equation together with the number of observations, certain other identifiers, and the uncorrected pass variance

$$\sum_1^{n_{\text{obs}}} w_i(f_{\text{obs}}-f)_i^2$$

Required partial derivatives for other unspecified parameters have the value 0.

Options.—With time transmission off, the iteration for ρ is not necessary, since $t_a=t$. The BLP, station, and orbit partial derivatives are modified by striking the terms in the $\partial f/\partial \mathbf{r}$, $\partial f/\partial \sigma$, and f expressions beginning with $1/c\lambda$. As given, the formulation is correct to order v/c but not to v^2/c^2.

Other Data Classes.—Since no range data and only limited quantities of optical data were processed in geodetic solutions performed at the Naval Weapons Laboratory, formulations for these data classes will be omitted. Many point positions were calculated from Doppler data which were treated as range differences; however, the formulas will be omitted, since they are fairly straightforward.

3.4.4.3.18 SOLUTION OF NORMAL EQUATIONS

After the normal equations are formed for each span of data, the BLP test described above is carried out to determine if the matrix is suitable for further processing. A matrix is considered to be satisfactory if each row is less than 10^{-5} for satellites with perigee heights of 600 km and 10^{-7} for satellites with perigee heights over 1000 km. The row and column corresponding to the scale parameter are then deleted and the matrix is augmented by two rows and columns corresponding to components of pole position. The elements of the rows and columns are computed from the elements corresponding to station coordinates, and $4\cdot10^{13}$ is added to the diagonal elements corresponding to each component of pole position to represent an a priori observation of the BIH values of pole position with 1-meter accuracy. The row and column corresponding to the longitude of the Maryland station are deleted to remove a longitude singularity from the solution.

An "equate" operation is performed to combine equivalent parameters. For example, a separate radiation parameter is established for the first and last half of each span for use in experiments even though the value is not expected to vary. The equate operation consists of deleting the row and column corresponding to the second radiation parameter after adding the row elements for the second parameter to those for the first parameter. The right-hand side of the matrix is then adjusted to account for any discrepancies in initial parameter values, such as the use of coordinates of neighboring stations which are separated by a distance which does not correspond to the survey distance. If the

initial parameters are P_0 and the desired parameters are P_1, the normal equations

$$[B]\,(\mathbf{P}^1-\mathbf{P}_0)=\mathbf{E}$$

can be written

$$[B]\,(\mathbf{P}^1-\mathbf{P}_1+\mathbf{P}_1-\mathbf{P}_0)=\mathbf{E}$$

so that

$$[B]\,(\mathbf{P}^1-\mathbf{P}_1)=\mathbf{E}+[B]\,(\mathbf{P}_0-\mathbf{P}_1)$$

Therefore, the second term in the last equation is the required adjustment to the right-hand side of the normal equations.

The final problem involves establishing which parameters are determinable. The solution for GM is usually suppressed by deleting the row and column corresponding to the parameters since it has been found to be ill-determined. Other gravitational parameters are deleted if their standard errors exceed empirical tolerances of about 10^{-8} or if the ratio of the normalized parameter to $10^{-5}/n^2$ exceeds an empirical tolerance of about 4. The tolerances are set after residuals are computed for solutions using various values for the tolerances.

Various methods are used to find the alternate solutions for test purposes. Some solutions are made for one order of a coefficient at a time, with stations and other orders held at best-determined values. Such solutions sometimes help isolate poorly determined coefficients. Other solutions (including the final one) are made using the entire matrix. In some cases, the higher degree coefficients are suppressed for each order, while in other solutions, parameter selection is based on the size of eigenvalues.

Methods of Point Positioning and Pole Position Computation.—While positions of observing stations are obtained in the course of a general geodetic solution, only a limited amount of the available observational data can be processed in such a solution because of the high cost of forming the large normal equations. Therefore, positions of many observing stations are obtained in least-squares solutions where the Earth's field and the positions of many of the stations are held at values determined in the last preceding general geodetic solution. A separate computer program is used for this purpose, because program efficiency is greater when the program objectives are more limited. But the mathematics is largely the same, so that only differences between the two programs will be described.

The first difference is in the use of a shorter time span of data for each set of orbit constants. A short span is desirable because the program is used to provide diagnostics on station and satellite performance, which should be obtained promptly. A two-day span of observation of one satellite is about the shortest span in which a useful solution can be obtained for the coordination of newly deployed stations. The short span also reduces the effect of some errors in the field.

The parameters of the solution include six orbit constants, one drag scaling parameter, two components of pole position, the coordinates of any newly deployed stations, and a frequency and tropospheric refraction scaling factor for each satellite pass. The radiation force is calculated on the basis of the average force determined in solutions using longer spans of data for the satellite (such as in general geodetic solutions). A value of 0.3 is used for Love's number while extraneous resonance parameters are not normally used.

Forces and normal equations are otherwise calculated in the manner described above for the general geodetic solution except that the variance for each data point is increased by 0.1 times the square of the tropospheric refraction correction before inversion for use as a weight in the formation of the normal equation.

The components of pole position are completely free parameters in these solutions, whereas in the general geodetic solutions the BIH values were used as a priori data. The integration method differs, although the difference is not numerically significant. A 60-sec integration interval and a tenth-order

process yields 1-meter numerical accuracy for a five-day interval, which includes the two-day time span in which data are fitted and a three-day prediction interval used for filtering data and evaluation. The integration is similar to that used in forming normal equations for geodetic solutions.

3.4.5 Satellite Triangulation and Trilateration (AFCRL Gulf Test)

(Donald H. Eckhardt, AFCRL)

The usual departure point for the adjustment of overdetermined systems is the method of least squares. This method is based rigorously on the method of maximum likelihood for normal deviates, which is the foundation on which the reduction technique for the systems used in the Gulf Test was directly constructed (sec. 3.5.1.5.1).

The principle of the method of maximum likelihood is to maximize the likelihood function or its logarithm L with respect to the parameters to be adjusted, ν^n, $n=1, 2, \ldots, N$. Consider these parameters as the elements of an N vector, $\boldsymbol{\nu}$. Then the conditions for a stationary point at $\boldsymbol{\nu}=\hat{\boldsymbol{\nu}}$ can be written as

$$(\partial L/\partial \nu^n)\,\hat{\boldsymbol{\nu}}=0$$

Suppose that $\tilde{\boldsymbol{\nu}}$ is an approximation to $\boldsymbol{\nu}$. By Taylor series expansion to the first order in $(\hat{\nu}^n-\tilde{\nu}^n)$, these conditions become

$$\left(\frac{\partial L}{\partial \nu^n}\right)_{\nu}+\sum_{l=1}^{N}\left(\frac{\partial^2 L}{\partial \nu^n \partial \nu^l}\right)_{\tilde{\nu}}(\hat{\nu}^l-\tilde{\nu}^l)=0$$

Let the inverse of the matrix

$$[-(\partial^2 L/\partial \nu^n \partial \nu^l)\,\tilde{\nu}] \qquad \text{be} \qquad [\eta^{nl}]$$

The first-order solution for $\hat{\boldsymbol{\nu}}$ becomes

$$\hat{\nu}^n=\tilde{\nu}^n+\sum_{l=1}^{N}\eta^{nl}\left(\frac{\partial L}{\partial \nu^n}\right)_{\tilde{\nu}} \qquad (3.41)$$

This array is the form used in the iterative solutions of the Gulf Test networks. It can be shown that, with such an iterative technique, $\hat{\boldsymbol{\nu}}$ converges in probability to the true parameter $\boldsymbol{\nu}$, and η^{nl} converges in probability to the expected value of $(\hat{\nu}^n-\nu^n)\,(\hat{\nu}^l-\nu^l)$; that is, $[\eta^{nl}]$ is the covariance matrix.

The elements of the vector $\boldsymbol{\nu}$ for the intervisible networks, as in the Gulf Test, are taken as the coordinates of N flash positions x_i^n $(n=1, 2, \ldots N)$, and the coordinates of M ground stations, y_i^m $(m=1, 2, \ldots M)$. (Subscripts always pertain to the three-vector of Cartesian space, and the convention of summation over repeated subscripts is adopted.) Estimates are available before the reduction of the coordinates of the stations $y_{i0}^m \approx y_i^m$ and of their covariances. The corrections for each station, $\Delta y_i^m \equiv y_i^m - y_{i0}^m$, are normally distributed with zero means and elements W_{ij}^m $(ij=1, 2, 3)$ of the inverse of the covariance matrix.

It is assumed that there is no correlation between stations and that each error ellipsoid defined by W_{ij}^m is an ellipsoid of revolution about the local vertical. Properly interpreted, the solution to be derived is valid in the limit as any error ellipsoid becomes infinitesimal (fixed station) or infinite (completely unknown station).

The range from station m to flash n is

$$r^{nm}=|x_i^n-y_i^m|$$

and the direction cosines from the station to the flash are

$$\mu_i^{nm}=(x_i^n-y_i^m)/r^{nm}$$

The direction cosines derived from observations are denoted by μ_{i0}^{nm}; the differences from the model are $\Delta\mu_i^{nm} \equiv \mu_i^{nm}-\mu_{i0}^{nm}$. It is assumed that the small angle $|\Delta\mu_i^{nm}|$ between the vectors $[\mu_i^{nm}]$ and $[\mu_{i0}^{nm}]$ is the resultant of two angles that are mutually orthogonal on the celestial sphere, each of which is normally distributed with zero mean and variance $1/u^{nm}$. For a missing observation, $1/u^{nm}$ is taken as zero.

The log likelihood for this model is

$$L=\text{constant}-\tfrac{1}{2}\sum_{n=1}^{N}\sum_{m=1}^{M}u^{nm}(\Delta\mu_i^{nm})^2-\tfrac{1}{2}\sum_{m=1}^{M}\Delta y_i^m W_{ij}^m \Delta y_j^m$$

Its first derivatives are, to the first order in $\Delta\mu_i^{nm}$,

$$\partial L/\partial x_i^n = \sum_{m=1}^{M} u^{nm}\Delta\mu_i^{nm}/r^{nm}$$

$$\partial L/\partial y_i^m = -\sum_{n=1}^{N} u^{nm}\Delta\mu_i^{nm}/r^{nm} - W_{ij}^m\Delta y_j^m$$

Its second derivatives are, to the 0th order in $\Delta\mu_i^{nm}$,

$$\partial^2 L/\partial x_i^n\partial y_j^m = u^{nm}(\delta_{ij}-\mu_i^{nm}\mu_j^{nm})/(r^{nm})^2$$

$$\partial^2 L/\partial x_i^m\partial x_j^m = -\sum_{m=1}^{M}\partial^2 L/\partial x_i^n\partial y_j^m$$

$$\partial^2 L/\partial y_i^m\partial y_j^m = -\sum_{n=1}^{N}\partial^2 L/\partial x_i^n\partial y_j^m - W_{ij}^m$$

where δ_{ij} is the Kronecker delta. All other second derivatives are zero. The second derivatives are calculated from the first approximations for x_i^n and y_i^m, and the covariance matrix is found by inversion. For reasonable first approximations, this matrix need be evaluated only once. The first derivatives are multiplied by the covariance matrix as in equation (3.41) to generate corrections to x_i^n and y_i^m (that is, to v^n), which are in turn used to update the first derivatives for iterative application of the equation. Iterations are continued until all of the corrections generated are significantly less than the solution variances.

The criterion that

$$|\hat{v}^n - \tilde{v}^n| < 100\,\eta^{nn}$$

was usually satisfied after the second iteration; one application of the first-order process is therefore usually quite sufficient. If station m is completely unknown, $W_{ij}^m = 0$, and the preceding formulas need no modification. If, however, the station is fixed, set $W_{ij}^m = \beta\delta_{ij}$ and let $\beta\to\infty$. Then $\partial^2 L/\partial y_i^m\partial y_j^m \to -\beta\delta_{ij}$, and the corresponding elements in the covariance matrix approach $\beta^{-1}\delta_{ij}$. These elements multiply only $\partial L/\partial y_j^m \to -\beta(y_j^m - y_{j0}^m)$ in the application of equation (3.41); the net result is that any y_i^m are replaced by y_{i0}^m after one iteration, and they are not modified thereafter. In practice, this is accomplished simply by dropping y_i^m as adjustment parameters. The foregoing solution is valid only for intradatum ties, but it can easily be extended for interdatum ties as well. For instance, suppose that for $m = 1, 2, \ldots M$, y_{i0}^m is referred to one datum, and for $m = M_i+1$, $M_i+2, \ldots M$, y_{i0}^m is referred to a second datum. Let the datum displacement be z_i, and in all of the preceding formulas replace y_{i0}^m by $y_{i0}^m + z_i$, when $m > M_i$.

The additional derivatives with respect to z_i of the modified log-likelihood function are, to the appropriate order,

$$\partial L/\partial z_i = \sum_{m=M+1}^{M} W_{ij}^m(y_j^m - y_{i0}^m - z_i)$$

$$\partial^2 L/\partial z_i\partial z_j = -\sum_{m=M+1}^{M} W_{ij}^m$$

$$\partial^2 L/\partial z_j\partial y_i^m = W_{ij}^m \qquad m > M_i$$

All other additional derivatives are zero. With the modified and new derivatives the datum displacement can be carried along with the coordinates of the stations and flashes in the vector $\mathbf{v}$.

In treating real data, u^{nm} and W_{ij}^m should be considered as weights rather than as known inverse variances or covariances. The solution covariance must then be scaled by the solution value of

$$\sigma^2 = \frac{\sum_{n=1}^{N}\sum_{m=1}^{M} u^{nm}(\Delta\mu_i^{nm})^2 + \sum_{m=1}^{M}\Delta y_i^m W_{ij}^m \Delta y_j^m}{2\times\text{number of observations} - N}$$

For the Gulf Test measurements, the weights u^{nm} were the variances calculated in the least-squares plate reductions of the Defense Mapping Agency/Aerospace Center (DMA/AC), and the adopted weights for W_{ij}^m had little influence in the determination of σ^2. Generally, σ^2 turned out to be quite close to unity, so the residuals of the Gulf Test adjustments (sec. 3.5.1.5.1) were consistent with the residuals of the preliminary plate adjustments.

3.4.6 Least-Squares Collocation Method for Combination of Satellite-Derived Gravitational and Terrestrial Gravity [1]

(Richard H. Rapp, OSU)

3.4.6.1 Introduction

The combination of a gravitational potential from satellite data and terrestrial gravity information has been a popular procedure for improving our knowledge of the Earth's gravity field. Such combination may be carried out in several ways.

Moritz (1970) considered methods of combination under a more general adjustment concept called "collocation." In his report Moritz derived certain equations that allow solutions obtained by the usual least-squares method to be converted to a solution corresponding to the least-squares collocation method. In this section we will extend the equations derived by Moritz. Actual combinations of satellite and terrestrial gravity information using recent solutions for the potential coefficients and terrestrial gravity fields are reported in section 3.5.2.

3.4.6.2 Basic Methods

Two methods of combination are examined. The first is a method that compares an estimate, Δg_T, of terrestrial anomaly to an anomaly Δg_S, computed from a set of satellite-derived coefficients. We form an adjustment model as follows

$$F = L_l - f(L_{x^0}) \tag{3.42}$$

where L_l is the column vector of observed anomalies and L_{x^0} are the given potential coefficients. An element of $f(L_{x^0})$ is given by

$$[f(L_{x^0})] = \frac{GM}{r^2}\sum_{n=2}^{n_{\max}}\left(\frac{a}{r}\right)^n (n-1) \sum_{m=0}^{n}(\bar{C}_n^{*m}\cos m\lambda + \bar{S}_n^m \sin m\lambda)\bar{P}_n^m(\sin\psi) \tag{3.43}$$

where GM is the geocentric gravitational constant, r is the geocentric radius, $n_{\max}$ is the maximum degree for which coefficients are to be found or are given, a is the equatorial radius, $\bar{C}_n^{*m}$, $\bar{S}_n^m$ are the normalized (to 4π) potential coefficients referring to an ellipsoid of specified flattening, $\bar{P}_n^m$ is the normalized (to 4π) associated Legendre polynomial, and ψ is the geocentric latitude.

The correction to the potential coefficients is the vector

$$\mathbf{V}_x = -(\mathbf{B}_x^t\mathbf{D}_l^{-1}\mathbf{B}_x + \mathbf{D}_x^{-1})\mathbf{B}_x\mathbf{D}_l^{-1}W \tag{3.44}$$

where $\mathbf{D}_l$ is the variance-covariance matrix of the observed anomalies, $\mathbf{D}_x$ is the variance-covariance matrix of the potential coefficients, and

$$\mathbf{B}_x = \frac{\partial F}{\partial \mathbf{L}_x} \qquad W \equiv F$$

The adjusted potential coefficients would be

$$L_x{}^a = L_{x^0} + V_x \tag{3.45}$$

The variance-covariance matrix $\mathbf{\Sigma}_x$ of the adjusted coefficients would be (for a standard error of unit weight)

$$\mathbf{\Sigma}_x = (\mathbf{B}_x^T\mathbf{D}_l^{-1}\mathbf{B}_x + \mathbf{D}_x^{-1})^{-1} \tag{3.46}$$

The second method is that derived by forming the difference between a given set of potential coefficients (L_{x^0}) and an estimate $L_x{}^c$, computed through the usual summation formula applied to a global field of terrestial anomaly estimates, L_l. Then

$$\overline{F} = L_{x^0} - L_x{}^c \tag{3.47}$$

where an element of $L_x{}^c$ would be

$$[L_x{}^a] = \frac{1}{4\pi\gamma(n-1)}\int\int_\sigma \Delta g\bar{P}_n^m(\sin\psi)\begin{Bmatrix}\cos m\lambda\\ \sin m\lambda\end{Bmatrix} d\sigma \tag{3.48}$$

where $d\sigma$ is an areal element on the unit sphere. The solution from the usual least-squares approach is

[1] The research reported in this section was sponsored by the Air Force Cambridge Research Laboratories, Bedford, Massachusetts.

$$\bar{V} = -\left(\left(\bar{\mathbf{B}}_l \mathbf{D}_l \mathbf{B}_l^T\right)^{-1} + \mathbf{D}_x^{-1}\right)^{-1} \left(\bar{\mathbf{B}}_l \mathbf{D}_l \mathbf{B}_l^T\right)^{-1} \bar{W} \tag{3.49}$$

where bars have been used to indicate results obtained from this second method. We have

$$\bar{\mathbf{B}}_l = \frac{\partial \bar{F}}{\partial L_l} \text{ and } \bar{W} \equiv \bar{F}$$

We may also express the anomaly residuals as

$$\bar{V}_l = \mathbf{D}_l \bar{\mathbf{B}}_l^T \mathbf{D}_x^{-1} \bar{V}_x \tag{3.50}$$

The adjusted quantities are

$$L_x^a = L_{x^0} + \bar{V}_x \quad \text{(for potential coefficients)} \tag{3.51}$$

$$L_l^a = L_l + \bar{V}_l \quad \text{(for anomalies)} \tag{3.52}$$

The variance-covariance matrix ($\bar{\mathbf{\Sigma}}_x$) of the adjusted potential coefficients would be (for standard error of unit weight)

$$\bar{\mathbf{\Sigma}}_x = \left(\left(\bar{\mathbf{B}}_l \bar{\mathbf{D}}_l \bar{\mathbf{B}}_l^T\right)^{-1} + \mathbf{D}_x^{-1}\right)^{-1} \tag{3.53}$$

We should note that the model represented by equation (3.47) is not quite as accurate as that represented by equation (3.43), since the shape of the ellipsoid is not considered in equaton (3.48).

3.4.6.3 Modifications for the Least-Squares Collocation Method

3.4.6.3.1 GENERAL CASE

The basic principle of the collocation method is

$$\mathbf{s}^T \mathbf{C}^{-1} \mathbf{s} + \mathbf{n}^T \mathbf{D}^{-1} \mathbf{n} = \text{a minimum} \tag{3.54}$$

where $\mathbf{s}$ is a signal vector, $\mathbf{C}$ is the covariance matrix of the signal, $\mathbf{n}$ is a noise vector, and $\mathbf{D}$ is the covariance matrix of the noise. Moritz showed that a solution of the combination methods carried out by the principle of equation (3.54) can be related to the solution obtained by the application of the principle that $V^T \mathbf{P} V =$ a minimum. (This is equivalent to $\mathbf{n}^T \mathbf{D}^{-1} \mathbf{n}$ used in equation (3.54).)

If $\mathbf{y}$ is a vector representing the adjusted anomalies and adjusted potential coefficients (in an order dependent on the statement of the combination solution) based on the application of the collocation principle and $\mathbf{y}_0$ is the corresponding vector for the usual least-squares solution, we have (Moritz, 1970, eq. (6-6))

$$\mathbf{y} = (\mathbf{I} - \mathbf{S})^{-1} \mathbf{y}_0 \tag{3.55}$$

or, with the development of $(\mathbf{I} - \mathbf{S})^{-1}$ into a series,

$$\mathbf{y} = (\mathbf{I} + \mathbf{S} + \mathbf{S}^2 \quad \cdots) \mathbf{y}_0 \tag{3.56}$$

where

$$\mathbf{S} = -\mathbf{R}\mathbf{D}\mathbf{H}^T \mathbf{C}^{-1} \mathbf{H} \tag{3.57}$$

$$\mathbf{R} = \mathbf{I} - \mathbf{T} \tag{3.58}$$

$$\mathbf{T} = \mathbf{D}\mathbf{G}^T (\mathbf{G}\mathbf{D}\mathbf{G}^T)^{-1} \mathbf{G} \tag{3.59}$$

$\mathbf{G}$ and $\mathbf{H}$ are matrices dependent on the method of combining the solutions being considered.

The error covariance matrix $\mathbf{E}$ in the collocation adjustment is related to the corresponding equation of the usual adjustment by

$$\mathbf{E} = (\mathbf{I} - \mathbf{S})^{-1} \mathbf{E}^0 \tag{3.60}$$

3.4.6.3.2 MODIFICATION FOR THE FIRST APPROACH

We first specify that we will have n unknown potential coefficients with m terrestrial anomalies. For a solution complete to degree 15, n would be 250. Using 5° equal area blocks, m would be 1654. In the case of this approach, Moritz has shown that

$$\mathbf{y} = \begin{matrix} m \\ n \end{matrix} \begin{bmatrix} \mathbf{g} \\ \mathbf{p} \end{bmatrix} \tag{3.61}$$

where **g** represents the adjusted anomalies and **p** the adjusted potential coefficients. Matrices needed to evaluate **S** are described in the following.

The matrix **D** is

$$\mathbf{D}=\begin{matrix} m \\ n \end{matrix}\overset{\begin{matrix} m & n \end{matrix}}{\begin{bmatrix} \mathbf{D}_l & 0 \\ 0 & \mathbf{D}_x \end{bmatrix}} \tag{3.62}$$

The matrix **H** is

$$\mathbf{H}=n\overset{\begin{matrix} m & n \end{matrix}}{[\mathbf{0}\ \mathbf{I}]} \tag{3.63}$$

The matrix **G** is

$$\mathbf{G}=M\overset{\begin{matrix} m & n \end{matrix}}{[\mathbf{I}\ \mathbf{B}_x]} \tag{3.64}$$

Under these circumstances Moritz (1970, eq. (6–16)) shows that

$$\mathbf{T}=\begin{matrix} m \\ + \\ n \end{matrix}\overset{m+n}{\begin{bmatrix} (\mathbf{I}-\mathbf{B}_x\mathbf{N}^{-1}\mathbf{B}_x{}^T\mathbf{D}_l^{-1})\ \mathbf{G} \\ \mathbf{N}^{-1}\mathbf{B}_x{}^T\mathbf{D}_l^{-1}\mathbf{G} \end{bmatrix}} \tag{3.65}$$

where $\mathbf{N}=\mathbf{B}_x{}^T\mathbf{D}^{-1}\mathbf{B}_x+\mathbf{D}_x{}^{-1}$.

Substituting these results (for **H**, **G**, and **T**) into equation (3.57) produces

$$\mathbf{S}=\begin{matrix} m \\ n \end{matrix}\overset{\begin{matrix} m & n \end{matrix}}{\begin{bmatrix} 0 & \mathbf{B}_x\mathbf{N}^{-1}\mathbf{C}^{-1} \\ 0 & -\mathbf{N}^{-1}\mathbf{C}^{-1} \end{bmatrix}} \tag{3.66}$$

Then

$$(\mathbf{I}-\mathbf{S})=\begin{bmatrix} \mathbf{I} & -\mathbf{B}_x\mathbf{N}^{-1}\mathbf{C}^{-1} \\ 0 & \mathbf{I}+\mathbf{N}^{-1}\mathbf{C}^{-1} \end{bmatrix} \tag{3.67}$$

and

$$(\mathbf{I}-\mathbf{S})^{-1}=\begin{bmatrix} \mathbf{I} & \mathbf{B}_x\mathbf{N}^{-1}\mathbf{C}^{-1}\ (\mathbf{I}+\mathbf{N}^{-1}\mathbf{C}^{-1}) \\ 0 & (\mathbf{I}+\mathbf{N}^{-1}\mathbf{C}^{-1})^{-1} \end{bmatrix} \tag{3.68}$$

Using equations (3.61) and 3.68) in equation (3.55), we have

$$\mathbf{g}=\mathbf{g}_0+\mathbf{B}_x\mathbf{N}^{-1}\mathbf{C}^{-1}\ (\mathbf{I}+\mathbf{N}^{-1}\mathbf{C}^{-1})\,\mathbf{p}_0 \tag{3.69}$$

$$\mathbf{p}=(\mathbf{I}+\mathbf{N}^{-1}\mathbf{C}^{-1})^{-1}\mathbf{p}_0 \tag{3.70}$$

The anomalies given by equation (3.69) are not of great practical significance since they are very much influenced by the neglect of higher-order potential coefficients. Consequently, we will not use equation (3.69). The variance-covariance matrix pertaining to the adjusted potential coefficients from the collocation procedure would be

$$\mathbf{\Sigma}_p=(\mathbf{I}+\mathbf{N}^{-1}\mathbf{C}^{-1})^{-1}\mathbf{\Sigma}_{p_0} \tag{3.71}$$

In this method **C** is a $n\times n$ diagonal matrix whose elements are the expected mean square value of the potential coefficients being estimated. The matrix $(\mathbf{I}+\mathbf{N}^{-1}\ \mathbf{C}^{-1})$ is not a symmetric matrix, so that computer algorithms designed for the inversion of nonsymmetric matrices must be used. This fact limits the number of unknowns that can be solved for in a given computer memory. Consequently, the series expansion for $(\mathbf{I}-\mathbf{S})^{-1}$ may be used. Retaining the first two terms in the series of equation (3.56), we can write

$$\mathbf{p}=(\mathbf{I}-\mathbf{N}^{-1}\mathbf{C}^{-1}+(\mathbf{N}^{-1}\mathbf{C}^{-1})\ (\mathbf{N}^{-1}\mathbf{C}^{-1})+\cdots)\,\mathbf{p}_0 \tag{3.72}$$

$$\mathbf{\Sigma}_p=(\mathbf{I}-\mathbf{N}^{-1}\mathbf{C}^{-1}+(\mathbf{N}^{-1}\mathbf{C}^{-1})\ (\mathbf{N}^{-1}\mathbf{C}^{-1})+\cdots)\,\mathbf{\Sigma}_{p_0} \tag{3.73}$$

Numerical tests indicated that at higher degree (say $n=20$) the error in the computed potential coefficient could reach 19 percent if only the first term in the series is retained. Stopping the series at the second term may still leave an error of the order of 8 percent.

Although this method yields meaningful potential coefficients directly, meaningful anomalies are not so obtained. This is a fault of the model used (i.e., a finite set of potential coefficients are being sought) and not the adjustment method. To obtain a set of anomalies consistent with the various estimates of the potential coefficients (either p or p_0) using the original terrestrial anomalies, a set of conditions may be imposed on these anomalies, the least-squares adjustment being performed to give an adjusted anomaly field.

3.4.6.3.3 MODIFICATIONS FOR THE SECOND APPROACH

We next turn to the evaluation of the matrix **S** (eq. (3.57)) for the second approach. In this case we have the adjusted variables as

$$\bar{\mathbf{y}} = \begin{matrix} n \\ m \end{matrix}\begin{bmatrix} \bar{\mathbf{p}} \\ \bar{\mathbf{g}} \end{bmatrix} \tag{3.74}$$

where the overbars designate quantities unique to this method.

The matrix **D** is

$$\mathbf{D} = \begin{matrix} n \\ m \end{matrix}\begin{bmatrix} \mathbf{D}_x & 0 \\ 0 & \mathbf{D}_l \end{bmatrix} \tag{3.75}$$

The matrix $\bar{\mathbf{H}}$ is

$$\bar{\mathbf{H}} = m\overset{n}{[\mathbf{0}}\ \overset{m}{\mathbf{I}}] \tag{3.76}$$

The matrix $\bar{\mathbf{G}}$ is

$$\bar{\mathbf{G}} = n\overset{n}{[\mathbf{I}}\ \overset{m}{\mathbf{B}_l}] \tag{3.77}$$

Using these results and results from equations (3.49) and (3.50), we can find

$$\bar{\mathbf{T}} = \begin{bmatrix} \bar{\mathbf{N}}^{-1}\bar{\mathbf{B}}_x{}^T\bar{\mathbf{M}}^{-1}\bar{\mathbf{G}} \\ \mathbf{D}_l\bar{\mathbf{B}}_l{}^T\bar{\mathbf{M}}^{-1}\ (\mathbf{I}-\bar{\mathbf{B}}_x\bar{\mathbf{N}}^{-1}\bar{\mathbf{B}}_x{}^T\bar{\mathbf{M}}^{-1})\bar{\mathbf{G}} \end{bmatrix} \tag{3.78}$$

where

$$\bar{\mathbf{M}} = \bar{\mathbf{B}}_l\bar{\mathbf{D}}_l\bar{\mathbf{B}}_l^T$$
$$\bar{\mathbf{N}} = \bar{\mathbf{M}}^{-1} + \mathbf{D}_x^{-1}$$

Substituting these results for $\bar{\mathbf{H}}$, $\bar{\mathbf{G}}$, and $\bar{\mathbf{T}}$ into equation (3.57), we find

$$\bar{\mathbf{S}} = \begin{matrix} n \\ m \end{matrix}\begin{bmatrix} \overset{n}{\mathbf{0}} & \overset{m}{\bar{\mathbf{N}}^{-1}\bar{\mathbf{M}}^{-1}\bar{\mathbf{B}}_l}\mathbf{D}_l\bar{\mathbf{C}}^{-1} \\ \mathbf{0} & -(\bar{\mathbf{I}}-\mathbf{D}_l\bar{\mathbf{B}}_l{}^T\bar{M}^{-1} \\ & \cdot(\bar{\mathbf{B}}_l-\bar{\mathbf{N}}^{-1}\bar{\mathbf{M}}^{-1}\bar{\mathbf{B}}_l))\mathbf{D}_l\bar{\mathbf{C}}^{-1} \end{bmatrix} \tag{3.79}$$

The matrix may be substituted into equation (3.55) and values of $\bar{\mathbf{p}}$ and $\bar{\mathbf{g}}$ (eq. 3.74) found as before. If we retain only the first term in $(\mathbf{I}-\mathbf{S})^{-1}$, we may also write for the coefficients

$$\bar{\mathbf{p}} = (\mathbf{I}+\bar{\mathbf{N}}^{-1}\bar{\mathbf{M}}^{-1}\bar{\mathbf{B}}_l\bar{\mathbf{D}}_l\bar{\mathbf{C}}^{-1})\,\mathbf{g}_0 \tag{3.80}$$

In these equations, $\bar{\mathbf{C}}$ represents the covariance matrix of the terrestrial anomalies. Thus, in its complete form, it will be a 1654 × 1654 matrix. Such a large matrix cannot be inverted easily at this time without excessive computer time. However, with the proper ordering of the anomalies (e.g., Isner, 1972) and the setting of covariances to zero for anomalies separated by a distance greater than some specified amount, a banded matrix could be obtained for $\bar{\mathbf{C}}$. This would make the inversion procedure somewhat easier. Such modifications of $\bar{\mathbf{C}}$ were not carried out. Consequently, we conclude at this time that the collocation concept is more easily applied (in practice) to the first approach than to the second.

The results obtained by means of method one are presented in section 3.52.

3.5 RESULTS

The DOD results deal almost entirely with station coordinates. The only exceptions are Rapp's geoid (sec. 3.5.2) and NWL computations (sec. 3.5.3) of Love's numbers and the polar motion.

Station coordinates are presented for (1) the western hemisphere (sec. 3.5.1.1), (2) North America, the West Indies, and Bermuda (sec. 3.5.1.1), (3) SECOR Equatorial Network (sec. 3.5.1.3), (4) TRANET Network (sec. 3.5.1.4), and (5) various points within the United States (sec. 3.5.1.5). The coordinates for the various points within the United States were obtained during tests of the PC–1000 camera and GEOCEIVER and are included partly because of their possible use as coordinates and partly because they show the performance of the instruments.

3.5.1 Coordinates of Tracking Stations

3.5.1.1 Stations in the Western Hemisphere

(Donovan N. Huber, DMA/AC)

3.5.1.1.1 INTRODUCTION

The Defense Mapping Agency/Aerospace Center (DMA/AC) has used PC–1000 and BC–4 data obtained through the NGSP in several geodetic solutions. The geometric applications of the data were directed toward specific-point positioning programs on the Air Force Eastern Test Range (AFETR), Bermuda, and Johnston Island. DMA/AC also undertook densification of the World Geometric Satellite (PAGEOS) Network (ch. 7) in South America. Data from ANNA 1B and GEOS 1 and 2 (ch. 2) and from ECHO 1 and PAGEOS (ch. 5) were used in these efforts (sec. 3.3.1).

3.5.1.1.2 EASTERN TEST RANGE

Table 3.11 presents the adjusted positions of five PC–1000 camera stations in the AFETR project. The initial coordinates were approximate values and were allowed to adjust freely. The positions for Hunter Air Force Base, Semmes, and Homestead on NAD 1927 (North America Datum) were held fixed. Only observations on ANNA 1B and GEOS–2 were used (table 3.6, sec. 3.3.1) for this project. Both case 1 and case 2 (see sec. 3.4.1) type observation-equations were employed.

Coordinates for three camera stations were determined also by the AFETR. Table 3.12 shows the difference between values of the AFETR and those in table 3.11. These differences are generally within the standard deviations shown in table 3.11.

3.5.1.1.3 BERMUDA

Geodetic positions (NAD 1927) for two stations, Aberdeen and Hunter, were held fixed, and the position of the Bermuda stations was allowed to adjust freely. Table 3.13 gives the final adjusted coordinates for Bermuda and the fixed values for Aberdeen and Hunter AFB. Only data from ECHO 1 and PAGEOS (table 3.6, sec. 3.3.1) were used for this solution. Since each observation involved at least one known station and Bermuda, only case 2 type observation equations were applicable (see sec. 3.4.1).

Several determinations of the coordinates of Bermuda on NAD 1927 exist. Three solutions in particular are in very close agreement: the PC–1000 determination, the AFETR determination, and a solution made by the U.S. National Ocean Survey (USNOS). In order to show the agreement between them in a meaningful way, the coordinate shifts from the local Bermuda 1957 Datum to NAD 1927 were derived for the three solutions. The derived shifts are given in table 3.14. As can be noted, the departure of each determination from the mean value is only a few meters.

3.5.1.1.4 JOHNSTON ISLAND

The latest solution for Johnston Island (table 3.15) was derived in November 1972. It is based on coordinates of Maui, Wake, and Christmas Islands determined by USNOS in their October 1972 World Net (WN) Adjustment (ch. 7). These stations being held fixed and the data listed in table 3.6 (sec. 3.3.1) being used, a relatively strong determination was achieved for Johnston Island. The strength of the tie to the World Net is indicated by the standard deviations.

3.5.1.1.5 SOUTH AMERICA

The latest solution for stations in South America was also referred to the WN adjustment. The five BC–4 camera positions shown in column 1 of Table 3.16 were weighted according to their sigmas as published by NOS. The sigmas are listed for the five stations along with their coordinates on the WN. The coordinates for Beltsville were held fixed, and two conditions on chord lengths were imposed in the adjustment. These chords were between the PC–1000 and BC–4 cameras collocated at Paramaribo and Natal.

Since WN positions for these two collocated PC–1000 stations could be computed accurately before any adjustment, this computation was made, and the resulting coordinates received a priori sigmas of 5 meters. Thus six stations were left to move freely in the solution: Brasilia, Asunción, Bogotá, Manaus, Curaçao, and Trinidad.

Internally, the results of the adjustment show that the PC–1000 stations are tied to the WN stations in South America to an accuracy of 4 meters (one sigma) in horizontal position and height. Combining this error with the errors given for the BC–4 stations produced an overall sigma of 6 meters horizontally and a sigma of 7 meters in geodetic height.

3.5.1.2 Stations in North America, West Indies, and Bermuda

(George Hadgigeorge, AFCRL)

3.5.1.2.1 INTRODUCTION

The solution involved a 29-station network on NAD 1927 (fig. 3.17, sec. 3.3.2). Data consisted of camera and ranging observations on 171 well-distributed passes. The camera observations were those made with the PC–1000 and MOTS camera systems, and the ranging data were those collected by SECOR and the NASA laser system (table 3.7, sec. 3.3.2). Prior to reduction the data were preprocessed and corrected, e.g., for polar motion and for UTC to UT corrections, and all data were fitted to a general conic of the form

$$ax^2+2bxy+cy^2+2dx+2ey+1=0$$

for evaluating randomness in the residuals. Additionally, two error models were used to discover errors in both sets of data.

3.5.1.2.2 RESULTS

Thirteen orbits were observed by four SECOR stations, two of which were observed simultaneously with cameras. Since most observations by SECOR were not simultaneous with the camera observations, constraints were applied to the distances and directions between the two SECOR and the two collocated camera stations (see fig. 3.18, sec. 3.3.2).

Measurements by laser systems were available from only one station and on only four orbits. Since the number of orbits was not sufficient to improve the station position, a constraint was applied to the distance and direction between the laser systems and optical collocated camera system (fig. 3.18). The weights used are given in table 3.17. Original coordinates for the stations are given in chapter 1.

The standard errors in the coordinates found by the short-arc method are given in table 3.18 (Hunter AFB coordinates were held fixed). Errors of 2 to 3 meters for stations in the continental United States and 3 to 6 meters for stations in the Caribbean reflect the precision and illustrate the strength of the solution. The determination of some coordinates was weaker than determination of others because of poor geometry and limited observations available from some stations. Table 3.18 also shows the finally adjusted coordinates of the stations. These coordinates are referred to NAD 1927 Datum.

A typical bias found in camera orientation ν, ω, and κ was 0″.2. The largest bias found was 1″.5. Biases found in the measurements by laser ranged from 2 to 15 meters, and biases on the SECOR ranges ranged from 4 to 35 meters. The random noise was approximately 1 to 2 meters for laser measurements and 1 to 5 meters for SECOR measurements.

In order to minimize errors included by the displacement of the Earth's center of mass relative to the center of the spheroid, another reduction was attempted. In this reduction the given NAD 1927 coordinates of all stations were transformed to Mercury Datum before the adjustment. After the adjustment was completed, the new coordinates were transformed back to NAD 1927.

A comparison of the results of the two methods reveals that high-quality determination of station locations may be sensitive to uncertainties in the coordinates of the

Earth's center of mass. If the station locations are referred to a datum whose origin does not coincide with the center of mass of the Earth, then either the first-degree coefficients of the potential should be constrained appropriately in the solution or the station locations should be transformed to a spheroid whose origin coincides more closely with the center of mass of the Earth before the adjustment is made.

3.5.1.3 Stations on the SECOR Equatorial Network

(M. A. Warden, W. D. Googe, and G. Dudley, DMA/TC)

3.5.1.3.1 PRELIMINARY GEOMETRIC ADJUSTMENTS

As field work progressed on the SECOR Equatorial Network, preliminary solutions were computed for each successive quadrilateral. These solutions were purely geometric; the three "known" stations were held fixed and satellite positions were computed from simultaneous ranges. The computed positions of the satellite were then held fixed, and the position of the unknown station was determined. The position of the unknown station was determined through the least-squares process described in section 3.4.3 with a three-sigma rejection criterion on the range. There was no limit on the number of observations used in solving for the position of a single station.

The geometric solution was used primarily to clean up data, e.g., to detect ambiguities in range, to remove data taken at low elevation, and to detect faulty corrections for ionospheric refraction. Faulty correction for ionospheric refraction can be due to local interference on the low-frequency carrier when the higher frequency carrier is relatively undisturbed. In addition to the station coordinates, estimates of satellite position and velocity vectors (in Earth-fixed coordinates), which were used later in the short-arc solution, were also provided by the geometric solution.

3.5.1.3.2 SHORT-ARC SOLUTION FOR EACH QUADRILATERAL

Although SECOR networks were designed for simultaneous observation, the final "quad" (set of four stations) by "quad" determination was done by the short-arc technique. The short-arc adjustment allowed the use of all ranging data collected at a station, whether or not observations were simultaneous with those at the other three stations; hence, it increased the amount of data and improved the geometry of the solution. In addition, fitting an orbit to the measured ranges served, in effect, to smooth the ranges.

A modification of Enkes' method was used to compute the reference orbit in which perturbation due only to the Earth's gravity was computed by numerical integration. The state vectors were then updated by an iterative fit to the measured ranges. This process was repeated for each satellite pass observed over the quad. The position and velocity vectors of each orbit and the coordinates of the four tracking stations were the parameters of a state vector which was adjusted by the method described in section 3.4.3. As each solution for a single quad was completed, its data were stored on punched cards for later adjustments.

3.5.1.3.3 ADJUSTMENT OF THE NETWORK

Having a preliminary quad-by-quad short-arc adjustment made it possible to prepare a simultaneous adjustment of the entire network soon after the last station in the network made its observation.

This adjustment was accomplished by a batch, least-squares, short-arc procedure; i.e., for each pass of a satellite the position and velocity vectors of the satellite were treated as unknown, as were the position vectors of the observing stations. The actual number of unknowns was

6 state vector unknowns for 594 passes	=3054
3 position unknowns for 37 stations	= 111
total unknowns	=3165

A total of 48 132 range observations entered into the adjustment.

The system of normal equations resulting from these data was, of course, singular, since the range observations supplied no orientation information and the short-arc dynamic constraint was not strong enough to fix the origin of the coordinate system. In the first adjustment this singularity was overcome by fixing the North American Datum (NAD 1927) coordinates of Herndon, Worthington, Ft. Stewart, Austin, and Larson after they had been shifted to a geocentric system by applying the shifts

$$\Delta X = -24 \text{ meters}$$
$$\Delta Y = 154 \text{ meters}$$
$$\Delta Z = 182 \text{ meters}$$

These shifts were derived by comparing the NAD 1927 coordinates to the Standard Earth II coordinates (Gaposchkin and Lambeck, 1970) of those points common to both systems.

In addition, the relative location of Azores 2 with respect to Azores 1 was held fixed. This solution was iterated three times, the observation equations being linearized each time on the basis of the solution obtained from the last iteration. The change in the solution from the second to the third iteration was completely negligible.

The normal equations from the third iteration, before any conditions were applied, were saved and subsequently the satellite coordinates eliminated. The result was a set of 111 normal equations containing all the information the ranges supplied about the relative location of the 37 tracking stations. All further solutions were obtained by applying conditions to these normal equations.

As was expected, this first solution was extremely weak. This weakness resulted principally from the weaknesses in geometry and data distribution. Undoubtedly, the best use of the SECOR results would be in combination with the results of other systems which can supply the directional control SECOR lacks, e.g., the BC–4 world net (ch. 7). However, it was desired to have a solution that was as "pure" SECOR as possible. The results (table 3.19) reported here are from a relatively pure solution.

Five stations of the network were located within the United States, and the relative coordinates of these on NAD 1927 were felt to be reliable. The eight pairs shown in table 3.20a were selected from these five stations, and weighted constraints were placed on the directions of these eight lines. Two of these direction constraints also served to tie Larson to Worthington and to Austin and thus to close the network.

The origin of the coordinate system was established by fixing the position of Worthington. The relative positions of the Azores stations were always held fixed.

At the time this solution was computed, the results of a preliminary BC–4 network adjustment (WGS–1) were available. According to H. Schmid, these are identical with those in ch. 7). Sixteen BC–4 stations had been collocated with SECOR stations, and directions were available for 14 lines observed by pairs of BC–4 cameras. These lines fell into two groups: the first group spanned the Atlantic and Africa from Paramaribo to Mashhad, and the second spanned the Pacific from Wake Island to Larson.

Since a pure solution was wanted, it was desirable to keep the number of directional constraints small and yet to employ enough directional constraints to achieve adequate control of direction throughout the network. Several ways of choosing directional constraints were investigated. The final method involved a systematic approach. A solution was made without any BC–4 constraints, and the uncertainty of the direction was computed from the SECOR solution for each of the BC–4 lines.

This method allowed the identification of the line that was most uncertain in direction

and therefore most in need of external directional constraints. In the next iteration the direction of this most uncertain line was constrained to the values obtained from the BC–4 observations, a solution was made, and the uncertainties of the remaining lines were examined. This procedure was followed through several iterations. After each iteration the uncertainties of the adjusted coordinates of the SECOR stations were examined. When the improvement in these uncertainties afforded by further BC–4 constraints became insignificant, the iterative procedure was stopped. The six sets of BC–4 direction contraints selected by this procedure are shown in table 3.20b. In practice, these directions are between BC–4 sites whose positions relative to the collocated SECOR sites were rigidly held. The directions from the BC–4 adjustment are not strictly compatible with those from NAD 1927, because of changes in the adopted longitude of the Naval Observatory. This should not seriously degrade the solution because both sets of directional constraints were incorporated into the solution with the a priori weights shown in tables 3.20a and 3.20b.

3.5.1.3.4 RESULTS AND ANALYSIS

The coordinates of the equatorial network stations obtained in the final adjustment (solution C–9) are shown in table 3.19. The standard deviation of a single measurement of range was 2.7 meters. The indicated standard deviation of the adjusted coordinates ranged from 4 to 8 meters. However, comparison of coordinates obtained by SECOR with those obtained by other systems showed much larger discrepancies. In order to obtain the best possible coordinates for the SECOR stations, a solution combining BC–4 and SECOR data ($B+S$ solution) was computed by using the normal equations for SECOR and the normal equations of the WGS 1 solution. This solution tended to be dominated by the BC–4 data, so that there was fair agreement between the combination solution and a pure BC–4 solution at the BC–4 stations. The differences between the combination solution and the SECOR solution were much larger, and many discrepancies as large as 50 meters were noted. The rms differences between the combination and SECOR solutions were 25 meters in latitude, 30 meters in longitude, and 26 meters in elevation. Furthermore, the differences are quite systematic in character, indicating large correlation between similar coordinates of adjacent stations. This means that the relative coordinates of adjacent stations may be quite accurate, even though accumulation of error may unfavorably affect the relative coordinates of widely separated points.

If the combination solution is adopted as a standard comparison, it follows that the coordinates determined by SECOR, with only a small amount of BC–4 directional control, have an accuracy of about 25 to 30 meters in each coordinate. Although these figures do not reflect the potential for very precise geodesy that some have seen in the system, they do meet the original design specifications of the SECOR measuring system.

In combination with other systems, however, SECOR can make a significant contribution. For example, table 3.21 gives the discrepancies between the chord distances from the $B+S$ solution and seven of the traverse distances used to scale the BC–4 net. The $B+S$ solution was scaled by SECOR alone, so these discrepancies are due to SECOR scale error as propagated through the BC–4 WGS 1 net or due to errors in the surveyed distances. Notice that the two large discrepancies in Europe largely cancel to give very good agreement on the line Tromso—Catania. Notice also that the only line directly observed in the SECOR net is the one in Africa.

3.5.1.4 Stations in the TRANET Network

(R. J. Anderle, NWL)

3.5.1.4.1 RESULTS

The Doppler system was used to position 37 of the 44 BC–4 sites in the PAGEOS network. The locations of the electrical center

of the antennas determined from the Doppler observations are given in table 3.22 in the CIO system. (Two stations were located in Wake and Seychelles.) Also shown in the table are the standard deviations of the solution. These errors give only the random error in station position resulting principally from uncertainties in the gravitational field. The Doppler system also has biases which are estimated to be 1 meter in pole position, 5 meters parallel to the spin axis, and 3 meters in height (which also implies 0.5 part per million in scale). The surveyed positions of the electrical centers in the local datum are given in table 3.10, section 3.3.4. Datum shifts based on the differences between the Doppler and terrestrial survey are given in table 3.23.

3.5.1.4.2 EVALUATION

Geometric Simulations.—Early simulations (Cohen and Hubbard, 1962) revealed that geometric solutions for station positions are particularly weak for Doppler or range difference observations of satellites. As a result, no geometric solutions for station positions have been carried out with actual Doppler or range difference data. Positions of Doppler stations are normally based on dynamic solutions using orbit constants best fitting observations over time periods of two or more days in order to obtain statistically strong solutions and to provide results for stations which are geographically isolated. However, numerous experiments have been conducted based on short-arc solutions, in which the orbital constants are based on data obtained during a period of about 30 min. Such experiments were particularly useful early in the program, when effects of uncertainties in the gravity field on the satellite orbit were orders of magnitude larger than they are now.

Dynamic Simulations.—Initial simulations of dynamic solutions indicated that accuracy of 10 meters in coordinates of a station could be obtained by such techniques (Anderle, 1963). The simulation was optimistic in that it neglected effects of all but a few gravitational terms but pessimistic in the effects of Doppler instrument error. More realistic simulations include the effects of neglected potential coefficients which can be predicted on the basis of the decrease in the magnitude of the coefficients with increasing degree, as shown in figure 3.29 (Anderle and Smith, 1968). It was found that synthetic fields could be constructed on the basis of this decay curve which could be used to predict the effects of neglected coefficients (Anderle *et al.*, 1969). The study showed that the effect on station positions of neglecting coefficients above sixth degree is 10 meters, whereas the effect of neglecting terms above 12th degree is only 2 meters (H. L. Green, unpublished report, 1969). Figure 3.30 shows the effects on the orbit of a Navy Navigation Satellite of neglecting coefficients above 12th degree in geodetic solutions. This curve does not include the effects of errors in resonance coefficients which can be quite large if they are not determined specifically for the satellite orbit under consideration (Anderle,

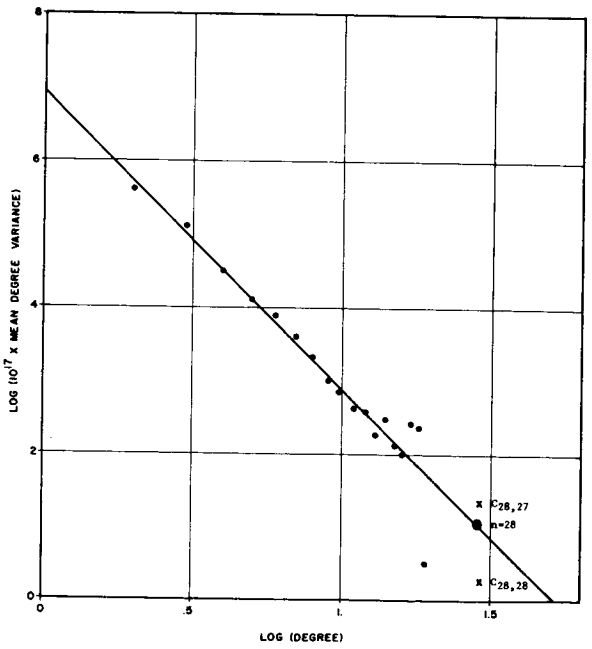

FIGURE 3.29.—Mean degree variances: NWL 8D solution.

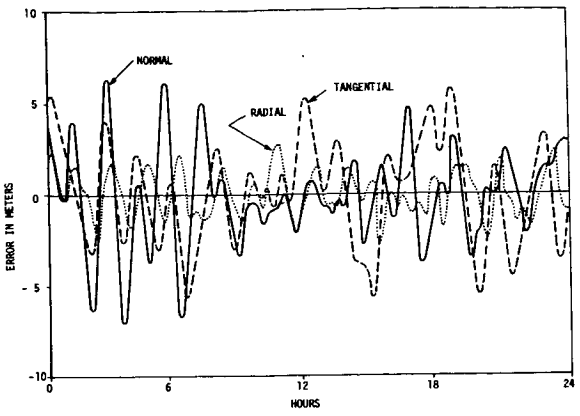

FIGURE 3.30.—Aliasing errors for 1100-kilometer polar orbit: NWL 8D simulation.

1965a). The rms of the errors shown in figure 3.30 is only 4 meters, which is consistent with the residuals of fit encountered when such a field is used to compute the orbit of a 600-nm polar satellite. However, this orbital condition was strongly represented in both the simulated and the actual solutions for potential coefficients; therefore, the effects of neglected coefficients on the orbit of this satellite were absorbed in errors in coefficients considered in the geodetic solution. If the lower order coefficients had been perfect, the neglected coefficients would have produced an rms error of 10 meters in the computed orbit, as shown in figure 3.31 (C. W. Malyevac, unpublished report, 1970). Such favorable aliasing of errors cannot be expected for all orbital conditions. More recent simulations show that the effects on computed station positions of neglecting coefficients above 17th degree are less than 2 meters.

Special Evaluation Tests.—Periodically, special evaluations of Doppler equipment or the dynamic method of station positioning were made. In the first test, results of short-arc computations of station position based on Doppler observations of the ANNA 1B satellite were compared with positions surveyed on the North American Datum. The results agreed to 5 to 10 meters, depending on the station geometry, which was essentially consistent with the expected effects of instrumentation error for the particular conditions (Nott, unpublished, 1964). In 1965 a more accurate terrestrial survey was conducted in the southeastern part of the United States, and the results were compared with both long- and short-arc solutions for station coordinates. The short-arc results agreed to 3 to 5 meters, which was again consistent with the effects of instrument error (R. W. Hill, unpublished report, 1966). The long-arc results disagreed with the survey by 5 to 10 meters, which exceeded the survey or instrument error. However, the results were based on a gravitational field which was only complete to sixth degree. It was later shown (R. W. Hill, unpublished report, 1971) that a Doppler ephemeris based on the NWL 9B coefficients gave agreement with laser system ranges to the satellite of 4 meters. When the geodimeter survey was completed across the United States in 1971, Doppler-derived positions agreed with the new survey to 1 meter in the eastern United States and 3 meters in the western United States (fig. 3.32). The 3-meter difference exceeds the expected uncertainty in the Doppler position, but the difference is close to the errors expected in both the satellite and the terrestrial survey.

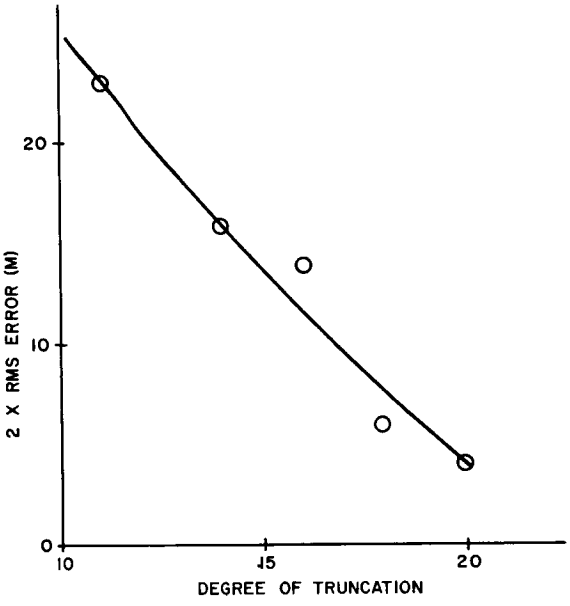

FIGURE 3.31.—Effect of neglected coefficients.

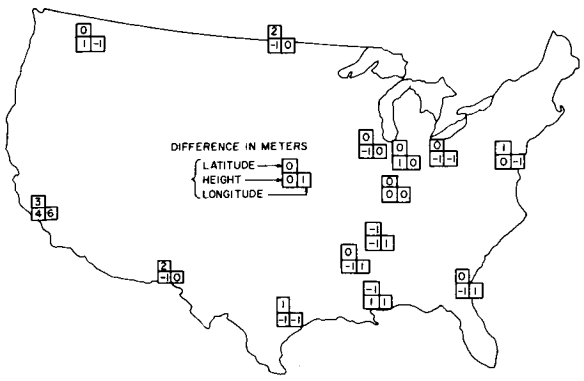

FIGURE 3.32.—Satellite versus geodimeter survey.

Tests for Consistency.—Tests are conducted periodically to determine the effect on geodetic solutions of changing the data sets, the station distribution, the number of satellites used, and the number of potential coefficients considered (Anderle, 1967a,b). The effects found are usually smaller than the effects of biases in the solution. Even the deletion of data from nearly a hemisphere in determining coefficients had only a small effect on the subsequent determination of the coordinates of stations in either hemisphere. However, one particularly valuable test involved the solution for station coordinates while constraining the zonal coefficients to various values. Table 3.24 shows how the z component of station position varies depending on which set of zonal coefficients is assumed to be correct. Biases as high as 100 meters can occur depending on which set of coefficients is used, as a result of correlation between odd zonal coefficients, orbital eccentricity, and the z component of station position. Note that the two sets of coefficients obtained simultaneously with station positions, the Goddard Space Flight Center GEM–2 and the NWL coefficients, give good agreement.

Tests Against External Standards.—It is desirable to test geodetic parameters obtained on the basis of dynamic analysis of Doppler satellite observations against external standards in order to determine if biases exist which are not tested in simulations or in tests for internal consistency. Unfortunately, the available standards either are not pertinent to the principal results or are not sufficiently accurate. Tests against terrestrial traverses were discussed earlier. While agreement of 1 to 3 meters was obtained for interstation distances, the traverse provides no test of the accuracy of the Doppler determination of datum origin or of worldwide Doppler positioning accuracy. Mean sea level would provide a worldwide evaluation of the accuracy of relative station heights if the distance of mean sea level from the center of the Earth were known. The most accurate worldwide geoid heights are those based on satellite observations, and these have uncertainties of several meters due to high-frequency geoidal undulations. Tests of NWL 10D satellite determinations of station height agree with those based on surveys above mean sea level to 9 meters for worldwide stations, which is consistent with effects of the high-frequency geoid undulations. Considering other terrestrial standards, the NWL 10D coefficients yield gravity anomalies and geoid heights which agree with terrestrial data to 18 mGal and 9 meters, respectively, on a worldwide basis. These differences are also reasonable, considering the neglected effects of high-frequency anomalies. Differences between Doppler and astronomic pole positions, discussed earlier, are not unreasonable, considering the expected accuracy of the two sets of data, but systematic variations are evident in the Doppler solutions due to resonance coefficients (Anderle, 1973). The Doppler solution for Love's number is about 20 percent lower than that found by analysis of terrestrial gravimetry data or by Newton in his analysis of Doppler data. However, the result is consistent with that obtained by Kozai in his analysis of camera data and that obtained by Douglas and others of Goddard Space Flight Center from analysis of camera observations of the GEOS–1 satellite. Qualitative agreement is obtained between tectonic features and density anomalies in the earth

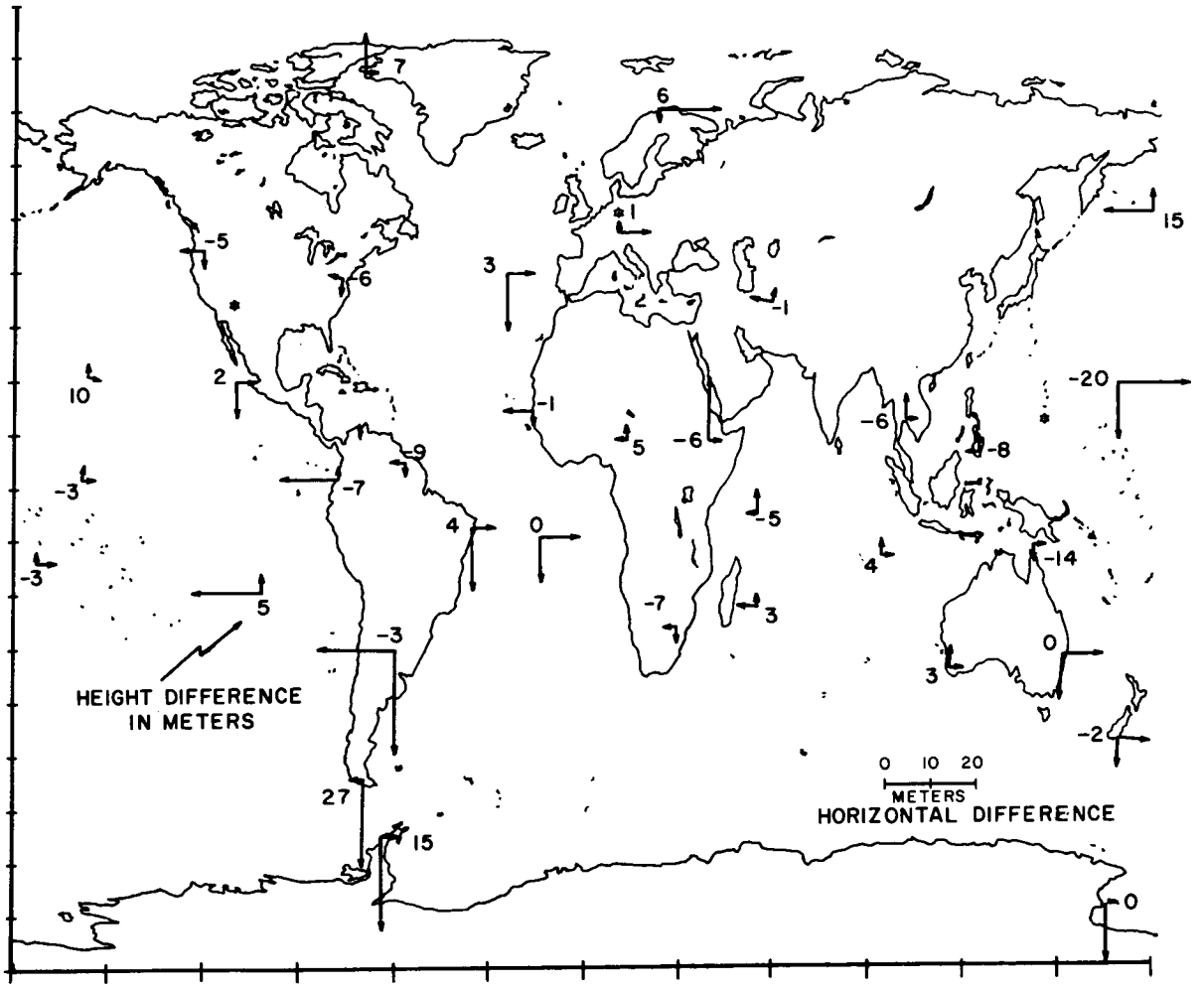

FIGURE 3.33.—Comparison of station coordinate solutions using geometric (optical) minus dynamic (Doppler).

corresponding to the computed coefficients (E. W. Schwiderski, unpublished report, 1967). Doppler-derived positions for BC–4 sites in the PAGEOS networks are compared in table 3.25 with the positions derived geometrically from the camera data. Many of the largest errors are in the South American area, as shown in figure 3.33. The error vectors on the figure depict the latitude and longitude error; the altitude error is shown numerically. It is believed that the latitude discrepancies are due to weak connections in the BC–4 net in this area. The remaining discrepancies are not unreasonable, considering the estimated accuracy of the BC–4 solutions.

3.5.1.5 Station Positions in the United States

From time to time, DOD has carried out small projects within the United States for testing techniques or instruments of satellite geodesy, but these tests also produced coordinates of stations. The projects, reported on briefly in the following section, were satellite triangulation by AFCRL using ANNA 1B carried out in 1963 and tests with the GEOCEIVERS conducted in 1971–1972.

3.5.1.5.1 GULF TEST PROJECT

(George Hadgigeorge, AFCRL)

A program in the southeastern United States, called the "Gulf Test," was undertaken in 1963 with a 10-station network of PC–1000 cameras observing the flashing beacon on ANNA 1B. The observations collected on the Gulf Test are shown in figure 3.34; coordinates of the stations are given in table 3.26. The "net numbers" in figure 3.34 represents a sequence of flashes of the ANNA beacon and the approximate satellite positions at the time of the flashing sequence.

One of the tests consisted of a reduction using all 33 nets and all observing stations. (Reduction was performed for AFCRL by Duane Brown of D. B. Associates.) Coordinates of stations AF640, AF641, AF643, and 3647 were determined by using stations 3648 and 3649 as known sites. Figure 3.34 shows the distribution of the flashing sequences used. The results of this adjustment have a mean spherical error of 4 meters relative to the coordinates on NAD 1927 (table 3.27).

Several other tests were made using the same data collected on the Gulf Test. One analysis which employed a different reduction technique was that used by Mancini (1965). From all available simultaneous data on each line, the geodetic azimuths were determined

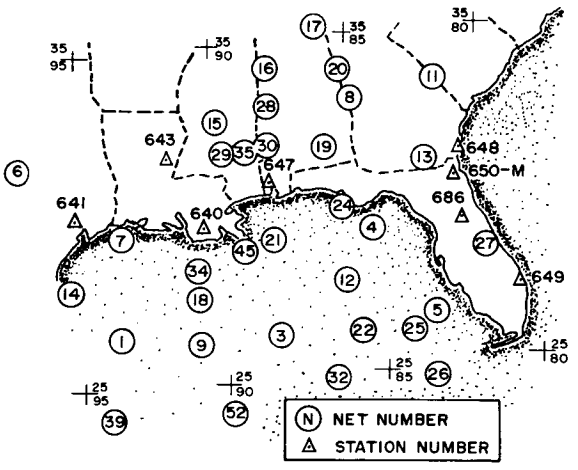

FIGURE 3.34.—Coordinates of stations AF640, AF641, AF643, and 3647 as determined from coordinates of stations 3648 and 3649 by the nets (circles) shown.

for several lines of the network on the condition that the two unit vectors from two stations to the satellite and the interstation vector are coplaner (see sec. 3.4.1). Some of the results obtained by Mancini are given in table 3.28.

The azimuths derived from the data are compared with the azimuth of the normal section obtained from the NAD 1927 coordinates by inverse computations. If these azimuths are used in a position computation with the distances given in the last column, the resulting coordinates agree within 5 meters or less with the NAD 1927 values.

3.5.1.5.2 GEOCEIVER TESTS BY DMA/AC

(Haschal L. White, DMA/AC)

Observations were made by DOD teams between 15 October and 12 December 1971 with small portable Doppler equipment (GEOCEIVER) on the network shown in figure 3.35. The network consisted of 22 sites, 19 connected (or scheduled to be connected) to the National Ocean Survey's Precision Geodimeter Traverse (HPGT) (Eos, Transactions American Geophysical Union, 1963, 1967). The observational program was accomplished in two phases. Over 10 000 passes of the Navy Navigation Satellites 1967 34A, 1967 48A, 1967 92A, 1968 12A, and 1970 67A were observed. Table 3.29 shows the stations occupied during phase 1 and phase 2.

Solutions using both the long-arc and the short-arc methods were made. Both adjustments were performed in the NWL–9D coordinate system; however, for comparison the derived coordinates were converted from the NWL–9D system to Modified Cape Canaveral Datum (MCCD). The following datum shifts were used to effect the transformation:

NWL to MCCD	*NWL to NAD 1927*
$\Delta X = 24$ meters	$\Delta X = 30$ meters
$\Delta Y = -150$ meters	$\Delta Y = -156$ meters
$\Delta Z = -179$ meters	$\Delta Z = -178$ meters

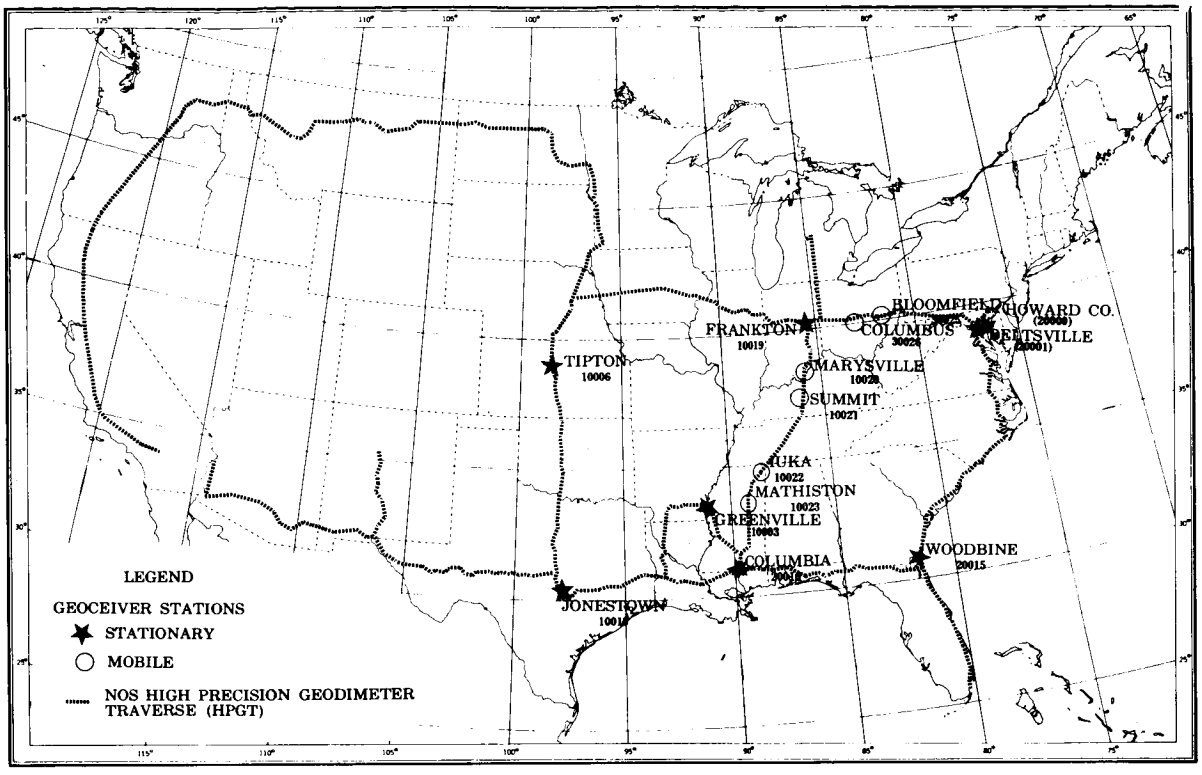

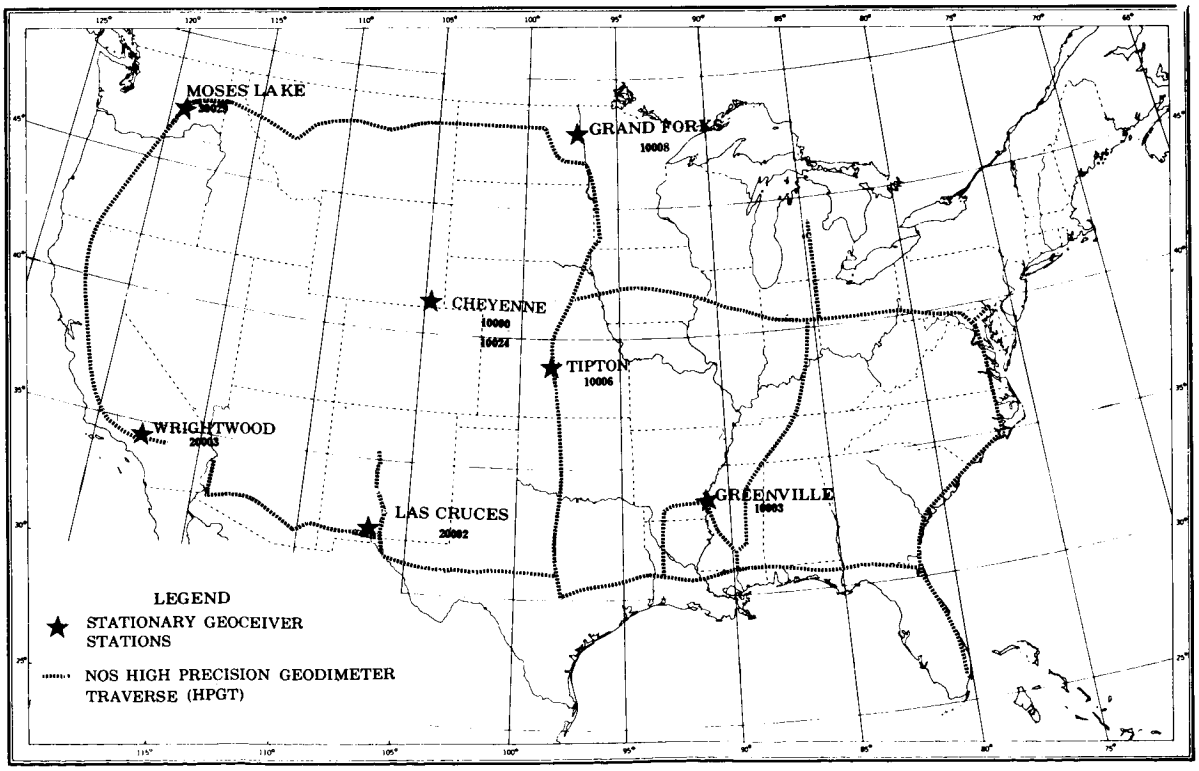

FIGURE 3.35.—GEOCEIVER network. (a) Operational test phase I. (b) Operational test phase II.

Results by the Short-Arc Method.—The procedure used in this solution has been described in various reports to the Department of Defense by Duane Brown Associates. GEOCEIVER data were used exclusively in the reduction but were used as ranges rather than range differences. Short-arc solutions were made in which either station Greenville or Tipton was held fixed in the adjustment and some interstation directions were used as constraints. Data obtained in phases 1 and 2 are summarized in table 3.30. Constraints used in solving with data from phase 1 are listed in table 3.31.

Table 3.32 shows the results for phase 1, phase 2, and phases 1 and 2 combined. The mean correction in longitude of 2 to 3 meters is larger than the mean correction in either the latitude or the geodetic height, the latter corrections being only a meter or less. In phase 1 this difference would be the result of a small timing bias, which was not completely removed from the Greenville (fixed) station data. In the phase 2 solution the large longitudinal difference at the Cheyenne stations leads one to suspect an error in the longitude on NAD 1927. Similarly, an error is probably in the longitude for Las Cruces and Moses Lake on MCCD because the HPGT was not complete, and the error propagated from a timing bias was not completely removed from the Tipton (fixed) station data. The longitudinal difference for the station at Wrightwood was less definitive than that at Cheyenne in different solutions.

The phase 1 and 2 solution shows longitudinal differences for Cheyenne similar to those obtained with the phase 2 solution and longitudinal differences slightly larger for Moses Lake (phase 2) and the Maryland stations (phase 1).

Latitudinal differences are typical of those with the other solutions, as are the geodetic height differences with the exception of Moses Lake and Wrightwood (NAD 1927).

Results Using Long-Arc Methods.—Precise ephemerides computed by USNWL using the TRANET station data were used in long-arc solutions. The ephemerides were available for Navy Navigation Satellites 1967–48A (phase 1 only) and 1967–92A (phase 1–2) in the NWL–9D coordinate system.

Again, the longitudes of the Cheyenne stations fared poorly, as did the MCCD longitude of Moses Lake. The Moses Lake longitudinal difference could be the result of not having the final adjusted values of the western loop of the HPGT.

Summary.—The short-arc, phase 1 results show typical accuracies in latitude and geodetic height of 2.5 meters or better, in comparison with the HPGT (MCCD) coordinates, and longitudinal differences of less than 4.5 meters. The phase 2 results are similar except for the stations for which only NAD 1927 coordinates were available (Cheyenne and Wrightwood) and for the slightly larger difference in the Moses Lake longitude.

The long-arc results show similar agreement. The maximum error in longitudinal error for the long-arc solution is 2.8 meters. (A more detailed description of these tests is included in a Tri-Service DMA Report 0001, July 1972. Requests for copies of this report should be directed to the Defense Mapping Agency, Washington, D. C.).

3.5.1.5.3 GEOCEIVER TESTS BY DMA/TC

(R. W. Smith and C. R. Schwarz, DMA/TC)

The point positioning technique (sec. 3.4.4) has proven to be extremely successful for producing precise geodetic positions based on observations from the miniaturized Doppler receivers. The positions obtained are referred to a center-of-mass coordinate system and are independent of other positions. For some applications, however, a precise relative position between two stations is desired. In these cases, the technique of section 3.4.4 is modified; this modified technique is known as translocation.

A translocation solution consists of the difference between two point position solutions, performed under special circumstances.

It is used only to determine the relative positions of two points, never to determine the position of a single point. The special circumstances are that each pass used in the individual point position solutions must be seen simultaneously by both stations and that each station must obtain the same number of data points. It is not necessary that the data be simultaneous.

This concept assumes that errors in the satellite ephemeris will, to a certain extent, affect both stations in a similar manner. These similar errors will cancel when the coordinates of the two stations are differenced, so that in many instances the relative positions between two stations can be determined more accurately than the position of either station can be.

The relative coordinates of 20 pairs of stations were determined by means of the translocation method and the DOD GEOCEIVER test data. These relative coordinates were compared with relative coordinates determined from the U.S. high-precision traverse. The discrepancies between the two determinations of relative position were examined in each coordinate and in the direction of the line joining the two stations. Some of these values are shown for NGSP stations in table 3.33. As was expected, these discrepancies were found to be larger for the longer lines. Ninety percent of all the linear discrepancies are contained within the bounds "0.5 meters plus 2 parts per million of the distance." This expression thus gives the accuracy (90 percent probability) to be applied to each component of relative position.

The accuracy expression for discrepancies found by translocation is valid for lines less than 800 km in length in either north-south or east-west orientation. When the separation is more than 800 km, the assumption that errors in the ephemeris affect both stations in the same way becomes less valid, and the translocation solution takes on the character of the difference of two point position solutions. The accuracy expression for discrepancies found by translocation applies to solutions containing 20 or more passes.

There is no evidence that any improvement can be gained by using more than about 35 passes, but the use of fewer than 20 passes may be expected to result in a less accurate solution. The application of the accuracy expression should also be limited to solutions similar to those from which the expression was derived.

3.5.2 Gravitational Potential and Geoid

3.5.2.1 Gravitational Potential and Geoid by the Least-Squares Collocation Method

(R. M. Rapp [2])

3.5.2.1.1 METHOD

The terrestrial data used for this comparison were the 1283 5° equal-area anomalies computed by Rapp (1972a), supplemented by model anomalies to form a complete set of 1654 5° anomalies. In the original computations a −2 mGal error was present for certain anomalies in the Canadian area. This error was removed; hence it is not reflected in the final solution given here.

The starting potential coefficients were those of GEM 3 (Lerch and Wagner, 1972). The standard deviation for each coefficient of GEM 3 was computed from

$$m = k\left(\frac{0.8\Delta_1^2 + 0.4\Delta_2^2 + 0.2\Delta_3^2}{0.8+0.4+0.2}\right)^{1/2} \quad (3.81)$$

where Δ_1, Δ_2, and Δ_3 are the mean differences between GEM 3 coefficients and those of GEM 1, the SAO Standard Earth II (Gaposchkin and Lambeck, 1970) and the SAO Standard Earth I (Lundquist and Veis, 1966). Values of k were chosen as ½, ¼, ⅛, and 1/16 to reflect various relative weighting schemes. The most realistic standard deviation for GEM 3 coefficients should be the $k = ½$ case.

[2] The research reported in this section was sponsored by the Air Force Cambridge Research Center, Bedford, Massachusetts.

3.5.2.1.2 SOLUTIONS

Using the original set of anomalies, a least-squares solution and a least-squares collocation solution were made with the four values of k. These solutions were complete to $n=20$ with additional resonance and zonal coefficients in degree 21 and 22. After making tests with each solution it was decided that the best overall solutions were achieved with $k=1/8$. The potential coefficients from the least-squares collocation solution (made with the corrected anomaly field) with $k=1/8$ are given in table 3.34. In this table, two sets of standard deviations are given. The first, designated SD 1, is based on the actual solution with $k=1/8$. As a guide to more realistic standard deviations, the standard deviations from a combination solution with $k=1/2$ are also given, as SD 2.

3.5.2.1.3 COMPARISONS OF SOLUTION

The results from the various sets of potential coefficients were examined by considering anomaly degree variances, terrestrial gravity comparisons, comparisons with astrogeodetic undulations, and comparisons with fitted orbits.

Comparisons of anomaly-degree variance were made to see the aliasing effect at the higher degrees that is caused by the truncation of the solution. This aliasing effect manifests itself by larger-than-expected values of the variances at high degree. In the comparisons made here it was found that the least-squares collocation adjustment significantly reduced the aliasing effect.

The comparisons of the terrestrial gravity field were made by computing anomalies from the potential coefficients, which were then compared with the starting anomalies by using the equations given by Kaula (1966a). The best agreement with the terrestrial gravity field was found with $k=1/2$. The usual least-squares and least-squares collocatiton coefficients showed no significant difference in anomaly agreement, although there was indication that the potential coefficients of the least-squares collocation solution were slightly (10 percent) more accurate than those of the usual least-squares solution.

Comparisons with the astrogeodetic geoid were made by computing undulations from the potential coefficients and comparing these undulations with the astrogeodetic undulations after a suitable transformation. The root-mean-square height after the adjustment was a measure of the goodness of a potential coefficient solution. Values of the rms deviations are given in table 3.35 for several solutions tested. In the North American Datum 1927, 3112 points were used, whereas in the Australian Datum, 1084 points were used. Of these solutions, the best is the least-squares collocation solution, although the difference between it and the usual least-squares solution is very minor. In several cases the other solutions tested are significantly poorer than those described in this paper.

Various sets of potential coefficients were used to obtain a best fitting orbit using laser data on a 7-day arc of GEOS-A. The fit to the orbit for these sets of coefficients is shown in table 3.36. We see that the least-squares collocation solution yields a better fit than the usual least-squares solution, although the differences decrease as k decreases. This set of potential coefficients yields better fit than all other sets tested except those of the SAO Standard Earth II.

The geoidal heights and anomalies derived from the potential coefficients of table 3.34 are shown in figures 3.36 and 3.37. Figure 3.38 shows the anomaly difference between the solution of this paper and the anomalies implied by the potential coefficients of the SAO Standard Earth II. They were computed from

$$N = R \sum_{n=2}^{n_{max}} \sum_{m=0}^{n} (\bar{C}_n^m \cos m\lambda + \bar{S}_n^m \sin m\lambda)\, \bar{P}_n^m(\sin \bar{\psi})$$

$$\Delta g = \gamma \sum_{n=2}^{n_{max}} (n-1) \sum_{m=0}^{n} (\bar{C}_n^m \cos m\lambda + \bar{S}_n^m \sin m\lambda)\, \bar{P}_n^m(\sin \psi)$$

using a flattening of 1/298.256.

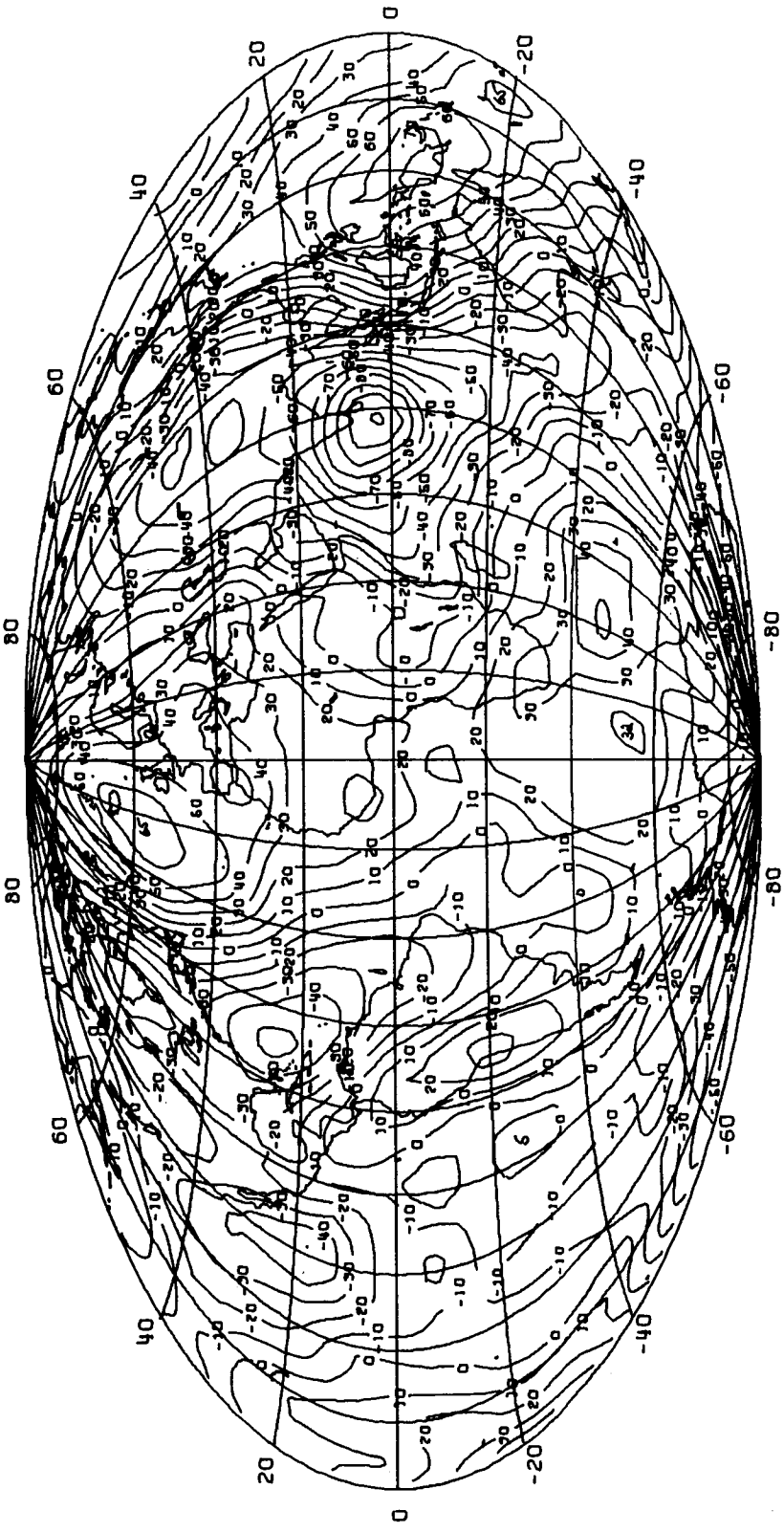

FIGURE 3.36.—Geoid undulations from recommended collocation coefficients; contour interval 10 meters, reference flattening = 1/298.256.

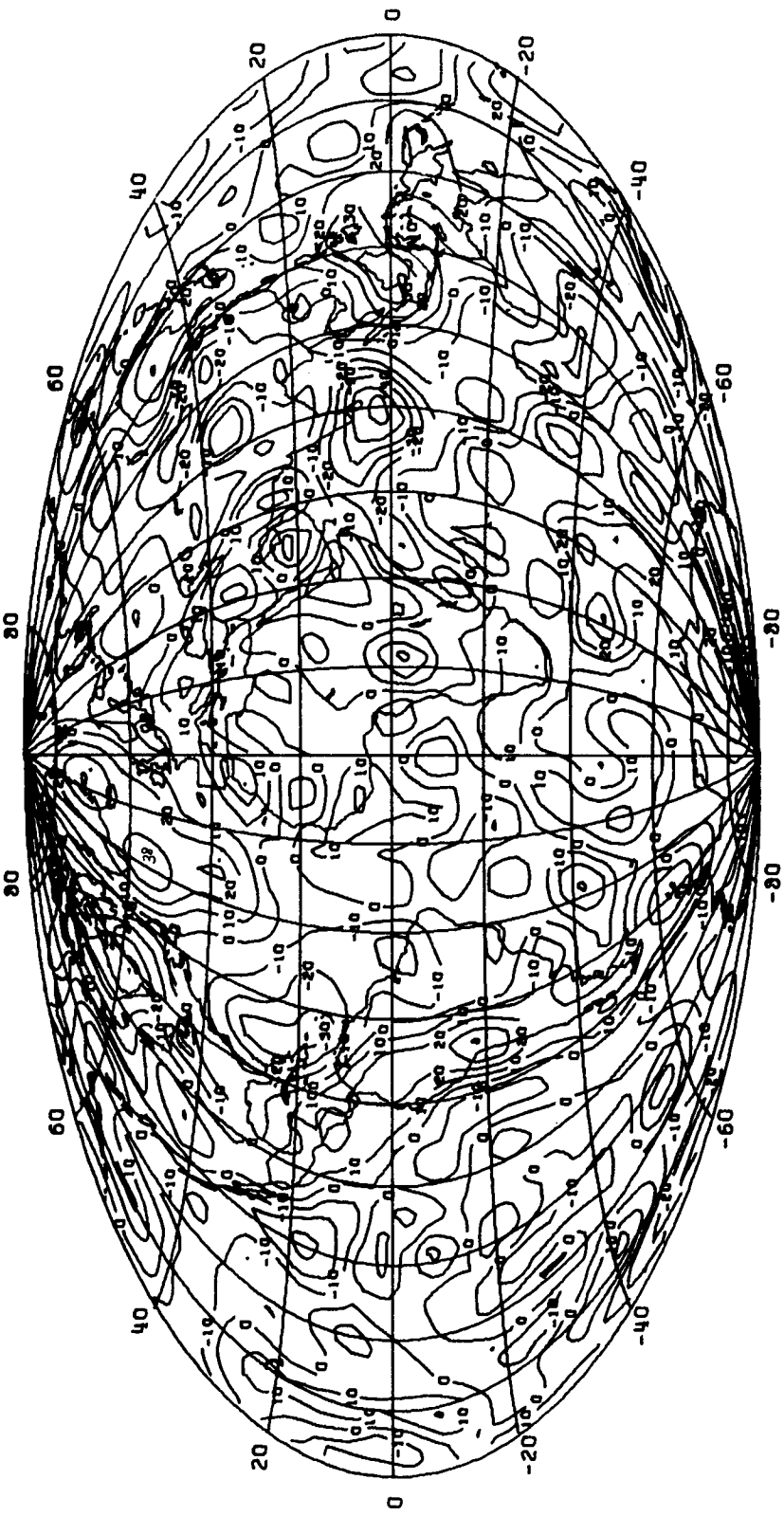

FIGURE 3.37.—Anomalies from recommended collocation coefficients; contour interval 10 mgals, reference flattening=1/298.256.

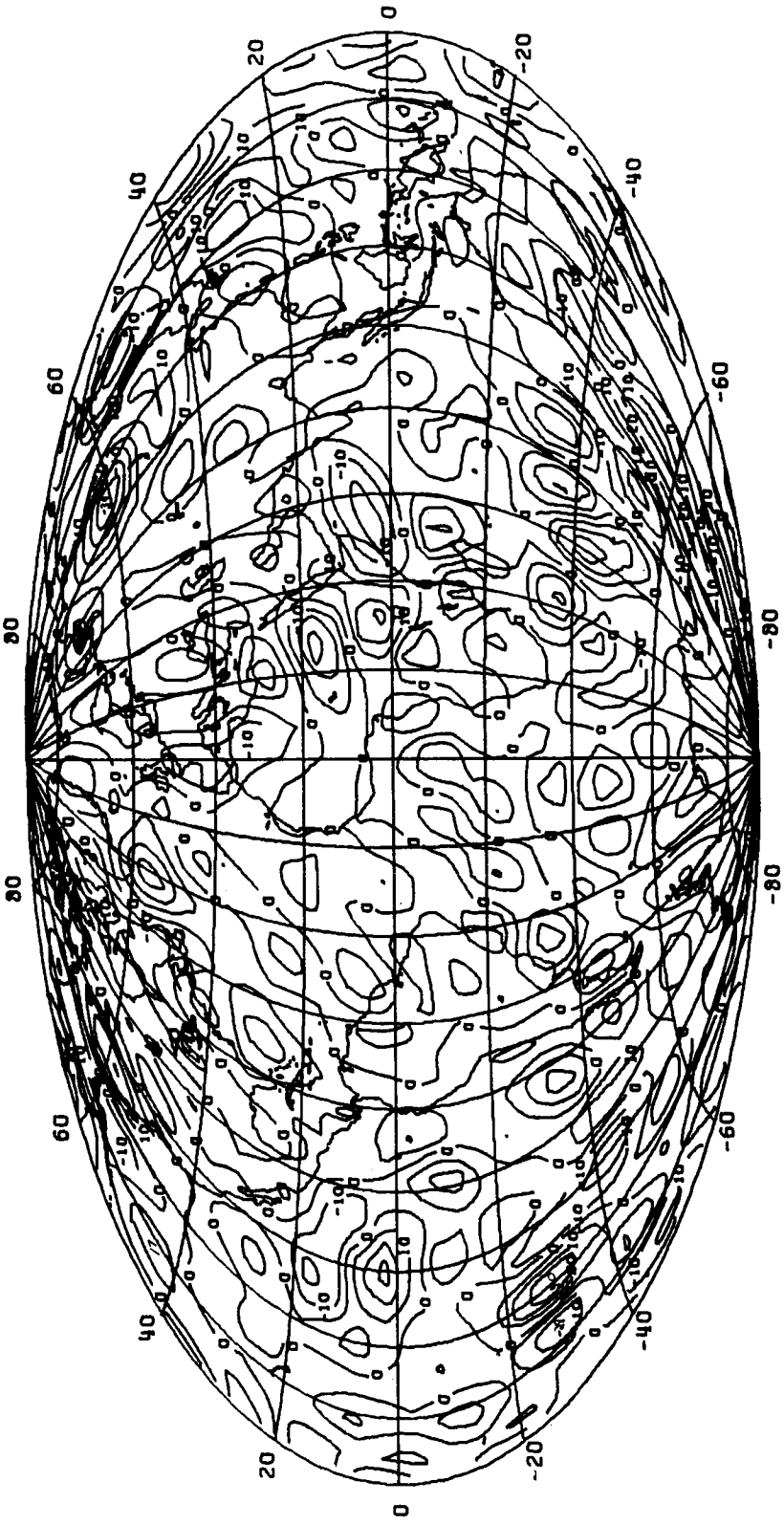

FIGURE 3.38.—Anomaly differences: collocation solution minus SAO Standard Earth II; contour interval 10 mgals; maximum difference=40 mgals; rms difference=10.8 mgals.

Comparison of various potential coefficients in terms of geoidal heights and differences of anomalies with respect to the potential coefficients given in table 3.34 is shown in table 3.37.

The largest anomaly and undulation differences between the potential coefficients of the SAO Standard Earth II and those given in table 3.34 occur in the South Pacific (20°S to 40°S, 130°W to 160°W). In this area there were only six known terrestrial anomalies used in this combination solution, and no terrestrial anomalies in this area for the SAO Standard Earth II solution.

3.5.2.1.4 SUMMARY

Highlights have been presented on the development of a combination gravimetric and satellite data solution using the concept of least-squares collocation. Interested readers will find more details on this development in Rapp (1973).

Comparisons made indicate that the least-squares collocation solution yields better estimates of certain quantities than those derived from the standard least-squares method. In some cases, however, the differences in the results were slight.

The difference between the coefficient of least-squares solution and that of the least-squares collocation solution was approximately 2 percent for degrees 2–12 and approximately 17 percent for degrees 13–20. It can be shown that this difference will increase linearly with higher degrees. For example, at $n=30$ the difference reaches a value of 42 percent.

3.5.2.2 Gravitational Potential From Doppler Data

(R. J. Anderle, NWL)

The last published solution by the Naval Weapons Laboratory is the NWL 5K set (Anderle, 1965b). Most potential coefficients determined recently are more accurate than these, which are only complete through seventh degree and sixth order. The set in current use at the Naval Weapons Laboratory is the NWL 9B set, which is complete through 19th degree and order, although the coefficients are not well determined. This solution was based on Doppler data from the satellites listed in table 3.9 (sec. 3.3.4.1). Since these data were insufficient for uniquely determining the full set of coefficients through 19th degree, a priori observation of zero for coefficients of degree n (except GM and $C_{2,0}$) was added with standard deviation of $10^{-5}/n^2$, in normalized form.

Three spans of data on polar satellites were chosen to obtain solutions for 27th-order gravity coefficients. Normal equations were formed for arc constants and for two pairs of 13th-, 14th-, and 27th-order gravity coefficients. Solutions were made for various combinations of the gravity coefficients and time spans for the drag parameters. The solutions for the 27th-order coefficients varied by 50 to 100 percent in the various tests. The following normalized coefficients were obtained under the conditions that gave the most consistent results for the three spans of data: The first data span listed, which is also the longest data span, gave the most consistent results in the various tests. The 28th-degree coefficient corresponds to an along-track effect on a polar satellite of 20-meter amplitude with an 8-day period; the 27th-degree coefficient corresponds to an along-track error of 5 meters at the orbit period modulated by the 8-day beat period (see inset).

3.5.3 Other Results

(R. J. Anderle, NWL)

3.5.3.1 Inertia Axis

Since the potential coefficients C_2^1, S_2^1 are parameters of the general geodetic solution,

Satellite	Span of Data	$^{c}27,27$	$^{D}27,27$	$^{c}28,27$	$^{s}28,27$
1967–92A	Days 286–302, 1968	.003	.001	−.022	.009
1967–92A	Days 214–224, 1970	.003	.004	−.037	.007
1966–76A	Days 59–69, 1967	.006	.001	−.024	−.012

it is possible to compute the orientation of the principal axis of inertia with respect to the reference axis. However, the computed orientation of the axis was found to be inconsistent even in quadrant when solutions were repeated with data from additional satellites. The unsatisfactory results are probably due to the fact that all even degree first-order coefficients produce small effects on the satellite orbit but correspond to large displacements in the moment of inertia. A normalized coefficient $C_2^1 = 10^{-8}$ produces a 5-meter effect on the orbit of a 1000–km polar satellite and corresponds to a 60-meter distance between inertia axis and reference axis at the Earth's surface.

3.5.3.2 Love's Number

The geodetic solution in current use, NWL 9B, yielded a value of Love's number of 0.25. A more recent solution, NWL 10D, gave a value of 0.26. The newer solution included data on the Timation 2 satellite and Baker-Nunn data on Vanguard 2, Vanguard 3, TELSTAR 1, ECHO 1 rocket, MIDAS 4, and TIROS 1. (The astronomical designations of the satellites for which optical data were processed are 1959 $\alpha 1$, 1959 $\eta 1$, 1962 $\alpha\epsilon 1$, 1960 i2, 1961 $\alpha\delta 1$, and 1960 $\beta 2$.) The NWL 10D solution also included additional Doppler data for polar satellites and optical data for ANNA 1B, GEOS–1, and GEOS–2, and omitted some data processed incorrectly for the NWL 9B solution. Simulations have shown that effects of neglected gravity coefficients on the computed value of Love's number are negligible. However, no tests have been made to determine the sensitivity of the solution to neglected atmospheric and oceanic tides. Since the solution is based on time spans of observation of 8 to 16 days, the results reflect primarily lunar tidal effects.

3.5.3.3 Solar Radiation

Since a solar radiation parameter is determined for each 8- to 16-day time span of data used in a general geodetic solution, the solutions provide a measure of the variation in radiation effects from one span to the next. Results for nearly spherical satellites were separated from those for satellites with solar panels, since the area to mass ratios for the latter satellites are difficult to compute. Radiation parameters for spherical satellites, shown in figure 3.39, show a consistency of about 10 percent. Radiation parameters for NAVSAT type satellites (fig. 3.40) show little if any correlation with the angle between the Sun and the orbit plane, although the effective cross-sectional area might have varied according to this angle for the gravity gradient stabilized navigation satellites or the magnetically stabilized Beacon-Explorer satellites.

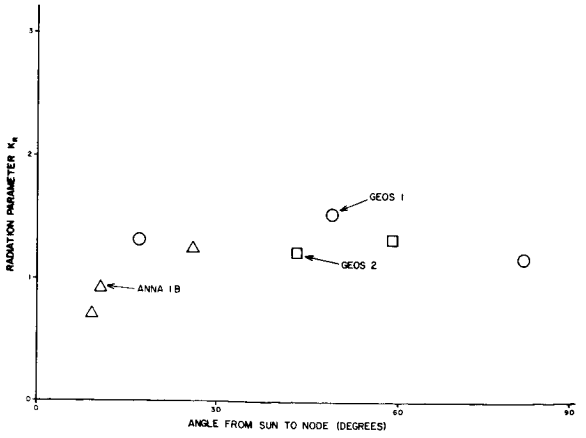

FIGURE 3.39.—Radiation parameter for spherical satellites.

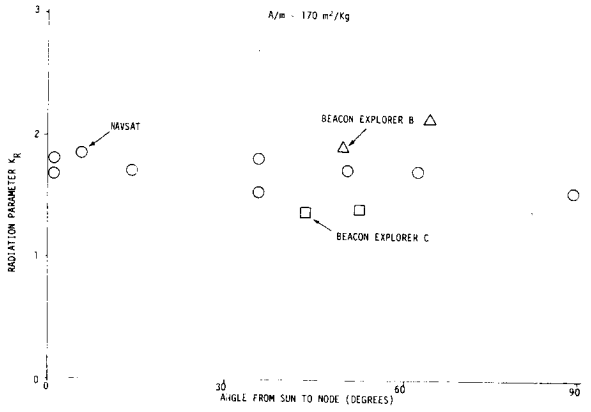

FIGURE 3.40.—Radiation parameters for NAVSAT-type satellites.

3.5.3.4 Atmospheric Drag Variations

Observations made in each 2-day time span are used to determine a scaling factor for atmospheric drag along with orbit constants. Sample results (Anderle, 1971a) are shown in figure 3.41 along with measures of solar flux, magnetic index, and the orientation of the angle between the angular momentum vector and the sun. Fairly strong correlation is evident between solar flux and drag, and some correlation exists between magnetic index and drag. A semiannual variation, which appears to correlate with the Sun angle, is readily apparent; however, the dominant effect is really a seasonal variation with some modulation due to Sun angle. Note that the 27-day rotation period of the Sun is reflected in both the solar flux data and the drag coefficient. The rapid changes in atmospheric density result in significant errors in predicting the satellite orbit. Figure 3.42 shows the prediction error 24 and 48 hours after the last data point used in predicting the satellite path. The prediction errors reflect the variations in drag to some extent, but the dominant period in the 24-hour prediction error is 17 days. This period is approximately twice the beat period corresponding to the 27th-order gravity coefficient. The rms of the prediction errors are

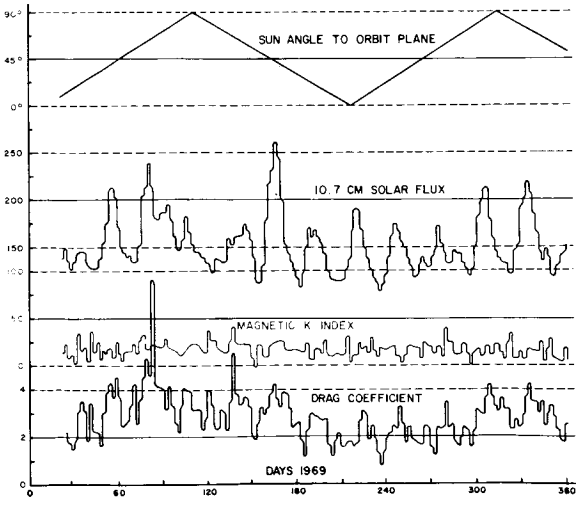

FIGURE 3.41.—Drag scaling factors and atmospheric characteristics for satellite 1967–92A for 1969.

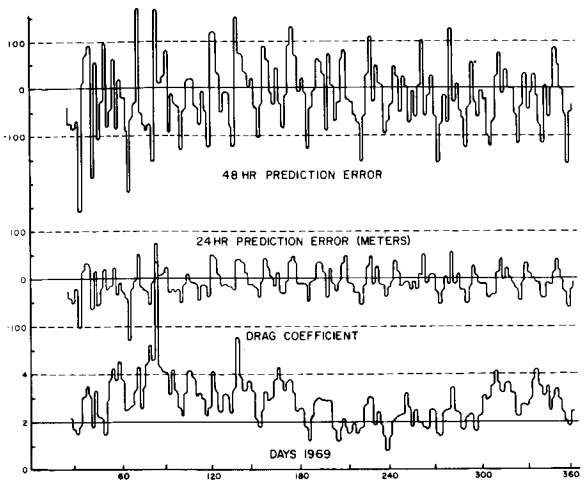

FIGURE 3.42.—Drag scaling factors and prediction errors for satellite 1967–92A for 1969.

about 20, 50, and 100 meter for 1-, 2-, and 3-day prediction intervals (L. K. Beuglass and M. S. Douglas, unpublished report, 1972). The errors were about 20 percent higher than these values in 1969 and 20 percent lower in 1971, but it is not known whether the improvement stems from improved computational techniques or from reduced levels of atmospheric density variations. The prediction error is primarily in the direction of the satellite motion; the error component that is directed radially outward from the center of the Earth is about 4 meters for any time span, whereas the error component normal to the orbit plane varies from 2 to 5 meters as the prediction interval increases from 1 to 3 days.

3.5.3.5 Earth's Rotational Rate

It should be possible to determine the rate of Earth's rotation from satellite observations by measuring discrepancies in the predicted motion of the orbit plane of the satellite with respect to a meridional plane of the Earth. Errors in the neighborhood of a meter per day might be expected, due to errors in Doppler observations or uncertainties in the gravity field, but much of the error will compensate in computing accumulated clock correction if the results are based on successive orbit computations.

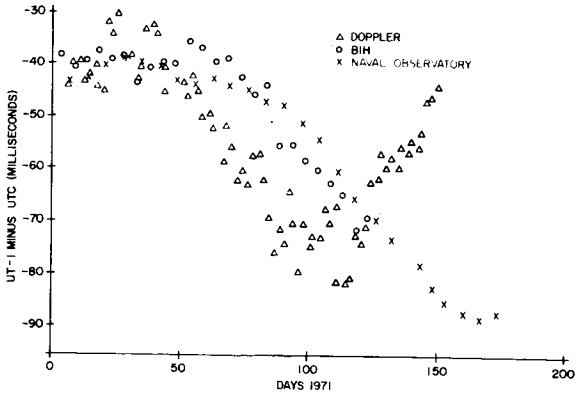

FIGURE 3.43.—Clock corrections.

Thus far, computations based on Doppler observations have given unsatisfactory results because effects of neglected atmospheric tides and biases of unknown origin exceed the seasonal and irregular variations in clock corrections. Sample results are shown in figure 3.43. Computations for different years and different satellites give biases of different magnitude and sign ranging as high as 1 meter per day (A. F. Buonaguro, unpublished report, 1972).

3.5.3.6 Pole Position

An independent determination of the components of pole position is made based on each two days of data processed for each satellite. The mean and standard error of the solutions falling within each contiguous 5-day time span in 1972 are shown in figures 3.44 and 3.45. Data were available for only one satellite during most of the year; during these periods the standard error of the 5-day mean (which contains only two or three solutions) was about 40 cm. From days 180 to 300, data from three satellites were available; during days 300 to 330, data from five satellites were available. Standard errors as low as 13 cm were obtained based on data from five satellites. BIH values are also shown on the figures. During the first six months of the year the NWL and BIH values differed by 0″.024 and 0″.002 in the x and y coordinates, respectively, on the average with standard deviations of the differences about the mean of 0″.029 and 0″.022, respectively (Anderle, 1973). The pole path is shown in figure 3.46, where the ellipses represent the standard error of the NWL solutions.

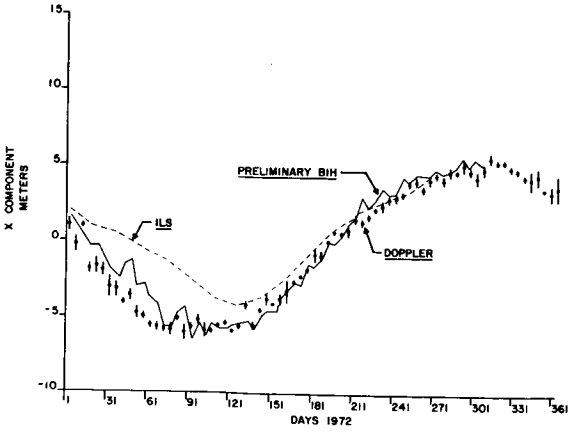

FIGURE 3.44.—X component of pole position for 1972.

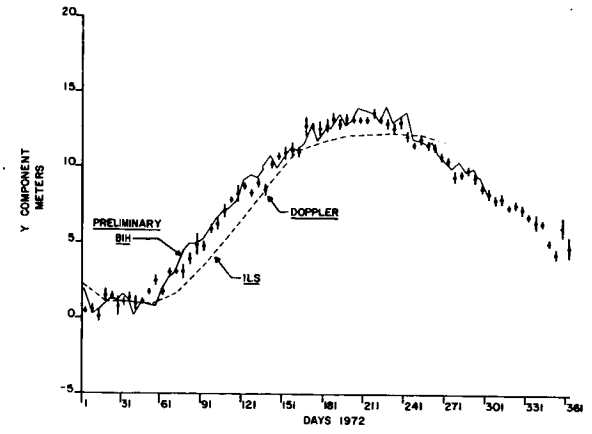

FIGURE 3.45.—Y component of pole position for 1972.

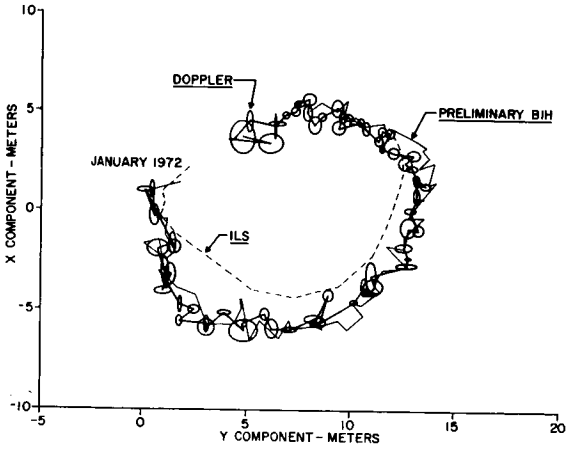

FIGURE 3.46.—1972 pole path.

3.5.3.7 Crustal Motion

Positions of Doppler equipment located at BC-4 sites in the PAGEOS network were determined over the course of seven years using the gravity field in use at the time. Positions of many of the sites have now been recomputed on the basis of ephemerides which were first recomputed using the NWL 9B gravity field, current values for the positions of base stations, and modern computational techniques. Positions of the base stations were also computed with respect to the new ephemerides. Thus solutions for base station positions were obtained for about 30 spans of data irregularly distributed over the 7-year period. Each span of data was about 10 days long. A least-squares linear fit was made to the solutions for each component of position of each station to determine whether significant variations in the solutions occurred over the 7-year time span. Each solution was weighted with the square of the number of passes in the solution. Results of the solution are shown in table 3.38. The standard errors of the computed drift rates are about 20 cm/yr with standard errors as low as 10 cm/yr for stations at extreme latitudes, which acquire more passes per day. The computed drifts are statistically significant for only a few of the components. In one example, the longitude of Japan, the drifts are not linear, as is shown in figure 3.47. Rather, there is a 300-cm change in the

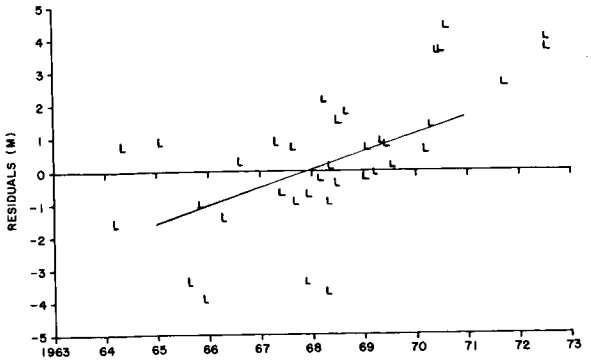

FIGURE 3.47.—Variations in the solutions for the longitude of Japan; drift 54±12 cm per year.

computed longitude of Japan at the end of 1969 or early in 1970. The station antennas were moved during this time period, but the old and new positions were well documented and the difference was under 1 cm. It is not known whether the computed change in longitude is physical or computational. Other stations are moved, opened, or closed periodically, and in some cases the changes affect the mean orbit and, in turn, positions of other stations computed from the mean orbit. Note in table 3.38 that the residuals of a 10-day solution for position are 1 to 2 meters. The residuals are larger for mid-latitude stations, which receive fewer passes per day, than statitons at extreme latitudes. Latitude residuals are usually better than height or longitude residuals. Average residuals for a group of stations are 1.5, 1.2, and 1.6 meters in longitude, latitude, and height, respectively.

APPENDIX

TABLE 3.1.—*Specifications of the PC—1000 Camera*

Camera body	
Focal length	1000 mm
Aperture	200 mm
Resolution	64 lines/mm
Distortion	< ±2 microns
Field of view	10° × 10°
Transmission factor	85–90%
Weight	62.3 kg
Photographic medium	
Glass	Kodak optically flat quality 190 mm × 215 mm × 6 mm
Emulsion	Spectroscopic 103 f

TABLE 3.2.—*Tabulation of Ranging Frequencies*

Ranging frequency (kHz)	Wavelength (m)	Unambiguous range (m)	Range resolution (m)
585.530	512	256	0.25
36.596	8 192	4 096	16
2.287	131 072	65 536	256
0.286	1 048 576	524 288	2 048

TABLE 3.3.—*SECOR Satellites*

Launch	Date	Incl. angle (degrees)	Period (minutes)	Apogee (kilometers)	Perigee (kilometers)
EGRS I	11 Jan 64	69.91°	103.4	928	916
EGRS III	9 Mar 65	70.09°	103.5	906	906
EGRS II	11 Mar 65	89.98°	97.5	992	982
EGRS IV	3 Apr 65	90.20°	111.4	1324	1266
EGRS V	10 Aug 65	69.24°	122.2	2427	1135
GEOS A	6 Nov 65	59.38°	120.3	2273	1119
EGRS VI	9 Jun 66	90.04°	125.2	3655	171
EGRS VII	19 Aug 66	90.01°	167.9	3743	3686
EGRS VIII	5 Oct 66	90.19°	167.6	3704	3677
EGRS IX	29 Jun 67	89.80°	172.1	3945	3794
GEOS B	11 Jan 68	105.80°	112.2	1573	1080
EGRS X	18 May 68	99.00°	106.0	1100	1100
EGRS XI	16 Aug 68	91.30°	172.0	3900	3900
EGRS XII	16 Aug 68	91.30°	172.0	3900	3900
EGRS XIII	14 Apr 69	99.90°	107.3	1141	1085
TOPO I	8 Apr 70	99.86°	107.0	1090	1081

TABLE 3.4.—*Characteristics of Lasers*

	Ranging laser	Photographic laser
Laser type	Ruby	Ruby
Wavelength	6943 Å	6936 Å
Beamwidth	1.45 mrad (after collimation)	2 mrad
Polarization	Linear	Linear
Cooling method	Water-cooled	Water-cooled
Mounting	Elevation over azimuth	Elevation over azimuth
Aiming method	Programmed	Programmed
Pulse length	30 nsec	2 msec
Energy per pulse	0.5 joule	250 joules
Pulsing method	Programmed, up to 10 pulses per pumping period with Pockels cell for Q-switching	Limited by capacitor

TABLE 3.5.—*Specifications on Flashing Lights in ANNA, GEOS–A, and GEOS–B*

Item	Satellites	
	ANNA–1B	GEOS–A and GEOS–B
Flashtubes	EG&G XFX-40; 4 lamps	EG&G helical lamps
Location	Two lamps each on top and bottom faces of solar cell belt	Four lamps on the Earth-facing side of the satellite
Light output	550 watt-seconds per tube	670 watt-seconds per tube
Flash sequence	Five consecutive flashes, 5.6-second interval between flashes	Five or seven flashes per sequence, 4.0-second interval between flashes
Flash duration	1 millisecond at ⅓ amplitude points	1 millisecond
Beam pattern	Figure 3.13	Figure 3.14
Flashes available	Approximately 100 per day	225 per orbital revolution 650 per day for 67% sun orbit 850 per day for 100% sun orbit
Expected life of flashtubes	20 000 flashes, minimum	90% intensity after 40 000 flashes
Energy available from battery		410,000 watt-sec per day, 67% sun orbit 580,000 watt-sec per day, 100% sun orbit
System weight	24 kg not including batteries	Approximately 27 kg not including batteries

TABLE 3.6.—*Camera Data Used To Derive Geodetic Coordinates*

Project	Station	Known stations	Unknown stations	Number of observations, by satellite					Period of observation
				ANNA 1B	GEOS-1	ECHO 1	PAGEOS	GEOS-2	
	PC-1000								
ETR	Swan Island, U.S.		X	16	16				May 65—Jun 66
	Grand Turk, U.K.		X	16	13				May 65—Jun 66
	Curaçao, N.A.		X	2	27				May 65—Jun 66
	Antigua, U.K.		X	9	18				May 65—Jun 66
	Trinidad, B.W.I.		X	1	8				May 65—Jun 66
	Semmes, AL	X		2	10				May 65—Jun 66
	Hunter AFB, GA	X		2	5				May 65—Jun 66
	Homestead AFB, FL	X		13	21				May 65—Jun 66
	PC-1000								
Bermuda	Bermuda		X			3	17		Oct 66—Apr 67
	Hunter AFB, GA	X				1	9		Oct 66—Apr 67
	Aberdeen, MD	X				2	8		Oct 66—Apr 67
	PC-1000								
Johnston Island	Johnston Island		X			5	18		Jul 67—Sep 67
	BC-4								
	Maui Island	X				1	7		Jul 67—Sep 67
	Wake Island	X				1	8		Jul 67—Sep 67
	Christmas Island	X				4	10		Jul 67—Sep 67
	BC-4								
South American Densification	Beltsville, MD	X					22		Oct 67—Dec 68
	Paramaribo, Surinam	X					37		Sep 67—Dec 68
	Quito, Ecuador	X					17	1	Sep 67—Aug 68
	Villa Dolores, Argentina	X					41		Sep 67—Mar 69
	Natal, Brazil	X					12		Jun 68—Feb 69
	PC-1000								
	Curaçao, N.A.		X				63	2	Aug 67—Aug 70
	Trinidad, B.W.I.		X				32	9	Aug 67—Feb 69
	Natal, Brazil		X				9	6	Jun 69—Aug 70
	Brasilia, Brazil		X				11	10	Mar 69—Aug 70
	Asunción, Paraguay		X				18	6	Feb 69—Aug 70
	Paramaribo		X				24	4	Aug 67—Feb 69
	Bogotá, Colombia		X				18	4	Aug 67—Feb 69
	Manaus, Brazil		X				9		Aug 68—Dec 69

TABLE 3.7.—*Observational Data for Station Positions in North America, the West Indies, and Bermuda*

Station number	Type	Number of sequences or orbits
5001	SECOR	8
5333	SECOR	10
5649	SECOR	11
5861	SECOR	8
7051	LASER	4
3405	PC–1000	14
3402	PC–1000	18
3657	PC–1000	19
3106	PC–1000	20
3861	PC–1000	28
3401	PC–1000	15
7040	MOTS–40	28
1022	MOTS–40	97
1034	MOTS–40	54
1042	MOTS–40	33
7037	MOTS–40	66
7036	MOTS–40	41
7039	MOTS–40	34
7075	MOTS–40	16
3648	PC–1000	7
3649	PC–1000	15
3404	PC–1000	8
3406	PC–1000	18
3407	PC–1000	5
1021	MOTS–40	12
7043	PTH–100	31
7045	MOTS–40	26
7072	MOTS–40	36
7076	MOTS–40	19

TABLE 3.8.—*SECOR Data*

Station number	Station	Total number of passes	Station number	Station	Total number of passes
5001	Herndon	11	5721	Mashhad	72
5706	Worthington	24	5722	Chagos	90
5648	Ft. Stewart	11	5723	Chiang Mai	96
5710	Bermuda	51	5724	Singapore	93
5709	Austin	18	5725	Hong Kong	101
5738	Puerto Rico	5	5726	Zamboanga	143
5711	Panama	28	5727	Darwin	73
5712	Paramaribo	70	5729	Manus	125
5713	Azores[1]	45	5728	Guam	134
5715	Dakar	152	5730	Wake	171
5735	Natal	57	5742	Palau	23
5736	Ascension	59	5731	Guadalcanal	61
5717	Ft. Lamy	145	5732	Pago Pago	48
5739	Azores[2]	64	5733	Christmas	73
5744	Catania	129	5411	Maui	81
5719	Cyprus	102	5410	Midway	41
5740	Rota	18	5734	Shemya	47
5741	Roberts Field	19	5201	Larson	22
5720	Addis Ababa	81			

TABLE 3.9.—*Orbital Data for Doppler Satellites*

Satellite	Internation designation	Inclination (°)	Period (min)	Perigee height (km)
TRANSIT 4B	1961 $\alpha\eta 1$	32.4	105.8	950
DIADEME 2	1967 14A	39.5	110.2	593
DIADEME 1	1967 11D	39.9	102.4	575
Beacon C	1965 32A	41.2	107.8	937
ANNA 1B	1962 $\beta\mu 1$	50.1	107.9	1083
TRANSIT 1B	1969 $\gamma 2$	51.2	95.8	289
GEOS-A	1965 89A	59.0	120.4	1115
TRANSIT 2A	1960 $\eta 1$	66.7	101.5	611
TRANSIT 4A	1961 $\sigma 1$	66.8	103.8	879
TIMATION 2	1969-082B	70.0	103.5	905
Beacon B	1964-64A	79.7	104.8	878
NAVSAT	1967-92A *et al.*	89.3	106.8	1043
GEOS-B	1968-002A	105.8	112.2	1080

TABLE 3.10.—*Survey Coordinates of Doppler Stations—Z System*[a]

Station No. (2000+)	Height MSL KM	Longitude			Latitude			Datum
		Deg	Min	Sec	Deg	Min	Sec	
018	0.0487	291.	13.	21.472	76.	32.	20.523	QOR
019	0.0382	166.	40.	03.444	−77.	50.	56.724	CMP
020	0.5910	55.	28.	48.630	−4.	40.	06.806	SEI
115	1.5804	28.	20.	53.205	−25.	56.	46.124	ARC
117	0.0092	189.	17.	07.643	−14.	20.	08.032	SAM
708	0.0103	166.	36.	39.128	19.	17.	27.064	AST
709	0.0916	115.	55.	47.572	−31.	36.	29.584	AUS
717	0.5871	55.	28.	48.738	−4.	40.	06.418	SEI
722	0.0812	345.	35.	38.840	−7.	58.	11.310	ASC
723	0.0086	96.	49.	47.730	−12.	11.	58.347	AST
727	0.0562	332.	54.	18.919	38.	45.	38.407	SWB
738	0.3722	240.	39.	47.400	47.	11.	08.060	NAD
739	0.0443	174.	06.	51.482	52.	43.	01.511	NAD
742	0.0498	283.	10.	27.170	39.	01.	39.500	NAD
744	0.0601	142.	12.	36.990	−10.	35.	06.210	AUS
765	0.3111	98.	58.	14.812	18.	46.	07.008	IND
766	0.0092	166.	36.	39.814	19.	17.	26.421	AST
805	0.2151	149.	33.	36.622	−30.	18.	39.601	AUS
809	0.0064	168.	18.	13.206	−46.	24.	49.311	GEO
811	0.0323	203.	31.	52.080	20.	49.	38.090	OHD
812	0.0289	14.	55.	05.883	37.	24.	38.796	ED
813	0.0275	342.	30.	53.268	14.	44.	40.311	YAF
815	0.0214	304.	47.	46.590	5.	27.	04.419	PRO
817	0.9946	59.	37.	42.916	36.	14.	30.096	ED
818	0.1093	18.	56.	30.700	69.	39.	44.270	ED
820	0.6110	294.	53.	39.460	−31.	56.	34.633	SAD
821	0.0147	122.	04.	03.700	6.	55.	26.800	LUZ
822	0.2983	15.	02.	05.612	12.	07.	50.939	ADI
825	0.0150	295.	56.	29.748	−64.	46.	34.916	AST
830	0.9431	11.	01.	30.259	47.	48.	08.330	ED
831	0.0263	249.	02.	40.587	18.	43.	43.666	ISA
832	0.0409	129.	42.	43.640	33.	04.	46.650	TD
837	0.0410	324.	49.	55.940	−5.	54.	45.410	PRO
838	0.1418	57.	25.	07.503	−20.	13.	41.720	AST
840	1.8908	38.	59.	49.242	8.	46.	09.503	ADI
844	2.6850	281.	34.	50.213	−00.	05.	51.268	SAD
846	0.2339	250.	34.	18.384	−27.	10.	38.061	EAS
847	0.0873	290.	46.	29.005	−52.	46.	51.133	SCD
849	0.0065	202.	35.	21.036	2.	00.	35.575	CHR

[a] Z system means that the coordinates are of the effective position applicable to observations made with the 150- and 400-MHz antennas at the station, which is a point $(1 + 150^2/400^2)$ of the distance from the 150- to the 400-MHz antenna.

TABLE 3.11.—*Horizontal and Vertical Coordinates, ETR Project, NAD 27*

No.	Camera station	Latitude	Longitude	Geodetic height (meters)	Horizontal sigma (meters)	Height sigma (meters)
3404	Swan Island	17° 24′ 16″.67 N	83° 56′ 29″.87 W	60.4	6.6	6.6
3405	Grand Turk	21° 25′ 46″.93 N	71° 08′ 46″.22 W	9.9	7.4	6.6
3406	Curaçao	12° 05′ 22″.24 N	68° 50′ 17″.39 W	36.6	10.0	7.0
3106	Antigua	17° 08′ 52″.69 N	61° 47′ 22″.07 W	24.7	10.0	8.7
3407	Trinidad	10° 44′ 31″.95 N	61° 36′ 37″.65 W	282.1	13.3	9.7
3648	Hunter AFB	32° 00′ 05″.87 N	81° 09′ 13″.64 W	15.4	0.0	0.0
3402	Semmes	30° 46′ 49″.35 N	88° 15′ 07″.63 W	76.4	0.0	0.0
3861	Homestead AFB	25° 30′ 24″.69 N	80° 23′ 17″.31 W	15.1	0.0	0.0

TABLE 3.12.—*AFETR Minus PC-1000, NAD 27*

Station	Latitude (meters)	Longitude[a] (meters)	Height (meters)
Grand Turk	−4.0	0.3	−6.1
Antigua	−0.3	−11.2	−9.5
Trinidad	−16.4	−3.9	−10.3

[a] Differences based on east longitudes positive.

TABLE 3.13.—*Horizontal and Vertical Coordinates, Bermuda Project, NAD 27*

No.	Camera station	Latitude	Longitude	Geodetic height (meters)	Horizontal sigma (meters)	Height sigma (meters)
3471	Bermuda	32° 22′ 58″.30 N	64° 41′ 00″.02 W	38.7	6.6	3.4
3657	Aberdeen	39° 28′ 18″.97 N	76° 04′ 15″.22 W	2.8	0.0	0.0
3648	Hunter AFB	32° 00′ 05″.87 N	81° 09′ 13″.64 W	15.4	0.0	0.0

TABLE 3.14.—*Bermuda 1957 Datum to NAD 27*

Solution	Latitude (seconds)	Latitude (meters)	Longitude (seconds)	Longitude (meters)
PC–1000	4.10	126.6	−1.84	−48.0
AFETR	4.27	131.8	−2.02	−52.7
USNOS	4.17	128.7	−1.63	−42.5
Mean	4.18	129.0	−1.83	−47.7

TABLE 3.15.—*Horizontal and Vertical Coordinates, Johnston Island Project, BC-4 World Net*[a]

No.	Camera station	Latitude	Longitude	Geodetic height (meters)	Horizontal sigma (meters)	Height sigma (meters)
3475	Johnston Island	16° 43′ 45.″72 N	169° 31′ 14.″53 W	24.7	5.4	5.8
6011	Maui (BC-4)	20° 42′ 27.″09 N	156° 15′ 21.″23 W	3089.5	0.0	0.0
6066	Wake (BC-4)	19° 17′ 28.″50 N	193° 23′ 19.″59 W	−2.0	0.0	0.0
6059	Christmas (BC-4)	02° 00′ 18.″83 N	157° 24′ 43.″32 W	32.3	0.0	0.0

[a] October 1972 WN adjustment; NWL-8D ellipsoid (a = 6 378 145.0 m; $1/f$ = 298.25).

TABLE 3.16—*Horizontal and Vertical Coordinates, South American Densification Project, BC-4 World Net*

No.	Camera station	Latitude	Longitude	Geodetic height (meters)	Horizontal sigma (meters)	Height sigma (meters)
3413	Natal	05° 54′ 57.″61 S	35° 10′ 04.″55 W	9.2	5.5	6.7
3414	Brasilia	15° 51′ 37.″34 S	47° 53′ 59.″47 W	1012.5	5.8	6.7
3431	Asunción	25° 18′ 57.″33 S	57° 34′ 47.″59 W	166.0	6.0	6.8
3476	Paramaribo	05° 26′ 53.″36 N	55° 12′ 18.″80 W	−36.9	5.5	6.4
3477	Bogotá	04° 49′ 01.″23 N	74° 04′ 27.″34 W	2558.9	5.9	7.3
3478	Manaus	03° 08′ 44.″82 S	59° 59′ 05.″76 W	44.3	9.1	10.1
3406	Curaçao	12° 05′ 26.″32 N	68° 50′ 16.″46 W	−24.7	5.6	6.5
3407	Trinidad	10° 44′ 35.″25 N	61° 36′ 36.″81 W	191.7	5.7	6.6
6002	Beltsville (BC-4)	39° 01′ 39.″44 N	76° 49′ 33.″06 W	0.5	0.0	0.0
6008	Paramaribo (BC-4)	05° 26′ 53.″93 N	55° 12′ 20.″21 W	−34.4	4.7	5.3
6009	Quito (BC-4)	00° 05′ 51.″24 S	78° 25′ 13.″50 W	2689.6	5.0	5.9
6019	Villa Dolores (BC-4)	31° 56′ 35.″32 S	65° 06′ 22.″52 W	614.9	4.9	6.1
6067	Natal (BC-4)	05° 55′ 38.″72 S	35° 09′ 56.″05 W	16.5	5.3	5.1

TABLE 3.17.—Standard Deviations Assumed for Input Parameters

Camera
- Orientation:
  - $\sigma_\nu = 1'' \; \sigma_\omega = 1'' \; \sigma_\kappa = 2''$
- Timing (interstation):
  - $\sigma_t = 1 \times 10^{-4}$ time sec (active)
- Measurement:
  - $\sigma_x = 3$ microns $\sigma_y = 3$ microns (plate coordinates)
  - $\sigma_k = 10$ microns (focal length)
  - $\sigma_\tau = 1 \times 10^{-4}$ sec (interval timing)

Laser
- $\sigma_a = 10$ m (zero set); $\sigma_r = 5$ m (range noise)
- $\sigma_\tau = 1.\times 10^{-4}$ sec (interval timing)

SECOR
- $\sigma_a = 30$ meters (zero set)
- $\sigma_r = 5$ meters (random range)
- $\sigma_\tau = 1 \times 10^{-4}$ sec (interval timing)

Initial conditions
- Position: $\sigma_x = \sigma_y = \sigma_z = 10\,000$ meters
- Velocity: $\sigma_{\dot{x}} = \sigma_{\dot{y}} = \sigma_{\dot{z}} = 5$ m/sec

TABLE 3.18.—*Adjusted Coordinates, NAD 1927*

Station	Geodetic							Rectangular					
	Latitude			Longitude (E)			Height	x	$\pm\sigma_{\Delta x}$	y	$\pm\sigma_{\Delta y}$	z	$\pm\sigma_{\Delta z}$
	Deg	Min	Sec	Deg	Min	Sec	(meters)	(meters)		(meters)		(meters)	
5648 ___	32	00	05.868	278	50	46.359	18.0	832 334.77	0	−5 349 731.00	0	3 360 414.47	0
5649 ___	32	00	04.040	278	50	43.170	20.0	832 516.59	0	−5 349 734.63	0	3 360 367.78	0
5001 ___	38	59	37.892	282	40	16.704	124.7	1 086 886.63	2.81	−4 843 080.19	3.90	3 991 669.31	2.54
5333 ___	33	25	32.404	269	05	11.133	49.2	−84 963.42	3.36	−5 328 097.19	4.84	3 493 299.63	3.95
5861 ___	25	29	21.182	279	37	39.421	19.5	963 495.79	2.30	−5 679 880.38	2.55	2 727 945.13	2.33
5051 ___	35	11	46.438	277	07	26.169	887.4	647 208.98	2.96	−5 178 465.88	2.85	3 656 001.72	2.03
5405 ___	21	25	46.687	288	51	13.865	.4	1 919 524.80	5.39	−5 621 243.75	5.24	2 315 603.91	4.68
5402 ___	30	46	49.285	271	44	52.433	79.3	167 292.27	3.40	−5 482 121.94	3.57	3 244 861.09	3.52
5657 ___	39	28	19.104	283	55	44.444	03.2	1 136 822.94	2.40	−4 785 337.44	3.67	4 032 706.97	2.54
5106 ___	17	08	52.141	298	12	37.961	−2.3	2 881 879.78	5.03	−5 372 309.13	5.32	1 868 357.20	5.19
5861 ___	25	30	24.694	279	36	42.759	13.6	961 794.02	2.30	−5 679 310.13	2.54	2 729 706.56	2.33
5401 ___	42	27	17.924	288	43	34.526	85.8	1 513 167.78	3.64	−4 463 167.78	5.62	4 282 883.00	4.20
5040 ___	18	15	26.224	294	00	22.179	49.6	2 465 086.66	3.60	−5 535 074.00	4.05	1 985 343.41	4.09
5022 ___	26	32	51.833	278	03	03.907	22.9	807 882.52	1.91	−5 652 139.19	2.22	2 833 328.25	2.15
5034 ___	48	01	21.390	262	59	21.465	263.4	−521 681.81	2.84	−4 242 203.50	3.16	4 718 549.38	3.27
5042 ___	35	12	06.782	277	07	40.986	916.9	647 539.05	2.00	−5 178 086.63	2.18	3 656 531.13	2.03
5037 ___	38	53	35.774	267	47	42.103	277.1	−191 261.40	2.39	−4 967 436.13	2.42	3 983 079.88	2.43
5036 ___	26	22	45.297	261	40	03.958	76.0	−828 467.56	3.21	−5 657 614.25	2.92	2 816 640.03	2.94
5039 ___	32	21	49.069	295	20	33.311	29.3	2 308 245.38	3.53	−4 873 752.19	3.74	3 394 394.00	3.39
5075 ___	46	27	21.208	279	03	10.585	285.3	692 650.55	3.13	−4 347 223.63	3.61	4 600 306.69	3.62
5649 ___	27	01	13.137	279	53	12.792	23.4	976 304.88	3.00	−5 601 545.50	3.57	2 880 069.72	3.38
5404 ___	17	24	16.595	276	03	29.715	75.3	642 535.59	4.93	−6 054 102.19	4.88	1 895 516.58	4.94
5406 ___	12	05	22.275	291	09	43.168	17.8	2 251 843.66	4.83	−5 816 042.81	5.83	1 327 008.58	5.34
5407 ___	10	44	31.834	298	23	22.817	249.6	2 979 940.41	6.58	−5 513 660.63	7.16	1 180 971.64	7.66
5021 ___	38	25	49.599	282	54	48.235	05.3	1 118 061.02	2.27	−4 876 471.44	2.94	3 942 791.88	3.07
5043 ___	39	01	51.327	283	10	19.335	49.8	1 130 737.78	2.31	−4 831 478.31	3.14	3 993 956.97	3.05
5045 ___	39	38	47.922	255	23	41.233	1804.7	1 240 450.92	3.55	−4 760 388.19	3.53	4 048 807.53	3.41
5072 ___	27	01	13.048	279	53	12.435	25.8	976 295.78	2.49	−5 601 550.50	2.96	2 880 068.31	3.09
5076 ___	18	04	32.157	283	11	26.604	486.1	1 384 189.60	3.47	−5 905 824.56	4.03	1 966 372.75	3.90

TABLE 3.19.—*Final SECOR Solutions (C9)*
Coordinates Referred to the Geocentric Ellipsoid With a = 6 378 155, $1/f = 298.255$

Station	Name	Latitude	Longitude (E)	Height (m)
5001 ---	Herndon	38° 59′ 37″.966	282° 40′ 16″.992	75.67
5706 ---	Worthington	43° 38′ 57″.907	264° 25′ 16″.392	436.00
5648 ---	Ft. Stewart	31° 55′ 19″.340	278° 26′ 00″.110	−21.88
5710 ---	Bermuda	32° 21′ 45″.871	295° 20′ 24″.466	−35.20
5738 ---	Puerto Rico	18° 29′ 40″.141	292° 50′ 52″.685	−26.85
5709 ---	Austin	30° 13′ 46″.740	262° 14′ 49″.182	158.01
5711 ---	Panama	8° 58′ 27″.262	280° 26′ 55″.476	−4.74
5712 ---	Paramaribo	5° 26′ 57″.946	304° 47′ 41″.841	−40.55
5713 ---	Azores 1	38° 45′ 36″.141	332° 54′ 24″.637	65.57
5715 ---	Dakar	14° 44′ 38″.309	342° 30′ 56″.967	4.32
5735 ---	Natal	−5° 54′ 58″.128	324° 49′ 54″.858	−8.81
5739 ---	Azores 2	38° 45′ 35″.728	332° 54′ 23″.259	65.57
5736 ---	Ascension	−7° 58′ 14″.839	345° 35′ 32″.864	44.51
5717 ---	Ft. Lamy	12° 07′ 50″.137	15° 02′ 07″.269	255.69
5744 ---	Catania	37° 26′ 35″.613	15° 02′ 43″.120	−27.97
5719 ---	Cyprus	35° 11′ 28″.107	33° 15′ 51″.444	124.44
5740 ---	Rota	36° 37′ 35″.825	353° 40′ 01″.264	−20.75
5741 ---	Roberts Field	6° 13′ 52″.981	349° 38′ 24″.775	−10.31
5720 ---	Addis Ababa	8° 46′ 10″.710	38° 59′ 52″.820	1830.43
5721 ---	Mashhad	36° 14′ 24″.206	59° 37′ 42″.344	917.10
5722 ---	Chagos	−7° 21′ 08″.471	72° 28′ 22″.094	−108.83
5723 ---	Chiang Mai	18° 46′ 09″.405	98° 58′ 03″.764	234.33
5724 ---	Singapore	1° 22′ 21″.996	103° 59′ 59″.262	0.50
5725 ---	Hong Kong	22° 11′ 54″.339	114° 13′ 14″.074	121.17
5726 ---	Zamboanga	6° 55′ 19″.277	122° 04′ 08″.752	66.54
5727 ---	Darwin	−12° 27′ 16″.337	130° 48′ 59″.380	71.60
5729 ---	Manus	−2° 02′ 20″.992	147° 21′ 41″.309	75.12
5728 ---	Guam	13° 26′ 21″.543	144° 38′ 05″.811	79.92
5730 ---	Wake	19° 17′ 29″.677	166° 36′ 41″.237	14.04
5742 ---	Palau	7° 20′ 39″.451	134° 29′ 28″.034	119.52
5731 ---	Guadalcanal	−9° 25′ 41″.143	160° 03′ 07″.386	84.22
5732 ---	Pago Pago	−14° 19′ 53″.290	189° 17′ 09″.642	72.83
5733 ---	Christmas	2° 00′ 18″.748	202° 35′ 17″.070	56.33
5411 ---	Maui	20° 49′ 54″.868	203° 32′ 00″.651	63.96
5410 ---	Midway	28° 12′ 43″.532	182° 37′ 53″.267	6.03
5734 ---	Shemya	52° 42′ 48″.803	174° 07′ 25″.747	30.20
5201 ---	Larson	47° 11′ 05″.211	240° 39′ 46″.017	328.18

TABLE 3.20a.—*Directional Constraints in Final Solution, Directions From NAD Coordinates*

From	To	Normal-Section-Azimuth	Sigma (m)	Elevation	Sigma (m)
Worthington	Herndon	102° 28′ 58″.13	4	−7°13′52″.78	4
Austin	Herndon	56° 59′ 4″.30	5	−9°27′ 9″.40	4
Ft. Stewart	Herndon	24° 54′ 44″.42	3	−3°55′40″.06	4
Worthington	Austin	188° 5′ 7″.06	4	−6°46′22″.99	4
Worthington	Ft. Stewart	131° 59′ 57″.92	4	−8° 3′15″.60	3
Austin	Ft. Stewart	78° 55′ 19″.11	4	−6°59′ ″.60	4
Worthington	Larson	290° 17′ 9″.65	4	−8°29′33″.86	4
Austin	Larson	321° 29′ 50″.08	6	−11°52′26″.27	5

TABLE 3.20b.—*Directional Constraints in Final Solution, Direction From the WGS 1 BBC–4 Solution*

From	To	Normal-Section-Azimuth	Sigma (m)	Elevation	Sigma (m)
Wake Island	Pago Pago	144° 35′ 16″.00	8	−20°10′37″.33	14
Maui	Wake Island	274° 19′ 33″.01	10	−17°28′ 2″.00	12
Wake Island	Christmas Island	111° 35′ 13″.77	8	−19°35′50″.34	14
Ascension Island	Natal	274° 17′ 38″.39	6	−10°21′11″.22	7
Mashhad	Catania	285° 38′ 9″.02	6	−17°41′39″.33	10
Catania	Ft. Lamy	180° 1′ 26″.35	6	−12°38′35″.84	8

TABLE 3.21.—*Precise Traverse Closures on B + S Solution Minus Survey*

	Meters	Parts per million
Beltsville—Moses Lake	0	0
Moses Lake—Wrightwood	8	6
Tromsø—Hohenpeissenburg	24	10
Catania—Hohenpeissenburg	−28	−23
Dakar—Ft. Lamy	6	2
Thursday—Culgoora	1	0
Tromsø—Catania	2	1

TABLE 3.22.—*Satellite-Derived Positions of Antennas of BC-4 Sites (NWL 9D System)*

Station number (add 2000)	Station name	Longitude (east)			Latitude[a]			Height[a]	Standard deviation (m)		
		Deg	Min	Sec	Deg	Min	Sec	(m)	Long	Lat	Ht
018	Thule Grnlnd	291	13	53.35	76	32	19.76	56.0	1.5	1.2	1.6
019	McMurdo, Ant.	166	40	25.73	−77	50	51.67	−20.0	1.5	1.2	1.6
020	Seychelles	55	28	45.69	−4	40	14.31	551.0	1.5	1.2	1.6
115	Pretoria, S. Af.	28	20	51.20	−25	56	48.24	1598.1	1.5	1.2	1.6
117	Amer. Samoa	189	17	2.40	−14	19	50.38	40.0	1.5	1.2	1.6
708	Wake Island	166	36	38.06	19	17	32.65	24.5	1.5	1.2	1.6
709	Perth, Aust.	115	55	52.06	−31	36	25.52	51.3	1.5	1.2	1.6
717	Seychelles	55	28	45.84	−4	40	13.90	547.9	1.5	1.2	1.6
722	Ascension Is.	345	35	39.69	−7	58	9.99	94.9	1.5	1.2	1.6
723	Cocos Island	96	50	3.02	−12	11	44.34	−30.8	1.5	1.2	1.6
727	Azores	332	54	22.38	38	45	37.95	108.1	1.5	1.2	1.6
738	Washington	240	39	42.48	47	11	7.53	342.5	1.5	1.2	1.6
739	Shemya Is.	174	6	39.72	52	42	55.54	40.9	1.5	1.2	1.6
742	Maryland	283	10	27.59	39	1	39.72	6.1	1.5	1.2	1.6
744	Australia	142	12	40.28	−10	35	.99	128.0	1.5	1.2	1.6
765	Thailand	98	58	2.07	18	46	11.61	267.0	1.5	1.2	1.6
766	Wake Island	166	36	38.76	19	17	31.97	25.0	1.5	1.2	1.6
805	Culgoora, Aust.	149	33	39.94	−30	18	34.01	236.5	1.5	1.2	1.6
809	New Zealand	168	18	12.76	−46	24	43.70	7.4	1.5	1.2	1.6
811	Hawaii	203	32	1.43	20	49	26.32	47.1	1.5	1.2	1.6
812	Sicily	14	55	2.74	37	24	34.60	65.3	1.5	1.2	1.6
813	Senegal	342	30	57.59	14	44	38.16	56.3	1.5	1.2	1.6
815	Surinam	304	47	40.67	5	26	52.75	−12.8	1.5	1.2	1.6
817	Iran	59	37	43.48	36	14	26.12	967.8	1.5	1.2	1.6
818	Norway	18	56	24.17	69	39	44.41	133.5	1.5	1.2	1.6
820	Argentina	294	53	36.52	−31	56	36.09	637.4	1.5	1.2	1.6
821	Zamboanga	122	4	7.15	6	55	21.60	80.3	1.5	1.2	1.6
822	Africa	15	2	5.97	12	7	53.60	305.7	1.5	1.2	1.6
825	Palmer Sta.	295	56	45.20	−64	46	27.77	22.8	1.5	1.2	1.6
830	Germany	11	1	25.69	47	48	5.12	977.2	1.5	1.2	1.6
831	Socorro, Mex.	249	2	42.11	18	43	56.95	−14.9	1.5	1.2	1.6
832	Japan	129	42	34.64	33	4	58.29	66.7	1.5	1.2	1.6
837	Brazil	324	49	55.44	−5	54	58.11	34.9	1.5	1.2	1.6
838	Mauritius	57	25	31.79	−20	13	52.83	138.3	1.5	1.2	1.6
840	Ethiopia	38	59	51.53	8	46	13.23	1871.9	1.5	1.2	1.6
844	Equador	281	34	47.96	−0	5	52.88	2700.9	1.5	1.2	1.6
846	Easter Is.	250	34	23.14	−27	10	35.65	222.7	1.5	1.2	1.6
847	Chile	290	46	32.49	−52	46	51.17	86.7	1.5	1.2	1.6
849	Christmas Is.	202	35	15.71	2	0	18.20	29.5	1.5	1.2	1.6
20126	Casey, Ant.	110	32	7.59	−66	16	44.70	3.0	1.5	1.2	1.6
	Mawson. Ant	Doppler observations not available									
	Tristan	Doppler observations not available									
	Pitcairn	Doppler observations not available									
	Diego Garcia	Doppler observations not available									
	Heard	Doppler observations not available									
	S. Georgia	Doppler observations not available									

[a] With respect to NWL8E ellipsoid semi-major axis 6 378 145 m and reciprocal flattening of 298.25.

TABLE 3.23.—*Datum Shifts for BC–4 Sites Based on Doppler Observations*

Datum	No. sites	Δx (meters)	Δy (meters)	Δz (meters)
Qornoq	1	+196	+132	−142
Camp Area 1962	1	−103	−125	+235
Southeast Island	2	−19	−186	−274
Arc 1950	1	−120	−128	−296
Samoa 62	1	−115	+140	+420
Wake Astro	1	+280	−35	+142
Australian	1	−120	−33	+144
Ascension Is. 58	1	−210	+81	+47
SW Base Gra. Is.	1	−52	+121	+14
NAD 27	2	−27	+161	+181
Indian	1	+253	+791	+358
Geodetic 1949	1	+75	−6	+198
Old Hawaiian	1	+56	−271	−197
European	3	−79	−105	−121
1967 Yof Astro	1	−35	+147	+88
Prov. SAD 56	2	−266	+125	−374
SAD 1969	2	−77	0	−43
Luzon	1	−101	−39	−101
Adindan	2	−150	−31	+199
Palmer Astro	1	+214	+28	+210
Isla Socorro Astro	1	+132	+219	+498
Tokyo	1	−135	+528	+676
Mauritius Astro	1	−788	+77	−294
Easter Is. 1967	1	+193	+154	+108
Prov. Chilean 63	1	−4	+194	+95
Christmas Is. 1967 Astro	1	+111	+258	−535

TABLE 3.24.—*Effect[a] of Zonal Coefficients on Z Component of Station Position–Zonal Gravitational Field*

Station	Kozai '69 (meters)	SAO '71 (meters)	French '71 (meters)	Wagner '72 (meters)	GEM 2 (meters)	NWL 10D (meters)
Brazil	−49	−56	−87	−113		1
Japan	−47	−53	−84	−109		1
Alaska	−42	−48	−75	−97		1
Greenland	−39	−44	−70	−91		2
Antarctica	−41	−47	−73	−95	3	0
Texas	−48	−54	−85	−109	−3	1
New Mexico	−49	−56	−87	−112	−4	0
Maryland	−41	−47	−77	−101	3	1
Australia	−45	−51	−82	−106	−1	4
So. Africa	−52	−58	−91	−118	−6	−1
Samoa	−50	−57	−91	−117	−1	3
Philippines	−48	−55	−89	−117	0	5
England	−51	−57	−86	−110	−8	−4
Seychelles	−56	−63	−97	−127	−7	−2

[a] Difference from a nominal set of station coordinates.

TABLE 3.25.—*Comparison of Doppler and BC-4 Station Position Determinations*

Site	Doppler minus BC-4			Estimated accuracy	
	Latitude (meters)	Longitude (meters)	Height (meters)	doppler (meters)	BC-4 (meters)
Thule	−9	−1	−7	2	5
Beltsville	5	2	6	2	5
Moses Lake	6	6	4	2	5
Shemya	−5	13	−15	2	6
Tromsø	2	−16	−6	2	4
Azores	13	−5	−3	2	5
Paramaribo	4	3	9	2	5
Quito	−2	12	7	2	6
Maui	−2	2	−11	2	5
Wake	15	−11	24	2	5
Iran	−3	4	−1	2	4
Catania	0	−1	−2	2	4
Argentina	23	16	3	2	5
Easter	−4	16	−5	2	7
Pago Pago	−3	−5	3	2	5
Thursday	2	−7	14	2	4
Invercargill	7	−8	2	2	4
Caversham	−4	−1	−3	2	5
Socorro	9	1	−3	2	5
Cocos	−3	0	−4	2	5
Addis Ababa	−12	−3	−6	2	4
Chile	25	4	−27	2	6
Mauritius	−3	4	−3	2	4
Zamboanga	−3	3	8	2	5
Palmer	24	−4	−15	2	9
McMurdo	16	0	0	2	6
Ascension	11	−10	0	2	5
Christmas	−2	−4	3	2	5
Culgoora	12	−9	0	2	4
Senegal	3	6	1	2	5
Ft. Lamy	−3	2	−5	2	4
Hohenpeissenberg	−1	−7	−1	2	4
Wake	15	−11	24	2	5
Brazil	15	−5	−4	2	5
Johannesburg	1	1	7	2	5
Chiang Mai	−3	−6	8	2	5
Mahe	−7	−1	6	2	5

TABLE 3.26.—*Coordinates of Stations Involved in Gulf Test (North American Datum 27)*

Station no.	Latitude			Longitude (W)			Height (meters)
	Deg	Min	Sec	Deg	Min	Sec	
AF640	29	33	44.801	90	40	44.187	2.0
AF641	29	35	39.885	95	09	14.040	8.2
AF643	31	19	15.908	92	31	31.910	26.8
3647	30	14	48.276	88	04	42.513	1.2
3648	32	00	05.868	81	09	13.641	12.2
3649	26	57	12.569	80	04	55.802	6.8
AF650M	30	13	05.457	81	41	47.806	6.4
AF686	28	34	26.025	81	19	39.070	28.6

TABLE 3.27.—*Determinations of Positions of Stations 3640, 641, 643, and 3647 From Positions at Stations 3648 and 3649*

Reference stations 3648 and 3649: $\sigma_\phi = \sigma_\lambda = \sigma_H = 0.03$ m
Unknown station: $\sigma_\phi = 200$ m, $\sigma_\lambda = 200$ m, $\sigma_H = 5$ m
Observations: 33 nets and a total of 142 flash-points

Station	Δx (m)	Δy (m)	Δz (m)	R (m)	Proportional error
Hunter (3648)	Known station				
Jupiter (3649)	Known station				
Houma (AF640)	0.0 ±3.9	−2.2 ±1.4	1.8 ±2.5	2.8 ±4.8	1:327 500
England (AF643)	−3.5 ±4.6	−2.4 ±1.4	3.4 ±2.3	5.3 ±5.4	1:199 600
Dauphin (3647)	1.0 ±2.9	−4.9 ±1.2	0.6 ±2.4	5.1 ±3.9	1:134 200
Ellington (AF641)	1.5 ±5.8	0.4 ±1.6	1.9 ±3.4	2.4 ±6.9	1:557 200

TABLE 3.28.—*Comparison of Azimuths*

Line		Forward azimuth	Distance (m)
641-3648	ANNA	75° 11′ 36″.7	1 365 165
	Normal section	75° 11′ 37″.5	
	ΔA_z	(−) 0″.8	
640-3648	ANNA	71° 04′ 34″.1	950 628
	Normal section	71° 04′ 34″.5	
	ΔA_z	(−) 0″.4	
643-3648	ANNA	83° 01′ 11″.0	1 080 640
	Normal section	83° 01′ 10″.1	
	ΔA_z	(+) 0″.9	

TABLE 3.29.—*NGSP Stations Occupied by GEOCEIVER, NAD 27*

Test No.	Name of locality	Coordinates λ	Coordinates φ	Near NGSP stations	Phase of service
10000	Cheyenne, WY	255° 07′ 57″.202	41° 08′ 00″.069	3902	II (Air Force)
10003	Greenville, MS	268° 59′ 51″.486	33° 28′ 42″.470	5333	I,II (Air Force)
10006	Tipton, KS	261° 27′ 29″.494	39° 13′ 26″.686		I,II (Air Force)
10008	Grand Forks, ND	262° 37′ 11″.198	47° 56′ 38″.593	3451, 1034, 7034	II (Air Force)
10013	Jonestown, TX	262° 01′ 17″.525	30° 26′ 48″.273	---	I (Air Force)
10019	Frankton, IN	274° 10′ 27″.186	40° 14′ 06″.956	---	I,II (Air Force)
10020	Marysville, IN	274° 21′ 07″.740	38° 35′ 20″.787	---	I (Air Force)
10021	Summit, KY	273° 55′ 10″.384	37° 33′ 06″.807	---	I (Air Force)
10022	Iuka, MS	271° 45′ 30″.291	34° 47′ 15″.547	---	I (Air Force)
10023	Mathiston, MS	270° 50′ 04″.504	33° 33′ 54″.655	---	I (Air Force)
10024	Cheyenne, WY	255° 07′ 57″.264	41° 08′ 00″.025	3902	II (Air Force)
20000	Howard Co., MD	283° 06′ 11″.314	39° 09′ 47″.514	2111	I,II (Navy)
20001	Beltsville, MD	283° 10′ 26″.756	39° 01′ 39″.492	3002, 2742, 6100, 7043, 1050	I (Navy)
20002	Las Cruces, NM	253° 14′ 48″.285	32° 16′ 43″.702	2103, 9001	II (Navy)
20003	Wrightwood, CA	242° 19′ 09″.484	34° 22′ 54″.537	---	II (Navy)
20015	Woodbine, GA	278° 19′ 07″.845	30° 56′ 54″.982	---	I (Navy)
20016	Columbia, MS	270° 16′ 28″.098	31° 12′ 44″.555	---	I (Navy)
30025	Bloomfield, OH	278° 15′ 39″.706	40° 05′ 11″.583	---	I (Army)
30026	Columbus, OH	276° 57′ 30″.248	40° 00′ 27″.648	---	I (Army)
30027	Greenville, OH	275° 23′ 26″.854	40° 09′ 51″.348	---	I (Army)
30028	Metamora, IL	270° 42′ 40″.598	40° 49′ 20″.343	---	I (Army)
30029	Moses Lake, WA	240° 39′ 48″.118	47° 11′ 07″.132	6002 (Identical)	II (Army)

TABLE 3.30.—*Short-Arc Passes Used in Solutions*

Number of stations observing pass	Phase I, days 288–301; number of passes		Phase II, days 319–346; number of passes	
	Pre-edit	Post-edit	Pre-edit	Post-edit
5	27	22	26	23
6	41	45	16	18
7	33	31	11	6
8	36	22	0	0
9	10	5	0	0
Total passes	147	125	53	47
North-to-south passes		56		14
South-to-north passes		69		33
Total single-station passes	990	818	303	265
Percentage of data loss (pre- to post-edit)		17%		13%

TABLE 3.31.—*Constraints Used in the Phase I Solutions*

Orbital

Position	Velocity
X = 10 km	$\dot{X}$ = 5 m/sec
Y = 10 km	$\dot{Y}$ = 5 m/sec
Z = 10 km	$\dot{Z}$ = 5 m/sec

Baseline

Parameter	Stations 10018 → 20001	Stations 10006 → 20016	Stations 20000 → 20001
Azimuth[a]	0.″001	60.″0	0.″001
Elevation[a] (angle)	0.″001	0.″001	0.″001
Range[a]	1000 m	1000 m	0.01 m

Station Coordinates

Coordinate	Greenville (10003)	All other stations
Latitude	0.″001	1.″0
Longitude	0.″001	1.″0
Geodetic height	0.01 m	30.0 m

Error Model Parameters

Parameter	Greenville (10003)	All other stations
Frequency offset	7.5 m/sec	7.5 m/sec
Frequency drift	0.2×10^{-3}	0.2×10^{-3}
Frequency bias	0.1×10^{-8}	0.1×10^{-8}
Time bias	0.1×10^{-5} sec	0.1×10^{-3} sec
Refraction	0.2 m	0.2 m
Zero set	10^7 m	10^7 m

[a] Angular and distance constraints between stations.

TABLE 3.32.—*Differences in GEOCEIVER Station Positions (Modified CCD) Surveyed Minus Tests Results*

GEOCEIVER stations		Phase I			Phase II			Phases I and II		
Number	Name	$\Delta\phi$ (sec)	$\Delta\lambda$ (sec)	ΔH (m)	$\Delta\phi$ (sec)	$\Delta\lambda$ (sec)	ΔH (m)	$\Delta\phi$ (sec)	$\Delta\lambda$ (sec)	ΔH (m)
10000	Cheyenne, WY				−0.05	−0.26	−1.6	−0.04	−0.29	−2.2
10003	Greenville, MS	0.00	0.00	0.0	0.06	−0.04	−2.4	0.03	−0.01	0.5
10006	Tipton, KS	0.00	0.13	−2.1	0.00	0.00	0.0	0.00	0.00	0.0
10008	Grand Forks, ND				−0.02	−0.07	−2.0	−0.02	0.11	−0.1
10018	Jonestown, TX	−0.03	0.16	−1.9				−0.01	0.01	3.2
10019	Frankton, IN	0.00	0.18	−1.9				0.04	0.25	−1.7
10022[a]	Iuka, MS	0.01	0.10	1.0				0.05	0.14	1.1
10023[a]	Mathiston, MS	0.01	0.08	−0.8				0.05	0.11	−0.5
10024	Cheyenne, WY				−0.05	−0.26	−1.6	−0.04	−0.29	−2.2
20000	Howard County, MD	−0.08	0.09	−1.1				−0.05	0.30	2.8
20001	Beltsville, MD	−0.08	0.09	−1.1				−0.05	0.30	2.8
20002	Las Cruces, NM				−0.05	0.23	1.6	−0.04	0.13	1.0
20003	Wrightwood, CA				0.02	0.17	−7.8	0.04	0.07	−7.5
20015	Woodbine, GA	−0.05	−0.13	2.4				0.00	−0.02	4.0
20016	Columbia, MS	0.00	0.03	−0.4				0.04	0.06	0.0
30025[a]	Bloomfield, OH	−0.03	0.13	0.4				0.01	0.27	1.7
30026[a]	Columbus, OH	−0.05	0.16	−1.3				−0.02	0.28	−0.5
30029	Moses Lake, WA				−0.05	0.27	−3.3	−0.01	0.36	−5.5

[a] Mobile stations.

TABLE 3.33.—*Comparison of Relative Positions and Distances as Determined by GEOCEIVER and by Precise Traverse*

From	To	Dist (km)	Passes	GEOCEIVER-Traverse			
				$\Delta\phi$ (m)	$\Delta\lambda$ (m)	Δh (m)	Δd (m)
Columbia, MS	Greenville, MS	278	122	1.11	1.08	−1.64	0.49
Greenville, MS	Meades Ranch, KS	929	39	1.56	−2.16	0.59	2.69
Meades Ranch, KS	Beltsville, MD	1867	24	−1.04	4.25	1.30	4.49

TABLE 3.34.—*Recommended Collocation-Derived Potential Coefficients and Their Standard Deviations (SD) ($\times 10^6$)*

n	m	$\bar{C}$	SD 1	SD 2	$\bar{S}$	SD 1	SD 2
2	0	−484.1718	0.0006	0.0024			
2	2	2.4257	0.0023	0.0094	−1.3856	0.0024	0.0097
3	0	0.9577	0.0005	0.0019			
3	1	2.0169	0.0052	0.0202	0.2508	0.0015	0.0061
3	2	0.9194	0.0086	0.0309	−0.6265	0.0044	0.0171
3	3	0.7186	0.0079	0.0299	1.4201	0.0096	0.0355
4	0	0.5470	0.0014	0.0058			
4	1	−0.5321	0.0019	0.0074	−0.4442	0.0031	0.0121
4	2	0.3544	0.0021	0.0084	0.6617	0.0031	0.0123
4	3	0.9736	0.0060	0.0219	−0.2195	0.0046	0.0175
4	4	−0.1674	0.0090	0.0311	0.3122	0.0044	0.0169
5	0	0.0681	0.0006	0.0024			
5	1	−0.0686	0.0014	0.0055	−0.0819	0.0022	0.0086
5	2	0.6568	0.0035	0.0131	−0.3166	0.0048	0.0175
5	3	−0.4719	0.0069	0.0229	−0.2312	0.0161	0.0349
5	4	−0.3150	0.0051	0.0184	0.0282	0.0043	0.0161
5	5	0.1489	0.0020	0.0081	−0.6787	0.0067	0.0236
6	0	−0.1610	0.0023	0.0088			
6	1	−0.0889	0.0022	0.0087	−0.0203	0.0040	0.0141
6	2	0.0682	0.0021	0.0080	−0.3680	0.0024	0.0092
6	3	0.0173	0.0038	0.0140	−0.0238	0.0056	0.0198
6	4	−0.1013	0.0076	0.0237	−0.4525	0.0046	0.0161
6	5	−0.2932	0.0071	0.0216	−0.5082	0.0035	0.0129
6	6	0.0384	0.0051	0.0180	−0.2296	0.0099	0.0278
7	0	0.0923	0.0012	0.0049			
7	1	0.2516	0.0027	0.0102	0.1306	0.0023	0.0086
7	2	0.3388	0.0037	0.0129	0.0851	0.0064	0.0187
7	3	0.2590	0.0048	0.0156	−0.2164	0.0102	0.0248
7	4	−0.2700	0.0100	0.0250	−0.0864	0.0021	0.0082
7	5	−0.0071	0.0041	0.0144	0.0531	0.0028	0.0106
7	6	−0.3288	0.0073	0.0208	0.1504	0.0056	0.0179
7	7	0.0645	0.0076	0.0222	0.0363	0.0090	0.0248
8	0	0.0621	0.0028	0.0101			
8	1	0.0241	0.0048	0.0156	0.0917	0.0047	0.0145
8	2	0.0486	0.0011	0.0043	0.0656	0.0018	0.0069
8	3	−0.0235	0.0023	0.0087	−0.0744	0.0075	0.0200
8	4	−0.2401	0.0067	0.0193	0.0680	0.0041	0.0138
8	5	−0.0928	0.0038	0.0130	0.0837	0.0033	0.0120
8	6	−0.0372	0.0028	0.0104	0.3010	0.0032	0.0115
8	7	0.0513	0.0039	0.0134	0.0725	0.0022	0.0085
8	8	−0.0909	0.0071	0.0206	0.0974	0.0023	0.0088
9	0	0.0322	0.0023	0.0086			
9	1	0.1593	0.0026	0.0094	0.0026	0.0013	0.0052
9	2	0.0258	0.0026	0.0094	−0.0169	0.0053	0.0155
9	3	−0.1522	0.0057	0.0154	−0.1500	0.0028	0.0102
9	4	0.0015	0.0042	0.0139	0.0259	0.0055	0.0159
9	5	−0.0201	0.0013	0.0050	−0.0698	0.0055	0.0165
9	6	0.0756	0.0052	0.0154	0.2248	0.0029	0.0104
9	7	−0.0561	0.0020	0.0075	−0.0098	0.0069	0.0178
9	8	0.1859	0.0037	0.0125	−0.0261	0.0060	0.0165
9	9	−0.0320	0.0034	0.0120	0.0756	0.0017	0.0067

TABLE 3.34.—*(Cont'd)*

n	m	$\bar{C}$	SD 1	SD 2	$\bar{S}$	SD 1	SD 2
10	0	0.0399	0.0033	0.0110			
10	1	0.0758	0.0028	0.0100	−0.1562	0.0056	0.0145
10	2	−0.0464	0.0030	0.0101	−0.0466	0.0042	0.0130
10	3	−0.0413	0.0017	0.0065	−0.1134	0.0066	0.0156
10	4	−0.0993	0.0042	0.0132	−0.1163	0.0043	0.0138
10	5	−0.1086	0.0022	0.0079	−0.0190	0.0094	0.0199
10	6	0.0001	0.0031	0.0108	−0.1245	0.0072	0.0172
10	7	−0.0070	0.0054	0.0149	−0.0299	0.0048	0.0142
10	8	0.0490	0.0027	0.0096	−0.1294	0.0040	0.0127
10	9	0.1287	0.0078	0.0173	−0.0595	0.0058	0.0155
10	10	0.0682	0.0042	0.0135	−0.0082	0.0033	0.0114
11	0	−0.0597	0.0035	0.0111			
11	1	−0.0146	0.0022	0.0081	0.0331	0.0011	0.0045
11	2	0.0360	0.0011	0.0044	−0.1135	0.0015	0.0059
11	3	−0.0136	0.0038	0.0117	−0.1190	0.0012	0.0048
11	4	0.0089	0.0046	0.0130	−0.1018	0.0080	0.0164
11	5	0.0271	0.0006	0.0023	0.0304	0.0070	0.0168
11	6	−0.0377	0.0055	0.0148	0.0577	0.0042	0.0133
11	7	0.0130	0.0025	0.0090	−0.1145	0.0017	0.0064
11	8	−0.0180	0.0061	0.0149	0.0424	0.0042	0.0127
11	9	−0.0063	0.0087	0.0169	0.0470	0.0040	0.0122
11	10	−0.1084	0.0014	0.0053	0.0032	0.0021	0.0076
11	11	0.0840	0.0039	0.0124	−0.0223	0.0019	0.0073
12	0	0.0429	0.0030	0.0100			
12	1	−0.0611	0.0047	0.0133	−0.0141	0.0028	0.0094
12	2	−0.0444	0.0057	0.0141	0.0384	0.0040	0.0121
12	3	0.1075	0.0044	0.0128	0.0846	0.0023	0.0081
12	4	−0.0220	0.0023	0.0081	−0.0143	0.0030	0.0101
12	5	0.0301	0.0013	0.0051	−0.0077	0.0037	0.0120
12	6	0.0588	0.0057	0.0150	−0.0089	0.0062	0.0154
12	7	−0.0223	0.0029	0.0099	0.0225	0.0062	0.0151
12	8	−0.0328	0.0022	0.0079	−0.0207	0.0043	0.0129
12	9	0.0239	0.0045	0.0131	0.0333	0.0031	0.0101
12	10	−0.0211	0.0021	0.0075	0.0508	0.0044	0.0124
12	11	0.0106	0.0040	0.0119	0.0290	0.0056	0.0140
12	12	−0.0116	0.0012	0.0045	0.0047	0.0043	0.0129
13	0	0.0428	0.0047	0.0122			
13	1	0.0048	0.0144	0.0162	−0.0324	0.0128	0.0150
13	2	−0.0149	0.0151	0.0172	−0.0661	0.0153	0.0168
13	3	−0.0931	0.0148	0.0168	0.0091	0.0151	0.0165
13	4	−0.0396	0.0147	0.0161	−0.0561	0.0147	0.0161
13	5	0.0504	0.0148	0.0160	0.0850	0.0150	0.0171
13	6	−0.0761	0.0155	0.0180	0.0677	0.0156	0.0180
13	7	−0.0453	0.0151	0.0171	0.0939	0.0156	0.0181
13	8	0.0461	0.0151	0.0173	−0.0152	0.0150	0.0178
13	9	0.0260	0.0068	0.0139	0.0705	0.0026	0.0089
13	10	−0.0010	0.0141	0.0160	0.0018	0.0140	0.0159
13	11	0.0004	0.0141	0.0157	−0.0615	0.0142	0.0158
13	12	−0.0304	0.0023	0.0081	0.0988	0.0025	0.0086
13	13	−0.0296	0.0046	0.0126	0.0949	0.0028	0.0094

TABLE 3.34.—*(Cont'd)*

n	m	$\bar{C}$	SD 1	SD 2	$\bar{S}$	SD 1	SD 2
14	0	−0.0296	0.0029	0.0094			
14	1	−0.0150	0.0008	0.0032	0.0062	0.0043	0.0113
14	2	−0.0383	0.0159	0.0164	0.0139	0.0159	0.0167
14	3	0.0536	0.0159	0.0165	−0.0213	0.0156	0.0164
14	4	0.0271	0.0158	0.0167	−0.0144	0.0158	0.0164
14	5	−0.0189	0.0158	0.0165	−0.0141	0.0160	0.0166
14	6	0.0725	0.0165	0.0176	−0.0196	0.0169	0.0176
14	7	0.0524	0.0169	0.0178	−0.0029	0.0165	0.0173
14	8	−0.0346	0.0167	0.0179	−0.0363	0.0165	0.0177
14	9	0.0404	0.0006	0.0026	0.0614	0.0027	0.0090
14	10	0.0042	0.0148	0.0160	−0.0601	0.0149	0.0163
14	11	0.0263	0.0137	0.0150	−0.0400	0.0138	0.0151
14	12	0.0082	0.0039	0.0108	−0.0233	0.0026	0.0086
14	13	0.0300	0.0020	0.0071	0.0076	0.0048	0.0119
14	14	−0.0517	0.0019	0.0068	−0.0081	0.0005	0.0021
15	0	−0.0008	0.0055	0.0117			
15	1	0.0385	0.0141	0.0150	−0.0150	0.0122	0.0135
15	2	−0.0073	0.0146	0.0153	−0.0064	0.0145	0.0152
15	3	0.0250	0.0151	0.0157	0.0432	0.0151	0.0157
15	4	0.0212	0.0148	0.0153	−0.0162	0.0147	0.0152
15	5	0.0732	0.0151	0.0155	0.0251	0.0151	0.0156
15	6	0.0167	0.0154	0.0159	−0.1048	0.0154	0.0158
15	7	0.0149	0.0165	0.0170	0.0698	0.0159	0.0165
15	8	−0.0260	0.0159	0.0165	0.0244	0.0155	0.0162
15	9	0.0317	0.0037	0.0105	0.0493	0.0028	0.0091
15	10	0.0218	0.0150	0.0160	0.0053	0.0148	0.0162
15	11	−0.0197	0.0137	0.0148	−0.0212	0.0137	0.0147
15	12	−0.0327	0.0031	0.0092	0.0165	0.0021	0.0071
15	13	−0.0034	0.0040	0.0105	0.0148	0.0029	0.0089
15	14	0.0026	0.0007	0.0027	−0.0212	0.0004	0.0018
15	15	−0.0474	0.0147	0.0154	0.0310	0.0148	0.0155
16	0	−0.0109	0.0015	0.0055			
16	1	0.0022	0.0143	0.0150	0.0315	0.0126	0.0132
16	2	0.0080	0.0136	0.0139	0.0020	0.0130	0.0135
16	3	0.0416	0.0144	0.0148	−0.0183	0.0141	0.0145
16	4	0.0565	0.0143	0.0147	0.0306	0.0139	0.0144
16	5	0.0157	0.0140	0.0143	0.0110	0.0142	0.0147
16	6	−0.0274	0.0144	0.0148	−0.0183	0.0141	0.0144
16	7	0.0186	0.0151	0.0155	0.0018	0.0147	0.0151
16	8	−0.0737	0.0153	0.0158	0.0168	0.0149	0.0155
16	9	−0.0294	0.0130	0.0144	−0.0642	0.0131	0.0142
16	10	−0.0396	0.0146	0.0155	−0.0078	0.0147	0.0161
16	11	0.0276	0.0136	0.0146	0.0012	0.0134	0.0143
16	12	0.0235	0.0003	0.0014	0.0006	0.0025	0.0078
16	13	0.0036	0.0025	0.0078	−0.0221	0.0034	0.0094
16	14	−0.0139	0.0008	0.0033	−0.0375	0.0011	0.0041
16	15	−0.0353	0.0132	0.0139	−0.0525	0.0131	0.0136
16	16	−0.0157	0.0152	0.0156	−0.0272	0.0149	0.0155
17	0	0.0199	0.0052	0.0102			
17	1	−0.0204	0.0131	0.0137	−0.0512	0.0116	0.0122
17	2	−0.0102	0.0127	0.0132	0.0066	0.0123	0.0130
17	3	0.0112	0.0131	0.0135	−0.0334	0.0129	0.0134
17	4	0.0032	0.0139	0.0142	0.0259	0.0135	0.0139
17	5	−0.0037	0.0132	0.0135	0.0010	0.0131	0.0136

TABLE 3.34.—*(Cont'd)*

n	m	$\overline{C}$	SD 1	SD 2	$\overline{S}$	SD 1	SD 2
17	6	−0.0554	0.0134	0.0137	−0.0212	0.0131	0.0135
17	7	0.0034	0.0138	0.0141	−0.0472	0.0134	0.0137
17	8	0.0334	0.0143	0.0146	−0.0035	0.0140	0.0144
17	9	0.0062	0.0143	0.0149	−0.0223	0.0142	0.0147
17	10	−0.0168	0.0138	0.0146	0.0382	0.0138	0.0147
17	11	−0.0046	0.0138	0.0148	0.0158	0.0133	0.0141
17	12	0.0228	0.0040	0.0098	−0.0003	0.0005	0.0020
17	13	0.0322	0.0026	0.0077	0.0398	0.0042	0.0100
17	14	−0.0159	0.0002	0.0009	0.0033	0.0018	0.0061
17	15	0.0422	0.0117	0.0123	0.0028	0.0116	0.0121
17	16	−0.0087	0.0130	0.0134	−0.0002	0.0132	0.0136
17	17	−0.0521	0.0146	0.0150	0.0120	0.0152	0.0155
18	0	0.0159	0.0016	0.0055			
18	1	−0.0559	0.0123	0.0127	−0.0569	0.0105	0.0110
18	2	−0.0076	0.0120	0.0123	0.0294	0.0119	0.0122
18	3	−0.0181	0.0114	0.0117	−0.0091	0.0117	0.0121
18	4	−0.0013	0.0127	0.0130	0.0318	0.0126	0.0129
18	5	0.0179	0.0126	0.0128	0.0029	0.0125	0.0127
18	6	−0.0004	0.0124	0.0127	−0.0003	0.0122	0.0125
18	7	−0.0003	0.0128	0.0131	−0.0053	0.0123	0.0126
18	8	0.0635	0.0131	0.0133	−0.0204	0.0129	0.0132
18	9	−0.0296	0.0133	0.0138	−0.0118	0.0132	0.0137
18	10	0.0480	0.0133	0.0138	0.0103	0.0132	0.0138
18	11	0.0025	0.0133	0.0141	−0.0340	0.0128	0.0136
18	12	−0.0472	0.0044	0.0104	−0.0162	0.0020	0.0064
18	13	−0.0037	0.0008	0.0031	−0.0885	0.0054	0.0106
18	14	−0.0213	0.0014	0.0050	−0.0117	0.0030	0.0080
18	15	−0.0707	0.0105	0.0109	−0.0343	0.0105	0.0110
18	16	0.0097	0.0111	0.0116	−0.0180	0.0111	0.0116
18	17	0.0288	0.0123	0.0127	−0.0315	0.0130	0.0133
18	18	−0.0141	0.0136	0.0138	−0.0231	0.0146	0.0149
19	0	0.0021	0.0038	0.0083			
19	1	−0.0206	0.0112	0.0115	0.0007	0.0100	0.0103
19	2	0.0283	0.0111	0.0114	−0.0104	0.0112	0.0116
19	3	0.0161	0.0108	0.0111	0.0019	0.0106	0.0109
19	4	0.0219	0.0116	0.0120	−0.0125	0.0114	0.0116
19	5	−0.0366	0.0118	0.0120	−0.0334	0.0118	0.0120
19	6	0.0573	0.0116	0.0119	0.0334	0.0114	0.0117
19	7	0.0445	0.0119	0.0122	−0.0328	0.0116	0.0118
19	8	0.0301	0.0119	0.0122	0.0230	0.0118	0.0121
19	9	0.0167	0.0122	0.0127	−0.0134	0.0121	0.0125
19	10	−0.0283	0.0124	0.0129	−0.0640	0.0122	0.0128
19	11	0.0161	0.0122	0.0129	0.0683	0.0120	0.0128
19	12	−0.0036	0.0053	0.0098	−0.0173	0.0018	0.0060
19	13	−0.0014	0.0033	0.0082	0.0094	0.0053	0.0104
19	14	0.0007	0.0004	0.0015	−0.0116	0.0016	0.0055
19	15	−0.0416	0.0094	0.0100	−0.0364	0.0094	0.0100
19	16	−0.0143	0.0094	0.0100	0.0419	0.0092	0.0098
19	17	0.0185	0.0102	0.0106	−0.0098	0.0103	0.0107
19	18	0.0549	0.0114	0.0117	0.0203	0.0116	0.0119
19	19	−0.0406	0.0126	0.0128	0.0238	0.0127	0.0130

TABLE 3.34.—*(Cont'd)*

n	m	$\bar{C}$	SD 1	SD 2	$\bar{S}$	SD 1	SD 2
20	0	0.0033	0.0005	0.0021			
20	1	−0.0062	0.0096	0.0101	0.0054	0.0085	0.0088
20	2	0.0331	0.0093	0.0095	0.0433	0.0095	0.0099
20	3	−0.0084	0.0090	0.0092	−0.0031	0.0091	0.0094
20	4	0.0137	0.0095	0.0097	−0.0526	0.0094	0.0096
20	5	0.0229	0.0095	0.0097	−0.0363	0.0093	0.0095
20	6	0.0077	0.0092	0.0095	−0.0206	0.0093	0.0095
20	7	−0.0501	0.0093	0.0094	0.0090	0.0092	0.0094
20	8	−0.0097	0.0093	0.0095	0.0198	0.0092	0.0094
20	9	0.0076	0.0093	0.0096	0.0243	0.0093	0.0096
20	10	−0.0586	0.0094	0.0097	0.0048	0.0095	0.0099
20	11	0.0095	0.0093	0.0098	−0.0233	0.0093	0.0099
20	12	0.0092	0.0012	0.0043	0.0075	0.0015	0.0050
20	13	0.0295	0.0031	0.0078	−0.0085	0.0064	0.0101
20	14	0.0126	0.0006	0.0023	−0.0027	0.0012	0.0043
20	15	0.0433	0.0082	0.0087	−0.0039	0.0083	0.0088
20	16	0.0141	0.0082	0.0088	−0.0443	0.0081	0.0087
20	17	0.0534	0.0086	0.0090	−0.0194	0.0087	0.0091
20	18	0.0184	0.0095	0.0097	0.0057	0.0096	0.0099
20	19	0.0039	0.0104	0.0105	0.0029	0.0102	0.0104
20	20	0.0176	0.0110	0.0112	−0.0094	0.0111	0.0113
21	0	−0.0018	0.0024	0.0065			
21	12	0.0077	0.0046	0.0078	−0.0308	0.0015	0.0050
21	13	−0.0162	0.0019	0.0058	0.0397	0.0036	0.0085
21	14	0.0023	0.0032	0.0073	0.0147	0.0012	0.0041
22	0	−0.0013	0.0024	0.0062			
22	12	−0.0527	0.0012	0.0042	−0.0228	0.0038	0.0070
22	13	−0.0170	0.0026	0.0062	−0.0121	0.0006	0.0009
22	14	0.0065	0.0034	0.0069	0.0093	0.0014	0.0045

TABLE 3.35.—*RMS Difference (After Adjustment) Between Astrogeodetic Geoidal Heights and Undulations Computed From Potential Coefficients*

Solution	North American Datum 1927 (meters)	Australian Datum (meters)
Least-squares collocation (k = ⅛)	4.34	1.96
LQ (k = ⅛)	4.39	2.03
GEM 3	5.29	2.11
GEM 4	4.38	3.73
SAO Standard Earth II	5.21	2.94
SAO Standard Earth III	6.06	2.64

TABLE 3.36.—*RMS Orbit Fit*

Solution	RMS fit (meters)
Least-squares collocation (k = ½)	±11.6
Least-squares (k = ½)	15.3
Least-squares collocation (k = ⅛)	5.0
Least-squares (k = ⅛)	5.2
GEM 3	6.4
GEM 4	7.4
SAO Standard Earth II	4.8
SAO Standard Earth III	7.9

TABLE 3.37.—*Differences in Geoidal Heights and Anomalies with Respect to Potential Coefficients Given in Table 3.34*

Solutions	Geoidal heights (meters)		Anomalies (meters)	
	RMS	Max	RMS	Max
Least-squares (k = ⅛)	±0.5	2	± 1.7	4
SAO SE II	5.9	22	10.8	40
GEM 3	3.3	12	7.6	28

TABLE 3.38.—*Consistency of Solutions for Station Positions From 1964 to 1972*

Station	No. spans of data	Avg no. passes	Longitude			Latitude			Height		
			Rate (cm/yr)	Std err (cm/yr)	Residuals (cm)	Rate (cm/yr)	Std err (cm/yr)	Residuals (cm)	Rate (cm/yr)	Std err (cm/yr)	Residuals (cm)
Brazil	32	34	−26	17	207	5	16	196	2	13	164
Japan	36	45	54	12	149	−26	11	134	−11	12	142
Alaska	39	88	−4	11	129	−30	12	148	47	13	158
Greenland	36	115	4	9	125	−17	6	77	−1	9	127
McMurdo	20	88	38	26	121	0	22	103	50	19	92
Seychelles	36	35	33	17	188	−7	18	196	−71	24	266
Hawaii	63	38	19	13	174	11	13	182	13	8	114
New Mexico	39	38	0	17	228	−25	11	141	40	16	206
England	33	61	−27	26	223	−9	24	203	109	28	242
Maryland	43	45	49	11	146	−8	9	113	63	11	143
Australia	37	43	20	12	153	−31	12	149	10	11	132
So. Africa	32	42	−20	15	157	6	16	162	61	18	186
Samoa	36	37	−6	18	213	−9	12	141	13	13	155
Philippines	34	35	46	16	189	−20	13	151	12	16	188
Maine	39	48	−1	11	140	−15	9	108	28	12	142
Minnesota	26	29	11	19	146	−8	12	95	42	17	135
California	49	26	−19	10	152	−16	6	93	23	8	118
Average					167			141			159

4

JET PROPULSION LABORATORY

P. B. Esposito
N. A. Mottinger
T. D. Moyer
D. W. Trask

4.1 INTRODUCTION

Determinations of tracking station locations and the gravitational constant of the Earth $GM_\oplus$ based on Doppler-tracking data from lunar and planetary spacecraft are presented in this chapter. The solutions for $GM_\oplus$ are consistent to within 0.4 km^3/sec^2, and the tracking station locations are consistent to within 1 meter for the coordinates well-determined by these data: the distance from the rotational axis (spin axis) of the Earth and the difference in longitude between two stations.

Participants in the National Geodetic Satellite Program (NGSP) made considerable use of the coordinates determined by the Jet Propulsion Laboratory (JPL) for its Deep Space Stations (DSS) by using data from planetary flight missions. The values of $GM_\oplus$ determined by JPL from near-Earth observations of the Mariner 9 spacecraft were also used. Because such determinations were made by JPL as part of other tasks and not directly as part of the NGSP, they are independent contributions supporting material in other chapters. Therefore they are discussed separately in this chapter, and the material is organized to bring out the values found and their errors, rather than being organized strictly according to the scheme used in other chapters.

The DSS instrumentation that JPL used is described briefly in section 4.2. Detailed descriptions are given in various JPL reports. The data used by JPL are described in sections 4.2, 4.3.3 (as used for finding locations of stations), and 4.5.3 (as used for finding $GM_\oplus$).

How the stations were located is detailed in section 4.3, the data used are discussed, and the results are given, together with an analysis of the errors in the results. Some theory pertaining to the determination of the spacecraft trajectories from such observations as distance and range rate is used in the determination of both station locations and $GM_\oplus$. This theory is presented in section 4.4. In section 4.5 the theory and data for determining $GM_\oplus$ are briefly described, and the values found for $GM_\oplus$ are discussed extensively.

4.2 INSTRUMENTATION AND GENERAL DATA

Two-way Doppler data obtained by the Deep Space Network (DSN) of the Jet Propulsion Laboratory were used to obtain the locations of the Deep Space Stations (DSS) and the gravitational constant of the Earth. The DSN is a global tracking network established by the NASA Office of Tracking and Data Acquisition for two-way communications with unmanned spacecraft traveling from Earth to interplanetary distances. The DSN, which operates under the system management and technical direction of JPL, comprises three main elements: Deep Space Instrumentation Facility (DSIF), Ground Communications Facility (GCF), and Space Flight Operations Facility (SFOF). The tracking station complexes of the DSIF, identified as DSS, are situated approximately 120 degrees apart in longitude to provide continuous coverage of distant spacecraft. The DSS serial designations and locations are listed in table 4.1: the coordinates are given in chapter 1.

4.2.1 Tracking Station

A simplified, two-way Doppler system is depicted in figure 4.1. The tracking station transmits a signal to the spacecraft. The signal received at the spacecraft is shifted in frequency by the well-known Doppler effect. The spacecraft then retransmits the received signal. The signal recorded at the ground receiver has been shifted further in frequency

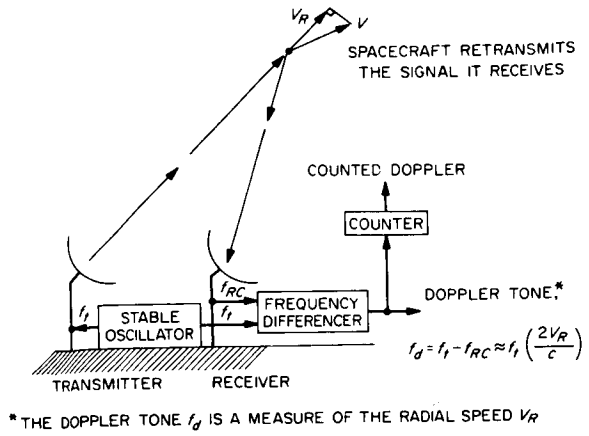

FIGURE 4.1.—Simplified Doppler system.

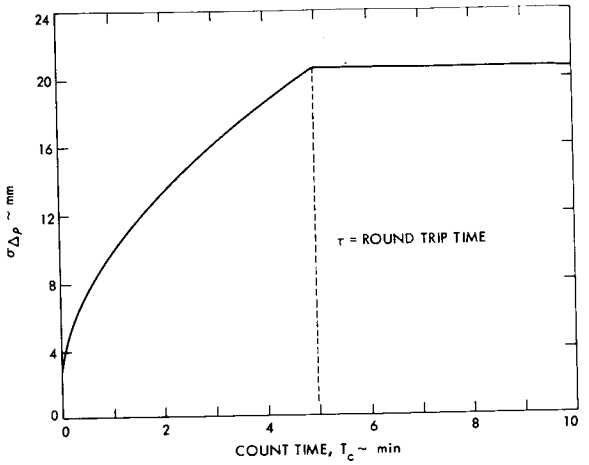

FIGURE 4.2.—Counted Doppler quality.

by the radial velocity of the receiver with respect to the spacecraft. The difference between the received frequency and the current transmitter frequency is called the Doppler tone.

In practice, the number of cycles in the Doppler tone is continuously counted, and the continuous count is sampled usually once each minute. These continuous-count Doppler tone samples are differenced to obtain the kind of data known as counted two-way Doppler, which is actually the increase in range between the DSS and the spacecraft that occurred during a sampling interval. In actual practice, the range differences accumulated over a 10-minute interval are normally used when the orbit of the spacecraft is being determined and physical constants (such as the DSS locations or $GM_\oplus$) are being solved for. The higher sampling rates are used for monitoring the quality of the data and other special analyses.

4.2.2 Quality of Data

The effective frequency at the counter is the same as the frequency received from the spacecraft (i.e., 2.3 MHz). This means that the length of each counted cycle of range difference is 65 mm. The typical quality of counted two-way Doppler data, which is shown as a function of counting time in figure 4.2, can be represented by the equation

$$\sigma^2(\Delta\rho) = k_1^2 + (k_2\sqrt{\text{minimum of } \tau, T_c})^2 = (k_2\sqrt{T_c})^2 + (k_3 T_c)^2 \qquad (4.1)$$

where

τ is the signal round trip time
T_c is the count time, i.e., the period over which the DSS-spacecraft range change occurs
k_1 represents a cumulative counting error that is independent of T
k_2 represents the cumulative count error that grows as the square root of T
k_3 represents a phase error that is proportional to T_c

Errors of the type of k_1 include quantization for roundoff error at the Doppler counter and phase jitter. For the current S-band system, $k_1 \approx 3$ mm (Trask, 1966; Trask and Hamilton, 1966), which includes receiver phase jitter and short-term variations in the path length of the signal as it passes through the transmission media (troposphere, stratosphere, and ionosphere).

For missions since Mariner 4, after the Doppler resolver (the time from the start of a Doppler count to the first positive-going zero crossing is counted with a 100–MHz counter) was introduced in the DSS, the quantization errors have been less than 0.4 mm. (The quantization error $\sigma_q = (LC/\sqrt{6})$, where LC is the value of the least count in

units of distance.) However, at the start of the Mariner 4 mission, $\sigma_q = 28$ mm (where only positive-going zero crossing was counted).

The k_2 term represents the short-term (white frequency) noise of the DSS reference oscillator (Trask and Hamilton, 1966; Motsch and Curkendall, 1967). For the rubidium standard, $k_2 = 3.8$ mm/s$^{1/2}$. The k_2 term represents the cycle dropout (add-in) behavior that may occur as a result of the momentary loss of lock of the receiver phase detector because of excessive phase jitter. This component is negligible under the strong signal-to-noise ratios that prevail during the tracking intervals used for this report.

An example of error of the type of k_3 is the quantization error due to the limited number of bits available for computing the spacecraft radial velocity. For the double-precision program now used at JPL, this term is negligible. However, for the single-precision program previously used, when the spacecraft velocity was between 16 and 32 km/s, $k_3 = 0.24$ mm/s.

The high-frequency noise visible in the data from the tracking stations is shown in figure 4.2. However, when DSS locations are being solved for from several days of data, long-term errors of a diurnal nature[1] become more important than this high-frequency noise.

An extensive effort has been carried out at JPL to correct the tracking data for these quantities. The nature and source of these corrections, as well as their size and/or effect on the determinations of the DSS locations, are outlined in sections 4.3 and 4.4. A further discussion of data used in determining locations of tracking stations is given in section 4.3.3.

[1] The importance of the diurnal type of error is explained in section 4.3.1. These diurnal errors are of two forms: those affecting the computation of the observables, such as the platform parameters (Universal Time 1 and polar motion), and those affecting the observable itself, such as the transmission media (the neutral particles of the troposphere and the charged particles of the ionosphere and space plasma).

4.3 RESULTS: LOCATIONS OF TRACKING STATIONS[2]

4.3.1 Solutions From Individual Flights

The latest determination of the set of locations of the eight stations in the DSN was made by processing Doppler radio-tracking data from three different spacecraft by means of computer programs and planetary ephemerides provided for the Mariner Mars 1971 (MM71) mission. The computer program was the satellite orbit determination program (SATODP) version C1.0, whose theoretical precepts are discussed by Moyer (1971).

Basic data supplied to the SATODP for determining station locations involve the radiometric data and a planetary ephemeris, from which the positions of bodies in the solar system are obtained. Owing to the high correlation between ephemerides and station locations, reduction of the data from the previous missions must be done with the same ephemeris that the current mission (MM71 in this case) is using. The planetary ephemeris designated development ephemeris 78 (DE78) was used during the phase of the MM71 mission covering the period from launch to arrival at Mars and hence was used in the determination of station locations for use by the MM71 mission.

This section documents the set of station locations obtained for the DSN by using the SATODP, ephemeris, and other quantities, including timing data giving Universal Time 1 (UT1), polar positions for the correction of polar motion, and data for correcting the effects on radio waves of both neutral and charged particles in the Earth's atmosphere.

The solutions derived are for all eight stations (table 4.1) in the DSN, but for clarity in discussing them, certain sets of solutions have been combined. For example, at the Goldstone, California, and Madrid, Spain, tracking complexes, there are multiple-antenna sites whose relative positions

[2] Theory is discussed in section 4.4; results on gravitational constants are given in section 4.5.

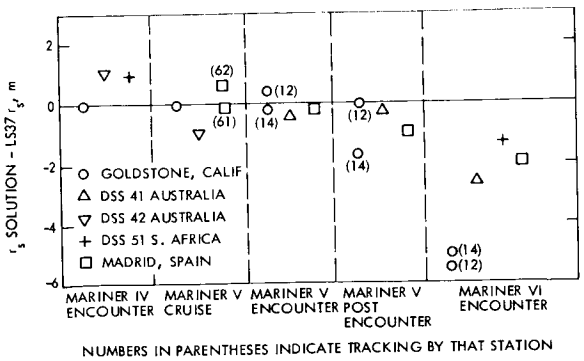

FIGURE 4.3.—Distance off spin axis: consistency among missions.

are known very accurately from geodetic surveys. At the Goldstone complex, locations from radio tracking for stations DSS 11, DSS 12, and DSS 14 have all been referred to the location of DSS 12, and at Madrid, locations of stations DSS 61 and DSS 62 have been referred to that of DSS 61. When this procedure has been used, a small number in parentheses is used to indicate the station that was actually tracking.

The differences shown in figures 4.3 and 4.4 are those for the stations at Goldstone (DSS 11, DSS 12, DSS 14), California; Woomera (DSS 41) and Tidbinbilla (DSS 42), Australia; Johannesburg, South Africa (DSS 51); and Madrid (DSS 61 and DSS 62), Spain. In these figures, the best estimate (location set 37) has been subtracted from the individual solutions to present a normalized plot showing how the solutions compare at the different stations. A summary of the entire solution is given in table 4.2 and the best estimate, location set 37 (LS37), in table 4.3.

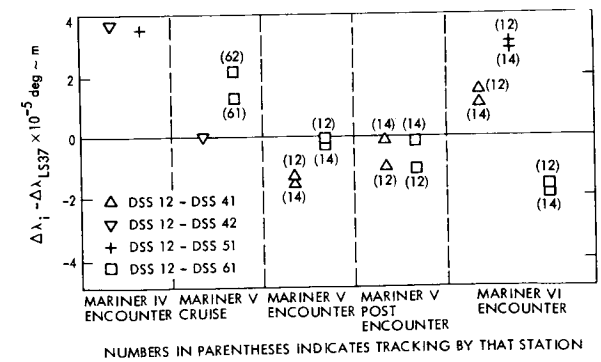

FIGURE 4.4.—Relative longitude: consistency among missions.

The various solutions for the spin axis at Goldstone show agreement to the ± 0.1-meter level. The Mariner 6 solutions show a definite bias at all stations, which may be because of the increased sensitivity of this mission to declination errors in the ephemeris. The large declination (-24 deg.) at encounter makes the solutions of this mission 8.5 times as sensitive to a declination error in the Mars ephemeris as those of Marine 4, which encounters Mars at -3-deg. declination.

The Mariner 6 solutions also have the largest uncertainties associated with them, primarily because of the inability to use the data acquired subsequent to the cold gas cooling (blow-down) occurring 45 minutes before encounter as required by an onboard experiment. The solutions from other missions show a spread of about 3 meters, but the rms deviation of all solutions except those of Mariner 6 is 0.8 meter.

Based on the error analysis, the true uncertainty for r_s values in solution LS37 is believed to be no better than 0.8 meter and no worse than approximately 2 meters.

Relative longitudes behave similarly to the spin axis estimates and are shown in figure 4.4. Best agreement is approximately 0.2×10^{-5} deg (~ 0.2 meter), whereas others range upward to 3.8×10^{-5} deg (~ 4 meters). Error analysis then shows the uncertainty of solution LS37 to be 0.5×10^{-5} deg; this may not be justified from the results shown in figure 4.4, which shows the rms to be 1.9×10^{-5} deg.

Assessment of the true uncertainty of the spin axis and relative longitudes is complicated by errors in the determination of planetary ephemerides, polar motion, and atmospheric refraction effects. Uncertainties in the measurements used to generate these items can be analyzed to produce statistics of the random uncertainty associated with each, but the detection of systematic errors within one item or between related items may be very difficult, if not impossible.

If the error is truly systematic, i.e., is a constant offset or bias, very consistent locations may be obtained, and the station locations may be used successfully when they are applied to support navigation using the same systematically perturbed item. Therefore an important criterion for accurate determination of station locations is that the locations are consistent from mission to mission.

Examples of this can be found in the plot (fig. 4.3) of spin axis solutions for Goldstone, California. Except for one solution, which may have been affected by high plasma activity in space, Mariner 4 and 5 solutions show a range of about 0.4 m. Marine 6 shows about a 4-meter mean offset at Goldstone and slightly smaller offsets at all other stations.

The significance of this offset can be determined if one knows the true uncertainty in all the spin axis solutions. Since the true uncertainty is unknown, approximations to it are made by examining the known sources of error. Estimates of the maximum effects of nine different error sources for the five mission phases analyzed are shown in Figures 4.5 and 4.6. The first is the contribution of the white (random) noise in the data. This is an estimate of merely the true observed data noise on the station locations. The next effect is that of errors in the ephemeris; these errors apply only to the spin axis and longitude but cancel for relative longitudinal determination.

Error in planetary declinations converts into error in r_s via the tangent of the declination times the error in the declination. For very small declinations the inability to determine the spacecraft declination does not affect the spin axis estimate. Mariner 6 encounter occurs at -24 deg declination, and a spin axis value from it is therefore more likely to show an offset because of declination error than are spin axis values from the other spacecraft, which encountered planets at small declinations or at zero declination.

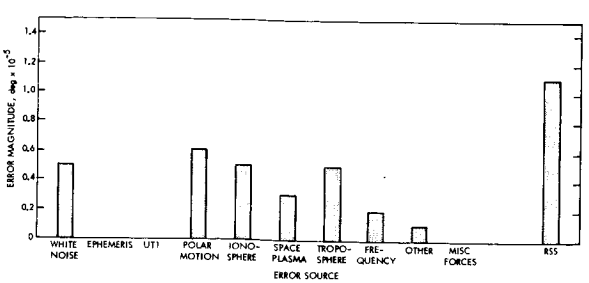

FIGURE 4.5—Error budget: relative longitude.

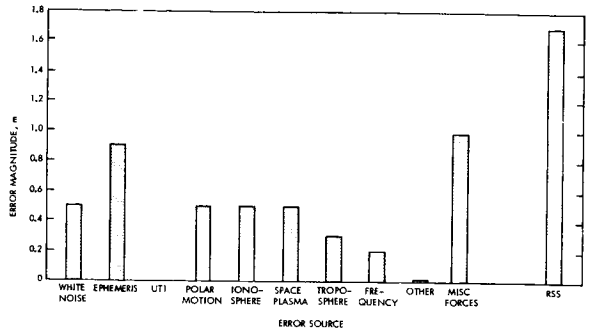

FIGURE 4.6.—Error budget: distance off spin axis

How does one determine the error in declination? Discussions with members of the JPL Ephemeris Development Group indicate that the best indication may be obtained by noting the differences in planetary position as given by various ephemerides.

There is a known error in DE78 that affected the derived station locations. Radar-measured distances to Mars taken during the 1971 opposition were erroneously time tagged because of equipment malfunction. The distances themselves were correct, but of course the incorrect time tags resulted in fallacious ephemeris elements for the planets when the data were reduced (Lieske *et al.*, unpublished, 1971). Correcting this error resulted in DE79. Comparison with DE78 indicates that the r_s solutions for Mariner 6 increase by only 0.03 meter and the Mariner longitude solutions by 0.45 meter.

Subsequent development of other ephemerides using more radar and Mariner 9 ranging data taken during the orbital phase has yielded DE80 and DE82. Comparing these with DE78 shows a maximum effect on the Mariner 4 spin axis solution of 0.14 meter when DE80 is used instead of DE78, but of 1.5 meters on the Mariner 6 spin axis solution. Entries in figures 4.5 and 4.6 are based on these differences between various ephemerides for the most sensitive mission.

UT1 does not affect either relative longitudes or spin axis values, as polar motion does. Henry Fliegel of JPL estimates a 0.7-meter error in both the X and Y components of the polar position as a result of errors in the measurements made by Bureau International de l'Heure (BIH) and of fitting their data in preparation for use in the orbit determination program.

Analysis of the errors in atmospheric refraction (ionospheric and tropospheric) is not easy because of difficulty in predicting the precise manner in which they cause station coordinate errors. Equivalent values for the errors in the ionospheric refraction model were made by Brendan Mulhall and Ka-Bing Yip and for the tropospheric refraction model by C. C. Chao, the JPL engineers who were responsible for the development of the corrections applied.

Entries for "frequency" and "other" in figures 4.5 and 4.6 are best estimates of possible errors caused by temperature effect on such items as electronic cables in the tracking system. The "miscellaneous forces" entry is for Mariner 6, for which data from the entire planetary fly-by could not be used because of the release of gas 45 minutes before encounter. Figures 4.5 and 4.6 show the worst possible error source cases for the five missions being analyzed. When the figures are prepared for each mission, uncertainties in r_s of about 1.1 meters are obtained for the Mariner 4 and 5 missions and 3.2 for Mariner 6. An rms of these yields an uncertainty of 0.6 meter for the r_s solutions in LS37. Analysis of relative longitude gives approximately 1.1×10^{-5} deg uncertainties for each rms to 0.5×10^{-5} deg for LS37. In view of the scatter of the solutions shown in figures 4.3 and 4.4, these results do not appear totally unrealistic for r_s but are perhaps optimistic by a factor of four for relative longitude.

4.3.1.1 Historical Behavior of the JPL Deep Space and Earth Satellite Solutions

Significant changes and improvements have been made in the station locations determined by processing radio-tracking data from deep space probes and in the work done with data from Earth satellites. In this section several different sets of JPL station locations derived between 1966 and the present will be compared with their counterparts derived from work done at the Smithsonian Astrophysical Observatory (SAO) and Wolf Research and Development Corporation (WRC) in cooperation with the Goddard Space Flight Center (GSFC).

The solutions originally determined by SAO were described in the Standard Earth 1966 (Lundquist and Veis, 1966) and were based on the data from Baker-Nunn cameras. A second set of locations was derived by SAO for the Standard Earth 1969 (Gaposchkin and Lambeck, 1970), which resulted from more camera data and the addition of laser-DME data. Only very cursory information about these differences will be provided here. The next set (WRC 1971) was prepared by WRC in cooperation with GSFC (Marsh *et al.*, 1971). They used a further augmented set of data from SAO that included not only more camera data but also more laser-DME and S-band, Doppler, and ranging data.

Four significant sets of locations derived at JPL will be compared with their appropriate counterparts. These sets are summarized in table 4.4. Certainly, similar tables prepared to show the progress in reducing data from cameras would show improvements in the development and application of various calibrations, constants, or corrections along with improvements in programs.

Disparity in some quantities such as longitude may be expected between solutions using camera data and JPL solutions because of differences in UT1 and discrepancies between the planetary ephemerides and the stellar catalogs in the definition of the origin of right ascension. Comparison of relative longitudes will remove this cause of conflict because they are independent of differences in UT1 and the ephemeris. Absolute longitudes will be handled separately.

There is another coordinate system in which the parameters best determined, r_s and relative longitudes, can be compared.

This system, used in interferometric tracking, involves the equatorial base line, which is the equatorial projection of the distance between stations. For stations 1 and 2, the base line r_b is given by

$$r_{b_{12}} = (r_{s_1}^2 + r_{s_2}^2 - 2r_{s_1} r_{s_2} \cos \Delta\lambda_{12})^{1/2} \quad (4.2)$$

where $\Delta\lambda_{12} = \lambda_2 - \lambda_1$, the relative longitude.

The evolution of the solutions for the distance off the spin axis and relative longitude made by processing Earth satellite and deep space probe data can be compared by studying figures 4.7 and 4.8, which show how the solutions compared with an average of the 1971 LS35 JPL solution and the WRC 1971 solution. In 1966 disparities in the spin axis solutions ranged from 12 to −18 meters, approximately. Since that time, solutions from both sources have been converging, and in 1971 the total difference was less than 3 meters.

Although the causes for the large change in the JPL solution for DSS 12 and the small change for DSS 41 are not known, part of it may derive from different sensitivities of the radio data to ionospheric refraction effects. The data used in 1966, the Ranger data, were taken at 900 MHz (L-band). The 900–MHz data are six times more sensitive to ionospheric refraction than the 2200–MHz (S-band) data available for the 1969 solutions. Uncertainties of 5 to 10 meters because of ionospheric refraction could exist in the 1966 solution. The fact that 2200–MHz data were corrected for the ionospheric effects could also cause a further shift between the 1966 and the 1969 solutions and at the same time reduce the uncertainty resulting from residual ionospheric refraction errors to less than 2 meters.

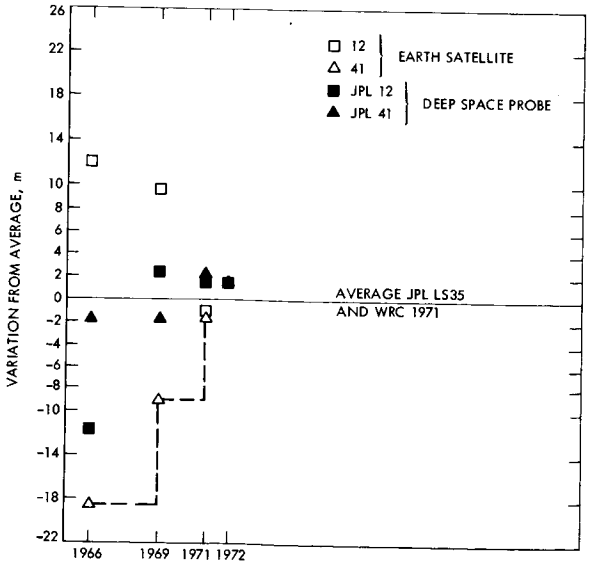

FIGURE 4.7.—History of spin axis distance.

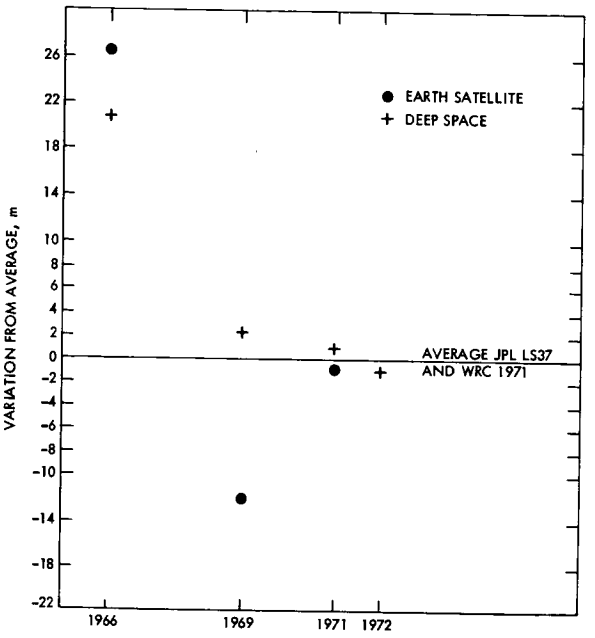

FIGURE 4.8.—History of longitudinal differences.

Another part of the differences may be due to seasonal variations in the ionosphere. DSS 12 and 41 are in different hemispheres; this fact, in conjunction with the seasonal ionospheric variations, would produce different effects on the estimated station locations. It is not known what specific items may be responsible for changes in the solutions.

The history of relative longitude determinations (fig. 4.8) likewise shows significant improvement in the agreement between the solutions from the two sources. As is true for distance off the spin axis, the charged particle effects may be responsible to a large degree for the changes between the 1966 and 1969 deep space solutions. The effect on the 1966 solutions could be in the 10- to 20-meter

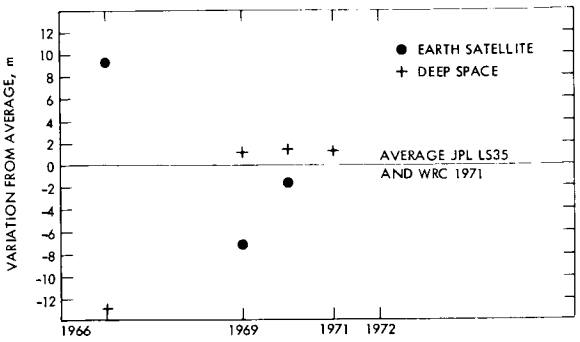

FIGURE 4.9.—History of equatorial base line: DSS 12 and DSS 41.

region. For the 1969 solutions it is probably 3 meters or less.

The same type of comparison is shown in figure 4.9, only for the equatorial base line project for DSS 12 and DSS 41. Note that less disparity exists between the 1966 solutions than was noted in either the r_s or the relative longitude figures just discussed; however, the 1969 to 1972 behavior is similar to the behavior of the relative longitudes (fig. 4.8). It is perhaps unexpected that the 1966 solutions should show smaller differences when they are studied from the base line viewpoint. Considering the large differences in longitude and distance off the spin axis previously studied, one might expect differences just as large in the base line. Because this is not the case, the exact cause is unknown at this time. One might expect that it is partially a result of the charged particle effects, which are so potentially significant to the 1966 deep space mission solutions.

4.3.1.2 Longitude Solutions

Longitude solutions are shown in figure 4.10. In analysis of LS35, a set very similar to LS37, the longitudes derived from Mariner 4 data were 16 meters east of the estimate based on combined Mariner 5 and 6 encounter data. This discrepancy was studied in minute detail because the individual solutions contained in earlier sets (i.e., LS25 in Mottinger, 1969) were not so disparate. By having the SATODP use the constants that were used to produce the Mariner 4 solution used in LS25,

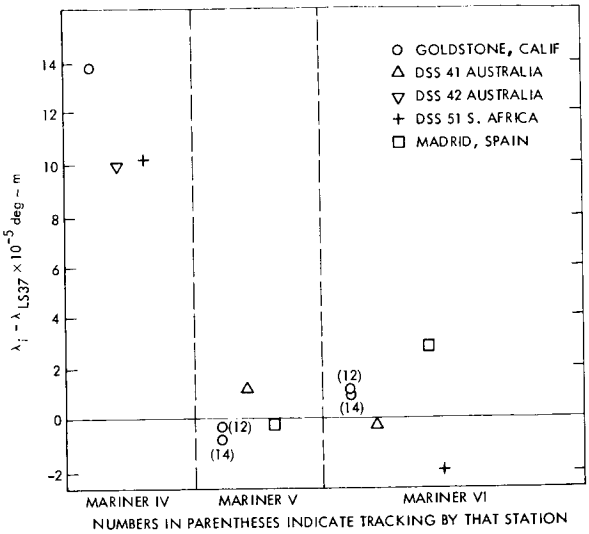

FIGURE 4.10.—Longitude determination: consistency among missions.

it was possible to obtain better than 1-meter agreement with those solutions. Thus it is indicated that the difference between LS25 and LS35 resulted from the changed constants for UT1, tropospheric and ionospheric refraction, polar motion, planetary ephemeris, and Mars pole direction. Since the old constants were known to be less accurate than the new constants, there was no choice but to accept the new solutions. To obtain longitudes in both LS35 and LS37, it was arbitrarily decided to de-weight the longitudes derived from Mariner 4 data but retain the spin axis values and the correlations that give relative longitudes.

Although this disparity has been reduced to approximately 14 meters in LS37 because of the application of the improved ionospheric refraction constants, the same basic policy of de-weighting the longitudes derived from Mariner 4 data was retained. Error analysis does not indicate that a 14-meter difference can be statistically justified. Some unknown factor is corrupting the solutions and is currently (1973) under intense investigation.

The uncertainty in LS35 and LS37 longitudes is difficult to assess. Using LS35 for Mariner 9 navigation support did not indicate that an error as large as 16 meters

was present. In fact, until initial postflight analysis of the Mariner 9 data provided station longitudes, it was felt that LS35 may have been accurate to 3 or 4 meters, or that a proper decision was made in completely ignoring the Mariner 4 longitudes when LS35 was being compiled for use by Mariner 9.

The station longitudes initially determined from the Mariner 9 phase using data from 5 days before Mars orbital insertion up to the insertion itself were 5 to 6 meters west of the LS35 longitudes, or approximately 20 meters from the Mariner 4 results. Ionospheric refraction constants have not been applied in this reduction, but indications are that the 5- to 6-meter difference may be reduced in half.

Plotting the uncorrected Mariner 9 longitudes as a function of time together with the other Mariner solutions suggests a strong linear relationship, which may be merely coincidental. Because it probably is coincidental, in reality the longitudes may be much more widely scattered than was previously believed. In an attempt to solve this problem, the computations most likely to affect longitude and right ascension are being thoroughly checked (1973). The analysis of what the uncertainties are for individual longitude solutions is shown in figure 4.11. Specifically, the root sum square (rss) of all contributing errors varies from 3.1×10^{-5} deg for Mariner 4 longitudes to 4.6×10^{-5} deg for Mariner 6 longitudes and is not sufficient to include the 14-meter difference existing between longitudes derived from different missions.

There may be some random error present, for example, in UT1 or the planetary ephemeris, or there may be programing errors ranging from an outright mistake to simply a misunderstanding of how certain quantities are to be handled when items related to longitude and/or right ascension are being computed.

The comparison with the longitudes derived from tracking Earth satellites is shown in figure 4.12. Although the more recent solutions are not so disparate as they were in 1966, the difference has not gone below the 18-meter level. The matter of determining longitudes is difficult because one must rely on either planetary ephemerides or star catalogs to determine the position of the spacecraft or satellite.

The longitudes obtained from the Ranger missions in 1966 depended on the lunar ephemeris, whereas those in 1969 depended on the planetary ephemeris. Part of the

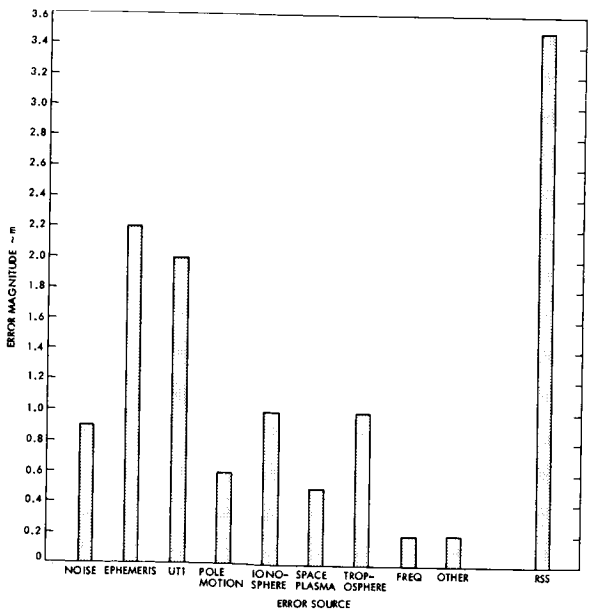

FIGURE 4.11.—Error budget: longitude.

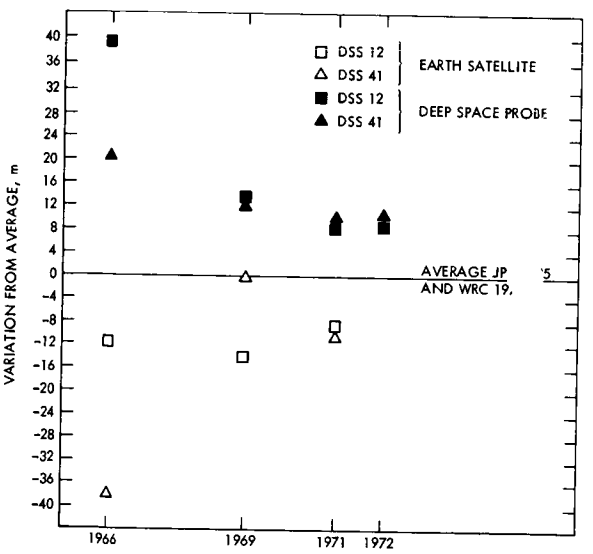

FIGURE 4.12.—Longitude history.

discrepancy between the solutions has been explained by Tom van Flandern of the U.S. Naval Observatory as an inconsistency in the definition of the origin of right ascension as given in the two ephemerides.

Similarly, changes in the source of UT1 have also affected the longitudes. SAO has consistently used UT1 from BIH, but it was not until 1971 that JPL switched from the U.S. Naval Observatory to BIH for this information. The removal of all inconsistencies between various reference frames is extremely difficult but, until it is done, exact agreement cannot be obtained. Ionospheric refraction effects may also have a strong influence on the longitudes; for the 900-MHz data of 1966, errors of 20 to 30 meters are believed to result. As was mentioned earlier, the 2200-MHz data used in 1969 and later are about one-sixth as sensitive. Actual ionospheric effects are illustrated in section 4.3.3.

4.3.2 Physical Principles

Why is it that one can accurately determine certain coordinates of a tracking station that has obtained Doppler data from a spacecraft and that this accuracy is almost independent of how distant the spacecraft is? The answer has more to do with the fact that the tracking station resides atop a spinning Earth than with any properties of the spacecraft trajectory. The role played by the spinning Earth can be visualized by referring to figure 4.13, remembering that the Doppler data are actually obtained by continuously counting cycles of the Doppler shift; i.e., they are a record of the change in range from the tracking stations to the spacecraft between times of taking data samples.

First, consider a plot of only that portion of the accumulated range change resulting from the rotation of the Earth for a distant spacecraft lying in the equatorial plane of the Earth. (The basis for this viewpoint was first discussed by Hamilton and Melbourne, 1966.) The example assumes a smooth, spherical Earth and ignores positional parallax due to the displacement of the tracking station during the tracking pass. The plot will start at zero and increase as a cosine curve of diurnal period, reaching a maximum at the time t_M that the spacecraft is on the observer's meridian. This accumulated range change will exactly equal r_s, the displacement

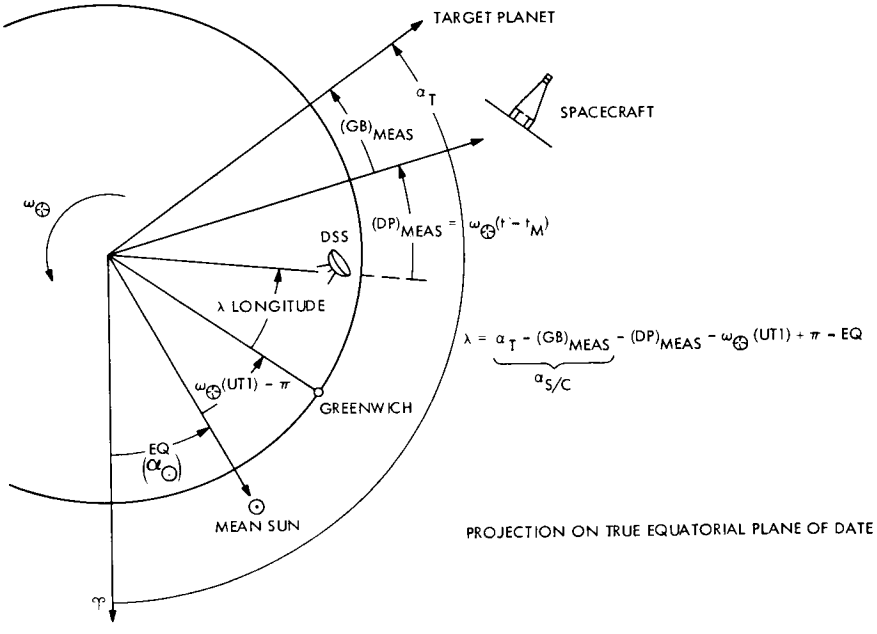

FIGURE 4.13.—DSS longitudes derived from tracking data correlated with other parameters.

of the tracking station from the spin axis (axis of rotation) of the Earth. After t_M, the accumulated range change following the cosine curve will decrease until it again reaches zero at the time the spacecraft disappears below the observer's horizon.

Note that, for the more general case shown in figure 4.14 in which the spacecraft is at some angle $\delta_{s/c}$ above the equatorial plane of the Earth, the amplitude of the accumulated range change is decreased by cos $\delta_{s/c}$. In fact, if the spacecraft were directly over the north pole ($\delta_{s/c}=90$ deg), there would be no change in the tracking-station/spacecraft range because of the rotation of the Earth. From the standpoint of station location determination, what is important is that the distance of the tracking station from the spin axis of the Earth can be determined from the amplitude. However, the accuracy of such a determination is limited, not only by the accuracy of the measurements, but also by uncertainties in the spacecraft position; i.e., r_s cos $\delta_{s/c}$ is the quantity actually determined, not r_s. Consequently, the better solutions for r_s are derived from tracking data when either the spacecraft declination is small ($\delta\sim 0$) and hence cos $\delta_{s/c}$ is relatively insensitive to errors in $\delta_{s/c}$, or when $\delta_{s/c}$ is well known.

The $\delta_{s/c}$ is well known when a spacecraft passes close by a target planet, such as Mars. In such a case the influence of the gravitational field of Mars on the spacecraft trajectory allows an accurate determination of the position of the spacecraft with respect to Mars, and the $\delta_{s/c}$ is inferred from the declination of Mars.

As with solutions for r_s, solutions for longitude λ can also be extracted from the cosine curve shown in figure 4.14. Only the information on λ comes from the phase of the curve instead of the amplitude. As the amplitude measurement is not a pure measure of r_s, neither is the phase measurement a pure measure of λ.

The change in tracking-station/spacecraft range ($\Delta\rho_{ER}$) caused by the rotation of the Earth can be written as

$$\Delta\rho_{ER}=r_s \cos \delta_{s/c} \sin\omega_\oplus (t-t_M) \qquad (4.3)$$

where

t_M time when the spacecraft is on the meridian plane of the tracking station

$\omega_\oplus (t-t_M)$ angle between the meridian planes of the spacecraft and the tracking station

$\omega_\oplus$ rotational rate of the Earth

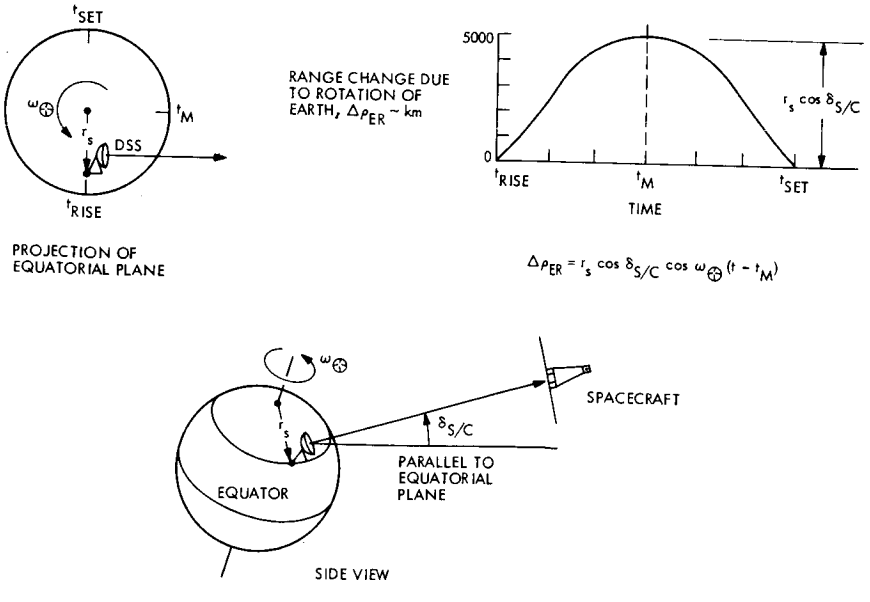

FIGURE 4.14.—Range change between spacecraft and DSS because of rotation of Earth.

Although the actual processing of the tracking data involves searching for the best values of a number of parameters to satisfy previously specified criteria (least-squares criterion nominally being employed), the part of the process related to the determination of station locations essentially finds an $r_s \cos \delta_{s/c}$ and t_M that best describe the $\Delta\rho_{ER}$ portion of the observations. Once the phase t_M of the diurnal $\Delta\rho_{ER}$ signature has been determined, the location of the meridian plane of the spacecraft is known as a function of time with respect to the meridian plane of the tracking station. In addition, the data reduction process determines the coordinates of the spacecraft; the spacecraft position with respect to the planet is well determined also, as mentioned previously, if the spacecraft trajectory has been significantly altered by the gravitational influence of the planet. These two measurements, labeled $(DP)_{meas}$ (DP for diurnal phase) and $(GB)_{meas}$ (GB for gravity bending), along with the other quantities involved in deriving the solutions for λ are shown in figure 4.13. From this figure it can be seen that

$$\lambda = \underbrace{\alpha_{TP} - (GB)_{meas}}_{\alpha_{s/c}} - \underbrace{(DP)_{meas} - \omega_\oplus \cdot \mathrm{UT1} + \pi - Eq}_{\omega_\oplus (t - t_M)} \tag{4.4}$$

where

α_{TP} is the right ascension of the planetary target and is computed from information contained in an ephemeris (JPL DE78 was used for the solutions in this chapter)

UT1 is used as a measure of the angular orientation of the Earth (Greenwich) with respect to the mean Sun; this angle is zero when it is noon at Greenwich; hence the angle of interest is $\omega_\oplus \mathrm{UT1} - \pi$

Eq indicates an equation relating the position of the mean Sun to Υ, the direction of the true vernal equinox of date used as the origin of the right ascension reference system of date

UT1 is supplied by BIH, the international timekeeping service headquartered in Paris. The equation designated Eq must match the equation used by BIH in deriving the UT1 data.

As can be seen from equation (4.4), the extraction of $(DP)_{meas}$ from the tracking data is not a determination of λ alone but of the combination

$$\alpha_{s/c} - \omega_\oplus \cdot \mathrm{UT1} - \lambda \tag{4.5}$$

where the right ascension of the spacecraft

$$\alpha_{s/c} = \alpha_{TP} - (GB)_{meas} \tag{4.6}$$

The fact that our solution for longitude depends on the ephemeris (as well as the UT1) used may account for the disappointing lack of agreement between longitudes found by JPL and those found by independent investigators, such as SAO (see sec. 4.3.1.1).

However, the differences in longitude, or relative longitudes, $\Delta\lambda_{ji}$ between two tracking stations are not functions of $\alpha_{s/c}$ or UT1 and do compare well with the values found by independent investigators, i.e.,

$$\Delta\lambda_{ij} = \lambda_i - \lambda_j = (DP)_{meas_i} - (DP)_{meas_j} \tag{4.7}$$

where i and j represent two tracking stations that alternately track the same spacecraft.

4.3.3 Tracking Data Used for Station Location

The data used in the latest analysis are essentially the same set of two-way Doppler data used for the solution set LS25 (Mottinger, 1969). Pertinent information for each set analyzed is presented in table 4.5, including the number of points in the current solution.

The summary of data used shows data for points above 15 deg elevation and data for which ionospheric refraction corrections are available. Tropospheric refraction corrections, as described subsequently, are based on empirical models and are believed to be accurate down to 5 deg elevation. However,

to be consistent with previous analysis, data were restricted to points above 15 deg elevation. Since the ionospheric refraction corrections currently must be derived from measurements taken at the antenna sites, only the Doppler data that were taken concurrently with these measurements can be used. Data not concurrent are omitted. The total amount of data that can be used varies from 70 to 99 percent of the total available.

The missions fall into two general categories. The first includes the encounter situation in which a set of data is taken bracketing the time of closest approach (encountering the target and extending for about 5 days before and after encounter). Mariner 4 and 5 are of this type; Mariner 6 is also, except that useful data stopped 45 minutes before encounter, when compressed gas was released to cool an onboard experiment. Hence only data taken during the approach to the planet are used; none taken after the time of closest approach are considered.

The second category covers the time when the probe is passing through the plane of the Earth's equator. At this time the estimates of station distance from the Earth's spin axis are insensitive to errors in the determination of the spacecraft declination. For Mariner 5 this situation occurred twice, once during the Earth-to-Venus cruise phase and again following the Venus encounter.

Other parameters in table 4.5 indicate the Sun-Earth-probe geometry over the range of data from which these values were reduced. Such information is useful in evaluating general ionospheric and space plasma influences on the Doppler shift as the signal propagates through space. Also included is the weight used in processing the data. This is expressed in hertz for the Doppler shift counted over 60 seconds. In actuality, the 1-minute count Doppler shift is further compressed to a 10-minute interval instead, and the weight is then divided by the square root of 10. It should be emphasized that, to account for unmodeled error sources, this weight is about an order of magnitude larger than the actual high-frequency noise in the data.

4.3.3.1 Corrections to Data: Platform (Earth) Parameters

The DSS locations are affected by much the same errors that affect navigation, namely the platform (Earth) parameters such as UT1 and polar motion, and the errors that affect the observables, such as the effects of the transmission media. (Parts of the following discussion are taken from Fliegel, 1971, pp. 10–13.)

The case of polar motion is shown in figure 4.15. As far as the tracking data are concerned, the pole of the Earth is on the spin axis. This means that if the crust of the Earth slips with respect to the spin axis, for the case illustrated, r_s shortens and the longitude between Greenwich and a DSS in the northern hemisphere increases. In the case of UT1, an error has no effect on r_s but affects the λ of all the DSS by the same (angular) amount; that is $\Delta\mathrm{UT1}=1$ msec will produce $\Delta\lambda=0.4$ meter at the modal latitude (35 deg) of DSS, as shown in figure 4.13, in which the tracking senses the angle $\omega_\oplus (t-t_0)$, where

$$\omega_\oplus(t-t_M) = (\alpha_{s/c}-\lambda-\omega_\oplus \mathrm{UT1}+\pi-\alpha_\odot) \tag{4.8}$$

Therefore, when λ is being determined, any errors in the other quantities on the right hand side of equation (4.2) will be reflected as errors in the solution of λ on a one-to-one (angular) basis.

Estimates of UT1 and polar motion are provided by BIH. These values are processed by a computer program described by Fliegel and Chao (Fliegel, 1971), and a set of polynomial coefficients are yielded that are then put into the SATODP and used in processing the radio-tracking data. In table 4.6 the relationship between International Atomic Time (IAT) and UT1 and also between IAT and Universal Time Coordinated (UTC) on the day of encounter is shown for the three missions used. UTC as defined in conjunction with all the time scales used in the orbit determination process (Moyer, 1971) is Greenwich Civil Time and is derived from

oscillations of a cesium atomic clock. Also shown in the table is the difference between UT1 and UTC both in milliseconds and in the equivalent number of meters. The pole positions, which relate the position of the Earth's spin axis with respect to the 1903.0 pole, are also listed for these same dates. When these corrections are used in the SATODP program, they result in the determination of station locations with respect to the 1903.0 pole, and thereby all solutions among the various missions can be made consistent.

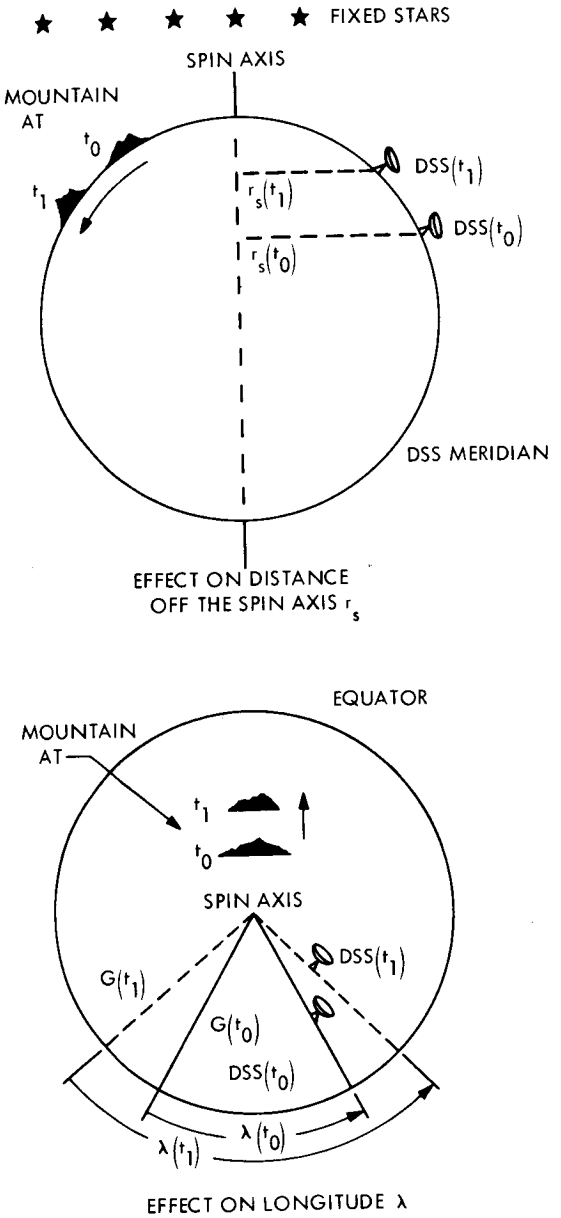

FIGURE 4.15.—Polar motion.

4.3.3.2 Correction for Effects of Transmission Media: Ionosphere

The ionosphere, which was ignored prior to preparations for the 1969 mission, is an example of an error source that can produce systematic errors in the DSS location solutions. The shift in r_s and λ, respectively, caused by applying the ionospheric corrections to the radio-tracking data is shown in figures 4.16 and 4.17. Note that, for the data spans considered, the shift in r_s is nearly always positive and averages 1.8 meters for the Goldstone complex. (Parts of the following discussion were taken from Mulhall, 1969, pp. 11–13.)

The errors in both r_s and λ caused by ignoring the ionosphere are significant. The effect of the ionospheric charged particles on the tracking is proportional to the number of charged particles in a column of unit area that contains the propagation path of the

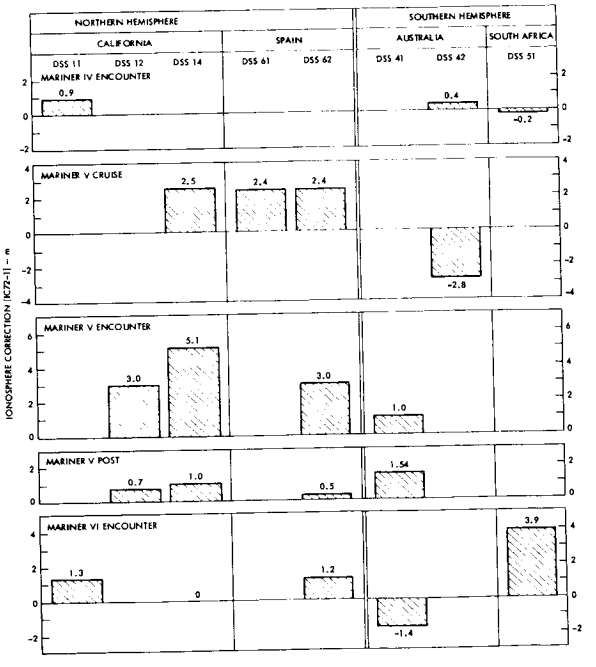

FIGURE 4.16.—Ionospheric refraction corrections to distances off spin axis.

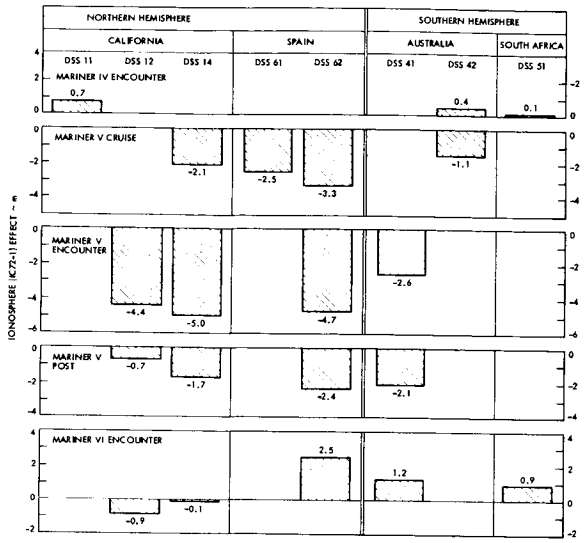

FIGURE 4.17.—Ionospheric refraction corrections to longitude.

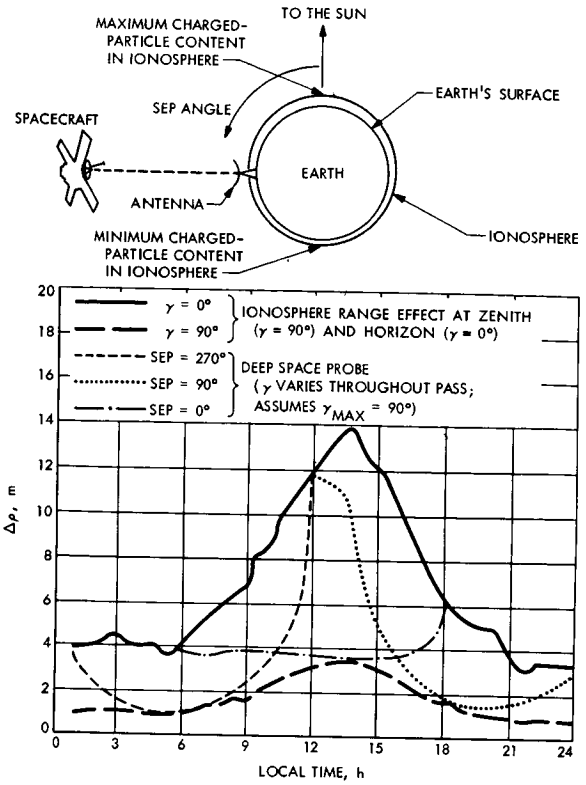

FIGURE 4.18.—Effect of ionosphere on radio tracking data.

radio signal between the DSS and the spacecraft. This columnar content is a function not only of the ray path, but also of the time of day, as illustrated in figure 4.18. The action of the ultraviolet rays of the sun on the ionosphere dissociates and ionizes the particles of the upper portion of the atmosphere. The maximum concentration of charged particles occurs near the subsolar point, whereas toward nightfall recombination dominates and a minimum number of charged particles exist on the night side of the earth. The dashed lines in figure 4.18 represent the error in counted cycles of Doppler shift ($\Delta\rho_I$) caused by the charged particles. The solid lines apply to a geostationary satellite at a constant elevation angle; the lower curve is for a spacecraft directly over the station ($\gamma=90$ deg) and the upper curve is for a spacecraft on the observer's horizon ($\gamma=0$ deg). In this case the error is generally a factor of 3 to 3.5 times greater than the error in the $\gamma=90$-deg case. The peaks of these curves usually occur between noon and 3 p.m. local time; that is, sometimes the rate of ionization exceeds the rate of the recombination even after high noon. However, the DSS locations are not derived from tracking geostationary spacecraft but from tracking planetary probes, in which case the Sun-Earth-probe angle (SEP) and not γ is relatively constant throughout the day. Dashed lines in figure 4.18 represent the history of $\Delta\rho_I$ for spacecraft at SEP=0, 90, and 270 deg. Each line starts as the spacecraft rises on the horizon ($\gamma=0$ deg), continues to the peak elevation angle, and then continues on until the spacecraft sets ($\gamma=0$ deg) (Ondrasik and Mulhall, 1969).

Errors in station locations will arise if the effect of the ionosphere, as illustrated in figure 4.18, is ignored. In particular, if the ionospheric refraction effect on $\Delta\rho_I$ is a curve shaped like a cosine wave centered at the midpoint of the pass, an error $\epsilon_{\dot{r}_s}$ in $\dot{r}_s$ equal to the amplitude of the cosine wave will result. (A similar relationship will exist between a sine-shaped $\Delta\rho_I$ and an error in λ.) This means that, for the three cases illustrated in figure 4.18, $\epsilon_{\dot{r}_s}$ will be positive for SEP=90 or 270 deg, depending on the actual

maximum elevation angle and the time of day at which the peak ionospheric activity occurs.

For past probes at planetary encounter, SEP $\approx$ 90 to 120 deg for Mars missions and SEP $\approx$ 45 deg for Venus missions. This means that ϵ_{r_s} will be larger for a Venus mission than for Mars missions. Exceptions can occur, however, because the charged particle content of the ionosphere does vary as a function of parameters not considered in the preceding discussion, such as a seasonal variation and changes in solar activity.

There still may be biases in the DSS solutions because of other error sources, such as the troposphere and the space plasma, although at present the extent of the effects of these sources has not been defined. In the case of the troposphere the current model is described later in this chapter.

The effect of charged particles in the space plasma may account for small systematic errors. Not only does the average number of charged particles in the column generally increase as the Earth-spacecraft distance increases, but, for the relatively small number of data sets included, the effects of the random fluctuations may not have been adequately averaged out. These random fluctuations result from concentrations of charged particles spewing out from the Sun, as was demonstrated by the model of charged particles in the space plasma described by Trask and Efron (1966). The model includes from three to five spiral arms that exist at any one time, each rotating with the solar equatorial period of about 28 days. Unfortunately, measurements of the effect of the space plasma during the periods of interest are rather sparse. The Mariner Venus-67 mission yielded the most information. It carried the Stanford dual-frequency experiment, which provided measurements of the columnar electron content in the space plasma during the time the spacecraft was in view of the Stanford, California, tracking station. The error caused by the space plasma during portions of this mission is discussed by Ondrasik *et al.* (1967). However, as described by Ondrasik *et al.*, the data were not obtained during all days of interest, and the fluctuations of the data obtained were of such a nature that it is difficult to predict what takes place between the setting of the spacecraft at the Goldstone tracking station and its rising the following day. An even lesser amount of data was available during the Mariner 2 (1962) and Mariner 4 (1964) missions, which did not measure the total electron content but only the charge density at the spacecraft. In the Mariner Mars 1969 spacecraft, no plasma experiments similar to those of previous missions were carried.

The ionospheric refraction correction reduces a 2-meter scatter about the mean of r_s from the Mariner 4 and 5 data to 1 meter about the mean and moves the mean about 2 meters. Previous analysis in 1969 revealed a larger net jump of the means and less of a reduction of the scatter than is currently observed. The Mariner 6 spin axis solutions are possibly displaced from the mean because of errors in the declination of Mars in the planetary ephemeris. These missions are especially sensitive to this kind of effect because of the large declination of -24 deg.

4.3.3.3 Corrections for Effects of Transmission Media: Troposphere

Corrections for the tropospheric effects on the Doppler shift in the spacecraft signal as it travels through the Earth's atmosphere are calculated by using a model described by Chao (1971). In this model, zenith range errors are computed for wet and dry components of the atmosphere by means of the following formulas that were determined from seasonally averaged data on surface weather:

$$\left.\begin{aligned} \Delta\rho_{z_{dry}} &= 2.276\, P_0 \\ \Delta\rho_{z_{wet}} &= 0.566\, \frac{(RH)}{\gamma}\left(1-\frac{c}{T_0}\right)^2 \\ &\quad \exp\left(\frac{AT_0-B}{T_0-C}\right) \end{aligned}\right\} \qquad (4.9)$$

where

$\Delta\rho_z$ zenith range correction in meters
P_0 surface pressure in bars

γ temperature lapse rate in °K/km
T_0 linearly extrapolated surface temperature in °K
$(RH)_0$ surface relative humidity, $0 \leq (RH)_0 \leq 1$
A 17.1486
B 4684.1331
C 38.45

where typically

$\Delta\rho_{dry}$ ($\gamma = 90$ deg) $\cong$ 2 meters
$\Delta\rho_{wet}$ ($\gamma = 90$ deg) $\cong$ 0.15 to 0.9 meter

To convert the zenith range error to the error in the line of sight to the spacecraft, tables have been constructed based on ray traces using typical refractivity versus height profiles. These are illustrated in figure 4.19, in which the total effect on range of the wet and dry components are shown as a function of elevation angle (Miller *et al.*, 1971).

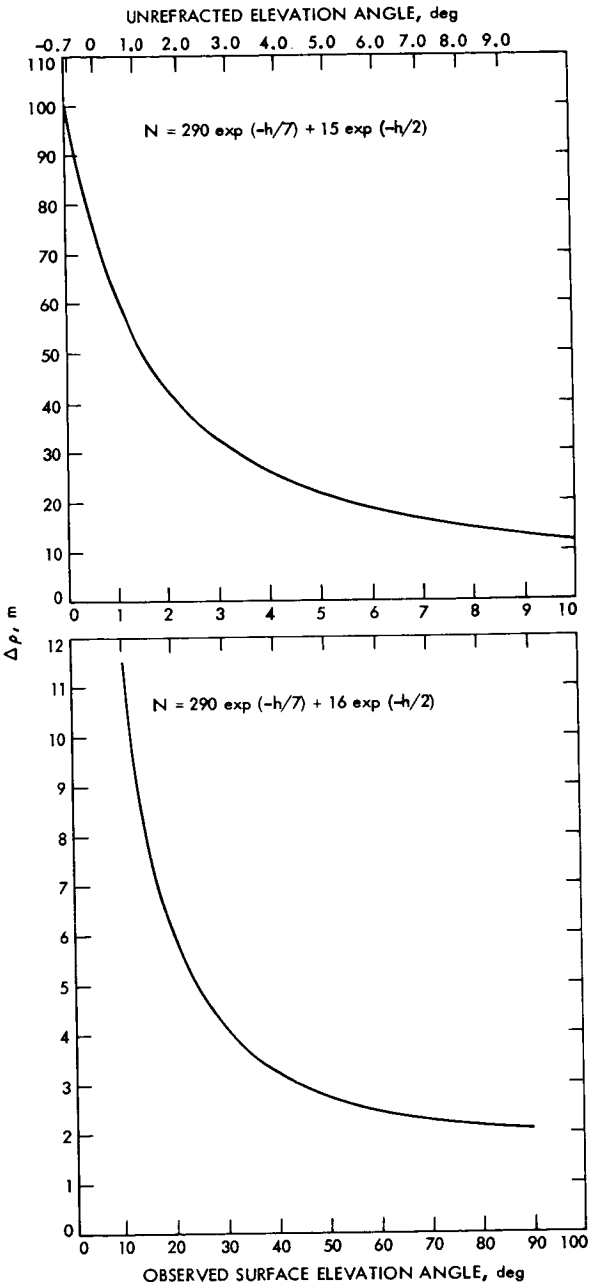

FIGURE 4.19.—Tropospheric effect on range.

4.4 THEORY [3]

The results given in sections 4.3 and 4.5 were derived for the most part by using a theory of spacecraft motion described in detail by Moyer (1971). This theory is incorporated in a program called the double-precision orbit-determination program (DPODP). The essential parts of the theory are considered to be (1) a description of the observables, (2) the corrections made to the observables, and (3) the differential equations of motion; of lesser importance are (4) the methods used for calculating the ephemerides of the bodies in the solar system and (5) the adjustment procedures. The ephemerides are calculated by numerical integration.

The equations of motion are Newton's equations plus relativistic perturbative accelerations derived from the one-body metric of the Brans-Dicke theory (Brans and Dicke, 1961). When the unknown parameter γ approaches unity, this metric reduces to the one-body isotropic metric of general relativity. JPL's ephemeris DE69 is the first to be based on isotropic relativistic coordinates. Previous ephemerides were based on the Schwarzschild coordinates of general relativity. This permanent change was made so that the precomputed n-body ephemerides would be compatible with the DPODP, which is based on isotropic coordinates.

[3] For additional theoretical discussions, see sections 4.3.2 and 4.5.2.

DE69 is based on a 60-year backward integration from the epoch of 2 August 1970, 0^hET to 1910. The observations consist of over 34 000 optical observations of the planets (except Pluto) and the Sun obtained from the 150- and 230-mm transit circles of the U. S. Naval Observatory from 1910 to 1968, radar range data for Mercury, Venus, and Mars from 1964 to 1968, and range observables for the Mariner 5 spacecraft near its encounter with Venus (data from 21 June to 12 November 1967). After being fitted to these data, the ephemerides were integrated forward from the 1970 epoch to 1976. DE69 consists of the latter portion of the 60-year integration from 28 October 1961 to the 1970 epoch and the forward integration from this epoch to 23 January 1976. The lunar ephemeris contained in DE69 is lunar ephemeris 16 (LE16); DE69 is described in O'Handley *et al.* (1969).

4.4.1 Observables

The theory used by JPL involves four kinds of observables: (1) frequency, (2) range, (3) angle, and (4) range difference. Since only frequencies (or, more correctly, count times) were used in deriving the results given in this chapter, only the theory involving these observables will be discussed in detail.

4.4.1.1 Light Time

In this section is given the formulation and procedure for solution of the light time problem, which is the first step in the computation of all observable quantities.

An electromagnetic signal is transmitted from a tracking station on Earth at time t_1. This signal is received by the spacecraft and retransmitted at time t_2. Alternatively, the signal may be transmitted directly by the spacecraft at time t_2. All observables are related to characteristics of this electromagnetic radiation, i.e., the angle of the incoming ray, the ratio of received to transmitted frequency, or the round trip transit time.

The transmitting station, the spacecraft, and the receiving station are referred to as direct participants, and t_1, t_2, and t_3, respectively, are their epochs of participation. The solution of the light time problem consists of these epochs of participation and the heliocentric position, velocity, acceleration, and jerk $\dddot{\mathbf{r}}$ of each direct participant evaluated at its epoch of participation. The rectangular components of these vectors are referred to the mean Earth equator and equinox of 1950.0.

Let the subscripts i or j equal 1, 2, or 3, where 1 refers to the transmitting station on Earth at the transmission time t_1, 2 refers to the spacecraft at the reflection time t_2, and 3 refers to the receiving station on Earth at the reception time t_3. The time for light to travel from point i at ephemeris time (coordinate time) t_i to point j at ephemeris time t_j is given by

$$t_j - t_i = \frac{r_{ij}}{c} + \frac{(1+\gamma)GM_\odot}{c^3} ln\left(\frac{r_i + r_j + r_{ij}}{r_i + r_j - r_{ij}}\right) \quad (4.10)$$

where

$$r_{ij} = ||\mathbf{r}_{ij}|| = ||\mathbf{r}_j^s(t_j) - \mathbf{r}_i^s(t_i)||$$
$$r_i = ||\mathbf{r}_i^s(t_i)||$$
$$r_j = ||\mathbf{r}_j^s(t_j)||$$

and

$\mathbf{r}_i^s(t_i), \mathbf{r}_j^s(t_j)$ heliocentric position vector of point i at transmission time t_i and point j at reception time t_j

c speed of light, km/s

$GM_\odot$ gravitational constant of the Sun, km^3/s^2

γ unknown free parameter of Brans-Dicke theory of relativity; the parameter γ is related to ω, the coupling constant of the scalar field, through $\gamma = (1+\omega)/(2+\omega)$

Solution of the light time equation (4.10) for a given leg of the light path gives the transmission time t_i for that leg. The time t_i is used to compute $\mathbf{r}_i^s(t_i)$ in the evaluation of the right-hand side of the light time equation and also appears explicitly in the left-hand side. The light time equation must be solved for t_i by an iterative technique. The

Newton-Raphson method is used in the DPODP (Moyer, 1971).

4.4.1.2 Frequency

Information about the velocity of a spacecraft is contained in the Doppler shift, not in the carrier frequency; it is the Doppler shift that is measured. The Doppler shift is therefore referred to as the Doppler observable. In this section is given the formulation for computation of Doppler observables, namely one-way, two-way, and three-way Doppler observables.

For one-way Doppler, an electromagnetic signal is transmitted continuously from the spacecraft and received at a tracking station on Earth. For two-way Doppler the signal is transmitted continuously from a tracking station on Earth, received and retransmitted by the spacecraft, and received continuously by the same tracking station. The signal may also be received by a different tracking station; in this case, the resulting observable is three-way Doppler. For each of these cases, the frequency of the received signal differs from that of the transmitted signal because of the Doppler shift. The observable is the average value of this frequency shift over a period of time called the count time, or count interval, T_c. It is proportional to the average range rate along the light path from the transmitter to the receiver during T_c or, more accurately, to the change in range along this light path during T_c. The count intervals for successive observables are contiguous.

The expression for computing each of these observables is obtained by expressing the frequency shift in a Taylor series, with coefficients evaluated at the midpoint of the count interval, and integrating term by term. The odd-order derivatives of the frequency shift vanish and the fourth- and higher-order even derivatives are ignored. Thus Doppler observables are computed from the frequency shift, and the second-order time derivative is evaluated along the light path whose reception time at the receiving station is the midpoint of the count interval.

For observables computed to an accuracy of 10^{-5} m/s, truncation of the Taylor series limits the count time to values as low as 1 to 10 sec when the spacecraft is very near the Earth or another planet. When the spacecraft is in heliocentric cruise, count times as large as 1000 sec may be used.

4.4.1.2.1 GENERAL EXPRESSIONS

An intermediate output from the electronic equipment at the receiving station on Earth is a signal whose frequency in cycles per second of station time (ST) is denoted by f. This signal contains the Doppler frequency shift (the transmitted frequency minus the received frequency, referred to as Doppler) and a bias frequency whose primary purpose is to keep f positive when the spacecraft range rate is negative. For one-way, two-way, and three-way Doppler, the expressions for f are

$$f_1 = C_1 - C_2 f_{S/C}\left(\frac{f_R}{f_T}\right) \tag{4.11}$$

$$f_2 = C_3\left[f_q(t_3) - f_q(t_1)\left(\frac{f_R}{f_T}\right)\right] + C_4 \tag{4.12}$$

$$f_3 = C_1 - C_5 f_q(t_1)\left(\frac{f_R}{f_T}\right) \tag{4.13}$$

where C_1 to C_5 are constants, defined subsequently. The spacecraft auxiliary transponder oscillator frequency, $f_{S/C}$, in cycles per UTC second (cycles of imaginary cesium atomic clock carried by the spacecraft), is determined by

$$f_{S/C} = f_{T_0} + \Delta f_{T_0} + f_{T_1}(t_2 - t_0) + f_{T_2}(t_2 - t_0)^2 \tag{4.14}$$

where

f_{T_0}	nominal value of $f_{S/C}$
$\Delta f_{T_0}, f_{T_1}, f_{T_2}$	unknowns
t_0	UTC epoch at start of time block
t_2	UTC value of spacecraft transmission time

In equations (4.11) through (4.13), f_R/f_T is the ratio of received to transmitted fre-

quency (for unity frequency multiplication at spacecraft). The received frequency f_R is measured in cycles per second of station time (ST) derived from the atomic frequency standard at the receiving station. For two-way or three-way Doppler the transmitted frequency f_T is measured in cycles per second of ST derived from the atomic frequency standard at the transmitting station. For one-way Doppler, f_T is measured in cycles per UTC second of an imaginary cesium atomic clock at the spacecraft.

The reference oscillator frequencies at the transmitting station are $f_q(t_1)$, $f_q(t_3)$, in cycles per second of ST (derived from the transmitted atomic frequency standard), evaluated at transmission time t_1 and reception time t_3, respectively. The frequency f_q is reset periodically but remains constant between settings. The Doppler formulation presumes that $f_q(t_3)$ is constant over the reception interval T_c for two-way Doppler and that $f_q(t_1)$ is constant over the transmission interval. If these intervals overlap for two-way Doppler, $f_q(t_1)$ must equal $f_q(t_3)$.

The Doppler tracking equipment originally operated in the L-band frequency range (390 to 1550 MHz). Later the system was changed to operate in the S-band range (1550 to 5200 MHz). In the interim period, some tracking data were obtained in the so-called L–S configuration (modified L-band tracking stations with an S-band transponder on the spacecraft). The only change in the Doppler formulation resulting from changing the frequency band is the change in the values of the coefficients C_1 through C_5, as shown in table 4.7. In that table, $K \equiv 10^6$ and $K_1(t_3)$ $[K_s(t_3)] \equiv$ the receiver's reference oscillator frequency at reception time (t_3) for L–S band (S-band) Doppler.

For two-way Doppler the reference frequency and received frequency are derived from the same atomic frequency standard. Hence two-way Doppler gives the most accurate measure of the Doppler frequency shift and the range rate from the tracking station to the spacecraft.

For one-way and three-way Doppler the reference signal and received signal are derived from different atomic frequency standards. Therefore these data types are less accurate than two-way Doppler. Furthermore, for one-way Doppler the signal transmitted from the spacecraft is currently derived from a crystal oscillator. Because of the large drift in frequency of this type of oscillator, one-way Doppler is very inaccurate and is rarely used in the determination of accurate spacecraft trajectories.

Define

$$f_{1_{bias}} = C_1 - C_2 f_{T_0} \tag{4.15}$$

$$f_{2_{bias}} = C_3[f_q(t_3) - f_q(t_1)] + C_4 \tag{4.16}$$

$$f_{3_{bias}} = C_1 - C_5 f_q(t_1) \tag{4.17}$$

Hence

$$f_1 - f_{1_{bias}} = C_2 f_{S/C}\left(1 - \frac{f_R}{f_T}\right) - C_2[\Delta f_{T_0} + f_{T_1}(t_2 - t_0) + f_{T_2}(t_2 - t_0)^2] \tag{4.18}$$

$$f_2 - f_{2_{bias}} = C_3 f_{q(t_1)}\left(1 - \frac{f_R}{f_T}\right) \tag{4.19}$$

$$f_3 - f_{3_{bias}} = C_5 f_q(t_1)\left(1 - \frac{f_R}{f_T}\right) \tag{4.20}$$

The signal with frequency f is input to an electronic counter whose register is incremented by one each time the magnitude of the signal changes from minus to plus. A total of N cycles are counted during the count time T_c. The Doppler observable F is

$$F = \frac{N}{T_c} - f_{bias} \tag{4.21}$$

where f_{bias} is computed from equation (4.15), (4.16), or (4.17). Since N is the integral of f over the count time T_c,

$$F = \frac{1}{T_c}\int_{t_{3_m}(ST)-(1/2)T_c}^{t_{3_m}(ST)+(1/2)T_c} (f - f_{bias})\, dt_3(ST) \tag{4.22}$$

where $t_3(ST)$ is the station time (ST) at the receiving station, derived from the station atomic frequency standard, and $t_{3_m}(ST)$ is

the epoch at the midpoint of the count interval T_c.

The transformation from UTC to ST at each tracking station is specified by

$$\text{UTC}-ST=a+bt+ct^2 \qquad (4.23)$$

where a, b, and c are specified by time block and t is in seconds past the start of the time block. Let the coefficients of equation (4.23) that apply for the receiving station at t_3 and for the transmitting station at t_1 be denoted by subscripts R and T, respectively. Also, define F by

$$1+F=\frac{(dST/d\text{UTC})_1}{(dST/d\text{UTC})_3} \qquad (4.24)$$

Then, since $dST/d\text{UTC}$ is extremely close to unity,

$$F \approx b_R(t_3)-b_T(t_1)+2t_3c_R(t_3)-2t_1c_T(t_1) \qquad (4.25)$$

where the transmission and reception times t_1 and t_3 are expressed as seconds past the start of the time blocks for a, b, and c used at t_1 and t_3, respectively. Also, define F_R/F_T by

$$\frac{F_R}{F_T}=\frac{\left(\frac{d\tau}{dt}\right)_1}{\left(\frac{d\tau}{dt}\right)_3}\frac{dt_1}{dt_2}\frac{dt_2}{dt_3} \qquad (4.26)$$

Define

$$\left(1-\frac{F_R}{F_T}\right)^*=\left(1-\frac{F_R}{F_T}\right)+\frac{T_c^2}{24}\left(1-\frac{F_R}{F_T}\right)^{\cdot\cdot} \qquad (4.27)$$

where T_c is the count interval. Define F_R/F_T for one-way Doppler by

$$\frac{F_R}{F_T}=\frac{\left(\frac{d\tau}{dt}\right)_2}{\left(\frac{d\tau}{dt}\right)_3}\frac{dt_2}{dt_3} \qquad (4.28)$$

The expressions for $F1$, $F2$, and $F3$ are

$$F1=C_2f_{S/C}\left[\left(1-\frac{F_R}{F_T}\right)^*+\Delta\right] -C_2[\Delta f_{T_0}+f_{T_1}(t_2-t_0)+f_{T_2}(t_2-t_0)^2] \qquad (4.29)$$

$$F2=C_3f_q(t_1) \times\left\{\left(1-\frac{F_R}{F_T}\right)^*-F\left[1-\left(1-\frac{F_R}{F_T}\right)^*\right]+\Delta\right\} \qquad (4.30)$$

$$F3=C_5f_q(t_1) \times\left\{\left(1-\frac{F_R}{F_T}\right)^*-F\left[1-\left(1-\frac{F_R}{F_T}\right)^*\right]+\Delta\right\} \qquad (4.31)$$

where $[1-(F_R/F_T)]^*$ is given by equation (4.27) in terms of $[1-(F_R/F_T)]$ and its second derivative with respect to $t_3(ST)$, $[1-(F_R/F_T)]^{\cdot\cdot}$, evaluated along the light path whose reception time at the receiving station, $t_3(ST)$, is the midpoint $t_{3_m}(ST)$ of the count interval T_c. Expressions for these quantities are derived from equation (4.26) for F_R/F_T for two-way and three-way Doppler and equation (4.28) for one-way Doppler.

Each of these expressions contains an additive correction, Δ, that accounts for the effects of the troposphere, the ionosphere, and the motion of the tracking point on the transmitting and receiving antennas during T_c. The computation of Δ is described in section 4.4.2.

4.4.1.2.2 DOPPLER FREQUENCY SHIFT

The expression for $[1-(F_R/F_T)]$ used to compute two-way and three-way Doppler and also the expression used to compute one-way Doppler are derived in this section. The definitions of F_R/F_T are equation (4.26) for two-way and three-way Doppler and equation (4.28) for one-way Doppler, evaluated along the light path whose reception time at the receiving station, $t_3(ST)$, is the midpoint of the count interval T_c. The expressions for $[1-(F_R/F_T)]$ are obtained as expansions in powers of $1/c$. To obtain the desired accuracy of 10^{-5} m/s for computed Doppler, all terms to order $1/c^3$ are retained.

The terms dt_1/dt_2 and dt_2/dt_3 are obtained by differentiation of the light time equations for the up and down legs of the light path. The light time equation for a given leg of the light path is equation (4.10). For the up and down legs it is given by

$$t_2-t_1=\frac{r_{12}}{c}+\frac{(1+\gamma)GM_\odot}{c^3}\,ln\left(\frac{r_1+r_2+r_{12}}{r_1+r_2-r_{12}}\right) \tag{4.32}$$

$$t_3-t_2=\frac{r_{23}}{c}+\frac{(1+\gamma)GM_\odot}{c^3}\,ln\left(\frac{r_2+r_3+r_{23}}{r_2+r_3-r_{23}}\right) \tag{4.33}$$

Solution of these equations gives the following quantities:

(1) t_1, t_2, t_3 are the ephemeris time (ET) values of transmission time at tracking station on Earth, reflection time at spacecraft (or transmission time for one-way Doppler), and reception time at tracking station on Earth, respectively. The station time (ST) value of t_3 is the midpoint of the count interval T_c.

(2) $\mathbf{r}_1$, $\mathbf{r}_2$, $\mathbf{r}_3$ are the heliocentric position vectors of transmitting station on Earth at t_1, spacecraft at t_2, and receiving station on Earth at t_3, respectively, with rectangular components referred to the mean Earth equator and equinox of 1950.0.

(3) $\dot{\mathbf{r}}_i$, $\ddot{\mathbf{r}}_i$, $\dddot{\mathbf{r}}_i$ are the heliocentric velocity acceleration and jerk vectors of participant i at its epoch of participation t_i ($i=1$, 2, or 3). The dots indicate differentiation of $\mathbf{r}_i$ with respect to ephemeris time.

The quantities on the right-hand sides of equation (4.32) and (4.33) are

$$r_{12}=[(\mathbf{r}_2-\mathbf{r}_1)\cdot(\mathbf{r}_2-\mathbf{r}_1)]^{1/2} \tag{4.34}$$

$$r_{23}=[(\mathbf{r}_3-\mathbf{r}_2)\cdot(\mathbf{r}_3-\mathbf{r}_2)]^{1/2} \tag{4.35}$$

$$r_1=(\mathbf{r}_1\cdot\mathbf{r}_1)^{1/2} \tag{4.36}$$

$$r_2=(\mathbf{r}_2\cdot\mathbf{r}_2)^{1/2} \tag{4.37}$$

$$r_3=(\mathbf{r}_3\cdot\mathbf{r}_3)^{1/2} \tag{4.38}$$

Differentiation of equations (4.32) and (4.33) gives

$$\frac{dt_1}{dt_2}=\frac{1-\frac{1}{c}\frac{\mathbf{r}_{12}}{r_{12}}\cdot\dot{\mathbf{r}}_2+\frac{(1+\gamma)GM_\odot}{c^3}\epsilon_{12}}{1-\frac{1}{c}\frac{\mathbf{r}_{12}}{r_{12}}\dot{\mathbf{r}}_1} \tag{4.39}$$

and an identical equation with the substitutions 1 goes to 2, and 2 goes to 3, where

$$\begin{aligned}
\mathbf{r}_{ij}&=\mathbf{r}_j-\mathbf{r}_i\\
\dot{\mathbf{r}}_{ij}&=\dot{\mathbf{r}}_j-\dot{\mathbf{r}}_i\\
\epsilon_{12}&=\frac{\dot{r}_1+\dot{r}_2-\dot{r}_{12}}{r_1+r_2-r_{12}}-\frac{\dot{r}_1+\dot{r}_2+\dot{r}_{12}}{r_1+r_2-r_{12}}\qquad 1\to 2,\ 2\to 3\\
\dot{r}_{12}&=\frac{\mathbf{r}_{12}}{r_{12}}\cdot\dot{\mathbf{r}}_{12}\\
\dot{r}_{23}&=\frac{\mathbf{r}_{23}}{r_{23}}\cdot\dot{\mathbf{r}}_{23}\\
\dot{r}_1&=\frac{\mathbf{r}_1}{r_1}\cdot\dot{\mathbf{r}}_1\\
\dot{r}_2&=\frac{\mathbf{r}_2}{r_2}\cdot\dot{\mathbf{r}}_2\\
\dot{r}_3&=\frac{\mathbf{r}_3}{r_3}\cdot\dot{\mathbf{r}}_3
\end{aligned} \tag{4.40}$$

The first term of equation (4.40) approaches $0\div 0$ as the distance from the light path to the center of the Sun approaches 0. However, because of the finite radius of the Sun (700 000 km), the limiting indeterminacy will not occur.

The quantities $(d\tau/dt)_1$, $(d\tau/dt)_2$, and $(d\tau/dt)_3$ are given by

$$\left(\frac{d\tau}{dt}\right)_i=\left[1-\frac{2\phi_i}{c^2}-\left(\frac{\dot{s}_i}{c}\right)^2\right]^{1/2}\qquad i=1,\ 2,\ \text{or}\ 3 \tag{4.41}$$

where ϕ_i is the Newtonian potential at participant i at its epoch of participation t_i, and $\dot{s}_i$ is the heliocentric velocity of participant i at its epoch of participation t_i.

The potential ϕ_i is given by

$$\phi_i=\sum_j\frac{\mu_j}{r_{ij}} \tag{4.42}$$

where the summation over j includes the Sun, all of the planets, and the Moon, and r_{ij} is the coordinate distance from the participant i to the center of the body j. The velocity $\dot{s}_i$ is obtained from

$$\dot{s}_i^2=\dot{\mathbf{r}}_i\cdot\dot{\mathbf{r}}_i \tag{4.43}$$

Substituting equations (4.39) and (4.41) into equation (4.26) and retaining all terms

to order $1/c^3$ give the desired expression for $[1-(F_R/F_T)]$ for two-way or three-way Doppler:

$$\left(1-\frac{F_R}{F_T}\right)=\frac{1}{c}(\dot{r}_{12}+\dot{r}_{23})+\frac{1}{c^2}\left[\dot{r}_{12}\dot{p}_{12}+\dot{r}_{23}\dot{p}_{23}-\dot{r}_{12}\dot{r}_{23}+(\phi_1-\phi_3)+\frac{1}{2}(\dot{s}_1^2-\dot{s}_3^2)\right]$$
$$+\frac{1}{c^3}\left\{\dot{r}_{12}\dot{p}_{12}^2+\dot{r}_{23}\dot{p}_{23}^2-\dot{r}_{12}\dot{r}_{23}(\dot{p}_{12}+\dot{p}_{23})-(\dot{r}_{12}+\dot{r}_{23})\left[(\phi_1-\phi_3)+\frac{1}{2}(\dot{s}_1^2-\dot{s}_3^2)\right]\right.$$
$$\left.-(1+\gamma)GM_\odot(\epsilon_{12}+\epsilon_{23})\right\} \qquad (4.44)$$

where

$$\dot{p}_{12}=\frac{\mathbf{r}_{12}}{r_{12}}\cdot\dot{\mathbf{r}}_1 \qquad \dot{p}_{23}=\frac{\mathbf{r}_{23}}{r_{23}}\cdot\dot{\mathbf{r}}_2$$

The expression for $[1-(F_R/F_T)]$ for one-way Doppler is

$$\left(1-\frac{F_R}{F_T}\right)=\frac{1}{c}(\dot{r}_{23})+\frac{1}{c^2}\left[\dot{r}_{23}\dot{p}_{23}+(\phi_2-\phi_3)+\frac{1}{2}(\dot{s}_2^2-\dot{s}_3^2)\right]$$
$$+\frac{1}{c^3}\left\{\dot{r}_{23}\dot{p}_{23}^2-\dot{r}_{23}\left[(\phi_2-\phi_3)+\frac{1}{2}(\dot{s}_2^2-\dot{s}_3^2)\right]-(1+\gamma)GM_\odot\epsilon_{23}\right\} \qquad (4.45)$$

4.4.1.2.3 SECOND DERIVATIVE OF DOPPLER FREQUENCY SHIFT

The computation of Doppler observables requires an expression for $[1-(F_R/F_T)]\cdot\cdot$. This term is the second derivative of $[1-(F_R/F_T)]$ with respect to the reception time t_3 (ST), evaluated along the light path whose reception time is the midpoint of the count interval T_c. The expression for $[1-(F_R/F_T)]\cdot\cdot$ for two-way and three-way Doppler and also the expression for one-way Doppler are obtained by differentiation of the corresponding expressions for $[1-(F_R/F_T)]$.

4.4.2 Antenna, Tropospheric, and Ionospheric Corrections to Observables

In section 4.4.2.1 the correction terms are defined for the Doppler observables that account for the effects of the offset of the tracking point on the moving antenna from the Earth-fixed station location, the troposphere, and the ionosphere. The evaluation of these corrections is described in section 4.4.2.2. Expressions are given for the antenna corrections. The general procedure for obtaining the tropospheric and ionospheric corrections is summarized in section 4.3.3. Details are given in Mulhall *et al.* (1970).

4.4.2.1 Definitions of Correction Terms

Equations (4.29), (4.30), and (4.31) for one-way, two-way, and three-way Doppler observables contain a term Δ that accounts for the effects of antenna offsets, the troposphere, and the ionosphere. The expression for Δ is obtained by comparing these equations to the equivalent differenced range Doppler formulation that contains correction terms for these effects.

Differenced range Doppler is computed from the difference of two range observables whose reception times are the end and start of the count interval T_c. Each of these range observables represents the time for the crest of a wave to travel from the transmitter to the receiver. In the presence of charged particles, the propagation speed for the crest of a wave is the phase velocity, which is greater than c.

The range corrections $\Delta_{A\rho}$, $\Delta_{T\rho}$, and $\Delta_{I\rho}$ in meters divided by 10^3c represent the time

delay in seconds caused by the antenna offset, the troposphere, and the ionosphere, respectively. For two-way and three-way range used to compute two-way and three-way differenced range Doppler, respectively, each of these corrections has a value $\Delta_{i\rho}(t_3)$ for the down leg of the light path and a value $\Delta_{i\rho}(t_1)$ for the up leg. For one-way range used to compute one-way differenced range Doppler, there are no up-leg corrections.

Comparing the correction terms of the differenced range Doppler formulation to the correction term Δ of the Taylor series Doppler formulation (eq. (4.29) through (4.31)) gives, for two-way or three-way Doppler,

$$\Delta = \frac{1}{10^3 c T_c} \times [\Delta\rho(t_{3_c}) + \Delta\rho(t_{1_c}) - \Delta\rho(t_{3_s}) - \Delta\rho(t_{1_s})] \quad (4.46)$$

where

- T_c count interval, s
- t_{3_c} epoch at end of reception interval T_c
- t_{3_s} epoch at start of reception interval T_c
- t_{1_c} epoch at end of transmission interval T_c'
- t_{1_s} epoch at start of transmission interval T_c'
- $\Delta\rho(t)$ sum of range corrections in meters because of the antenna offset, the troposphere, and the ionosphere for up leg with transmission time t or for down leg with reception time t

That is,

$$\Delta\rho(t) = \Delta_A\rho(t) + \Delta_T\rho(t) + \Delta_I\rho(t) \quad (4.47)$$

The antenna and troposphere corrections are the same as those used for a range observable; the ionosphere correction has the same magnitude but the opposite sign (negative in eq. (4.46) and (4.47)) as that used for a range observable. For one-way Doppler the light path consists of a down leg only, and

$$\Delta = \frac{1}{10^3 c T_c}[\Delta\rho(t_{3_c}) - \Delta\rho(t_{3_s})] \quad (4.48)$$

Given the midpoint t_{3_m} of the reception interval T_c in any time scale, the epochs t_{3_c} and t_{3_s} in the same time scale are given to sufficient accuracy by

$$t_{3_c} = t_{3_m} + \frac{1}{2}T_c \quad (4.49)$$

$$t_{3_s} = t_{3_m} - \frac{1}{2}T_c \quad (4.50)$$

where T_c is given in seconds of station time (ST). The light time solution for the Doppler observable has a reception time t_{3_m} and a transmission time t_{1_m}, which is the midpoint of the transmission interval T_c. Given t_{1_m} in any time scale, t_{1_c} and t_{1_s} in the same time scale are given approximately by

$$t_{1_c} \approx t_{1_m} + \frac{1}{2}T_c \quad (4.51)$$

$$t_{1_s} \approx t_{1_m} + \frac{1}{2}T_c \quad (4.52)$$

4.4.2.2 Evaluation of One-Leg Range Corrections

This section gives the formulation for computation of corrections to the one-way range from the tracking station to the spacecraft resulting from (1) the offset of the tracking point on the antenna from the station location $\Delta_A\rho$; (2) the troposphere $\Delta_T\rho$; and (3) the ionosphere $\Delta_I\rho$.

4.4.2.2.1 ANTENNA CORRECTION

The antennas at the tracking stations of the DSN, Manned Space-Flight Network (MSFN), and Air Force Eastern Test Range (AFETR) have four different types of mounts: (1) hour angle and declination (*HA–dec*), (2) azimuth and elevation (A_z–E_l), (3) X and Y angles (MSFN), and (4) X' and Y' angles (MSFN). For the 26-meter (85-ft) *HA–dec*, A_z–E_l, and X'–Y' antennas the two mutually perpendicular axes do not intersect. The offset between the two axes

(the perpendicular distance between them) is denoted by b and ranges from about 1 to 7 meters. The axis that has a fixed position relative to the Earth will be denoted as the primary axis (the HA, A_z or X' axis). Owing to the offset b between the two axes, rotation of the antenna about the primary axis causes the secondary axis to move relative to the Earth.

The two mutually perpendicular axes of an HA–dec, A_z–E_l, or X'–Y' antenna are shown in figure 4.20. The primary axis (HA, A_z, or X') is in the plane of the paper, and the secondary axis (dec, E_l, or Y') is normal to it. The offset between the two axes is b. The positions of the station location and spacecraft are indicated. The second angle (dec, E_l, or Y') is indicated by θ.

Each range tracking system is calibrated so that the tracking point lies on the secondary (moving) axis. That is, the calibrated range observable obtained from the tracking station corresponds to a one-way range $\hat{\rho}$ measured from the secondary axis to the spacecraft. However, the computed range observable is based on the one-way range $\hat{\rho}$ measured from a specific point on the antenna which is fixed relative to the Earth. This point is called the station location.

Its geocentric position is represented by spherical or cylindrical coordinates, which are solve-for parameters. For all antennas the station location is the intersection of the primary axis with the plane perpendicular to it, which contains the secondary axis.

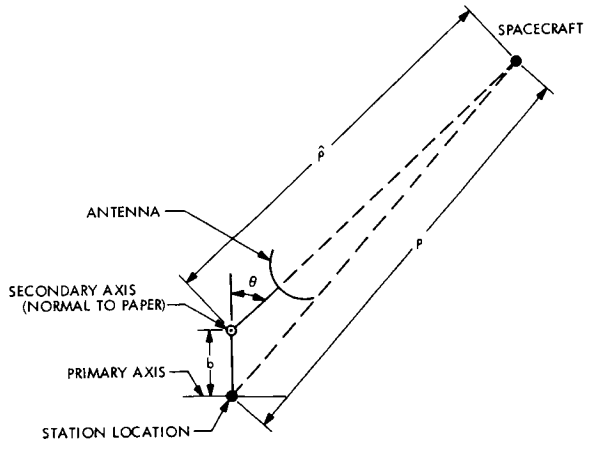

FIGURE 4.20.—Antenna correction.

The computed range for the up or down leg of the light path is r_{12} or r_{23} (denoted as ρ in fig. 4.20) plus $\Delta_A\rho$ for that leg. The sum $\rho+\Delta_A\rho$ must equal $\hat{\rho}$. Hence, the antenna correction $\Delta_A\rho$ is given by

$$\Delta_A\rho=\hat{\rho}-\rho \tag{4.53}$$

The maximum displacement of the secondary axis from the tracking station to the spacecraft line is less than 10 m. The maximum effect of this transverse displacement on $\hat{\rho}-\rho$ is about 0.5×10^{-3} m (for a spacecraft range of 10^5 m), which is insignificant. Thus the significant part of $\hat{\rho}-\rho$ is caused by the component of b along the direction to the spacecraft. Since $b<10$ m and $\rho>10^5$ m,

$$\hat{\rho}\approx\rho-b\cos\theta \tag{4.54}$$

to an accuracy of better than 10^{-3} m and

$$\Delta_A\rho=-b\cos\theta \tag{4.55}$$

From equation (4.46) the Doppler observable formulation includes antenna corrections for the up and down legs of the light paths which have reception times equal to the end and start of the reception interval T_c. The tracking point for Doppler observables is located along the spacecraft-to-secondary axis line at a constant distance r_c from this axis. Hence each of the four antenna corrections is given by equation (4.55) plus the constant r_c. However, since the round trip range correction at the beginning of the count interval T_c is subtracted from the corresponding correction at the end of T_c, the effect of r_c on Δ and hence on Doppler observables is zero. Therefore, equation (4.55) applies also for Doppler observables.

For the 26-m HA–dec antennas of the DSN,

$$\Delta_A\rho=-b\cos\delta \tag{4.56}$$

where δ is the observed declination of the spacecraft and $b=6.706$ m. These antennas

are located at DSN/DSS 11, 12, 41, 42, 51, 61, and 62.

For the 26-m A_z–E_l antenna at DSS 13,

$$\Delta_A\rho = -b \cos \gamma \qquad (4.57)$$

where γ is the observed elevation of the spacecraft and $b = 0.9144$ m.

For the 26-m X'–Y' antennas of the MSFN,

$$\Delta_A\rho = -b \cos Y' \qquad (4.58)$$

where Y' is the observed angle Y' to the spacecraft and $b = 1.2192$ m. These antennas are located at station MAD at Madrid, Spain; DRA at Canberra, Australia; and GDS at Goldstone, California.

The axis offset b is zero for the 64-m (210-ft) A_z–E_l antenna at DSS 14, the 9-m (30-ft) X–Y antennas of the MSFN, and all antennas of the AFETR (stations 73 to 77, 79 to 84, and 87). Therefore there are no antenna corrections for these stations.

4.4.2.2.2 TROPOSPHERE AND IONOSPHERE CORRECTIONS

These corrections are discussed in section 4.3.3.

4.4.3 Equations of Motion

The differential equations of motion are

$$\frac{d^2\mathbf{r}}{dt^2} = \sum_{j=1}^{J} \frac{\mathbf{F}_j}{m} \qquad (4.59)$$

where $\mathbf{r}$ is the location of the satellite and the $\mathbf{F}_j$ are forces acting on the satellite. The following accelerations ($\mathbf{F}_j/m$) are accounted for by JPL: (1) the Newtonian point-mass acceleration relative to the center of integration (the point selected as origin); (2) the perturbative acceleration from general relativity; (3) the direct acceleration of the spacecraft because of the oblateness of a nearby planet or the Moon; (4) the indirect acceleration of the center of integration (if it is the Earth or the Moon) because of the oblateness of the Earth and the Moon; (5) the acceleration resulting from solar radiation pressure; (6) the acceleration caused by small forces originating in the spacecraft, such as those from operation of the attitude control system and from gas leaks; and (7) the acceleration from motor operation. The formulation for computation of the first six of these terms of spacecraft acceleration is contained in this section.

The total acceleration is integrated numerically to give the spacecraft ephemeris, with ephemeris time (ET) as the independent variable. The acceleration is computed at each integration step and is used to produce three sum-and-difference arrays, one for each rectangular component of position. Each sum-and-difference array contains two sums and ten differences of an acceleration component. The arrays may be interpolated at any ET epoch to give the rectangular components of position, velocity, acceleration, and jerk ($\dddot{\mathbf{r}}$) of the spacecraft relative to the current center of integration. The rectangular components are referred to the mean Earth equator and equinox of 1950.0. The x axis is directed along the mean equinox of 1950.0, the z axis is normal to the mean Earth equator of 1950.0, directed north, and the y axis completes the right-handed system.

The center of integration is located at the center of mass of the Sun, the Moon, or one of the nine planets. It may be specified as one of these bodies, or it may be allowed to change as the spacecraft passes through the sphere of influence of a planet (relative to the Sun) or of the Moon (relative to the Earth). For this case the center of integration will be that body within whose sphere of influence the spacecraft lies. At a change in center of integration the position and velocity of the spacecraft relative to the old center of integration are incremented by the position and velocity, respectively, of the old center relative to the new center.

The 1950.0 rectangular components of the spacecraft position and velocity vectors at the injection epoch are solve-for parameters (unknowns) and may be referred to any body (not necessarily the center of integration).

The injection epoch must be specified in the A1 (atomic time), UTC, or ST time scales and transformed to ET. The injection position and velocity vectors are transformed to values relative to the initial center of integration and are used to start the sum-and-difference arrays.

The equations for computing each term of the total spacecraft acceleration relative to the center of integration are given in the following paragraphs.

4.4.3.1 Gravitational Acceleration of a Point Mass

The point mass gravitational acceleration of the spacecraft S/C relative to the center of integration C includes all gravitational acceleration except those arising from the oblateness of the various bodies. The point mass acceleration is given by

$$\ddot{\mathbf{r}} = \ddot{\mathbf{r}}_{S/C} - \ddot{\mathbf{r}}_C \tag{4.60}$$

where $\ddot{\mathbf{r}}_{S/C}$, $\ddot{\mathbf{r}}_C$ are the inertial gravitational acceleration of the spacecraft and the center of integration, respectively, computed by treating each body of the solar system as a point mass. These inertial accelerations are relative to the barycenter of the solar system and have rectangular components referred to the mean Earth equator and equinox of 1950.0.

Each of these accelerations is computed from

$$\ddot{\mathbf{r}}_i = \sum_{j\neq i} \frac{GM_j(\mathbf{r}_j-\mathbf{r}_i)}{r^3_{ij}} \left\{ 1 - \frac{2(1+\gamma)}{c^2} \sum_{l\neq i} \frac{GM_l}{r_{il}} - \frac{1}{c^2} \sum_{k\neq j} \frac{GM_k}{r_{jk}} + \gamma \left(\frac{\dot{s}_i}{c}\right)^2 + (1+\gamma)\left(\frac{\dot{s}_j}{c}\right)^2 \right.$$
$$\left. - \frac{2(1+\gamma)}{c^2} \dot{\mathbf{r}}_i \dot{\mathbf{r}}_j - \frac{3}{2c^2}\left[\frac{(\mathbf{r}_i-\mathbf{r}_j)\,\dot{\mathbf{r}}_j}{r_{ij}}\right]^2 + \frac{1}{2c^2}(\mathbf{r}_j-\mathbf{r}_i)\,\ddot{\mathbf{r}}_j \right\}$$
$$+ \frac{1}{c^2} \sum_{j\neq i} \frac{GM_j}{r^3_{ij}} \{(\mathbf{r}_i-\mathbf{r}_j)\,[(2+2\gamma)\dot{\mathbf{r}}_i - (1+2\gamma)\dot{\mathbf{r}}_j]\}\,(\dot{\mathbf{r}}_i-\dot{\mathbf{r}}_j) + \frac{3+4\gamma}{2c^2} \sum_{j\neq i} \frac{GM_j \ddot{\mathbf{r}}_j}{r_{ij}} \tag{4.61}$$

where the subscript i refers to S/C or center of integration and where $\mathbf{r}_j$ is the position vector of body j, $\dot{\mathbf{r}}_j$ is the heliocentric (strictly barycentric) velocity vector of body j, and $\ddot{\mathbf{r}}_j$ is the Newtonian acceleration of body j computed from

$$\ddot{\mathbf{r}}_j = \sum_{k\neq j} \frac{GM_k(\mathbf{r}_k-\mathbf{r}_j)}{r^3_{jk}} \tag{4.62}$$

The magnitude of $(\mathbf{r}_j-\mathbf{r}_i)$ is r_{ij}, GM_j is the gravitational constant of body j in km^3/s^2, and $\dot{s}_j$ is the magnitude of $\dot{\mathbf{r}}_j$.

The $1/c^2$ term of equation (4.61) is the Newtonian acceleration. The remaining $1/c^2$ terms are relativistic perturbative accelerations derived from the Brans-Dicke theory; these terms revert to those of general relativity when $\gamma \to 1$. The summation over $j \neq i$ includes the Sun, the nine planets, and the Moon. For each of these perturbing bodies the user has three options: (1) computing the Newtonian acceleration and the relativistic perturbative acceleration; (2) computing the Newtonian acceleration only, or (3) ignoring the acceleration caused by that body.

The summation over $k \neq j$ in equations (4.61) and (4.62) and over $1 \neq i$ in equation (4.61) includes all bodies of the solar system that are treated as specified in options (1) or (2) and included in the j summation of equation (4.61).

4.4.3.2 Direct Acceleration of Spacecraft Because of Oblateness

The acceleration of the spacecraft relative to the center of integration because of the oblateness of the bodies of the solar system consists of the direct acceleration of the spacecraft minus the indirect acceleration of the center of integration. The direct acceleration of the spacecraft because of the oblate-

ness of a body is computed only when the spacecraft is within the so-called harmonic sphere for the body. The radii of the harmonic spheres may be changed by input; the nominal values for the Earth, Mars, and the Moon are 2.5×10^6, 1.0×10^6, and 2×10^5 km, respectively. The formulation for computing the direct acceleration of the spacecraft because of the oblateness of a body is given in this section. The indirect acceleration of the center of integration caused by oblateness, computed only when the center of integration is the Earth or the Moon, accounts for the oblateness of each of these two bodies. The formulation is given in section 4.4.3.3.

The direct acceleration of the spacecraft because of the oblateness of a body is derived from the generalized potential function for that body (*Proceedings of the Eleventh General Assembly*, Berkeley, 1961, pp. 173–174, 1962):

$$V=\frac{GM}{r}\left[1+\sum_{n=1}^{\infty}\sum_{m=0}^{n}\left(\frac{A_p}{r}\right)^n P_n^m(\sin\psi)\,(C_{nm}\cos m\lambda+S_{nm}\sin m\lambda)\right] \quad (4.63)$$

where

- GM gravitational constant of the body, km^3/s^2
- r,ψ,λ radius, latitude, and longitude (positive east of prime meridian) of the spacecraft relative to the body
- a_p mean equatorial radius of the body (an adopted constant used for V)

The inertial acceleration of the spacecraft is computed in a rectangular coordinate system $(x'y'z')$ with the x' axis directed outward along the instantaneous radius to the spacecraft, the y' axis directed east, and the z' axis directed north. These axes relative to body-fixed axes $x_by_bz_b$ are shown in figure 4.21, where x_b is along the intersection of the prime meridian and equator of the body, z_b is directed north along the axis of rotation of the body, and y_b completes the right-handed system. The transformation from body-fixed

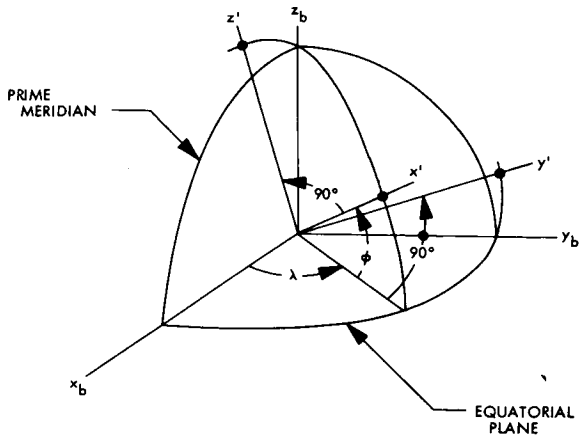

FIGURE 4.21.—Body-fixed x_b, y_b, and z_b axes relative to x', y', and z' axes.

coordinates $\mathbf{r}_b=(x_b,y_b,z_b)^T$ to $\mathbf{r}'=(x',y',z')^T$ coordinates is given by

$$\mathbf{r}'=R\mathbf{r}_b \quad (4.64)$$

where

$$R=\begin{bmatrix}\cos\psi\cos\lambda & \cos\psi\sin\lambda & \sin\psi\\ -\sin\lambda & \cos\lambda & 0\\ -\sin\psi\cos\lambda & -\sin\psi\sin\lambda & \cos\psi\end{bmatrix} \quad (4.65)$$

The position vector of the spacecraft relative to the body (denoted as body i) with rectangular components referred to the mean Earth equator and equinox of 1950.0 is $\mathbf{r}-\mathbf{r}_i^C$, where $\mathbf{r}$ is the position vector of the spacecraft relative to the center of integration with rectangular components referred to the mean Earth equator and equinox of 1950.0; that is, the 1950.0 position vector and $\mathbf{r}_i^C$ is the 1950.0 position vector of body i relative to the center of integration C. The transformation from these 1950.0 body-centered coordinates to body-fixed coordinates $\mathbf{r}_b$ is denoted as

$$\mathbf{r}_b=T^T(\mathbf{r}-\mathbf{r}_i^C) \quad (4.66)$$

The overall transformation from $(\mathbf{r}-\mathbf{r}_i^C)$ to $\mathbf{r}'$ is thus

$$\mathbf{r}'=RT^T(\mathbf{r}-\mathbf{r}_i^C)\equiv G(\mathbf{r}-\mathbf{r}_i^C) \quad (4.67)$$

The inverse transformation is

$$(\mathbf{r}-\mathbf{r}_t^C)=G^T\,\mathbf{r}'=TR^T\mathbf{r}' \qquad (4.68)$$

If $\mathbf{r}_b$ from equation (4.66) is used, the sines and cosines of ψ and λ and the angle λ are computed from

$$\sin\psi=\frac{z_b}{r} \qquad (4.69)$$

$$\cos\psi=\frac{(x_b^2+y_b^2)^{1/2}}{r} \qquad (4.70)$$

$$\sin\lambda=\frac{y_b}{(x_b^2+y_b^2)^{1/2}} \qquad (4.71)$$

$$\cos\lambda=\frac{x_b}{(x_b^2+y_b^2)^{1/2}} \qquad (4.72)$$

The formulation for the transformation T for the planets, Sun, and Moon is specified by Sturms (1971).

Let $\ddot{\mathbf{r}}'$ denote the inertial acceleration of the spacecraft because of the oblateness of any body with rectangular components along the instantaneous directions of the x', y', and z' axes. This acceleration can be broken down into $\ddot{\mathbf{r}}'(J)$ due to the zonal harmonics J_n, and $\ddot{\mathbf{r}}'(C,S)$ due to the tesseral harmonics C_{nm} and S_{nm}. Given these terms, the direct acceleration of the spacecraft because of the oblateness of any body, with rectangular components referred to the mean Earth equator and equinox of 1950.0, is given by

$$\ddot{\mathbf{r}}=G^T\ddot{\mathbf{r}}'=G^T\,[\ddot{\mathbf{r}}'(J)+\ddot{\mathbf{r}}'(C,S)] \qquad (4.73)$$

The components of $\ddot{\mathbf{r}}'(J)$ and $\ddot{\mathbf{r}}'(C,S)$ are given by

$$\ddot{\mathbf{r}}'(J)=\frac{GM}{r^2}\sum_{n=1}^{n_1}J_n\left(\frac{a_p}{r}\right)^n\begin{bmatrix}(n+1)P_n\\0\\-\cos\psi\,P_n'\end{bmatrix} \qquad (4.74)$$

$$\ddot{\mathbf{r}}'(C,S)=\frac{GM}{r^2}\sum_{n=1}^{n_2}\sum_{m=1}^{n}\left(\frac{a_p}{r}\right)^n \times\begin{bmatrix}-(n+1)P_n^m\{C_{nm}\cos m\lambda+S_{nm}\sin m\lambda\}\\ m\sec\psi\,P_n^m\{-C_{nm}\sin m\lambda+S_{nm}\cos m\lambda\}\\ \cos\psi\,P_n^{m\prime}\{C_{nm}\cos m\lambda+S_{nm}\sin m\lambda\}\end{bmatrix} \qquad (4.75)$$

where the primes indicate derivatives with respect to $\sin\psi$.

The Legendre polynomial P_n is computed recursively from

$$P_n=\frac{2n-1}{n}\sin\psi\,P_{n-1}-\left(\frac{n-1}{n}\right)P_{n-2} \qquad (4.76)$$

starting with

$$P_0=1 \qquad (4.77)$$

$$P_1=\sin\psi \qquad (4.78)$$

The derivative of P_n with respect to $\sin\psi$, denoted P_n', is given by

$$P_n'=\sin\psi\,P_{n-1}'+nP_{n-1} \qquad (4.79)$$

starting with

$$P_1'=1 \qquad (4.80)$$

The function $\sec\psi\,P_n^m$ is computed by first generating

$$\sec\psi\,P_n^n=(2n-1)\cos\psi\,(\sec\psi\,P_{n-1}^{n-1}) \qquad (4.81)$$

starting with

$$\sec\psi\,P_1^1=1 \qquad (4.82)$$

and continuing until $n=n_2$, and then generating

$$\sec\psi\,P_n^m=\left(\frac{2n-1}{n-m}\right)\sin\psi\,(\sec\psi\,P_{n-1}^m)-\left(\frac{n+m-1}{n-m}\right)(\sec\psi\,P_{n-2}^m) \qquad (4.83)$$

For each value of m between 1 and n_2, n is varied from $m+1$ to n_2. The general term P_a^b is zero if $b>a$. The function P_n^m is obtained by multiplying $(\sec\psi\,P_n^m)$ by $\cos\psi$.

The function $\cos\psi\,P_n^{m'}$, where $P_n^{m'}$ is the derivative of P_n^m with respect to $\sin\psi$, is computed from

$$\cos\psi\,P_n^{m'}=-n\sin\psi\,(\sec\psi\,P_n^m)+(n+m)\,(\sec\psi\,P_{n-1}^m) \qquad (4.84)$$

4.4.3.3 Indirect Acceleration of Center of Integration Because of Oblateness

As was previously mentioned, the indirect oblateness acceleration of the spacecraft relative to the center of integration is the negative of the acceleration of the center of integration because of oblateness. It is computed only when the center of integration is the Earth or Moon and accounts for the oblateness of both of these bodies.

The force of attraction between the Earth and Moon consists of the following: force 1, the attraction between the point mass Earth and point mass Moon; (2) force 2, attraction between the oblate part of the Earth and the point mass Moon; (3) force 3, attraction between the oblate part of the Moon and the point mass Earth, and (4) force 4, the attraction between the oblate part of the Earth and the oblate part of the Moon.

Force 1 is accounted for in section 4.4.3.1. The formulation in this section will account for forces 2 and 3 but will ignore force 4.

Let $\ddot{\mathbf{r}}_M(E)$ be the inertial acceleration of the point mass Moon because of the oblateness of the Earth and $\ddot{\mathbf{r}}_E(M)$ be the inertial acceleration of the point mass Earth because of the oblateness of the Moon. These accelerations, with rectangular components referred to the mean Earth equator and equinox of 1950.0, may be computed from the formulation of section 4.4.3.2. In the computation of $\ddot{\mathbf{r}}_M(E)$ the Moon is treated as the spacecraft of section 4.4.3.2, and $\mathbf{r}-\mathbf{r}_i^C$ in equation (4.66) is replaced by $\mathbf{r}_M^E$. Similarly, in the computation of $\ddot{\mathbf{r}}_E(M)$ the Earth is treated as the spacecraft and $\mathbf{r}-\mathbf{r}_i^C$ is replaced by $\mathbf{r}_E^M$.

The acceleration of the Earth because of the oblateness of the Earth and Moon is

$$\ddot{\mathbf{r}}_E = \ddot{\mathbf{r}}_E(M) + \ddot{\mathbf{r}}_E(E) = \ddot{\mathbf{r}}_E(M) - \frac{GM_\leftmoon}{GM_\oplus}\ddot{\mathbf{r}}_M(E) \qquad (4.85)$$

where $\ddot{\mathbf{r}}_E(E)$ is the inertial acceleration of the Earth because of the force of attraction between the oblate part of the Earth and the point mass Moon.

Similarly,

$$\ddot{\mathbf{r}}_M = \ddot{\mathbf{r}}_M(E) + \ddot{\mathbf{r}}_M(M) = \ddot{\mathbf{r}}_M(E) - \frac{GM_\oplus}{GM_\leftmoon}\ddot{\mathbf{r}}_E(M) \qquad (4.86)$$

where $\ddot{\mathbf{r}}_M(M)$ is the inertial acceleration of the Moon due to the force of attraction between the oblate part of the Moon and the point mass Earth.

The contribution to the spacecraft acceleration relative to the center of integration is the negative of the acceleration of the center of integration, or

$$\ddot{\mathbf{r}} = \pm GM_i\left[\frac{1}{GM_\oplus}\ddot{\mathbf{r}}_M(E) - \frac{1}{GM_\leftmoon}\ddot{\mathbf{r}}_E(M)\right] \qquad (4.87)$$

where $\pm GM_i = +GM_\leftmoon$ if Earth is the center of integration and $\pm GM_i = -GM_\oplus$ if the Moon is center of integration.

Sturms' algorithm for computation of this acceleration accounts for J_2, C_{22}, and S_{22} of the Earth and Moon. Equation (4.87), evaluated with these harmonic coefficients, is equivalent to Sturms' formulation.

4.4.3.4 Acceleration of Spacecraft Because of Solar Radiation Pressure and Small Forces Originating in Spacecraft

In this section is given the model for representing the acceleration of the spacecraft because of solar radiation pressure and small forces originating in the spacecraft, such as those from operation of the attitude control system (particularly if using uncoupled attitude control jets) or from gas leaks. The model applies to any spacecraft that has one axis (the roll axis) continuously oriented toward the Sun and uses a star or planet tracker to orient the spacecraft about the roll axis. The various Mariner spacecraft are of this type.

The solar radiation pressure model accounts for the acceleration of the spacecraft because of solar radiation pressure acting along three mutually perpendicular spacecraft axes, one of which is the roll axis. Normally, the solar panels are oriented normal

to the roll axis so that the largest component of the force because of solar radiation pressure is along the roll axis. However, the model can also account for the small forces acting along the other two spacecraft axes and arising from departures of the spacecraft shape from rotational symmetry about the roll axis.

The small-force model accounts in a crude fashion for the acceleration arising from small forces originating in the spacecraft. The component of this acceleration along each spacecraft axis is represented as a quadratic. The model has been expanded to allow this acceleration to be represented alternatively as an exponential decay with components along each spacecraft axis.

The acceleration of the spacecraft because of solar radiation pressure and small forces originating in the spacecraft is represented by

$$\begin{aligned}\ddot{\mathbf{r}} = &\left\{[a_r + b_r(t-T_{AC1}) + c_r(t-T_{AC1})^2][u(t-T_{AC1}) - u(t-T_{AC2})]\right.\\ &\left.+\Delta a_r + \frac{C_1 A_p}{m r_{sp}^2} G_r u^*(t-T_{SRP})\right\}\mathbf{U}_{SP}\\ &+\left\{[a_x + b_x(t-T_{AC1}) + c_x(t-T_{AC1})^2][u(t-T_{AC1}) - u(t-T_{AC2})]\right.\\ &\left.+\Delta a_x + \frac{C_1 A_p}{m r_{sp}^2} G_x u^*(t-T_{SRP})\right\}\mathbf{X}^*\\ &+\left\{[a_y + b_y(t-T_{AC1}) + c_y(t-T_{AC1})^2][u(t-T_{AC1}) - u(t-T_{AC2})]\right.\\ &\left.+\Delta a_y + \frac{C_1 A_p}{m r_{sp}^2} G_y u^*(t-T_{SRP})\right\}\mathbf{Y}^* \qquad (4.88)\end{aligned}$$

The value for each Δa_i is obtained by linear interpolation between input points. The acceleration is started at the epoch of the first point and ended at the epoch of the last point.

$$C_1 = \frac{JA_E^2}{c} \times \frac{1\ \text{km}^2}{10^6\ \text{m}^2} = 1.010 \times 10^8 \frac{\text{km}^3\ \text{kg}}{s^2 m^2}$$

where

- J solar radiation constant, equals 1.3525×10^3 watts/m^2 (Plamondon, 1969; 20 July 1970, Plamondon stated that a more accurate reduction of the data gave a value of 1.348 $\times 10^3$ watts/m^2), equals 1.3525×10^3 kg/s^3
- A_E equals 1.496×10^8 km
- A_p the nominal area of the spacecraft projected onto the plane normal to the Sun-spacecraft line, m^2

The terms in this equation are defined as follows:

- $\mathbf{U}_{SP}$ the unit vector from the Sun to the spacecraft
- $\mathbf{X}^*$, $\mathbf{Y}^*$ the unit vectors along the spacecraft x and y axes ($\mathbf{X}^* \times \mathbf{Y}^* = \mathbf{U}_{SP}$) (defined subsequently)
- a_i, b_i, c_i solve-for coefficients of acceleration polynomials, where $i = r$, x, or y, km/s^2, km/s^3, km/s^4
- t ephemeris time
- T_{AC1}, T_{AC2} the epochs at which the acceleration polynomials are turned on and off, respectively
- $u(t-T_{AC1})$ equals 1 for $t \geq T_{AC1}$, 0 for $t < T_{AC1}$, $T_{AC1} \rightarrow T_{AC2}$
- Δa_r, Δa_x, Δa_y known input acceleration, km/s^2

m the instantaneous mass of the spacecraft, kg

r_{SP} the distance from the Sun to the spacecraft, km

T_{SRP} the epoch at which acceleration because of solar radiation pressure is turned on (epoch of solar panel unfolding)

$u^*(t-T_{SRP})$ equals 1 for $t \geq T_{SRP}$ if the spacecraft is in the sunlight, or equals 0 for $t < T_{SRP}$ if the spacecraft is in shadow of a planet or the Moon

G_r the unknown effective area for acceleration of the spacecraft in the radial direction because of solar radiation pressure divided by the nominal area A_p

G_x the unknown effective area for acceleration of the spacecraft in the direction of its positive x axis (along $\mathbf{X}^*$ vector) divided by A_p

G_y the unknown effective area for acceleration of the spacecraft in the direction of its positive y axis (along $\mathbf{Y}^*$ vector) divided by A_p

The unit Sun-spacecraft vector $\mathbf{U}_{SP}$ is computed from

$$\mathbf{U}_{SP}=\frac{\mathbf{r}-\mathbf{r}_s^C}{||\mathbf{r}-\mathbf{r}_s^C||} \tag{4.89}$$

where $\mathbf{r}$ is the position vector of the spacecraft relative to the center of integration with the rectangular components referred to the mean Earth equator and equinox of 1950.0, and $\mathbf{r}_s^C$ is the 1950.0 position vector of the Sun relative to the center of integration C.

The spacecraft $\mathbf{X}^*$ and $\mathbf{Y}^*$ unit vectors are obtained as a rotation of the tangential $\mathbf{T}$ and normal $\mathbf{N}$ vectors through the angle K.

$$\begin{bmatrix}\mathbf{X}^*\\ \mathbf{Y}^*\end{bmatrix}=\begin{bmatrix}\cos K & \sin K\\ -\sin K & \cos K\end{bmatrix}\begin{bmatrix}\mathbf{T}\\ \mathbf{N}\end{bmatrix} \tag{4.90}$$

The angle K is an input (non-solve-for) constant. Computation of the unit vectors $\mathbf{T}$ and $\mathbf{N}$ requires the unit vector $\mathbf{U}_r$, the unit vector from the spacecraft to the reference body that orients the spacecraft about the roll axis (Sun-spacecraft line). The reference body may be a star, a planet, or the Moon. If the reference body is a star,

$$\mathbf{U}_r=\begin{bmatrix}\cos\delta\cos\alpha\\ \cos\delta\sin\alpha\\ \sin\delta\end{bmatrix} \tag{4.91}$$

where the right ascension α and declination δ of the star are referred to the mean Earth equator and equinox of 1950.0. If the reference body B is a planet (normally the Earth) or the Moon,

$$\mathbf{U}_r=\frac{\mathbf{r}_B^C-\mathbf{r}}{||\mathbf{r}_B^C-\mathbf{r}||} \tag{4.92}$$

where $\mathbf{r}_B^C$ is the 1950.0 position vector of the reference body B relative to the center of integration C. The unit normal vector $\mathbf{N}$ (normal to Sun-spacecraft-reference body plane) is computed from

$$\mathbf{N}=\frac{\mathbf{U}_r\times\mathbf{U}_{SP}}{||\mathbf{U}_r\times\mathbf{U}_{SP}||} \tag{4.93}$$

The unit tangential vector $\mathbf{T}$ (tangent to Sun-spacecraft-reference body plane) is

$$\mathbf{T}=\mathbf{N}\times\mathbf{U}_{SP} \tag{4.94}$$

Given $\mathbf{T}$ and $\mathbf{N}$, the vectors $\mathbf{X}^*$ and $\mathbf{Y}^*$ are given by equation (4.90). The angle K may be selected to achieve a specific orientation of $\mathbf{X}^*$ and $\mathbf{Y}^*$ relative to the spacecraft.

4.4.4 Application of Theory to Specific Problems

The precise way in which the preceding theory is applied to specific problems varies somewhat according to whether locations of stations, gravitational constants, or locations of spacecraft are to be determined. Only the

first two of these problems concern the NGSP. The application of theory to these two is given in sections 4.3.3 (station location) and 4.5.2 (gravitational constant).

4.5 RESULTS: GEOCENTRIC GRAVITATIONAL CONSTANT DETERMINED FROM SPACECRAFT TRACKING DATA

4.5.1 Introduction

Within the last decade, most of the determinations of the geocentric gravitational constant have been the result of the analysis of data from the near-Earth phase of lunar and interplanetary missions. A relatively recent review of the status of the value of the universal gravitational constant, G, as well as the geocentric gravitational constant, $GM_\oplus$, is presented by Sagitov (1970). In that paper a small segment of results from spacecraft tracking is displayed. A general review of the application of spacecraft-tracking data to the determination of planetary gravitational constants as well as a tabulation of recently determined geocentric and lunar gravitational constants are given by Melbourne (1970). The purpose of this section is to present the details of the determination of $GM_\oplus$ using the analysis of Mariner 9 data as a representative example and to investigate the major sources of error. In addition, other $GM_\oplus$ values deduced from the analysis of spacecraft-tracking data will be reviewed and compared.

4.5.2 Basis of Determination of Geocentric Gravitational Constant

During the first several days of flight the gravitational attraction of the Earth dominates the spacecraft motion. It is simply the variation in the gravitational attraction as reflected in the spacecraft Doppler shift and range measurements that enables $GM_\oplus$ to be determined from the data.

At launch the speed the spacecraft must have in order to escape from the Earth's gravitational grasp is given by $v = (2\mu/R)^{1/2} =$ 11.2 km/s. The variation of the geocentric speed, radial speed, and distance during the first 24 hours after the Mariner 9 launch is given in figure 4.22. It is evident that both the velocity magnitude and the radial speed undergo a large variation within several hours after launch. It is within this time interval that one has the most important data for the direct determination of GM. Of course, additional data are necessary to establish the hyperbolic orbit of the spacecraft, determine other quantities pertinent to the analysis, and allow a separation of GM from other parameters (e.g., the initial state of the spacecraft) that enter into the analysis.

With respect to the cruise phase of an interplanetary mission, $GM_\oplus$ is not directly determined. However, since the Earth revolves about the center of mass of the Earth-Moon system with a period of approximately 27 days, a sinusoidal Doppler shift with an amplitude of 12 m/s is embedded in the Doppler data. This particular effect in the Doppler data can be approximated by

$$\dot{\rho} = n_\zeta a_\zeta \frac{\mu}{1+\mu} \cos\beta \sin(\lambda - \lambda_\zeta) \qquad (4.95)$$

where n_ζ, a_ζ, μ, and λ_ζ are the lunar mean motion, perturbed mean distance from the

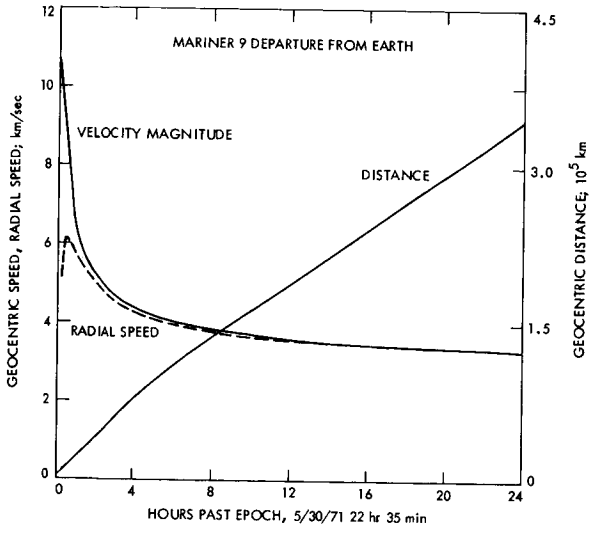

FIGURE 4.22.—Mariner 9 velocity and distance variation during first day of flight.

Earth, the ratio of the mass of the Moon to the mass of the Earth, and the longitude of the Moon, respectively. In addition, λ and β represent the longitude and latitude of the spacecraft with respect to the lunar orbital plane (Melbourne, 1970). Consequently, the Earth-Moon mass ratio (μ^{-1}) can be inferred from the Doppler data from which $GM_{\oplus}$ can be deduced providing $GM_{\mathbb{C}}$ is well known, or vice versa. A review of the evaluation of μ^{-1} from the cruise phase of interplanetary spacecraft is given by Null (1970), and the Mariner 9 result is given by Wong (1973).

4.5.3 Determination of Geocentric Gravitational Constant From Mariner 9 Tracking Data: A Representative Analysis

4.5.3.1 Modeling the Mariner 9 Trajectory

During the first several days of flight the gravitational attraction of the Earth dominates the spacecraft motion. The Earth's gravitational coefficients are not estimated, however; their influence on the trajectory is calculated. The nominal values of these coefficients were taken from works by Kozai (1969) and Gaposchkin and Lambeck (1970). Since the spacecraft was 20 000 km above the Earth's surface when the Deep Space Net first acquired the spacecraft, no attempt has been made to model atmospheric drag. However, refraction of the radio signal because of the troposphere has been modeled according to an algorithm described by Berman (1970). At present, no ionospheric corrections have been applied to the data; however, its expected that the influence of the ionosphere on the propagation of the 2200-MHz (S-band) radio signal will be modeled eventually.

The motion of the Mariner 9 spacecraft is determined by a numerical integration of the equations of motion. These equations account for the basic Newtonian motion as well as for perturbations because of harmonics in the Earth's gravitational field, solar radiation pressure, planetary and lunar effects, spacecraft attitude control forces, etc. Perturbations resulting from solar radiation pressure are modeled as a three-dimensional force along the pitch, roll, and yaw axes of the spacecraft. The model is parameterized, and each component of the force can be estimated. Usually, the spacecraft maintains a fixed orientation in space by locking onto the Sun and Canopus by way of star sensors. However, on occasion, the spacecraft will drift from this orientation. To rotate the spacecraft to its original orientation, a pair of coupled gas jets, located on the ends of opposite solar cell panels, will fire synchronously. In the process of achieving the desired orientation, a net translational acceleration of magnitude 10^{-11} to 10^{-12} km/s^2 may be imparted to the spacecraft. In addition, intermittent gas leakage is responsible for a constant acceleration within the same magnitude interval, as was mentioned previously. These forces generally occur in a random manner and ordinarily are negligible. However, when data arcs consisting of one to several weeks are being analyzed, a perturbation of this type will influence the trajectory and consequently must be modeled.

The motion of the Moon as well as of the planets is deduced from the analysis of transit-circle, radar, and previous spacecraft data. One of the results of such an analysis is the generation of a planetary ephemeris. JPL's most recent development ephemeris, DE80, has been employed in the analysis of the Mariner 9 data (O'Handley, *et al.*, 1969). The spacecraft was launched in a direction away from the Moon and reached a geocentric distance of 400 000 km 30 hours after launch. Thus the influence of the Moon's gravitational force on the spacecraft has been minimized.

Tracking station coordinates are referred to the mean pole, equator, and prime meridian of 1903.0. Their nominal values, in cylindrical coordinates (longitude λ, distance perpendicular to the Earth's spin axis r_s, and distance parallel to spin axis z), are given in table 4.8 (Mulhall *et al.*, 1970). These coordinates can be refined in the analysis of the Mariner data.

In summary, the pertinent models and parameters employed in the analysis along with their nominal values and a priori standard deviations are shown in table 4.9. The initial conditions are in a geocentric space-fixed reference system and are with respect to the Earth's mean equator and equinox of 1950.0.

4.5.3.2 Data Analysis

The data were divided into two groups consisting of data over a short arc, which encompassed the first day of data, and data over a longer arc, which included data from launch to launch plus 5 days. On 5 June 1971, 22 minutes UTC, the first midcourse maneuver was performed which, in addition to imparting a velocity change of 6.7 m/s to the spacecraft, served as a demarcation point for the data analyzed. Most of the direct information on GM comes from the short arc. However, the longer arc provides additional information on the gravitational constant, refines the spacecraft trajectory, and reduces the correlations between the initial state of the spacecraft and the Earth's gravitational constant.

Data were analyzed by way of a classical least-squares algorithm. In addition to minimizing the sum of squares of the weighted residuals, the least-squares estimator has the capability of interpreting a priori estimates of parameters as data. The parameter estimation equation is

$$\Delta x = (A^T W A + \tilde{\Lambda}_x^{-1})^{-1}(A^T W \Delta z + \tilde{\Lambda}_x^{-1}\tilde{\Delta} x) \quad (4.96)$$

with the estimated parameter covariance matrix given by

$$\Lambda_x = (A^T W A + \tilde{\Lambda}_x^{-1})^{-1} \quad (4.97)$$

The residuals (observed data minus computed data) for the Doppler and range data are represented by Δz, corrections to the estimated parameters are represented by Δx, and corrections to a priori values of estimated parameters are indicated by $\tilde{\Delta} x$. A diagonal weighting matrix, W, is assumed to be the inverse of the data noise covariance matrix, and $\tilde{\Lambda}_x$ represents the a priori parameter covariance matrix. Numerically evaluated partial derivatives of the data with respect to the estimated parameters are contained in the A matrix.

The basic set of estimated parameters for the short arc consists of the location and velocity of the spacecraft at epoch, station locations, and the Earth's gravitational constant. A typical set of Doppler shift residuals resulting from such an analysis is shown in figure 4.23 and the quantity of data analyzed has been tabulated in table 4.10. The Dopp-

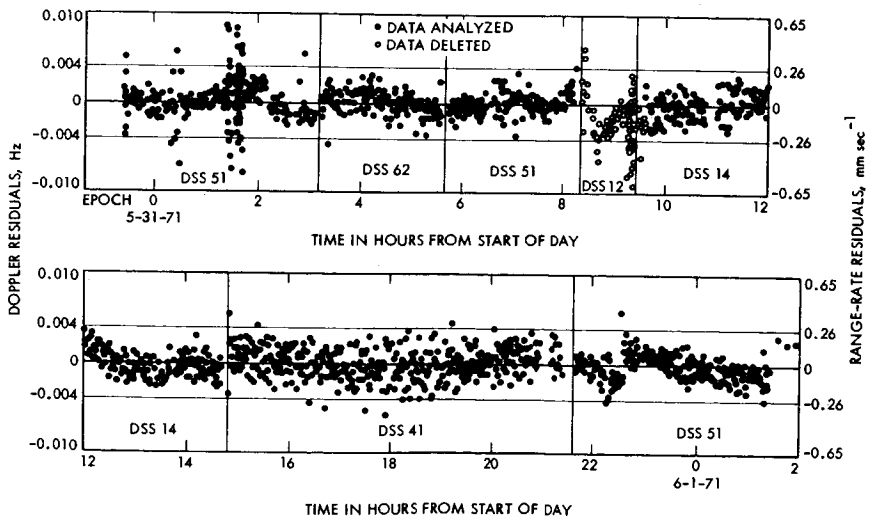

FIGURE 4.23.—Mariner 9 Doppler shift residuals.

ler shift residuals are confined within a band of width ± 0.004 Hz, which amounts to ± 0.26 mm/s in range rate. The DSS 12 data occur at very low elevation angles (3 to 12 deg) and have been deleted from the analysis. However, the residuals are shown and serve as an excellent reminder of the influence of the Earth's atmosphere on the propagating radio signal. On 31 May 1971, 22 hours 32 minutes, there occurs a slight discontinuity in the residual trend because of a scan platform unlatch on the Mariner spacecraft. Telemetry information indicates that this operation imparted a velocity increment to the spacecraft of about 4 mm/s. This type of perturbation is being modeled as an impulsive force.

The data analysis involved several sequences in which the length of arc, quantity and type of data, and estimated parameters were varied. This procedure was adopted to determine the sensitivity of certain parameters in the analysis, establish the stability of the solution, and investigate possible biases in the data. Analysis of the 1-day arc reveals that the expected level of perturbations because of attitude control forces has a minor influence on the *GM* solution. However, in such a short arc the initial location and velocity of the spacecraft exhibit moderate to high correlations with the geocentric gravitational constant. Analysis of the 5-day arc of data yields a *GM* solution consistent with respect to the short arc. However, the cumulative influence of the random attitude control forces over this long arc, if not modeled properly, will exert an influence in the orbit refinement that will affect the *GM* solution. Although the results of the short- and long-arc analyses are basically consistent, the long-arc analysis requires additional investigation before conclusive results are available.

4.5.3.3 Sources of Error

In addition to the previously mentioned analysis, the adequacy of a solution has been investigated by noting trends or patterns in the residuals, using a converged solution to predict data outside the data arc analyzed, and conducting a sensitivity analysis on parameters designated as "consider" parameters. With respect to these parameters, certain parameters cannot be refined by the near-Earth data; however, their uncertainties may have an influence on the estimated parameters, especially *GM*. These parameters are designated as consider parameters simply because their effects are considered in the orbit determination. For example, if one assumes that a reasonable error in J_2 is 0.5×10^{-7}, then this uncertainty can be translated into a corresponding change in the estimated parameters. In addition, a consider covariance matrix can be evaluated which will degrade the covariance matrix obtained from equation (4.97). A change or error in a consider parameter maps into a change in an estimated parameter according to a first-order Taylor series

$$\delta \bar{x} = S_{xy}\, \delta y \tag{4.98}$$

where the sensitivity matrix is defined as a matrix of partial derivatives of the estimated parameters x with respect to the consider parameters y

$$S_{xy} = \partial \bar{x} / \partial \bar{y} \tag{4.99}$$

The consider covariance matrix is given by

$$\Lambda_x(\text{consider}) = \Lambda_x[\text{eq. (4.100)}] + S_{xy} \tilde{\Lambda}_y S_{xy}^T \tag{4.100}$$

where $\tilde{\Lambda}_y$ represents a priori covariance matrix on the consider parameters.

Consider-parameters and reasonable uncertainties are listed in table 4.11, along with their influence on the value of *GM* for the 1-day data arc.

The parameters a_r, a_x, a_y represent constant accelerations acting along the spacecraft roll, pitch, and yaw axes. If one assumes that this type of perturbation was acting over 1 day, then it can have a relatively large impact (with respect to the other consider parameters) on the value of *GM*. The importance of such a perturbation increases as

the data arc is extended. Consequently, it must be modeled in the orbit refinement. Uncertainties in the Earth's gravitational harmonics, the Moon's gravitational constant, heliocentric orbital elements of the Earth, geocentric orbital elements of the Moon, and the astronomical unit have a negligible effect on the Earth's gravitational constant.

A preliminary estimate of *GM* deduced from the analysis of the Mariner 9 data is $GM_{\oplus}=398\,600.8\pm0.4$. This standard deviation is conservative insofar as the Doppler data have been weighted by a factor of 4 larger than the rms variation in the residuals. At present, the formal standard deviation deduced from equation (4.97) is 0.15. This conservative approach is justified insofar as the long-arc data (5 days) are still in the preliminary stage of analysis. Furthermore, analysis has been performed on data within the interval of launch to launch plus 20 days, in which the first midcourse maneuver has been modeled. Preliminary analysis of this data arc indicates results consistent with the preceding estimate. With the completion of the analysis, it is anticipated that the uncertainty in *GM* will be reduced by a factor of 2.

The Mariner 9 data have been analyzed with the JPL orbit determination program, described in detail by Moyer (1971).

4.5.4 Comparison and Critique of Previous Results

The purpose of this section is to review the results for $GM_{\oplus}$ of previous spacecraft missions and to comment on the accuracy of the results. Some of the values for *GM* have been abstracted from JPL Flight Path Reports, which are more oriented toward the engineering aspects of the mission than to a scientific analysis of the data. This statement is offered as a caution and not as a criticism; these documents fulfilled their purpose in an excellent manner. On the other hand, they are the only source of the *GM* values deduced from some of the earlier spacecraft missions. It is in this spirit that the following comments pertaining to each of the individual *GM* determinations are offered.

With respect to current knowledge of *GM*, the results listed in table 4.12 for Ranger 3, 4, and 5 are only of historic interest. These first evaluations of *GM* demonstrated a feasible technology and began a trend that ultimately led to a revision of the then accepted current value of the Earth's gravitational constant, i.e., 398 603.2 km^3/s^2.

Solutions from Ranger 6 through 9 are given individually in their respective flight path reports. However, a more definitive analysis was conducted; the results are summarized by Sjogren *et al.* (1966), and presented in table 4.12. The results from these different sources do not differ in any significant way. It is noteworthy that the report by Sjogren *et al.* (1966), represents a detailed analysis of the Ranger data, giving a clear explanation of the method of analysis and delineating the major sources of error.

The result of a statistical combination of the data from Ranger 6, 7, 8, and 9 is given by Vegos and Trask (1967) and is also shown in table 4.12. Note that the analysis yielded a standard deviation of 0.4; yet the authors summarized their result with a realistic standard deviation of 0.7 km^3/s^2. The results of this overall analysis led to the adoption by JPL of $GM_{\oplus}=398\,601.2$ km^3/s^2 (Melbourne *et al.*, 1968).

Lunar Orbiter 2 results exist for *GM*; however, as evidenced by the title of the report, "Consistency of Lunar Orbiter II Ranging and Doppler Data" (Mottinger and Sjogren, 1967), the authors were primarily concerned with a comparison of data types (Doppler and range). This is the reason why two results are given for *GM*: *GM*(Doppler) = $398\,600.9\pm2.1$ and *GM*(Doppler+range) = $398\,600.4\pm0.7$. As a result of this study, some small biases had been detected in the range data, which led the authors to increase their formal standard deviations from 1.23 and 0.26 to those given in the preceding equations.

The Surveyor results have been described in flight path reports by Thorton *et al.*

(1968), O'Neil *et al.* (1968), and Labrum *et al.* (1968), and have been summarized by Wong (1968). However, after a close review of these reports, some hesitation is felt about tabulating these six values, as has been done for the Ranger results. The reasons for caution are as follows:

(1) For Surveyor 3, 5, 6, and 7 the *GM* values deduced from the analysis (Wong, 1968) are almost identical to two decimal places (i.e., 398 601.11 for Surveyor 3, 6, and 7 and 398 601.10 for Surveyor 5); yet the standard deviations associated with these results are 0.8, 0.5, 0.8, and 0.6, respectively. It would appear that either the standard deviations are grossly exaggerated, which seems dubious, or it is a fortuitous coincidence that these results agree exactly.

(2) In the Surveyor 4 determination an a priori standard deviation of 1.0 km^3/s^2 was used for *GM*. As a result of the analysis, $\sigma(GM) = 0.99$, which is equivalent to saying that the data analyzed have no information about *GM* to the level of 1.0 km^3/s^2.

(3) In the report by O'Neil *et al.* (1968), which is a somewhat definitive post-flight analysis, the values deduced for *GM* from Surveyor 1 and 3 are $398\,600.6 \pm 0.6$ and $398\,600.8 \pm 0.7$, respectively; yet in the report by Wong (1968) these values had been revised upward to $398\,601.3 \pm 0.8$ and $398\,601.1 \pm 0.8$ without comment on the reasons for the revision.

(4) And finally, Wong (1968) comments that all the Surveyor determinations were analyzed by using an a priori σ of 1.0 km^3/s^2. Since the standard deviations resulting from the analysis are not significantly lower, the solutions were guided by the a priori information. Thus it is implied that the resultant values were not determined by the data alone but were aided by the somewhat tight a priori information. As a result of these conditions, the Surveyor determinations should be viewed with concern and caution.

Data from Mariner 4, 5, 6, 7, and 9 have been analyzed for *GM*. The results from Mariner 4 and 5 taken from Null *et al.* (1967) and Pease *et al.* (1969) are $398\,601.8 \pm 1.4$ and $398\,601.5 \pm 0.4$, respectively. The error analysis that exists in these reports is more in the nature of verification that the spacecraft will arrive at the target planet within the constraints necessary to ensure a successful mission, as opposed to an analysis of data strictly to determine $GM_\oplus$. Thus at present one must satisfy oneself with a tabulation of results deduced from a navigation or engineering document.

Although the Mariner 6 and 7 near-Earth data have been analyzed, it appears that no effective results are available, as is indicated by the following statement: "Comparison between the uncertainty of the estimate and the input a priori indicates that the data has very little information on the gravitational constant of the Earth" (Gordon *et al.*, 1970, pp. 2–205). With all due respect, a reanalysis of these data has been undertaken to determine quantitatively the sensitivity of the Mariner 6 and 7 data to *GM*.

The analysis of the Mariner 9 data appears in this report and is essentially the same as that presented at the International Symposium on Earth Gravity Models and Related Problems (Esposito and Wong, 1972). Current results (1974) indicate a value in essential agreement with that presented at the symposium.

An analysis of the Pioneer 7 data from *GM* has been reported in the literature and a preliminary result given as $GM = 398\,601.9 \pm 0.6$ (Anderson and Hilt, 1969). The preliminary nature of this result is further emphasized by the fact that the authors of the Pioneer 7 analysis state that the quoted standard deviation ". . . should probably be multiplied by a factor of 3 at this early stage of the analysis of data" (Anderson and Hilt, 1969, p. 104a).

Finally, some relatively recent results are available from the Venera 4, 5, 6, and 7 spacecraft. The results shown in table 4.13 have been taken directly from a similar tabulation in the paper by Akim *et al.* (1972), one column having been omitted. As shown in this table, individual results are available from each spacecraft; however, no corre-

sponding measure of uncertainty is listed. The summarized result is the best estimate of GM from the analysis, and the associated error is identified as the maximum possible error. One notes an inconsistency in the first row of table 4.13. Using the quoted numbers for $\mu_\oplus$ and μ_ζ, one finds $\mu_\oplus/\mu_\zeta$ equals 81.3020, which does not agree with the corresponding entry in the last column.

4.6 SUMMARY

The DSS location determinations reported here were obtained from tracking data from intervals of approximately 2 weeks when the Mariner 4 and 6 spacecraft were closest to Mars and during a like period when Mariner 5 passed by Venus, plus two other periods when the Mariner 5 spacecraft was at low declination. One of these low-declination periods occurred before the closest approach of the spacecraft to the planet Venus and one after. The resultant solutions for the distance off the spin axis r_s are probably accurate to better than ± 1 meter for the Goldstone tracking station; the best determinations for the overseas stations were slightly less accurate, both because fewer tracking data are available for these stations and because high-quality data on corrections for charged particles, such as exist at Goldstone, are lacking. The accuracy of the solutions is reasonably consistent with the accuracy of the r_s solutions when one recalls that two stations are involved, at least one of which is an overseas station with the limitations previously described.

An accurate determination of $GM_\oplus$ can be obtained from the analysis of tracking data from most lunar and planetary missions. Two data sets in particular have been extensively analyzed: the Ranger Block III Missions (Ranger 6, 7, 8, and 9, which were the only lunar missions to be tracked from launch to impact), which yielded $GM_\oplus = 398\ 601.2\ km^3/s^2$ and the near-Earth data of Mariner 9 (a spacecraft headed for Mars), which gave $GM_\oplus = 398\ 600.8\ km^3/s^2$. The Mariner 9 was attractive because the tracking data were obtained sooner after injection than was true for previous planetary missions.

APPENDIX

TABLE 4.1.—*Deep Space Station Locations*

Deep space communications complex	Location	Deep space station (DSS)	Serial designation
Goldstone	California	Pioneer	DSS 11
Goldstone	California	Echo	DSS 12
Goldstone	California	Mars	DSS 14
Canberra	Australia	Woomera	DSS 41
Canberra	Australia	Tidbinbilla	DSS 42
----------	South Africa	Johannesburg	DSS 51
Madrid	Spain	Robledo	DSS 61
		Cebreros	DSS 62

TABLE 4.2.—*Station Locations Using Ionospheric Refraction Corrections IC72–1*

DSS	Data source	Distance off spin axis (km)	Geocentric longitude (deg)	Distance along spin axis[a] (km)	Run ID[b]
12	Mariner 4 encounter	5212.0525	243.194655	3673.763	M4E204-G(DSS 11)
	Mariner 5 cruise	525	553	----------	M5C105-F
	Mariner 5 encounter	529	514	----------	M5E204-G
		523	511	----------	(DSS 14)
	Mariner 5 postencounter	524	594	----------	M5P105-G
		506	603	----------	(DSS 14)
	Mariner 6 encounter	470	528	----------	M6E201-H
		477	526	----------	(DSS 14)
		525	516	----------	LS37
41	Mariner 5 encounter	5450.2015	136.887503	−3302.243	M5E204-G
	Mariner 5 postencounter	2016	580	----------	M5P105-G
	Mariner 6 encounter	1993	488	----------	M6E201-H
		2019	492	----------	LS37
42	Mariner 4 encounter	5205.3504	148.981364	−3674.646	M4E204-G
	Mariner 5 cruise	484	301	-	M5C105-F
		494	264	----------	LS37
51	Mariner 4 encounter	5742.9410	27.6855	−2768.744	M4E204-G
	Mariner 6 encounter	9384	396	----------	M6E201-H
		9400	417	----------	LS37
61	Mariner 5 cruise	4862.6084	355.751001	4114.885	M5C105-F
		90	0989	----------	(DSS 62)
	Mariner 5 encounter	81	0972	----------	M5E204-G(DSS 62)
	Mariner 5 postencounter	73	1063	----------	M5P105-G(DSS 62)
	Mariner 6 encounter	63	1002	----------	M6E201-H
		83	0974	----------	LS37

[a] Not estimated but included for completeness.
[b] Nomenclature in parentheses shows whether the solution was obtained for a different station and transferred by using differences in surveyed values.

TABLE 4.3.—*Location Set 37: DE78, BIH UT1 and Pole, Ionospheric Corrections*

DSS	Radius (km)	Latitude (deg)	Longitude (deg)	Distance off spin axis (km)	Z (km)	X (km)	Y (km)
11	6 372.010 662	35.208 034 7	243.150 585	5 206.340 875	3 673.763	−2 351.429 21	−4 645.079 76
12	6 371.994 953	35.118 657 67	243.194 516	5 212.052 480	3 665.628	−2 350.442 67	−4 651.979 18
14	6 371.993 758	35.244 345 65	243.110 471	5 203.997 795	3 677.052	−2 353.621 05	−4 641.342 59
41	6 372.559 094	−31.211 408 32	136.887 492	5 450.201 884	−3 302.243	−3 978.718 75	3 724.848 67
42	6 371.709 798	−35.219 662 48	148.981 264	5 205.349 415	−3 674.646	−4 460.978 38	2 682.412 05
51	6 375.523 730	−25.739 303 98	27.685 417	5 742.939 970	−2 768.744	5 085.441 737	2 668.265 696
61	6 370.026 548	40.238 900 70	355.750 974	4 862.608 319	4 114.885	4 849.243 171	−360.278 126
62	6 369.967 330	40.263 192 89	355.632 167	4 860.818 070	4 116.908	4 846.700 634	−370.196 262

TABLE 4.4.—*Description of JPL Station Location Sets*

Location set	Description
4	Combination of solutions from Ranger 6, 7, 8, and 9, each of which impacted the Moon; used lunar ephemeris 3, with UT1 from Richmond, Florida, and IPMS polar motion; analysis done in 1966 and 1967 on the SPODP (Warner *et al.*, 1968)
25	Derived by using DPODP (Moyer, 1971); data from Mariner 4 and 5 analyzed by using DE69, Richmond UT1, and BIH polar motion, but with ionosphere calibrations applied; analysis done in 1969
35	Derived by using the SATODP (Moyer, 1971); data from Mariner 4, 5, and 6 analyzed by DE78, BIH polar motion and UT1, the Chao troposphere, and ionospheric refraction corrections IC71–1; analysis was done in 1971 (Madrid *et al.*, 1973)
37	Same basic data as LS35; used improved ionospheric refraction corrections (IC72–1 in place of IC71–1); improved combination technique; analysis done in 1972

TABLE 4.5.—*Data Summary by Mission*

Mission	Number of Doppler data points	Tracking span	Data weight[a] (H_2)	Sun-Earth probe angle (deg)	Declination (deg)
Mariner 4 encounter	362	1965 7/10 to 7/21	0.05	77	−3
Mariner 5 cruise	439	1967 7/28 to 9/16	0.05	35-20-35	−8 to −18
Mariner 5 encounter	759	1967 10/14 to 10/25	0.05	45	6
Mariner 5 postencounter	704	1967 10/28 to 11/21	0.05	43	2 to −2
Mariner 6 encounter	604	1969 7/26 to 7/31	0.08	117	−24
Total	3268	4 hr 30 min			

[a] Data weight for a 60-sec count time point.

TABLE 4.6.—*Timing Relationship and Position of Pole*

	IAT.1–UTC	IAT.1–UT1	UT1–UTC (msec)	UT1–UTC (m)	Pole (m) X	Pole (m) Y
Mariner 4 encounter (15 Jul 65)	4.027	4.020	7	2.8	0.17	14.3
Mariner 5 encounter (19 Oct 67)	6.048	5.946	102	40.8	−0.42	6.58
Mariner 6 encounter (31 Jul 69)	7.635	7.616	19	7.6	3.95	7.15

TABLE 4.7.—*Value of Coefficients C_1 Through C_5*

	L-band	L–S band	S-band
C_1	930.15K	9.375K + 30K_1	96 (240/221)K_8 + K
C_2	31/32	30/96	1
C_3	30 (96/89)	----------	96 (240/221)
C_4	$10^{-1}K$	----------	K
C_5	(96/89) (31/32)	30 (240/221)	96 (240/221)

TABLE 4.8.—*Tracking Station Coordinates*

Station	λ (deg)	r_s (km)	z (km)
DSS 12	243.194 51	5 212.052	3 665.628
DSS 14	243.110 46	5 203.998	3 677.052
DSS 41	136.887 49	5 450.202	−3 302.243
DSS 51	276.853 92	5 742.942	−2 768.744
DSS 62	355.632 16	4 860.818	4 116.908
σ (a priori)	0.000 1	0.010	0.030

TABLE 4.9.—*Nominal Parameters of the Mariner 9 Trajectory*

Parameter	Nominal value	A priori sigma
Epoch	30 May 1971, 22 hr 35 min UTC	---
X, km	−6 053.477	10^6
Y, km	267.767	10^6
Z, km	2 475.587	10^6
X, km/s	−1.997 454	1.0
Y, km/s	−10.747 680	1.0
Z, km/s	−3.388 601	1.0
$GM_\oplus$, km^3/s^2	398 601.20	5.0
$GM_\mathbb{C}$, km^3/s^2	4 902.784	0.05
J_2	$1\,082.628 \times 10^{-6}$	---
J_3	-2.538×10^{-6}	---
J_4	-1.593×10^{-6}	---
$C_{2,2}$	1.558×10^{-6}	---
$S_{2,2}$	-0.881×10^{-6}	---

TABLE 4.10.—*Statistical Characteristics of Data Analyzed*

Tracking station (DSS)	Amount of Doppler data	Tracking interval (hr:min)	Mean residual (μHz)	RMS residual (mHz)
51	628	10:11	−11.5	1.89
62	139	2:22	54.2	1.32
12	202	1:02	(Deleted from analysis)	
14	288	5:14	−64.2	1.40
41	373	6:36	53.7	1.76

Tracking station	Amount of range data	Tracking data interval	Mean residual (ns)	RMS residual (ns)
14	127	4:19	0.084	5.97

TABLE 4.11.—*Influence of Consider Parameters on* $GM_\oplus$ *Determination*

Consider parameter	Assumed uncertainty	Absolute value of change in $GM_\oplus$ (km^{3}s^2)
a_r, a_s, a_w, km/s^2	0.5×10^{-11}	0.06, 0.08, 0.10
Z (DSS 51), m	30.0	0.05
$GM_\mathbb{C}$, km^3/s^2	0.05	0.004
J_2, J_3, J_4	0.5×10^{-7}	negligible
$C_{2,2}, S_{2,2}$	0.5×10^{-7}	0.001, 0.001
Earth orbital elements (Set III)	1.0×10^{-7}	negligible
Moon orbital elements (Set III)	0.12×10^{-5}	negligible
Astronomical unit, km	3.0	negligible

TABLE 4.12.—*Earth's Gravitational Constant Determined From Spacecraft Data*

Spacecraft	$GM_\oplus \pm$ standard deviation (398 xxx.xx km^3/s^2)	Reference
Ranger 3	601.63 ± 2.5	(a, b)
Ranger 4	601.87 ± 13.3	(b, c)
Ranger 5	599.20 ± 13.2	(b)
Ranger 6	600.69 ± 1.1	(d, e)
Ranger 7	601.34 ± 1.5	(e, f)
Ranger 8	601.14 ± 0.7	(e)
Ranger 9	601.42 ± 0.6	(e, g)
Combined Rangers (6, 7, 8, 9)	601.20 ± 0.7	(e, h)

[a] Sjogren, 1962.
[b] Sjogren *et al.*, 1963.
[c] Hamilton *et al.*, 1962.
[d] Sjogren *et al.*, 1964.
[e] Sjogren *et al.*, 1966.
[f] Wallenhaupt *et al.*, 1964.
[g] Vegos *et al.*, 1968.
[h] Vegos and Trask, 1967.

TABLE 4.13.—*GM Deduced From Venera 4, 5, 6, and 7 Data*

Data span	$\mu_\oplus$ (km^3/s^2)	μ_ς (km^3/s^2)	$\mu_\oplus/\mu_\varsigma$
Before and after trajectory correction:			
Venera 4, 5, 6, 7	398 600.37	4902.716	81.3005
Venera 4	398 600.89	4902.806	81.3006
Venera 5	398 600.26	4902.702	81.3022
Venera 6	398 600.72	4902.638	81.3033
Venera 7	398 599.45	4902.808	81.3002
Venera 5, 6	398 600.57	4902.682	81.3026
Before trajectory correction:			
Venera 5	398 599.72	4902.717	81.3018
Venera 6	398 600.73	4902.642	81.3033
Summary	398 600.37±1.0	4902.716±0.10	

5

NASA GODDARD SPACE FLIGHT CENTER

J. H. Berbert
J. Brownd
T. Felsentreger
D. Harris
T. S. Johnson
M. A. Khan
F. Lerch
J. Marsh
J. Murphy
B. Putney
J. Reece
J. Richardson
M. Sandson
P. Schmidt
D. Smith
S. Vincent
C. Wagner

5.1 INTRODUCTION [1]

The contribution of Goddard Space Flight Center (GSFC) to the National Geodetic Satellite Program (NGSP) is marked by its breadth and diversity. Goddard developed and operated all of the major types of tracking systems, including those using optical, electronic range-and-range-rate, and laser technologies. Even the MINITRACK data were used to derive geodetic results.

The methods used at GSFC for the analysis of these data also reflected an unusual diversity. For example, general-perturbation methods were used to determine resonances. Special perturbations were also used for this purpose, as well as for gravimetric geodetic studies. Numerical integration was used mainly to obtain the general simultaneous solutions for the gravitational potential coefficients, locations of tracking stations, and the Earth's equatorial radius. Numerical integration was also used in the studies of polar motion, distances between stations, and solid-Earth tides.

The types of data employed in the solutions were similarly varied. Observations of some two dozen satellites by Baker-Nunn cameras gave much of the strength to the general solutions. The MINITRACK optical tracking system (MOTS) cameras obtained observations of the flashing lights on the satellites known as GEOS 1 and 2 and of the lights on PAGEOS and ECHO, which were especially useful in the geometric geodetic studies. Electronic range-and-range-rate observations of medium-altitude satellites were useful in helping to fix scale and in evaluating resonance terms associated with their orbits. Range-and-range-rate observations of synchronous satellites formed the basis for strength in the solutions for low-order harmonics. MINITRACK observations of nearly resonant orbits were also used to obtain better values of the corresponding terms of gravitational field representation. Scale was fixed more accurately by the laser system range measurements. In the later stages of the NGSP analyses, the satellite data were blended with surface gravimetry in the general solutions for the geopotential and site locations.

Perhaps the most important use of the data from the laser systems was the determination of polar motion, distances between sites, and solid-Earth tides, since these studies played a key role in pointing the way to the NASA Earth and Ocean Physics Applications Program (EOPAP). The interpretation of the geodetic results in terms of geophysical phenomena, such as those associated with plate tectonics, is another important aspect of the applications program that has been pursued at GSFC.

5.2 INSTRUMENTATION

In its development of satellite-tracking systems, GSFC had to consider two objectives at the same time. The primary objective was to keep track of the satellites by computing orbits from the tracking-system data, and it was for this purpose that PRIME MINITRACK, NASA's first tracking system, and the Goddard range-and-range-rate system (GRARR) were developed. (PRIME MINITRACK is discussed in sec. 5.2.2.2 and GRARR is discussed in sec. 5.2.2.3.) However, this objective could not stand alone:

---

[1] Chris Massey, of Computing and Software, Inc., was responsible for setting up and executing the many computer runs in the study presented in section 5.6.3.9. Her able assistance is gratefully acknowledged.

The work described in section 5.6.3.10 was undertaken by Ronald Kolenkiewicz, James G. Marsh, and Joel Mashbaum of Goddard Space Flight Center, and Bruce C. Douglas, Peter J. Dunn, Steven M. Klosko, and Ronald G. Williamson, of Wolf Research and Development Corporation, Riverdale, Maryland, in addition to the author.

Unless the tracking-station locations were known accurately, the orbits themselves would contain errors. A secondary objective was therefore adopted: To correct the poorly known coordinates of the observing stations. A third objective, similar to the second, was to calibrate accurately the tracking systems themselves, since errors in the calibration constants also affect the orbits.

The first and third objectives had the greatest effect on development. PRIME MINITRACK was an electronic all-weather system accurate enough to keep track of satellites but not accurate enough for other purposes such as geodesy. Also, the system was difficult to calibrate by using natural radio sources. To solve the calibration problem, the MOTS camera (sec. 5.2.2.1) was developed. Placed at the center of the PRIME MINITRACK array (sec. 5.2.2), it photographed a flashing beacon carried by an airplane flying in the near field of the system. Experience with the camera showed that it gave sufficiently accurate measurements to allow it to be used as a geodetic tool for finding the positions of PRIME MINITRACK, and the design of the camera was therefore modified to give it geodetic capabilities.

Neither of the other systems, GRARR and laser distance-measuring equipment (DME), posed any particular problems in their calibration and were in fact of sufficient accuracy (the laser DME, particularly) that they, like the MOTS cameras, could be used geodetically.

It should be remembered that an indispensable part of every tracking system is the satellite. The MOTS camera can be used for tracking any satellite that is sufficiently bright, but PRIME MINITRACK can observe only those satellites carrying a MINITRACK beacon (about 136 MHz) and GRARR requires a suitable transponder in the satellite. In theory, laser DME can track any satellite reflecting enough light back to the receiving telescope, and satellites have been tracked this way in experiments. In practice, however, laser DME is used only on satellites carrying corner-cube reflectors. Descriptions of the geodetically important satellites carrying corner-cube reflectors are given in chapters 2 and 9. The satellites carrying transponders for GRARR (GEOS 2 and 3) are described in chapter 2. (The satellites carrying MINITRACK beacons are too numerous to describe.)

A great many observations were made by the MOTS cameras on flashing beacons carried on satellites ANNA 1B, GEOS 1, and GEOS 2. These lights are described in chapter 3.

Three satellites, ECHO 1, ECHO 2, and PAGEOS, were not extensively observed by NASA for geodetic purposes but were the basis for NGS's entry into an observational program. (Of these, PAGEOS was by far the most important.) These satellites were constructed by NASA; they are described in the following text. The four principal tracking systems used by GSFC for geodetic purposes —the MOTS–40 camera systems, PRIME MINITRACK, GRARR, and laser DME—are described next. NASA also has a number of 5-cm pulsed radars that have been used geodetically. These are described in chapter 6.

5.2.1 Satellites

(Søren W. Henriksen)

5.2.1.1 ECHO Satellites

The idea of using balloon-like satellites for reflectors in communications networks, for investigation of atmospheric densities, and as beacons in geodetic projects was conceived by J. O'Sullivan of NASA/Langley. It was put into effect on 12 August 1960 with the launching of ECHO 1, a balloon 30 meters in diameter (see table 5.1). It was sent into orbit neatly folded up, but was inflated after ejection from its container. The method of inflation was as follows. The sphere was carefully folded and placed in its container under low pressure to avoid entrapping air between the folds, since this air might cause damage to the sphere during inflation. As an added precaution against these air pockets, the sphere was punctured by 243 holes $\frac{1}{16}$ inch (1.59 mm) in diameter.

To provide enough pressure to inflate the sphere after it was in orbit, 10 pounds (4.5 kg) of benzoic acid powder and 9 pounds (4 kg) of anthraquinone were placed in the sphere. The benzoic acid sublimated to furnish the initial pressure necessary to inflate the sphere. The anthraquinone, which has a lower vapor pressure, was used to maintain a sufficient pressure to keep the sphere inflated for approximately seven days, assuming an equivalent micrometeorite impact aperture growth of 1.4 inch^2 (0.22 mm^2) per day. The success of this satellite led to the launching on 25 January 1964 of a similar satellite, ECHO 2, which was 41 meters in diameter (table 5.2). Both satellites carried MINITRACK beacons (sec. 5.2.2.2) located at diametrically opposite points on the surface. Figures 5.1 and 5.2 show the structure of ECHO–2.

5.2.1.2 PAGEOS

PAGEOS (table 5.3) was launched on 24 June 1966. It was very similar in size and structure to ECHO 1, but lacked the two MINITRACK beacons. Because its purpose was entirely geodetic, the satellite was placed at 4250 km, high enough to allow it to be seen simultaneously by observers 2000- to 3000-km apart at optimum distances from the zenith. Figure 5.3 shows the launching and inflation of PAGEOS. The description below was given by J. Rolff (1966).

The SAO Baker-Nunn camera at Olifantsfontein, South Africa, took pictures first

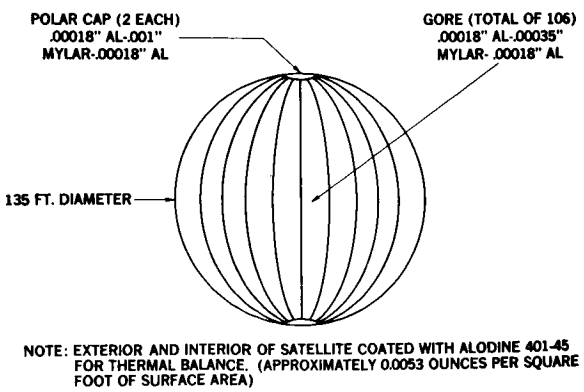

FIGURE 5.1.—Echo inflated balloon.

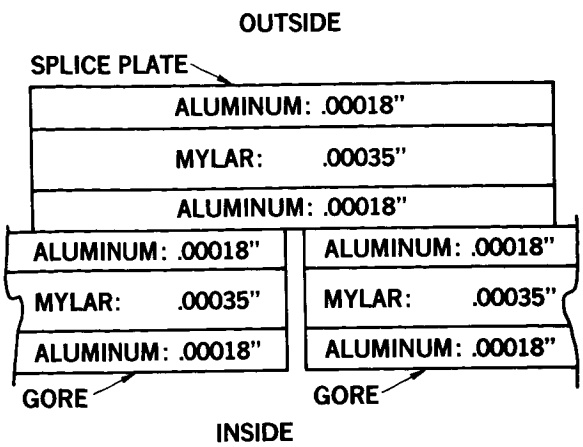

FIGURE 5.2.—Balloon fabrication detail.

of the ignition of the Agena rocket booster/payload combination, and then of the thrust buildup prior to separation of the payload, of the separation itself, and finally of the balloon inflation. Times are Universal Time. The camera was tracking along a great circle across the sky at the same angular velocity as the satellite. Stars are represented by shutter-broken trails. The satellite was about 4200 km above the Earth during this event.

The reflected sunlight from the satellite surface is a function of the camera-satellite-Sun angle, or phase angle Ψ. For a 0 degree phase angle, the diffuse component accounts for about 8 percent of the light reflected toward the observer. As the phase angle increases, the diffuse component diminishes according to the formula given in figure 5.4. The phase factor $F(\Psi)$ is unity for $\Psi=0$ degree, $1/\pi$ for $\Psi=90$ degrees, and 0 for $\Psi=180$ degrees. With a 30-degree camera elevation angle and the Sun 18 degrees below the horizon, the phase angle may vary from 12 degrees minimum to 132 degrees maximum and result in a variation of the diffuse component from 8 to 0.5 percent of the total reflected light.

5.2.2 Tracking Stations

Tracking stations are the ground half of a tracking system, the other half being the

satellite. (The satellite portion is discussed in chapters 2 and 3, and the orbital characteristics are summarized in table 1.10.) The tracking station portion as designed and used by GSFC is described in the following text.

As mentioned earlier, the primary responsibility and interest of GSFC was to determine orbits, and its tracking stations were designed primarily with this in mind and only secondarily with a view to geodetic use. This was definitely true of PRIME MINITRACK (sec. 5.2.2.2) and GRARR (sec. 5.2.2.3), and its was also true of the MOTS camera (sec. 5.2.2.1) which was developed first as an instrument for calibrating PRIME MINITRACK. The laser DME (sec.

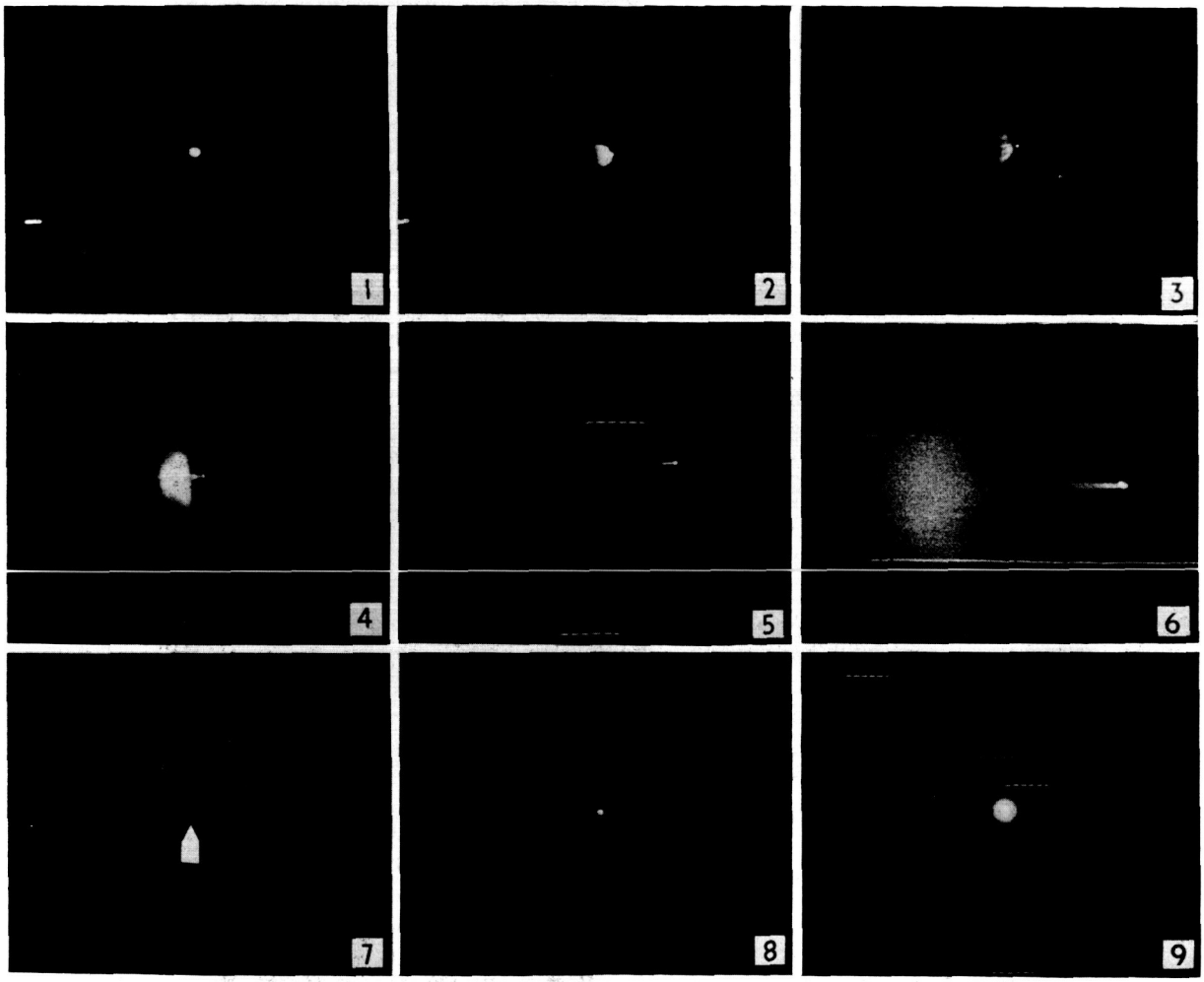

FIGURE 5.3.—Launching and inflating of PAGEOS as photographed by Baker-Nunn camera. Frame 1: $01^h24^m37.5557^s$; the first frame that gives an indication of Agena ignition; exposure time, 0.4 sec. Frame 2: $01^h24^m39.5557^s$; thrust buildup; exposure time, 0.4 sec. Frame 3: $01^h24^m41.555^s$; thrust buildup; exposure time, 0.4 sec. Frame 4: $01^h24^m59.5554^s$; the bright central cone of the rocket exhaust cloud, as well as the hemispheric outer cloud, is distinct; exposure time, 0.4 sec. Frame 5: $01^h25^m51.0551^s$; exhaust cloud had moved away from the rocket and was beginning to expand; exposure time, 1.6 sec. Frame 6: $01^h26^m14.2093^s$; this longer exposure time of 13.2 sec reveals more detail in the exhaust cloud structure. Frame 7: $01^h27^m45.5266^s$; the tiny dot is the image of the PAGEOS balloon satellite after it had achieved orbit, but before the inflation process had begun; at this point the satellite was of magnitude +8; exposure time, 0.4 sec. Frame 8: $01^h27^m55.5268^s$; partial inflation; the unfolding balloon is estimated at a stellar magnitude of +4 in this frame; exposure time, 0.4 sec. Frame 9: $01^h28^m01.5268^s$; the satellite had reached full inflation by this time; the halo is caused by the extreme brilliancy of the satellite, a +2 stellar magnitude.

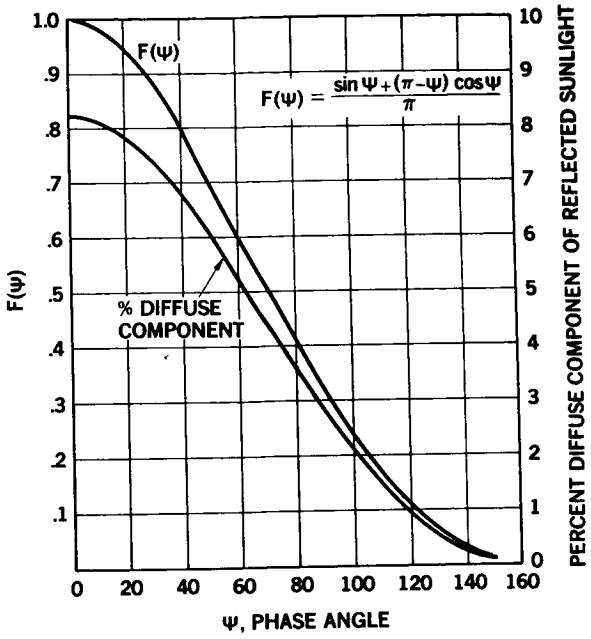

FIGURE 5.4.—Diffuse sunlight reflected from PAGEOS as a function of phase angle.

5.2.2.4) was developed for very precise tracking, although its geodetic application was certainly considered in the design. The line of development was nearly linear. PRIME MINITRACK came first, MOTS was developed as an adjunct to it, GRARR was developed for more accurate tracking of satellites at greater distances than PRIME MINITRACK could handle, and the laser DME was developed to increase accuracy still further. (It is interesting to note how optical instrumentation has alternated with electronics in the sequence.)

Accuracy of measurement was an extremely important factor in GSFC's development of its tracking systems. But the accuracy of an instrument is a function not only of its design but also of the way the measurements made by the instrument are tied to the true values of the quantity being measured; i.e., of the way the instrument is calibrated (see, e.g., ch. 1). Since an uncalibrated system is useless if accuracy is needed, the calibration constants of a system are as important and indispensable to the system as the power supply and the timing subsystem. The calibration procedures are hence described along with the system itself. But it is difficult, in the NGSP at any rate, to separate the calibration of the systems from their evaluation as carried out by GSFC and Wallops Flight Center. (For further insight into the problems of calibration, see section 6 of this chapter, and chapters 6 and 11.)

5.2.2.1 MOTS Camera System

(D. Harris)

The MOTS–40 camera, shown in figure 5.5, utilizes an $f/5.0$, 40-inch (1-meter) focal-length lens system previously used in the K–22 aerial reconnaissance cameras. The camera, equatorially mounted and sidereally driven, provides images of tenth-magnitude stars with exposures of 35 seconds on Kodak spectroscopic glass plates. The original design of the plateholder provided an 11-degree by 14-degree field of view on 8- by 10-inch plates 0.060 inch thick. (A 24-inch (610-mm) focal length camera was also built, but had little use. It was designated the MOTS–24.)

In this original form, the camera was installed at each MINITRACK site for the purpose of calibrating the electronic tracking equipment. An airplane carrying a transmitter and a xenon lamp that flashed in a time-coded sequence flew through the tracking beam of the antennas on a clear night. The light was photographed against the stellar background by comparing the positions of the flashing light relative to the star background with positions determined by the electronic tracking system to obtain a calibration. Since the accuracy of the MINITRACK system is approximately 20″, a camera system with an accuracy of about 2″ was deemed sufficiently accurate for calibration (Harris *et al.*, 1963).

In May 1960, the cameras were modified for the purpose of tracking the brighter satellites (sunlight-illuminated). By 12 August 1960, the launch date of the ECHO balloon-satellite, the new MOTS system was ready to provide useful data on the positions of the satellite.

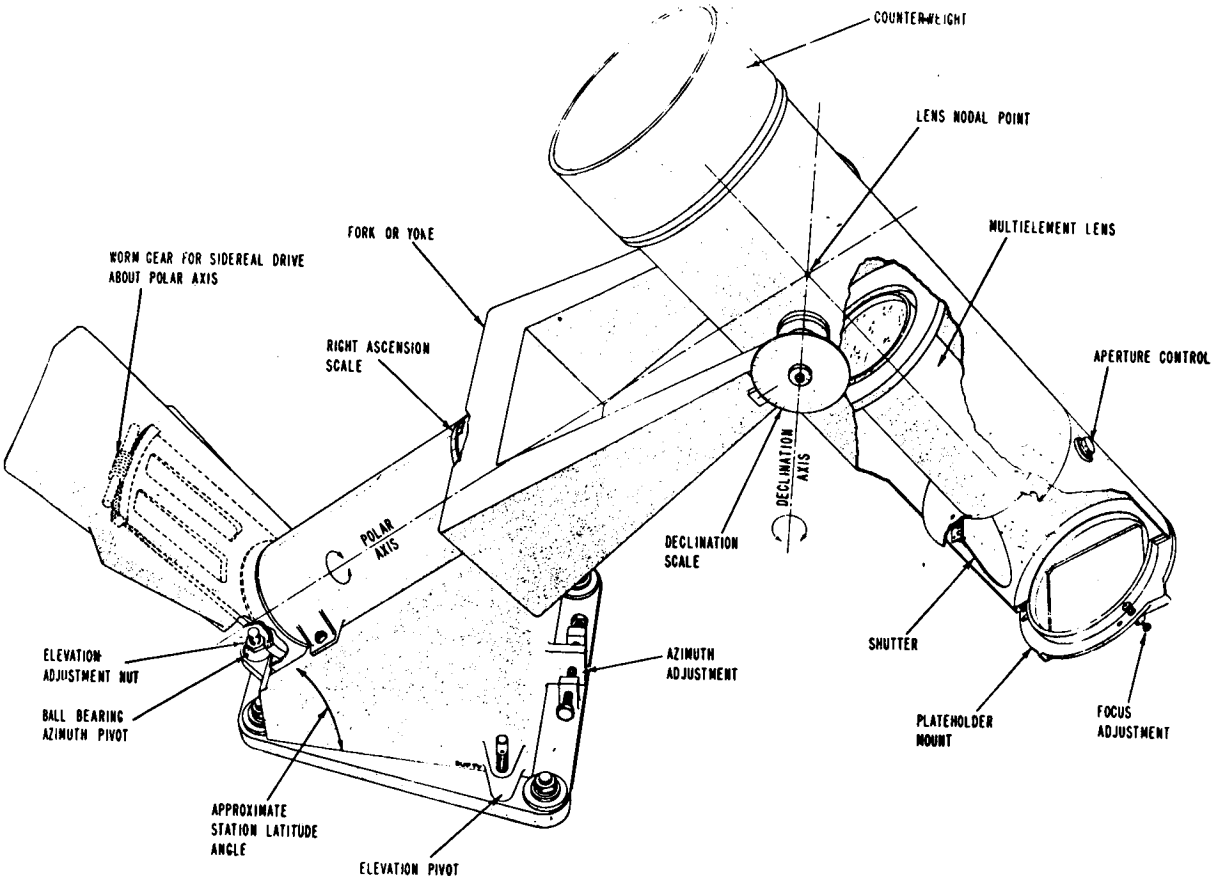

FIGURE 5.5.—The MOTS–40 astrographic camera.

To adapt the camera for tracking, a solenoid assembly was attached to it, and a special plateholder was designed to allow lateral motion of the plate when pushed by the solenoid. By means of an electronic circuit, the heart of which is a one-shot multivibrator, a time-coded pulse was taken from a digital clock, activating the solenoid and moving the spring-loaded photographic plate approximately 0.5 mm for the duration of the pulse. The time code was thus inscribed to identify breaks in the trail of the passing source. By maintaining the solenoid-pulse duration at 30 per cent or less of the timing interval between successive pulses, two images of each star were formed which were easily identifiable. By measuring the positions of the breaks in the trial with respect to the star background, the position of the source at the time of each break in its trail could be determined.

The sidereal drive is started by applying a precise 60-cycle signal to a reversible, 1-rpm synchronous motor. The 60-cycle frequency standard supplying 120 volts to the motor is accurate to $\pm 1 \times 10^{-6}$ Hz, and the motor will operate at the proper frequency with voltages as low as 90 volts. The motion is transmitted through the gear train, terminating at a worm gear. This worm gear, rotating at one revolution every 89.753 seconds, in turn meshes with a gear sector of 27 degrees. This sector was manufactured on the basis of 2-⅔ teeth per degree. Thus, in 24 hours of tracking (assuming a full 360-degree gear), the camera lags behind the stars by 1.46 seconds, resulting in a delay of 0.″9125 per hour for stars at the celestial equator.

Since exposure times are generally limited to less than 2 minutes (35 seconds for a satellite such as GEOS 1 or GEOS 2), the error introduced is no more than 0.″03.

The above description assumes the perfect meshing of perfect gears, which does not occur in the MOTS camera. Analysis of the drive system reveals that at all stations a periodic oscillation of the order of 90 seconds exists in the drive. The peak amplitudes in right ascension vary between ±2″ and ±4″ at the equator for the camera systems tested.

The effect of this oscillation must be considered in view of the procedure employed in photographing a satellite. For a flashing satellite such as GEOS 1 or GEOS 2, the exposure time is limited to 35 seconds, beginning 5 seconds after the exposure starts. Differences in results are obtained for the flashing light positions when the exposure begins at different points in the drive cycle. For the worst-case condition, the beginning and end flash points exhibit the maximum error of ±2″. For some stations tested, this value may be as much as ±4″ or at little as ±1″.

Operations on passive satellites such as PAGEOS require exposures of 60 to 120 seconds and cover more closely the full drive cycle: They thereby tend to provide an average displacement close to 0″ for star images. For the broken trail of the satellite, the displacements will approximately equal the error introduced by the cyclic nature of the grear train and result in errors of 0″ to 3″ for the average camera.

As indicated previously, the original plate-holder provided an 11-degree by 14-degree field of view on the 8×10 inch (14-cm by 25-cm) glass plates. In preparation for photographing the GEOS satellites, a new modification was made to lay the plate emulsion against the focal plane of the camera. Accordingly, the new field of view recorded onto the plate was changed to a 10-degree circle. Also during the operation, a set of four fiducial marks was photographed onto the plate to aid in reduction.

Calibration of MOTS Cameras (Søren W. Henriksen).—Various methods have been used for calibrating the MOTS cameras. When the camera was used for calibrating PRIME MINITRACK, the astrometric method was used (ch. 1). When the camera was used for photographing satellites, either the astrometric method or the photogrammetric method was used (ch. 7). Both methods were reasonably similar to those used by the other NGSP participants. A GSFC document (X–514–71–19, 1971) describes the methods in detail and compares their usefulness for NASA's purposes.

5.2.2.2 PRIME MINITRACK
(P. Schmidt)

PRIME MINITRACK is an interferometer (Mengel, 1956; Watkins, 1969) that provides direction cosines describing the position of a beacon relative to a given tracking station. The beacon transmits at a nominal 136 MHz. No ranging information is available, and at present no attempt is made to utilize the available one-way Doppler frequency for calculation of range-rate. The relationships between direction cosines and the conventional definitions of azimuth and elevation are given in figure 5.6. The calculated direction cosines do not provide a measure of either elevation angle of arrival or elevation of the spacecraft but rather an elevation angle between the two which, to a first order, is the angle of arrival corrected for tropospheric refraction.

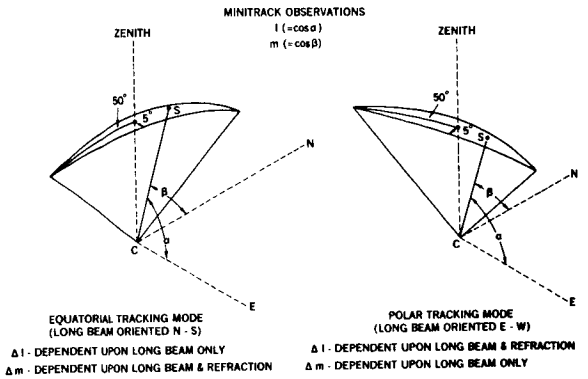

FIGURE 5.6.—Dimensions of fine beam of 136–MHz MINITRACK antenna array.

Typical resolution of the MINITRACK system is 0.1 mrad (20″). Figure 5.7 shows the layout of the antennas and figure 5.8 shows the internal workings of the system. The method by which phase differences are converted to direction is described by Watkins (1969) as follows.

> The electronics of the MINITRACK system divides the 360 electrical-degree phase-measurement into 1000 parts of 0.36 electrical degrees each. This measurement represents the upper precision limit of the equipment. If it is assumed that the fine-beam baseline is approximately 100 meters [see figure 5.9], the resulting accuracy in terms of space angle can be estimated approximately by the following procedure. The direction cosine l (considering the east-west baseline) is related to the electrical phase angle by the equation

$$l=\cos\alpha=\frac{d}{B}=\frac{n\lambda}{B}=\frac{\phi}{2\pi}\frac{\lambda}{B}$$

where

ϕ = electrical angle in radians
λ = signal wavelength $\cong$ 2.2 meters at 136.555 MHz
B = antenna separation or base-line length $\cong$ 100 meters
d = phase difference in linear measure
n = phase difference in number of wavelengths of signal

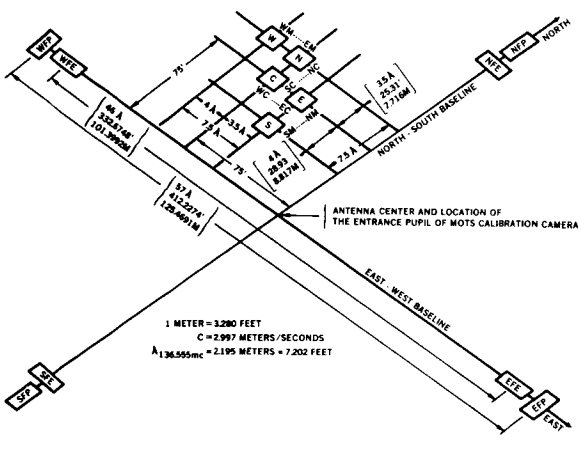

FIGURE 5.7.—Prime MINITRACK antenna layout.

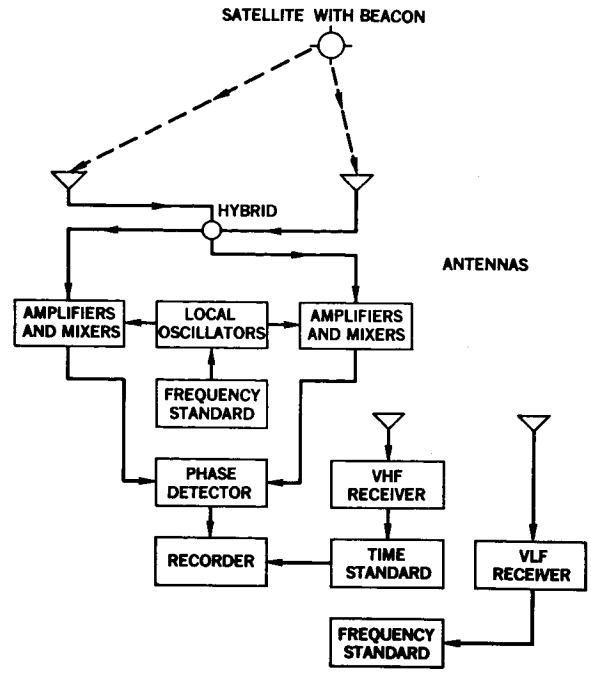

FIGURE 5.8.—Prime MINITRACK structure.

If ϕ is measured in degrees, the equation becomes

$$l=\cos\alpha=\frac{\phi}{360^\circ}\frac{2.2}{100}$$

To find the error in l and α,

$$\Delta l=-\sin\alpha\Delta\alpha=\frac{2.2}{360\times100}\Delta\phi$$

$$=\frac{2.2}{3.6}\times10^{-4}\Delta\phi$$

Calibration of PRIME MINITRACK (Søren W. Henriksen).—In the very early days of PRIME MINITRACK, J. A. O'Keefe suggested that the system might be calibrated in the same way that camera-type tracking systems are calibrated—by using celestial objects of known direction to establish the direction reference system of the system. Of course, using the visible stars as a reference was out of the question, but a small number of radio stars (also called radio sources or radio objects) had recently been discovered and their directions measured.

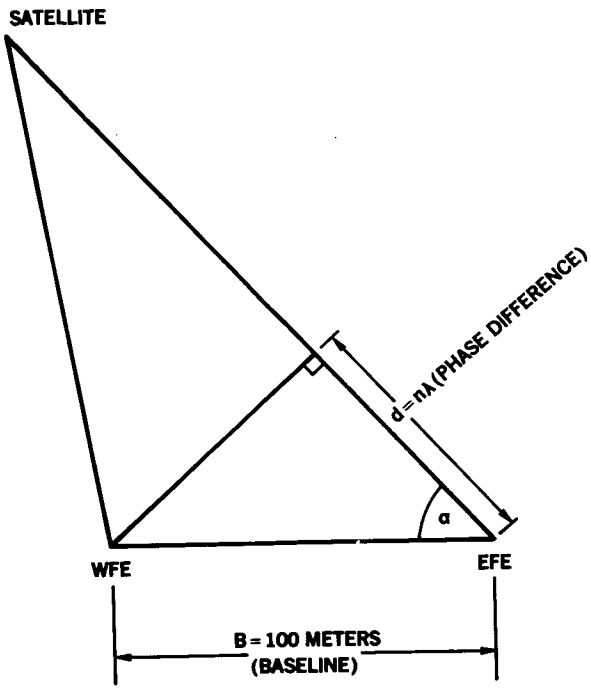

FIGURE 5.9

If the data that are now available on radio stars had been available then and if the Sun had been a little quieter, the method probably would have worked. As it was, the method had to be given up, with recourse taken to a more expensive and cumbersome method that used a radio transmitter (beacon) carried about the antenna field in an airplane (see, e.g., Kahn, 1957; Harris *et al.*, 1963; Berbert *et al.*, 1963.)

The direction of the beacon is found by photographing a flashing light attached near the beacon against a stellar background. The same technique is used in reducing the plates and data as in reducing the photography of artificial satellites. The same camera, the MOTS, is in fact used for both calibration and satellite tracking. It is located at the intersection of the fine-array base lines (see above), this point being assumed to be the electrical center of the arrays. The differences between the direction cosines found photographically and the direction cosines found by PRIME MINITRACK constitute the calibration constants for that MINITRACK.

A few minor points may be mentioned. First, the flashing light is considerably closer to the observer than a satellite is. The correction to be made for parallactic refraction is correspondingly greater. Second, the radio beacon used for calibration is much closer to the antenna arrays than a radio beacon in a satellite and the radiation pattern close to the arrays is different from the pattern at great distances. This circumstance must be considered in the calibration. Third, the measured phase-difference depends not only on the geometric arrangement of the antennas, but also on the length and temperature of the connecting cables, on the condition of the receiver circuits, and on other factors. A calibration constant therefore does not really remain constant but changes slightly with temperature and time. The correction for temperature of the cables is given by Watkins (1969). The corrections for other changes with time have not been fully determined.

5.2.2.3 Goddard Range and Range Rate System (GRARR)

(P. Schmidt *et al.*)

GRARR (also known as GRRR, GRR, or Gr/R) measures phase and rate of change of phase. These quantities are easily converted into distance and rate of change of distance. Figure 5.10 is a block diagram showing how GRARR functions. (The specifications for GRARR are given in table 5.4.) A carrier is modulated by frequencies corresponding to wavelengths of from 1.874×10^6 meters to about 3000 meters. The modulated wave is sent to a transponder (fig. 5.11) in the satellite, where it is shifted in frequency (but not in phase) and sent back to the receiving station. There, the carrier is demodulated and the phases of the modulating waves are compared with the phases of the transmitted waves. The phase differences translate directly into distances:

$$d_f = \frac{c}{f}\frac{\Delta\phi}{2} \qquad (5.1)$$

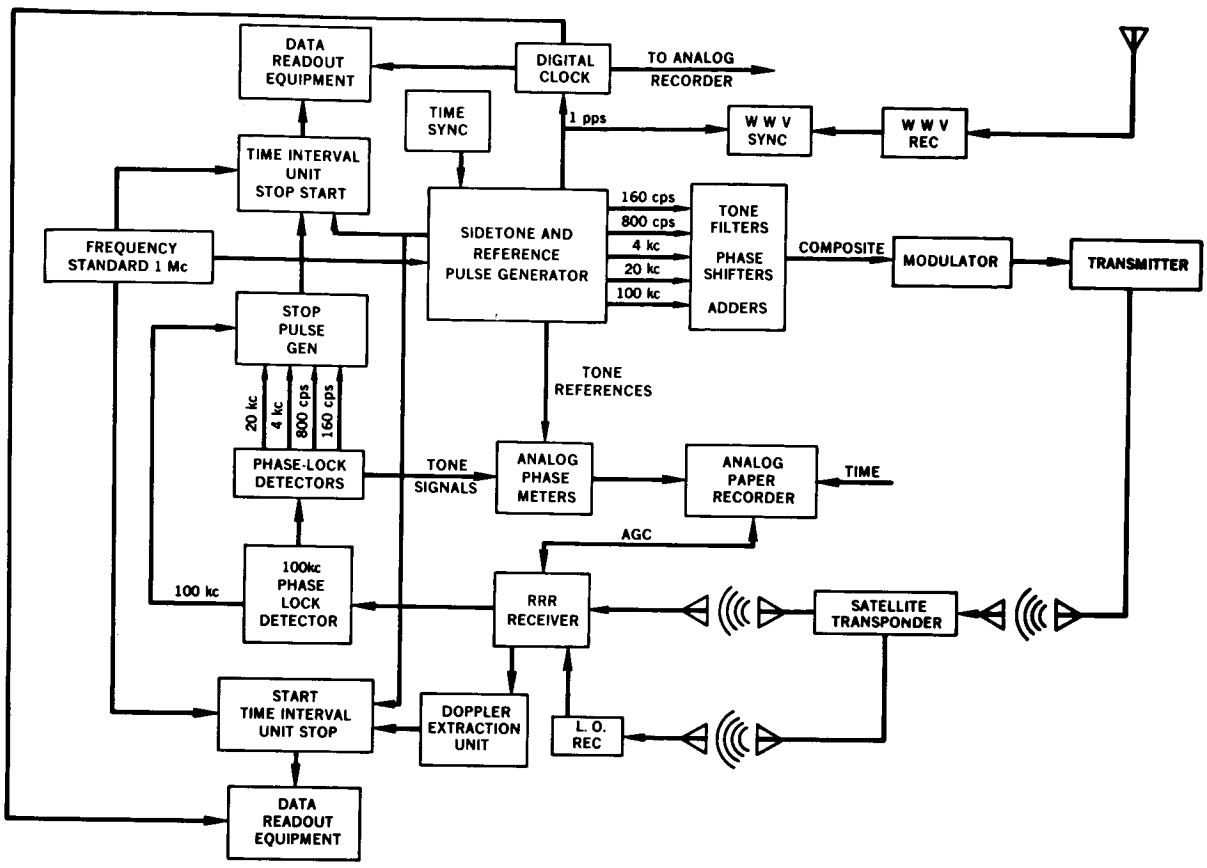

FIGURE 5.10.—Generalized diagram of GRARR.

where d_f is the distance corresponding to frequency f at which phase difference $\Delta\phi$ is measured.

The frequency shift Δf caused by motion of the transponder with respect to the receiver on the ground is measured on the carrier frequency. Operation of the system in terms of frequency-measuring is shown in figure 5.12.

The range measurement is based on the measured propagation delay as evidenced by the zero crossings of the phase-delayed ranging tone. As usual, the assumption is made that the signal time-delay or phase shift is equal for transmission from the ground to the vehicle and from the vehicle back to the ground. The total two-way time-delay is equal to the total number of full cycles that the lowest ranging tone is shifted plus the relative incremental phase-shift of the tone as measured at the ground. This measured time-delay includes, of course, such delays as those in the cable or wave guide as well as the time-delay in the transponder. Thus, the one-way range measurement is given by

$$R=\frac{c}{2}\left[\frac{N}{F_L}+T_R-T_T-T_B\right]\text{km} \qquad (5.2)$$

where R is the range, c is the speed of light equal to 2.997925×10^5 km/sec, N is the number of full cycles of phase shift at the lowest sidetone frequency F_L (usually, $F_L=$ 8 Hz), T_R is the incremental time-difference as measured at the ground receiver, T_T is the delay in the transponder, and T_B is the delay in ground instrumentation.

The ambiguity represented by N/F_L can be resolved by computing an orbit. The time associated with this range, Universal Time Coordinated (UTC), is the measured time

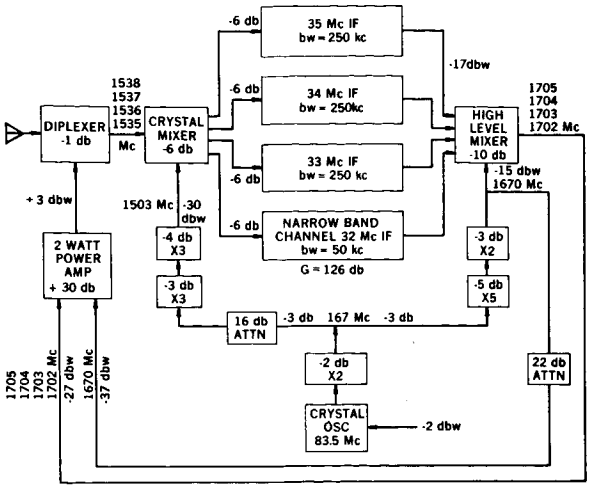

FIGURE 5.11.—Transponder for GRARR.

corrected for propagation time. The time is presented as day of year, hours, minutes, and seconds to the nearest microsecond.

In the GRARR system, there is a raw-data frame time, T_F, followed by four frames of data at a rate T_{DR}. The appropriate time for subsequent frames is therefore given by

$$T_S = T_F + kT_{DR} \text{ sec} \qquad (5.3)$$

where T_S is the frame time, T_F is the basic frame time, T_{DR} is the data rate, and $k = 0,1,2,3,$

It should be noted that the time T_S is associated with the positive-going zero crossing of the lowest-ranging frequency just prior to an incremental time-delay T_R. The time relationships are indicated in figure 5.13. The time T_S corresponds to the time that all transmitted range-tones pass upward

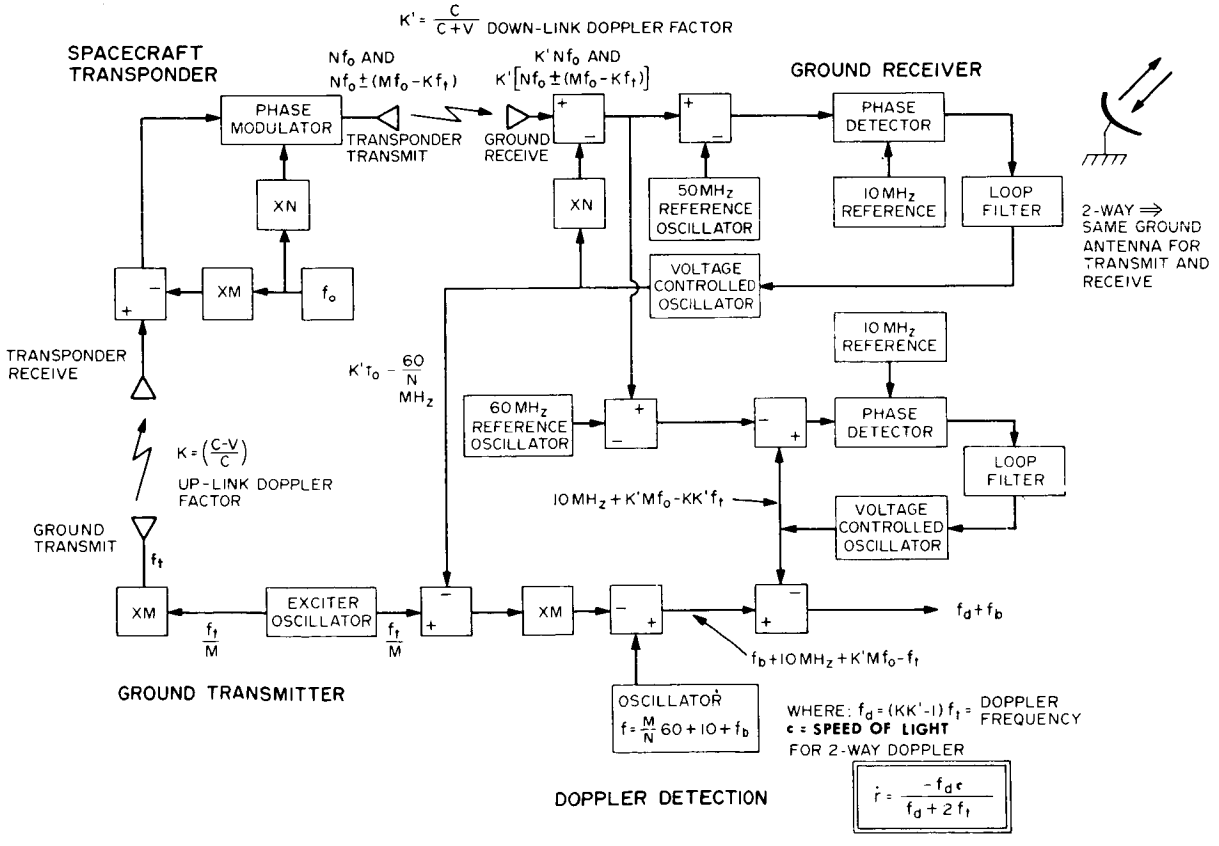

FIGURE 5.12.—Doppler tracking by GRARR.

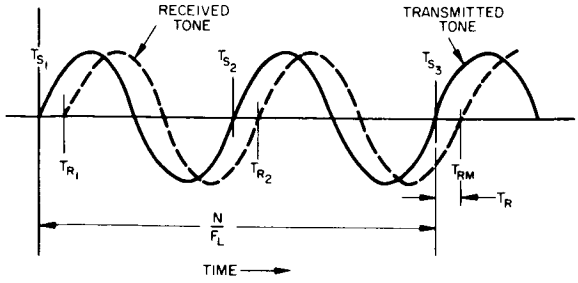

FIGURE 5.13.—Timing in GRARR.

through zero. The ground time of measurement, which is not influenced by ambiguity, is given by

$$T_{RM}=T_S+T_R+T_W \qquad (5.4)$$

where T_{RM} is the range time tag (ground measurement time) and T_S is the frame time, (T_W is the time increment corresponding to the difference between the transmitted and received sidetone frequencies.)

For tracking data recorded after November 1968, correction for propagation time has been made at the station.

GRARR Range Rate.—The overall electronics of the GRARR system are such that it is equivalent to having a coherent transponder with a turnaround constant of $k=1$ (see fig. 5.12). The formula for $\dot{r}_s$ is

$$\dot{r}_s=-\left(\frac{\frac{\Delta N}{\Delta T}-f_b}{\frac{\Delta N}{\Delta T}-f_b+2f_t}\right)c=\frac{-f_d c}{f_d+2f_t}\text{km/sec} \qquad (5.5)$$

where

- $\dot{r}_s$ is the average range-rate
- c equals 2.997925×10^5 km/sec
- f_b is the inserted bias
- ΔN represents a fixed number of counted cycles
- ΔT is the time required to count ΔN cycles in the form of number of cycles of a reference frequency
- f_g is the transmitter frequency (both S-band and VHF are used)
- f_d is the average Doppler frequency shift

The time associated with the range rate is UTC (ground measurement time) corrected for propagation delay and referred to the center of the count interval. Note that the Doppler count ΔT starts at T_S (figure 5.13). The time, T_{RM}, is therefore given by

$$T_{RM}=T_S+\frac{\Delta T}{2}+T_W \qquad (5.6)$$

where ΔT is the measured Doppler interval required to accumulate ΔN cycles of phase change from the carrier.

Calibration and Evaluation of GRARR (Søren W. Henriksen).—GRARR is calibrated in the same way as other phase-measuring types of distance-measuring equipment. The transponder is mounted on, but well off from, a high tower at a suitable surveyed distance from the tracking equipment. The distance to the transponder is measured by the tracking system and compared with the distance already known from survey. The difference between the two gives the calibration constants that concern time-distance properties of the system. Determination of the other constants is more difficult and problematical.

The equation giving the correction to the measured range r is, as a function of the calibration constants (a_i),

$$\Delta r=a_1+a_2 r+a_3\frac{dr}{dt}+a_4\frac{d^2r}{dt^2}+\frac{a_5}{r}\frac{dr}{dt}+a_6\sec\zeta$$

where ζ is the zenith distance.

Using data from measurements made on 30 passes of GEOS–1 by various camera systems and the GRARR, Lerch *et al.* (1969) evaluated the performance of the GRARR at Rosman, North Carolina. The results for the A-channel of the system were (table 5.4)

$\sigma_a = \pm 10.3$ meters and $\sigma_t = \pm 0.004$ second, where σ_a and σ_t are the standard deviations in range and time, respectively.

The equation assumed for the range was

$$R_{TRUE} = R_{OBS} + \epsilon_a + \frac{dR}{dt}\epsilon_t + 3 \sec \zeta + b - 9.7$$

where b is a constant and ϵ_a and ϵ_t are constant or slowly changing over long periods. The data from cameras were used to establish the orbit from which distances were taken to compare with the GRARR data.

5.2.2.4 GSFC Laser DME

(T. S. Johnson, NASA/GSFC)

The instrumentation may be divided into three major subsystems: (1) tracking pedestal and receiver optics, (2) laser transmitter, and (3) ranging and data-control subsystem. These are connected to form a digitally controlled optical radar system capable of tracking reflecting satellites (fig. 5.14).

The laser transmitter and receiver detector are mounted on a modified Nike-Ajax radar pedestal. All the original mechanical and electronic equipment designed especially for radar functions has been removed. The elevation axis was modified to allow mounting the laser transmitter and a 400-mm-aperture receiving telescope. A 32-power viewfinder used for visual observation of the satellites was mounted parallel to the laser and the receiving telescope on the top portion of the elevation axis. The bottom of the elevation axis carried the counterweight assembly and affords additional mounting surface for other instrumentation. One end of the elevation axis has been modified to permit mounting a 17-bit optical encoder: On the azimuth axis, the slip-ring assembly was used to mount the 17-bit azimuth encoder and a coaxial, rotary water-joint to supply cooling water to the laser transmitter.

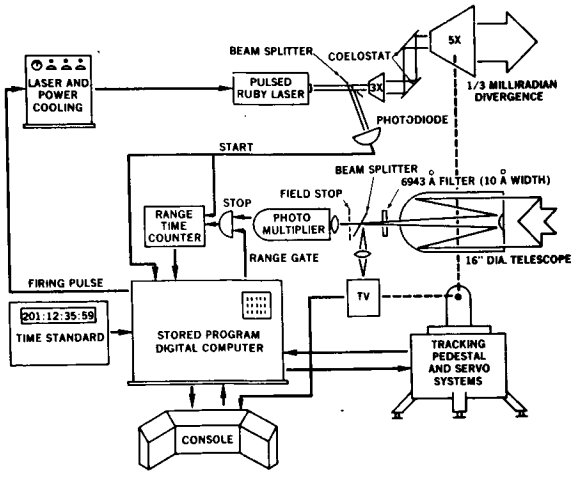

FIGURE 5.14.—Mobile laser system.

A special-purpose computer was modified for use in controlling the tracking pedestal. This computer selects various angular positions as determined from its control and compares them with the actual position of the azimuth and elevation shaft encoders, generating appropriate servo-error signals to drive the pedestal to the correct position. The primary positional input to the programmer is through a specially prepared tape containing the predicted azimuth and elevation and range for each second of time. The pedestal may also be positioned manually. The programmer also serves as the data-recording terminal, recording time, angles, station-housekeeping information, and the measured range.

In the programmed mode of operation, the tracking precision of the pedestal can be monitored by recording the programmer error output, which is the actual difference between the position of the pedestal as determined by the encoders and the command position generated by the programmer. The dynamic positional precision of the tracking pedestal has been found to be ± 0.005 degree peak-to-peak in both axes with typical drive tapes. On the other hand, the tracking accuracy of the system with respect to actual satellite position is affected by the encoder alignment, deflections, boresight precision, and the accuracy of the predicted drive tapes for any pass.

The laser transmitter-system includes a water-cooled ruby laser, a Q-switching mechanism, output-beam-sampling unit, and 10-

power collimating optics with a boresight viewer, all mounted on an adjustable base plate.

The water-cooled ruby laser contains a linear xenon flashlamp and a ruby ⅜-inch (9.4 mm) in diameter by 5-½ inches (140 mm) long positioned at the pseudo-confocal points of a circular, aluminum-coated, Pyrex reflector 4 inches (100 mm) in diameter. The ruby rod, sealed by O-rings, and the flashlamp are contained within a single Pyrex water-jacket. The Q-switching mechanism at the rear of the laser contains a totally-reflecting prism rotated at 24 000 rpm and an optical cell containing a cryptocyanine-and-methanol solution. A magnetic pickup is used to sense the position of the rotating prism with respect to the ruby axis.

An output-beam sampling-unit containing a quartz pellicle oriented at Brewster's angle with respect to the output of the ruby is mounted at the front of the laser. With this, a small fraction of the ruby's output is reflected onto an FW114A biplaner photodiode, whose output is used to start the range measurement, and which serves as a remote monitor of the laser output. A 10-power, simple Galilean optical system then reduces the divergence of the laser beam from approximately 10 mrad to a measured 1.2 mrad.

The receiver is based on a 16-inch (400-mm)-aperture Cassegrainian telescope with with an effective focal length of 300 inches (7.6 m). The detector assembly is in a light-tight housing bolted on the rear of the telescope with an adjustable iris located at the focal point to determine the field of view. An interference-filter holder and photomultiplier housing follow the adjustable iris. An AMPEREX 56TVP photomultiplier is used as the detector. A reflex viewer with a flip-in mirror precedes the adjustable iris for boresighting and acquisition of the satellite during twilight conditions.

The photomultiplier housing contains an automatic threshold-adjusting unit. Its output is used to terminate the range measurement. This device senses the maximum amplitude of both the transmitted pulse and the received pulse, and adjusts the triggering threshold to one-half that amplitude. If the pulses are symmetrical, thus will result in a lens jitter throughout the dynamic range of the unit. Data taken during routine operations with this unit and in postflight pulse-height correction—much less correction is needed since the half-maximum unit compensates within its dynamic range for variation in pulse height—have consistently been better than 40 cm and occasionally have been as low as 26 cm, even with relatively long durations of transmitter pulse (fig. 5.15).

The ranging and data-control system controls the operation of the laser transmitter and detector as well as measures and records the range. Ranging measurements are made using a timer with a minimum reading of 1 nsec and with appropriate starting and stopping pulses from the laser beam-sampling unit and the detector avalanche circuit. Information contained in the timing unit is stored and transferred to the output tape of the programmer before the timer is reset to zero.

The rotating, Q-switching, TIR prism cannot maintain exact synchronism with on-time pulse, and the laser may therefore fire several milliseconds after the command time. An uncertainty of this magnitude in the time of observation is not compatible with the accuracy requirements, so a delay-time counter was incorporated in the data-control unit to

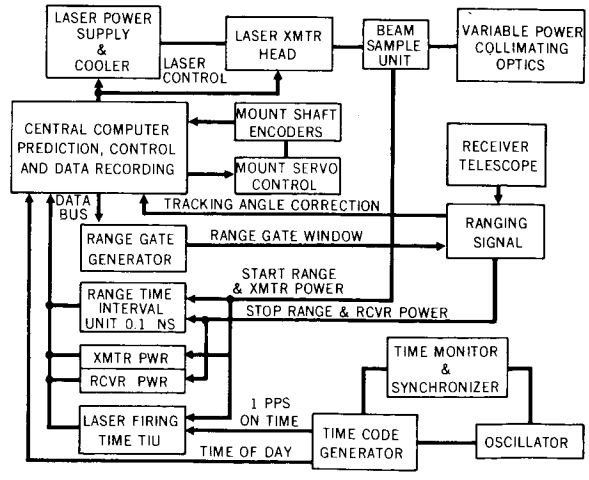

FIGURE 5.15.—Laser system.

measure accurately the time of firing with respect to on-time. This counter is started by the on-time pulse and stopped by a signal from the laser beam-sampling unit, giving the absolute time at which the laser fires to within 10 μsec. The output of the delay counter is recorded on the output tape as indicated above.

The characteristics of the mobile laser systems are summarized in table 5.5.

Calibration of Laser DME.—Pulses are fired at a target a known distance of 2 to 4 km from each laser, and the round-trip time is measured. The delays in the systems are computed from

$$\Delta t_i = t_{Ri} - \frac{2DA}{c}$$

where Δt_i is the delay computed from the i^{th} calibration point, t_{Ri} is the i^{th} measured round-trip time to the target, D is the distance between the laser and the target, and c is the speed of light.

$$A = (2.753/10000)\ (288.16/29.92)(P/T) + 1.0$$

where P is the atmospheric pressure in millibars and T is the local temperature in Kelvin, or

$$A = 1.0002919$$

when the pressure, temperature, or both are not known.

All Δt_i that are negative or greater than 200×10^{-9} sec are rejected as erroneous. The Δt_i are averaged and the resultant value is used as the calibration correction.

$$\Delta t = \sum_{i=1}^{N} \Delta t_i / N$$

where N is the number of measurements.

The laser, however, provides an additional piece of information with each measurement: the height of the received pulse. The received energy is a function of the pulse height and Δt_i is fitted to a function of the measured pulse heights.

The function fitted to the calibration data is half of a Gaussian function.

$$f(p_i) = \frac{1}{\sqrt{2\pi\sigma^2}} e^{-\frac{1}{2}\frac{(p_i - \mu)^2}{\sigma^2}}$$

and

$$\Delta t_i = \beta_0 + \beta f(p_i)$$

where β and β_0 are constants, p is the return-pulse height, and μ is the pulse height where Δt is a maximum.

The maximum error in time is assumed to be at zero pulse-height; thus, $\mu = 0$.

In order to set the spread of the function, the full bell is assumed to be centered at zero. Since only positive values are possible for pulse-height, the estimate of σ^2 uses an imaginary point $(-p, \Delta t)$ corresponding to each point $(p, \Delta t)$. Thus, $\hat{\sigma}^2$ is computed

$$\hat{\sigma}^2 = \Sigma p^2 / 2N$$

where N is the original number of points.

The model for the curve is

$$Y_i = \beta_0 + \beta f(p_i) + \epsilon_i$$

where Y_i is the error in time.

Points that are $2.645\hat{\sigma}$ from the resulting function are deleted.

5.3 DATA

The results given in section 5.6 rest basically on three sets of data corresponding to the three different major sets of solutions: (1) the Goddard Earth Model (GEM) series (sec. 5.6.1.6), (2) Goddard '73 (sec. 5.6.1.2), and (3) the detailed global geoid (sec. 5.6.2). In the first solution the largest set of data is used for determining GEM 5 and GEM 6. This set is summarized in section 5.3.1, and the data include average gravity anomalies, which were used in deriving GEM 6, but not GEM 5.

The solution for Goddard '73 used only observations from camera and laser systems and the gravitational field of GEM 1. The GEM 1 field is not given here (see Lerch *et al.*, GSFC X–533–72). This set is summarized in section 5.3.2.

The detailed global geoid of Vincent and Marsh used GEM 4 as a basis for the gravitational potential (see Lerch *et al.*, NASA X–592–72–476, 1972) and average gravity anomalies from the Aeronautical Chart and Information Center [now known as the Defense Mapping Agency, Aerospace Center (DMA/AC)] rather than from Ohio State University, which were used for GEM 6. The sources are not independent, however, and most of the values in the two sets come from the same original data. Because of the volume of data involved, only the sources are given in section 5.3.3: The data themselves can be obtained from GSFC.

In accordance with the scheme adopted for this report, the procedures used for preprocessing the various data are described in section 5.3.4. Although GSFC also handled data from TRANET, C-band radar and SECOR (see ch. 3) in its work, it usually accepted these after they had been preprocessed by the observing group. The only exception to this rule is the preprocessing applied by Berbert's group (sec. 5.5) as part of the intercomparison. For the results given in section 5.6, the only preprocessing done by GSFC was applied to data from MOTS cameras, PRIME MINITRACK (sec. 5.3.4.2), GRARR (sec. 5.3.4.3), and NASA's laser DME (sec. 5.3.4.4).

5.3.1 Data Used for GEM 5 and GEM 6

GEM 5 has been computed from observations on approximately 350 7-day-long arcs by camera, electronic, and laser systems on 27 satellites close to the earth. In addition, data over approximately 100 one- and two-day arcs of GEOS were employed to improve the station coordinates. The tracking systems providing observational data included: Baker-Nunn cameras (ch. 9), MINITRACK, MOTS cameras, laser DME, GRARR systems, C-band radar systems (ch. 6), and TRANET (Doppler) systems (chs. 2 and 3). GEM 6 has been computed from a combination of GEM 5 and surface gravimetric data and from simultaneous observation by the BC 4 (chap. 7), laser DME, and MOTS. The gravimetric data consist of a global collection of 555- by 555-km, equal-area anomalies computed by Rapp (1972a). Simultaneous observations from the North American MOTS and laser systems and from the BC–4 stations (ch. 7) have been processed by means of geometric theory and the result included in the solution for GEM 6.

The data used in the solutions are described in tables 5.6 through 5.16. In addition, two figures are used to illustrate certain properties of the data. The station locations are in figure 5.16, and base lines to BC–4 stations in figure 5.17. The stations involved are listed in table 5.17. Their coordinates on local datums are given in chapter 1 (table 1.26).

5.3.2 Data Used for Goddard '73

Over 64 000 observations from camera systems and 7000 observations of ranges by laser DME on the satellites GEOS 1, GEOS 2, BE–C, D1–C, and D1–D have been used in combination to determine the locations of 75 tracking stations distributed globally. Dynamical methods were used. One-hundred-and-fifty arcs 2 days in length were used. This solution is called Goddard '73, or GSFC '73, and is given in section 5.6.2.

Table 5.18 presents the number of observations by station used in Goddard '73. Stations which were collocated and forced to adjust in parallel are indicated with brackets. Figure 5.18 shows the distribution of stations involved. The coordinates (on local datums) of these stations are given in chapter 1 (table 1.26). The gravitational field used was GEM 1 (Lerch *et al.*, 1972b), augmented by using coefficients of C_n^m, S_n^m of orders 12, 13, and 14 from the Smithsonian Astrophysical Observatory's (SAO's) 1969 Standard Earth II Model (Gaposchkin and Lambeck, 1970).

5.3.3 Data Used for Detailed Global Geoid

(S. Vincent and J. Marsh)

The detailed global geoid described in section 5.6.3 was derived from two kinds of

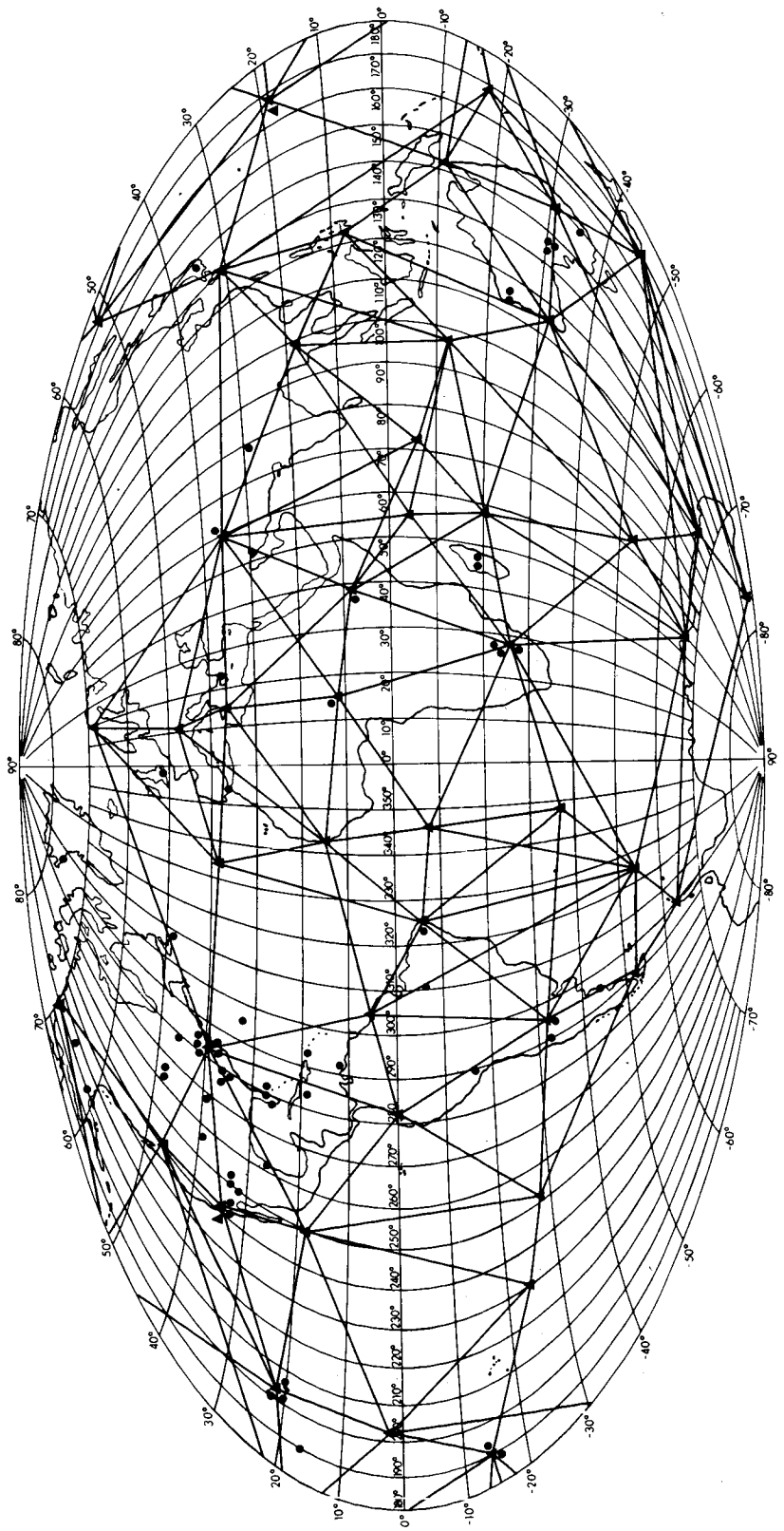

FIGURE 5.16.—Stations used in GEM 6.

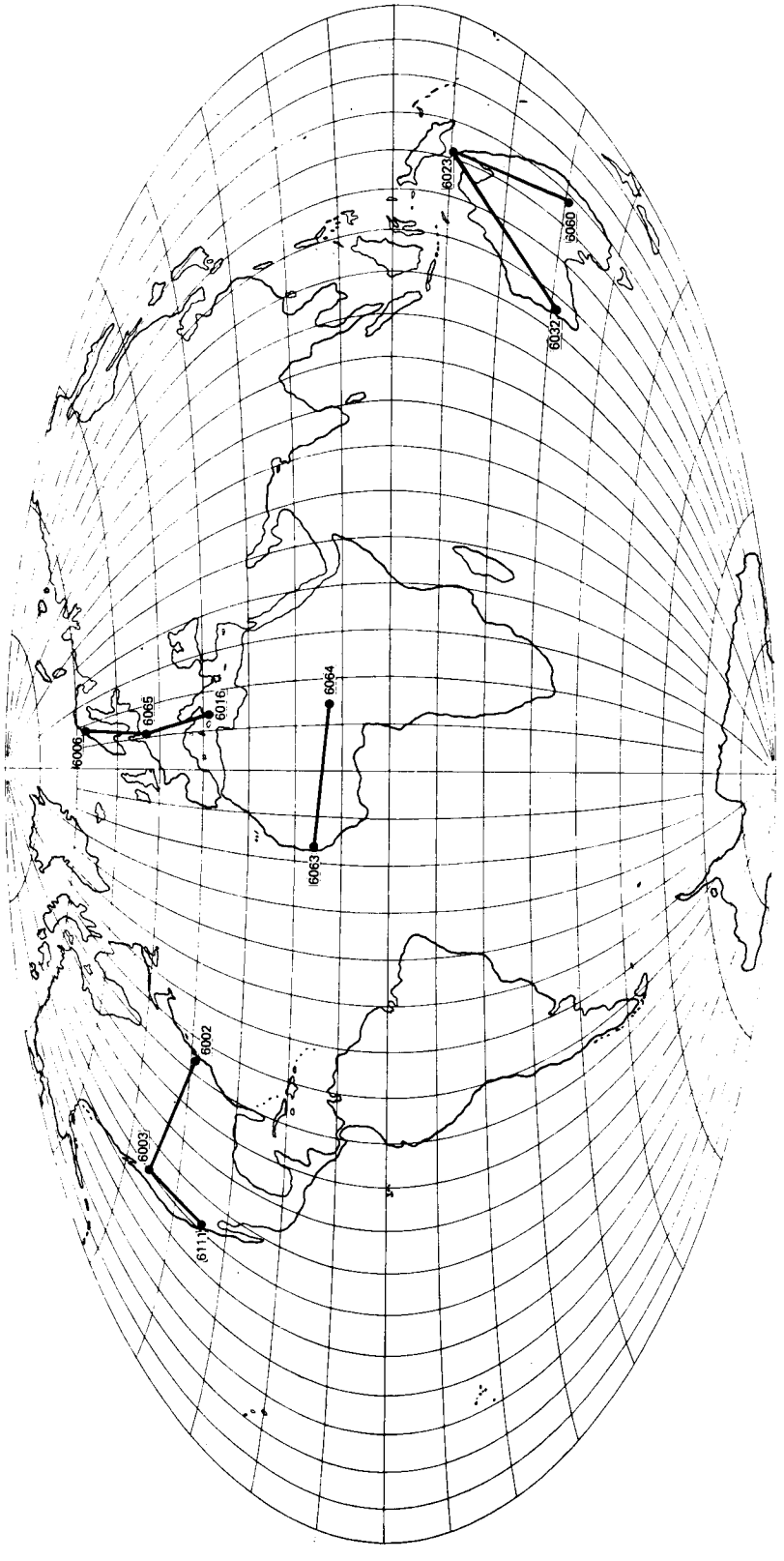

FIGURE 5.17.—BC–4 baselines and ties.

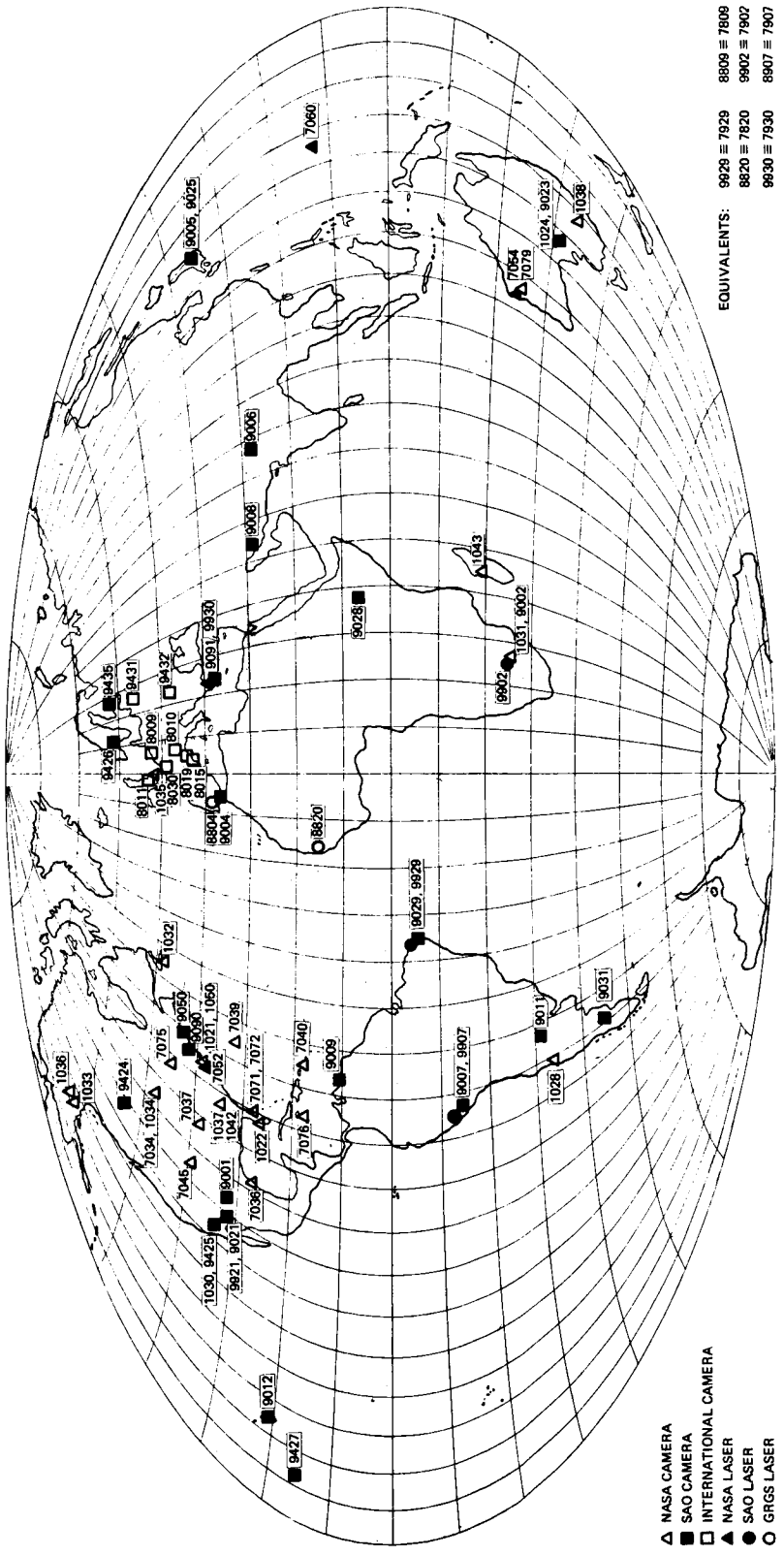

FIGURE 5.18.—Stations used in Goddard '73.

data: (1) the coefficients $\{C_n^m, S_n^m\}$ of GEM 4 (Lerch *et al.*, 1972c) and (2) mean gravity anomalies from a number of different sources.

5.3.3.1 Data From GEM 4

GEM 4 is a set of tracking-station coordinates and a set of coefficients $\{C_n^m, S_n^m\}$ that are derived from about 400 000 observations on 27 satellites and from 1707 5-degree by 5-degree mean gravity anomalies. The coefficients $\bar{C}_n^m$, $\bar{S}_n^m$ are given in table 5.19.

5.3.3.2 Surface Data Used for Detailed Global Geoid

A compilation of 23 947 records of mean, free-air, gravity-anomaly values of 1-degree by 1-degree were obtained from DMA/AC. This gravity collection was augmented with data from the worldwide 1-degree by 1-degree collection of the National Oceanic and Atmospheric Agency (NOAA), from Hawaii Institute of Geophysics and from many other sources. Some of the data were in the form of free-air anomalies at points, Bouguer anomalies, or free-air-gravity contour maps. The free-air anomalies at points were compiled into average 1-degree by 1-degree values. Bouguer anomalies were first converted to free-air anomalies before averaging.

In general, the DMA/AC and Hawaii 1-degree by 1-degree mean free-air anomalies were used as a base in the computations of the detailed geoid. Whenever possible, local data collected by local agencies were used in preference to data supplied by others. When these data were not sufficient, then DMA/AC or Hawaii data were used when available to fill in the voids. Data for specific regions were as follows.

Canadian data were obtained from the following sources:

(1) Data were obtained from D. Nagy of the Gravity Division, Earth Physics Branch, Department of Energy, Ottawa, Ontario, in the form of 1-degree by 2-degree means, which were converted into 1-degree by 1-degree means by assigning equal value to each of the two squares.

(2) Canadian oceanographic data in the North Atlantic were obtained from the Atlantic Oceanographic Laboratory, Bedford Institute.

(3) Data from R. H. Rapp of Ohio State University were in the form of 1-degree by 1-degree mean anomalies, which were compiled from point gravity data.

Sources of data for the North Atlantic, United States, and Northeast Pacific were as follows:

(1) Data for the United States were in the form of 1-degree by 1-degree values (Strange and Wollard, 1964).

(2) Continental shelf (east coast) point-data were obtained from NOAA, and were reduced to 1-degree by 1-degree values.

(3) Continental shelf point-station data from the U.S. east coast and U.S. Gulf coast were obtained from DMA/AC.

(4) Point anomalies and 1-degree by 1-degree data were provided for the North Atlantic and the Gulf coast. (Bowin, unpublished, 1971; Talwani, unpublished, 1971.)

(5) North Atlantic data were provided in 1-degree by 1-degree form (Strang Van Heese, unpublished, 1970).

(6) Data in the North Atlantic were provided by the Centre National pour l'Exploitation de Oceans (CNEYO), Paris, France.

(7) Pacific Ocean data offshore from Washington and Oregon were obtained from NOAA.

(8) A complete SEAMAP data-series in the northeast Pacific was obtained from NOAA.

(9) Hawaiian data were provided by the Hawaii Institute of Geophysics.

Data sources for Eurasia, Africa, and Australia were as follows:

(1) Data on eastern Europe were provided in the form of 1-degree by 1-degree means, 20-minute by 12-minute means, 10-minute by 6-minute means, and 30-minute by 30-minute means (Arnold, 1964).

(2) A collection of 1-degree by 1-degree mean gravity data was provided for Europe (Tengström, unpublished, 1965).

(3) Point anomalies and contour maps furnished data in the Mediterranean (Bowin, unpublished, 1971; Morelli, unpublished, 1970).

(4) Data in 1-degree by 1-degree form were collected in Eurasia and Africa by ACIC and the Hawaii Institute of Geophysics.

(5) Point anomaly data in Kenya (1971) and Tanzania (1968) were obtained from the Department of Geophysics and Planetary Physics, University of Newcastle Upon Tyne, England.

(6) Mean values in 1-degree by 1-degree form for Australia were obtained by Mather.

Miscellaneous data were obtained from the following sources:

(1) Mean values of 1-degree by 1-degree were obtained in Mexico and South America (Wollard, unpublished, 1968).

(2) Japanese Sea data in the areas of seamounts and trenches were supplied by Tomoda, University of Tokyo.

(3) Several contour maps in Venezuela were obtained from Dutch oil companies.

5.3.3.3 Constants

The values used were:

$W_o = 6263687.5$ kgal m
$\gamma_e = 978032.2$ mgal
$a_e = 6378.142$ km
$1/f = 298.255$
$GM = 3.986009 \times 10^5$ km^3/sec^2

5.3.4 Data Preprocessing

(Søren W. Henriksen)

To avoid introducing observables such as temperature and pressure into the observation equations, the effects of these observables on distance, direction, and frequency are computed before setting up the observation equations and the effects are then removed from the observations. This preliminary treatment of observations is called preprocessing. GSFC is concerned with preprocessing of four kinds of data: those from (1) MOTS cameras, (2) PRIME MINITRACK, (3) laser DME, and (4) GRARR (sec. 5.2.2). Although the NASA center also uses data from other instruments, it accepts such data as they are preprocessed by the observing organization.

5.3.4.1 Preprocessing of Data from the MOTS Cameras

The approximate procedure is outlined in chapters 1 and 7. The actual procedure differs in some details, however, and these details have been changed from time to time so that actually three different procedures have been used for MINITRACK, GEOS 1, and GEOS 2. The general procedure is as follows:

(1) Measure the photograph to get coordinates x_i, y_i of the stellar images and x_{sj}, y_{sj} of the satellite images.

(2) Correct the x_i, y_i and x_{sj}, y_{sj} for errors in the measuring engine.

(3) Identify the stars, find their coordinates α_i, δ_i and bring these up to the time T of observation.

(4) Using $\{\alpha_i, \delta_i\}$ and $\{x_i, y_i\}$, compute corrections (in terms of parameters $\{a_{klm}\}$).

(5) Using $\{x_{sj}, y_{sj}\}$ and $\{a_{klm}\}$, compute $\{\alpha_{sj}, \delta_{sj}\}$.

We will consider these steps as individual stages:

(1) Measurement stage: About 50 images of stars of magnitudes $7^m.5$ to $9^m.0$ are measured. Each image is measured five times and the average of the four closest is taken. Satellite images $\{x_{sj}, y_{sj}\}$ and the principal point or fiducial marks are also measured to give $\{x_{oj}, y_{oj}\}$.

(2) Corrections for errors in measuring engine: Derivation of the correction is covered in chapter 1, section 3. The result is a new set $\{x_i', y_i'\}$ of coordinates.

(3) Determination of α_i, δ_i of stars: The stars are identified, their coordinates located in the SAO Star Catalog (ch. 1), and the coordinates are brought up to the time of observation by the usual procedure: i.e., correct for proper motion (eq. (5.16) to (5.18)); apply precession (eq. (5.19)); ap-

ply nutation (eq. (5.20) to (5.22)); and correct for annual and diurnal aberration (eq. (5.23) and (5.24)). The time T is UTC. The result is $\{\alpha_i, \delta_i\}$.

(4) Correction for nonideality of camera and atmosphere:

(a) The MINITRACK version is as follows: Compute from x_o, y_o the approximate coordinates α_o, δ_o of the plate center. Compute from $\{x_i, y_i\}$, $\{\alpha_i, \delta_i\}$, and α_o, δ_o the standard coordinates $\{\xi_i, \eta_i\}$ and $\{\xi_o, \eta_o\}$ (eq. (5.10)). Then, using the equations

$$\left.\begin{aligned} \xi_i &= \sum_{k,l} a_{1kl} x^k y^l \qquad k=1 \text{ to } K \\ \eta_i &= \sum_{k,l} a_{2kl} x^k y^l \qquad l=1 \text{ to } L \end{aligned}\right\} \tag{5.7}$$

compute, by least squares, the values of the $\{a_{1kl}, a_{2kl}\}$. Some of the a_{1kl}, a_{2kl} have defined values as follows: $a_{102}=0$, $a_{103}=0$, $a_{220}=0$, $a_{130}=0$, $a_{ikl}=0$ for $(i+j)>3$. The coefficients a_{100} and a_{200} are corrections to the approximate plate center coordinates ξ_o, η_o. Refraction is taken care of by the coefficients at least insofar as it varies quadratically from the plate center.

(b) The GEOS 1 version is as follows: The equations used in the MINITRACK version (eq. (5.7)) are also used in the GEOS 1 version. However, since the equations are derived from a projective geometry (see eq. (5.8) and (5.9)), the coefficients are not independent, and the conditions on the coefficients are more complicated. They are given by setting the following coefficients equal to zero: a_{101}, a_{121}, a_{103}, a_{141}, a_{123}, a_{105}, a_{201}, a_{212}, a_{230}, a_{214}, a_{232}, a_{250}, and all a_{ikl} for which $k=l>5$. Also, there are relations between the coefficients, and these are given by equations (5.11) through (5.14). (Note that θ enters nonlinearly.) The rest of the procedure is the same as for the MINITRACK version except that instead of using standard coordinates ξ, η, the projected coordinates $\bar{\xi}$, $\bar{\eta}$ are used. They are derived from

$$\bar{\xi} = (a_1 l + a_2 m + a_3 n)/D \tag{5.8}$$

$$\bar{\eta} = (b_1 l + b_2 m + b_3 n)/D \tag{5.9}$$

where

$$D \equiv c_1 l + c_2 m + c_3 n$$

The a_i, b_i, and c_i are constants computed from the right ascension and declination using equations (5.25) and (5.26), and the l, m, and n are direction cosines of a particular image computed from equation (5.27). Corrections for refraction are first computed by using Garfinkel's (1944) formula. They are then adjusted, along with the $\{a_{ikl}\}$, during the adjustment of equation (5.7) (see eqs. (5.28) to (5.31)).

(c) The GEOS 2 version is similar to the GEOS 1 version, with the following differences: relation (5.13) is not used at all, with equation (5.15) being used instead; and the correction for refraction is not changed during adjustment.

(5) Computation of $(\alpha_{si}, \delta_{si})$, the satellite coordinates: These coordinates are computed from the inverse of equation (5.10) after refraction has been corrected for. Then equations (5.18) to (5.22) are applied.

(6) Equations: For plate constants and other constants, let $\bar{x}$, $\bar{y}$ be measured coordinates of image and ξ, η be standard coordinates of image.

$$\begin{aligned} \xi &= \cot\delta \sin(\alpha-\alpha_o)/D \\ \eta &= [\cos\delta_o - \cot\delta \sin\delta_o \cos(\alpha-\alpha_o)]/D \end{aligned} \tag{5.10}$$

where

$$D \equiv \sin\delta_o + \cos\delta_o \cot\delta \cos(\alpha-\alpha_o)$$

and

$$\left.\begin{aligned} x_1 &= \bar{x} - x_p \\ y_1 &= \bar{y} - y_p \end{aligned}\right\} \tag{5.11}$$

$$\Delta y = y_1 (K_o + K_1 r^2 + K_2 r^4) \tag{5.12}$$

$$dx = -\left[\left(1+2\frac{(x_1)^2}{r^2}\right)\sin\theta - \frac{2x_1y_1}{r^2}\cos\theta\right] (J_1 r^2 + J_2 r^4) \tag{5.13}$$

$$dy = -\left[\frac{2x_1y_1}{r^2}\sin\theta - \left(1+2\frac{(y_1)^2}{r^2}\right)\cos\theta\right] (J_1 r^2 + J_2 r^4)$$

$$\left.\begin{aligned} x &= x_1 + \Delta x + dx \\ y &= y_1 + \Delta y + dy \end{aligned}\right\} \quad (5.14)$$

$$\left.\begin{aligned} \Delta x &= x_1 (K_1 r^2 + K_2 r^4 + K_3 r^6) \\ \Delta y &= y_1 (K_1 r^2 + K_2 r^4 + K_3 r^6) \end{aligned}\right\} \quad (5.15)$$

$$\left.\begin{aligned} \alpha_1 &= \alpha + (\mu_\alpha + \frac{1}{2}\Delta\mu_\alpha)\,\Delta T \\ \delta_1 &= \delta + (\mu_\delta + \frac{1}{2}\Delta\mu_\delta)\,\Delta T \end{aligned}\right\} \quad (5.16)$$

where μ_α and μ_δ are proper motion in right ascension and declination and $\Delta\mu_\alpha$ and $\Delta\mu_\delta$ are

$$\left.\begin{aligned} \Delta\mu_\alpha &= 2\mu_\alpha\mu_\delta \tan\delta_0\ \Delta T \\ \Delta\mu_\delta &= -\mu_\alpha^2 \sin\delta\cos\delta\ \Delta T \end{aligned}\right\} \quad (5.17)$$

where

$$\Delta T = T + t - T_o \quad (5.18)$$

T being the beginning of the nearest Besselian year and t being the fraction of a tropical year T. The value of t is taken from the Nautical Almanac for the current year. During the last half of the year, the value of t will be negative since the tabulated value of t refers to the beginning of the next Besselian year.

$$\begin{aligned} \zeta_o &= [23''.04948 + 0.00014\,(T_o - 1950)]\Delta T \\ &\quad + 3''.0 \times 10^{-5}\Delta T^2 + 1''.7 \times 10^{-8}\,\Delta T^3 \\ \theta &= [20''.04255 - 0.000085\,(T_o - 1950)]\Delta T \\ &\quad - 4''.3 \times 10^{-5}\,\Delta T^2 - 4.1 \times 10^{-8}\,\Delta T^3 \\ z &= \zeta_o + 7.9 \times 10^{-5}\,\Delta T^2 \end{aligned} \quad (5.19)$$

where T_o is the epoch of the catalog and ΔT is the interval in years from T_o to the epoch of observation computed as indicated in the previous paragraph. The "nutation in longitude" is taken from the "Sun, 196X" column tables in the current Nautical Almanac. The true obliquity of the ecliptic (ϵ) is taken from the 10th column of the same table. The mean obliquity ϵ_m of the ecliptic is found from

$$\begin{aligned} \epsilon_m &= 23.445787 - 1.30125 \times 10^{-4}\,\Delta T \\ &\quad - 1.64 \times 10^{-10}\,\Delta T^2 \end{aligned} \quad (5.20)$$

The nutation is then determined from

$$\Delta\epsilon = \epsilon - \epsilon_m \quad (5.21)$$

The nutation is then applied to the precessed coordinates α_p, δ_p by the following expressions

$$\begin{aligned} \delta &= \delta_p + \arcsin\,(\Delta\epsilon \sin\alpha_p + \Delta\psi \cos\alpha_p \sin\epsilon_m) \\ \sin\alpha &= (\sin\alpha_p \cos\delta_p - \Delta\epsilon \sin\delta_p \\ &\quad + \Delta\psi \cos\epsilon_m \cos\delta_p \cos\alpha_p)/\cos\delta \\ \cos\alpha &= [\cos\alpha_p \cos\delta_p - \Delta\psi\ (\sin\delta_p \sin\epsilon_m \\ &\quad + \cos\delta_p \cos\epsilon_m \sin\alpha_p)\,]/\cos\delta \end{aligned} \quad (5.22)$$

Annual aberration is set equal to 20″.47, and

$$\begin{aligned} \delta &= \delta' + \arcsin\,[-K\cos\odot\cos\epsilon_m\,(\tan\epsilon_m\cos\delta' \\ &\quad - \sin\alpha'\sin\delta') - K\cos\alpha'\sin\delta'\sin\odot] \end{aligned} \quad (5.23a)$$

$$\begin{aligned} \alpha &= \alpha' + \arcsin\,[(-K\cos\alpha'\cos\odot\cos\epsilon_m \\ &\quad - K\sin\alpha'\sin\odot)/\cos\delta] \end{aligned} \quad (5.23b)$$

where α', δ' are the coordinates before correction and α, δ are the corrected coordinates. For diurnal aberration,

$$\left.\begin{aligned} \delta &= \delta' + \arcsin\,(\bar{D}\sin\delta\sin h) \\ \alpha &= \alpha' + \arcsin\,(\bar{D}\cos h/\cos\delta) \end{aligned}\right\} \quad (5.24)$$

where the primed and unprimed right ascensions denote the uncorrected and corrected coordinates, respectively, and $\bar{D}$ is equal to 0″.319 cos ψ, where ψ is the station latitude.

$$\begin{aligned} [A] &\equiv \begin{bmatrix} a_1 & a_2 & a_3 \\ b_1 & b_2 & b_3 \\ c_1 & c_2 & c_3 \end{bmatrix} \\ &\equiv \begin{bmatrix} -\sin\kappa & \cos\kappa & 0 \\ -\cos\kappa & -\sin\kappa & 0 \\ 0 & 0 & 1 \end{bmatrix} \\ &\quad \begin{bmatrix} \sin\omega & 0 & \cos\omega \\ 0 & 1 & 0 \\ \cos\omega & 0 & \sin\omega \end{bmatrix} \begin{bmatrix} \sin\nu & \cos\nu & 0 \\ -\cos\nu & \sin\nu & 0 \\ 0 & 0 & 1 \end{bmatrix} \end{aligned} \quad (5.25)$$

where ν, ω, and κ are the elements of exterior orientation of the camera and are determined from the right ascension and declination of the star, satellite, or plate center, as may be required, and

$$\begin{aligned}\nu &= \arctan\left[\cos\delta \sin H \,(\cos\delta \sin\phi \cos H - \sin\delta \cos\phi)^{-1}\right]\\ \omega &= \arcsin\left[\cos\delta \cos\phi \cos H + \sin\delta \sin\phi\right]\\ \kappa &= \arccos\left[\sin\nu \sin\phi \sin H + \cos\nu \cos H\right]\end{aligned} \tag{5.26}$$

The direction cosines l, m, and n are computed from the measured and corrected plate coordinates $\{x, y\}$.

$$\begin{bmatrix} l \\ m \\ n \end{bmatrix} = [A]^T \begin{bmatrix} x - x_p \\ y - y_p \\ k \end{bmatrix} \tag{5.27}$$

where x_p, y_p are the coordinates of the plate center and k is approximately the principal distance.

5.3.4.2 Correction of Stellar Coordinates for Refraction

Corrections for refraction are applied to coordinates of each star by Garfinkel's method (1944). The auxiliary angle $\bar{\theta}$ is computed from $\cot 2\bar{\theta} = \gamma_0 \cot \zeta_0$, and γ_0 is $8.1578\,(273/T)^{1/2}$. The coefficients $\eta_1, \eta_2, \ldots, \eta_5$ are determined from

$$\left.\begin{aligned}\eta_1 &= a\\ \eta_2 &= a\,(2/3 + b)\\ \eta_3 &= a\,(2/7 + 17/11\, b + 2b^2)\\ \eta_4 &= a\,(1/14 + 87/77\, b + 185/44\, b^2 + 5\, b^3)\\ \eta_5 &= a\,(1/126 + 70/143\, b + 3155/748\, b^2 + 815/66\, b^3 + 14 b^4)\end{aligned}\right\} \tag{5.28}$$

where

$$\begin{aligned} a &= 2\, d\gamma_0 (1 + d)\\ b &= 2d\, \gamma_0 \end{aligned} \tag{5.29}$$

and where d is a function of the index of refraction n at the observer:

$$d = (n^2 - 1)/2\, n^2 \tag{5.30}$$

The index of refraction n is dependent on the pressure p_o in millibars, the temperature T_o in degrees Kelvin, and the wavelength λ_o in microns (μm) of the light observed

$$n = 1 + [(77.34 + 0.44\, \lambda_0^2) P_o/T_o] \times 10^{-6} \tag{5.31}$$

In the plate reduction, λ_o is assumed to be 0.54 μm and a and b are constants.

After the satellite's zenith-distance ζ_0 has been found, corrections are applied for atmospheric refraction to get the corrected zenith-distance ζ.

$$\zeta_1 = \zeta_o + \Delta\zeta$$

where $\Delta\zeta$ is found by the same procedures used for correcting stellar coordinates. Since the satellite is not at infinite distance, $\Delta\zeta$ overcorrects for refraction, and the correct ζ is computed from

$$\zeta = \arctan\left[\sin\beta/(\cos\beta - f_R)\right]$$

where

$$\begin{aligned} f_R &\equiv (R_o + H_o)/(R_o + H_s)\\ \beta &\equiv \zeta - \arcsin\,(n f_R \sin\zeta_1) \end{aligned}$$

Here, R_o is the radius of curvature in the meridian, H_o is the height of the observer above mean sea level, H_s is the height of the satellite above mean sea level, and n is the index of refraction at the observer.

An additional correction $\Delta\zeta_2$ is added when a flash at time t_2 is used, but refraction has been computed for a neighboring flash at time t_i:

$$\Delta\zeta_2 = 0.3 \times 10^{-3} \sin A_z \cos\phi \operatorname{cosec}^2 \zeta\,(t_2 - t_1)$$

where A_z is the azimuth of the ray.

5.4 THEORY

To understand the theory used by GSFC in deriving its results, one must remember that the primary objective of GSFC has been keeping track of satellites. Even in geodetic problems, it has principally relied on the theory of orbits, and the theory for static satellite geodesy has been "tacked onto" the dynamics. This dynamic theory, embodied in a computer program (now called GEODYNE and used also by NASA at Wallops

Flight Center and a few other nongovernmental groups), is described in section 5.4.1 and was used to derive GEM 5, GEM 6, and Goddard '73 (See results, sec. 5.6.) Those modifications made to the theory in deriving GEM 5 and GEM 6, principally by way of introducing the equations of geometric satellite geodesy, are given in section 5.4.

Besides the general theory, a number of theories for more specialized purposes have been used from time to time. One, embodied in a program called ROAD, was analytic in nature (the theory of sec. 5.4.1 depends on numerical integration). Another, derived by Murphy and Felsentreger, is also analytic and handles luni-solar perturbations (sec. 5.4.4), and still another (sec. 5.4.5) describes analytically the effects of solar radiation pressure.

The detailed global geoid derived by Vincent and Murphy (sec. 5.6.3) does not use the theory of satellite geodesy at all but overlaps a geoid derived from satellite geodesy (GEM 4) with geops computed by the Stokes formula (sec. 5.4.3). Similarly, the theories of M. A. Khan on the hydrostatic flattening of the Earth (sec. 5.4.5.1), isostatic gravity anomalies (sec. 5.4.5.2), and comparisons of the geopotential with other geophysical quantities (sec. 5.4.5.3) rest primarily on classical gravimetric theory and only indirectly on the theory of satellite geodesy.

5.4.1 General Theory for Dynamic Satellite Geodesy

(B. Putney)

GSFC and Wallops Flight Center (ch. 6) use the same straightforward theory for dynamic satellite geodesy. The differential equations of motion (sec. 5.4.1.4) are integrated numerically (sec. 5.4.1.6) to give the position of a satellite as a function of time. The positions are computed for the times of observation and the approximate positions of the observers to give computed values for the observables (sec. 5.4.1.3). The residuals are computed, the observation equations are set up, and an adjustment is made (sec. 5.4.1.5) to the assumed values of the observers' positions, orbital elements, and other quantities. To incorporate observations other than NASA's or older solutions, the adjustment procedure contains special provision for introduction of such results. This provision is called Bayesian least squares and is treated in detail in ch. 6.

The theory is embodied in a program called GEODYNE.

5.4.1.1 Coordinate Systems

The following three coordinate systems are used: (1) geodetic coordinates λ, ϕ, h; (2) topocentric right ascension and declination; and (3) topocentric North-zenith coordinates x, y, z. The first two systems are the standard ones used by all geodesists and astronomers (e.g., Bomford, 1962; Smart, 1962).

5.4.1.1.1 GEODETIC COORDINATE SYSTEM

The system of topocentric North-normal coordinates has as axes the vectors $\hat{N}$, $\hat{E}$, and $\hat{Z}$, which are defined in terms of the geodetic coordinates λ and ψ of a point on the surface as

$$\hat{N}=\begin{bmatrix} -\sin\phi\cos\lambda \\ -\sin\phi\sin\lambda \\ \cos\phi \end{bmatrix}$$

$$\hat{E}=\begin{bmatrix} -\sin\lambda \\ \cos\lambda \\ 0 \end{bmatrix}$$

$$\hat{Z}=\begin{bmatrix} \cos\phi\sin\lambda \\ \cos\phi\sin\lambda \\ \sin\phi \end{bmatrix}$$

where ϕ is the geodetic latitude and λ is the geodetic longitude of the observer.

This system is the one to which such measurements as azimuth and elevation, X and Y angles, and direction cosines are related.

5.4.1.1.2 ASTRONOMIC COORDINATE SYSTEMS

The choice of appropriate coordinate systems for computing the orbits is controlled by several factors.

First, in the case of a satellite moving in the Earth's gravitational field, the most suitable reference system for computing orbits is a system with its origin at the Earth's center of mass, referred to as a geocentric reference system.

Second, the satellite equations of motion must be integrated in an inertial coordinate system. Also, the Earth is rotating at a rate $\dot{\theta}_g$, which is the rate of change of the Greenwich hour angle.

Finally, the Earth both precesses and nutates, thus changing the directions of both the Earth's axis of rotation and the true equinox of date in inertial space.

True Coordinate System of Date.—At any given time, the axis of rotation of the Earth $(+Z)$ and the direction of the true equinox of date $(+X)$ may be used to define a right-handed geocentric coordinate system. This system is known as the true coordinate system of date. The other coordinate systems will be defined in terms of this system. The inertial coordinate system is the true coordinate system of date defined at 0^h0 of the reference day for each satellite. This is the system in which the satellite equations of motion are integrated. This is a right-handed, Cartesian, geocentric coordinate system, with the X axis directed toward the true equinox of 0^h0 of the reference day and with the Z axis directed parallel to the Earth's axis of rotation toward north at the same time. The Y axis is defined so that the coordinate system is orthogonal.

It should be noted that the inertial system differs from the true system of date by the variation in time of the directions of the Earth's axis of rotation and the true equinox of date. This variation is described by the effects of precession and nutation.

5.4.1.1.3 VARIATIONS IN THE COORDINATE SYSTEMS

Polar Motion.—Consider the point P which is defined by the intersection of the Earth's axis of rotation at some time t with the surface of the Earth. At some time $t+\Delta t$ the intersection will be at some point P' which is different from P. Thus, the axis of rotation appears to be moving relative to a fixed position on the Earth; hence the term "motion of the pole" is introduced.

A rectangular coordinate system has been established with its center at a point F fixed on the surface of the Earth, F being near the point P around 1900, and measurements have been taken of the rectangular coordinates of the point P during the period 1900.0 to 1906.0. It was observed that the point P moves in roughly circular motion in this coordinate system with two distinct periods, one period of approximately 12 months and one period of 14 months. The mean position of P during this period is defined to be the point P_o, the mean pole of 1900.0 to 1906.0.

The mean is taken over a 6-year period in order to average out both the 12-month term (six periods) and the 14-month term (five periods) simultaneously. The radius of this observed circle varies between 5 and 11 meters.

In addition to the periodic motion of P about P_o, by taking 6-year means of P in the years after 1900 to 1906, there is found a secular motion of the mean position of the pole away from its original mean position P_o in the years 1900 to 1906 at the rate of approximately $0''.0032$ per year in the direction of the meridian 60 degrees west, and a libration with a period of approximately 24 years with a coefficient of about $0''.022$. The short periodic motions over a period of 6 years average about $0''.2$ to $0''.3$.

This motion of the pole means that the observing stations are moving with respect to the $\hat{N}$, $\hat{E}$, $\hat{Z}$-coordinate system. The station positions must be corrected for this effect.

The position of the instantaneous or true pole is computed by linear interpolation in a Bureau International de l'Heure (BIH) table of observed values for the true pole relative to the mean pole of 1900 to 1906. The increment of the table is 10 days. The table gives the coordinates of the true pole relative to the mean pole, measured in seconds of arc.

Consider the station vector **X** in a system referred to the mean pole and the same vector **Y** in the system referred to the true pole of date. The transformation between **Y** and **X** consists of a rotation ζ about the X_2 axis and a rotation η about the X_1 axis; i.e.,

$$\mathbf{Y}=R_1(\eta)\,R_2(\zeta)\mathbf{X}$$

$$=\begin{bmatrix}1 & 0 & 0\\ 0 & \cos\eta & \sin\eta\\ 0 & -\sin\eta & \cos\eta\end{bmatrix}\begin{bmatrix}\cos\zeta & 0 & -\sin\zeta\\ 0 & 1 & 0\\ \sin\zeta & 0 & \cos\zeta\end{bmatrix}\mathbf{X}$$

Because ζ and η are small angles, their cosines are set equal to 1 and their sines equal to their values in radians. Consequently,

$$\mathbf{Y}=\begin{bmatrix}1 & 0 & -\zeta\\ \zeta\eta & 1 & \eta\\ \zeta & -\eta & 1\end{bmatrix}\mathbf{X}$$

Greenwich Hour Angle θ_g.—The computation of the Greenwich hour angle is quite important because it provides the orientation of the Earth relative to the true system of date. This angle is the major variable in relating the Earth-fixed system to the inertial reference frame in which the satellite equations of motion are integrated.

The evaluation of θ_g is discussed in detail in the *Explanatory Supplement to the Astronomical Ephemeris and the American Ephemeris and Nautical Almanac* (1961).

$$\theta=\theta_{g_0}+\Delta t_1\,\dot{\theta}_1+\Delta t_2\,\dot{\theta}_2+\Delta\alpha$$

where Δt_1 is the integral number of days since January 0.0 UT of the reference year, Δt_2 is the fractional (UT) part of a day for the time of interest, θ_{g_0} is the Greenwich hour angle on January 0.0 UT of the reference year, $\dot{\theta}_1$, is the mean advance of the Greenwich hour angle per mean solar day, $\dot{\theta}_2$ is the mean daily rate of advance of Greenwich hour angle $(2\pi+\theta_1)$, and $\Delta\alpha$ is the equation of equinoxes (nutation in right ascension).

The initial θ_{g_0} is obtained from the proper table in the Nautical Almanac of values containing the Greenwich hour angle on January 0.0 for each year.

Precession and Nutation.—The inertial coordinate system in which the equations of motion are integrated is defined by the true equator and equinox of date for 0^h0 of the reference day. However, the Earth-fixed coordinate system is related to the true equator and equinox of date at any given instant. Thus, it is necessary to consider the effects that change the orientation in space of the equatorial plane and the ecliptic plane. These phenomena are the combined gravitational effect of the Moon and the Sun on the Earth's equatorial bulge and the effect of the gravitational pulls of the various planets on the Earth's orbit. The first of these affects the orientation of the equatorial plane; the second affects the orientation of the plane of the ecliptic. Both affect the relationship between the inertial and Earth-fixed reference systems.

These phenomena cause precession and nutation, both for the axis of rotation of the Earth and for the pole of the ecliptic. The precession and nutation provide the relationship between the inertial system defined by the true equator and equinox of the reference date and the "instantaneous" system defined by the true equator and equinox of date at any given instant.

The luni-solar effects cause the Earth's axis of rotation to precess and nutate about the pole of the ecliptic. This precession will not affect the angle between the equatorial plane and the ecliptic (the "obliquity of the ecliptic"), but will affect the position of the equinox in the plane of the ecliptic. Thus, the effect of luni-solar precession is entirely in celestial longitude. The nutation will affect

both. Consequently, we have nutation in longitude and nutation in obliquity.

The effect of the planets on the Earth's orbit will cause both secular and periodic deviations. However, the ecliptic is defined as the mean plane of the Earth's orbit. Periodic effects were not considered to be a change in the orientation of the ecliptic; instead, they were considered to be a perturbation of the Earth's celestial latitude.

The secular effect of the planets on the ecliptic's plane is separated into two parts, planetary precession and secular change in obliquity. The effect of planetary precession is entirely in right ascension. As is the convention, all of the secular effects are considered under the category of precession. The periodic effects are nutation in longitude and nutation in obliquity.

5.4.1.1.4 TIME SCALES

Three principal time scales are currently used: ephemeris time (ET), atomic time (A1), and universal time (UT1, UT2, UTC). These are defined in chapter 1.

The following equation is used by GSFC to calculate (UT2−UT1) for any year:

$$(\mathrm{UT2}-\mathrm{UT1}) = +^{s}.022 \sin 2\pi t - ^{s}.012 \cos 2\pi t - ^{s}.006 \sin 4\pi t + ^{s}.007 \cos 4\pi t$$

where t is the fraction of the tropical year elapsed from the beginning of the Besselian year for which the calculation is made (1 tropical year equals 365.2422 days).

This difference (UT2−UT1) is known as the seasonal variation. The time difference (A1−UT1) is computed by linear interpolation from a table of values. The spacing for the table is 10 days, which matches the increment for the "final time of emission" published by the U.S. Naval Observatory in the bulletin *Time Signals*. The differences for this table are determined from the relation (A1−UT1) = (A1−UTC) − (UT1−UTC). The values for (UT1−UTC) are obtained from "Circular D", BIH. The difference (A1−UTC) is determined according to the following procedure.

UTC contains discontinuities both in epoch and in frequency because an attempt is made to keep the difference between a UTC clock and a UT2 clock less than $^{s}.1$. By international agreement, adjustments are made in steps of $^{s}.1$ and only at the beginning of the month; i.e., at $0^{h}0$ UT of the first day of the month. The general formula used to compute (A1−UTC) is

$$(\mathrm{A1}-\mathrm{UTC}) = a_0 + a_1 (t - t_0)$$

Both a_0 and a_1 are given in the table. The values in the table for a_0 are the values of (A1−UTC) at the time of each particular step adjustment. The values in the table for a_1 are the values for the new rates of change between the two systems after each step adjustment. Values for a_0 and a_1 are published by both the U.S. Naval Observatory and BIH.

5.4.1.2 Observables and Related Derivatives

Measurements.—The observations are geometric in nature. The computed values for the observables are obtained by applying these geometric relationships to the computed values for the relative positions and velocities of the satellite and the observer at the time of the observations.

In addition to the geometric relationships, a timing bias and a constant bias are associated with a measurement from a given station. The model for an observable is therefore

$$C_{t+\Delta t} = f_t(\mathbf{r},\dot{\mathbf{r}},\mathbf{r}_{ob}) + b + \dot{f}_t(\mathbf{r},\dot{\mathbf{r}},\mathbf{r}_{ob})\,\Delta t$$

where $C_{t+\Delta t}$ is the computed value of the observable taken at time $t+\Delta t$, $\mathbf{r}$ is the Earth-fixed position vector of the satellite, $\mathbf{r}_{ob}$ is the Earth-fixed position vector of the station, $f_t(\mathbf{r}, \dot{\mathbf{r}}, \mathbf{r}_{ob})$ is the geometric relationship defined by the particular observable at time t, b is a bias on the observable, and Δt is the timing bias associated with the observable. The functional dependence of f_t was explicitly stated for the general case. Many of the observables are functions only of the position vectors and hence are not functions of the satellite velocity $\dot{\mathbf{r}}$.

One requires the partial derivatives of the observables with respect to the quantities being determined: the true position of date and velocity of the satellite, the parameters of the force model, the station positions, and the biases.

These quantities are implicitly divided into a set α which is not concerned with the dynamics of satellite motion and a set β which is.

The partial derivatives associated with the α, the station positions and the biases, are computed for the given times of observation. The partial derivatives with respect to the quantities β, the position and velocity and the parameters of the force model, must be determined according to a chain rule:

$$\frac{\partial C_{t+\Delta t}}{\partial \beta} = \frac{\partial C_{t+\Delta t}}{\partial \mathbf{x}_t} \frac{\partial \mathbf{x}_t}{\partial \beta}$$

where $\mathbf{x}_t$ is the vector describing the satellite position and velocity in true coordinates of date. The partial derivatives $\partial C_{t+\Delta t}/\partial \mathbf{x}_t$ are computed directly at the given times of obsevation, but the partial derivatives $\partial \mathbf{x}_t/\partial \beta$ may not be so obtained. The $\partial \mathbf{x}_t/\partial \beta$ relate the true position of date and the velocity of the satellite at the given time to the quantities at epoch through the satellite dynamics.

The partial derivatives $\partial \mathbf{x}_t/\partial \beta$ are called the variational partials and are obtained by numerical integration of the variational equations. These equations are analogous to the equations of motion.

First, consider the partial derivatives of the values associated with the quantities in β. We have

$$\frac{\partial C_{t+\Delta t}}{\partial \beta} = \frac{\partial f_t}{\partial \mathbf{x}_t} \frac{\partial \mathbf{x}_t}{\partial \beta}$$

Note that we have dropped the partial derivative with respect to β of the differential product $\dot{f}_t \Delta t$. We have done so because we use a first-order approximation in our model; hence, higher-order terms are assumed to be negligible. This linearization is also completely consistent with the assumptions made in the solution to the estimation equations.

The partial derivatives $\partial f_t/\partial \mathbf{x}_t$ are computed by transforming the partial derivatives $\partial f_t/\partial \mathbf{r}$ and $\partial f_t/\partial \dot{\mathbf{r}}$ from the Earth-fixed system to the true system of date.

In summary, the partial derivatives required for computing the $\partial C_{t+\Delta t}/\partial \beta$, the partial derivatives of the computed value for a given observable, are the variational partials and the Earth-fixed geometric partial derivatives.

The partial derivatives of the computed values with respect to the station positions are simply related to the partial derivatives with respect to the satellite position at time t:

$$\frac{\partial C_{t+\Delta t}}{\partial \mathbf{r}_{ob}} = \frac{\partial f_t}{\partial \mathbf{r}_{ob}} = \frac{\partial f_t}{\partial \mathbf{r}}$$

where $\mathbf{r}$ is the satellite position vector in Earth-fixed coordinates. This simple relationship is a direct result of the symmetry in the coordinates of the position.

The partial derivatives with respect to the biases are

$$\frac{\partial C_{t+\Delta t}}{\partial b} = 1$$

$$\frac{C_{t+\Delta t}}{\partial (\Delta t)} = f_t$$

Let us coinsider the calculation of the geometric function f_t and its derivatives. The derivatives have been shown to be the partial derivatives with respect to the satellite position and velocity at time t and the rate of change of the function f_t.

The basic types of observation are right ascension and declination, range, range rate, direction cosines l and m, angles X and Y, and azimuth and elevation. The geometric relationship corresponding to each of these observations follows. It should be noted that, in addition to the geocentric or inertial coordinate systems, topocentric coordinate systems are used for some of the relationships.

(1) Range: Consider the station-satellite vector: $\boldsymbol{\rho} = \mathbf{r} - \mathbf{r}_{ob}$, where $\mathbf{r}$ is the satellite position (x, y, z) in the geocentric Earth-fixed system and $\mathbf{r}_{ob}$ is the station position in the same system. The range S is then the magnitude of the vector $\mathbf{S}$, which is one of the measurements.

(2) Range rate: The rate of change of this vector $\boldsymbol{\rho}$ is $\dot{\boldsymbol{\rho}} = \dot{\mathbf{r}}$, since $\dot{\mathbf{r}}_{ob} = 0$. Let us consider that $\dot{\rho} = \rho\hat{u}$ where $\hat{u}$ is the unit vector in the direction of $\boldsymbol{\rho}$. Thus, we have $\dot{\boldsymbol{\rho}} = \dot{\rho}\hat{u} + \rho\dot{\hat{u}}$. The quantity $\dot{\rho}$ in the above equations is the value for the range rate and is determined by $\dot{\rho} = \hat{u} \cdot \dot{\mathbf{r}}$.

(3) Right ascension and declination: These angles are computed from the components of the Earth-fixed station-satellite vector and the Greenwich hour angle θ_g:

$$\alpha = \tan^{-1}\left(\frac{\rho_2}{\rho_1}\right) + \theta_g$$
$$\delta = \sin^{-1}\left(\frac{\rho_3}{\rho}\right)$$

where ρ_1, ρ_2, ρ_3 are the geocentric coordinates of the $\boldsymbol{\rho}$ vector.

(4) Direction cosines: There are three direction cosines associated with the station-satellite vector in the topocentric North-zenith-system. These are $l = \hat{u} \cdot \hat{E}$, $m = \hat{u} \cdot \hat{N}$, and $n = \hat{u} \cdot \hat{Z}$.

(5) X and Y angles: The X and Y angles are computed by

$$X_a = \tan^{-1}\left(\frac{l}{n}\right)$$
$$Y_a = \sin^{-1}(m)$$

(6) Azimuth and elevation: The azimuth and elevation are computed by

$$A_z = \tan^{-1}\left(\frac{l}{m}\right)$$
$$E_l = \sin^{-1}(n)$$

Partial Derivatives of the Observables.—The partial derivatives with respect to satellite position and velocity are given below. All are in the geocentric, Earth-fixed system. (The r_i refer to the Earth-fixed components of $\mathbf{r}$.)

(1) Range:

$$\frac{\partial \rho}{\partial r_i} = \frac{\rho_i}{\rho}$$

(2) Range rate:

$$\frac{\partial \dot{\rho}}{\partial r_i} = \frac{1}{\rho}\left[\dot{r}_i - \frac{\dot{\rho}\rho_i}{\rho}\right]$$
$$\frac{\partial \dot{\rho}}{\partial \dot{r}_i} = \frac{\rho_i}{\rho}$$

(3) Right ascension:

$$\frac{\partial \alpha}{\partial r_i} = \frac{-\rho_2}{\sqrt{\rho_1^2 + \rho_2^2}}$$
$$\frac{\partial \alpha}{\partial r_2} = \frac{\rho_1}{\sqrt{\rho_1^2 + \rho_2^2}}$$
$$\frac{\partial \alpha}{\partial r_3} = 0$$

(4) Declination:

$$\frac{\partial \delta}{\partial r_i} = \frac{-\rho_1\rho_3}{\rho^2\sqrt{\rho_1^2 + \rho_2^2}}$$
$$\frac{\partial \delta}{\partial r_2} = \frac{-\rho_2\rho_3}{\rho\sqrt{\rho_1^2 + \rho_2^2}}$$
$$\frac{\partial \delta}{\partial r_3} = \frac{\sqrt{\rho_1^2 + \rho_2^2}}{\rho^2}$$

(5) Direction cosines:

$$\frac{\partial l}{\partial r_i} = \frac{1}{\rho}\left[E_i - l v_i\right]$$
$$\frac{\partial m}{\partial r_i} = \frac{1}{\rho}\left[N_i - m\mu_i\right]$$
$$\frac{\partial n}{\partial r_i} = \frac{1}{\rho}\left[Z_i - n u_i\right]$$

(6) X and Y angles:

$$\frac{\partial X_a}{\partial r_i} = \frac{nE_i - lZ_i}{\rho\,(1 - m^2)}$$
$$\frac{Y_a}{lr_i} = \frac{N_i - mu_i}{\rho\sqrt{1 - m^2}}$$

(7) Azimuth and elevation:

$$\frac{\partial A_z}{\partial r_i} = \frac{mE_i - lN_i}{\rho\sqrt{1 - n^2}}$$
$$\frac{\partial E_l}{\partial r_i} = \frac{Z_i - nu_i}{\rho\,(1 - n^2)}$$

The derivatives of each observable type with respect to time are presented below. All are in the geocentric Earth-fixed system.

(1) Range:

$$\dot{\rho}=\hat{u}\cdot\dot{\mathbf{r}}$$

(2) Range rate: The range rate-derivative deserves special attention. Remembering that $\dot{\boldsymbol{\varrho}}=\dot{\mathbf{r}}$, we write

$$\dot{\rho}=\hat{u}\cdot\dot{\boldsymbol{\varrho}}$$

Thus,

$$\ddot{\rho}=\dot{\hat{u}}\cdot\dot{\boldsymbol{\varrho}}+\hat{u}\cdot\ddot{\boldsymbol{\varrho}}$$

Because

$$\dot{\boldsymbol{\varrho}}=d/dt\,(\rho\hat{u})+\rho\dot{\hat{u}}+\dot{\rho}\hat{u}$$

we may substitute above for $\hat{u}$:

$$\ddot{\rho}=1/\rho\,(\dot{\boldsymbol{\varrho}}\cdot\dot{\boldsymbol{\varrho}}-\dot{\rho}\hat{u}\cdot\dot{\boldsymbol{\varrho}})+\hat{u}\cdot\ddot{\boldsymbol{\varrho}}$$

or, since $\dot{\rho}=\hat{u}-\dot{\boldsymbol{\varrho}}$ we may write

$$\ddot{\rho}=1/\rho\,(\dot{\boldsymbol{\varrho}}\cdot\dot{\boldsymbol{\varrho}}-\dot{\rho}^2+\rho\cdot\ddot{\boldsymbol{\varrho}}).$$

To obtain $\ddot{\boldsymbol{\varrho}}$, we use the limited gravitational potential

$$U=\frac{GM}{r}\left(1-\frac{C_2{}^0a_e{}^2}{r^2}P_2{}^0(\sin\psi)\right)$$

The gradient of this potential with respect to the Earth-fixed position coordinates of the satellite is the part of $\ddot{\boldsymbol{\varrho}}$ due to the potential

$$\frac{\partial U}{\partial r_i}=-\frac{GM}{r^3}\left[1-\frac{3a_e{}^2C_2{}^0}{2r^2}\left(5\sin^2\psi-1-2\frac{\dot{z}}{r_i}\right)\right]r_i$$

We must add to this the effect of the rotation of the coordinate system. (The Earth-fixed coordinate system rotates with respect to the true coordinates of date with a rate $\dot{\theta}_g$, the rate of change of the Greenwich hour angle.)

The components of $\ddot{\boldsymbol{\varrho}}$ are then

$$\ddot{\rho}_1=\frac{\partial U}{\partial r_1}+[\dot{x}\cos\theta_g+y\sin\theta_g]\dot{\theta}_g+\dot{r}_2\,\dot{\theta}_g$$

$$\ddot{\rho}_2=\frac{\partial U}{\partial r_2}+[-\dot{x}\sin\theta_g+y\cos\theta_g]\,\dot{\theta}_g-\dot{r}_1\,\theta_g$$

$$\ddot{\rho}_3=\frac{\partial U}{\partial r_3}=\frac{\partial U}{\partial z}$$

These transforms are used on the satellite velocity components $\dot{x}$ and y in the true coordinates of date.

It should be noted that all quantities in this formula except for those in brackets are values in an Earth-fixed system. The magnitude r is invariant with respect to the transformations of the coordinate system.

The derivatives with respect to time are:

(3) Right ascension:

$$\dot{\alpha}=\frac{u_1\dot{r}_2-u_2\dot{r}_1}{\rho\,(1-u_3^2)}$$

(4) Declination:

$$\dot{\delta}=\frac{r_3-\dot{\rho}u_3}{\rho\sqrt{1-u_3^2}}$$

(5) Direct cosines:

$$\dot{l}=\frac{\dot{\boldsymbol{\varrho}}\cdot\hat{E}-l\dot{\rho}}{\rho}$$

$$\dot{m}=\frac{\dot{\boldsymbol{\varrho}}\cdot\hat{N}-m\dot{\rho}}{\rho}$$

(6) X and Y angles:

$$\dot{X}_a=\frac{\dot{\boldsymbol{\varrho}}\cdot(n\hat{E}-l\hat{Z})}{\rho\,(1-m^2)}$$

$$\dot{Y}_a=\frac{\dot{\boldsymbol{\varrho}}\cdot\hat{N}-m\dot{\rho}}{\rho\sqrt{1-m^2}}$$

(7) Azimuth:

$$\dot{A}_z=\frac{\dot{\boldsymbol{\varrho}}\cdot(m\hat{E}-l\hat{N})}{\rho\,(1-m^2)}$$

(8) Elevation:

$$\dot{E}_l=\frac{\dot{\boldsymbol{\varrho}}\cdot\hat{Z}-m\dot{\rho}}{\rho\sqrt{1-m^2}}$$

5.4.1.3 Force Model

In a geocentric, inertial, rectangular coordinate system, the equations of motion for a spacecraft are of the form:

$$\ddot{\mathbf{r}}=\frac{GM\mathbf{r}}{r^3}+\mathbf{A} \qquad (5.32)$$

where $\mathbf{r}$ is the position vector of the satellite, G is the gravitational constant, M is the mass

of the Earth, and **A** is the acceleration caused by the asphericity of the Earth, extraterrestrial gravitational forces, atmospheric drag, and solar radiation.

This equation provides a system of second-order equations which, given the position and velocity components at epoch, may be integrated to obtain the position and velocity at any other time.

There is an alternative way of expressing the equations of motion given above:

$$\ddot{\mathbf{r}} = -\nabla V + \mathbf{A}_D + \mathbf{A}_R \qquad (5.33)$$

where V is the gravitational potential and $\mathbf{A}_D$ contains the accelerations due to solar radiation pressure. This relation is merely a regrouping of terms coupled with a recognition of a potential field.

The system in which these equations of motion are integrated corresponds to the true system at 0^{h}0 of the reference day.

The accelerations for $\ddot{\mathbf{r}}$ are evaluated in the true system of date. Thus, the inertial position and velocity resulting from the integration must be transformed to the true system of date for the evaluation of the accelerations and the computed accelerations must be transformed from the true system of date to the inertial system.

The variational equations have the same relationship to the variational partials as the satellite-position vector has to the equations of motion. The variational partials are defined as the $\partial \mathbf{x}_t / \partial \beta$, where $\mathbf{x}_t$ spans the true position and velocity of the satellite at a given time in a true system and β spans the epoch parameters.

The variational partials may be partitioned according to the satellite position and velocity vectors at the given time. Thus, the required partials are $\partial \mathbf{r} / \partial \beta$, $\partial \dot{\mathbf{r}} / \partial \beta$, where $\mathbf{r}$ is the satellite velocity vector (x, y, z) in the true system of date and $\dot{\mathbf{r}}$ is the satellite velocity vector, $(\dot{x}, \dot{y}, \dot{z})$ in the same system. The first of these, $\partial \mathbf{r} / \partial \beta$, can be obtained by the double integration of

$$\frac{d^2}{dt^2} \frac{\partial \mathbf{r}}{\partial \beta}$$

or rather, since the order of differentiation may be exchanged, $\partial \dot{\mathbf{r}} / \partial \beta$ can be obtained. Note that the second set of partials, $\partial \mathbf{r} / \partial \beta$, may be obtained by a first-order integration of $\partial \dot{\mathbf{r}} / \partial \beta$. Hence, we recognize that the quantity to be integrated is $\partial \dot{\mathbf{r}} / \partial \beta$. Using the second form for the equations of motion (eq. 5.33), we find the variational equations to be given by

$$\frac{\partial \ddot{\mathbf{r}}}{\partial \beta} = \frac{\partial}{\partial \beta}(-\nabla V + \boldsymbol{A}_R + \mathbf{A}_D)$$

where V is the potential due to gravitational effects, $\mathbf{A}_R$ is the acceleration due to radiation pressure, and $\mathbf{A}_D$ is the acceleration due to drag. At this point, we must consider a few items.

(1) The potential is a function only of position. Thus, we have

$$\frac{\partial}{\partial \beta}\left(\frac{\partial V}{\partial r_i}\right) = \sum_{m=1}^{3} \left(\frac{\partial^2 V}{\partial r_i \partial r_m}\right) \frac{\partial r_m}{\partial \beta}$$

(2) The partials of solar radiation pressure are zero with respect to the coefficients defining the potential, the drag coefficient, and the satellite velocity, and the partials with respect to the satellite position are negligible.

(3) (Drag is a function of position and velocity.) The partials are zero with respect to the potential coefficients and the satellite emissivity, but we have

$$\frac{\partial \mathbf{A}_D}{\partial \beta} = \frac{\partial A_D}{\partial \boldsymbol{x}_t} \frac{\partial \mathbf{x}_t}{\partial \beta} + \frac{\partial \mathbf{A}_D}{\partial C_D} \frac{\partial C_D}{\partial \beta} + \frac{\partial \mathbf{A}_D}{\partial C_D} \frac{\partial \dot{C}_D}{\partial \beta}$$

Let us write our variational equations in matrix form, where the following definitions apply:

- n is the number of parameters in β at epoch.
- F is a $3 \times n$ matrix whose j^{th} column vectors are $\partial \dot{\mathbf{r}} / \partial \beta_j$.
- U_{2c} is a 3×6 matrix whose last three columns are zero and whose first three columns are such that the i, j^{th} element is given by $\partial^2 U / \partial r_i \, \partial r_j$.

D_r is a 3×6 matrix whose j^{th} column is defined by $\partial \mathbf{A}_D/\partial x_{t_j}$.

X_m is a $6\times n$ matrix whose i^{th} row is given by $\partial \mathbf{x}_t/\partial \beta_j$. Note that X_m contains the variational partials.

f is a $3\times n$ matrix whose first six columns are zero and whose last $n-6$ columns are such that the i, j^{th} element is given by $\partial/\partial\beta_j[-(\nabla U+\mathbf{A}_D+\mathbf{A}_R]$. Note that the first six columns correspond to the first six elements of β, which are the position and velocity at epoch. (This matrix contains the direct partials of $\mathbf{x}$ with respect to β.) We may now write $F=[U_{2c}+D_r]X_m+f$. This is a matrix form of the variational equations.

Note that U_{2c}, D_r, and f are evaluated at the current time, whereas X_m is the output of the integration. Initially, the first six columns of X_m plus the six rows form an identity matrix; the rest of the matrix is zero (for $i=j$, $X_{m_{ij}}=1$; for $i\neq j$, $X_{m_{ij}}=0$).

Potential of the Earth.—The Earth's potential is described by a series of spherical harmonics, and it is most conveniently expressed in a coordinate system where ϕ' is the geocentric latitude of the satellite, λ is the longitude of the satellite, and r is the geocentric distance of the satellite.

The Earth's gravitational field is represented by:

$$V=\frac{GM}{r}\left\{1+\sum_{n=2}^{nmax}\sum_{m=0}^{n}\left(\frac{a_e}{r}\right)^n P_n^m(\sin\phi')\,[C_{nm}\cos m\lambda+S_{nm}\sin m\lambda]\right\}$$

where $nmax$ is the upper limit for the summation (highest degree).

The relationships between the normalized coefficients ($\bar{C}_{nm}$, $\bar{S}_{nm}$) and the unnormalized coefficients are as follows:

$$C_{nm}=\left[\frac{(n-m)\,!\,(2n+1)\,(2-\delta_{om})}{(n+m)\,!}\right]^{1/2}\bar{C}_{nm}$$

where δ_{om} is the Kronecker delta ($\delta_{om}=1$ for $m=0$ and $\delta_{om}=0$ for $m\neq 0$). A similar expression is valid for the relationship between $\bar{S}_{nm}$ and S_{nm}.

The gravitational accelerations in true coordinates of date ($\ddot{x}$, $\ddot{y}$, $\ddot{z}$) are computed from the potential, $V(r,\phi',\lambda)$, by the chain rule; e.g.,

$$\ddot{x}=\frac{\partial V}{\partial r}\frac{\partial r}{\partial x}+\frac{\partial V}{\partial \phi'}\frac{\partial \phi'}{\partial x}+\frac{\partial V}{\partial \lambda}\frac{\partial \lambda}{\partial x}$$

The accelerations $\ddot{y}$ and $\ddot{z}$ are determined in a similar way. The partial derivatives of V with respect to r, ϕ', and λ are given by

$$\frac{\partial V}{\partial r}=\frac{GM}{r^2}\left[1+\sum_{n=2}^{nmax}\left(\frac{a_e}{r}\right)^n\sum_{m=0}^{n}(C_{nm}\cos m\lambda+S_{nm}\sin m\lambda)\,(n+1)P_n^m(\sin\phi')\right]$$

$$\frac{\partial V}{\partial \lambda}=\frac{GM}{r}\sum_{n=2}^{nmax}\left(\frac{a_e}{r}\right)^n\sum_{m=0}^{n}(S_{nm}\cos m\lambda-C_{nm}\sin m\lambda)\,mP_n^m(\sin\phi')$$

$$\frac{\partial V}{\partial \phi'}=\frac{GM}{r}\sum_{n=2}^{nmax}\left(\frac{a_e}{r}\right)^n\sum_{m=0}^{n}(C_{nm}\cos m\lambda+S_{nm}\sin m\lambda)\,[P_n^m(\sin\phi')-m\tan\phi'\,P_n^m(\sin\phi')]$$

The partial derivatives of r, ϕ', and λ with respect to the satellite coordinates $\{r_i\}$ are

$$\frac{\partial r}{\partial r_i}=\frac{r_i}{r}$$

$$\frac{\partial \phi'}{\partial r_i}=\frac{1}{\sqrt{x^2+y^2}}\left[-\frac{zr_i}{r^2}+\frac{\partial z}{\partial r_i}\right]$$

$$\frac{\partial \lambda}{\partial r_i}=\frac{1}{\sqrt{x^2+y^2}}\left[\frac{\partial y}{\partial r_i}-\frac{y}{x}\frac{\partial x}{\partial r_i}\right]$$

The Legendre functions are computed via recursion formulas.

(1) Zonals: $m=0$

$$P_n^o(\sin\phi')=\frac{1}{n}[(2n-1)\sin\phi'\,P_{n-1}^o(\sin\phi')-(n-1)P_{n-2}^o(\sin\phi')]$$

$$P_n^o(\sin\phi')=\sin\phi'$$

(2) Tesserals: $m\neq 0$ and $m\leq n$

$$P_n^m(\sin\phi')=P_{n-2}^m(\sin\phi')+(2n-1)\cos\phi'\,P_{n-1}^{m-1}(\sin\phi')$$

$$P_1^1(\sin\phi')=\cos\phi'$$

(3) Sectorials: $m=n$

$$P_n^m = (2n-1)\cos\phi' P_{n-1}^{n-1}(\sin\phi')$$

The relationship for the derivatives is given by

$$\frac{d}{d\phi'}P_n^m(\sin\phi')) = P_n^{m+1}(\sin\phi') - m\tan\phi' P_n^m(\sin\phi')$$

It should also be noted that multiple-angle formulas are used for evaluating the sine and cosine of $m\lambda$.

The variational equations require the computation of the matrix U_{2c}, whose elements are given by

$$(U_{2c})_{i,j} = \frac{\partial^2}{\partial r_i}\frac{V}{\partial r_j}$$

where $r_i = \{x, y, z\}$, the true position of date of the satellite.

Because the Earth's field is in terms of r, $\sin\phi'$, and λ, we write

$$U_{2c} = C_1^T U_2 C_1 + \sum_{k=1}^{3}\frac{\partial V}{\partial e_k}C_{2k}$$

where e_k ranges over the elements r, $\sin\phi'$, and λ, U_2 is the matrix whose i, j^{th} element is given by $\partial^2 V/\partial e_i \partial e_j$, C_1 is the matrix whose i, j^{th} element is given by $\partial e_i/\partial r_j$, and C_{2k} is a set of three matrices whose i, j^{th} elements are given by $\partial^2 e_k/\partial r_i \partial r_j$.

We compute the second partial derivatives of V with respect to r, ϕ', and λ as in inset.

The elements of U_2 have nearly been computed. What remains is to transform from (r, ϕ, λ). This transformation affects only the partials involving ϕ:

$$\frac{\partial V}{\partial \sin\phi} = \frac{\partial V}{\partial\phi'}\frac{\partial\phi'}{\partial\sin\phi}$$

$$\frac{\partial^2 V}{\partial \sin\phi'^2} = \frac{\partial\phi'}{\partial\sin\phi'}\left(\frac{\partial^2 V}{\partial\phi'^2}\right)\frac{\partial\phi'}{\partial\sin\phi'}\frac{\partial}{\partial\phi'}\frac{\partial^2\phi'}{\partial\sin\phi'^2}$$

where

$$\frac{\partial\phi'}{\partial\sin\phi'} = \sec\phi'$$

$$\frac{\partial^2 V}{\partial r^2} = \frac{2GM}{r^3} + \frac{GM}{r^3}\sum_{n=2}^{nmax}(n+1)(n+2)\left(\frac{a_e}{r}\right)^n \sum_{m=0}^{n}(C_{nm}\cos m\lambda + S_{nm}\sin m\lambda)P_n^m(\sin\phi')$$

$$\frac{\partial^2 V}{\partial r\partial\phi'} = -\frac{GM}{r^2}\sum_{n=2}^{nmax}(n+1)\left(\frac{a_e}{r}\right)^n \sum_{m=0}^{n}(C_{nm}\cos m\lambda + S_{nm}\sin m\lambda)\frac{\partial}{\partial\phi'}[P_m^n(\sin\phi')]$$

$$\frac{\partial^2 V}{\partial r\partial\lambda} = \frac{GM}{r^2}\sum_{n=2}^{nmax}(n+1)\left(\frac{a_e}{r}\right)^n \sum_{m=0}^{n} m(-C_{nm}\sin m\lambda + S_{nm}\cos m\lambda)P_n^m(\sin\phi')$$

$$\frac{\partial^2 V}{\partial\phi'^2} = \frac{GM}{r}\sum_{n=2}^{nmax}\left(\frac{a_e}{r}\right)^n \sum_{m=0}^{n}(C_{nm}\cos m\lambda + S_{nm}\sin m\lambda)\frac{\partial^2}{\partial\Phi^2}[P_n^m(\sin\phi')]$$

$$\frac{\partial^2 V}{\partial\phi'\partial\lambda} = \frac{GM}{r}\sum_{n=2}^{nmax}\left(\frac{a_e}{r}\right)^n \sum_{m=0}^{n} m(-C_{nm}\sin m\lambda + S_{nm}\cos m\lambda)\frac{\partial}{\partial\phi'}[P_n^m(\sin\phi')]$$

$$\frac{\partial^2 V}{\partial\lambda^2} = -\frac{GM}{r}\sum_{n=2}^{nmax}\left(\frac{a_e}{r}\right)^n \sum_{m=0}^{n} m^2(C_{nm}\cos m\lambda + S_{nm}\sin m\lambda)P_n^m(\sin\phi')$$

where

$$\frac{\partial}{\partial\phi'}(P_n^m(\sin\phi')) = P_n^{m+1}(\sin\phi') - m\tan\phi' P_n^m\sin\phi')$$

$$\frac{\partial^2}{\partial\phi'^2}(P_n^m(\sin\phi')) = P_n^{m+2}(\sin\phi') - (m+1)\tan\phi' P_n^{m+1}(\sin\phi') - m\tan\phi'[P_n^{m+1}(\sin\phi') - m\tan\phi' P_n^m(\sin\phi')] - m\sec^2\phi' P_n^m(\sin\phi')$$

$$\frac{\partial^2\phi'}{\partial \sin\phi'^2}=\sin\phi'\sec^3\phi'$$

For the C_1 and C_{2k} matrices, the partials of r, $\sin\phi'$, and λ are obtained from the formulas

$$r=\sqrt{x^2+y^2+z^2}$$
$$\sin\phi'=\frac{z}{r}$$
$$\lambda=\tan^{-1}\left(\frac{y}{x}\right)-\theta_g$$

We have for C_1

$$\frac{\partial r}{\partial r_i}=\frac{r_i}{r}$$
$$\frac{\partial \sin\phi'}{\partial r_i}=\frac{-zr_i}{r^3}+\frac{1}{r}\frac{\partial z}{\partial r_i}$$
$$\frac{\partial\lambda}{\partial r_i}=\frac{1}{x^2+y^2}\left[x\frac{\partial y}{\partial r_i}-y\frac{\partial x}{\partial r_i}\right]$$

The C_{2k} are symmetric. The necessary elements are given by

$$\frac{\partial^2 r}{\partial r_i\partial r_j}=\frac{r_ir_j}{r^3}+\frac{1\partial r_i}{r\partial r_j}$$
$$\frac{\partial^2\sin\phi'}{\partial r_i\partial r_j}=\frac{3zr_ir_j}{r^5}-\frac{1}{r^3}\left[r_j\frac{\partial z}{\partial_i}+r_i\frac{\partial z}{\partial_j}+z\frac{\partial r_i}{\partial_j}\right]$$
$$\frac{\partial^2\lambda}{\partial r_i\partial r_j}=\frac{-2r_j}{(x^2+y^2)^2}\left[x\frac{\partial y}{\partial r_i}-y\frac{\partial x}{\partial r_i}\right]+\frac{1}{x^2+y^2}\left[\frac{\partial x}{\partial r_j}\frac{\partial y}{\partial r_j}-\frac{\partial y}{\partial r_j}\frac{\partial x}{\partial r_j}\right]$$

If coefficients C_{nm} or S_{nm} are being estimated, we require their partials in the f matrix. These partials are:

$$\frac{\partial}{\partial C_{nm}}\left(-\frac{\partial V}{\partial r}\right)=(n+1)\frac{GM}{r^2}\left(\frac{a_e}{r}\right)^n\cos(m\lambda)P_n^m(\sin\phi')$$
$$\frac{\partial}{\partial C_{nm}}\left(-\frac{\partial V}{\partial\lambda}\right)=m\frac{GM}{r}\left(\frac{a_e}{r}\right)^n\sin(m\lambda)P_n^m(\sin\phi')$$
$$\frac{\partial}{\partial C_{nm}}\left(\frac{\partial V}{\partial\phi'}\right)=\frac{GM}{r}\left(\frac{a_e}{r}\right)^n\cos(m\lambda)\left[P_n^{m+1}(\sin\phi')-m\tan\phi'\,P_n^m(\sin\phi')\right]$$

The partials for S_{nm} are identical except that $\cos(m\lambda)$ is replaced by $\sin(m\lambda)$ and $\sin(m\lambda)$ is replaced by $-\cos(m\lambda)$.

These partials are converted to true coordinates of date by means of the chain rule; e.g.,

$$\frac{\partial}{\partial C_{nm}}\left(-\frac{\partial V}{\partial x}\right)=\frac{\partial}{\partial C_{nm}}\left(-\frac{\partial V}{\partial r}\right)\frac{\partial r}{\partial x}+\frac{\partial}{\partial C_{nm}}\left(-\frac{\partial V}{\partial\lambda}\right)\frac{\partial\lambda}{\partial x}+\frac{\partial}{\partial C_{nm}}\left(-\frac{\partial V}{\partial\phi'}\right)\frac{\partial\phi'}{\partial x}$$

The gravitational potential originating from solid-earth tides caused by a single disturbing body is given by

$$U_D(r)=\frac{k_2}{2}\frac{GM_d}{R_d^3}\frac{R_e^5}{r^3}[3(\hat{R}_d\times\hat{r})^2-1]=\frac{k_2}{2}\frac{GM_e}{R_e}\left(\frac{M_d}{M_e}\right)\left(\frac{R_e}{R_d}\right)^3\left(\frac{R_e}{r}\right)^3[3(\hat{R}_d\cdot\hat{r})^2-1]$$

and the resultant accelerations on a satellite due to this potential are

$$-\nabla U_D=\frac{k_2}{2}\frac{GM_d}{R_d^3}\frac{R_e^5}{r}\{[3-15(\hat{R}_d\cdot\hat{r})^2]r+6(\hat{R}_d\cdot\hat{r})R_d\}$$

where k_2 is the tidal coefficient of degree 2, called the Love number, G is the universal gravitational constant, M_e is the mass of the Earth, R_e is the mean Earth-radius, M_d is the mass of the disturbing body, M_e is the mass of the Earth, R_d is the distance from the center of mass of the Earth to the center of mass of the disturbing body, r is the distance from the center of mass of the Earth to the satellite, $\hat{R}_d$ is the unit vector, and $\hat{r}$ is the unit vector from the center of mass of the Earth to the satellite.

Third-Body Gravitational Perturbations (Luni-Solar Forces).—The gravitational perturbations caused by a third body on the orbit of a satellite are treated by defining a function, R_d, which is the third-body disturbing potential. This potential takes on the form

$$R_d = \frac{GMm_d}{r_d}\left[\left(1-\frac{2r}{r_d}S+\frac{r^2}{r_d{}^2}\right)^{-1/2}\frac{r}{r_d}S\right]$$

where m_d is the mass of the disturbing body, $\mathbf{r}_d$ is the geocentric true of date position vector to the disturbing body, S is equal to the cosine of the angle between $\mathbf{r}$ and $\mathbf{r}_d$, and $\mathbf{r}$ is the geocentric true position of date vector of the satellite. All perturbations are computed from:

$$\mathbf{a}_d = -GMm_d\left[\frac{\mathbf{d}}{D_d}+\frac{1}{r_d}\frac{\mathbf{r}_d}{r_d}\right]$$

where

$$\mathbf{d} = \mathbf{r}-\mathbf{r}_d$$
$$D_d = [r_d^2-2r\,r_d\,S+r^2]^{3/2}$$

Then the matrix U_{2c}, whose i, j^{th} element is given by

$$\frac{\partial^2 R_d}{\partial r_i\,\partial r_j} = -\frac{GMm_d}{D_d}\left[\frac{\partial r_i}{\partial r_j}+\frac{3d_i\,d_j}{D_d{}^{2/3}}\right]$$

is computed. This matrix is a fundamental part of the variational equations.

Lunar, Solar, and Planetary Ephemerides.—Ephemerides in true coordinates of date for the Moon, the Sun, Venus, Mars, Jupiter, and Saturn are used. The actual ephemerides are computed from Everett's fifth-order interpolation formula. The tabular interval, h, is 0.5 day for Moon and the equation of the equinoxes and 4.0 days for the other bodies.

All coordinates are true. The quantities contained in the ephemerides are the geocentric positions of the Moon and the corresponding second and fourth differences, the positions of the Sun relative to the Earth-Moon barycenter and the corresponding second and fourth differences, the heliocentric positions of Venus, Mars, Jupiter, and Saturn and the corresponding second and fourth differences, and the equation of the equinoxes and its second and fourth differences. This ephemeris was prepared from a planetary ephemeris of Jet Propulsion Laboratory (JPL) which corresponded to the JPL development ephemeris 69 (O'Handley *et al.*, 1969).

The formulation for Everett's fifth-order interpolation is:

$$\begin{aligned} y(t_j+sh) = {} & y_jF_0(1-s)+d_j^2F_2(1-s) \\ & +d_j^4F_4(1-s)+y_{j+1}F_0(s) \\ & +d_{j+1}^2F_2(s)+d_{j+1}^4F_4(s) \end{aligned}$$

where

$$\begin{aligned} F_0(s) &= sF_2(s) \\ &= [(s-1)\,(s)\,(s+1)]/6F_4(s) \\ &= [(s-2)\,(s-1)\,(s)\,(s+1)\,(s+2)]/120 \end{aligned}$$

The quantity s is the fractional interval for the interpolation. The quantities d_j are obtained from the ephemeris.

Solar Radiation Pressure.—The force due to solar radiation can have a significant effect on the orbits of satellites with a large area-to-mass ratio. The accelerations due to solar radiation pressure are

$$\mathbf{A}_R = -\nu C_R\frac{A_s}{m_s}P_s\hat{r}_s$$

where ν is the eclipse factor, so that $\nu=0$ when the satellite is in the Earth's shadow and $\nu=1$ when the satellite is illuminated by the Sun, C_R is a factor depending on the reflectivity of the satellite, A_s is the cross-sectional area of the satellite, m_s is the mass of the satellite, P_s is the solar radiation pressure in the vicinity of the Earth, and $\hat{r}_s$ is the (geocentric) true unit vector of date pointing to the Sun.

The unit vector $\hat{r}_s$ is determined as part of the computations of the luni-solar planetary ephemeris.

The eclipse factor ν is determined as follows: Compute $D=\mathbf{r}\cdot\hat{r}_s$, where $\mathbf{r}$ is the true position vector of date of the satellite. If D is positive, the satellite is always in sunlight. If D is negative, compute the vector $\mathbf{P}_R=\mathbf{r}-D\hat{r}_s$. This vector is perpendicular to $\hat{r}_s$. If its magnitude is less than an Earth radius i.e., if $\mathbf{P}_R\cdot\mathbf{P}_R<a_e^2$, the satellite is in shadow.

The satellite is assumed to be specularly reflecting with reflectivity ρ_s; thus, $C_R+1+\rho_s$.

When a radiation pressure coefficient C_R is being determined, the partials for the f matrix in the variational equations must be

computed. The i^{th} element of this column matrix is given by

$$\delta_i = -\nu \frac{A_s}{m_s} p_s$$

Atmospheric Drag.—A satellite moving through an atmosphere experiences an atmospheric drag. Acceleration due to this force is given by

$$\mathbf{A}_D = -\tfrac{1}{2} C_D \frac{A_s}{m_s} \rho_D \boldsymbol{v}_r \mathbf{v}_r$$

where C_D is the drag coefficient, A_s is the cross-sectional area of the satellite, m_s is the mass of the satellite, ρ_D is the density of the atmosphere, at the satellite position, and $\mathbf{v}_r$ is the velocity vector of the satellite relative to the atmosphere.

Both A_s and C_D are treated as constants. Although A_s depends somewhat on the satellite attitude, the use of a mean cross-sectional area does not lead to significant errors at this time. The factor C_D varies slightly with satellite shape and atmospheric composition. However, it has been treated as a satellite-dependent constant.

The relative velocity vector $\mathbf{v}_r$ is computed under the assumption that the atmosphere rotates with the Earth. The components of this vector in a true system of date are then

$$\dot{x}_r = \dot{x} - \dot{\theta}_g y, \quad \dot{y}_r = \dot{y} - \dot{\theta}_g x, \quad \dot{z}_r = \dot{z}$$

The quantities $\dot{x}$, $\dot{y}$, and $\dot{z}$ are the components of $\dot{\mathbf{r}}$, the satellite velocity in true coordinates of date.

The direct partials for the f matrix of the variational equations when the drag coefficient C_D is being determined are given by

$$f = -\frac{1 A_s}{2 m_s} \rho_D \boldsymbol{v}_r \mathbf{v}_r$$

When drag is present, the D_r matrix in the variational equations must also be computed. This matrix, which contains the partial derivatives of the drag acceleration with respect to the Cartesian orbital elements, is

$$D_r = -\frac{1}{2} C_D \frac{A_s}{m_s} \left[\rho_D \boldsymbol{v}_r \frac{\partial \mathbf{v}_r}{\partial \mathbf{x}_t} + \rho_D \frac{\partial \boldsymbol{v}_r}{\partial \mathbf{x}_t} \mathbf{v}_r + \frac{\partial \rho_D}{\partial x_t} \boldsymbol{v}_r \mathbf{v}_r \right]$$

where $\mathbf{x}_t$ is $(x, y, z, \dot{x}, \dot{y}, \dot{z})$;

$$\frac{\partial \mathbf{v}_r}{\partial \mathbf{x}_t} = \begin{bmatrix} 0 & -\dot{\theta}_g & 0 \\ -\dot{\theta}_g & 0 & 0 \\ 0 & 0 & 0 \\ 1 & 0 & 0 \\ 0 & 1 & 0 \\ 0 & 0 & 1 \end{bmatrix}$$

$$\frac{\partial \boldsymbol{v}_r}{\partial \mathbf{x}_t} \mathbf{v}_r = \frac{1}{\boldsymbol{v}_r} \begin{bmatrix} -\dot{y}_r \theta_g \dot{x}_r & -\dot{y}_r \theta_g \dot{y}_r & -\dot{y}_r \theta_g \dot{z}_r \\ \dot{x}_r \theta_g \dot{x}_r & \dot{x}_r \theta_g \dot{y}_r & \dot{x}_r \theta_g \dot{z}_r \\ 0 & 0 & 0 \\ \dot{x}_r \ \dot{x}_r & \dot{x}_r \ \dot{y}_r & \dot{x}_r \ \dot{z}_r \\ \dot{y}_r \ \dot{x}_r & \dot{y}_r \ \dot{y}_r & \dot{y}_r \ \dot{z}_r \\ \dot{z}_r \ \dot{x}_r & \dot{z}_r \ \dot{y}_r & z_r \ \dot{z}_r \end{bmatrix}$$

and $\partial \rho_D / \partial \mathbf{x}_t$ is the matrix containing the partial derivatives of the atmospheric density with respect to $\mathbf{x}_t$. Because the density is not a function of the satellite velocity, the required partials are $\partial \rho_D / \partial \mathbf{r}$.

Atmospheric Density.—The atmospheric density is the least well-known factor in the computation of drag. The program uses the Jacchia-Nicolet model, which gives densities from 120–1000 km with an extrapolation formula for higher altitudes (Jacchia, 1965.)

The formula for computing the exospheric temperature has been modified according to Jacchia's later papers. The density computed from the exospheric temperature is based on data provided in the 1965 report, which presents density distribution versus altitude and exospheric temperature.

The model of the atmosphere proposed by Nicolet considers that the fundamental parameter is the temperature. Other physical parameters such as the pressure and density are derived from the temperature.

To calculate the fundamental parameter, the exospheric temperature, Jacchia considered the four factors of solar activity variation, semi-annual variation, diurnal variation, and variation in geomagnetic activity.

In addition to the density, the partial derivatives of the density with respect to the

Cartesian position coordinates are required. These partials are used in computing the contribution of drag to the variational equations. The density is given by

$$\rho_D = \exp\ (C_0 + C_1 h + C_2 h^2 + C_3 h^3)$$

where h is the geodetic height and the C_i are coefficients which are polynomials in temperature as determined by the model. We then have

$$\frac{\partial \rho_D}{\partial \mathbf{r}} = \rho_D (C_1 + 2C_2 h + 3C_3 h^2) \frac{\partial h}{\partial \mathbf{r}}$$

where $\mathbf{r}$ is the true position of date vector of the satellite (x, y, z).

5.4.1.4 Adjustment Procedures

Bayesian Least-Squares Method.—It should be noted that the functional relationships between the observations and parameters being solved for are in general nonlinear, and an iterative procedure is necessary to solve nonlinear normal equations. The Newton-Raphson iteration formula is used to solve these equations.

The Bayesian estimation formula is

$$dx^{(n+1)} = (B^T W B + V_A^{-1})^{-1} [B^T W dm + V_A^{-1} (x^{(n)} - x_A)]$$

where x_A is the a priori estimate of x, V_A is the a priori covariance matrix associated with x_A, W is the weighting matrix associated with the observations, $x^{(n)}$ is the n^{th} approximation to x, dm is the vector of residuals $(O-C)$ from the n^{th} approximation and $dx^{(n+1)}$ is the vector of corrections to the parameters; i.e.,

$$x^{n+1} = x^n + dx^{(n+1)}$$

B is the matrix of partial derivatives of the observations with respect to the parameters where the i, j^{th} element is given by $\partial m_i / \partial x_j$.

The iteration formula given by this equation solves the nonlinear normal equations formed by minimizing the sum of squares of the weighted residuals.

Separation of Bias in Electronic Instruments.—For certain types of electronic tracking data (e.g., Doppler data), biases exist that are different from one pass to the next. In many cases, these biases are of no interest per se, although their existence must be appropriately accounted for if the data are to be used in an orbit or for estimation of geodetic quantities. In addition, a desired set of electronics data involving hundreds of passes of the satellite over various stations and the complete solution for each bias would require an excessive amount of storage.

The effects of such biases can be removed by separating the biases from the other parameters being adjusted. The forms that this separation takes can be seen from the solution of the equation $\delta_m = B_e\ \Delta b + B \Delta x + \epsilon$ where δm is the vector of residuals, Δb is the set of corrections that should be made to the biases, B_e is the matrix of partial derivatives of the measurements with respect to the biases (the elements of this matrix are either 1 or 0), Δx is the set of corrections to be made to all the other adjustable parameters, B is the matrix of partial derivatives of the measurements with respect to the x parameters, and ϵ is the measurement noise vector.

The least-squares solution of the above equation is:

$$\begin{bmatrix} \Delta \hat{b} \\ \Delta \hat{x} \end{bmatrix} = \begin{bmatrix} B_e{}^T W B_e & B_e{}^T W B \\ B^T W B_e & B^T W B \end{bmatrix}^{-1} \begin{bmatrix} B_e{}^T W \delta m \\ B^T N \delta m \end{bmatrix}$$

where W the weight matrix $(W^{-1} = E\ (\epsilon \epsilon^T))$ is taken to be completely diagonal. The $\Delta \hat{x}$ part can be shown to be

$$\Delta \hat{x} = [B^T W B - B^T W B_e (B_e{}^T W B_e)^{-1} B_e{}^T W B]^{-1}$$
$$x [B^T W \delta m - B^T W B_e (B_e{}^T W B_e)^{-1} B_e{}^T W \delta m]$$

To remove the effects of bias, the last equation states that the normal matrix $B^T W B$ must have $B^T W B_e\ (B_e{}^T W B_e)^{-1} B_e{}^T W \delta m$ subtracted from it. Because of the assumed independence of different measurements, it follows that these quantities which must be subtracted are a sum of contributions for different passes over various stations

$$B^T W B_e (B_e^T W B_e)^{-1} B_e^T W B =$$
$$\sum_{p=1}^{n_b} B_p^T W_p B_{e_p} (B_{e_p}^T W_p B_{e_p})^{-1} B_{e_p}^T W_p B_p$$

$$B^T W B_e (B_e^T W)^{-1} B_e^T W \delta m =$$
$$\sum_{p=1}^{n_b} B_p^T W_p B_{e_p} (B_{e_p}^T W_p B_{e_p}) B_{e_p}^T W_p \delta m_p$$

where n_b is the total number of passes during which there are biases in the data and the subscript p denotes an array for measurements of pass p. The computation of the right side of the equations requires the arrays $B_p^T W_p B_p = na \times 1$ array, $B_{e_p}^T W_p B_{e_p} = 1 \times 1$ array, $B_{e_p}^T W_p \delta m_p = 1 \times 1$ array, where na is the number of adjusted parameters other than biases affecting the arc during which the biases occur. Thus, $na+2$ storage locations must be assigned for every bias which exists at any one time.

The individual biases may be adjusted on the basis of the orbital elements from the previous iteration and force model parameters. This bias can then be used along with the accumulated arrays to correct the sum of weighted squared residuals properly.

5.4.1.5 Numerical Integration Procedures

The equations of motion and the variational equations are integrated to obtain the position and velocity and the attendant variational partials at each observation time. Values at the actual observation time are obtained by interpolation between values at even-numbered steps in the integration.

Let us first consider the integration of the equations of motion. These equations are three second-order differential equations in position, and would be formulated as six first-order equations in position and velocity if a first-order integration scheme were used for their solution.

For reasons of increased accuracy and stability, the position vector $\mathbf{r}$ is obtained by a second-order integration of the acceleration $\ddot{\mathbf{r}}$, whereas the velocity vector $\dot{\mathbf{r}}$ is obtained as the solution of a first-order system. These are both multistep methods requiring at least one derivative evaluation on each step.

Integration of Position and Velocity Components.—To integrate the position components, the predictor formula

$$\mathbf{r}_{n+1} = \left(S_2 + \sum_{p=0}^{q} \gamma_p^* \ddot{\mathbf{r}}_{n-p} \right) h^2$$

is applied, followed by a Cowell corrector formula

$$\mathbf{r}_{n+1} = \left(S_2 + \sum_{p=0}^{q} \gamma_p^* \ddot{\mathbf{r}}_{n-p+1} \right) h^2$$

The velocity components are obtained using the predictor formula

$$\dot{\mathbf{r}}_{n+1} = \left(S_1 + \sum_{p=0}^{q+1} \beta_p^* \ddot{\mathbf{r}}_{n-p} \right) h$$

followed by an Adams-Moulton corrector formula

$$\dot{\mathbf{r}}_{n+1} = \left(S_1 + \sum_{p=0}^{q+1} \beta_p \ddot{\mathbf{r}}_{n-p+1} \right) h$$

where S_1 and S_2 are the first and second sums of the accelerations.

In these formulas, h is the integration step size, q has the value order of the integration less 2, γ_p, γ_p^*, β_p, and β_p^* are coefficients whose values are given in standard texts on numerical integration. Table 5.20 compares the GSFC formulas with those used by other participants in the study.

Integration of the Variational Equations.—Let us next consider the integration of the variational equations (sec. 5.4.1.3). We may write these equations as

$$\ddot{Y} = [AB] \begin{bmatrix} Y \\ \dot{Y} \end{bmatrix} + f$$

where

$$\begin{bmatrix} Y \\ \dot{Y} \end{bmatrix} = X_m$$

and, partitioning according to position and velocity partials, we have

$$[AB] = [U_{2c} + D_r]$$

See section 5.4.1.3 for definitions of the matrices involved.

Because A, B, and f are functions only of the orbital parameters, the integration can be and is performed by using only corrector formulas. (Note that A, B, and f must be evaluated with the final correction values of $\mathbf{r}_{n+1}$ and $\dot{\mathbf{r}}_{n+1}$.)

In the above corrector formulas, we substitute the equation for $\dot{Y}$ and solve explicitly for Y and $\dot{Y}$:

$$\begin{bmatrix} Y_{n+1} \\ \dot{Y}_{n+1} \end{bmatrix} = (I-H)^{-1} \begin{bmatrix} \bar{Y}_n \\ \bar{\dot{Y}}_n \end{bmatrix}$$

Under certain conditions, a reduced form of this solution is used. It can be seen from the variational and observation equations that if drag is not a factor, and there are no range rate, Doppler, or altimeter rate measurements; the velocity variational partials are not used. There is then no need to integrate the velocity variational equations. In the integration algorithm, the B matrix is zero and $(I-H)$ is reduced to a 3×3 matrix.

Backwards integration involves only a few simple modifications to these normal or forward integration procedures. The step size is made negative, and the time completion test needs to be rephrased. The step size for these integration procedures can be selected on the basis of perigee height and the eccentricity of the orbit, if it is desired.

For a starting scheme, a Taylor series approximation is used to predict initial values of position and velocity. With these starting values, the sum array (S_1 and S_2 variables) is evaluated. The loop is closed by interpolating for the positions and velocities not at epoch, and their accelerations are evaluated. The sums are now again evaluated.

Interpolation.—In this procedure, interpolation is used for two functions: (1) interpolation of the orbit elements and variational partials to the observation times; and (2) interpolation for midpoints when the integrator is decreasing the step size in the varistep mode of integration.

The formulas used are:

$$X(t+\Delta t) = \left(S_2(t) + \left(\frac{\Delta t}{h} - 1 \right) S_1(t) + \sum_{i=0}^{n} C_i(\Delta t) f_{n-i} \right) h^2$$

for positions and

$$\dot{X}(t+\Delta t) = \left(S_1(t) + \sum_{i=0}^{n} C_i(\Delta t) f_{n-i} \right) h$$

for velocities. Here S_1 and S_2 are the first and second sums carried along by the integration, the f are the back values of acceleration, h is the step size, and C_i, C' are the interpolation coefficients.

5.4.2 Theory Used for Obtaining GEM 5 and GEM 6

(F. J. Lerch)

A Goddard Earth Model consists of a gravitational potential expressed in a series of spherical harmonics and tracking station locations expressed in a geocentric coordinate system. The models described in section 5.6.1, GEM 5 and GEM 6, are part of a series of solutions derived from an expanding set of measurements from satellite tracking and surface gravity. GEM 5 is based upon tracking data only, while GEM 6 is based upon a combination of tracking data and gravimetric data. Previous solutions GEM 1 and 2 (Lerch *et al.*, 1972b) are similarly organized; the odd and even numbers refer, respectively, to models derived from tracking data and models derived from tracking plus gravimetric data. The odd-numbered models are complete in harmonics to degree and order 12, and the even-numbered models are complete to degree and order 16. All solutions contain coefficients of higher-degree zonal harmonics and selected tesseral harmonics extending to degree 22. The solutions derived from tracking and gravimetry are

adjusted for the reference value of equatorial gravity given in table 5.7.

A brief description of GEM 1 through GEM 6, including basic data employed, is presented in table 5.21. A detailed description of the data employed in deriving GEM 5 and GEM 6 is given in section 5.3.1.

The theory used in deriving the GEM's is essentially the same theory as described in the preceding section. However, that theory is based entirely on dynamics, and does not provide directly for use of geometry or gravimetric data. In addition to the theory of section 5.4.1, a theory for geometric satellite geodesy (sec. 5.4.2.1), a theory for conversion of gravimetric values to a form compatible with dynamic satellite theory (sec. 5.4.2.2), and a method of combining the operations of geometric and gravimetric geodesy with the equations given in section 5.4.1 are used in deriving the GEM's. (See sec. 5.4.2.3.)

The overall design of the geopotential and station determination warrants discussion, notably the truncation of the spherical harmonics in the gravitational potential; the selection of weekly arc lengths in processing the orbital data; and the orientation, origin, and scale for the system of tracking stations. With regard to truncation, the prime considerations are the frequency spectrum of orbital perturbations, satellite sensitivity to terms of high-degree, aliasing effects, relative contributions of the satellite and gravimetric data, and certain deficiencies in the modeling.

Several factors enter into the resolution of the potential coefficients in the satellite solution and govern the truncation in the spherical harmonic model for GEM 5. Formal standard deviations of the coefficients defined in the solution are not altogether dependable. They tend to be optimistic since observations and orbital effects are not perfectly modeled. Although the numerical integration of the modeled forces provides a formal accuracy of better than a meter in orbital position, uncertainties in the forces modeled such as the drag function and exclusion of other unknowns such as tidal effects limit the ability to resolve the orbital position.

For an average (rms) size coefficient of degree n, the potential coefficients decrease, approximately according to the rule of Kaula of $10^{-5}/n^2$. This condition, coupled with the fall-off at altitude in the potential itself, results in greatly diminished effects in orbital perturbations, employing previous estimates of the coefficients, and shows relatively little sensitivity among the satellites to resolve potential terms beyond degree 12 except for zonal and satellite-resonant terms. When the sensitivity level is lowered to take advantage of stochastic averaging of observation errors, resolution of potential terms out to degree 16 is seen. However, when the solution is extended to include higher-degree terms, correlations tend to increase among the higher-degree coefficients, resulting in some unexpectedly large values for the coefficients. Also, certain aliasing errors become more pronounced with the increased correlations, where adjacent terms near the point of truncation tend to absorb effects of the potential beyond this point.

The truncation of the spherical harmonics of GEM 5 was designed to be suitable for satellite applications and as a model for combination with surface gravity data, where higher-degree terms complete to degree and order 16 may be more effectively resolved. The satellite data are considerably more effective in the determination of the lower-degree terms than the gravimetry data, and approximately equal sensitivity is reached at degree 10.

For the above reasons, the general truncation in GEM 5 was chosen to be complete through degree and order 12. Selected higher-degree resonant and zonal terms, out to degree 22, were also included because of their enhanced effects on the orbits.

Satellite data are processed in weekly orbital arcs. The arc length was found to be adequate to provide good resolution in the coefficients including the zonal terms, which are generally derived from their long-term orbital perturbations. The potential gives

rise to a frequency spectrum of harmonics in orbital perturbations which are adequately covered among the weekly orbital arcs and associated data. Perturbations contain many short-period terms of less than one orbital revolution, as well as terms of approximately m cycles per day, where m is the order of the spherical harmonics. Satellite resonant effects generally last less than one week. Long-period and secular zonal effects are appreciable over one week of time. Better resolution of the resonant and zonal terms may be expected to be achieved with longer arcs. But in a previous analysis employing 14-day arc lengths, the observation residuals were significantly increased over those for the weekly arcs. This was particularly so for satellites with large atmospheric drag effects, even though two empirical drag parameters were employed.

The spherical coordinates of the potential and the station coordinates are modeled in a center-of-mass reference system which is oriented to the mean pole (CIO) of 1900–1905, (Bomford, 1971a). Satellite orbital motion provides the basis of a center-of-mass origin, particularly for the tracking stations that are processed dynamically. Orientation to the CIO pole is provided through use of polar motion data distributed by the BIH. Stations processed in the geometrical mode, as with the BC–4 world triangulation network, are similarly oriented and are tied to the stations in the dynamic system through use of local datum coordinates from survey. The scale for the station coordinates is principally determined from the reference value of GM, which provides the scale for the satellite orbits through the gravitational potential. However, the eight base-line distances employed in the geometric analysis for the BC–4 network will contribute somewhat to this scale in the combination solution, GEM 6.

In the spherical harmonic model of the potential, certain low-degree and low-order coefficients are of interest in the modeling. Coefficients $\bar{C}_{10}$, $\bar{C}_{11}$, and $\bar{S}_{11}$ are set to zero so as to correspond to a center-of-mass reference system, and $\bar{C}_{21}$ and $\bar{S}_{21}$ correspond to a shift in position of the mean pole. For an offset of 5 meters in the mean pole, the coefficients ($\bar{C}_{21}$, $\bar{S}_{21}$) would be on the order of 10^{-9}, which is below the recovery capability. However, values of these coefficients are estimated in the solution to serve as a measure of the error for the low-degree coefficients.

5.4.2.1 Geometric Satellite Geodesy

(J. Reece, Computer Sciences Corp.)

The mathematical analysis leading to the geometric adjustment of coordinates of tracking stations is based on (1) two cameras observing the satellite simultaneously, (2) three cameras observing the satellite simultaneously, (3) four cameras observing the satellite simultaneously, and (4) two cameras and one laser observing the satellite simultaneously.

Condition equations resulting from a given set of simultaneous observations are of two types: (1) coplanarity equations, which require that the two observing stations and the satellite lie in the same plane, and (2) length equations, which require that the observation satisfying the two-station coplanarity relationship also agree with the range from a third station.

Corresponding to each event is an equation

$$\sum_{i}^{m} a_i v_i + \sum_{j}^{n} b_j x_j + c = 0 \qquad (5.34)$$

where

a_i, b_i	are known constants given by equations (5.46) through (5.51)
c	is the discrepancy in the condition equation
v_i	are the residuals
x_j	are the unknown corrections to the station coordinates
m	is the number of observed quantities
n	is the number of unknown coordinates

Additional condition equations are employed for the solution. Conditions (i.e., con-

straints) may be either statistical or absolute. Statistical constraints specify coordinate relationships and take the form of equation (5.34). Absolute constraints fix certain relationships between unknowns and are of the form

$$\sum_{k=1}^{l} p_k x_k + e = 0 \qquad (5.35)$$

where

p_k is a known constant
e is the discrepancy
x_k are the unknown corrections to station coordinates
l is the number of coordinates involved in the constraint

Three types of condition equations may be applied.

(1) Coordinate equations, which require a given coordinate value to remain at or near a given value throughout the adjustment.

(2) Distance equations, which require the distance between two stations to remain at or near a given value throughout the adjustment.

(3) Coordinate-shift equations, which require the differences between coordinates of two stations to retain a specified relationship. The equations are set up as follows.

(1) For a two-camera event, one coplanarity equation is used.

(2) For a three-camera event, three coplanarity equations are used.

(3) For a four-camera event, five coplanarity equations are used.

(4) For a two-camera, single-laser event, one coplanarity equation and one length equation are used.

These equations lead to an equation in the form

$$Av + Bx + c = 0 \qquad (5.36)$$

If we let the aggregate of constraints be of the form

$$Px + e = 0$$

the resulting expression to be minimized is

$$v^T W v - 2k^T (Av + Bx + c) - 2\lambda^T (Px + e) \qquad (5.37)$$

where W is the weight matrix for observations, and k and λ are Lagrangian multipliers. Assuming the existence of a matrix of normal equations

$$J = B^T (AW^{-1}A^T)^{-1} B \qquad (5.38)$$

and defining an intermediate matrix $M = AW^{-1}A^T$, we find that the value of vector x is

$$x = -J^{-1}[(I - P^T (PJ^{-1}P^T)^{-1} PJ^{-1}B^T M^{-1} c + P^T (PJ^{-1}P^T)^{-1} e] \qquad (5.39)$$

The matrix of normal equations is obtained in a step-wise manner as each event is processed. Since the matrix $AW^{-1}A^T$ is quasi-diagonal (i.e., $AW^{-1}A^T$ is composed of symmetric submatrices located along the principal diagonal with each submatrix of the order of the number of observations in the event), it is easily inverted. Each symmetric submatrix is inverted as it occurs, and the inverse is placed in the appropriate position in the $(AW^{-1}A^T)^{-1}$ matrix. This leads to the normal equations $(B^T (AW^{-1}A^T)^{-1} B)$ by forming and summing subsets of the normal equations. The matrix $AW^{-1}A^T$ required for a large solution may be on the order of $20\,000 \times 20\,000$, but the largest submatrix requiring inversion is 5×5.

Development of the coplanarity and length equations is discussed in the following text.

Coordinate System.—The observations in α and δ are transformed from right ascension α and declination δ to earth-fixed angles β and γ. The conversion of α and δ as corrected for precession, nutation, and polar motion to the angles β and γ is straightforward. The topocentric angle γ is measured with respect to the equatorial plane and is equivalent to δ, i.e., $\gamma = \delta$. The angle β is measured from the

Greenwich meridian in a plane parallel to the equator and is

$$\beta = \alpha - GHA \tag{5.40}$$

where GHA is the Greenwich hour angle at the epoch of the observation.

Coplanarity Equations.—The coplanarity equations require that the volume of the parallelepiped defined by the two station-to-satellite vectors and the station-to-station vector and their respective errors be zero. The two station-to-station vectors are defined in the local terrestrial coordinates as

$$\underline{\rho}_i(x_i\, y_i\, z_i) = u_i\hat{i} + v_i\hat{j} + w_i\hat{k} \tag{5.41}$$

where

$$\begin{aligned} u_i &= \cos\gamma_i \cos\beta_i \\ v_i &= \cos\gamma_i \sin\beta_i \\ w_i &= \sin\gamma_i \end{aligned}$$

The station-to-station vector $\mathbf{p}_3$ is defined in spherical coordinates by

$$\beta_3 = \tan^{-1}\left(\frac{y_2 - y_1}{x_2 - x_1}\right) \qquad 0 \le \beta_3 \le 2\pi \tag{5.42}$$

$$\gamma_3 = \tan^{-1}\left[\frac{z_2 - z_1}{(x_2 - x_1)^2 + (y_2 - y_1)^2)^{1/2}}\right] \qquad -\frac{\pi}{2} \le \gamma_3 < \frac{\pi}{2} \tag{5.43}$$

$$r_3 = ((x_2 - x_1)^2 + (y_2 - y_1)^2 + (z_2 - z_1)^2)^{1/2} \tag{5.44}$$

The volume of the parallelepiped defined by vectors is given by their triple scalar product, which is

$$F_0 = \begin{bmatrix} \cos\gamma_1 \cos\beta_1 & \cos\gamma_2 \cos\beta_2 & \cos\gamma_3 \cos\beta_3 \\ \cos\gamma_1 \sin\beta_1 & \cos\gamma_2 \sin\beta_2 & \cos\gamma_3 \sin\beta_3 \\ \sin\gamma_1 & \sin\gamma_2 & \sin\gamma_3 \end{bmatrix} = C \tag{5.45}$$

The coefficients of the expansion are

$$a_1 \equiv \frac{\partial F_0}{\partial \beta_1} = \cos\gamma_1 \sin\gamma_2 \cos\gamma_3 \cos(\beta_3 - \beta_1) - \cos\gamma_1 \cos\gamma_2 \sin\gamma_3 \cos(\beta_2 - \beta_1) \tag{5.46}$$

$$a_2 \equiv \frac{\partial F_0}{\partial \gamma_1} = \cos\gamma_1 \cos\gamma_2 \cos\gamma_3 \sin(\beta_3 - \beta_2) - \sin\gamma_1 \cos\gamma_2 \sin\gamma_3 \sin(\beta_2 - \beta_1) + \sin\gamma_1 \sin\gamma_2 \cos\gamma_3 \sin(\beta_3 - \beta_1) \tag{5.47}$$

$$a_3 \equiv \frac{\partial F_0}{\partial \beta_2} = \cos\gamma_2 [\cos\gamma_1 \sin\gamma_3 \cos(\beta_2 - \beta_1) - \sin\gamma_1 \cos\gamma_3 \cos(\beta_3 - \beta_2)] \tag{5.48}$$

$$a_4 \equiv \frac{\partial F_0}{\partial \gamma_2} = -\cos\gamma_1 \cos\gamma_2 \cos\gamma_3 \sin(\beta_3 - \beta_1) - \sin\gamma_1 \sin\gamma_2 \cos\gamma_3 \sin(\beta_3 - \beta_2) - \cos\gamma_1 \sin\gamma_2 \sin\gamma_3 \sin(\beta_2 - \beta_1) \tag{5.49}$$

$$b_1 \equiv \frac{\partial F_0}{\partial \beta_3} = \cos\gamma_3 [\sin\gamma_1 \cos\gamma_2 \cos(\beta_3 - \beta_2) - \cos\gamma_1 \sin\gamma_2 \cos(\beta_3 - \beta_1)] \tag{5.50}$$

$$b_2 \equiv \frac{\partial F_0}{\partial \gamma_3} = \cos\gamma_1 \cos\gamma_2 \cos\gamma_3 \sin(\beta_2 - \beta_1) - \sin\gamma_1 \cos\gamma_2 \sin\gamma_3 \sin(\beta_3 - \beta_2) + \cos\gamma_1 \sin\gamma_2 \sin\gamma_3 \sin(\beta_3 - \beta_1) \tag{5.51}$$

Since β_1, γ_1, β_2, and γ_2 are observations, $\Delta\beta_1$, $\Delta\gamma_1$, $\Delta\beta_2$, and $\Delta\gamma_2$ are residuals and are designated v_1, v_2, v_3, and v_4, respectively.

The variables to be solved for are corrections to the station coordinates. The transformation of unknowns from interstation range and directions to coordinates are given by equation (5.61), providing an equation of the form of equation (5.34). This equation makes adjustments to the interstation angles β_3 and γ_3.

Length Equations.—The length equation is developed for two cameras and a laser DME observing the satellite simultaneously. Assume the existence of two cameras (A and B), a laser DME (L), and a satellite (S), when directions from the cameras to the satellite are observed simultaneously (A to S and B to S) and a range is observed at the same time from L to S. These quantities and auxiliary vectors and angles are shown in figure 5.19. Assumed values of coordinates of the cameras and the laser system are used to calculate initial estimates of the directions and distances between the cameras and the laser. By taking scalar products of the station-to-station and station-to-satellite vec-

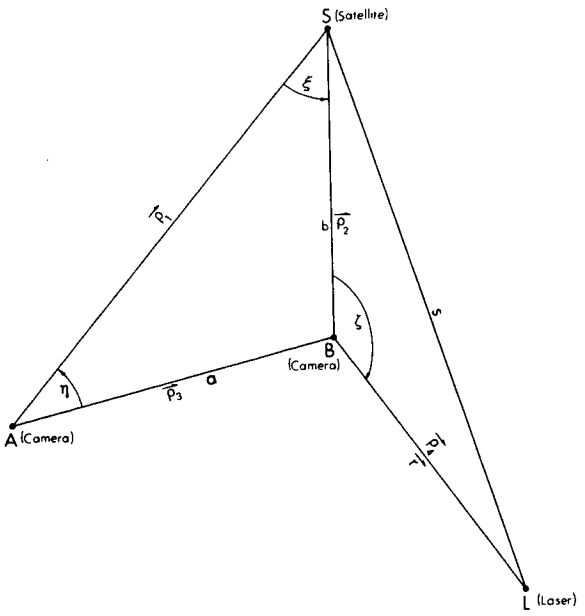

FIGURE 5.19.—Geometry for two camera and one laser DME observing simultaneously.

tors, the cosines of the angles, ξ, η, and ζ are obtained as follows:

$$\cos \xi = \rho_1 \cdot \rho_2 = \sin \gamma_1 \sin \gamma_2 + \cos \gamma_1 \cos \gamma_2 \cos (\beta_2 - \beta_1) \quad (5.52)$$

$$\cos \eta = \rho_1 \cdot \rho_3 = \sin \gamma_1 \sin \gamma_3 + \cos \gamma_1 \cos \gamma_3 \cos (\beta_3 - \beta_1) \quad (5.53)$$

$$\cos \zeta = \rho_2 \cdot \rho_4 = \sin \gamma_2 \sin \gamma_4 + \cos \gamma_2 \cos \gamma_4 \cos (\beta_4 - \beta_2) \quad (5.54)$$

where

$\beta_1, \gamma_1, \beta_2, \gamma_2$	are directions to the satellite
β_3, γ_3	are the interstation angles for the two cameras
β_4, γ_4	are the interstation angles for one camera and the laser system

From figure 5.19, the law of cosines will give, corresponding to the laser length s

$$F = r^2 + b^2 - 2br \cos \zeta - s^2 = 0 \quad (5.55)$$

and the law of sines will give for b above

$$b = a \frac{\sin \eta}{\sin \xi} \quad (5.56)$$

Through the use of equations (5.52) through (5.54), we expand F linearly about the values of a, r, β_3, γ_3, β_4, γ_4, obtained from the initial station coordinates, and the values of β_1, γ_1, β_2, γ_2, and s_o obtained from the observations. Then, we have using differentials as adjustments ($d \equiv \Delta$)

$$F = F_o + \frac{\partial F}{\partial a} da + \frac{\partial F}{\partial r} dr + \frac{\partial F}{\partial \beta_3} d\beta_3 + \cdots + \frac{\partial F}{\partial s} ds = 0 \quad (5.57)$$

Divide F through by $q = 2(r - b \cos \xi)$ and denote the result by

$$a_1 d\beta_1 + a_2 d\gamma_1 + a_3 d\beta_2 + a_4 d\gamma_2 + a_5 ds + b_1 d\gamma_3 + b_2 d\gamma_3 + b_3 da + b_4 d\beta_4 + b_5 d\gamma_4 + b_6 dr + C = 0 \quad (5.58)$$

where $C = F_o/q$, and the differentials on the a_1 coefficients are the observation residuals v_i for $i = 1$ to 5. This represents the laser length equation. The coefficients and C are evaluated from the initial values, where F_o is obtained from the misclosure of equation (5.55). The coefficients in equation (5.58) are obtained as follows:

$$P_1 = b \cot \xi [\cos \gamma_2 \sin (\beta_2 - \beta_1)]$$

$$P_2 = b \cot \xi [\cos \gamma_1 \sin \gamma_2 - \sin \gamma_1 \cos \gamma_2 \cos (\beta_2 - \beta_1)]$$

$$P_3 = -P_1$$

$$P_4 = b \cot \xi [\sin \gamma_1 \cos \gamma_2 - \cos \gamma_1 \sin \gamma_2 \cos (\beta_2 - \beta_1)]$$

$$P_5 = \frac{a \cos \eta}{\sin \xi} [\cos \gamma_1 \cos \gamma_3 \sin (\beta_3 - \beta_1)]$$

$$P_6 = \frac{a \cos \eta}{\sin \xi} [\cos \gamma_1 \sin \gamma_3 - \sin \gamma_1 \cos \gamma_3 \cos (\beta_3 - \beta_1)]$$

$$P_7 = -P_5$$

$$P_8 = \frac{a \cos \eta}{\sin \xi} [\sin \gamma_1 \cos \gamma_3 - \cos \gamma_1 \sin \gamma_3 \cos (\beta_3 - \beta_1)]$$

$$P_9 = \frac{br \sin \zeta}{b - r \cos \zeta} [\cos \gamma_2 \cos \gamma_4 \sin (\beta_4 - \beta_2)]$$

$$P_{10}=\frac{br\sin\zeta}{b\text{-}r\cos\zeta}[\cos\gamma_2\sin\gamma_4 - \sin\gamma_2\cos\gamma_4\cos(\beta_4-\beta_2)]$$
$$P_{11}=-P_9$$
$$P_{12}=\frac{br\sin\zeta}{b\text{-}r\cos\zeta}[\sin\gamma_2\cos\gamma_4 - \cos\gamma_2\sin\gamma_4\cos(\beta_4-\beta_2)]$$
$$a_1=P_1/\sin\xi-P_5/\sin\eta$$
$$a_2=P_2/\sin\xi-P_6/\sin\eta$$
$$a_3=P_1/\sin\xi-P_9/\sin\zeta$$
$$a_4=P_4/\sin\xi-P_{10}/\sin\zeta$$
$$a_5=-s/(b-rs\cos\zeta)$$
$$b_1=P_5/\sin\eta$$
$$b_2=-P_8/\sin\eta$$
$$b_3=\sin\eta/\sin\xi$$
$$b_4=P_9/\sin\zeta$$
$$b_5=-P_{12}/\sin\zeta$$
$$b_6=(r-b\cos\zeta)/(b-r\cos\zeta)$$

The coplanarity and length equations are transformed from γ, β, r variables to x, y, z variables by using the relationships

$$\left.\begin{aligned} x_2-x_1&=r\cos\gamma\cos\beta\\ y_2-y_1&=r\cos\gamma\sin\beta\\ z_2-z_1&=r\sin\gamma\end{aligned}\right\} \quad (5.59)$$

Differentiating these expressions yields equation (5.60). Inverting equation (5.60) produces the transformation equation (5.61). Equations (5.60) and (5.61) are found in inset below.

Other Condition Equations.—The three types of condition equations derived for the geometric solution are: (1) coordinate equations, (2) distance equations, and (3) coordinate-shift equations. These equations may be applied either to effect an absolute constraint or a statistical constraint.

The coordinate equation computes one of the following: (1) it fixes the coordinates of one or more stations exactly at some a priori values, or (2) it statistically weights coordinates of one or more stations according to some a priori assessment of errors.

The distance equation for the absolute constraint fixes the distances between two stations in the adjustment. For the statistically weighted constraint, a distance between two stations is weighted according to its estimated uncertainty from a priori information.

The absolute constraint form of the coordinate-shift equation causes rectangular space coordinates of a pair of stations to assume a given difference relationship. As is true with the coordinate and distance equations, the statistically weighted constraint form of the coordinate-shift equation causes the differences in coordinates of pairs of stations to shift together in accordance with a variance obtained from an a priori model.

(1) Coordinate equation: Assume the input coordinates of the i^{th} station are the coordinates about which a priori information is available. Let the input values of x_i, y_i, z_i, be x_{i0}, y_{i0}, z_{i0}. Error increments are applied to write the following constraint equations:

$$x_{i0}+dx=x_0$$
$$y_{i0}+dy=y_0$$
$$z_{i0}+dz=z_0$$

or

$$\begin{bmatrix} dx_2-dx_1\\ dy_2-dy_1\\ dz_2-dz_1\end{bmatrix}=\begin{bmatrix} -r\cos\gamma\sin\beta & -r\sin\gamma\cos\beta & \cos\gamma\cos\beta\\ r\cos\gamma\cos\beta & -r\sin\gamma\sin\beta & \cos\gamma\sin\beta\\ 0 & r\cos\gamma & \sin\gamma\end{bmatrix}\begin{bmatrix} d\beta\\ d\gamma\\ dr\end{bmatrix} \quad (5.60)$$

$$\begin{bmatrix} d\beta\\ d\gamma\\ dr\end{bmatrix}=\begin{bmatrix} \frac{-\sin\beta}{r\cos\gamma} & \frac{\cos\beta}{r\cos\gamma} & 0\\ \frac{-\sin\gamma\cos\beta}{r} & \frac{-\sin\gamma\sin\beta}{r} & \frac{\cos\gamma}{r}\\ \cos\gamma\cos\beta & \cos\gamma\sin\beta & \sin\gamma\end{bmatrix}\begin{bmatrix} dx_2-dx_1\\ dy_2-dy_1\\ dz_2-dz_1\end{bmatrix} \quad (5.61)$$

$$\left.\begin{aligned} dx+C_1&=0\\ dy+C_2&=0\\ dz+C_3&=0 \end{aligned}\right\} \qquad (5.62)$$

where

$$\begin{aligned} C_1&=x_{i0}-x_0\\ C_2&=y_{i0}-y_0\\ C_3&=z_{i0}-z_0 \end{aligned}$$

In conformity with previous notation, replacing dx, dy, dz by x_{3i-2}, x_{3i-1}, x_{3i} results in

$$\left.\begin{aligned} x_{3i-2}-C_1&=0\\ x_{3i-1}-C_2&=0\\ x_{3i}-C_3&=0 \end{aligned}\right\} \qquad (5.63)$$

as absolute constraint equations for the station coordinates. The constraints fix the station coordinates at their input values. If statistically weighted constraints are to be applied, the above equations are modified to the following:

$$\left.\begin{aligned} v_1+x_{3i-2}-C_1&=0\\ v_2+x_{3i-1}-C_2&=0\\ v_3+x_{3i}\ -C_3&=0 \end{aligned}\right\} \qquad (5.64)$$

(2) Distance equation: The absolute constraint form of the distance equation fixed the distance between a pair of stations. The statistically weighted constraint form of equation treats a distance from ground surveys or other sources in a statistically weighted fashion according to its estimated uncertainty. The distance equation is:

$$\begin{aligned} -dr+\cos\gamma\cos\beta\ (dx_2-dx_1)&\\ +\cos\gamma\sin\beta\ (dy_2-dy_1)&\\ +\sin\gamma\ (dz_2-dz_1)&=0 \end{aligned} \qquad (5.65)$$

If the stations are the correct distance apart, $dr=0$, but if not, let $C=dr$. If the r^{th} and s^{th} ground stations are involved, the equation is written as

$$\begin{aligned} \cos\gamma\cos\beta\ (dx_s-dx_r)+\cos\gamma\sin\beta&\\ (dy_s-dy_r)+\sin\gamma\ (dz_s-dz_r)+C&=0 \end{aligned} \qquad (5.66)$$

In conformity with the previous notation, the terms dx_s, dy_s, dz_s, dx_r, dy_r, and dz_r are replaced by x_{s-2}, x_{s-1}, x_s, x_{r-2}, x_{r-1}, and x_r to obtain the distance equation

$$\begin{aligned} \cos\gamma\cos\beta\ (x_{s-2}-x_{r-2})+\cos\gamma\sin\beta&\\ (x_{s-1}-x_{r-1})+\sin\gamma\ (x_s-x_r)+C&=0 \end{aligned} \qquad (5.67)$$

To convert this to the statistically weighted form, an unknown difference, v, is added to the above equation, yielding

$$\begin{aligned} v+\cos\gamma\cos\beta\ (x_{s-2}-x_{r-2})+\cos\gamma\sin\beta&\\ (x_{s-1}-x_{r-1})+\sin\gamma\ (x_s-x_r)+C&=0 \end{aligned} \qquad (5.68)$$

(3) Coordinate-shift equation: If local surveys have established the geometric relationship between two tracking stations on a local datum, quantities

$$\left.\begin{aligned} d_1&=x_2-x_1\\ d_2&=y_2-y_1\\ d_3&=z_2-z_1 \end{aligned}\right\} \qquad (5.69)$$

may be known with substantial accuracy. The coordinates x_1, y_1, z_1, x_2, y_2, and z_2 may not be well known in a barycentric coordinate system. If the coordinates of the two stations do not reflect the survey information, the differences x_2-x_1, y_2-y_1, and z_2-z_1 are not the same as those given by the local survey. The coordinate shift is an equation requiring the corrections to corresponding coordinates of the j^{th} and k^{th} stations to reproduce the differences in surveyed coordinates. Differentiating equation (5.69) results in

$$\left.\begin{aligned} dx_2-dx&=D_1-(x_2-x_1)\ \text{computed}\\ dy_2-dy_1&=D_2-(y_2-y_1)\ \text{computed}\\ dz_2-dz_1&=D_3-(z_2-z_1)\ \text{computed} \end{aligned}\right\} \qquad (5.70)$$

After replacing dx_2, dy_2, dz_2, dx_1, dy_1, and dz_1, by dx_{k-2}, dx_{k-1}, dx_k, dx_{j-2}, dx_{j-1}, and dx_j, respectively, the coordinate-shift equations are written as

$$\left.\begin{aligned} dx_{k-2} - dx_{j-2} &= c_1 \\ dx_{k-1} - dx_{j-1} &= c_2 \\ dx_k - dx_j &= c_3 \end{aligned}\right\} \qquad (5.71)$$

If an uncertainty is to be attributed to the local surveys, an unknown difference v_i is added to each of the above equations to obtain the statistically weighted constraint form of the coordinate-shift equations:

$$\left.\begin{aligned} v_1 + dx_{k-2} - dx_{j-2} &= c_1 \\ v_2 + dx_{k-1} - dx_{j-1} &= c_2 \\ v_3 + dx_k - dx_j &= c_3 \end{aligned}\right\} \qquad (5.72)$$

5.4.2.2 Surface Gravity

(J. Richardson, Computer Science Corp.)

Conversion of Rapp's Gravity Formula to the GSFC Formula.—The anomalies published by Rapp (1972a) were referred to a gravity formula consistent with the following constants:

$$\begin{aligned} a_e &= 6\,378\,137.8 \text{ meters} \\ f &= 1/298.258 \\ GM &= 3.986\,013 \times 10^{14} \text{ m}^3/\text{sec}^2 \end{aligned}$$

The gravity formula given by Rapp which is consistent with these constants and includes a term of -0.87 mGal for eliminating the mass of the atmosphere is

$$\gamma_{EA} = 978\,033.5\ (1 + .005\,302\,43 \sin^2\phi - 0.000\,005\,87 \sin^2 2\phi \text{ (mGal)} \qquad (5.73)$$

where the subscript EA stands for equal area.

The parameters used in the GEM 6 solution are

$$\begin{aligned} a_e &= 6\,378\,155 \text{ meters} \\ f &= 1/298.255 \\ GM &= 3.986013 \times 10^{14} \text{ m}^3/\text{sec}^2 \\ \omega &= 0.7292115146 \times 10^{-4} \text{ rad/sec} \end{aligned}$$

The parameters above yield the gravity formula

$$\gamma_R = 978\,029.1\ (1 + 0.0053025 \sin^2\phi - 0.00000585 \sin^2 2\phi) \qquad (5.74)$$

where the subscript R stands for reference. Equations (5.73) and (5.74) are used to convert Rapp's data from the equal-area system to the GSFC system through the relationship

$$\Delta g_R = \Delta g_{EA} + \gamma_{EA} - \gamma_R \qquad (5.75)$$

which becomes

$$\Delta g_R = \Delta g_{EA} + 4.4 \qquad (5.76)$$

With this conversion, the equal-area anomalies were used to generate a set of data used for computing normal equations, as described in the following section.

Normal Equations Using Surface Gravity.—Mean free-air gravity anomalies are used to estimate potential coefficients describing the Earth's gravitational field. The analysis required to perform this estimation is as follows. The gravity potential at a point p on the Earth's surface is expressed as

$$W(p) = V(p) + \Phi(p) \qquad (5.77)$$

where

$$V(p) = \frac{GM}{r_p}\left\{1 + \sum_{n=2}^{\infty}\sum_{m=0}^{n}\left[\left(\frac{a_e}{r_p}\right)^n P_n^m(\sin\psi_p)\right.\right. \left.\left.(C_n^m \cos(m\lambda_p) + S_n^m \sin(m\lambda_p))\right]\right\} \qquad (5.78)$$

$$\Phi(p) = \tfrac{1}{2}\,\omega^2\, r_p^2 \cos^2\psi_p \qquad (5.79)$$

The earth's equatorial radius is a_e, and r_p is the geocentric distance to p. The gravity anomaly (Δg) at the point p is expressed in terms of potential coefficients as

$$\begin{aligned} \Delta g_p &= (g_0)_p - (g_c)_p \\ &= \Delta g_0 + \frac{GM}{r_p^2}\left[\sum_{n=2}^{\infty}\sum_{m=0}^{n}(n-1)\left(\frac{a_e}{r_p}\right)^n \right. \\ &\quad \left. (C^*{}_n^m \cos(m\lambda_p) + S_n^m \sin(m\lambda_p)) P_n^m(\sin\psi_p)\right] \end{aligned} \qquad (5.80)$$

where

g_0 is observed gravity derived from the relationship $g_0 = \Delta g + \gamma_0$

γ_0 is normal gravity on the reference surface of the observation

g_c is an estimate of gravity computed from the a priori coefficients, to a sufficient approximation

$$g_c=\left\{\left(\frac{\partial W}{\partial r}\right)^2+\frac{1}{r^2}\left(\frac{\partial W}{\partial \psi}\right)^2\right\}^{1/2} \qquad (5.81)$$

Δg_0 is a constant term representing the variation of mean gravity from the reference system

C_n^{*m} represents the difference between the values of the coefficients and values consistent with the flattening of the ellipsoid to which the anomalies are referred

The observation equations are formed from equation (5.80) as follows:

$$\Delta g_p=K_{00}+K_{20}\Delta C_{20}+\cdots+K_{nm}\Delta C_n^m\cos(m\lambda_p)+\cdots+K_{nm}\Delta S_n^m\sin(m\lambda_p) \qquad (5.82)$$

where

K_{00} = the constant coefficient of Δg_0 for all observations, which is used to estimate Δg_0 simultaneously with the spherical harmonic coefficients

$$K_{nm}=\frac{GM}{r_p^2}(n-1)\left(\frac{a_e}{r_p}\right)^n P_n^m(\sin\psi_p) \qquad (5.83)$$

$$\left.\begin{aligned}\Delta C_n &= C_{nm}^{(s)}-C_{nm}^{(0)}\\ \Delta S_n &= S_{nm}^{(s)}-S_{nm}^{(0)}\end{aligned}\right\} \qquad (5.84)$$

where $C_{nm}^{(s)}$, $S_{nm}^{(s)}$ are the coefficients of the spherical harmonics for the solution model of the gravity field, and the superscript 0 indicates coefficients of the a priori model of the gravity field.

The set of a priori coefficients used in computing the coefficients $C_{nm}^{(0)}$ and $S_{nm}^{(0)}$ corresponds to the coefficients used in the orbital computations, thereby allowing the results from the computations of gravity anomaly to be combined with normal equations derived from satellite-tracking data.

In matrix notation, the set of observation equations is

$$Ax=\delta g \qquad (5.85)$$

where A is an l-by-k matrix (for l observations and k coefficients) of the form

$$a_{ij}=K_{00}+K_{ij}\left\{\begin{matrix}\sin\\ \cos\end{matrix}\right\}(j\lambda_i) \qquad (5.86)$$

where K_{ij} is defined in equation (5.83), where the choice of sine or cosine factor is determined by the occurrence of a sine or cosine term in the j^{th} row of x, and

x is a k-element solution vector of corrections to the coefficients of the spherical harmonics

δg is an l-element vector representing l residuals in observations of gravity

The associated system of weighted least-squares normal equations may be written as

$$(A^TWA)x=(A^TW)\delta g \qquad (5.87)$$

where W is a matrix of weights and is usually inversely proportional to the variance of the measurements ($\sigma_{\Delta g}^2$).

5.4.2.3 Combination of Different Sets of Data

(Mark Sandson, Computer Sciences Corporation)

For GEM 5, the gravitational potential and the station coordinates are computed by using only the orbital (dynamic) theory. For GEM 6, the orbital theory is combined with geometric theory and gravimetric theory.

The dynamic theory is used to generate systems of arc-specific normal equations; i.e., one system of normal equations is generated for a given week-long arc. These systems of normal equations are written in terms of arc-dependent variables (orbital elements) and arc-independent variables (gravitational potential and station parameters). Processing continues by reducing these systems of normal equations to systems written in arc-independent variables only. Once this is done, normal equations using any number of arcs and/or surface and geometric data are combined. The elimination of orbital elements from satellite-specific systems of normal equations is described in this section.

The normal equations formed for individual arcs are of the form

$$\begin{bmatrix} B_1 & B_3^T \\ B_3 & B_2 \end{bmatrix} \begin{bmatrix} X_1 \\ X_2 \end{bmatrix} = \begin{bmatrix} b_1 \\ b_2 \end{bmatrix} \tag{5.88}$$

where

B_1 is the $k \times k$ matrix of coefficients involving partial derivatives with respect to arc-independent variables only

B_2 is the $(n-k) \times (n-k)$ matrix of coefficients involving arc-dependent partial derivatives only

B_3 is the $(n-k) \times -k$ matrix of coefficients involving product term partial derivatives of arc-independent and arc-dependent variables

X_1 is the k-dimensional vector $X_1, \ldots, X_k$ involving arc-independent variables (gravitational parameters and tracking station coordinates)

X_2 is the $(n-k)$-dimensional vector $X_{k+1}, \ldots, X_n$ involving arc-dependent variables (satellite vectors, tracking system biases, and drag and radiation pressure coefficients)

b_1 is the k-dimensional portion of the right-hand vector associated with the arc-independent and product-term partial derivatives (B_1 and B_3^T)

and

b_2 is the $(n-k)$-dimensional portion of the right-hand vector associated with the arc-dependent and product term partial derivatives (B_2 and B_3)

The back substitution solution for X_2 gives

$$X_2 = B_2^{-1} (b_2 - B_3 X_1) \tag{5.89}$$

Using this result to find X_1 produces the expression

$$B_1 X_1 + B_3^T [B_2^{-1} (b_2 - B_3 X_1)] = b_1 \tag{5.90}$$

which yields the equation

$$(B_1 - B_3^T B_2^{-1} B_3) X_1 = b_1 - B_3^T B_2^{-1} b_2 \tag{5.91}$$

Equation (5.91) is the reduced system of normal equations in arc-independent variables only. A reduced set of normal equations is formed for each arc prior to its aggregation to form a multiarc solution for the arc-independent variables. Once equation (5.91) is solved, the result is substituted into equation (5.89) to produce an estimate of X_2, the arc-dependent variables.

A notational simplification is obtained by

$$\begin{aligned} B^* &= B_1 - B_3^T B_2^{-1} B_3 \\ b^* &= b_1 - B_3^T B_2^{-1} b_2 \\ X^* &= X_1 \end{aligned} \tag{5.92}$$

which produces a reduced set of normal equations of the form

$$B^* X^* = b^* \tag{5.93}$$

The combined, reduced, normal equations are formed by simple matrix addition, where

$$C = \sum_{i=1}^{N} B_i^*$$

$$c = \sum_{i=1}^{N} b_i^*$$

and where N is the number of systems of normal equation to be combined. In the GEM solutions, each of the N normal equations is weighted by a factor $(1/\text{rms}^2)$, where rms is the weighted rms of residuals for the system of normal equations used. The resulting combined normal equations are of the form

$$CX^* = c \tag{5.94}$$

Solving equation (5.94) yields

$$X^* \quad C^{-1} c \tag{5.95}$$

from which X^* is used to obtain estimates of the gravitational potential and the coordinates of the stations.

5.4.3 Theory Used to Derive the Detailed Global Geoid

(S. Vincent and J. Marsh)

In section 5.6.3, a model is presented of the geoid which covers the entire earth with a contour interval of 2 meters. This model was derived by first computing geoidal heights using a gravitational potential derived by dynamic satellite geodesy and adding to these additional geoidal heights derived from gravimetric data.

The geoidal height at any point P on the Earth can be computed by means of the well-known formula of Stokes:

$$N(\psi, \lambda) = \frac{R}{4\pi\bar{\gamma}} \int_{\lambda'=0}^{2\pi} \int_{\psi'=-\frac{\pi}{2}}^{\pi/2} \Delta g_T(\psi', \lambda') S(\theta) \cos\psi' \, d\psi' \, d\lambda' \qquad (5.96)$$

where

ψ, λ	are the geocentric latitude and longitude of the fixed point
ψ', λ'	are the geocentric latitude and longitude of the variable point
$N(\psi, \lambda)$	is the geoidal height at ψ, λ
R	is the mean radius of the Earth
$\bar{\gamma}$	is the mean value of gravity over the Earth
$\Delta g_T(\psi', \lambda')$	is the free-air gravity anomaly at the variable point

and

$$S(\theta) = \frac{1}{\sin(\theta/2)} - 6\sin(\theta/2) + 1 + 5\cos\theta - 3\cos\theta \ln\sin(\theta/2) + \sin^2(\theta/2)$$

where

$$\theta = \cos^{-1}[\sin\psi \sin\psi' + \cos\psi \cos\psi' \cos(\lambda - \lambda')] \qquad (5.97)$$

In order to combine surface data and data derived from GEM 4 (Lerch *et al.*, 1972c) for computing the geoidal height at point P, the Earth is divided into two areas, a local area (A_1) surrounding the point P, and the remainder of the Earth (A_2). Also, each gravity anomaly in each area is partitioned into two parts, Δg_s and Δg_2. The Δg_s value is defined as that part of the gravity anomaly which can be represented by the coefficients in a spherical harmonic expansion of the gravitational potential derived from satellite observations. The Δg_2 value is defined as the remainder of the gravity anomaly. Using this division, one can write equation (5.96) in the form:

$$N(\psi,\lambda) = N_1 + N_2 + N_3 \qquad (5.98)$$

where

$$N_1 = \frac{R}{4\pi\bar{\gamma}} \int_0^{2\pi} \int_{-\frac{\pi}{2}}^{\frac{\pi}{2}} [\Delta g_s(\psi',\lambda') S(\theta) \cos\psi' \, d\psi' \, d\lambda']$$

$$N_2 = \frac{R}{4\pi\bar{\gamma}} \int_{A_1} \int [\Delta g_2(\psi',\lambda') S(\theta) \cos\psi' \, d\psi' \, d\lambda']$$

$$N_3 = \frac{R}{4\pi\bar{\gamma}} \int_{A_2} \int [\Delta g_2(\psi',\lambda') S(\theta) \cos\psi' \, d\psi' \, d\lambda'] \qquad (5.99)$$

How each of the three components presented in equation (5.99) is handled in the computations is now considered.

Given a set of coefficients $\bar{C}_n^m$, $\bar{S}_n^m$, a number of methods exist for computing the N_1 component of the geoidal height.

In the present case, N_1 was not computed by using the integration indicated in equation (5.99). Instead, the procedure described by Bacon *et al.* (unpublished, 1970) was used. Briefly, this procedure consists of fixing a value of the potential W_o and computing the component N_1 as

$$N_1 = r - r_e \qquad (5.100)$$

where r is the radial distance to the equipotential surface defined by W_o and the potential coefficients of the GEM 4 gravitational potential model and r_E is the radial distance to a selected reference—an ellipsoid defined by a semimajor axis a_e and flattening f.

The radial distance r to the equipotential surface W_o at a particular latitude and longitude ψ, λ is determined by using the equation

$$W_o=\Omega(r,\psi,\lambda)=\frac{GM}{r}\left[1+\sum_{n=2}^{k}\sum_{m=0}^{n}\left(\frac{a_e}{r}\right)^n(\bar{C}_n^m\cos m\lambda+\bar{S}_n^m\sin m\lambda)\bar{P}_n^m(\sin\psi)\right]+\frac{\omega^2r^2}{2}\cos^2\psi \quad (5.101)$$

where r is the geocentric radius, the only unknown in this equation. Values of $r_1=R+\epsilon$, $r_2=R-\epsilon$, and $r_3=(r_1+r_2)/2$ are chosen for substitution into equation (5.101) for evaluation of the functions $\Omega_1(r_1,\psi,\lambda)$, $\Omega_2(r_2,\psi,\lambda)$, and $\Omega_3(r_3,\psi,\lambda)$.

The r_i for which $|\Omega_i-W_o|$ is a maximum is identified and eliminated from consideration. The two remaining values of r_i are labeled r_1 and r_2 and are used for calculation of $r_3=(r_1+r_2)/2$. The potential functions are evaluated with these arguments and the worst-value elimination process is repeated. The process continues until an r is chosen so that $|\Omega(r,\psi,\lambda)-W_o|\leq10^{-12}$. With this value of r and the value of r_E computed from the input values of a_e and f of the reference ellipsoid, a component N_1 is computed. The area A_1 for a point at which the geoid was being computed was defined to consist of a 20-degree by 20-degree area centered on the point. The formula used was

$$N_2=\frac{R}{4\pi\bar{\gamma}}\sum_{j=1}^{400}\overline{\Delta g}_2(\psi_j',\lambda_j')S(\theta_j)\cos\psi_j'\Delta\psi'\Delta\lambda' \quad (5.102)$$

where

$\overline{\Delta g}_2(\psi_j',\lambda_j')$ is the mean value of $\overline{\Delta g}_2$ within the j^{th} 1-degree by 1-degree square

$S(\theta)_j$ is the value of Stokes' function at the center of the j^{th} 1-degree by 1-degree square

$\Delta\psi'$ $=\Delta\lambda'=1^\circ$

The value of Δg_2 used for each 1-degree by 1-degree square was computed from the formula

$$\overline{\Delta g}_2=\overline{\Delta g}_e-\overline{\Delta g}_s$$

The $\overline{\Delta g}_e$ values are mean 1-degree by 1-degree free-air anomalies provided by surface gravity data. Values of Δg_e for each 1-degree by 1-degree square were computed by carrying out the computation

$$\overline{\Delta g}_e=\Delta g_{IF}+\gamma_{IF}+P.C.-\gamma_N$$

where

Δg_{IF} is the mean value of free-air anomaly referred to the International Gravity Formula (1924)

γ_{IF} is the value of surface gravity as computed from the International Gravity Formula (1924)

$P.C.$ is the Potsdam correction, 13.7 mGal

γ_N $=978\,032.2\,(1+0.0053025\sin^2\psi-0.00000585\sin^2 2\psi$ mGal (Rapp, 1969)

In carrying out the computations, γ_{IF} and γ_n were evaluated at the center of each 1-degree by 1-degree square.

The $\overline{\Delta g}_s$ values are that part of the mean 1-degree by 1-degree free-air anomalies represented by the GEM 4 harmonic coefficients used in computing N_1. The $\overline{\Delta g}_s$ values are obtained by evaluating the following equation at the center of each 1-degree by 1-degree square:

$$\overline{\Delta g}_s=\bar{\gamma}\sum_{n=2}^{k}\sum_{m=0}^{n}(n-1)\,[\bar{C}_n^m\cos m\lambda'+\bar{S}_n^m\sin m\lambda']\bar{P}_n^m(\sin\psi') \quad (5.103)$$

where $\bar{\gamma}$ is the mean value of gravity over the Earth in milligals.

In equation (5.103), the $\overline{C_2^\circ}$ and $\overline{C_4^\circ}$ terms do not represent the complete coefficients, but rather the difference between the complete coefficients and the coefficients compatible with the ellipsoid used in computing N_1. The differences used were $\overline{\Delta C_2^\circ}=0.01954\times10^{-6}$ and $\overline{\Delta C_4^\circ}=-0.2417\times10^{-6}$ (fully normalized). For the procedure described above to produce correct results, the quantities $\overline{\Delta g}_e$, $\overline{\Delta g}_s$, and the a and f which define the ellipsoid used to compute N_1 must all be compatible. Compatibility implies that the values of C_2° and C_4° used to compute the values of theoretical gravity needed to obtain $\overline{\Delta g}_e$ and $\overline{\Delta g}_s$ are the same as the values of $\overline{C_2^\circ}$ and

$\overline{C_4^0}$, implied by the reference ellipsoid. Correct results in the absolute sense also depend upon the value of W_0 chosen to represent the true value of the potential of the geoid.

The effects of not making $\overline{\Delta g_e}$, $\overline{\Delta g_s}$, a_e, and f compatible are twofold. First, all the computed geoidal heights may be in error by a constant. In addition, there will be a systematic error as a function of latitude. The effect of selecting an incorrect value of W_0 would be to introduce a constant error in all geoidal heights.

In the calculations described here, the term N_3 in equation (5.98) was set equal to zero. This is equivalent to assuming that the GEM 4 values for gravitation are adequate for the area A_2 at a distance of more than 10 degrees from the computation point.

5.4.4 Theory Used for Special Purposes

The theory presented in sections 5.4.1 and 5.4.2 is satisfactory for determining orbits, tracking station locations, and gravitational potential. For other purposes, theories having special applications are preferred. It may be remembered that the theory of section 5.4.1 involves numerical integration of the differential equations of motion. Such a procedure is excellent from a computational point of view, but it does not give any advanced insight into the physical results. When this is needed, an analytic theory must be used. GSFC found that an analytic theory was particularly needed to account for the luni-solar and solar-radiation pressure perturbations of the orbits of near-earth satellites. This theory is given in the next two sections. Note that the equations are truncated. The full expansion, too lengthy to be given here, will be found in Murphy and Felsentreger (1966) for luni-solar perturbations. The theory for perturbation by solar radiation pressure is given in various internal publications by GSFC. In sections 5.6.4.1 and 5.6.4.2, typical perturbations are evaluated by means of these theories.

In order to get a better grip on the relations between dynamic satellite geodesy and the structure of the solid earth, M. A. Khan developed the theory of the hydrostatic flattening of the earth as far as terms to the second order in J2. This theory is given in section 5.4.4.3. The new figure and the constants needed to convert from the International Gravity Formula (1924) to the formula appropriate to the hydrostatic figure are given in section 5.6.4.3.

Because dynamic satellite geodesy uses the Earth's gravitational field in the form of a series of associated Legendre polynomials, whereas gravimetric geodesy adds on the centrifugal force and expresses the result as gravity anomalies, conversion from one form to the other is laborious. Khan used the theory of isostatic gravity anomalies and an expression of the Earth's topography in spherical harmonies to expand the isostatic potential into spherical harmonics. This theory is given along with the results in section 5.6.4.4.

5.4.4.1 Luni-Solar Gravitational Perturbations (J. Murphy and T. Felsentreger)

The disturbing function for the Sun (or Moon) is

$$R=\frac{GM'}{r'}\left[\frac{r^2}{r'^2}P_2(S)+\frac{r^3}{r'^3}P_3(S)+\cdots\cdots\right]$$

which can be expanded in terms of artificial satellite orbital elements and solar (lunar) ephemeris quantities. In this expression,

- m' is the ratio of the mass of the Sun (or Moon) to the mass of the Sun (or Moon) plus the mass of the Earth
- r' is the geocentric distance of the Sun (Moon)
- r is the geocentric distance of the satellite
- S $=\cos(r\,r')$.

Only secular and long-period terms from the second and third Legendre polynomials are considered (i.e., only those terms not dependent upon the mean anomaly of the satellite). In addition, terms from the third

Legendre polynomial having the eccentricity of the disturbing body as a multiplier are neglected. The Earth's equatorial plane is adopted as the fundamental plane.

The secular and long-period part of the disturbing function then, is

$$R=n'^2m'a^2\left\{\left[\left(1+\frac{3}{2}e^2\right)P+\frac{15}{8}e^2Q\right]-\frac{a}{a'}\left[\left(\frac{15}{64}e+\frac{45}{256}e^3\right)Y+\frac{175}{64}e^3Z\right]\right\}$$

where

$$P=\frac{1}{4}\left(1-\frac{3}{2}\sin^2 i\right)\left(1-\frac{3}{2}\sin^2 i'\right)[1+3e'\cos(\lambda'-\omega'-\Omega')]$$
$$+\frac{3}{16}\sin 2i\sin 2i'\left[\cos(\Omega'-\Omega)+\frac{3}{2}e\cos(\lambda'-\omega'-\Omega)+\frac{3}{2}e'\cos(\lambda'-\omega'-2\Omega'+\Omega)\right]+\cdots$$

$$Q=\cos^4\frac{i}{2}\cos^4\frac{i'}{2}\left[\cos(2\lambda'-2\omega-2\Omega)-\frac{1}{2}e'\cos(\lambda'+\omega'+\Omega'-2\omega-2\Omega)+\frac{7}{2}e'\cos(3\lambda'-\omega'-\Omega'-2\omega-2\Omega)\right]$$
$$+\frac{1}{2}\sin^2 i\left(1-\frac{3}{2}\sin^2 i'\right)\left[\cos^2\omega+\frac{3}{2}e'\cos(\lambda'-\omega'-\Omega'-2\omega)+\frac{3}{2}e'\cos(\lambda'-\omega'-\Omega'+2\omega)\right]+\cdots$$

$$Y=-\frac{3}{4}\sin i(1-5\cos^2 i)\sin i'(1-5\cos^2 i')\cos(\lambda'-\Omega'+\omega)$$
$$+\frac{1}{4}\cos^2\frac{i}{2}(1+10\cos i-15\cos^2 i)\sin^2\frac{i'}{2}(1-10\cos i-15\cos^2 i)\cos(\lambda'-2\Omega'+\omega+\Omega)$$
$$+\frac{1}{4}\sin^2\frac{i}{2}(1+10\cos i-15\cos^2 i)\sin^2\frac{i'}{2}(1+10\cos i'-15\cos^2 i')\cos(\lambda'+\omega-\Omega)$$
$$-\frac{5}{8}\sin i(1-2\cos i-3\cos^2 i)\sin i'(1+2\cos i'-3\cos^2 i')\cos(\lambda'-3\Omega'+\omega+2\Omega)$$
$$-\frac{5}{8}\sin i(1+2\cos i-3\cos^2 i)\sin i'(1-2\cos i'-3\cos^2 i')\cos(\lambda'+\Omega'+\omega-2\Omega)+\cdots$$

and

$$Z=\frac{3}{16}\sin^3 i\sin i'(1-5\cos^2 i')\cos(\lambda'-\Omega'+3\omega)$$
$$-\frac{3}{16}\sin^2 i\cos^2\frac{i}{2}\sin^2\frac{i'}{2}(1-10\cos i'-15\cos^2 i')\cos(\lambda'-2\Omega'+3\omega+\Omega)$$
$$-\frac{3}{16}\sin^2 i\sin^2\frac{i}{2}\cos^2\frac{i'}{2}(1+10\cos i'-15\cos^2 i')\cos(\lambda'+3\omega-\Omega)+\cdots$$

The disturbing function R is substituted into the variation equations for de/dt and di/dt, and these equations are integrated to obtain perturbations δe and δi. Then, the following equations are integrated:

$$\frac{d(\delta M)}{dt}=\frac{dM}{dt}-n+\frac{d\dot{M}}{de}\delta e+\frac{d\dot{M}}{di}\delta i$$
$$\frac{d(\delta\omega)}{dt}=\frac{d\omega}{dt}+\frac{d\dot{\omega}}{de}\delta e+\frac{d\dot{\omega}}{di}\delta i$$
$$\frac{d(\delta\Omega)}{dt}=\frac{d\Omega}{dt}+\frac{d\dot{\Omega}}{de}\delta e+\frac{d\dot{\Omega}}{di}\delta i$$

where $\dot{M}$, $\dot{\omega}$ and $\dot{\Omega}$ are expressed by

$$\dot{M}=n\left\{1-\frac{3C_2^0a_e^2}{4a^2(1-e^2)^{3/2}}(1-3\cos^2 i)+\frac{3(C_2^0)^2a_e^2}{128a^4(1-e^2)^{1/2}}\right.$$
$$[10-25e^2+16\sqrt{1-e^2}-6(10-15e^2+16\sqrt{1-e^2})\cos^2 i+(130-25e^2+144\sqrt{1-e^2})\cos^4 i]$$
$$\left.-\frac{45C_4^0a_e^4e^2}{128a^4(1-e^2)^{1/2}}(3-30\cos^2 i+35\cos^4 \mathrm{i})\right\}$$

$$\dot{\omega}=n\left\{-\frac{3C_2^0a_e^2}{4a^2(1-e^2)^2}(1-5\cos^2 i)+\frac{3(C_2^0)^2a_e^2}{128a^4(1-e^2)^4}\right.$$
$$[-10-25e^2+24\sqrt{1-e^2}-6(6-21e^2+32\sqrt{1-e^2})\cos^2 i+5(86-9e^2+72\sqrt{1-e^2})\cos^4 i]$$
$$\left.-\frac{15C_4^0a_e^4}{128a^4(1-e^2)^4}[3(4+3e^2)-18(8+7e^2)\cos^2 i+7(28+27e^2)\cos^4 i]\right\}$$

$$\dot{\Omega}=n\left\{-\frac{3C_2^0a_e^2\cos i}{2a^2(1-e^2)^2}+\frac{3(C_2^0)^2a_e^2\cos i}{32a^4(1-e^2)^4}[4-9e^2+12\sqrt{1-e^2}-(40-5e^2+36\sqrt{1-e^2})\cos^2 i]\right.$$
$$\left.-\frac{15C_4^0a_e^4(2+3e^2)\cos i}{32a^4(1-e^2)^4}(3-7\cos^2 i)\right\}$$

Integration of the variation equations is accomplished by assuming that a, e, i, a', e', and i' are constants and that ω, Ω, λ', ω', and Ω' are linear functions of time. The secular motions for ω and Ω are $\dot{\omega}$ and $\dot{\Omega}$ as expressed above. Thus

$$\delta e=-\frac{\sqrt{1-e^2}}{na^2e}A_1$$

$$\delta i=\frac{\cos i}{na^2\sqrt{1-e^2}\sin i}A_1-\frac{1}{na^2\sqrt{1-e^2}\sin i}A_2$$

$$\delta\omega=-\frac{\cos i}{na^2\sqrt{1-e^2}\sin i}A_5+\frac{\sqrt{1-e^2}}{na^2e}A_4+\frac{d\dot{\omega}}{de}A_6+\frac{d\dot{\omega}}{di}A_7$$

$$\delta\Omega=\frac{1}{na^2\sqrt{1-e^2}\sin i}A_5+\frac{d\dot{\Omega}}{de}A_6+\frac{d\dot{\Omega}}{di}A_7 \qquad \delta M=-\frac{2}{na}A_3-\frac{1-e^2}{na^2e}A_4+\frac{d\dot{M}}{de}A_6+\frac{d\dot{M}}{di}A_7$$

Expressions for the various A_i are as follows:

$$A_1=\int\frac{\partial R}{\partial\omega}\,dt$$
$$=-\frac{15}{64}n'^2m'a^2e^2\left\{-4\sin^2 i\left(1-\frac{3}{2}\sin^2 i'\right)\right.$$
$$\left[\frac{2\cos 2\omega}{2\dot{\omega}}-3e'\frac{\cos(\lambda'-\omega'-\Omega'-2\omega)}{\dot{\lambda}'-\dot{\omega}'-\dot{\Omega}'-2\dot{\omega}}+3e'\frac{\cos(\lambda'-\omega'-\Omega'+2\omega)}{\dot{\lambda}'-\dot{\omega}'-\dot{\Omega}'+2\dot{\omega}}\right]$$
$$+3\sin^2 i\sin^2 i'\left[\frac{2\cos(2\lambda'-2\Omega'-2\omega)}{2(\dot{\lambda}'-\dot{\Omega}'-\dot{\omega})}-e'\frac{\cos(\lambda'+\omega'-\Omega'-2\omega)}{\dot{\lambda}'+\dot{\omega}'-\dot{\Omega}'-2\dot{\omega}}+7e'\frac{\cos(3\lambda'-\omega'-3\Omega'-2\omega)}{3\dot{\lambda}'-\dot{\omega}'-3\dot{\Omega}'+2\dot{\omega}}\right]$$
$$\left.-3\sin^2 i\sin^2 i'\left[\frac{2\cos(2\lambda'-2\Omega'+2\omega)}{2(\dot{\lambda}'-\dot{\Omega}'+\dot{\omega})}-e'\frac{\cos(\lambda'+\omega'-\Omega'+2\omega)}{\dot{\lambda}'+\dot{\omega}'-\dot{\Omega}'+2\dot{\omega}}+7e'\frac{\cos(3\lambda'-\omega'-3\Omega'+2\omega)}{3\dot{\lambda}'-\dot{\omega}'-3\dot{\Omega}'+2\dot{\omega}}\right]\right\}$$
$$+\cdots$$

(See following page.)

$$-m'\frac{a^3}{a'^4}\left(\frac{15}{64}e+\frac{45}{256}e^3\right)\left[-\frac{3}{4}\sin i\ (1-5\cos^2 i)\ \sin i'(1-5\cos^2 i')\frac{\cos\ (\lambda'-\Omega'+\omega)}{\dot\lambda'-\dot\Omega'+\dot\omega}\right.$$
$$-\frac{3}{4}\sin i\ (1-5\cos^2 i)\ \sin i'\ (1-5\cos^2 i')\ \frac{\cos\ (\lambda'-\Omega'-\omega)}{\dot\lambda'-\dot\Omega'-\dot\omega}$$
$$+\frac{5}{4}\sin i\ (1-5\cos^2 i)\ \sin^3 i'\frac{\cos\ (3\lambda'-3\Omega'+\omega)}{3\dot\lambda'-3\dot\Omega'+\dot\omega}$$
$$\left.+\frac{5}{4}\sin i\ (1-5\cos^2 i)\ \sin^3 i'\frac{\cos\ (3\lambda'-3\Omega'-\omega)}{3\dot\lambda'-3\dot\Omega'-\dot\omega}\right]+\cdots$$
$$-\frac{175}{64}m'\frac{a}{a'^4}e^3\left[\frac{9}{16}\sin^3 i\sin i'(1-5\cos^2 i')\frac{\cos\ (\lambda'-\Omega'+3\omega)}{\dot\lambda'-\dot\Omega'+3\dot\omega}\right.$$
$$+\frac{9}{16}\sin^3 i\sin i'\ (1-5\cos^2 i')\frac{\cos\ (\lambda'-\Omega'-3\omega)}{\dot\lambda'-\dot\Omega'-3\dot\omega}$$
$$\left.-\frac{15}{16}\sin^3 i\sin^3 i'\frac{\cos(3\lambda'-3\Omega'+3\omega)}{3\dot\lambda'-3\dot\Omega'+3\dot\omega}\ -\frac{15}{16}\sin^3 i\sin^3 i'\frac{\cos(3\lambda'-3\Omega'-3\omega)}{3\dot\lambda'-3\dot\Omega'-3\dot\omega}\right]+\cdots$$

$$A_2=\int\frac{\partial R}{\partial\Omega}dt$$
$$=\frac{3}{32}n'^2\,m'\,a^2\left(1+\frac{3}{2}e^2\right)$$
$$\left\{-\sin 2i\sin 2i'\left[2\frac{\cos\ (\Omega'-\Omega)}{\dot\Omega'-\dot\Omega}+3e'\frac{\cos\ (\lambda'-\omega'-\Omega)}{\dot\lambda'-\dot\omega'-\dot\Omega}-3e'\frac{\cos\ (\lambda'-\omega'-2\Omega'+\Omega)}{\dot\lambda'-\dot\omega'-2\dot\Omega'+\dot\Omega}\right]\right.$$
$$-2\sin^2 i\sin^2 i'\left[\frac{2\cos\ (2\Omega'-2\Omega)}{2\,(\dot\Omega'-\dot\Omega)}+3e'\frac{\cos\ (\lambda'-\omega'+\Omega'-2\Omega)}{\dot\lambda'-\dot\omega'+\dot\Omega'-2\dot\Omega}-3e'\frac{\cos\ (\lambda'-\omega'-3\Omega'+2\Omega)}{\dot\lambda'-\dot\omega'-3\dot\Omega'+2\dot\Omega}\right]$$
$$-4\sin^2 i\cos^4\frac{i'}{2}\left[2\frac{\cos\ (2\lambda'-2\Omega)}{2\,(\dot\lambda'-\dot\Omega)}-e'\frac{\cos\ (\lambda'+\omega'+\Omega'-2\Omega)}{\dot\lambda'-\dot\omega'+\dot\Omega'-2\dot\Omega}+7e'\frac{\cos\ (3\lambda'-\omega'-\Omega'-2\Omega)}{3\dot\lambda'-\dot\omega'-\dot\Omega'-2\dot\Omega}\right]$$
$$+2\sin 2i\sin i'\cos^2\frac{i'}{2}\left[2\frac{\cos\ (2\lambda'-\Omega'-\Omega)}{2\dot\lambda'-\dot\Omega'-\dot\Omega}-e'\frac{\cos\ (\lambda'+\omega'-\Omega)}{\dot\lambda'+\dot\omega'-\dot\Omega}+7e'\frac{\cos\ (3\lambda'-\omega'-2\Omega'-\Omega)}{3\dot\lambda'-\dot\omega'-2\dot\Omega'-\dot\Omega}\right]$$
$$+4\sin^2 i\sin^4\frac{i'}{2}\left[\frac{2\cos\ (2\lambda'-4\Omega'+2\Omega)}{2\,(\dot\lambda'-2\dot\Omega'+\dot\Omega)}-e'\frac{\cos\ (\lambda'+\omega'-3\Omega'+2\Omega)}{\dot\lambda'+\dot\omega'-3\dot\Omega'+2\dot\Omega}+7e'\frac{\cos\ (3\lambda'-\omega'-5\Omega'+2\Omega)}{3\dot\lambda'-\dot\omega'-5\dot\Omega'+2\dot\Omega}\right]$$
$$+2\sin 2i\sin i'\sin^2\frac{i'}{2}$$
$$\left.\times\left[2\frac{\cos\ (2\lambda'-3\Omega'+\Omega)}{2\dot\lambda'-3\dot\Omega'+\dot\Omega}-e'\frac{\cos\ (\lambda'+\omega'-2\Omega'+\Omega)}{\dot\lambda'+\dot\omega'-2\dot\Omega'+\dot\Omega}+7e'\frac{\cos\ (3\lambda'-\omega'-4\Omega'+\Omega)}{3\dot\lambda'-\dot\omega'-4\dot\Omega'+\dot\Omega}\right]\right\}+\cdots$$

$$A_3=\int\frac{\partial R}{\partial a}dt$$
$$=2n'^2\,m'\,a\left\{\left[\left(1+\frac{3}{2}e^2\right)\int Pdt+\frac{15}{8}e^2\int Qdt\right]\right.$$
$$\left.-\frac{3a}{2a'}\left[\left(\frac{15}{16}e+\frac{45}{256}e^3\right)\int Ydt+\frac{175}{64}e^3\int Zdt\right]\right\}$$

and

$$A_4=\int\frac{\partial R}{\partial e}dt$$
$$=3n'^2\,m'\,a^2\left\{e\left[\int Pdt+\frac{5}{4}\int Qdt\right]-\frac{a}{a'}\left[\left(\frac{5}{64}+\frac{45}{256}e^2\right)\int Ydt+\frac{175}{64}e^2\int Zdt\right]\right\}$$

where

$$\int P dt = \frac{1}{16}\left(1-\frac{3}{2}\sin^2 i\right)\alpha_1 + \frac{3}{32}\sin^2 i\,(\alpha_2) + \frac{3}{32}\sin^2 i\,(\alpha_3)$$

$$\int Q dt = \frac{1}{4}\cos^4\frac{i}{2}(\alpha_4) + \frac{1}{16}\sin^2 i\ (\alpha_5) + \frac{1}{4}\sin^4\frac{i}{2}(\alpha_6) + \frac{1}{4}\sin i\cos^2\frac{i}{2}(\alpha_7) + \frac{1}{4}\sin i\sin^2\frac{i}{2}(\alpha_8)$$

$$\int Y dt = \frac{1}{4}\sin i\ (1-5\cos^2 i)\ (\alpha_9) + \frac{1}{4}\cos^2\frac{i}{2}(1+10\cos i-15\cos^2 i)\ (\alpha_{10})$$
$$+\frac{1}{4}\sin^2\frac{i}{2}(1-10\cos i-15\cos^2 i)\ (\alpha_{11}) + \frac{5}{8}\sin^2 i\sin^2\frac{i}{2}(\alpha_{15})$$

$$\int Z dt = \frac{1}{16}\sin^3 i\ (\alpha_{16}) + \frac{3}{16}\sin^2 i\cos^2\frac{i}{2}(\alpha_{17}) + \frac{3}{16}\sin^2 i\sin^2\frac{1}{2}(\alpha_{18})$$
$$+\frac{3}{8}\sin i\cos^4\frac{i}{2}(\alpha_{19}) + \frac{3}{8}\sin i\sin^4\frac{i}{2}(\alpha_{20}) + \frac{1}{4}\cos^6\frac{i}{2}(\alpha_{21}) + \frac{1}{4}\sin^6\frac{i}{2}(\alpha_{22})$$

where

$$\alpha_1 = 4a_{61} + 3a_{62}$$
$$a_{61} = \left(1-\frac{3}{2}\sin^2 i'\right)\left[1+3e'\frac{\sin\ (\lambda'-\omega'-\Omega')}{\dot\lambda'-\dot\omega'-\dot\Omega'}\right]$$
$$a_{62} = \sin^2 i'\left[\frac{2\sin\ (2\lambda'-2\Omega')}{2\,(\dot\lambda'-\dot\Omega')} - e'\frac{\sin\ (\lambda'+\omega'-\Omega')}{\dot\lambda'+\dot\omega'-\dot\Omega'} + 7e'\frac{\sin\ (3\lambda'-\omega'-3\Omega')}{3\dot\lambda'-\dot\omega'-3\dot\Omega'}\right]$$

and so on, the other α_i being similar functions of terms a_j similar to a_{61} and a_{62}.

$$A_5 = \int \frac{\partial R}{\partial i} dt$$
$$= \frac{3}{16}n'^2 m' a^2\left(1+\frac{3}{2}e^2\right)[\sin i\cos i\ (-\alpha_1+\alpha_3) + \cos 2i\ (\alpha_2)] + \cdots$$

$$A_6 = \int \delta e\ dt$$
$$= \frac{\sqrt{1-e^2}}{na^2 e}\int A_1\ dt$$
$$= \frac{15}{128}\frac{n'^2}{n}m'e\sqrt{1-e^2}\Bigg\{-4\sin^2 i$$
$$\left(1-\frac{3}{2}\sin^2 i'\right)\left[\frac{4\sin 2\omega}{4\dot\omega^2} - 6e'\frac{\sin\ (\lambda'-\omega'-\Omega'-2\omega)}{(\dot\lambda'-\dot\omega'-\dot\Omega'-2\dot\omega)^2} + 6e'\frac{\sin\ (\lambda'-\omega'-\Omega'+2\omega)}{(\dot\lambda'-\dot\omega'-\dot\Omega'+2\dot\omega)^2}\right]$$
$$+3\sin^2 i\sin^2 i'\left[\frac{4\sin\ (2\lambda'-2\Omega'-2\omega)}{4\,(\dot\lambda'-\dot\Omega'-\dot\omega)^2} - 2e'\frac{\sin\ (\lambda'+\omega'-\Omega'-2\omega)}{(\dot\lambda'+\dot\omega'-\dot\Omega'-2\dot\omega)^2} + 14e'\frac{\sin\ (3\lambda'-\omega'-3\Omega'-2\omega)}{(3\dot\lambda'-\dot\omega'-3\dot\Omega'-2\dot\omega)^2}\right]$$
$$-3\sin^2 i\sin^2 i'\left[\frac{4\sin\ (2\lambda'-2\Omega'+2\omega)}{4\,(\dot\lambda'-\dot\Omega'+\dot\omega)^2} - 2e'\frac{\sin\ (\lambda'+\omega'-\Omega'+2\omega)}{(\dot\lambda'+\dot\omega'-\dot\Omega'+2\dot\omega)^2} + 14e'\frac{\sin\ (3\lambda'-\omega'-3\Omega'+2\omega)}{(3\dot\lambda'-\dot\omega'-3\dot\Omega'+2\dot\omega)^2}\right]$$
$$+8\,(a_{140}-a_{142}-a_{143}+a_{144}-a_{146}-a_{148}) + 4\,(a_{141}-a_{147}) + 16\,(a_{145}+a_{149}+a_{150}+a_{151})\Bigg\} + \cdots$$

where

$$a_{140} = \cos^4\frac{i}{2}\cos^4\frac{i'}{2}$$
$$\left[\frac{4\sin\ (2\lambda'-2\omega-2\Omega)}{4\,(\dot\lambda'-\dot\omega-\dot\Omega)^2} - 2e'\frac{\sin\ (\lambda'+\omega'+\Omega'-2\omega-2\Omega)}{(\dot\lambda'+\dot\omega'+\dot\Omega'-2\dot\omega-2\dot\Omega)^2} + 14e'\frac{\sin\ (3\lambda'-\omega'-\Omega'-2\omega-2\Omega)}{(3\dot\lambda'-\dot\omega'-\dot\Omega'-2\dot\omega-2\dot\Omega)^2}\right]$$

$$a_{141}=\cos^4\frac{i}{2}\sin^2 i'$$
$$\left[\frac{4\sin(2\Omega'-2\omega-2\Omega)}{4(\dot\Omega'-\dot\omega-\dot\Omega)^2}+6e'\frac{\sin(\lambda'-\omega'+\Omega'-2\omega-2\Omega)}{(\dot\lambda'-\dot\omega'+\dot\Omega'-2\dot\omega-2\dot\Omega)^2}-6e'\frac{\sin(\lambda'-\omega'-3\Omega'+2\omega+2\Omega)}{(\dot\lambda'-\dot\omega'-3\dot\Omega'+2\dot\omega+2\dot\Omega)^2}\right]$$

$$a_{142}=\sin^4\frac{i}{2}\cos^4\frac{i'}{2}$$
$$\left[\frac{4\sin(2\lambda'+2\omega-2\Omega)}{4(\dot\lambda'+\dot\omega-\dot\Omega)^2}-2e'\frac{\sin(\lambda'+\omega'+\Omega'+2\omega-2\Omega)}{(\dot\lambda'+\dot\omega'+\dot\Omega'+2\dot\omega-2\dot\Omega)^2}+14e'\frac{\sin(3\lambda'-\omega'-\Omega'+2\omega-2\Omega)}{(3\dot\lambda'-\dot\omega'-\dot\Omega'+2\dot\omega-2\dot\Omega)^2}\right]$$

etc.

$$A_7=\int\delta i\,dt$$
$$=\frac{\cos i}{na^2\sqrt{1-e^2}\sin i}\int A_1\,dt-\frac{1}{na^2\sqrt{1-e^2}\sin i}\int A_2\,dt$$
$$=-\frac{e\cot i}{1-e^2}A_6-\frac{3}{32}\frac{n'^2}{n}\frac{m'}{\sqrt{1-e^2}\sin i}$$
$$\left(\left(1+\frac{3}{2}e^2\right)\left\{-\sin 2i\sin 2i'\left[2\frac{\sin(\Omega'-\Omega)}{(\dot\Omega'-\dot\Omega)^2}+3e'\frac{\sin(\lambda'-\omega'-\Omega)}{(\dot\lambda'-\dot\omega'-\dot\Omega)^2}-3e'\frac{\sin(\lambda'-\omega'-2\Omega'+\Omega)}{(\dot\lambda'-\dot\omega'-2\dot\Omega'+\dot\Omega)^2}\right]\right.\right.$$
$$\left.\left.-\sin^2 i\sin^2 i'\left[\frac{4\sin(2\Omega'-2\Omega)}{4(\dot\Omega'-\dot\Omega)^2}+6e'\frac{\sin(\lambda'-\omega'+\Omega'-2\Omega)}{(\dot\lambda'-\dot\omega'+\dot\Omega'-2\dot\Omega)^2}-6e'\frac{\sin(\lambda'-\omega'-3\Omega'+2\Omega)}{(\dot\lambda'-\dot\omega'-3\dot\Omega'+2\dot\Omega)^2}\right]\right\}\right)+\cdots$$

In these expressions,

a' is the semimajor axis of the Sun's (Moon's) orbit relative to the Earth
e' is the eccentricity of the Sun's (Moon's) orbit relative to the Earth
i' is the inclination of the Sun's (Moon's) orbital plane to the Earth's equatorial plane
n' is the mean motion of the Sun (Moon) relative to the Earth
λ' is the mean longitude of the Sun (Moon) measured in the Earth's equatorial plane from the mean equinox of date to the mean ascending node of the Sun's (Moon's) orbit, and then along the orbit
Ω' is the longitude of mean ascending node of the Sun's (Moon's) orbit on the Earth's equator measured from the mean equinox of date
ω' is the argument of perigee of the Sun's (Moon's) orbit measured from the mean ascending node on the Earth's equator

Murphy and Felsentreger (1966) have shown that these luni-solar forces can produce perturbations in orbits which are comparable in size to long-period, zonal harmonic effects. (See Results and Analysis.)

As is true of gravitational potential harmonic effects, luni-solar resonances can occur which cause unusually large perturbations in satellite orbits. Felsentreger (1966) has shown that a 550-year-period perturbation, caused by a nearly constant longitude of perigee, is observable in the eccentricity of the Relay 2 satellite. This perturbation can be explained by two terms in the luni-solar gravitational disturbing function presented previously; namely,

$$F_R=\frac{15}{64}a^2e^2(1+\cos i)^2$$
$$[n_\odot^2 m_\odot\sin^2 i_\odot\cos 2(\Omega_\odot-\omega-\Omega)+n_\varsigma^2 m_\varsigma\sin^2 i_\varsigma\cos 2(\Omega_\varsigma-\omega-\Omega)]$$

where

$n_\odot, n_\mathfrak{c}$ is the mean motion of the Sun (Moon) relative to the Earth
$m_\odot, m_\mathfrak{c}$ is the ratio of the mass of the Sun (Moon) to the mass of the Sun (Moon) plus the mass of Earth
$i_\odot, i_\mathfrak{c}$ is the inclination of the Sun's (Moon's) orbital plane to the Earth's equatorial plane
$\Omega_\odot, \Omega_\mathfrak{c}$ is the longitude of the mean ascending node of the Sun's (Moon's) orbit on the Earth's equator measured from the mean equinox of date

Direct analytical integration of the second (lunar) term cannot be performed because the motions of $i_\mathfrak{c}$, $\Omega_\mathfrak{c}$, and $\omega+\Omega$ are all commensurate. However, a transformation made to the ecliptic as the basic reference plane makes analytical integration possible. The disturbing function F_R then becomes

$$\begin{aligned}F_R=\frac{15}{64}a^2e^2(1+\cos i)^2\{&n_\odot{}^2m_\odot\sin^2 i_\odot\cos 2\,(\Omega_\odot-\omega-\Omega)\\&+n_\mathfrak{c}{}^2m_\mathfrak{c}[\sin^2 i_\odot\,(\cos^2 i''-\tfrac{1}{2}\sin^2 i'')\cos 2(\omega+\Omega)\\&-\sin i''\cos i''\sin i_\odot\,(1-\cos i_\odot)\cos(\Omega''+2\omega+2\Omega)\\&+\sin i''\cos i''\sin i_\odot\,(1+\cos i_\odot)\cos(\Omega''+2\omega-2\Omega)\\&+\tfrac{1}{4}\sin^2 i''\,(1-\cos i_\odot)^2\cos 2\,(\Omega''+\omega+\Omega)\\&+\tfrac{1}{4}\sin^2 i''\,(1+\cos i_\odot)^2\cos 2\,(\Omega''-\omega+\Omega)]\}\end{aligned}$$

where

i'' is the inclination of the Moon's orbital plane to the ecliptic $=5^\circ.1453964$
Ω'' is the longitude of the mean ascending node of the lunar orbit on the ecliptic measured from the mean equinox of date

Then, the perturbation in eccentricity is

$$\begin{aligned}(\delta e)_R=\frac{15}{32}a\sqrt{a}\,e\sqrt{1-e^2}(1+\cos i)^2\Bigg\{&-\frac{n_\odot^2 m_\odot\sin^2 i_\odot}{2(\dot\omega+\dot\Omega)}-\cos 2(\Omega_\odot-\omega-\Omega)\\&+n_c^2 m_c\Bigg[-\frac{\sin^2 i_\odot\cos^2 i''-\frac{1}{2}\sin^2 i''}{2(\dot\omega+\dot\Omega)}\cos 2(\omega+\Omega)\\&+\frac{\sin i''\cos i''\sin i_\odot\,(1-\cos i_\odot)}{\dot\Omega''+2(\dot\omega+\dot\Omega)}\cos(\Omega''+2\omega+2\Omega)\\&+\frac{\sin i''\cos i''\sin i_\odot\,(1+\cos i_\odot)}{\dot\Omega''-2(\dot\omega+\dot\Omega)}\cos(\Omega''-2\omega-2\Omega)\\&-\frac{\sin^2 i''(1-\cos i_\odot)^2}{8(\dot\Omega''+\dot\omega+\dot\Omega)}\cos 2(\Omega''+\omega+\Omega)\\&+\frac{\sin^2 i''(1+\cos i_\odot)^2}{8(\dot\Omega''-\dot\omega-\dot\Omega)}\cos 2(\Omega''-\omega-\Omega)\Bigg]\Bigg\}\end{aligned}$$

The accuracy of this expression in explaining the observable perturbation in e is shown in Results and Analysis.

5.4.4.2 Solar Radiation Pressure

(J. Murphy and T. Felsentreger)

The force of solar radiation pressure on the surface of a satellite causes a long-period perturbation of the orbit. This perturbation can be significant for satellites having appreciable area-to-mass ratios. The long-period part of the solar radiation-pressure disturbing function is (Murphy and Felsentreger, 1966)

$$\begin{aligned}R_p = -F\frac{3ae}{2}\Big[&\cos^2\frac{i}{2}\sin^2\frac{i_\odot}{2}\cos(\omega+\Omega+\lambda_\odot)\\&+\cos^2\frac{i}{2}\cos^2\frac{i_\odot}{2}\cos(\omega+\Omega-\lambda_\odot)\\&+\sin^2\frac{i}{2}\cos^2\frac{i_\odot}{2}\cos(\omega-\Omega+\lambda_\odot)\\&+\sin^2\frac{i}{2}\sin^2\frac{i_\odot}{2}\cos(\omega-\Omega-\lambda_\odot)\\&-\frac{1}{2}\sin i\sin i_\odot\cos(\omega+\lambda_\odot)\\&+\frac{1}{2}\sin i\sin i_\odot\cos(\omega-\lambda_\odot)\Big]\end{aligned}$$

where

$$F = (4.63\times10^{-6}\ \text{kg/msec}^2)\ \ (A/m)$$

and

A is the effective area of the satellite in the direction of the Sun, and

m is the mass of satellite.

The perturbations in the orbital elements are

$$\delta e = \frac{\sqrt{1-e^2}}{na^2e}B_1$$

$$\delta i = \frac{\cos i}{na^2\sqrt{1-e^2}\sin i}B_1 - \frac{1}{na^2\sqrt{1-e^2}\sin i}B_2$$

$$\delta M = -\frac{2}{na}B_3 - \frac{1-e^2}{na^2e}B_4 + \frac{d\dot{M}}{de}B_6 + \frac{d\dot{M}}{di}B_7$$

$$\delta\omega = \frac{\cos i}{na^2\sqrt{1-e^2}\sin i}B_5 + \frac{\sqrt{1-e^2}}{na^2e}B_4 + \frac{d\dot{\omega}}{de}B_6 + \frac{d\dot{\omega}}{di}B_7$$

$$\delta\Omega = \frac{1}{na^2\sqrt{1-e^2}\sin i}B_5 + \frac{d\dot{\Omega}}{de}B_6 + \frac{d\dot{\Omega}}{di}B_7$$

where

$$\begin{aligned}B_1 &= \int\frac{\partial R_p}{\partial\omega}dt\\&= -F\frac{3ae}{2}\Big[\cos^2\frac{i}{2}\sin^2\frac{i_\odot}{2}\frac{\cos(\omega+\Omega+\lambda_\odot)}{\dot\omega+\dot\Omega+\dot\lambda_\odot}\\&\quad+\cos^2\frac{i}{2}\cos^2\frac{i_\odot}{2}\frac{\cos(\omega+\Omega-\lambda_\odot)}{\dot\omega+\dot\Omega-\dot\lambda_\odot}\\&\quad+\sin^2\frac{i}{2}\cos^2\frac{i_\odot}{2}\frac{\cos(\omega-\Omega+\lambda_\odot)}{\dot\omega-\dot\Omega+\dot\lambda_\odot}\\&\quad+\sin^2\frac{i}{2}\sin^2\frac{i_\odot}{2}\frac{\cos(\omega-\Omega-\lambda_\odot)}{\dot\omega-\dot\Omega-\dot\lambda}\\&\quad-\frac{1}{2}\sin i\sin i_\odot\frac{\cos(\omega+\lambda_\odot)}{\dot\omega+\dot\lambda}\\&\quad+\frac{1}{2}\sin i\sin i_\odot\frac{\cos(\omega-\lambda_\odot)}{\dot\omega-\dot\lambda_\odot}\Big]\end{aligned}$$

$$\begin{aligned}B_2 &= \int\frac{\partial R_p}{\partial\Omega}dt\\&= -F\frac{3ae}{2}\Big[\cos^2\frac{i}{2}\sin^2\frac{i_\odot}{2}\frac{\cos(\omega+\Omega+\lambda_\odot)}{\dot\omega+\dot\Omega+\dot\lambda_\odot}\\&\quad+\cos^2\frac{i}{2}\cos^2\frac{i_\odot}{2}\frac{\cos(\omega+\Omega-\lambda_\odot)}{\dot\omega+\dot\Omega+\dot\lambda_\odot}\\&\quad-\sin^2\frac{i}{2}\cos^2\frac{i_\odot}{2}\frac{\cos(\omega-\Omega+\lambda_\odot)}{\dot\omega-\dot\Omega+\dot\lambda_\odot}\\&\quad-\sin^2\frac{i}{2}\sin^2\frac{i_\odot}{2}\frac{\cos(\omega-\Omega-\lambda_\odot)}{\dot\omega-\dot\Omega-\dot\lambda_\odot}\Big]\end{aligned}$$

$$\begin{aligned}B_3 &= \int\frac{\partial R_p}{\partial a}dt\\&= -F\frac{3e}{2}\Big[\cos^2\frac{i}{2}\sin^2\frac{i_\odot}{2}\frac{\sin(\omega+\Omega+\lambda_\odot)}{\dot\omega+\dot\Omega+\dot\lambda_\odot}\\&\quad+\cos^2\frac{i}{2}\cos^2\frac{i_\odot}{2}\frac{\sin(\omega+\Omega-\lambda_\odot)}{\dot\omega+\dot\Omega-\dot\lambda_\odot}\\&\quad+\sin^2\frac{i}{2}\cos^2\frac{i_\odot}{2}\frac{\sin(\omega-\Omega+\lambda_\odot)}{\dot\omega-\dot\Omega+\dot\lambda_\odot}\\&\quad+\sin^2\frac{i}{2}\sin^2\frac{i_\odot}{2}\frac{\sin(\omega-\Omega-\lambda_\odot)}{\dot\omega-\dot\Omega-\dot\lambda_\odot}\\&\quad-\frac{1}{2}\sin i\sin i_\odot\frac{\sin(\omega+\lambda_\odot)}{\dot\omega+\dot\lambda_\odot}\\&\quad+\frac{1}{2}\sin i\sin i_\odot\frac{\sin(\omega-\lambda_\odot)}{\dot\omega-\dot\lambda}\Big]\end{aligned}$$

$$\begin{aligned}B_4 &= \int\frac{\partial R_p}{\partial e}dt\\&= \frac{a}{e}B_3\end{aligned}$$

$$B_5=\int\frac{\partial R_p}{\partial i}dt$$
$$=F\frac{3ae}{4}\Bigg[\sin i\sin^2\frac{i_\odot}{2}\frac{\sin(\omega+\Omega+\lambda_\odot)}{\dot\omega+\dot\Omega+\dot\lambda_\odot}$$
$$+\sin i\cos^2\frac{i_\odot}{2}\frac{\sin(\omega+\Omega-\lambda_\odot)}{\dot\omega+\dot\Omega-\dot\lambda_\odot}$$
$$-\sin i\cos^2\frac{i_\odot}{2}\frac{\sin(\omega-\Omega+\lambda_\odot)}{\dot\omega-\dot\Omega+\dot\lambda_\odot}$$
$$-\sin i\sin^2\frac{i_\odot}{2}\frac{\sin(\omega-\Omega-\lambda_\odot)}{\dot\omega-\dot\Omega-\dot\lambda_\odot}$$
$$+\cos i\sin i_\odot\frac{\sin(\omega+\lambda_\odot)}{\dot\omega+\dot\lambda_\odot}$$
$$-\cos i\sin i_\odot\frac{\sin(\omega-\lambda_\odot)}{\dot\omega-\dot\lambda_\odot}\Bigg]$$

$$B_6=\int\delta e\,dt$$
$$=-\frac{\sqrt{1-e^2}}{na^2e}\int B_1dt$$
$$=\frac{3}{2}F\frac{\sqrt{1-e^2}}{na}\Bigg[\cos^2\frac{i}{2}\sin^2\frac{i_\odot}{2}\frac{\sin(\omega+\Omega+\lambda_\odot)}{(\dot\omega+\dot\Omega+\dot\lambda_\odot)^2}$$
$$+\cos^2\frac{i}{2}\cos^2\frac{i_\odot}{2}\frac{\sin(\omega+\Omega-\lambda_\odot)}{(\dot\omega+\dot\Omega-\dot\lambda_\odot)^2}$$
$$+\sin^2\frac{i}{2}\cos^2\frac{i_\odot}{2}\frac{\sin(\omega-\Omega+\lambda_\odot)}{(\dot\omega-\dot\Omega+\dot\lambda_\odot)^2}$$
$$+\sin^2\frac{i}{2}\sin^2\frac{i_\odot}{2}\frac{\sin(\omega-\Omega-\lambda_\odot)}{(\dot\omega-\dot\Omega-\dot\lambda_\odot)^2}$$
$$-\frac{1}{2}\sin i\sin i_\odot\frac{\sin(\omega+\lambda_\odot)}{(\dot\omega+\dot\lambda_\odot)^2}$$
$$+\frac{1}{2}\sin i\sin i_\odot\frac{\sin(\omega-\lambda_\odot)}{(\dot\omega-\dot\lambda_\odot)^2}\Bigg]$$

$$B_7=\int\delta i\,dt$$
$$=\frac{\cos i}{na^2\sqrt{1-e^2}\sin i}\int B_1dt$$
$$-\frac{1}{na^2\sqrt{1-e^2}\sin i}\int B_2dt$$
$$=-\frac{e\cot i}{1-e^2}B_6$$
$$+\frac{3}{2}F\frac{e}{na^2\sqrt{1-e^2}\sin i}$$
$$\Bigg[\cos^2\frac{i}{2}\sin^2\frac{i_\odot}{2}\frac{\sin(\omega+\Omega-\lambda_\odot)}{(\dot\omega+\dot\Omega+\dot\lambda_\odot)^2}$$
$$+\cos^2\frac{i}{2}\cos^2\frac{i_\odot}{2}\frac{\sin(\omega+\Omega-\lambda_\odot)}{(\dot\omega+\dot\Omega-\dot\lambda_\odot)^2}$$
$$-\sin^2\frac{i}{2}\cos^2\frac{i_\odot}{2}\frac{\sin(\omega-\Omega+\lambda_\odot)}{(\dot\omega-\dot\Omega+\dot\lambda_\odot)^2}$$
$$-\sin^2\frac{i}{2}\sin^2\frac{i_\odot}{2}\frac{\sin(\omega-\Omega-\lambda_\odot)}{(\dot\omega-\dot\Omega-\dot\lambda_\odot)^2}\Bigg]$$

An indirect, long-period variation in the orbit is caused by passage of the satellite in and out of the Earth's shadow. This effect is best observed in the semimajor axis, which undergoes no long-period motion from any other source. The perturbation in the semimajor axis is

$$\delta a_R=-2\frac{a^3}{\mu}FC\cos E+D\sqrt{1-e^2}\sin E\Bigg]_{E_2}^{E_1}$$

where

$$C=-\cos^2\frac{i}{2}\cos^2\frac{i_\odot}{2}\cos(\omega+\Omega-\lambda_\odot)$$
$$-\sin^2\frac{i}{2}\cos^2\frac{i_\odot}{2}\cos(\omega-\Omega-\lambda_\odot)$$
$$-\cos^2\frac{i}{2}\sin^2\frac{i_\odot}{2}\cos(\omega+\Omega+\lambda_\odot)$$
$$-\sin^2\frac{i}{2}\sin^2\frac{i_\odot}{2}\cos(\omega-\Omega-\lambda_\odot)$$
$$-\tfrac{1}{2}\sin i\sin\frac{i}{2}[\cos(\omega-\lambda_\odot)-\cos(\omega+\lambda_\odot)]$$

$$D=\cos^2\frac{i}{2}\cos^2\frac{i_\odot}{2}\sin(\omega+\Omega-\lambda_\odot)$$
$$+\sin^2\frac{i}{2}\cos^2\frac{i_\odot}{2}\sin(\omega-\Omega+\lambda_\odot)$$
$$+\cos^2\frac{i}{2}\sin^2\frac{i_\odot}{2}\sin(\omega+\Omega+\lambda_\odot)$$
$$+\sin^2\frac{i}{2}\sin^2\frac{i_\odot}{2}\sin(\omega-\Omega-\lambda_\odot)$$
$$+\tfrac{1}{2}\sin i\sin i_\odot[\sin(\omega-\lambda_\odot)$$
$$-\sin(\omega+\lambda_\odot)]$$

and where E is the eccentric anomaly of the satellite and E_1, E_2 are the eccentric anomalies of the satellite at the exit from and entrance into the Earth's shadow. Thus, δa_0 is the perturbation after one revolution.

The TELSTAR 2 satellite provides a good subject for a study of this effect. A long-period variation with an approximate amplitude of 0.0000140 Earth radii and a period of about a year was observed in the semimajor axis. (See Results and Analysis.)

5.4.4.3 Tidal Deformation of the Earth

The deformation of the Earth caused by lunar and solar tides can produce observable perturbations of satellite orbits. The magnitude of these tidal effects depends upon the

elastic properties of the Earth as described by Love numbers. The Love numbers appear as coefficients in the expansion of the exterior tidal potential in terms of spherical harmonics.

The assumption is usually made that the Love numbers are "global"; i.e., that they are constant over the whole Earth. Musen and Felsentreger (1973) have derived a perturbation theory, assuming that the Love numbers are not global constants, but vary along the parallels of latitude; i.e.,

$$k_2 = k_{20} + k_{21} P_{10}(\nu) + k_{22} P_{20}(\nu) + \cdots$$
$$k_3 = k_{30} + k_{31} P_{10}(\nu) \cdots,$$

where ν is the latitude. The theory is developed by performing a single averaging along the parallels of altitude.

The tidal disturbing function on the surface of the Earth has the form

$$R = \frac{Gm'}{a'^3}\left(\frac{a'}{r'}\right)^3 \sum_{j=0}^{4} A'_j a_j + \frac{Gm'}{a'^4}\left(\frac{a'}{r'}\right)^4 \sum_{j=1}^{2} B'_j b_j$$

where the A'_j, B'_j are functions of lunar (solar) coordinates, the a_j are functions of the k_2 Love number and coordinates on the surface of the Earth, and the b_j are functions of the k_3 Love number and coordinates on the surface of the Earth. Also, r' is the distance of the Moon (Sun) from the center of the Earth and a' is the semimajor axis of the lunar (solar) orbit defined in such a manner that the constant part in the expansion of a'/r' is equal to 1.

The expansion of the exterior tidal potential is obtained from Dirichlet's theorem, and differential equations for tidal perturbations of satellite elements are obtained by taking into account the deviation of k_2 and k_3 from constants along the parallels of latitude. The perturbations are obtained by numerically integrating these differential equations. Terms for short periods (equal to the periods of the satellite or less) were removed from the differential equations by averaging over the instantaneous orbit of the satellite.

The perturbative equations are

$$\sin i \frac{d\delta_2\Omega}{dt} = +\frac{n\alpha^2\alpha'^3}{2(1-e^2)^2} \times \frac{m'}{M} \times \left(\frac{a'}{r'}\right)^3 V_{21}^{(s)}$$

$$\frac{d\delta_2 i}{dt} = -\frac{n\alpha^2\alpha'^3}{2(1-e^2)^2} \times \frac{m'}{M} \times \left(\frac{a'}{r'}\right)^3 V_{21}^{(c)}$$

$$\frac{d\delta_2\pi}{dt} = +\frac{3n\alpha^2\alpha'^3}{(1-e^2)^2} \times \frac{m'}{M} \times \left(\frac{a'}{r'}\right)^3 V_{20} + 2\sin^2\frac{i}{2} \times \frac{d\delta_2\Omega}{dt}$$

$$\frac{d\delta_2 e}{dt} = 0$$

$$\frac{d\delta_2 L}{dt} = +\frac{6n\alpha^2\alpha'^3}{(1-e^2)^{3/2}} \times \frac{m'}{M} \times \left(\frac{a'}{r'}\right)^3 \times V_{20} \frac{e}{1+\sqrt{1-e^2}} \times \frac{d\delta_2\pi}{dt} + 2\sqrt{1-e^2}\sin^2\frac{i}{2}\frac{d\delta_2\Omega}{dt}$$

$$\sin i \frac{d\delta_3\Omega}{dt} = +\frac{n\alpha^3\alpha'^3 e}{(1-e^2)^3} \times \frac{m'}{M} \times \left(\frac{a'}{r'}\right)^3 \left(V_{30}\sin\omega - \frac{1}{2}V_{32}^{(c)}\sin\omega + \frac{1}{2}V_{32}^{(s)}\cos\omega\right)$$

$$\frac{d\delta_3 i}{dt} = +\frac{n\alpha^3\alpha'^3 e}{(1-e^2)^3} \times \frac{m'}{M} \times \left(\frac{a'}{r'}\right)^3 \left(V_{30}\cos\omega + \frac{1}{2}V_{32}^{(c)}\cos\omega + \frac{1}{2}V_{32}^{(s)}\sin\omega\right)$$

$$\frac{d\delta_3\pi}{dt} = +\frac{n\alpha^3\alpha'^3}{(1-e^2)^3 e} \times \frac{m'}{M} \times \left(\frac{a'}{r'}\right)^3 \times (1+4e^2)\left(V_{31}^{(c)}\cos\omega + V_{31}^{(s)}\sin\omega\right) + 2\sin^2\frac{i}{2}\frac{d\delta_3\Omega}{dt}$$

$$\frac{d\delta_3 e}{dt} = +\frac{n\alpha^3\alpha'^3}{(1-e^2)^2} \times \frac{m'}{M} \times \left(\frac{a'}{r'}\right)^3 \left(V_{31}^{(c)}\sin\omega - V_{31}^{(s)}\cos\omega\right)$$

$$\frac{d\delta_3 L}{dt} = +\frac{8n\alpha^3\alpha'^3 e}{(1-e^2)^{5/2}} \times \frac{m'}{M} \times \left(\frac{a'}{r'}\right)^3 \left(V_{31}^{(c)}\cos\omega + V_{31}^{(s)}\sin\omega\right) + \frac{e}{1+\sqrt{1-e^2}} \times \frac{d\delta_3\pi}{dt} + 2\sqrt{1-e^2}\sin^2\frac{i}{2}\frac{d\delta_3\Omega}{dt}$$

$$\sin i \frac{d\delta_4\Omega}{dt} = +\frac{n\alpha^4\alpha'^3}{2(1-e^2)^4}\times\frac{m'}{M}\times\left(\frac{a'}{r'}\right)^3 \times\left\{+\left(1+\frac{3}{2}e^2\right)V_{41}^{(s)} +\frac{3}{4}e^2[+(-V_{41}^{(s)}+V_{43}^{(s)})\cos 2\omega +(+V_{41}^{(c)}-V_{43}^{(c)})\sin 2\omega]\right\}$$

$$\frac{d\delta_4 i}{dt} = +\frac{n\alpha^4\alpha'^3}{2(1-e^2)^4}\times\frac{m'}{M}\times\left(\frac{a'}{r'}\right)^3 \times\left\{\left(1+\frac{3}{2}e^2 V_{41}^{(c)} +\frac{3}{4}e^2[+(+V_{41}^{(c)}+V_{43}^{(c)})\cos 2\omega +(+V_{41}^{(s)}+V_{43}^{(s)})\sin 2\omega]\right.$$

$$\frac{d\delta_4\pi}{dt} = +\frac{n\alpha^4\alpha'^3}{(1-e^2)^4}\times\frac{m'}{M}\times\left(\frac{a'}{r'}\right)^3 \times\left\{+\left(+10+\frac{15}{2}e^2\right)V_{40} +\left(\frac{3}{2}+\frac{15}{4}e^2\right)(+V_{42}^{(c)}\cos 2\omega +V_{42}^{(s)}\sin 2\omega)\right\}+2\sin^2\frac{i}{2}\frac{d\delta_4\Omega}{dt}$$

$$\frac{d\delta_4 e}{dt} = +\frac{3n\alpha^4\alpha'^3}{2(1-e^2)^3}\times\frac{m'}{M}\times\left(\frac{a'}{r'}\right)^3 \times(V_{42}^{(c)}\sin 2\omega - V_{42}^{(s)}\cos 2\omega)$$

$$\frac{d\delta_4 L}{dt} = +\frac{10n\alpha^4\alpha'^3}{(1-e^2)^{7/2}}\times\frac{m'}{M}\times\left(\frac{a'}{r'}\right)^3 \times\left\{\left(1+\frac{3}{2}e^2\right)V_{40} +\frac{3}{4}e^2(V_{42}^{(c)}\cos 2\omega+V_{42}^{(s)}\sin 2\omega)\right\} +\frac{e}{1+\sqrt{1-e^2}}\times\frac{d\delta_4\pi}{dt} +2\sqrt{1-e^2}\sin^2\frac{i}{2}\frac{d\delta_4\Omega}{dt}$$

where

- λ', μ', ν' = equatorial components of the unit vector r'° directed from the center of the Earth toward the Moon (Sun)
- ϵ = the eccentricity of the meridian of the Earth
- $\pi = \omega + \Omega$ = the longitude of perigee of the satellite
- L = mean anomaly $+\pi$ = the mean longitude of the satellite
- α = $R/\bar{a}$
- $\alpha' = R'/a'$ = the lunar (solar) parallactic factor
- M = mass of the Earth
- m' = mass of the Moon (Sun)
- R = equatorial radius of the Earth

The $V_{ij}^{(c)}$, $V_i^{(s)}$ are trigonometric functions of i, Ω, α', λ', ν', μ', and the k_i. Also, indirect effects are represented by

$$\frac{d\delta_5\Omega}{dt} = -(n_0\,\Omega_1\tan i)\,\delta i$$

$$\frac{d\delta_5\pi}{dt} = (+5\sin i - \tan i)\,n_0\,\Omega_1\,\delta i$$

$$\frac{d\delta_7 L}{dt} = (+8\sin i - \tan i)\,n_0\,\Omega_1\,\delta i$$

where

- n_0 = mean motion of the satellite
- $\Omega_1 = -3\gamma_2'\theta+\frac{3}{8}\gamma_2'^2[(-5+12\eta+9\eta^2)\,\theta +(-35-36\eta-5\eta^2)\,\theta^2] +\frac{5}{4}\gamma_4'[(5-3\eta^2)(3\theta-7\theta^3)]$
- $\gamma_2' = +\frac{1}{2}\frac{C_2^0R^2}{a^2}\eta^{-4}$
- $\gamma_4' = -\frac{3}{8}\frac{C_4^0R^2}{a^4}\eta^{-8}$
- $\eta = \sqrt{1-e^2}$
- $\theta = \cos i,$

This theory has been used to compute theoretical tidal perturbations for various satellites. These theoretical effects have agreed quite well with observations. (See Results and Analysis.)

5.4.4.4 Hydrostatic Figure of the Earth
(M. H. Khan)

If the Earth were a fluid body, it would respond instantaneously to any stresses, including those caused by its rotation, until it attained a state of zero stress. The figure that the Earth would assume if it were in such a state is called the hydrostatic-equilibrium figure, or simply a hydrostatic figure or an equilibrium figure. Because hydrostatic shape indicates a state of zero stress, any

departures from this state are particularly interesting, since they show the extent of available stresses in the interior of the Earth which can be invoked to explain any geophysical mechanisms that may be found or assumed to exist in the Earth's interior. Apart from its traditional appeal, the problem is particularly interesting for this reason to modern geophysicists.

The mathematical theory of hydrostatic equilibrium for the Earth, to the first order of small qualities, was originally developed by Clairaut (1743). Radau (1885) simplified the solution of Clairaut's differential equation by making an important substitution. The original purpose of the theory was that, with the then-known data, the theory would provide useful information about the distribution of density in the Earth. It was found, however, that with the then-known data, the theory led to no discrimination between widely varying laws of density. But it did yield more accurate values of flattening for the Earth (assuming, of course, hydrostatic equilibrium) than were likely to be obtained by geodetic surveys.

This result stimulated further interest in the theory, and its development was extended to the second order by Callandreau (1889) and later by Darwin (1900). DeSitter (1938) modified the development and studied its actual application to the Earth. Subsequent applications of the second-order theory have been made by Bullard (1948) and Jeffreys (1963).

With the advent of artificial Earth satellites, it became possible to determine the actual flattening of the Earth directly from the second-degree harmonic coefficient of geopotential. The same coefficient, coupled with the precessional constant of the Earth, also yields accurate values of the Earth's polar moment of inertia, and hence the hydrostatic theory can now be used to yield the hydrostatic flattening as distinct from the actual flattening of the Earth. Thus, one could study the departures of the actual Earth from its equilibrium state. Such studies were conducted by O'Keefe (1960), Henriksen (1960), Caputo (1965), and Khan (1967) in the post-artificial Earth satellite era. Since there is a fundamental difference in the pre- and post-artificial Earth satellite applications of the hydrostatic theory, Khan (1968, 1969) revised and extended the second-order theory to suit readily the new applications and data types.

Theory of the External Field.—The external gravitational potential V of a body symmetrical with respect to its equatorial plane and polar axis is given by equation (1.14). This equation reduces to

$$V=\frac{GM}{r}\left[1+\left(\frac{a_e}{r}\right)^2 C_2^0 P_2(\sin\psi)+\left(\frac{a_e}{r}\right)^4 C_4^0 P_2(\sin\psi)-0(f^3)\right] \tag{5.104}$$

if accuracy is wanted only to the order of the square of flattening F.

The potential of gravity is

$$W=V+\frac{1}{3}\omega^2 r^2\,[1-P_2(\sin\psi)] \tag{5.105}$$

where ω is the rate of rotation of the body.

Let the equation of an equipotential surface be

$$\frac{a_e}{r}=1+\left(f+\frac{3}{2}f^2\right)\sin^2\psi-\frac{1}{2}f^2\sin^4\psi 0(f^3) \tag{5.106}$$

which in terms of the mean radius a_e and Legendre's polynomials is expressible to the second degree as

$$r=a_e(1+\alpha_2 P_2+\alpha_4 P_4)$$

$$r=a_e\left[1-\left(\frac{2}{3}f+\frac{23}{63}f^2\right)P_2(\sin\psi)+\frac{12}{35}f^2 P_4(\sin\psi)\right] \tag{5.106a}$$

Substitution of equations (5.104) and (5.106) (or (5.106a)) in equation (5.105) yields

$$C_2^o = -\frac{2}{3}f + \frac{1}{3}f^2 + \frac{1}{3}m - \frac{2}{21}mf - 0(f^3) \quad (5.107a)$$

$$C_4^o = \frac{4}{5}f^2 - \frac{4}{7}mf - 0(f^3) \quad (5.107b)$$

where

$$m = \frac{\omega^2 a^3 (1-f)}{GM}$$

Theory of the Internal Field.—The condition of hydrostatic equilibrium for any point in the earth's interior is given by

$$\frac{dp}{dr} = \rho \frac{dW}{dr} \quad (5.108)$$

where the pressure p and the density ρ are related to the point under consideration. Thus, surfaces of constant W are also surfaces of constant p and ρ; i.e., the surfaces of equal density are equipotential surfaces. Let one such surface with a uniform density ρ' be expressed as

$$r = a'\ (1 + \Sigma \alpha_n P_n) \quad (5.109)$$

where α_n and ρ' are functions of a'. Let r_1 be the value of a for the surface of constant density a point. Then, the potential $W(r_1)$ on this surface is the sum of potentials from (1) matter inside the shell r_1, (2) matter outside the shell r_1, and (3) rotational potential; i.e.,

$$\begin{aligned} W(r_1) = {} & \frac{4}{3}\pi G \int_0^{r_1} \rho' \frac{\partial}{\partial a'} \\ & \left(\frac{a'^3}{r} + \sum \frac{3}{2n+1} \frac{a'^{n+3}}{r^{n+1}} \alpha_n P_n \right) da' \\ & + \frac{4}{3}\pi G \int_{r_1}^{a} \rho' \frac{\partial}{\partial a'} \\ & \left(\frac{3}{2} a'^2 + \sum \frac{3}{2n+1} \frac{r^n}{a'^{n-2}} \alpha_2 P_n \right) da' \\ & + \tfrac{1}{2}\omega^2 r_1^2 (1 - \sin^2 \psi') \end{aligned} \quad (5.110)$$

The mean density ρ_0 within the surface r_1 is

$$\rho_0 = \frac{3}{r_1^3} \int_0^{r_1} \rho' a'^2 da' \quad (5.111)$$

Development of the first-order theory can be found in Jeffreys (1962). The principal results of this theory are the following equations

$$\rho_0 \left(\frac{d^2\alpha_2}{dr^2} - \frac{6\alpha_2}{r^2} \right) + \frac{6\rho}{r} \left(\frac{d\alpha_2}{dr} + \frac{\alpha_2}{r} \right) = 0 \quad (5.112)$$

This is Clairaut's (1743) differential equation.

Let a new dependent variable η be

$$\eta = \frac{d \log \alpha_2}{d \log r} = \frac{r d\alpha_2}{\alpha_2 dr} \quad (5.113)$$

$$\frac{d}{dr}(\rho_0 r^5 \sqrt{1+\eta}) = 5\rho_0 r^4 \bar{\psi}(\eta) \quad (5.114)$$

where

$$\bar{\psi}(\eta) = \frac{1 + \frac{1}{2}\eta - \frac{1}{10}\eta^2}{\sqrt{1+\eta}} \quad (5.115)$$

and $\rho_0(a)$ is the mean density of the mass bounded by a. This is Radau's equation, as the substitution in equation (5.113) was conceived by Radau (1885). The importance of the substitution lies in the fact that, for any reasonable law of density variation, the function $\psi(\eta)$ has the remarkable property of never departing from 1 by more than 8 parts in 10^4. Then to an accuracy of this order

$$\frac{d}{dr}(\rho_0 r^5 \sqrt{1+\eta}) = 5\rho_0 r^4 \quad (5.116)$$

To the same degree of accuracy, the polar moment of inertia C is

$$C = \frac{8}{3}\pi \int_0^a \rho(r) r^4 dr \quad (5.117)$$

which, on integration by parts, becomes

$$C = \frac{2}{3}Ma^2 - \frac{4}{15}Ma^2\sqrt{1-\eta(a)} \quad (5.118)$$

or

$$\eta(a) = \left[\frac{5}{2} - \frac{15}{4} \frac{C}{Ma^2} \right]^2 - 1 \quad (5.119)$$

But from equation (5.113) the value of η at $r=a$ is

$$\eta(a)=\frac{a}{\alpha_2(a)}\left(\frac{d\alpha_2}{dr}\right)_a$$

which is

$$\eta(a)=\frac{5}{3}\frac{m}{\alpha_2(a)}-2 \qquad (5.120)$$

In the choice of this coefficient $\alpha_2(a)$, the external potential theory is linked to the hydrostatic theory. Equations (5.106) or (5.106a), (5.107), and (5.108) of the external potential theory are derived without any assumption about the density distribution inside the Earth. Hence, these are valid whether or not hydrostatic equilibrium exists in the Earth. Thus, if the Earth were in hydrostatic equilibrium, the exterior surface defined by equation (5.109) must match the surface defined by equation (5.106) or (5.106a). This should be obvious by intuition: if the hydrostatic theory were true for the Earth, the surfaces defined by the theories of the external and internal fields must be coincident at the outer boundary. To the first order, equation (5.106a) becomes

$$r=r_0\left[1-\frac{2}{3}f_h P_2(\sin\phi)\right]+O(f^2) \qquad (5.121)$$

and

$$\alpha_2=-\frac{2}{3}f_h$$

where the subscript h refers to hydrostatic flattening. Consequently, it can be shown that

$$f_h=\frac{5}{2}m\Big/\left[1+\left(\frac{5}{2}-\frac{15}{4}\frac{C}{Ma^2}\right)\right] \qquad (5.122)$$

The development of the second-order theory is somewhat complicated but follows exactly the procedure given by Jeffreys (1962). Now all terms $\leq O(f^2)$ must be retained and the simplifying assumptions modified accordingly. The treatment given below follows deSitter (1938) and Khan (1968, 1969).

Development of the second-order theory becomes somewhat simpler if we choose as an independent variable the mean radius of a surface of equal density (deSitter, 1938). Further simplification is possible by expressing the mean radius in terms of the mean radius of the outer surface as unity and the density in terms of mean density of the body as unity. With these modifications the potential W at any point (r, ψ) within the Earth (equation 5.110), correct to the second order, is

$$\begin{aligned}W=\frac{4}{3}\pi G\Bigg[&3\int_0^\beta\frac{\rho}{r}\beta^2 d\beta\\&-\frac{2}{5}\left\{\int_0^\beta\frac{\rho}{r^3}\frac{d}{d\beta}\left(\alpha'+\frac{2}{7}\alpha^2\right)\beta^5\right]d\beta\\&+\int_\beta^1 r^2\rho\frac{d}{d\beta}\left[\alpha'+\frac{16}{21}\alpha^2\right]\Bigg\}P_2(\sin\psi')\\&+\Bigg\{\frac{12}{35}\int_0^\beta\frac{\rho}{r^5}\frac{d}{d\beta}[\alpha^2\cdot\beta^7]\,d\beta\\&+\frac{32}{105}\int_\beta^1 r^4\cdot\rho\frac{d}{d\beta}(\beta^{-2})\,d\beta\Bigg\}P_4(\sin\psi')\\&+\frac{1}{3}\alpha^2r^2\,[1-P_2(\sin\psi')]\end{aligned} \qquad (5.123)$$

where β is the mean radius of an arbitrary surface of equal density, expressed in terms of the mean radius of the outer surface as unity, and ρ is the density, expressed in terms of the mean density as unit. Units of ρ are different from the previously used ρ'. In this notation, $\rho(\beta)$ the mean density within the surface β (corresponding to equation (5.111)) is

$$\rho(\beta)=\frac{3}{\beta^3}\int_0^\beta\rho\beta^2 d\beta \qquad (5.124)$$

so that for the surface $r=a$; i.e., $\beta=1$,

$$\rho(r)=\rho(1)=1 \qquad (5.125)$$

The equivalent of equation (5.109), which defines a surface of equal density, also in this case an equipotential surface (equation (5.106)), becomes

$$r=\beta\left[1-\left(\frac{2}{3}\alpha'+\frac{4}{9}\alpha^2\right)P_2(\sin\psi')+\frac{12}{35}\alpha^2P_4(\sin\psi')\right] \quad (5.126)$$

where for convenience of algebraic manipulation, the quantity α' is introduced:

$$\alpha'=\alpha-\frac{5}{42}\alpha^2$$

In the second-order theory, $\alpha'^2=\alpha^2$. Substitution of

$$\frac{1}{r},\ \frac{1}{r^3},\ \frac{1}{r^5},\ r^2 \text{ and } r^4$$

from equation (5.127) in equation (5.123) and the condition that the resulting equation must define an equipotential surface, yields

$$\left[\alpha'+\frac{2}{7}\alpha^2-\frac{1}{2}m(\beta)\right]\frac{3}{\beta^3}\int_0^\beta\rho\beta^2d\beta-\frac{3}{5\beta^5}\int_0^\beta\rho\frac{d}{d\beta}\left[\left(\alpha'+\frac{2}{7}\alpha^2\right)\beta^5\right]d\beta+\left(\frac{4}{7}\alpha-\frac{3}{5}\right)\int_\beta^1\rho\frac{d}{d\beta}\left(\alpha'+\frac{16}{21}\alpha^2\right)d\beta-\frac{4}{21}\alpha m(r_1)=0 \quad (5.127)$$

where

$$m(\beta)=\frac{\omega^2\beta^3}{GM}$$

and

$$m(r_1)=\frac{\omega^2r_1^3}{GM}$$

with β and r_1, denoting the radius of the same surface in different units. Also

$$9\frac{\alpha^2}{\beta^3}\int_0^\beta\rho\beta^2d\beta+\frac{3}{\beta^7}\int_0^\beta\rho\frac{d}{d\beta}[\alpha^2\cdot\beta^7]\,d\beta+\frac{8}{3}\beta^2\int_\beta^1\rho\frac{d}{d\beta}(\beta^{-2})\,d\beta-\frac{6\alpha}{\beta^5}\int_0^\beta\rho\frac{d}{d\beta}\left[\left(\alpha'+\frac{2}{7}\alpha^2\right)\beta^5\right]d\beta=0 \quad (5.128)$$

The manipulation of equation (5.128) and the introduction of the variable η which is now defined as

$$\eta=\frac{d\log\alpha'}{d\log\beta}=\frac{\beta}{\alpha'}\frac{d\alpha'}{d\beta} \quad (5.129)$$

yields

$$\beta\frac{d\eta}{dr}+\eta^2+5\eta-2\zeta(1+\eta)-\frac{4}{21}\zeta\xi=0 \quad (5.130)$$

where

$$\zeta=-\frac{\beta}{\rho(\beta)}\frac{d\rho(\beta)}{d\beta}=3\left(1-\frac{\rho}{\rho(\beta)}\right) \quad (5.131)$$

as yielded by the differentiation of equation (5.124). Also,

$$\xi=7m(\beta)(1+\eta)-3\alpha(1+\eta)^2-4\alpha \quad (5.132)$$

For $r=a$—i.e., $\beta=1$—it yields after simplification

$$\eta(a)f_h'=3f_h'-\frac{6}{7}f_h^2+\frac{4}{7}mf_h-J_h\left(5+\frac{10}{21}f_h+\frac{20}{21}m\right) \quad (5.133)$$

where $\eta(a)$ denotes the value of η for the outer surface on which α and α' also become α', $(a)=f_h'$ and $\alpha(a)=f_h$; i.e., f_h denotes the value of hydrostatic flattening for the outer surface and J_h is the hydrostatic counterpart of $J=-\frac{3}{2}C_{20}^o$.

Equation (5.130) yields the second-order counterparts of equations (5.114) and (5.115); i.e.,

$$\frac{d}{d\beta}[\rho(\beta)\beta^5\sqrt{1+\eta}]-5\rho(\beta)\beta^4\psi(\eta) \quad (5.134)$$

where

$$\psi(\eta)=\frac{1+\frac{1}{2}\eta-\frac{1}{10}\eta^2+\frac{2}{105}\zeta\xi}{\sqrt{1+\eta}} \quad (5.135)$$

Integration of equation (5.135) yields

$$\int_0^\beta\rho(\beta)\beta^4\psi(\eta)\,d\beta=\frac{1}{5}\rho(\beta)\beta^5\sqrt{1+\eta}$$

or

$$\int_0^\beta \rho(\beta)\beta^4 d\beta = \frac{1}{5}\rho(\beta)\beta^5 \frac{\sqrt{1+\eta}}{1+\lambda} = \frac{3}{20}\frac{M\beta^2\sqrt{1+\eta}}{\pi \quad 1+\lambda}$$

which for the outer surface yields

$$\int_0^1 \rho(\beta)\beta^4 d\beta = \frac{3}{2}\frac{M}{\pi}\frac{\sqrt{1+\eta(a)}}{1+\lambda(a)} \quad (5.136)$$

where $1+\lambda$ is the average value of the function $\psi(\eta)$ over the range of integration and $\lambda(a)$ denotes the value of λ for the outer surface.

The polar moment of inertia C is given by the second-order counterpart of equation (5.117); i.e.,

$$C = \frac{8}{3}\pi\int_0^\beta \rho\beta^4 d\beta + \frac{2}{3}(C-A) \quad (5.137)$$

where A is the moment of inertia of the body around its equatorial diameter. Integrating the above equation by parts, we have

$$C = \frac{2}{3}M - \frac{16}{9}\pi\int_0^1 \rho(\beta)\beta^4 d\beta + \frac{2}{3}(C-A) \quad (5.138)$$

and, substituting equation (5.137) in equation (5.138), we find

$$C = \frac{2}{3}Ma^2\left(1-\frac{2}{3}f_h\right) - \frac{4}{15}Ma^2\left(1-\frac{2}{3}f_h\right)\frac{\sqrt{1+\eta(a)}}{1+\lambda(a)} + \frac{2}{3}(C-A) \quad (5.139)$$

where a is now the equatorial radius. Consequently,

$$\frac{3}{2}\frac{C}{Ma^2} = 1-\frac{2}{3}f_h - \frac{2}{5}\left(1-\frac{2}{3}f_h\right)\frac{\sqrt{1+\eta(a)}}{1+\lambda(a)} + J_{2h} \quad (5.140)$$

or

$$\eta(a) = [1+\lambda(a)]^2\left[\frac{5}{2}\left(1-\frac{2}{3}f_h + J_{2h} - \frac{3}{2}\frac{C}{Ma^2}\right)\left(1-\frac{2}{3}f_h\right)^{-1}\right]^2 - 1 \quad (5.141)$$

and from equation (5.133)

$$[1+\lambda(a)]^2\left[\frac{5}{2}\left(1-\frac{2}{3}f_h + J_{2h} - \frac{3}{2}\frac{C}{Ma^2}\right)\left(1-\frac{2}{3}f_h\right)^{-1}\right]^2 - 1 = 3 - \frac{6}{7}f_h'^{-1}f_h^2 + \frac{4}{7}mf_h f_h'^{-1} - \frac{3}{2}J_{2h}f_h'^{-1}\left(5+\frac{10}{21}f_h+\frac{20}{21}m\right) \quad (5.142)$$

whereas the polar moment of inertia is determined by

$$\frac{C}{Ma^2} = \frac{C_2^0}{H} \quad (5.143a)$$

where

$$C_2^0 = \frac{C-A}{Ma^2}$$

and

$$H = \frac{C-A}{C}$$

The quantity C_2^0 is directly determinable from the orbital motion of an artificial Earth satellite to a high degree of accuracy. The quantity H is determined also with high accuracy from the precession of the Earth's axis. Thus, in equation (5.142), if $\lambda(a)$ can be assigned an appropriate value, a knowledge of C_{2h}^0 should yield f_h, since the polar moment of inertia has already been determined by equation (5.143). But $C_{2h}^0 \neq C_2^0$ in the case of the Earth, and thus C_{2h}^0 is not known. We have reasoned earlier, however, that the solutions of external potential and internal potential theories must match at the outer boundary; i.e., equations (5.104a) and (5.142) must be simultaneously satisfied for the outer boundary. To avoid any confusion, rewrite equation (5.107a) as

$$C_{2h}^0 = -\frac{2}{3}f_h + \frac{1}{3}f_h^2 + \frac{1}{3}m - \frac{2}{21}mf_h \quad (5.143b)$$

Equation (5.142) can then be solved immediately with the help of equation (5.143a).

However, equations (5.133) and (5.141), or equation (5.142) can be recast to obtain a

more convenient expression, which gives f_h explicitly in terms of other parameters. To do this, write equation (5.141) as

$$\eta(a) = \frac{25}{4} F^2 q'^2 \left(\frac{1-\Delta_1}{1-\Delta_2} \right) - 1 \qquad (5.144)$$

where

$$\left.\begin{aligned} q &= \frac{C}{Ma^2}\frac{3}{2} \\ q' &= 1-q \\ \Delta_1 &= \frac{\frac{2}{3}\left(f_h - J_h - \frac{2}{3} f_h^2 \right)}{q'} \\ \Delta_2 &= \frac{2}{3}\left(f_h - \frac{2}{3} f_h^2 \right) \\ F &= 1+\lambda(a) \end{aligned}\right\} \qquad (5.145)$$

It is instructive to note that Δ_1 and Δ_2 are both of the order of flattening. Simplifying equation (5.144), one obtains

$$\begin{aligned} \eta(a) &= \frac{25}{4} F^2 q'^2 [1 + 2(\Delta_2 - \Delta_1) \\ &\quad + (\Delta_1^2 + 3\Delta_2^2 - 4\Delta_1\Delta_2)] - 1 \\ &= \eta_0 + \eta_1 + \eta_2 \end{aligned} \qquad (5.146)$$

where

$$\left.\begin{aligned} \eta_0 &= \frac{25}{4} F^2 q'^2 - 1 \\ \eta_1 &= \frac{25}{2} F^2 q'^2 (\Delta_2 - \Delta_1) \\ &= \frac{25}{3} F^2 q' \left(J_h - q f_h + \frac{2}{3} q f_h^2 \right) \\ &\text{and} \\ \eta_2 &= \frac{25}{4} F^2 q'^2 (\Delta_1^2 + 3\Delta_2^2 - 4\Delta_1\Delta_2) \end{aligned}\right\} \qquad (5.147)$$

Note that the quantity η_1 is of the order of f_h, whereas η_2 is of the order of f_h^2.

With this value of $\eta(a)$, equation (5.133) can be written as

$$A f_h^2 + (\eta_0 - 3 + \delta_1) f_h + 5J_h + \delta_2 = 0 \qquad (5.148)$$

where

$$\left.\begin{aligned} A &= \frac{17}{14} - \frac{5}{42}\eta_0 - \frac{25}{3} F^2 q q' \\ \delta_1 &= \frac{25}{3} F^2 q' J_h - \frac{4}{7} m + \frac{10}{21} J_h \\ &\text{and} \\ \delta_2 &= \frac{20}{21} m J_h \end{aligned}\right\} \qquad (5.149)$$

Note that δ_1 is approximately of the order of f_h, whereas δ_2 is of the order of f_h^2.

Equation (5.148) gives the required expression for f_h which, correct to the second order of small quantities, is

$$f_h = \frac{1}{3-\eta_0} \left[(5J_h + \delta_2) + \frac{(5J_h + \delta_2)\delta_1}{3-\eta_0} + \frac{25 A J_h^2}{(3-\eta_0)^2} \right] \qquad (5.150)$$

Also, from equation (5.143b)

$$f_h = J_h \left(1 + \frac{5}{14} m + \frac{1}{2} J_h \right) + \frac{1}{2} m + \frac{3}{56} m^2 \qquad (5.151)$$

Simultaneous solution of equations (5.150) and (5.151) would then yield the correct value of f_h.

5.5 COMPARISON OF TRACKING SYSTEMS

(J. H. Berbert)

The NGSP compared the observations from the different types of geodetic observation systems used by NASA (MINITRACK, MOTS, GRARR, C-band radar, and laser), the Smithsonian Astrophysical Observatory (Baker-Nunn, laser), the Air Force (PC–1000), the Army (SECOR), the Navy (TRANET), and the Coast and Geodetic Survey (BC–4). These comparisons were made to aid decisions on how to weight and combine the data properly from the different systems for the World Datum and Earth Gravity Field Model, and to indicate which systems would be most useful for future geodetic research and applications. An investigation was designed to determine the relative accuracy and precision of these systems to better than 10 meters.

5.5.1 Methods Used

If reference orbits accurate to better than 10 meters were available, then these orbits could be used to determine the errors in the systems. However, because of errors in the survey and gravity field, the most accurate orbits at the time this investigation was initiated were estimated to be in error at 100 to 1000 meters.

Therefore, a collection technique was used to minimize the effects of uncertainties in the relative station locations and in the Earth's gravitational field by installing accurate reference tracking systems close to the systems to be compared and precisely determining their relative positions. This approach also allowed local synchronization of the system clocks. The laser and camera systems available at GSFC, which were thought to be acccurate to 1 to 2 meters and 1″ to 2″, respectively, were chosen as the reference systems for the investigation.

The GSFC laser and camera systems were shipped to selected sites, where they tracked the GEOS satellite simultaneously with the other systems. A reference orbit was determined by a least-squares fit of the reference data (R) on each pass and used to compute reference quantities (C) for the systems to be compared. The actual observations (O) from the systems being compared (called comparison systems) were first preprocessed to remove the known errors and to achieve compatibility with the reference quantities (C), and then differenced with the reference quantities to form the residuals (O-C). Measurement biases (B) and timing biases (T), both relative to the reference systems, were then derived from the residuals (O-C) by means of the relationship

$$(O\text{-}C)_i = B - T\,\dot{C}_i + E_i$$

where $\dot{C}_i$ is the time rate of change of the quantity (C_i) and E_i is the noise component in the observations.

This procedure has the following characteristics:

(1) The orbit program corrects for the parallax errors due to the different locations of the systems.

(2) Errors in the reference trajectory due to errors in the gravitation are held to within ± 1 meter during the 15-minute duration or less of a single pass (table 5.22, ref. 1). These errors are not inherent in the observations (R), but are inherent in the quantities (C) computed for the comparison systems, owing to imperfect smoothing of the observations by the orbit.

(3) By local synchronization of the clocks of the reference and comparison systems, timing errors due to clock differences are held to ± 0.1 msec or less. This is equivalent to ± 0.5 meter or less in range measurement for the maximum range rates. The program corrects for known time differences between the observations (R) and the comparison system observations (O) when the quantities (C) for the comparison systems are generated.

(4) Except for the small errors cited above, the reference orbits produce reference quantities (C) and residuals (O-C) for nearly collocated systems, which are as accurate as the data (R) to which these orbits are fitted. Thus, the reference orbits produce quantities which are accurate to the 1- to 2-meter accuracy of the laser data. This level of derived range accuracy produces a derived range rate accuracy of 0.5 to 2.0 cm/sec. Likewise, the reference orbits produce angles (C) for nearby systems, which are accurate to 1″ to 2″, the accuracy of the camera systems (R) within the camera data span. Thus, to the extent that measurement and timing biases, assumed constant over one pass, are adequate error models, the bias differences are determined to at least the accuracy of the point-by-point accuracies quoted above for the reference systems.

5.5.2 Tests Performed

During this investigation, one comparison of cameras and a series of five comparisons of laser systems were performed to determine

whether these reference systems were consistent to within their estimated accuracies of 1″ to 2″ and 1 to 2 meters, respectively.

Other systems were compared against collocated, reference laser systems and/or cameras in the following tests: (1) GRARR, at Rosman, North Carolina; (2) Two C-band radars, SECOR and TRANET, at Wallops Flight Center, Virginia; (3) GRARR and C-band, at Carnarvon, Australia; and (4) MINITRACK, at all sites.

5.5.2.1 Camera Comparison Test

An intercomparison of some of the different types of cameras was conducted at Jupiter, Florida, where the MOTS–40, MOTS–24, and PTH–100 cameras were located within 30 meters of each other. They operated simultaneously with the Baker-Nunn and K–50 cameras and with a PC–1000 and a BC–4 camera (300-mm focal length) from November 1965 to May 1966 to track GEOS 1. Details are given in table 5.22, reference 2.

Combined Data Orbits.—The flashing lights (ch. 3), were programmed in sequences of seven flashes. The first flash fell on the even minute and subsequent flashes were spaced at 4-second intervals for a total duration of 24 seconds.

For each seven-flash sequence, observed simultaneously by two or more of the cameras, an initial set of orbital elements was differentially corrected to obtain a least-squares fit over the 24-second span of data to all the observations made by these cameras. For each participating camera, an rms of the seven right-ascension residuals and an rms of the seven declination residuals were calculated for each sequence. The mean rms, averaged over the indicated number of sequences, is given on the left side of table 5.23 for each camera.

These results tend to verify the accuracy estimates of 1″ to 2″ for the MOTS–40 and PTH–100 reference cameras, since data from these cameras are consistent with data reduced from different camera systems by independent organizations.

The larger rms values for the MOTS–24 and the BC–4 cameras are probably due to both the shorter focal length and the smaller aperture of these cameras. The shorter focal length makes the observations more sensitive to measuring errors and the smaller aperture makes the flashing light and stellar images less distinct and more difficult to center on the measuring system crosshairs. Also, some of the BC–4 right-ascension observations may have been affected by timing problems (table 5.22, ref. 2).

5.5.2.2 Biases Relative to the MOTS–40

To determine whether there were any consistent angular biases, orbits computed from observations by MOTS–40 and at least one other camera were selected for further analysis. For each 24-second orbit from MOTS–40 data, the means of the seven right-ascension residuals and of the seven declination residuals were subtracted from those for the other participating cameras. The resulting differences in the means are a close approximation to the angular biases for the comparison cameras relative to the MOTS–40. These differences in means are averaged over the indicated number of sequences and the average (B) is given on the right side of table 5.23 for each camera, along with the rms fluctuation (σ) of each set of differences about its average value. The total rms ($\sqrt{B^2+\sigma^2}$) is also given.

These results support the accuracy estimates for the cameras, since the average of the mean differences (B) is generally less than 1″ and the rms fluctuation (σ) of these mean differences about their average is generally less than 2″.

5.5.2.3 Comparison of Laser Systems

Five tests were performed during the two years from October 1968 to October 1970. Three of the tests were conducted at the Goddard Optical Research Facility (GORF)

between the prototype Goddard laser system (GODLAS) and the transportable Goddard laser system (MOBLAS, MOBLA2, or MOBLA3). The other two tests were at the Smithsonian Astrophysical Observatory site at Mt. Hopkins, Arizona, between the SAO laser system (HOPLAS) and the MOBLAS (called HOMLAS or HOMLA2 in these tests). Details on all five tests are given in table 5.22, reference 3.

In each test, the range, azimuth, and elevation (RAE) observed by MOBLAS were used to form a reference orbit on each pass by adjusting an initial set of orbital elements by least squares. The adjustment results in a zero mean for the residuals in range and azimuth. The mean of the residuals in elevation was usually different from zero by a few seconds, owing to correlation with the ranges, which were more heavily weighted. The residuals appear random, no systematic effects remaining except the nonzero mean of the residuals in elevation. Therefore, the rms of the residuals in range and azimuth may be interpreted as noise.

The residuals obtained from the MOBLAS orbit for the other laser systems were then used to determine a measurement bias (B) and a time bias (T) for each pass, as described earlier. After fitting this error model to the residuals, the remainders E_i appear random with zero mean, and may therefore be interpreted as the noise in the observations from the comparison laser systems.

The results of all five tests are shown in table 5.24 and figure 5.20.

GORF–1 Test.—GODLAS was compared with MOBLAS at the Goddard Optical Research Facility in October and November 1968. The assembly of MOBLAS had been completed just before this experiment, and this test included some of the first passes taken by MOBLAS. Five passes were observed simultaneously in this test.

The initial analysis of the GORF–1 data indicated that GODLAS and MOBLAS had average rms errors in the range of 1.86 and 1.23 meters, respectively, after a reference orbit had been fitted to the ranges from

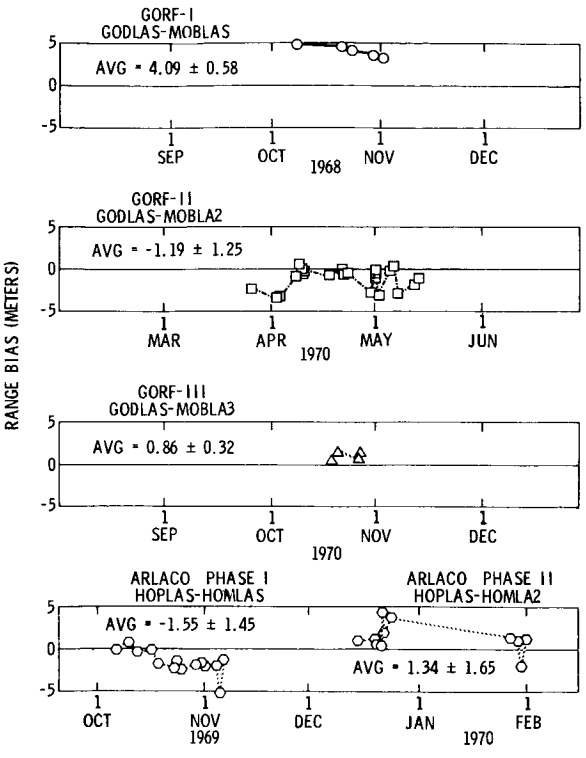

FIGURE 5.20.—Summary of four laser/laser intercomparison tests: relative range bias versus date.

MOBLAS on each pass and GODLAS range and time biases had been solved for on each pass. The average bias in range of GODLAS with respect to MOBLAS was 4.1 meters for the five passes, and the rms fluctuation of the five biases about this average was ± 0.6 meter.

The GSFC Optical Systems Branch analyzed the calibration technique used with MOBLAS during this test. They established that MOBLAS was calibrated at a signal level that was two orders of magnitude larger than the level expected for the returned signal. It was later determined that MOBLAS reads short by 4.6 meters under these conditions.

If the MOBLAS data are corrected by adding 4.6 meters to each range measurement, the bias of GODLAS (with respect to the orbit computed from MOBLAS data as shown in the second line of table 5.24) is reduced from 4.1 ± 0.6 meters to -0.5 ± 0.6 meters. The noise remains the same.

In all tests conducted after the GORF–1 test, MOBLAS was calibrated for the level expected from the returned signal.

ARLACO Laser Test.—The Arizona laser collocation (ARLACO) test was conducted from October 1969 through January 1970. MOBLAS was collocated with the SAO laser system, HOPLAS, at the Mt. Hopkins Observatory in Arizona. Halfway through the test, MOBLAS was moved 10 meters to the west, thus breaking the experiment into two tests, ARLACO–1 and ARLACO–2.

An analysis of the data from the first two passes revealed a range bias of 5.5 meters and a time bias of 100 msec for HOPLAS with respect to the orbit computed from MOBLAS data. Of the 5.5 meters, 4.8 meters were traced to a change in the internal delay in the HOPLAS system since the last calibration. The 100-msec time bias was due to an intentional offset in the times of HOPLAS observations to avoid interference with observations by MOBLAS, but the offset was overlooked in the preprocessing. After these discrepancies were corrected, the comparison was continued.

For the 14 passes observed during October and November 1969, the HOPLAS ranges had an average noise of 1.34 meters and the MOBLAS ranges had an average noise of 1.06 meters. The average bias of the HOPLAS ranges with respect to the orbit from the MOBLAS data was -1.6 ± 1.5 meters.

During the second phase of ARLACO, December 1969 and January 1970, data were taken on 11 passes. The noises for HOPLAS and MOBLAS were 1.09 and 1.00 meters, respectively, and the average bias of the HOPLAS ranges with respect to the orbit computed from MOBLAS was 1.3 ± 1.7 meters.

GORF–2 Test.—The GORF–2 test was conducted between March 1970 and May 1970. At that time, MOBLAS was the same as it was during the Carnarvon laser collocation (CALACO) experiment. Data were taken on 21 passes. GODLAS AND MOBLAS had an average noise level of 1.00 and 1.06 meters, respectively, and an average bias of -1.2 ± 1.3 meters for the GODLAS ranges with respect to the orbit computed from the MOBLAS data.

GORF–3 Test.—Between the GORF–2 and GORF–3 tests, both the MOBLAS and GODLAS systems were modified to incorporate a more sophisticated pulse-detection scheme. Pulse height was measured and the pulse threshold detection level was set at one-half the measured pulse height. In addition, a quantitative measure of the MOBLAS pulse height was made, recorded, and used in a programme correction of the range measurements on the MOBLAS. This feature was present in the GODLAS during earlier tests.

The results of the GORF–3 tests, although not applicable to the earlier laser comparisons with GRARR, C-Band, SECOR, and TRANET, show significant reductions in the laser system noise and relative range bias, with all quantities at the submeter level.

Summary of Laser Results.—The tests support the estimated single-pass accuracy of 1 to 2 meters for the Goddard reference-laser systems. The average of the biases derived on each pass for the GODLAS ranges with respect to the orbit computed from MOBLAS data lies between -1.2 ± 1.3 meters and 0.9 ± 0.3 meters for the three GORF tests. The average of the biases for the SAO HOPLAS with respect to the orbit computed from MOBLAS data lies between -1.6 ± 1.5 meters and 1.3 ± 1.7 meters for the two ARLACO tests.

5.5.3 Comparison of Other Systems With the Laser and Camera Systems

Besides the tests described above, three other comparisons were conducted between a laser system and other systems during this investigation. These were: (1) the Rosman laser collocation test (ROLACO) to compare GRARR on GEOS 1 (table 5.22, ref. 4), (2) the Wallops Island collocation experiment

(WICE) to compare the FPQ–6 and FPS–16 C-band radars; (3) a SECOR system and a TRANET system on GEOS 2 (table 5.22, refs. 5 and 6); and (4) the Carnarvon laser collocation experiment (CALACO) to compare another GRARR and FPQ–6 radar on GEOS 2 (table 5.22, ref. 7). GODLAS was used as the reference laser for the ROLACO and WICE tests, and MOBLAS was used for the CALACO test.

The data were analyzed in these tests as in the laser intercomparison tests. The residuals in range, azimuth, and elevation (RAE) from laser systems were minimized in the least-squares sense by adjusting a set of orbital elements for each pass to form a reference RAE orbit. The mean and rms of the comparison system residuals about the RAE orbit were computed for each type of observation and for each pass. In the tables accompanying this section, the average mean and the average rms are given over the number of passes indicated. These are designated as "mean before" and "rms before," since they are determined from residuals before fitting an error model. In addition, the rms fluctuation of the means for each pass about the average mean for all passes and the fluctuation of the rms's for each pass about the average rms are given in the same columns.

On each pass, the residuals for the comparison systems were used to determine a measurement bias (B) and a station time bias (T) relative to the laser system. The term "station time bias" is used to indicate that each type of observation from a given comparison system contributes to the determination of the time bias of that system. In these tables, only the average B and T over the indicated number of passes is given, along with the rms fluctuation of the single-pass B and T about the given average. Since T is usually small, the average bias B is almost the same as the mean before fitting the error model. The mean after fitting the error model is not given in the tables, since it is always zero. The column headed "rms after" is the rms of the average residual after fitting the error model, along with the rms fluctuation in the rms's for each pass about the average rms. These numbers represent the noise in the observations by the comparison system.

The reference RAE orbits closely fit the observations from the laser system within the laser data span; they therefore produce reference ranges and angles for nearby systems with essentially the same accuracy or bias as the laser system data. From the previous laser intercomparison tests, the range biases for the laser system are below 2 meters with respect to other laser systems. As will be shown later, in tests involving camera observations, the biases in the laser system angles with respect to camera observations are below 30″. Error analyses indicate the range-rate accuracies from the laser system RAE orbits are within 0.5 to 2.0 cm/sec.

To evaluate the observed angle from data supplied by camera, observations from a collocated camera are used instead of the laser system azimuth and elevation observations in forming reference orbits. These orbits are designated range, right ascension, and declination (RRD) orbits. The RRD orbits closely fit the laser system range and camera angle observations and therefore produce reference ranges and range rates for nearly collocated systems with essentially the same accuracy as the RAE orbits. However, they produce improved angles with the 1″ to 2″ accuracy of the camera data.

5.5.3.1 ROLACO Test

The results of the July through December 1966 GEOS 1 ROLACO test of the Rosman GRARR versus GODLAS are summarized in table 5.25 and in the plot of the derived GRARR relative range biases against date in figure 5.21. After an orbit was fitted to the data from the laser system, the remaining rms noise was 1.8 meters for the system.

An earlier evaluation of the Rosman GRARR by means of short-arc reference orbits of GEOS 1 which were generated with data taken the first week of January 1966 from four eastern U.S. SECOR stations indicated this GRARR had a range bias of

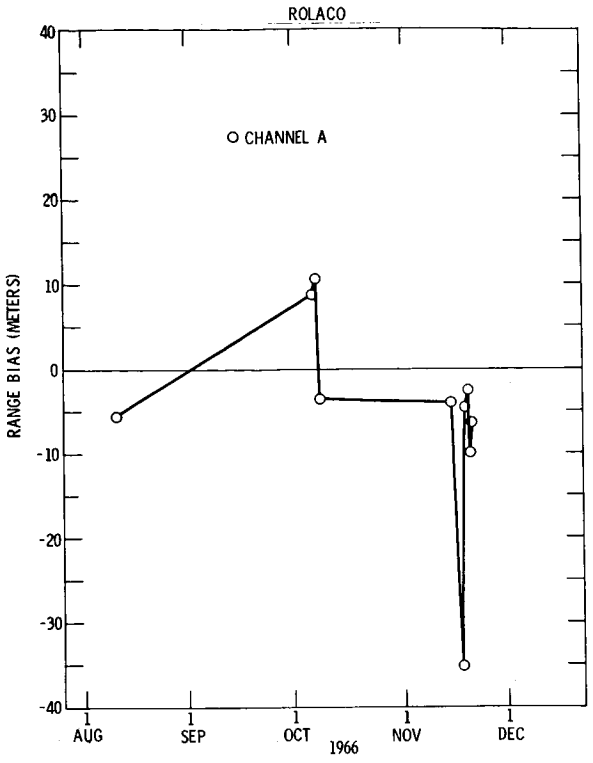

FIGURE 5.21.—Rosman GRARR range bias versus date, GEOS 1 transponder channel A laser (GODLAS) reference orbits.

-20.5 ± 4.9 meters (table 5.22, ref. 8). Investigations into the cause of this bias led to the discovery of several small errors in the GRARR calibration and preprocessing procedures which accounted for -9.7 meters of the GRARR range bias (table 5.22, ref. 9), leaving a net bias of -10.8 ± 4.9 meters for the Rosman GRARR at that time.

For the ROLACO test, the GRARR calibration and preprocessing procedures were changed to add the above corrections, resulting in an average single-pass bias in the GRARR range data relative to the laser orbit of -5.3 meters with an rms fluctuation of 12.4 meters about this average value for the 10 bias values obtained. The average GRARR time bias relative to the laser was -2.1 ± 1.2 msec. All 10 passes were on GRARR channel A. More details are given in reference 4 of table 5.22.

In an independent comparison of the Rosman GRARR observations with accurate orbits obtained from camera observations, Lerch, Marsh, and O'Neill (table 5.22, ref. 10) reported average range and time biases on channel A of -10.0 ± 8.8 meters and -2.4 ± 2.4 msec on 12 passes relative to a 5-day orbit, and -5.6 ± 1.6 meters and -1.9 ± 5.1 msec on 14 passes relative to another 5-day orbit a week later. These results included the correction for bias of -9.7 meters. The -10.0-meter GRARR channel A bias obtained here is in remarkable agreement with the -10.8-meter GRARR channel A bias obtained with respect to SECOR orbits during the same first week in January 1966. The long-arc GRARR results obtained for the second week of January 1966 are consistent with the ROLACO test results for data taken 6 to 12 months later. Lerch et al. also reported average biases on channel C of 18.1 meters and -1.4 msec on 3 passes during the first 5-day orbit.

5.5.3.2 WICE Test

The WICE statistics for the two C-band radars, the SECOR, TRANET, and laser systems and the camera systems are summarized in tables 5.26 and 5.27. Table 5.26 gives the results for all the available passes, using GODLAS data to generate reference RAE orbits. Table 5.27 gives the results for those passes which had collocated data from the PTH–100 camera combined with the laser system data to generate reference RRD orbits. Both the RAE and the RRD orbits provide reference ranges with essentially the accuracy of the laser system data. The accuracy of the angles from the RAE orbit is determined by the accuracy of the laser system angles (about 30″), whereas the accuracy of the reference angles from the RRD orbit is determined by the camera angles (1″ to 2″).

In figures 5.22, through 5.25, the pass-to-pass variations in the derived biases in range, range rate, azimuth, and elevation are shown for the participating systems. More details may be found in references 5 and 6 of table 5.22. The tables and figures show the char-

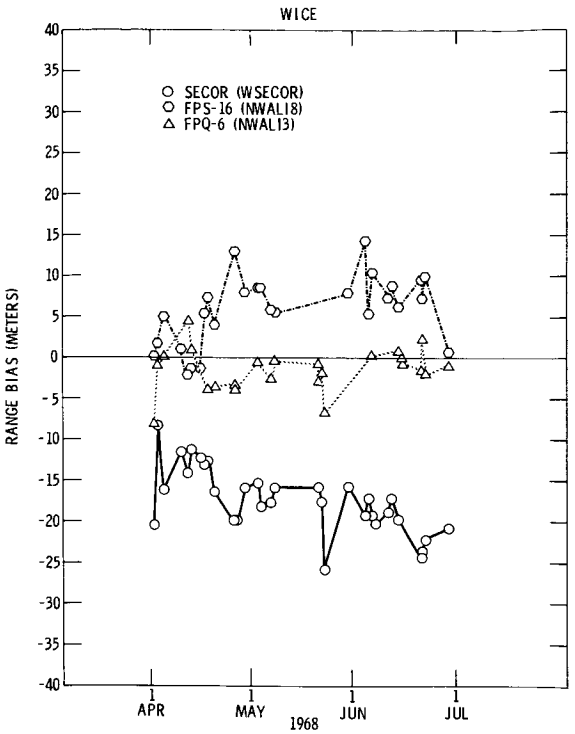

FIGURE 5.22.—FPQ–6, FPS–16, and SECOR range bias versus date, laser (GODLAS) reference orbits.

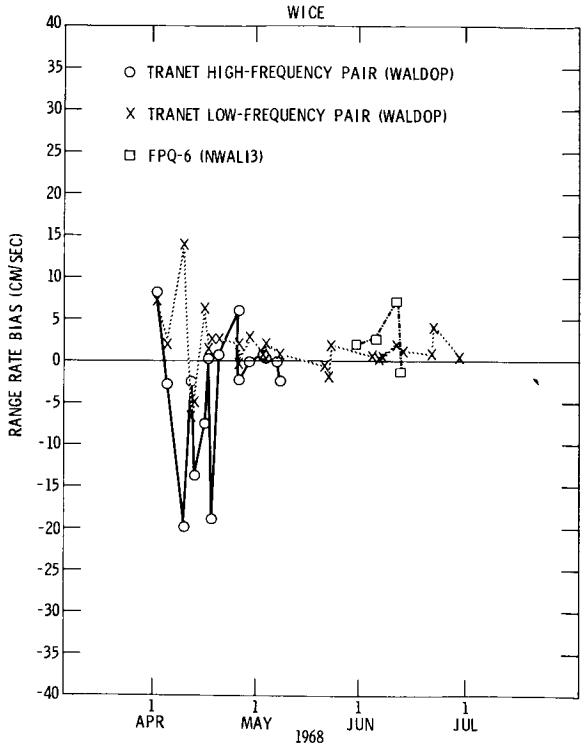

FIGURE 5.23.—TRANET and FPQ–6 range rate bias versus date, laser (GODLAS) reference orbits.

acteristics of the participating systems, as outlined below.

RMS and Bias in Range for WICE.—The rms noise in data from GODLAS was reduced in this test from the earlier ROLACO value of 1.8 meters to 1.3 meters. After error modeling, the rms noise in the C-band radar and SECOR ranges was also less than 2 meters. The data from the FPQ–6 receiver were the smoothest, averaging 1.0 meter over the 34 RAE orbits and 0.8 meter over the 21 RRD orbits.

In the 34 simultaneous trackings by laser systems and by the FPQ–6 on a beacon (transponder), there were 10 passes in which the radar tracked both beacon and satellite surface on the same pass; i.e., the beacon was tracked on the first third of the pass, the surface on the middle third of the pass, and the beacon again on the last third of the pass. For these passes, the bandwidth of the FPQ–6 receiver was optimized to receive a 1.0-μsec-wide pulse rather than the 0.6-μsec-wide pulse used in tracking beacons. The pulse-width mismatch resulted in the ranges from the beacon tracking being short by approximately 30 meters, and these ranges were corrected by adding 30 meters. If these 10 passes are ignored, the remaining 24 passes (beacon only), shown in figure 5.22, yield essentially the same results as all 34 passes, except the average bias in range is changed from -1.6 ± 2.6 meters to -2.0 ± 2.7 meters (see table 5.26).

In the 27 sets of data from FPS–16 on a beacon, the average of the range biases is 5.7 ± 4.1 meters, resulting in a net difference between the biases of 7.3 meters in the two radars.

The radar calibration techniques used in WICE were analyzed by Wallops Flight Center. The results of the analysis and tests verifying the analysis indicated that the FPQ–6 and FPS–16 (see ch. 6) were miscalibrated and their range data should be corrected by algebraically adding -0.6 meter

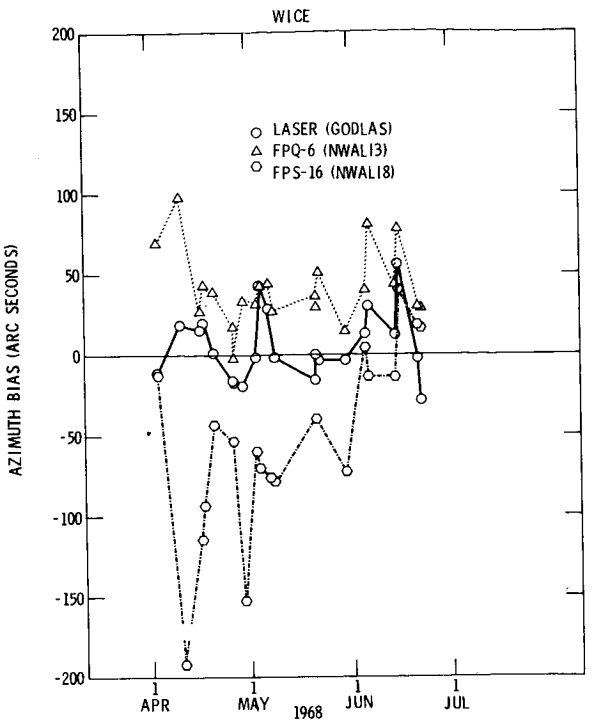

FIGURE 5.24.—Azimuth bias versus date for the Goddard laser, FPQ–6 radar, and FPS–16 radar collocated at Wallops Island, Virginia. WALMOT camera/GODLAS range reference orbits.

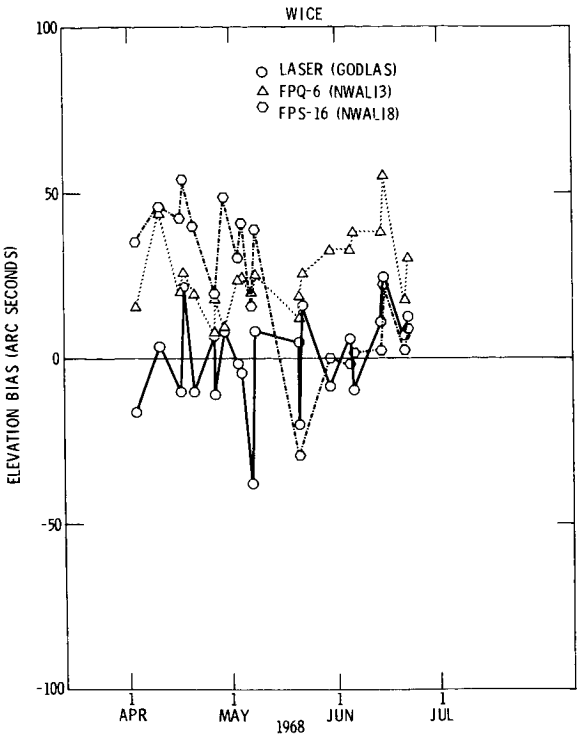

FIGURE 5.25.—Elevation bias versus date for the Goddard laser, FPQ–6 radar, and FPS–16 radar collocated at Wallops Island, Virginia. WALMOT camera/GODLAS range reference orbits.

to the FPQ–6 and −7.9 meters to the FPS–16 measurements.

If this correction is made, the range bias on the FPQ–6 of -1.6 ± 2.6 meters shifts to -2.2 ± 2.6 meters, as shown in table 5.26. The average FPQ–6 range noise of 1.0 ± 0.3 meters and time bias of 0.3 ± 0.3 msec remain unchanged. If the FPS–16 data are corrected for the −7.9-meter calibration error, the average range-bias changes from 5.7 ± 4.1 meters to -2.2 ± 4.1 meters. The two collocated C-band, average range-biases of the beacon track then agree with each other to better than 0.1 meter. The results in tables 5.26 and 5.27 were obtained before the post-test calibration analysis and hence do not include these corrections except where indicated.

FPQ–6 skin-track data (data obtained by reflection from the satellite surface) were successfully taken on 8 of the 10 passes where skin tracking was attempted. No FPS–16 skin-tracks were attempted. The average range rms noise and average range bias for the skin-track portion of the eight FPQ–6 passes were 8.6 ± 2.0 meters and -5.2 ± 2.7 meters, respectively. The corresponding averages for the beacon track portion of the same eight passes were 1.1 ± 0.4 meters for range noise and -1.8 ± 2.2 meters for range bias. Thus, the FPQ–6 skin track range bias is 3.4 meters more negative than the FPQ–6 beacon track range bias on the eight common passes.

There were 16 passes that were common to the 24 FPQ–6 and 27 FPS–16 beacon-only passes. If the derived biases for the two radars are differenced on each of the 16 common passes, the average range bias difference of the FPS–16 relative to the FPQ–6 is 6.3 ± 5.6 meters. If the calibration analysis corrections of −0.6 and −7.9 meters are ap-

plied, this average range bias difference is reduced to -1.0 ± 5.6 meters.

Note that the pass-to-pass variation in range bias in the radars (table 5.26) was ± 2.6 meters for the 34 FPQ–6 biases and ± 4.1 meters for the 27 FPS–16 biases when taken relative to the laser system. The pass-to-pass variation in range bias increased to ± 5.6 meters when the FPS–16 biases were taken relative to the FPQ–6 biases, indicating the uncorrelated nature of the range bias in the two radar systems. The correlation coefficient between the FPQ–6 and FPS–16 range bias values for the common 16 passes is -0.22, indicating the pass-to-pass variations in bias are probably not due to the laser system.

The difference in FPQ–6 average range bias obtained with all 20 beacon-1 (112-meter delay) tracks relative to the bias obtained with all 14 beacon-2 (740-meter delay) tracks is -1.6 meters (see table 5.26). A similar comparison with the FPS–16 for 14 beacon-1 and 13 beacon-2 tracks leads to a value of $+2.6$ meters. Thus, if a consistent range bias exists between beacon-1 and beacon-2 tracks for both radars, it is obscured by the pass-to-pass fluctuations in range bias for the two radars.

The average range bias of -17.5 ± 4.0 meters in SECOR appears realistic to within the estimated laser-system accuracy of 1 to 2 meters, especially since the analysis of the radar calibration discovered the -7.9-meter error on the FPS–16 and reduced its bias relative to the laser system from 5.7 to -2.2 meters. An analysis of the SECOR calibration and preprocessing procedures by the Army Map Service led to correction of several minor preprocessing errors, which changed the derived biases by 1 or 2 meters in earlier submissions of these data. However, the analysis failed to account for the large bias shown in table 5.26 for the latest submission.

The temporal variation in the biases shown in figure 5.22 suggests that the delay characteristics of the satellite transponder may have been changing slowly with time. A linear extrapolation of the SECOR range bias values in figure 5.22 intersects the zero bias about one month before the launch of GEOS 2 on 11 January 1968, when presumably the last calibration of the transponder could have been made.

Range Rate RMS and Bias for WICE.—The FPQ–6 radar obtained range rate skin-track observations on four of the laser passes. These data were relatively noisy because of the low signal levels involved in skin-tracking GEOS 2. However, the average range-rate bias of $+2.4$ cm/sec is not unreasonable, considering the estimated orbit accuracy of ± 0.5 to ± 2.0 cm/sec in range rate.

The WICE TRANET station could track on the two lower GEOS 2 Doppler beacon frequencies (162 and 324 MHz, designated by TRAN–59) or on the higher pair (324 and 972 MHz, designated by TRAN–35). In order to conserve spacecraft power, the 972-MHz beacon was turned off part way through these tests, so fewer passes were obtained by TRAN–35.

The initial analysis of the TRANET data yielded range-rate positive biases of 21.2 ± 7.7 cm/sec and 18.4 ± 5.5 cm/sec for TRAN–59 and TRAN–35. An analysis of the editing and preprocessing procedures of the Naval Weapons Laboratory (NWL) indicated that at least some of this bias was due to the omission of time correction for satellite-to-station transit and the tropospheric refraction correction prior to solving for a per-pass bias, which were then provided with the observations on each pass.

This per-pass bias absorbs the bias component of the error due to neglecting the two corrections. When the user applies the per-pass bias provided as well as the two omitted corrections, he overcorrects by the amount of the bias component absorbed in the per-pass bias provided by NWL. Since the correction for transit time is always a negative time correction, which adjusts the observation times back to when the signals left the satellite, the net result is always a positive range rate bias.

Agreen and Marsh (table 5.22, ref. 11) compared observations from 5 TRANET sta-

tions against 13 optical-reference 2-day orbits generated from worldwide camera data. They reported a positive average range rate bias for all five participating TRANET stations of 8.2 to 10.2 cm/sec ± 2.4 to 3.4 cm/sec relative to the optical orbits. It has not yet been explained why the TRANET positive range rate biases found in this analysis were only about half the magnitude of those found in the WICE test.

As a result of the WICE analysis, NWL again preprocessed the early WICE TRANET data. This time, the two corrections mentioned were made before solving for the per-pass bias. These final results are also given in table 5.26, where it is shown that the biases with respect to the RAE orbits are now reduced to 1.4 ± 3.5 cm/sec for TRAN 59 and -3.2 ± 7.5 cm/sec for TRAN 35. The results with fewer RRD orbits are slightly better.

The TRANET biases for a single pass are plotted against time in figure 5.23, where the wider fluctuations in derived biases at the beginning of the test may reflect a learning period for the operators.

Angle RMS and Bias for WICE.—The biases in azimuth and elevation from pass to pass relative to the angles from RRD orbit based on camera data indicate that the angle biases of the laser system are substantially less than the angle biases of the radar. However, the rms values indicate the radar point-to-point angle data are smoother than the laser system data.

In the angle residuals statistics, the camera right-ascension residuals are multiplied by cos (declination) and the laser and radar azimuth residuals are multiplied by cos (elevation) in order to compare these residuals on the same sky-angle scale as the declination and elevation residuals. The sky-angle scale is also more useful for interpreting the results as radar boresight error or for relating the angle observation errors to target position errors.

The average angle biases in the laser system and the radars derived from the RRD orbits differ from those derived from the RAE orbits by less than 6″. The average angle rms's derived from the RRD orbits differ from those from the RAE orbits by less than 10″. Thus, the RAE orbits based on data from the laser system appear adequate for determining average angle biases and rms to 10″ or better in tests such as WICE.

The average azimuth and elevation biases in the laser system data changed, respectively, from $0'' \pm 0''$ and $-6'' \pm 13''$ for the RAE orbits to $5'' \pm 21''$ and $0'' \pm 15''$ for the RRD orbits, indicating that the RAE orbits are adequate for determining pass-to-pass angle biases to about 22″ or better (in the 1-σ sense) in such tests.

The FPQ–6 and FPS–16 average station time biases derived from the beacon track are both 0.3 ± 0.3 msec relative to the laser, indicating the laser might have a -0.3-msec timing error. However, the FPQ–6-derived time bias of 0.1 ± 0.7 msec on eight range data skin tracks and the SECOR-derived time bias of -0.6 ± 0.5 msec are not consistent with this interpretation.

The larger derived TRANET time biases evident on the RRD range rate evaluations are due to the high correlation between the derived range-rate and time biases and to relaxing the a priori constraint on time bias from 0.2 msec on the RAE orbits to 2.0 msec on the RRD orbits.

5.5.3.3 CALACO Test

The CALACO test results for the collocated GRARR, FPQ–6 C-band radar, MOBLAS laser, and PTH-100 camera are summarized in tables 5.28 and 5.29 and figures 5.26 through 5.30. The statistics derived from the laser RAE orbits are given in table 5.28 and those from the RRD orbits in table 5.29. The temporal variation in the derived C-band range and timing biases and in the GRARR range, range rate, and timing biases are given in figures 5.26 through 5.30.

After sending the preprocessed C-band observations, the radar coordinator at Wallops Station advised us of an equipment problem that caused a time error of an unknown integral, multiple of 10 msec. This error was

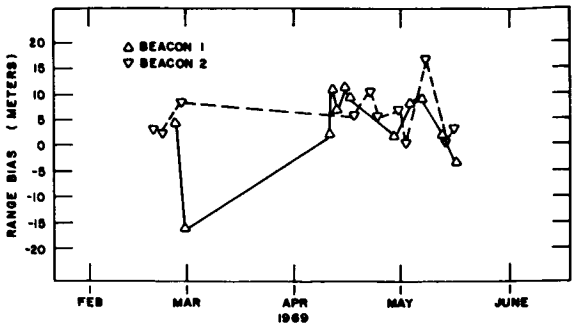

FIGURE 5.26.—CALACO NCARVN C-band range bias versus time.

constant within a pass, but varied from pass to pass. It was not feasible to determine the unknown integers by comparison with the worldwide, long-arc orbits. However, comparison of the radar observations with the laser system observations enabled us to determine these integers and to correct the radar observation times by the proper multiple of 10 msec before the normal intercomparison procedure.

Range RMS and Bias for CALACO.—The MOBLAS range average-rms noise remaining after fitting the orbits is 1.3 ± 0.2 meters, which is similar to the rms noise of 1.2 meters observed in the prior GORF–1 test.

The FPQ–6 C-band range rms noise, after removing a measurement and timing bias, is 1.1 ± 0.4 meters, similar to the previous results for the two C-band radars at Wallops Station.

The Carnarvon GRARR range rms noise of 3.0 ± 0.2 meters on GEOS 2 is smoother

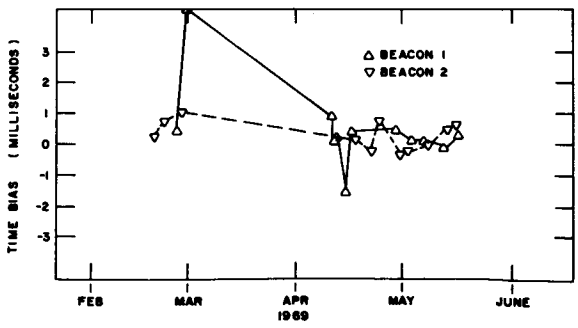

FIGURE 5.27.—CALACO NCARVN C-band timing bias versus time.

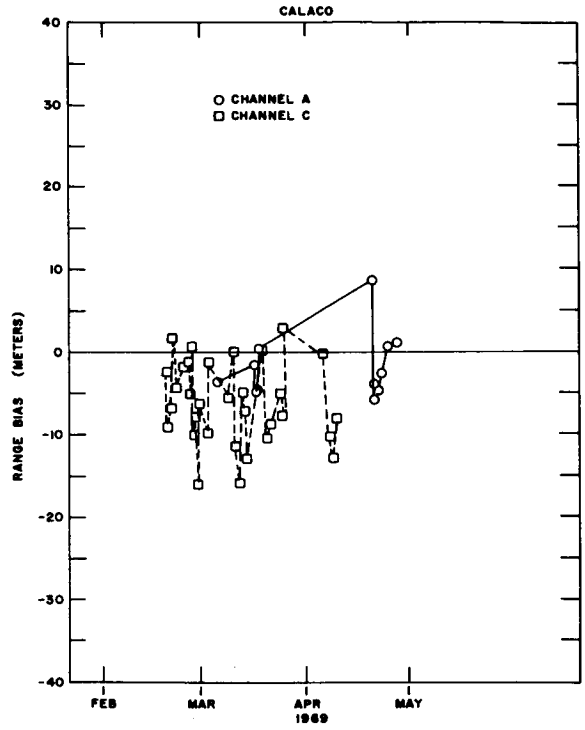

FIGURE 5.28.—Carnarvon GRARR range bias versus date for GEOS 2 transponder channels A and C, laser (CRMLAS) reference orbits.

than the 6.8 ± 2.1-meter value obtained for the Rosman GRARR on GEOS 1. The difference could be due to the setup of the ground systems, the different transponders, or the greater height of GEOS 1.

An average range bias of -15.0 ± 6.5 meters was initially found for the FPQ–6 relative to the laser system. In attempting to explain this large bias, it was determined that the radar range calibrations were performed on a distant range target without correction for the delay introduced by the atmosphere. By using values of atmospheric pressure, temperature, and humidity collected for the laser system and camera passes, the actual delay through the atmosphere to the range calibration target was calculated to be 20.0 ± 0.7 meters larger than the assumed value. Thus, the radar calibration preprocessing for this station produced ranges that were too short by 20.0 ± 0.7 meters on each pass.

A post-test calibration correction for this refraction bias was computed for each pass

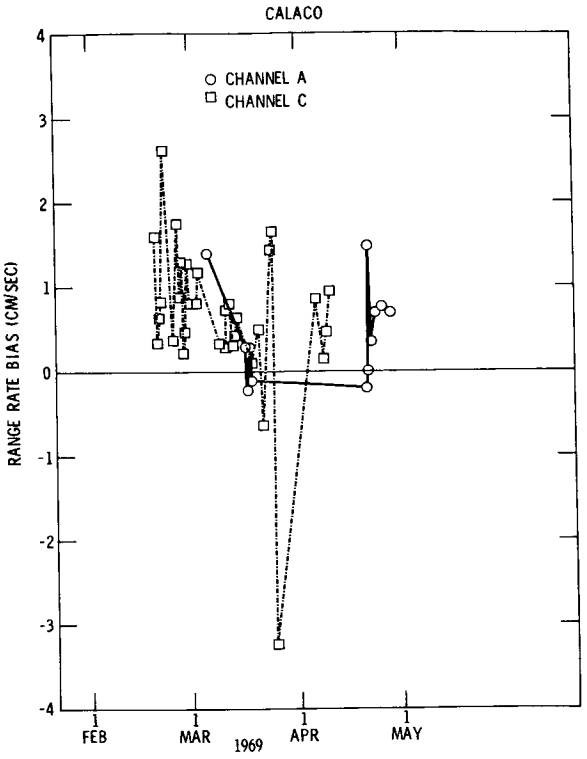

FIGURE 5.29.—Carnarvon GRARR range rate bias versus date for GEOS 2 transponder channels A and C laser (CRMLAS) reference orbits.

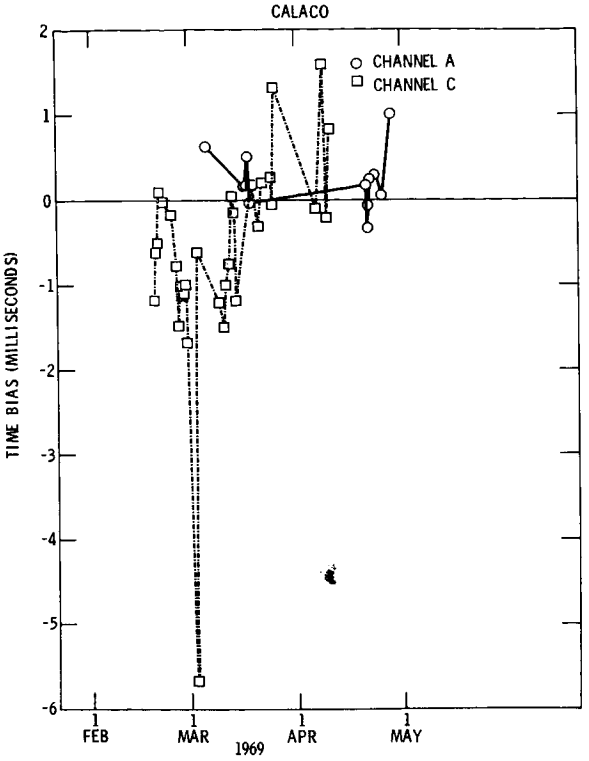

FIGURE 5.30.—Carnarvon GRARR time bias versus date for GEOS 2 transponder channels A and C, laser (CRMLAS) reference orbits.

and applied to the range bias previously derived for that pass. As shown in table 5.28, this step improved the average range bias from -15.0 ± 6.5 meters to 5.0 ± 6.7 meters. Users of these radar data should make certain that this refraction bias correction is applied.

Correction by the user of the remaining radar average range-bias of 5.0 meters relative to the laser system reduces the pass-to-pass total rms error of that radar at that time from ± 8.4 meters to ± 6.7 meters. This assumes the following definition of total rms error:

$$\text{total rms error} = \sqrt{B^2 + \sigma^2}$$

where σ is the pass-to-pass bias fluctuation about B ($\sigma = \pm 6.7$ meters in this case) and B is the average range bias ($B = 5.0$ meters in this case).

When the FPQ–6 average range biases for the two C-band beacons are compared, the beacon-1 bias minus the beacon-2 bias is -1.7 meters before the above refraction correction is made and -1.5 meters after it is made. This difference is similar in magnitude and consistent in sign with the -1.6-meter difference obtained between beacon-1 and beacon-2 for the Wallops FPQ–6, but it is not consistent with the $+2.6$-meter difference obtained with the Wallops FPS–16.

Similarly, a 3.2-meter difference in average range bias was noted between channels A and C of GRARR. This range bias difference was significant at the 1 percent level in a statistical test on the probability of a chance occurrence of such a difference. Application of the derived range bias corrections of -1.7 meters for channel A and -4.9 meters for channel C reduces the total rms range error from ± 4.0 meters to ± 3.6 meters for chan-

nel A and from ±8.9 meters to ±7.4 meters for channel C.

Range Rate RMS and Bias for CALACO.—The Carnarvon GRARR range rate rms noise of 1.4±0.7 cm/sec is smoother than the values obtained during the WICE test for the C-band skin track data or for the TRANET Doppler data.

Without regard to channel, the GRARR average range rate bias of 0.5±2.4 cm/sec and the values for the individual channels are all smaller than the values for the WICE range rate systems and are within the estimated accuracy of the orbits based on laser system data. Correction for the derived range rate biases for GRARR in this test or for the FPQ–6 or TRANET in the WICE test (after the preprocessing correction noted) is not justified, since this does not improve the accuracy of the pass-to-pass range rate data significantly, owing to the variability in the derived pass-to-pass biases.

Angle RMS and Bias for CALACO.—Results for the 14 CALACO passes, with camera angle data added to the laser data to form RRD reference orbits, are given in table 5.29. The zero means and small rms for the residuals in laser range and the camera angle observation indicate that the RRD orbits have adjusted closely to these observations (R). Then, the RRD orbits produce observations (C) having essentially the same bias as R for evaluation of observations (O) from nearly collocated systems.

For both the radar and the laser systems, the angle-residual average rms in table 5.29 lies between 31 and 38 arc seconds. The average of the angle residual means is 30 arc seconds or less for both systems and is smaller for the laser system than for the radar.

Station Time Bias for CALACO.—The Carnarvon FPQ–6 radar-derived average station time bias of 0.3 to 0.5 msec relative to MOBLAS is consistent with the 0.3-msec value derived for both radars relative to GODLAS in WICE. This result might indicate that a systematic error, having the appearance of a time bias, exists in the laser systems, were it not for the −0.6 msec value obtained for SECOR in WICE and the 0.0-msec value obtained for GRARR in the CALACO test.

Comparison of MINITRACK With MOTS–40 Cameras.—The MOTS–40 calibration camera at the center of each MINITRACK site observed GEOS flash sequences within the MINITRACK beam. The 24-sec reference orbits from these cameras were used to determine a per-pass bias for simultaneous MINITRACK observations. The results indicated that the MINITRACK observation of per-pass biases relative to the camera orbits were about 10″ to 20″ (table 5.22, ref. 12).

A long-arc comparison of MINITRACK observations relative to a 5-day camera orbit indicated an rms for the MINITRACK per-pass angle biases of about ±40″ (table 5.22, ref. 13).

It was noted in these studies that the MINITRACK biases were smaller when the refraction corrections normally introduced in the orbit differential correction (DC) program were suppressed or when only those observations near the base-line bisecting-plane, which are therefore nearly immune to refraction error, were used. This effect was traced to an overcorrection for refraction in the DC program resulting from use of a single-path refraction correction rather than a differential two-path refraction correction required for an interferometer (table 5.22, refs. 14 through 17).

5.5.4 Summary and Conclusions

In this investigation, it has been assumed that the most important indicators of accuracy in the observations are the per-pass measurement bias (B), the time bias (T), and the pass-to-pass fluctuations (σ) in these biases. The point-to-point noise within a pass has little effect on the results, since these solutions are determined by the orbit adjusted to the observations, and this orbit smooths out the nearly random noise of the data

points within a pass, provided there are enough data points.

If the pass-to-pass fluctuation (σ) in the measurement bias (B) is random, then this parameter also is averaged out to some extent in the results, provided enough passes are used in the solutions. The stable component of the pass-to-pass bias has the most damaging effect on the solutions.

A composite error indicator used to help summarize the intercomparison test results is the total rms error, which equals $\sqrt{B^2+\sigma^2}$. This error probably best estimates the relative accuracy of the GEOS observation systems for NGSP applications.

The pass-to-pass biases (B) were determined relative to orbits determined from the reference laser systems and cameras. Estimates of the accuracy of the reference system observations were supported by a test of collocated camera and by five collocated-laser tests. Other GEOS observation systems were evaluated against collocated lasers and cameras in three major tests performed at Rosman, North Carolina, at Wallops Flight Center, Virginia, and at Carnarvon, Australia. Summaries of the various tests are available in a single document in reference 18 of table 5.22.

5.5.4.1 Cameras

The Jupiter camera-intercomparison test results support the 1″ to 2″ accuracy per seven-flash sequence for most of the cameras tested, since for all but the MOTS–24 and BC–4 (300 mm) cameras, which have shorter focal lengths and smaller apertures, the mean rms with respect to the combined data orbits were within 2″ or better (table 5.23).

A few NASA sites originally had MOTS–24 cameras, but these were all replaced by MOTS–40 cameras prior to GEOS 1.

The NGS World Geometric Survey project (ch. 7) at first used the 300-mm focal-length BC–4 cameras, but later converted to the 450-mm focal-length version, thereby improving the BC–4 plate scale by 50 percent. Also, the C&GS observations were shutter chops of the relatively bright, continuous trails of the ECHO and PAGEOS balloons rather than of the GEOS flashes, thereby increasing the number of observations available for averaging and improving the detectability and measurability of the images on the photographic plate.

5.5.4.2 Laser Systems

The results support the 1- to 2-meter accuracy over one pass, since, except for the initial few passes with the new systems in the GORF 1 and ARLACO 1 tests, the total rms error of the comparison systems with respect to the reference systems was within 2.2 meters (table 5.30).

After the calibration error on the first few passes for MOBLAS was corrected, the total rms error for the GODLAS ranges with respect to an orbit computed from MOBLAS data was only 0.8 meter for GORF 1. The total rms error for GODLAS with respect to MOBLAS for GORF 2 was 1.8 meters, and for GORF 3, the error was 0.9 meter.

5.5.4.3 Accuracies of Ranging Systems

Unsuspected systematic errors were discovered in the observations from most of the systems. The systematic errors identified were usually traced to the calibration or preprocessing procedures rather than to faults in the system.

Table 5.30 summarizes the average and standard deviation of the range biases for each pass derived for the comparison systems with respect to the reference systems.

The total rms error, before applying corrections discovered as a result of the tests, represents typical system accuracy for a pass under normal operating conditions. However, an extra effort was made to remove known errors from the calibration and preprocessing procedures.

The probable sources of the identified biases and their measured corrections are also given in table 5.30, along with the improved average range biases and total rms errors after these corrections had been applied. These improved, total rms errors represent

potential system accuracies for one pass only if the effort is expended to detect and correct the small calibration and preprocessing errors, such as those discovered in these tests.

The normal error estimates are probably best for relative data weighting for the NGSP solutions. The potential error estimates are useful for simulations investigating what is possible with these systems if the extra effort is made.

5.5.4.4 Accuracies of Range Rate Systems

The range rate observations by GRARR and radar are probably unbiased, within the ability of these tests to detect a bias.

The TRANET data originally submitted for WICE, as well as all other TRANET data in the Geodetic Satellite Data Service (GSDS), are affected by per-pass negative Doppler-frequency biases, equivalent to the positive range rate biases resulting from the NWL preprocessing procedures.

These biases could be removed by reprocessing all the TRANET data and applying the corrections to transit time and tropospheric refraction before solving for the per-pass base-frequency bias provided by NWL. This was done for the WICE TRANET observations on all 26 passes; the range rate average bias ($B \pm \sigma$) and the total rms error ($\sqrt{B^2+\sigma^2}$) were reduced from 21.2 ± 7.7 cm/sec and 22.6 cm/sec to 1.4 ± 3.5 cm/sec and 3.8 cm/sec, respectively, for TRAN–59 relative to the laser. Similarly, for TRAN–35, the total rms error was reduced from 19.2 cm/sec to 8.2 cm/sec.

Alternatively, the use of the TRANET observations could be improved by recognizing the existence of an a priori, positive, range rate bias and solving for this bias, under an appropriate a priori constraint, along with the orbit, survey, and gravity field parameters.

A more exact procedure would be to determine, with the use of a nominal orbit, the transit time and tropospheric-refraction Doppler-frequency correction-profile versus time in each pass. Then the mean positive-frequency bias component in this profile should be solved for and the result used to remove the positive bias component from the base frequency (F_B) provided by NWL. This should remove the net negative Doppler frequency bias component or the net positive range-rate bias component from the TRANET observations.

Range rate ($\dot{R}$) was related to the TRANET observations by means of the following equation:

$$\dot{R} \pm \frac{c\ (F_B - F_M)}{F_M}$$

where F_M is the measured frequency provided by NWL, F_B is the base frequency provided by NWL, and c is the speed of light (2.997925×10^8 m/sec).

5.5.4.5 Accuracies of Angle Systems

No obvious angle biases were detected in the Jupiter camera test. The camera angles appear to be accurate to 1″ to 2″ whereas the laser angles appear accurate to better than 30″ and the C-band angles appear to be accurate in the region of 30″ to 70″.

The MINITRACK angles appear accurate to 10″ to 20″, provided the correct refraction theory is applied.

5.5.4.6 Station Time Biases

The time bias in the Rosman GRARR of -2.1 ± 1.2 msec relative to the laser was not supported by the 0.0 ± 1.2-msec value found for the Carnarvon GRARR relative to the laser.

The time biases in Wallops FPQ–6 and FPS–16 of 0.3 ± 0.3 msec relative to the laser were supported by the 0.4 ± 1.1-msec value found for the Carnarvon FPQ–6. It seems likely that either the C-bands or the lasers have a systematic error, which behaves like an 0.3-msec time bias for the C-bands or like a -0.3-msec time bias for the lasers.

5.5.4.7 General Remarks

The measurement biases discovered in these tests are recommended for correcting

the observations only in those cases where the probable source of the bias has been identified and measured, and only for the specific laser and C-band observations affected, as indicated in table 5.30.

All the TRANET and MINITRACK observations were affected by the biases discussed; hence, all these data should be corrected as indicated.

The sources of the GRARR and SECOR range biases on GEOS 2 were not identified, so it is not known whether these values apply only to the specific GRARR's and SECOR's tested in collocation or to all GRARR's and SECOR's at all times.

The camera angle accuracies of 1″ to 2″ are far more accurate than the laser or C-band angle accuracies of 30″ to 70″. However, at a satellite distance of, say, 1.5 million meters, an angle accuracy of 1″ is equivalent to only 7.3 meters in satellite position component normal to the line of sight.

The laser range accuracies of 1 to 2 meters during GEOS 1 and 2 were already better than the range accuracies of the C-band, GRARR, and SECOR electronic systems or the total rms errors of 3 to 18 meters, as summarized in table 5.30. Improvements now being made in the lasers indicate an increase in accuracy of an order of magnitude should soon be achieved.

Results obtained with Doppler observations appear competitive with those obtained so far with laser observations. Improvements in the GRARR, unified-S-band, Doppler systems and the TRANET GEOCEIVER Doppler systems would enable a readout of the Doppler cycle count without destroying the continuity of the count over longer intervals. This should increase the accuracy of results obtained with the Doppler observations.

5.6 RESULTS

As explained previously, the primary objective of determining and predicting the positions of satellites led inevitably to a second objective of determining better values for the geodetic quantities that affected the accuracy of the orbital determinations. The secondary objective has been attained by the determination of GEM 5, GEM 6, and Goddard '73. These three sets of results provide coordinates of tracking stations and values for the gravitational potential and geoid, and the accuracies of these quantities strongly affect the accuracies of predicted orbits.

GEM 5 and GEM 6 (sec. 5.5.1) were derived by using a vast amount of data (sec. 5.3.1) and by combining both static and dynamic satellite geodesy. (The adjustment for GEM 6 also used data on gravity anomalies.) Goddard '73 was derived from data recorded by the MOTS, Baker-Nunn, and some European cameras and from the laser systems of NASA, SAO, and Groupe de Recherches de Geodesie Spatiale (GRGS).

A more fundamental difference between GEM and Goddard '73 than the set of data used is the difference in the theories used. Both were derived from the dynamic theory presented in section 5.4.1, but GEM was also derived from geometric theory (sec. 5.4.2), whereas Goddard '73 was not.

One of the most useful results from dynamic satellite geodesy, to the geodesist at least, is the figure of the Earth (the geoid). It is the only connection between heights measured by leveling (most of the measured heights throughout the world) and geodetic heights found by satellite geodesy. Lerch *et al.* (sec. 5.6.2.1) derive a geoid from GEM 5 and GEM 6. But these geoids do not show the small variations in the geoid. The small variations (to within ± 0.5 meter) are given by the geoid of Vincent and Marsh (sec. 5.6.2.2), which was derived from gravity anomalies to provide the fine detail (sec. 5.4.3).

Results of two other investigations of geoid and the gravitational field are given in sections 5.6.4.3 and 5.6.4.4. In the former, the contribution to the geoid given by C_2^0 terms alone is derived on the basis of the theory of hydrostatic flattening (sec. 5.4.4.3); in the latter, the effect of isostatic compensation on the potential derived from satellite geodesy is given.

Orbital perturbations resulting from lunisolar gravitation and from solar radiation

pressure (secs. 5.4.4.1 and 5.4.4.2) have been determined, and typical values are given in sections 5.6.4.1 and 5.6.4.2.

In accordance with the scheme used throughout this volume, the results are organized according to their geodetic nature. Section 5.6.1 deals with geometric results (point coordinates) and contains tracking station coordinates from GEM 5, GEM 6, and Goddard '73. Section 5.6.2 deals with the geoid—a partly geometric, partly dynamic concept—and gives the geoids derived from GEM 5 and GEM 6 and from a combination of GEM 4 with gravity data. Section 5.6.3 treats the gravitational potential, and contains the $\{\bar{C}_n^m, \bar{S}_n^m\}$ coefficients of GEM 5 and GEM 6. Section 5.6.4 contains a number of results of special applications.

5.6.1 Coordinates of Tracking Stations

Two sets of coordinates are presented. Set 1, for GEM 6, was derived by a combination of dynamics and geometry (secs. 5.4.1 and 5.4.2). The second set, for Goddard '73, was derived by using only data from optical tracking systems and using only dynamics (sec. 5.4.1).

5.6.1.1 Station Coordinates in GEM 5 and GEM 6

(J. Reece and J. Brownd, Computer Sciences Corp.)

5.6.1.1.1 PRESENTATION OF RESULTS

In conjunction with the derivation of the GEM 6 gravitational field, positions were derived for some 138 tracking stations. Positions for all stations except the BC–4 were derived with the use of dynamic satellite geodesy. The positions of the BC–4 stations were derived by using geometric theory of simultaneous observations between BC–4 cameras and constraints on relative positions from ground surveys to tie a subset of BC–4 stations to other camera and Doppler stations.

In addition, constraints were applied to the relative positions of other closely spaced pairs of stations. These relative-position constraints (sec. 5.4.2.1) reflect results of surveys on local datums for 47 pairs of stations. In our judgment, such ties for these stations would strengthen the solution. Table 5.31 lists the ties, the Δx, Δy, Δz survey differences, an estimated uncertainty in meters used for weighting, and the residual from the solution. Except for Doppler stations, uncertainties were estimated in a formal way from Simmons rule:

$$\sigma = 0.029 D^{2/3}$$

where D is the distance between the stations in kilometers. The Doppler stations are uncertain by an additional 3 meters, owing to a lack of information concerning the relationship of the surveyed point to the electrical (phase) center of the Doppler antennas. The weighting is not critical. A wide variation in weights results in nearly the same solution.

In arriving at the station positions, a set of chord distances between BC–4 stations and associated error estimates were also enforced. These chord distances, taken from Mueller (unpublished, 1973), with the error estimates assigned in this solution are presented in table 5.32. The observations used in the solution are described in section 5.3.2 and the theory used in section 5.4.2. The coordinates were derived as part of GEM 6 and are given in table 5.33.

This solution for 741 unknowns required some attention to numerical analysis to obtain a numerically correct solution of the combined normal equations. The solution was obtained by Cholesky's method and an iterative improvement method. Of the unknowns, 327 were corrections to assumed coefficients of the Earth's gravitational potential and 414 were corrections to assumed coordinates of 138 stations, not all of which are independent.

The final results are presented in table 5.33 in the form of latitude, longitude, and geodetic height with respect to an ellipsoid having a semimajor axis of 6 378 155 meters and a flattening of 1/298.255.

Before discussing the results, the consequences of the applied constraints should be

examined. First, comparisons of GEM 6 station coordinates with GEM 4 station coordinates, as well as with other solutions not involving the BC–4 stations, indicate that most positions derived dynamically are essentially unaffected by inclusion of the BC–4 network. The only exceptions are Doppler stations 2019, 2722, 2723, and 2738. Only a small number of Doppler data were available to determine the positions of these stations, and they are very weakly determined from calculations using dynamics. These four Doppler stations do not have any substantial effect on the positions of the BC–4 stations; rather, these positions are to a large extent a function of the BC–4 and base-line data used in the solution.

It should also be noted that this solution contains a number of Doppler stations whose latitudes exceed in absolute value the inclination of the orbits of the satellites observed (GEOS 1, GEOS 2, BE–B, and BE–C). At these stations, the observations are unevenly distributed about the local zenith. Consequently, the along-track error typical of well-distributed data is not canceled. As can be expected, then, the positions of these stations, especially in longitude, are coupled to the potential more than they would be if observational data on high-inclination or polar orbits had been used.

The validity of attempting to enforce in a single solution both a value of GM, which would serve to scale the dynamically derived positions, and chord distances, which could represent a scale not compatible with the GM scale, may be questioned. As a practical matter, the effect of enforcing the base lines is rather small except for a few stations tied to the base lines. A comparison of solutions with and without base lines showed that only 8 of the 47 BC–4 stations in the solution had their positions changed more than 5 meters. Of these stations, five were tied directly to base lines and the remaining three were directly adjacent to one of the five. Since the base lines are considered accurate to at least 1 ppm, this solution was retained as being better for stations 6003, 6006, 6007, 6008, 6063, 6065, and 6111.

5.6.1.1.2 COMPARISON WITH OTHER RESULTS

The JPL deep-space system (DSS) solution (Mottinger, 1969) does not yield the complete position of a station. The well-determined parameters are distances from spin axis and differences between the longitudes of the stations. In order to compare GEM 6 with the JPL solution, only the x, y coordinates were used (table 5.34). The GEM 6 coordinates for the DSS sites were obtained by using connections on the local datum between the camera stations and the DSS stations. In table 5.35, direct comparisons are given with spin axis distance (D) and longitude (λ). Tables 5.34 and 5.35 show good agreement between the two solutions after a 1.4-ppm difference in scale is removed. The scale difference is probably due to the value of GM used in the GEM 6 dynamic solution. The 3-meter rms is within the estimate of random error given for both GEM 6 and JPL DSS solutions.

Very long base-line interferometry (VLBI) has been used to determine the projection of the chord distance between the Goldstone, California, and the Rosman, North Carolina, antennas on the equatorial plane using signals from 15 quasars (Ramasastry, unpublished, 1973). Repeated VLBI measurements yielded estimates of the projection of the chord distance on the equatorial plane which are consistent to within a few centimeters. Comparison of the equatorial projection of the chord distance obtained from VLBI with that inferred from the determination of the distance between two nearby camera stations using GEM 6 gives agreement within 3 meters (table 5.36).

In tables 5.37 through 5.41, GEM 6 is compared with five other solutions. The solutions are (1) GEM 4 (Lerch *et al.*, 1972c), (2) Goddard '73 (sec. 5.6.2), (3) the SAO Standard Earth III Model (ch. 9), (4) the NWL 9D (ch. 3) (Anderle, 1973), and (5) the Ohio State University WN 4 solution (Mueller, 1973). Systematic differences between the solutions were estimated using positions common to both by solving for a translation

in space to make the origins coincide, and by using three rotations about coordinate axes to orient the coordinate systems and a scale difference. The systematic quantities are indicated in tables 5.37 through 5.41 together with the rms of the random differences after the seven systematic parameters were removed.

The comparison of GEM 6 with GEM 4, shown in table 5.37, was carried out by solving for 7 parameters using 62 common stations of GEM 6 and GEM 4. Three additional 7-parameter solutions were made with subsets of the 62 stations common to the solutions. These included 23 MOTS-SPEOPTS camera stations, 13 Doppler stations, and 19 Baker-Nunn cameras. The comparison indicates that the coordinate systems of GEM 6 and GEM 4 are referred to the same center of mass for all practical purposes and that there are negligible differences of scale and rotation. Hence, the coordinate systems of GEM 6 and GEM 4 are nearly identical. The solutions from subsets of stations indicate, however, a significant shift of the z axes of the Baker-Nunn camera network of nearly 4 meters between GEM 4 and GEM 6.

Table 5.38 presents results from 7-parameter solutions comparing GEM 6 with Goddard '73. First, a solution using 47 stations shows that a significant difference occurs in rotation about the z axis of 0.2″. The translation of origin, scale difference, and other rotation parameters are negligible.

Three solutions were made to compare GEM 6 with the positions in SAO's Standard Earth III Model. One solution was carried out with all 68 stations; the second was carried out with only 17 Baker-Nunn camera stations, and a third was carried out with only the 47 BC–4 camera stations. The results are shown in table 5.39.

The first solution using 68 stations shows significant magnitudes for the parameters used to transform from the GEM 6 coordinate system to the SAO coordinate system. The apparent displacement of the center of mass is nearly 11 meters, the scale difference is -0.5 ppm, and significant rotations are found, particularly about the z axis. The second solution using 17 Baker-Nunn cameras shows a large translation in z of 15 meters, whereas the shifts in x and y are somewhat smaller than those found with the 68-station solution. The rotation angles are negligible except for ω, a result that also agrees well with the first solution.

In conjunction with the other two solutions, the third solution using 47 BC–4 cameras may be interpreted to show that the BC–4 cameras were successfully tied into their respective center-of-mass systems, although the shift along the z axis is half that of the second solution. The rotation ϵ about the x axis is large in this solution, and apparently dominates the rotation of the second solution in obtaining the first solution. The rms of the solutions are 10, 7.7, and 10 m, respectively.

Two comparisons made with the NWL 9D coordinate system are displayed in table 5.40. One was obtained by using the Doppler stations of GEM 6 that are common with the stations of NWL 9D. The other uses surveys connecting Doppler stations with BC–4 stations to place the BC–4 stations in the NWL 9D system. The BC–4 station positions for GEM 6 are used in conjunction with the BC–4 positions derived from NWL 9D to obtain the solution.

The first solution uses 12 Doppler stations and shows a displacement of 10 meters, the z component being nearly 8 meters, a scale difference of -0.3 ppm, and a significant rotation ω about the z axis. The other two rotations are negligible.

The second solution using 20 BC–4 cameras to compute the relationship between the NWL 9D and the GEM 6 coordinate systems shows a translation of nearly 6 meters, a scale difference of -0.5 ppm, and significant rotations about the x and z axes of $\epsilon=0.3$ arc second and $\omega=0.66$ arc second, respectively.

The principal agreement between the solutions is the rotation about the z axis, a negligible rotation about the y axis, reasonably close scale differences, and compatible values of the y translation. The translations in x differ in sign and in magnitude by 9 meters, and the translations in z disagree by nearly 4 meters but have the same sign.

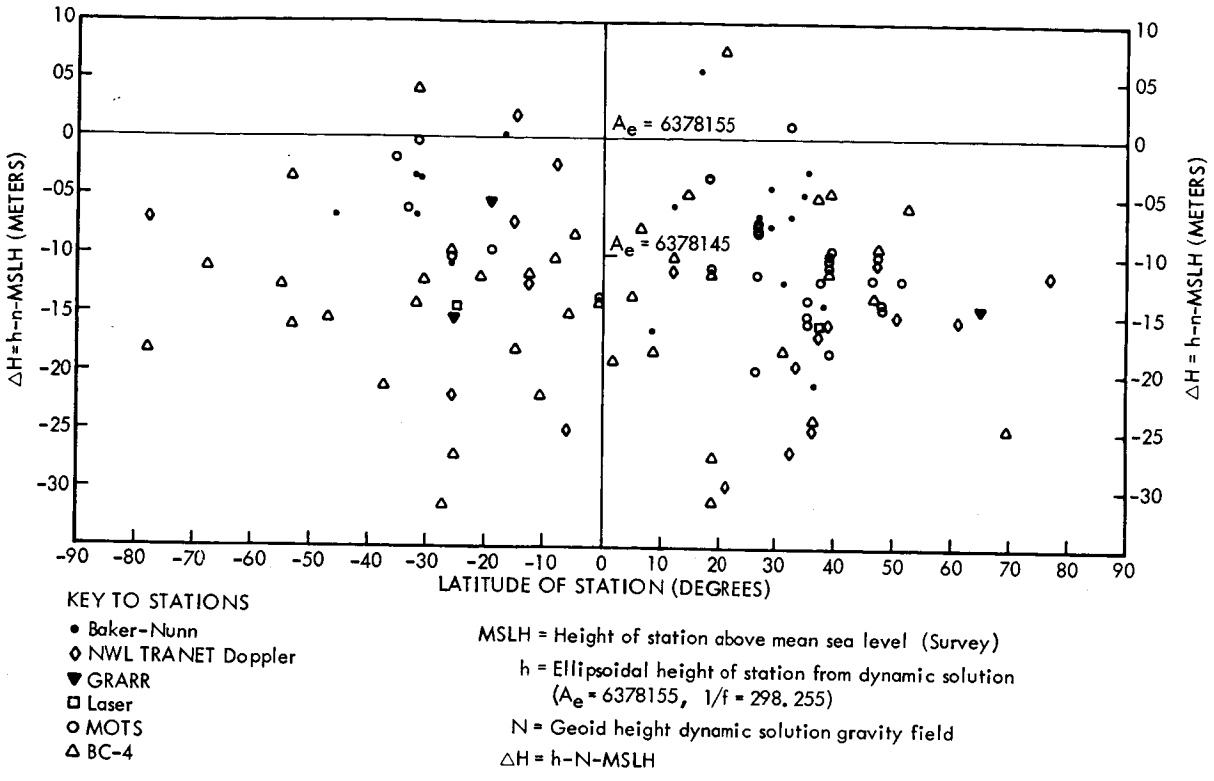

FIGURE 5.31.—Station heights above geoid computed by GEM 6 versus surveyed height.

Table 5.41 presents the 7 parameters obtained from a solution using 45 BC–4 stations in GEM 6 and the Ohio State University WN 4 solution (Mueller, 1973). (This model differs slightly from WN 14, ch. 8.) These results show a scale difference of 1.9 ppm, while the solutions have negligible differences in orientation, as indicated by the estimates of the three rotations. The translation between origins has a magnitude of 25 meters. In the World Net (WN) 4 solution, $\Delta x = 12$ meters, $\Delta y = 12$ meters, and $\Delta z = -6.0$ meters were used to transform to the geocenter. The signs of the OSU translations and the sign given in table 5.41 agree, but the Δx and Δz terms differ by 8 and 3 meters, respectively. The rms of the position differences is ± 10 meters. Examination of residuals reveals a systematic trend between GEM 6 and the WN 4 solution in a series of stations in Europe, Africa, and the South Atlantic.

Table 5.42 compares Δy differences from the seven-parameter solutions for nine BC–4 stations in these areas. In these comparisons, Δy is nearly equivalent to longitude. Other Δy differences shown in table 5.42 are from GEM 6 SAO Standard Earth III and the GEM 6 BC–4 stations tied to NWL 9D by ground ties. Systematic differences are evident, but the dispersion of results is so large that it is difficult to form any reasonable hypothesis to account for the differences.

5.6.1.1.3 COMPARISON WITH HEIGHTS ABOVE MEAN SEA LEVEL

Heights of stations above the geoid as determined from GEM 6 are compared in figure 5.31 with heights above mean sea level as determined by survey. The following difference is plotted for each of 138 tracking stations:

$$\Delta H = (h - N) - MSLH \text{ (meters)}$$

where h is the height of the station above the ellipsoid used in GEM 6, based upon a ref

erence of $a_e = 6\,378\,144$ meters and $1/f = 298.255$, N is the geoidal height derived from GEM 6, and *MSLH* is the height above mean sea level from survey.

The differences ΔH are shown in figure 5.31 by a symbol signifying the tracking system providing the data. A key for the symbols is given with the figure.

Table 5.43 shows solutions that estimate four systematic differences in the coordinate system based upon a comparison of heights. Three of the parameters constitute a translation of the origin, and the fourth is a change to the semimajor axis a_e. Five solutions are presented in table 5.43. Results are given first for 114 stations representing a combination of the various tracking systems used in GEM 6, with results next given from subsets of stations by data type, as follows: 29 MOTS-SPEOPTS camera stations, 40 BC–4 camera stations, 19 Baker-Nunn camera stations, and 18 Doppler stations. The geoidal heights used in the solution were computed from GEM 6, the geodetic heights were from GEM 6, and the MSLH were from various geodetic surveys.

The first solution (114 stations) shows a displacement of the origin of nearly 2.3 meters and a best-fitting equatorial radius a_e of 6 378 144 meters. The next four solutions use subsets of stations to estimate the systematic differences. The derived semimajor axis ranges from 6 378 141 to 6 378 149.3 meters, or a total excursion of nearly 8 meters. The solutions using MOTS–SPEOPTS cameras and the Baker-Nunn cameras give the largest semimajor axes, and the BC–4 network results in the smallest semimajor axis, the Doppler station solution occupying a central posion.

It may be recalled from table 5.41 that the WN 4 solution for GEM 6 gave a scale difference of 1.9 ppm, which results in a derived semimajor axis of 6 378 129 meters. This agrees with an independent geometric adjustment we have made using the BC–4 camera data. Apparently, the ties made between the BC–4 cameras and other tracking stations dominated the terrestrial base lines in the solutions for the station heights away from the base lines. The range of 8 meters in determinations of a_e apparently reflects possible systematic differences between the data from the tracking systems for which the comparisons were made.

Displacement differences for the Baker-Nunn and Doppler solutions agree in sign and to better than 2 meters in magnitude of each component of the shift. The MOTS camera displacements agree in sign with the Baker-Nunn and Doppler solutions, but the magnitude of the x components disagrees by 6 to 8 meters. The z component agrees with the Doppler solution, but differs from the Baker-Nunn solutions by 2 meters.

These differences reflect errors in the computed geoid from GEM 6 and in the selection process due to spacing of the stations as well as the error in station height. Thus, there tend to be uncertainties in the origin greater than the formal uncertainties and discrepancies in certain areas between derived station heights and the derived geoid.

5.6.1.1.4 COMPARISON WITH POSITIONS ON NATIONAL OR INTERNATIONAL DATUMS

Station coordinates in the GEM 6 system are compared with coordinates in national or international datums by first computing the datum shifts involved and then using these to transform the coordinates. We refer to coordinates in the national or international datums as surveyed coordinates.

Let λ_s, ψ_s, h_s be the geodetic coordinates of a particular station as determined by survey on the ground. These are converted to rectangular coordinates x_s, y_s, z_s by using the specifications of the datum. Here, x_s, y_s, z_s will be referred to as "surveyed" coordinates. The surveyed coordinates are transformed to the system of GEM 6 by the equation

$$\begin{pmatrix} x_s' \\ y_s' \\ z_s' \end{pmatrix} = \begin{pmatrix} \Delta x + x_o \\ \Delta y + y_o \\ \Delta z + z_o \end{pmatrix} + (1+s) \begin{pmatrix} 1 & \omega & -\psi \\ -\omega & 1 & \epsilon \\ \psi & -\epsilon & 1 \end{pmatrix} \begin{pmatrix} x_s - x_o \\ y_s - y_o \\ z_s - z_o \end{pmatrix} \tag{5.152}$$

where

$\begin{pmatrix} x_s' \\ y_s' \\ z_s' \end{pmatrix}$ are surveyed coordinates transformed to the GEM 6 system

$\begin{pmatrix} x_s \\ y_s \\ z_s \end{pmatrix}$ are surveyed coordinates in the original datum

$\begin{pmatrix} x_o \\ y_o \\ z_o \end{pmatrix}$ are surveyed coordinates of the adopted datum origin

s is the scale difference

ω is the rotation about the z axis

ψ is the rotation about the y axis

ϵ is the rotation about the x axis

Table 5.44 shows the adopted origins λ_0, ϕ_0, h_o, which lead to x_o, y_o, z_o for the calculations outlined above. With the exception of the North American Datum 1927 (NAD 1927), the adopted origins for our calculations do not agree with the origins of the four datums whose solutions are derived.

By including the coordinates of the origin of the datums, the translation parameters (Δx, Δy, Δz) are then exactly equal to the shift of the local datum at the datum origin. Also, the correlations between translation and rotation parameters are minimized.

Table 5.45 presents solutions for seven parameters of four major datums using the coordinates of cameras and the rms of the differences in the station coordinates. In each solution, individual stations are weighted equally. The average rms error for each datum is 4.5 meters. Coordinate differences for each solution are shown in table 5.46.

A special comment is warranted on the solution for the European datum 1950, known as ED50. The solution uses only five stations for its determination. A number of other stations connected to ED50 were rejected because they did not fit with any reasonable hypothesis concerning the accuracy of the triangulation on ED50.

5.6.1.1.5 SUMMARY AND CONCLUSIONS

Coordinates of the 138 tracking stations in GEM 6 provide datum shifts for establishing a unified world geodetic system for 11 different datums. Results with respect to an ellipsoid having a semimajor axis of 6 378 155 and a flattening of 1/298.255 are presented in table 5.33. Table 5.47 shows the translations for transforming 11 datums to the GEM 6 system, and table 5.45 gives the translation, scale difference, and three rotations for transforming four major datums to the GEM 6 system.

Radial positions and heights above mean sea level from a survey of the stations indicate a mean radius a_e for the Earth of 6 378 143.7 meters. Results have been presented in table 5.43 and figure 5.31, where variations ranging from 6 378 141.0 to 6 378 149.3 meters can been seen for subsets of the tracking systems. Also, an independent geometric solution using the BC–4 data gives an a_e of 6 378 129.0 meters based upon DME base lines.

Systematic differences of coordinates in dynamic solutions such as GEM 6, Goddard '73, NWL 9D, and classical geodetic triangulation may be removed by estimating seven parameters. Three parameters are translations, three are rotations, and one is a scale change. After the systematic differences are removed, coordinates of major tracking systems in GEM 6, such as the MOTS-SPEOPTS cameras, Baker-Nunn cameras, and laser DME stations, agree with the Goddard '73 solution and with classical geodetic triangulations so well that the coordinates of major tracking stations in GEM 6 are believed to be known with an rms accuracy of 5 meters or better in each coordinate. In the GEM 6 system, coordinates of Doppler stations are known to an rms of 8 meters or better and BC–4 coordinates of cameras are known to an rms of 10 meters or better.

A significant difference of nearly 12 meters exists between the coordinate origins (center of mass) derived from station positions of the GEM 6 (or Goddard '73) and Standard Earth III Model, and an 11-meter systematic difference exists between GEM 6 and NWL 9D. There are systematic differences in the rotation parameters, especially about the z axis, which are estimated from station co-

ordinates derived by geometric or dynamic theory. Pending a resolution of the differences in the rotation parameters estimated from the various solutions, the rotation parameters associated with the datum transformations need not be interpreted as datum tilts or absolute deflections in the classical geodetic sense.

Figure 5.32 shows displacements of the Greenwich meridian (the angle ω converted to meters) and the mean pole (the angles ϵ and ψ converted to meters at the pole) with respect to the zero meridian and pole of GEM 6.

Coordinates of BC–4 cameras derived by different investigators through geometric theory give relatively large dispersions in the magnitudes of the seven parameters used to estimate systematic differences in the solutions in comparison with corresponding results from dynamic solutions. In addition, relatively large rms differences exist after systematic differences are removed. The BC–4 camera network has fewer observations per station on the average, than the stations in dynamic solutions.

Stations derived through dynamic processing of observations are connected through orbital constraints with many other stations, compared with the relatively few BC–4 stations connected by observations.

In the comparison of independent solutions by different investigators, the GEM 6 solution is especially useful. It contains observational data of many different classes. Hence, solutions of other investigators can be compared with GEM 6 and can be indirectly compared with each other, even when direct comparisons are not possible.

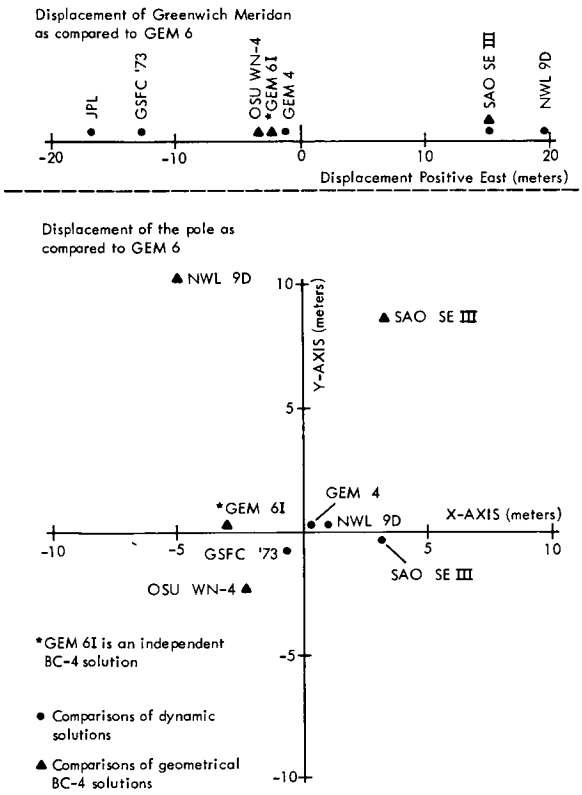

FIGURE 5.32.—Relations of coordinate system of GEM 6 and various other models.

5.6.1.2 Station Coordinates in Goddard '73 (J. Marsh)

5.6.1.2.1 PRESENTATION OF RESULTS

Table 5.48 presents the values determined for our stations, which are referred to in this text as Goddard '73 or GSFC '73. The coordinates are in a center-of-mass system oriented with the z axis parallel to the axis through the CIO pole and the x axis in the zero meridian defined by BIH's longitudes. The solutions were derived through the use of the equations described in section 5.4.1.

A total of 150 two-day arcs were used in the final solution. Experience with observations of the GEOS flash and laser DME data has indicated that two-day arcs are short enough to accommodate errors in the model and yet long enough to provide adequate strength. The dominant source of error was uncertainty in the values of the 12th- and 13th-order resonance coefficients of the gravitational model. Resonance produces an orbital perturbation of about 600 meters, primarily along track, on the GEOS satellites with a period of about six days. Resonance-caused errors on the order of a few tens of meters were for the most part absorbed in the orbital elements of two-day arcs. To reduce unmodeled errors in the orbit further, passes

were selected in all directions on all sides of the stations. When the solution is designed properly, this geometry leads to favorable cancellation of errors.

In order to utilize accurately surveyed ties between adjacent stations, the coordinates of certain stations were constrained to adjust together. A list of the stations with constrained coordinates is presented in table 5.49. It is noted that no other constraints were employed in the solution, since it was believed that the laser system data could be used to reveal systematic differences (due to the incompatibility of parameters such as scale) which might otherwise be obscured. Also, the camera data provide a direct measure of latitude and longitude with proper modeling of UT1 and polar motion.

The goal was to produce a global solution accurate to 5 meters. Our previous work employed the gravitational coefficients of SAO 1969 Standard Earth II (Gaposchkin and Lambeck, 1970), which was found to be the best available at that time. Lerch *et al.* (1972 b, c) at GSFC have produced the GEM series of gravitational models, which are considered in section 5.6.1. Our solution was computed first, with GEM 1 modified with the resonance coefficients in SAO's Standard Earth II and repeated using all the coefficients in SAO's Standard Earth II. Generally, the results using GEM 1 gave a more consistent set of coordinates, a smaller rms of fit to the data, and the best overall results. We have adopted the solution with GEM 1 and the 12th-, 13th-, and 14th-order terms resonance coefficients) of SAO's Standard Earth II for the Goddard '73. The results obtained with these two models are compared in section 5.6.5.

A total of 65,000 camera observations and some 350 passes from laser systems were used in our final simultaneous solution. The data from NASA and CNES (Centre National d'Etudes Spatiales) laser systems were sampled, leaving from 10 to 20 points per pass where possible. For those systems with slower data rates, all data available were used. The formal rms of fit to this set of data after adjustment is presented in table 5.50.

5.6.1.2.2 THE RELATIONS OF MAJOR GEODETIC DATUMS TO A GEOCENTRIC REFERENCE SYSTEM

The relations of North American Datum 1927, European Datum 1950, South American Datum 1969, and Australian Geodetic Datum to the geocentric reference of Goddard '73 have been established through the derivation of values for seven parameters (three translation, three rotation, and one scale) for each datum. For the Arc Datum, the two available stations have been used to derive the translation parameters.

Surveyed coordinates were obtained primarily from the "NASA Director of Observatiton Station Locations" (1971).

North American Datum (1927).—Fourteen stations (12 on the continent and 1 each on the islands of Jamaica and Puerto Rico) have been used to establish the orientation of North American Datum 1927 with respect to a geocentric reference system established by Goddard '73. Figure 5.33 presents values for the seven orientation parameters, their correlation coefficients, associative residuals in X, Y, and Z, and chord-length differences. The scale difference indicates that North American Datum 1927 is smaller than the geocentric solution by 0.9 ± 0.2 ppm. This value is in good agreement with the 0.8 ppm derived from the comparison of Goddard '73 with JPL's spin-axis distances. The residuals in X, Y, and Z have rms values of 3.4, 2.6, and 3.8 meters, respectively.

European Datum (1950).—Nine stations have been used in relating European Datum 1950 to this global reference system. Figure 5.34 presents information for the European datum similar to that presented in Figure 5.33 for North American Datum 1927. The comparison of our solution with that of CNES indicated a mean scale difference of 0.3 ppm for chords to San Fernando, Spain. The overall scale difference derived in the seven-parameter solution was 5.0 ± 0.4 ppm. This large difference is primarily attributed

TRANSFORMATION PARAMETERS FOR THE NORTH AMERICAN 1927 DATUM AND THE GEOCENTRIC REFERENCE SYSTEM

ΔX	ΔY	ΔZ	Δℓ	OMEGA	PSI	EPSILON
−42.7 ± 1	161.6 ± 1	179.8 ± 2	.9 ppm	−1".1	−".2	−".05
			± .2	± .04	± .04	± .07

CHORD LENGTH AGREEMENT

	1022	9021	9001	7076	7075	7072	7050	7045	7040	7037	7036	7034	1042	1030
9021	7.4													
9001	2.7	4.3												
7076	0.5	1.8	−2.7											
7075	7.4	8.9	8.9	10.8										
7072	−3.6	9.1	4.9	−5.6	16.1									
7050	5.6	0.8	0.7	5.3	−2.4	15.2								
7045	4.3	8.2	10.8	2.3	0.9	8.6	−5.0							
7040	−7.5	−1.6	−5.4	−2.6	5.2	−10.1	7.6	−2.6						
7037	−0.9	4.7	2.6	−1.1	7.5	5.7	−3.8	0.7	−5.3					
7036	6.8	1.3	−5.0	1.7	9.1	6.1	4.5	3.6	−2.1	−0.5				
7034	0.9	7.0	8.0	1.5	−3.1	8.0	−9.3	−1.1	−3.3	2.9	2.6			
1042	−4.0	6.6	3.5	−1.5	11.2	4.5	3.6	3.3	−6.9	1.8	2.8	3.1		
1030	8.7	2.0	7.7	4.0	7.9	11.3	2.0	7.4	0.6	6.2	3.3	7.7	8.1	
1021	−7.8	−1.2	−3.6	−1.2	9.2	1.8	13.0	−5.2	−3.5	−5.2	−4.1	−3.2	−6.2	8.4

CORRELATION COEFFICIENTS

	ΔX	ΔY	ΔZ	Δℓ	OMEGA	PSI
ΔY	.209					
ΔZ	.248	.453				
Δℓ	.007	.579	−.337			
OMEGA	.849	.184	.224	$-.37\times10^{-15}$		
PSI	.624	.131	.160	$-.24\times10^{-15}$	.170	
EPSILON	−.266	−.795	−.929	$.17\times10^{-14}$	−.241	−.166

RESIDUALS BY STATION FOR NORTH AMERICAN 1927 DATUM ORIENTATION SOLUTION

STATION NAME	NUMBER	RESIDUALS IN METERS X	Y	Z
HOPKIN	9021	1.4	−2.2	3.0
1ORGAN	9001	−1.3	4.2	3.7
1SUBBR	7075	−0.6	−4.2	−6.1
1JUM40	7072	−3.6	3.9	5.1
GODLAS	7050	4.2	−4.7	−7.1
1DENVR	7045	−3.0	−1.6	−3.6
1PURIO	7040	6.8	0.5	−0.6
1COLBA	7037	−1.6	1.9	2.0
1EDINB	7036	1.1	1.2	−1.5
1UNDAK/1GFORK	7034	−3.9	1.7	−1.6
1ROSMA	1042	−2.6	1.8	2.7
1MOJAV	1030	2.2	−1.6	0.7
1BPOIN	1021	5.0	1.9	5.3
1FTMYR	1022	−4.2	−1.0	−2.1
RMS OF FIT		3.4 m	2.6 m	3.8 m

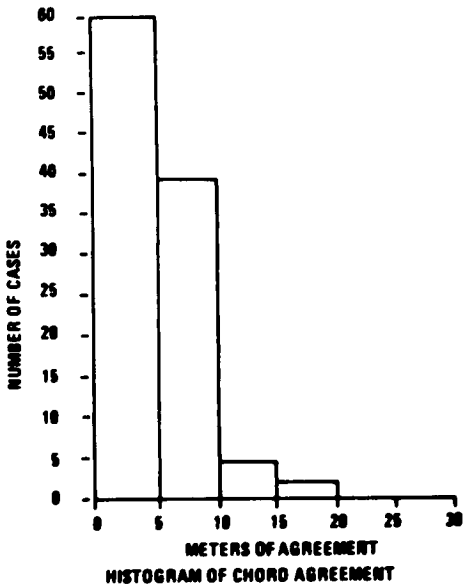

FIGURE 5.33.—The orientation and chord length agreement between the North American 1927 datum and Goddard 1973 solution.

TRANSFORMATION PARAMETERS FOR THE EUROPEAN 1950 DATUM AND THE GEOCENTRIC REFERENCE SYSTEM

ΔX	ΔY	ΔZ	Δℓ	OMEGA	PSI	EPSILON
−149.0 ± 3	−103.0 ± 3	−92.5 ± 3	5.0 ppm ± .4	0".60 ± .08	−1".9 ± .12	0".65 ± .08

CORRELATION COEFFICIENTS

	ΔX	ΔY	ΔZ	Δℓ	OMEGA	PSI
ΔY	.023					
ΔZ	−.481	−0.60				
Δℓ	−.488	−.073	−.512			
OMEGA	−.111	.758	.024	$-.60 \times 10^{-16}$		
PSI	.863	.049	−.849	$-.13 \times 10^{-14}$	−.045	
EPSILON	−.089	−.769	.173	$.60 \times 10^{-15}$	−.190	−.120

RESIDUALS BY STATION FOR EUROPEAN 1950 DATUM ORIENTATION SOLUTION

STATION NAME	NUMBER	RESIDUALS IN METERS X	Y	Z
UZHGOR	9432	0.8	−5.1	1.3
GREECE	9091	1.2	5.5	0.3
1SPAIN	9004	−0.0	4.2	4.3
MUDONI	8030	−5.5	−1.6	−5.5
NICEFR	8019	−3.3	0.5	−4.3
ZIMWLD	8010	1.8	−4.0	−5.1
DELFTH	8009	0.8	3.6	3.8
1WNKFL	1035	−1.2	8.4	7.4
HAUTEP	8015	5.5	−3.5	−2.1
RMS OF FIT		3.8 m	3.6 m	4.3 m

CHORD LENGTH AGREEMENT

	1035	9432	9091	9004	8030	8019	8015	8010
9432	13.3							
9091	1.7	1.1						
9004	2.6	17.2	3.9					
8030	−1.8	12.2	3.1	8.9				
8019	−1.5	10.9	2.4	7.9	8.7			
8015	−4.2	4.8	−2.1	13.5	−1.5	−3.7		
8010	−0.1	5.8	0.8	15.5	2.1	5.5	1.8	
8009	−0.8	15.2	6.7	5.8	−1.1	2.8	−2.5	8.1

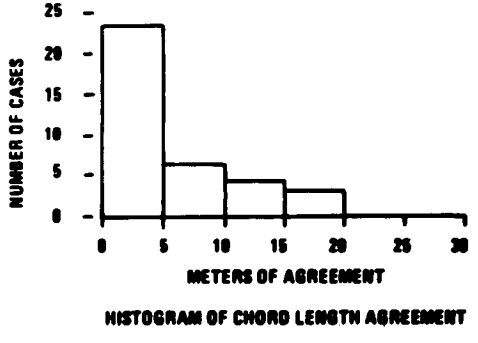

HISTOGRAM OF CHORD LENGTH AGREEMENT

FIGURE 5.34.—The orientation and chord length agreement between the corrected European 1950 datum and Goddard 1973 solution.

to a systematic scale error in European Datum 1950 resulting from the unavailability of the geoidal heights throughout the system at the time of its reduction in 1950. The values used for the chords derived have been modified to account for this error. After correction, 23 of a total of 36 chords show differences of 5 meters or less.

The residuals in X, Y, Z have rms values of 3.0, 3.6, and 4.3 meters, respectively.

South American Datum (1969).—Five stations tied to the South American Datum 1969 were used in this study. A scale difference of -1.8 ± 0.2 ppm was derived. Curaçao was omitted from the analysis, since chords from this station to Natal, Brazil, and Arequipa, Peru, differed from survey values by -16.1 and 21.7 meters, respectively. However, the differences between our values and those of GEM 4 and SAO's Standard Earth II were on the order of a few meters. The differences in X, Y, Z for this datum are somewhat larger than for the North American and European datums, their rms values being 4.6, 4.0, and 8.2 meters, respectively. Figure 5.35 presents these results.

Australian Geodetic Datum (1965) and Arc Datum.—Only three separate locations were available for comparison in Australia. Figure 5.36 presents the results for Australian Geodetic Datum 1965. The translation and orientation parameters showed high correlations, which might be expected because of the small number of stations. The correlation coefficients for scale were in general less than 0.3; therefore, it is concluded that the scale difference of 1.9 ± 0.4 ppm is a well-determined value.

Translation parameters (in meters) are presented below for the two stations on Arc Datum which were independently adjusted in our solution.

	ΔX	ΔY	ΔZ
Johannesburg, Republic of South Africa	−124.2	−108.8	−296.2
Olifantsfontein, Republic of South Africa	−125.2	−107.8	−300.8

Comparison of the satellite-derived chord connecting these two stations with the surveyed value indicated a difference of 1.9 meters.

5.6.1.2.3 ANALYSIS OF RESULTS

Comparison of Coordinates in Goddard '73 With Coordinates Determined by JPL and McDonald Observatory.—In any analysis, evaluation of the results is one of the most difficult and important tasks. In satellite geodesy, it is useful to compare the results of several investigators, but in many cases the solutions are not truly independent. Fortunately, the results of JPL for spin-axis distance and longitudinal differences are both highly accurate and are obtained without using near-Earth satellites.

As noted by Mottinger (1969), JPL's data from interplanetary spacecraft do not yield a complete position for a station. The well-determined parameters are the distance of a station from the Earth's spin axis and the differences between longitudes of the stations. The Earth-fixed Z component of the station position is poorly determined. Thus, complete positions of DSS stations rely on independent determinations (see ch. 4).

In no case is a camera or laser tracking station precisely contiguous to a DSS station. In all cases except in Spain, the stations are very close, so close that significant survey error can generally be regarded as unlikely.

The procedure used to infer coordinates of a camera-type tracking station from the DSS solutions follows. The local- to center-of-mass shift for the DSS radar was calculated and then applied to the local coordinates of the nearby camera-type tracking stations. In cases where two cameras were nearby and their coordinates independently determined, coordinates of both are presented. The resulting camera coordinates were then used to calculate spin-axis distances and longitudinal differences. A comparison of the spin-axis distances is given in table 5.51 for the Goddard '73 and JPL LS25.

In previous solutions that used SAO's Standard Earth II (1969) gravitational

TRANSFORMATION PARAMETERS FOR THE PROVISIONAL SOUTH AMERICAN DATUM AND THE GSFC '73 GEOCENTRIC REFERENCE SYSTEM

ΔX	ΔY	ΔZ	Δℓ	OMEGA	PSI	EPSILON
−44.1 ± 2	8.9 ± 2	−46.4 ± 2	−1.8 ppm ± .2	0".74 ± .08	−0".25 ± .05	0".28 ± .08

CORRELATION COEFFICIENTS

	ΔX	ΔY	ΔZ	Δℓ	OMEGA	PSI
ΔY	.484					
ΔZ	−.424	−.564				
Δℓ	−.295	.481	.276			
OMEGA	.058	.762	−.571	$.97 \times 10^{-15}$		
PSI	−.158	.241	−.532	$.24 \times 10^{-15}$	.211	
EPSILON	.481	.774	−.897	$.93 \times 10^{-15}$	.629	.298

RESIDUALS BY STATION FOR PROVISIONAL SOUTH AMERICAN DATUM ORIENTATION SOLUTION

STATION NAME	NUMBER	RESIDUALS IN METERS X	Y	Z
COMRIV	9031	−4.4	1.3	3.0
NATALB	9029	−1.8	−2.7	−1.5
1VILDO	9011	−1.6	5.9	3.2
1QUIPA	9007	−0.8	1.3	9.9
1SATAG	1028	8.6	−5.7	−14.7
RMS OF FIT		4.6 m	4.0 m	8.2 m

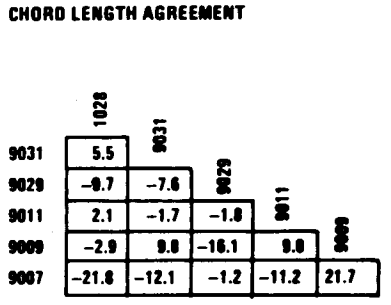

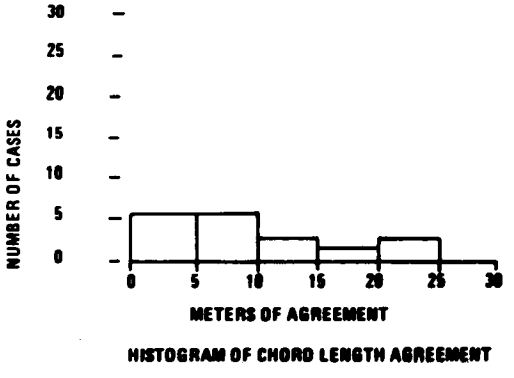

FIGURE 5.35.—The orientation and chord length agreement between the provisional South American 1969 datum and Goddard 1973 solution.

TRANSFORMATION PARAMETERS FOR THE AUSTRALIAN GEODETIC DATUM AND THE GSFC '73 GEOCENTRIC REFERENCE SYSTEM

ΔX	ΔY	ΔZ	Δℓ	OMEGA	PSI	EPSILON
−137.2 ± 15	−49.5 ± 5	155.0 ± 21	1.9 ppm ± .4	0".34 ± .26	0".18 ± .64	0".38 ± .54

CHORD LENGTH AGREEMENT

	1038	7054
7054	5.2	
9023	−3.5	9.7

CORRELATION COEFFICIENTS

	ΔX	ΔY	ΔZ	Δℓ	OMEGA	PSI
ΔY	−.833					
ΔZ	−.979	.849				
Δℓ	.095	−.326	.060			
OMEGA	−.969	.711	.944	$.117 \times 10^{-13}$		
PSI	−.988	.839	.993	$.118 \times 10^{-13}$	.943	
EPSILON	−.974	.877	.992	$.120 \times 10^{-13}$	.939	.980

RESIDUALS BY STATION FOR AUSTRALIAN GEODETIC DATUM ORIENTATION SOLUTION

STATION NAME	NUMBER	RESIDUALS IN METERS X	Y	Z
CRMLAS	7054	−1.3	−0.4	−0.2
1ORROL	1038	−2.0	−1.7	−0.7
AUSBAK	9023	3.3	2.1	0.9
RMS OF FIT		2.4 m	1.6 m	0.7 m

FIGURE 5.36.—The orientation and chord length agreement between the Australian geodetic datum and Goddard 1973 solution.

model, we found little systematic difference in the spin-axis distances for the cameras and nearby JPL radars (Marsh *et al.*, 1971). This was probably due to two factors. First, SAO's coordinates of 1969 contained some constraints based on JPL's results, and we held SAO's coordinates as fixed initially in our previous work. Second, the orbital semi-major axes were able to accommodate an error in GM.

In our recent work, we included scale-providing data from laser systems. Also, no a priori constraints were employed on station coordinates. These solutions produced spin-axis distances which were systematically larger than those of JPL when a value of $GM = 3.986013 \times 10^5$ km^3/sec^2 was used. However, when GM was changed to the more recent value of 3.986008×10^5 km^3/sec^2 (Esposito and Wong, 1972), this disagreement was reduced.

The spin-axis distances obtained when the value of $GM = 3.986008 \times 10^5$ km^3/sec^2 was used indicated a scale difference of $+0.8 \times 10^{-6}$ for these distances. The GM implied by this scale difference would be about 3.986000×10^5 km^3/sec^2. Allowing for this scale difference, the rms difference between JPL and Goddard '73 results is 2.6 meters. (The reason for this scale difference is not known at this time.)

Analysis of measurements by laser systems to the lunar retro-reflectors, recorded at McDonald Observatory by the Lunar Laser Group (Williams *et al.*, 1972, unpublished), has yielded the distance of the observing site from the spin axis of the Earth with an accuracy of ± 3 meters. Table 5.52 presents a comparison of the Lunar Laser Group results and those obtained from recent solutions using camera and laser system data, including Goddard '73. When the 0.8-ppm scale factor as determined from the comparison with JPL's values is subtracted from the scale factor of Goddard '73, the agreement with the Lunar Laser Group is 30 cm.

Table 5.51 also presents the longitudinal differences between JPL's stations and Goddard '73 after removal of a longitudinal rotation of 0.27″ (8 meters at the equator). It is noted that both SAO's Standard Earth II and GSFC 1971 were rotated in longitude by about 0.75″ with respect to JPL's solution. In our present solutions using the potential of Standard Earth II, with no a priori information being supplied by SAO's station coordinates, our longitudes rotated into agreement with JPL's longitude. With the use of GEM 1, a rotation of 0.27″ in longitude again appeared. When this rotation is removed, the rms agreement in longitude is 2.6 meters. The rotation may be related to least-squares accommodation of errors in the coefficients of tesseral harmonics.

Comparison With the Station Coordinates of Standard Earth III (1973) and GEM 4.—Lerch *et al.* (1972c) of GSFC published a set of potential coefficients and station coordinates of GEM 4. Gaposchkin (1973) of SAO solved for a gravitational potential and station coordinates, using an iterative process. This section will assess the level of agreement between Goddard '73 and these models.

The accuracy of coordinates derived by means of dynamic techniques varies. In a least-squares determination of orbital position, larger errors normally occur over areas with limited or no tracking for near-Earth satellites. Therefore, the isolated stations with limited sets of data have the poorest determinations of coordinates. In order to assess more realistically the difference between Goddard '73 and the GEM 4 and Standard Earth III, seven stations with known larger uncertainties in position were omitted from the analysis.

GEM 4 used $GM = 3.986013 \times 10^5$ km^3/sec^2. To compare these values with our own, a transformation with seven parameters was computed using 34 independent common stations. Table 5.53 presents the results of this solution. The scale difference of 0.46 ppm is very close to the expected value, since the Goddard '73 solution used a value of $GM = 3.986008 \times 10^5$ km^3/sec^2. The translational parameters, ΔX, ΔY, and ΔZ are 50 cm or less in each case. A rotation of about 0.3 arc second in longitude is noted in the table.

The rms of fit for the 34 stations, as shown in Table 5.53, indicates agreement to better than 5 meters between Goddard '73 and GEM 4. This agreement is especially significant in that GEM 4 used a different technique than Goddard '73 by simultaneously solving for a gravitational model complete with zonals and the station coordinates, and a different gravitational model was employed.

A similar analysis was performed using 24 stations common to Goddard '73 and Standard Earth III (ch. 9). Here, the differences were larger. The rms of fit for the 24 stations was 8.9, 10.5, and 13.4 meters in X, Y, and Z, respectively. A comparison of Standard Earth III with respect to geoidal height indicated a 25-meter discrepancy between the heights in Europe and those of North America and Australia. This discrepancy largely accounts for the greater differences between Goddard '73 and Standard Earth III.

Evaluation of Radial Positions.—The comparisons of longitudinal differences and spin-axis distances presented in the preceding section provide an excellent means of assessing the precision of the geocentric X and Y coordinates. This precision has been shown to be a very few meters. These comparisons are insensitive to the values of the Z coordinate. Systematic errors as large as 5 meters can occur in Z due to errors in zonal harmonics (Anderle, 1973). Other errors are also present, primarily due to uncertainties in modeling tesseral and sectorial harmonics. Errors in Z will be propagated into errors in the heights above the reference ellipsoid for stations not on the equator.

Certain gravimetric geoids have been used to evaluate the radial coordinates. On a global basis, we have used the geoid (Marsh *et al.*, 1973) corresponding to the gravitational field of GEM 4. Comparisons of this geoid with detailed gravimetric geoids indicated that the accuracy is generally on the order of 5 to 10 meters.

The detailed gravimetric geoid of Vincent and Marsh (sec. 5.6.3), which is based upon a combination of surface gravity data and satellite data, has been used in the areas of North America, Europe, and Australia. The accuracy of the detailed geoid has been estimated at about 2 meters.

Figure 5.37 presents a plot of Δh versus station latitude:

$$\Delta h = (h_{el} - h_{msl}) - N$$

where h_{el} is the height of the station above the reference ellipsoid, h_{msl} is the height of the station above mean sea level obtained from survey data, and N represents the geoidal heights from GEM 4.

Thus, the differences shown in figure 5.37 represent the sum of errors in the height dynamically determined, the surveyed height above mean sea level, and the satellite geoid height. The rms difference for this comparison is 5.6 meters, after removal of the systematic difference. This systematic difference is due to the difference in semimajor axes used for the geoidal heights (6 378 142 meters) and the reference figure for the station coordinates (6 378 155 meters). This result agrees well with those of Mueller (unpublished, 1973) and Lerch (1972c), who both indicated that a reference ellipsoid of 6 378 155 meters is too large by at least 10 meters. This plot indicates no significant trend in the residuals as a function of latitude, which means that displacement of the origin of the coordinate system along the Z axis must be less than a few meters.

Figure 5.38 presents a comparison of the station heights in North America, Europe, and Australia versus the heights from the detailed gravimetric geoid. The overall rms difference for these three areas is 4.1 meters, reflecting the increased accuracy of the detailed geoid over the global satellite geoid. The ellipsoid implied by this more accurate comparison would have a semimajor axis of 6 378 142 $\pm$ 2 meters. It is also important to note that no significant scale differences are indicated for these areas. This indicates that a small value is an upper bound to the systematic error in the definition of mean sea level for these three continents.

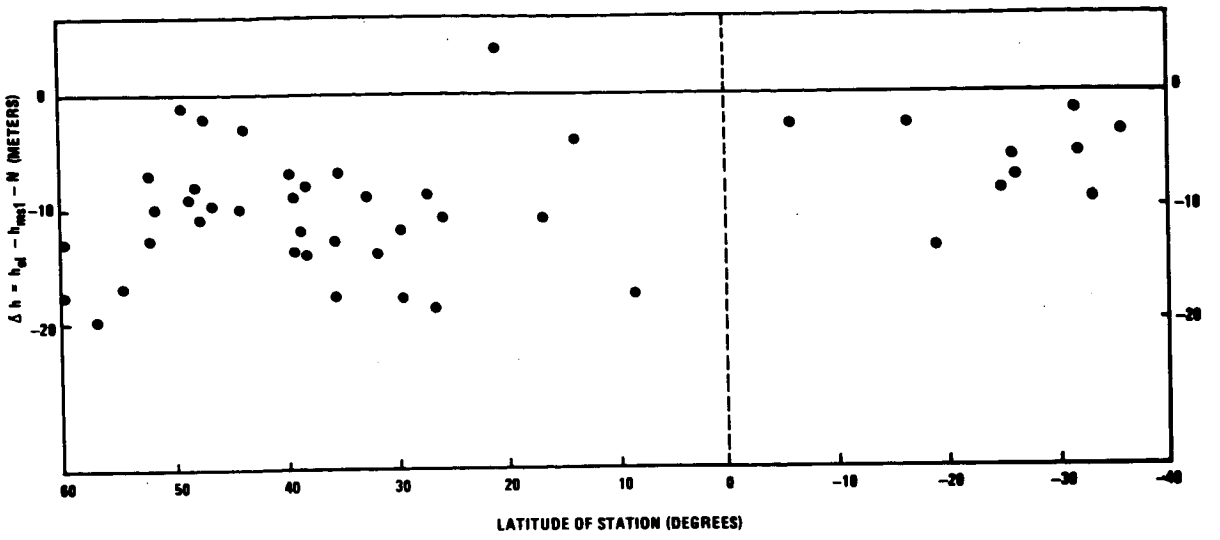

FIGURE 5.37.—Comparison of geoidal heights calculated from Goddard 1973 and GEM 4 solutions.

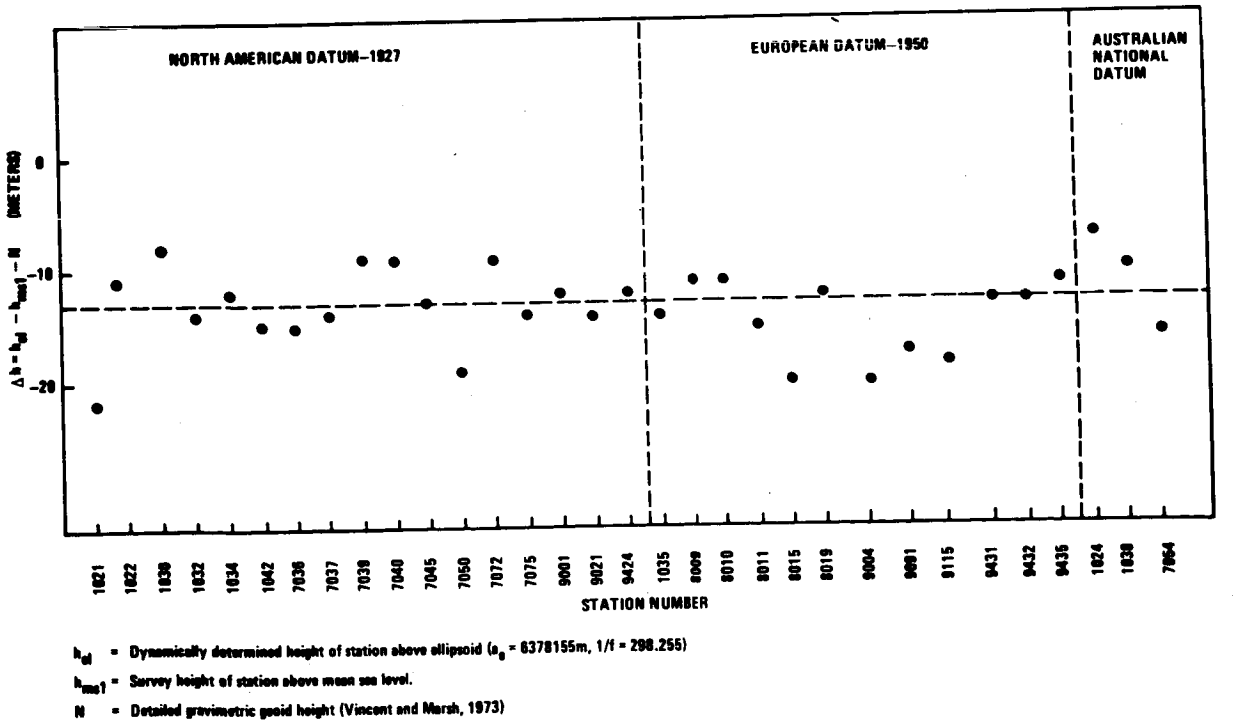

FIGURE 5.38.—Comparison of geoidal heights computed from Goddard 1973 data and detailed global geoid.

Both noise and systematic errors in the Z coordinates are assessed to be less than 4 meters rms for the Goddard '73.

Comparison of Chord Lengths on the North American and European Datums.—This section presents a comparison of chord lengths computed from the Goddard '73 coordinates with chord lengths computed from coordinates of Reece and Marsh (1973) for North America, Cazenave *et al.* (1972a) for Europe, and the VLBI solution coordinates of Ramasastry *et al.* (1973, unpublished).

Simultaneous observations of the GEOS 1 and GEOS 2 flashing lamps taken by NASA's MOTS and SPEOPT cameras were used by Reece *et al.* to find coordinates of 13 sites on the North American Datum. Scale was provided by using data of laser systems at Greenbelt and Wallops Island simultaneously with camera data. Goddard '73 also provided coordinates for these stations. Figure 5.39 presents a histogram of the agreement between the two solutions. Of the 77 common chords, 63 agree to 5 meters or better.

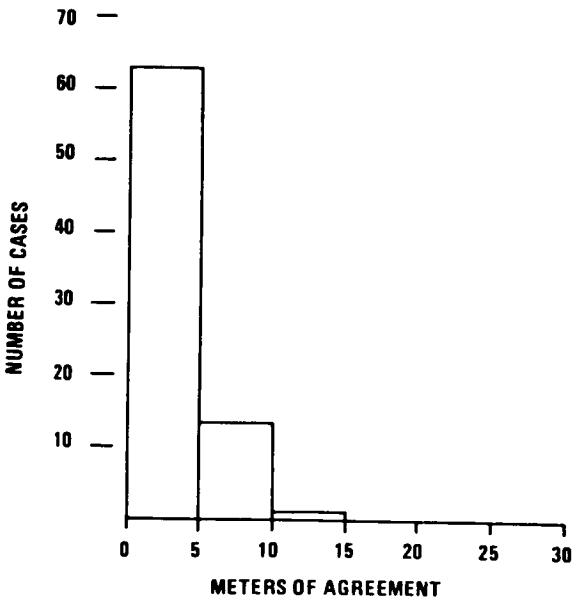

FIGURE 5.39.—Histogram of agreement in North America of chords calculated from Reece's solution and the Goddard 1973 solution.

CNES in France (Cazenave *et al.*, 1972) used purely geometric techniques with data from cameras and laser systems to find the chord lengths between San Fernando, Spain, and eight other sites in Europe.

Table 5.54 compares the chord lengths obtained from Goddard '73 with the geometric solution of CNES. The agreement between Goddard '73 and CNES is good, six of the eight chords agreeing to 4.5 meters. The disagreement of the chord to Greece may be due to the fact that this station is on the periphery of the geometric network and therefore is constrained in only limited directions in the CNES solution. However, the mean difference between CNES and Goddard '73, including Greece, is still only a few meters. When Greece is eliminated, the mean scale difference between Goddard '73 and CNES is 0.3 ppm.

Goddard '73, when compared with these independent geometrical solutions of Reece and Cazenave and the VLBI solution of Ramasastry, indicates agreement to better than 5 meters in almost all cases. This is consistent with our error analysis, which indicated that the coordinates of Goddard '73 in North America and Europe are accurate to 3 meters (1σ).

5.6.1.2.4 SUMMARY

Table 5.55 presents final estimates for the uncertainties in coordinates of Goddard '73 stations, based upon error analyses and comparisons. For most stations, a standard deviation of 5 meters ($1\ \sigma$) in each coordinate is estimated.

5.6.2 The Geoid

5.6.2.1 The Geoid From GEM 5 and GEM 6

(J. Richardson, Computer Sciences Corporation)

Contour maps of geoidal heights determined with the potentials of GEM 5 and GEM 6 are presented in figures 5.40 and 5.41, respectively. The major features of high and

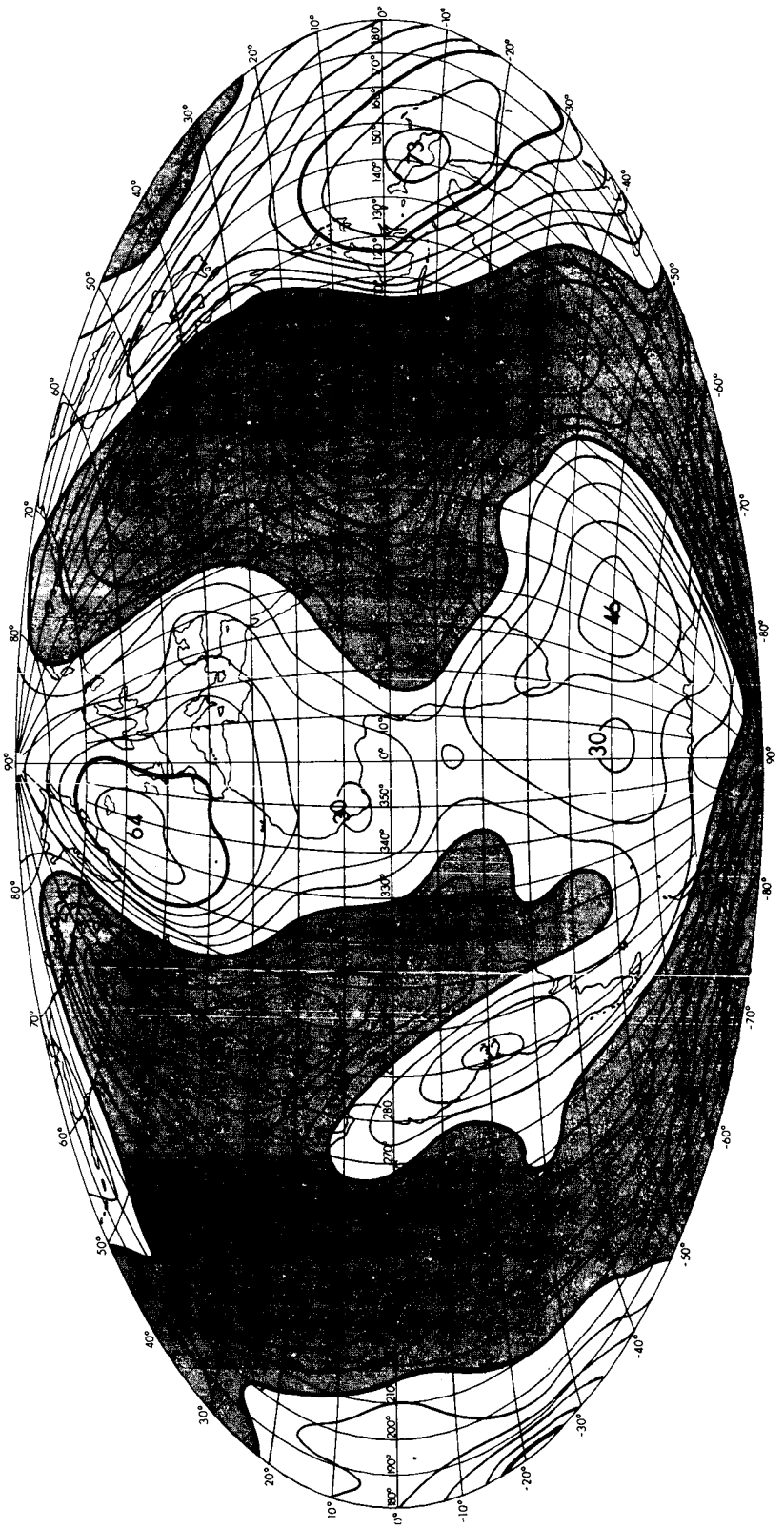

FIGURE 5.40.—Geoidal heights from GEM 5 (10-m intervals).

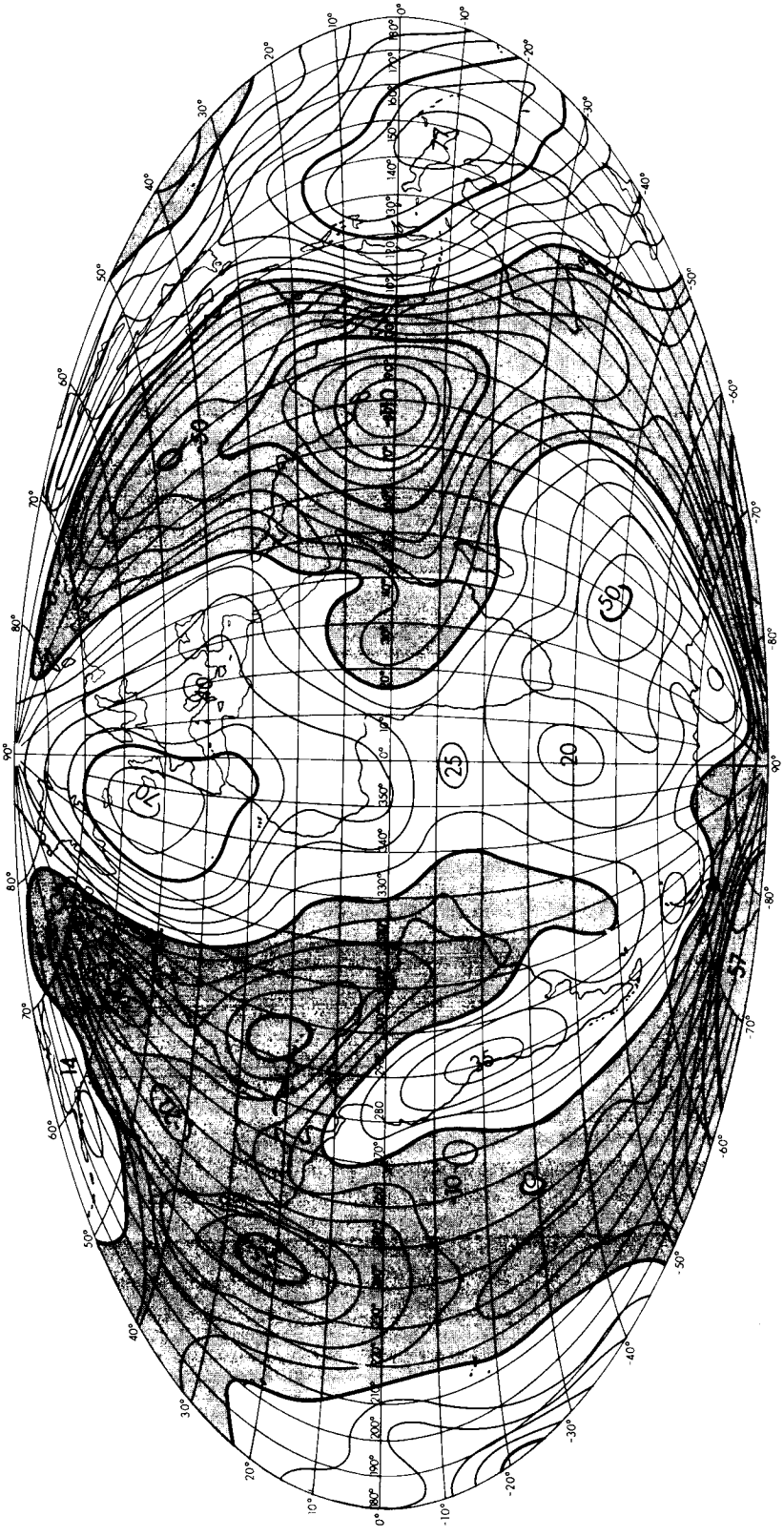

FIGURE 5.41.—Geoidal heights from GEM 6 (10-m intervals).

low points on these geoids are exhibited in table 5.56 for eight main features.

There is good agreement between the two models in the major features. The largest difference, 8 meters, occurs at the northeast Pacific low. A profile of geoidal height found with the use of zonal coefficients from GEM 6 is given in figure 5.42. An rms of differences between geoidal heights computed from the zonal harmonic coefficients of Cazenave *et al.* (1971) and from those of GEM 6 is 0.2 meter; the maximum difference is less than 1 meter. The zonal terms of the two models, which agree very well in individual coefficients, are seen to have little effect on differences in geoidal height. In general, a global rms of differences in geoidal height ΔN between two models may be estimated from the Bruns formula (Heiskanan and Moritz, 1967) ($N = T\gamma$) as follows

$$rms_{\Delta N} = \left[R_e^2 \sum_{n=0}^{N} \sum_{m=0}^{n} (\Delta \bar{C}_{nm}^2 + \Delta \bar{S}_{nm}^2) \right]^{1/2} \qquad (5.153)$$

where $\Delta\bar{C}$, $\Delta\bar{S}$ are differences in the normalized coefficients of degree n and order m between the two models, R_e is the mean radius for the Earth, and N is the highest degree in the models.

With the use of equation (5.153), comparisons of the rms differences of geoidal heights determined with GEM 6 and various other models are as follows:

GEM 2	*GEM 4*	*GEM 5*	*EXP (20×20)*
3m	3m	5m	4m

The average rms difference for these models is seen to be 4 meters, whereas the GEM 5 geoid has an average rms difference of 5

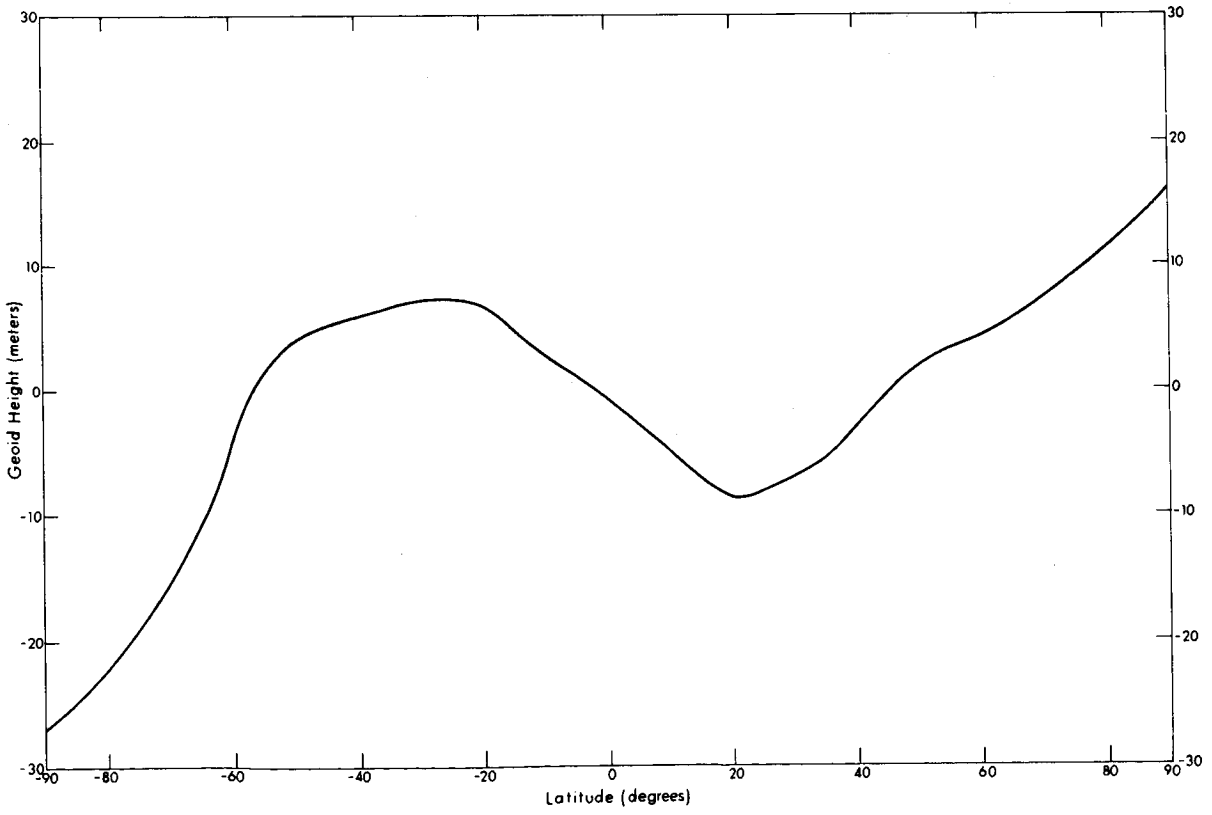

FIGURE 5.42.—Profile of geoidal heights using only zonal harmonics in GEM 6.

meters. The relative magnitude of the difference for GEM 5, which is complete to degree and order 12, is due to the omission of some higher-degree terms, from degree 13 through degree 16. (The model EXP is defined in section 5.6.3).

To estimate the error in the GEM 6 geoid, a comparison was made with a detailed geoid in North America, Eurasia, and Australia (Vincent *et al.*, 1972) where data on 1-degree by 1-degree gravity anomalies were used. The rms of geoidal height differences for these areas was about 3.5 meters. However, large variations in geoidal height exist in certain areas. For example, a difference of 12 meters exists in the vicinity of the Puerto Rican Trench.

Based upon these tests, an estimate of the rms error in geoidal height when GEM 6 is used is approximately 4 meters.

5.6.2.2 Detailed Global Geoid

(S. Vincent and J. Marsh)

From data obtained mainly from DMA/AC and the Hawaiian Institute of Geophysics, but supplemented by data collected from many other sources (see sec. 5.3.2), and with the use of the theory described in section 5.4.3, a detailed global geoid was constructed using GEM 4 as a source of values for long-wavelength harmonics. Comparisons with

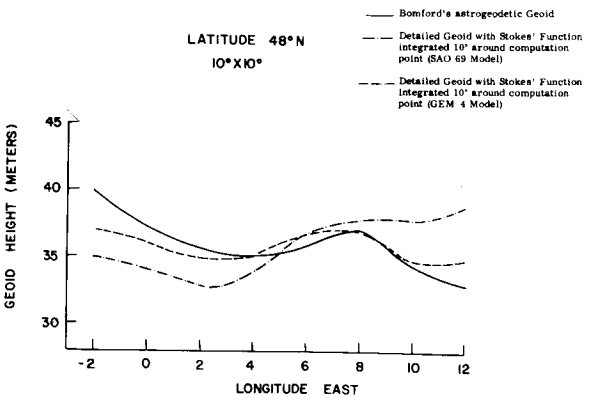

FIGURE 5.43.—Comparison between Bomford's astrogeodetic geoid and the detailed global geoids (GEM 4 and SAO Standard Earth II) integrated 10° around computation point for Europe.

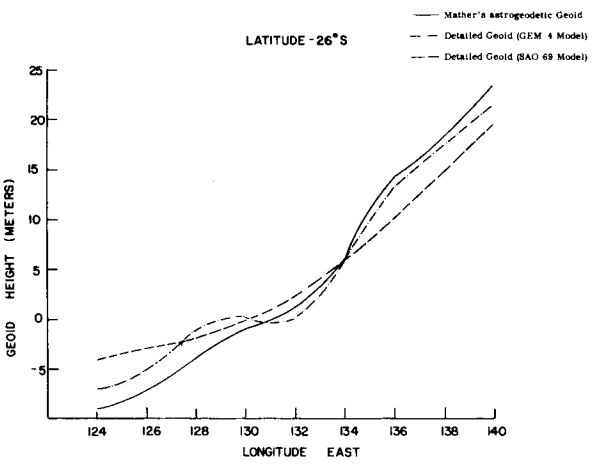

FIGURE 5.44.—Comparison between the astrogeodetic geoid for Australia by Mather *et al.* and the detailed global geoids (GEM 4 and SAO Standard Earth II) in Australia.

Bomford's geoid for Europe (Bomford, 1971b) (fig. 5.43) and with Mather's geoid for Australia (Mather, 1970) (fig. 5.44) showed that the geoid based on GEM 4 agreed much better than did the geoid of Standard Earth II.

The detailed global geoid is shown in figure 5.45 on the Miller projection with 2-meter intervals. It is compared in figure 5.46 with the GEM 4 geoid.

Analysis of Results.—To evaluate the accuracy of the detailed global geoid for the areas computed, a number of comparisons were made. The first comparison was made with the astrogeodetic geoid data of D. A. Rice (personal communication, 1973) for the United States. Rice supplied 1100 points distributed over the United States, of which 200 well-distributed points were selected for comparison. Before any comparisons could be made, Rice's data were transformed from the North American Datum 1927 to a geocentric coordinate system. The rms difference between Rice's values and values from the Goddard geoid is on the order of ± 2 meters.

As a means of evaluating the scale of the geoid, detailed geoidal heights and reference ellipsoid parameters were used together with

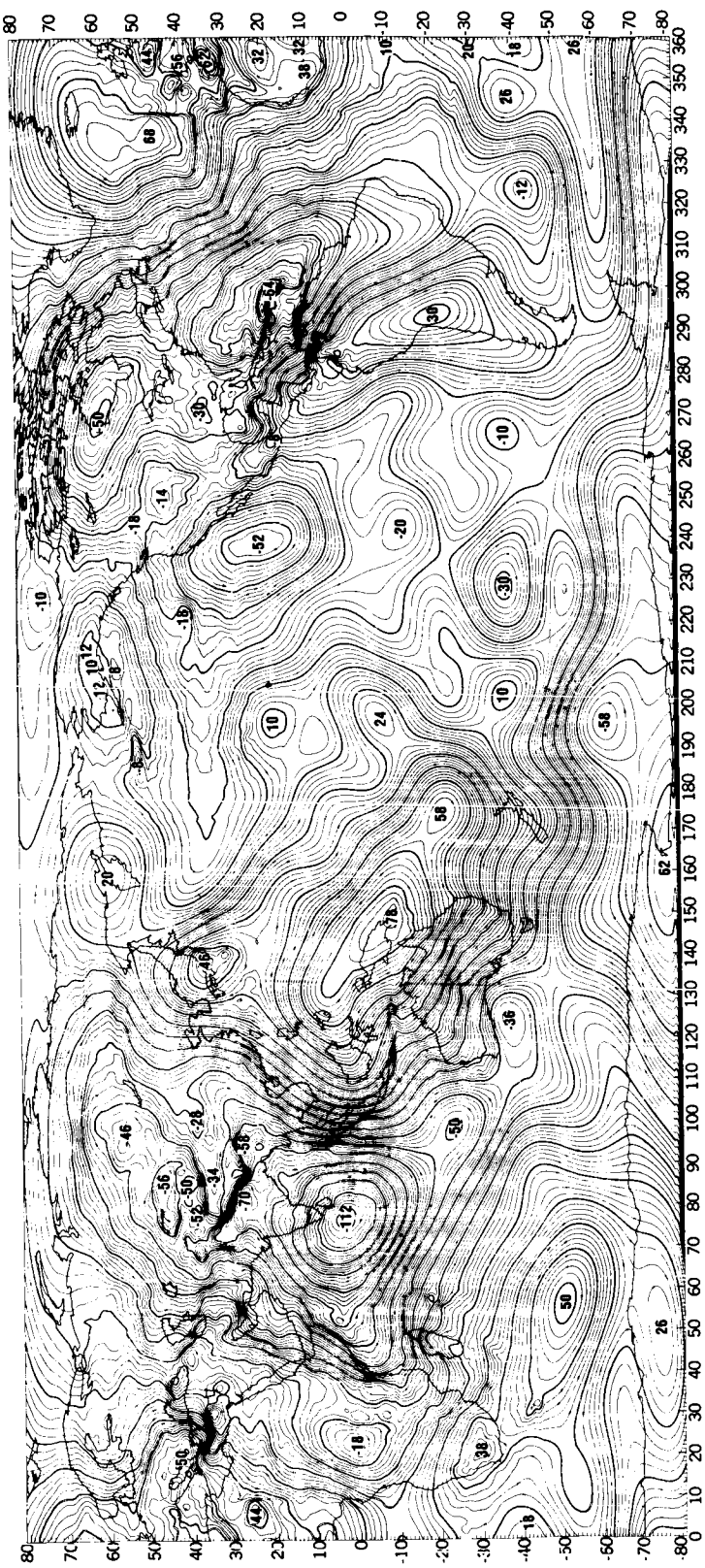

FIGURE 5.45.—Detailed global geoid.

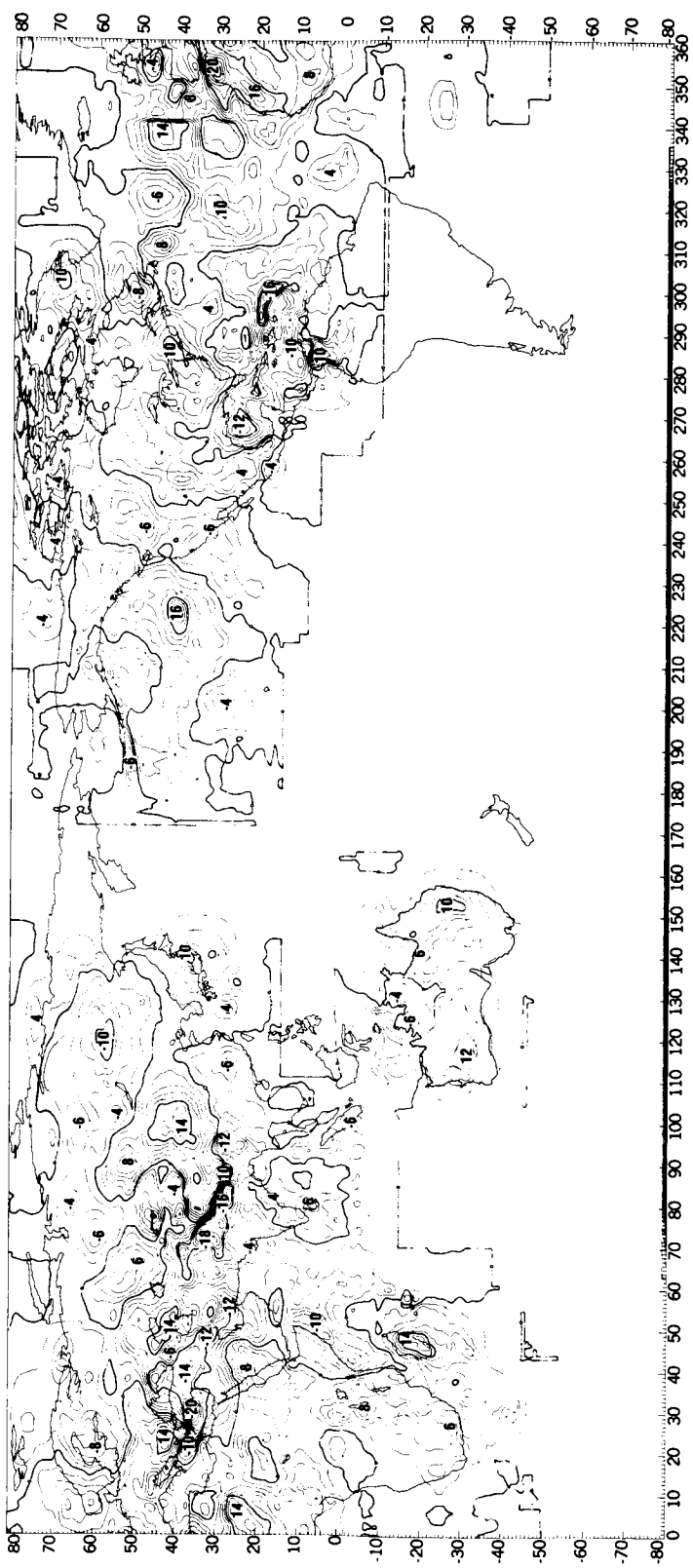

FIGURE 5.46.—Difference between detailed global geoid and the geoid from GEM 6.

heights above mean sea level taken from the NASA Directory of Observation Station Locations (1971) to compute geocentric radii for 32 satellite-tracking stations. These radii were then compared with geocentric radii derived from satellite observations. (See table 5.57). No systematic difference was detectable. This level of agreement must be considered excellent, especially when the uncertainties in the various data used in deriving the parameters are taken into account. Of the various sources of the differences, the most probable are (1) errors in values of r_e, W_o, and a_e, (2) errors in station coordinates obtained from dynamic theory, (3) errors in mean sea level heights for some tracking stations, and (4) errors in geoidal heights at tracking stations due to the use of simple free-air anomalies rather than terrain-corrected free-air anomalies.

Theoretically, terrain-corrected free-air anomalies provide more accurate estimates of geoidal height than simple free-air anomalies. The effect of using the simple anomalies is to produce geoidal heights which are systematically too negative in the vicinity of land areas with rugged relief. Dimitrijevich (1972) has shown that the value of the difference in the United States ranges from in excess of +3.5 meters in the rugged mountains of the west to about +0.2 meter in the east. Since most tracking stations used in the comparisons are on large land masses and several are in areas of rugged relief, 1- to 2-meter differences may arise. It should be noted that differences due to this source are not the result of errors in basic parameters but the result of using a slightly incorrect form of surface gravity anomalies in the computations.

Another evaluation of scale was conducted by comparing Mather's (1970) gravimetric geoid with our geoid. Mather's geoid was computed on the basis of Rapp's model complete to (12, 12). The comparisons were made along two latitudes, −24 degrees and −26 degrees (table 5.58). In both instances, there was a variation of less than 2 meters rms and no systematic scale differences.

Conclusions.—The geoid presented here has an accuracy of ±2 m. over the continents and 5 to 7 m. where data are sparse.

The use of a consistent set of parameters refers this geoid to an absolute datum. Comparisons of the detailed global geoid with astrogeodetic geoids and station positions derived by dynamic satellite geodesy show no systematic scale differences.

There seems to be no conclusive evidence of a rotation with respect to North American Datum 1927. However, a slight rotation, which is prominent along the east-west profile, exists in the European and Australian datums. This rotation could be attributed to long-wavelength errors in coefficients in GEM 4, a rotation of the astrogeodetic geoid, or a combination of both.

5.6.3 Gravitational Potential of GEM 5 and GEM 6

5.6.3.1 Presentation of Results

The gravitational potential in terms of normalized associated Legendre polyomials, as defined by the coefficients $\bar{C}_n^m$ and $\bar{S}_n^m$, is given in table 5.59 for GEM 5 and in table 5.60 for GEM 6.

5.6.3.2 Analysis of Results

Zonal Harmonics (F. Lerch, GSFC).—Coefficients of the zonal harmonics have been determined by Cazenave *et al.* (1971) and Kozai (1969) by analyses of orbital perturbations of long periods, whereas GSFC, in its work on GEM, determined the coefficients of the zonal harmonics by analysis of orbital perturbations of short period (7 days). Table 5.61 compares the zonal coefficients in GEM, Standard Earth II, and the solution of Cazenave *et al.* (1972b). The solution of Cazenave *et al.* resulted from a combination of Kozai's normal equations (used in Standard Earth II) with corresponding equations for three low-inclination satellites (SAS, PEOLE, and DIAL). The rms differences from the coefficients of Cazenave *et al.* are as follows:

Solutions with data on satellites of low inclination (rms×10⁹)		*Solutions without data from satellites of low inclination (rms×10⁹)*	
GEM 3	9.5	SE-II	16.3
GEM 4	7.6	GEM 1	22.5
GEM 5	8.9	GEM 2	9.1
GEM 6	7.4		

Solutions without low-inclination satellite data employ satellites whose inclinations are greater than 28 degrees.

The rms agreement with the values of Cazenave *et al.* is much better for the solutions that contain the data on low-inclination satellites than for the solutions which lack these data. The comparisons of the coefficients of Cazenave *et al.* with the coefficients of GEM 1, 3, and 5 show progressively better agreement, as do the comparisons with the coefficients of GEM 2, 4, and 6.

The rms difference of 7.4×10^{-9} between the values of GEM 6 and the values of Cazenave *et al.* is approaching the accuracy given by the standard deviations from each of the solutions. The rms of the standard deviations is 5×10^{-9} for the GEM 6 solution and 4.5×10^{-9} for the Cazenave *et al.* solution. Secular and long-period zonal perturbations were computed from these models and are presented in a subsequent section. In this analysis, the solutions that include low-inclination data yield improved results over solutions not including these data.

Comparison With Gravity Anomalies (F. Lerch, GSFC, and J. Richardson, Computer Sciences Corporation).—Data on surface gravity were employed for testing models derived only from tracking data as well as models derived by adding gravimetric data. Rapp's 5-degree equal-area (555-km squares) average gravity anomalies were employed in the comparisons. These consisted of 1654 blocks of anomalies, of which 1283 blocks were based upon actual measurements of gravity. For these 1283 blocks, mean square differences $E\ [(G_T-G_S)^2]$ between the 5-degrees average gravity anomaly (G_T) and the value (G_S) computed from the potential given in various models are listed in table 5.62.

Three subsets of the 1283 blocks are also presented in table 5.62. These subsets are based upon the number (n) of 1-degree equal-area anomalies in a 5-degree block that were based directly upon observations. The four samples selected for the comparisons consist of the 1283 blocks for $n\geq1$, 1044 blocks for $n\geq5$, 563 blocks for $n\geq15$, and 211 blocks for $n=25$.

Models are listed in table 5.62 in the order of increasing agreement with the data on surface gravity. The average reduction in $E[(G_T-G_S)^2]$ between GEM 1 and GEM 5 is about 8 mGal^2 for the four samples. This improvement is significant for satellite models, considering that the total reduction for this quantity is about 32 mGal^2 when surface gravity data are included, as in the case of the GEM 4 and 6 models.

GEM 6 was computed with the gravity data from Rapp included in its solution. For this reason, GEM 6 is in better agreement with the data than GEM 4. The improvement in GEM 3 and GEM 5 relative to GEM 1 is attributed to the inclusion of electronic and laser DME data.

The result in table 5.62 for Standard Earth II is somewhat unexpected, since this model used a set of average gravity anomalies in its solution. However, these data were based upon an earlier collection and were fewer than Rapp's data.

Gravity anomalies were computed for GEM 5 and GEM 6 with the use of equation (5.41). The results are plotted in figures 5.47 and 5.48.

The value $E\,(G_T-G_S)^2$ for the mean square gravity anomaly differences is due to: (1) errors (ϵ_S) of commission caused by errors in the potential coefficients in the solution, (2) errors (ϵ_T) in the data, and (3) errors (δ_g) of omission caused by excluding higher-degree coefficients from the solution. The solution (EXP in table 5.62) is derived in a manner similar to that for GEM 6 except that the EXP solution is complete to degree and order 20 in spherical harmonics. This

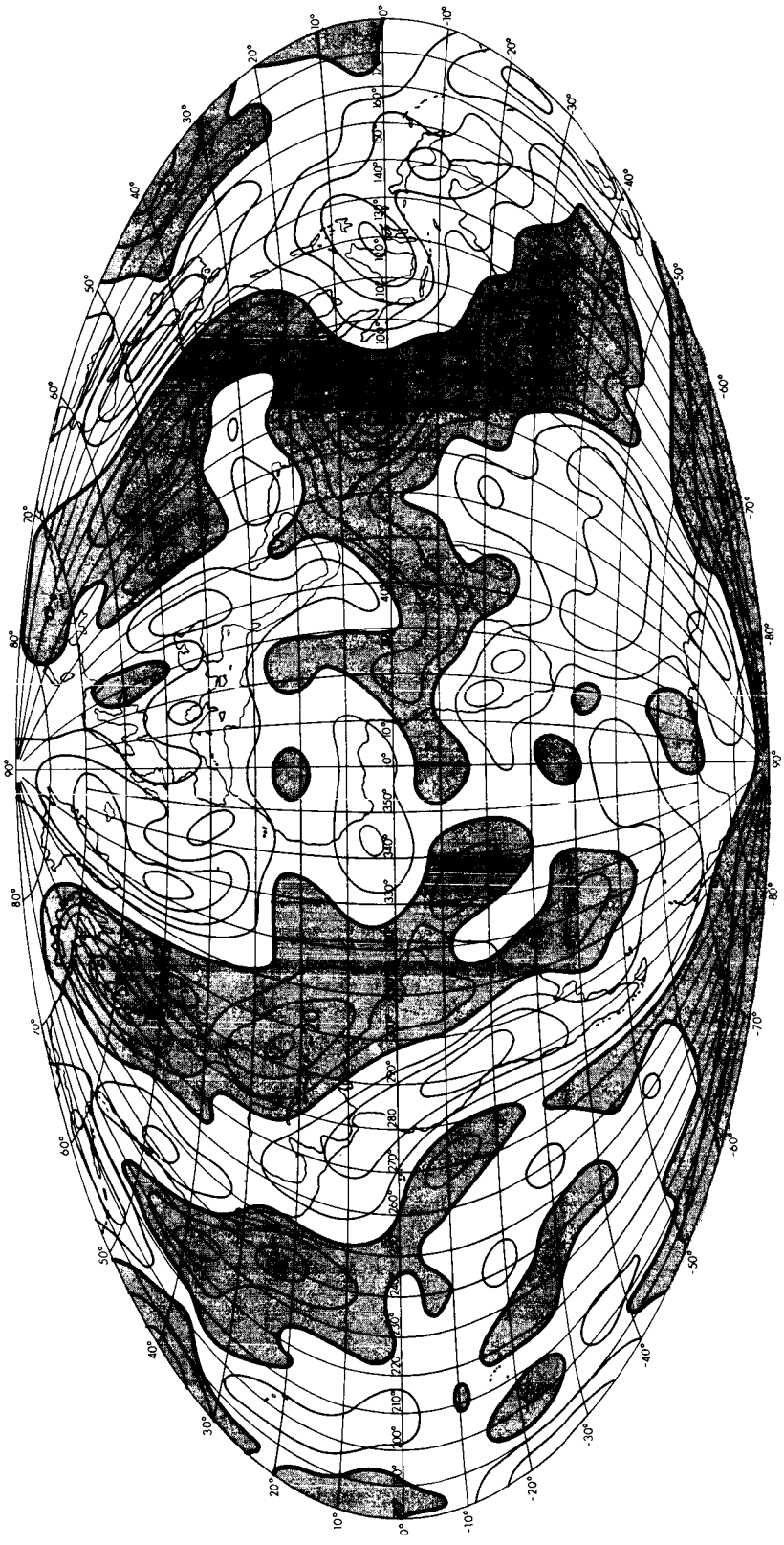

FIGURE 5.47.—GEM 5 computed mean gravity anomalies (10-mGal intervals).

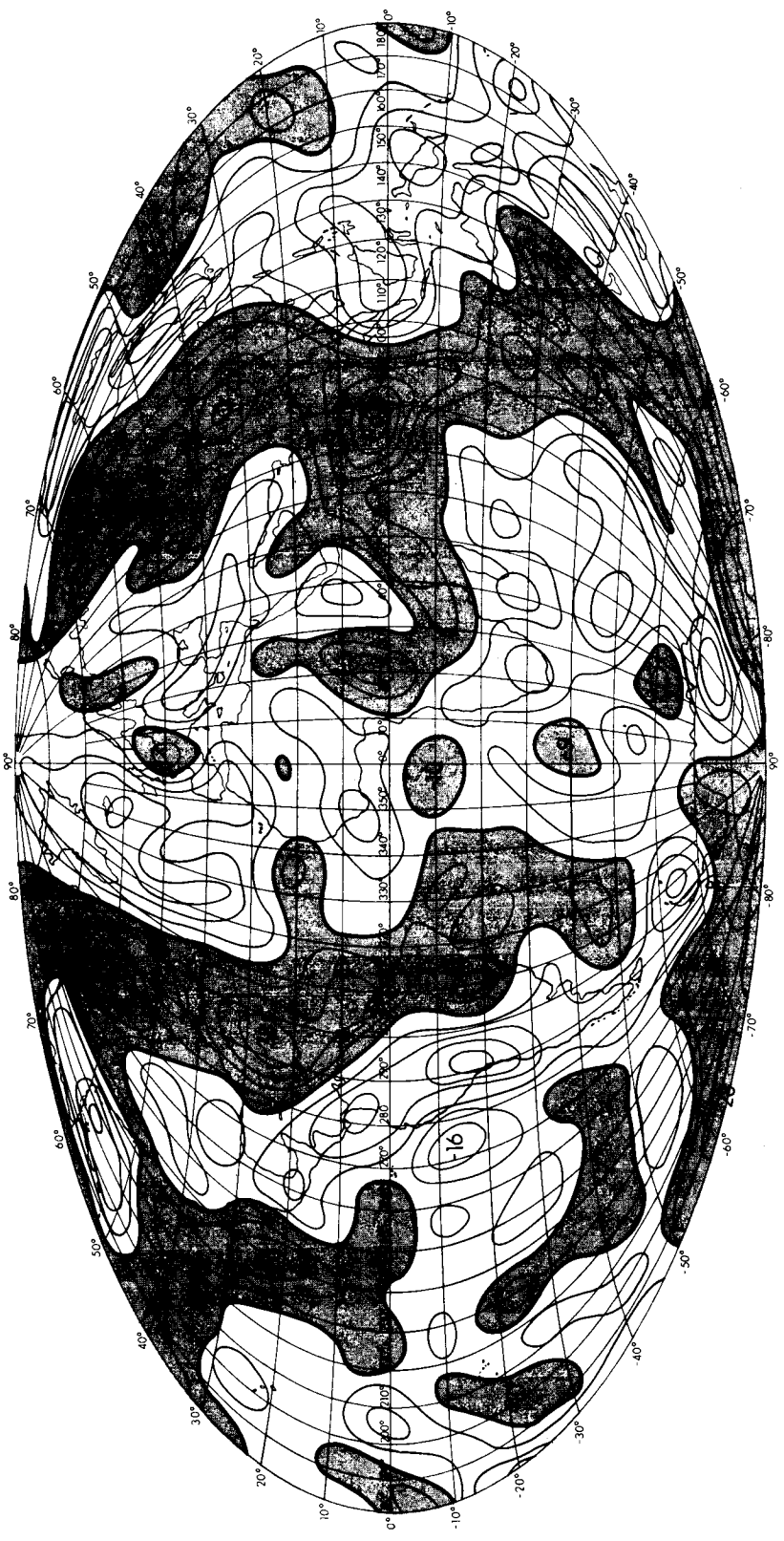

FIGURE 5.48.—GEM 6 computed mean gravity anomalies (10-mGal intervals).

extension is obtained from the contributions of the surface-gravity data. The EXP model shows a considerable reduction in $E(G_T - G_S)^2$ relative to GEM 6. Also, since 5-degree mean gravity anomalies correspond ideally to a model complete to degree and order 36 in harmonics, the primary source of the value (total error) is due to the omission errors δ_g.

Kaula (1966a) provided a statistical technique for estimating the mean square of the errors (ϵ_T, ϵ_S, δ_g) in $E(G_T - G_S)^2$ for a given solution and the data. The following quantities are defined for the statistical error estimates:

$E[(G_T - G_S)^2]$	mean square difference between the terrestrial anomaly G_T and the anomaly G_S computed from the solution
$E(G_T^2)$	mean square of the terrestrial anomalies
$E(G_S^2)$	mean square of anomaly computed from the solution
$E(G_T G_S)$	estimate of the variance of G_Π, the true contribution to G_S
$E(\epsilon_T^2)$	mean square value of error in terrestrial anomaly
$E(\delta_g^2)$	mean square value of neglected higher-degree terms in the G_S set (omission error)
$E(\epsilon_S^2)$	mean square error in the solution G_S (commission error)

For a given argument Q, the preceding quantities $E(Q)$ are computed from

$$E(Q) = \sum_{i=1}^{K} \frac{Q_i}{K}$$

where the subscript i corresponds to a 5-degree equal-area block and K is the number of blocks containing terrestrial gravity anomalies G_T.

$$E(\epsilon_T^2) = E\left[\frac{E(G_T^2)}{n}\right]$$

$$E(\epsilon_S^2) = E(G_S^2) - E(G_H^2)$$

$$E(\delta_g^2) = E((G_T - G_S)^2) - E(\epsilon_T^2) - E(\epsilon_S^2)$$

where n is the number of 1-degree anomalies in a 5-degree block.

The statistical estimates were applied to three samples of the 5-degree test anomalies for the GEM 5, GEM 6, and EXP models. The resulting estimates are listed in table 5.63. Samples of the 1283 blocks of observed data were chosen for $n \geq 10$, 15, and 20. The error estimates are expected to be most valid for GEM 5, since the solution is independent of the test data.

The estimate for $E(\delta_g^2)$ represents the amount of information that remains to be extracted from the gravity data corresponding to a given solution. For the three models in table 5.63, the $E(\delta_g^2)$ averaged over the three samples reduces from 119 mGal^2 for the 12×12 GEM 5 model to 93 mGal^2 for the 16×16 GEM 6 model, and to 70 mGal^2 for the 20×20 EXP model. These omission (or truncation) errors are decreasing by about 25 mGal^2 as the maximum degree increases by 4. At this rate, the truncation error would be exhausted for a field complete to degree 32. Ideally, this exhaustion would occur at degree 36 for a global set of 5-degree anomalies.

The mean square errors of commission $E(\epsilon_S^2)$, due to errors in the potential coefficients in the solution, are estimated more realistically for the GEM 5 satellite model, since its solution is independent of the test data. The rms error for GEM 5 is about 6 mGal for the three samples. Corresponding errors for GEM 6 and EXP are about 5 and 4 mGal, respectively.

Gravity anomaly degree variances for the GEM 5, GEM 6, and EXP models are listed in table 5.64. Values are quite consistent from degree 2 to 12 for the three solutions. For these coefficients, a maximum difference of 3 mGal^2 is seen at degree 7 between GEM 5 and each of the combination solutions. Degree variances are listed beyond degree 12 for the GEM 5 satellite model, but these include only the effects of the zonal and selected satellite resonant terms. Similarly, the results agree very well between the GEM 6 and EXP model through degree 16. The sharp rise in the EXP (20×20) result for degrees 19 and 20 is possibly related to the so-called aliasing effect. This effect is due to

the truncation of the spherical harmonics. Some of the remaining information in the gravity anomaly (δ_g) for higher-degree terms (>20) is absorbed into adjacent degree terms in the solution due to relatively common frequency components.

Table 5.64 includes a value corresponding to the harmonic of degree zero, Δg_o, which was derived in the combination solutions as an adjustment for the reference value of equatorial gravity γ_e. Since $\Delta g_o = 3$ mGal, the reference value of γ_e given in the introduction is adjusted to 978 032.1 mGal (γ'_e) so as to correspond to the observed gravity data. The observed and computed gravity anomalies used in the comparisons above referred to normal gravity with the adjusted γ'_e.

Effects of Different Models of the Gravitational Potential on Satellite Observation Residuals (F. Lerch, GSFC, and J. Brownd, Computer Sciences Corporation).—Orbits have been derived from several sets of tracking observations with the use of various models of the gravitational field. The rms of the residuals found by using the different models is used as a measure for comparing them. Results are presented in the following areas of data analysis: (1) unified S-band (USB) tracking data on 11 daily arcs of the ERTS–1 satellite (table 5.65); (2) 7-day arcs of camera data on 23 satellites (table 5.66); (3) BE–C laser DME data on 22 short arcs (table 5.67); and (4) long-term zonal perturbations on 21 satellites (table 5.68).

The USB tracking data were processed for 11 stations using each of the GEM models and the Standard Earth II Model. The results are listed in table 5.65. These data provided global coverage for the orbit on 11 day-long arcs of the ERTS 1 satellite. For each day-long arc, the number of two-way range rate observations and station passes is listed. The rms of the residuals is given for each arc along with the average for the 11 arcs corresponding to each of the models. The average rms is least for GEM 6. In general, the GEM's yield an rms of from 30 to 45 percent relative to Standard Earth II. GEM 4 shows the largest rms among the GEM's.

Table 5.66 presents the weighted rms of residuals for a week-long arc on each of the 23 satellites that contain data from cameras. The rms values are weighted corresponding to the standard deviation of 2″, representing the accuracy of the camera data. Ideally, then, the rms values should be close to unity (they may be scaled by a factor of 2 for conversion to arc seconds). The average rms value per satellite is listed at the bottom of table 5.66 for each of the models. Models GEM 1 and 3 and GEM 6 all agree to within 0.″37 with the GEM 5 value of 2.″37 in the average rms value per satellite. The GEM 4 and Standard Earth II values are 0.″63 and 1.″07 larger than the GEM 5 value. This average rms of 2.″37 per satellite for the GEM 5 solution approaches the ideal value of 2″.

Twenty-two short arcs measured by the laser system on BE–C, which is independent of the solutions, have been processed using each GEM. The BE–C arcs are three revolutions in length; each consists of four consecutive passes with data which were collected by GODLAS at Greenbelt, Maryland during a 5-month period starting in July 1970. The rms of the residuals are listed in table 5.67 for the individual arcs, along with an average rms per arc. The results agree to within 0.3 meter for the GEM 1, GEM 5, and GEM 6 models.

These average rms values range from 1.33 to 1.65 meters. As shown in table 5.67, somewhat larger average rms values have been obtained for GEM 3 (2.0 meters) and for Standard Earth II (2.51 meters), and a value as large as 4.05 meters has been obtained for GEM 4. On a single pass, all the above models generally give rms values of about 50 cm, corresponding closely to the estimate of the accuracy of GODLAS.

A preliminary solution (PGS 2) for the gravitational potential, which is based upon camera data as is GEM 1 but which is complete to degree and order 16 in harmonics and includes a number of selected higher-degree terms, gave an average rms value of 1.06 meters for the 22 four-pass arcs. Results for individual arcs for PGS 2 are listed in table 5.67 along with the results for the

other models. These results more closely approach the accuracy of the data.

Solutions for zonal coefficients were tested by Wagner (1972) on 21 satellites, including the low-inclination satellite SAS and PEOLE for their secular and long-period effects on mean elements obtained from week-long arcs. Wagner uses as a test criterion the rms of the weighted variations in the mean element of each solution. These rms values are listed with those of other solutions (not included in his work) for comparison in table 5.68. Only about half of the 21 satellites used in Wagner's work were used in the other models.

The models that contain the data from the low-inclination satellites, GEM 3 through 6 and the Cazenave *et al.* (1971) model compare favorably in this test. Considering that the GEM's were based upon week-long orbital arcs and the model of Cazenave *et al.* (1971) was based upon satellite long-term zonal effects, it verifies that good zonal recovery may be achieved from short-term zonal effects. The Standard Earth II, GEM 1, and GEM 2 solutions do not compare as well in these tests because they do not contain the effects of low-inclination satellites. Wagner's result is expected to have the lowest rms, since his solution is based entirely upon the test data.

A summary of the results in tables 5.65 through 5.68 and table 5.62 is presented in table 5.69. The rms values of residuals for the different categories of data show, on the average, better results for GEM 5 and GEM 6. In ordering the models for evaluation, a simplified ranking scheme is used, where the rank as given in the table is derived from the sizes of the rms values from the different comparisons.

5.6.3.3 Geodetic Parameters

The reference values of the Earth's ellipsoid and normal gravity are listed below, along with the corresponding adjusted values based upon the GEM 6 solution.

	Reference Value	*Adjusted Value*
a_e (equatorial radius)	6 378 155 m	6 378 144 m
f (flattening)	1/298.255	1/298.256
g_e (equatorial gravity)	978 029.1 mGal	978 032.1 mGal

The adjusted value of a_e was derived in sec. 5.6.1.1 from an analysis of the GEM 6 station coordinates and heights of stations above mean sea level. Another estimate of a_e may be derived from the reference value of $GM = 398\,601.3$ km^3/sec^2 and the adjusted value of g_e, as derived from surface gravity data (Lerch *et al.*, 1972). This value for a_e is 6 378 142 meters and is well within the variational results associated with the above value of a_e, as shown by table 5.43.

5.6.4 Other Results

5.6.4.1 Luni-Solar Gravitational Perturbations

(J. Murphy and T. L. Felsentreger)

The magnitudes of luni-solar perturbations relative to the zonal harmonic effects are indicated in table 5.70, which gives the amplitudes and periods of some of the principal terms in the eccentricity perturbation of the TELSTAR 2 satellite.

The results of analyzing the orbital eccentricity of TELSTAR 2 are shown in figure 5.49. In this figure, the dots represent the "mean" values of eccentricity derived from an orbital theory containing Earth's zonal harmonic effects through C_5^0. If no perturbations are left in the elements, the mean values should be fairly constant. As indicated in figure 5.49, a quite substantial long-period variation remains in the eccentricity. However, after removal of the long-period and solar gravitational effects and solar radiation pressure, this variation is reduced to almost nothing. Similar results were obtained for the inclination, the argument of perigee, and the longitude of the node.

Figure 5.50 illustrates the effect of removing the resonant perturbation $(\delta e)_R$ from the eccentricity of the RELAY 2 satellite. The resultant mean eccentricity is practically a

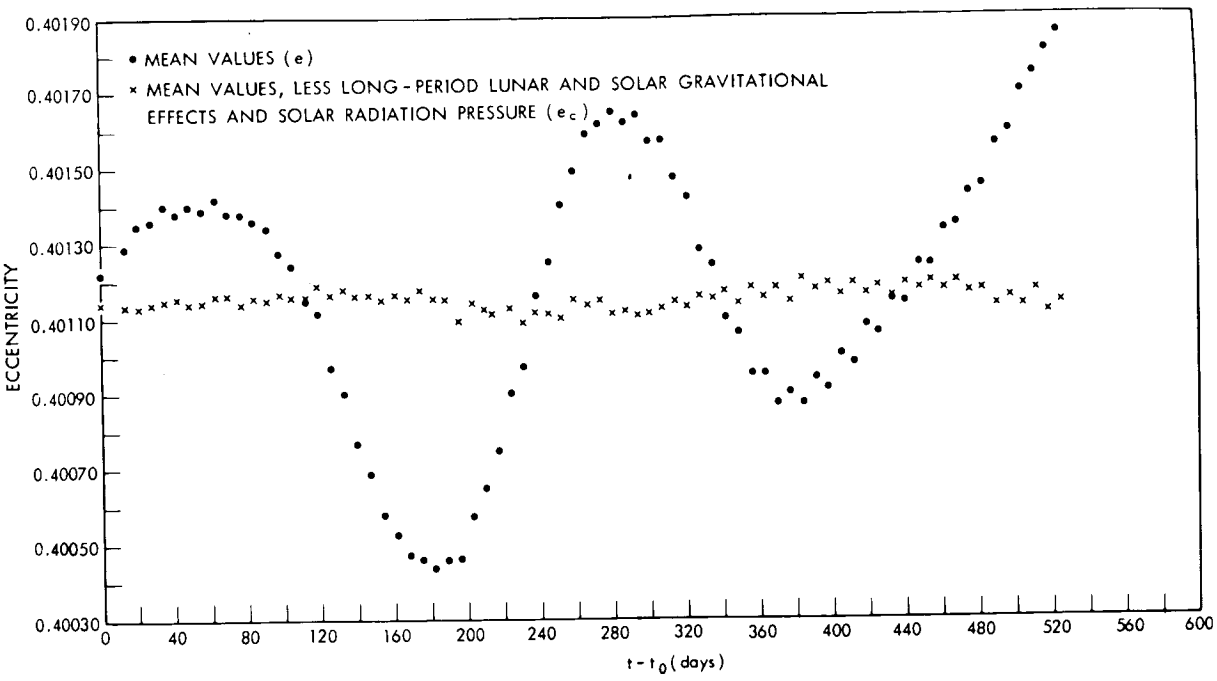

FIGURE 5.49.—Eccentricity of Telstar 2 orbit.

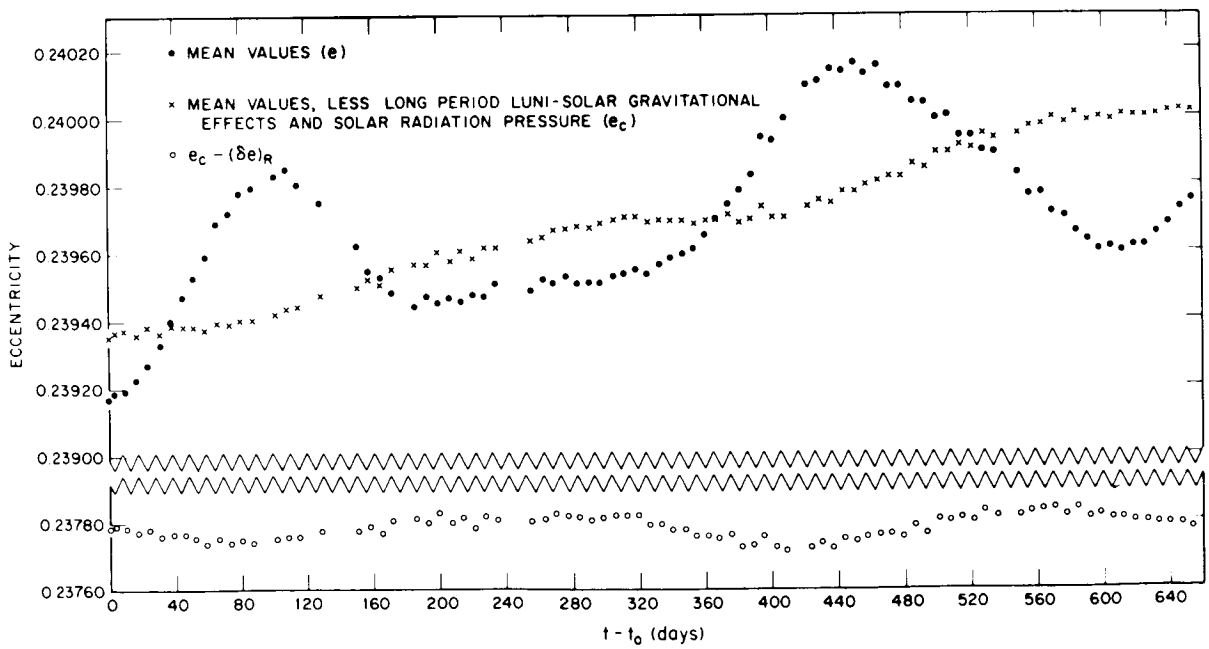

FIGURE 5.50.—Eccentricity of Relay 2 orbit.

constant, as it should be if all perturbations have been removed.

The remaining variation in $e_c - (\delta e)_R$ is in phase with the argument of perigee, with a period of about 325 days. The values of $e_c - (\delta e)_R$ were fit by means of least squares to an expression of the form

$$e_0 + B_1 \sin \omega + B_2 \cos \omega$$

indicating that this variation can be explained by a trigonometric term with a period of 325 days and with an amplitude of $B_1^2 + B_2^2 = 0.00004242$. The closeness of the fit is indicated in figure 5.51. The peturbation formula for e due to Earth zonal harmonic C_3° contains such a term:

$$\delta e = -\tfrac{1}{2} \frac{C_3^\circ \sin i}{C_2^\circ a} \sin \omega$$

A value of C_3° of -2.285×10^{-6} was used in the orbit theory. However, the remaining variation in e indicates that a value of -2.504×10^{-6} should have been used. This value is more in line with recent determinations.

5.6.4.2 Solar Radiation Pressure

The TELSTAR 2 satellite provides a good subject for study of the solar radiation pressure effect (sec. 5.4.4.2). A variation with approximate amplitude of 0.0000140 Earth radii and a period of about a year was observed in the semimajor axis, as depicted by the dots in figure 5.52. Inclusion of the shadowing radiation-pressure successfully accounted for this variation, as shown in figure 5.52.

5.6.4.3 Tidal Deformation of the Earth

Figure 5.53 shows the theoretical tidal perturbation on the BE–C satellite using a value of 0.3 for k_{20} only (Musen and Felsentreger, 1973). This perturbation agrees quite well with observational data.

5.6.4.4 Figure of the Hydrostatic Earth
(M. A. Khan)

The following data are adopted in the computation of f_h:

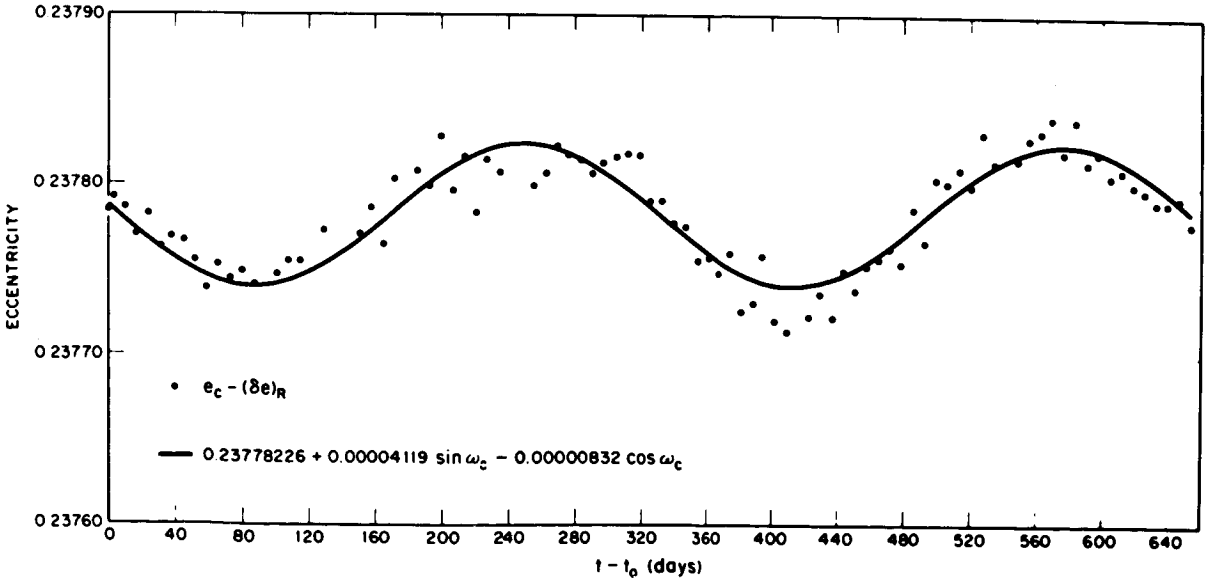

FIGURE 5.51.—Eccentricity of Relay 2 orbit.

$$C_2^\circ = -1082.646 \times 10^{-6}$$

$$H = 3273.64 \times 10^{-6}$$

Therefore,

$$\frac{C}{Ma^2} = 0.33071598$$

$$m = 3449.80 \times 10^{-6}$$

$$\lambda(a) = 0$$

The resulting value of the hydrostatic flattening is

$$f_h = \frac{1}{299.75 \pm 0.05}$$

The corresponding value of hydrostatic C_2° is

$$C_{2_h}^\circ = -1071.66 \times 10^{-6}$$

The value of actual flattening f corresponding to $C_2^\circ = -1082.692 \times 10^{-6}$ is

$$f = \frac{1}{298.25 \pm 0.05}$$

and therefore

$$f - f_h = 16.722 \times 10^{-6}$$

The choice of $\lambda(a) = 0$ needs some justification. The value of $\lambda(a)$ lies between 1.3×10^{-6} (Bullard, 1948), as calculated from the known density distribution of the Earth. Thus, it may appear at first sight that the choice of λ is not compatible with the second-order theory. However, selection of $\lambda(a) = 0$ instead of $\lambda(a) = 1.3 \times 10^{-4}$ results in f_h being

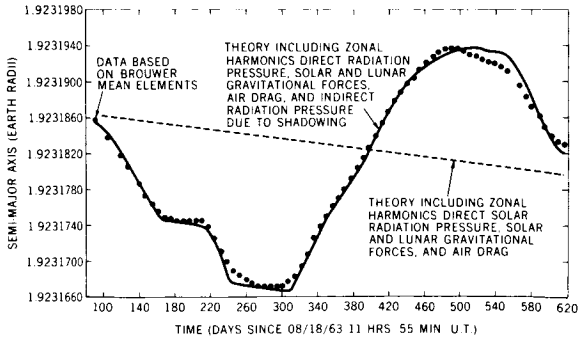

FIGURE 5.52.—Semimajor axis of Telstar 2 orbit versus time.

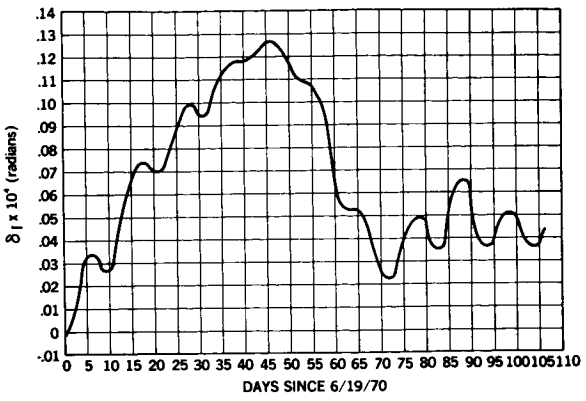

FIGURE 5.53.—Tidal perturbations in orbit of BE–C.

greater by 6×10^{-7} only, whereas the difference $f - f_h = 16.722 \times 10^{-6}$. Hence, our choice of $\lambda(a) = 0$, and consequently $\psi(\eta) = 1$, does not affect the value of f_h to any significant degree. This is demonstrated in figure 5.54.

Size of the Hydrostatic Earth.—The size of the ellipsoid of the hydrostatic Earth can be computed by assuming that it is volumetrically equivalent to the actual Earth. Thus, if a and b are the equatorial and polar radii of the actual Earth and a_h and b_h their hydrostatic counterparts, we have

$$a_h = a\left(\frac{1-f}{1-f_h}\right)^{1/3}$$

For $a = 6\,378\,140$ meters and $C = 6\,356\,755$ meters (corresponding to $f = 1/298.255$), we obtain

$$a_h = 6\ 378\ 104 \text{ meters}$$

$$b_h = 6\ 356\ 826 \text{ meters}$$

which result in

$$a - a_h = 36 \text{ meters}$$

$$b - b_h = -71 \text{ meters}$$

Gravity Field Referred to the Hydrostatic Figure.—As discussed earlier, since the hydrostatic figure is a figure of zero stress, it constitutes a geophysically meaningful reference figure for gravity anomalies for use in

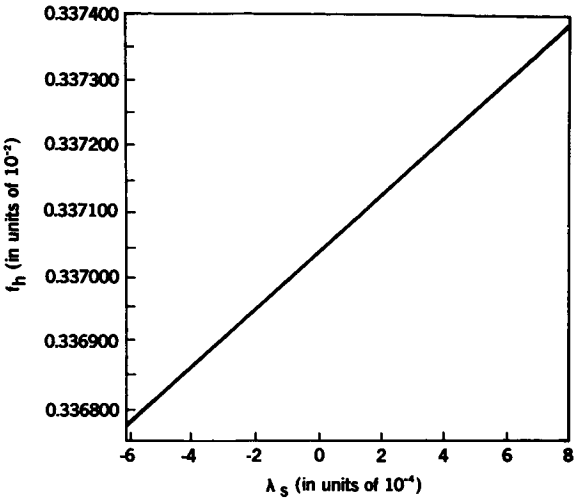

FIGURE 5.54.—Influence of $\lambda(a)$ on the value of f_h (after Khan, 1968).

studying the internal state of the Earth. These gravity anomaly maps are generally available with reference to either the International Gravity Formula or Gravity Formula 1967. Table 5.71 lists the conversion factors to be applied to these anomalies in order to refer them to the hydrostatic reference figure. Note that these are the conversion factors for the gravity anomalies alone. To convert absolute gravity values from the International Gravity Formula to values on the hydrostatic ellipsoid, the Potsdam correction must also be taken into account. The geoid referred to the hydrostatic Earth is shown in figure 5.55.

5.6.4.5 Earth's Isostatic Gravity Anomalies (M. A. Khan)

If gravity anomalies are to be used for deriving information on the mass distribution of the Earth, the gravity effect of the obvious surface features must first be removed. One such important effect is the surface topography and its subsurface compensation. When the gravity effect, which is likely to result from a compensated topographic feature (on the basis of an assumed compensation model), is removed from the free-air gravity anomalies, the isostatic gravity anomalies result. These anomalies are the most suitable for use in geophysical interpretation of subsurface features.

The conventional methods of applying the isostatic correction, the gravity effect which would result from a compensated topographic feature, are time-consuming, cumbersome, and not too gracefully computerized, though they have the advantages of greater precision, a factor important in accurate gravity surveys such as those made for exploration of natural resources. But for purposes of global geophysical interpretation, the isostatic correction is most easily computed by treating the Earth's topography as a variable-surface-mass layer which is compensated by a variable-mass layer of opposite sign at an appropriate depth of compensation. The basic isostatic model in such computations is the same as the conventional Airy-Heiskenan model of isostatic compensation.

Theory.—The theory of the method is summarized by Jeffreys (1962) and Khan (1972). The gravitational potential of a mass anomaly represented by a surface density $\sigma_{nm} S_n^m$ at $r=R$ is

$$V_{nm}=\frac{4\pi G}{2n+1}\sigma_{nm}S_n^m\frac{R^{n+2}}{r^{n+1}} \qquad (5.154)$$

where G is the gravitational constant and S_n^m is the surface spherical harmonic of degree n and order m.

The compensation of this surface density layer, located at $r=R-d$, where d is the depth of compensation, produces a potential

$$V_{nm}^c=V_{nm}\,[(R-d)/R]^n \qquad (5.155)$$

Hence, the potential due to the isostatic reduction is

$$V_{nm}^i=\frac{4\pi G}{2n+1}\sigma_{nm}S_n^m\frac{R^{n+2}}{r^{n+1}}\left[1-\left(\frac{R-d}{R}\right)^n\right] \qquad (5.156)$$

The gravity effect of this potential must be accounted for in converting free-air gravity anomalies to isostatic gravity anomalies.

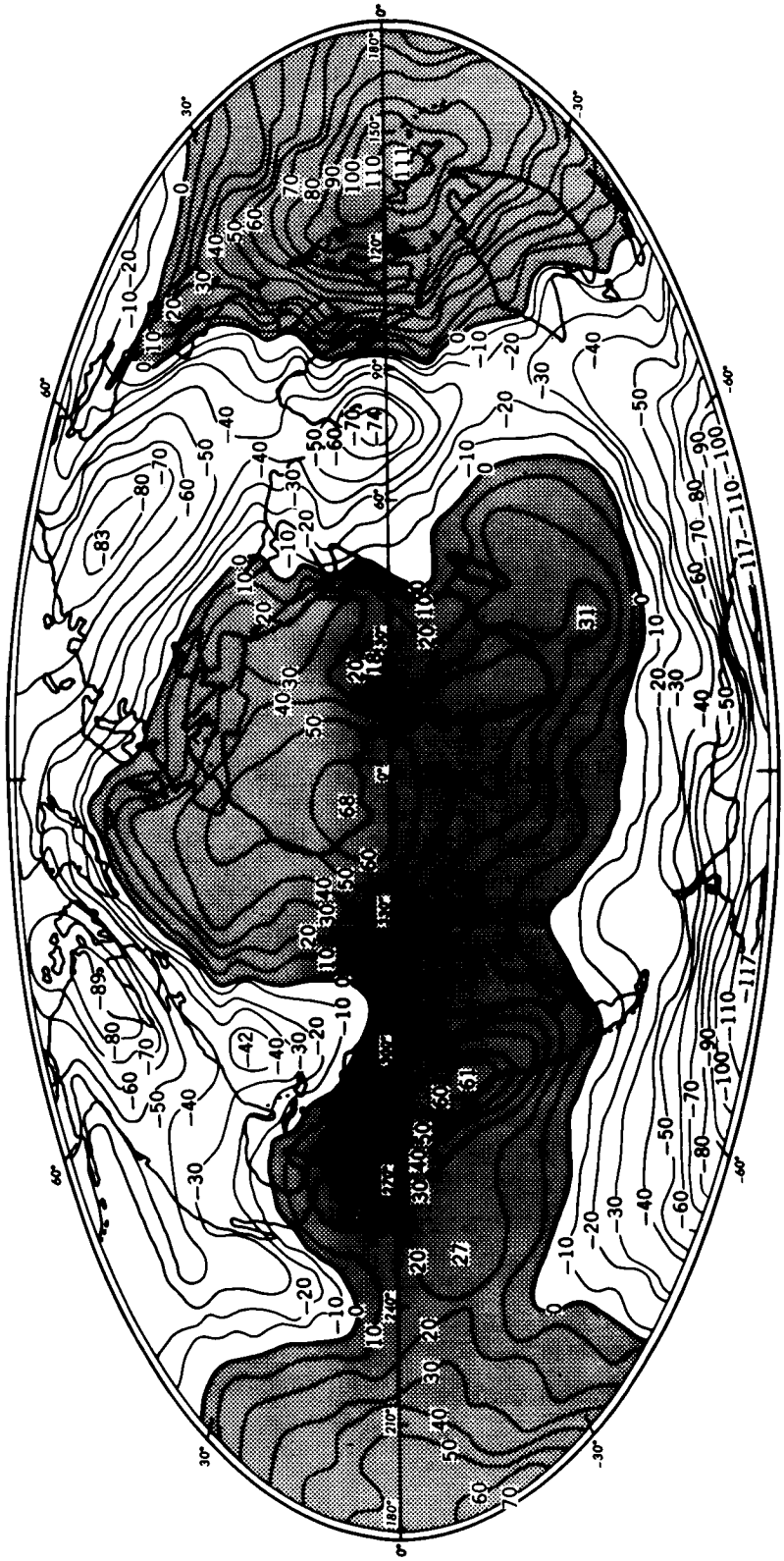

FIGURE 5.55.—Geoid based on GEM 6 in meters. Flattening 1/299.75 contour in intervals of 10 meters.

For a reasonable depth of compensation, the factor in the brackets stays close to zero. For a high-altitude satellite, the effect of equation (5.156) will be further attenuated because of the large distance of the satellite from the source of anomaly. But for low-altitude satellites, the isostatic reduction effect must be taken into account.

Equation (5.156) is used to compute spherical harmonic coefficients of isostatic reduction potential.

Data Used.—The set of spherical harmonic coefficients of global topography on which the isostatic reduction potential coefficients are based is reported by Balmino *et al.* (1973). Their analysis of global topography is based on the data used by Lee and Kaula (1967). However, Lee and Kaula's analysis had errors of incorrect dimension and incorrect contribution of ice to equivalent rock, which have been corrected in more recent analysis.

The basic gravity model in computing the free-air gravity anomalies, which are then used to compute the isostatic gravity anomaly field in conjunction with the model gravity anomalies, is GEM 4 (Lerch *et al.*, 1972c), which was obtained from a combination of orbital data and surface gravity data.

Results.—On the assumption that the compensation for the topographic load is achieved in the manner of the Airy-Heiskenan hypothesis at a compensation depth of 30 km, the spherical harmonic coefficients of the isostatic reduction potential U are computed using equation (5.156). Values are given in table 5.72. The degree power spectra of these coefficients are compared in table 5.73 with the power spectra of the isostatic reduction coefficients given by Uotila (1964).

5.6.4.7 Estimation of Accuracy of Various Computed Gravitational Potentials
(C. Wagner)

One of the goals of NGSP was to determine the gravitational potential through degree and order 15, but the accuracy with which this should be accomplished was not specified. However, a widely quoted goal (Strange, 1968, (unpublished) of no more than 0.2 mGal at the Earth's surface per spherical harmonic coefficient would provide about a 3-mGal error over the full set through degree 15. These requirements are more severe for the high-degree coefficients (being inversely proportional to $n-1$) because of the greater sensitivity of gravity anomalies to the short-wavelength terms. For example, with the error above, the requirements on fully normalized coefficients range from 20×10^{-8} for second-degree to only 1.4×10^{-8} for 15th-degree terms.

How severe is the total error budget? A simple calculation using Kaula's rule for the normalized potential coefficients (10^{-5}/deg^2) shows that the rms anomaly for this full set is only 18 mGal. To leave an error of 3 mGal implies an overall determination to an accuracy of about 20 percent, which is quite modest. Yet comparisons of recent satellite-gravimetry combination models and comparisons of them with unused surface data show discrepancies of 8 mGal on the average (Gaposchkin, 1970 and Wagner, 1970, unpublished). In terms of potential coefficients (fully normalized), these comparisons show differences (Lerch, 1972, unpublished) on the order of 5×10^{-8} (rms), which meets the accuracy requirements for only as high as fifth-degree harmonics. It is clear that, overall, the determination of the (15, 15) field is still far from adequate. Nevertheless, it is reasonable to inquire whether some parts of the field are better determined than others compared to the apparent overall average accuracy figure of 5×10^{-8}.

In general, there are only two classes of harmonic terms for which we can make judgments with accuracy. These are the zonal harmonics, which alone have secular effects on all satellite orbits, and the resonant harmonics (of specific orders), which have characteristic long-period effects on orbits whose periods are commensurate with the Earth's rotation. A previous study (Wagner, unpublished, 1972) has shown that the coefficients of zonal harmonics of less than degree 11 are

now known individually to an accuracy of better than 2×10^{-8}. This satisfies the stated accuracy requirements for the NGSP.

The orbits examined here have periods of 24 hours, 12 hours, 2^h40^m, and 1^h43^m. The orbits of the highest satellites are dominated by resonance with the (2, 2) harmonic, although the effects of terms of higher degree and order are observable. The other orbits are not dominated by any single resonant harmonic. Only the 24-hour period orbits are examined here in detail [but see Wagner, unpublished, 1972]. The results for orbits with a 24-hour period are given in detail in this section and are summarized in table 5.74. For an orbit of 12 hours the result is given in table 5.75, for an orbit of 2^h40^m, in table 5.76, and for an orbit of 1^h43^m period in table 5.77.

The potentials evaluated are representative of the best satellite and combined satellite-surface fields produced up to 1973, using a variety of satellites, types of data, and methods of solution. Their characteristics are summarized in table 5.78. The SAO Standard Earth I is the M1 field of the first Smithsonian Standard Earth (Lundquist and Veis, 1966.) It is complete through degree and order 8 with selected higher degree terms to (16, 14). This field includes the strong ninth-order resonance from TELSTAR 1, but only its influence on (15, 9).

The APL 5.0 (1967) is perhaps the best field yet published using Doppler data alone (ch. 2). It is nearly complete through (12, 12) with selected higher-degree resonant terms (none of ninth order). The Standard Earth II field is the second Smithsonian Standard Earth Model (Gaposchkin and Lambeck, 1970), complete through (16, 16) with selected higher-degree terms to (22, 14). However, it does not contain data from the strong, ninth-order, resonant TELSTAR orbit. The fields of GEM 3 and 4 contain this orbital information. GEM 3 is complete through (12, 12) and GEM 4 through (16, 16), both having selected higher-degree terms to (22, 14).

The data used are mainly sets of Keplerian mean elements of long arcs for the resonant orbits, determined by various organizations from different kinds of tracking data. Arcs vary in length from 1 month to over 6 years. The idea was simply to see how much of the total resonance could be explained by the five chosen potentials. The unexplained amount, expressed as a percentage of the total, should be a direct measure of the error in the set of resonance coefficients for that potential.

24-Hour Satellites.—For the deeply resonant (librating) 24-hour satellites, most of the arcs have nearly stationary ground tracks. The best of these allow precise accelerations to be calculated by fitting the semimajor axis and longitude to a model which adjusts the (2, 2) coefficients by a least-squares process. The trajectories are calculated by numerical integration of Lagrange's planetary equations expressed in mean elements. Subsequently, the longitudinal accelerations ($\ddot{l}$) are calculated from the adjusted values by a formula for orbits with stationary ground tracks (i.e., see Wagner, 1968b). It should be noted that this formula shows that coefficients (2, 2) account for about 80 percent of the resonant acceleration on the 24-hour satellite. The longitude (l) is defined as $(M+\omega)/s+\Omega-\theta_c$, where M is the satellite mean anomaly, ω is the argument of perigee, s is the commensurate number of revolutions per day, Ω is the right ascension of the ascending node, and θ_c is the hour angle of Greenwich.

Accelerations from measurement were compared with values computed using the five potentials. The results are given in table 5.74. The data on SKYNET (R. H. Merson, unpublished, 1972) are from radar range and angle tracking using a program which adjusts, by least squares, the (2, 2) coefficient directly to the tracking data. The ATS 3 data were derived in a similar way directly from range and range rate data.

Where the orbits are not sufficiently stationary, the full resonance effect is taken to be the rms residual in longitude, mean anomaly, or semimajor axis from a trajectory fitted by least squares to these observed

elements by a model without resonance coefficients. The results of these tests on two very long (nonstationary) arcs of SYNCOM 2 and 3 are shown in table 5.79. For SYNCOM 2, the longitude varies over an amplitude of only 10 degrees, providing a fairly local test of the field. For SYNCOM 3, on the other hand, the longitude span is worldwide. In both tests, the superiority of the GEM 4 solution is evident.

Summary of Results.—The resonance terms in GEM 3 and GEM 4 explain all but about 0.3 percent of the data (table 5.75). If this difference were distributed among the resonance terms according to their dominance, a shift of the order of 0.5×10 in the normalized coefficient of the (2, 2) harmonic would be necessary to explain the accelerations completely. These accelerations are worldwide.

GEM 3 and GEM 4 can explain all but about 1 percent of the resonant effect in the long arcs of SYNCOM 2 and 3. A shift of from 2 to 4×10^{-8} in coefficient (2, 2) is required to explain its proportion of the error (80 percent). The lower number applies to the worldwide sample on SYNCOM 3. However, the SYNCOM 2 sample is for a very limited libration with small acceleration. In addition, the SYNCOM 3 data are so poor that the "noise only" (resonant) solution is only marginally superior to the GEM solutions. Therefore, the overall results of the 24-hour satellite imply an error of no more than 2×10^{-8} in the dominant low-order coefficients.

Conclusions.—Current values for fully normalized coefficients of order 2, 3, 4, 9, and 14 as judged by independent, resonant satellite data range in accuracy from 2 to 5×10^{-8}. Except for order 9, these accuracies satisfy the modest requirements of the NGSP.

5.6.4.8 Polar Motion and Earth Tides

(David E. Smith)

With the increase in man's knowledge of the Earth's gravitational field and the positions of tracking stations, our ability to compute the orbital behavior of geodetic-type satellites has steadily improved. This advance in capabilities has enabled the relatively small orbital perturbations caused by the Earth and ocean tides to be observed and the variation of latitude of the tracking stations to be detected. The early work in the area of tides was done by Newton (1968) and Kozai (1968b) and by Anderle (1970, unpublished) for polar motion. Since 1970, work has been in progress at GSFC to improve the identification of the tidal perturbations of three satellites, Beacon Explorer C, GEOS 1, and GEOS 2. Efforts are also being made to measure the variation in latitude of a station with greater precision over shorter averaging times than has so far been possible.

The theoretical analysis of tidal perturbations on a satellite orbit began with Kozai in 1965, with a simple first-order development of the perturbations of the Keplerian elements (Kozai, 1965). In this analysis, the tidal disturbing function was represented by a second-degree spherical harmonic. More recently, Musen and Estes (1972) and Musen and Felsentreger (1973) have conducted combined numerical analytical developments in which the effect of more complex tidal potentials have been investigated.

To a person on the Earth's surface, the apparently dominant motions of the Sun and Moon are the daily passages of these bodies across the sky, arising from the Earth's rotation. To a satellite orbiting the Earth, the dominant motions of these bodies are their much slower motions across the celestial sphere. Similarly, the major frequency of the Earth tides as seen on the surface of the Earth is semidiurnal, caused by the Earth's rotation. To a satellite, this frequency is nonexistent. Viewed from space, the satellite sees the gravity field elongated slightly in the direction of the Sun and Moon—possibly offset slightly—but (to first order) is unaffected by the rotation of the Earth when the tides are considered. Thus, to a satellite, the dominant tidal periods are much longer than those of the surface tides and are determined by the relative rotations of the satellite

orbit with respect to the orbit of the Moon and the "apparent" orbit of the Sun.

In contrast to some of the earlier work, the approach taken at GSFC to observe the tides was exclusively numerical, and only the orbit inclinations were analyzed. The differencing of long and short orbital arcs was the principal technique used in all the investigations. In this technique, the short orbital arc adjusts to absorb the perturbation, whereas the long orbital arc, because of its length, is unable to adjust and, in effect, ignores the perturbation. Subtracting the long-arc orbits from the short-arc orbit reveals the perturbation together with any other badly modeled long-period effects.

This approach has the advantage that very complex perturbing forces which cannot easily be represented analytically can be taken into account in the numerically integrated long arc. The major disadvantage is that numerical integration of very long arcs (several hundred days) requires special care and considerable computer time.

5.6.4.8.1 TIDES

Beacon Explorer C.—The time orbit of Beacon Explorer C (BE–C) is nearly circular at an altitude of about 1000 km and inclined to the equator at 41 degrees. During the latter part of 1970 and most of 1971, a laser tracking system at GSFC tracked BE–C as part of a polar-motion experiment (Smith *et al.*, 1972b) and an international satellite geodesy experiment (ISAGEX). From the data collected during these experiments, the orbital inclination of BE–C was determined on 36 occasions over the 17-month period.

The latitude of the tracking station is about 39 degrees north, and, because this is similar to the maximum northerly latitude reached by the satellite, there are four consecutive observable passes each day. Orbit parameters were fitted through each four-pass arc and an ephemeris generated through the observations. From the ephemeris, the four maximum northerly latitudes were determined (Dunn *et al.*, 1973, unpublished) for each four-pass arc. At the position of maximum latitude, the argument of latitude of the satellite is $\pi/2$, by definition, and the latitude is equal to the inclination of the osculating orbit.

A "long" orbital arc was then fitted through 3 weeks of data and an ephemeris generated through the observations and projected for a total of 5 months. From the ephemeris, the values of maximum latitude (inclination) during the short four-pass arcs were derived. In all the orbital computations, the effects of terrestrial, lunar and solar gravity, solar radiation pressure, and air drag were included. When the long-arc maximum latitudes were subtracted from the short-arc maximum latitudes, a distinctive pattern in the residuals was evident. This pattern was subsequently shown to be the perturbation of the inclination by the Earth and ocean tides.

By adopting a second-degree spherical harmonic expansion for each tidal potential, the residual pattern could be almost completely explained throughout the 5-month period when Love's number (k_2) for the Earth was taken as

$$k_2 = 0.245 \pm 0.005$$

and a phase lag

$$\phi = 3.2 \pm 0.5 \text{ degrees}$$

was introduced (Smith *et al.*, 1973a).

The 5-month analysis containing 28 days of measurements was then extended to 17 months by including a further 8 days of data. The same long arc derived from 3 weeks of data was extended for the full 17-month period. Although only isolated days of data were available, the additional data were equally well satisfied by the results of the 5-month analysis (Kolenkiewicz *et al.*, 1973, unpublished).

Figure 5.56 shows the tidal perturbation of the BE–C orbital inclination for the full 17-month period. It is interesting to note that the last point in Figure 5.56 is at a local minimum on the perturbation curve and that the third point is at a local maximum: both

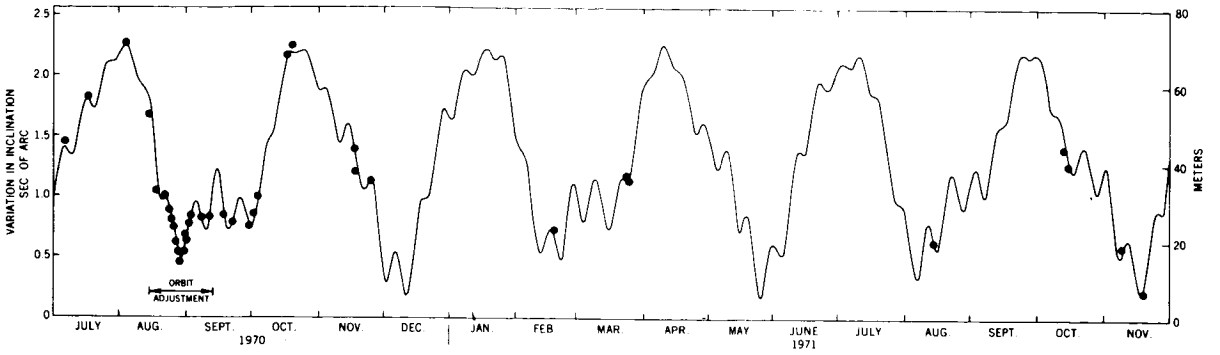

FIGURE 5.56.—Tidal perturbation of BE–C inclination for $k_2=0.245$, $\phi=3.2$. Solid dots, laser data; solid line, theory.

points appear to agree with the theoretical curve, indicating that the amplitude is quite well defined. The rms deviation of the observed points about the theoretical curve is 0.045 arc second. The GEODYN program system was used for this analysis.

GEOS–1.—Optical measurements (i.e., by camera) of 7700 flash observations of GEOS 1 over a 65-day period in 1966 were used in this investigation. The data were obtained by the worldwide camera networks of SAO and NASA and supplemented by several international cameras.

The perturbation of the inclination of GEOS 1 by the Earth and ocean tides has a peak-to-peak variation of about 2″, and during the period being investigated, March 11 to May 15, it changed by about 1″.5 (Douglas *et al.*, 1972, unpublished).

In order to circumvent a resonance problem with terms of 12th order in the field, the length of the short-arc orbital determination was chosen at 6.5 days, equal to the beat period of the resonance. Seven of these short arcs could be derived from the observational data. A single long arc was fitted through the 65-day period, and the values of the long-arc osculating orbital inclination were subtracted from the short-arc osculating inclination. In this analysis, the Earth and ocean tides were represented by second-degree spherical harmonics, and the computations were repeated for different values of Love's number, k_2.

Figure 5.57 shows the residuals between the short- and the long-arc inclinations of GEOS 1 for several values of k_2, with zero phase lag. The short and long arcs were differenced every six hours of the short arc, and figure 5.57 shows that the differences are largely constant during a short arc. Thus, the short arc must be averaging through the resonance errors and unmodeled tidal effects, as had been anticipated.

The residual patterns in figure 5.57 indicate that the trends reverse between $k_2=0.21$ and 0.24 and, by interpolation, that the pattern almost disappears for $k_2=0.22\pm0.02$.

The standard deviation of 0.02 assigned to this result is considered a rather arbitrary value and reflects the difficulty of assessing the true accuracy of the result from the technique being applied. This value is, of course, somewhat smaller than that obtained from BE–C, and from figure 5.57 it is apparent that applying a value of k_2 near 0.25 (BE–C value) would leave residuals in the GEOS 1 inclination of at least 0.2 arc second. This apparent discrepancy is discussed elsewhere in this section. This analysis was conducted using the GEODYN program system.

GEOS 2.—The data used in this investigation were mean orbital elements over a 2-year period derived from optical flash data obtained by worldwide tracking stations (Douglas *et al.*, 1973). The short-arc orbits were 2 days in length, and the mean elements

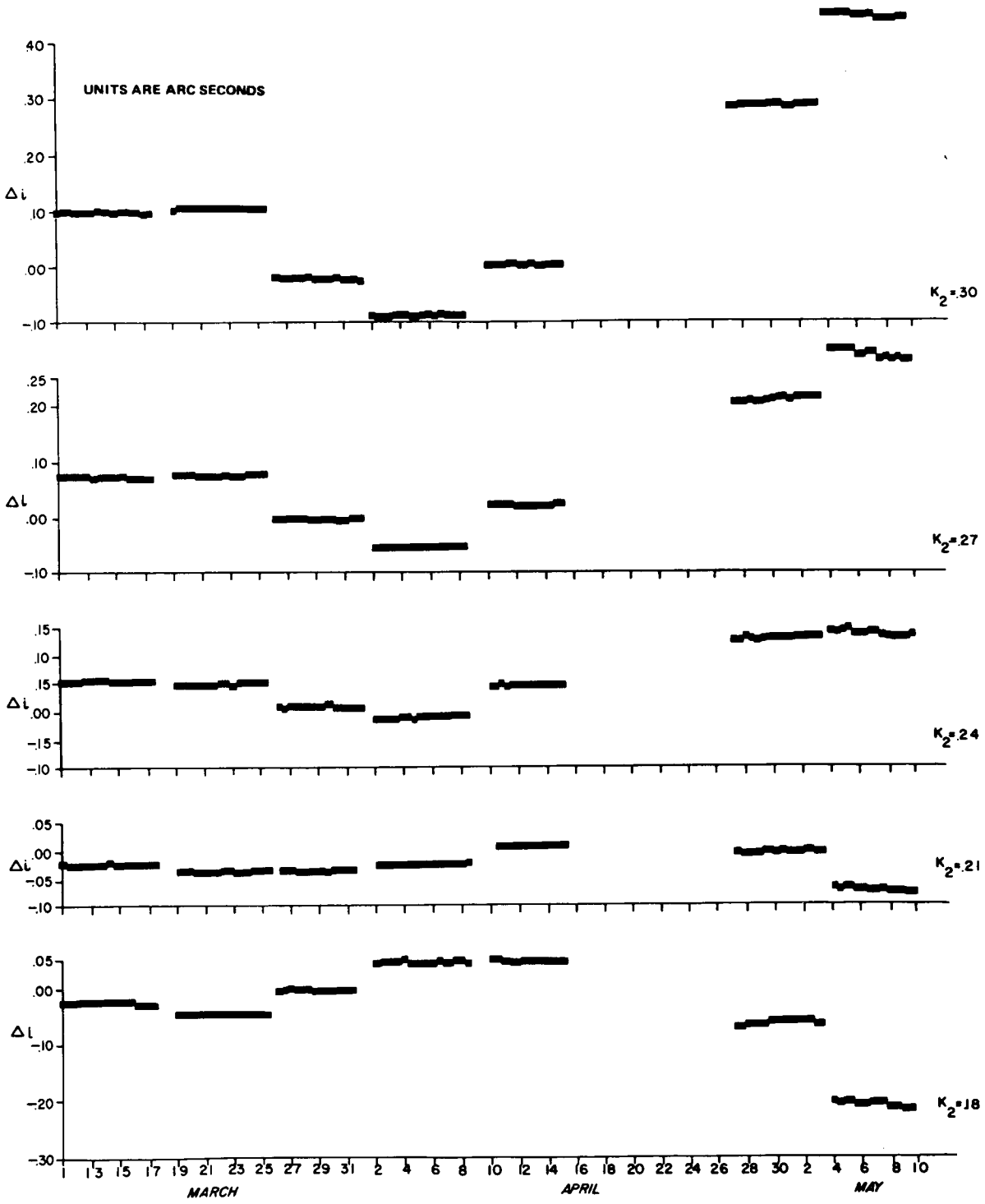

FIGURE 5.57.—Differences between long (65^d) and short (6^d.5) arc inclination for various values of k_2.

were derived by a combined analytical-numerical averaging technique from osculating elements obtained with the GEODYN program. The parameters investigated for the tidal effect were the variations in mean orbital inclination.

The ROAD computer program, which simultaneously integrates all long-period and secular effects on the orbit, was used to analyze the inclination values. In essence, ROAD uses the mean orbital parameters as data, and adjusts epoch orbital or other parameters such as tidal constants to best fit the data (elements). The absence of high-frequency terms in the perturbing function permits integration step sizes of 1 to 2 days, with consequent saving in computer time.

Figure 5.58 shows the residuals in inclination for the 2-year GEOS 2 arc when the tides are neglected ($k_2=0$) and after k_2 has been solved for (see the lower graph of the figure). The recovered value of k_2 was

$$k_2=0.31\pm0.01$$

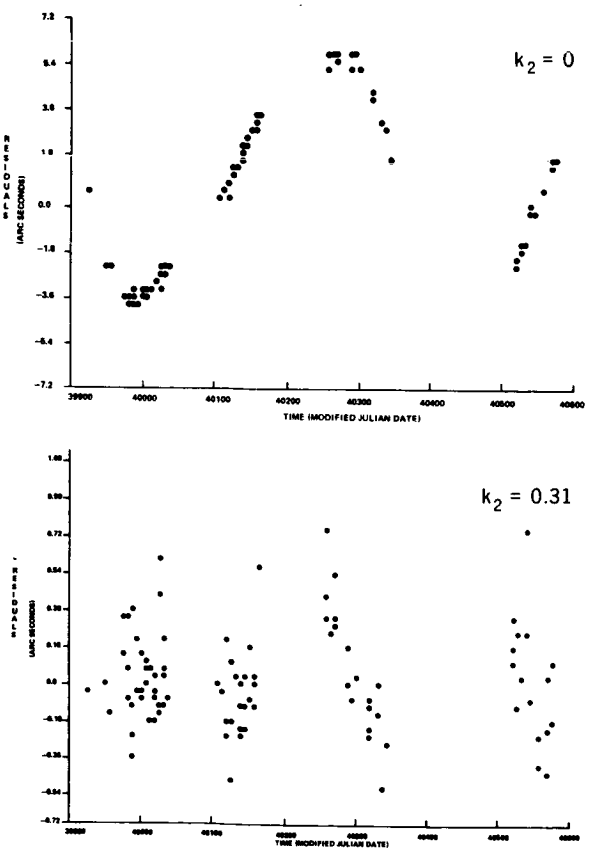

FIGURE 5.58.—GEOS 2 residuals in orbital inclination.

The amplitude of the tidal perturbation in inclination is very large, with about 10 arc seconds of variation, and the recovered best fit value of k_2 reduces the spread in residuals to about 1.2 arc seconds; that is, to about 12 percent. The lower part of figure 5.58 suggests that the final residuals are not completely random and that the signature of some unknown or poorly modeled perturbation may still remain. The phase angle was not recoverable from these data except to confirm that it was very small.

Discussion.—If the values of k_2 derived from the analyses of the BE–C and the GEOS 1 and 2 orbits are accepted, then they strongly suggest that k_2 is dependent on the satellite and its orbit and, consequently, that our model of the tides is inadequate. The present model, a second-degree spherical harmonic, is probably the simplest possible model, which can in principle be made more complex by increasing the degree and order of the spherical harmonic expansion. Such an expansion could satisfy any potential arising from the tidal response of the Earth if the response were independent of rotation of the Earth; or, in other words, if the response potential were only a function of the location of the point on the Earth's surface with respect to the rising body of the tide. Such a situation would imply that the tides were stationary in a coordinate system rotating with the rising body of the tide.

In reality, this situation does not exist, principally because the Earth's surface is composed of both continents and oceans, and the distribution of the continents significantly affects the tidal response of the oceans. Thus, the representation of the Earth and ocean tides must allow for a variation in response with geographical position. In effect, this implies making the coefficients of the spherical harmonic expansion a function of time.

Lambeck and Cazenave (1973) have assessed the contribution that the oceans could make to the tidal perturbations of satellites. Although their appraisal is not definitive, they find significant perturbations from certain components of the ocean tides that might explain the divergence of values described here for k_2. It therefore appears to be incorrect to recover k_2 from these analyses, and in the future, it may be more appropriate to determine the perturbations of the orbit due to the ocean tides. By assuming a value of k, from, say, seismicity, it may be possible to deduce the phase and amplitude of certain components of the ocean tides from these types of data. This approach implies that we know the solid Earth tide (not completely true) and that, if we can measure the total tidal perturbation, any residual can be ascribed to the oceans. This approach is both exciting and promising, and will surely receive considerable attention in the years to come.

5.6.4.8.2 POLAR MOTION

Originally, the BE–C laser data used in the tidal analysis were obtained for the purpose of trying to detect polar motion, and the first part of this investigation was the determination of the tidal perturbations. The basic concept of the experiment was to use the orbital plane of the satellite as an external reference for determining motions of the Earth. In particular, changes in the latitude of the tracking station would look like changes in the orientation of the orbital plane. Further, if the observations from which the orbit is determined are in the region of the maximum northerly (or southerly) latitude reached by the satellite, then the station latitude changes would appear as changes in the orbital inclination. However, since the orbital plane of the satellite is not fixed in space but undergoes significant perturbation, the major problem of the analysis is the complete modeling of the perturbations of the orbit, including those of the Earth and ocean tides.

After the tides, the perturbing force of greatest magnitude is the Earth's gravitational field (the higher-degree and order harmonics), but the perturbing force of solar radiation pressure is the most difficult to model. Fortunately, the technique of measuring the inclination at the apex of the orbit (maximum latitude) and analyzing the inclination with a "short-arc minus long-arc" approach tends to minimize the gravitational model errors. Further, the radiation pressure perturbations of the inclination of BE–C cover both short periods ($\sim$35 days) on the order of 8 meters in amplitude and long periods (thousands of days) of very large amplitude. The larger perturbations arise because there is almost no motion of perigee with respect to the Sun. Neither of these periods gets confused with the annual or 14-month periods of polar motion, even though the amplitudes of the perturbations are at least as large as those of polar motion.

Figure 5.59 shows the inclination perturbations of BE–C for tides and solar radiation pressure on the same scale as the latitude variation arising from polar motion of the Goddard tracking station according to BIH. Figure 5.59 (Dunn *et al.*, 1973, unpublished) indicates that a detailed knowledge of the tides and solar radiation pressure is essential for computing polar motion at the submeter level. Indeed, as discussed by Dunn *et al.*, it was necessary to include the variations in cross-sectional areas of BE–C arising from spacecraft attitude changes for the present results to be obtained.

In order to observe the variation of latitude of the Goddard station in the laser range data, it was necessary to compute the short, four-pass orbital arcs without including polar motion in the orbit determination program, GEODYN. As already noted, this approach causes the actual variation in latitude of Goddard to be forced into the computed value of the orbital inclination of BE–C. If all other perturbing forces are properly modeled, then the differences between the short- and long-arc values of maximum latitude reveal the variation in latitude of the tracking station (Smith *et al.*, 1972c). Figure

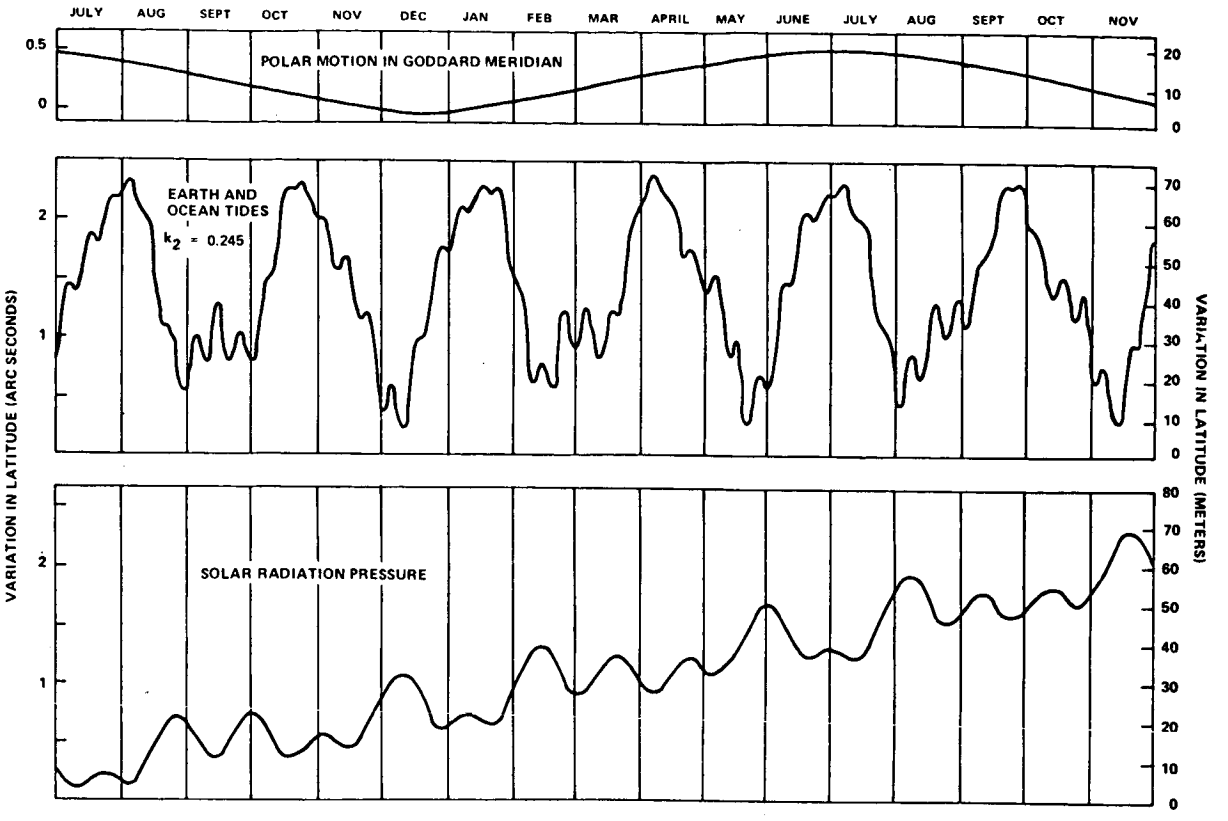

FIGURE 5.59.—Large inclination perturbations.

5.60 shows this variation obtained from the laser data over the 17-month period.

In a direct comparison with the BIH smoothed variation of the Goddard latitude, the laser data had an rms deviation of 0".045 or 1.38 meters (Kolenkiewicz *et al.*, 1973, unpublished). A careful examination of these laser residuals about the BIH curve suggests that they are not just noise, but probably contain more information about polar motion or about the perturbations of the orbit. It is also of interest to note that the rms deviation of the polar motion is almost identical to the average rms deviation (1.32 meters) of the laser ranges about the short, four-pass orbital arcs. From the analysis of data collected on a single pass, it is known that the actual rms noise of the laser data is on the order of 50 cm and that the larger fit through four passes is caused by errors in the field.

The field used throughout this analysis was the GEM 1, which is a field derived from optical tracking data complete to degree and order 12 with selected higher resonance and zonal terms (Smith *et al.*, 1973b; Lerch *et al.*, 1972, unpublished). No laser tracking data were used in the GEM 1 solution, and it can be presumed that these data would have improved the solution and, in particular, the fit to the laser data used in the polar motion analysis. Thus, it is probable that the polar motion residuals will decrease with a better field.

5.6.4.8.3 CONCLUSIONS

The orbits of three satellites have been analyzed to provide values for the second-degree Love number for the Earth. The differences between these values, which are considerably larger than the projected standard errors, strongly suggest that the perturbations observed arise not only from the tidal deforma-

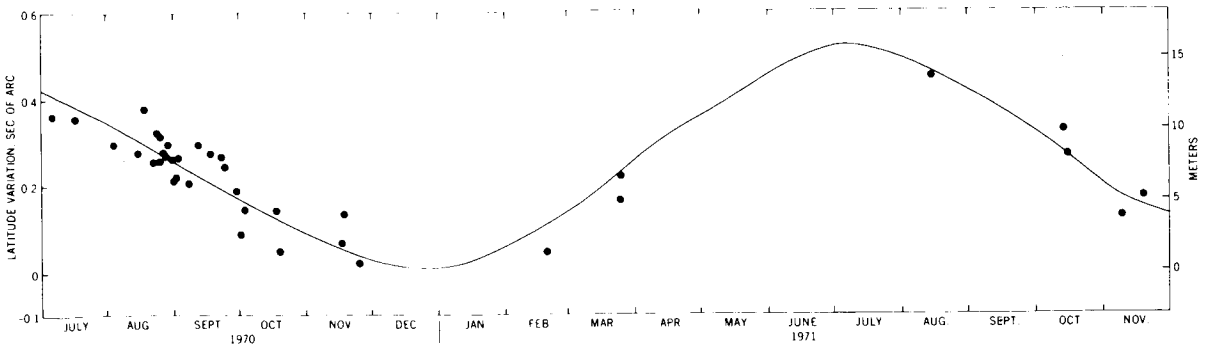

FIGURE 5.60.—Variation in latitude of the Goddard laser tracking station. Solid dots, determined from laser data; solid line, BIH smoothed values.

tion of the solid Earth but also from the oceans. For a definitive description of the ocean tidal components of these perturbations, it will be necessary to investigate the tidal perturbations of several other satellites in slightly different orbits. Thus, it appears that the study of Earth tides from satellite perturbations may be leading us toward increasing our knowledge of the ocean tides, which had not been anticipated a few years ago.

The determination of polar motion (variation in latitude) from laser tracking of near-Earth satellites to an accuracy of 1 to 1.5 meters has been accomplished in an environment in which the basic orbit determination capability is still at the 5- to 10-meter level. The conception and exploitation of technique that has enabled consistent results to be obtained over a reasonably long period of time suggest that monitoring the pole of rotation of the Earth at the 10-cm level from laser tracking should be realizable in a few years.

Further, since these results were obtained with only one tracking system, it seems that the contribution of a single tracking station ought not to be underestimated. At the level of about 10 cm, a single station will have the basic capability of monitoring its own secular motion in latitude, and therefore can contribute to our understanding and determination of tectonic motions and sea-floor spreading as well as to our knowledge of the rotation of the Earth.

APPENDIX

TABLE 5.1.—*Characteristics of ECHO 1 (1960 1)*

Launch:
- Date: 12 August 1960
- From: Atlantic Missile Range
- Rocket: Thor-Delta, three-stage

Orbital Elements

a, km	e	i	P	h_p, km	h_a, km
8226	0.012	47°.2	118^m.3	1752	1943

Structure: 82 gores, 2 polar caps of Mylar polyester, 243 holes 1/10″ in diameter in surface for escape of gases
- Diameter: 100 ft (30 m)
- Area: 31 400 ft² (2920 m²)
- Thickness: 13 μ (0.5 mil)
- Coating: Aluminium (1-μ thick), vapor-deposited
- Total weight: 76 kg

Reflectivity: 98 percent for radio waves up to 20 GHz (see also data on PAGEOS, table 5.3).
Beacons: Two, 107.94 MHz
Power: 70 solar cells, 5 to 8 mW
References: Bryant (1961); Jakes (1961)

TABLE 5.2.—*Characteristics of ECHO 2 (1964 4A, ECHO A-12)*

Launch:
- Date: January 25, 1964
- From: Western Test Range
- Rocket: Thor-Agena B

Orbital Elements

a, km	e	i	P	h_a, km	h_p, km
7727	0	81°.5	108^m.8	1189	1509

Structure
- Diameter: 135 ft (41 m)
- Thickness: 0.00035 mil (9.8 μ)
- Coating: Aluminum foil with Alodyne coating 4.5-μ thick (see fig. 5.2)
- Weight: 281 kg (618 lb)

Beacons: Two, 136.170 MHz and 136.020 MHz
Power: 35 mW output per beacon

TABLE 5.3.—*Characteristics of PAGEOS (1966 56A)*

Launch

Date: 24 June 1966
From: Western Test Range
Rocket: Thor Agena D

Orbital Elements: 01^h34^m00, 24 June 1966

a, km	e	i	Ω	ω	M_c
10 614.79	0.00248	86°.974	377°.125	248°.328	108°.411

Structure: 84 gores, 2 polar caps, vent holes (0.1587 mm in diameter) in caps

Diameter: 30 m
Thickness: 12 μ
Coating: vapor-deposited aluminum
Weight: 53 kg

Reflectivity: 0.36 λ to 0.7 λ

$R_{specular}$ 0.862 ± 0.0046
$R_{diffuse}$ 0.029 ± 0.0046
R_{total} 0.891 ± 0.0032

Reference: Bowker (1967); Roloff (1966); Teichmann (1968)

TABLE 5.4.—*Characteristics of GRARR*

Transmitter

Operating frequency:	2270.1328 MHz, channel C 2271.9328 MHz, channel A
Type of emission:	CW
Type of modulation:	Phase (by coherent range tones)
RF power output:	1 kW to 10kW
Power amplifier:	Klystron, 5-cavity, liquid-cooled

Antenna

Reflection and feed:	14-foot (4.6 m) parabola with Cassegrainian feed
Frequency:	1705 MHz nominal, receiving 2271 MHz nominal, transmitting
Beamwidth:	2.5 degrees, transmitting
Gain:	33 dB, receiving 35 dB, transmitting

Receiver

Carrier frequency:	1705.000 MHz
Intermediate frequencies:	60 MHz and 10 MHz (dual conversion)
Noise figure:	3 dB, max
Dynamic signal range:	−70 to −151 dBm

Distances are measured by measuring the phase shift in 8 (6) frequencies phase-modulated onto the UHF carriers. The modulating frequencies are

f(kHz)	λ (km)	f(Hz)	λ (km)
500	0.6	800	375
100	3.0	160	1 875
20	15.0	32	9 375
4	75.0	8	37 500

TABLE 5.5.—*Characteristics of Mobile Laser System*

Laser energy/pulse	0.5 Joule
Pulse width	15–25 nanoseconds
Repetition rate	1 pps
Beam divergence	⅓ milliradian
Receiver aperture	16 inches (40.6 cm)
Receiver field-of-view	⅓ milliradian
Spectral filter	10 Å at 6943 Å
Range resolution	10 nanoseconds (1.5 meters)
Timing accuracy	± 50 microseconds to USNO

TABLE 5.6.—*Satellites*

Satellite name	a (meters)	e	i (degrees)	Perigee hgt (km)	Period (rev/day)
TELSTAR-1	9 669 530.1	0.2421	44.79	951.3	9.13
TIROS-9	8 020 761.2	0.1167	96.42	706.7	12.09
GEOS-1	8 067 353.6	0.0725	59.37	1107.5	11.98
SECOR-5	8 154 869.9	0.0801	69.23	1140.1	11.79
OV1-2	8 314 700.2	0.1834	144.27	414.8	11.45
ALOU-2	8 097 474.4	0.1508	79.83	502.0	11.91
ECHO-1RB	7 968 879.1	0.0121	47.22	1501.0	12.20
D1-D	7 614 681.9	0.0842	39.45	589.0	13.07
BE-C	7 503 563.5	0.0252	41.17	941.9	13.36
D1-C	7 344 163.4	0.0526	40.00	586.6	13.79
ANNA-1B	7 504 950.8	0.0070	50.13	1075.8	13.35
GEOS-2	7 710 806.6	0.0308	105.79	1114.2	12.82
OSCAR-7	7 404 041.3	0.0242	89.70	847.7	13.63
5BN-2	7 463 226.9	0.0058	89.95	1062.5	13.47
COURIER-1B	7 473 289.0	0.0174	28.34	966.5	13.44
GRS	7 228 289.3	0.0604	49.72	421.3	14.13
TRANSIT-4A	7 321 521.7	0.0079	66.83	896.0	13.86
BE-B	7 304 785.0	0.0143	79.70	901.8	13.74
OGO-2	7 345 633.6	0.0739	87.37	424.8	13.79
INJUN-1	7 312 542.4	0.0076	66.81	895.0	13.88
AGENA-R	7 297 251.5	0.0010	69.91	920.2	13.93
MIDAS-4	9 995 760.5	0.0121	95.84	3504.8	8.69
VANGUARD-2	8 306 759.8	0.1645	32.89	566.7	11.47
VANGUARD-2S	8 309 120.5	0.1648	32.87	562.2	11.46
VANGUARD-3S	8 511 504.6	0.1906	33.35	517.9	11.06
SAS	6 922 505.3	0.0030	3.03	523.5	15.07
PEOLE	7 006 154.9	0.0162	15.01	515.4	14.80

TABLE 5.7.—*Constants Describing the Coordinate System and Gravity*[a]

Mean equatorial radius	$a_e = 6\,378\,155$ m
Flattening	$f = 1/298.255$
Rotation rate	$\omega = 0.7292115146 \times 10^{-4}$ rad/sec
Geocentric gravitational constant	$GM = 3.986013 \times 10^{14}$ m^3/sec^2
Mean equatorial gravity	$G_e = 978\,029.1$ mGal

[a] The z-axis is parallel to that passing through the CIO, and the x-axis is defined by the BIH's conventional longitude.

TABLE 5.8.—*Weights Assigned to the Observations*

Observation	Standard deviation
GRARR: range	8 meters
range-rate	3 cm/sec
Laser: range	8 meters
Camera: declination (δ)	2″
right ascension ($\alpha \cos \delta$)	2″
MINITRACK: direction cosines	3×10^{-4}
NWL Doppler: range-rate	4 cm/sec
C-band radar: range	10 meters
Surface-gravity data	See table 5.7

TABLE 5.9.—*Assumed Values of Normalized Gravitational Potential* ($\times 10^6$)

Zonals

Index n	m	Value	Index n	m	Value	Index n	m	Value	Index n	m	Value	Index n	m	Value
2	0	−484.1669	3	0	0.9593	4	0	0.5310	5	0	0.0693	6	0	−0.1392
7	0	0.0935	8	0	0.0286	9	0	0.0229	10	0	0.0772	11	0	−0.0421
12	0	0.0084	13	0	0.0237	14	0	0.0136	15	0	0.0313	16	0	−0.0328
17	0	−0.0144	18	0	0.0380	19	0	0.0346	20	0	0.0008	21	0	−0.0220

Sectorials and tesserals

Index		Value		Index		Value		Index		Value	
n	m	$\bar{C}$	$\bar{S}$	n	m	$\bar{C}$	$\bar{S}$	n	m	$\bar{C}$	$\bar{S}$
2	2	2.3796	−1.3509	3	1	1.9359	0.2557	3	2	0.7349	−0.5387
3	3	0.5608	1.6207	4	1	−0.5724	−0.4691	4	2	0.3300	0.6619
4	3	0.8517	−0.1908	4	4	−0.0530	0.2300	5	1	−0.0791	−0.1030
5	2	0.6303	−0.2317	5	3	−0.5207	0.0070	5	4	−0.2646	0.0640
5	5	0.1560	−0.5930	6	1	−0.0470	−0.0269	6	2	0.0690	−0.3657
6	3	−0.0540	0.0310	6	4	−0.0441	−0.5178	6	5	−0.3135	−0.4585
6	6	−0.0400	−0.1549	7	1	0.1967	0.1558	7	2	0.3644	0.1626
7	3	0.2499	0.0180	7	4	−0.1321	−0.1022	7	5	0.0760	0.0540
7	6	−0.2089	0.0630	7	7	0.0550	0.0970	8	1	−0.0757	0.0655
8	2	0.0260	0.0390	8	3	−0.0370	0.0040	8	4	−0.2122	−0.0120
8	5	−0.0530	0.1182	8	6	−0.0170	0.3180	8	7	−0.0087	0.0310
8	8	−0.2479	0.1020	9	1	0.1170	0.0121	9	2	−0.0040	0.0349
9	9	0.1854	0.2099	10	1	0.1050	−0.1261	10	2	−0.1049	−0.0420
10	3	−0.0650	0.0300	10	4	−0.0740	−0.1110	10	9	0.1036	−0.0644
11	1	−0.0530	0.0149	11	11	0.0257	0.0560	12	1	−0.1630	−0.0707
12	2	−0.1030	−0.0050	12	11	−0.0541	−0.3107	12	12	−0.0327	−0.0054
13	12	−0.0697	0.0751	13	13	−0.0552	0.1243	14	1	−0.0150	0.0053
14	11	0.0002	−0.0001	14	12	0.0033	−0.0276	14	13	0.0231	0.0550
14	14	−0.0458	−0.0254	15	9	−0.0009	−0.0018	15	12	−0.0764	−0.0012
15	13	−0.0225	0.0306	15	14	0.0021	−0.0222	16	14	−0.0168	0.0007
17	13	0.0365	0.0491	17	14	−0.0135	−0.0017				

TABLE 5.10.—*Observations by Baker-Nunn Cameras in Seven-day Arcs Used for Potential and Station Coordinate Estimation*

	SAO Baker-Nunn Stations																					
Satellite	9001	9002	9003	9004	9005	9006	9007	9008	9009	9010	9011	9012	9021	9023	9025	0928	9031	9050	9091	9424	9425	9426	9427
TELSTAR 1	135	117	101	57	55	73	65	71	71	44	78	103											
GEOS 1	996	658		779	66	138	429	107	307	1127	424	255		809				96		108		15	13
SECOR 5	11	22		9	2	11	7	10	11	6	23	10		23									
OVI 2	57	35		35	16	63	43			48	2	30		69		66							
ECHO 1RB	68	121	202	97	59	51	63	112	56	83	158	50											
DID	789	73		603	67	534	53			327		245		134		139	85			6	69		65
BE C	170	340		179	10	434	73	60	47	148	145	171		503		37	95				27		10
DIC	42	44		40	21	70	5			55		43		95		7					15		15
ANNA 1B	350	143		150		168		51	88		238	109		210									
GEOS 2		572		843		80	321			68		371	331	370	66	204	438		894	14	183		34
OSCAR 7	28	59		34		176	97	49	47	17	93	207		123									
5BN 2	27	24		3	5	19	9	11	16	8	18	18		21									
COURIER 1B	52	168		106	36	154	176			125		132		243		218	47						
GRS	30	6		34			12	31	7	9	13	18		15									
TRANSIT 4A	93	82	142	64	31	10	26	16	21	33	64	59											
BE B	11	26		26	1	1	5			25		10		57		12	60						
OGO 2	37	7		30	7	21	13	27	12	15	9	43		4						3			3
INJUN 1	33	62	36	18	54		3	15	41	22	21	75											
AGENA R	90	46	33	51	5	36	47	16	16	47	51	51		21									
MIDAS 4	1180	74		675	530	820	212	595	573	631	169	650		118						323		255	576
VANG-2-ROC	19	21	18	1	5	17	18	8	11		24	27		20									
VANG-2-SAT	72	16	13	101	10	30	17	6	12	14	6	8											
VANG-3-SAT	16	51	120	51	25	4	17	9	48	30	63	36											
Total	4306	2767	665	3986	1005	2910	1711	1194	1381	2882	1599	2721	331	2835	66	683	725	96	894	454	294	270	716

TABLE 5.11.—*Observations in Seven-Day Arcs Used for Potential and Station Coordinate Estimation*[a]

Station	GEOS-		GEOS-2		BE-B		BE-C		DI-C		DI-D		PEOPLE	
	Arcs	Passes	Arcs	Passes	Arcs	Passes	Arcs	Passes	Arcs	Passes	Arcs	Passes	Arcs	Passes
R and RR														
1122 Tananarive			3	8										
1123 Tananarive			2	5										
1126 Rosman			11	85										
1128 Fairbanks			11	125										
1152 Carnarvon			11	63										
Doppler														
2014 Anchorage	12	472												
2017 Tafuna	9	245			5	120	4	150						
2018 Thule			11	528	5	263								
2019 Antarctica	9	122			2	39								
2100 Wahiawa	12	352					4	143						
2103 Las Cruces	12	407					4	132						
2106 Lasham	12	476												
2111 Howard County	12	513					4	127						
2115 Pretoria			4	108										
2117 Tafuna			10	145										
2203 Wallops			5	67										
2722 Ascension					3	63	4	160						
2723 Cocos Is.					4	62	1	2						
2738 Moses Lake							4	128						
2739 Shemya	1	40												
2742 Beltsville	2	75												
2745 Stoneville	2	70												
2815 Paramaribo			3	15										
2817 Mashhad			3	74										
2820 Villa Dolores			4	48										
2822 Ft. Lamy				24										
2837 Natal			5	68										
C-band														
4050 Pretoria			1	3										
4082 Merritt Is.			1	15										
4740 Bermuda			1	12										
4741 Tananarive			1	4										
4760 Bermuda			1	12										
4840 Wallops			1	16										
4860 Wallops			1	25										
4946 Woomera			1	12										
Laser														
7050 Greenbelt			3	12			2	7	2	5	1	7		
7052 Wallops			5	15										
7053 Greenbelt			1	4										
7054 Carnarvon			1	4										
7060 Guam													1	8
9020 Dakar													1	2
9901 Organ Pass					1	5	2	6	2	13	1	20		
9907 Arequipa													3	19
9929 Natal													4	47

TABLE 5.11.—*(Cont'd)*

Station	GEOS–1		GEOS–2		BE–B		BE–C		DI–C		DI–D		PEOPLE	
	Arcs	Passes	Arcs	Passes	Arcs	Passes	Arcs	Passes	Arcs	Passes	Arcs	Passes	Arcs	Passes
Optical														
1021 Blossom Pt	9	20	1	3										
1022 Ft. Myers	9	49	9	40										
1024 Woomera	3	17												
1028 Santiago	1	2	9	26										
1030 Goldstone	9	47	11	68										
1031 Johannesburg	4	11	9	21										
1032 St. John's	1	1	1	3										
1034 E. Grand Fk	6	28												
1035 Winkfield	1	3	8	19										
1036 Fairbanks			3	6										
1037 Rosman			12	56										
1038 Orroral			7	27										
1042 Rosman	7	25	5	20										
1043 Tananarive	3	6	5	8										
7034 E. Grand Fk			10	30										
7036 Edinburg	6	30	10	37										
7037 Columbia	6	21	10	50										
7039 Bermuda	5	16	10	31										
7040 San Juan	3	7	10	27										
7043 Greenbelt	6	14												
7072 Jupiter	3	11												
7075 Sudbury	6	18	9	25										
7076 Kingston	3	14	9	27										
9001 Organ Pass	10	82	1	6	1	6	2	14	2	29	1	29		
9002 Olifants	8	27	7	27			1	2	1	3				
9004 San Fernando	11	58	4	41	1	4	2	5	2	13	1	15		
9005 Tokyo	5	11							2	6	1	4		
9006 Naini Tal	8	82	2	7	1	6	2	15	1	15	1	25		
9007 Arequipa	5	19	6	20					1	5	1	3		
9008 Shiraz	5	25												
9009 Curacao	3	14												
9010 Jupiter	9	44	1	1	1	2	2	8	2	14	1	16		
9011 Villa Dolores	6	27												
9012 Maui	4	30					1	2						
9023 Woomera	7	34	6	19			1	5						

[a] Minitrack data from SAS satellite not included in this listing

TABLE 5.12.—*Seven Day Electronic-Optical Arcs Used in GEM Solutions (by Satellite and Time Period)*[a]

Satellite	Time period	Number of stations (1) and station passes (2) used							
		GRARR		Doppler		Laser		Camera	
		(1)	(2)	(1)	(2)	(1)	(2)	(1)	(2)
DIC	4/22/67 to 4/28/67					2	6	6	25
DIC	4/30/67 to 5/ 8/67					2	12	8	68
DID	5/ 9/67 to 5/17/67					2	27	7	98
BE-B	12/23/64 to 12/29/64			4	113				
BE-B	1/ 2/65 to 1/ 8/65			4	122				
BE-B	1/25/65 to 1/31/65			4	124				
BE-B	2/24/65 to 3/ 3/65			4	85				
BE-B	3/21/65 to 3/28/65			3	108				
BE-B	5/12/67 to 5/19/67			1	2	1	5	4	18
BE-C	6/29/65 to 7/ 6/65			6	203				
BE-C	7/ 9/65 to 7/15/65			6	216				
BE-C	7/25/65 to 7/31/65			6	221				
BE-C	8/29/65 to 9/ 5/65			6	200				
BE-C	4/ 2/67 to 4/10/67					2	6	5	30
BE-C	4/20/67 to 4/27/67					2	7	6	23
GEOS-1	11/17/65 to 11/24/65			8	271			10	39
GEOS-1	11/25/65 to 12/ 1/65			8	237			16	70
GEOS-1	1/21/66 to 1/27/66			8	311			16	59
GEOS-1	1/28/66 to 2/ 5/66			8	213			22	68
GEOS-1	4/17/66 to 4/24/66			7	284			27	133
GEOS-1	5/11/66 to 5/18/66			6	243			13	67
GEOS-1	6/16/66 to 6/23/66			6	234			6	6
GEOS-1	7/ 2/66 to 7/ 9/66			7	258			7	16
GEOS-1	7/23/66 to 7/30/66			7	185			15	94
GEOS-1	8/13/66 to 8/21/66			6	217			17	68
GEOS-1	10/29/66 to 11/ 5/66			6	208			3	7
GEOS-1	11/15/66 to 11/22/66			6	142			12	55
GEOS-2	2/25/68 to 3/ 1/68	3	12	4	47	1	1	23	81
GEOS-2	3/16/68 to 3/24/68	4	29	3	50			23	82
GEOS-2	3/28/68 to 4/ 4/68	4	23	4	40	1	2	24	92
GEOS-2	4/22/68 to 4/29/68	4	25	3	116	1	3	27	82
GEOS-2	6/ 3/68 to 6/10/68	3	29	5	110	1	4	22	73
GEOS-2	6/13/68 to 6/19/68	1	2	6	141	1	3	27	132
GEOS-2	6/21/68 to 6/28/68	3	33	5	136	1	3	28	140
GEOS-2	7/12/68 to 7/18/68	3	45	4	107			1	2
GEOS-2	7/25/68 to 8/ 1/68	4	30	4	92			15	41
GEOS-2	8/ 9/68 to 8/16/68	3	18	4	131			8	15
GEOS-2	8/31/68 to 9/ 7/68	3	20	3	31	1	5	22	67
GEOS-2	10/19/68 to 10/26/68	3	20	2	51	1	4	22	73
GEOS-2[b]	2/ 5/69 to 2/12/69					2	10		
PEOLE[c]	6/ 3/71 to 6/ 5/71					4	13		
PEOLE	6/ 6/71 to 6/10/71					1	9		
PEOLE	6/11/71 to 6/15/71					2	41		
PEOLE	6/16/71 to 6/19/71					2	13		

[a] In addition to the above arcs, four SAS-A arcs, nine TIROS arcs, and two ALOUETTE arcs with MINITRACK data only were used in the GEM solutions

[b] C-band tracking data from 8 stations with 105 station passes are also included.

[c] MINITRACK data were also used with each PEOLE arc.

TABLE 5.13.—*MOTS and SPEOPTS Camera Observations in Seven-Day Arcs Used for GEM Gravitational and Station Solutions*

Station	GEOS-1	GEOS-2
1021 Blossom Pt.	636	
1022 Ft. Myers	1737	1021
1024 Woomera	616	
1028 Santiago	233	382
1030 Goldstone	1569	1405
1031 Johannesburg	690	328
1032 St. John's	46	56
1033 Fairbanks	129	
1034 East Grand Forks	1531	
1035 Winkfield	145	263
1036 Fairbanks		434
1037 Rosman	112	1179
1038 Orroral		617
1042 Rosman	861	421
1043 Tananarive	95	170
7034 East Grand Forks		564
7036 Edinburg	1272	704
7037 Columbia	1765	1074
7039 Bermuda	651	555
7040 San Juan	914	472
7043 Greenbelt	601	
7045 Denver	1349	999
7071 Jupiter	145	
7072 Jupiter	615	
7073 Jupiter	108	
7074 Jupiter	151	
7075 Sudbury	484	47
7076 Kingston	638	20
7077 Greenbelt	90	41
7079 Carnarvon		14

TABLE 5.14.—*Station Passes in Two-Day Arcs Used for GEM Station Position Solutions*

Station	GEOS 1	GEOS 2	Station	GEOS 1	GEOS 2
MOTS			2817 Mashhad		84
1021 Blossom Pt.	49		2822 Fort Lamy		26
1022 Ft. Myers	68	50	2837 Natal		27
1024 Woomera	31		SPEOPTS		
1028 Santiago	12	35	7034 East Grand Forks		35
1030 Goldstone	76	87	7036 Edinburg	45	33
1031 Johannesburg	26	28	7037 Columbia	78	40
1032 St. John's	6	15	7039 Bermuda	25	28
1034 East Grand Forks	70		7040 San Juan	47	30
1035 Winkfield	4	16	7043 Greenbelt	42	
1036 Fairbanks		53	7045 Denver	63	37
1037 Rosman		78	7050 Greenbelt (laser)		25
1038 Orroral		31	7052 Wallops (laser)		13
1042 Rosman	60		7054 Carnarvon (laser)		33
1043 Tananarive	4	13	7072 Jupiter	36	
GRARR			7075 Sudbury	13	14
1123 Tananarive		14	7076 Kingston	18	22
1126 Rosman		34	Baker-Nunn		
1128 Fairbanks		95	9001 Organ Pass	47	
1152 Carnarvon		43	9002 Olifantsfontein	44	38
Doppler			9004 San Fernando	42	62
2014 Anchorage	149		9005 Tokyo	31	
2017 Tafuna	81		9006 Naini Tal	51	11
2018 Thule		253	9007 Arequipa	24	45
2100 Wahiawa	119		9008 Shiraz	48	
2103 Las Cruces	135		9009 Curaçao	26	
2106 Lasham	139		9010 Jupiter	39	4
2111 Howard County	152		9011 Villa Dolores	35	
2115 Pretoria		26	9012 Maui	50	32
2117 Tafuna		81	9023 Woomera	41	42

TABLE 5.15.—*Summary of Simultaneous Observations used for Geometrical Station Asjustment*

Event Type	Number of events
MOTS–SPEOPTS–LASER system data (U.S. area)	
Two-camera	3870
Three-camera	1614
Four-camera	584
Laser/two-camera	42
BC–4 World geometric network data	
Two-camera	5896
Three-camera	1332
Four-camera	99

TABLE 5.16—*Average Gravity Anomalies (Δg) Over 550-km by 550-km Areas According to R. Rapp (1972a)*[a]

ϕ	λ	Δg	M	N	ϕ	λ	Δg	M	N	ϕ	λ	Δg	M	N	ϕ	λ	Δg	M	N	ϕ	λ	Δg	M	N
87.5	60.0	2.	13.	3	87.5	180.0	5.	7.	13	87.5	300.0	4.	8.	8	82.5	20.0	10.	10.	7	82.5	60.0	18.	14.	2
82.5	180.0	−1.	6.	16	82.5	220.0	5.	4.	20	82.5	260.0	6.	10.	7	82.5	300.0	−12.	5.	15	82.5	340.0	9.	13.	4
77.5	11.5	−8.	10.	8	77.5	34.0	−2.	12.	3	77.5	56.5	−10.	9.	5	77.5	79.0	−9.	12.	4	77.5	146.5	−15.	15.	1
77.5	169.0	−7.	10.	7	77.5	191.5	4.	3.	24	77.5	214.0	−12.	2.	25	77.5	236.5	−2.	2.	25	77.5	259.0	−8.	2.	25
77.5	281.5	1.	5.	18	77.5	304.0	15.	6.	12	77.5	326.5	−8.	8.	7	77.5	349.0	19.	11.	4	72.5	8.0	17.	10.	10
72.5	24.5	−3.	5.	19	72.5	41.0	0.	12.	3	72.5	57.0	−7.	7.	11	72.5	73.5	−8.	10.	5	72.5	90.0	−7.	10.	9
72.5	106.5	−11.	4.	20	72.5	123.0	5.	3.	25	72.5	172.0	−1.	15.	1	72.5	188.0	−4.	6.	16	72.5	204.5	−16.	3.	25
72.5	221.0	−12.	2.	25	72.5	237.0	−8.	4.	19	72.5	253.5	−19.	6.	18	72.5	270.0	−6.	3.	23	72.5	286.5	−3.	4.	22
72.5	303.0	−6.	5.	16	72.5	319.0	16.	11.	7	72.5	335.5	9.	9.	8	72.5	352.0	13.	13.	2	67.5	6.5	11.	4.	24
67.5	19.5	−1.	2.	24	67.5	32.5	0.	7.	10	67.5	45.0	−3.	10.	6	67.5	57.5	−8.	9.	7	67.5	83.5	−9.	5.	18
67.5	96.5	−16.	3.	25	67.3	109.5	−23.	3.	25	67.5	122.5	−20.	3.	25	67.5	135.0	3.	3.	25	67.5	147.5	8.	3.	25
67.5	150.5	13.	3.	25	67.5	173.5	19.	3.	25	67.5	186.5	2.	3.	25	67.5	199.5	−3.	3.	22	67.5	212.5	14.	3.	25
67.5	225.0	4.	4.	21	67.5	237.5	−3.	2.	25	67.5	250.5	−24.	2.	25	67.5	263.5	−29.	7.	14	67.5	276.5	−34.	5.	15
67.5	289.5	−20.	2.	25	67.5	302.5	19.	3.	25	67.5	315.0	1.	12.	5	67.5	327.5	20.	12.	3	67.5	340.5	27.	9.	11
62.5	5.5	11.	2.	25	62.5	16.5	−10.	2.	24	62.5	27.5	−7.	4.	23	62.5	38.5	−1.	4.	19	62.5	49.5	1.	4.	20
62.5	60.0	−4.	12.	4	62.5	70.5	−11.	13.	2	62.5	81.5	−19.	5.	18	62.5	92.5	−30.	3.	25	62.5	103.5	−37.	4.	25
62.5	114.5	−27.	3.	25	62.5	125.5	−24.	3.	25	62.5	136.5	1.	3.	25	62.5	147.5	19.	3.	25	62.5	158.5	17.	4.	24
62.5	169.5	24.	4.	22	62.5	180.0	14.	11.	6	62.5	190.5	−2.	5.	19	62.5	201.5	12.	5.	19	62.5	212.5	24.	3.	24
62.5	223.5	27.	6.	17	62.5	234.5	10.	5.	18	62.5	245.5	−19.	2.	25	62.5	256.5	−31.	2.	25	62.5	267.5	−39.	3.	25
62.5	278.5	−28.	3.	25	62.5	289.5	−12.	3.	21	62.5	300.0	3.	4.	19	62.5	310.5	−12.	5.	17	62.5	321.5	6.	14.	3
62.5	332.5	27.	9.	9	62.5	343.5	27.	5.	18	62.5	354.5	16.	5.	19	57.5	4.5	1.	2.	24	57.5	13.5	0.	1.	25
57.5	23.0	−16.	5.	18	57.5	32.5	−2.	3.	24	57.5	41.5	2.	5.	18	57.5	50.5	6.	4.	19	57.5	60.0	7.	2.	25
57.5	69.5	−17.	2.	25	57.5	78.5	−17.	2.	25	57.5	87.5	−17.	3.	25	57.5	97.0	−30.	3.	25	57.5	106.5	−16.	4.	25
57.5	115.5	−36.	3.	25	57.5	124.5	−33.	3.	25	57.5	133.5	−10.	3.	25	57.5	143.0	2.	12.	5	57.5	152.5	12.	13.	3
57.5	161.5	17.	4.	22	57.5	170.5	4.	7.	13	57.5	130.0	−15.	8.	12	57.5	189.5	12.	5.	20	57.5	198.5	25.	9.	10
57.5	207.5	9.	3.	24	57.5	217.0	6.	6.	15	57.5	226.5	12.	5.	18	57.5	235.5	13.	4.	20	57.5	244.5	−5.	3.	25
57.5	253.5	−13.	2.	25	57.5	263.0	−26.	2.	25	57.5	272.5	−40.	3.	25	57.5	281.5	−39.	3.	25	57.5	290.5	−27.	3.	24
57.5	300.0	−15.	6.	16	57.5	309.5	7.	3.	9	57.5	318.5	6.	12.	5	57.5	327.6	24.	11.	5	57.5	346.5	5.	8.	12
57.5	355.5	16.	3.	24	52.5	4.0	−7.	1.	25	52.5	12.0	8.	1.	25	52.5	20.5	0.	2.	23	52.5	29.0	4.	3.	24
52.5	37.0	0.	4.	21	52.5	45.0	−2.	4.	22	52.5	53.0	−8.	3.	25	52.5	61.0	4.	1.	25	52.5	69.5	−1.	6.	15
52.5	78.0	−21.	3.	23	52.5	86.0	−11.	3.	25	52.5	94.0	−23.	3.	25	52.5	102.0	−33.	3.	25	52.5	110.5	−10.	10.	7
52.5	119.0	3.	12.	4	52.5	127.0	4.	10.	8	52.5	159.5	15.	8.	12	52.5	168.0	6.	8.	9	52.5	176.0	−4.	4.	24
52.5	184.0	−24.	3.	24	52.5	192.0	3.	3.	23	52.5	200.5	−1.	6.	13	52.5	209.0	7.	13.	3	52.5	217.0	5.	9.	8
52.5	225.0	−2.	5.	20	52.5	233.0	12.	2.	25	52.5	241.0	6.	2.	25	52.5	249.5	−3.	1.	25	52.5	258.0	1.	2.	25
52.5	266.0	−9.	2.	25	52.5	274.0	−26.	2.	25	52.5	232.0	−32.	3.	24	52.5	290.5	−10.	2.	25	52.5	290.0	−20.	3.	25
52.5	307.0	−1.	5.	20	52.5	323.0	21.	9.	9	52.5	331.0	12.	10.	7	52.5	339.5	−3.	12.	4	52.5	348.0	15.	5.	21
52.5	356.0	11.	3.	24	47.5	3.5	5.	1.	25	47.5	11.0	10.	0.	25	47.5	18.5	18.	2.	24	47.5	25.5	20.	4.	21
47.5	33.0	9.	3.	24	47.5	40.5	−4.	3.	25	47.5	47.5	−14.	6.	14	47.5	55.0	−23.	6.	14	47.5	62.5	−11.	5.	15
47.5	69.5	−14.	2.	25	47.5	77.0	−27.	3.	25	47.5	84.5	−35.	3.	25	47.5	92.0	−16.	3.	25	47.5	99.5	−20.	4.	25
47.5	106.5	0.	9.	10	47.5	114.0	−4.	12.	5	47.5	121.5	10.	6.	13	47.5	128.5	8.	6.	15	47.5	136.0	6.	10.	7
47.5	143.5	−1.	10.	10	47.5	165.5	13.	14.	1	47.5	172.5	5.	9.	9	47.5	180.0	11.	10.	10	47.5	187.5	16.	9.	10
47.5	194.5	12.	10.	6	47.5	202.1	6.	9.	8	47.5	209.5	−2.	11.	4	47.5	216.5	−5.	12.	3	47.5	224.0	−2.	10.	8
47.5	231.5	−10.	4.	23	47.5	238.5	−7.	1.	25	47.5	246.0	8.	1.	25	47.5	253.5	14.	2.	25	47.5	260.5	7.	2.	25
47.5	268.0	2.	1.	25	47.5	275.5	−11.	1.	25	47.5	283.0	−15.	2.	25	47.5	290.5	−7.	1.	25	47.5	297.5	−10.	2.	25
47.5	305.0	12.	3.	24	47.5	312.5	18.	4.	22	47.5	319.5	6.	4.	20	47.5	327.0	23.	3.	24	47.5	334.5	35.	5.	20
47.5	341.5	16.	4.	22	47.5	349.0	4.	3.	24	47.5	356.5	0.	2.	25	42.5	3.5	12.	3.	23	42.5	10.5	13.	3.	23
42.5	17.0	22.	4.	20	42.5	23.5	21.	7.	11	42.5	30.5	−8.	6.	15	42.5	37.5	−23.	5.	17	42.5	44.5	10.	5.	16
42.5	51.0	−30.	11.	6	42.5	57.5	−7.	3.	20	42.5	64.5	−20.	2.	25	42.5	71.5	−32.	3.	25	42.5	78.5	−7.	4.	25
42.5	85.0	−20.	4.	25	42.5	91.5	−28.	4.	25	42.5	98.5	−5.	4.	25	42.5	105.5	4.	9.	10	42.5	112.0	−2.	14.	2
42.5	118.5	4.	12.	4	42.5	125.5	18.	5.	16	42.5	132.5	4.	5.	18	42.5	139.5	13.	3.	25	42.5	146.0	−17.	7.	16
42.5	166.5	−2.	13.	3	42.5	173.5	4.	10.	7	42.5	130.0	1.	12.	3	42.5	186.5	−5.	13.	2	42.5	193.5	−3.	15.	1
42.5	200.5	−4.	7.	12	42.5	207.5	0.	11.	4	42.5	214.0	−1.	13.	3	42.5	220.5	−11.	9.	11	42.5	227.5	−7.	6.	20
42.5	234.5	−11.	2.	25	42.5	241.5	10.	1.	25	42.5	248.0	22.	1.	25	42.5	254.5	15.	2.	25	42.5	261.5	−2.	2.	25

42.5	268.5	−10.	0.	25	42.5	275.0	−11.	1.	25	42.5	281.5	−11.	1.	25	42.5	288.5	0.	1.	25	42.5	295.5	−6.	4.	25
42.5	302.5	−18.	4.	25	42.5	309.0	12.	5.	19	42.5	315.5	4.	4.	23	42.5	322.5	13.	3.	25	42.5	329.5	27.	4.	25
42.5	336.5	25.	3.	25	42.5	343.0	2.	3.	24	42.5	349.5	5.	3.	23	42.5	356.5	8.	2.	25	37.5	3.0	14.	4.	21
37.5	9.5	23.	5.	18	37.5	16.0	7.	4.	23	37.5	22.0	−3.	7.	14	37.5	28.5	−1.	8.	11	37.5	35.0	25.	9.	11
37.5	41.0	9.	8.	8	37.5	47.5	42.	5.	13	37.5	54.0	1.	6.	17	37.5	60.0	−15.	3.	25	37.5	66.0	−25.	4.	23
37.5	72.5	−6.	4.	24	37.5	79.0	−11.	4.	25	37.5	35.0	−8.	4.	25	37.5	91.5	9.	4.	25	37.5	98.0	10.	5.	23
37.5	104.0	6.	7.	15	37.5	110.5	−13.	10.	6	37.5	117.0	−18.	8.	9	37.5	123.0	8.	8.	10	37.5	129.5	14.	4.	20
37.5	136.0	24.	3.	25	37.5	142.0	23.	3.	24	37.5	148.5	1.	9.	9	37.5	155.0	3.	8.	8	37.5	161.0	−2.	6.	13
37.5	167.5	−3.	9.	8	37.5	174.0	1.	11.	7	37.5	180.0	−3.	13.	3	37.5	192.5	−9.	11.	5	37.5	199.0	−7.	9.	8
37.5	205.0	−4.	7.	13	37.5	211.5	4.	10.	10	37.5	218.0	−20.	5.	21	37.5	224.0	−18.	7.	15	37.5	230.5	−25.	2.	25
37.5	237.0	−17.	1.	25	37.5	243.0	−1.	1.	25	37.5	249.5	7.	2.	25	37.5	256.0	9.	2.	25	37.5	262.0	−11.	3.	25
37.5	268.5	−7.	1.	25	37.5	275.0	−5.	0.	25	37.5	281.0	−0.	1.	25	37.5	287.5	−22.	2.	25	37.5	294.0	−22.	4.	22
37.5	300.0	−17.	5.	19	37.5	306.0	−14.	5.	20	37.5	312.5	−2.	4.	21	37.5	319.0	16.	4.	25	37.5	325.0	33.	4.	25
37.5	331.5	40.	3.	25	37.5	338.0	15.	4.	23	37.5	344.0	5.	5.	17	37.5	350.5	6.	4.	22	37.5	357.0	11.	3.	25
32.5	3.0	3.	1.	25	32.5	9.0	−10.	4.	19	32.5	15.0	0.	5.	18	32.5	21.0	8.	6.	16	32.5	27.0	−35.	4.	24
32.5	32.5	−17.	4.	25	32.5	38.0	25.	5.	17	32.5	44.0	−4.	12.	5	32.5	50.0	13.	4.	23	32.5	56.0	17.	4.	25
32.5	62.0	25.	7.	15	32.5	68.0	12.	7.	14	32.5	74.0	−38.	3.	25	32.5	80.0	42.	4.	25	32.5	86.0	24.	5.	25
32.5	91.5	8.	5.	25	32.5	97.0	11.	4.	25	32.5	103.0	−10.	5.	20	32.5	109.0	−22.	10.	7	32.5	115.0	−26.	7.	14
32.5	121.0	0.	9.	9	32.5	127.0	17.	9.	10	32.5	133.0	19.	6.	14	32.5	139.0	−20.	5.	17	32.5	145.0	−4.	7.	14
32.5	150.5	−5.	9.	9	32.5	156.0	−7.	7.	12	32.5	162.0	−13.	8.	11	32.5	168.0	−16.	8.	9	32.5	174.0	−10.	12.	5
32.5	180.0	−4.	14.	1	32.5	186.0	−24.	11.	6	32.5	192.0	−14.	13.	3	32.5	198.0	−4.	8.	9	32.5	204.0	−4.	13.	4
32.5	209.5	−3.	7.	13	32.5	215.0	−13.	11.	8	32.5	221.0	−9.	6.	17	32.5	227.0	−18.	4.	23	32.5	233.0	−19.	7.	15
32.5	239.0	−22.	3.	23	32.5	245.0	−12.	2.	25	32.5	251.0	−1.	2.	25	32.5	257.0	−4.	2.	25	32.5	263.0	−7.	3.	25
32.5	268.5	0.	3.	25	32.5	274.0	−2.	2.	25	32.5	280.0	−5.	2.	24	32.5	286.0	−38.	4.	22	32.5	292.0	−26.	4.	22
32.5	298.0	−9.	4.	22	32.5	304.0	−15.	5.	20	32.5	310.0	−4.	5.	20	32.5	316.0	10.	4.	23	32.5	322.0	27.	4.	24
32.5	327.5	17.	7.	14	32.5	333.0	5.	10.	10	32.5	339.0	−3.	7.	13	32.5	345.0	5.	4.	23	32.5	351.0	26.	3.	23
32.5	357.0	41.	2.	25	27.5	3.0	−10.	1.	25	27.5	8.5	4.	3.	23	27.5	14.0	3.	8.	9	27.5	20.0	2.	8.	12
27.5	25.5	1.	8.	11	27.5	31.0	6.	7.	13	27.5	36.5	1.	7.	12	27.5	42.0	6.	9.	11	27.5	48.0	−10.	4.	23
27.5	53.5	−15.	4.	25	27.5	59.0	8.	4.	25	27.5	55.0	8.	4.	24	27.5	70.5	−10.	3.	25	27.5	76.0	−18.	3.	25
27.5	81.5	−71.	4.	24	27.5	87.0	−27.	4.	25	27.5	93.0	−31.	4.	25	27.5	98.5	−7.	5.	25	27.5	104.0	−25.	5.	21
27.5	110.0	−20.	7.	14	27.5	115.5	−8.	8.	10	27.5	121.0	4.	8.	9	27.5	126.5	26.	8.	9	27.5	132.0	−17.	13.	3
27.5	138.0	16.	8.	9	27.5	143.5	−11.	11.	5	27.5	149.0	0.	13.	4	27.5	155.0	29.	10.	8	27.5	160.5	−4.	14.	3
27.5	166.0	−9.	11.	6	27.5	171.5	−9.	9.	10	27.5	177.0	−4.	10.	9	27.5	183.0	−13.	13.	3	27.5	188.5	−1.	8.	12
27.5	194.0	6.	10.	7	27.5	200.0	8.	10.	5	27.5	205.5	−2.	11.	7	27.5	211.0	−5.	6.	16	27.5	216.5	2.	7.	15
27.5	222.0	−13.	10.	10	27.5	228.0	−14.	10.	6	27.5	233.5	−17.	9.	8	27.5	239.0	−23.	8.	12	27.5	245.0	−18.	5.	21
27.5	250.5	−7.	2.	25	27.5	256.0	15.	1.	25	27.5	261.5	−4.	1.	25	27.5	267.0	−9.	2.	25	27.5	273.0	−2.	4.	20
27.5	278.5	3.	2.	25	27.5	284.0	−18.	5.	21	27.5	290.0	−25.	7.	11	27.5	295.5	−17.	5.	16	27.5	301.0	−29.	5.	20
27.5	306.5	−21.	4.	22	27.5	312.0	−2.	4.	21	27.5	318.0	8.	5.	18	27.5	323.5	−2.	4.	22	27.5	329.0	0.	5.	21
27.5	335.0	−10.	5.	20	27.5	340.5	0.	5.	20	27.5	346.0	14.	5.	18	27.5	351.5	11.	5.	18	27.5	357.0	−3.	6.	17
22.5	2.5	20.	2.	25	22.5	8.0	26.	2.	25	22.5	13.5	3.	3.	25	22.5	18.5	3.	5.	17	22.5	24.0	−17.	7.	13
22.5	29.5	4.	15.	1	22.5	35.0	−3.	9.	11	22.5	40.5	33.	9.	8	22.5	45.5	−10.	11.	6	22.5	51.0	−31.	4.	21
22.5	56.5	−15.	13.	3	22.5	67.0	−6.	8.	11	22.5	72.5	2.	3.	25	22.5	78.0	1.	3.	25	22.5	83.5	−1.	4.	25
22.5	88.5	−9.	4.	21	22.5	94.0	−22.	5.	23	22.5	99.5	−19.	5.	25	22.5	104.5	−19.	5.	20	22.5	110.0	−11.	7.	11
22.5	115.5	−9.	9.	8	22.5	121.0	0.	7.	10	22.5	126.5	−1.	7.	12	22.5	131.5	1.	11.	6	22.5	137.0	1.	9.	6
22.5	142.5	1.	11.	4	22.5	153.0	8.	13.	4	22.5	158.5	−13.	10.	7	22.5	164.0	−10.	10.	5	22.5	174.5	−6.	11.	5
22.5	180.0	−9.	8.	13	22.5	185.5	2.	8.	10	22.5	190.5	6.	6.	15	22.5	196.0	10.	6.	13	22.5	201.5	24.	6.	17
22.5	207.0	5.	6.	18	22.5	212.5	−7.	8.	10	22.5	217.5	−5.	8.	11	22.5	223.0	−8.	8.	10	22.5	228.5	−12.	8.	13
22.5	233.5	−9.	10.	6	22.5	244.5	−9.	13.	5	22.5	250.0	−10.	6.	17	22.5	255.5	11.	3.	23	22.5	260.5	20.	3.	25
22.5	256.0	1.	3.	25	22.5	271.5	12.	2.	24	22.5	276.5	−1.	3.	24	22.5	282.0	−6.	3.	25	22.5	287.5	−53.	5.	25
22.5	293.0	−35.	4.	24	22.5	298.5	−28.	5.	21	22.5	303.5	−22.	4.	24	22.5	309.0	−23.	4.	23	22.5	314.5	5.	6.	18
22.5	319.5	0.	5.	18	22.5	325.0	0.	5.	18	22.5	330.5	8.	5.	20	22.5	336.0	−3.	4.	21	22.5	341.5	4.	5.	21
22.5	346.5	−3.	4.	21	22.5	352.0	−14.	5.	16	22.5	357.5	−5.	6.	15	17.5	2.5	7.	1.	25	17.5	7.5	6.	2.	25
17.5	13.0	−3.	2.	24	17.5	18.5	−11.	5.	11	17.5	23.5	5.	7.	12	17.5	34.0	10.	10.	6	17.5	39.5	4.	8.	13
17.5	44.5	8.	8.	11	17.5	49.5	−20.	8.	12	17.5	54.5	3.	11.	6	17.5	60.0	2.	15.	1	17.5	65.5	−11.	8.	9
17.5	70.5	−19.	8.	10	17.5	75.5	−23.	4.	24	17.5	80.5	−10.	3.	24	17.5	86.0	−13.	7.	14	17.5	91.5	−20.	8.	11
17.5	96.5	−9.	5.	20	17.5	101.5	−17.	2.	24	17.5	107.0	−10.	6.	14	17.5	112.5	−2.	14.	2	17.5	117.5	15.	14.	2
17.5	122.5	34.	8.	11	17.5	127.5	5.	12.	4	17.5	133.0	3.	11.	6	17.5	138.5	1.	8.	9	17.5	143.5	24.	9.	10

TABLE 5.16—*(Cont'd)*

ϕ	λ	Δg	M	N	ϕ	λ	Δg	M	N	ϕ	λ	Δg	M	N	ϕ	λ	Δg	M	N	ϕ	λ	Δg	M	N
17.5	148.5	17.	10.	8	17.5	154.0	−7.	15.	1	17.5	159.5	−9.	12.	5	17.5	164.5	−8.	11.	6	17.5	169.5	−6.	9.	11
17.5	174.5	−9.	8.	10	17.5	180.0	−2.	7.	12	17.5	185.5	0.	12.	5	17.5	190.5	−11.	8.	11	17.5	195.5	1.	12	4
17.5	200.5	8.	8.	11	17.5	206.0	22.	8.	8	17.5	211.5	1.	11.	6	17.5	216.5	2.	13.	3	17.5	221.5	−11.	9.	9
17.5	227.0	−8.	13.	3	17.5	232.5	−10.	13.	4	17.5	237.5	−12.	12.	3	17.5	242.5	−15.	8.	8	17.5	247.5	−13.	11.	6
17.5	253.0	−12.	4.	23	17.5	258.5	−7.	4.	23	17.5	263.5	30.	4.	22	17.5	268.5	14.	3.	24	17.5	274.0	21.	4.	23
17.5	279.5	4.	4.	25	17.5	284.5	−2.	4.	25	17.5	289.5	16.	4.	24	17.5	294.5	−45.	3.	25	17.5	300.0	−36.	4.	25
17.5	305.5	−17.	10.	7	17.5	310.5	−12.	11.	6	17.5	315.5	−12.	10.	6	17.5	320.5	−16.	11.	4	17.5	326.0	−5.	14.	2
17.5	331.5	2.	15.	1	17.5	336.5	24.	8.	8	17.5	341.5	1.	9.	10	17.5	347.0	12.	3.	22	17.5	352.5	1.	9.	11
17.5	357.5	6.	4.	21	12.5	2.5	1.	3.	22	12.5	7.5	8.	7.	15	12.5	12.5	8.	4.	18	12.5	18.0	2.	11.	4
12.5	23.5	−4.	12.	3	12.5	28.5	5.	10.	5	12.5	33.5	−4.	16.	1	12.5	38.5	22.	5.	16	12.5	43.5	4.	6.	17
12.5	48.5	3.	5.	15	12.5	54.0	−4.	4.	21	12.5	59.5	−9.	5.	17	12.5	64.5	−5.	13.	3	12.5	69.5	−35.	6.	16
12.5	74.5	−30.	6.	16	12.5	79.5	−24.	6.	17	12.5	90.0	−6.	9.	7	12.5	95.5	−10.	5.	20	12.5	100.5	−6.	5.	19
12.5	105.5	−6.	3.	25	12.5	110.5	1.	8.	13	12.5	115.5	8.	7.	14	12.5	120.5	29.	5.	17	12.5	126.0	36.	7.	14
12.5	131.5	8.	13.	3	12.5	136.5	1.	10.	7	12.5	141.5	25.	10.	8	12.5	146.5	−22.	5.	16	12.5	151.5	−3.	8.	13
12.5	156.5	11.	8.	9	12.5	152.0	−6.	10.	5	12.5	167.5	−5.	13.	3	12.5	177.5	17.	12.	5	12.5	182.5	13.	14.	2
12.5	187.5	−9.	13.	4	12.5	192.5	−6.	9.	8	12.5	198.0	6.	6.	14	12.5	213.5	2.	11.	6	12.5	218.5	0.	13.	4
12.5	244.5	−9.	12.	5	12.5	254.5	−3.	13.	4	12.5	259.5	2.	11.	6	12.5	264.5	5.	9.	10	12.5	270.0	7.	5.	18
12.5	275.5	33.	5.	20	12.5	280.5	−8.	7.	14	12.5	285.5	−17.	4.	23	12.5	290.5	−33.	6.	19	12.5	295.5	−25.	5.	21
12.5	300.5	−36.	4.	24	12.5	306.0	−34.	5.	20	12.5	311.5	−23.	7.	12	12.5	316.5	−11.	5.	19	12.5	321.5	−16.	12.	5
12.5	326.5	−9.	12.	3	12.5	331.5	−4.	9.	8	12.5	336.5	−9.	7.	13	12.5	342.0	11.	6.	14	12.5	347.5	10.	7.	15
12.5	352.5	11.	3.	23	12.5	357.5	3.	2.	25	7.5	2.5	17.	6.	15	7.5	7.5	23.	6.	12	7.5	12.5	19.	8.	11
7.5	17.5	2.	12.	2	7.5	22.5	−5.	12.	3	7.5	38.0	25.	6.	12	7.5	43.5	5.	13.	3	7.5	48.5	−10.	15.	1
7.5	53.5	−36.	5.	19	7.5	58.5	−10.	5.	15	7.5	63.5	−24.	6.	13	7.5	68.5	−41.	5.	18	7.5	73.5	−43.	5.	18
7.5	78.5	−29.	5.	21	7.5	83.5	−35.	5.	17	7.5	88.5	−14.	7.	14	7.5	93.5	−23.	4.	23	7.5	98.5	8.	3.	25
7.5	103.5	5.	12.	4	7.5	109.0	0.	7.	12	7.5	114.5	7.	6.	16	7.5	119.5	42.	11.	6	7.5	124.5	54.	7.	12
7.5	129.5	4.	10.	7	7.5	134.5	23.	8.	11	7.5	139.5	5.	8.	10	7.5	144.5	7.	8.	11	7.5	149.5	−5.	7.	13
7.5	154.5	−59.	7.	10	7.5	159.5	5.	15.	1	7.5	169.5	37.	15.	1	7.5	180.0	5.	9.	5	7.5	185.5	−9.	14.	3
7.5	190.5	−6.	6.	15	7.5	195.5	−1.	13.	3	7.5	200.5	22.	9.	7	7.5	240.5	−6.	13.	4	7.5	245.5	−4.	13.	5
7.5	251.0	−4.	12.	5	7.5	256.5	0.	11.	6	7.5	261.5	2.	12.	5	7.5	266.5	3.	12.	6	7.5	271.5	10.	8.	12
7.5	276.5	25.	4.	23	7.5	281.5	21.	5.	19	7.5	286.5	27.	3.	22	7.5	291.5	3.	8.	11	7.5	296.5	−2.	11.	5
7.5	301.5	−12.	11.	4	7.5	306.5	−23.	9.	9	7.5	311.5	−34.	7.	15	7.5	316.5	−23.	7.	14	7.5	322.0	−12.	8.	11
7.5	327.5	7.	8.	11	7.5	332.5	−1.	6.	13	7.5	342.5	7.	8.	8	7.5	347.5	29.	6.	13	7.5	352.5	27.	3.	25
7.5	357.5	15.	2.	25	2.5	7.5	17.	10.	8	2.5	12.5	10.	12.	4	2.5	17.5	−11.	9.	8	2.5	22.5	−29.	7.	13
2.5	27.5	−4.	8.	10	2.5	32.5	2.	4.	20	2.5	37.5	−2.	12.	4	2.5	42.5	−11.	13.	2	2.5	47.5	−30.	7.	14
2.5	52.5	−29.	5.	17	2.5	57.5	−19.	4.	20	2.5	62.5	−21.	4.	20	2.5	67.5	−24.	10.	9	2.5	72.5	−42.	5.	17
2.5	77.5	−43.	9.	10	2.5	82.5	−50.	8.	12	2.5	87.5	−16.	8.	10	2.5	92.5	−12.	5.	19	2.5	97.5	−13.	6.	18
2.5	102.5	14.	8.	9	2.5	107.5	16.	6.	14	2.5	112.5	13.	11.	6	2.5	117.5	1.	15.	1	2.5	122.5	24.	8.	11
2.5	127.5	9.	8.	11	2.5	132.5	23.	13.	3	2.5	137.5	−1.	14.	2	2.5	142.5	4.	7.	15	2.5	147.5	11.	7.	15
2.5	152.5	11.	8.	11	2.5	157.5	2.	11.	5	2.5	177.5	4.	12.	5	2.5	182.5	3.	8.	12	2.5	187.5	−1.	8.	13
2.5	192.5	3.	14.	2	2.5	197.5	14.	12.	5	2.5	267.5	2.	15.	1	2.5	272.5	0.	14.	2	2.5	277.5	8.	7.	13
2.5	282.5	24.	3.	25	2.5	287.5	26.	2.	25	2.5	292.5	3.	15.	1	2.5	302.5	−11.	14.	2	2.5	307.5	−4.	12.	5
2.5	312.5	−2.	15.	1	2.5	317.5	−11.	11.	6	2.5	322.5	−5.	8.	13	2.5	327.5	10.	6.	18	2.5	332.5	5.	9.	13
2.5	342.5	−7.	9.	6	2.5	347.5	−8.	10.	6	2.5	352.5	5.	12.	4	2.5	357.5	2.	15.	1	−2.5	7.5	14.	15.	1
−2.5	12.5	−9.	11.	6	−2.5	17.5	−21.	5.	18	−2.5	22.5	−37.	2.	25	−2.5	27.5	1.	5.	20	−2.5	32.5	−7.	4.	23
−2.5	37.5	13.	7.	16	−2.5	42.5	−31.	5.	19	−2.5	47.5	−19.	6.	12	−2.5	52.5	−13.	4.	20	−2.5	57.5	−16.	4.	23
−2.5	62.5	−20.	6.	17	−2.5	67.5	−24.	10.	8	−2.5	72.5	−39.	6.	14	−2.5	77.5	−37.	9.	9	−2.5	82.5	−54.	5.	20
−2.5	87.5	−32.	6.	15	−2.5	92.5	−19.	8.	11	−2.5	97.5	4.	6.	15	−2.5	102.5	9.	9.	11	−2.5	107.5	30.	6.	17
−2.5	112.5	12.	13.	3	−2.5	117.5	8.	7.	13	−2.5	122.5	−3.	7.	16	−2.5	127.5	9.	5.	21	−2.5	132.5	24.	7.	17
−2.5	137.5	2.	7.	11	−2.5	142.5	28.	3.	23	−2.5	147.5	37.	3.	25	−2.5	152.5	17.	6.	16	−2.5	157.5	18.	10.	7
−2.5	177.5	−6.	8.	11	−2.5	182.5	4.	13.	3	−2.5	187.5	−1.	9.	8	−2.5	197.5	15.	12.	5	−2.5	202.5	6.	15.	1
−2.5	277.5	0.	9.	7	−2.5	282.5	8.	8.	11	−2.5	287.5	25.	11.	5	−2.5	292.5	15.	13.	3	−2.5	297.5	−2.	15.	1
−2.5	302.5	−8.	13.	2	−2.5	307.5	−0.	12.	4	−2.5	312.5	−30.	5.	22	−2.5	317.5	−29.	6.	19	−2.5	322.5	−1.	9.	10
−2.5	327.5	−7.	6.	16	−2.5	332.5	−5.	6.	19	−2.5	337.5	−10.	8.	14	−2.5	342.5	−12.	10.	7	−2.5	347.5	6.	10.	8

-2.5	352.5	3.	12.	3	-7.5	7.5	-7.	12.	4	-7.5	12.5	10.	11.	3	-7.5	17.5	-4.	14.	2	-7.5	22.5	-11.	9.	12
-7.5	27.5	-9.	5.	21	-7.5	32.5	5.	4.	23	-7.5	38.0	-1.	5.	20	-7.5	43.5	-35.	5.	19	-7.5	48.5	-18.	6.	14
-7.5	53.5	-2.	8.	9	-7.5	58.5	-6.	10.	8	-7.5	63.5	-8.	12.	5	-7.5	68.5	-5.	7.	12	-7.5	73.5	-4.	11.	6
-7.5	78.5	-15.	13.	3	-7.5	83.5	-13.	13.	4	-7.5	88.5	-6.	13.	2	-7.5	93.5	-11.	11.	5	-7.5	98.5	8.	10.	10
-7.5	103.5	-15.	4.	23	-7.5	109.0	18.	4.	21	-7.5	114.5	17.	5.	20	-7.5	119.5	-4.	5.	21	-7.5	124.5	-5.	5.	24
-7.5	129.5	-26.	3.	25	-7.5	134.5	8.	5.	16	-7.5	139.5	16.	4.	21	-7.5	144.5	25.	3.	25	-7.5	149.5	20.	3.	25
-7.5	154.5	36.	3.	25	-7.5	159.5	23.	3.	25	-7.5	164.5	-36.	4.	25	-7.5	169.5	-23.	10.	9	-7.5	174.5	0.	9.	9
-7.5	180.0	1.	8.	8	-7.5	185.5	-5.	14.	2	-7.5	190.5	-2.	9.	6	-7.5	200.5	22.	10.	6	-7.5	220.5	10.	14.	1
-7.5	276.5	-8.	12.	3	-7.5	281.5	-8.	12.	4	-7.5	236.5	-13.	9.	8	-7.5	291.5	5.	13.	3	-7.5	296.5	2.	14.	1
-7.5	311.5	-26.	7.	17	-7.5	316.5	-28.	4.	25	-7.5	322.0	-4.	4.	25	-7.5	327.5	-17.	6.	15	-7.5	332.5	-6.	14.	3
-7.5	337.5	-4.	11.	8	-7.5	342.5	-4.	6.	18	-7.5	347.5	3.	6.	18	-7.5	352.5	-4.	13.	2	-7.5	357.5	-3.	12.	3
-12.5	12.5	6.	13.	2	-12.5	18.0	4.	14.	1	-12.5	23.5	2.	11.	4	-12.5	28.5	-15.	7.	13	-12.5	33.5	-6.	9.	12
-12.5	38.5	-13.	11.	7	-12.5	43.5	-26.	5.	13	-12.5	48.5	11.	8.	10	-12.5	54.0	-5.	6.	14	-12.5	59.5	-27.	11.	4
-12.5	64.5	4.	8.	10	-12.5	69.5	2.	11.	4	-12.5	79.5	-12.	13.	3	-12.5	84.5	-9.	13.	3	-12.5	90.0	-17.	12.	4
-12.5	95.5	-10.	5.	15	-12.5	100.5	-8.	5.	17	-12.5	105.5	3.	7.	12	-12.5	110.5	-8.	4.	20	-12.5	115.5	-26.	5.	21
-12.5	120.5	2.	3.	23	-12.5	126.0	23.	2.	25	-12.5	131.5	27.	2.	24	-12.5	136.5	19.	4.	21	-12.5	141.5	15.	3.	25
-12.5	146.5	11.	3.	25	-12.5	151.5	19.	4.	25	-12.5	156.5	25.	4.	23	-12.5	162.0	11.	4.	25	-12.5	167.5	16.	6.	18
-12.5	172.5	-5.	15.	1	-12.5	177.5	-2.	11.	5	-12.5	182.5	17.	9.	7	-12.5	187.5	14.	8.	11	-12.5	192.5	17.	9.	10
-12.5	198.0	9.	12.	5	-12.5	280.5	-10.	10.	5	-12.5	285.5	-2.	10.	6	-12.5	290.5	13.	11.	6	-12.5	295.5	33.	11.	6
-12.5	306.0	-16.	15.	1	-12.5	311.5	5.	3.	15	-12.5	316.5	-8.	4.	25	-12.5	321.5	-3.	5.	20	-12.5	326.5	-15.	7.	14
-12.5	342.0	-4.	11.	5	-12.5	347.5	-5.	8.	12	-12.5	352.5	-3.	12.	3	-12.5	357.5	-2.	13.	2	-17.5	7.5	2.	14.	2
-17.5	13.0	5.	12.	2	-17.5	18.5	4.	15.	1	-17.5	23.5	0.	10.	6	-17.5	28.5	10.	7.	14	-17.5	34.0	-1.	7.	13
-17.5	39.5	-15.	8.	10	-17.5	44.5	4.	6.	17	-17.5	49.5	18.	8.	12	-17.5	54.5	-8.	6.	14	-17.5	60.0	21.	6.	16
-17.5	65.5	-4.	9.	7	-17.5	70.5	1.	14.	2	-17.5	75.5	8.	13.	4	-17.5	80.5	-8.	7.	12	-17.5	86.0	-15.	8.	10
-17.5	91.5	-29.	6.	15	-17.5	96.5	-20.	7.	12	-17.5	101.5	-22.	8.	10	-17.5	107.0	-12.	9.	6	-17.5	112.5	-21.	7.	15
-17.5	117.5	-5.	4.	20	-17.5	122.5	11.	2.	25	-17.5	127.5	13.	1.	25	-17.5	133.0	4.	1.	25	-17.5	138.5	9.	2.	25
-17.5	143.5	20.	1.	25	-17.5	148.5	15.	3.	25	-17.5	134.0	11.	4.	25	-17.5	159.5	1.	5.	20	-17.5	164.5	18.	9.	10
-17.5	169.5	24.	10.	8	-17.5	174.5	20.	10.	5	-17.5	180.0	18.	8.	11	-17.5	190.5	6.	9.	7	-17.5	200.5	9.	15.	1
-17.5	206.0	16.	15.	1	-17.5	211.5	22.	13.	1	-17.5	216.5	1.	14.	1	-17.5	268.5	1.	15.	1	-17.5	279.5	-11.	14.	1
-17.5	284.5	4.	13.	3	-17.5	289.5	57.	8.	11	-17.5	294.5	33.	6.	17	-17.5	300.0	19.	9.	7	-17.5	305.5	1.	13.	4
-17.5	310.5	-21.	8.	13	-17.5	315.5	-23.	4.	25	-17.5	320.5	-14.	4.	23	-17.5	326.0	-16.	6.	13	-17.5	357.5	0.	11.	3
-22.5	2.5	4.	9.	8	-22.5	8.0	-4.	12.	3	-22.5	13.5	4.	12.	3	-22.5	18.5	10.	10.	6	-22.5	24.0	2.	10.	7
-22.5	29.5	8.	4.	20	-22.5	35.0	-14.	10.	8	-22.5	40.5	-14.	5.	18	-22.5	45.5	22.	5.	21	-22.5	51.0	9.	8.	10
-22.5	56.5	7.	5.	21	-22.5	61.5	19.	6.	15	-22.5	57.0	30.	5.	16	-22.5	72.5	16.	6.	15	-22.5	78.0	0.	11.	8
-22.5	83.5	-8.	13.	3	-22.5	88.5	-11.	12.	5	-22.5	94.0	-14.	12.	5	-22.5	99.5	-28.	8.	10	-22.5	104.5	-7.	14.	3
-22.5	110.0	5.	11.	6	-22.5	115.5	5.	3.	21	-22.5	121.0	-1.	4.	21	-22.5	126.5	-11.	1.	25	-22.5	131.5	-9.	2.	25
-22.5	137.0	8.	2.	25	-22.5	142.5	5.	2.	25	-22.5	147.5	22.	2.	25	-22.5	153.0	8.	10.	8	-22.5	158.5	7.	12.	6
-22.5	164.0	34.	6.	15	-22.5	169.5	23.	10.	6	-22.5	174.5	24.	11.	5	-22.5	180.0	4.	15.	1	-22.5	185.5	-20.	7.	15
-22.5	190.5	-19.	8.	7	-22.5	239.0	3.	13.	3	-22.5	244.5	4.	12.	5	-22.5	287.5	-1.	9.	8	-22.5	293.0	61.	5.	18
-22.5	298.5	-1.	10.	9	-22.5	303.5	0.	12.	4	-22.5	309.0	-19.	4.	22	-22.5	314.5	-4.	5.	19	-22.5	319.5	-12.	7.	13
-22.5	325.0	-14.	10.	6	-22.5	357.5	2.	15.	1	-27.5	3.0	3.	13.	3	-27.5	8.5	-2.	10.	7	-27.5	14.0	23.	7.	13
-27.5	20.0	15.	3.	23	-27.5	25.5	17.	2.	25	-27.5	31.0	35.	4.	20	-27.5	36.5	-10.	8.	10	-27.5	42.0	3.	7.	13
-27.5	48.0	15.	6.	15	-27.5	53.5	5.	11.	7	-27.5	59.0	3.	7.	10	-27.5	65.0	10.	12.	4	-27.5	70.5	21.	12.	4
-27.5	76.0	20.	11.	7	-27.5	81.5	-6.	13.	4	-27.5	87.0	-3.	12.	5	-27.5	93.0	-6.	12.	5	-27.5	98.5	-5.	13.	5
-27.5	104.0	-12.	10.	9	-27.5	110.0	-20.	8.	9	-27.5	115.5	0.	3.	22	-27.5	121.0	-8.	5.	19	-27.5	126.5	-16.	4.	23
-27.5	132.0	-7.	4.	21	-27.5	138.0	-10.	1.	25	-27.5	143.5	-5.	1.	25	-27.5	149.0	12.	1.	25	-27.5	155.0	4.	5.	18
-27.5	160.5	4.	9.	8	-27.5	166.0	13.	13.	3	-27.5	171.5	5.	13.	2	-27.5	177.0	0.	13.	3	-27.5	183.0	30.	11.	6
-27.5	188.5	-11.	9.	9	-27.5	245.0	0.	13.	3.	-27.5	250.5	-2.	9.	9	-27.5	256.0	2.	15.	1	-27.5	261.5	-2.	14.	2
-27.5	290.0	55.	5.	18	-27.5	295.5	8.	2.	25	-27.5	301.0	12.	5.	17	-27.5	306.5	-7.	6.	16	-27.5	312.0	-10.	5.	19
-27.5	318.0	-12.	13.	2	-27.5	323.5	-7.	10.	6	-27.5	351.5	-3.	15.	1	-32.5	3.0	4.	14.	1	-32.5	9.0	5.	10.	5
-32.5	15.0	2.	6.	15	-32.5	21.0	20.	2.	25	-32.5	27.0	12.	3.	23	-32.5	32.5	17.	8.	11	-32.5	38.0	-2.	9.	8
-32.5	44.0	35.	10.	6	-32.5	50.0	9.	12.	4	-32.5	62.0	-6.	10.	4	-32.5	74.0	20.	9.	5	-32.5	91.5	12.	15.	1
-32.5	97.0	-19.	8.	8	-32.5	103.0	-24.	8.	7	-32.5	109.0	-26.	8.	10	-32.5	115.0	-15.	4.	21	-32.5	121.0	-15.	3.	24
-32.5	127.0	-15.	6.	16	-32.5	133.0	-17.	5.	17	-32.5	139.0	0.	2.	25	-32.5	145.0	-0.	3.	23	-32.5	150.5	21.	3.	25
-32.5	156.0	-10.	8.	11	-32.5	152.0	-1.	15.	1	-32.5	174.0	25.	13.	2	-32.5	180.0	-6.	13.	2	-32.5	186.0	-2.	13.	4
-32.5	192.0	-15.	10.	7	-32.5	215.0	1.	13.	3	-32.5	221.0	7.	12.	4	-32.5	227.0	2.	12.	5	-32.5	233.0	5.	13.	3
-32.5	239.0	3.	12.	5	-32.5	245.0	-1.	12.	5	-32.5	251.0	-3.	11.	6	-32.5	257.0	-4.	7.	12	-32.5	263.0	-10.	9.	6

TABLE 5.16—*(Cont'd)*

φ	λ	Δg	M	N	φ	λ	Δg	M	N	φ	λ	Δg	M	N	φ	λ	Δg	M	N	φ	λ	Δg	M	N
−32.5	268.5	−3.	9.	5	−32.5	274.0	0.	9.	5	−32.5	280.0	0.	8.	5	−32.5	286.0	−6.	7.	11	−32.5	292.0	30.	3.	23
−32.5	298.0	11.	1.	25	−32.5	304.0	19.	3.	24	−32.5	310.0	5.	9.	8	−32.5	316.0	0.	12.	4	−32.5	322.0	4.	10.	5
−32.5	327.5	−12.	12.	2	−32.5	333.0	4.	12.	3	−32.5	339.0	4.	15.	1	−32.5	351.0	−3.	12.	3	−32.5	357.0	11.	13.	3
−37.5	9.5	−3.	13.	3	−37.5	22.0	−3.	9.	10	−37.5	28.5	5.	7.	12	−37.5	35.0	5.	8.	7	−37.5	41.0	13.	10.	5
−37.5	55.0	−1.	12.	4	−37.5	72.5	−2.	12.	4	−37.5	79.0	−6.	7.	10	−37.5	85.0	−5.	8.	7	−37.5	91.5	−3.	9.	7
−37.5	98.0	−11.	10.	5	−37.5	104.0	−21.	12.	5	−37.5	136.0	3.	9.	5	−37.5	142.0	2.	4.	19	−37.5	148.5	18.	6.	15
−37.5	155.0	−10.	8.	8	−37.5	161.0	−7.	10.	5	−37.5	167.5	4.	11.	5	−37.5	174.0	28.	7.	14	−37.5	180.0	−16.	5.	18
−37.5	192.5	−24.	11.	8	−37.5	218.0	−3.	13.	3	−37.5	224.0	−2.	13.	3	−37.5	230.5	3.	12.	3	−37.5	237.0	4.	13.	3
−37.5	243.0	−3.	18.	2	−37.5	249.5	−4.	13.	2	−37.5	262.0	−7.	8.	9	−37.5	268.5	−1.	15.	1	−37.5	281.0	1.	15.	1
−37.5	287.5	22.	6.	17	−37.5	294.0	0.	2.	25	−37.5	306.0	11.	3.	22	−37.5	306.0	6.	7.	14	−37.5	312.5	−10.	11.	5
−37.5	319.0	−2.	15.	1	−37.5	338.0	6.	14.	2	−37.5	350.5	5.	13.	3	−42.5	30.5	70.	9.	5	−42.5	71.5	−4.	11.	4
−42.5	146.0	18.	8.	8	−42.5	152.5	−7.	12.	5	−42.5	166.5	3.	13.	3	−42.5	173.5	10.	5.	18	−42.5	180.0	12.	9.	10
−42.5	186.5	−20.	10.	7	−42.5	193.5	−14.	13.	3	−42.5	258.5	−5.	8.	9	−42.5	281.5	−0.	12.	3	−42.5	288.5	35.	6.	15
−42.5	295.5	0.	7.	13	−42.5	302.5	−9.	7.	14	−42.5	309.0	−10.	9.	8	−42.5	315.5	−4.	14.	2	−42.5	356.5	−7.	15.	1
−47.5	40.5	11.	15.	1	−47.5	69.5	15.	10.	5	−47.5	158.0	−9.	12.	5	−47.5	165.5	34.	11.	5	−47.5	172.5	17.	13.	4
−47.5	180.0	−1.	15.	1	−47.5	187.5	−19.	7.	14	−47.5	194.5	0.	15.	1	−47.5	253.5	2.	14.	2	−47.5	268.0	1.	15.	1
−47.5	275.5	10.	9.	9	−47.5	283.0	−19.	13.	2	−47.5	290.5	−6.	7.	13	−47.5	297.5	−9.	10.	7	−47.5	305.0	−12.	6.	16
−52.5	69.5	13.	12.	4	−52.5	159.5	−1.	12.	5	−52.5	158.0	12.	12.	4	−52.5	192.0	−6.	10.	6	−52.5	249.5	7.	13.	2
−52.5	282.0	4.	9.	8	−52.5	290.5	4.	8.	8	−52.5	299.0	1.	5.	18	−52.5	307.0	−3.	12.	5	−52.5	323.0	26.	14.	3
−57.5	50.5	7.	14.	1	−57.5	152.5	−1.	12.	5	−57.5	189.5	−23.	8.	10	−57.5	198.5	−11.	12.	2	−57.5	253.5	−4.	14.	2
−57.5	290.5	15.	11.	7	−57.5	300.0	15.	8.	7	−57.5	309.5	9.	6.	13	−57.5	318.5	9.	13.	3	−57.5	327.5	13.	14.	2
−57.5	337.0	14.	13.	3	−62.5	5.5	4.	14.	2	−62.5	16.5	15.	8.	8	−62.5	27.5	−0.	14.	1	−62.5	49.5	6.	15.	1
−62.5	70.5	30.	10.	4	−62.5	81.5	12.	9.	10	−62.5	92.5	−17.	11.	7	−62.5	103.5	19.	13.	3	−62.5	114.5	−28.	13.	2
−62.5	125.5	−18.	12.	3	−62.5	136.5	−5.	12.	3	−62.5	147.5	−11.	14.	1	−62.5	158.5	−3.	9.	9	−62.5	169.5	−1.	14.	1
−62.5	190.5	−10.	9.	5	−62.5	201.5	−4.	12.	2	−62.5	245.5	3.	13.	2	−62.5	256.5	−2.	15.	1	−62.5	289.5	0.	12.	3
−62.5	300.0	38.	6.	15	−62.5	310.5	28.	11.	7	−67.5	6.5	2.	12.	5	−67.5	19.5	−9.	6.	14	−67.5	32.5	26.	7.	13
−67.5	45.0	4.	6.	18	−67.5	57.5	35.	7.	13	−67.5	70.5	17.	6.	13	−67.5	83.5	14.	6.	16	−67.5	96.5	20.	5.	18
−67.5	109.5	15.	7.	15	−67.5	122.5	−16.	8.	10	−67.5	135.0	4.	10.	6	−67.5	147.5	−15.	8.	9	−67.5	160.5	−12.	5.	15
−67.5	173.5	−8.	8.	8	−67.5	186.5	−10.	6.	15	−67.5	199.5	−16.	10.	5	−67.5	212.5	2.	13.	1	−67.5	225.0	−15.	12.	3
−67.5	237.5	−16.	11.	6	−67.5	250.5	−4.	12.	2	−67.5	253.5	15.	12.	2	−67.5	276.5	−5.	10.	5	−67.5	289.5	14.	12.	5
−67.5	302.5	7.	15.	1	−72.5	8.0	10.	14.	2	−72.5	24.5	7.	10.	6	−72.5	90.0	10.	7.	12	−72.5	106.5	−31.	10.	7
−72.5	139.0	−17.	9.	8	−72.5	155.5	−23.	8.	5	−72.5	172.0	−16.	13.	2	−72.5	204.5	−17.	11.	3	−72.5	237.0	−14.	15.	2
−72.5	253.5	−2.	15.	1	−72.5	270.0	9.	11.	5	−72.5	286.5	22.	10.	8	−77.5	79.0	16.	11.	5	−77.5	101.5	−14.	8.	12
−77.5	124.0	−2.	14.	1	−77.5	146.5	−36.	6.	13	−77.5	159.0	−7.	8.	11	−77.5	191.5	−17.	9.	11	−77.5	214.0	−16.	9.	9
−77.5	236.5	−6.	4.	20	−77.5	259.0	−14.	4.	22	−77.5	281.5	5.	9.	9	−77.5	304.0	−3.	13.	3	−77.5	326.5	−15.	10.	8
−82.5	60.0	28.	9.	7	−82.5	140.0	−32.	7.	11	−82.5	180.0	−30.	5.	17	−82.5	220.0	−13.	10.	9	−82.5	260.0	−6.	3.	24
−82.5	300.0	−16.	6.	14	−87.5	180.0	−19.	6.	14	−87.5	300.0	−12.	8.	10										

"Center of region at latitude φ, longitude λ; M = standard deviation (in mGal) of average gravity anomaly (in mGal); N = number of observations in area.

TABLE 5.17—*Stations Involved in GEM 5 and GEM 6*

Name	Number
BC–4	
BELTSV	6002
MOSELK	6003
SHEMYA	6004
TROMSO	6006
TRCERA	6007
PARMBO	6008
QUITO	6009
MAUIO	6011
WAKEIS	6012
KANOYA	6013
CATNIA	6016
MASHAD	6015
VILDOL	6019
EASTER	6020
TUTILA	6022
THRUSD	6023
INVERC	6031
CAVERS	6032
SOCORO	6038
PITCRN	6039
COCOSI	6040
ADISBA	6042
CERROS	6043
HEARDI	6044
MAURIT	6045
ZAMBGA	6047
PALMER	6050
MAWSON	6051
WILKES	6052
MCMRDO	6053
ASCENS	6055
XMASIL	6059
CULGDA	6060
SGAISL	6061
DAKAR	6063
FORTLY	6064
HOHNBG	6065
NATALB	6067
JOBURG	6068
TRSUNA	6069
CHIMAI	6072
DGOGRA	6073
MAHE	6075
PRTVLA	6078
WRIGHT	6111
PRBARW	6123
WRIGHT	6134

Name	Number
Baker-Nunn	
1ORGAN	9001
1OLFAN	9002
WOOMER	9003
ISPAIN	9004
1TOKYO	9005
1NATAL	9006
1QUIPA	9007
1CURAC	9008
1SHRAZ	9009
1JUPTR	9010
1VILDO	9011
1MAUIO	9012
HOPKIN	9021
AUSBAK	9023
DODAIR	9025
DEZEIT	9028
COMRIV	9031
JUPGEO	9049
AGASSI	9050
GREECE	9091
COLDLK	9424
EDWAFB	9425
OSLONR	9426
JOHNST	9427
Laser	
GODLAS	7050
WALLAS	7052
CRMLAS	7054
GRARR	
MADGAR	1122
MADGAS	1123
ROSRAN	1126
ULASKR	1128
CARVON	1152
Radar	
ETRPRE	4050
ETRMRT	4082
NBER34	4740
NWALI8	4840
NWALI3	4860
NBERO5	4760
WOO38	4946

Name	Number
Doppler	
ANCHOR	2014
TAFUNA	2017
THOLEG	2018
MCMRDO	2019
WAHIWA	2100
LACRES	2103
LASHM2	2106
APLMND	2111
PRETOR	2115
ASAMOA	2117
WALDOP	2203
ASCION	2722
COCOSL	2723
MOSLAK	2738
STNVIL	2745
MESHED	2817
FRTLMY	2822
NATLDP	2837
MOTS	
1BPOIN	1021
1FTMYR	1022
1OOMER	1024
1QUITO	1025
1SATAG	1028
1MOJAV	1030
1JOBUR	1031
1NEWFL	1032
1GFORK	1034
1WNKFL	1035
1ULASK	1036
1ROSMN	1037
1ORORL	1038
1ROSMA	1042
1TANAN	1043
1UNDAK	7034
1EDINB	7036
1COLBA	7037
1BERMD	7039
1PURIO	7040
1GFSCP	7043
1DENVR	7045
1JUM24	7071
1JUM40	7072
1JUPC1	7073
1JUBC4	7074
1SUDBR	7075
1JAMAC	7076
1GFSCN	7077
WALMOT	7078

TABLE 5.18.—*Number of Observations by Station Selected for Goddard '73*

Station number	Number of observations	Station number	Number of observations
1021	918	7050	1812
1022	3969	7052	178
1024	624 [a]	7054	214
9023	2938	7079	194
1028	1234	7060	1078
1030	4266	7071	202
1031	2236	7072	976
1032	148	7075	1350
1033	230	7076	1412
1034	2194	8820;7820	326
7034	893	8009	472
1035	632	8010	1290
1036	558	8011	458
1037	1832	8015	802
1042	1436	7815	503
1038	1186	8809	1233
1043	504	8019	516
7036	2364	8030	236
7037	4168	9001	1844
7039	1568	9002	2770
7040	1868	9902	346
7045	3078	9004	3193
9009	310	80;8804	939
9011	1318	9005	58
9012	1296	9025	84
9021	854	9006	366
9921	197	9007	1506
9028	398	8907	300
9029	386	9008	174
9929	135	9031	508
9050	156	9426	[b]28
9091	1322	9427	166
9930	60	9431	660
9424	78	9432	522
9425	1026	8435	250

[a] Bracket indicates constrained stations

[b] Only one pair of observations for each pass was reduced precisely.

TABLE 5.19.—*Coefficients in GEM 4*

	n	m	GEM 4		n	m	GEM 4		n	m	GEM 4
C	2	0	−484.1690	C	6	1	−0.0905	C	16	2	0.0108
S	2	0	0.0	S	6	1	0.0084	S	16	2	0.0217
C	3	0	0.9570	C	7	1	0.2553	C	3	3	0.7063
S	3	0	0.0	S	7	1	0.1334	S	3	3	1.4231
C	4	0	0.5412	C	8	1	0.0297	C	4	3	0.9713
S	4	0	0.0	S	8	1	0.0578	S	4	3	−0.2187
C	5	0	0.0692	C	9	1	0.1536	C	5	3	−0.4701
S	5	0	0.0	S	9	1	0.0088	S	5	3	−0.2506
C	6	0	−0.1528	C	10	1	0.0757	C	6	3	0.0169
S	6	0	0.0	S	10	1	−0.1438	S	6	3	−0.0127
C	7	0	0.0910	C	11	1	−0.0199	C	7	3	0.2558
S	7	0	0.0	S	11	1	0.0371	S	7	3	−0.2281
C	8	0	0.0515	C	12	1	−0.0592	C	8	3	−0.0262
S	8	0	0.0	S	12	1	−0.0466	S	8	3	−0.0809
C	9	0	0.0312	C	13	1	0.0183	C	9	3	−0.1700
S	9	0	0.0	S	13	1	−0.0753	S	9	3	−0.1049
C	10	0	0.0502	C	14	1	−0.0453	C	10	3	−0.0483
S	10	0	0.0	S	14	1	0.0371	S	10	3	−0.0976
C	11	0	−0.0561	C	15	1	0.1043	C	11	3	−0.0205
S	11	0	0.0	S	15	1	0.0419	S	11	3	−0.0887
C	12	0	0.0389	C	16	1	−0.0314	C	12	3	0.1389
S	12	0	0.0	S	16	1	0.0082	S	12	3	0.0429
C	13	0	0.0477	C	2	2	2.4237	C	13	3	−0.0335
S	13	0	0.0	S	2	2	−1.3895	S	13	3	0.0301
C	14	0	−0.0266	C	3	2	0.9164	C	14	3	0.0386
S	14	0	0.0	S	3	2	−0.6322	S	14	3	−0.0157
C	15	0	−0.0050	C	4	2	0.3511	C	15	3	0.0150
S	15	0	0.0	S	4	2	0.6652	S	15	3	0.0552
C	16	0	−0.0093	C	5	2	0.6620	C	16	3	0.0306
S	16	0	0.0	S	5	2	−0.3145	S	16	3	−0.0160
C	17	0	0.0174	C	6	2	0.0679	C	4	4	−0.1811
S	17	0	0.0	S	6	2	−0.3795	S	4	4	0.3153
C	18	0	0.0113	C	7	2	0.3305	C	5	4	−0.3107
S	18	0	0.0	S	7	2	0.0748	S	5	4	0.0321
C	19	0	0.0090	C	8	2	0.0511	C	6	4	−0.1005
S	19	0	0.0	S	8	2	0.0739	S	6	4	−0.4601
C	20	0	0.0090	C	9	2	0.0534	C	7	4	−0.2939
S	20	0	0.0	S	9	2	−0.0171	S	7	4	−0.1064
C	21	0	−0.0076	C	10	2	−0.0457	C	8	4	−0.2480
S	21	0	0.0	S	10	2	−0.0667	S	8	4	0.0466
C	22	0	−0.0038	C	11	2	0.0158	C	9	4	0.0212
S	22	0	0.0	S	11	2	−0.1250	S	9	4	0.0139
C	2	1	−0.0078	C	12	2	−0.0449	C	10	4	−0.0934
S	2	1	−0.0004	S	12	2	0.0532	S	10	4	−0.1177
C	3	1	2.0164	C	13	2	0.0194	C	11	4	0.0027
S	3	1	0.2498	S	13	2	−0.1477	S	11	4	−0.0937
C	4	1	−0.5330	C	14	2	−0.0370	C	12	4	−0.0423
S	4	1	−0.4614	S	14	2	0.1169	S	12	4	−0.0168
C	5	1	−0.0741	C	15	2	0.0008	C	13	4	−0.0543
S	5	1	−0.0786	S	15	2	−0.1010	S	13	4	−0.0737

TABLE 5.19.—*(Cont'd)*

	n	m	GEM 4		n	m	GEM 4		n	m	GEM 4
C	14	4	0.0346	C	7	6	−0.3230	C	13	7	−0.0526
S	14	4	0.0064	S	7	6	0.1664	S	13	7	0.1473
C	15	4	0.0099	C	8	6	−0.0476	C	14	7	0.1313
S	15	4	−0.0254	S	8	6	0.2841	S	14	7	−0.0797
C	16	4	0.0308	C	9	6	0.0651	C	15	7	−0.0214
S	16	4	0.0733	S	9	6	0.2210	S	15	7	0.0968
C	5	5	0.1700	C	10	6	−0.0178	C	16	7	0.0298
S	5	5	−0.6845	S	10	6	−0.1220	S	16	7	−0.0462
C	6	5	−0.2964	C	11	6	−0.0211	C	8	8	−0.1075
S	6	5	−0.5115	S	11	6	0.0443	S	8	8	0.1158
C	7	5	0.0035	C	12	6	0.0634	C	9	8	0.2182
S	7	5	0.0321	S	12	6	−0.0252	S	9	8	0.0052
C	8	5	−0.0884	C	13	6	−0.1284	C	10	8	0.0418
S	8	5	0.0848	S	13	6	0.0378	S	10	8	−0.1256
C	9	5	−0.0320	C	14	6	0.0534	C	11	8	0.0011
S	9	5	−0.0548	S	14	6	−0.0323	S	11	8	0.0639
C	10	5	−0.0682	C	15	6	−0.0174	C	12	8	−0.0317
S	10	5	−0.0070	S	15	6	−0.0481	S	12	8	0.0060
C	11	5	0.0736	C	16	6	−0.0407	C	13	8	0.0412
S	11	5	0.0332	S	16	6	−0.0189	S	13	8	−0.0192
C	12	5	0.0399	C	7	7	0.0752	C	14	8	0.0007
S	12	5	−0.0048	S	7	7	0.0130	S	14	8	−0.0605
C	13	5	0.0418	C	8	7	0.0494	C	15	8	−0.1600
S	13	5	0.0548	S	8	7	0.0679	S	15	8	0.0290
C	14	5	0.0428	C	9	7	−0.0685	C	16	8	0.0301
S	14	5	−0.0311	S	9	7	−0.0212	S	16	8	−0.0248
C	15	5	0.0237	C	10	7	0.0110	C	9	9	−0.0273
S	15	5	−0.0175	S	10	7	−0.0337	S	9	9	0.0801
C	16	5	0.0160	C	11	7	0.0223	C	10	9	0.1062
S	16	5	0.0334	S	11	7	−0.1104	S	10	9	−0.0724
C	6	6	0.0313	C	12	7	−0.0335	C	11	9	−0.0505
S	6	6	−0.2348	S	12	7	0.0005	S	11	9	0.0857

TABLE 5.19.—(*Cont'd*)

	n	m	GEM 4		n	m	GEM 4		n	m	GEM 4
C	12	9	0.0081	C	16	11	0.0046	C	18	13	−0.0027
S	12	9	0.0208	S	16	11	−0.0064	S	18	13	−0.0834
C	13	9	0.0137	C	12	12	−0.0117	C	19	13	−0.0068
S	13	9	0.1196	S	12	12	0.0049	S	19	13	−0.0012
C	14	9	0.0116	C	13	12	−0.0306	C	20	13	0.0312
S	14	9	0.0460	S	13	12	0.0994	S	20	13	−0.0637
C	15	9	0.0066	C	14	12	0.0098	C	21	13	−0.0190
S	15	9	0.0769	S	14	12	−0.0268	S	21	13	0.0257
C	16	9	0.0409	C	15	12	−0.0341	C	22	13	−0.0137
S	16	9	−0.0608	S	15	12	0.0153	S	22	13	−0.0348
C	10	10	0.0786	C	16	12	0.0256	C	14	14	−0.0521
S	10	10	−0.0232	S	16	12	−0.0076	S	14	14	−0.0074
C	11	10	−0.0727	C	17	12	0.0261	C	15	14	0.0025
S	11	10	−0.0063	S	17	12	−0.0011	S	15	14	−0.0216
C	12	10	−0.0057	C	18	12	−0.0568	C	16	14	−0.0108
S	12	10	0.0312	S	18	12	−0.0229	S	16	14	−0.0374
C	13	10	−0.0128	C	19	12	−0.0256	C	17	14	−0.0155
S	13	10	0.0171	S	19	12	−0.0203	S	17	14	0.0060
C	14	10	0.0273	C	20	12	0.0121	C	18	14	−0.0234
S	14	10	−0.1311	S	20	12	−0.0023	S	18	14	−0.0043
C	15	10	0.0503	C	21	12	0.0072	C	19	14	0.0005
S	15	10	0.0345	S	21	12	−0.0347	S	19	14	−0.0109
C	16	10	−0.0602	C	22	12	−0.0537	C	20	14	0.0117
S	16	10	−0.0093	S	22	12	−0.0333	S	20	14	−0.0035
C	11	11	0.0900	C	13	13	−0.0274	C	21	14	0.0042
S	11	11	−0.0255	S	13	13	0.0930	S	21	14	0.0134
C	12	11	0.0052	C	14	13	0.0318	C	22	14	0.0215
S	12	11	0.0305	S	14	13	0.0087	S	22	14	0.0071
C	13	11	−0.0443	C	15	13	−0.0023	C	15	15	−0.0788
S	13	11	−0.0215	S	15	13	0.0107	S	15	15	0.0308
C	14	11	0.0980	C	16	13	0.0064	C	16	15	−0.0544
S	14	11	−0.0331	S	16	13	−0.0213	S	16	15	0.0090
C	15	11	−0.0567	C	17	13	0.0319	C	16	16	−0.0048
S	15	11	0.0568	S	17	13	0.0423	S	16	16	−0.0036

TABLE 5.20.—*Comparison of Formulas Used by GSFC With Those Used by DOD, JPL, and APL*

Name	Used by	Type	General Form[a]
Runge-Kutta	APL	Onestep	$Y_{n+1} = Y_n + h\Phi(X_n, Y_n, h)$
Cowell[b]	NASA	Multistep	$Y_{n+1} = 2Y_n - Y_{n-1} + h^2 \sum_m \gamma_m \nabla^m f_{n+1}$
Störmer[b]	NASA	Multistep	$Y_{n+1} = 2Y_n - Y_{n-1} + h^2 \sum_m \gamma_m \nabla^m f_n$
Adams-Bashford[b]	NASA	Multistep	$Y_{n+1} + Y_n + h \sum_m \gamma_m \nabla^m f_n$
Adams-Moulton[b]	NASA	Multistep	$Y_{n+1} + Y_n + h \sum_m \gamma_m \nabla^m f_{n+1}$
Second-sum	JPL	Multistep $\binom{2 \text{ sum}}{10 \text{ diff}}$	Moyer (1971)
Second-difference	DOD/NWL	Multistep	Herrick (1971)

[a] h = step-size
γm = constant
f_m = given function
Φ = adjustment function

[b] Note that Cowell's and Störmer's methods apply to function f without first derivative, whereas the Adams-type equations apply to first-order equations.

TABLE 5.21.—*Description of Goddard Earth Models*

Solution	Extent of spherical harmonics	Station coordinates	Tracking data	Gravimetric data
GEM 1	12 × 12		120 000 camera obs. on 23 satellites, MINITRACK obs. on 2 satellites	
GEM 2	16 × 16	46 stations	GEM 1 data	1707 5° × 5° mean gravity-anomalies based on 21 000 1° × 1° values
GEM 3	12 × 12		400 000 camera, laser DME and electronics obs. on 27 satellites including data from SAS and PEOLE at low inclination	
GEM 4	16 × 16	61 stations	GEM 3 data	1705 5° × 5° mean gravity-anomalies based on 21 000 1° × 1° values
GEM 5	12 × 12		GEM 3 data with different weighting	
GEM 6	16 × 16	134 stations	GEM 5 data plus data from BC–4 cameras	Rapp's 5° equal-area mean gravity anomalies based on 23 000 1° × 1° values

TABLE 5.22.—*References for Intercomparison of GEOS Observation Systems*

1. Brown, D. C.: Short Arc Optical Survey of the GEOS North American Tracking Network. NASA/GSFC X-550-68-439, Nov. 1968.
2. Rawlinson, F. G.; Harris, D. W.; Berbert, J. H.; and Oosterhout, J. D.: The Jupiter Camera Intercomparison Test. NASA/GSFC X-590-73-344, Nov. 1973.
3. Berbert, J. H.; and Carney, D. V.: Five Laser/Laser Intercomparison Tests. NASA/GSFC X-590-73-345, Nov. 1973.
4. Berbert, J. H.; Maresca, P.; Norris, P.; and Reich, R.: Intercomparison of Collocated Laser Optical and GRARR Radio Ranging System Tracks on GEOS-A. NASA/GSFC X-514-67-447, Sept. 1967.
5. Berbert, J. H.; and Parker, H. C.: Comparison of C-band, SECOR, and TRANET with a Collocated Laser on 10 Tracks of GEOS-2. NASA/GSFC X-514-68-458, Nov. 1968.
6. Berbert, J. H.; Parker, H.; and Carney, D.: Comparison of C-band, SECOR, and TRANET with Collocated Laser and Camera on 35 tracks of GEOS-2. NASA/GSFC X-550-72-451, Nov. 1972.
7. Berbert, J. H.; Hlavin, J. M.; and Carney, D. V.: Carnarvon Laser Collocation Experiment (CALACO). NASA/GSFC X-550-72453, Dec. 1972.
8. Berbert, J.; Reich, R.; and Stephenson, J.: Evaluation of Range Accuracy for the Goddard Range and Range Rate System at Rosman. NASA/GSFC X-514-66-513, Oct. 1966.
9. GSFC Operations Evaluation Branch *et al.*; Final Report on GRARR/GEOS-A Data Validation. NASA/GSFC I-514-68-111, June 1968.
10. Lerch, F. J.; Marsh, J. G.; and O'Neill, B.: Evaluation of the Goddard Range and Range Rate System at Rosman by Intercomparison with GEOS-1 Long Arc Orbital Solutions. NASA TN D-5036, June 1969.
11. Agreen, R. W.; and Marsh, J. G.: An Intercomparison of Navy TRANET Doppler Data and Optical Data from the GEOS-1 Satellite. NASA/GSFC X-552-69-539, Dec. 1969.
12. Berbert, J. H.; and Carney, D.: GEOS MOTS/MINITRACK Collocation Study. NASA/GSFC X-514-69-102, Dec. 1973.
13. Marsh, J. G.; Doll, C. E.; Sandifer, R. J.; and Taylor, W. A.: Intercomparison of the MINITRACK and Optical Tracking Networks using GEOS-1 Long Arc Orbital Solutions. NASA TN D-5337, Feb. 1970.
14. Schmid, P. E.: NASA MINITRACK Interferometer Refraction Corrections. NASA/GSFC X-551-69-434, Oct. 1969, and NASA TN D-5966, Mar. 1971.
15. Berbert, J. H.; and Parker, H. C.: GEOS Satellite Tracking Corrections, for Refraction in the Troposphere. NASA/GSFC X-514-70-55, Feb. 1970.
16. Berbert, J. H.; and Parker, H. C.: GEOS Satellite Tracking Corrections for Refraction in the Ionosphere, NASA/GSFC X-514-70-467, Dec. 1970.
17. Mallinckrodt, A. J.: Refraction Errors of Short Horizontal Baseline Interferometers. NASA/GSFC X-514-70-465, Dec. 1970.
18. Proceedings of the GEOS-2 Program Review Meeting 22-24 June 1970, vol. 2, Tracking System Intercomparison with GEOS-2, edited by CSC, Nov. 1970.

TABLE 5.23.—*Camera Intercomparisons at Jupiter*

Camera	Combined data orbits mean rms (arc sec)			MOTS 40 orbits mean difference (arc sec)				
	No. of seqs	$\Delta\alpha \cos\delta$	$\Delta\delta$	No. of seqs	$B \pm \sigma$ $\Delta\alpha \cos\delta$	$\sqrt{B^2+\sigma^2}$ Tot rms	$B \pm \sigma$ $\Delta\delta$	$\sqrt{B^2+\sigma^2}$ Tot rms
SAO Baker-Nunn	35	1.39	1.38	31	−0.74 ± 1.25	1.45	0.08 ± 1.14	1.14
SAO K–50	12	1.41	1.57	10	−0.42 ± 2.07	2.11	−0.82 ± 1.26	1.50
Air Force PC–1000	28	1.62	1.42	19	−0.11 ± 1.69	1.69	−0.72 ± 1.50	1.66
NASA MOTS–40	53	1.61	1.47	53	0 ± 0	0	0 ± 0	0
NASA MOTS–24	20	2.30	1.96	18	−0.85 ± 1.95	2.13	0.60 ± 1.56	1.67
NASA PTH–100	18	1.87	1.54	14	−1.03 ± 2.14	2.37	0.52 ± 1.57	1.65
NASA BC–4—300	22	6.07	4.27	15	−3.95 ± 7.96	8.89	1.06 ± 2.95	3.13

TABLE 5.24.—*Comparison Laser Versus MOBLAS Laser Tests*

Test	Date	No. of passes	Comp laser	RMS range noise (meters)		Avg range bias ($B \pm$ Sigma) (meters)
				Comp laser	MOBLAS	Comp laser—MOBLAS
GORF–1[a]	Oct–Nov. 1968	5	GODLAS	1.86	1.23	4.1 ± 0.6
GORF–1	Oct.–Nov. 1968	5	GODLAS	1.86	1.23	−0.5 ± 0.6
ARLACO–1	Oct.–Nov. 1969	14	HOPLAS	1.34	1.06	−1.6 ± 1.5
ARLACO–2	Dec. 1969–Jan. 1970	11	HOPLAS	1.09	1.00	1.3 ± 1.7
GORF–2	Mar.–May 1970	21	GODLAS	1.00	1.06	−1.2 ± 1.3
GORF–3	Oct. 1970	4	GODLAS	0.59	0.59	0.9 ± 0.3

[a] MOBLAS had a calibration error of 4.6 meters

TABLE 5.25.—*ROLACO RAE Statistics*

System	Name	Measurement	No. passes	Mean before	RMS before	RMS after	Measurement bias (B)	Station time bias (T) (milliseconds)
Reference system								
Laser	GODLAS	Range (meters)	15	-------	1.8 ± 0.8	---------	----------	----------
		Azimuth (arc sec)	15	-------	91 ± 62	---------	----------	----------
		Elevation (arc sec)	15	-------	37 ± 25	---------	----------	----------
Comparison system								
GRARR	Rosman	Range (meters)	10	-------	-------	6.8 ± 2.1	−5.3 ± 12.4	−2.1 ± 1.2
		Range rate (cm/sec)	9	-------	6.9 ± 5.8	---------	----------	----------

TABLE 5.26.—*WICE (RAE Orbit) Statistics*

System	Name	Measurement	No. passes	Mean before	RMS before	RMS after	Measurement bias (B)	Station time bias (T) (milliseconds)
Laser	GODLAS	Range (meters)	35	0.0 ± 0.0	1.3 ± 0.2			
C-band	FPQ-6 (−0.6 m added)	Range (meters)	34			1.0 ± 0.3	−2.2 ± 2.6	0.3 ± 0.3
C-band	FPQ-6	Range (meters)	34	−1.4 ± 2.5	2.5 ± 2.0	1.0 ± 0.3	−1.6 ± 2.6	0.3 ± 0.3
C-band	FPQ-6 (beacon only)	Range (meters)	24			1.0 ± 0.2	−2.0 ± 2.7	0.3 ± 0.3
C-band	FPQ-6 (beacon segment)	Range (meters)	8			1.1 ± 0.4	−1.8 ± 2.2	0.3 ± 0.2
C-band	FPQ-6 (skin track)	Range (meters)	8			8.6 ± 2.0	−5.2 ± 2.7	0.1 ± 0.7
C-band	FPQ-6 (beacon 1, all)	Range (meters)	20	−2.0 ± 2.2	2.6 ± 2.0	0.9 ± 0.2	−2.2 ± 2.4	0.3 ± 0.3
C-band	FPQ-6 (beacon 2, all)	Range (meters)	14	−0.5 ± 2.6	2.3 ± 1.9	1.2 ± 0.3	−0.6 ± 2.5	0.3 ± 0.3
C-band	FPQ-16 (−7.9 m added)	Range (meters)	27			1.4 ± 0.4	−2.2 ± 4.1	0.3 ± 0.3
C-band	FPS-16	Range (meters)	27	5.9 ± 4.1	6.7 ± 3.2	1.4 ± 0.4	5.7 ± 4.1	0.3 ± 0.3
C-band	FPS-16 (beacon 1)	Range (meters)	14	7.2 ± 3.3	7.6 ± 2.9	1.2 ± 0.2	7.0 ± 3.4	0.3 ± 0.3
C-band	FPS-16 (beacon 2)	Range (meters)	13	4.5 ± 4.2	5.7 ± 3.1	1.6 ± 0.5	4.4 ± 4.3	0.3 ± 0.3
SECOR	WSECOR	Range (meters)	32	−18.1 ± 3.7	18.4 ± 3.6	1.8 ± 0.4	−17.5 ± 4.0	−0.6 ± 0.5
C-band	FPQ-6	Range rate (cm/sec)	4			9.8 ± 4.2	2.4 ± 2.9	0.2 ± 0.2
TRANET	TRAN59 (early)	Range rate (cm/sec)	24			8.5 ± 5.1	21.2 ± 7.7	0.0 ± 0.0
TRANET	TRAN35 (early)	Range rate (cm/sec)	15			12.1 ± 10.2	18.4 ± 5.5	0.0 ± 0.0
TRANET	TRAN59 (final)	Range rate (cm/sec)	26	1.5 ± 3.7	5.6 ± 3.5	4.5 ± 2.0	1.4 ± 3.5	0.0 ± 0.1
TRANET	TRAN35 (final)	Range rate (cm/sec)	16	−3.7 ± 7.9	9.3 ± 9.6	6.1 ± 7.0	−3.2 ± 7.5	0.0 ± 0.0
Laser	GODLAS	Azimuth × cos el (arc-sec)	35	0 ± 0	53 ± 33	53 ± 53	0 ± 0	
C-band	FPQ-6	Azimuth × cos el (arc-sec)	34	38 ± 37	53 ± 44	21 ± 18	38 ± 37	
C-band	FPS-16	Azimuth × cos el (arc-sec)	27	−52 ± 57	78 ± 55	41 ± 33	−51 ± 56	
Laser	GODLAS	Elevation (arc-sec)	35	−6 ± 13	30 ± 11	27 ± 9	−6 ± 13	
C-band	FPQ-6	Elevation (arc-sec)	34	23 ± 15	27 ± 14	11 ± 4	23 ± 15	
C-band	FPS-16	Elevation (arc-sec)	27	24 ± 23	35 ± 19	19 ± 7	24 ± 23	

TABLE 5.27.—*WICE (RRD Orbit) Statistics*

System	Name	Measurement	No. passes	Mean before	RMS before	RMS after	Measurement bias (B)	Station time bias (T) (milliseconds)
Laser	GODLAS	Range (meters)	22	0.0 ± 0.0	1.3 ± 0.2	1.5 ± 0.2		
C-band	FPQ-6 (−0.6 m added)	Range (meters)	21			0.8 ± 0.1	−2.2 ± 1.8	0.4 ± 0.3
C-band	FPQ-6	Range (meters)	21	−1.7 ± 1.8	2.4 ± 1.2	0.8 ± 0.1	−1.6 ± 1.8	0.4 ± 0.3
C-band	FPS-16 (−7.9 m added)	Range (meters)	21			1.1 ± 0.3	−0.8 ± 3.5	0.3 ± 0.2
C-band	FPS-16	Range (meters)	16	7.1 ± 3.4	7.6 ± 2.9	1.1 ± 0.3	7.1 ± 3.5	0.3 ± 0.2
SECOR	WSECOR	Range (meters)	20	−17.5 ± 3.3	17.8 ± 3.2	1.7 ± 0.3	−16.8 ± 3.8	−0.7 ± 0.3
TRANET	TRAN59	Range rate (cm/sec)	15	2.2 ± 4.1	5.7 ± 4.7	3.9 ± 1.9	0.3 ± 3 7	0.8 ± 1.5
TRANET	TRAN35	Range rate (cm/sec)	10	−0.5 ± 3.2	5.0 ± 1.8	2.7 ± 0.7	−2.2 ± 4.7	0.6 ± 0.8
Laser	GODLAS	Azimuth × cos el (arc-sec)	22	11. ± 23.	64. ± 46.	57. ± 42.	5. ± 21.	
C-band	FPQ-6	Azimuth × cos el (arc-sec)	21	46. ± 21.	51. ± 22.	17. ± 15.	38. ± 20.	
C-band	FPS-16	Azimuth × cos el (arc-sec)	16	−43. ± 40.	62. ± 31.	31. ± 18.	−52. ± 50.	
Laser	GODLAS	Elevation (arc-sec)	22	1. ± 13.	30. ± 10.	27. ± 9.	0. ± 15.	
C-band	FPQ-6	Elevation (arc-sec)	21	26. ± 10.	28. ± 9.	10. ± 3.	25. ± 12.	
C-band	FPS-16	Elevation (arc-sec)	16	26. ± 19.	34. ± 16.	18. ± 6.	24. ± 19.	
Camera	WALLOP	Rt asc. × cos dec (arc-sec)	22	0.4 ± 0.9	1.6 ± 0.8			
Camera	WALLOP	Dec (arc-sec)	22	0.2 ± 1.5	1.7 ± 1.1			

TABLE 5.28.—*CALACO (RAE Orbit) Statistics*

System	Name	Measurement	No. passes	Mean before	RMS before	RMS after	Measurement bias (B)	Station time bias (T) (milliseconds)
Laser	CRMLAS	Range (meters)	92	0.0 ± 0.0	1.3 ± 0.2			
C-band	NCARVN (+20 ± 0.7 m added)	Range (meters)	23			1.1 ± 0.4	5.0 ± 6.7	0.4 ± 1.1
C-band	NCARVN	Range (meters)	23	−13.1 ± 4.4	13.3 ± 4.4	1.1 ± 0.4	−15.0 ± 6.5	0.4 ± 1.1
C-band	NCARVN (beacon 1)	Range (meters)	12	−13.3 ± 4.1	13.3 ± 4.1	1.0 ± 0.2	−15.8 ± 7.5	0.5 ± 1.4
C-band	NCARVN (beacon 2)	Range (meters)	11	−13.0 ± 4.5	13.2 ± 4.4	1.2 ± 0.5	−14.1 ± 4.6	0.3 ± 0.5
C-band	NCARVN (beacon 1 corrected)	Range (meters)	12			1.0 ± 0.2	4.1 ± 7.9	0.5 ± 1.4
C-band	NCARVN (beacon 2 corrected)	Range (meters)	11			1.2 ± 0.5	5.6 ± 4.9	0.3 ± 0.5
GRARR	CARVON (A + C)	Range (meters)	64	−4.1 ± 6.4	7.6 ± 4.0	3.0 ± 0.2	−4.0 ± 6.7	0.0 ± 1.2
GRARR	CARVON (A)	Range (meters)	17	−1.5 ± 3.7	4.8 ± 1.6	3.0 ± 0.2	−1.7 ± 3.6	0.2 ± 0.5
GRARR	CARVON (C)	Range (meters)	47	−5.1 ± 6.9	8.6 ± 4.1	2.9 ± 0.2	−4.9 ± 7.4	−0.1 ± 1.4
GRARR	CARVON (A + C)	Range rate (cm/sec)	64	0.5 ± 0.9	1.7 ± 0.8	1.4 ± 0.7	0.5 ± 2.4	
GRARR	CARVON (A)	Range rate (cm/sec)	17	0.3 ± 0.1	1.6 ± 0.8	1.3 ± 0.4	−0.2 ± 0.7	
GRARR	CARVON (C)	Range rate (cm/sec)	47	0.6 ± 0.9	1.7 ± 0.8	1.5 ± 0.7	0.8 ± 2.7	
Laser	CRMLAS	Azimuth × cos el (arc-sec)	92	0. ± 0.	30. ± 17.			
C-band	NCARVN	Azimuth × cos el (arc-sec)	23	−17. ± 32.	54. ± 56.	42. ± 55.	−17. ± 32.	
Laser	CRMLAS	Elevation (arc-sec)	92	−8. ± 14.	22. ± 13.			
C-band	NCARVN	Elevation (arc-sec)	23	22. ± 28.	36. ± 23.	15. ± 18.	22. ± 28.	

TABLE 5.29.—*CALACO (RRD Orbit) Statistics*

System	Name	Measurement	No. passes	Mean before	RMS before
Laser	CRMLAS	Range (meters)	14	0.0 ± 0.0	1.3 ± 0.2
C-band	NCARVN	Range (meters)	5	−9.3 ± 4.2	9.5 ± 4.1
GRARR	CARVON	Range (meters)	12	−6.4 ± 7.0	8.9 ± 5.2
GRARR	CARVON	Range rate (cm/sec)	12	0.3 ± 1.3	1.7 ± 0.7
Laser	CRMLAS	Azimuth × cos el (arc-sec)	14	10. ± 24.	35. ± 23.
C-band	NCARVN	Azimuth × cos el (arc-sec)	5	−28. ± 8.	38. ± 10.
Laser	CRMLAS	Elevation (arc-sec)	14	−26. ± 11.	31. ± 9.
C-band	NCARVN	Elevation (arc-sec)	5	30. ± 6.	35. ± 5.
Camera	1CARVN	Rt. asc × cos dec (arc-sec)	14	0.0 ± 0.0	0.9 ± 0.3
Camera	1CARVN	Declin (arc-sec)	14	0.0 ± 0.8	1.4 ± 0.7

TABLE 5.30.—*Range System Accuracies, Typical and Potential (in Meters)*

		Before correction				After correction	
Test	Range system	Avg bias $B \pm \sigma$	Total rms $(B^2 + \sigma^2)^{1/2}$	Bias source	Added correction	Avg bias $B \pm \sigma$	Total rms $(B^2 + \sigma^2)^{1/2}$
GORF-1	MOBLAS	−4.1 ± 0.6	4.1	Cal sig level	4.6	0.5 ± 0.6	0.8
ARLACO-1	HOPLAS	(2 passes) 5.5 ± 0.6	5.5	Cal change	−4.8	(14 passes) −1.6 ± 1.5	2.2
ROLACO	GRARR (A)	−15.0 ± 12.4	19.5	Cal	9.7	−5.3 ± 12.4	13.5
CALACO	GRARR (A)	−1.7 ± 3.6	4.0	Unknown			
CALACO	GRARR (C)	−4.9 ± 7.4	8.9	Unknown			
WICE	FPS-16	5.7 ± 4.1	7.0	Cal, survey	−7.9	−2.2 ± 4.1	4.7
WICE	FPQ-6	−1.6 ± 2.6	3.1	Calib	−0.6	−2.2 ± 2.6	3.4
CALACO	FPQ-6	−15.0 ± 6.5	16.3	Cal refr	20.0 ± 0.7	5.0 ± 6.7	8.4
WICE	SECOR	−17.5 ± 4.0	18.0	Unknown			

TABLE 5.31.—*Constraints on Relative Position*

Station pair		Relative position constraints (meters) Δx	Δy	Δz	Est stand dev (meters) σ	Differences with respect to constrained values (meters) δx	δy	δz
2017	2117	−3.75	6.28	−2.02	4.23	6.03	3.19	10.73
2018	2018	0.00	0.00	0.00	5.12	17.39	−17.12	−0.68
2822	6064	−12.06	13.60	23.74	3.00	−1.66	2.03	1.07
2837	6067	46.13	290.25	−1248.20	3.00	−10.56	0.71	3.59
1038	6060	304 147.18	114 912.15	494 900.60	2.04	−6.45	12.01	6.91
2019	6053	−130.35	808.62	87.15	3.00	−0.48	9.33	−3.28
2722	6055	−78.06	−172.20	−160.45	3.00	7.44	−6.64	2.98
2723	6040	19.71	0.69	14.10	3.00	1.93	−1.73	−3.74
1152	6032	−47 149.40	−424 141.91	676 055.82	2.50	10.97	2.19	−3.32
6019	9011	−52.01	−37.07	18.82	0.01	0.01	0.00	0.00
1021	7043	12 681.43	44 984.51	51 158.99	0.49	−1.48	−2.67	−2.86
1022	7071	168 409.91	50 582.89	45 732.81	0.93	0.60	6.44	2.51
1034	7034	0.08	0.66	−0.74	0.01	0.00	0.00	0.00
1037	1042	−7.58	−0.59	0.50	0.01	0.00	0.00	0.00
7043	7050	−38.21	−36.26	−31.23	0.01	0.00	0.01	0.01
7043	7052	130 836.64	−50 256.13	−100 969.38	0.90	3.61	−2.64	2.65
7043	7077	−652.92	−1710.84	−1877.61	0.06	0.01	0.00	0.00
7043	7078	130 867.90	−50 025.41	−100 693.72	0.90	−0.77	−0.53	0.42
7071	7072	4.08	5.48	11.42	0.01	−0.20	0.04	0.72
7071	7073	10.32	6.62	9.32	0.01	0.19	−0.03	−0.72
7071	7074	11.03	8.97	15.81	0.01	0.00	0.00	0.00
2738	6003	3.96	−23.90	21.87	3.00	8.19	−16.28	−4.58
1025	6009	17 214.35	4034.43	58 089.41	0.46	−0.01	0.05	0.04
2817	6015	7.76	4.05	−10.20	3.00	−11.17	−3.60	11.18
6111	6134	−53.77	−90.12	−305.26	0.01	0.00	0.00	0.00
6002	7043	−56.27	−499.54	−568.43	0.02	0.00	0.00	0.00
6011	9012	−49.58	118.93	−35.81	0.01	0.00	0.00	0.00
7071	9010	19.05	3.07	3.92	0.01	0.01	0.01	0.01
9003	9023	6011.64	−17 986.56	−27 467.42	0.30	−0.02	−0.04	0.42
4740	7039	−674.06	699.92	1476.31	0.04	0.00	0.00	0.00
4760	7039	−683.27	706.55	1488.25	0.04	0.00	0.00	0.01
1037	1126	−334.06	−403.53	−571.31	0.02	0.01	0.00	−0.01
1152	7054	54.96	−51.86	−135.62	0.01	0.00	0.00	0.00
2203	7052	−116.78	−336.48	−389.60	3.00	5.76	2.27	0.02
2115	4050	354.70	970.65	296.73	3.00	1.51	−3.76	3.73
4082	7071	65 691.26	62 291.57	1 377 355.55	0.87	−0.74	−0.31	−1.78
4840	4860	−2384.64	711.85	1660.19	0.06	0.00	−0.01	0.00
4840	7052	−2425.68	685.03	1630.22	0.06	−0.01	0.00	0.01
1024	4946	−21 762.84	24 680.80	54 300.42	0.46	0.28	−0.20	−0.60
1031	6068	59.69	−55.46	51.19	0.01	0.00	0.00	0.00
6068	9002	28 722.17	46 167.12	−7673.38	0.42	0.50	−0.44	0.47
7072	9049	4.82	−3.60	−12.97	0.01	0.01	0.01	0.00
6111	9425	−1159.33	43 554.59	52 281.60	0.48	0.38	0.07	0.09
6042	9028	2992.55	−3032.66	−2462.26	0.08	0.00	0.01	0.00
2100	6011	38 128.97	−180 272.68	−83 071.46	3.04	−12.07	1.62	5.85
9005	9025	36 256.49	10 061.56	30 386.63	0.38	0.27	−0.11	0.52
7901	9001	0.00	0.00	0.00	4.23	−20.28	−1.41	7.34
2106	1035	−22 330.33	23 266.93	17 999.44	3.03	−2.97	21.42	−1.57

TABLE 5.32.—*Constraints on Surface Distance*

Station pair		Distance (meters)	Estimated relative standard deviation (ppm)	Residual after adjustment (meters)
6002	6003	3 485 363.23	1.00	6.58
6006	6016	3 545 871.56	1.00	1.68
6006	6065	2 457 765.81	0.70	−1.04
6016	6065	1 194 793.60	0.85	2.92
6023	6060	2 300 209.80	0.50	−1.72
6032	6060	3 163 623.87	1.00	−5.54
6063	6064	3 485 550.76	0.85	−2.32
6003	6111	1 425 876.45	0.90	−2.03

TABLE 5.33.—*GEM 6 Station Coordinates*

Station		Latitude			Longitude			Height	Sigma[a]
Name	Number	Deg	Min	Sec	Deg	Min	Sec	(meters)	(meters)
Station positions for BC-4									
BELTSV	6002	39	1	39.706	283	10	27.538	0.1	3
MOSELK	6003	47	11	6.660	240	39	43.768	331.6	9
SHEMYA	6004	52	42	48.985	174	07	26.363	38.3	22
TROMSO	6006	69	39	44.108	18	56	29.299	109.3	15
TRCERA	6007	38	45	36.426	332	54	25.707	99.9	11
PARMBO	6008	5	26	53.866	304	47	40.707	−30.2	15
QUITO	6009	− 0	5	51.408	281	34	47.674	2685.5	17
MAUIO	6011	20	42	27.235	203	44	38.433	3057.8	4
WAKEIS	6012	19	17	28.643	166	36	39.443	−15.6	12
KANOYA	6013	31	23	42.733	130	52	16.579	76.1	17
CATNIA	6016	37	26	38.374	15	2	45.352	38.6	9
MASHAD	6015	36	14	25.459	59	37	43.740	947.7	9
VILDOL	6019	−31	56	35.317	294	53	38.999	625.1	4
EASTER	6020	−27	10	36.330	250	34	22.636	199.6	22
TUTILA	6022	−14	19	54.394	189	17	8.692	15.5	11
THRUSD	6023	−10	35	3.276	142	12	39.420	107.9	10
INVERC	6031	−46	24	58.309	168	19	31.502	−11.5	9
CAVERS	6032	−31	50	25.036	115	58	31.671	−18.1	7
SOCORO	6038	18	43	58.568	249	2	41.347	−23.0	10
PITCRN	6039	−25	4	6.765	229	53	12.572	295.2	25
COCOSI	6040	−12	11	43.990	96	50	2.460	−47.8	11
ADISBA	6042	8	46	12.504	38	59	52.089	1865.2	5
CERROS	6043	−52	46	52.600	290	46	34.090	78.3	11
HEARDI	6044	−53	1	9.425	73	23	34.212	34.8	16
MAURIT	6045	−20	13	52.901	57	25	31.944	133.1	11
ZAMBGA	6047	6	55	20.395	122	4	8.907	59.3	14
PALMER	6050	−64	46	26.371	295	56	53.697	23.1	15
MAWSON	6051	−67	36	4.268	62	52	22.242	28.8	11
WILKES	6052	−66	16	44.937	110	32	7.169	−5.5	11
MCMRDO	6053	−77	50	41.846	166	38	31.279	−56.0	10
ASCENS	6055	− 7	58	15.213	345	35	34.770	70.1	9
XMASIL	6059	2	0	18.617	202	35	16.306	2.3	11
CULGDA	6060	−30	18	34.411	149	33	40.993	226.2	7
SGAISL	6061	−54	17	0.709	323	30	21.877	2.0	12
DAKAR	6063	14	44	42.292	342	31	0.697	44.3	9
FORTLY	6064	12	7	54.697	15	2	7.246	296.4	7
HOHNBG	6065	47	48	3.758	11	1	25.916	970.1	12
NATALB	6067	− 5	55	38.935	324	50	4.707	13.2	10
JOBURG	6068	−25	52	58.963	27	42	23.644	1539.2	3
TRSUNA	6069	−37	3	53.227	347	41	5.670	25.3	9
CHIMAI	6072	18	46	10.593	98	58	2.372	245.9	14
DGOGRA	6073	− 7	21	6.513	72	28	20.592	−77.9	12
MAHE	6075	− 4	40	14.620	55	28	47.950	534.4	12
PRTVLA	6078	−17	41	31.834	168	18	24.472	54.4	37
WRIGHT	6111	34	22	54.548	242	19	5.990	2247.7	6
PRBARW	6123	71	18	48.393	203	21	8.504	−34.0	26
WRIGHT	6134	34	22	44.455	242	19	5.765	2161.8	6

TABLE 5.33.—*(Cont'd)*

Station		Latitude			Longitude			Height	Sigma[a]
Name	Number	Deg	Min	Sec	Deg	Min	Sec	(meters)	(meters)
Station positions for Laser									
GODLAS	7050	39	1	14.387	283	10	18.638	11.1	3
WALLAS	7052	37	51	36.199	284	29	23.965	−42.4	3
CRMLAS	7054	−24	54	15.965	113	42	58.252	−3.5	4
Station positions for Baker-Nunn									
1ORGAN	9001	32	25	25.079	253	26	48.996	1619.1	4
1OLFAN	9002	−25	57	35.837	28	14	52.459	1559.0	3
WOOMER	9003	−31	6	2.124	136	47	3.319	155.5	4
ISPAIN	9004	36	27	46.818	353	47	36.958	60.0	3
1TOKYO	9005	35	40	22.968	139	32	16.563	84.9	5
1NATAL	9006	29	21	34.781	79	27	27.517	1871.0	4
1QUIPA	9007	−16	27	56.628	288	30	24.604	2484.7	4
1CURAC	9009	29	38	13.839	52	31	11.372	1580.3	6
1SHRAZ	9008	12	5	25.186	291	9	44.532	−23.2	5
1JUPTR	9010	27	1	14.120	279	53	13.357	−24.8	3
1VILDO	9011	−31	56	34.597	294	53	36.609	625.1	4
1MAUIO	9012	20	42	26.175	203	44	33.983	3042.8	4
HOPKIN	9021	31	41	3.302	249	7	18.599	2341.0	7
AUSBAK	9023	−31	23	25.694	136	52	43.649	134.0	4
DODAIR	9025	36	0	20.304	139	11	31.565	883.7	5
DEZEIT	9028	8	44	51.242	38	57	33.407	1904.1	5
COMRIV	9031	−45	53	12.290	292	23	9.413	192.5	6
JUPGEO	9049	27	1	13.948	279	53	12.993	−28.1	3
AGASSI	9050	42	30	21.542	288	26	30.583	129.9	22
GREECE	9091	38	4	44.849	23	55	58.658	487.2	5
COLDLK	9424	54	44	34.634	249	57	23.125	669.4	15
EDWAFB	9425	34	57	50.677	242	5	8.030	748.9	6
OSLONR	9426	60	12	39.200	10	45	2.938	617.0	17
JOHNST	9427	16	44	38.879	190	29	9.343	18.8	8
Station positions for GRARR									
MADGAR	1122	−19	1	16.314	47	18	15.185	1349.6	50
MADGAS	1123	−19	1	14.392	47	18	11.335	1387.6	7
ROSRAN	1126	35	11	45.528	277	7	26.240	828.1	3
ULASKR	1128	64	58	18.964	212	29	12.728	338.8	3
CARVON	1152	−24	54	11.015	113	42	59.302	2.5	4
Station positions for C-Band									
ETRPRE	4050	−25	56	37.592	28	21	28.937	1588.6	12
ETRMRT	4082	28	25	28.943	279	20	7.649	−30.7	5
NBER34	4740	32	20	53.337	295	20	46.909	−26.9	4
NWALI8	4840	37	50	29.160	284	30	53.007	−39.4	4
NWALI3	4860	37	51	37.279	284	29	25.864	−36.4	4
NBERO5	4760	32	20	52.837	295	20	47.119	−24.9	4
WOOR38	4946	−30	49	5.877	136	50	17.532	124.3	6

TABLE 5.33.—*(Cont'd)*

Station		Latitude			Longitude			Height	Sigma[a]
Name	Number	Deg	Min	Sec	Deg	Min	Sec	(meters)	(meters)
Station positions for Doppler									
ANCHOR	2014	61	17	0.168	210	10	29.035	63.9	5
TAFUNA	2017	−14	19	49.937	189	17	3.046	27.4	5
THOLEG	2018	76	32	20.047	291	13	52.647	47.4	10
MCMRDO	2019	−77	50	52.257	166	40	25.770	−33.1	11
WAHIWA	2100	21	31	15.531	202	0	10.436	395.6	4
LACRES	2103	32	16	44.522	253	14	45.428	1150.7	5
LASHM2	2106	51	11	9.367	358	58	25.532	217.8	4
APLMND	2111	39	9	48.588	283	6	11.907	96.0	4
PRETOR	2115	−25	56	48.272	28	20	52.046	1582.6	6
ASAMOA	2117	−14	19	50.265	189	17	2.891	39.5	5
WALDOP	2203	37	51	52.094	284	29	32.286	−38.0	12
ASCION	2722	− 7	58	9.757	345	35	40.701	88.6	10
COCOSL	2723	−12	11	44.560	96	50	3.054	−44.3	16
MOSLAK	2738	47	11	7.247	240	39	43.766	338.3	15
STNVIL	2745	33	25	32.087	269	5	9.799	−2.5	46
MESHED	2817	36	14	26.485	59	37	44.239	950.8	5
FRTLMY	2822	12	7	53.927	15	2	6.787	298.5	7
NATLDP	2837	− 5	54	57.998	324	49	55.950	3.9	6
Station positions for MOTS									
1BPOIN	1021	38	25	50.253	282	54	48.699	−38.2	3
1FTMYR	1022	26	32	53.359	278	8	4.161	−35.9	3
1OOMER	1024	−31	23	24.970	136	52	15.455	128.6	5
1QUITO	1025	− 0	37	21.567	281	25	16.401	3571.8	19
1SATAG	1028	−33	8	58.448	289	19	53.576	709.3	5
1MOJAV	1030	35	19	47.931	243	5	59.055	886.2	3
1JOBUR	1031	−25	53	0.843	27	42	26.404	1537.2	3
1NEWFL	1032	47	44	29.838	307	16	46.121	64.2	8
1GFORK	1034	48	1	21.344	262	59	19.513	216.4	3
1WNKFL	1035	51	26	46.148	359	18	8.330	97.3	5
1ULASK	1036	64	58	37.046	212	28	31.715	284.1	8
1ROSMN	1037	35	12	7.388	277	7	41.321	864.1	3
1ORORL	1038	−35	37	32.106	148	57	14.825	943.5	4
1ROSMA	1042	35	12	7.408	277	7	41.021	864.1	3
1TANAN	1043	−19	0	31.860	47	17	59.360	1362.2	6
1UNDAK	7034	48	1	21.344	262	59	19.513	215.4	3
1EDINB	7036	26	22	46.743	261	40	7.459	20.9	3
1COLBA	7037	38	53	36.207	267	47	40.940	227.4	3
1BERMD	7039	32	21	49.826	295	20	35.069	−14.9	4
1PURIO	7040	18	15	28.817	294	0	23.584	−10.4	3
1GFSCP	7043	39	1	15.716	283	10	20.528	10.1	3
1DENVR	7045	39	38	48.056	255	23	38.640	1757.8	3
1JUM24	7071	27	1	14.010	279	53	12.657	−26.9	3
1JUM40	7072	27	1	14.388	279	53	12.844	−26.1	3
1JUPC1	7073	27	1	14.372	279	53	13.060	−26.6	3
1JUBC4	7074	27	1	14.570	279	53	13.107	−25.9	3
1SUDBR	7075	46	27	21.306	279	3	10.514	235.5	5
1JAMAC	7076	18	4	34.700	283	11	27.038	417.9	5
1GFSCN	7077	38	59	57.438	283	9	37.906	7.1	3
WALMOT	7078	37	51	47.543	284	29	27.717	−39.6	5

[a] Estimated error of Cartesian coordinates

TABLE 5.34.—*Comparisons With JPL's DSS*

Four-parameter solution (GEM 6—JPL):
Scale = 1.42×10^{-6} $\bar{\Delta\lambda} = -0.50$
$\bar{\Delta x} = -3.2$ m $\bar{\Delta y} = -0.8$ m

Site	Differences	
	Δx(m)	Δy(m)
Goldstone, Cal.	+1.4	+6.9
Woomera, Aus.	−3.3	+1.1
Tidbinbilla, Aus.	+1.6	−3.0
Johannesburg, RSA	+1.6	−2.3
Madrid, Spain	0.0	−2.1
	rms(m)	3.0

TABLE 5.35.—*Direct Comparisons of Spin Axis Distance (D) and Longitude (λ) (GEM 6—JPL)*

Site	ΔD (m)	$\Delta D/D$ ($\times 10^6$)	$\Delta\lambda$ (sec)	$\Delta D - \Delta\bar{D}$ (m)	$\Delta\lambda - \Delta\bar{\lambda}$ (sec)
Goldstone, Cal.	2.8	0.5	−0.67	−5.1	−0.19
Woomera, Aus.	12.7	2.2	−0.35	4.8	0.16
Tidbinbilla, Aus.	6.7	1.3	−0.34	−1.2	+0.17
Johannesburg, RSA	5.4	0.9	−0.57	−2.2	−0.06
Madrid, Spain	4.4	0.9	−0.63	−3.5	−0.12
Average	7.9 ($\bar{\Delta D}$)	1.2	−0.51 ($\bar{\Delta\lambda}$)		

TABLE 5.36.—*GEM 6—VLBI Using x,y Coordinates Goldstone, Cal. to Rosman, N.C.*

Solution	Equatorial baseline (meters)
VLBI	3 050 034.8
GEM 6	3 050 035.5

TABLE 5.37.—*Comparison of GEM 6 With GEM 4*

	62 stations	23 MOTS–SPEOPTS camera stations	19 BN camera stations	13 Doppler stations
Δx (m)	0.54 ± 1.4	−0.58 ± 2.7	0.30 ± 2.4	0.85 ± 3.1
Δy (m)	−0.44 ± 1.4	−0.13 ± 2.7	0.03 ± 2.4	−0.50 ± 3.3
Δz (m)	0.22 ± 1.4	−0.56 ± 2.8	3.8 ± 2.4	−1.5 ± 3.1
s ($\times 10^6$)	−0.02 ± 0.22	−0.01 ± 0.42	0.07 ± 0.37	−0.01 ± 0.48
ϵ ('')	0.00 ± 0.05	0.02 ± 0.10	0.02 ± 0.09	−0.10 ± 0.14
ψ('')	−0.02 ± 0.05	−0.08 ± 0.13	0.02 ± 0.10	−0.07 ± 0.11
ω('')	0.04 ± 0.05	0.04 ± 0.12	0.00 ± 0.86	0.06 ± 0.12
rms (m)	±3.3	±2.8	±0.12	±3.7

TABLE 5.38.—*Comparison of Coordinate Systems of GEM 6 and Goddard '73*

	45 BC–4 stations
Δx (m)	+20 ± 1.5
Δy (m)	+12 ± 1.5
Δz (m)	−9 ± 1.5
s ($\times 10^6$)	+1.9 ± 0.23
ϵ ('')	−0.07 ± 0.06
ψ('')	+0.07 ± 0.06
ω('')	+0.08 ± 0.06
rms (m)	±11

TABLE 5.39.—*Comparison of Coordinate Systems of GEM 6 and Standard Earth III*

	68 stations	17 BN stations	47 BC–4 stations
Δx (m)	+4.2 ± 1.22	1.9 ± 2.4	+4.8 ± 1.46
Δy (m)	−5.3 ± 1.22	−3.5 ± 2.4	−6.2 ± 1.46
Δz (m)	+9.5 ± 1.22	15.0 ± 2.4	+7.4 ± 1.46
s ($\times 10^6$)	0.49 ± 0.05	0.84 ± 0.38	+0.23 ± 0.05
ϵ ('')	+0.19 ± 0.05	−0.01 ± 0.09	+0.23 ± 0.05
ψ('')	−0.08 ± 0.05	−0.10 ± 0.11	−0.09 ± 0.06
ω('')	−0.46 ± 0.05	−0.51 ± 0.09	−0.47 ± 0.06
rms (m)	±10	±8	±10

TABLE 5.40.—*Comparison of Coordinate Systems of GEM 6 and NWL 9D*

	12 Doppler stations	20 BC–4 stations
Δx (m)	−6.2 ± 1.3	4.3 ± 2.3
Δy (m)	3.1 ± 1.5	1.4 ± 2.3
Δz (m)	8.3 ± 1.4	1.9 ± 2.3
s ($\times 10^6$)	−0.30 ± 0.21	−0.41 ± 0.35
ϵ ('')	0.01 ± 0.06	0.30 ± 0.09
ψ ('')	−0.03 ± 0.06	0.15 ± 0.09
ω ('')	−0.59 ± 0.06	−0.65 ± 0.09
rms (m)	±2.8	±7.9

TABLE 5.41.—*Comparison of Coordinate Systems of GEM 6 and WN–4*

	43 Stations
Δx (m)	0.5 ± 0.7
Δy (m)	0.6 ± 0.6
Δz (m)	2.1 ± 0.7
s ($\times 10^6$)	0.44 ± 0.1
ϵ ('')	0.00 ± 0.03
ψ ('')	0.04 ± 0.03
ω ('')	0.35 ± 0.03
rms (m)	±4.6

TABLE 5.42.—*Comparison of Shifts Δy in Origins of Coordinate Systems of GEM 6, WN–4, Standard Earth III, and NWL–9D*

	6006	6065	6007	6016	6063	6064	6055	6067	6069
GEM 6—WN–4	32	28	26	24	26	12	22	12	20
GEM 6—Standard Earth III	22	21	8	17	11	8	9	−2	11
GEM 6—Doppler BC 4 Ties	23	1	9	4	−2	−3	13	4	

TABLE 5.43.—*Diameter and Origin of Best-Fitting Spheroid ($f = 1/298.255$)*

	114 stations	29 MOTS–SPEOPTS cameras	40 BC–4 stations	19 BN stations	18 Doppler stations
Δx (m)	−1.5 ± 0.18	−0.85 ± 0.58	3.2 ± 0.26	−8.9 ± 0.40	−6.8 ± 0.40
Δy (m)	−1.3 ± 0.18	0.52 ± 0.51	−1.1 ± 0.27	−0.85 ± 0.36	0.4 ± 0.52
Δz (m)	−1.5 ± 0.19	−4.8 ± 0.58	0.49 ± 0.30	−2.7 ± 0.49	−4.8 ± 0.49
Δa (m)	−11.32 ± 0.10	−8.0 ± 0.30	−14.0 ± 0.16	−5.7 ± 0.25	−11.70 ± 0.27
rms (m)	±7.7	±4.3	±8.3	±4.3	±7.5
a_e (m)	6 378 143.7	6 378 147.0	6 378 141.0	6 378 149.3	6 378 143.

TABLE 5.44.—*Origins Used in Solution for Relation of GEM 6 to North American Datum 1927, South American Datum 1969, European 1950, and Australian 1965*

Datum	λ_0 Longitude			ϕ_0 Latitude			h_0 Height
NAD 1927	261°	27′	29″.494	39°	13′	26″.686	0
SAD 1969	290	0	0	−20	0	0	0
Europe	15	0	0	40	0	0	0
Australia	124	0	0	−33	0	0	0

TABLE 5.45.—*Relation of GEM 6 Coordinate System to North American Datum1927, South American Datum 1969, European 1950, and Australian 1965*

	GEM 6—NAD 1927	GEM 6—AUS 65	GEM 6—SAD 1969	GEM 6—ED 1950
No. stations[a]	33	10	9	5
Δx (m)	−24 ± 2.1	−135 ± 4.0	−63 ± 3.7	−83 ± 5.1
Δy (m)	151 ± 2.3	−39 ± 4.0	0 ± 3.6	−116 ± 5.1
Δz (m)	187 ± 2.1	133 ± 3.9	−32 ± 3.5	−120 ± 5.7
s ($\times 10^6$)	1.7 ± 1.2	2.4 ± 2.2	−1.3 ± 1.2	−0.3 ± 1.6
ϵ (″)	−0.2 ± 0.5	−1.0 ± 0.7	0.6 ± 0.3	0.6 ± 0.6
ψ (″)	0.1 ± 0.3	−1.2 ± 0.6	−0.2 ± 0.3	0.4 ± 1.0
ω (″)	−0.8 ± 0.3	0.4 ±0.5	0.0 ± 0.4	−0.6 ± 0.4
rms (m)	4.0	±4.9	±6.0	±2.6

[a] The signs of Δx, Δy, Δz should be reversed to find the displacement of the coordinate origin

TABLE 5.46.—*Differences Between Coordinates of Stations in GEM 6 and Coordinates of the Same Stations in North American Datum 1927, South American Datum 1969, European 1950, and Australian 1965*

Station	Meters		
	Δx	Δy	Δz
North American Datum 1927			
1021	4	0	−5
1022	−1	−2	3
1030	1	−4	3
1034	−2	1	3
1037	−1	0	7
1042	−1	0	7
1126	−1	0	7
2203	0	7	−5
4082	0	5	7
4840	6	−4	−5
4860	6	−4	−5
6002	2	−2	−7
6111	−2	2	−4
6134	−2	2	−4
7034	−2	1	3
7036	2	0	1
7037	0	1	5
7043	2	−2	−7
7045	−3	−5	2
7050	2	−2	−7
7052	6	−4	−5
7071	−1	5	5
7072	−1	5	6
7073	−0	5	5
7074	−1	5	5
7075	−2	−2	−1
7077	2	−2	−7
7078	2	−2	−8
9001	−8	2	−2
9010	−1	5	5
9021	−5	−5	−4
9049	−1	5	6
9425	−1	2	4
		rms 4.0	
South American Datum 1969			
1025	−8	−8	−3
1028	13	−9	−4
2837	17	4	−5
6008	0	3	−1
6009	−7	−8	−3
6019	−3	3	8
6067	6	4	−2
9009	−9	8	−10
9011	−3	3	8
9031	−7	0	12
		rms 7.3	

TABLE 5.46.—(*Cont'd*)

Station	Meters		
	Δx	Δy	Δz
Australian 1965			
1024	3	−7	−3
1038	−3	0	−5
1152	−6	−1	4
4946	4	−7	−3
6023	3	5	9
6032	0	4	−3
6060	−7	10	6
7054	−6	−1	4
9003	6	−2	−5
9023	6	−2	−5
		rms 4.9	
European 1950			
1035	−6	−4	−8
6015	10	2	11
9004	6	1	10
9008	−8	−1	−9
9091	−1	1	−5
		rms 2.6	

TABLE 5.47.—*Shifts of Various Datums to Coordinate System of GEM 6*

Datum	No. of sites	Meters[a]		
		Δx	Δy	Δz
NAD 1927	33	−22	155	187
SAD 1969	10	−66	3	−33
Europe 1950	4	−81	−115	−122
Australia 1965	10	−130	−41	134
ADIND	5	−147	−3	211
Old Hawaiian	4	61	−284	−182
ARC	5	−126	−110	−296
Tokyo	3	−147	509	686
Samoa	1	−114	124	426
Madagascar	2	−172	−237	−119
Johnston Island	1	177	−80	−209

[a] The signs of Δx, Δy, Δz should be reversed to find the displacement of the coordinate origin

TABLE 5.48.—*Locations of Tracking Stations in Goddard '73 Model*

Station Name	Number	Geodetic coordinates[a] Geodetic latitude (deg, min, sec)	East longitude (deg, min, sec)	Height (meters)	Standard deviation Lat (sec)	Lon (sec)	Ht (m)
1BPOIN	1021	38 25 49.826	282 54 49.027	− 50.26	0.061	0.066	1.93
1FTMYR	1022	26 32 53.336	278 8 4.582	− 36.87	0.046	0.036	0.81
1OOMER	1024	−31 23 25.041	136 52 15.828	123.10	0.044	0.041	0.89
1SATAG	1028	−33 8 58.452	289 19 53.702	705.21	0.052	0.049	1.33
1MOJAV	1030	35 19 47.914	243 5 59.462	886.09	0.043	0.037	0.85
1JOBUR	1031	−25 53 0.900	27 42 26.547	1534.93	0.047	0.041	1.01
1NEWFL	1032	47 44 29.639	307 16 46.883	67.64	0.088	0.153	4.08
1COLEG	1033	64 52 18.268	212 9 37.190	156.20	0.121	0.363	5.46
1GFORK	1034	48 1 21.332	262 59 20.064	213.47	0.038	0.047	1.10
1WNKFL	1035	51 26 45.970	359 18 8.895	100.80	0.044	0.065	1.76
1ULASK	1036	64 58 36.948	212 28 31.733	287.51	0.078	0.197	3.05
1ROSMN	1037	35 12 7.330	277 7 41.756	861.79	0.044	0.039	0.90
1ORORL	1038	−35 37 32.012	148 57 14.927	941.43	0.052	0.054	1.45
1ROSMA	1042	35 12 7.345	277 7 41.456	861.92	0.044	0.039	0.90
1TANAN	1043	−19 0 31.858	47 17 59.420	1356.32	0.061	0.056	1.64
1UNDAK	7034	48 1 21.332	262 59 20.064	213.47	0.038	0.047	1.10
1EDINB	7036	26 22 46.733	261 40 7.840	20.35	0.049	0.039	0.95
1COLBA	7037	38 53 36.179	267 47 41.417	225.04	0.042	0.039	0.91
1BERMD	7039	32 21 49.787	295 20 35.615	− 16.84	0.050	0.043	1.12
1PURIO	7040	18 15 28.771	294 0 24.034	− 9.46	0.053	0.039	1.03
1DENVR	7045	39 38 48.065	255 23 39.119	1759.45	0.042	0.041	1.01
GODLAS	7050	39 1 14.268	283 10 18.955	2.46	0.044	0.051	0.74
WALLAS	7052	37 51 36.191	284 29 24.506	− 49.68	0.056	0.055	1.00
CRMLAS	7054	−24 54 15.609	113 42 58.681	− 1.46	0.063	0.065	0.92
GMILAS	7060	13 18 33.581	144 44 13.951	126.82	0.055	0.077	0.80
1JUM24	7071	27 1 13.868	279 53 13.092	− 31.04	0.061	0.055	1.60
1JUM40	7072	27 1 14.277	279 53 13.272	− 30.89	0.061	0.055	1.60
1SUDBR	7075	46 27 21.352	279 3 10.907	230.50	0.044	0.056	1.33
1JAMAC	7076	18 4 34.515	283 11 27.437	415.28	0.056	0.042	1.12
1CARVN	7079	−24 54 22.615	113 43 16.381	− 9.46	0.063	0.065	0.92
DAKLAS	8820	14 46 3.458	342 35 28.210	28.69	0.115	0.123	2.21
DELFTH	8009	52 0 6.468	4 22 16.292	56.54	0.053	0.076	1.95
ZIMWLD	8010	46 52 37.225	7 27 54.171	941.68	0.048	0.063	1.63
MALVRN	8011	52 8 36.002	358 1 54.808	145.02	0.058	0.092	2.69
HAUTEP	8015	43 55 57.739	5 42 45.360	691.16	0.040	0.046	0.77
HAULAS	8809	43 55 56.787	5 42 44.871	690.13	0.040	0.046	0.77
HAUTLS	8815	43 55 55.780	5 42 44.465	690.14	0.040	0.046	0.77

TABLE 5.48.—(*Cont'd*)

Station Name	Number	Geodetic coordinates[a] Geodetic latitude (deg, min, sec)	East longitude (deg, min, sec)	Height (meters)	Standard deviation Lat (sec)	Lon (sec)	Ht (m)
NICEFR	8019	43 43 32.980	7 17 59.324	415.51	0.052	0.062	1.59
MUDONI	8030	48 48 22.175	2 13 46.696	205.89	0.059	0.087	2.60
1ORGAN	9001	32 25 24.805	253 26 49.169	1615.84	0.052	0.047	1.24
1OLFAN	9002	−25 57 36.013	28 14 52.626	1558.13	0.045	0.040	0.78
OLILAS	9902	−25 57 36.013	28 14 52.626	1555.92	0.045	0.040	0.78
1SPAIN	9004	36 27 46.764	353 47 37.190	56.48	0.041	0.038	0.71
SAFLAS	8804	36 27 45.516	353 47 36.388	55.88	0.041	0.038	0.71
SAFLAS	80	36 27 45.516	353 47 36.388	55.88	0.041	0.038	0.71
1TOKYO	9005	35 40 22.708	139 32 17.258	78.41	0.112	0.131	3.46
1NATOL	9006	29 21 34.473	79 27 27.796	1863.09	0.077	0.081	2.21
1QUIPA	9007	−16 27 56.834	288 30 24.664	2476.01	0.049	0.040	0.83
ARELAS	9907	−16 27 56.834	288 30 24.664	2476.53	0.049	0.040	0.83
1SHRAZ	9008	29 38 13.786	52 31 12.030	1566.93	0.116	0.139	4.39
1CURAC	9009	12 5 25.109	291 9 44.992	− 20.72	0.105	0.098	3.28
1VILDO	9011	−31 56 34.777	294 53 36.556	622.71	0.052	0.052	1.28
1MAUIO	9012	20 42 26.097	203 44 34.433	3040.82	0.054	0.045	1.22
HOPKIN	9021	31 41 2.993	249 7 18.799	2338.61	0.054	0.052	0.98
HOPLAS	9921	31 41 3.191	249 7 18.792	2338.00	0.054	0.052	0.98
AUSBAK	9023	−31 23 25.788	136 52 43.828	131.50	0.044	0.041	0.89
DODAIR	9025	36 0 20.012	139 11 32.248	877.29	0.112	0.132	3.46
DEZEIT	9028	8 44 51.256	38 57 33.837	1897.72	0.068	0.066	1.79
NATALB	9029	− 5 55 40.252	324 50 7.373	28.52	0.066	0.061	1.20
NATLAS	9929	− 5 55 40.252	324 50 7.373	29.14	0.066	0.061	1.20
COMRIV	9031	−45 53 12.463	292 23 9.539	186.85	0.062	0.079	1.98
AGASSI	9050	42 30 21.759	288 26 30.541	131.07	0.126	0.183	4.50
GREECE	9091	38 4 44.567	23 55 59.285	489.38	0.047	0.050	1.10
GRELAS	9930	38 4 42.473	23 55 57.668	496.42	0.047	0.050	1.10
COLDLK	9424	54 44 34.260	249 57 23.234	665.23	0.133	0.234	6.11
EDWAFB	9425	34 57 50.648	242 5 8.202	745.29	0.063	0.062	1.75
OSLONR	9426	60 12 39.545	10 45 4.869	593.98	0.187	0.360	9.74
JOHNST	9427	16 44 38.967	190 29 9.707	3.33	0.105	0.108	3.36
RIGALA	9431	56 56 55.437	24 3 32.470	11.11	0.050	0.094	1.92
UZHGOR	9432	48 38 1.831	22 17 55.471	216.12	0.050	0.071	1.79
HELSIK	8435	60 9 43.199	24 57 7.633	41.59	0.080	0.153	2.66

[a] a_e = 6378155.m, $1/f$ = 298.255

TABLE 5.49.—*Stations Constrained To Adjust in Parallel*

Station	Pair
Mt. Hopkin, Arizona	9921–9021
Woomera, Australia	1024–9023
Carnarvon, Australia	7054–7079
Natal, Brazil	9929–9029
Jupiter, Florida	7071–7072
Haute Provence, France	8809–8015
Dionysis, Greece	9930–9091
Tokyo, Japan	9005–9025
Rosman, North Carolina	1037–1042
Olifantsfontein, Republic of South Africa	9902–9002
Arequipa, Peru	8907–9007
San Fernando, Spain	8804–9004

TABLE 5.50.—*RMS of Fit to the Data*

	Number of observations	RMS of fit
Right ascension	32 122	1".62
Declination	32 301	1".54
Range	7 043	4.6 m

TABLE 5.51.—*Comparison of Distances and Longitudinal Differences*

Location	Code number	JPL Station ΔX, ΔY Used for solution[a]	Spin-axis distance (Goddard '73)–[JPL (LS25)] (meters)	(ppm)	$[\Delta r - (\bar{\Delta r}_{ppm} \times r)]$	$\Delta\lambda - \Delta\bar{\lambda}$ Longitudinal difference (Goddard '73)–[JPL (LS25)][b] [c] (arcsec)	(meters)
Goldstone, California	1030	DSN 12	3.2	0.61	−1.0 m	0".00	0.0
Edwards AFB, California	9425	DSN 12	6.3	1.20	2.1 m	0".11	−3.2
Woomera, Australia	9023	DSN 41	8.1	1.49	3.7 m	0".18	4.9
Johannesburg, Rep of S. Africa	1031	DSN 51	2.6	0.45	−2.0 m	0".02	0.6
Olifantsfontein, Rep of S. Africa	9002	DSN 51	1.3	0.23	−3.3 m	−0".03	−0.8
Orroral, Australia	1038	DSN 42	7.0	1.35	2.8 m	−0".13	−3.1
San Fernando, Spain	9004	DSN 61	1.6	0.31	−2.5 m	0".03	1.0
			$\bar{\Delta r}_{ppm}$ =	0.8			

[a] ΔX, ΔY is the difference between survey X, Y and JPL-determined X, Y
[b] $\Delta\lambda$ is the difference between surveyed longitude and JPL-determined longitude
[c] A mean longitudinal rotation of 0".27 has been applied to GSFC's value

TABLE 5.52.—*Spin Axis Distance of the McDonald Observatory*

Goddard '73	5 492 420.7 m
Goddard '73[a]	5 492 416.3 m
Lunar Laser	5 492 416.0 m
Standard Earth II	5 492 417.0 m
Standard Earth III	5 492 413.4 m

[a] Modified to account for scale difference of 0.8 ppm as determined from comparison of Goddard '73 and JPL values

TABLE 5.53.—*Solution for Orientation between GEM 4 and Goddard '73 Using 34 Common Stations*

ΔX (meters)	ΔY (meters)	ΔZ (meters)	Δl (ppm)	ω	ψ	ϵ
-0.5 ± 0.2	-0.1 ± 0.2	0.5 ± 0.2	0.45	0".26	0".11	0".01
			± 0.03	± 0.01	± 0.01	± 0.01

Correlation coefficients

	ΔX	ΔY	ΔZ	Δl	ω	ψ
ΔY	0.012					
ΔZ	−0.019	0.057				
Δl	−0.140	0.415	−0.242			
ω	0.426	0.194	0.073	0.462×10^{-16}		
ψ	0.236	−0.079	−0.259	-0.186×10^{-18}	−0.216	
ϵ	0.015	−0.303	−0.495	-0.124×10^{-15}	−0.067	0.141

RMS of fit (meters)

X	Y	Z
3.8	4.3	3.6

TABLE 5.54.—*Comparison of Chord Lengths From Station 9004 (San Fernando, Spain) (European Datum of 1950)*[a]

	Survey SAT (m)		Survey SAT (ppm)		GSFC—CNES	
Number	CNES	GSFC '73	CNES	GSFC '73	(m)	(ppm)
9432	−20.5	−22.5	−7.7	−8.5	−2.0	−0.8
9431	−21.5	−14.9	−6.8	−4.7	6.6	2.1
9091	−26.1	−12.6	−9.8	−4.7	13.3	5.1
8019	−14.7	−12.7	−10.5	−9.1	2.0	1.4
8015	−16.8	−17.9	−12.9	−13.7	−1.1	−0.8
8011	−12.2	−8.3	−6.9	−4.7	3.9	2.2
8010	−17.6	−19.8	−10.8	−12.2	−2.3	−1.4
8009	−6.5	−10.8	−3.3	−5.6	−4.3	−2.3

[a] The local survey values are based on the 1971 Bomford geoid

TABLE 5.55.—*Estimated Uncertainty in the Coordinates*

Stations	Uncertainty in each coordinate (m)	Stations	Uncertainty in each coordinate (m)
1021	5	7072	3
1022	3	7075	3
1028	5	7076	3
1030	3	8820	10
1031	3	8009	3
1032	7	8010	3
1033	10	8011	5
1034	3	8015	3
1035	3	8019	3
1036	5	8030	5
1038	5	9001	3
1042	3	9002	3
1043	5	9004	3
1037	3	9005	7
1039	3	9006	7
1040	3	9007	3
1045	3	9008	10
9009	7	9031	5
9011	3	9050	7
9012	3	9091	3
9021	3	9424	10
9028	5	9425	3
9029	5	9426	10
7050	3	9427	10
7052	7	9431	3
7054	5	9432	3
7060	7	8435	5

TABLE 5.56.—*Major Features of the Geoid*

Number	Geographic name	Approximate		Height	
		Latitude (°)	Longitude (°)	GEM 5	GEM 6
1	Solomon Island high	−10	150	73	77
2	Indian low	0	80	−110	−110
3	British Isle high	50	350	64	70
4	Bahama low	30	290	−53	−55
5	Antartica high	−55	50	46	50
6	North East Pacific low	20	240	−47	−55
7	Antartica low	−70	200	−60	−57
8	South America high	−20	290	32	35

TABLE 5.57.—*Comparison Between Station Heights Derived by Dynamic Satellite Geodesy and Gravimetric Geoid (meters)*

Station name	Station no.	Geoid height[a] (GEM 4)[b]	Geoid height (Goddard '73)[c]	Geoid height (gravimetric)	1–3	2–3
United States						
St. Johns	1032		12	13		−1
Blossom Point	1021		−43	−34		−9
Ft. Myers	1022	−28	−29	−31	3	2
Goldstone	1030	−34	−30	−35	1	5
E. Grand Forks	1034	−25	−27	−28	3	1
Rosman	1042	−30	−34	−32	2	−2
Edinburg	7036	−24	−27	−25	1	−2
Columbia	7037	−32	−35	−34	2	−1
Greenbelt	7050		−40	−34		−6
Denver	7045	−19	−18	−18	−1	0
Organ Pass	9001		−22	−23		1
Mt. Hopkins	9021		−30	−29		−1
Jupiter	7072	−32	−32	−36	4	4
Cold Lake	9424		−27	−29		2
Sudbury	7075	−34	−32	−37	−2	5
Caribbean						
Bermuda	7039	−36	−35	−39	3	4
San Juan	7040	−45	−46	−50	5	4
Europe						
Malvern	8011		45	47		−2
Winkfield	1035	49	47	48	1	−1
Delft	8009		45	43		2
Zimmerwald	8010		52	50		2
Haute Provence	8015		45	52		−7
Nice	8019		52	51		1
San Fernando	9004	43	43	50	−7	−7
Naini Tal	9006		−51	−60		9
Dionysos	9091	28	35	40	−12	−5
Oslo	9115		35	36		−5
Uzhgorod	9432		40	40		0
Helsinki	9435		15	13		2
Riga	9431		16	16		0
Australia						
Woomera	1024	12	6	0	12	6
Orroral	1038	25	23	20	5	3
Carnarvon	7054	−25	−20	−17	−8	−3
				rms =	±5.5 m	±4.1 m

[a] Geoid height equals height of tracking station above reference ellipsoid minus height of tracking station above mean sea level

[b] Lerch *et al.* (1972)

[c] (Sec. 5.6.2.)

TABLE 5.58.—*Comparison Between the Geoid of Mather* et al. *(Mather 1970), and the Detailed Global Geoid for Australia*

Longitude	Mather's geoid	Detailed geoid	Difference
Latitude (−24°S)			
114	−16	−15	−1
116	−11	−9	−2
118	−8	−6	−2
120	−4	−2	−2
122	−2	−1	−1
124	−1	−1	0
126	−0	1	−1
128	3	4	−1
130	4	6	−2
132	7	8	−1
134	12	14	−2
136	20	20	0
138	26	26	0
Latitude (−26°S)			
114	−18	−17	−1
116	−14	−13	−1
118	−11	−10	−1
120	−9	−8	−1
122	−8	−8	0
124	−6	−7	1
126	−5	−5	0
128	0	−1	1
130	0	0	0
132	−1	0	−1
134	6	6	0
136	12	12	0
138	18	17	1
140	22	21	1

Absolute mean = ±0.87

TABLE 5.59.—*Normalized Coefficients in GEM 5* ($\times 10^6$)

Zonals

Index			Index			Index			Index			Index		
n	m	Value	n	m	Value	n	m	Value	n	m	Value	n	m	Value
2	0	−484.1662	3	0	0.9605	4	0	0.5363	5	0	0.0659	6	0	−0.1457
7	0	0.0956	8	0	0.0430	9	0	0.0272	10	0	0.0587	11	0	−0.0547
12	0	0.0338	13	0	0.0498	14	0	−0.0260	15	0	−0.0081	16	0	−0.0046
17	0	0.0215	18	0	0.0052	19	0	0.0031	20	0	0.0152	21	0	−0.0101
22	0	−0.0121												

Sectorials and tesserals

Index		Value		Index		Value		Index		Value	
n	m	$\bar{c}$	$\bar{s}$	n	m	$\bar{c}$	$\bar{s}$	n	m	$\bar{c}$	$\bar{s}$
2	1	−0.0012	−0.0087	2	2	2.4282	−1.3802	3	1	2.0055	0.2449
3	2	0.9296	−0.6126	3	3	0.7285	1.4052	4	1	−0.5396	−0.4525
4	2	0.3495	0.6719	4	3	0.9794	−0.2201	4	4	−0.1691	0.3026
5	1	−0.0579	−0.0893	5	2	0.6533	−0.3110	5	3	−0.4403	−0.2440
5	4	−0.2996	0.0261	5	5	0.1373	−0.6577	6	1	−0.0756	−0.0145
6	2	0.0595	−0.3560	6	3	0.0284	−0.0095	6	4	−0.1018	−0.4537
6	5	−0.2858	−0.5174	6	6	0.0307	−0.2265	7	1	0.2535	0.1244
7	2	0.3409	0.1049	7	3	0.2740	−0.2104	7	4	−0.3044	−0.1071
7	5	0.0028	0.0708	7	6	−0.3299	0.1584	7	7	0.0275	0.0661
8	1	0.0099	0.0836	8	2	0.0469	0.0719	8	3	−0.0289	−0.0721
8	4	−0.2410	0.0562	8	5	−0.0814	0.0773	8	6	−0.0545	0.3172
8	7	0.0685	0.0604	8	8	−0.0976	0.0826	9	1	0.1598	0.0063
9	2	0.0170	0.0023	9	3	−0.1269	−0.1234	9	4	0.0056	0.0347
9	5	−0.0250	−0.0839	9	6	0.0630	0.2220	9	7	−0.0711	−0.0387
9	8	0.1595	−0.0350	9	9	−0.0389	0.0884	10	1	0.0883	−0.1740
10	2	−0.0434	−0.0300	10	3	−0.0503	−0.1219	10	4	−0.0740	−0.1015
10	5	−0.1163	−0.0480	10	6	−0.0056	−0.0795	10	7	−0.0135	−0.0247
10	8	0.0304	−0.1288	10	9	0.1117	−0.0542	10	10	0.0696	−0.0405
11	1	−0.0203	0.0215	11	2	0.0326	−0.0883	11	3	0.0052	−0.1343
11	4	0.0390	−0.0657	11	5	0.0181	0.0310	11	6	0.0003	0.0478
11	7	0.0125	−0.1086	11	8	−0.0246	0.0534	11	9	0.0195	0.0630
11	10	−0.0972	0.0036	11	11	0.0632	−0.0245	12	1	−0.0831	−0.0302
12	2	−0.0280	0.0225	12	3	0.0842	0.0576	12	4	0.0033	−0.0201
12	5	0.0100	0.0146	12	6	0.0681	0.0404	12	7	−0.0149	0.0160
12	8	−0.0230	−0.0160	12	9	0.0289	0.0426	12	10	−0.0071	0.0359
12	11	0.0036	0.0389	12	12	−0.0125	−0.0090	13	9	0.0952	0.0851
13	12	−0.0282	0.1002	13	13	−0.0598	0.0689	14	1	−0.0150	0.0053
14	9	0.0378	0.0644	14	11	0.0002	−0.0001	14	12	0.0070	−0.0366
14	13	0.0145	0.0264	14	14	−0.0455	−0.0045	15	9	0.0643	0.0588
15	12	−0.0348	0.0154	15	13	−0.0226	−0.0022	15	14	0.0037	−0.0191
16	12	0.0269	−0.0088	16	13	0.0009	−0.0132	16	14	−0.0217	−0.0406
17	12	0.0167	−0.0009	17	13	0.0104	0.0188	17	14	−0.0133	−0.0022
18	12	−0.0599	−0.0212	18	13	−0.0225	−0.0619	18	14	−0.0109	−0.0033
19	12	−0.0290	−0.0289	19	13	−0.0244	−0.0300	19	14	0.0002	0.0007
20	12	0.0073	−0.0000	20	13	−0.0020	−0.0317	20	14	0.0078	−0.0087
21	12	−0.0217	−0.0226	21	13	−0.0270	0.0108	21	14	0.0096	0.0073
22	12	−0.0399	−0.0053	22	13	−0.0412	−0.0159	22	14	−0.0080	0.0024

TABLE 5.60.—*Normalized Coefficients in GEM 6* ($\times 10^6$)

Zonals

Index			Index			Index			Index			Index		
n	m	Value	n	m	Value	n	m	Value	n	m	Value	n	m	Value
2	0	−484.1661	3	0	0.9607	4	0	0.5362	5	0	0.0661	6	0	−0.1451
7	0	0.0961	8	0	0.0426	9	0	0.0264	10	0	0.0606	11	0	−0.0528
12	0	0.0306	13	0	0.0470	14	0	−0.0206	15	0	−0.0045	16	0	−0.0077
17	0	0.0192	18	0	0.0091	19	0	0.0044	20	0	0.0143	21	0	−0.0098
22	0	−0 0138												

Sectorials and tesserals

Index		Value		Index		Value		Index		Value	
n	m	$\bar{c}$	$\bar{s}$	n	m	$\bar{c}$	$\bar{s}$	n	m	$\bar{c}$	$\bar{s}$
2	1	−0.0009	−0.0032	2	2	2.4251	−1.3883	3	1	2.0021	0.2482
3	2	0.9332	−0.6311	3	3	0.6969	1.4260	4	1	−0.5403	−0.4648
4	2	0.3461	0.6695	4	3	0.9655	−0.2073	4	4	−0.1636	0.3051
5	1	−0.0684	−0.0842	5	2	0.6651	−0.3112	5	3	−0.4656	−0.1947
5	4	−0.2485	0.0360	5	5	0.1845	−0.7119	6	1	−0.0734	0.0150
6	2	0.0643	−0.3740	6	3	0.0115	0.0099	6	4	−0.0867	−0.4655
6	5	−0.2747	−0.5464	6	6	0.0173	−0.2627	7	1	0.2501	0.1385
7	2	0.3463	0.0875	7	3	0.1988	−0.1844	7	4	−0.2807	−0.1408
7	5	0.0265	0.0228	7	6	−0.3074	0.1213	7	7	0.0624	0.0048
8	1	0.0102	0.0579	8	2	0.0610	0.0860	8	3	−0.0378	−0.0667
8	4	−0.2311	0.0284	8	5	−0.0570	0.0622	8	6	−0.0947	0.2528
8	7	0.0658	0.0819	8	8	−0.0832	0.0701	9	1	0.1426	0.0137
9	2	0.0552	−0.0216	9	3	−0.1299	−0.0727	9	4	−0.0125	−0.0147
9	5	−0.0036	−0.0686	9	6	0.0163	0.1267	9	7	−0.0566	−0.0037
9	8	0.2519	−0.0101	9	9	−0.0275	0.0873	10	1	0.0927	−0.1343
10	2	−0.0419	−0.0703	10	3	−0.0383	−0.0998	10	4	−0.0699	−0.1247
10	5	−0.0525	−0.0377	10	6	−0.0550	−0.1342	10	7	0.0174	−0.0237
10	8	0.0473	−0.1213	10	9	0.0960	−0.0749	10	10	0.1365	−0.0391
11	1	−0.0087	0.0431	11	2	−0.0123	−0.1176	11	3	−0.0334	−0.0841
11	4	−0.0263	−0.1033	11	5	0.0842	0.0406	11	6	−0.0421	−0.0353

TABLE 5.60.—(*Cont'd*)

Sectorials and tesserals

Index		Value		Index		Value		Index		Value	
n	m	$\bar{c}$	$\bar{s}$	n	m	$\bar{c}$	$\bar{s}$	n	m	$\bar{c}$	$\bar{s}$
11	7	0.0041	−0.1123	11	8	−0.0204	0.0714	11	9	−0.0349	0.0393
11	10	−0.0464	−0.0333	11	11	0.0696	−0.0356	12	1	−0.0717	−0.0477
12	2	−0.0530	0.0621	12	3	0.0694	0.0371	12	4	−0.0488	−0.0158
12	5	0.0624	0.0230	12	6	0.0531	0.0280	12	7	−0.0261	0.0127
12	8	−0.0187	−0.0031	12	9	−0.0002	0.0251	12	10	0.0231	−0.0012
12	11	0.0066	0.0359	12	12	−0.0123	−0.0103	13	1	−0.0157	−0.0216
13	2	−0.0454	−0.0867	13	3	−0.0460	0.0454	13	4	0.0298	−0.0670
13	5	0.0586	0.0469	13	6	−0.0848	0.0577	13	7	−0.0414	0.0482
13	8	−0.0055	−0.0347	13	9	0.0271	0.0588	13	10	−0.0240	−0.0044
13	11	−0.0576	−0.0830	13	12	−0.0261	0.0991	13	13	−0.0543	0.0722
14	1	−0.0038	0.0480	14	2	−0.0150	0.0429	14	3	0.0653	0.0032
14	4	0.0019	0.0010	14	5	−0.0144	−0.0216	14	6	0.0166	−0.0442
14	7	0.0426	0.0030	14	8	−0.0007	−0.0414	14	9	0.0140	0.0552
14	10	−0.0380	−0.0797	14	11	0.0614	−0.0313	14	12	0.0047	−0.0413
14	13	0.0211	0.0281	14	14	−0.0448	−0.0016	15	1	0.0333	−0.0224
15	2	0.0370	−0.0641	15	3	−0.0457	0.0279	15	4	−0.0070	0.0163
15	5	0.0136	0.0358	15	6	−0.0130	−0.1076	15	7	0.0751	0.0668
15	8	−0.0261	−0.0242	15	9	0.0116	0.0385	15	10	0.0351	−0.0480
15	11	−0.0090	−0.0106	15	12	−0.0338	0.0145	15	13	−0.0191	−0.0000
15	14	0.0036	−0.0189	15	15	−0.0444	0.0356	16	1	0.0321	−0.0091
16	2	−0.0200	0.0639	16	3	−0.0083	−0.0205	16	4	0.0252	0.0306
16	5	0.0120	0.0173	16	6	0.0321	0.0136	16	7	−0.0003	−0.0286
16	8	−0.0456	−0.0046	16	9	−0.0652	−0.0676	16	10	0.0118	0.0386
16	11	0.0189	−0.0078	16	12	0.0197	−0.0195	16	13	0.0034	−0.0139
16	14	−0.0172	−0.0430	16	15	−0.0475	−0.0378	16	16	−0.0376	−0.0119
17	12	0.0137	−0.0012	17	13	0.0145	0.0204	17	14	−0.0111	−0.0013
18	12	−0.0636	−0.0269	18	13	−0.0137	−0.0580	18	14	−0.0127	−0.0006
19	12	−0.0309	−0.0300	19	13	−0.0205	−0.0291	19	14	−0.0006	0.0011
20	12	−0.0056	−0.0154	20	13	0.0114	−0.0282	20	14	0.0055	−0.0098
21	12	−0.0324	−0.0175	21	13	−0.0241	0.0108	21	14	0.0094	0.0078
22	12	−0.0435	−0.0065	22	13	−0.0324	−0.0151	22	14	−0.0077	−0.0007

TABLE 5.61.—*Comparison of Zonal Coefficients (Normalized Coefficients* $\times 10^6$)

Degree	Cazenave *et al.* 1971	GEM 1	GEM 2	GEM 3	GEM 4	GEM 5	GEM 6	Standard Earth II
2	−484.170	−484.177	−484.167	−484.171	−484.169	−484.166	−484.166	−484.166
3	0.961	0.962	0.955	0.958	0.957	0.961	0.961	0.959
4	0.540	0.557	0.537	0.547	0.541	0.536	0.536	0.531
5	0.068	0.062	0.073	0.068	0.069	0.066	0.066	0.069
6	−0.155	−0.178	−0.145	−0.162	−0.153	−0.146	−0.145	−0.139
7	0.094	0.105	0.087	0.092	0.091	0.096	0.096	0.094
8	0.051	0.080	0.040	0.062	0.051	0.043	0.043	0.029
9	0.027	0.008	0.033	0.030	0.031	0.027	0.026	0.023
10	0.051	0.021	0.065	0.040	0.050	0.059	0.061	0.077
11	−0.049	−0.020	−0.055	−0.056	−0.056	−0.055	−0.053	−0.042
12	0.038	0.059	0.021	0.046	0.039	0.034	0.031	0.008
13	0.039	0.002	0.043	0.049	0.048	0.050	0.047	0.024
14	−0.016	−0.037	−0.009	−0.030	−0.027	−0.026	−0.021	0.014
15	0.015	0.047	0.004	−0.007	−0.005	−0.008	−0.005	0.031
16	−0.008	−0.013	−0.026	−0.012	−0.009	−0.005	−0.008	−0.033
17	0.005	−0.035	0.007	0.020	0.017	0.022	0.019	0.014
18	0.023	0.018	0.023	0.016	0.011	0.005	0.009	0.038
19	0.018	0.045	0.015	0.008	0.009	0.003	0.004	0.035
20	0.014	−0.002	−0.001	0.003	0.009	0.015	0.014	0.001
21	−0.016	−0.031	−0.012	−0.008	−0.008	−0.010	−0.010	−0.022
22				−0.001	−0.004	−0.012	−0.014	

TABLE 5.62.—*Comparisons of Terrestrial 5-Degree Anomalies* (G_T) *With Anomalies* (G_S) *Computed from Various Models*[a]

	$E[(G_T - G_S)^2]$ mGal^2			
Model (harmonics)	1283 blocks $n \geq 1$	1044 blocks $n \geq 5$	563 blocks $n \geq 15$	211 blocks $n \geq 25$
GEM 1 (12 × 12)	170	177	183	182
SE–II (16 × 16)	174	182	180	179
GEM 3 (12 × 12)	164	169	172	175
GEM 5 (12 × 12)	161	168	174	176
GEM 4 (16 × 16)	161	151	142	131
GEM 6 (16 × 16)	143	142	139	125
EXP (20 × 20)	131	125	105	86

[a] Satellite-derived solutions—GEM 1, 3, 5; combination solutions (satellite/gravimetry)—SE–II, GEM 4, 6, EXP; all solutions contained higher-degree zonal and selected resonance terms extending to degree 21 or 22.

TABLE 5.63.—*Statistical-Error Estimates for Gravity Models Derived From 5-Degree Terrestrial Anomalies G_T and Anomalies G_S Obtained from Potential Coefficients ($mGal^2$)*

$n \geq$ (blocks)	$E(G_T - G_S)^2$	$E(G_T G_S)$	$E(G_S^2)$	$E(G_T^2)$	$E(\epsilon_S^2)$	$E(\epsilon_T^2)$	$E(\delta_g^2)$
GEM 5 (12 × 12)							
10 (771)	165	190	228	318	37	19	109
15 (563)	174	193	228	330	36	16	122
20 (401)	171	182	214	322	32	14	125
GEM 6 (16 × 16)							
10 (771)	136	214	246	318	32	19	85
15 (563)	139	218	244	330	26	16	97
20 (401)	134	210	232	322	22	14	98
EXP (20 × 20)							
10 (771)	109	236	264	318	28	19	62
15 (563)	105	240	256	330	15	16	74
20 (401)	95	235	242	322	8	14	73

TABLE 5.64.—*Gravity Anomaly Degree Variances ($mGal^2$)*

Degree n	GEM 5	GEM 6	EXP
0	–	9.0	9.0
2	7.3	7.3	7.3
3	33.5	33.6	33.5
4	19.5	19.3	19.3
5	20.4	21.6	21.1
6	18.6	20.0	19.7
7	20.1	17.4	17.1
8	10.5	8.4	8.4
9	10.0	8.8	8.5
10	10.8	11.4	10.7
11	7.1	7.7	7.5
12	4.0	4.1	4.2
13	5.2	10.6	9.3
14	1.7	5.9	6.2
15	1.9	8.5	6.7
16	0.7	6.8	7.5
17	0.3	0.3	5.5
18	2.4	2.4	7.7
19	1.0	1.0	12.5
20	0.5	0.5	10.9
21	0.8	0.9	0.8
22	1.6	1.5	1.5

TABLE 5.65.—*RMS (cm/sec.) Value of Residuals of Two-Way Doppler from USB Tracking on Daily Arcs of ERTS1*[a]

Daily arc (1972)	No. of obs. (passes)	GEM 1	GEM 3	GEM 4	GEM 5	GEM 6	SE-II[b]
7/23	2610 (27)	4.9	6.2	10.3	5.6	6.4	9.1
7/28	1924 (19)	4.9	5.5	4.7	5.5	4.0	9.4
7/29	1183 (18)	5.3	5.3	4.8	5.5	4.3	11.2
7/30	1167 (17)	5.4	6.2	5.6	6.1	3.7	8.7
7/31	989 (15)	5.9	5.7	5.4	5.7	6.2	9.8
8/1	1280 (19)	6.8	5.9	6.0	6.0	6.1	10.4
8/2	1239 (20)	6.4	5.3	6.1	5.2	4.9	11.7
8/4	1176 (18)	7.4	6.0	6.3	6.4	5.5	13.0
8/8	1026 (17)	6.1	6.0	9.1	6.4	6.3	9.1
8/9	1309 (20)	6.2	7.0	10.5	6.8	6.3	10.4
8/10	1686 (20)	5.8	6.1	9.9	6.1	6.9	10.1
	Average rms	5.9	5.9	7.2	5.9	5.5	10.3

[a] Orbital elements: a = 7 283 207 m, e = 0.0001, i = 99.12°; 11 USB Stations: ACN3, BDA3, CRO3, CYI3, GDS8, GDSA, GWM3, HAW3, HSK8, MAD8, and MIL3; average of 7 stations participated per arc.

[b] Standard Earth (II) Gaposchkin and Lambeck (1970).

TABLE 5.66.—*Weighted RMS of Residuals in Camera Observations for a Week-Long Arc on Each of 23 Satellites* ($\sigma = 2''$)

Satellite	GEM 1	GEM 2	GEM 3	GEM 4	GEM 5	GEM 6	SE-II[a]
TELSTAR	0.9	0.9	0.9	0.9	0.9	1.0	2.5
GEOS-1	0.8	1.0	0.8	0.8	0.8	0.8	1.0
SECOR	1.3	1.2	1.3	1.2	1.3	1.2	1.3
OVI-2	2.0	2.3	2.0	2.3	2.0	2.2	2.1
ECHO	1.1	1.1	1.1	1.3	1.1	1.1	1.3
DI-D	1.5	1.7	1.5	1.7	1.4	1.7	2.5
BE-C	0.9	1.0	0.9	1.0	0.9	1.0	1.1
DI-C	1.1	1.5	1.2	1.8	1.0	1.3	1.9
ANNA-1B	1.1	1.3	1.3	1.5	1.1	1.3	1.3
GEOS-2	0.9	0.9	0.8	0.9	0.9	0.9	1.2
OSCAR	1.0	1.2	1.4	1.6	1.0	1.1	1.2
5BN-2	2.5	1.6	4.1	3.3	1.4	1.8	2.7
COURIER	1.2	1.4	1.3	1.3	1.2	1.2	1.1
GRS	1.9	2.3	2.0	2.6	1.8	2.0	4.3
TRANSIT	1.0	1.0	1.0	1.1	1.0	1.1	1.1
BE-B	1.2	1.3	1.4	1.6	1.3	1.6	1.4
OGO-2	1.6	2.9	1.3	2.9	1.4	2.6	2.9
INJUN	1.1	1.3	1.1	1.6	1.0	1.3	1.5
AGENA	1.7	1.6	1.6	1.8	1.6	1.5	2.4
MIDAS	0.8	0.8	0.8	0.8	0.8	0.8	0.8
VANG-2R	0.8	0.8	0.8	0.8	0.8	0.9	0.8
VANG-2S	1.5	1.7	1.4	1.6	1.4	1.7	1.5
VANG-3S	1.3	1.3	1.2	1.3	1.2	1.4	1.7
Average rms (unweighted)	2.″54	2.″79	2.″71	3.″10	2.″37	2.″74	3.″44

[a] Gaposchkin and Lambeck (1970)

TABLE 5.67.—*RMS Value (m) of Residuals of Laser-System Measurements from Short Arcs of BE-C*

Date YYMMDD	Time HHMMSS	No. pts.	GEM 1	GEM 3	GEM 4	GEM 5	GEM 6	SE-II[a]	PGS 2
700706	205829	493	1.2	3.4	3.9	2.0	1.4	1.4	0.9
700818	040000	1712	2.1	1.4	1.3	1.8	2.1	1.4	1.2
700822	040435	1777	1.7	2.3	5.2	2.2	1.2	3.7	0.8
700824	024423	1338	1.5	1.2	1.8	1.2	1.8	0.9	1.1
700825	035555	1197	1.2	2.4	5.5	1.3	3.0	1.4	1.3
700826	031510	1072	0.9	2.3	6.0	1.3	2.2	2.5	0.9
700827	023425	1498	1.3	2.7	5.3	2.0	1.3	3.1	0.8
700828	015324	1269	1.3	1.5	3.3	1.6	1.0	2.7	0.7
700829	011340	1579	1.3	0.9	0.8	1.1	1.2	1.1	1.0
700831	014527	1008	0.7	2.0	5.1	1.0	2.5	1.6	1.0
700901	010340	2001	1.2	3.3	7.5	2.0	2.4	3.6	1.0
700902	002214	1875	1.4	2.4	5.3	2.0	1.1	3.5	0.8
700902	230000	1567	1.2	1.1	2.1	1.4	0.7	1.9	0.8
700907	221312	1349	1.5	2.0	4.0	1.4	1.1	3.6	1.0
700911	193306	775	1.1	2.8	5.4	1.7	1.9	2.7	0.9
700929	140000	615	1.0	1.1	1.9	1.0	1.0	2.5	1.1
701001	130000	690	1.9	0.8	1.7	1.4	1.7	1.7	1.7
701003	135548	818	0.9	2.0	7.3	1.0	2.6	3.0	2.2
701017	080000	568	2.2	1.9	3.2	2.2	1.3	4.0	1.1
701116	222815	506	1.1	2.9	5.1	1.7	2.3	2.1	1.2
701117	214802	723	1.1	1.9	5.0	1.3	1.6	3.4	1.0
701124	185600	1285	1.5	1.6	2.5	1.6	0.9	3.4	0.9
Average rms			1.33	2.00	4.05	1.54	1.65	2.51	1.06

[a] Gaposchkin and Lambeck (1969)

TABLE 5.68.—*Comparison of Models for Long-Term Orbital Perturbations Due to Zonal Coefficients*

Solution	RMS
Standard Earth II	5.49
GEM 2	4.80
GEM 1	3.62
Cazenave *et al.*	3.28
GEM 3	2.92
GEM 4	2.89
GEM 5	3.13
GEM 6	2.97
Wagner	1.50

Table 5.69. TABLE 5.69.—*Summary of Comparisons of Various Models: RMS of Residuals*

Model	Camera data on week-long arcs for 23 satellites (arc sec)	USB Doppler[a] data on 11 day-long ERTS-1 arcs (cm/sec)	Laser data[a] on 22 BE-C short arcs (meters)	Long-term zonal perturbations on 21 satellites (relative measure)	5° average gravity anomalies (mGal)	Rank
GEM 1	2".54	5.9	1.33	3.62	13.3	4
GEM 3	2".71	5.9	2.00	2.92	13.0	3
GEM 4	3".10	7.2	4.05	2.89	12.1	5
GEM 5	2".37	5.9	1.54	3.13	13.0	2
GEM 6	2".74	5.5	1.65	2.97	11.7	1
S.E. II	3".44	10.3	2.51	5.49	13.3	6

[a] Data in these two categories were independent of the solutions for all models.

TABLE 5.70.—*Principal Long-Period Terms in Zonal Harmonic and Luni-Solar Perturbations in Eccentricity of Telstar 2*

Source	Amplitude	Argument	Period (days)
C_3°/C_2°	373×10^{-6}	ω	296
C_4°/C_2°	−60	2ω	148
C_2°	17	2ω	148
C_5°/C_2°	5	ω	296
C_5°/C_2°	−1	3ω	99
Lunar gravitation	−220	$2(\Omega_\mathbb{C}-\omega-\Omega)$	1121
Lunar gravitation	192	$\Omega_\mathbb{C}-2\omega-\Omega$	261
Lunar gravitation	−95	2ω	148
Lunar gravitation	33	$2(\lambda_\mathbb{C}-\omega-\Omega)$	14
Lunar gravitation	11	$2\lambda_\mathbb{C}-\Omega_\mathbb{C}-2\omega-\Omega$	14
Lunar gravitation	−11	$\Omega_\mathbb{C}+2\omega-\Omega$	103
Solar gravitation	245	$2(\lambda_\odot-\omega-\Omega)$	219
Solar gravitation	221	$2\lambda_\odot-\Omega_\odot-2\omega-\Omega$	607
Solar gravitation	−106	$2(\Omega_\odot-\omega-\Omega)$	1111
Solar gravitation	90	$\Omega_\odot-2\omega-\Omega$	261
Solar gravitation	−42	2ω	148
Solar gravitation	−35	$2(\lambda_\odot-\Omega_\odot-\omega)$	781
Solar gravitation	8	$\lambda_\odot-\omega_\odot-2\omega-\Omega$	917
Solar gravitation	−6	$\Omega_\odot+2\omega-\Omega$	103
Solar radiation pressure	42	$\omega+\Omega-\lambda_\odot$	437
Solar radiation pressure	−24	$\omega-\lambda_\odot$	1562

TABLE 5.71.—*Corrections in Milligals for the Interconversion of the International (1967) and Equilibrium Reference Ellipsoids*

Latitude (deg)	[a](1)	[b](2)	[c](3)	Latitude (deg)	[a](1)	[b](2)	[c](3)
90.00	9.10	−9.00	−18.11	45.00	2.31	−2.28	−4.59
89.00	9.10	−9.00	−18.10	44.00	2.07	−2.04	−4.11
88.00	9.09	−8.99	−18.07	43.00	1.83	−1.81	−3.64
87.00	9.07	−8.97	−18.03	42.00	1.59	−1.57	−3.16
86.00	9.04	−8.94	−17.97	41.00	1.35	−1.33	−2.69
85.00	9.00	−8.90	−17.90	40.00	1.12	−1.10	−2.22
84.00	8.95	−8.86	−17.81	39.00	0.88	−0.87	−1.75
83.00	8.90	−8.80	−17.71	38.00	0.65	−0.64	−1.29
82.00	8.84	−8.74	−17.59	37.00	0.42	−0.41	−0.82
81.00	8.77	−8.68	−17.45	36.00	0.09	−0.18	−0.37
80.00	8.70	−8.60	−17.30	35.00	−0.04	0.04	0.08
79.00	8.61	−8.52	−17.13	34.00	−0.27	0.26	0.53
78.00	8.52	−8.43	−16.94	33.00	−0.49	0.48	0.97
77.00	8.42	−8.33	−16.75	32.00	−0.70	0.70	1.40
76.00	8.31	−8.22	−16.53	31.00	−0.92	0.91	1.83
75.00	8.20	−8.11	−16.31	30.00	−1.13	1.12	2.25
74.00	8.08	−7.99	−16.06	29.00	−1.34	1.32	2.66
73.00	7.95	−7.86	−15.81	28.00	−1.54	1.52	3.06
72.00	7.81	−7.73	−15.54	27.00	−1.74	1.72	3.45
71.00	7.67	−7.58	−15.26	26.00	−1.93	1.91	3.84
70.00	7.52	−7.44	−14.96	25.00	−2.12	2.09	4.21
69.00	7.37	−7.28	−14.65	24.00	−2.30	2.27	4.57
68.00	7.21	−7.12	−14.33	23.00	−2.48	2.45	4.92
67.00	7.04	−6.96	−14.00	22.00	−2.65	2.62	5.26
66.00	6.87	−6.79	−13.65	21.00	−2.81	2.78	5.59
65.00	6.69	−6.61	−13.30	20.00	−2.97	2.94	5.90
64.00	6.50	−6.43	−12.93	19.00	−3.12	3.09	6.21
63.00	6.31	−6.24	−12.56	18.00	−3.27	3.23	6.50
62.00	6.12	−6.05	−12.17	17.00	−3.41	3.37	6.77
61.00	5.92	−5.85	−11.77	16.00	−3.54	3.50	7.03
60.00	5.72	−5.65	−11.37	15.00	−3.66	3.62	7.28
59.00	5.51	−5.45	−10.96	14.00	−3.78	3.74	7.52
58.00	5.30	−5.24	−10.54	13.00	−3.89	3.84	7.73
57.00	5.08	−5.02	−10.11	12.00	−3.99	3.95	7.94
56.00	4.87	−4.81	−9.67	11.00	−4.09	4.04	8.13
55.00	4.64	−4.59	−9.23	10.00	−4.18	4.12	8.30
54.00	4.42	−4.37	−8.79	9.00	−4.25	4.20	8.46
53.00	4.19	−4.14	−8.33	8.00	−4.32	4.27	8.60
52.00	3.96	−3.91	−7.87	7.00	−4.39	4.33	8.72
51.00	3.73	−3.68	−7.41	6.00	−4.44	4.39	8.83
50.00	3.50	−3.45	−6.95	5.00	−4.49	4.43	8.92
49.00	3.26	−3.22	−6.48	4.00	−4.53	4.47	9.00
48.00	3.02	−2.99	−6.01	3.00	−4.56	4.50	9.06
47.00	2.79	−2.75	−5.54	2.00	−4.58	4.52	9.10
46.00	2.55	−2.51	−5.06	1.00	−4.59	4.53	9.12
				0.0	−4.59	4.54	9.13

[a] Column (1): For change from the "Reference Ellipsoid 1967" to the International Reference Ellipsoid, add the correction to the gravity anomaly. For reverse operation subtract the correction.

[b] Column (2): For change from the "Reference Ellipsoid, 1967" to the Equilibrium Reference Ellipsoid, add the correction to the gravity anomaly. For reverse operation subtract the correction.

[c] Column (3): For change from the International Reference Ellipsoid to the Equilibrium Reference Ellipsoid, add the correction to the gravity anomaly. For reverse operation subtract the correction.

TABLE 5.72.—*Spherical Harmonic Coefficients of Isostatic Gravity Anomaly Potential*

n	m	C_{nm}	S_{nm}	n	m	C_{nm}	S_{nm}
2	0	−0.104 19D−06	0.0	10	0	0.707 41D−07	0.0
2	1	−0.938 39D−07	−0.979 87D−07	10	1	0.552 00D−07	−0.125 77D−06
2	2	0.254 15D−05	−0.137 54D−05	10	2	0.103 49D−07	−0.457 72D−07
3	0	0.100 25D−05	0.0	10	3	−0.172 02D−07	−0.741 45D−07
3	1	0.206 21D−05	0.213 93D−06	10	4	−0.574 94D−07	−0.132 10D−06
3	2	0.106 04D−05	−0.769 73D−06	10	5	−0.948 51D−07	−0.146 63D−07
3	3	0.673 45D−06	0.126 50D−05	10	6	−0.434 84D−07	−0.101 14D−06
4	0	−0.326 10D−06	0.0	10	7	0.599 03D−08	−0.452 11D−07
4	1	−0.462 275D−06	−0.385 97−06	10	8	0.241 86D−07	−0.967 29D−07
4	2	0.480 97D−06	0.646 57D−06	10	9	0.562 34D−07	−0.711 98D−07
4	3	0.859 25D−06	−0.173 02D−06	10	10	0.504 08D−07	−0.259 34D−08
4	4	−0.167 64D−06	0.173 28D−06	11	0	−0.357 55D−07	0.0
5	0	0.234 08D−06	0.0	11	1	−0.665 8D−07	0.544 14D−07
5	1	−0.578 46D−06	−0.484 76D−07	11	2	0.294 86D−07	−0.112 19D−06
5	2	0.674 31D−06	−0.263 82D−06	11	3	−0.175 24D−07	−0.756 64D−07
5	3	−0.518 21D−06	−0.251 86D−06	11	4	−0.102 39D−07	−0.707 64D−07
5	4	−0.477 73D−06	0.605 95D−07	11	5	0.522 32D−07	0.276 68D−07
5	5	0.193 84D−06	−0.764 30D−06	11	6	−0.257 48D−07	0.431 25D−07
6	0	−0.219 37D−06	0.0	11	7	0.307 48D−07	−0.814 47D−07
6	1	−0.859 78D−07	0.590 80D−07	11	8	−0.226 51D−07	0.420 19D−07
6	2	0.534 99D−07	−0.346 70D−06	11	9	−0.353 7D−07	0.546 00D−07
6	3	−0.665 26D−08	−0.703 91D−07	11	10	−0.959 05D−07	−0.247 79D−07
6	4	−0.168 78D−06	−0.403 87D−06	11	11	0.104 36D−06	−0.136 15D−07
6	5	−0.262 17D−06	−0.451 98D−06	12	0	0.503 54D−07	0.0
6	6	0.241 64D−07	−0.242 57D−06	12	1	−0.651 70D−07	−0.305 45D−07
7	0	0.156 83D−06	0.0	12	2	−0.383 68D−07	0.457 47D−07
7	1	0.238 85D−06	0.790 46D−07	12	3	0.138 97D−06	0.668 75D−07
7	2	0.264 61D−06	0.687 69D−07	12	4	−0.298 94−07	−0.180 41D−07
7	3	0.277 06D−06	−0.236 00D−06	12	5	0.412 41D−07	0.105 97D−07
7	4	−0.224 21D−06	−0.121 01D−06	12	6	0.362 89D−07	−0.181 57D−07
7	5	0.497 42D−08	0.253 43D−07	12	7	−0.290 33D−07	0.148 96D−07
7	6	−0.302 50D−06	0.199 31D−06	12	8	−0.128 43D−07	−0.452 07D−08
7	7	0.894 48D−07	0.473 06D−07	12	9	−0.141 68D−07	0.122 09D−07
8	0	0.494 33D−07	0.0	12	10	−0.216 66D−08	0.362 34D−07
8	1	0.369 098D−07	0.689 24D−07	12	11	−0.725 84D−09	0.104 58D−08
8	2	0.157 10D−08	0.732 52D−07	12	12	0.264 17D−07	0.280 66D−07
8	3	−0.429 30D−07	−0.103 42D−06	13	0	0.131 67D−07	0.0
8	4	−0.241 55D−07	0.269 61D−07	13	1	0.278 07D−07	−0.740 15D−08
8	5	−0.641 17D−07	0.773 02D−07	13	2	0.225 46D−07	−0.118 89D−06
8	6	−0.751 22D−07	0.253 43D−06	13	3	−0.504 19D−08	0.159 36D−07
8	7	−0.181 60D−07	0.553 16D−07	13	4	−0.516 59D−07	−0.692 80D−07
8	8	−0.252 92D−07	0.159 58D−06	13	5	0.407 51D−07	0.419 15D−07
9	0	0.831 07D−07	0.0	13	6	−0.118 90D−06	0.414 81D−07
9	1	0.134 29D−06	−0.177 67D−07	13	7	−0.480 19D−07	0.165 60D−06
9	2	0.546 12D−07	−0.318 12D−07	13	8	0.521 32D−07	−0.188 02D−07
9	3	−0.168 50D−06	−0.111 60D−06	13	9	0.116 70D−07	0.853 60D−07
9	4	0.267 24D−07	−0.750 35D−08	13	10	−0.178 52D−07	0.482 16D−07
9	5	−0.475 21D−07	−0.804 59D−07	13	11	−0.265 11D−07	0.363 07−08
9	6	0.721 95D−07	0.157 59D−06	13	12	−0.166 08D−07	0.786 61D−07
9	7	−0.709 52D−07	0.179 04D−07	13	13	−0.220 05D−08	0.910 34D−07
9	8	0.172 33D−06	−0.238 5D−07	14	0	0.988 51D−08	0.0
9	9	−0.155 08D−07	0.107 08D−06	14	1	−0.508 00D−07	0.164 22D−07

TABLE 5.72. —*(Cont'd)*

n	m	C_{nm}	S_{nm}	n	m	C_{nm}	S_{nm}
14	2	−0.232 06D−07	0.135 47D−06	16	6	−0.250 89D−07	−0.145 09D−07
14	3	0.346 57D−07	−0.106 48D−07	16	7	0.321 21D−07	−0.356 68D−07
14	4	0.204 12D−07	0.262 44D−07	16	8	−0.120 20D−07	−0.283 37D−07
14	5	0.526 09D−07	−0.271 00D−07	16	9	0.480 61D−07	−0.344 38D−07
14	6	0.590 95D−07	−0.436 47D−07	16	10	−0.829 02D−07	−0.428 19D−08
14	7	0.129 43D−06	−0.722 97D−07	16	11	0.237 91D−08	−0.120 18D−07
14	8	0.609 06D−08	−0.682 48D−07	16	12	0.998 66D−08	−0.860 36D−08
14	9	−0.501 49D−08	0.450 78D−07	16	13	−0.631 05D−08	−0.350 28D−07
14	10	−0.271 03D−08	−0.127 59D−06	16	14	−0.847 97D−08	−0.183 34D−07
14	11	0.990 35D−07	0.304 86D−10	16	15	−0.536 14D−07	0.866 99D−08
14	12	0.726 69D−08	0.270 52D−08	16	16	0.565 09D−08	0.414 25D−08
14	13	0.160 43D−07	0.125 51D−07	17	0	0.194 10D−07	0.0
14	14	−0.334 79D−07	−0.477 72D−08	17	12	0.121 85D−07	−0.275 58D−07
15	0	−0.300 95D−07	0.0	17	13	0.111 73D−07	0.358 63D−07
15	1	0.995 59D−07	0.503 38D−07	17	14	−0.251 39D−07	−0.101 37D−07
15	2	0.133 32D−07	−0.946 98D−07	18	0	0.358 81D−08	0.0
15	3	0.529 43D−08	0.233 04D−07	18	12	−0.560 34D−07	−0.714 79D−08
15	4	0.327 13D−07	−0.135 68D−07	18	13	−0.559 07D−08	−0.633 67D−07
15	5	0.245 60D−07	−0.175 69D−07	18	14	−0.232 71D−07	0.183 60D−07
15	6	−0.249 01D−07	−0.318 33D−07	19	0	0.230 79D−07	0.0
15	7	−0.368 7D−07	0.802 14D−07	19	12	−0.285 36D−07	−0.164 82D−07
15	8	−0.152 38D−06	0.112 23D−07	19	13	−0.694 54D−08	0.118 67D−07
15	9	0.271 01D−08	0.624 73D−07	19	14	−0.319 29D−08	−0.133 46D−08
15	10	0.582 45D−07	0.320 33D−07	20	0	−0.112 03D−08	0.0
15	11	−0.663 03D−07	0.444 04D−07	20	12	0.175 15D−07	0.152 20D−08
15	12	−0.194 89D−07	−0.137 70D−07	20	13	0.144 48D−07	−0.581 46D−07
15	13	0.982 28D−08	0.219 88D−07	20	14	0.203 48D−07	0.129 48D−07
15	14	−0.197 80D−07	−0.530 94D−08	21	0	0.181 36D−08	0.0
15	15	−0.786 10D−07	0.364 91D−07	21	12	0.976 46D−09	−0.344 15D−07
16	0	0.108 14D−07	0.0	21	13	−0.532 62D−08	0.267 51D−07
16	1	−0.211 71D−07	−0.449 67D−08	21	14	−0.794 27D−08	0.826 36D−08
16	2	0.152 09D−07	0.225 77D−07	22	0	0.125 84D−08	0.0
16	3	0.516 14D−07	−0.211 38D−08	22	12	−0.562 75D−07	−0.330 49D−07
16	4	0.384 17D−07	0.569 03D−07		13	−0.125 78D−07	−0.444 35D−07
16	5	0.233 91D−07	0.385 16D−07		14	0.191 61D−07	0.308 58D−08

TABLE 5.73.—*Power Spectra of the Isostatic Anomaly Potential*

n	Khan's	Uotila's
2	0.05	0.13
3	0.27	1.02
4	0.61	2.25
5	1.06	3.69
6	0.60	2.26
7	0.71	2.16
8	0.65	2.03
9	0.91	3.11
10	1.08	3.60
11	0.87	2.97
12	0.75	2.38
13	1.17	3.75
14	1.16	2.93
15	1.22	3.42
16	1.04	4.04

TABLE 5.74.—*Precise Accelerations on 24-Hour Satellites*

Semimajor axis = 6.6105 Earth radii
Eccentricity = <0.001
Mean motion ~ 1 rev/day

Satellite	λ (deg)	i (deg)	$\ddot{\lambda}$ (10^5 rad/sid day^2)	$\sigma(\ddot{\lambda})$ (10^8 rad/sid day^2)	Weighted residuals, $(0-C)/\sigma$, computed from: GEM 4	GEM 3	SE II	APL	SE I	Resonant field
SKYNET 1, 1	39.58	2.17	3.0553	5.0	4.0	2.9	6.4	5.4	15.4	0.3
SKYNET 1, 5	45.64	1.36	2.8409	1.6	11.4	8.1	16.2	8.4	32.1	0.4
SKYNET 1, 7	50.04	1.21	2.5865	1.8	7.4	4.6	9.8	−0.4	15.4	0.5
ATS 3, 1	314.90	0.29	−2.3140	4.0	−6.3	−4.7	−10.0	−3.0	−31.2	0.5
INTELSAT 2 F4, 1	181.20	0.90	1.9139	14.8	1.4	1.8	3.1	5.6	0.5	0
ATS 5	105.04	1.05	−0.0112	0.4	12.0	−8.8	−1.5	−108.8	154.8	1.5
INTELSAT 2 F3, 1	350.00	1.00	0.1395	2.6	−1.1	1.2	8.0	14.0	17.5	−1.9
INTELSAT 2 F3, 2	347.50	1.10	−0.0925	4.6	1.0	2.4	5.7	9.3	9.1	1.1
SYNCOM 3, 11	167.40	0.60	0.6084	5.0	0.7	1.4	6.0	16.5	1.3	−2.6
SYNCOM 2, 8	65.90	31.85	0.9763	28.4	−1.0	−1.1	−1.3	−2.4	−2.2	−1.0
SYNCOM 3, 14	158.40	2.50	−0.3834	7.2	1.1	1.5	4.2	11.9	3.5	−0.2
ATS 3, 4	265.20	0.50	−0.8387	2.4	−3.8	−7.3	−9.1	−21.7	4.0	−4.7
Statistics:										
RMS measurement			2.25							
RMS residuals (10^8 rad/day^2)					7.4	5.9	10.0	41.9	59.9	2.2

Comments:
RMS measurement $\sigma = 1.2 \times 10^{-8}$ rad/day^2 ^{4} $[12/\sum (1/\sigma)^2]^{1/2}$
RMS residual = $[\sum$ (weighted residuals)^2 $\sum (1/\sigma)^2]^{1/2}$
SKYNET measurements are from R. H. Merson. SYNCOM, INTELSAT, and ATS 5 measurements were computed by the ROAD program from Kepler element data. ATS 3 measurements were computed by the GEODYN program from radar range and range rate data. The resonant field includes all relevant terms through (5, 5) and uses data from all the above satellites except ATS 3, 4.

TABLE 5.75.—*Tests on INTELSAT 2F1, 1328-Day Arc*

Orbit: a = 4.165 Earth radii, e = 0.64, i = 18°, n ≈ 2 rev/day

Field used in orbit determination	RMS semimajor axis residual (m)	RMS mean anomaly residual (degs)	RMS mean resid × 100/ nonres RMS mean resid	RMS along track residual (km)
GEM 4 (1972)	241	0.26	0.33	120
GEM 3 (1972)	237	0.25	0.32	118
SAO SE II (1970)	247	0.47	0.60	217
APL 5.0 (1967)	696	1.58	2.03	730
SAO SE I (1966)	507	1.25	1.60	580
Nonresonant	9650	78.00	100.00	36100
Resonant	228	.04	0.05	17

Comments: Data span: MJD 40059-41387. Orbit data used: 131 sets of Brouwer mean elements from MINITRACK observations over about one week of observations per set. Radiation pressure effects included; CR = 1.08, A/M = 0.1 cm^2/g for resonant fields, all potential effects are included giving at least 0.005 of maximum acceleration ($\ddot{M}$) due to (2,2): from (2,2)→(11,2), (4,4)→(11,4), and (6,6)→(13,6). The resonant field is GEM 4 with adjusted coefficients for (2,2), (3,2), (4,2) and (5,2).

TABLE 5.76.—*Tests on COSMOS 382 Rocket (1970 103B) Data*

Field Used in Orbit Determination	RMS Semimajor Axis Residual (m)	RMS Mean Anomaly Residual (deg)	RMS along Track Residual (km)
GEM 4 (1972)	11.6	0.162	27.5
GEM 3 (1972)	11.3	0.158	26.8
SAO SE II (1970)	55.0	0.690	116.5
APL 5.0 (1968)	68.5	1.460	247.0
SAO SE I (1966)	26.3	0.438	74.2
Nonresonant	26.4	0.444	75.1
Resonant	7.9	0.023	3.9

Comments: Data are mean Kepler elements from DOD (North American Air Defense Command), MJD 40928-41355. "Mean" off-resonant beat-period = 125 days. Orbit inclination = 51.5°, eccentricity = 0.18. Minimum perigee height = 1600 km. Resonant field has adjusted (9,9), (10,9), (11,9) and (12,9) coefficients (with some high correlations) and GEM 4 (13,9)→(16,9) and zonal coefficients. SAO SE I has no significant resonant effects on this orbit

TABLE 5.77.—*Tests on ERTS 1 (58 = day arc)*

Orbit: a = 1.142, e = 0.0015, i = 99.1°, n ≈ 14, primary beat period = 19 days.

Field Used in Orbit Determination	RMS Semimajor Axis Residual (m)	RMS Axis Resid × 100/ Nonres RMS Axis Resid	RMS Inclination Residual (10^{-4} deg)
GEM 4 (1972)	1.48	37	5.95
GEM 3 (1972)	1.49	37	5.95
SAO SE II (1970)	1.31	33	6.70
APL 5.0 (1967)	4.58	114	9.25
Nonresonant	4.03	100	9.00
Resonant	.30	8	—

TABLE 5.78.—*Potentials Used in Comparisons*

Potential	Total number of distinct orbits	Number of reasonant satellites of order	
		9	14
SAO SE I (1966)	14	1	7
APL 5.0 (1967)	7	0	1
SAO SE II (1970)	19	1	8
GEM 3 (1972)	25	2	9
GEM 4 (1972)	25	2	9

TABLE 5.79.—*Tests on Two Long 24-Hour Satellite Arcs*

Field used in orbit determination	Orbits tested: SYNCOM 2 (Data span: 1300 days, i ≈ 31°) PMS longitude residual (deg)	RMS × 100/ nonres RMS	RMS along track residual (km)	SYNCOM 3 (Data span: 1900 days, i ≈ 4°) RMS longitude residual (deg)	RMS × 100/ nonres RMS	RMS along track residual (km)
GEM 4 (1972)	0.096	1.2	71	0.187	.8	138
GEM 3 (1972)	0.101	1.3	74	0.200	.8	148
SAO SE II (1970)	0.236	3.1	174	0.307	1.2	227
APL 5.0 (1967)	0.502	6.5	370	0.750	3.0	554
SAO SE I (1966)	0.574	7.4	422	0.254	1.0	188
Nonresonant	7.75	100.0	5680	25.0	100.0	10300
Resonant	0.040	.52	30	0.134	.5	99

Comments: Only semimajor axis and longitude ($M + \omega + N - \theta_e$) data used in orbit determinations. All resonant effects through (5,5) used except for nonresonant field test. resonant field has adjustment for terms through (4,4).

Data are from DOD, range and range rate tracking

Data are from DOD, range and range rate tracking (MJD 39665-40175), NASA X-Y angle tracking (of beacon), MJD 40833-41580

6

NASA WALLOPS FLIGHT CENTER

J. Belgin
A. Borrego
R. L. Brooks
D. J. Dempsey
N. M. Fubara
K. Guard
M. Hillhouse
C. D. Leitao
C. F. Martin
G. Mourad
N. A. Roy
H. R. Stanley

6.1 INTRODUCTION

(N. A. Roy, Wolf Research and Development Corporation (WRC), and H. R. Stanley, National Aeronautics and Space Administration/Wallops Flight Center (NASA/WFC))

6.1.1 Objectives

The major accomplishments of the GEOS–B, C-band systems project may be assessed in terms of the project objectives. The objectives of the project were grouped into three categories: (1) primary objectives that must be met for the project to be successful; (2) secondary objectives that were sufficiently important to warrant serious consideration in the project effort; and (3) other objectives that were important to the project and for which additional effort would be desirable if sufficient time, data, and funding were available.

The first of five primary objectives was to calibrate and evaluate the C-band radar systems. The noise level of the various radars were evaluated by analyzing data from many short-arc passes of GEOS–2 over a single station. The results of these analyses showed that AN/FPQ–6 radars typically had a precision of $\simeq$0.8 meter in range and 10″ to 15″ in angle. The AN/FPS–16 radars typically had a precision of of $\simeq$1.5 meters in range and 20″ to 25″ in angle.

Special tests were performed to evaluate the retroreflector (Van Atta Array) on GEOS–2 and to provide estimates of comparative range accuracy of retroreflector and transponder tracking. During these tests it was found that a pulsewidth/bandwidth-dependent bias existed when the radars were calibrated by using one pulsewidth but were tracked by use of another pulsewidth. The correction to be applied to these data was found to be about half the difference (in meters) between the pulsewidth used during calibration and pulsewidth received from the transponder. The radar ranges were also compared directly with ranges obtained by the Goddard Space Flight Center (GSFC) laser distance measuring equipment (DME) located at Wallops during a Wallops Island collocation experiment (WICE). The agreement between the two systems averaged 0.2 meter, with a σ of 2.9 meters. A range bias resulting from the use of a non-point-source target for reference was discovered for AN/FPS–16 at Wallops. This turned out to be a constant +7.9 meters.

Data from many revolutions and passes over many stations were reduced and analyzed to determine biases in azimuth and elevation. These analyses showed no indication that lag, droop, or other dynamic errors were significant contributors to angular error. However, most radars exhibited an azimuth bias that was dependent on the secant of the elevation angle. The proper correction factor was determined and applied to the data.

The second primary objective was to determine the adequacy of specific mathematical models for the C-band system. A detailed and comprehensive mathematical error model for the radar was developed. The detailed model was tested and evaluated, and a simple deterministic model was developed for use in the data reduction procedure. This simplified model has been evaluated and found to be adequate for describing the form and function of systematic radar errors. The adequacy of the model has been further corroborated, if somewhat indirectly, by the quality of the geodetic results obtained during the network evaluations.

The third primary objective was to evaluate the feasibility of using satellites and C-band systems for geodetic as well as calibration purposes. Data from 3 weeks of concentrated tracking in January and February 1969 from more than 20 globally distributed radar stations were reduced and analyzed. The results demonstrated clearly that it was possible to determine ranging and timing biases, to remove atmospheric and trans-

ponder-induced biases, and to identify and remove errors induced in data handling from the data collected at the various remote sites while obtaining high-quality geodetic results. In most instances, biases determined at Wallops were confirmed by the controlling agencies. Station positions, distances between stations, and gravitational potential coefficients were estimated during the project.

The fourth primary objective was to provide scale for solutions using only angular data and to confirm surveyed locations of sites. The C-band radar data were used to provide scale for geometric solutions at Ohio State University, with excellent results reported. Improved center-of-mass station positions were obtained for more than 20 globally distributed stations to an accuracy of 10 meters or better. Distances between these stations were compared with distances surveyed to first-order accuracy, and agreement was generally found to be better than 3 meters.

The fifth primary objective was to determine the short- and long-term stability of the radar system. Tests covering periods of 1 hour to 3 years have shown that the radar and satellite systems are stable over extensive periods of time. System drift is negligible provided sufficient time (2 to 3 hours) is allowed for warming up the radar.

The secondary study objective was to study long- versus short-arc methods of reducing orbital data as applied to calibration problems. Short-arc methods have been shown to be adequate for determining precision. However, biases in the measurements tend to be hidden in the least-squares fit. Relative timing biases, relative station position errors, and relative biases in the measurements (and, therefore, relative accuracy) may be recovered from short-arc solutions that involve data from two or more stations, where one station has been chosen as the reference or datum station.

Long arcs (up to 2 days) allow for more accurate orbit determinations from which estimates of measurement accuracy can be made. Error analyses have shown that orbital accuracy degrades after 2 days because of uncertainties in the gravitational potential models. Improved station coordinates were determined along with radar measurement and timing biases by means of 2-day arc solutions.

A sixth objective was to study the feasibility of using satellites both to evaluate shipborne instrumentation and to locate ships. Ships were located by means of orbital solutions determined by data from land-based radars. The principal error source was found to be the ship's inertial navigation system (SINS), which was used for determining the ship's motion during the satellite tracking.

A seventh objective was to investigate the feasibility of contributing to the knowledge of the gravitational potential model and to determine the adequacy of existing models for specific purposes in missile and space-vehicle testing. The usefulness of C-band radar data for determining gravitational potential coefficients was clearly demonstrated during these studies. Effective resonant coefficients C_{14}^{13} and S_{14}^{13} were determined using data from four, geographically well-distributed radar sites. The coefficients have been verified in subsequent orbital solutions.

An eighth objective was to determine and analyze the spectral content of the radar data. The spectral content of the range, azimuth, and elevation data of the Wallops radars were evaluated by performing power spectral density analysis of typical tracking data. The results indicate that the performance of the radars is consistent with design criteria. Specifically, the results demonstrate that the precision of the data can be improved by low-pass digital filtering to remove most of the random error while preserving the signal content.

A ninth objective was to develop and implement a data-compaction scheme compatible with C-band data to be sent to various users. A spectral analysis study was conducted to determine the optimum data recording and sampling rates for C-band radars and to determine an optimum method of filtering and sampling the data.

It was determined that the signal content of range, azimuth, and elevation measure-

ments made by a C-band radar was concentrated at frequencies below 0.05 Hz. The optimum method of filtering and sampling to preserve the statistical information content of the data consisted of filtering the data using a low-pass filter with a sharp cutoff at 0.5 Hz, then sampling the data at one sample every 10 seconds. It was also determined that filtering is not necessary for data that are to be used in long-arc orbital determinations, because data selected without filtering yielded essentially the same orbit, with the same residual rms, as data filtered before selecting.

A tenth and final objective was to determine the effectiveness of using C-band radar for checking out remote-site instrumentation. The determination of improved geodetic coordinates for ships and isolated land-based radars and the associated calibration constants of such radars is a clear indication of the effectiveness of C-band radar data.

6.1.2 Agencies and Radar Systems Involved

Agencies participating in the GEOS–2 C-band tests are listed in table 6.I, along with the number of GEOS–2 missions scheduled for each agency. The total amount of usable data obtained by each agency is also shown.

6.2 INSTRUMENTATION

6.2.1 Functional Description of Radar Sets AN/FPQ–6 and AN/TPQ–18

The fixed and transportable versions of MIPIR (AN/FPQ–6 and AN/TPQ–18) have identical performance characteristics. The radar subsystems may be functionally grouped under microwave system (transmitter, antenna, and receiver), target acquisition system, target tracking (angle and range servos) system, data-processing system, and system-control system. An ultrastable frequency synthesizer and multiplier unit, a power amplifier, and a modulator form the transmitter. A solid-surface 8.8-meter paraboloidal reflector illuminated by a monopulse, polarization-diversified feed comprises the Cassegrainian antenna. This structure is supported by a two-axis (azimuth-elevation) pedestal, featuring a low-friction hydrostatic azimuth bearing, antibacklash drive gearing, and precision, single-speed, 20-bit angle-shaft encoding subsystem. The acquisition-system features reflect test range needs; a diverse complement of aids facilitate detection and lock-on.

A 46-meter boresight tower for calibration is also part of the system. It comprises radiation antenna, optical targets, and a C-band test source. The angle or antenna-positioning subsystems are high-torque-to-inertial electrohydraulic servo loops. Tracking signals are supplied to the antenna positioning and ranging servos by a low-noise broadband three-channel receiver subsystem. An all-electronic, digital, ranging subsystem affords unambiguous range coverage to $\simeq$60 000 km (32 000 n. mi.) at high pulse repetition rates with a granularity (least significant bit in the range) of about 2 meters. The data processing system contains a 4096-word stored program for a militarized computer (RCA FC–2101).

6.2.1.1 Target Tracking System

6.2.1.1.1 ANGLE SERVOS

Commutated-error video, either local or remote in origin, is converted to hydraulic-value control signals in the azimuth and elevation servo loops. These dc signals, with amplitudes and polarities dependent on the magnitude and direction of the antenna pointing error, determine the slew rate of the antenna and direction of rotation about each axis.

Two angle servo preamplifiers, similar except that the gain in the azimuth channel depends on the secant of the elevation angle, provide initial received-signal gain for the servo errors. Two angle error amplifiers provide additional gain as well as demodulate the error signals. Phase compensation and bandwidth control networks follow. A variable bandwidth is available in the tracking mode. A pedestal-velocity-feedback loop, employing a tachometer generator, affords rate compensation. Current feedback around the valve

driver stage stablizes gain in this loop. The technique of modulation, ac amplification, and demodulation permits less complex circuitry than drift-stablized dc amplifier control.

6.2.1.1.2 RANGE SERVOS

Digital techniques in the range system provide an unambiguous measurement interval of ≃60 000 km (32 000 n. mi.) with high pulse-repetition rates, about 2-meter granularity, and excellent precision. In a conventional pulse-type radar, the unambiguous range is inversely related to the pulse repetition frequency (prf), severely curtailing the sampling rate at longer ranges. Range extensions in the AN/FPQ–6 are achieved by reducing the repetition rate. A low repetition rate, i.e., 2.5 pulses per second (pps), provides the time scale, and a relatively high one (160 or 640 pps) is the ranging-pulse repetition frequency. The maximum range is established by the 2.5–pps repetition rate.

By dividing this time base into either 64 or 256 zones, depending on the prf employed, as many transmissions as zones may occur before the first pulse is received. True range is determined by locating a return within a zone (apparent or ambiguous range) and adding it to the rf transmission that caused it. Ambiguity resolution is a two-step process called find and verify. Verification is attempted immediately following target lock-on and, if not successful, the system switches to the find process.

The find process determines the target location zone, and the verify process confirms that the correct zone is found. In the find mode, two successive transmitter pulses are delayed about 14 630 meters. Concurrently, double range gates are generated in each pulse repetition period, the second gate being about 14 630 meters from the first. The number of pulses following the two delayed pulses are counted until two video pulses are detected in the delayed range gates.

The verify process is then started. For verification, one transmitter pulse and the range gate in the assumed zone are delayed ≃14 630 meters. The gate is then checked for the presence of a target return. The verify process is repeated until four video pulses are detected. Failure to verify causes the find process to repeat.

To avoid interference between received and transmitted pulses (because the transmitted pulse cannot be excluded by the receiver), the system is capable of delaying alternately the transmitter pulse time and the range gate delay time. This technique enables time separation of the transmitter pulses and target returns, without changing the sampling rate, when the received signals are in the predetermined interference region. To exclude signals caused by ground reflections, a blanking region of ≃14 630 meters about the time positions of the transmitted pulses is also allowed.

Automatic tracking is accomplished in a type-2 servo loop. Split gates are superimposed on the gated video and coupled with a time discriminator to derive range errors. The magnitude of the range error is dependent on the time position of the target return with respect to the center of the tracking gate. The sign of the range error is established by the relative energy levels bracketed by the split gates (early and late). The range error voltage is integrated, converted to a ramp voltage with a slope and sign equivalent to the magnitude and direction of the range error, and then changed in an analog-to-digital converter to a series of pulses proportional to this error. The pulse rate depends on the slope of the ramp voltage and consequently on the magnitude of the range error. These pulses are then used to correct the range counter and reposition the track gate.

The range tracker also generates precise timing signals for its internal operation, as well as the system triggers. A prf sequencer is included to eliminate interference caused by the nearly simultaneous arrival at the transponder of interrogation pulses from several radars in a tracking chain.

6.2.1.2 Data System

The data system enables the collection, processing, display, and transmission of data.

For explanatory purposes, this system has been divided into three sections: angle, data handling, and data processing. The angle section consists of azimuth and elevation encoders (transducers) and their associated digital circuits. The data handling section accepts data from various sources to enable communication in the form of digital data and control commands with the data processor, other portions of the radar, and external sources.

Inputs to the data handling section include the outputs from the angle section, range information from the range tracking subsystem, and analog angle-servo-error information from the angle tracking subsystem. The servo-error data are converted to digital form and supplied to the data processing section, where these signals are processed and summed with the outputs of the angle encoder outputs to compensate for dynamic lag in the angle subsystem. The data processor is programed to correct, in addition to dynamic lag, the encoder for certain systematic errors such as nonorthogonality, antenna droop, encoder bias, and pedestal-leveling error. After correction the angle and range data are supplied to the console for display and to output circuits for immediate use by external equipment.

The transducer signal processor is a correlating, resolving, and pulse counting technique to form a 20-bit binary word for each coordinate. Basically, the encoder circuit amplifies and shapes a reference marker, representing the zero reference position of the boresight axis, and uses it to start and synchronize a 20-stage high-speed counter.

A variable marker is amplified, shaped, and used to stop the high-speed counter temporarily; it represents the angular position of the boresight axis at that instant.

The signal processing circuit for each coordinate contains the following: an automatic-frequency-control (AFC) sample pulse generator; a marker-pulse shaping and synchronizing circuit; the high-speed counter and its control circuit, including an automatic-check signal generator and sequencer and delayed reference marker generator; and the up-down counter and its control circuit, including the up-down signal processing circuit, the read control circuit, and the output buffer.

An angle-error signal-processing section (or analog section) and digital circuits comprise the data handling section. In combination with the data processor, these circuits correct the raw pedestal-position data for known errors and make the result available to the user as serial readout from either three parallel lines or a single line. The analog section translates the pedestal tracking-error voltages (commutated ac) from the angle servo preamplifiers into filtered, dc error signals. The dc signals are then sent to the digital portion of the data handling section, where they are converted into digital form and applied to the data processor.

The data processor uses these error data to correct the pedestal angular-position raw data for dynamic tracking lag. The elevation error signal is the output of the elevation servo preamplifier. The azimuth error signal is picked off in the azimuth servo preamplifier and represents the error in the antenna traverse plane rather than the error in the horizontal plane. Also included in the data handling section are converters and decoders for decimal readout of the data at the console and signal processing for meter displays of the dynamic tracking lag and noise components of the angle servos.

6.2.1.3 Coherent-Signal Processing Modification

The coherent-signal processing (csp) modification enables tracking at radial velocities up to $\simeq$18 000 m/sec, radial accelerations up to $\simeq$1800 m/sec^2 and radial rates of acceleration (jerk) of $\simeq$1200 m/sec^3. In addition, target radial rates of acceleration of $\simeq$9150 m/sec^3 may be tracked for a duration of 0.03 sec at a prf of 640 pps. At target velocities up to $\simeq$18 000 m/sec and target accelerations between 0 and $\simeq$910 m/sec^2, acquisition time will be between 1.5 and 5.0 sec at a prf of 640 pps. With a prf of 160 pps and target velocity up to $\simeq$18 000 m/sec and a target

accelerating up to $\simeq$450 m/sec^2, acquisition time will be between 6 and 10 sec. When a csp modification is incorporated in the radar, the tracking range is improved by at least a factor of 2 at a prf of 640 pps. At 160 pps the improvement is at least a factor of 1.9.

6.2.2 General Performance Characteristics of Radar Set AN/FPS–16

The tracking accuracy of the AN/FPS–16 is 0.1 mil rms in azimuth and elevation and $\simeq$4.5 meters rms in range.

Three types of output data are provided for azimuth, elevation, and range: digital, potentiometer, and synchro. However, only the digital data are of interest for missions requiring precise data.

Digital data are available for serial readout in binary form with least significant digit first. For azimuth and elevation coordinates, 17-bit data with a granularity of 0.0488 mil for the least significant digit are supplied. For the range coordinate, 20-bit data with a granularity of $\simeq$1.8 meters for the least significant digit are supplied.

The accuracy of the digital output is better than 0.1 mil rms in angle (azimuth and elevation) and better than 3.5 meters rms in range.

The full range of the range tracking system is from 0 to $\simeq$475 000 meters. The actual usable range coverage is determined by radar-receiver recovery time, target echo area for skin tracking, and transponder characteristics (sensitivity, power, and antenna) for transponder tracking. The useful range tracking coverage is from 450 to 275 000 meters on a 1.0–m^2 skin target and from 450 to 475 000 meters on a transponder-assisted target.

The coverage in azimuth is a full and continuous 360 deg. The elevation coverage is from -10 deg to $+190$ deg. The plunge (angles in excess of 90 deg) is very useful as a calibrating feature. The radar will track through -90 deg elevation provided that azimuth and elevation lag errors do not exceed the antenna beamwidth. The maximum tracking rates are 7300 m/sec in range, 750 mils/sec in azimuth, and 400 mils/sec in elevation.

The radar has the capability for echo (skin) or transponder (beacon) tracking at operator option with provisions for monitoring either the transponder signal when echo tracking is being performed or the echo signal when transponder tracking is occurring. An adjustment is provided to allow compensation in the range data for any transponder-induced delay. This compensation is necessary to allow switching from transponder tracking to echo tracking, or vice versa, without loss of track.

Aided tracking is available at operator option for azimuth, elevation, and range. Either automatic frequency control or manual frequency control is provided for both echo and transponder tracking receivers at operator option.

The receiver-frequency coverage is 5400 to 5900 MHz, tunable from operator console for both skin and beacon. The transmitter frequency is from 5400 to 4900 MHz tunable at 250 kW, and at 5480 $\pm$ 30 MHz fixed at 1 mW. Acquisition may be either automatic or semiautomatic. One of 12 pulse repetition frequencies is available at operator option. The frequencies are 285, 341, 366, 394, 467, 682, 732, 853, 1024, 1280, 1364, and 1707 pps. The prf can be changed without loss of track.

One of the three following pulsewidths is available at operator option: 0.25, 0.5, and 1.0 μsec. The pulsewidth can be changed without loss of track.

6.2.3 GEOS–2 C-Band Transponder [1]

Selection of the GEOS–2 C-band transponder was based on criteria that satisfied as many of the requirements of the individual participants as was practical while still meeting the requirements of off-the-shelf availability and the constraints placed on it by the spacecraft. To this end, the GEOS–2 satellite contains two Vega, model-313C, radar trans-

[1] J. T. McGoogan, A. R. Selzer, H. R. Stanley, C. L. Davis, and W. D. Stevenson, all of NASA/WFC, contributed greatly to this section.

ponders (modified version of the Vega model 302C–2). The two model-313C transponders are identical except for internal delay time.

One transponder, known as the long-delay transponder or transponder 2, has a nominal internal delay of 4.96 μsec; the other, known as the short-delay transponder or transponder 1, has a nominal internal delay of 0.75 μsec. This difference is intended to make real-time identification of the transponders easier for all users.

The following characteristics are common to both model-313C transponders.

(1) Receiver system: recovery time, less than 70 μsec; interrogation frequency, 5690 MHz; stability, better than ±2 MHz; bandwidth, 10 to 14 MHz; sensitivity, −70 dBm for 99-percent reply; pulse code, two-pulse with 8-μsec spacing (leading edge to leading edge; pulsewidth, 0.5 μsec (nominal); pulse rise time, 0.1 μsec (nominal).

(2) Transmitter system: output frequency, 5765 MHz; stability, ±3 MHz; maximum prf, 2600 pps; pulse delay jitter for signal level 0 to −55 dBm, less than 20 nsec, and for signal level −55 dBm to −65 dBm, less than 50 nsec; pulsewidth, 0.5 μsec; power output, 400 watts (nominal).

(3) Antenna system: the antenna is a small, quartz-loaded, cavity-backed helix; its polarization is right-handed and circular, and its beamwidth is 120 deg.

6.2.4 GEOS–2 Reflector

Even though the transponder-delay variation resulting from variations in received signal strength can be corrected with calibration curves, there exist long-term variations that are not amenable to this method of correction. During the expected life of the satellite, aging of components was expected to cause slow variations in the signal delay in the transponder. In addition, components such as the silicon-controlled rectifier used with the fixed-delay multivibrator are very susceptible to delay changes because of radiation. Therefore a means of measuring these long-term changes in delay during the satellite life was required so that corrections could be made.

The use of a passive reflecting array to enhance the radar-skin return signal so that both echo and transponder tracking might be accomplished on the same satellite pass was the most promising solution to this problem. Either direct measurements of the time displacement between the signal returned by the reflector and the signal returned by the transponder or the differencing of the range measurements acquired from both modes of operation yields the delay corrections needed.

Characteristics of the passive reflecting array are summarized as follows: (1) frequency range is 5690±20 MHz (nominal); (2) polarization is left-handed and circular for receiving, and right-handed and circular for transmitting; (3) coverage angle is 3 dB down from peak value at ±35° from normal to array in any plane containing normal; and (4) effective radar scattering cross section, 9 dB above a 1-m^2 target.

6.3 DATA

(R. L. Brooks, WRC, and C. D. Leitao, NASA/WFC)

6.3.1 Stations Involved

The tracking stations involved in the calibration and geodetic investigation projects are given in table 6.2. Those involved particularly in the calibration project are listed in table 6.3, together with the number of passes made by each station and the average range rms for each station from short-arc orbits fitted to the radar data. The data are from a 3-week period of intensive tracking from 28 January to 17 February 1969. The coordinates of the stations that contributed data used in the National Geodetic Satellite Program (NGSP) for geodetic purposes are given in chapters 1 and 8. The data were reduced by using the following models and data restrictions: [2]

[2] The A/OMEGA program was developed by WRC for NASA. It is a definitive orbit and geodetic parameter estimation program capable of simultaneously processing observations from multiple arcs and many satellites.

(1) Station coordinates (from SAO 1969 Standard Earth Datum): $a_e = 6378155$, $f = 1/298.26$, and $GM = 3.986013 \times 10^{20}$ cm^3/sec^2.

(2) Gravitational model: SAO 1969 Standard Earth.

(3) Data rate: one observation every 20 seconds.

(4) Data type: range data where elevation was greater than 10 deg; the corresponding angle data were given zero weight in the solution.

(5) Timing: UTC time corrected to UT1 time.

6.3.2 Data Handling

The generalized flow of radar data is shown in figure 6.1. The radar data are recorded on tape at the radar site, generally at a rate of 10 or 20 samples per second. These data are usually totally uncorrected except that the AN/FPQ–6 radar instrumentation includes an RCA 4101, general-purpose computer, which corrects for the following: (1) servo lag (optional), (2) RF axis shift, (3) encoder bias, (4) droop (applied to elevation only), (5) secant error (applied to azimuth only), (6) nonorthogonality; and (7) pedestal mislevel. The form and function of the error corrections are shown in figure 6.2.

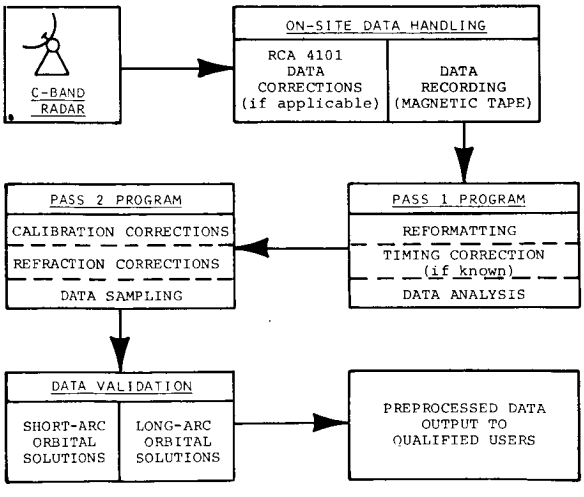

FIGURE 6.1.—C-band data preprocessing.

Note that no corrections to range are made and that no mission-by-mission calibration corrections are applied at the radar site.

The purpose of the pass-1 handling of the raw data is as follows: (1) to apply appropriate bit weights to the information on the data tapes received from the radar site; (2) to compute first differences of the raw data; (3) to correct radar data time tags by applying time corrections, if they are known a priori; (4) to put out data in a format suitable for further computer processing; and (5) to perform preliminary data analysis. Pre- and post-mission calibration measurements are printed as a part of the output.

Three corrections are applied to the data during pass-2 handling: (1) refraction correction, (2) propagation time correction, and (3) combined range corrections.

The tropospheric refraction correction uses an index of refraction measured at the Earth's surface and a dependence on the cosecant of the elevation angle. The refractive index μ is computed from

$$\mu - 1 = \left[\frac{103.49\ (P-e)}{T} + \frac{86.26}{T}\left(1 + \frac{5748}{T}e\right) \right] \times 10^{-6}$$

where P is the total atmospheric pressure (mm Hg), e is the partial pressure of water vapor (mm Hg), and T is the absolute temperature (°C). If temperature, pressure, and relative humidity are not known, a nominal value of 0.2919×10^{-3} for $\mu - 1$ is assigned. The refraction-corrected ranges R_c are

$$R_c = R_o - [(\mu - 1)\ (s)/(\sin E_c + 0.026)]$$

where E_c, the corrected elevation angle measurement, equals $E_o - (\mu - 1)/[0.01644 + 0.93\ (\tan E_o)]$, E_o being the observed elevation angle; R_c is the corrected range; R_o is the observed range; s is the scale height of the atmosphere, approximately 7.6 km; and 0.026 equals the Earth's curvature correction.

The measurement-time tags are corrected in the propagation-time correction step to the

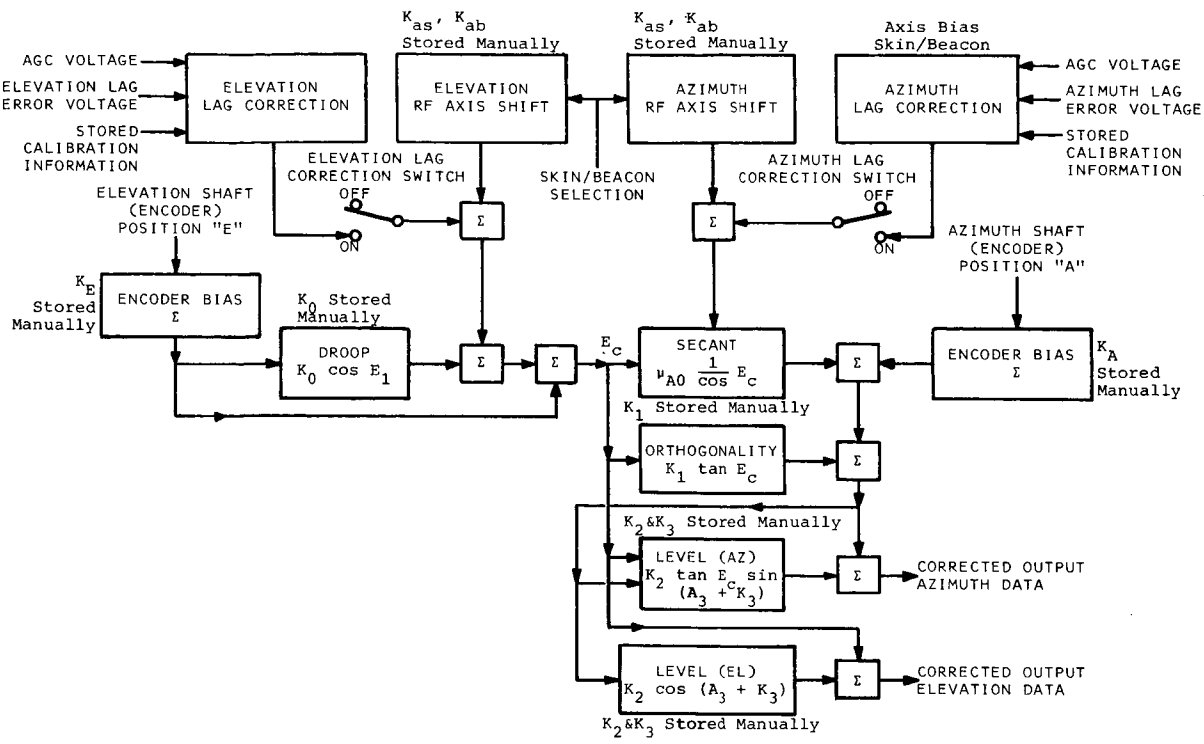

FIGURE 6.2.—AN/FPQ–6 error correction program.

time the radar pulse left the satellite by the relationship

$$T_c = T_o - R_c/c$$

where T_c is the corrected time of observation in sec, T_o is the time of sample at radar and c, velocity of light, equal 299 792.5 km/sec.

The total combined range correction is calculated from

$$R_{TC} = R_s - R_c - R_T - R_R$$

where R_{TC} is the total correction to range, R_s is the surveyed distance to the calibration target, R_c is the radar distance to calibration target, and R_T is the nominal delay in the transponders (transponder-1 delay is 112 meters, transponder-2 delay is 739 meters).

6.3.3 Data Validation

The internal consistency of each set of tracking data is checked by making single-station, single-pass, orbital solutions. Gross errors, such as assignment of the wrong correction for transponder delay, will become apparent at this stage. Long-arc, multiple-station, orbital solutions are then found to ascertain data accuracy. These solutions may be used to solve for measurement and timing biases, if they exist.

6.4 THEORY [3]

(C. F. Martin and Keith Guard, WRC)

6.4.1 Rationale of the Reduction Process

The basic problem in orbit determination is to calculate, from a given set of observations of the spacecraft, a set of numbers specifying the orbit of the spacecraft. Because there are generally more observations than unknowns, the unknowns are over-determined. Therefore a statistical estimation

[3] The material in this section was assembled with the help of T. V. Martin and Clyde Goad, both of WRC.

scheme is necessary to estimate the best set of unknowns. The unknowns include not only the orbital elements but also station coordinates and instrumental errors. The scheme selected is a partitioned, Bayesian, least-squares method. The complete development of this procedure is presented later in this section.

It should be noted that the relationships between the observations and unknowns are in general nonlinear; thus an iterative procedure is necessary to solve the resultant nonlinear equations. The Newton-Raphson iteration formula is used to solve these equations. The procedure used in the determination of the orbit and estimation of the unknown is as follows:

(1) An orbit is computed by the methods of numerical integration given in section 6.4.6, with the functions given later in this section for the forces and with a set of assumed elements.

(2) The quantitities corresponding to each observation are computed from appropriate geometric relationships.

(3) The observations are corrected for timing and measurement biases, as well as for propagation time and station position error.

(4) A linear equation relating the observations O_i, the corresponding computed values C_i, and the vector of the unknown to be determined P is defined. The relationship is given by

$$O_i - C_i = \sum_j \frac{\partial C_i}{\partial P_j} dP_j - dO_i \qquad (6.1)$$

where i denotes the i^{th} observation or association with it, dP_j is the correction to the j^{th} unknown, and dO_i is the error of observation associated with the i^{th} observation. The basic problem of estimation for these unknowns is to determine a solution to these equations. The procedure adopted for solving the problems is now shown.

(5) Using the method of least squares, with the best estimate for orbital elements and other unknowns to be determined as the known a priori, solve equation (6.1) for dP_j.

(6) Adjust the a priori parameter-vector by the correction dP_j, and, using the corrected value with its variance/covariance matrix as known a priori, repeat the procedure.

A Bayesian solution has the advantage that any known, a priori, information such as estimates of the orbital elements and other unknowns and their variances can be included in the solution. In the absence of valid estimates of any parameter, the associated variance can be designated as a very large number, indicating ignorance of the value. The resulting reduction, if a state of ignorance is assumed for all parameters, is equivalent to a weighted least-squares solution of the linearized equations. Also, constraints on the values of the parameters can be realized by use of the a priori covariance matrices.

A number of schemes can be used for estimation. One method is a batch scheme that uses all observations simultaneously to estimate the set of unknowns. An alternative would be a scheme that uses the observations sequentially to calculate an updated set of parameters from each additional observation. Although batch and sequential schemes are essentially equivalent, practical numerical problems often occur when sequential schemes are used, especially when highly accurate observations are being processed. Therefore a batch scheme was chosen.

6.4.2 Equations

6.4.2.1 Equations of Motion

In a geocentric, inertial, rectangular coordinate system, the equations of motion for a spacecraft are of the form

$$\ddot{\mathbf{r}} = -\frac{GM\,\mathbf{r}}{r^3} + \mathbf{A}$$

where $\mathbf{r}$ is the position vector of the satellite, G is the gravitational constant, M is the mass of the Earth, and $\mathbf{A}$ is the acceleration caused by the asphericity of the Earth, extraterrestrial gravitational forces, atmospheric drag, and solar radiation. This provides a system of

second-order equations which, given the position and velocity components at the epoch, may be integrated to obtain the position and velocity at any other time. Throughout this discussion, if a vector, such as **r**, has been defined, then the appearance of that symbol in italics, as r, indicates the Euclidian norm (magnitude) of the vector.

There is an alternative way of expressing the equations of motion:

$$\ddot{\mathbf{r}} = \nabla V + \mathbf{A}_D + \mathbf{A}_R$$

where V is the potential field of gravitation, $\mathbf{A}_D$ contains the drag acceleration, and $\mathbf{A}_R$ contains the acceleration resulting from solar radiation pressure. This equation is, of course, just a regrouping of terms coupled with a recognition of the existence of a potential field.

6.4.2.2 Force Model

6.4.2.2.1 EARTH FORCES

The Earth's gravitation field is represented by the gradient of the potential of a solid body having the form of an ellipsoid of revolution with small irregular variations expressed by a sum of spherical harmonics as follows:

$$V = \frac{GM}{r}\left[1 + \sum_{n=2}^{nmax}\sum_{m=0}^{n}\left(\frac{a_e}{r}\right)^n p_n^m(\sin\phi')\,(C_{nm}\cos m\lambda + S_{nm}\sin m\lambda)\right]$$

where r is the geocentric distance to the satellite, $nmax$ is the upper limit for the summation (highest degree), and a_e is the Earth's mean equatorial radius.

6.4.2.2.2 SOLAR AND LUNAR GRAVITATIONAL PERTURBATIONS

The perturbations caused by a third body on a satellite orbit are treated by defining a function R_d which is the third-body disturbing potential. This potential takes on the following form:

$$R_d = \frac{GM_d}{r_d}\left[\left(1 - \frac{2r}{r_d}S + \frac{r^2}{r_d{}^2}\right)^{-1/2} - \frac{r}{r_d}S\right]$$

where M_d is the mass of the disturbing body, $\mathbf{r}_d$ is the geocentric true position of date vector to the disturbing body, S is the cosine of the enclosed angle between **r** and $\mathbf{r}_d$, and **r** is the geocentric true position of date vector of the satellite.

The third-body perturbations considered in A/OMEGA are for the Sun and the Moon. Both are computed by

$$\mathbf{a}_d = -GM_d\left[\frac{\mathbf{d}}{D_d} + \frac{1}{r_d}\frac{\mathbf{r}d}{r_d}\right]$$

6.4.2.2.3 SOLAR RADIATION PRESSURE

The force resulting from solar radiation can have a significant effect on the orbits of satellites with a large area to mass ratio. The acceleration from solar radiation pressure is formulated as

$$\mathbf{A}_R = \nu\, C_R \frac{A_s}{m_s} P_s\, \hat{r}_s$$

where

- ν eclipse factor such that $\nu = 0$ when the satellite is in the Earth's shadow and $\nu = 1$ when the satellite is illuminated by the Sun
- C_R factor depending on the reflective characteristics of the satellite
- A_s cross-sectional area of the satellite
- m_s mass of the satellite
- P_s solar radiation pressure in the vicinity of the Earth
- r_s geocentric true unit vector of date pointing to the Sun

The unit vector $\hat{r}_s$ is determined as part of the lunisolar ephemeris computations.

6.4.2.2.4 ATMOSPHERIC DRAG

A satellite moving through an atmosphere experiences drag. The acceleration because of this force is given by

$$\mathbf{A}_D = -\frac{1}{2} C_D \frac{A_s}{m_s} \rho_D \, v_r \, \mathbf{v}_r \qquad (6.2)$$

where

- C_D satellite drag coefficient
- A_s cross-sectional area of the satellite
- m_s mass of the satellite
- ρ_D density of the atmosphere at the satellite position
- $\mathbf{v}_r$ velocity vector of the satellite relative to the atmosphere

Both A_s and C_D are treated as constants. Although A_s depends somewhat on satellite attitude, the use of a mean cross-sectional area does not lead to significant errors for geodetically useful satellites. The factor C_D varies slightly with satellite shape and atmospheric composition. However, for any geodetically useful satellite, it may be treated as a satellite-dependent constant. The velocity vector $\mathbf{v}_r$ is computed under the assumption that the atmosphere rotates with the Earth.

The atmospheric density is the factor which is least well-known in the computation of drag; however, it is essential to the computation of realistic perturbations from drag. The solution is to use the Jacchia-Nicolet model of the atmosphere, which is perhaps the best model currently available. In this model, densities between 120 and 1000 km are given with a formula for extrapolating to higher altitudes.

The formulas for computing the exospheric temperature have in some cases been modified according to Jacchia's later papers (Jacchia, 1965, 1971). The computation of the density from the exospheric temperature is also based on data from Jacchia's later report.

6.4.3 Measurement Model

The measurement model is

$$C_{t+\Delta t} = f_t(\mathbf{r}, \dot{\mathbf{r}}, \mathbf{r}_{ob}) + b + \dot{f}_t(\mathbf{r}, \dot{\mathbf{r}}, \mathbf{r}_{ob}) \Delta t \qquad (6.3)$$

where

- $C_{t+\Delta t}$ computed equivalent of the observation taken at time $t+\Delta t$
- $\mathbf{r}$ Earth-fixed position vector of the satellite
- $\mathbf{r}_{ob}$ Earth-fixed position vector of the station
- $f_t(\mathbf{r}, \dot{\mathbf{r}}, \mathbf{r}_{ob})$ geometric relationship defined by the particular observation type at time t
- b constant bias on the measurement
- Δt timing bias associated with the measurement

The functional dependence of f_t was explicitly stated for the general case. Many of the measurements are functions only of the position vectors and are hence not functions of the satellite velocity-vector $\dot{\mathbf{r}}$. For notational convenience, f_t will appear without the explicit functional dependence.

The current types of observation are right ascension and declination, range, range rate, direction cosines l and m, angles X and Y, azimuth and elevation, and altimeter height. The radars used in the calibration and evaluation effort measure range, range rate, azimuth, and elevation angles; therefore only these measurements will be described.

6.4.3.1 Range

Consider the station-to-satellite vector

$$\boldsymbol{\varrho} = \mathbf{r} - \mathbf{r}_{ob} \qquad (6.4)$$

where $\mathbf{r}$ is the satellite position vector (x, y, z) in the geocentric Earth-fixed system and $\mathbf{r}_{ob}$ is the station vector in the same system. The magnitude of this vector ϱ is one of the measurements.

6.4.3.2 Range Rate

The time rate of change of ϱ is

$$\dot{\varrho} = \dot{\mathbf{r}} \qquad (6.5)$$

The velocity of the observer in the Earth-fixed system is zero. Consider that

$$\varrho = \rho \hat{\mu} \tag{6.6}$$

where $\hat{\mu}$ is the unit vector in the direction of ϱ.

6.4.3.3 Angle

The azimuth and elevation angles are computed by

$$\left.\begin{aligned} A_z &= \tan^{-1}\left(\frac{l}{m}\right) \\ E_l &= \sin^{-1}(n) \end{aligned}\right\} \tag{6.7}$$

where l, m, n are the direction cosines of $\hat{\mu}$.

6.4.3.4 Error Model

6.4.3.4.1 EFFECTS OF SYSTEMATIC ERRORS ON RANGE DATA

Since an important aspect of calibration is the identification of sources of systematic errors, a series of radar experiments designed to assist in determining the magnitude and sign of systematic errors in the range data was performed. The identified errors are listed in table 6.4. It should be noted that this tabulation is by no means comprehensive or general in nature. It gives errors that have been identified and measured at Wallops. Some of the errors are inherent in the procedure used to gather and process the data.

6.4.3.4.2 ANGULAR ERROR

The theoretical model for azimuth and elevation errors contains the following terms: (1) Azimuth errors: zero-set bias, dynamic lag, nonorthogonality, pedestal leveling, skin/beacon collimation, and encoder nonlinearity; and (2) Elevation errors: zero-set bias, dynamic lag, droop, pedestal leveling, skin/beacon collimation, and encoder nonlinearity.

Corrections for all of these errors are applied to the WFC AN/FPQ–6 data obtained during GEOS–2 tracking missions, with the exception of the encoder nonlinearity corrections and the dynamic-lag corrections. The azimuth and elevation lag errors are computed in real time, but the results are recorded rather than applied in real time. The recorded corrections can, of course, be applied during post-mission data reduction, and therefore the magnitudes of lag error presented in the tables are based on the assumption that such a correction will be carried out after the mission.

6.4.3.4.3 REFRACTION CORRECTIONS

The refraction correction $\Delta\rho$ applied to range observation is computed as follows:

$$\Delta\rho = \frac{2.77 n_s}{328.5\,(0.026 + \sin E_l)} \tag{6.8}$$

where E_l is the elevation angle computed from the initial estimate of the satellite position and n_s is the index of refraction at the surface. If the value n_s is not specified, it is assumed to be 1.

For range rate the correction $\Delta\dot{\rho}$ is derived from the range correction:

$$\frac{2.77\, n_s \cos E_l}{328.5\,(0.026 + \sin E_l)^2}\dot{E}_l \tag{6.9}$$

where $\dot{E}_l$ is the computed rate of change of elevation. For observations of range or range rate from certain stations, there is a correction to account for the mean daily variation of the index of refraction at the surface. This correction, which is a correction to the product $(2.77/328.5)\ n_s$, is computed by linear interpolation in an hourly table.

For elevation observations the correction ΔE_l is computed as follows:

$$\Delta E_l = \frac{n_s 10^3}{16.44 + 930 \tan E_l} \tag{6.10}$$

Azimuth is not affected by refraction.

6.4.3.5 Data Preprocessing

The function of data preprocessing is to convert and correct the data. These corrections and conversions relate the data to the physical model and to the coordinate and time reference systems used. The corrections and conversions are (1) to transform all observation times to Atomic Time (A1) at the satellite, (2) to correct range measurements for transponder delay, and (3) to correct for refraction.

The transponder delay correction $\Delta\rho_d$ is computed as a polynomial in the range rate:

$$\Delta\rho_d = a_0 + a_1\dot{\rho} + a_2\dot{\rho}^2 \qquad (6.11)$$

where a_0, a_1, and a_2 depend on the characteristics of the particular satellite.

6.4.4 Adjustment Equations: Bayesian Least-Squares Estimation

Consider a vector $\mathbf{z}$ of N independent observations whose values can be expressed as known functions of M quantities denoted by the vector $\mathbf{x}$. The following nonlinear regression equation holds:

$$\mathbf{z} = \mathbf{f}(\mathbf{x}) + \boldsymbol{\delta} \qquad (6.12)$$

where $\boldsymbol{\delta}$ is the N vector denoting the noise on the observations. Given $\mathbf{z}$, the functional form of $\mathbf{f}$, and the statistical properties of $\boldsymbol{\delta}$, the estimate of $\mathbf{x}$ that is "best" in some sense must be obtained.

Bayes' theorem in probability holds for probability density functions and can be written as follows:

$$p(\mathbf{x}|\mathbf{z}) = \frac{p(\mathbf{x})}{p(\mathbf{z})} p(\mathbf{z}|\mathbf{x}) \qquad (6.13)$$

where $p(\mathbf{x}|\mathbf{z})$ is the joint conditional probability density function for the vector $\mathbf{x}$, given that the data vector $\mathbf{z}$ has occurred, $p(\mathbf{x})$ is the joint probability density function for the vector $\mathbf{x}$, $p(\mathbf{z})$ is the joint probability density function for the vector $\mathbf{z}$, and $p(\mathbf{z}|\mathbf{x})$ is the joint conditional density function for the vector $\mathbf{z}$, given that $\mathbf{x}$ has occurred.

Often $p(\mathbf{x})$ is referred to as the a priori density function of $\mathbf{x}$, and $p(\mathbf{x}|\mathbf{z})$ is referred to as the a posteriori conditional density function. In any Bayesian estimation scheme this a posteriori density function must be determined and from this function determine a best estimate of $\mathbf{x}$, which can be denoted $\hat{\mathbf{x}}$.

To obtain the a posteriori conditional density function, an assumption must be made concerning the statistical properties of the noise on the observations: the noise vector $\boldsymbol{\delta}$ has a joint normal distribution with mean vector $\mathbf{0}$ and a variance-covariance matrix $\sum_z$. $\sum_z$ is an $N \times N$ matrix and is assumed diagonal; that is, the observations are considered to be independent and uncorrelated. The best estimate of $\mathbf{x}$, $\hat{\mathbf{x}}$, is defined as that vector maximizing the a posteriori density function; this is equivalent to choosing the mean value of this distribution. An estimator of this type has been referred to as the maximum likelihood estimate in the Bayesian sense.

A further assumption is that the a priori density function $p(\mathbf{x})$ is a joint normal distribution and is written as follows:

$$p(\mathbf{x}) = \left[\frac{\mathrm{Det}(\sum_A^{-1})}{2\pi}\right]^{\frac{M}{2}} \exp\left[-\frac{1}{2}(\mathbf{x}-\mathbf{x}_A)^T \times \sum_A^{-1}(\mathbf{x}-\mathbf{x}_A)\right] \qquad (6.14)$$

where $\mathbf{x}_A$ is the a priori estimate of the parameter vector and $\sum_A$ is the a priori variance-covariance matrix associated with the a priori parameter vector. $\sum_A$ is an $M \times M$ matrix, which may or may not be diagonal.

The conditional density function $p(\mathbf{z}|\mathbf{x})$ can be written as

$$p(\mathbf{z}|\mathbf{x}) = \left[\frac{\mathrm{Det}(\sum_z^{-1})}{2\pi}\right]^{\frac{N}{2}} \exp\left\{-\frac{1}{2}[\mathbf{z}-\mathbf{f}(\mathbf{x})]^T \times \sum_A^{-1}[\mathbf{z}-\mathbf{f}(\mathbf{x})]\right\} \qquad (6.15)$$

It can be shown that maximizing the a posteriori density function $p(\mathbf{x}|\mathbf{z})$ is equivalent to maximizing the product $p(\mathbf{x})p(\mathbf{z}|\mathbf{x})$ because the density function $p(\mathbf{z})$ is a constant

valued function. Further, this reduces to minimizing the following quadratic form:

$$(\mathbf{x}-\mathbf{x}_A)^T\sum_A^{-1}(\mathbf{x}-\mathbf{x}_A) + [\mathbf{z}-\mathbf{f}(\mathbf{x})]^T\sum_z^{-1}[\mathbf{z}-\mathbf{f}(\mathbf{x})] \quad (6.16)$$

This results in the following set of M nonlinear equations:

$$B^T\sum_z^{-1}[\mathbf{z}-\mathbf{f}(\hat{\mathbf{x}})] + \sum_A^{-1}(\mathbf{x}-\mathbf{x}_A) = 0 \quad (6.17)$$

where B is an $N\times M$ matrix with elements

$$B_{NM} = \frac{\partial f_N(\mathbf{x})}{\partial x_M}\mathbf{x}=\hat{\mathbf{x}} \quad (6.18)$$

This equation defines the Bayesian least-squares estimation procedure. It has not been stated how the a priori parameter vector and variance-covariance matrix were obtained. In practice, these a priori values are almost always estimates that have been obtained from some previous data. In these cases the Bayesian estimates are identical to the classical maximum likelihood estimates that would be obtained if all the data were used; in this context the a priori quantities can be considered as additional observations.

The variance-covariance matrix of $\hat{\mathbf{x}}$, V is given by

$$V = \left[B^T\sum_z^{-1}B + \sum_A^{-1}\right]^{-1} \quad (6.19)$$

6.4.5 Iteration Method

A set of M nonlinear equations in M unknowns $\hat{\mathbf{x}}$ has been defined in equation (6.17); these equations are solved by means of the Newton-Raphson iteration formula. Equation (6.17) can be written as

$$\mathbf{F}(\hat{\mathbf{x}}) = 0 \quad (6.20)$$

The iteration formula is

$$\hat{\mathbf{x}}^{(n+1)} = \hat{\mathbf{x}}^{(n)} - \left(\frac{\partial \mathbf{F}(\hat{\mathbf{x}})}{\partial \hat{\mathbf{x}}}\right)^{-1}\mathbf{F}(\hat{\mathbf{x}}^{(n)}) \quad (6.21)$$

where $\hat{\mathbf{x}}^{(n)}$ is the n^{th} approximation to the true solution $\hat{\mathbf{x}}$. Now

$$F(\hat{\mathbf{x}}) = B^T\sum_z^{-1}[\mathbf{z}-\mathbf{f}(\hat{\mathbf{x}})] + \sum_A^{-1}(\hat{\mathbf{x}}-\mathbf{x}_A) = 0 \quad (6.22)$$

Then differentiating and neglecting second derivatives gives

$$\left(\frac{\partial \mathbf{F}(\hat{\mathbf{x}})}{\partial \hat{\mathbf{x}}}\right) = \left[\left(B^T\sum_z^{-1}B\right)\right] + \sum_A^{-1} \quad (6.23)$$

Substituting equation (6.23) in equation (6.21) gives

$$\hat{\mathbf{x}}^{(n+1)} - \hat{\mathbf{x}}^{(n)} = \left(B^T\sum_z^{-1}B + \sum_A^{-1}\right)^{-1}\left\{B^T \times \sum_z^{-1}[\mathbf{z}-\mathbf{f}(\hat{\mathbf{x}})^{(n)}] + \sum_A^{-1}(\hat{\mathbf{x}}^{(n)}-\mathbf{x}A)\right\} \quad (6.24)$$

Now let $\hat{\mathbf{x}}^{(n+1)}-\hat{\mathbf{x}}^{(n)}$, the correction to the n^{th} approximation, be denoted by $d\mathbf{x}^{(n-1)}$, and let $\mathbf{z}-\mathbf{f}(\hat{\mathbf{x}}^{(n)})$, the vector of residuals from the n^{th} approximation, be denoted by $d\mathbf{z}^{(n)}$. Equation (6.24) then becomes

$$d\mathbf{x}^{(n-1)} = \left(B^T\sum_z^{-1}B + \sum_A^{-1}\right)^{-1} \times \left[B^T\sum_z^{-1}d\mathbf{z}^{(n)} + \sum_A^{-1}(\hat{\mathbf{x}}^{(n)}-\mathbf{x}_A)\right] \quad (6.25)$$

6.4.6 Computational Methods

Direct numerical integration of both the equations of motion and the variational equations is used to obtain the position, the velocity, and the attendant variational partials at each observation time. The integrator output is not required at actual observation times; it is given on an even integration step. An interpolation technique is used to obtain values at the actual observation time. The specific numerical methods used for this integration and interpolation are now presented.

First consider the integration of the equations of motion. These equations are three second-order differential equations in posi-

tion and may be formulated as six first-order equations in position and velocity if a first-order integration scheme is used for their solution. For reasons of increased accuracy and stability, the position vector $\mathbf{r}$ is obtained by a second-order integration of the accelerations $\ddot{\mathbf{r}}$, whereas the velocity vector $\dot{\mathbf{r}}$ is obtained as the solution of a first-order system. These are both 10-point multistep methods requiring two evaluations of the derivative on each step.

To integrate the position components, a Störmer predictor

$$\mathbf{r}_{n+1}=2\mathbf{r}_n-\mathbf{r}_{n-1}+(\Delta h)^2\sum_{p=0}^{q}\gamma_{qp}^{*}\ddot{\mathbf{r}}_{n-p} \qquad (6.26)$$

is applied, followed by a Cowell corrector,

$$\mathbf{r}_{n+1}=2\mathbf{r}_n-\mathbf{r}_{n-1}+(\Delta h)^2\sum_{p=0}^{q}\gamma_{qp}\ddot{\mathbf{r}}_{n-p+1} \qquad (6.27)$$

The velocity components are integrated by using an Adams-Bashforth predictor,

$$\dot{\mathbf{r}}_{n+1}=\dot{\mathbf{r}}_n+\Delta h\sum_{p=0}^{q}\beta_{qp}^{*}\ddot{\mathbf{r}}_{n-p} \qquad (6.28)$$

followed by an Adams-Moulton corrector,

$$\dot{\mathbf{r}}_{n+1}=\dot{\mathbf{r}}_n+\Delta h\sum_{p=0}^{q}\beta_{qp}\ddot{\mathbf{r}}_{n-p+1} \qquad (6.29)$$

In these integration formulas, Δh is the integration step size, q has the value 9, and γ_{qp}, γ_{qp}^{*}, β_{qp}^{*}, and β_{qp} are coefficients.

6.4.7 Unmodeled Errors

The assumptions inherent in the least-squares orbital solution are never completely satisfied, primarily because of various systematic errors existing in the measurements and force model. Various procedures can be used to minimize these errors, such as careful data preprocessing, use of the best available set of gravitational coefficients, inclusion of all significant perturbative forces, and estimation of model errors. However, the number of such model errors that can be successfully estimated is limited by computer storage and running time considerations, as well as by the information contained in the data themselves. Furthermore, there are limitations on our knowledge of the most significant errors and on our ability to model certain types, particularly force model errors.

It follows that the assumptions underlying the least-squares orbital solution can never be completely correct. As a corollary, this means that solution accuracy estimates, which assume that all systematic effects have been modeled, will give overly optimistic error estimates.

Realistic estimates of the accuracy of a least-squares orbital solution can be calculated, provided that error estimates for the ignored quantities are available. As a by-product of this calculation, the effects on the orbital solution of each individual error source are available and may be used to identify the importance of various error sources on a particular solution.

6.4.8 Extension of Error Analysis (ORAN)

The mathematics used to calculate the effects on an orbital determination (and/or instrumentation calibration) of certain inaccurate assumptions made in the minimum-variance type reduction of orbital tracking data are outlined in this section; in particular, the effects of ignoring the presence of various systematic errors are discussed. In general, the order in which the operations are performed is not specified.

Consider first the propagation of unmodeled errors into the orbital elements and bias parameters estimated for a single arc. The measurements may be related to the orbital elements and biases by the matrix equation

$$(m)_{nm\times 1}=(A)_{nm\times 6}\,(a)_{6\times 1}+(K)_{nm\times na}\,(k)_{na\times 1}+(B)_{nm\times nu}(\gamma)_{nu\times 1}+(\epsilon)_{nm\times 1} \qquad (6.30)$$

where

m column vector representing the deviation of the actual measurement from that for some approximate orbit (Also called the discrepancy vector)

A matrix giving the partial derivatives of the measurements with respect to the epoch orbital elements, evaluated along the approximate orbit

a column vector representing the deviation of the true orbital elements at epoch from those for the approximate orbit

K matrix giving the partial derivatives of the measurements with respect to those biases that are adjusted

B same as K but with respect to parameters that are not to be adjusted

k deviations of the adjusted quantities from their approximate (or estimated) values

γ same as k but refers to quantities that are not to be adjusted

ϵ column vector representing the random noise on the measurements

nm total number of measurements

na number of adjustable biases

nu number of unadjusted biases

With γ known, the minimum-variance solution of equation (6.30) for a and k is

$$\begin{bmatrix} \hat{a} \\ \hat{k} \end{bmatrix} = \begin{bmatrix} A^TWA & A^TWK \\ K^TWA & K^TWK \end{bmatrix}^{-1} \begin{bmatrix} A^TW \\ K^TW \end{bmatrix} (m - B\gamma)$$

$$= \begin{bmatrix} M_a & M_{ak} \\ M_{ak}^T & M_k \end{bmatrix} \begin{bmatrix} A^TW \\ K^TW \end{bmatrix} (m - B\gamma) \quad (6.31)$$

where

$$W^{-1} = E(\epsilon\,\epsilon^T) \quad (6.32)$$

$$M_k = [K^TWD - K^TWA\ (A^TWA)^{-1}A^TWK]^{-1} \quad (6.33)$$

$$M_{ak} = -QM_k, \text{ with } Q = (A^TWA)^{-1}A^TWK \quad (6.34)$$

$$M_a = (A^TWA)^{-1} + QM_kQT \quad (6.35)$$

The variances of these estimates, if the unmodeled quantities are neglected, are given by

$$\left.\begin{aligned} \text{Var}(\hat{a})_{mod} &= M_a \\ \text{Var}(\hat{k})_{mod} &= M_k \end{aligned}\right\} \quad (6.36)$$

and the covariance is given by

$$\text{Cov}(\hat{a}\hat{k}^T)_{mod} = M_{ak} \quad (6.37)$$

The contribution of the unadjusted quantities to the total variance will be computed as

$$\frac{\partial \hat{n}}{\partial \gamma} = -M_{ak}^TA^TWB - M_kK^TWB \quad (6.38)$$

With the use of equations (6.34) and (6.35), equation (6.38) may be rewritten in the more convenient form

$$\frac{\partial \hat{a}}{\partial \gamma} = -(A^TWA)^{-1}\left[A^TWB + A^TWK\frac{\partial \hat{k}}{\partial \gamma}\right] \quad (6.39)$$

As such, the total variance of the $\hat{a}$ estimate is not computed. To see the expression that should be used to compute the total variance of $\hat{k}$, compute the expected value

$$\begin{aligned} \text{Var}\,\hat{k} &= E(\hat{k}\,\hat{k}^T) \\ &= E[M_{ak}^TA^TW + M_kK^TW] \\ &\quad (m - B\gamma)\,(m - B\gamma)^T \\ &\quad \times [M_{ak}^TA^TW + M_kK^TW]^T \end{aligned} \quad (6.40)$$

If it is assumed that

$$E(m\,m^T) = E(\epsilon\,\epsilon^T) = W^{-1} \quad (6.41)$$

$$E(m\,\gamma^T) = 0 \quad (6.42)$$

$$E(\gamma\,\gamma^T) = \text{Var}\,\gamma \quad (6.43)$$

then equation (6.40) may be written as

$$\begin{aligned} \text{Var}\,\hat{k} &= (M_{ak}^TA^T + M_kK^T)\,(M_{ak}^TA^TW \\ &\quad + M_kK^TW)^T + (M_{ak}^TA^TWB \\ &\quad + M_kK^TWB)\,\text{Var}\,\gamma\,(M_{ak}^TA^TWB \\ &\quad + M_kK^TWB)^T \\ &= M_k + \frac{\partial \hat{k}}{\partial \gamma}\text{Var}\,\gamma\left(\frac{\partial \hat{k}}{\partial \gamma}\right)^T \end{aligned} \quad (6.44)$$

6.5 RESULTS

6.5.1 Introduction

(C. D. Leitao, NASA/WFC, and R. L. Brooks, WRC)

The most significant instrumental and geodetic accomplishments have been the following:

(1) The range accuracy of properly operated and ground-calibrated C-band radars was ascertained. The WFC station results indicate that the AN/FPS–16 and AN/FPQ–6 radars are capable of providing ranges to satellites with an accuracy of 1 to 4 meters.

(2) The pulse Doppler system of WFC's AN/FPQ–6 was used to derive ranges from range-rate measurements. The resulting ranges exhibit noise values as low as 0.0006 meter.

(3) Radar data were filtered to reduce storage requirements and computer time, but statistical content was retained.

(4) Range, angle, and timing biases were determined.

(5) Coordinates and intersite distances for participating radars were determined.

(6) Geoidal profiles and geodetic positions of Apollo tracking ships were determined from data acquired with ship-borne and land-based radars.

(7) A set of resonant geopotential coefficients was estimated from C-band radar data on GEOS–2.

(8) Geodetic positions for underwater, acoustic-transponder arrays were determined.

6.5.2 Description of Results

6.5.2.1 Achievable Range Accuracy

(H. R. Stanley NASA/WFC and D. J. Dempsey, RCA)

Generally speaking, the C-band radars are unmatched as geodetic instrumentation in terms of dependability, consistency, and precision. To evaluate their accuracy, the following comparisons were made:

(1) Radar parameters were varied during the tracking of GEOS–2. Residuals from short-arc reduction show effects on the range measurements of changing parameters such as pulsewidth, bandwidth, and prf. Some of these effects are shown in figure 6.3. The increased measurement noise in the 180- to 280-sec time interval is because of skin tracking of GEOS–2. The remainder of the data is from transponder tracking.

(2) Range residuals from collocated radars were compared to assess relative accuracies. Eight meters of the observed-range differences WFC AN/FPS–16 minus AN/FPQ–6 (shown in fig. 6.4) are attributable to the AN/FPS–16 use of a water tank for calibration, rather than a point source.

(3) Range residuals from collocated radars and lasers have been compared as an independent check (table 6.5). The average range difference in the WICE was only 0.5 meter (laser minus AN/FPQ–6).

(4) Unweighted WICE radar and laser range measurements were compared with

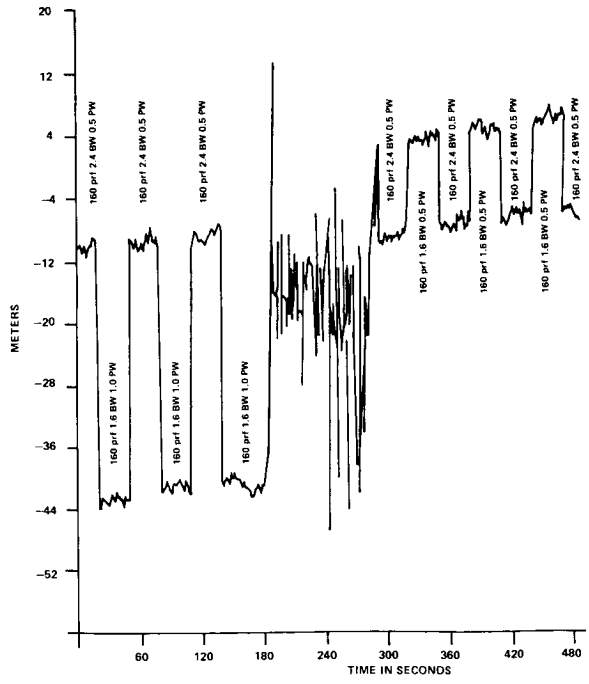

FIGURE 6.3.—Effects on range measurements of radar parameter variations.

ranges to an orbit determined from camera observations. The results are shown in tables 6.6a and 6.6b.

6.5.2.2 Spectral Analysis and Data Compaction

(Keith Guard, WRC)

The goals were to evaluate and analyze the spectral content of the data and to develop a data compaction scheme for supplying C-band data to the National Space Science Data Center (NSSDC). (See ch. 1.)

6.5.2.2.1 SPECTRAL ANALYSIS

Determination of spectral content, or power spectral-density estimation, is concerned with decomposition of the time domain signal into periodic components, as a function of frequency, and determination of the average power in each component. The term "power" used in this context refers to the mean squared amplitude of the component, in analogy to the mean squared amplitude of a sinusoidal voltage passed through a unit resistance.

The spectral density of the signal component of the data from range, azimuth, and elevation measurement when a satellite is being tracked is concentrated at frequencies lower than 0.05 Hz. A low-pass filter, with sharp cutoff at 0.05 Hz, will retain all signal content of the data and reject almost all noise content.

6.5.2.2.2 DATA COMPACTION

For much geodetic work, such as the estimation of potential coefficients or the determination of station positions, long arcs of data must be processed. At the sampling rate of 10 observations per second an excessive number of observations must be processed. The solution is not necessarily simply to discard data. A method based on selecting each N^{th} point and discarding $N-1$ of every N points will throw away information with the discarded points. In the frequency domain representation this method of data

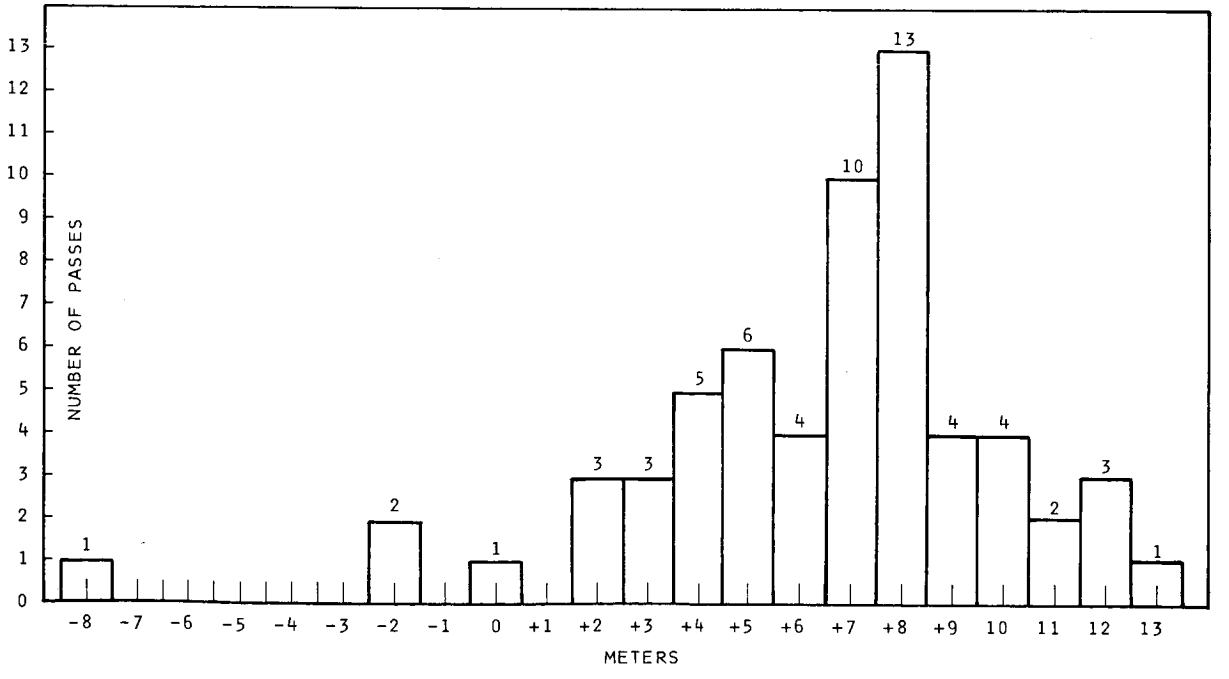

FIGURE 6.4.—Range differences, AN/FPS–16 minus AN/FPQ–6 (WICE collocation experiment).

compaction introduces aliasing or frequency foldover of the higher-frequency noise components into the lower-frequency signal components of the spectrum.

A data smoothing or filtering scheme must be used so that the frequency of observations, or sampling rate, is significantly reduced while most of the original information is retained. The design goal is to reduce to a minimum the amount of data necessary to maintain the statistical-information content of the noncompacted data. The filtering operation must decrease the bandwidth of the noise content of the data, so that the cutoff frequency f_c is reduced. Then the data selection interval can be chosen to avoid frequency foldover effects and to minimize serial correlation of the data.

Filtering before selection of data improves the rms of the residuals in a short-arc fit, over simply selecting raw data. In one typical test (data from WICE test 80) the rms of the residuals from the unfiltered range data was 0.762 meter and from the filtered range data 0.388 meter; noise with an rms value of 0.656 meter has thus been filtered out of the data.

Data filtered before selection produce essentially the same orbital elements as data selected without filtering, for both short-arc and long-arc orbital reduction. This result demonstrates that filtering does not change the statistical content of the data and that the accuracy of the data is unaffected by filtering.

6.5.2.2.3 TIMING TRUNCATION PROBLEM IN NSSDC FORMAT

In the course of this investigation, a time truncation problem with the NSSDC format was covered. After a digital filtering program was applied to C-band range data on the GEOS–2 satellite, an orbit was fitted to the data and residuals with respect to the orbit were computed. A plot of the residuals showed a number of discontinuities, or jumps.

Investigation revealed that the jumps resulted from a truncation of the timing data on the input to the orbital program. The times were given to four decimal places, in seconds, as specified in the NSSDC format. When the fourth digit changed, the computed range jumped. These orbital data were the first with sufficient precision to detect this jump of less than ½ meter in a range of over three million meters. A segment of the plotted residuals is shown in figure 6.5.

6.5.2.2.4 CONCLUSIONS

On the basis of the preceding results, it was concluded that the radar data that were to be stored for general scientific use be filtered with a low-pass filter, with cutoff frequency at 0.1 Hz, then sampled at one sample per 10 sec. The 0.1–Hz filter would reduce the random noise content essentially to zero and provide for negligible error contribution caused by frequency folding or aliasing when the data were sampled at one sample per 10 sec. The one sample per 10 sec is recommended as the smallest sampling that simultaneously provides negligible serial correlation for short-arc residuals and negligible effects of frequency folding for a 0.1-Hz cutoff filter.

Data that are to be used only for long-arc reductions can be compacted by simply select-

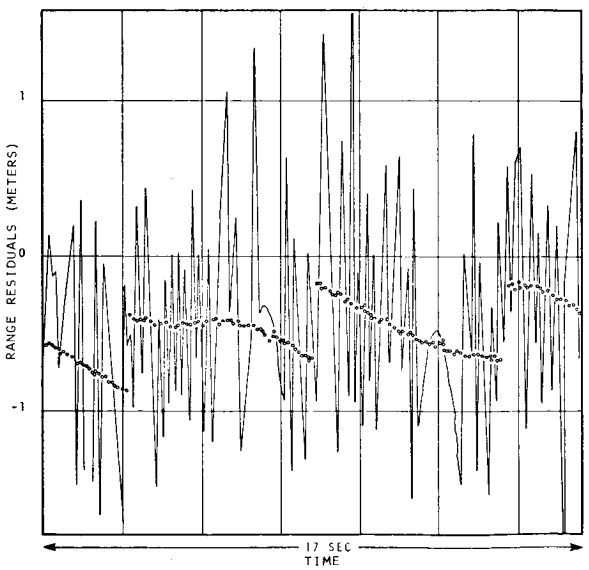

FIGURE 6.5.—Effect of truncation of timing data.

ing data at one point per 10 sec or one point per 20 sec. The slight increase in bias and low-frequency error, which can theoretically be expected to result from frequency folding, apparently does not appreciably affect the orbital reduction.

Data should not be sampled at greater than 20-sec intervals, pending further investigation, since the frequency folding of the low-frequency noise might appreciably affect the data.

6.5.2.3 Determination of Biases [4]

Data from several stations and throughout eight arcs were reduced to determine range biases, timing biases, and improved station coordinates on the SAO 1969 Standard Earth Datum. The biases and coordinates were estimated in an iterative solution, the range time tag, the bias should be subtracted algebraically from the time tag.

6.5.2.3.1 TIMING BIASES

The estimated timing biases are listed by station in table 6.7. To correct the recorded time tag, the bias should be subtracted algebraically from the time tag.

At the request of NASA/WFC, the Weapons Research Establishment personnel investigated and verified that a software error (one record skip at 40 pps) had caused a -0.025-sec time bias in the WOOMERA data. The software error has since been corrected.

The timing error at WFC did not result from timing at the radar but was caused by a freak occurrence of a -0.1000-sec error in the time generated by Wallops Station Central Timing. The cause of this error has been removed, and this timing bias is not expected to reoccur.

Unfortunately, the radar at Carnarvon, Australia (NCARNV), had a variable timing bias, in increments of 10 msec, during this period of concentrated tracking. As a result, the January-February 1969 NCARNV data were not usable. The cause of this error has also been corrected.

The remaining timing biases listed in table 6.7 are presumed to have their origin in the site timing hardware and are considered to be stable. There were no apparent timing biases at the two Bermuda radars or at Tananarive, Ascension, Antigua, or Merritt Island.

6.5.2.3.2 RANGE BIASES

The recovered range biases are listed by station in table 6.8. To correct the range observations from a particular station, the estimated bias should be algebraically subtracted from the observation. All the biases listed in table 6.8 may be explained on the basis of pulsewidth mismatch.

The GEOS–2 transponder transmitted pulsewidth was determined by NASA/WFC personnel to be 0.6 ± 0.3 μsec. The estimated range biases are valid only for C-band radar tracking of GEOS–2 or for other transponders that return a 0.6-μsec pulsewidth. However, unless the radar pulsewidths are changed, the same relative biases may be used for other transponder tracking.

6.5.2.3.3 ANGLE BIASES

In an effort to estimate angle biases, the azimuth and elevation measurements of the radars were compared with an orbit determined by range measurements from several stations and six arcs. The angle biases were determined on a pass-by-pass basis, and these values were in turn averaged. Those biases are listed in table 6.9.

There is no practical means of verifying the angle biases except to see them reoccur in independent orbital solutions. The Wallops C-band radar angle biases have been observed to be stable for 4 years.

[4] These investigations relied heavily on the help of Renzo Mitchell, RCA; J. T. McGoogan and W. F. Townsend, NASA/WFC; W. T. Wells, WRC; and S. K. Garoutte, AFWTR.

6.5.2.3.4 REMARKS ON CALIBRATION
(D. J. Dempsey, RCA)

It was of course anticipated that each radar could have time or measurement biases or that the station coordinates might be in error. In the course of this study, several other problem areas were encountered and resolved. The most significant of these were pulsewidth mismatch and refraction.

Since the radar can only be calibrated by using its own transmitter-output pulsewidth, a transponder-generated return pulse will introduce some pulsewidth-dependent range bias. The range bias B_ρ caused by the pulsewidth mismatch is approximately

$$B_\rho = 0.5\,(P_R - P_C)\ (150\ \text{m}/\mu\text{sec})$$

where P_R is the received pulsewidth from transponder in μsec and P_C is the radar nominal pulsewidth in μsec.

The effect of the pulsewidth mismatch was made particularly noticeable when it was observed that a 15-meter range discrepancy existed between Bermuda AN/FPS–16 and AN/FPQ–6 radars, the AN/FPQ–6 measuring longer. On request, Bermuda personnel measured the radar pulsewidths and found that their norminal 0.5-μsec pulsewidths actually were 0.38 μsec (AN/FPQ–6) and 0.55 μsec (AN/FPS–16).

Radar range measurments are made on a well-surveyed calibration target, both before and after each track to obtain zero-set corrections. The multistation reductions currently being performed have promoted the realization that significant range errors (in that indicated range measurements are short) will result if refraction effects are not taken into account during the calibration. This error is nominally as large as 13 meters for the Carnarvon AN/FPQ–6 radar, because their range calibration target is approximately 48 km distant. For other radars, this error is normally 1 to 2 meters.

6.5.2.3.5 WHITE SANDS MISSILE RANGE INVESTIGATIONS
(Arturo Borrego, WSMR)

White Sands Missile Range (WSMR) started tracking the GEOS satellite early in 1969 and obtained data intermittently through 1972. Some of the data were turned over to NASA and other missile ranges in support of their experiments, and some were utilized to measure instrumentation performance. The instruments used were the AN/FPS–16 radars.

The most significant finding uncovered through use of the GEOS–2 tracking data was a timing error in several WSMR radars. By processing the data through the NASA-developed ORAN program the error magnitude was identified as 50 msec.

WSMR was not able to fully utilize the calibration potential of the GEOS–2 C-band project. Participation in the C-band project was rather limited considering the number of C-band radars in use at WSMR. Nevertheless, some significant error sources were uncovered, and it is expected that the experience gained will allow WSMR to make more effective use of future calibration satellite programs.

6.5.2.3.6 PACIFIC MISSILE RANGE INVESTIGATIONS: SOURCES OF ACCURACY DEGRADATION
(John Belgin, PMR)

Some of the sources that were found to affect the accuracy of the radars tracking the GEOS–B satellite are as follows.

(1) Pulsewidth matching: Some of the radars have been directed to use a pulsewidth of 1 μsec. While the actual transponder reply is 0.6 μsec, there is a difference of 0.2 μsec between the two centroids when the same leading edge is referenced. The 0.2-μsec difference results in a range bias that represents $\simeq$ 30 meters of range error that must be added to the data to maintain calibration.

(2) Timing: A constant timing error of approximately 2 to 3 msec in the range machine in radar 003004 (Point Mugu) was still present when it was transferred to radar 003002 (also at Point Mugu) in December 1968. There was also a variable timing error because of the trigger being nonsynchronous with the 10-sample/sec read pulse. Although the Engineering Section was cognizant of the error, the values from the regression techniques gave a more exact value of the error magnitude.

(3) Angular bias: Radar 003002 has consistently exhibited a large bias in azimuth and elevation. It has been determined that a combination of survey, zero set, and rf collimation errors is the reason for the large bias.

(4) Transponder delay setup: After examination of the transponder delay inserted into each radar and conversations with the radar personnel, it was concluded that there were several different methods being used for transponder delay setup. It was also noted that not all the methods had a high degree of accuracy.

(5) Downrange timing/survey error: There is an indication that a timing error and/or survey error exists at the Johnston Island radar tracking sites. This is under investigation (1972).

(6) AN/FPQ–10 cyclic error: On all GEOS–B operations the AN/FPQ–10 radar data had a cyclic error in slant range. The error was a function of range rate and had a maximum magnitude of $\simeq$ 35 meters (peak to peak) at a slant range of $\simeq$ 6500 m/sec and was present in data from all AN/FPQ–10 radars. A significant portion of the error was because of the lack of the velocity circuit in the range register.

6.5.2.4 Determination of Tracking Station Coordinates

(R. L. Brooks, WRC, and C. D. Leitao, NASA/WFC)

With the assumption that the uncertainty in (ϕ, λ, h) of all stations except NWALI3 was 10 sec in latitude and longitude and 10 meters in geodetic height, the data were reduced by means of the theory given previously to estimate the geodetic coordinates.

The WFC AN/FPQ–6 radar, NWALI3, was chosen as the origin because there was greater familiarity with its data, there was confidence in its accuracy, it is located on the North American Datum (NAD), and it is easily transformed to the SAO 1969 Standard Earth Datum (Lundquist and Veis, 1966). The estimated station coordinates on the datum used for SAO 1969 Standard Earth Datum are given in table 6.10.

6.5.2.4.1 INTERSITE CHORD DISTANCES

Intersite chord distances have been computed using NAD coordinates, and the results have been compared with the recovered intersite chord distances on the Common World Datum. This comparison is shown in figure 6.6.

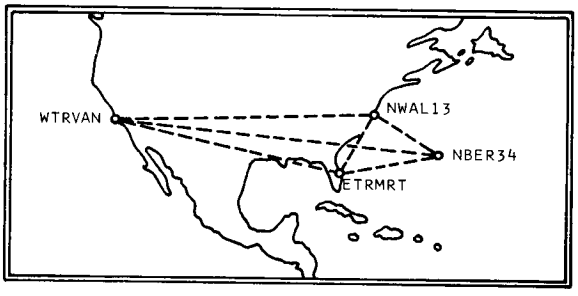

RADAR SITE	TYPE DATUM	WTRVAN	ETRMRT	NBER34
NWAL13	N.Am.	3 960 251	1 149 602	1 160 594
	C-Band	3 960 243	1 149 614	1 160 599
	C. C.	-	1 149 612	
NBER34	N.Am.	4 997 851	1 593 091	
	C-Band	4 997 854	1 593 106	
ERTMRT	N.Am.	3 770 614	CHORD DISTANCES IN METERS	
	C-Band	3 770 612		

FIGURE 6.6.—Comparison of intersite chord distances: North American datum versus C-band datum.

6.5.2.4.2 LATITUDE, LONGITUDE, AND HEIGHT

Jury (unpublished, 1972) has analyzed several sets of results from satellite geodesy to ascertain their agreement at Antigua, Bermuda, and Ascension in the Atlantic Ocean area. The C-band results compare favorably (agreement within 5 meters), with one exception; there was a 10-meter difference for Bermuda, which has one of the best-determined station positions.

Jury's results are affected not only by uncertainties or inconsistencies in the local surveys, but also by uncertainties in the parameters required to transform from the various datums to the common datum used for comparison. AFETR has adopted the transformed C-band position of Ascension as its standard for the AFETR Coordinate Manual.

Vincent *et al.* (unpublished, 1971) have determined the precision of several investigators' solutions for geoid height on a worldwide basis. These results are shown in table 6.11. It can be seen from this table that C-band results are consistent with current and past geoid determinations.

6.5.2.4.3 EASTERN TEST RANGE INVESTIGATIONS

(Milton Hillhouse, AFETR)

Eastern Test Range investigations with GEOS–2 C-band radar data have been primarily concerned with geodetic survey improvements and transponder array positioning in ocean areas. In this section the role played by C-band tracking radars in reducing survey uncertainties for the MISTRAM/MRS system is described. This special effort was undertaken because survey uncertainties at the MISTRAM/MRS sites at Grand Turk, Antigua, Bermuda, and Trinidad affected the MINUTEMAN–3 (MM–3) velocity accuracies after burnout. The flight interval of interest was between 300 and 900 sec. This circumstance led AFETR to place the MISTRAM/MRS vans at new locations. It had been shown that, if a survey improvement could be effected for these four X-band sites relative to the Florida mainland, a significant contribution would be made toward improving the MM–3 velocity accuracies.

Theoretical studies performed early in the calibration satellite effort had indicated that, even with a moderate amount of data, a significant improvement over existing uncertainties could be obtained. The limitation on studies of this type is that the physical situation assumed in the study may not completely describe the actual situation under which the data are collected relative to data availability, noise in the data, and the significant parameters in the solution. The last two limitations apply to the error propagation obtained from the actual reduction.

This study was the first attempt at AFETR to use C-band pulse radar data from satellites in short-arc solutions for survey improvement. The conclusions reached were:

(1) The method can properly determine any major inconsistencies.

(2) Weaknesses in the adjustment will be identifiable from internal comparisons.

(3) When the results were internally consistent, comparison with adjustments obtained by other means were, for the most part, consistent within the uncertainties quoted.

(4) The results were obtained relatively quickly, in comparison to results using ballistic cameras.

6.5.2.5 Geoidal Profile Above Puerto Rican Trench

(N. A. Roy, WRC, and H. R. Stanley, NASA/WFC)

The object of the experiment was to determine whether it would be possible to use shipborne radar tracking of a satellite to position a ship precisely enough to measure the depression (with respect to a fitted ellipsoid) of the sea surface believed to exist across the Puerto Rican Trench.

Heights of the USNS Vanguard, and thus the heights of the sea surface across the Puerto Rican Trench, were estimated from the orbital parameters of the GEOS–2 satel-

lite as determined by land-based and ship-borne C-band radars. The estimated ocean surface profile has been compared with a profile determined in 1966 by von Arx using different techniques. As will be shown, the results indicate that a depression (with respect to a fitted ellipsoid) of the sea surface exists over the trench, and that ship positions may be accurately determined in open ocean areas. A calibration area for satellite-borne altimeters has been provided also.

Extensive error analyses performed before the experiment showed that ground-based range tracking of the satellite from two stations, Antigua and Grand Turk, in addition to the ship, on two consecutive revolutions of the GEOS–2 satellite would be sufficient for ship height determination to within 2 to 3 meters. Precise height determination is more difficult than estimation of latitudes and longitudes with comparable accuracies.

The error analyses showed that the ship height estimation is sensitive to nearly all measurement, timing, and navigation biases that might occur. This result indicated that two consecutive revolutions of the satellite were necessary to lessen the effects of any biases and that a very precise navigation system would be needed if only range measurements from the ship were to be used.

During the period 25 June through 5 July 1970, tracking data were acquired by land-based radars and the radar aboard the Vanguard as the ship cruised in the test areas shown in figure 6.7. Test 9 was made dockside at San Juan.

The experiment plan was as follows: (1) use the land-based C-band radar to refine the position of Grand Turk relative to Antigua to obtain the best base line possible; (2) determine the GEOS–2 orbital parameters using the range data from Antigua and Grand Turk for each pair of consecutive revolutions; and (3) then, holding the determined GEOS–2 orbit fixed, use the ship's radar range data to determine the ship's latitude, longitude, and height (height above the spheroid) at the beginning of the first GEOS–2 pass.

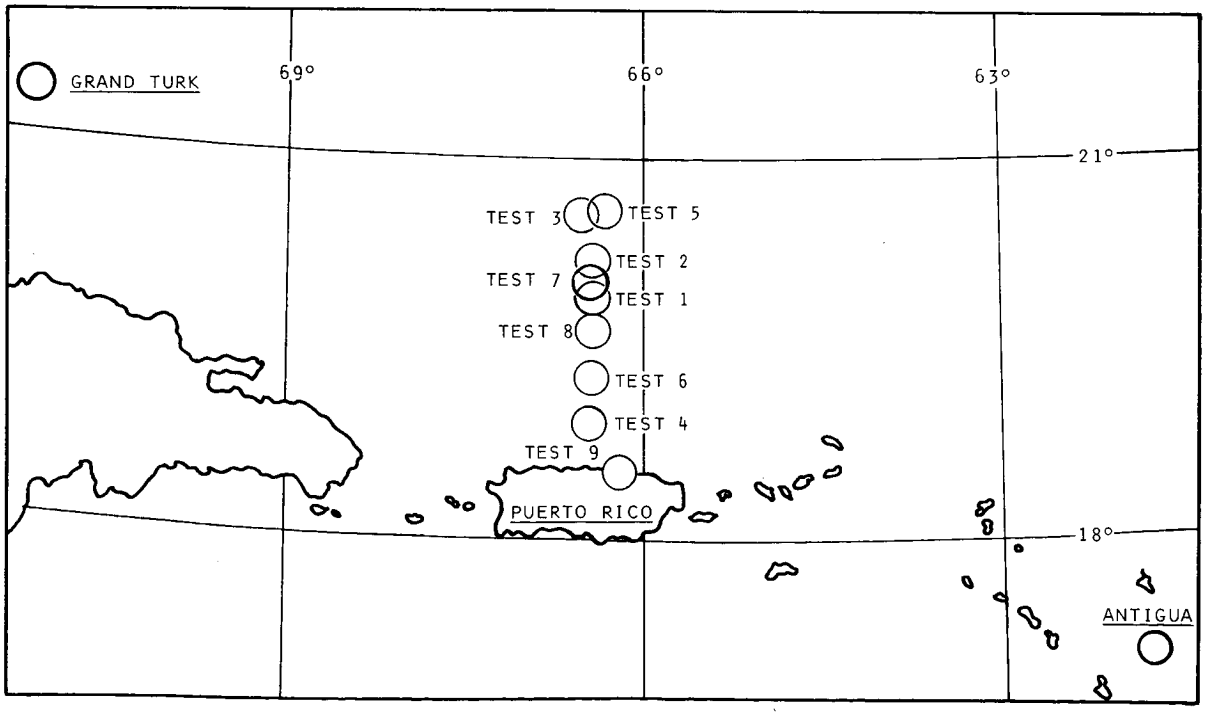

FIGURE 6.7.—Ship test location for ocean surface profiling experiment.

The results are compared with the results of von Arx (1966) in figure 6.8. The von Arx results were obtained from both gravimetric and astrogeodetic measurements during his experiment in 1966, and the results are shown by the solid and dashed lines. Since von Arx used a different reference spheroid, his results have been transformed to the SAO Standard Earth II Ellipsoid.

The results of this experiment conclusively show that it is possible and feasible to use shipborne radar tracking of satellites to position a ship precisely enough to measure geoidal profiles in areas of rather severe geoidal undulations, such as the Puerto Rican Trench.

6.5.2.6 Estimation of Resonance Coefficients

(C. F. Martin, WRC)

A set of 13th-order resonance coefficients for the SAO M–1 model was estimated by the use of only C-band radar data. These coefficients are listed in table 6.12. As another test of the coefficients, camera data from 5 days in the 28 April to 4 May 1968 period were reduced both with and without the use of the estimated coefficients. The solution with the coefficients had an rms of fit of 3.95 arc sec, compared with an rms of fit of 6.16 arc sec obtained when the coefficients were not used.

Although the model (SAO Standard Earth I, Gaposchkin, 1966 a, c) used to obtain these results has since been supplanted, the techniques used are still valid.

6.5.2.7 Positioning Transponder Arrays in the Bahamas and Off Puerto Rico

(G. Mourad and N. M. Fubara, Battelle Memorial Institution)

The use of shipboard C-band radar for positioning (locating) arrays of underwater acoustic transponders was investigated in two experiments, one in the Bahamas and the other over the Puerto Rico Trench.

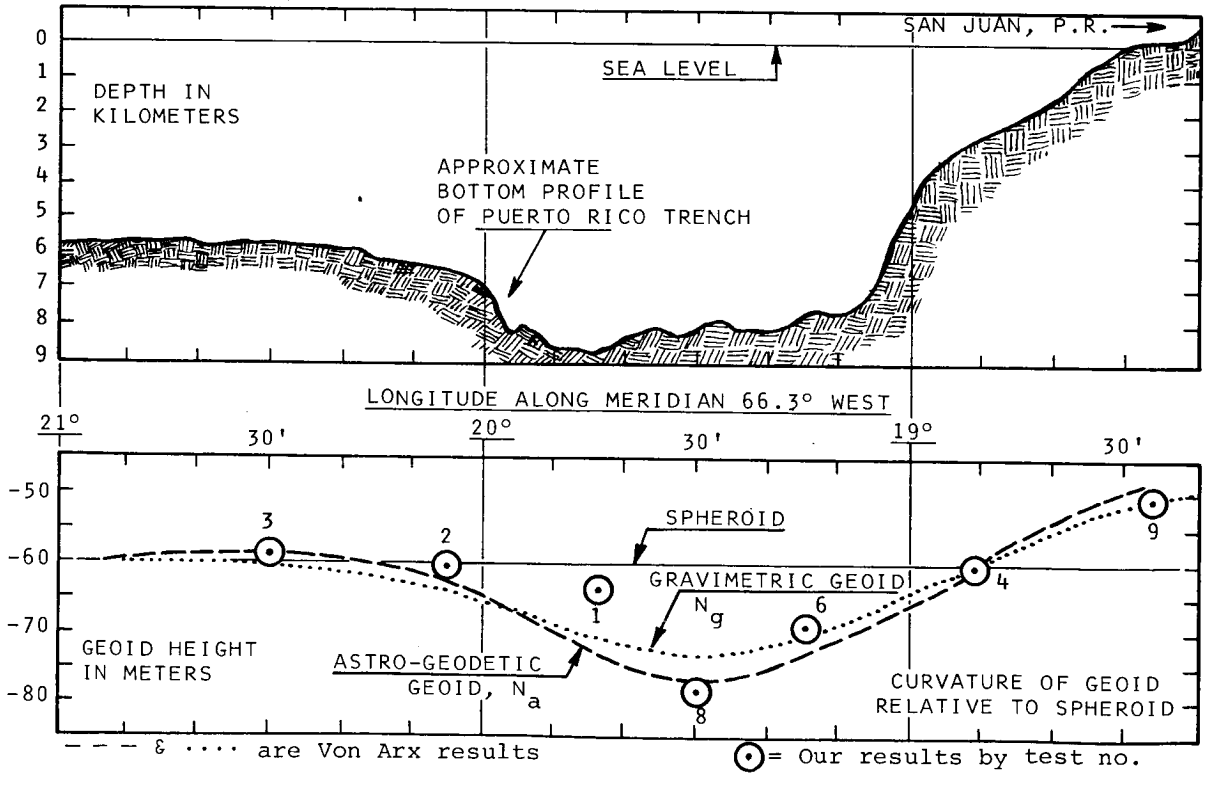

FIGURE 6.8.—Puerto Rican Trench profile along meridian 66°3 west.

The Bahamas experiment was conducted in September 1969 in an area where a transponder array was already implanted on the ocean bottom at a depth of about 5000 meters by the U.S. Navy. The location of the array, which consisted of four transponders forming a quadrangle of about 5 km on each side, is shown in figure 6.9.

The location of the Puerto Rico Trench experiment, which was conducted during July 1970, is shown in figure 6.10. A traverse about 200 km long consisting of eight stations across the Puerto Rico Trench was made and the profile measured. Four transponders were emplaced in about 5000 meters of water at the northern end of the traverse to provide the necessary geodetic control for the traverse.

The following accurately-timed simultaneous measurements were made: (1) acoustic measurement ranges between ship and transponders as the ship made various predetermined tracks over and around the array; (2) determination of the ship's position by the three land-based LORAC transmitters (Bahamas experiment only); (3) radar measurement of ranges between ship and GEOS–2 satellite during its passes; (4) measurement at the ship of the Doppler shift in the satellite signal; and (5) determination of the astronomic position using a special star-tracking device, INS.

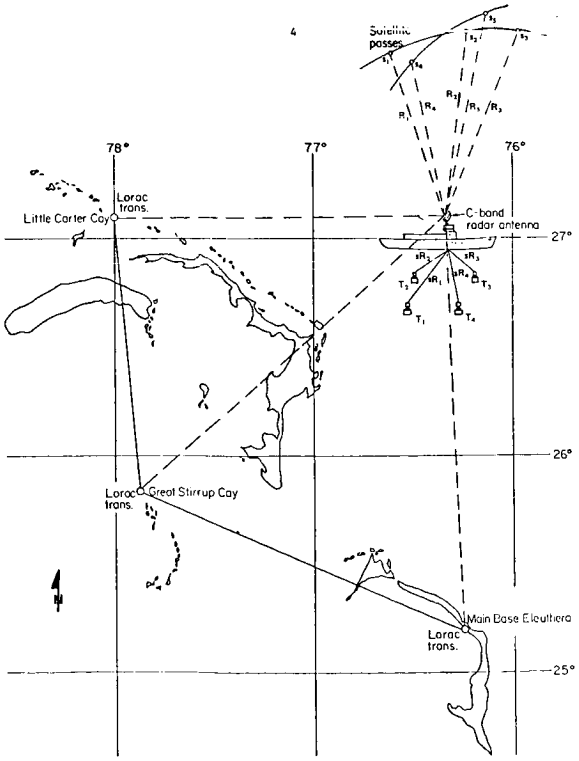

FIGURE 6.9.—The Bahamas experiment.

6.5.2.7.1 REVIEW OF DATA REDUCTION AND ANALYSIS

The determination of three-dimensional coordinates of geodetic control on the ocean bottom involves the solution of two problems: (1) accurate determination of geodetic positions of the survey ship, and (2) the simultaneous determination of the ship's position relative to the transponders by acoustic ranging. The solution of the first problem is the main purpose of the measurements from the C-band radar, Doppler receivers, and/or LORAC receivers as in steps (2), (3), and (4) of the preceding paragraph.

The most commonly used technique for locating transponders on the bottom from measurements on the surface is that of line crossing. However, this technique has serious accuracy limitations, requires stringent control of ship's heading and speed, and also requires accurately determined transponder depth. Details of this technique are described in Mourad (1970), Mourad *et al.* (1972), and Fubara (1971). To overcome these limitations and meet the objectives of the two experiments, several new high-precision techniques were developed. These techniques are described in detail by Fubara and Mourad (unpublished, 1972).

6.5.2.7.2 RESULTS OF THE BAHAMAS EXPERIMENT

In table 6.13 are given the adjusted geodetic coordinates of the transponders and their standard errors in geographic coordinates (based on the 1960 Fischer Ellipsoid $a=6\,378\,166$ and $1/f=298.3$) as determined by using the two available sound-velocity

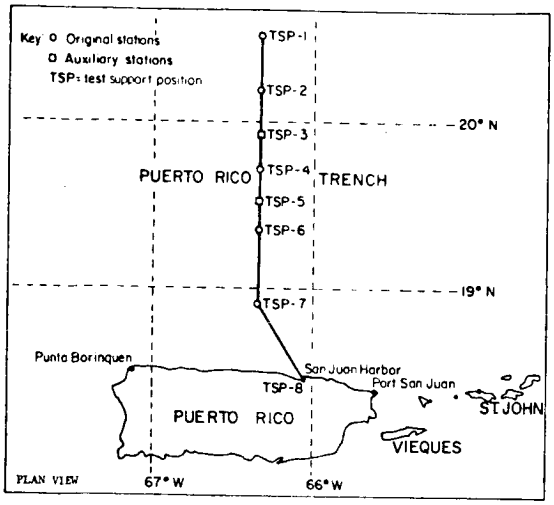

Ship Track Traverse Across the Puerto Rican Trench

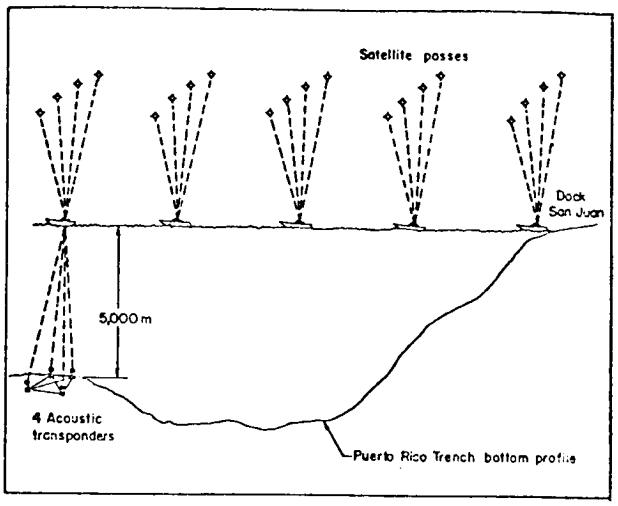

Cross Section

FIGURE 6.10.—The Puerto Rican Trench experiment.

profiles. The influence of variations in the velocity of sound on the coordinates was significant. However, the standard errors for each transponder did not vary greatly. This was expected, because the same set of "observed" ranges and weighting criteria were used, and sound velocity is only a scaling parameter. The data used to obtain these coordinates included approximately 1500 acoustic ranges from the ship to the three transponders. The ship positions used were derived from the LORAC positioning system. SINS data were used in the line crossing computations. Several corrections made to the raw data in an attempt to eliminate systematic errors included the corrections for effects of the ship's velocity on the acoustic data and for antenna offset from the bathymetric navigation system (BNS) transducer. As was expected, increase in the number of observations improved the precision of the adjusted coordinates of the transponders.

6.5.2.7.3 RESULTS OF THE PUERTO RICO TRENCH EXPERIMENT

The results are shown in tables 6.14 and 6.15. The maximum error was in side 2–4, which had only one pair of usable coplanar ranges instead of the ideal minimum of three pairs. Such precision indicators are consistent with the type of data involved in the computations; they are as expected from earlier simulation studies (Fubara and Mourad, unpublished, 1972). It should be noted that the lengths of sides are small relative to the average depth, whereas the theory showed that optimum results should be obtained when the ratio is between 2 and 2.5. The geographic coordinates and the ellipsoidal height of each transponder as deduced from the computations are shown in table 6.16.

6.5.2.8 Positioning Transponder Arrays in Open Ocean

(Milton Hillhouse, AFETR)

This study was directed toward the problem of determining the geodetic position of a transponder array in the open ocean. The transponder array is used for scoring the accuracy of impact of missiles; hence the location of the array must be known quite accurately. The approach used in the investigation was to have a ship locate itself by tracking a satellite whose orbit is accurately determined by land-based sensors. Then the ship may interrogate the transponders in the target array and thus locate the geodetic

position of the array. This discussion is confined to the methods and accuracy achieved in ship location only.

All data were obtained by tracking the transponder in the GEOS–B satellite. The orbit of GEOS–B was determined in every case from tracking data obtained by AFETR pulse radars. Three methods of determining ship motion were investigated: (1) direct solution for average ship velocity vector in least-squares solution; (2) use of SINS data for relative ship position; and (3) use of ocean-bottom-transponder interrogation data for relative ship position.

The land-based radar range data and the ship's radar range data were used to estimate the orbit and to locate the position of the ship simultaneously. Results for this limited series of tests indicated no significant improvement when radar range bias was also adjusted. The results also indicated that a one-revolution fit is about equal to a two-revolution fit. Because the ship moves during the test, it was not considered feasible to constrain the survey adjustment in the same manner as a fixed radar site is constrained.

The actual survey accuracy achieved and the number of separate satellite passes required depend to a large extent on the accuracy of the reference orbit, the accuracy of the ship's tracking data and ship's motion determination, and the geometry of the different passes used. Where unknown and unmodeled errors exist, it will be essential to obtain sufficient passes to examine the errors present for each test. It is always desirable to obtain satellite passes on each side of the ship for which the geodetic survey is desired.

6.6 CONCLUSIONS

(H. R. Stanley, NASA/WFC, and N. A. Roy, WRC)

The results show that the Wallops radars and the laser system are of comparable accuracy and that this accuracy is achievable by all similar types of radar. System reliability for the radars is nearly 99 percent, and stability of the systems is excellent over both the short and the long term. A radar calibration technique that allows for the remote calibration of radar sets on a global scale has been demonstrated.

The geodetic results obtained during the project were quite good but were certainly not indicative of ultimate performance capabilities. A good first effort is represented by 10- to 15-meter station positioning, since most other tracking networks did not yield such good results in their calibration stages. The analyses indicate that a well-designed experiment with good geographic distribution of radars can yield positions accurate to ± 5 meters relative to the center of mass.

The system performance throughout the experiment was exceptional. The radars performed according to specifications in every instance. None of the problems encountered (range biases, timing errors, etc.) are traceable to radar hardware malfunctions. The system reliability has also proved to be exceptionally high throughout the project.

APPENDIX

TABLE 6.1.—*Agencies Participating in GEOS–2 C-Band Tests*

Agency	Number of GEOS–2 tracks scheduled	Usable data (sec)
Eastern Test Range	265	155 876
SAMTEC	70	45 799
Manned Space Flight Center	844	465 756
Wallops Flight Center	648	452 713
Pacific Missile Range	107	36 853
White Sands Missile Range	5	830
Edwards Air Force Base	2	626
Flight Research Center	32	15 267
CNES	4	1 790
Weapons Research Establishment	36	11 168
Royal Aircraft Establishment	19	1 783
Totals	2 032	1 188 461 (330 hours)

TABLE 6.2.—*Radar Stations Involved in Calibration of AIVD/OR Geodetic Projects*

	Radar system and serial number	NGSP number	NGSP designation
White Sands Missile Range			
Talos Site	FPS–16 (XN–3)	4140	WSMTAL
"C" Station	FPS–16 (S/N–1)	4141	WSC112
Halloman (KING–1)	FPS–16 (S/N–4)	4142	WSH122
"C" Station	FPS–16 (S/N–6)	4143	WSC113
Halloman (KING–1)	FPS–16 (S/N–9)	4144	WSH123
Stallion	FPS–16 (S/N–12)	4145	WSS127
Phillips Hill	FPS–16 (S/N–16)	4146	WSP124
Stallion	FPS–16 (S/N–22)	4147	WSS128
Green River, Utah	FPS–16 (S/N–26)	4148	WSC218
"C" Station	FPS–16 (S/N–28)	4149	WSC114
Green River, Utah	FPS–16 (S/N–33)	4150	WSC219
Tularosa	FPS–16 (S/N–40)	4151	WST125
Blanding, Utah	MPS–25 (XN–1)	4152	WSBLU1
Blanding, Utah	MPS–25 (XN–2)	4153	WSBLU2
Eglin Gulf Test Range			
Site A–20	FPS–16 (S/N–17)	4340	EGLA21
Site A–20	FPS–16 (S/N–20)	4341	EGLA23
Site D–3	FPS–16 (S/N–23)	4342	EGLD31
Site D–3	FPS–16 (S/N–27)	4343	EGLD32
Site A–20	FPS–16 (S/N–31)	4344	EGLA22
Site D–4	FPS–16 (S/N–32)	4345	EGLD42
Site D–4	FPS–16 (S/N–39)	4346	EGLD41
Site A–20	FPS–16 (S/N–42)	4347	EGLA24
Instrumentation Ship			
Range Tracker (WIR)	FPS–16 (S/N–27)	4940	ISTA01
Watertown (WTR)	CAPRI (S/N–1)	4910	ISTA06
Huntsville (WTR)	CAPRI (S/N–2)	4911	ISTA07
Wheeling (PMR)	FPS–16 (S/N–46)	4941	ISTA08
Vanguard (WTR)	FPS–16 (V) (S/N–47)	4942	ISTA19
Redstone (WTR)	FPS–16 (V) (S/N–48)	4943	ISTA20
Mercury (WTR)	FPS–16 (V) (S/N–49)	4944	ISTA21
Twin Falls (ETR)	FPS–16 (S/N–25)	4945	ISTA11
Air Force Flight Test Center			
Edwards AFB	FPS–16 (S/N–38)	4540	EDAFB3
Edwards AFB	FPS–16 (S/N–41)	4541	EDAFB4
Edwards Catsite	MPS–9	4592	EDAFB2
Eastern Test Range			
GBI	FPS–16 (XN–2)	4040	ETRGB5
Cape Kennedy	FPS–16 (S/N–11)	4041	ETRCAK
Ascension Island	FPS–16 (S/N–14)	4042	ETRAS6
PAFB (storage)	FPS–16 (S/N–19)	4043	ETRPA1
PAFB (storage)	FPS–16 (S/N–43)	4044	ETRPA2
Pretoria So. Africa	MPS–25 (S/N–5)	4050	ETRPRE
Patrick AFB	FPQ–6 (S/N–1)	4060	ETRPAT
Antigua	FPQ–6 (S/N–2)	4061	ETRANT
Asunción	TPQ–18 (S/N–1)	4080	ETRAS8
Grand Turk	TPQ–18 (S/N–2)	4081	ETRGRT
Merritt Island	TPQ–18 (S/N–3)	4082	ETRMRT
GBI	TPQ–18 (S/N–4)	4083	ETRGB8

TABLE 6.2.—

	Radar system and serial number	NGSP number	NGSP designation
Western Test Range			
Vandenberg	TPQ–18 (S/N–5)	4280	WTRVAN
Pillar Point	FPS–16 (S/N–5)	4240	WTRPPS
Tranquillon	FPS–16 (S/N–18)	4241	WTRTB2
Tranquillon	FPS–16 (S/N–21)	4242	WTRTB1
Pillar Point	FPQ–6 (S/N–6)	4260	WTRPPQ
Pacific Missile Range			
Point Mugu	FPS–16 (S/N–2)	4440	PMRPM1
Point Mugu	FPS–16 (S/N–3)	4441	PMRPM2
San Nicolas	FPS–16 (S/N–7)	4442	PMRSN2
San Nicolas	FPS–16 (S/N–13)	4443	PMRSN3
San Nicolas	FPS–16 (S/N–15)	4444	PMRSN4
San Nicolas	FPQ–19 (S/N–1)	4400	PMRSN5
San Nicolas	FPQ–19 (S/N–4)	4401	PMRSN6
Point Mugu	FPS–16 (S/N–10)	4445	PMRPM3
Point Mugu	FPS–16 (S/N–24)	4446	PMRPM4
Barking Sands	MPS–25 (S/N–2)	4450	PMRBK1
Johnston Island	MPS–25 (S/N–3)	4451	PMRJI3
Johnston Island	MPS–25 (S/N–4)	4452	PMRJI4
Makaha Ridge	FPQ–10 (S/N–2)	4402	PMRMR1
Makaha Ridge	FPQ–10 (S/N–3)	4403	PMRMR2
Barking Sands	MPS–26	4420	PMRBK2
Point Mugu	MPS–26	4421	PMRPM5
Point Mugu	MPS–26	4422	PMRPM6
Naval Research Laboratories			
Chesapeake Bay Annex	FPS–16 (X/N–1)	4950	NRLCBA
Atomic Energy Commission			
Tonopah, Nevada	MPS–25 (S/N–1)	4951	AECTON
Elec. Environment Test Range			
Ft. Huachuca	FPS–16 (S/N–29)	4952	EETRFH
Rome Air Development Center			
Verona, N.Y.	FPQ–4 (S/N–1)	4970	RADCV1
Verona, N.Y.	FPQ–4 (S/N–2)	4971	RADCV2
Weapons Research Laboratories Australia			
Red Lake	FPS–16 (S/N–35)	4946	WOOR38
Mirikara	FPS–16 (S/N–36)	4947	WOOR39
Royal Aircraft Establishment U.K.			
Aberporth	FPS–16 (S/N–44)	4948	RAEAB4
Aberporth	FPS–16 (S/N–45)	4949	RAEAB5
NASA			
Canary Island	MPS–26	4720	NCANIS
Bermuda	FPS–16 (S/N–34)	4740	NBER34
Wallops Flight Center	FPS–16 (S/N–8)	4840	NWALI8
Bermuda	FPQ–6 (S/N–5)	4760	NBERO5
Wallops Flight Center	FPQ–6 (S/N–3)	4860	NWALI3
Carnarvon	FPQ–6 (S/N–4)	4761	NCARNV
Tananarive	CAPRI	4741	NTANAN
Ely, Nevada	MPS–19	4690	NELYNV
Kauai, Hawaii	FPS–16 (S/N–30)	4742	WTRKAU
Ely, Nevada	CAPRI	4610	NELHAR
CNES, France			
French Guiana		4953	KOUROU

TABLE 6.3.—*Participating Radars*

Site	NGSP number	Radar type	Number of GEOS–2 passes	Average range rms (m)
Wallops Flight Center	4860	AN/FPQ–6	51	1.2
Wallops Flight Center	4840	AN/FPS–16	32	1.4
Bermuda	4760	AN/FPQ–6	45	1.4
Bermuda	4740	AN/FPS–16	44	1.4
Kauai, Hawaii	4742	AN/FPS–16	23	2.1
Tananarive	4741	CAPRI	9	1.6
Ascension Island	4080	AN/FPQ–18	8	1.8
Carnarvon	4761	AN/FPQ–6	27	1.3
Antigua	4061	AN/FPQ–6	37	1.4
Merritt Island	4082	AN/TPQ–18	26	1.4
Vandenberg AFB	4280	AN/TPQ–18	8	1.4
Canary Island	4720	MPS–26	28	5.1
Ely, Nevada	4610	HAIR (CAPRI)	4	3.1
Woomera	4946	AN/FPS–16	10	2.4
Pretoria	4050	MPS–25	9	1.7
Makaha Ridge	4402	FPQ–10	14	5.3

TABLE 6.4.—*Identification and Magnitude of Sources of Systematic Range Errors for the Wallops Flight Center AN/FPQ–6 Radar*

Range error source	Skin track corrections (m)	Beacon no. 1 corrections (m)	Beacon no. 2 corrections (m)
Local oscillator mode select	0	0	0
Range target size (fsr assumed)	0	0	0
Propagation error (fsr assumed)	+0.9	+0.9	+0.9
PRF select	0	0	0
Beacon track mismatch (cal. in 0.5 μsec, 2.4 MHz; and track in 2.4 MHz)	0	[a]−6.2	[a]−5.0
Beacon pulsewidth-dependent error (interrogate with 0.5 μsec)	0	0	0
Computed GEOS–2 transponder delay error	0	−2.7	+1.2
Total track correction	+0.9	−8.0	−2.9

[a] These values are a function of the radar's actual pulsewidth.

TABLE 6.5.—*Differences Between Ranges Measured by AN/FPQ-6 and by Laser System (WICE)*

Date YYMMDD	Range difference (m)	Date YYMMDD	Range difference (m)
68403	0	680426	+3
680405	−1	680503	0
680410	+2	680507	+1
680412	−5	680508	−2
680413	−1	680521	0
680418	+4	680522	0
680420	+2	680523	+4
680426	+2	680614	−2

TABLE 6.6*a*.—*Range Measurements: Solution from Camera Data*

Site	Measurement type	Number of observations[a]	RMS (arc sec)
Tananarive, Malagasy	Declination	20	2.9
	Right ascension	21	2.8
Johannesburg, South Africa	Declination	23	5.9
	Right ascension	22	5.0
Santiago, Chile	Declination	25	1.6
	Right ascension	19	6.6
Columbia, Missouri	Declination	28	3.4
	Right ascension	26	8.4
Mojave, California	Declination	68	4.6
	Right ascension	63	4.9
Fort Meyers, Florida	Declination	63	5.3
	Right ascension	55	4.7
Rosman, North Carolina	Declination	53	1.4
	Right ascension	53	3.9
Edinburg, Texas	Declination	14	5.1
	Right ascension	9	8.4
	All measurements	562	4.7

[a] Arc of 5½ days, 28 April to 4 May 1968.

TABLE 6.6*b*.—*Range Measurements: Mean Residuals (Unweighted)*

Site	Measurement type	Number of observations[a]	Mean (m)
Wallops AN/FPQ-6 radar	Range	776	1.6
NASA/GSFC laser	Range	248	0.6

[a] Range measurements were throughout 5½ -day period.

TABLE 6.7.—*Estimated Timing Biases*

Radar site		Estimated timing bias (sec)	Verified
Woomera	AN/FPS-16	−0.0249	Yes
Vandenberg AFB	AN/TPQ-18	+0.0243	Yes
Makaha Ridge	FPQ-10	−0.0087	
Canary Island	MPS-26	+0.0065	
Ely, Nevada	HAIR	+0.0126	Partial
Pretoria	MPS-25	+0.0046	
Kauai	AN/FPS-16	+00.58	
WFC	AN/FPQ-6	−0.1000	Yes
WFC	AN/FPS-16	−0.1000	Yes
Carnarvon	AN/FPQ-6	−0.010, −0.020, −0.030	Yes

TABLE 6.8.—*Estimated Range Biases*

Site	Radar	Estimated range bias (m)	Pulsewidth (PW) mismatch
Canary Island	MPS-26	+9.7	
WFC	AN/FPQ-6	0	measured 0.60 μsec
Antigua	AN/FPQ-6	−22.6	nominal 1.0 μsec
WFC	AN/FPS-16	0	measured 0.60 μsec
Ely, Nevada	HAIR	−6.5	
Ascension	AN/TPQ-18	−30.0	nominal 1.0 μsec
Merritt Island	AN/TPQ-18	−21.0	nominal 1.0 μsec
Makaha Ridge	FPQ-10	−50.3	nominal 1.0 μsec
Vandenberg AFB	AN/TPQ-18	+20.1	
Bermuda	AN/FPQ-6	+14.9	measured 0.38 μsec
Tananarive	CAPRI	+13.8	
Bermuda	AN/FPS-16	0	measured 0.60 μsec
Woomera	AN/FPS-16	−29.6	
Pretoria	MPS-25	3.8	
Kauai	AN/FPS-16	−27.9	nominal 1.0 μsec

TABLE 6.9.—*Angle Biases From Multistation Long-Arc Solutions*

Site	Radar	Azimuth bias (arc sec)	Elevation bias (arc sec)
WFC	AN/FPQ-6	29.8	43.2
WFC	AN/FPS-16	−17.5	−11.5
Bermuda	AN/FPQ-6	49.2	68.5
Bermuda	AN/FPS-16	3.4	10.1
Antigua	AN/FPQ-6	15.3	18.1
Merritt Island	AN/TPQ-18	17.9	−11.4
Canary Island	MPS-26	129.9	457.7
Woomera	AN/FPS-16	10.4	−50.9
Kauai	AN/FPS-16	−8.8	−42.5
Makaha Ridge	FPQ-10	66.0	−100.0
Tananarive	CAPRI	−10.9	−123.6
Ascension	AN/TPQ-18	31.9	45.1
Pretoria	MPS-25	96.6	−3.8
Ely, Nevada	HAIR	11.0	−20.0
Vandenberg AFB	AN/TPQ-18	−34.9	82.0

TABLE 6.10.—*Estimated Station Positions*

Station	Number	Latitude	Longitude E	Geodetic height (m)
ETRPRE	4050	−25°56′38″.7	28°21′28″.3	1584.7
ETRANT	4061	17°08′36″.8	298°12′26″.0	−18.6
ETRAS8	4080	−7°58′21″.2	345°35′54″.6	120.9
ETRMRT	4082	28°25′28″.9	279°20′07″.2	−35.0
WTRVAN	4280	34°39′57″.4	239°25′06″.7	83.9
PMRMR1	4402	22°08′02″.6	200°16′18″.3	477.6
NELHAR	4610	39°18′30″.2	244°54′47″.1	2761.8
NCANIS	4720	27°45′46″.6	344°21′58″.1	186.2
NBER34	4740	32°20′52″.9	295°20′46″.8	−41.4
NTANAN	4741	−19°00′07″.0	47°18′52″.6	1328.8
WTRKAU	4742	22°07′23″.4	200°20′03″.1	1157.7
NBERO5	4760	32°20′52″.4	295°20′47″.0	−39.7
NCARNV[a]	4761	−24°53′47″.4	113°43′01″.7	39.3
NWALI8	4840	37°50′28″.9	284°30′53″.1	−54.4
NWALI3	4860	37°51′37″.0	284°29′25″.9	−51.8
WOOR38	4946	−30°49′06″.9	136°50′17″.8	98.4

[a] This position was obtained from the October 1969 data analyses; results are not yet completed.

TABLE 6.11.—*Precision of Geoidal Height for Each Investigator*

Investigator	Number of stations	Absolute averages (m)
Marsh, Douglas, and Klosko	46	10
Mueller (orbital)	22	12
Mueller (geometric)	22	9
SAO	42	14
Hadgigeorge	25	5
Berbert	11	6
C-band	12	9
Mancini	14	18
ACIC	11	8
NWL	42	9

TABLE 6.12.—*Residuals Before and After Estimation*[a] of C_{14}^{13}, S_{14}^{13}

Station	Number of weighted measurements	RSS before adjustments (m)	RSS after adjustment (m)
WFC	144	58.7	14.8
Carnarvon	84	44.2	26.5
Tananarive	46	72.2	14.8
Kauai	65	86.4	49.4
Total	339	64.2	27.8

[a] Estimated values of 13th-order resonance coefficients: $C_{14}^{13} = 1.176 \times 10^{-21}$; $S_{14}^{13} = 6.549 \times 10^{-21}$.

TABLE 6.13.—*Transponder Coordinates Using Different Sound Velocity Profiles*[a]

Transponder number	Navy sound velocity profile[b]	Standard error[c]	Average sound velocity profile[d]	Standard error[c]
2 ϕ	27°08′14″.75	0″.24	27°08′14″.43	0″.24
λ	−76°23′14″.60	0″.19	−76°23′13″.93	0″.10
[e] h	−5018.0 m	3.38 m	−4998.3 m	3.38 m
3 ϕ	27°08′22″.05	0″.23	27°08′21″.21	0″.24
λ	−76°20′03″.73	0″.19	−76°20′04″.13	0″.21
[e] h	−5016.6 m	2.76 m	−4998.7 m	2.89 m
4 ϕ	27°05′44″.92	0″.19	27°05′45″.45	0″.19
λ	−76°21′35″.51	0″.20	−76°21′35″.44	0″.20
[e] h	−5016.6 m	1″.99 m	−4995.2 m	2.98 m

[a] 1960 Fischer Ellipsoid, a = 6 378 166 mi; $1/f$ = 298.3.
[b] Compass Island curve.
[c] Precision estimates relative to LORAC network coordinates.
[d] Mean curve.
[e] A geoidal height of −60 m (i.e., geoid is 60 m below the ellipsoid) was assumed.

TABLE 6.14.—*Horizontal Distances Between Transponders*

Side	Length (m)	Standard errors (m)
1–2	7172.2	± 6.8
2–3	5697.1	±14.8
3–4	6435.9	± 5.3
4–1	6418.1	± 7.6
1–3	9135.3	± 9.6
2–4	9364.1	±15.5

TABLE 6.15.—*Computed Depths of Transponders*

Transponder	Mode of computation and precision			
	FIXCOR		LESSA	
	Depth (m)	Standard error (m)	Depth (m)	Standard error (m)
1	5663.8	±3.7	5668.7	±28.6
2	5683.0	±4.6	5691.3	±24.3
3	5630.0	±4.2	5638.4	±19.2
4	5682.5	±5.3	5709.3	±18.3

TABLE 6.16.—*Geographic Coordinates of Transponders*

Transponder	Latitude (N) standard error[a]	Longitude (W) standard error[a]	Geodetic height standard error[a] (m)
1	20°29′53″.84	66°14′51″.34	−5720.7
	±1″.10	±1″.18	±20.2
2	20°27′39″.36	66°18′31″.37	−5743.3
	±0″.90	±0″.76	±16.0
3	20°30′15″.50	66°20′36″.28	−5690.4
	±0″.87	±0″.25	±10.5
4	20°32′33″.47	66°17′46″.64	−5761.3
	±0″.62	±1″.32	±12.7

[a] Precision estimate relative to SINS coordinates.

☆ U. S. GOVERNMENT PRINTING OFFICE : 1977 O - 588-174 (PART 1)